به نام خدا

مرکز دانلود رایگان
مهندسی متالورژی و مواد

---

www.Iran-mavad.com

COMPREHENSIVE MATERIALS PROCESSING

EDITOR-IN-CHIEF

Saleem Hashmi

Dublin City University, Dublin, Ireland

ASSOCIATE EDITORS-IN-CHIEF

Gilmar Ferreira Batalha

University of São Paulo, São Paulo, Brazil

Chester J. Van Tyne

Colorado School of Mines, Golden, CO, USA

Bekir Yilbas

King Fahd University of Petroleum and Minerals, Dhahran, Saudi Arabia

VOLUME 12

THERMAL ENGINEERING OF STEEL ALLOY SYSTEMS

VOLUME EDITOR

George Krauss

Colorado School of Mines, Golden, CO, USA

ELSEVIER

AMSTERDAM • BOSTON • HEIDELBERG • LONDON • NEW YORK • OXFORD
PARIS • SAN DIEGO • SAN FRANCISCO • SINGAPORE • SYDNEY • TOKYO

Elsevier
Radarweg 29, PO Box 211, 1000 AE Amsterdam, Netherlands
The Boulevard, Langford Lane, Kidlington, Oxford OX5 1GB, UK
225 Wyman Street, Waltham, MA 02451, USA

British Library Cataloguing in Publication Data
A catalogue record for this book is available from the British Library

Library of Congress Cataloging-in-Publication Data
A catalog record for this book is available from the Library of Congress

ISBN: 978-0-08-096532-1

Printed and bound in Italy
14 15 16 17 18 19 10 9 8 7 6 5 4 3 2 1

Project Manager: Gemma Tomalin
Associate Project Manager: Joanne Williams

EDITOR-IN-CHIEF

Saleem Hashmi graduated from East Pakistan University of Engineering and Technology in 1967, and in 1972 he completed his master's and PhD degrees from the University of Manchester. He was appointed as a postdoctoral fellow with UMIST, Manchester, in January 1973, and in October 1973, he joined Sheffield Hallam University as a lecturer. In 1976, he was promoted to senior lecturer, then to principal lecturer in 1977, and to reader in 1984.

In January 1987, Professor Hashmi founded the School of Mechanical & Manufacturing Engineering at Dublin City University. While in the process of establishing this school, he attracted substantial external research funding to set up the Material Processing Research Centre (MPRC), a research center of excellence in the field of material processing. To this day, he continues his affiliation with Dublin City University as an emeritus professor in the school he founded 27 years ago.

In 1990, Professor Hashmi established Advances in Materials and Processing Technologies (AMPT), a much needed international conference in materials processing. He continues to be the Chairperson of the Steering Committee for this series of conferences. In 1998, he was appointed as editor-in-chief of Elsevier *Journal of Material Processing Technology* and continued in this role until 2008.

In 1995, Professor Hashmi was awarded the higher doctorate degree of DSc, by the University of Manchester, the highest academic degree any university in the United Kingdom can award.

Professor Hashmi has supervised or co-supervised 110 PhD and 55 MEng research students to successful completion. Over the years, he has also acted as an external examiner and expert assessor for PhD candidates and engineering departments with universities in Ireland, the United Kingdom, India, Pakistan, Bangladesh, Hong Kong, Canada, Australia, and Malaysia. He is a Chartered Engineer (CEng), a Fellow of the Institution of Mechanical Engineers, UK (FIMechE) and also a Fellow of the Institution of Engineers of Ireland (FIEI). He has published over 430 papers and 12 books and is still publishing.

This page intentionally left blank

EDITORIAL BOARD

Chester J. Van Tyne is the FIERF (Forging Industry Education and Research Foundation) professor at Colorado School of Mines (CSM) in Golden, Colorado. He received his undergraduate and graduate degrees from Lehigh University and worked for Bethlehem Steel as a research engineer for a short period before joining Lafayette College in the Metallurgical Engineering Department as a professor in 1980. In 1988, he joined the Metallurgical and Materials Engineering Department at CSM. He is actively engaged in the research operations of the Advanced Steel Processing and Products Research Center at CSM. His research interests are in metal deformation processes especially forging, sheet stamping, and friction during metalworking operations.

Gilmar F. Batalha graduated as a mechanical engineer from the University of Brasilia in 1982. He completed his MSc in Mechanical Engineering at the Federal University of Santa Catarina (1987), his PhD in Mechanical Engineering (1995) and habilitation/livre-docencia in manufacturing processes (2010) at the Department of Mechatronics and Mechanical Systems, Polytechnic School of Engineering, University of Sao Paulo, where he has been a tenured professor since 1989. He has had postdoctoral research experience at the Friedrich Alexander University Erlangen–Nuremberg, Germany (1997–98). He was a visiting professor at Ecole Centrale de Lille, France (2004–06), and at the Faculty of Mechanical Engineering of the Silesian University of Technology, Gliwice, Poland (2012–13). He served as an adjunct professor at the Faculty of Engineering, UDESC, Joinville, Brazil (1984–89). He has been an advisor on several PhD theses and master's dissertations, coordinator of the Laboratory of Manufacturing Engineering of the EPUSP, and is responsible for several international and national cooperation agreements for exchange of students and researchers as well as for consultancy with the industry. He is the volume editor for the *Materials Modeling and Characterization* volume in Elsevier's *Comprehensive Materials Processing series*.

Sergio T. Button received his PhD in Mechanical Engineering from School of Mechanical Engineering, University of Campinas, Brazil, in 1990. He is currently full professor of Manufacturing Processes at the University of Campinas. His main research fields include metal forming and numerical simulation. Currently, his research is focused on cross wedge rolling and hot stamping. He is the coauthor of 2 books and more than 100 papers in international journals and conferences. He is the editor and reviewer of many international journals, and participates in the organization of three national and international scientific conferences.

David Cameron is currently scientific advisor to Miktech Oy, Finland, and adjunct professor in Dublin City University, Ireland. From 2003 to 2013, he was professor of Material Technology in Lappeenranta University of Technology, Finland, where he established the Advanced Surface Technology Research Laboratory (ASTRaL). He obtained his doctorate from the University of Glasgow in 1980 and has spent his research career working on thin-film technology. He was a senior research fellow at the Royal Signals and Radar Establishment in the United Kingdom until 1982 when he joined the School of Electronic Engineering at Dublin City University, becoming associate professor. His research focus is on atomic layer deposition and its industrialization.

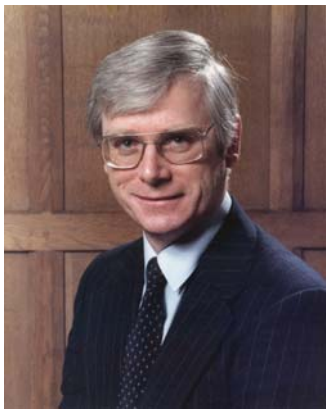

Joseph A. McGeough is an honorary professorial fellow in the School of Engineering at the University of Edinburgh. He is a graduate from the universities of Glasgow (BSc and PhD) and Aberdeen (DSc). He held research appointments at the universities of Leicester, Queensland, and Strathclyde. As a student he gained numerous county, university, and national championship athletic awards. His industrial training began as an undergraduate vacation apprentice for a firm of electrical contractors based at ICI ltd Nobel Division, and he subsequently undertook postgraduate experience at International Research and Development, Newcastle upon Tyne, before returning to university service. He was successively a lecturer, senior lecturer, and reader in Engineering at Aberdeen University, and then moved to Edinburgh University to take up its Regius Chair of Engineering. His research work has dealt mainly with manufacturing processes for which he has been awarded Institution of Mechanical Engineers and the Society for Underwater Technology prizes. He has been the recipient of a Royal Society/SERC (Science and Engineering (now Engineering and Physical Sciences) Research Council) Industrial Fellowship in order to transfer the results of his research to industry. His publications include *Principles of Electrochemical Machining*, *Advanced Methods of Machining*, and *Micromachining of Engineering Materials* (editor). His latest book is *The Engineering of Human Joint Replacements* (2013), which contains details of the materials and manufacturing processes used in this field. He is a fellow of the Institution of Mechanical Engineers, International Academy for Production Engineering, Royal Society of Edinburgh, and Royal Academy of Engineering.

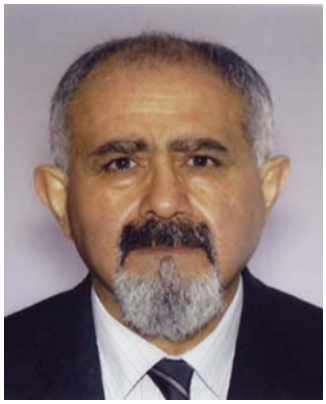

Emin Bayraktar is a full university professor and research director at Supmeca/Paris, School of Mechanical and Manufacturing Engineering, Paris, France. He was awarded a PhD degree in Mechanical Engineering by IST/OSU and a second PhD degree in Materials Science and Engineering in Paris. Subsequently, Professor Bayraktar was awarded a higher doctorate degree of habilitation (DSc) in Mechanics of Materials in recognition of his research contributions at Paris 6, University Marie-Curie. His teaching and research expertise lies on the processing and manufacturing of the composite materials and damage analysis. Recently he has been appointed as an adjunct professor in UNICAMP-Campinas, Brazil, on the new design of composites for the application in aeronautical engineering. He is on the editorial board of a number of scientific journals. He is also a member of the Steering Committee for the International Conference Series on Advances in Materials and Processing Technologies (AMPT).

Bekir S. Yilbas received his PhD degree in Mechanical Engineering from Birmingham University. He was awarded the Doctor of Engineering degree in 2005 by Birmingham University due to his significant contribution to his field of study. He has published 375 journal papers in reputable international journals and presented over 60 papers at international conferences. He has served as an editorial board member of international journals, including *International Journal of Machine Tool and Manufacture Design, Research and Application, International Journal of Subsurface Sensing Technologies and Applications, Journal of Materials Processing Technology, Journal of Achievements in Materials and Manufacturing Engineering, International Journal of Nanomanufacturing, and Archives of Materials Science and Engineering*. He has received numerous awards in recognition of his research work.

Nabil Bassim was born and raised in Cairo, Egypt. Dr. Bassim received a BSc in Chemical Engineering from Cairo University in 1965. He went to the University of Virginia, United States, where he received his MSc in Chemical Engineering (Nuclear Engineering option), and a PhD in Materials Science in 1973. He moved to Canada where he is now professor of Materials Science and Engineering at the University of Manitoba. He served for years as associate dean of research at the Faculty of Engineering and was director of International Programs for the faculty. His areas of research interest include mechanisms and mechanics of plastic deformation, dislocation theory, fracture and fatigue, and nondestructive evaluations. He has patents on the use of acoustic emission for monitoring of structures. He also has an interest in studying the behavior of materials at high strain rates and large strains as they affect processes such as metal forming and machining. He has published over 120 papers and supervised numerous MSc and PhD theses.

Syed H. Masood is professor of Mechanical and Manufacturing Engineering at Swinburne University of Technology in Melbourne, Australia, where he is also the program coordinator of the master's program in advanced manufacturing technology. He obtained his PhD from the University of Queensland, Australia; MEng from the University of New Brunswick, Canada; PG Dip from IIT Delhi; and BSc Eng Hons from Aligarh Muslim University, India. Professor Masood has worked previously at Central Queensland University, Rockhampton, and PNG University of Technology, Papua New Guinea. He has published over 275 technical articles in international journals, books, and conferences in different areas of advanced manufacturing. His current research interests include additive manufacturing technologies, especially fused deposition modeling and direct metal deposition, plastics manufacturing processes, material development, and material characterization.

Mustafizur Rahman is currently a professor at the Department of Mechanical Engineering at National University of Singapore (NUS), and has been with NUS since 1982. He obtained his BSc in Engineering from Bangladesh University of Engineering and Technology (BUET), MEng and PhD from Tokyo Institute of Technology, Japan. His research interests include micro-/nanomachining, design and development of miniature machine tools and devices for micro-/nanomachining, and high-speed machining of difficult-to-machine materials. He has received Outstanding Achievement Awards from the Singapore Institute of Engineers and the Japan Society of Mechanical Engineers in 2003 and 2005, respectively.

George Krauss is currently university emeritus professor at the Colorado School of Mines and a metallurgical consultant specializing in steel microstructural systems. Dr. Krauss received the BSc in Metallurgical Engineering from Lehigh University in 1955 and the MSc and ScD degrees in Metallurgy from the Massachusetts Institute of Technology in 1958 and 1961, respectively, after working at the Superior Tube Company as a development engineer in 1956. In 1962–63, he was an NSF postdoctoral fellow at the Max Planck Institut für Eisenforschung in Düsseldorf, Germany. He served at Lehigh University as assistant professor, associate professor, and professor of Metallurgy and Materials Science from 1963 to 1975, and in 1975 joined the faculty of the Colorado School of Mines as the AMAX Foundation professor in Physical Metallurgy. He was the John Henry Moore professor of Metallurgical and Materials Engineering at the time of his retirement from the Colorado School of Mines in 1997.

In 1984, Dr. Krauss was a principal in the establishment of the Advanced Steel Processing and Products Research Center, an NSF Industry-University cooperative research center at the Colorado School of Mines, and served as its first director until 1993. He has authored the book *Steels: Processing, Structure, and Performance*, (ASM International, 2005), coauthored the book *Tool Steels*, fifth edition, (ASM International, 1998), and edited or coedited conference volumes on tempering of steel, carburizing, zinc-based coatings on steel, and microalloyed forging steels. He has published over 330 papers and lectured widely in technical conferences, universities, corporations, and ASM International chapters, presenting a number of keynote, invited, and honorary lectures. He presented the Edward DeMille Campbell Memorial Lecture of ASM International in 2000, the Howe Memorial Lecture of ISS in 2003, and the Adolf Martens Memorial Steel Lecture of AIST in 2010.

Dr. Krauss has served as the president of the International Federation of Heat Treatment and Surface Engineering (IFHTSE), 1989–91, and as President of ASM International, 1996–97. He is a fellow of ASM International, TMS, and IFHTSE. He has been awarded the Adolf Martens Medal of the German Society for Heat Treatment and Materials, the Charles S. Barrett Silver Medal of the Rocky Mountain Chapter of ASM, the George Brown Gold Medal of the Colorado School of Mines, and several other professional and teaching awards, including the ASM Albert Easton White Distinguished Teacher Award in 1999. He is an honorary member of the Iron and Steel Institute of Japan, a distinguished member of the Iron and Steel Society, an honorary member of ASM International, and an honorary member of the Japan Institute of Metals.

CONTRIBUTORS TO VOLUME 12

L. Albano
Universidade de São Paulo, São Carlos, São Paulo, Brazil

M.A. Aronov
IQ Technologies Inc., Akron, OH, USA

J. Bodin
Swerea IVF, Mölndal, Sweden

L.C.F. Canale
Universidade de São Paulo, São Carlos, São Paulo, Brazil

K.D. Clarke
Los Alamos National Laboratory, Los Alamos, NM, USA

A. Dalke
Institute of Materials Engineering, Freiberg, Germany

T. Ericsson
Linköping University, Linköping, Sweden

K.O. Findley
Colorado School of Mines, Golden, CO, USA

J. Grosch
Technische Universität Berlin, Berlin, Germany

F. Hoffmann
IWT Stiftung Institut für Werkstofftechnik, Bremen, Germany

T. Inoue
Saitama Institute of Technology, Fukaya, Japan

N.I. Kobasko
IQ Technologies Inc., Akron, OH, USA

G. Krauss
Colorado School of Mines, Golden, CO, USA

H. Kristoffersen
Swerea IVF, Mölndal, Sweden

B. Liščić
University of Zagreb, Zagreb, Croatia

D. Loveless
Inductoheat Inc., Rochester, MI, USA

T. Lübben
IWT Stiftung Institut für Werkstofftechnik, Bremen, Germany

L. Meekisho
Portland State University, Portland, OR, USA

A.B. Nissan
Colorado School of Mines, Golden, CO, USA

V.I. Rudnev
Inductoheat Inc., Madison Heights, MI, USA

S. Segerberg
Heattec Värmebehandling, Halmstad, Sweden

S. Singer
University of Zagreb, Zagreb, Croatia

M.A.J. Somers
Technical University of Denmark, Kgs. Lyngby, Denmark

H.-J. Spies
Institute of Materials Engineering, Freiberg, Germany

G.E. Totten
Portland State University, Portland, OR, USA

E. Troell
Swerea IVF, Mölndal, Sweden

J. Vatavuk
Universidade Presbiteriana Mackenzie, São Paulo, Brazil

H.-W. Zoch
IWT Stiftung Institut für Werkstofftechnik, Bremen, Germany

This page intentionally left blank

CONTENTS OF VOLUME 12

Editor-in-Chief v

Editorial Board vii

Contributors to Volume 12 xi

Preface xv

12.01 Introduction to Thermal Engineering of Steel Alloy Systems 1
G Krauss

12.02 Introduction to Steel Heat Treatment 3
L C F Canale, J Vatavuk and *G E Totten*

12.03 Hardenability of Steel 39
L C F Canale, L Albano, G E Totten and *L Meekisho*

12.04 Controlling the Cooling Process — Measurement, Analysis, and Quality Assurance 99
E Troell, H Kristoffersen, J Bodin and *S Segerberg*

12.05 Calculation of the Heat Transfer Coefficient Based on Experiments by the Liscic Probes 123
B Liščić and *S Singer*

12.06 Metallo-Thermo-Mechanical Coupling in Quenching 177
T Inoue

12.07 Intensive Quenching 253
N I Kobasko and *M A Aronov*

12.08 Residual Stresses Produced by Quenching of Martensitic Steels 271
T Ericsson

12.09 Distortion Engineering: Basics and Application to Practical Examples of Bearing Races 299
T Lübben, F Hoffmann and *H-W Zoch*

12.10 Austenite Formation and Microstructural Control in Low-Alloy Steels 345
K D Clarke

12.11 Quench and Tempered Martensitic Steels: Microstructures and Performance 363
G Krauss

12.12 Microstructure and Properties of Gas Carburized Steels 379
J Grosch

12.13 Development of Compound Layer and Diffusion Zone during Nitriding and Nitrocarburizing of Iron and Steels 413
M A J Somers

12.14 Case Structure and Properties of Nitrided Steels 439
H-J Spies and *A Dalke*

12.15 Induction Hardening: Technology, Process Design, and Computer Modeling 489
V I Rudnev and *D Loveless*

12.16 Microstructures and Mechanical Performance of Induction-Hardened Medium-Carbon Steels 581
A B Nissan and *K O Findley*

PREFACE

In recent years considerable advances have taken place in materials and their processing technologies, the pace of which is progressing at an accelerated rate. It is therefore vitally important that researchers, academics, design engineers, and manufacturing technologists be up to date with these new developments. Such developments open up excellent opportunities to improve effective utilization of material resources, improve efficiency, reliability, durability, and cost effectiveness of the products. This comprehensive series will serve researchers all over the world in keeping them fully abreast of such new developments.

Comprehensive Materials Processing is a one-stop resource consolidating and enhancing the literature of the materials processing and manufacturing universe. The work addresses recent progress in materials technologies and science as well as covering recent developments in specific manufacturing processes involved with materials for applications in engineering, biomedical, environmental protection, health and safety, and sensor materials and technologies. The authoritative analysis of these processes will assist scientists and engineers in the selection, design, and usage of materials, whether required in the lab or in action across industry.

As the editor-in-chief of this comprehensive series, a truly collaborative work, I am greatly indebted to the volume editors, internationally renowned experts in their fields, for guiding and selecting the topics for their respective volumes, commissioning authors, and reviewing the content so meticulously. Their true dedication to the scientific community is reflected in the time and energy they have given to this project. My sincere thanks are also due to all of the authors—researchers and materials practitioners who have contributed extensive coverage of literature review as well as recent works of research to this huge project. Their insight and specialist knowledge in their respective fields is reflected in the high quality of this work.

Myself, the three associate editors-in-chief, and all of the volume editors are greatly appreciative of all the hard work undertaken to turn this idea into a publishable work. Our special thanks go to Gemma Tomalin, the project manager, along with Joanne Williams, and the rest of the team at Elsevier who served successively to keep the project on track through friendly nudges in order to ensure timely completion. We are also hugely grateful to Mohamed Imrankhan for his dutiful coordination of the proofs.

The extensive academic discussion of core theories and applications, supplemented by applied case studies and advanced multimedia features has drawn together numerous areas of research and I sincerely hope that this work will prove to be of great help to both the young and experienced members of the international research community, academics, and industrial practitioners for many years to come.

Saleem Hashmi
Editor-in-Chief

This page intentionally left blank

12.01 Introduction to Thermal Engineering of Steel Alloy Systems

G Krauss, Colorado School of Mines, Golden, CO, USA

Acknowledgments 2

This volume is part of the multivolume work titled **Comprehensive Materials Processing**, designed to characterize the processing of materials from initial manufacture to finished products with specific sets of properties for given applications. Hardenable steels, in particular low-alloy carbon steels, are especially suited for this objective in view of the dramatic changes produced in microstructure and properties by final heat treatment. Steels are produced by solidification of liquid steel with controlled chemistry, and many processing steps, including hot rolling and intermediate heat treatments, lead to the final processing that is the subject of this volume. Steels are widely used for structural applications of all sorts, and there are many combinations of steel chemistry and final heat treatment parameters that produce high strength material for vast numbers of demanding applications. Steel chemistry and processing produce microstructures with many components and properties, making a given finished steel part truly an alloy structural system.

Final heat treatment processing of low alloy steels consists of three stages: **austenitizing, quenching, and tempering**. The great versatility of steels is a result of the fact that the high-temperature crystal structure of steels, termed austenite, must transform to other crystal structures on cooling. Austenite and its formation are described in Chapter 12.10, and the various microstructures that depend on cooling rates are characterized in the early Chapter 12.02. For strengthening the desired crystal structure formed on cooling is martensite, the component that produces the hardest microstructure that can be formed in any steel. The toughness or fracture resistance of martensite formed directly on cooling is low, and therefore steels hardened by martensite are heated in a **tempering** heat treatment step to increase fracture resistance as described in Chapter 12.11.

Martensite forms only if the time-dependent formation of softer microstructures can be avoided on cooling. Generally this aspect is accomplished by rapid cooling, typically called **quenching**, and carbon and alloy contents determine the appropriate cooling rates necessary to form martensite in a given steel. The latter aspects of martensite formation are the subject of characterization termed **hardenability** as described in Chapter 12.03.

Quenching or cooling is a complex process requiring understanding the coupling of cooling media and internal changes in sections of steel that develop during cooling to understand its effects on steel structure and properties. Heat transfer analysis and the measurement of cooling rates during the stages of quenching with various media are described in Chapters 12.04 and 12.05. The surfaces of steel parts cool more rapidly than part interiors, resulting in gradients in temperature, microstructures, and stresses as the austenite transforms and cooling proceeds. Critical to this process is the fact that volume expansion occurs when austenite with its atomic close-packed crystal structure transforms to phases stable at lower temperatures, including martensite, during quenching. Databases and the mathematical modeling of the interrelated time-, temperature-, mechanical-dependent factors during quenching are presented in the Chapter 12.06. The effects of very rapid cooling are described in Chapter 12.07.

A major consequence of the various gradients operative during quenching is the development of residual stresses superimposed on the hardened microstructures produced during the quench. The measurement and development of residual stresses in through-hardened steels and steels surface hardened by induction and laser heating are described in Chapter 12.08. Not only are residual stresses produced during quenching, but distortion, i.e., part dimensional and shape changes, may also be a severe consequence of the mechanical gradients produced during quenching. A detailed analysis of distortion is given in Chapter 12.09.

There are two approaches to producing hardened microstructures in low-alloy carbon steels: through hardening and surface hardening. Parts that are through-hardened depend on steels that are selected to have sufficient hardenability for producing martensitic microstructures throughout most of the part cross section. The Chapter 12.11 describes the roles that steel carbon content and tempering play in strengthening and potential embrittlement of through-hardened steels.

There are many hardening techniques that are designed to strengthen only the surface of steel parts. Three examples, carburizing, nitriding, and induction hardening, are described in detail in this volume. Not only is surface strength increased relative to part interiors, but also beneficial residual surface stresses are produced by surface hardening techniques.

Carburizing and nitriding are examples of processes that produce changes in surface chemistry, i.e., thermochemical processes. Carburizing is described in Chapter 12.12. The nitriding process and the complex surface changes produced by nitriding and nitrocarburizing are described in detail in Chapter 12.13 and the effects of microstructures produced by nitriding on mechanical performance are described in Chapter 12.14. Induction hardening is a thermal surface modification technique: only the surface is heated and quenched to martensite while the core structure remains unheated. The technology and modeling of the very short time, high-temperature surface heating during induction hardening are described in detail in Chapter 12.15, and the interactions of case and core microstructures and the effects on fatigue of induction hardened steels are described in Chapter 12.16.

The chapters noted present comprehensive reviews and state-of-the art descriptions of the various facets of thermal engineering of hardenable steels. All have been written by experts that have long and detailed knowledge in their areas of expertise.

There are areas of subject overlap between some of the chapters, but that overlap only adds to the understanding of some of the complex phenomena that occur in the quenching and tempering of steels. There are chapters devoted to the processing, its control, and its effects, and there are chapters devoted to finished microstructures and properties. This coverage is of vital importance to the mechanical, materials, and manufacturing engineers that must specify and select steels and heat treatments for the demanding structural applications for which quench and tempered steels are well suited.

Acknowledgments

The editor expresses his sincere thanks and appreciation to all of the chapter authors for the time and effort devoted to sharing their expertise and the preparation of their valuable contributions to this volume.

12.02 Introduction to Steel Heat Treatment

LCF Canale, Universidade de São Paulo, São Carlos, São Paulo, Brazil
J Vatavuk, Universidade Presbiteriana Mackenzie, São Paulo, Brazil
GE Totten, Portland State University, Portland, OR, USA

12.02.1	**Introduction**	3
12.02.2	**Steel Classification**	3
12.02.3	**Fe–C Diagram**	8
12.02.3.1	Effect of Alloying Elements on Eutectoid Concentration and the Eutectoid Temperature	9
12.02.4	**Steel Transformation**	10
12.02.4.1	Principles	10
12.02.4.2	Microstructures of Steels	11
12.02.4.2.1	Ferrite and Pearlite	11
12.02.4.2.2	Bainite	16
12.02.4.2.3	Martensite	18
12.02.5	**Time-Temperature-Tranformation Diagrams**	22
12.02.5.1	Isothermal Transformation Diagrams	22
12.02.5.2	Continuous Cooling Transformation Diagrams	23
12.02.6	**Hardenability**	24
12.02.6.1	Grossmann Hardenability	26
12.02.6.2	Jominy Curves	27
12.02.7	**Tempering**	28
12.02.7.1	Tempering Reactions	34
References		36

12.02.1 Introduction

Despite of a great number of available materials, steels have been used in many applications because of the facility to get them and also to the different properties obtained by the heat treating process, including low costs, taking in account a worldwide raw material and steel production about 6.10^9 t per year.

Steels are Fe–C alloys (maximum C content is about 2%) that can contain other alloying elements, according the application. Even low variations in those composition may lead to great differences in mechanical properties, since the final structure may change according to manufacturing processing route as well as heat treatment cycles applied.

The desired shape of a component may be made by casting, welding, forging, rolling, and powder metallurgy. Invariably a steel component is subjected to a finishing heat treatment at some temperature below its melting point and cooled to provide desired changes in structure in order to produce required structure and properties.

Indeed there is, for all the materials, a closed relationship between the internal structure, processing, and final properties as shown in **Figure 1**. This is particularly important in the case of steels (*1*). Any change in one of these three aspects may cause changes in either or both of the others.

For steel phase transformations, products that take place are related to the cooling rate from austenitization temperature. Extremely slow to fast prompts yield strength variation from 200 MPa (microstructure of ferrite and carbide) to 2500 MPa (martensitic microstructure). A survey on these correlations has been published (*2*) and the balance of this chapter describes these relationships and their causes.

12.02.2 Steel Classification

Steels may be classified according to their application. In this case names such as spring steel and bearing steel are related to a specific composition to meet the requirements for such application.

However, steels are commonly classified as in the following (*3*):

- **Plain carbon steels** – These steels are solid solutions of iron and small amounts of manganese, phosphorous, sulfur, and silicon. These steels may be further classified as **low-carbon or mild steels**, which contain <0.25% carbon; **medium-carbon steels**, which contain 0.25–0.60% carbon; **high-carbon steels**, which contain 0.60–1.0% carbon and **ultrahigh carbon steels**, which contain up to 1.25–2.0% carbon.

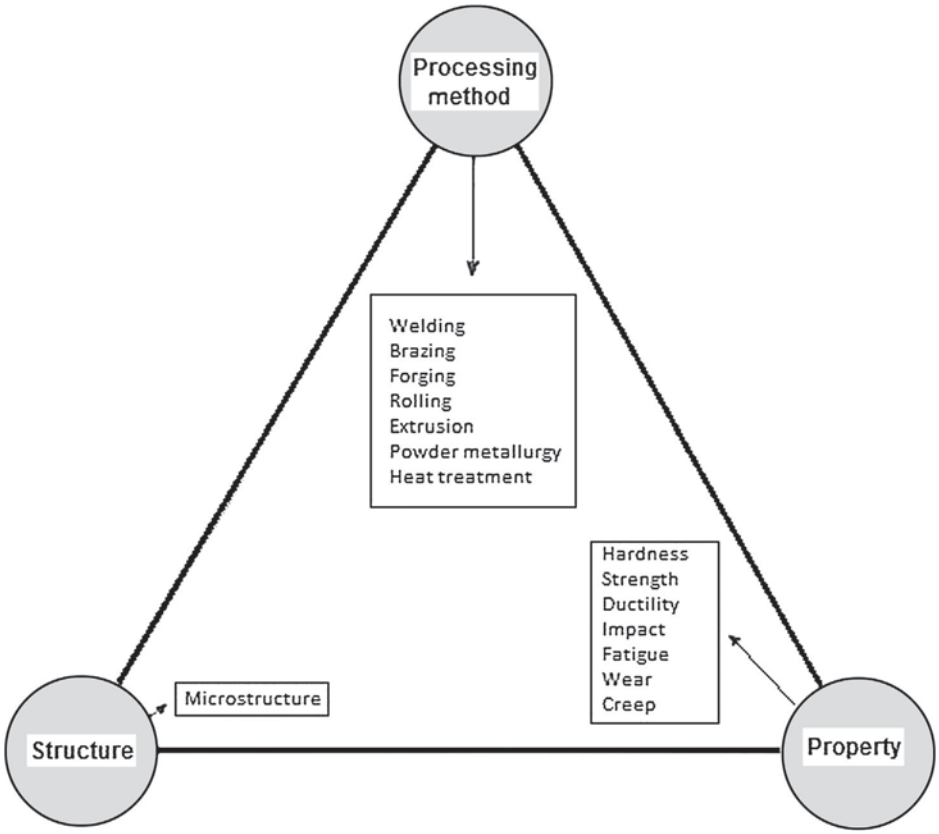

Figure 1 Relationship between structure, properties, and processing methods. Adapted from Askeland, D. R. *The Science and Engineering of Materials*, 4th ed.; PWS Publishing Company: Boston, 1989.

- **Low-alloy steels.** Typical alloying elements for these steels include nickel, chromium, molybdenum, manganese, and silicon. Low-alloy steels may be further classified by carbon content as noted for plain carbon steels. Low-carbon alloy steels are typically used with ferrite-pearlite microstructures and are relatively ductile. Medium-carbon alloy steels have carbon contents to 0.5% and are quenched to martensite and tempered to provide high strength.
- **High-strength, low-alloy steels.** These steels are microalloyed with very low amounts of niobium, vanadium, and/or titanium and may be finish processed by low-temperature hot-rolling (controlled rolling) to produce very fine ferrite grains (*4*,*5*).
- **Stainless steels.** These high-alloy steels contain a minimum of 12% chromium to provide corrosion resistance and are divided into several different types.
  Ferritic stainless steels. Alloyed only with chromium. Interstitial contents of carbon and nitrogen are low to provide toughness. Sometimes carbide-forming elements such as niobium or titanium are added to form carbides to further reduce carbon in solution.
  Austenitic stainless steels. In addition to chromium, nickel is added to stabilize austenite to room temperature. Again, carbon content is kept low to prevent intergranular corrosion associated with chromium-carbide formation on austenite grain boundaries.
  Martensitic stainless steels. Grades with various amounts of chromium and carbon are quenched and tempered to provide high hardness and strength.
  Duplex stainless steels. Chromium, nickel, and molybdenum are balanced to provide microstructures of ferrite and austenite.
  Precipitation hardened stainless steels. Better toughness than obtained with martensitic stainless steels and higher strengths than in the other types of stainless steels are provided by precipitation of intermetallic compounds of nickel and aluminum.
- **Tool steels.** These steels are used to form or machine other steels and materials, and have high contents of carbon and carbide-forming alloying elements such as chromium, molybdenum, tungsten, vanadium, titanium, and niobium. Tempering at high temperatures may be used for secondary hardening by fine carbide precipitation. The steels may be produced by conventional steel making or by powder metallurgy, which reduces alloy element segregation (*6*–*8*).

There are many standards that classify the different types of steel. Many nations have their own classification system for steels and cast irons. The most commonly used classifications are DIN system (Germany), the American Iron and Steel Institute (AISI), and Society of Automotive Engineers (SAE) system. Many countries adopted similar classification as AISI/SAE classification, including the Brazilian Technical Standards Association (ABNT). The American Society for Testing and Materials (ASTM) uses another system, which is not based on composition but on the steel product and application; for example, railroad rails, boiler tubes, plate, and bolts. The American Society of Mechanical Engineers (ASME) devised a similar system, but it is generally limited to boiler and heat

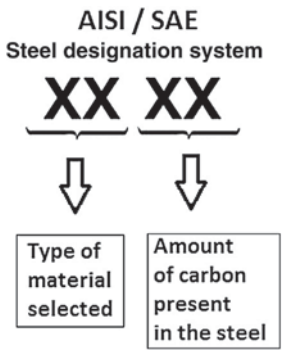

Figure 2 System for designation of steel.

exchanger steels and other materials that are covered by the boiler code specifications (ASME, n.d.). Figure 2 shows the system used for the AISI/SAE classification.

In this system, the third and fourth digits refer to carbon content in hundredths of weight percent. The following steels are classified in the four-digit system according to alloy content as follows.

- *Carbon Steels:*
  - The first digit is '1' as in 10xx, 11xx, and 12xx.
  - The second digit describes processing: '1' is resulfurized and '2' is resulfurized and rephosphorized.
- *Manganese Steel:*
  - The first digit is '1' as in 13xx and is, indeed, a carbon steel. However, since manganese is a normal by-product of carbon steel making, the AISI/SAE has decided not to classify it as an alloy steel.
  - The second digit is always '3.'
- *Nickel Steel:*
  - The first digit is '2' as in 23xx and 25xx.
  - The second digit designates the percentage of nickel in the steel.
- *Nickel–Chromium Steel:*
  - The first digit is '3' as in 31xx, 32xx, and 33xx.
  - The second digit designates the percentage of nickel and chromium in the steel.
- *Molybdenum Steels:*
  - The first digit is '4' as in 40xx and 44xx.
  - The second digit designates the percentage of molybdenum in the steel.
- *Chromium Steel:*
  - The first digit is '5' as in 51xx and 52xx.
  - The second digit designates the percentage of chromium in the steel.
- *Chromium–Vanadium Steel:*
  - The first digit is '6' as in 61xx.
  - The second digit designates the percentage of chromium and vanadium in the steel.
- *Tungsten–Chromium Steel:*
  - The first digit is '7' as in 72xx.
  - The second digit designates the percentage of tungsten and chromium.
- *Silicon–Manganese Steel:*
  - The first digit is '9' as in 92xx.
  - The second digit designates the percentage of silicon and manganese in the steel.
- *Triple Alloy Steels:*
  - These steels contain three alloys.
  - The first digit can be '4,' '8,' or '9' depending on the predominate alloy.
  - The second digit designates the percentage of the remaining two alloys.

Table 1 shows these steels (*9*).

Alloying elements are added with specific purposes. Each element exhibits a specific influence on the final requirements for a specific application. The most common alloying elements are as follows (*5,10*).

Aluminum (Al): Improves nitriding treatment response, grain refining, removes O in the steel melting. Typical ranges: <2%.

Sulfur and Phosphorus (S and P): Add machinability, reduce weldability, promote hot shortness (sulfur) and cold shortness (phosphorus), reducing ductility and toughness. These elements among others promote the martensite temper embrittlement phenomena. Nowadays typical ranges: <0.04%.

Table 1 Steel designations according to AISI/SAE

AISI/SAE designation number	*Type and description*
Carbon steels	
10xx	Plain carbon (Mn. 1.00% max.)
11xx	Resulfurized
12xx	Resulfurized and rephosphorized
15xx	Plain carbon (max. Mn. range 1.00–1.65%)
Manganese steels	
13xx	Mn 1.75
Nickel steels	
23xx	Ni 3.50
25xx	Ni 5.00
Nickel–chromium steels	
31xx	Ni 1.25; Cr 0.65, 0.80
32xx	Ni 1.75; Cr 1.07
33xx	Ni 3.50; Cr 1.50, 1.57
34xx	Ni 3.00; Cr 0.77
Molybdenum steels	
40xx	Mo 0.20, 0.25
44xx	Mo 0.40, 0.52
Chromium–molybdenum steels	
41xx	Cr 0.50, 0.80, 0.95; Mo 0.12, 0.20, 0.25, 0.30
Nickel–chromium–molybdenum steels	
43xx	Ni 1.82; Cr 0.50, 0.80; Mo 0.25
43BVxx	Ni 1.82; Cr 0.50; Mo 0.12, 0.25; V 0.03 min
47xx	Ni 1.05; Cr 0.45; Mo 0.20, 0.35
81xx	Ni 0.30; Cr 0.40; Mo 0.12
86xx	Ni 0.55; Cr 0.50; Mo 0.20
87xx	Ni 0.55; Cr 0.50; Mo 0.25
88xx	Ni 0.55; Cr 0.50; Mo 0.35
93xx	Ni 3.25; Cr 1.20; Mo 0.12
94xx	Ni 0.45; Cr 0.40; Mo 0.12
97xx	Ni 1.00; Cr 0.20; Mo 0.20
98xx	Ni 1.00; Cr 0.80; Mo 0.25
Nickel–molybdenum steels	
46xx	Ni 0.85, 1.82; Mo 0.20, 0.25
48xx	Ni 3.50; Mo 0.25
Chromium steels	
50xx	Cr 0.27, 0.40, 0.50, 0.65
51xx	Cr 0.80, 0.87, 0.92, 0.95, 1.00, 1.05
50xxx	Cr 0.50; C 1.00 min
51xxx	Cr 1.02; C 1.00 min
52xxx	Cr 1.45; C 1.00 min
Chromium–vanadium steels	
61xx	Cr 0.60, 0.80, 0.95; V 0.10, 0.15
Tungsten–chromium steels	
72xx	W 1.75; Cr 0.75
Silicon–manganese steels	
92xx	Si 1.40, 2.00; Mn 0.65, 0.82, 0.85; Cr 0.00, 0.65
High-strength low-alloy steels	
9xx	Various SAE grades
Boron steels	
xxBxx	B denotes boron steels
Leaded steels	
xxLxx	L denotes leaded steels

Chromium (Cr): Increases corrosion resistance, hardenability, hot strength, form hard wear-resistant carbide in a wide range of tool steels. Typical ranges: <0.3–12%. Class D cold-working tool steel, the Cr content is around 12%. Stainless steels require more than 11% in the composition in order to guarantee a continuous passive layer based on a nanometric oxide layer rich in Cr, but there are some austenitic grades with up to 25% and even 27% in some internal specifications of worldwide steel producing companies.

Nickel (Ni): Austenite former increases hardenability and toughness mainly in low-alloyed steels. Typical ranges: 0.3–5%. In austenitic stainless steels, a higher range can be found (8–20%), and even higher for some specific applications as is the case of the super austenitic stainless steels.

Copper (Cu): Aids atmospheric corrosion resistance. Typical ranges: 0.2–0.5%. It takes part in some grades of precipitation hardened tool and stainless steels.

Manganese (Mn): Austenite former increases hardenability/combines with S to reduce its adverse effects. Typical ranges: 0.3–2%. In hard field steels, the Mn content can reach 12%. In some austenitic stainless steels, class 2XX, developed during the Second World War, in order to save costs, Mn additions reduced the Ni content in this kind of steel.

Silicon (Si): Removes O in steel making increases hardenability promoting ferrite solid solution strengthening and toughness reduction. During the tempering heat treatment, the silicon enhances the transformation temperature from epsilon carbide to cementite, avoiding the embrittlement martensite tempering phenomena. Typical ranges: 0.2–2.5%.

Molybdenum (Mo): Grain refining increases the hardenability and the hot strength in tool steels. In stainless steel, its effect is to enhance creep resistance and corrosion resistance, reducing localized attack (pitting corrosion). Typical ranges depend on the steel class, typically 0.1–0.5% for low-alloyed steels, 2–4% in stainless steels, and up 5% in high-speed steels (*6*).

Vanadium (V): Grain refining increases hardenability, forms wear-resistant carbide, and increases temper resistance in martensite. Typical ranges depend on the steel class: from 0.1 to 0.3% for low-alloyed steels; around 2% in tool steels. Higher vanadium additions in tool steels can be done using powder metallurgy techniques.

Boron (B): Increases hardenability but this effect is related to the carbon content. Typical ranges: 0.0005–0.003%.

Lead (Pb): Aids machinability. Typical ranges: <0.3%.

Nitrogen (N): Acts like C strengthening. Typical ranges: <0.1%.

In some cases, Si is considered an impurity, while S and P are always considered impurities. The effect of these elements on mechanical properties will depend largely on the way in which impurities are distributed throughout the structure of the steel. The effect is less deleterious when such impurities are evenly distributed throughout the structure. Although considered impurities, S and Pb are sometimes intentionally added to improve machinability (*11*).

Some alloying elements form very stable carbides when added to steel, promoting a hardening effect, and result in improved wear resistance. In addition to Cr, Mo, and V, the presence of Ti, Nb, and W perform similarly by forming hard carbides in the microstructure such as Cr_7C_3, W_2C, Mo_2C, V_4C_3, NbC, and TiC. Others form complex carbides containing Fe and one or more metals. For example, M_6C is a complex carbide and may be represented by $Fe_4\ W_2C$ and $Fe_4\ Mo_2C$ (M represents the total metal atoms). Alloying elements have different carbide-forming tendencies. Those elements can be also present in the steel in other forms. For example, Ni can be also found as $NiAl_3$; Al and Ti can form nitrides and Mn forms MnS inclusions (*11*).

Figure 3 shows the carbide-forming tendency for some of the more commonly utilized elements.

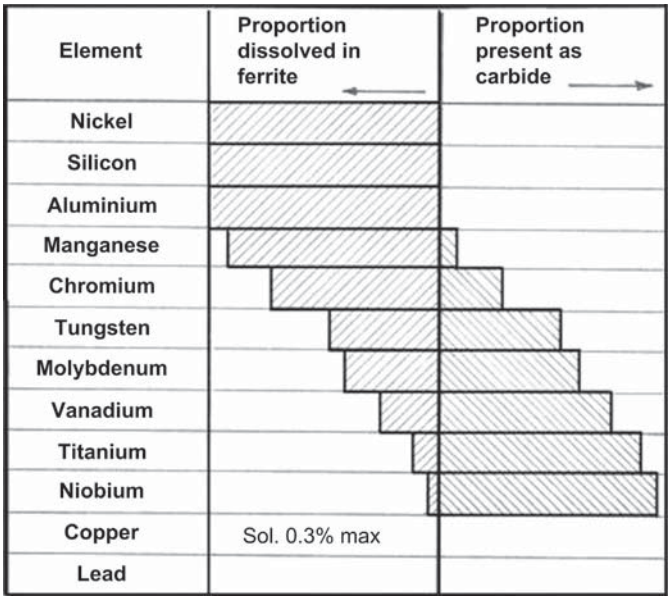

Figure 3 Tendency of the alloying elements on the carbide formation. Adapted from Higgins, R. A. *Engineering Metallurgy. Part 1. Applied Physical Metallurgy*, 5th ed.; Robert E. Krieger Publishing Company: Malabar, FL, 1983, p 559.

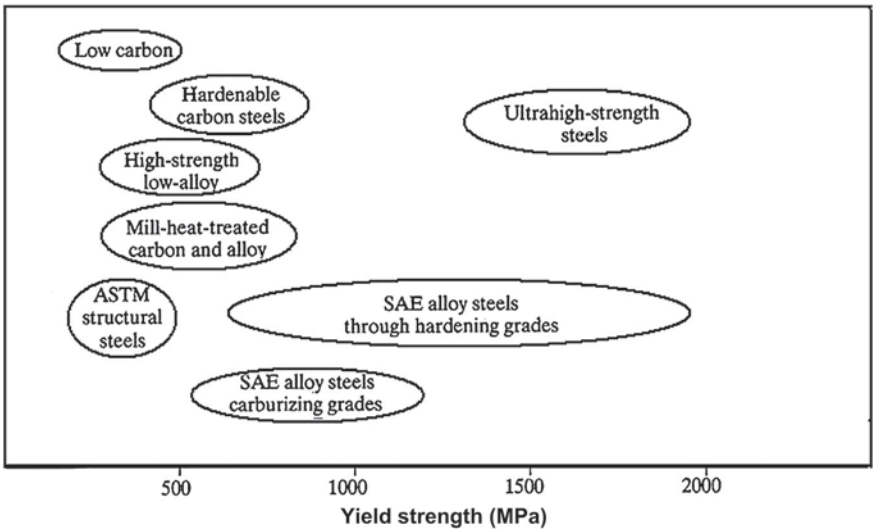

Figure 4 Yield strength ranges of steels. Adapted from Budinski, K. G.; Budinski, M. K. *Engineering Materials – Properties and Selection*, 7th ed.; Prentice Hall, 2002, (chapters 8–16).

Final mechanical properties are influenced by chemical composition and the heat treating process, and a wide range of properties can be achieved with different combinations of these variables, as illustrated by the variation of yield strength for different steels shown in Figure 4.

New steel classes have been developed to meet more advanced automotive industry requirements to satisfy emission requirements, vehicle safety, and reduced weight. Therefore, new grades of low-carbon steels for structural and die-stamped products have been developed.

12.02.3 Fe–C Diagram

The Fe–C metastable diagram, shown in Figure 5, is one of the most useful tools to study steel transformation and together continuous cooling transformation (CCT) and isothermal transformation (IT) curves are the basis for understanding the steel heat treatment process. In this discussion, the portion of the Fe–C diagram representing 0–2.0% C will be emphasized. Ferrous alloys with more than approximately 2% C are designated as cast iron. However, cast irons are not the focus of this chapter.

Since the carbon range for steel studies lies between 0 and 2%, a simplified version of the Fe–C phase diagram shown in Figure 6 is typically used. For easy reference, solid solutions that are formed in steels are designated as austenite when gamma (γ) iron is the solvent and ferrite when alpha (α) iron is the solvent (*12*).

Ferrite is a near carbon-free solid solution of one or more elements in a body-centered cubic arrangement. Fully ferritic steels are obtained only when the carbon content is very low (*13–15*). These designations refer only to structures and imply nothing about composition or properties.

Austenite is a microstructural phase characterized by a face-centered cubic iron crystal structure. It is the solid solution microstructure produced prior to hardening of the steel.

Cementite is another phase observed in Figure 6. It is a brittle compound of iron and carbon (iron carbide) with the approximate chemical formula Fe_3C and is characterized by an orthorhombic crystal structure. When it occurs as a phase in steel, the chemical composition will be affected by the presence of Mn and other carbide-forming elements.

Pearlite is a microstructure characterized by a lamellar aggregate of ferrite and cementite. It is formed from austenite, and the lamellae may be coarse or thin depending on the cooling rate and temperature range where they are formed (isothermal heat treatment) (*13–15*). It is also possible to obtain ferrite and spherical cementite structure; however, this does not form a lamellar pearlitic microstructure.

Figures 5 and 6 show phase field boundaries marked by critical temperature ranges A_1, A_3, and A_{CM}. A_1 is the temperature between the two-phase ferrite/cementite field and the temperature at which austenite forms, A_3 is the temperature range between the austenite/ferrite two-phase field and the single-phase austenite field, and A_{CM} is the temperature range between the austenite/cementite two-phase field and the single-phase austenite field. The austenite phase field defined by the critical temperatures A_3 and A_{CM} and the solidus temperature range shows that austenite exists over a large temperature/composition range, an observation that holds not only for Fe–C alloys but also for alloy steels, although the critical temperatures will vary somewhat because of alloying. The temperatures between A_1 and A_3 and between A_1 and A_{CM} are termed intercritical temperatures and define respectively the two phase fields austenite/ferrite and austenite/cementite.

Looking at Figure 6, an austenitic area is observed. This area covers a broad range of composition and temperature confirming illustrating that the austenitic microstructure is not related to one composition. Alloy steels form austenite at elevated

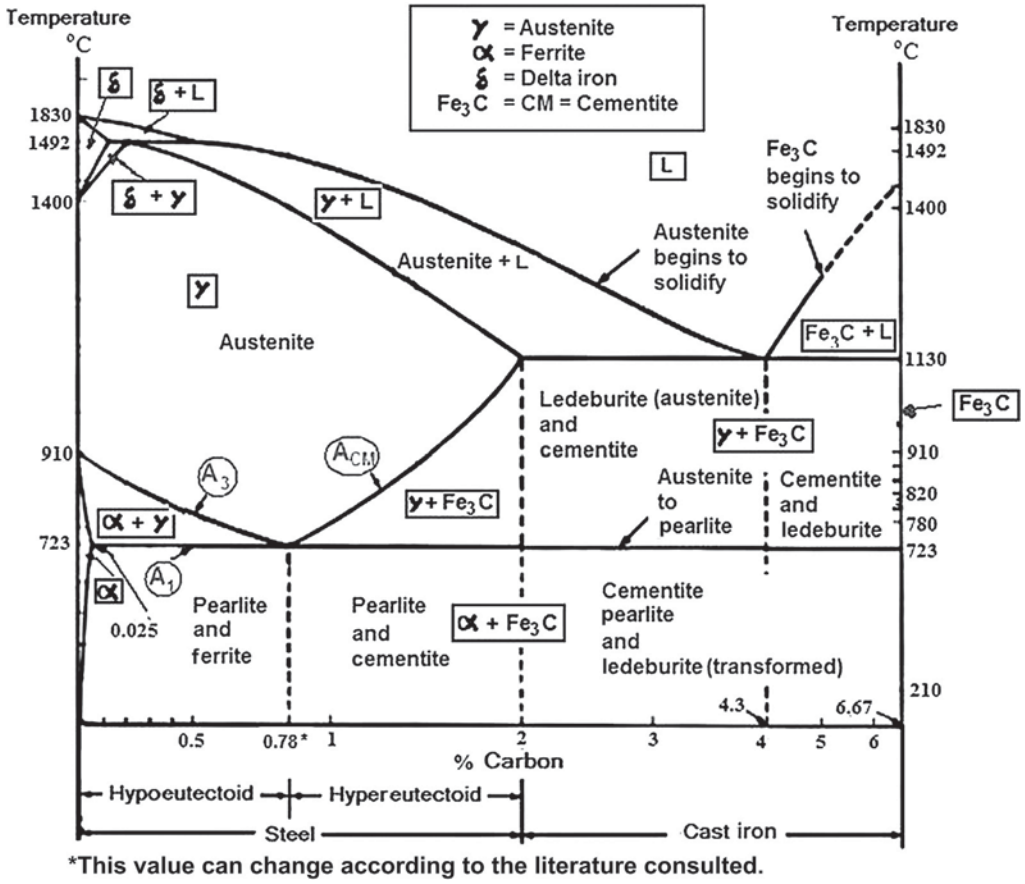

Figure 5 Fe–C metastable diagram.

temperature in the same way as plain carbon steels. The temperature range between the line A_1 (723 °C) and the line A_3, or line A_{CM}, 2 phases coexists; austenite and ferrite (between A_1 (723 °C) and line A_3), or austenite and cementite (between 723 °C and line A_{CM}).

The steel compositions at approximately 0.8% C is designated as the eutectoid composition. Compositions containing less than 0.8% C are hypoeutectoid compositions and those containing more than 0.8% C are named hypereutectoid compositions.

At slow cooling rates, liquid steel solidifies to austenite between the lines liquidus and solidus. Below the solidus line all of the structure is solidified as austenite. In the case of eutectoid steel, during slow cooling, the austenite structure is maintained up to line A_1 at which time it will transform in pearlite.

At room temperature, the eutectoid composition of steel is formed as pearlite as seen in Figure 6. During slow cooling, austenite in hypoeutectoid steels will begin to transform below line A_3 since undercooling is necessary to provide a driving force for the solid-state nucleation process. Between A_3 and A_1 (723 °C), ferrite is formed from austenite and austenite is becoming richer in carbon up to 0.8% C at 723 °C, also known as the eutectoid temperature. Just below this temperature, the remaining austenite transforms to coarse pearlite. For a eutectoid composition, undercooling is necessary to provide a driving force for the solid-state nucleation process so that at room temperature the microstructure of hypoeutectoid steel will be composed of ferrite and pearlite. The relative amount of ferrite and pearlite are dependent on the carbon content and alloying elements in the steel.

During slow cooling of hypereutectoid steels, austenite transformation will begin to transform below the A_{CM} line. The driving force of this reaction is also undercooling. Austenite begins to transform to cementite around the grain boundary and the remaining austenite decreases in carbon proportional to the degree of transformation. At 723 °C, the remaining austenite contains 0.8% C and below the eutectoid temperature transformation to pearlite occurs. At room temperature, hypereutectoid steels contain cementite as a network around pearlite. The relative phase composition of cementite and pearlite will vary according to the carbon content and the presence of alloying elements in the steel.

12.02.3.1 Effect of Alloying Elements on Eutectoid Concentration and the Eutectoid Temperature

The addition of alloying elements to steel will vary the position of the A_1, A_3, and A_{CM} boundaries and the eutectoid composition in the Fe–C diagram as shown in Figure 7 (*11*).

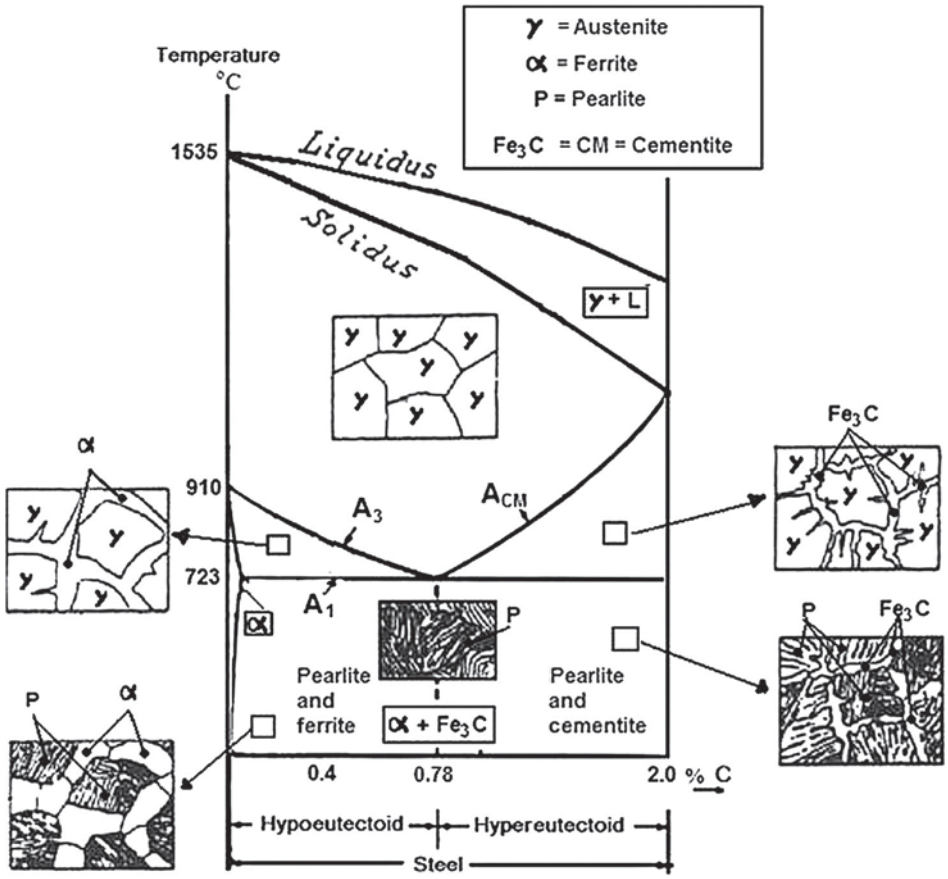

Figure 6 Simplified Fe–C phase diagram related to the steel transformations. Adapted from Honeycombe, R. W. K. *Steel Microstructure and Properties*, 2nd ed.; Edward Arnold (Publishers) Ltd, 1995, p 324.

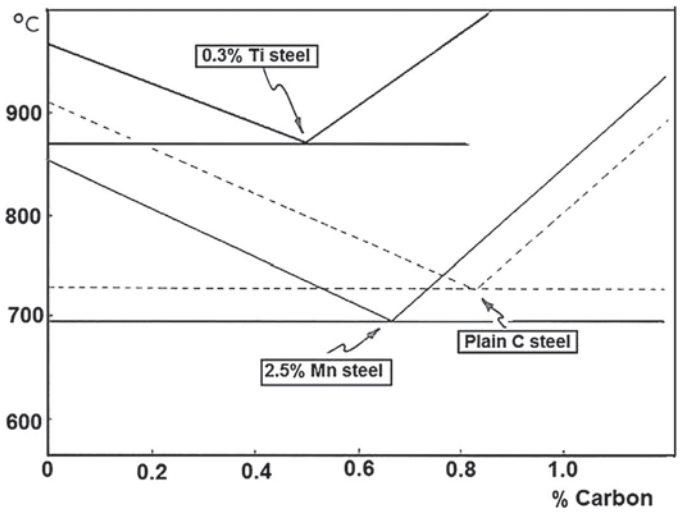

Figure 7 Influence of alloy addition on the main points of Fe–C diagram. Adapted from Higgins, R. A. *Engineering Metallurgy. Part 1. Applied Physical Metallurgy*, 5th ed.; Robert E. Krieger Publishing Company: Malabar, FL, 1983, p 559.

12.02.4 Steel Transformation

12.02.4.1 Principles

For high cooling rates, the description of the transformation process must also include time, and therefore conventional Fe–C diagrams are insufficient to describe the steel transformations. Cooling the solid solution of austenite with increased cooling rates

leads to an incomplete diffusion process. Metastable phases, not present in the conventional Fe–C diagram, may also occur (*2*). During fast nonequilibrium cooling, the formation of products requiring a very high driving force occurs. Starting from martensite, the higher strain energy solid-state reaction produces a diffusionless structure. For bainite reactions, the driven force is still sufficiently high to overcome some of the strain energy but the reaction occurs by short-range interstitial diffusion processes, the extent of which depends on the reaction temperature (upper or lower bainite) as will be seen subsequently. These reactions are associated with good matching interfaces whose movement requires dislocation slipping mechanisms.

12.02.4.2 Microstructures of Steels

During industrial heat treatment processes where high cooling rates are used, three groups of microstructures can be differentiated as shown in **Figure 8**:

- Pearlite microstructures whose growth is primarily diffusion controlled;
- Bainite microstructures whose growth is partly diffusion controlled; and
- Martensite microstructures whose growth is primarily diffusionless.

The temperature range of the formation of these three groups depends on the chemical composition of the steel and the cooling rate. Excellent summaries of microstructures in steel are provided in Refs. (*16–19*).

In the subsequent discussion, isothermal transformation of low-alloyed steel after austenitization is assumed. In high-alloy steels, carbides other than M_3C or nonmetallic and intermetallic eutectoids other than pearlite may be formed, but these transformations will not be discussed here.

12.02.4.2.1 Ferrite and Pearlite

In an unalloyed eutectoid steel, the carbon concentration is about 0.8% C and the transformation temperature occurs at the lowest temperature within the austenite range as shown in **Figure 6**. For these steels, austenite transforms between about 700 °C and 600 °C by a simultaneous precipitation of ferrite and cementite in a metastable, lamellar-like arrangement, called pearlite as shown in **Figures 9** and **10** (*12,20*).

The interlamellar distance of pearlite decreases with decreasing transformation temperature. The interlamellar spacing reduction promotes an increase of pearlite hardness, from 15 HRC with a 1 μm spacing to 40 HRC when the interlamellar spacing is reduced to 0.1 um (*21*). In most practical applications, pearlite exhibits such a small interlamellar distance that ferrite and cementite plates cannot be resolved with light optical microscopy and conventional magnification. It depends also on the cutting plane angle with respect to the pearlite lamellae.

In hypoeutectoid steels in general, a transformation to proeutectoid ferrite starts at the austentite grain boundaries. The thickening rate of this grain boundary ferrite requires some time to complete the reaction. Therefore, the rate of ferrite volume fraction transformed below Ac1 increases with decreasing grain size of austentite. This phenomenon is clearly demonstrated in **Figure 11** for a bimodal austenite grain size distribution in a 0.45 wt.% carbon steel.

The large austenite grain size labeled by the larger circle in **Figure 15** produces a localized low ferrite and high pearlite content. In the smaller circle, in the relatively small austenite grain size region, the ferrite content increases as the pearlite content decreases.

When the ferrite volume fraction is lower than the typical value for the annealed condition, the carbon content of pearlite is lower than the eutectoid composition, which indicates a lamellar structure with a lower volume fraction relative to cementite and a correspondingly higher volume fraction for ferrite. For the same carbon content steel in the proeutectoid ferritic range, the higher the heat extraction rate (cooling rate), the lower the ferrite contribution to the microstructure that is formed.

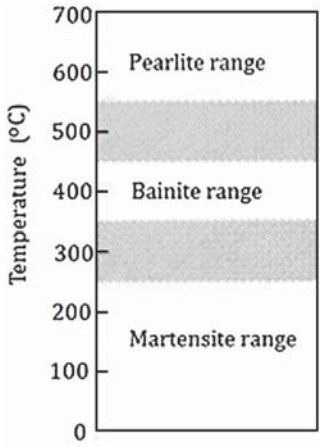

Figure 8 Temperature range of the formation of microstructures in unalloyed steels. Adapted from Hougardy, H. *Umwandlung and Gefüge unlegierter Stähle, eine Einführung*; Verlag Stahleisen mbH Düsseldorf, 1990.

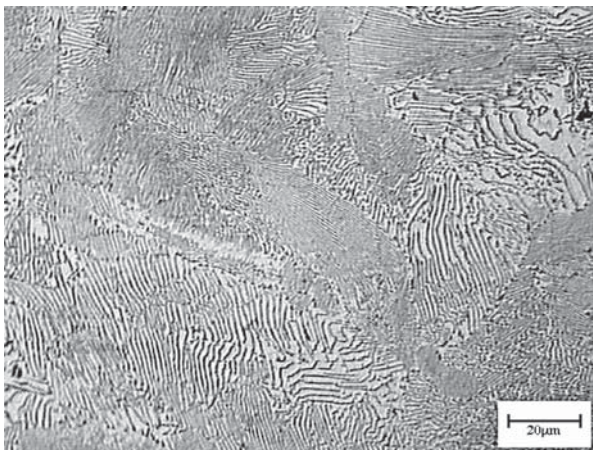

Figure 9 Pearlite: ferrite (while) and cementite (gray or black) in an arrangement of parallel plates. Etched 2% Nital. Courtesy of Dr Rosamel Muñoz, University of São Paulo.

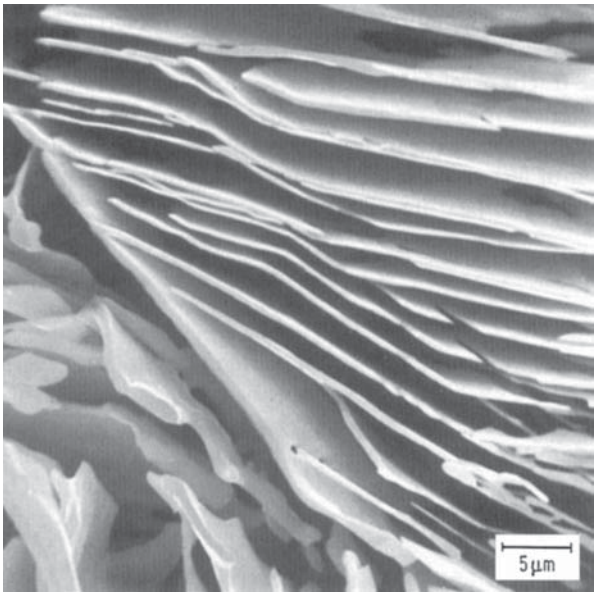

Figure 10 Coarse pearlite after deep etching 4 min in 5% Nital. The scanning electron microscope image shows bright-appearing cementite plates separated by dark or black areas where the ferrite has been dissolved by the heavy etching. The relatively high interlamellar spacing of the cementite/ferrite areas is related to the cutting plane angle with respect to the orientation of the pearlite lamellae. Reproduced from Hougardy, H. *Umwandlung and Gefüge unlegierter Stähle, eine Einführung*; Verlag Stahleisen mbH Düsseldorf, 1990.

In addition to volume fraction of ferrite and pearlite, their distribution patterns are directly related to the relative amounts of the component microstructure. This is the case of the banded structure observed in the longitudinal cross-section of bars that were subjected to an intensive plastic deformation during steel manufacturing followed by a lower cooling rate from the austenite temperature or due to annealing heat treatment. When the microstructure is observed from the transversal bar cross-section, it is very difficult to identify the banded structure, as shown in **Figure 12**.

Banded structure is related to the segregation process during solidification when the liquid between the dendrites and the tips of the dendrite branches becomes richer relative to the solute contents. This occurs when both the liquid and the solid phases are different with respect to alloying element solubility. Such a process is called microsegregation and it is difficult to be eliminated. Microsegregation, also called interdendritic chemical segregation, may exhibit the banding phenomenon after thermomechanical processing. Some degree of banding is found in all types of steels. However, in the case of higher cooling rates, as expected in the normalizing heat treatment, the banded structure may not be observed, depending on the section size. Nonbanded structure is shown in **Figure 13**.

The solid-state nucleation process of ferrite from austenite occurs at austenite grain boundaries when the ferrite nuclei possess *good matching interfaces* with one of the adjacent austenitic grains and are incoherent with the other side of the austenite grain. When the heat extraction rate is low, the driving force for the austenite to ferrite reaction is low and ferrite grows through the incoherent

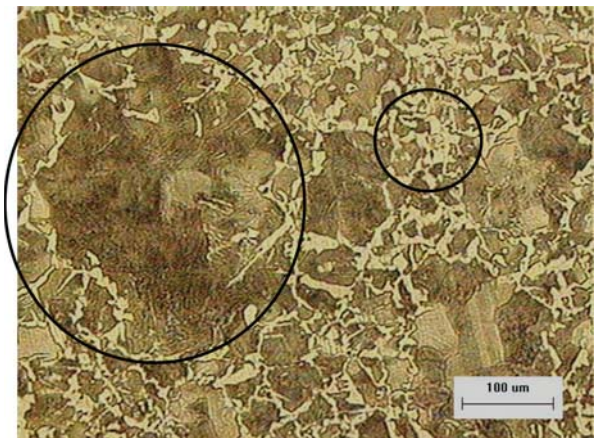

Figure 11 Microstructure from the cross-section of SAE 1045 steel bar showing a bimodal previous austenite grain size. Air cooled from 950 °C. 2% Nital etched.

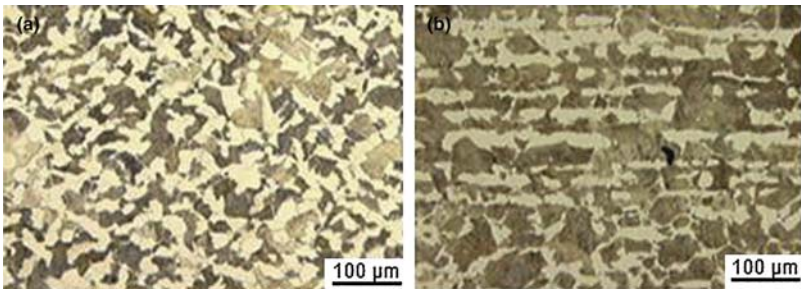

Figure 12 Microstructure of a bar of SAE 1045 annealed from 900 °C. (a) Transversal cross-section and (b) longitudinal cross-section showing banded structure. 2% Nital etched.

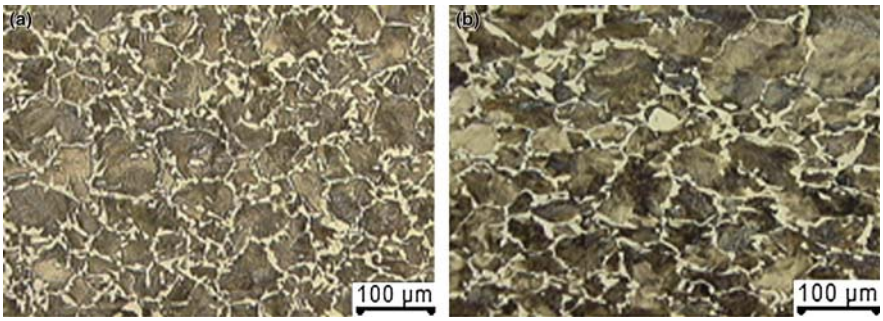

Figure 13 Microstructure of a bar of SAE 1045 normalized from 900 °C. (a) Transversal cross-section and (b) longitudinal cross-section. 2% Nital etched.

interface. For higher cooling rates, the driving force is higher, which promotes the growth mechanism in the *good matching interface* side producing Widmanstatten ferrite shown in Figure 14 (*6*,*22*). The Widmanstatten ferrite (also called acicular ferrite) plates thicken in a discontinuous way by a ledge growth mechanism (*6*).

For similar heat extraction rates, increasing the austenite grain size may lead to a higher driving force for ferrite to austenite transformation with a Widmanstatten structure contribution and a lower proeutectic ferrite content as seen in Figure 15.

Lower steel carbon content enhances the ferrite content, and the previous austenite grain boundary became difficult to be visualized, especially with slow cooling rates.

The hypereutectoid carbon steels are related to carbon contents that are greater than the eutectoid composition. When this grade of steels is slow cooled from the austenite temperature, proeutectoid cementite nucleates at the austenite grain boundaries and grows at the expense of austenite carbon until reaching the eutectoid temperature. Further cooling initiates the austenite decomposition process by a eutectoid reaction producing pearlite. The final structure consists of grain boundary proeutectoid cementite and pearlite, as shown in Figure 16.

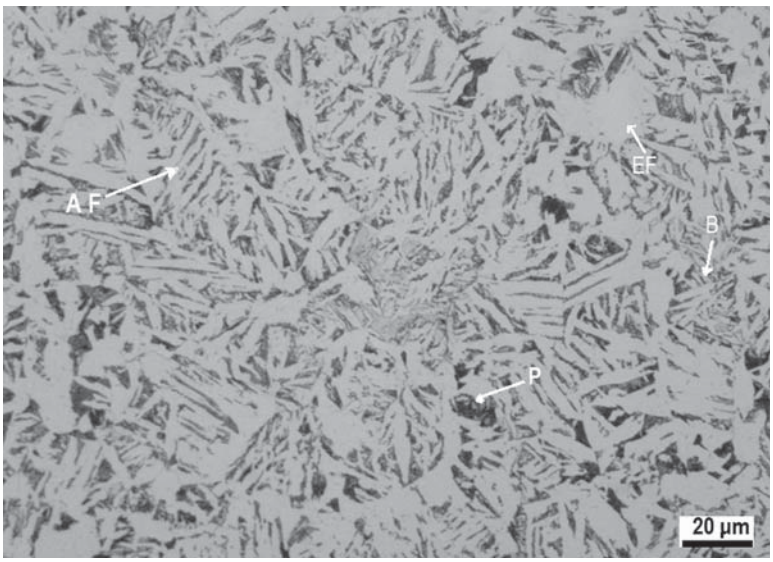

Figure 14 Acicular ferrite (AF) in as-rolled 4027 alloy steel (Fe – 0.27% C – 0.8% Mn – 0.25% Si – 0.25% Mo) revealed by etching with 2% Nital. There are also patches of equiaxed ferrite (EF), occasional patches of pearlite (P), and considerable bainite (B) in the matrix. Courtesy of George Vander Voort.

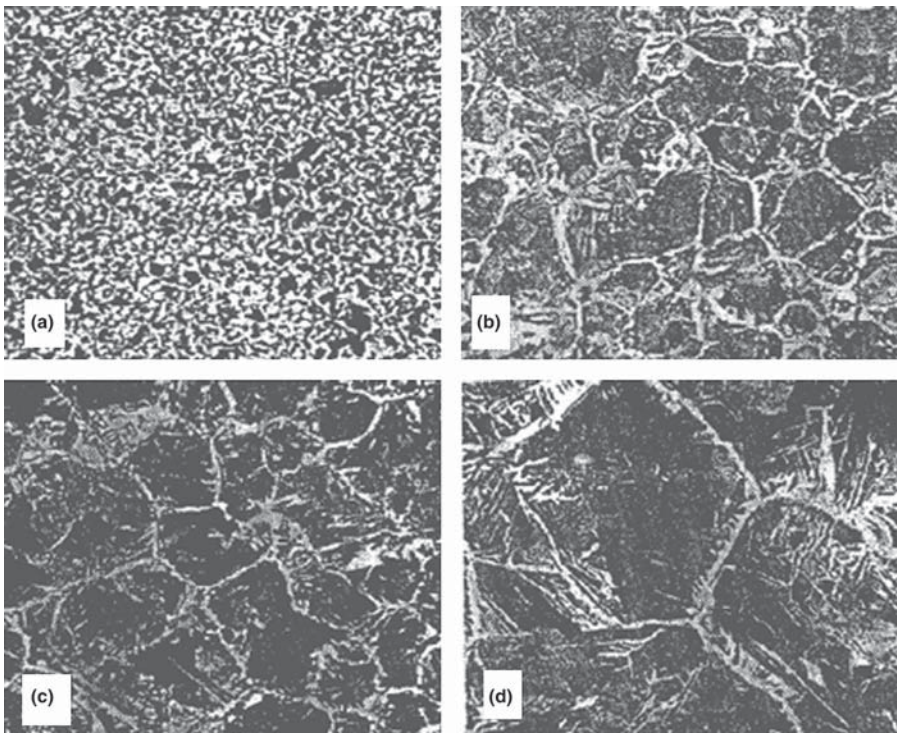

Figure 15 Steel with 0.45% wt.% C air cooled from 1 – (a) 800 °C; (b) 960 °C; (c) 1050 °C; (d) 1150 °C. 2% Nital etched. Magnification: 100×. Reproduced from Lakhtin, Y. *Engineering Physical Metallurgy (translated from the Russian by Nicholas Weinstein)*, 2nd ed.; Mir Publishers: Moscow, 2009, p 471.

Even when the carbon content reaches 1.3%, which is 0.5% higher than the eutectoid composition, the volume fraction of proeutectoid cementite is low while the same difference in terms of carbon for hypoeutectoid (steel with about 0.3% C) produces a high proeutectoid ferrite volume fraction. This difference is explained by the lever rule.

Under some cooling conditions, cementite can precipitate as Widmanstatten structure as shown in **Figure 17**.

For many industrial applications, ferrite and cementite mixtures must be based on the spheroidized morphology to improve processing during manufacture. This microstructure is close to the equilibrium. There are a number of heat treatment processes to obtain this microstructural feature. Usually this control is provided by maintaining the steel in a temperature range close to the eutectoid temperature for a time sufficient to spheroidize the lamellar structure. **Figure 18** shows the spheroidized structure.

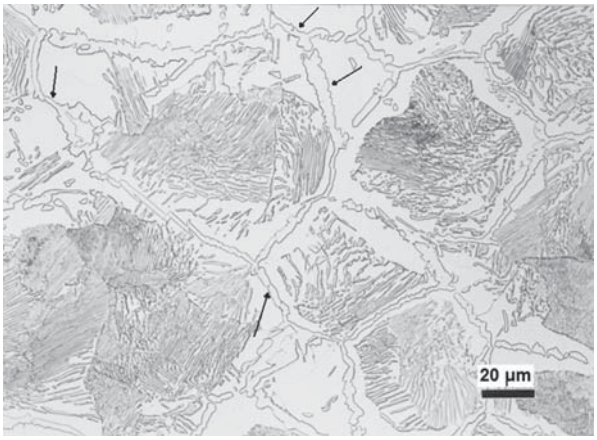

Figure 16 Proeutectoid cementite and pearlite in a hypereutectoid steel with 1.2% C. Picral etch. Courtesy of George Vander Voort.

Figure 17 Microstructure of as-rolled Fe – 1.31% C – 0.35% Mn – 0.25% Si high-carbon water hardenable tool steel. Note the Widmanstatten intragranular cementite that precipitated as proeutectoid cementite before the eutectoid reaction. Originals at 1000×. 4% Picral etch. Courtesy of George Vander Voort.

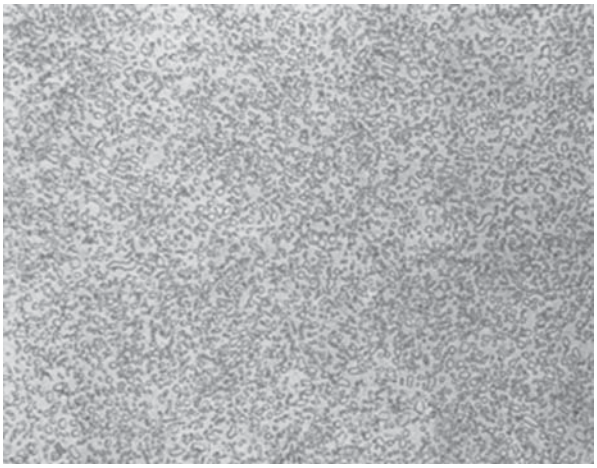

Figure 18 Ferrite (matrix) and cementite (globules) in an SAE 52100 alloy steel for bearings (Fe – 1.05% C – 0.35% Mn – 1.45% Cr) etched with 4% picral. Original at 1000×.

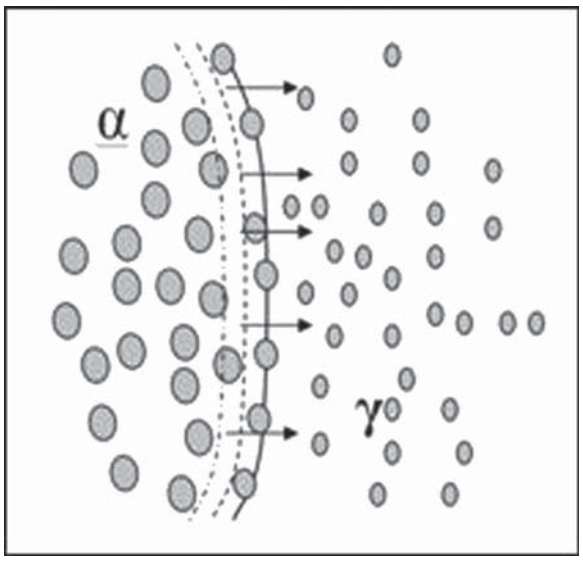

Figure 19 Eutectoid transformation (interface moving from the left to right), consuming austenite containing stabilized carbides, with no lamellar cooperative growing process, but only the growing of the γ undissolved carbides during the γ/α interface movement.

When steel compositions contain carbide-forming alloying elements such as Cr in SAE 52100 composition, a globulized structure is expected in the annealed condition without additional heat treatment. The mechanism responsible for this structure development can be explained by **Figure 19**.

12.02.4.2.2 Bainite

In many steels, a bainitic structure may be obtained by an isothermal or continuous cooling process conducted within an appropriate temperature range. In the carbon steels, bainite is directly related to isothermal heat treatment because, as in the continuous cooling process, the pearlite reaction almost totally consumes the austenite, thus making the bainite nucleation process, which is essentially a eutectoid reaction, more difficult (*23*,*24*).

Bainitic structure can be divided in two groups: upper bainite and lower bainite. Typically, lower bainite differs from upper bainite by the iron-based carbide precipitates within the ferrite plates with a preferred orientation. Upper bainite consists of small subunits of ferrite plates separated by carbide films.

Lower bainite behaves similar to martensite in terms of the ferrite austenite Kurdjumov–Sachs orientation relationship, and the habit plane austenite-bainite is of the (225) type, the same habit plane found in the high-carbon martensite (1.0–1.4 wt.% C). Macroscopically, a habit plane is the interface plane between austenite and martensite (*6*). During the high-speed martensite reaction, the carbon atoms are unable to move from their interstitial positions and are retained in the octahedral-type interstitial sites in martensite while the bainite transformation (lower or upper bainite) occurs with a lower rate with some contribution from temperature-dependent short-range carbon diffusion. Another difference between the austenite-martensite and austenite-bainite transformations is the iron-based carbides that precipitate in one variant of the orientational relationship in the lower bainite (in carbon steels, the lower bainite, metastable epsilon carbides precipitate inside of the laths with an angle of 55° relative to the lath axis) while in the tempered martensite, the precipitates (epsilon carbides and cementite) are found in several different orientational relationships.

The transformation kinetics are reflected in isothermal transformation diagrams (time-temperature-transformation (TTT) diagrams), which follow the general model developed by Bain and Paxton and then extended for all steel alloys (*25*). In isothermal cooling, bainite transformation begins according to the corresponding TTT diagram and then the fraction of bainite transformed gradually increases with the holding time at the isothermal temperature. **Figures 20** and **21** illustrate examples of lower bainite obtained in AISI O1 cold-working steel (0.8% C) austenitized at 860 °C cooled isothermally at 320 °C in a molten salt bath with interruptions at 5 and 10 min to show the lower bainite transformation kinetics in contrast to the martensite matrix due to the quenching of the remaining austenite. **Figures 20** and **21** show the bainite transformation after 5 and after 10 min, respectively (*26*).

Figure 22 shows upper bainite in SAE 5160 steel isothermally heat treated 830 °C (1525 °F) – 30 min, 538 °C (1000 °F) for 60 s – water quenched (remaining austenite forms martensite).

Until recently, phase nucleation processes (excluding the martensite reaction) were considered to occur at austenite grain boundaries and inside the grains and may, or may not, be associated with inclusion interfaces. More recently, it has been demonstrated by tridimensional microstructural construction using a computer code based image acquisition after sequential polishing and etching and removal of a slice of material that most reactions excluding martensite begin at austenite grain boundaries as shown in **Figure 23**. As a result, it was concluded that many morphologies that included induced phase transformation theories were incorrect (*27*).

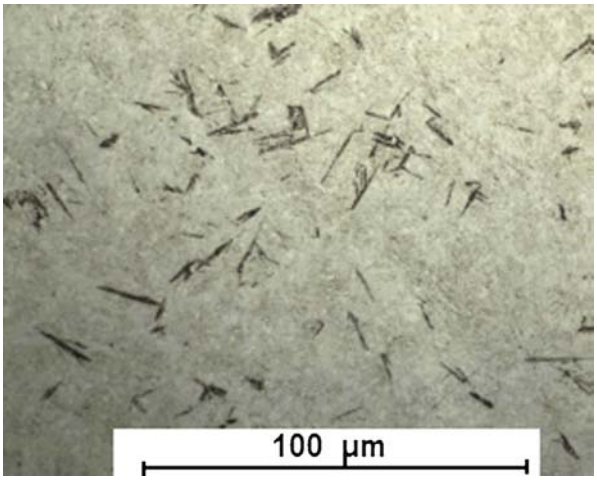

Figure 20 Beginning of bainitic transformation in AISI O1 steel. Lower bainite laths – dark area, formed after 5 min cooling at 320 °C molten salt bath. Matrix: martensite. 2% Nital etched. Reproduced from Vatavuk, J.; Santos, D. *Estudo das transformações bainíticas, Scientific Report*; Laboratório de Engenharia dos Materiais, Universidade Presbiteriana Mackenzie, 2008, p 15.

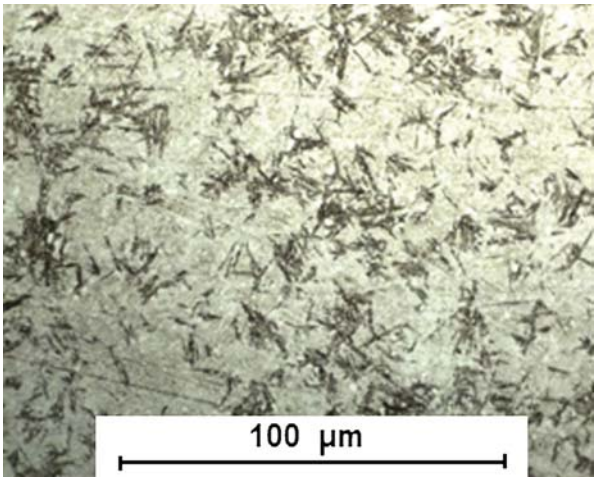

Figure 21 Bainitic transformation in AISI O1 steel. Lower bainite laths – dark area, formed after 10 min cooling at 320 °C molten salt bath. Matrix: martensite. 2% Nital etched. Reproduced from Vatavuk, J.; Santos, D. *Estudo das transformações bainíticas, Scientific Report*; Laboratório de Engenharia dos Materiais, Universidade Presbiteriana Mackenzie, 2008, p 15.

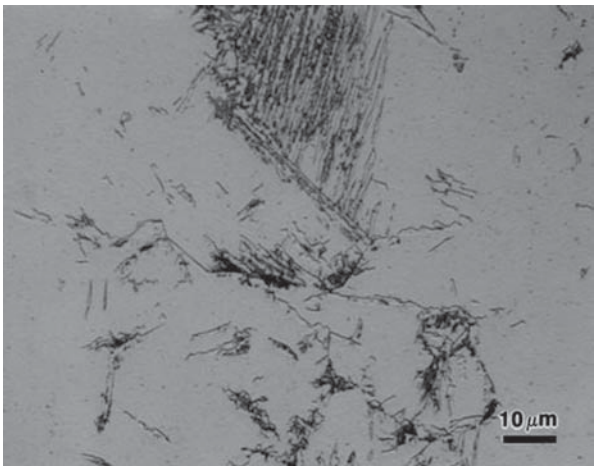

Figure 22 Upper bainite: 5160 alloy steel (Fe – 0.6% C – 0.85% Mn – 0.25% Si – 0.75% Cr). Isothermally heat treated to form a small amount of upper bainite (dark areas). Matrix: martensite. 4% picral etch. Courtesy of George Vander Voort.

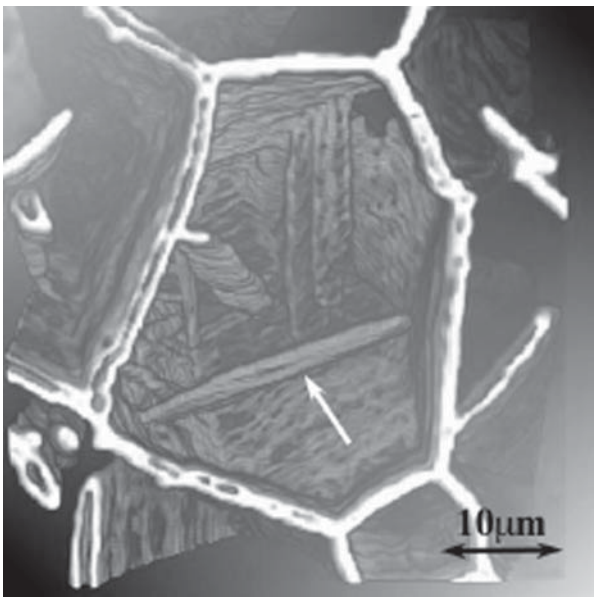

Figure 23 Three-dimensional reconstruction of proeutectoid cementite precipitates in a grain boundary. Reproduced from Kral, M. V.; Mangan, M. A.; Rosemberg, R. O.; Spanos, G. *Three Dimensional Analysis of Microstructure*; U.S. Naval Research Laboratory, Department of the Navy, 1999, p 7.

Bainitic transformations are controlled by short-range diffusion associated with an evolution of a substantial strain energy. This transformation occurs matching interface movement (*military transformation*) since it occurs in an organized atomic motion across the moving boundary. Conversely, *civilian transformation* indicates that the transformation occurs without organization of atomic movement across the moving boundary. These transformations can be monitored by the polishing method where a previously polished surface is observed after transformation. When allotrimorphic ferrite (an incoherent side-growing process) occurs, the polished topography remains the same, indicating a civilian diffusion-controlled transformation. When the driving force to ferrite austenite transformation increases, the acicular ferrite reaction predominates (a semicoherent, side-growing process), and the polished topography indicates the phase transformation process. Bainitic and martensitic transformations occur by the same topography change, indicating a military transformation (*28*).

Banded structure may be observed after isothermal heat treatment. Figure 24 shows bainitic transformation in AISI O1 steel austenitized at 860 °C, cooling at 320 °C in a molten salt bath for different times. IT is observed at the beginning as shown in Figure 24(a) where there is a banded transformation (martensite and bainite). Banding is promoted by a difference in segregation effects resulting in hardenability differences (*26*). Figure 24(b) and 24(c) show that the banded structure gradually disappears as the bainite reaction proceeds – even in the higher hardenability regions.

12.02.4.2.3 Martensite

Ferrous martensite is a body-centered tetragonal crystallographic structure with lattice parameters related to the carbon content of the steel:

$$c/a = 1 + 0.0467 \times (\%\ \text{carbon}) \qquad [1]$$

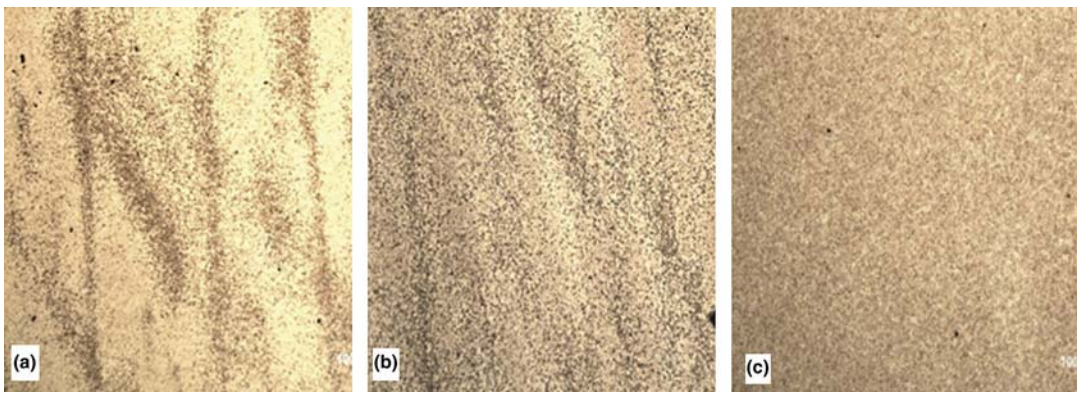

Figure 24 (a) Bainitic transformation after 10 min. (b) Bainitic transformation after 20 min. (c) Bainitic transformation after 40 min. 2% Nital etched.

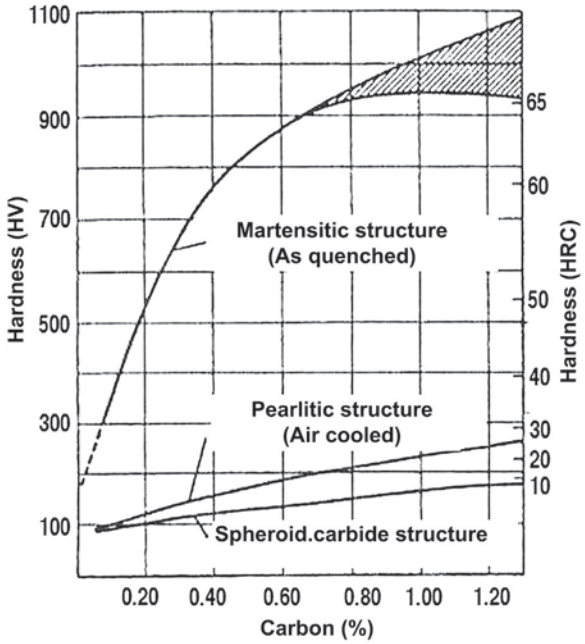

Figure 25 Hardness of martensite as a function of carbon content. Reproduced from Bain, E. C.; Paxton, H. W. *Alloying Elements in Steel*; ASM: Metals Park, OH, 1966, p 291.

This expression shows the higher the carbon content, greater is the difference between the lattice parameters a and c. Martensite is typically hard (800–900 HV maximum) and brittle. Figure 25 shows that hardness varies with C content and is strongly related to distortions caused by the C atom in the body-centered tetragonal structure.

Austenite to martensite transformation is a diffusionless reaction and as shown by Bain (*29*), it occurs by a face-centered-cubic lattice shearing of austenite (Bain distortion) as shown in Figure 26.

Bain distortions are large, lead to variation of shape of the polycrystalline system, and are compensated through *lattice-invariant deformation*, which may occur by a *dislocation slide mechanism*, mechanical twinning, diffusion-induced creep, or a mixture of mechanisms depending on the composition of the steel. Although these deformations are lattice-invariant because although they result in a change in shape, the crystal structure is unchanged from the initial structure. Generally, lattice-invariant deformation is affected by the deformation temperature, which is directly related to the martensite transformation temperatures. Carbon exhibits the greatest influence on M_s temperature and is responsible for the martensite morphology of steels.

The martensite start temperature (M_s) is the temperature at which martensite starts to form on cooling. The martensite finish temperature (M_f) is the temperature at which martensite transformation on cooling is essentially finished. There are several empirical equations to calculate M_s temperature, including (*6,25,30*):

$$M_s = 539 - 432(\%C) - 30.4(\%Mn) - 17.7(\%Ni) - 12.1(\%Cr) - 7.5(\%Mo) \quad [2]$$

For medium-carbon steel:

$$M_s = 520 - 320(\%C) - 50(\%Mn) - 30(\%Cr) - 20[\%(Ni + Mo)] - 5[\%(Cu + Si)] \quad [3]$$

$$M_s = 561 - 474(\%C) - 33(\%Mn) - 17(\%Ni) - 17(\%Cr) - 21(\%Mo) \quad [4]$$

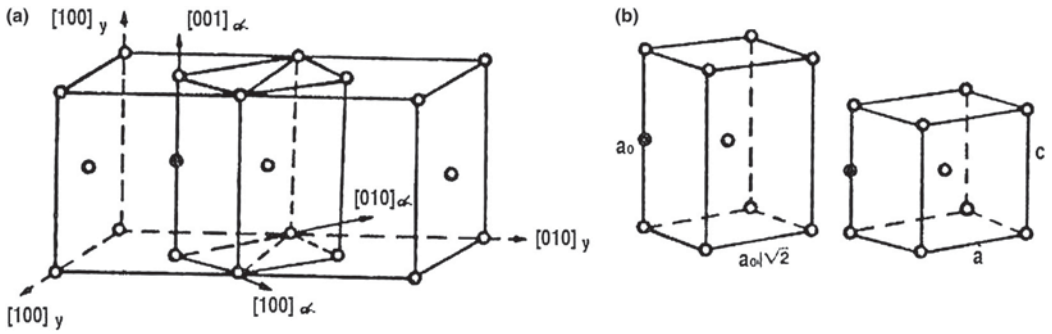

Figure 26 (a) BCT (body-centered tetragonal) cell in austenite. (b) BCT cell before (left) and after (right) the lattice deformation from austenite to martensite. Reproduced from Honeycombe, R. W. K. *Steel Microstructure and Properties*, 2nd ed.; Edward Arnold (Publishers) Ltd, 1995, p 324; Bain, E. C.; Paxton, H. W. *Alloying Elements in Steel*; ASM: Metals Park, OH, 1966, p 291.

As the transformation temperature increases, the probability of plastic deformation by a dislocation glide mechanism increases. Low temperatures lead to plastic deformation by mechanical twinning. Therefore, martensite morphology is shown to be dependent on the alloying element content, with the greatest single contribution provided by the carbon content.

Martensitic transformations are constrained by the crystallography of the initial crystal structure and transformations occur by a dislocation (slip) or a twinning mechanism. **Figures 27–29** show the morphological aspects of martensite as function of carbon content for steels using optical microscopy. One structure of martensite is lath martensite, which is characterized by lath-shaped (needle-like) structure a few micrometers long and less than 1 μm thick (*31*). Lath martensite occurs when the carbon content is less than 0.6% C.

For lath martensite, the deformation mechanism of invariant lattice is the dislocation slip. Morphologically, this martensite exhibits lath packets that are separated by a low boundary angle with a misorientation of less than 5° (*32,33*). (A packet is defined as a group of laths with almost the same habit plane and blocks, which contain a group of laths with almost the same orientation. Blocks may be further subdivided into subblocks. Usually, packet size is assumed to be equal to the effective grain size (*34*).) Substructure hardening transformation is essentially independent of the grain size (*35*).

The dislocation density found in martensite may vary from 0.3 to 0.9 $\times$ 10^{13} cm of dislocations per cubic centimeter of the crystal. This dislocation density is greater than the maximum that may be obtained by increasing the percentage of cold plastic deformation. Some observations made by transmission electronic microscopy show a very small cellular structure size (about 0.2–0.3 μm) inside the lath (*36*).

Figure 29 illustrates the microstructure of a high C content steel as observed by optical microscopy. The white areas indicate retained austenite (see white arrow).

The second common morphology of carbon steels and alloy steels is *plate* or *lenticular* martensite. Plate martensite may exhibit a platelike grain structure. Plate martensite is formed when the carbon content is greater at approximately 0.6% C. When the carbon

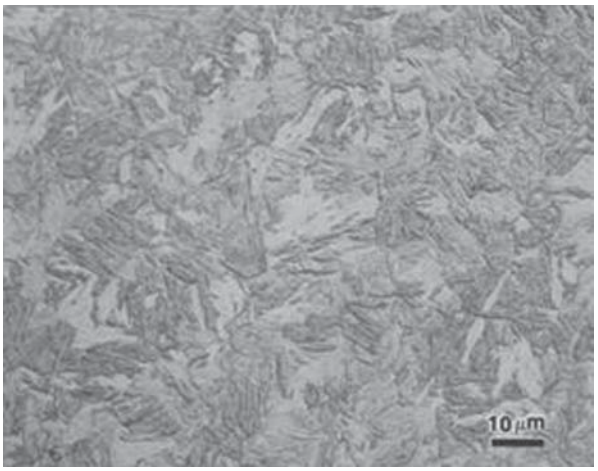

Figure 27 Lath (low-carbon) martensite in SAE 8620 alloy steel (Fe – 0.2% C – 0.8% Mn – 0.55% Ni – 0.5% Cr – 0.2% Mo) after heat treatment (954 °C, 1750 °F – 1 h, water quench).

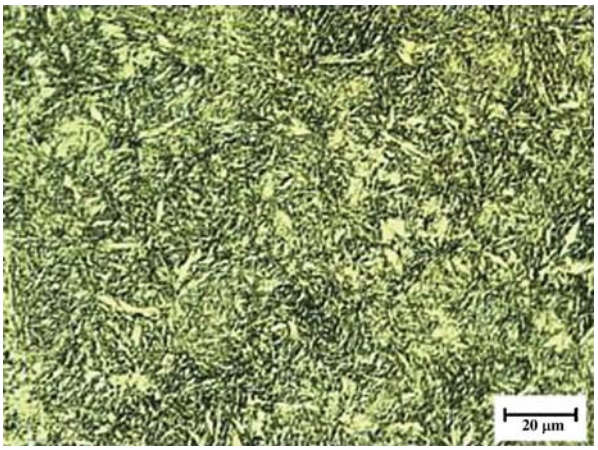

Figure 28 High-carbon martensite (0.8% C). Nital etched.

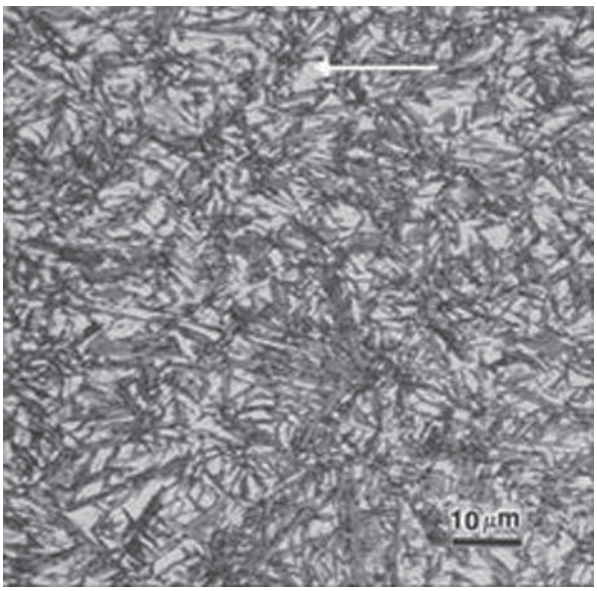

Figure 29 Microstructure of quenched 1.3% C steel. Dark needles of plate martensite. Arrow shows retained austenite. 2% Nital etched.

content is between 0.6 and 1.0% C, a mixture of lath and plate martensite may be observed microscopically (*37*). **Figures 28** and **29** illustrate a *twinned martensite* or *plate martensite* for high-C martensite. The spacing of the twinned substructure of the plate martensite, approximately 10 Angströms, can be resolved through transmission electron microscopy (*38*).

As the carbon content increases, so-called high-carbon martensite twins begin to replace dislocations within the plates (*37*). The percentage of slip martensite and twinned martensite in carbon steels and tool steels may be experimentally determined and can be inferred in **Figure 30**. As the carbon content increases, the amount of lath martensite decreases. The untransformed austenite increases with the reduction in the M_s temperature. The increase of the retained austenite volume fraction reduces the as-quenched hardness.

When the martensitic transformation occurs at different times at the surface and in the core of the steel, the variations in the volume and size contribution increase and residual tensile stresses are developed in the surface after the heat treatment and quenching. The volume variation during the transformation from austenite to martensite in a 1% C steel is about 4% (the transformation to pearlite results in 2.4% of expansion) and decreases with an increase in C in the steel composition (*6*). This occurs because of the different C effect in austenite relative to martensite. In the first case, the deformation exhibits a volumetric character while, in the second, the effect is more directional (*39*). This behavior can be seen in **Figure 31**.

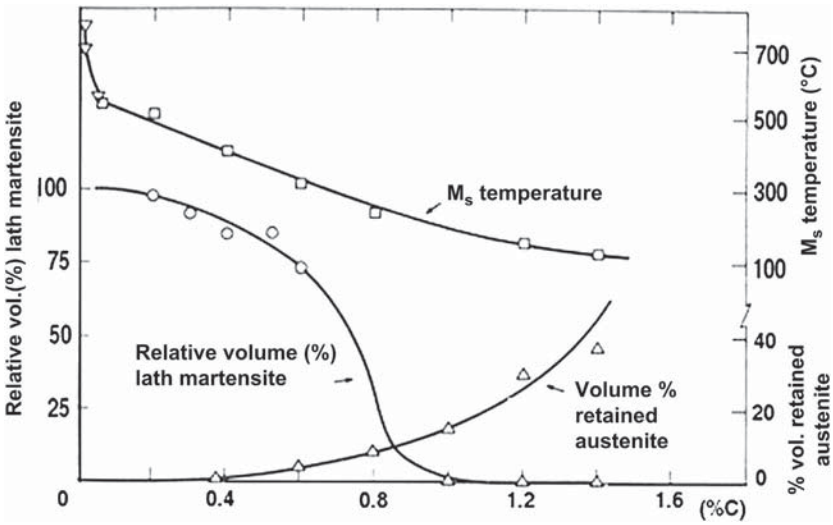

Figure 30 Effect of C content on the lath martensite volume and retained austenite volume fraction and also M_s temperature. Adapted from Speich, G. R. *Trans. Metall. Soc. Am. Inst. Mech. Eng.* **1969**, *245* (12), 2553–2564; Speich, G. R.; Leslie, W. C. Tempering of Steel. *Metall. Trans.* **May 1972**, *3* (5), 1043–1054.

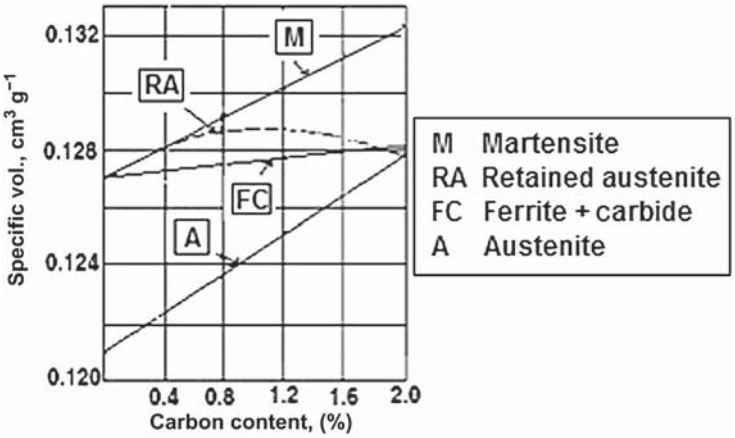

Figure 31 Specific volume (D*V*/*V*) of carbon steels at room temperature. Adapted from Narazaki, M.; Totten, G. E.; Webster, G. M. Hardening by Reheating and Quenching. Handbook of Residual Stress and Deformation. Totten, G. E.; Howes, M.; Inoue, T. ASM International, Materials Park, OH, USA, 2002, p 499.

Figure 31 shows that the difference in specific volume between austenite and martensite is about 15% from very low carbon content to very high-carbon content (2% C). Also for low-carbon steel, the change in volume from the as-annealed condition to as-hardened condition is negligible. However, that difference is increased with increasing C content. These observations are important during the component design process. Furthermore, as the C content increases, the potential for embrittlement of the plate martensite increases (*40*). However, since retained austenite also increases with C content, this fraction of retained austenite will improve toughness and reduce volume variation as shown in the curve A–FC of Figure 31. This results in lower load to the cold surface because of the incomplete transformation of the core. The lower low yield strength of the core is similar to the low mechanical resistance exhibited by austenite, which decreases the potential to develop tensile stress in the surface of the steel.

Figure 31 also shows that for 2% carbon, it could be theoretically possible to obtain complete transformation to martensite. However, this does not occur in practice. The retained austenite line matches the austenite line for very high carbon content. That is the case for a Hatfield-type steel, which contains a high manganese content (12%) that guarantees an austenitic microstructure even though the carbon amount is approximately 1.2%. In this situation, it is possible to quench very large components with complex geometry with a low risk of developing cracks – even with increasing quenchant severity (*41*).

The ability to form martensite is described in terms of hardenability, which is related to the presence of other alloying elements in addition to carbon. For example, molybdenum, chromium, and nickel increases hardenability while cobalt lowers the hardenability of steel. The effect of alloying elements on the hardenability has a multiplying character so that it may be beneficial to use small quantities of alloying elements together than a higher content of a specific element. A higher hardenability allows martensite transformation with a slower cooling rate. This is beneficial for reducing tensile residual stresses in the component surface.

12.02.5 Time-Temperature-Tranformation Diagrams

Under very slow cooling rates that simulate equilibrium conditions, the formation of ferrite, coarse pearlite, and cementite may be predicted from the Fe–C metastable diagram. However, martensite and bainite are nonequilibrium microstructures. The formation of these products and the proportions of each are dependent on austenitization conditions (which influence austenite grain size), amount of alloying elements in solution, time and temperature cooling history of the particular alloy, and composition from the transformation diagrams for the steel alloy. Two of the most commonly used diagrams are time-temperature-transformation (TTT) or alternatively designated IT and CCT diagrams. These diagrams are strongly affected by chemical composition and austenite grain size since they are related with the nucleation and rate of growth of pearlite, bainite, primary ferrite, and primary iron carbide.

12.02.5.1 Isothermal Transformation Diagrams

IT diagrams can be developed using a dilatometric method where the length of the steel test specimen is recorded as a function of time at the transformation temperature. When phase transformation occurs, the pattern of contraction or dilation varies with the percentages of the transformed constituent. These diagrams can be constructed from a set of steel test specimens that are heated through the critical zone until they are totally transformed to austenite. At this point, each test specimen is quickly transferred to a constant temperature bath held at the desired transformation temperature. The test specimens are held at the desired temperature for different times and then quenched. The transformation is monitored microscopically. The amount of untransformed austenite (retained austenite) during the isothermal process is determined in the as-quenched martensite. The same procedure is repeated for a wide range of isothermal baths. By this process, it is possible to determine the initial time and final time of pearlite and/or ferrite transformations for each temperature. A typical IT diagram for AISI 4340 steel is shown in Figure 32 (*42*).

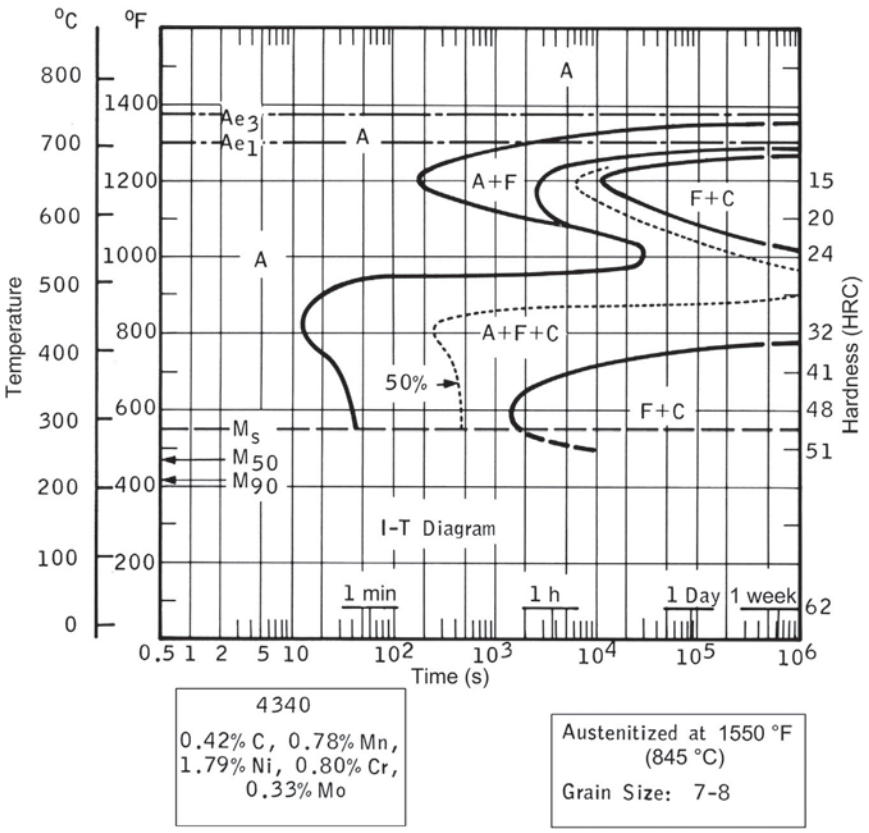

Figure 32 IT diagram for AISI 4340 steel. Reproduced from *Atlas of Isothermal Transformation and Cooling Transformation Diagrams*; ASM International: Materials Park, OH, 1980.

Austenite is stable only at elevated temperatures and martensite is formed on cooling. The cooling rate required to facilitate martensite formation is dependent on the composition of the alloy. **Figure 32** shows the line representing the temperature at which martensite transformation begins (M_s). The temperature at which 50% of the austenite was transformed to martensite is indicated by M_{50}. And M_{90} represents the point where 90% of the austenite has transformed to martensite. The M_s temperatures of many steels have been determined experimentally and they also may be approximated using one of several available empirical equations. Lines A_s and A_f are the critical temperatures that illustrate the critical temperature range where the steel is only partially austenitized. Subscripts A, F, and C indicate austenite, ferrite, and cementite, respectively.

IT diagrams can only read along the isotherms. Some heat treatments such as austempering to produce bainite microstructure and isothermal annealing may utilize IT diagrams for process design. However, this procedure is to be contrasted to that where the heat treatment involves variation of temperature with time.

12.02.5.2 Continuous Cooling Transformation Diagrams

CCT curves correlate the temperatures for each phase transformation, the amount of transformation product obtained for a given cooling rate with time, and the cooling rate necessary to obtain martensite. These correlations are obtained from CCT diagrams by using the different cooling rate curves (*43*). Using CCT curves, it is possible to determine the critical cooling rate, which is the time required to avoid formation of pearlite for the particular steel being quenched and which is normally defined as that cooling rate equivalent to, or faster than, the rate indicated by the 'nose' of the pearlite transformation curve to maximize the formation of martensite. If the temperature–time cooling curves for the quenchant and the CCT curves of the steel are plotted on the same scale, then they may be superimposed to select the steel grade, which will provide the desired microstructure and hardness for a given cooling condition (*44*). This assumption is limited to bars up to 100 mm quenched in oil and bars up to 150 mm quenched into water.

CCT diagrams may be constructed in various forms. Steel may also be continuously cooled at different specified rates using a dilatometer and the proportion of transformation products formed after cooling to various temperatures intermediate between the austenitizing temperature and the M_s temperature and these data are used to construct a CCT diagram. **Figure 33** is a CCT diagram for a steel containing 0.39% C – 1.49% Si – 1.41% Mn – 0.74% Cr – 0.51% Mo (austenitized at 885 °C for 20 min), which shows the transformation ranges under continuous cooling conditions and defines the bainite start and ferrite start half-cooling times curves for the beginning and ending of the different phase transformations.

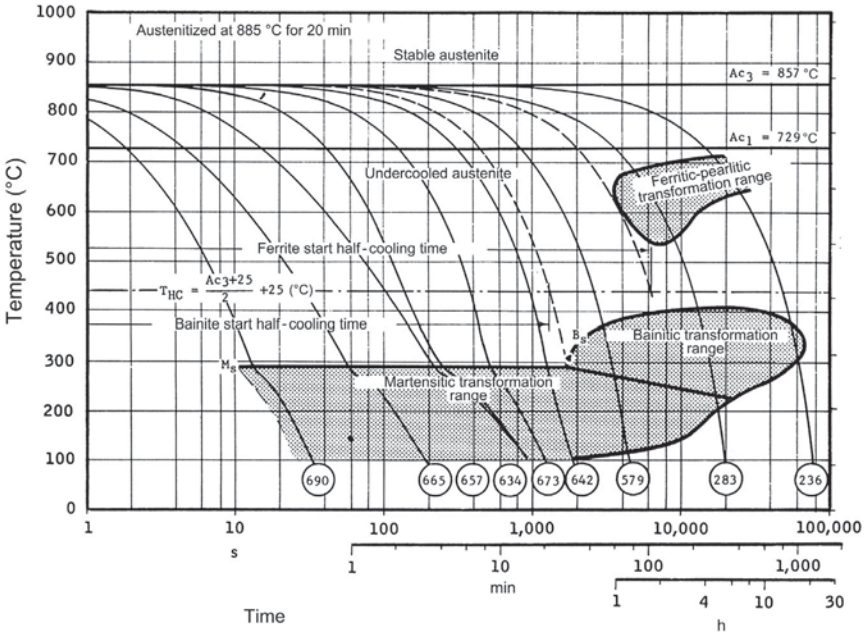

Figure 33 CCT diagram for steel containing 0.39% C – 1.49% Si – 1.41% Mn – 0.74% Cr – 0.51% Mo. Reproduced from Vatavuk, J.; Goldenstein, H. Aços Hadfield contendo carbonetos de nióbio e titânio. In *Anais do II Encontro de Tecnologia e Utilização dos Aços Nacionais. Rio de Janeiro*; ABM, COPPE (UFRJ), 18–22 de maio de 1987; pp 151–169.

There are other methods of determining a CCT diagram, such as the CCT diagram illustrated in **Figure 34** (*45*). In this case, instead using a dilatometer, the CCT curve was generated by a Jominy test bar. The corresponding Jominy curve is shown along with a diagram for a particular quenchant and agitation condition, which permits the prediction of cross-sectional hardness for a round bar (*46*).

There are a number of heat treatment processes where only the use of a CCT diagram is appropriate and for these cases, if IT diagrams are used, a wrong conclusion may be obtained. Scheil has shown that transformation begins later in time for a continuous cooling process than for an isothermal process (*47*).

Another type of CCT diagram is illustrated in **Figure 35**. The cooling curves are not shown because the diagrams are presented in terms of bar diameters. Different cooling curves would apply at the center and surface of a bar. This CCT diagram refers only to the center of a bar, but the structures at other positions can be inferred. The structures that can be expected in as-cooled bars, whether air cooled, or oil or water quenched, are indicated in each CCT diagram. In the case of **Figure 35**, the lines shown are representative of a 10 mm bar (*48*).

Furthermore:

- Since increasing the austenitizing temperature will shift the curves to longer transformation times, it is necessary to use CCT diagrams generated at the desired austenitizing temperature.
- Grain size will affect both IT and CCT diagrams and is usually specified in the diagrams. **Figure 36** shows difference in the IT diagrams for two different grain size (*49*).

Usually grain size is referred by an ASTM number (G), which is a grain size designation bearing a relationship to average intercept distance at 100 diameters magnification according to the equation:

$$G = 10.00 - 2\log_2 L \qquad [5]$$

Where L = the average intercept distance at 100 diameters magnification. The smaller the ASTM grain size, the larger the diameter of the grains. Steel chemical composition has a strong influence on IT and CCT diagrams.

The presence and amount of alloying elements will determine the ability to obtain martensite during fast cooling from the austenitizing temperature. This is designated as hardenability. **Figures 37** and **38** illustrate this by comparing CCT diagrams for two different steel compositions where both contain similar amounts of C, Si, and Mn but different amounts of Mo (*44*). Hardenability is discussed in more detail in the following section.

12.02.6 Hardenability

Hardenability is the ability of the Fe–C alloy to be hardened by forming martensite. Hardenability is not 'hardness' but a qualitative measure of the rate at which hardness decreases with distance from the surface because of decreased martensite content (*13*). High hardenability means the ability of the alloy to produce a high martensite content throughout the volume of the steel. The ability to achieve a certain hardness level is associated with the highest attainable hardness, which depends on the carbon content of the steel

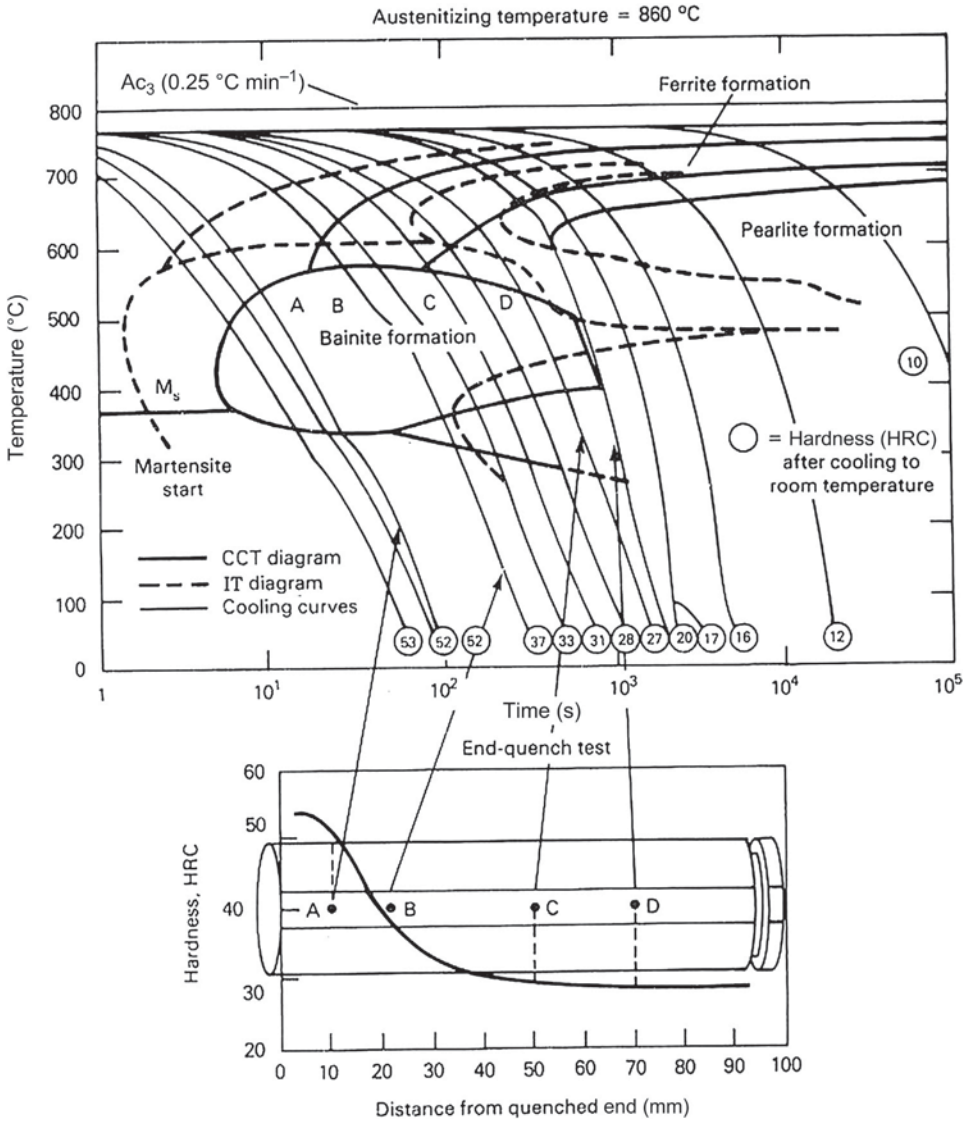

Figure 34 Experimentally determined CCT diagram (solid lines) for a DIN 42CrMo4 steel IT diagram. Numbers inside the circles are hardness values. Reproduced from Houdremont, E. Strength of Martensite. *Trans. ASM* **June 1962**, *55* (2), 347–361.

and more specifically on the amount of carbon dissolved in the austenite after austenitizing. However, with increasing carbon concentration, martensitic transformation from austenite becomes more difficult, resulting in a greater tendency for retained austenite and correspondingly lower strength. Hardenability also refers to the hardness distribution within a cross-section from the surface to the core under specified quenching conditions. It depends on the carbon content, which is interstitially dissolved in austenite and the amount of alloying elements substitutionally dissolved in the austenite during austenitization. Also, increasing carbon content influences the M_f temperature relative to M_s during rapid cooling as shown in **Figure 39** (*50*). In this figure, it is evident that for steels with carbon content above 0.6%, the transformation of austenite to martensite will be incomplete if the cooling process is stopped at 0 °C or higher.

The depth of hardening depends on the following factors:

- Size and shape of the cross-section,
- Hardenability of the material,
- Quenching conditions.

The cross-section shape exhibits a significant influence on heat extraction during quenching and, therefore, on the hardening depth. Heat extraction is dependent on the surface area exposed to the quenchant. Grain size also influences hardenability. **Figure 40** shows this relationship.

D_I means ideal critical diameter and is defined as the largest bar diameter that can be quenched to produce 50% martensite at the center after quenching in an 'ideal' quench, i.e., under 'infinite' quenching severity. The ideal quench is one that reduces surface

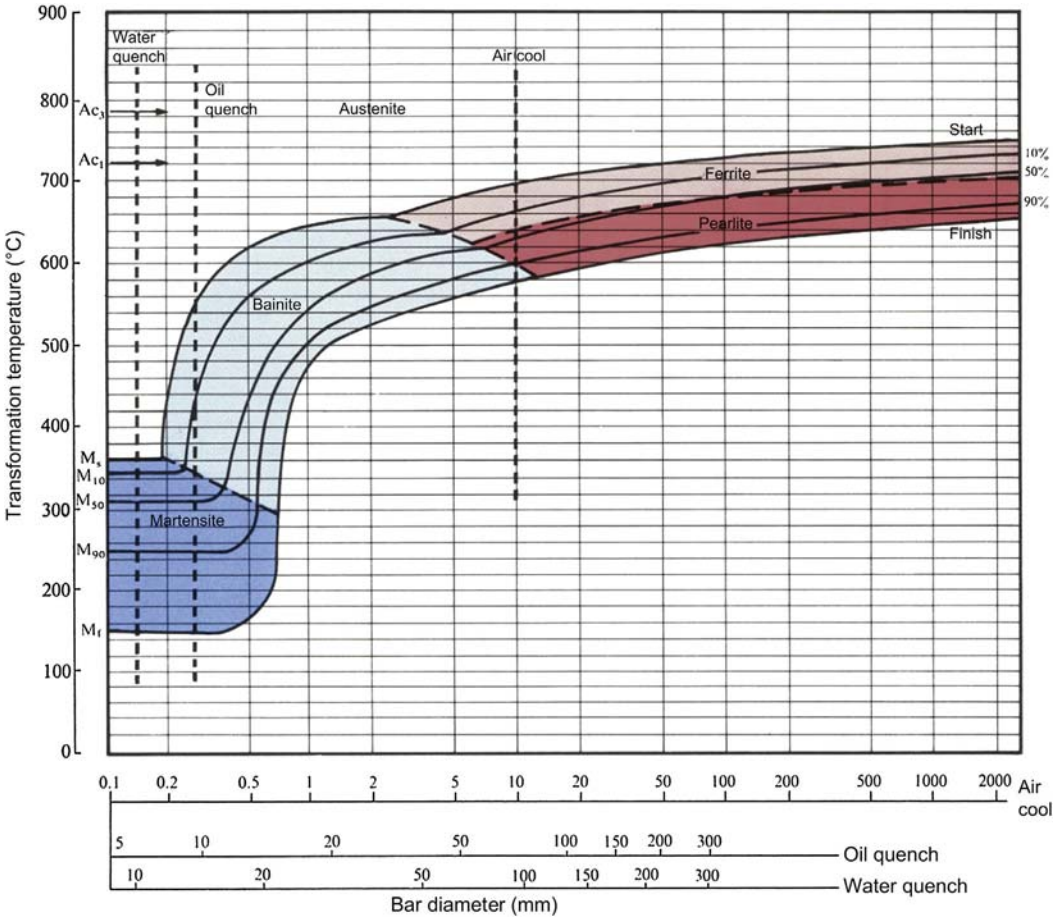

Figure 35 CCT diagram for an SAE 1040 steel. Reproduced from Atkins, M. *Atlas of Continuous Cooling Transformation Diagrams for Engineering Steels*; ASM: Metals Park, Ohio, USA; British Steel Corporation: Sheffield, England. Printed in the USA, 1980, p 260.

temperature of an austenitized steel to the bath temperature instantaneously. Under these conditions, the cooling rate at the center of the bar depends only on the thermal diffusivity of the steel (*47*). The ideal critical diameter may be calculated from:

$$D_I = D_I \text{ Base (carbon concentration and grain size)} \times \text{fMn} \times \text{fSi} \times \text{fCr} \times \text{fMo} \times \text{fV} \times \text{fCu} \times \text{fNi} \times \text{fn} \quad [6]$$

Where fn is a multiplicative factor for the particular substitutionally dissolved alloying element. These values are found in **Table 2**.

Boron exhibits an unusual effect on steel hardenability, even in low concentration (e.g., 0.001%) and is usually treated separately. The influence of boron is modified greatly by the carbon content and elements such as Ti and N in low concentrations. The main effect on this element is retarding the formation of primary ferrite and pearlite, and it exhibits a low effect on the bainite transformation rate (*51*).

The effect of quenching conditions on the depth of hardening is dependent not only on the quenchant being used and its physical and chemical properties but also on process parameters such as bath temperature and agitation.

There are numerous methods to estimate steel hardenability and the two most common are Grossmann hardenability and Jominy curve determination.

12.02.6.1 Grossmann Hardenability

Grossmann's method of measuring hardenability uses a number of cylindrical steel bars of different diameters hardened in a given quenching medium (*30*). After sectioning each bar at midlength and metallographic examination, the bar with 50% martensite at its center is selected and the diameter of this bar is designated as the critical diameter D_{crit}. Other bars with diameters smaller than D_{crit} will possess more martensite and correspondingly higher hardness values and bars with diameters larger than D_{crit} will contain 50% martensite only up to a certain depth as shown in **Figure 41** (*13*). The D_{crit} value is valid only for the quenching medium and conditions used to determine this value. To determine the hardenability of a steel independent of the quenching medium, Grossmann introduced the term ideal critical diameter, D_I, which was defined previously.

To identify a quenching medium and its condition, Grossmann introduced the quenching intensity (severity) value H. **Table 3** provides a summary of Grossmann H-values for different quenching media and different quenching conditions (*52*). Although

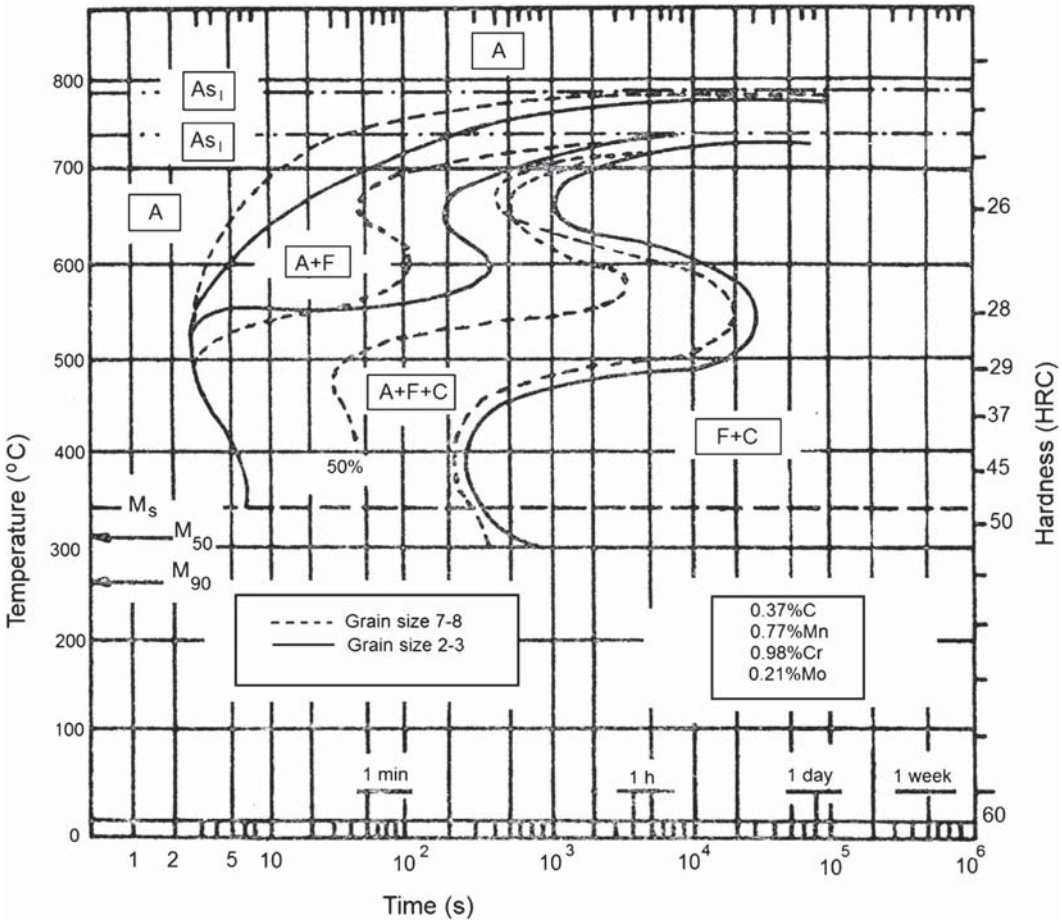

Figure 36 IT diagrams for ASTM 2–3 grain size and ASTM 7–8 grain size. Adapted from Pereira, R. L. *Tratamentos Térmicos dos Metais*. 3rd ed.; Escola de Engenharia de São Carlos, Universidade de São Paulo, 1979, p 422.

these data have been published in numerous reference texts for many years, they are of relatively limited quantitative value. One of the most obvious reasons is that quenchant agitation is not adequately defined and is often unknown, yet it exhibits enormous effects on quench severity.

There is a correlation between D_{crit} and D_I as shown in **Figure 42**. Once quench severity is known, this graph permits the interconversion of D_{crit} and D_I (*53*).

12.02.6.2 Jominy Curves

Jominy bar end-quench test is the most familiar and commonly used procedure for measuring steel hardenability. This test has been standardized and is described in ASTM A 255, SAE J406, DIN 50191, and ISO 642. For this test, a 100 mm (4 in.) long by 25 mm (1 in.) diameter round bar is austenitized to the proper temperature, dropped into a fixture, and one end rapidly quenched with 24 °C (75 °F) water from a 13 mm (0.5 in.) orifice under specified conditions (*54*). The austenitizing temperature is selected according to the specific steel alloy being studied; however, most steels are heated in the range of 870–900 °C (1600–1650 °F).

In the Jominy end-quench test, a cylindrical specimen is heated to the desired austenitizing temperature and well-defined time, which is material composition dependent, and then it is quenched at one end with water. The cooling velocity decreases with increasing distance from the quenched end. After quenching, parallel flats are ground on opposite sides of the bar and hardness measurements made at 1/16 in. (1.6 mm) intervals along the bar, as illustrated in **Figure 43** (*30*).

Hardness as a function of distance from the quenched end is measured and plotted and, together with measurement of the relative areas of the martensite, bainite, and pearlite that is formed, it is possible to compare the hardenability of different steels using Jominy curves. As the slope of the Jominy curve increases, the ability to harden the steel (hardenability) decreases. Conversely, decreasing slopes (or increasing flatness) of the Jominy curve indicate increasing hardenability (ease of hardening). **Figure 44** illustrates that steel hardenability is dependent on the steel chemistry, that unalloyed steels exhibit poor hardenability, and that Jominy curves provide an excellent indicator of relative steel hardenability (*1*).

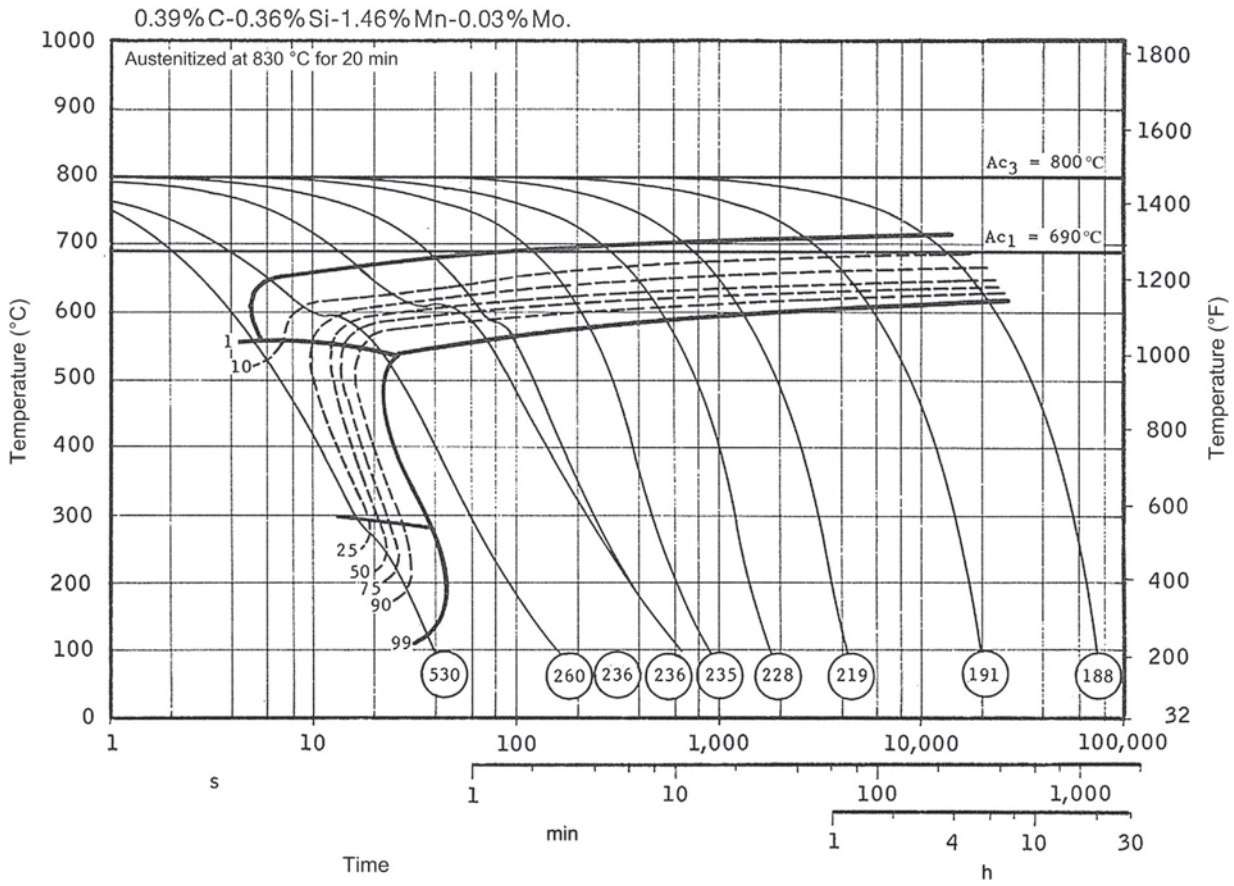

Figure 37 CCT diagram for a steel containing 0.39% C – 0.36% Si – 1.46% Mn – 0.03% Mo.

Hardenability is susceptible to minor changes in composition. An interesting example is a 24 cm diameter axle manufactured with an SAE 4340 steel. The longitudinal section (near the core) showed a banded microstructure as shown in Figure 45. This component was austenitized at 880 °C, oil quenched (60 °C), and tempered at 630 °C (*55*).

A similar situation was observed in all sections: near the surface, in the middle of the radius, and in the core, as shown in Figure 45. An estimated band thickness shows values about 200 μm, wide enough to conglomerate many austenite grains with sizes of about 40 μm. In metallurgical terms, it looks like two different steels. Analysis of the composition of the dark areas and the white areas was performed. The D_I value was calculated for both compositions. This calculation was made using multiplicative factors and Table 2. It was found that for the dark area the $D_I = 375$ mm and for the white areas the $D_I = 137$ mm. This means that within the same component, due the banding, hardenability is very different when promoting martensite formation in the core (although D_I for the steel composition is 176 mm) and bainite in the surface, an atypical microstructure distribution.

Quenchant selection for a particular steel is dependent on the hardenability of the steel being hardened. For through-hardened steels, this is relatively straightforward and procedures such as Jominy hardenability characterization can usually be readily applied. For carburized steels, this is considerably more complex since the hardenability of the case is substantially different from the hardenability of the core.

12.02.7 Tempering

Tempering is a term historically associated with the heat treatment of martensite in steels to change the microstructure and mechanical properties by holding the steel component isothermally at a temperature below which austenite cannot form. When steel is hardened the as-quenched martensite not only is very hard but also has low toughness. Tempering, also known as 'drawing,' is the thermal treatment of hardened and normalized steels to obtain improved toughness and ductility, lower hardness, and improved dimensional stability. During tempering, solid-state reactions occur and the as-quenched martensite is transformed into tempered martensite, which, at higher tempering temperatures, is composed of highly dispersed spheroids of cementite (carbides) dispersed in a soft matrix of ferrite, resulting in reduced hardness and increased toughness. The objective is to allow hardness to decrease to the desired level and then to stop the solid-state reactions as the sequence of carbide precipitation by cooling. The extent of the tempering effect is determined by the temperature and time of the process (*56*).

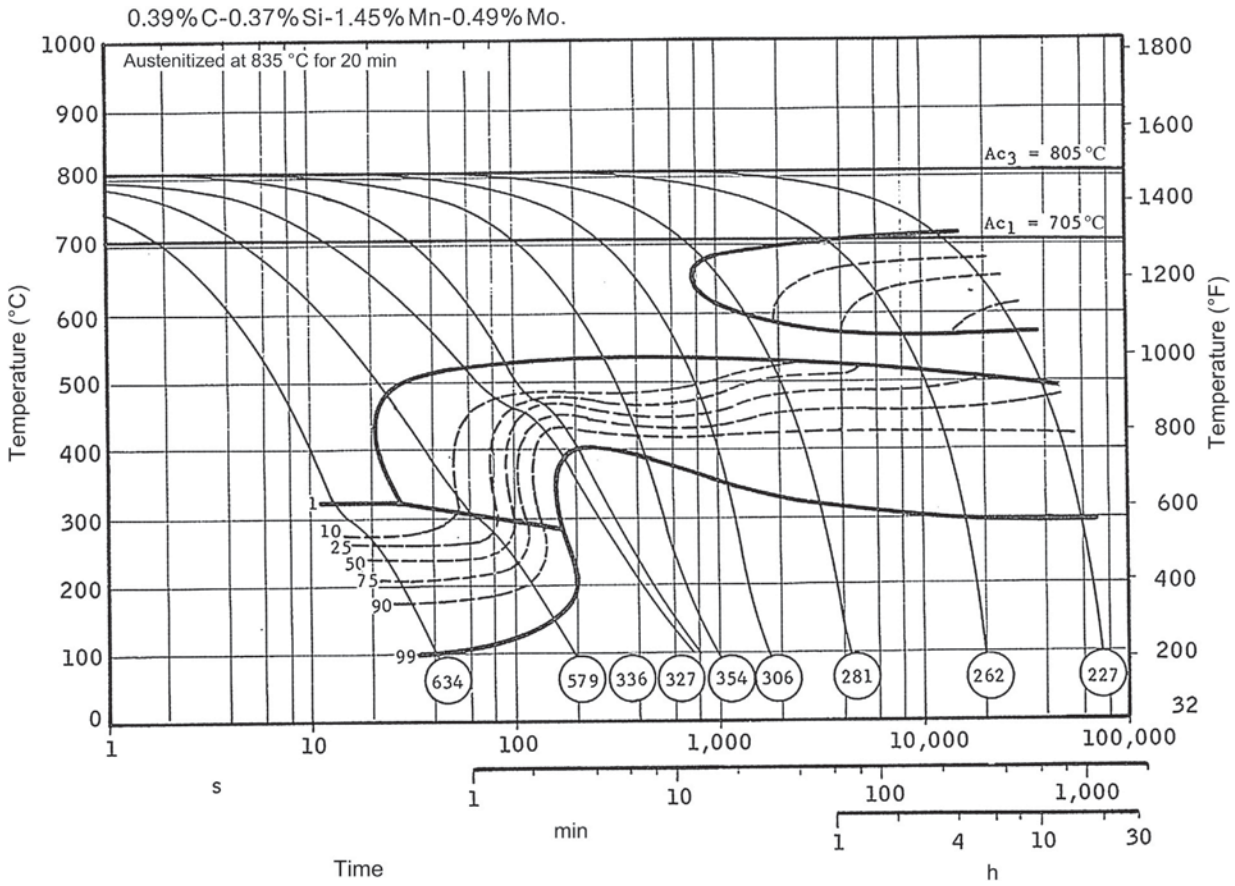

Figure 38 CCT diagram for a steel containing 0.39% C – 0.37% Si – 1.45% Mn – 0.49% Mo.

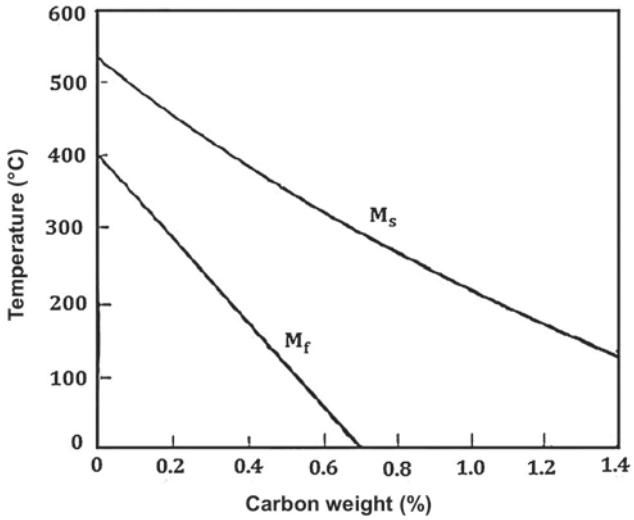

Figure 39 Influence of the carbon content in steels on the temperature of the start of martensite formation (M_s) and the end of martensite formation (M_f).

The tempering process may be conducted at any temperature up to the lower critical temperature (Ac1). When steel is tempered in air, the heated oxide film on the surface of the steel exhibits a color, known as 'tempering color,' which is characteristic of the surface temperature. Table 4 provides a summary of characteristic surface temperatures for tempering and their colors (*57*).

Figure 46 illustrates the effect of carbon content and tempering temperature on hardness of carbon steels (*58*). The specific tempering conditions that are selected are dependent on the desired strength and toughness.

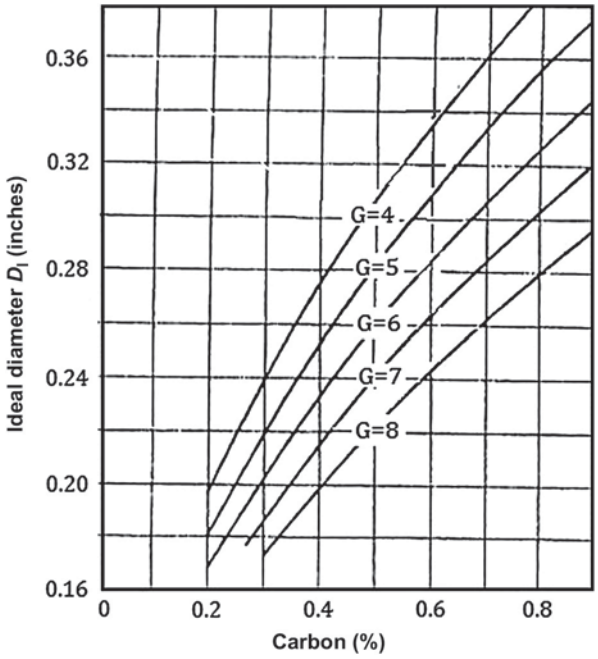

Figure 40 Influence of grain size (ASTM number) in the hardenability (D_I).

Table 2 Hardenability factors for carbon content, grain size, and selected alloying elements in steel

	Carbon grain size no.			*Alloying element*				
Alloy content (%)	*6*	*7*	*8*	*Mn*	*Si*	*Ni*	*Cr*	*Mo*
0.05	0.0814	0.0750	0.0697	1.167	1.035	1.018	1.1080	1.15
0.10	0.1153	0.1065	0.0995	1.333	1.070	1.036	1.2160	1.30
0.15	0.1413	0.1315	0.1212	1.500	1.105	1.055	1.3240	1.45
0.20	0.1623	0.1509	0.1400	1.667	1.140	1.073	1.4320	1.60
0.25	0.1820	0.1678	0.1560	1.833	1.175	1.091	1.54	1.75
0.30	0.1991	0.1849	0.1700	2.000	1.210	1.109	1.6480	1.90
0.35	0.2154	0.2000	0.1842	2.167	1.245	1.128	1.7560	2.05
0.40	0.2300	0.2130	0.1976	2.333	1.280	1.146	1.8640	2.20
0.45	0.2440	0.2259	0.2090	2.500	1.315	1.164	1.9720	2.35
0.50	0.2580	0.2380	0.2200	2.667	1.350	1.182	2.0800	2.50
0.55	0.273	0.251	0.231	2.833	1.385	1.201	2.1880	2.65
0.60	0.284	0.262	0.241	3.000	1.420	1.219	2.2960	2.80
0.65	0.295	0.273	0.251	3.167	1.455	1.237	2.4040	2.95
0.70	0.306	0.283	0.260	3.333	1.490	1.255	2.5120	3.10
0.75	0.316	0.293	0.270	3.500	1.525	1.273	2.62	3.25
0.80	0.326	0.303	0.278	3.667	1.560	1.291	2.7280	3.40
0.85	0.336	0.312	0.287	3.833	1.595	1.309	2.8360	3.55
0.90	0.346	0.321	0.296	4.000	1.630	1.321	2.9440	3.70
0.95	–	–	–	4.167	1.665	1.345	3.0520	–
1.00	–	–	–	4.333	1.700	1.364	3.1600	–

Figure 47 shows other modifications of mechanical properties that occur when an oil-quenched AISI 4340 steel is tempered at temperatures above 200 °C (*59*).

Typically, tempering times are a minimum of approximately 1 h. Thelning has reported a 'rule of thumb' of 1–2 h in.$^{-1}$ of section thickness after the load has reached a preset temperature (*60*) After heating, the steel is cooled to room temperature in still air. The recommended tempering conditions, in addition to recommended heat treating cycles, for a wide range of carbon and alloy steels are provided in SAE AMS 2759. In some manufacturing circumstances, rapid cooling processes can be applied after tempering treatment to obtain a tangential compressive residual state of stresses on the component surface with acceptable distortion.

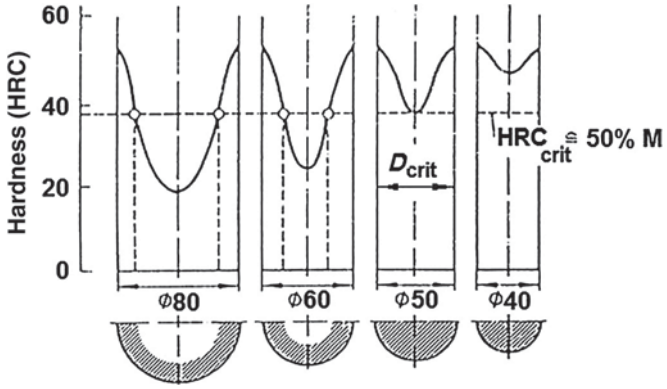

Figure 41 Determination of critical diameter D_{crit} according to Grossmann.

Table 3 Effect of agitation on quench severity as indicated by Grossmann quench severity factors (H-factors)

	Grossmann H-factor		
Agitation	*Oil*	*Water*	*Caustic soda or brine*
None	0.25–0.3	0.9–1.0	2
Mild	0.30–0.35	1.0–1.1	2–2.2
Moderate	0.35–0.4	1.2–1.3	–
Good	0.4–0.5	1.4–1.5	–
Strong	0.5–0.8	1.6–2.0	–
Violent	0.8–1.1	4	5

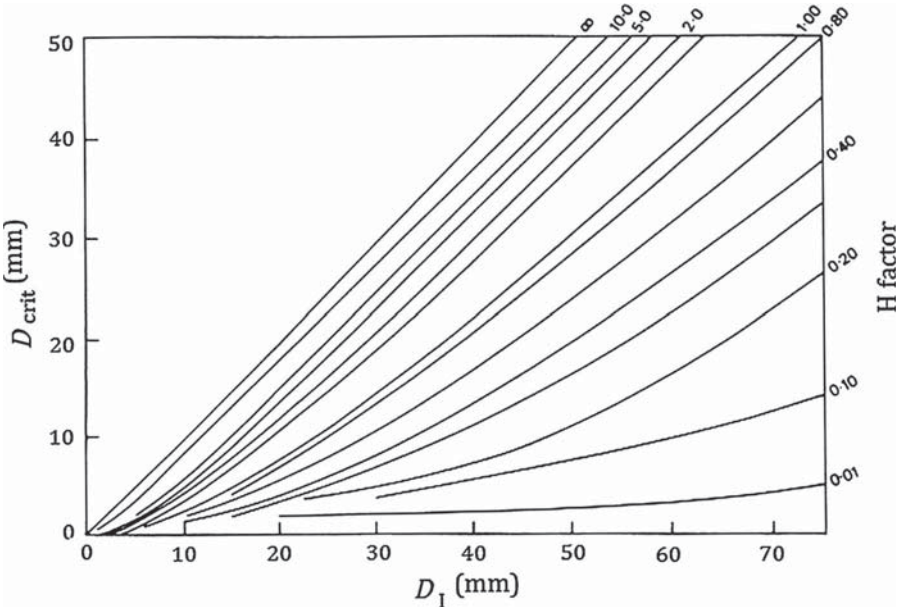

Figure 42 Chart correlating D_{crit}, D_I, and quench severity (H).

Tempering times and temperatures may also be calculated by various methods. One of the more common methods is to use the Larsen–Miller equation. The Larsen–Miller equation, although originally developed for prediction of creep data, has been used successfully for predicting the tempering effect of medium/high-alloy steels (*61*).

The interrelationship between tempering temperature, time, and steel chemistry has been reported by Spies (*62*):

$$HB = 2.84H_h + 75(\%C) - 0.78(\%Si) + 14.24(\%Mn) + 14.77(\%Cr) + 128.22(\%Mo) - 54.0(\%V) - 0.55T_t + 435.66 \quad [7]$$

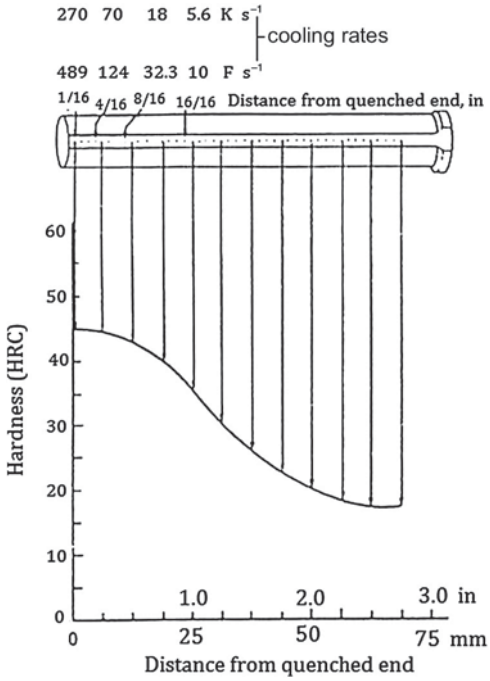

Figure 43 Measuring hardness on the Jominy test specimen and plotting hardenability curves. Reproduced from Sverdlin, A. V.; Ness, A. R. Fundamental Concepts in Steel Heat Treatment: Chapter 1. In *Steel Heat Treatment Handbook*; Totten, G. E., Howes, M. A. H., Eds.; Marcel Dekker, Inc.: New York, NY, 1997; pp 1–44.

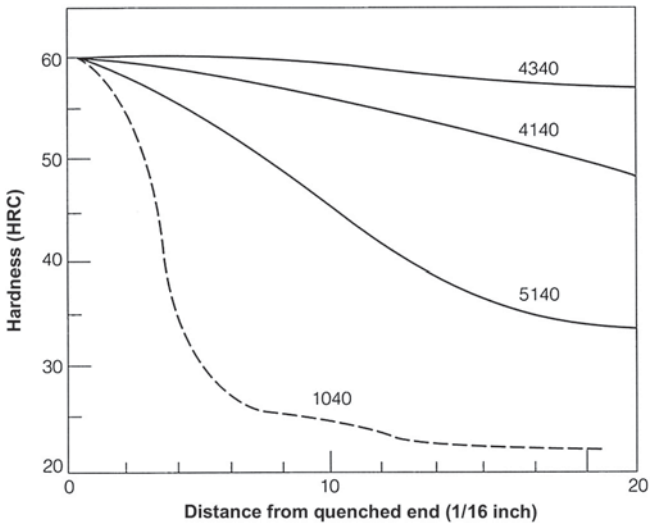

Figure 44 Jominy curve comparison of the hardenability of different steels, alloyed and unalloyed. Adapted from Askeland, D. R. *The Science and Engineering of Materials*, 4th ed.; PWS Publishing Company: Boston, 1989.

Where:

HB is the Brinell hardness after hardening and tempering,
H_h is the Rockwell (HRC) hardness after hardening,
T_t is the tempering temperature in °C.
OBS: This equation was developed for the following conditions:

$$H_h = 20 - 65\text{HRC},\quad T_t = 500 - 600°\text{C}\ \text{and}\ \text{C} = 0.20 - 0.54\%,\ \text{Si} = 0.17 - 1.40\%,\ \text{Mn} = 0.50 - 1.90\%,\ \text{Cr} = 0.03 - 1.20\% \quad [8]$$

An average relationship between hardness after hardening (H_h) and hardness after hardening and tempering (H_t) can be obtained from:

$$H_h = (T_t/167 - 1.2)H_t - 17\quad (\text{HRC}) \quad [9]$$

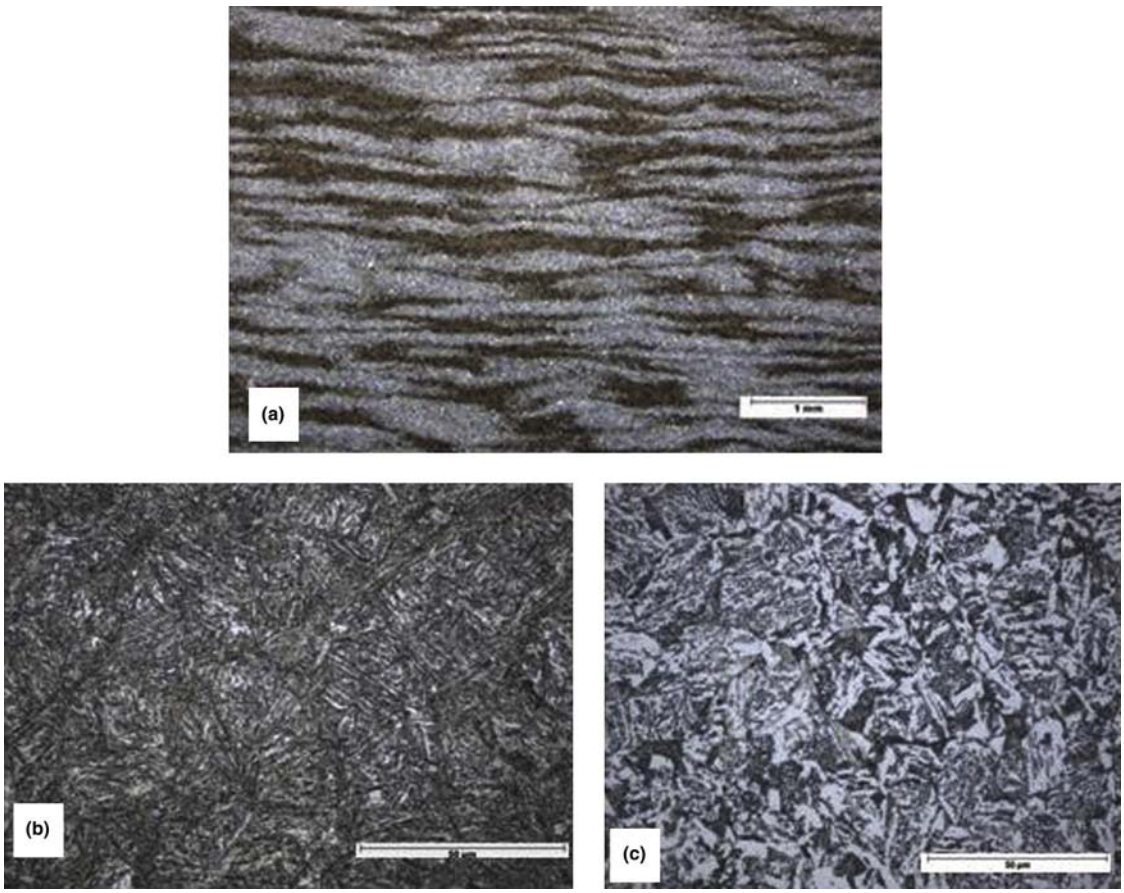

Figure 45 Aspect of the cross-section close to the core (a). Dark areas present tempered martensite (as evident on (b)) while lighter regions are compound by a mixture of microstructures, mainly bainite, as shown in (c). Nital 2% etched.

Table 4 Colors of tempering heats

(°F)[a]	(°C)[a]	Color of oxides	(°F)[b]	(°C)[b]
370	188	Faint yellow	460	238
390	199	Light straw	510	265
410	210	Dark straw	560	293
430	221	Brown	610	321
450	232	Purple	640	337
490	254	Dark blue	660	349
510	265	Light blue	710	376

[a]*Temp. held for 1 h.*
[b]*Temp. held for 8 min.*

Where:

H_t = hardness after hardening and tempering (HRC),
T_t = tempering temperature (°C).

This equation is valid for 490 °C < T_t < 610 °C and for a tempering time of 1 h.

The tempering temperature for a specified hardness after hardening and tempering is also possible to calculate when chemical composition and the degree of hardening are known (*55*):

$$T_t = 647\left[S\left(60\sqrt{C}+20\right)/H_t - 0.9\right]1/4 - 3.45\,SH_t + (537-561S)(\%C) + 505S(\%V) + 219S(\%Mo) + 75S(\%Cr) + 66S(\%Si) - 51 \quad (^\circ C) \qquad [10]$$

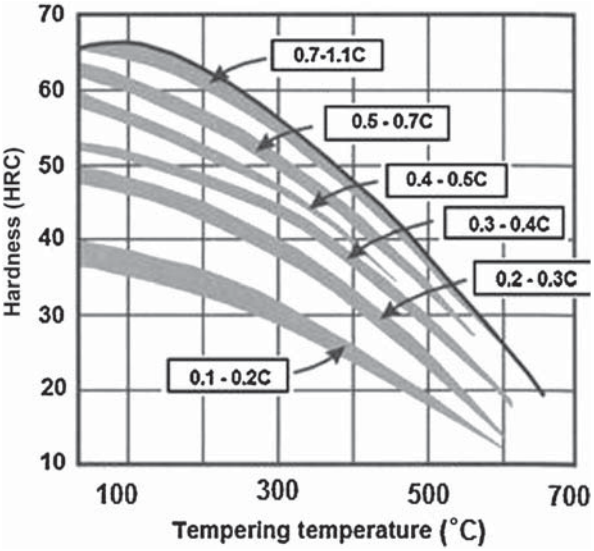

Figure 46 Effect of carbon content in the hardness of tempered plain steels. Adapted from Seco/Warwick. *Heat Treating Data Book*, 8th ed.; Seco/Warwick Corporation: USA, 2000, p 96.

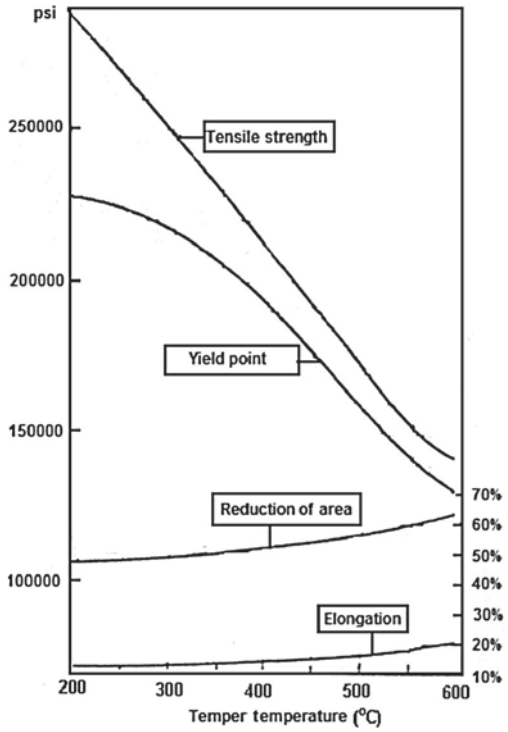

Figure 47 Changes in the mechanical properties of the AISI 4340 steel with the tempering temperature. Reproduced from Krauss, G. Tempering of Steel. In *Principles of Heat Treatment of Steel*; ASM International: Materials Park, OH, USA, 1980; pp 187–227 (chapter 8).

where:

H_t = hardness after hardening and tempering (HRC),
S = degree of hardening, $S \leq 1.0$; and alloying elements are given in weight percent.

This equation is valid for a tempering time of 2 h.

12.02.7.1 Tempering Reactions

Tempering is a process where the microstructure approaches equilibrium under thermal activation. It follows that the tendency to temper depends on how far the starting microstructure deviates from equilibrium (*63*).

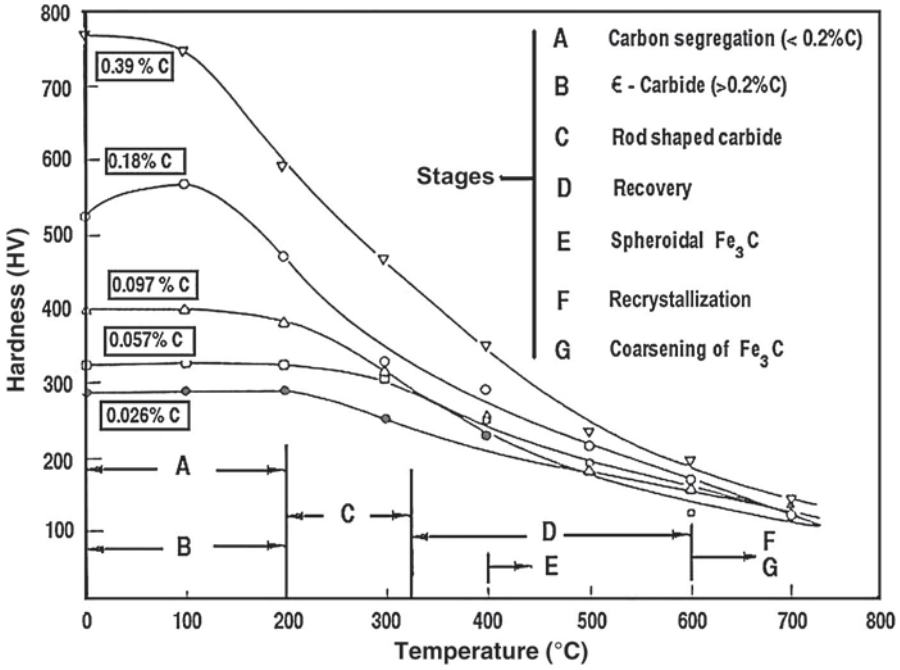

Figure 48 Hardness as function of tempering temperature for plain carbon steels. Reproduced from Speich, G. R.; Leslie, W. C. Tempering of Steel. *Metall. Trans.* **May 1972**, *3* (5), 1043–1054.

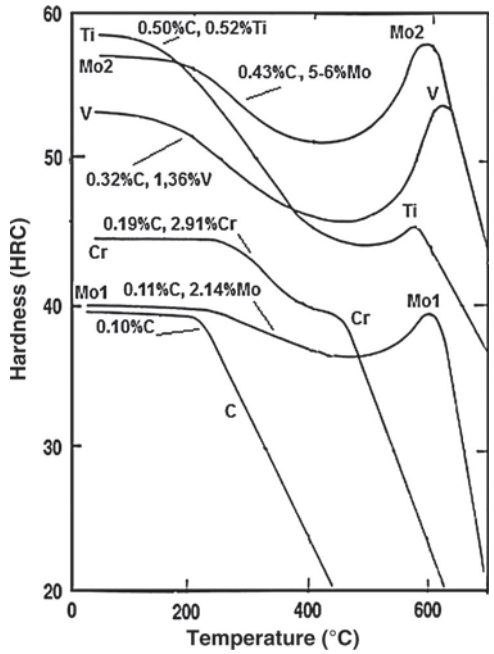

Figure 49 Effects of Ti, V, Cr, and Mo on the tempering hardness behavior. Reproduced from Speich, G. R.; Leslie, W. C. Tempering of Steel. *Metall. Trans. May 1972*, *3* (5), 1043–1054.

During tempering, the martensitic structure is subjected to a sequence of solid-state reactions often superposed, defined as temper stages (*32*,*59*,*63*). These processes involve carbon segregation, carbide precipitation, retained austenite decomposition, and recrystallization of martensitic structure.

Stage 1 – In high-carbon steels, precipitation of excess carbon begins with the formation of a transition carbide, such as ε-carbide ($Fe_{2.4}C$) or η-carbide (Fe_2C), which can grow at temperatures as low as 50 °C. This stage begins at room temperature extending until 250 °C. The ratio between the ε-carbides and ferrous structure is due to a precipitation-hardening effect of martensite in high-C steels that are tempered between 50 and 100 °C.

Stage 2 – Tempering at higher temperatures, in the range 200–300 °C for 1 h, induces retained austenite to decompose into a mixture of cementite and ferrite. When austenite is present as a film, cementite also precipitates as a continuous array of particles that have the appearance of a film (*32,59,63*). The martensite of steels with less than 0.5% of C contains retained austenite ranging from less than 2% up to 6% for 0.8% C steels. There are some indications that austenite decomposes into ferrite and cementite, but at present there is no consensus if this structure can be correlated to the lower bainite, typically present from isothermal decomposition of austenite in the temperature range of 230–300 °C.

Stage 3 – Tempering at even higher temperatures leads to a coarsening of the cementite particles, with those located at the plate boundaries growing at the expense of the intraplate particles. This precipitation is responsible for the embrittlement phenomenon observed between the temperatures of 250 and 400 °C and can be avoided by Si addition, because it is an element insoluble in cementite, just allowing the cementite formation at temperatures where the Si diffusion occurs. That is considered a slow process because this alloy element is substitutional. The Si accumulated in the ferrous matrix adjacent to Fe_3C carbide in the growing process increases the C activity in this region by decreasing the C flow to the growing particle and consequently reducing its growth velocity (*33,64,65*). This reaction begins to occur at temperatures on order of 100 °C, indicating the interposition between the tempering stages. It is possible to assume that at temperatures between 260 and 360 °C, the kinetic reactions are higher.

Cementite can also be observed during quenching when the M_s temperature is elevated as is the case of a steel with low C content, mainly in the martensite formed immediately below M_s temperature. This phenomenon is known as self-tempering (*32*). In carbon steels, *Stage 3* marks the end of the tempering process unless the steel is tempered for a long time or if it is subjected to an excessively high tempering temperature. When this occurs, cementite growth corresponds to the coalescence of this carbide and is sometimes called *Stage 4* of tempering (*6*).

In a general way, the inflection point of the curve relating hardness with tempering time is an indication that a new metallurgical process is being initiated. The effect of the tempering temperature for steels with increasing carbon contents can be inferred in **Figure 48**.

In low-carbon martensite, epsilon carbide appears only during the tempering reaction when the carbon content is greater than 0.2%. The high dislocation density of the lath martensite consumes at least 0.2% of the carbon due to segregation along dislocation lines (*36*).

Alloyed steels may have another stage where precipitation of alloy carbides including M_2C (Mo-rich), M_7C_3, M_6C, $M_{23}C_6$ (Cr-rich), V_4C_3, and TiC, etc., occurs, where the M refers to a combination of metal atoms. However, all of these carbides require long-range diffusion of substitutional atoms. They can only precipitate when the combination of time and temperature is sufficient to allow this diffusion. Alloy carbides grow at the expense of less stable cementite. If the concentration of strong carbide-forming elements such as Mo, Cr, Ti, V, and Nb is large, then all of the carbon can be accommodated in the alloy carbide, thereby completely eliminating cementite. **Figure 49** illustrates the effect of alloying elements on the hardness as a function of tempering temperature in carbon steels (*36*).

Hardness increased with additions of Ti, V, Mo, and Cr, is related to alloy carbide precipitation. This phenomenon is common for tool steels and can affect their toughness. However, Nb additions do not present the same effect. The absence of the Nb effect is related to its low solubility in austenite, and the principal effect is the precipitation of stable primary carbides whose shape depends on the addition of other elements such as titanium. Alloying elements are added to ensure improved performance of different steel grades, especially tool steels. When considering alloy design, effects such as precipitation-hardening effects, solid solubility at different temperatures, hardenability characteristics, carbon consumption during formation, and its characteristics during solidification must be considered. The concept of steel matrix must be considered if alloy development is based on an existing steel grade. Even the matrix composition must be considered since it is directly related to the austenitizing temperature. As the austenitizing temperature increases, different carbides, even those that are more stable, begin to dissolve, which consumes part of the matrix composition. Niobium, which can be useful for improving wear resistance, for example, forms a hard carbide since its solubility in the ferrous matrix is negligible, even at high austenitizing temperatures, with a low influence in the other solid-state reactions, which indicates a low impact in conventional heat treating routes. As for plain carbon steel, hardness decreases with increasing tempering temperature. Consequently, the yield strength and tensile strength decrease as well. However, elongation at fracture and ductility increases as well.

References

1. Askeland, D. R. *The Science and Engineering of Materials*, 4th ed.; PWS Publishing Company: Boston, 1989.
2. Eisenhüttenleute, V. J. *Steel: A Handbook for Material Research and Engineering*. Springer-Verlag: Berlin, Heidelberg, New York, Tokyo; Verlag Stahlesien mbH Düsseldorf, 1991, 1992; Vol. 1.
3. Capudean, Bob. *Carbon Content, Steel Classifications and Alloy Steels*, August 28, 2003. http://www.thefabricator.com/Metallurgy/Metallurgy_Article.cfm?ID=685.
4. Bottrel Coutinho, C. *Materiais Metálicos para Engenharia;* Fundação Christiano Ottoni. Escola de Engenharia da Universidade Federal de Minas Gerais, 1992. p 405.
5. Washko, S. D.; Aggen, G. *Properties and Selection: Irons, Steels, and High-Performance Alloys*; In: *ASM Handbook*. 10th ed.; 2009; Vol. 1, p 2521.
6. Honeycombe, R. W. K. *Steel Microstructure and Properties*, 2nd ed.; Edward Arnold (Publishers) Ltd: London, 1995. p 324.
7. Goldenstein, H.; Vatavuk, J. Aço ferramenta para trabalho a frio contendo carbonetos de nióbio. In *Anais do XXXIX Congresso da ABM Belo Horizonte, MG* **1984,** *2*. pp 337–387.
8. Salgado, L.; Ambrozio Filho, F.; Vatavuk, J.; Rossi, J. F. *A metalurgia do pó aplicada à indústria automobilística*. SAE USA Technical Paper N° 982961, 1998, pp 1–8.
9. http://www.engineershandbook.com/Tables/carbonsteelalloys.htm.
10. Budinski, K. G.; Budinski, M. K. *Engineering Materials – Properties and Selection*, 7th ed.; Prentice Hall: Upper Saddle River, NJ, 2002, (chapters 8–16).

11. Higgins, R. A. *Engineering Metallurgy. Part 1. Applied Physical Metallurgy,* 5th ed.; Robert E. Krieger Publishing Company: Malabar, FL, 1983. p 559.
12. Colpaert, H. Micrografia. In *Metalografia dos Produtos Siderúrgicos Comuns;* Paulo, São, Blücher, Edgard, Eds., 3rd ed.; da Universidade de São Paulo, 1974; pp 121–198. Capítulo 3.
13. Davis, J. R. *ASM Materials Engineering Dictionary;* ASM International: Materials Park, OH, 1992.
14. Tarney, E. Heat Treatment of Tool Steels. *Tool. Prod.* **May 2000,** 102–104.
15. Horstmann, D. Das Zustandsschaubild Eisen-Kohlenstoff. In *Bericht des Werkstoffausschusses des Vereins Deutscher Eisenhüttenleute Nr. 180,* 6. Aufl.; Verlag Stahleisen, 1985.
16. Rose, A.; Schrader, A. *De Ferri Metallographia;* Verlag Stahleisen mbH Düsseldorf, 1966; Vol. 2 (the text is written in English, French and German).
17. Narazaki, M.; Totten, G. E. Classification and Mechanisms of Steel Transformation. Steel Heat Treatment: Metallurgy and Technologies. In *Steel Heat Treatment Handbook;* Totten, G. E., Ed., 2nd ed.; CRC Press Taylor & Francis Group: Boca Raton, FL, 2007; pp 91–120 (chapter 2).
18. ASM Handbook; Metallography and Microstructures, Vandervoort, G. R., Ed.; ASM International: Materials Park, OH, 2004; Vol. 9, p 1184.
19. Geels, K.; Fowler, D. B.; Kopp, W-U.; Ruckert, M. *Metallographic and Materialographic Specimen Preparation, Light Microscopy, Image Analysis and Hardness Testing;* ASTM International: West Conshohocken, 2007; p 727.
20. Hougardy, H. *Umwandlung and Gefüge unlegierter Stähle, eine Einführung;* Verlag Stahleisen mbH Düsseldorf, 1990.
21. Reed Hill, R. E. *Physical Metallurgy Principles,* 2nd ed.; D. Van Nostrand Company: New York, NY, USA, 1973; p 919.
22. Hume-Rothery, W. *Estrutura das Ligas de Ferro;* Editora Edgar Blücher Ltda. Editora da Universidade de São Paulo, 1968; p 214.
23. Lakhtin, Y. *Engineering Physical Metallurgy* (translated from the Russian by Nicholas Weinstein), 2nd ed.; Mir Publishers: Moscow, 2009; p 471.
24. Hillert, M.; Purdy, G. R. On the Misuse of the Term Bainite. *Scr. Mater.* **2000,** *43,* 831–833.
25. Bain, E. C.; Paxton, H. W. *Alloying Elements in Steel;* ASM: Metals Park, OH, 1966; p 291.
26. Vatavuk, J.; Santos, D. *Estudo das transformações bainíticas*, Scientific Report; Laboratório de Engenharia dos Materiais, Universidade Presbiteriana Mackenzie, 2008; p 15.
27. Kral, M. V.; Mangan, M. A.; Rosemberg, R. O.; Spanos, G. *Three Dimensional Analysis of Microstructure;* U.S. Naval Research Laboratory. Department of the Navy, 1999; p 7.
28. Shewmon, P. G. *Transformation in Metals. Materials Science and Engineering Series;* Mc Graw-Hill Book Company: USA, 1969; p 393.
29. Bain, E. C. The Nature of Martensite. *Trans. AIME* **1924,** *70,* 25–46.
30. Sverdlin, A. V.; Ness, A. R. Fundamental Concepts in Steel Heat Treatment: Chapter 1. In *Steel Heat Treatment Handbook;* Totten, G. E., Howes, M. A. H., Eds.; Marcel Dekker, Inc.: New York, NY, 1997; pp 1–44.
31. Marder, A. R.; Krauss, G. The Morphology of Martensite in Iron-Carbon Alloys. *Trans. ASM* **1967,** *60,* 651–660.
32. Speich, G. R. *Trans. Metall. Soc. Am. Inst. Mech. Eng.* **1969,** *245* (12), 2553–2564.
33. Nakada, N.; Tsuchiyama, T.; Takaki, S.; Miyano, N. Temperature Dependence of Austenite Nucleation Behavior from Lath Martensite. *ISIJ Int.* **2011,** *51* (2), 299–304.
34. Morito, S.; Saito, H.; Ogawa, T.; Furuhara, T.; Maki, T. Effect of Austenite Grain Size on the Morphology and Crystallography of Lath Martensite in Low Carbon Steels. *ISIJ Int.* **2005,** *45* (1), 91–94.
35. Morito, S.; Yoshida, H.; Maki, T.; Huang, X. Effect of Block Size on the Strength of Lath Martensite in Low Carbon Steels. *Mater. Sci. Eng. A* **2006,** *438–440,* 237–240.
36. Speich, G. R.; Leslie, W. C. Tempering of Steel. *Metall. Trans.* **May 1972,** *3* (5), 1043–1054.
37. Herring, D. H. Martensite. *Ind. Heat.* **June 2011,** 18–20.
38. Speich, G. R.; Leslie, W. C. Tempering of Steel. *Metall. Trans.* **May 1972,** *3* (5), 1043–1054 (tens of Angstroms).
39. Narazaki, M.; Totten, G. E.; Webster, G. M. Hardening by Reheating and Quenching. In *Handbook of Residual Stress and Deformation;* Totten, G. E., Howes, M., Inoue, T., Eds.; ASM International: Materials Park, OH, USA, 2002; p 499.
40. Kelly, A.; Nicholson, R. B. *Strengthening Methods in Crystals. Materials Science Series;* Applied Science Publishers Ltd: London, 1971, (printed in Great Britain by Galliard Limited, Great Yarmouth, England).
41. Vatavuk, J.; Goldenstein, H. Aços Hadfield contendo carbonetos de nióbio e titânio. In *Anais do II Encontro de Tecnologia e Utilização dos Aços Nacionais. Rio de Janeiro;* ABM, COPPE (UFRJ), 18–22 de maio de 1987; pp 151–169.
42. *Atlas of Isothermal Transformation and Cooling Transformation Diagrams;* ASM International: Materials Park, OH, 1980.
43. Rose, A.; Strassburg, W. Anwendung des Zeit-Temperatur-Umwandlungs-Schaubildes für kontinuierliche Abkülung auf Fragen der Wärmbehandlung. *Arch. Eissenhüttenwes.* **1953,** *24* (11/12), 505–514.
44. Cias, W. W. *Austenite Transformation Kinetics of Ferrous Alloys;* Climax Molybdenum Company, 1978, p 83.
45. Houdremont, E. Strength of Martensite. *Trans. ASM* **June 1962,** *55* (2), 347–361.
46. Totten, G. E.; Bates, C. E.; Clinton, N. A. Measuring Hardenability and Quench Severity. In *Quenchants and Quenching Technology;* ASM International: Materials Park, OH, 1993; pp 35–68 (chapter 2).
47. Scheil, E. *Arch. Eisenhüttenwes.* **1934/35,** *8*, 565–567; 144–206.
48. Atkins, M. *Atlas of Continuous Cooling Transformation Diagrams for Engineering Steels;* ASM: Metals Park, Ohio, USA; British Steel Corporation: Sheffield, England, 1980; Printed in the USA, 1980, p 260.
49. Pereira, R. L. *Tratamentos Térmicos dos Metais,* 3rd ed.; Escola de Engenharia de São Carlos, Universidade de São Paulo, 1979; p 422.
50. Sinha, A. K. Iron-Carbon Alloys; *Ferrous Physical Metallurgy;* Butterworth: Boston, MA, 1989; pp 1–42, (chapter 1).
51. Brooks, C. *Principles of the Heat Treatment of Plain Carbon and Low Alloy Steels;* ASM International: Materials Park, OH, USA, 1996; p 490.
52. Krauss, G. Glossary of Selected Terms. In *Steels: Heat Treatment and Processing Principles;* ASM International: Materials Park, OH, 1990; pp 453–468.
53. Grossmann, M. A.; Asimow, M. Hardenability and Quenching. *The Iron Age* **April 25, 1940,** *36*, 25–29.
54. Standard Terminology Relating to Metallography ASTM E7-01. ASTM International, West Conshohocken, PA.
55. Vatavuk, J. *Análise de falha em eixo SAE 4340;* Scientific Report; Laboratório de Ciência dos Materiais, Universidade Presbiteriana: Mackenzie 2010; p 12.
56. Vatavuk, J.; Canale, L. C. F. Steel Failures Due to Tempering and Isothermal Heat Treatment. In *Failure Analysis of Heat Treated Steel Components;* Canale, L. C. F., Mesquita, R. A., Totten, G. E., Eds.; ASM International: Materials Park, OH, 2008; pp 285–310.
57. Bhadeshia, H. K. D. H.; Edmonds, D. V. *Metal Sci.* **1983,** *17,* 411–419.
58. Seco/Warwick. *Heat Treating Data Book,* 8th ed.; Seco/Warwick Corporation: USA, 2000; p 96.
59. Krauss, G. Tempering of Steel. In *Principles of Heat Treatment of Steel;* ASM International: Materials Park, OH, USA, 1980; pp 187–227 (chapter 8).
60. Blackwood, R. R.; Jarvis, L. M.; Hoffman, D. G.; Totten, G. E. Conditions Leading to Quench Cracking Other Than Severity of Quench. In *Heat Treating Including the Liu Dai Symposium, Proc. 18th Conference;* Wallis, R. A., Walton, H. W., Eds.; ASM International: Materials Park, OH, 1998; p 575.
61. Clarke, P. C. Close Tolerance Heat Treatment of Gears. *Heat Treat. Metals* **1998,** *25* (3), 61–64.
62. Spies, H. J.; Münch, G.; Prewetz, A. Möglichkeiten der Optimierung der Auswahl vergütbarer Baustähle durch Berechnung der Härt-und-vergütbarkeit. *Neue Hütte* **1977,** *8* (22), 443–445.
63. http://www.msm.cam.ac.uk/phasetrans/2004/Tempered.Martensite/tempered.martensite.html.
64. Nam, W. J.; Choi, H. C. Effect of Silicon, Nickel and Vanadium on Impact Toughness in Spring Steels. *Mater. Sci. Technol.* **1997,** *13,* 568–574.
65. Nam, W. J.; Choi, H. C. Effect of Si on Mechanical Properties of Low Alloy Steels. *Mater. Sci. Technol.* **1999,** *15,* 527–530.

This page intentionally left blank

12.03 Hardenability of Steel

LCF Canale and L Albano, Universidade de São Paulo, São Carlos, São Paulo, Brazil
GE Totten and L Meekisho, Portland State University, Portland, OR, USA

11.18.1	**Introduction**	483
11.18.2	**Nano-Surface Generation by Grinding**	483
11.18.3	**In-Process Dressing of Super Abrasive Wheel**	484
11.18.4	**History of ELID Grinding**	486
11.18.5	**Classifications of ELID Grinding**	488
11.18.5.1	Electrolytic In-Process Dressing	488
11.18.5.2	Electrolytic Interval Dressing	489
11.18.5.3	Electrodeless ELID	491
11.18.5.4	Electrodeless ELID	491
11.18.5.5	Ion Shot ELID	491
11.18.6	**Fundamental Study on ELID Grinding**	492
11.18.7	**Study Related to Control of ELID Grinding Process**	499
11.18.8	**Study Related to ELID Grinding Machine Development**	504
11.18.9	**Study Related to Application of ELID Grinding**	508
11.18.9.1	ELID on Ceramics	508
11.18.9.2	ELID on Coated Film	510
11.18.9.3	ELID on Metal	511
11.18.9.4	ELID on Optical Glasses	514
11.18.9.5	ELID on Silicon Wafer	517
11.18.10	**Conclusions**	520
References		520

12.03.1 Introduction

Plain-carbon and low- and medium-alloy steels are typically hardened by heating to the austenization temperature and then cooled rapidly to form the desired structure, typically martensite, in order to maximize the attainable strength. Martensite is characteristically hard and brittle. When the cross-section size is sufficiently large, the hardness varies across the section, with the greatest hardness at the surface and with lower hardness at the center, which is due to increasing amounts of softer pearlitic structure. The variation of the steel structure across the section is due to a gradation of cooling rates ranging from fastest at the surface to slowest at the center, and the hardness distribution across the section is dependent on the transformation characteristics and composition of the steel.

Krauss has defined hardenability to be the relative ability of a ferrous alloy to form martensite when quenched from a temperature above the upper critical temperature (Ac_3), known as the austenitizing temperature, as hardenability (*5*). Therefore, steel hardenability refers to the potential to be hardened by a thermal treatment. The greater the hardenability of a steel, the greater will be the depth of hardening when quenched from the Ac_3 temperature. Hardenability should not be confused with hardness, which is a material property and refers to the resistance to penetration, which is proportional to strength. Hardness is dependent only on carbon content in the steel, whereas hardenability refers to the ability to achieve a certain hardness at a certain depth and a quality that depends on both the carbon content as shown in **Table 1** (*1*) and the presence and amount of the alloying elements. The actual depth of hardness depends on:

- Size and shape of the cross section
- Hardenability of the material
- Quenching conditions

The effect of quenching conditions on the depth of hardening is not only dependent on the quenchant being used and its physical and chemical properties, but also on process parameters such as bath temperature and agitation. These effects will be discussed subsequently.

The focus of this chapter will be on plain-carbon and low-alloy carbon steels. Plain-carbon steels typically contain no additional major concentrations of alloying elements other than carbon. Low-alloy carbon steels are a category of steels that exhibit mechanical properties superior to plain carbon steels due to the addition of alloying elements including nickel, chromium, molybdenum, vanadium, manganese, and copper. Total alloy content can range from 2.07% up to 10% chromium, a level just below that of stainless

Table 1 Effect of carbon concentration and martensite content on the as-quenched hardness of steel[a]

	Hardness (HRC)				
Carbon %	*99% martensite*	*95% martensite*	*90% martensite*	*80% martensite*	*50% martensite*
0.10	38.5	32.9	30.7	27.8	26.2
0.12	39.5	34.5	32.3	29.3	27.3
0.14	40.6	36.1	33.9	30.8	28.4
0.16	41.8	37.6	35.3	32.3	29.5
0.18	42.9	39.1	36.8	33.7	30.7
0.20	44.2	40.5	38.2	35.0	31.8
0.22	45.4	41.9	39.6	36.3	33.0
0.24	46.6	43.2	40.9	37.6	34.2
0.26	47.9	44.5	42.2	38.8	35.3
0.28	49.1	44.8	43.4	40.0	36.4
0.30	50.3	47.0	44.6	41.2	37.5
0.32	51.5	48.2	45.8	42.3	38.5
0.34	52.7	49.3	46.9	43.4	39.5
0.36	53.9	50.4	47.9	44.4	40.5
0.38	55.0	51.4	49.0	45.4	41.5
0.40	56.1	52.4	50.0	46.4	42.4
0.42	57.1	53.4	50.9	47.3	43.4
0.44	58.1	54.3	51.8	48.2	44.3
0.46	59.1	55.2	52.7	49.0	45.1
0.48	60.0	56.0	53.5	49.8	46.0
0.50	60.9	56.8	54.3	50.6	46.8
0.52	61.7	57.5	55.0	51.3	47.7
0.54	62.5	58.2	55.7	52.0	48.5
0.56	63.2	58.9	56.3	52.6	49.3
0.58	63.8	59.5	57.0	53.2	50.0
0.60	64.3	60.0	57.5	53.8	50.7

[a]Reproduced from Totten, G. E.; Bates, C. E.; Clinton, N. A. Measuring Hardenability and Quench Severity. In *Quenchants and Quenching Technology*; ASM International: Materials Park, OH, USA, 1993; pp 35–68. ISBN: 978-0-8717-0448-1 (chapter 2).

steels. The primary function of the alloying elements in low-alloy steels is to increase hardenability in order to optimize mechanical properties and toughness after heat treatment. This chapter describes factors that affect steel hardenability and methods to quantify it.

12.03.2 Discussion

Time-temperature-transformation (TTT) diagrams, which are also called isothermal-transformation (IT) diagrams (*2,3*), are developed by heating small samples of steel to the temperature where the austenite structure is completely formed, that is, austenitizing temperature, then rapidly cooling to a temperature intermediate between the austenitizing and M_s temperature, and then holding for a fixed period of time until the transformation is complete, at which point the transformation products are determined. This procedure is repeated until a TTT diagram is constructed, such as those shown in **Figure 1** for AISI 1045 and AISI 4140 steel (*143,144*). TTT diagrams can only be read along the isotherms shown, and these diagrams strictly apply only to those transformations conducted at constant temperature. By comparing the position of the nose of the pearlite transformation, it is evident from transformation times that the AISI 1045 plain-carbon steel is considerably less hardenable than AISI 4140.

However, relatively few commercial heat treatments are conducted isothermally. Instead, steel is heated to the austenitizing temperature and then continuously cooled in a quenching bath at a temperature and at a cooling rate suitable for the alloy and section size being treated. To better model this process, steel samples can be cooled at different specified rates, and the proportion of transformation products formed after cooling to various temperatures intermediate between the austenitizing and M_s temperatures are determined and a continuous-cooling-transformation (CCT) diagram is constructed like those shown for AISI 1045 and AISI 4140 steel in **Figure 2** (*143,144*). CCT curves provide data on the temperatures for each phase transformation, the amount of phase transformation product obtained for each cooling rate with respect to time, and the cooling rate necessary to obtain martensite. CCT diagrams can only be read along the curves for different cooling rates. The CCT diagrams show from the displacement of the AISI 4140 transformation curve to the right relative to the curve for AISI 1045 plain-carbon steel that it is the more hardenable steel.

12.03.2.1 Critical Cooling Rate

The oldest concept of assessing hardenability based on transformation diagrams is the critical cooling rate (*4*). Krauss has defined the critical cooling rate of a steel as "the rate of continuous cooling required to prevent undesirable transformation. For Steel, it is the

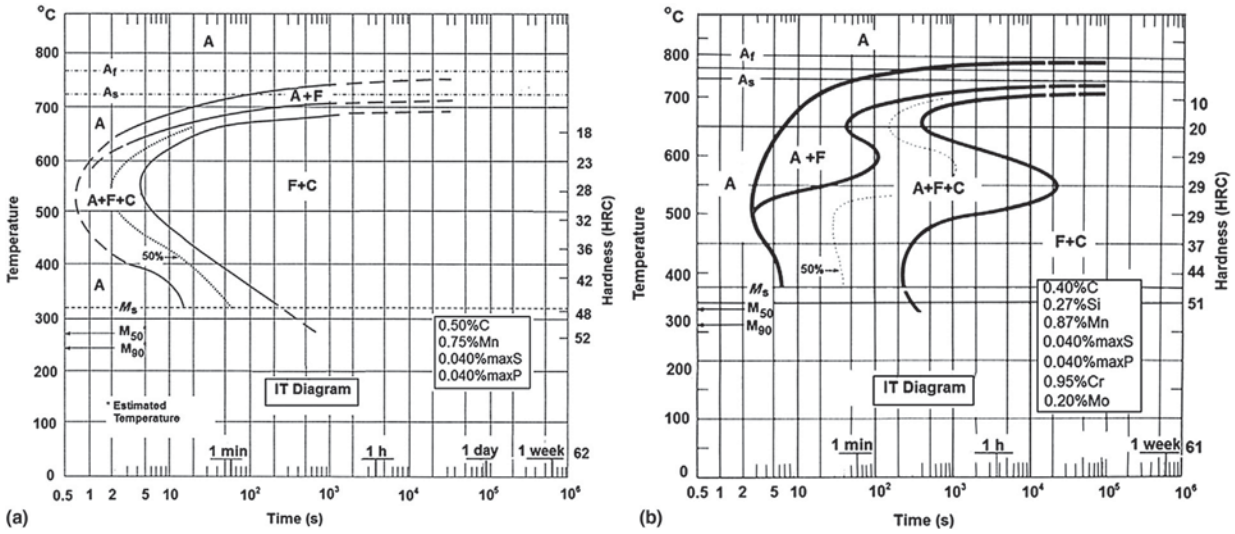

Figure 1 Representations of TTT diagrams for AISI 1045 (on left) and AISI 4140 (on right). Reproduced from Boyer, H. E.; Gray, A. G. *Atlas of Isothermal Transformation and Cooling Transformation Diagrams*; ASM International: Metals Park, OH, 1977.

minimum rate at which austenite must be continuously cooled to suppress transformations above the M_s temperature" (5) or the slowest cooling rate that will produce 100% martensite. Since the cooling curve from which the critical cooling rate is derived is not linear, there are various methods for its determination. Using the TTT curve for the alloy of interest, examples include the time to cool halfway between the austenitizing temperature and the temperature of the quench bath; average cooling rate calculated from the (austenitizing temperature–quenchant bath temperature)/elapsed time to cool; or the slope of the tangent to the transformation curve denoting the onset of austenite precipitation at a given temperature (the nose method (6)) such as 700 °C – although the selection of this temperature is not obvious (7). Sverdlin and Ness have reported that the so-called nose method provides an

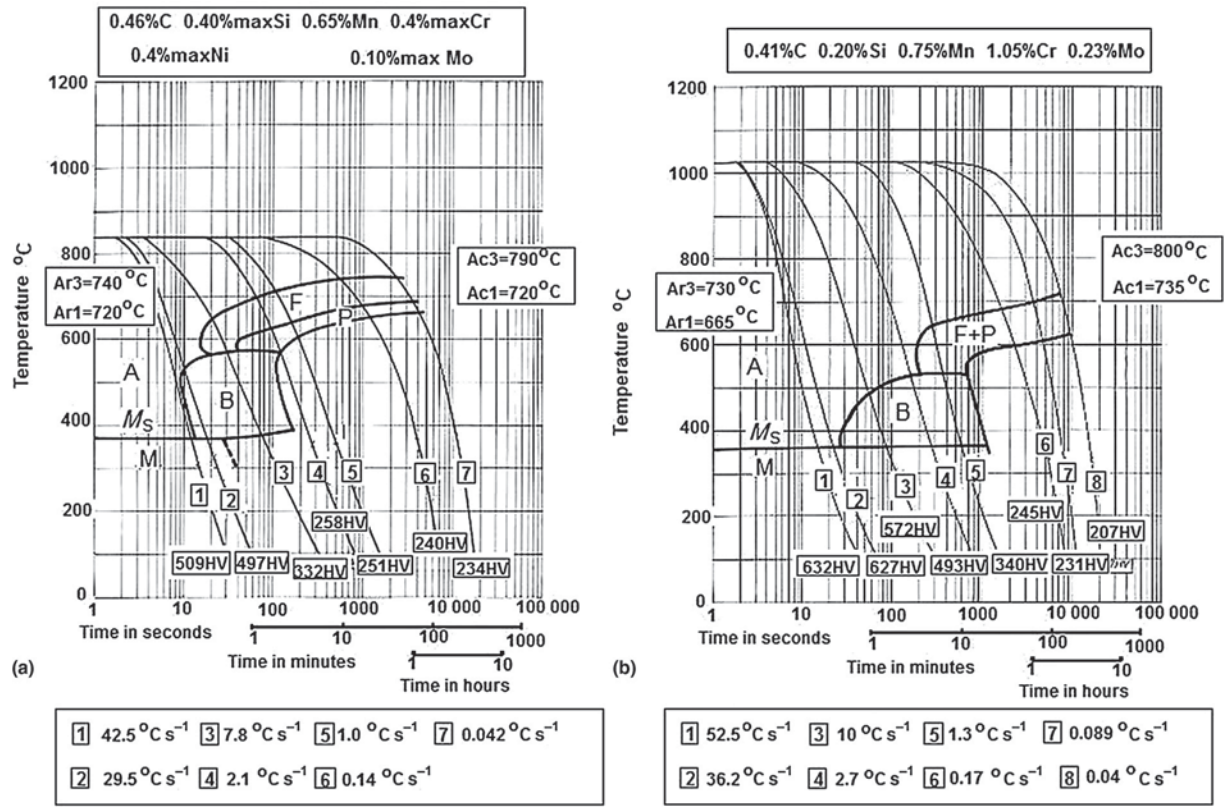

Figure 2 CCT diagrams for AISI 1046 (on left) and AISI 4140 (right). (Diagrams modified from Atkins, M. *Atlas of Continuous Cooling Transformation Diagrams for Engineering Steels*; ASM International: Metals Park, OH, 1980.).

estimate that is approximately 1.5 times the true critical cooling rate (*8*). Furthermore, the critical cooling rates have been obtained from either the TTT or CCT diagrams, which are clearly different. Therefore, the method by which the critical cooling rate is calculated must be provided.

A CCT diagram for a eutectoid steel is shown in **Figure 3** (*145*). Cooling curves for different cooling processes include a water and an oil quench and a normalizing and a full-annealing cooling process. Cooling after normalizing is typically performed by removing the load and cooling in air at ambient temperature. Typically, the full-annealing process is conducted by heating the steel in the furnace and then shutting off the heat and cooling the load in the furnace (furnace cooling). For this steel, the structure formed after normalizing is a coarse pearlite, and a fine pearlite structure is formed after full-annealing. Quenching in oil produces a mixed structure of pearlite and martensite. The fastest cooling occurred in water, and a fully martensitic structure is formed. The dashed line in **Figure 3**, which represents the critical cooling rate curve and a cooling rate in excess of the critical cooling rate, is necessary if a fully martensitic structure is to be achieved (*145*).

Zeng and Xu developed a regression equation to obtain the minimal critical cooling rate (V_M) and a 100% martensitic structure based on the steel composition (*9*):

$$\log V_M = 4.5 - 2.7C - 0.95Mn - 0.18Si - 0.38Cr - 0.43Ni - 1.17Mo - 1.29\ C{\cdot}Cr - 0.33\ Cr{\cdot}Mo$$

where V_M is in $^\circ C\,s^{-1}$. This equation can be applied to hypoeutectoid carbon steels and low-medium alloy steel. Alternatively, the V_M value can be obtained from the CCT diagram using the following equation (*9*):

$$V_M = \frac{T_A - T_N}{I_N}$$

where T_A is the austenitization temperature (°C), T_N is the corresponding temperature (°C) at the nose of the CCT curve (if there are two noses, use the temperature at the nose of the lower curve) and I_N is the incubation time (s).

Fu et al. provided a detailed description of three primary computational methods for determining the critical cooling rate based on a CCT curve; these methods include the modified Maynier Model, the Eldis Model, and the Isothermal Curve Model (*10*). Although all three models can be used, the Isothermal Curve Model produced the best results where agreement within ±6% with respect to experimental results were obtained.

Previously, it has been shown that the maximum as-quenched hardness exhibited by carbon and low-alloy steels is predominantly due to the carbon content (see **Table 1**). The TTT and CCT diagrams above show that hardness is also dependent on the cooling rate, which typically decreases from the surface to the center of a cross section of steel. Steel hardness depends on the degree

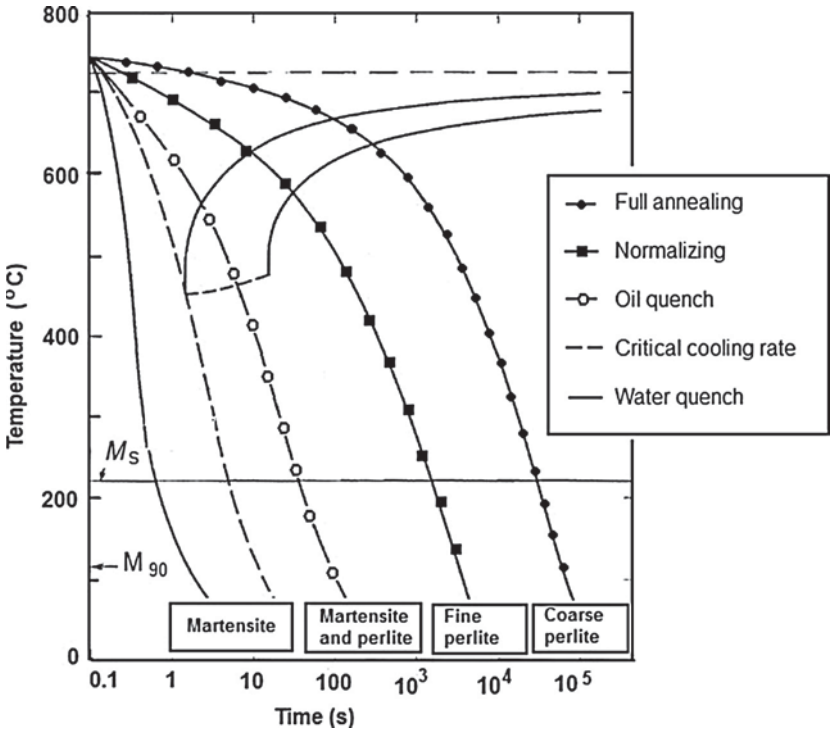

Figure 3 Microstructure formation as a function of cooling rate. (Modified from Diggs, T. G.; Rosenberg, S. J.; Geil, G. W. Heat Treatment and Properties of Iron and Steel; National Bureau of Standards Monograph 88, November 1, 1966.).

of transformation to martensite, which increases with the cooling rate up to the critical cooling rate. Cooling rates greater than the critical cooling rate do not produce correspondingly greater hardness.

Cooling rates generally decrease from the surface to the center of a section of steel. If the cooling rate at the center is equal or greater than the critical cooling rate, then maximum hardness over the entire cross section will be obtained. However, when the cooling rate is less than the critical cooling rate, correspondingly lower hardnesses will be achieved. **Figure 4** shows the hardness distributions of different section sizes of AISI 6140 round bars after quenching in oil (*17*). The greatest cross-sectional hardness was only achieved with the smallest cross-sectional size (1/2 inch). Also shown in **Figure 4** is cross-sectional hardness for AISI 1045 for a range of bar diameters. As with AISI 6140, the 1045 steel also exhibited progressively poorer hardness uniformity across the section, but also the figure clearly shows that the 6140 low-alloy steel is significantly more hardenable than the 1045 plain-carbon steel.

The rate of change of the hardness through the section is dependent on section size, hardenability of the steel, and quench severity. Steel hardenability and quench severity will be discussed subsequently.

12.03.2.2 Fracture Classification

When steel is quenched, typically a transition takes place from martensite at the surface to the softer, unhardened core. In the 1930s, Shepherd developed a fracture test that applies only to high-carbon and highly alloyed tool steels, which was designated as the P (penetration) – F (fracture) test. This test, which is seldom used today, was based on the transition of brittle fracture characteristics exhibited by martensite to a ductile fracture (*11*). This transition occurs at approximately 50% martensite (*12*,*13*). The two regions are distinguishable by etching; therefore this method provided a means of determining the depth of hardening and hardenability of high carbon and highly alloyed tool steels (*14*).

The P–F test is performed by utilizing four test specimens (one-inch diameter × three-inch round bars), which are normalized at 1600 °F for a minimum of 40 min. One test bar is heated in a vertical position to 1450, 1500, 1550, and 1600 °F and then quenched in a two-inch pipe with flow of 10% brine solution. After quenching, the bars are notched in the middle with a thin 1/16–3/32-inch friction wheel to a depth not exceeding 1/16 inch. The bar is then fractured by a transverse impact. The grain size or fracture (F) – value is determined on one of the broken halves and expressed as the number or quarter number corresponding to the appropriate standard sample. The penetration test is performed on a smooth and polished surface not less than one inch from the original end of the remaining half of the broken sample bar. The hardness is measured macroscopically to the nearest half of 1/64 inch and is expressed as the numerator of a fraction (*11*).

The P–F characteristic is composed of eight (8) numbers. The first four (4) numbers represent the P-value in 1/64 inch on the test bars heated to 1450, 1500, 1550, and 1600 °F, respectively. The last four numbers represent the fracture grain size (F-value) for the same bars heated at the same four temperatures, respectively. These values are then written in the following manner:

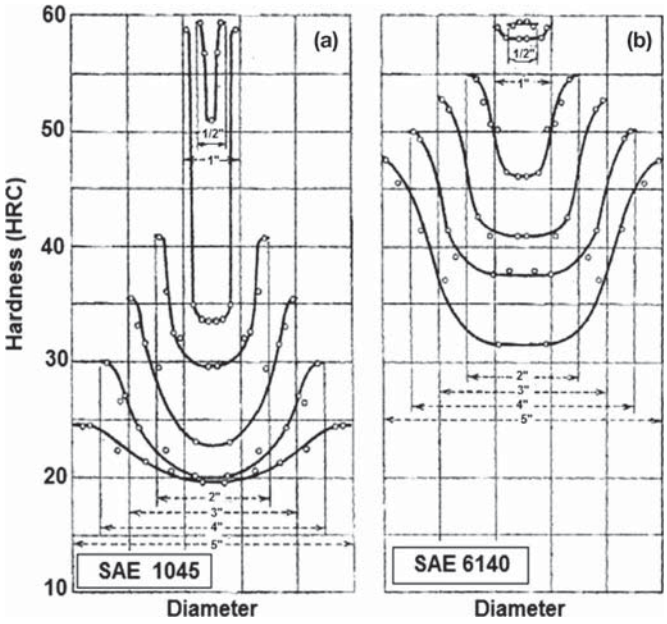

Figure 4 U-curve comparison of the hardenability of (a) AISI 1045 plain-carbon steel and (b) AISI 6140 low-alloy steel with increasing cross-sectional diameters. Reproduced from Crafts, W.; Lamont, J. L. Hardness and Hardenability. In *Hardenability and Steel Selection*; Pittman Publishing: New York, NY, 1949; pp 84–110 (chapter 5).

Table 2 Classification of standard P–F values[a]

Type	*P – characteristic*	*F – characteristic*
1	3/64 inch or less change	Not more than one (1) number
2	More than 3/64 inch change but does not through-harden	More than one (1) number
3	Through-hardens at 1600 °F	More than 1 $^{3}/_{4}$ number change

[a]Reproduced from Davis, J. R. Classification and Properties of Tool and Die Steels. In *ASM Specialty Handbook – Tool Materials*; ASM International: Materials Park, OH, USA, 1995; pp 119–153.

5. 6. 8. 12 / 9. 8. 6. 4.

Davis has reported that a P–F value of 6–8 indicates a hardened case depth (P-value) of 6/64 in (2.4 mm) and a fracture grain size (F-value) of 8. Water-hardened, fine-grained tool steels exhibit F-values of ≥8. Deep-hardenability steels exhibit P-values of ≥12. Medium-hardenability steels exhibit P-values of 9–11, and shallow-hardenability steels exhibit P-values of 6–8 (*15*).

Table 2 summarizes the P–F characteristic assigned to tool steels as Type 1, 2, or 3 (*15*). However, a more discriminating classification involving two numbers may be used such as Type 2-1, which would indicate an intermediate P-characteristic but a stable F-characteristic. Furthermore, hardenability will decrease with increasing amounts of undissolved carbides at the hardening temperature. It should be noted that one of the limitations of the Shepherd P–F test is that hardenability of high carbon and highly alloyed tool steels is not only dependent on composition but also on austenitizing, which has a very strong effect on the dissolution of carbides that form and are retained as a function of austenitizing temperature in those steels. The amount of retained carbides controls the amount of carbon in the austenite, which in turn controls hardenability and fracture characteristics of the quenched microstructures.

Figure 5 illustrates the correlation of bar diameter and hardened case depth for three W1 tool steels, shallow, medium, and deep hardenability, with the same total carbon content (1%) (*15*).

While P–F classification can be used to assess the depth of hardening, it is limited to those steels where the transition from brittle to ductile fracture is sufficiently sharp, such as tool steels for which the Shepherd P–F test was developed and is seldom used today (*12*).

12.03.2.3 Steel-Hardening Criterion

Although it is typically difficult to quantitatively assess martensite content microscopically as 100% martensite is obtained, traditional use of fracture tests showed that it was possible to identify 50% martensite (also known as half-hardening (*16*)) by etching with reasonable precision because the hardness gradient is typically sharp in this region and therefore can be well correlated with the position where the dark, martensitic microstructure begins (*17*). Therefore, this critical 50% martensite position can be identified by fracture tests, microscopic examination, or hardness tests, and represents the position where the variation of hardness with cooling rate is greatest – at least for plain-carbon and low-alloy steels. Grossmann et al. further refined this criterion by stating that the reference point was 50% martensite when subjected to an infinite quench as shown in Figure 6 (*88*).

One criticism of this approach is that it does not account for other nonmartensitic constituents, such as proeutectoid ferrite and pearlite or bainite. This is especially problematic with higher hardenability steels where the hardenability variation obtained by the 50% criterion and that obtained by 99.9% martensite may be considerable (*18*). Therefore, some authors have used a greater transformation criterion, such as 90% used by Grange for studies of medium- and high-carbon steels (*19*) and Hwang et al. for boron steels (*20*).

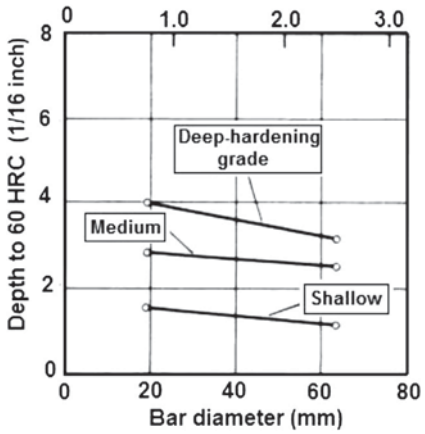

Figure 5 Effect of bar diameter and depth of hardening for shallow, medium, and deep hardenability grades of W1 tool steel containing total 1% carbon content. Reproduced from Davis, J. R. Classification and Properties of Tool and Die Steels. In *ASM Specialty Handbook – Tool Materials*; ASM International: Materials Park, OH, USA, 1995; pp 119–153.

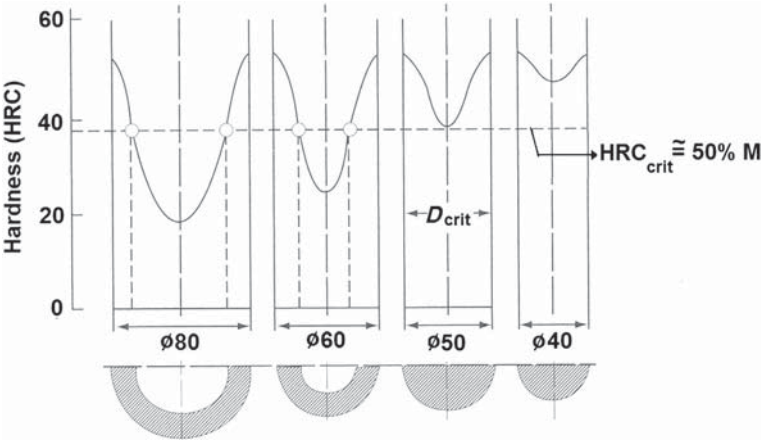

Figure 6 Illustration of the critical round-bar diameter by Grossmann's methodology. Reproduced from Liščič, B. Hardenability. Steel Heat Treatment Handbook. In *Steel Heat Treatment: Metallurgy and Technologies*; Totten, G. E., Ed., 2nd ed.; CRC Press Taylor & Francis Group: Boca Raton, FL, 2007; pp 213–276. ISBN: 978-0-8493-8455-4 (chapter 5).

That diameter where 50% martensite is formed when subjected to a specific quench was designated by Grossmann as the critical diameter, D_C of the steel. This could easily be identified graphically by plotting the centerline hardness versus the bar diameter as shown in Figure 7 (*17*). The ideal critical diameter, D_I is that bar diameter that produces 50% martensite when subjected to an infinite quench. The infinite quench is the quench that reduces the surface temperature of an austenitized steel to the bath temperature instantaneously and is typically assumed to be salt brine.

Using a hardenability criterion, steels can be classified as either shallow hardening or deep hardening (or through hardening) (*21*). Shallow hardening steels typically exhibit a very limited depth of hardening and are generally defined as those steels whose critical diameter is less than 1 inch (25 mm) and include plain-carbon steels with low concentrations of Mn and Si, and other alloying elements (*22*). For deep hardening steels, the cross-sectional hardness is uniform throughout. Some alloy steels are classified as deep hardening, such as tool steels and high-speed steels (HSS). Tool steels are used primarily to make tools employed in manufacturing processes as well as for machining of metals, wood, and plastics. High-speed steels are molybdenum and tungsten based and are used for high-speed machining applications such as high-speed machining, cutting-off tools (knives, drills, milling cutters, etc.), and rolls for cold rolling. Examples of high-speed steel alloys include M2, M4, and M42. The hardenability of most medium-carbon, low-alloy steels is intermediate between these two steel classes. This discussion will focus primarily on the hardenability of plain-carbon and medium-carbon low-alloy steels.

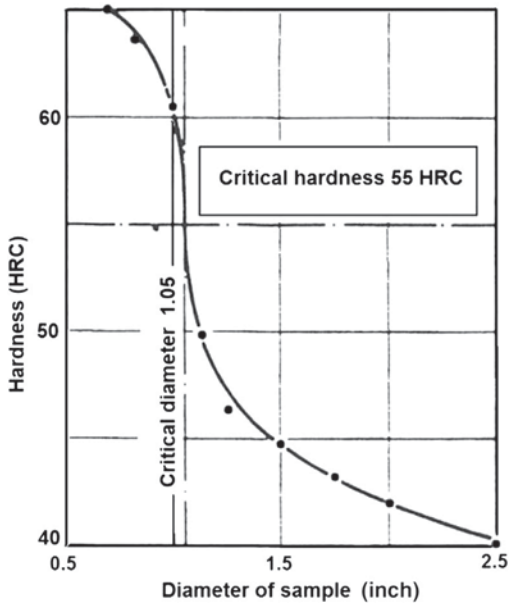

Figure 7 Determination of the critical round-bar diameter of a steel from a plot of bar diameter versus hardness. Reproduced from Crafts, W.; Lamont, J. L. Hardness and Hardenability. In *Hardenability and Steel Selection*; Pittman Publishing: New York, NY, 1949; pp 84–110 (chapter 5).

12.03.2.3.1 Effect of Steel Composition and Grain Size

Alloying elements are incorporated into steels for one, or more, of the following reasons: (1) to improve mechanical properties by controlling hardenability and permitting higher tempering temperature while maintaining high strength and ductility; (2) to improve high- or low-temperature mechanical properties; (3) to increase resistance to chemical attack or thermal oxidation; and (4) to influence special properties such as magnetic permeability and neutron absorption (*23*). Of these, improvement of mechanical properties is among the most important, and the addition of alloying elements improve mechanical properties by varying the size of dispersed carbides in ferrite and by changing the properties of ferrite and cementite phases. The presence of alloying elements in steel helps reduce the need for a rapid quench cooling, which is generally necessary with low-hardenability, plain-carbon steels. Reducing the cooling rate necessary to achieve the desired hardness also reduces the potential for distortion and cracking. Furthermore, the presence of alloying elements typically increases the depth of hardening, thus increasing the potential for fully hardening thick section sizes.

Although carbon steels primarily contain carbon as the alloying element, alloy steels may contain a range of potential alloying elements as shown in **Table 3** (*24*). The effect of steel composition on hardenability has been studied by many authors (*16*,*25*,*26*) but the methodology still used today is essentially unchanged from when Grossmann first proposed it (*27*). In this work, hardenability was shown to be a function of grain size and steel composition and was calculated in terms of the 'ideal critical diameter' (D_I), which, as discussed previously, was defined as the largest bar diameter that can be quenched to produce 50% martensite at the center after quenching in an 'ideal' quench, that is, under infinite quenching severity. This is a microstructural definition, and there is no reference to hardness (*28*). The use of hardness measurements to determine the position where 50% martensite occurs does not account for the fact that the nonmartensitic structures may be pearlitic or bainitic, with each contributing differently to the overall as-quenched hardness. The ideal quench is one that reduces the surface temperature of an austenitized steel to the quenching bath temperature instantaneously (*27*). Under these conditions, the cooling rate at the center of the bar depends only on the thermal diffusivity of the steel.

Assuming 'half-hardening' as the hardening criterion, we can estimate the hardenability by multiplying a base value that is a function of the carbon content by a hardenability-dependent multiplying factor (f). For hypereutectoid steels, hardenability varies with the square root of the carbon content, which becomes the baseline for these calculations. This baseline value refers to the size of an ideal round bar that will half-harden at the center (*16*). The effect of small quantities of various elements on the formation of pearlite or bainite during hardening of plain-carbon steel has been studied by (*25*). The ideal critical diameter may be calculated from:

$$D_I = D_{\text{IBase}}(\text{carbon concentration and grain size}) \times f_{\text{Mn}} \times f_{\text{Si}} \times f_{\text{Cr}} \times f_{\text{Mo}} \times f_{\text{V}} \times f_{\text{Cu}} \times f_{\text{Ni}} \times f_X$$

Table 3 Effects of alloying elements on steel properties[a]

Element[b,c,d]	*Effect on Steel Properties*[b]
Boron (B)	Small amounts substantially increase hardenability. Boron-treated steels will usually contain 0.0005–0.003% boron. Although boron is effective with low-carbon alloy steels, its effectiveness decreases with increasing carbon content. Boron is not recommended for steels containing >0.6% carbon.
Manganese (Mn)	Increases hardenability and is a carbide former (Mn_3C) above a threshold value. In constructional steel alloys, manganese substantially increases the critical cooling rate and therefore facilitates deep hardening.
Nickel (Ni)	Increases hardenability by decreasing the critical cooling rate necessary to produce hardening as a result of quenching and affects austenite transformation by depressing A_c and A_r critical temperatures. Nickel does not form carbide structures. When combined with chromium, nickel produces alloy steels with higher elastic ratios, greater hardenability, higher impact strength, and fatigue resistance than is possible with carbon steels.
Chromium (Cr)	Chromium is a strong carbide former, and in the presence of carbon and iron, chromium forms a complex series of carbide structures. Complex chromium carbides dissolve in austenite slowly. Chromium greatly increases hardenability and increases oxidation and corrosion resistance and increases the Ac_3 critical temperature. If sufficient austenitizing times are utilized, chromium provides a substantial improvement in the depth of hardening because the critical cooling rate is decreased.
Molybdenum (Mo)	Molybdenum increases the Ac_3 critical temperature in constructional steels at concentrations of 0.1–0.60% and depending on the molybdenum and carbon content, may form complex carbide structures. Increases hardenability and is more potent than chromium but often used in combination with nickel and/or chromium. In solid solution, molybdenum decreases transformation rates, and this increases the depth of hardening.
Vanadium (V)	Vanadium is a strong carbide-forming element. Increases hardenability and promotes finer grain size. The presence of vanadium decreases high-temperature grain growth. Vanadium exhibits a secondary hardening effect upon tempering and increases hardness at elevated temperatures.
Silicon (Si)	Silicon increases the critical temperature by amounts that vary with the carbon content; therefore required austenitizing temperatures are increased. Silicon is not a carbide former. Provides relatively small increase in hardenability and strengthens low-alloy steels but primarily used in low concentrations as a potent deoxidizer.

[a]Reproduced from Heine, H. J. Understanding the Hardenability of Steel. *Heat Treat.* **March/April 1994,** 31–34.

[b]The addition of two or more elements is more effective than the addition of a single element.

[c]The effects of sulfur and phosphorus on thermal treatment are negligible.

[d]Cobalt (Co), tungsten (W), titanium (Ti), and copper (Cu) are used primarily as alloying elements for stainless steel.

where f_X is a multiplicative factor for the particular substitutionally dissolved alloying element. The D_{IBase} value and alloying factors are provided in Table 4 (*1*). (*Note*: This is not an exhaustive listing of alloying factors but contains those that are commonly encountered, and they permit calculations to illustrate the effect of steel chemistry variation on hardenability.)

Alternatively, the multiplying factor '*f*' that varies linearly may be calculated from:

$$f = 1 + ax$$

where *a* is a constant for each element and *x* is the weight percent (%) of the element present in the steel. These factors are summarized in Table 5 (*16*).

While the use of such multiplicative relationships has been generally validated by various authors and continues to be widespread, there are a number of important limitations to this approach for the assessment of steel hardenability. One potential problem is that a multiplying factor assigned to an element is not always directly proportional to the total amount of that element. Another potential limitation to the multiplicative approach is that there is the potential for interaction effects, so that when two or more elements are present together, their net effect may be different than if only one of the elements is present alone (*28*,*29*).

Jatczak used 90% martensite for his hardenability criterion instead of 50% martensite for high-carbon steels because of the effect of carbon on hardenability. For high-carbon steels (0.60–1.10% C), the austenitizing temperature must also be included in the hardenability determination. In these high-carbon steels, some of the carbon content may be retained in carbides rather than in solution in the austenite, depending on austenitizing temperatures. More carbides are dissolved at higher austenitizing temperatures, increasing hardenability, as will be shown in Figures 60–62.

For this reason, Jatczak's data was limited to those steels that were quenched from 925 °C (1700 °F) (*28*,*30*).

Doane also showed in his review that the effect of manganese of up to 1% is greater for either low- or high-carbon steels than medium-carbon steels (*28*). The effect of silicon may vary greatly with carbon content and is much greater in high-carbon steels than in low-carbon steels. Furthermore, the magnitude of the effect of nickel on hardenability is dependent on the carbon content, and the effect is greatest in medium carbon steels. Jatczak reported that there was an interaction between manganese and nickel for steels austenitized below 925 °C (1700 °F) (*30*). If nickel is present in concentrations greater than 0.75%, there is a synergistic effect of nickel and molybdenum in low-carbon steels.

Finally, Doane also reported that the effect of chromium on hardenability is greatest in medium-carbon steels, although the effect is still large for low-carbon and carburized steels (*28*,*29*). At lower austenitizing temperatures, the effect of chromium on hardenability is less because of the stability of the carbides that are formed.

In summary, the multiplicative approach to estimating steel hardenability using the factors developed by Grossmann does provide a good approximation of D_I for medium-carbon low-alloy steels using the 50% martensite criterion. However, there are exceptions that may lead to significant errors such as chromium/molybdenum steels. The factors and approach used by Jatczak is generally favored for carbon steels containing 0.60–1.10% carbon, in addition to high-carbon surface layers present in carburized

Table 4 Alloy factors for the calculation of ideal diameter[a]

	Base ideal diameter (D_I) for the following grain size			*Alloying factor f_X where element X is*				
Carbon %	*No. 6*	*No.7*	*No. 8*	*Mn*	*Si*	*Ni*	*Cr*	*Mo*
0.05	0.0814	0.0750	0.0697	1.167	1.035	1.018	1.1080	1.15
0.10	0.1153	0.1065	0.0995	1.333	1.070	1.036	1.2160	1.30
0.15	0.1413	0.1315	0.1212	1.500	1.105	1.055	1.3240	1.45
0.20	0.1623	0.1509	0.1400	1.667	1.140	1.073	1.4320	1.60
0.25	0.1820	0.1678	0.1560	1.833	1.175	1.091	1.5400	1.75
0.30	0.1991	0.1849	0.1700	2.000	2.210	1.109	1.6480	1.90
0.35	0.2154	0.2000	0.1842	2.167	1.245	1.128	1.7560	2.05
0.40	0.2300	0.2130	0.1976	2.333	1.280	1.246	1.8640	2.20
0.45	0.2440	0.2259	0.2090	2.500	1.315	1.164	1.9720	2.35
0.50	0.2580	0.2380	0.2200	2.667	1.350	1.182	2.0800	2.50
0.55	0.2730	0.2510	0.2310	2.833	1.385	1.201	2.1880	2.65
0.60	0.284	0.262	0.2410	3.000	1.420	1.219	2.2960	2.80
0.65	0.295	0.273	0.2551	3.167	1.455	1.237	2.4040	2.95
0.70	0.306	0.283	0.260	3.333	1.490	1.255	2.5120	3.10
0.75	0.316	0.293	0.270	3.500	1.525	1.273	2.6200	3.25
0.80	0.326	0.303	0.278	3.667	1.560	1.291	2.7280	3.40
0.85	0.336	0.312	0.287	3.833	1.595	1.309	2.8360	3.55
0.90	0.346	0.321	0.296	4.000	1.630	1.321	2.9440	3.70
0.95	–	–	–	4.167	1.665	1.345	3.0520	–
1.00	–	–	–	4.333	1.700	1.364	3.1600	–

The ideal diameter (D_I) is calculated from: $D_I = D_{IC} \cdot f_{Mn} \cdot f_{Si} \cdot f_{Ni} \cdot f_{Cr} \cdot f_{Mo}$; where D_{IC} is the D_I factor for carbon and *f* is the factor for the alloying element.

[a]Reproduced from Totten, G. E.; Bates, C. E.; Clinton, N. A. Measuring Hardenability and Quench Severity. In *Quenchants and Quenching Technology*; ASM International: Materials Park, OH, USA, 1993; pp 35–68. ISBN: 978-0-8717-0448-1 (chapter 2).

Table 5 Effect of carbon and alloying elements on hardenability[a]

Element	*Pearlitic hardenability factor*	*Bainitic hardenability factor*
Carbon factor		
50% pearlite or bainite	$0.338 \times (\%C)^{0.5}$	$0.494 \times (\%C)^{0.5}$
Essentially all martensite	$0.254 \times (\%C)^{0.5}$	$0.272 \times (\%C)^{0.5}$
Manganese	$1 + 4.10 \times (\%Mn)$	$1 + 4.10 \times (\%Mn)$
Phosphorous	$1 + 2.83 \times (\%P)$	$1 + 2.83 \times (\%P)$
Sulfur	$1 - 0.62 \times (\%S)$	$1 - 0.62 \times (\%S)$
Silicon	$1 + 0.64 \times (\%Si)$	$1 + 0.64 \times (\%Si)$
Chromium	$1 + 2.33 \times (\%Cr)$	$1 + 1.16 \times (\%Cr)$
Nickel	$1 + 0.52 \times (\%Ni)$	$1 + 0.52 \times (\%Ni)$
Molybdenum	$1 + 3.14 \times (\%Mo)$	1
Copper	$1 + 0.27 \times (\%Cu)$	$1 + 0.27 \times (\%Cu)$

These calculations assume an ASTM grain size of 7.
[a]Reproduced from Holloman, J. H.; Jaffe, L. D. Hardenability. In Ferrous Metallurgical Design: Design Principles for Fully Hardened Steel; John Wiley & Sons: New York, NY, USA, 1947; pp 196–214 (chapter 6).

steels (to be discussed later in this review) using the 90% martensite criterion (*31*). Therefore, to assure minimum error, these computational approaches must be used with appropriate caution.

D_I is dependent on the carbon content at a given grain size of the steel (*27*). Grain size refers to the dimensions of grains or crystals in a polycrystalline metal exclusive of twinned regions and subregions when present. Typically, the metallurgical structures formed on cooling are formed on the austenitic grain boundaries. Increased grain size results in a reduction of the grain boundary area per unit volume, which shifts the transformation start curves to longer times, increasing the depth of hardening due to the corresponding improvement in hardenability (*32*). Conversely, the finer the grain size, the greater the propensity for pearlite nucleation and the lower the hardenability (*33*). Grain size is the single greatest factor affecting hardenability. With the exception of very high hardenability steels, it is important to obtain a precise assessment of the grain size since a difference between an increase in the ASTM grain size from 6 to 7 may result in a hardenability difference of up to 10% (*27*). **Figure 8** illustrates the dependence of critical diameter on grain size for shallow-hardening steels after water quenching and 90% transformation to martensite (*19*).

Grain size is usually estimated or measured on the cross section of an aggregate of grains. Common units are (1) average diameter, (2) average area, (3) number of grains per linear unit, (4) number of grains per unit area, and (5) number of grains per unit volume. Grain size may be determined according to ASTM E112, where standard comparison charts are provided (*34*).

12.03.2.4 Vanadium and Boron Effects

The Grossmann equation provided above for calculation of the D_I does not include the effects of vanadium or boron on hardenability (*1*). Usually, vanadium is not added to improve hardenability in quenched and tempered steels. Typically, it is added to improve secondary hardening during tempering. Since vanadium is a strong carbide former, high austenitizing temperatures and time are required to achieve solution.

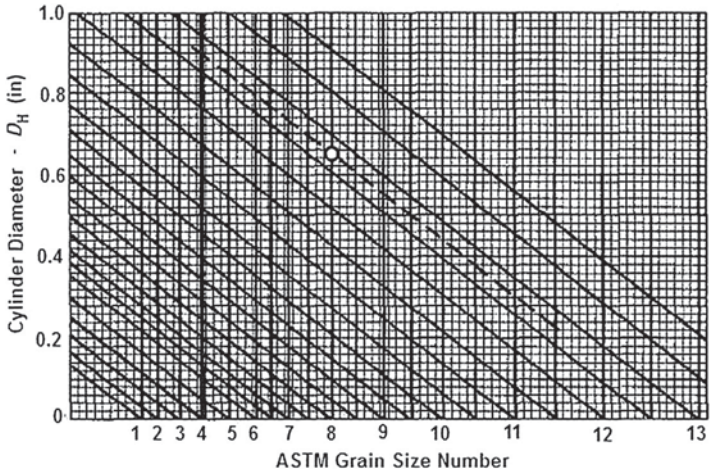

Figure 8 Chart for predicting hardenable diameter (90% martensite, water-quenched) for any grain size different from that at which hardenability was measured or estimated. Reproduced from Grange, R. A. Estimating the Hardenability of Carbon Steels. *Metall. Trans.* **Oct 1973,** *4*, 2231–2244.

Although vanadium, a grain growth inhibitor, at low concentrations of up to 0.1% does increase hardenability, further increases may actually result in decreased hardenability because hardenability is dependent on the composition of free vanadium at the austenitization temperature, not on the overall total vanadium concentration in the steel. Woodhead has reported that if the vanadium concentration is sufficient and if the austenitizing temperature is high enough, the presence of vanadium may exhibit a marked inhibition in pearlite formation (*35*).

Pacyna et al. showed that up to 0.14%, vanadium increases the hardness and hardenability slightly by decreasing slightly the onset temperature of ferrite precipitation and increasing the time for pearlite transformation (*36*). This is important since vanadium carbides, which may be present in the steel, do not readily dissolve at most standard austenitization temperatures and thus do not affect the kinetics of phase transformation. Only when dissolved in austenite at concentrations of 0.14–0.77% the effect is much stronger.

The effect of boron on steel hardenability is treated separately because of its unusual effect. The purpose of boron addition to hypoeutectoid carbon and low-alloyed steels is to improve hardenability. The presence of boron has no effect on eutectoid steels and decreases hardenability in hypereutectoid steels. As the grain size decreases, the hardenability effect increases. Increasing hardenability by boron addition does not decrease the M_s temperature (*37*).

The greatest effect on hardenability typically occurs at 3–15 ppm. To be effective, boron must be in a solid solution with austenite. However, the solubility of boron in austenite is very low. At 912 °C, boron solubility in austenite is 0.001% and increases with increasing temperature to a maximum value of 0.005% at the eutectic composition. In α – iron, the solubility is essentially zero (*37*). Since boron has only limited solubility in austenite, it readily concentrates in the grain boundaries. As steel is cooled from the austenitizing temperature, its solubility is reduced further.

Boron increases hardenability at concentrations as low as 0.0010% of boron (*38*), although it has only a minimal effect on the bainite transformation rate. Concentrations as low as 100 ppm boron may exhibit the same hardenability effect as other alloying elements at much higher concentrations. The reason for the decreasing effectiveness with increasing content is that boron must be free ('effective') since boron structures formed in steel, such as borocarbides $(Fe_{23}BC)_6$ and reaction products with oxygen and nitrogen in the steel, do not redissolve even at high austenitizing temperatures (*22*). Furthermore, increasing austenitizing temperatures decreases hardenability by increasing segregated boron concentration by the preferred precipitation of these structures in the austenite grain boundaries due to grain coarsening and a nonequilibrium segregation mechanism (*20*). Therefore, at concentrations greater than 30 ppm, the insoluble boron reaction products become segregated in the austenite grain boundaries, which reduces hardenability by delaying the formation of ferrite and pearlite. **Figure 9** correlates effective boron content and the boron multiplying factor (*39*). Alternatively, the effect of boron may be determined from the boron factor (BF) (*37*):

$$\mathrm{BF} = \frac{D_\mathrm{I}\ \text{with B}}{D_\mathrm{I}\ \text{without B}}$$

where the D_I value with boron is derived from the Jominy hardenability curve and the D_I value without B is obtained from the chemical composition of the steel.

The influence of boron on the hardenability of construction steels containing nitrogen, titanium, and zirconium was studied by Kapadia et al. The hardenability of these steels was dependent on the interaction of boron, titanium, and zirconium with the nitrogen in the steel. Only the free, unbound ('effective') boron exhibited any observed increase in hardenability. The maximum effect was observed when the effective boron was approximately 0.001% by weight as shown in **Figure 10** (*39*).

The D_I values for various steel alloys are listed in **Table 6** (*40*). The SAE-AISI designation of 'H' following the alloy designation indicates that the steels are produced to a specific hardenability range (*41*).

12.03.2.5 Quench Severity

Fourier published his work on the flow of heat flow in *Théorie analytique de la chaleur* in 1922, which was later translated into English (*42*). This work was based on Newton's law of cooling, which states that "the rate of change of the temperature of an object is proportional to the difference between its own temperature and the ambient temperature". Fourier's fundamental discovery was that some discontinuous functions are the sum of an infinite series. In addition, Fourier proposed a partial differential equation for conductive diffusion of heat that continues to be taught today. As a result of this work and Newton's law of cooling, Fourier solved the differential equation for the cooling of an infinitely long round bar. To simplify the analysis, it was assumed that the thermal conductivity, λ, and the surface heat abstraction coefficient '*C*' were temperature independent and were related by a term '*h*', which was equal to C/λ (*43*).

Heindlhofer subsequently reported that while Newton's law of cooling was generally valid for small temperature differences at low temperatures, it was not valid for large temperature differences such as those typically encountered in the quenching of steel (*44*). However, Russell studied the cooling process that typically occurs during the quenching of steel and developed a series of tables that could be used for the analysis of cooling of plates and cylinders (*45*). This work was followed by the presentation of mathematical calculations that could be used for end-quenched bars (*46,47*).

Grossmann and coworkers followed Russell's work and demonstrated a correlation of as-quenched hardness of round bars, with calculated cooling times obtained using the mathematical approach proposed by Russell (*48*). In this work, the preference was to

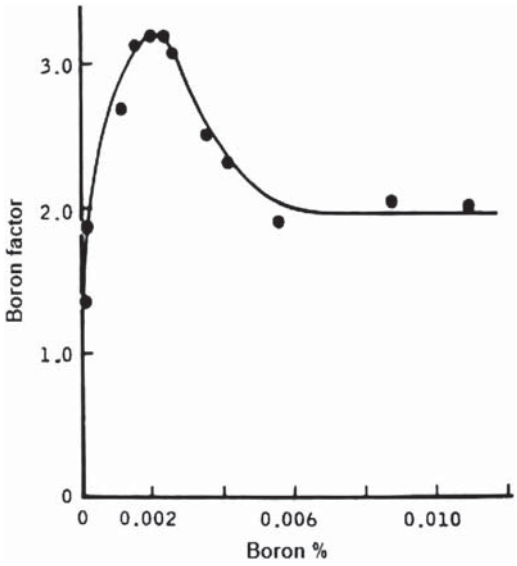

Figure 9 Correlation of the boron hardenability factor with the boron content in the steel alloy. Reproduced from Maalekian, M. *Christian Doppler Laboratory for Early Stages of Precipitation – The Effects of Alloying Elements on Steels – I.* Report CDL/ESOP Report; Technical Universität Graz, Institut für Werkstoffkunde, Schweißtechnik und Spanlose Formgebungsverfahren: Graz, Austria, Oct 2007; pp 1–36.

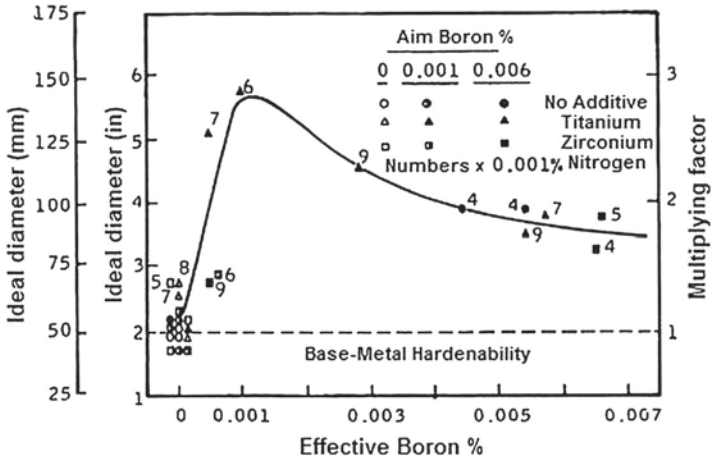

Figure 10 The correlation of the effective boron content of construction steels containing nitrogen, titanium, and zirconium with the ideal diameter (hardenability). Reproduced from Kapadia, B. M.; Brown, R. M.; Murphy, W. J. The Influence of Nitrogen, Titanium and Zirconium on the Boron Hardenability Effect in Constructional Alloy Steel. *Trans. Metall. Soc. AIME* **1968,** *242*, 1689–1694.

use bar diameters instead of radii, and therefore, they defined the term 'H' as $H = h/2 = C/2\lambda$. Details of the development and use of steel hardenability and quench severity, which were based on the work of these earlier workers, will now be provided.

The rate of cooling of hot steel is dependent on (1) the initial temperature of the hot steel before cooling begins, (2) the size, shape, and the cross-section size of the piece being cooled, (3) the thermophysical properties of both the quenchant and the steel, including specific heat capacity, thermal diffusion, and thermal conductivity, (4) temperature-dependent viscosity of the quenchant, and (5) the quenchant temperature. Russell developed a numerical treatment of the quenching process based on Newton's law of cooling, which assumes that the rate of cooling is proportional to the difference in temperature between the surface of the object and the surroundings (quenchant) (*49*). This approach can be described numerically as follows (*50*):

$$dQ = \alpha A(T_S - T_M)dt$$

For a cylinder, this equation is expressed as:

$$dQ = \frac{\lambda}{r}A(T_C - T_S)dt$$

where

Table 6 D_I ranges for various steel alloys

Steel	D_I *range*	*Steel*	D_I *range*	*Steel*	D_I *range*
1045	0.9–1.3	4135H	2.5–3.3	8625H	1.6–2.4
1090	1.2–1.6	4140H	3.1–4.7	8627H	1.7–2.7
1320H	1.4–2.5	4317H	1.7–2.4	8630H	2.1–2.8
1330H	1.9–2.7	4320H	1.8–2.6	9632H	2.2–2.9
1335H	2.0–2.8	4340H	4.6–6.0	8635H	2.4–3.4
1340H	2.3–3.2	X4620H	1.4–2.2	8637H	2.6–3.6
2330H	2.3–3.2	4620H	1.5–2.2	8640H	2.7–3.7
2345	2.5–3.2	4621H	1.9–2.6	8641H	2.7–3.7
2512H	1.5–2.5	4640H	2.6–3.4	8642H	2.8–3.9
2515H	1.8–2.9	4812H	1.7–2.7	8645H	3.1–4.1
2517H	2.0–3.0	4815H	1.8–2.8	8647H	3.0–4.1
3120H	1.5–2.3	4817H	2.2–2.9	8650H	3.3–4.5
3130H	2.0–2.8	4820H	2.2–3.2	8720H	1.8–2.4
3135H	2.2–3.1	5120H	1.2–1.9	8735H	2.7–3.6
3140H	2.6–3.4	5130H	2.1–2.9	8740H	2.7–3.7
3340	8.0–10.0	5132H	2.2–2.9	8742H	3.0–4.0
4032H	1.6–2.2	5135H	2.2–2.9	8745H	3.2–4.3
4037H	1.7–2.4	5140H	2.2–3.1	8747H	3.5–4.6
4042H	1.7–2.4	5145H	2.3–3.5	8750H	3.8–4.9
4042H	1.8–2.7	5150H	2.5–3.7	9260H	2.0–3.3
4047H	1.7–2.4	5152H	3.3–4.7	9261H	2.6–3.7
4053H	1.7–2.4	5160H	2.8–4.0	9262H	2.8–4.2
4063H	1.8–2.7	6150H	2.8–3.9	9437H	2.4–3.7
4068H	1.7–2.4	8617H	1.3–2.3	9440H	2.4–3.8
4130H	1.8–2.6	8620H	1.6–2.3	9442H	2.8–4.2
4132H	1.8–2.5	8622H	1.6–2.3	9445H	2.8–4.4

Reproduced from Grossmann, M. A.; Bain, E. C. *Principles of Heat Treatment*, 5th ed.; American Society for Metals: Metals Park, OH, USA, 1964. Krauss, G. Hardness and Hardenability. In *Steels: Heat Treatment and Processing Principles*; ASM International: Materials Park, OH, 1990; pp 145–178. ISBN: 0-87170-370-X (chapter 6).

Q is the heat transferred from the hot steel to the cooler quenchant (J);
α is the interfacial heat transfer coefficient ($W\,m^{-2}\,K$);
A is the surface area (m^2);
T_S is the surface temperature of the steel body (K);
T_M is the temperature of the quenchant (K);
T_C is the temperature at the center of the cylindrical body (K);
r is the radius of the cylinder (m);
D is the diameter of the cylinder (m);
λ is the thermal conductivity of the steel ($W\,m^{-1}\,K$); and
t is the cooling time (s).

The heat transfer coefficient, α, is proportional to the temperature difference between the metal surface and the quenchant. The amount of heat conducted is proportional to the temperature difference between the center and surface of the cylindrical body and is characterized by the thermal conductivity of the steel. These calculations show that the cooling process depends on the ratio α/λ:

$$\frac{\alpha}{\lambda} = \frac{1}{r}\left[\frac{(T_C - T_S)}{(T_S - T_M)}\right]$$

where the ratio α/λ has been referred to as the 'relative heat transfer coefficient' and is commonly designated as h (m^{-1}). Heat transfer coefficients for water, oil, and brine under increasing agitation conditions are provided in **Table 7**. (The term *brine* refers to an aqueous solution of sodium chloride unless otherwise noted.)

Grossmann developed the term '*HD*', which is a quantitative representation of quench severity correlated to heat transfer by complex, coupled interfacial convection/conduction processes, and was designated as (*51*):

$$HD = hR = Bi = \left(\frac{\alpha}{\lambda}\right)R$$

where

H is the heat transfer equivalent consisting of the ratio of the heat transfer factor ($h/2$) to thermal conductivity, indicating the heat dissipation rate from the steel to the quenching medium (per inch);
D is the bar diameter (inch);

Table 7 Calculated heat transfer coefficient variations, derived from Grossmann *H*-values, with quenchant and agitation[a]

Quenchant	*Agitation*	α ($W\,m^{-2}\,K$)
Brine	None	2700
Brine	Violent	6800
Water	None	1400
Water	Violent	2000
Oil	None	270
Oil	Medium	480
Oil	Good	680
Oil	Violent	960

[a]Reproduced from Tensi, H. M.; Liscić, B. Determination of Quenching Power of Various Fluids. In *Quenching Theory and Technology*, 2nd ed.; CRC Press: Boca Raton, FL, 2010; pp 315–358. ISBN: 978-0-8493-9279-5 (chapter 11) and Grossmann, M. A. The Nature of the Quenching Process. In *Elements of Hardenability*; American Society for Metals: Metals Park, OK, USA, 1952; pp 61–91 (chapter 3).

R is the radius to any point in the cross section of a cylindrical bar (inch); and
Bi is the Biot number, which is a dimensionless number that represents the ratio of the resistance to heat transfer from the inside of the body to the surface of the body (*52*). For simplification, it is assumed that the thermal conductivity is temperature-independent. In this case, the H-value depends only on the heat transfer coefficient at the surface of the body (h) and therefore on the cooling properties of the quenchant.

Instead of the Biot number, Grossmann et al. used the term *HD*, a dimensionless number, to indicate quench severity and *H* as a heat transfer factor. By combining terms, the simple form of this equation that is encountered most often is:

$$H = \frac{h}{2\lambda}$$

These calculations presume that the heat transfer coefficient is constant throughout the entire cooling process, which it is not, especially for vaporizable quenchants such as water and oil where the cooling mechanism changes as the steel cools from full-film boiling (vapor-blanket cooling) to nucleate boiling to convective cooling, with each cooling process characterized by a very different heat transfer coefficient. However, the Grossmann description of quenching continues to be used today – approximately 75 years later (*51*). **Table 8** provides a summary of *H*-values for different quenching media and degrees of agitation reported previously by Grossmann (*53*).

Although it is possible to determine *H*-values by quenching steel bars, it is often inconvenient because the procedure is time consuming and requires sacrificing the steel test bars of different diameters. Unless substantial quantities of steel with the required composition and grain size are available for bars of different diameters, it is difficult to compare *H*-value variations over time because normal lot-to-lot variations in steel composition necessarily produce data scatter. Furthermore, several steels with different hardenabilities are required to obtain test precision when evaluating quenchants ranging from agitated water and brines to poorly agitated oils. Therefore, an alternative method for determining the *H*-value that does not require sacrificing and metallographic characterization of steels test specimens is desirable.

Monroe and Bates have described the use of cooling curve analysis using A Type 304 stainless steel probe to estimate *H*-values based on a finite-difference heat transfer program (*54*). Cooling curves were collected for the cylindrical Type 304 stainless steel test bars where the length was at least four times the diameter, with a Type K thermocouple inserted into the geometric center of the probe. The probe diameters were 13, 25, 38, and 50 mm (0.5, 1.0, 1.5, and 2.0 inch). The calculated time-temperature profiles were analyzed to determine the cooling rate at 705 °C (1300 °F) as a function of imposed quench severity and bar diameter. These data were analyzed statistically to fit the cooling rate data obtained for the different probe diameters, and the following equation was developed (*55*):

$$H = AX^{C}\exp\left(BX^{C}\right)$$

where

H is the Grossmann *H*-value (the heat transfer equivalent as defined above);
X is the cooling rate in $^{\circ}F\,s^{-1}$ at 705 °C (1300 °F); and
A, *B*, *C*, *D* are curve fitting parameters summarized in **Table 9** (*55*).

Table 8 Grossmann H – values for different quenching media[a]

Quenching conditions	*Air*	*Oil*	*Water*	*Brine*
No circulation	0.02	0.25–0.30	0.9–1.0	2
Mild circulation	–	0.30–0.35	1.0–1.1	2–2.2
Moderate circulation	–	0.35–0.40	1.2–1.3	–
Good circulation	–	0.40–0.50	1.4–1.5	–
Strong circulation	0.05	0.5–0.8	1.6–2.0	–
Violent circulation	–	0.8–1.1	4	5

[a]Reproduced from Grossmann, M. A. The Nature of the Quenching Process. In *Elements of Hardenability*; American Society for Metals: Metals Park, OK, USA, 1952; pp 61–91 (chapter 3).

Table 9 Statistical modeling parameters for Grossmann *H*-value determination using instrumented type 304 stainless steel probes[a]

Cylindrical probe diameter[c]		*Curve-fitting parameters*			
mm	*inch*	*A*	*B*	*C*	*D*
13	0.5	0.002802	0.1857×10^{-7}	1.201	2.846
25	1.0	0.002348	0.2564×10^{-9}	1.508	4.448
38	1.5	0.002309	0.5742×10^{-9}	1.749	5.076
50	2.0	0.003706	0.03456×10^{-10}	1.847	6.631

[a]Reproduced from Dakins, M. E.; Bates, C. E.; Totten, G. E. Estimating Quench Severity with Cooling Curves. *Heat Treat.* **April 1992,** 24–26.
[b]A Type K thermocouple is press-fitted or soldered to the geometric center of the probe. Totten, G. E.; Bates, C. E.; Clinton, N. A.; Cooling Curve Analysis. In *Handbook of Quenchants and Quenching Technology*; Totten, G. E., Bates, C. E., Clinton, N.A., Eds.; ASM International, Materials Park, OH, 1993. ISBN: 978-0-8717-0448-1, pps 69–128.
[c]Infinite probe dimensions where the length of the bar is at least four times the diameter to minimize end-cooling effects.

The use of this model and Type 304 stainless steel probes, as well as the cooling rate curves obtained from the experimental time–temperature cooling curve data, provides a nondestructive and reproducible determination of *H*-values provided by various quenchant media.

Round bars, square bars, and plates exhibit different depths of hardening, which is dependent on the total surface area exposed to the quenchant. The total surface area significantly affects heat extraction during quenching and, therefore, the depth of hardening. This is why rectangular-shaped bars achieve a relatively lower depth of hardening than round bars of the same cross-sectional size (*56*). **Figure 11** can be used to convert the diameter or thickness of square bars and plates to the equivalent diameter of the circular cross-sectional size (*1*). The equivalent diameter is considered to be the diameter of a circle that can be transcribed in the section of interest. Alternatively, Aerospace Standard AS 1260 can be used for comparing the hardening response to shapes other than round bars (*57*).

Figure 12 illustrates the degree of hardening with increasing bar size for a water and an oil quench (*53,91,150*). As the cross-sectional size of the bar is increased, the size of the unhardened core (D_U), where there is <50% martensite, increases more rapidly for the less severe oil quench than for the water quench. Quench severity was defined above as the product of the heat transfer equivalent '*H*' and the diameter '*D*' of a cylindrical bar. This means that the heat flow remains constant; therefore the *HD* value is unchanged. Grossmann et al. constructed a chart correlating the ratio of the unhardened diameter to the total diameter (D_U/D) to the *HD* value of a cylindrical steel bar quenched in water and in oil with known *H*-values (see **Figure 13**).

The shape of the family of curves in **Figure 13** is also interesting since they indicate that the value of D_U/D increases faster as the value of *H* decreases, which means that experimentally it becomes increasingly difficult to obtain any hardening as the diameter of the bar increases (*75*). These curves also indicate that two different steels with different hardenabilities may exhibit the same critical diameters in two different quenching media, but the unhardened core at all diameters would be greater than the critical diameter which would be different (*13,51,58*).

One classical way of using this concept for determining the critical diameter is to quench a single bar with a known diameter (*D*) and quenchant *H*-value and measure the diameter of the unhardened core (D_U). Then the point corresponding to *HD*, D_U/D is

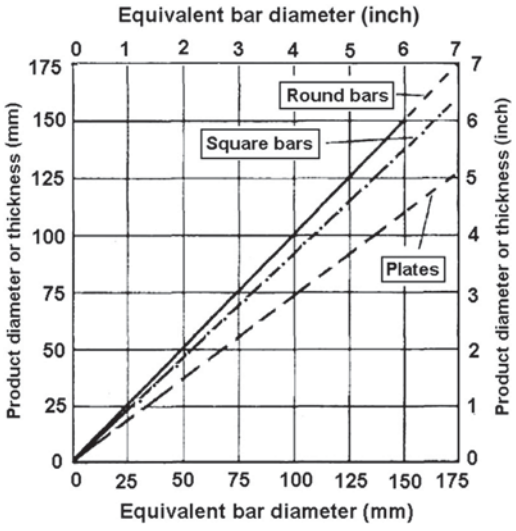

Figure 11 Relationship between through-quenched round-bar diameter and through-quenched thickness of plates and square bars. Reproduced from Totten, G. E.; Bates, C. E.; Clinton, N. A. Measuring Hardenability and Quench Severity. In *Quenchants and Quenching Technology*; ASM International: Materials Park, OH, USA, 1993; pp 35–68. ISBN: 978-0-8717-0448-1 (chapter 2).

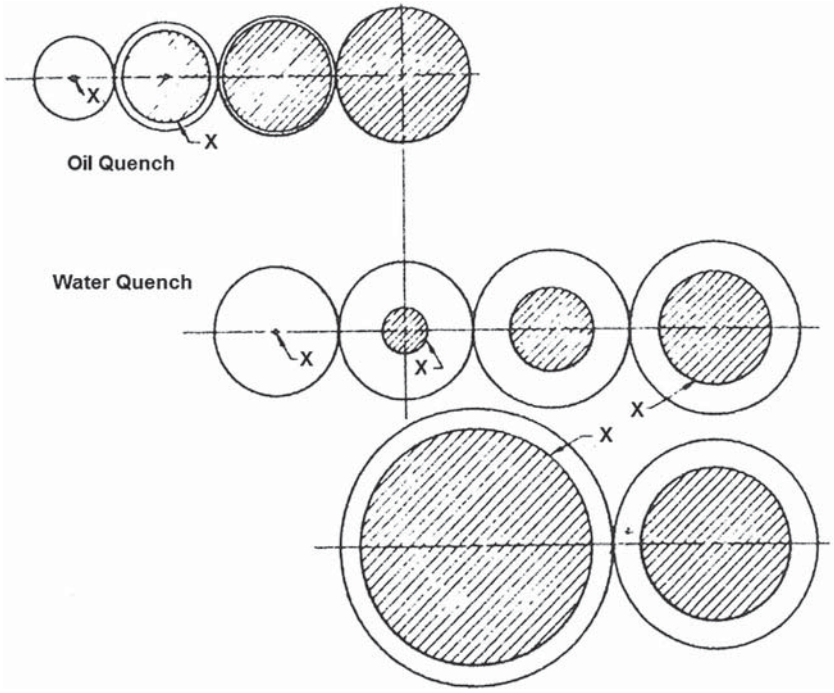

Figure 12 Schematic illustration of AISI 3140 quenched in oil and water. The shaded region indicates the unhardened core (<50% martensite) for each quenching condition. As expected, a water quench provides better through-hardening than a less severe oil quench at the same bar diameter. Reproduced from Grossmann, M. A. Hardenability Tests. In *Elements of Hardenability*; American Society for Metals: Metals Park, OK, 1952; pp 1–42 (chapter 1).

located and the curve on which it is located is followed to $D_U/D = 0$ (on the X-axis) in **Figure 13** and then the value of HD is known. Dividing the value of HD by H gives the critical diameter D_{crit} (*13*).

Figure 14(a) (for large bars) and **Figure 14(b)** (for small bars) can be used to determine the ideal critical diameter (D_I – value) for any steel if the critical diameter (D_{crit}) and H-value for the quenching medium is known or if the D_I – value and H-value are

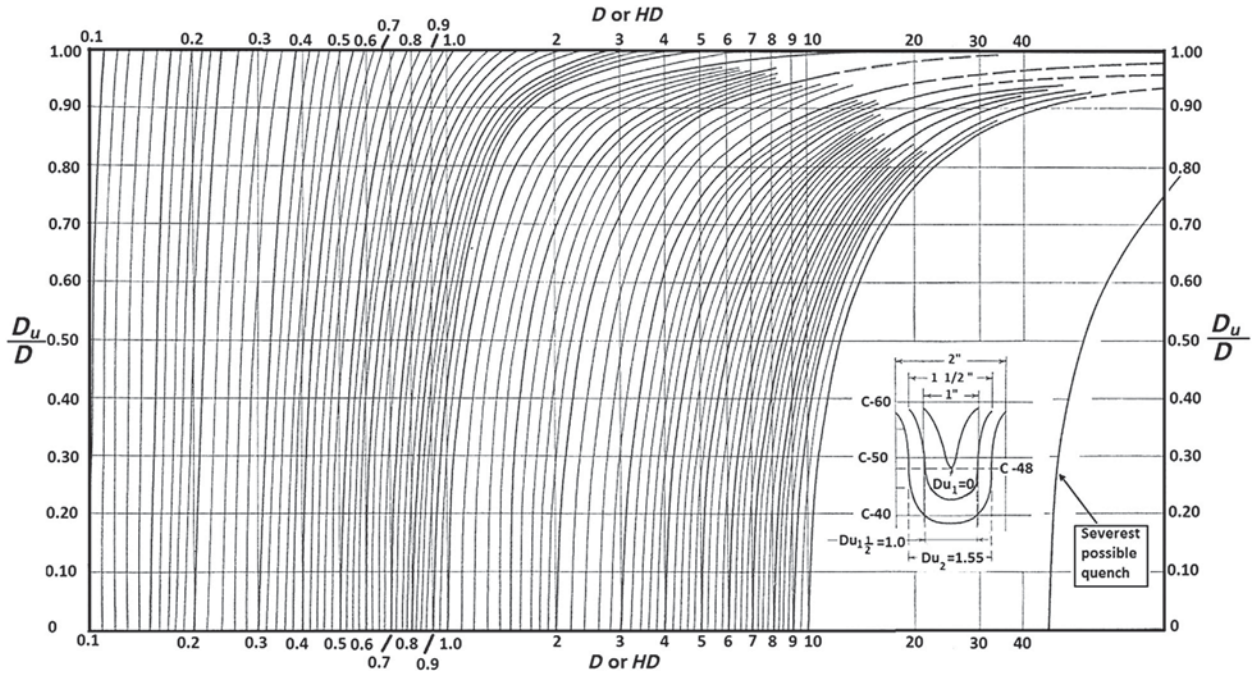

Figure 13 Grossmann's interrelationship between quench severity (HD), bar diameter (D), and depth of hardening (D_U/D). Reproduced from Crafts, W.; Lamont, J. L. Quenching. In *Hardenability and Steel Selection*; Pittman Publishing: New York, NY, 1949; pp 53–83 (chapter 4).

known; then the D_{crit} can be determined (*40,146*). These conversions indicate that D_I is not only a measure of steel hardenability, but is also independent of the quenching medium.

12.03.2.6 Jominy Hardenability

The most commonly used test for evaluating steel hardenability is the Jominy bar end-quench test, which was developed by Jominy and Boegehold (*59*). The Jominy end-quench test provides a faster alternative to assess steel hardenability than the more time-consuming development of TTT and CCT diagrams. There are many international standards describing this important test, including ASTM A255 (*60*), SAE J406 (*61*), JIS G 0561 (*62*), DIN 50191 (*63*), and ISO 642 (*64*).

In this section, the Jominy end-quench testing procedure and its relationship to quenchant immersion tests to assess quench severity will be discussed.

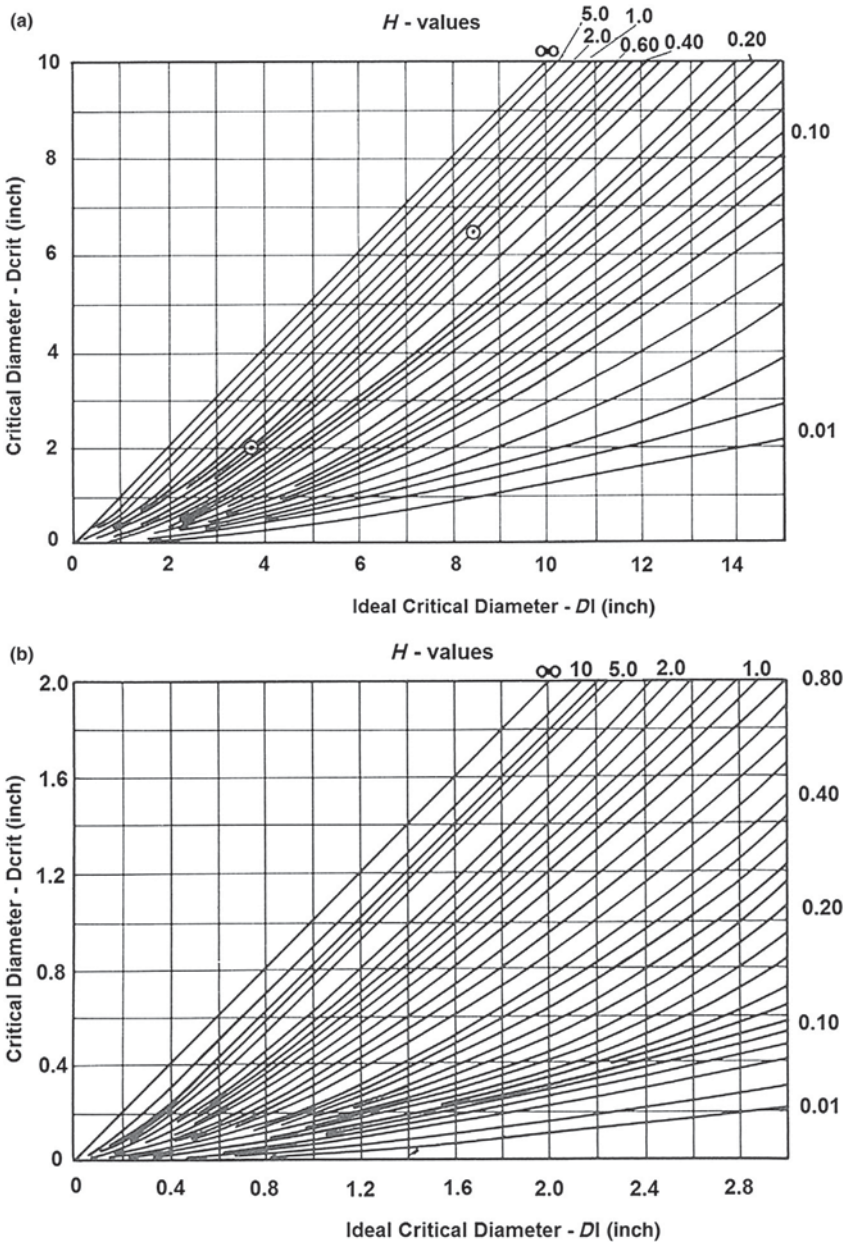

Figure 14 Charts for the interconversion of the critical diameter and ideal critical diameter if the Grossmann hardenability (H) value is known. (a) For large bars and (b) for small bars. Reproduced from Krauss, G. Hardness and Hardenability. In *Steels: Heat Treatment and Processing Principles*; ASM International: Materials Park, OH, 1990; pp 145–178. ISBN: 0-87170-370-X (chapter 6).

12.03.2.6.1 The Jominy End-Quench Hardenability Testing Procedure

The Jominy end-quench test utilizes a 100 mm (4 inch) long by 25 mm (1 inch) diameter round bar of the steel of interest (see **Figure 15(a)**) is first normalized to eliminate any differences in microstructure due to previous hot working (*147*). After normalizing, the test bar is heated to the specified austenitizing temperature. The austenitizing temperature is dependent on the specific steel alloy being evaluated and may be as low as 815 °C (1500 °F). Most carbon and low-alloy steels are heated in the range of 870–900 °C (1600–1650 °F). It is important that precautions be taken to prevent decarburizing and scaling during the time the Jominy test bar is heated.

When the Jominy test bar has equilibrated at the austenitizing temperature, it is dropped into a fixture as shown in **Figure 15(a)**, where one end of the test bar is cooled with 24 °C (75 °C) water emitted from a 13-mm (0.5-inch) orifice under standardized conditions. In this way, one end of the test bar is cooled at a fast cooling rate typical of highly agitated water, and the opposite end is cooled slowly in still air. At intermediate locations from the quenched end, quench severities comparable to still-water quenching, oil quenching, and forced-air cooling are encountered, as shown in **Figure 15(b)** (*147*).

After quenching, a 0.38-mm (0.015-inch) flat is ground along the length of both sides of the test bar to remove any decarburized material. It is important that temperature increases during the grinding process be minimized to prevent any subsequent tempering of the steel. Hardness is typically measured at 1.5 mm (1/16 or 0.0625 inch) for alloy steels as shown in **Figure 15(b)** (*147*). However, for low-hardenability carbon steels hardness is typically measured at 0.65 mm (1/32 or 0.031 inch) (*65*).

When heating the Jominy test bar, it is important to clearly specify the austenitizing temperature and to show that the heating time is sufficient to assure that the temperature within the bar is uniform throughout. If the austenitizing temperature is too low, the necessary carbide dissolution may be incomplete, which in addition to a nonuniform temperature will result in depressed Jominy curves indicating poorer than expected hardenability due to the accelerated formation of nonmartensitic transformation products on cooling (*66*). **Figure 16** illustrates the effect of austenitizing temperature on the hardenability of AISI 4150 steel. Heating to the proper austenitizing temperature is especially important for low-hardenability steels (*56*).

Weinman et al. reported that the most important factor affecting the correlation of Jominy bar hardness with that of quenched rounds in commercial steels was longitudinal and transverse segregation effects due to nonuniform heating, with the greater effect being longitudinal segregation (*67*). In addition to chemical composition and grain size, austenite homogeneity is reported to exhibit one of the greatest effects on Jominy end-quench hardness results (*68*).

Important experimental variables that may influence Jominy end-quench test results include austenitizing time and temperature, degree of oxidation or decarburization that may occur during austenitization, consistency of the flat surface ground on the Jominy bar prior to hardness measurement, water temperature, height of the water jet, orifice diameter, and transfer time from the furnace to the test fixture. All tests must be conducted in accordance with the international standard being used (*1*).

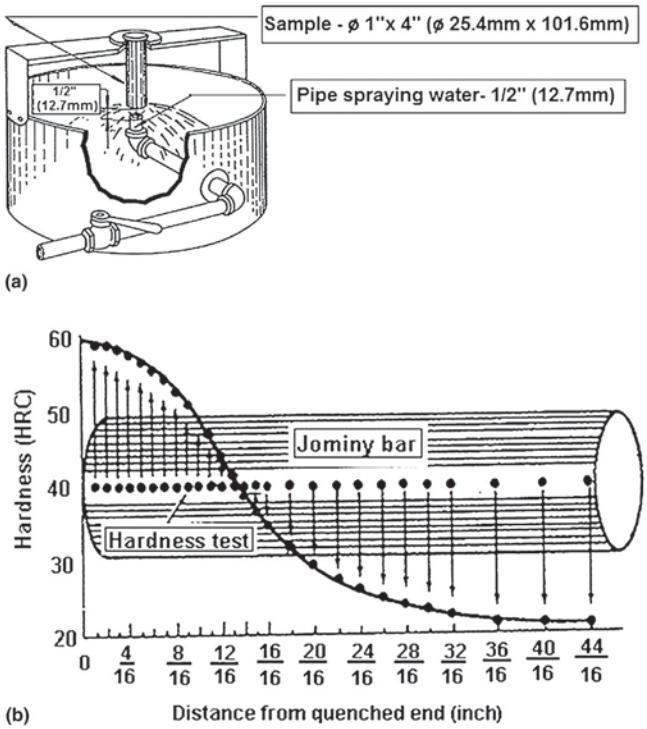

Figure 15 (a) Schematic illustration of a typical quenching apparatus used for the heated Jominy test bar. (Modified from Dorivaldo Batista Nogueira Junior, Universidade São Francisco, Internet: http://amigonerd.net/trabalho/2320-ensaio-jominy. (b) Illustration of a typical Jominy curve generated from a Jominy test bar after end-quenching and grinding. Reproduced from Dorivaldo Batista Nogueira Junior, Universidade São Francisco, Internet: http://amigonerd.net/trabalho/2320-ensaio-jominy.

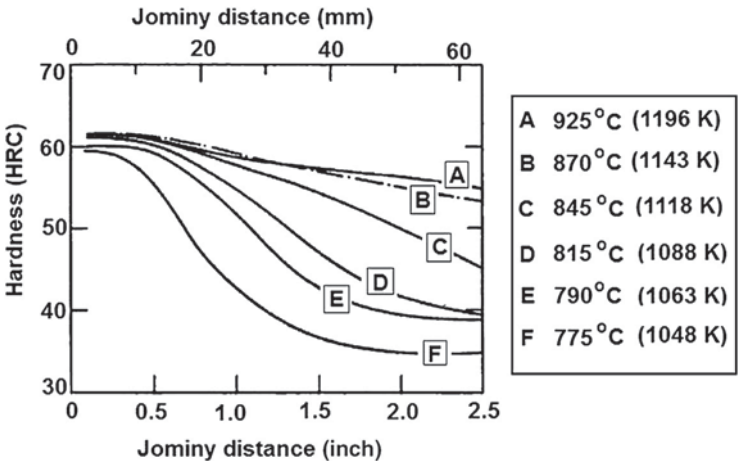

Figure 16 Effect of varying austenitizing temperature on the hardenability of AISI 4150 steel as exemplified by Jominy curve behavior. The austenitizing temperature is provided at the right in both °C and K. Reproduced from Jackson, C. R.; Christenson, A. L. The Effect of Quenching Temperature on the Results of the End-Quench Hardenability Test. *Trans. Am. Inst. Min. Metall. Eng.* **1944,** *158*, 125–137.

Figure 17 shows four (4) different positions along the Jominy bar that correspond to the indicated cooling time-temperature curves and microstructures shown on a CCT diagram (*38*). The highest fraction of martensite would be expected for cooling curve A, which would correspond to the fastest cooling and highest hardness obtained closest to the water-cooled end. Because of the slow cooling obtained at the air-cooled end (position D), a pearlitic microstructure would be expected, with the lowest hardness indicating that hardening did not occur for the steel indicated by this CCT diagram. Intermediate cooling would give either mixed martensitic/pearlitic, bainitic, or ferrite/pearlite microstructures, depending on the cooling rate and transformation behavior.

Various workers such as Weinman et al. have obtained cooling time–temperature curves by welding thermocouple wires, either 22 or 28 gage, at 1.5 mm depths at different positions along the length of a Jominy test bar (*67*). Cooling time–temperature curve data was obtained during the quench using a high-speed recorder or an oscillograph.

The so-called 'Jominy equivalent cooling rate' is the cooling rate at 704 °C (1300 °F) for each Jominy position for which there is a cooling time–temperature curve (*69,70*). The 704 °C temperature is used because the Jominy equivalent cooling rate is approximately independent of the steel composition because the thermophysical properties of carbon and low-alloy steels are very similar at this temperature, though not identical (*7*). Although the cooling rate at 704 °C is traditionally used, there are reports that the cooling rate over the temperature interval of 700–500 °C is preferred (*69*). The Jominy equivalent cooling rates are often shown along with hardness and Jominy position correlations. Alternatively, if the hardness and Jominy position are known, the corresponding Jominy equivalent cooling rate can be determined from Figure 18. However, the Jominy equivalent cooling rate corresponds to the distance from the quenched end at the surface. The cooling rate at the center of the bar is dependent on the bar diameter. Nevertheless, the amount of martensite formed dictates the steel hardness, and the hardness is a function of the cooling rate. Thus, if the hardness is known at any position, the Jominy equivalent cooling rate can be determined.

Figure 19 shows Jominy curves for a series of AISI 8600 (nickel-chromium-molybdenum) steel with increasing carbon content (*148*). These data show that hardenability increases with increasing carbon content, as is evident by the decreasing change in hardness with increasing Jominy distance (*J*-values) along the Jominy test bar.

Jominy curves comparisons also illustrate the inherent differences in hardenability of different steel grades at the same 0.4% carbon content. The nominal composition of these steels is shown in Table 10. Figure 20 shows that, as expected, plain-carbon (1000 series) steel is the least hardenable of those alloys tested; of the remaining, the following order of hardenability was observed (*148*):

$$1040 < 5140 < 8640 < 4140 < 4340$$

The Jominy end-quench test provides valid data for steels with an ideal diameter (D_I) of approximately 25–160 mm (1–6 inch). The D_I may be less than 25 mm; however, this usually requires Vickers hardness measurements closer to the quenched end and closer together than is typically possible with Rockwell hardness measuring equipment. Also, Weinman et al. have reported that Jominy end-quench cooling curves do not correlate well with oil-quenched round bar results when appreciable amounts of pearlite and ferrite are formed (*67*).

One illustration of the use of Jominy curves other than simply for steel hardenability comparison is provided by the example illustrated in Figure 20 for AISI 4140. Assume that the as-quenched hardness of the surface of 4140 is $R_c = 50$ and at the center the as-quenched hardness is 40. What is the cooling rate and % martensite in these two locations? To answer this question, the distance from the quenched end of the Jominy bar is determined for both hardness values if the Jominy equivalent cooling rates are not provided on the plot of the Jominy data. In this case, the cooling rate at each Jominy position is determined from Figure 18. If the Jominy equivalent cooling rate is provided on the plot as shown in Figure 20, the cooling rate may be determined by reading it

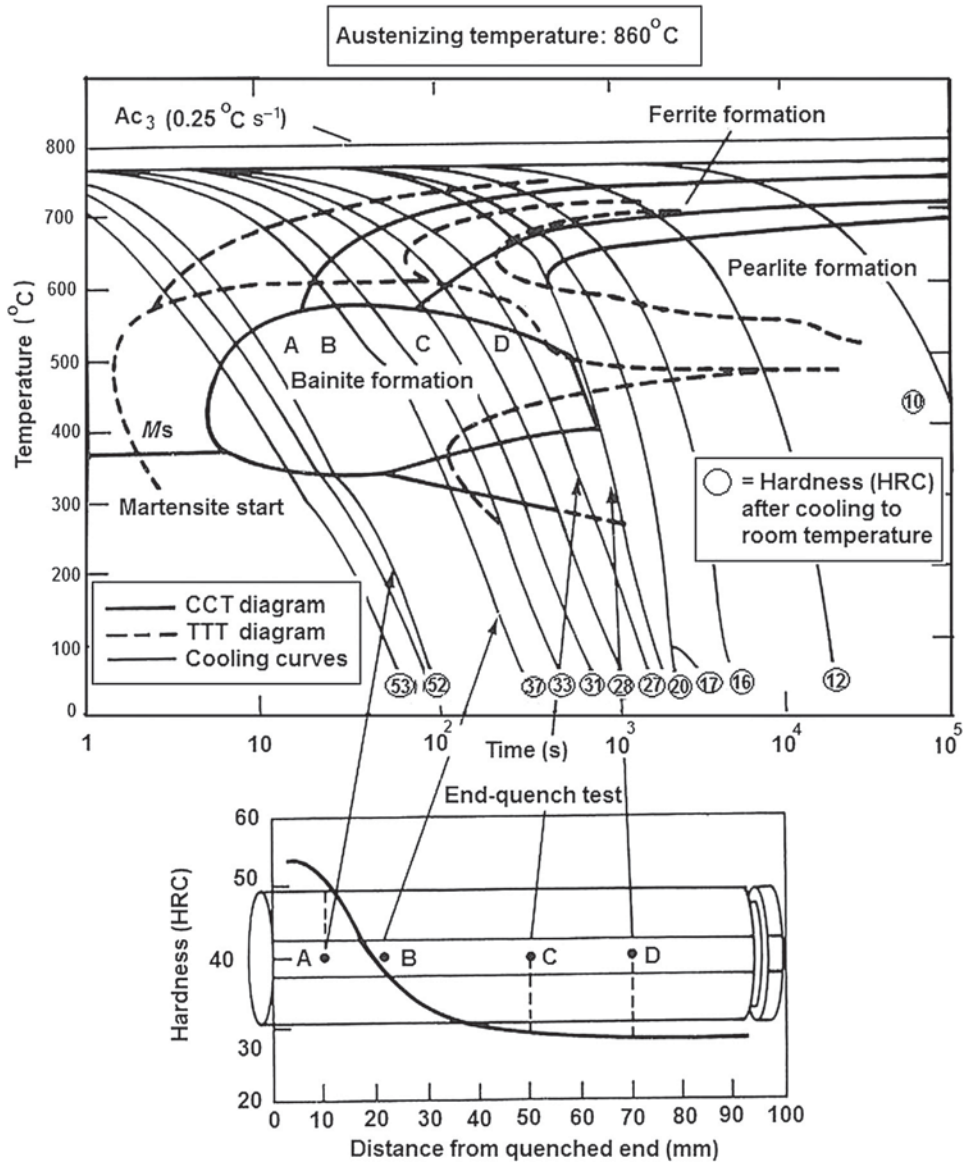

Figure 17 Superposition of cooling curves obtained along a Jominy test bar on the TTT curve of a steel. Note the fastest cooling on the water-quenched end yielding a martensitic microstructure and the slowest cooling on the air-quenched end yielding a pearlitic microstructure and lowest hardness. Intermediate cooling rates and microstructures are obtained between these two cooling limits. Reproduced from *Steel Casting Handbook – Supplement 11: Hardenability and Heat Treatment*; Steel Founders Society of America: 780 Mcardle Dr # G Crystal Lake, IL 60014-8155, 1985; pp 3–20.

directly from the figure. The % martensite is determined from the scale on the right side of **Figure 20**. The data is summarized in **Table 11**. This example also shows that since the % martensite is < 50 at the center, the AISI 4140 bar in this example is not through-hardened.

By further inspection of the Jominy curves shown in **Figure 20**, AISI 4340 is considerably more hardenable than 4140 and would be expected to exhibit a significantly greater core hardness. AISI 8640 would exhibit a lower hardness. AISI 1040 would not be hardened under these quenching conditions.

Similarly, if the cooling rate is known for a given quenching medium, it is possible to determine which Jominy curve intersects that cooling rate; from the hardness it is possible to use a conversion chart, similar to **Table 12**, to obtain the as-quenched strength that the steel alloy should produce.

12.03.2.6.2 Hardenability Bands

As discussed previously, steel hardenability is dependent on composition, which varies within specified limits for each steel grade. However, there is a normal variation in hardenability that may be encountered for any grade of steel within its compositional specification limits, and in some cases, tighter control of the composition is necessary for an application where that steel may be

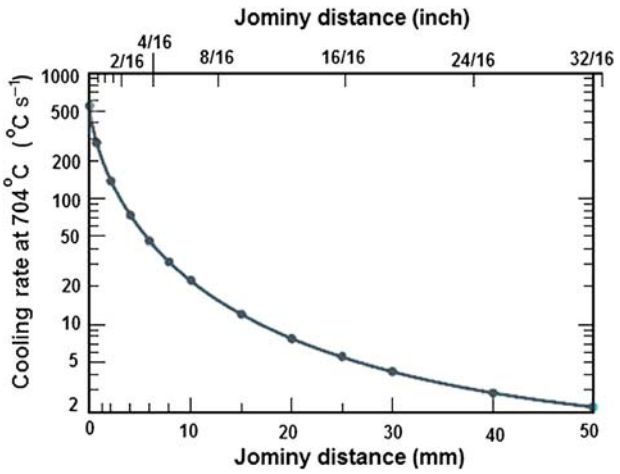

Figure 18 Jominy equivalent cooling rate – Jominy distance correlation. The cooling rates are surface cooling rates at each position where hardness is measured on the Jominy bar. Since the cooling rate is essentially independent of steel composition, this curve can be used for any carbon steel.

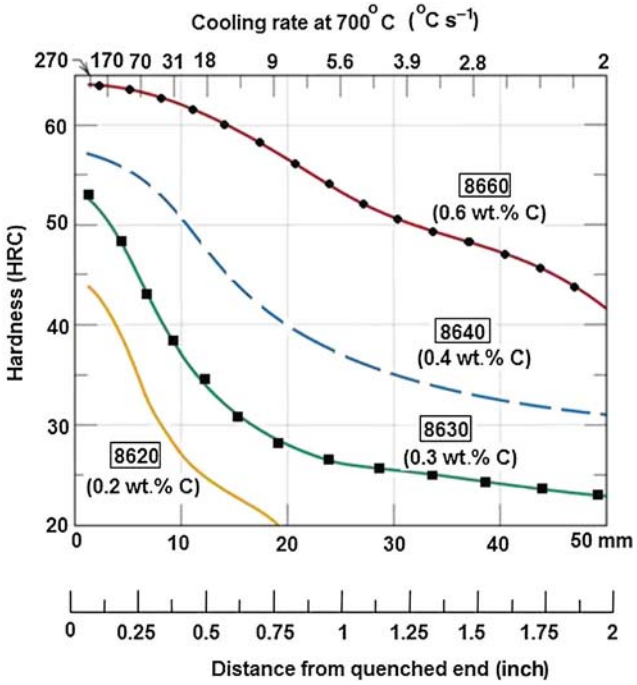

Figure 19 Illustration of the effect of increasing carbon content of an AISI 8600 series steel alloy on Jominy hardenability. (Modified from Callister, W. D.; Rethwisch, D. G. Applications and Processing of Metal Alloys. In *Fundamentals of Materials Science and Engineering, An Integrated Approach*, 3rd ed.; John Wiley & Sons Inc.: New York, NY, 2008; pp 358–413 (chapter 11).).

Table 10 Selected SAE steel alloy grade generic compositions

SAE steel alloy series	*Carbon and steel alloy grade*
1040	Plain carbon (Mn 1.00% max)
5140	Cr (0.8–1.1%)
8640	Ni (0.6%), Cr (0.50–0.7%), Mo (0.20%)
4140	Cr (0.5–1.0%), Mo (0.2%)
4340	Ni (1.8%), Cr (0.50–0.80%), Mo (0.3%)

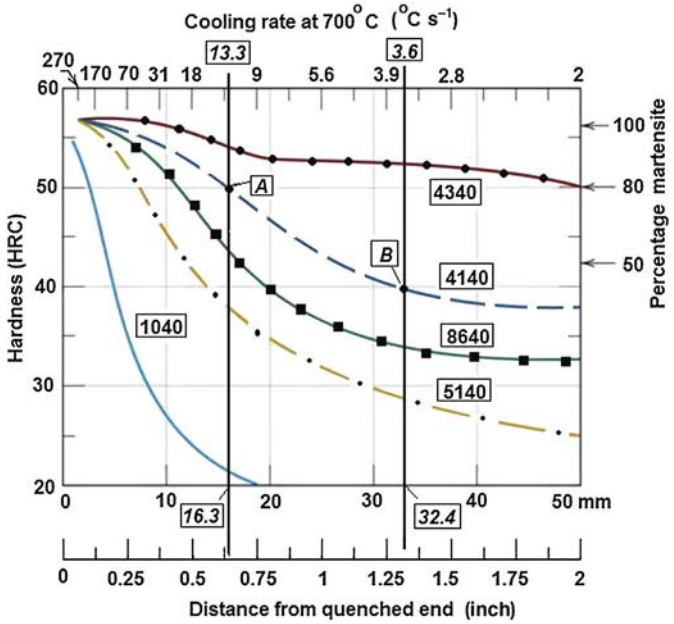

Figure 20 Illustration of the effect of steel alloy composition on Jominy hardenability for different alloys with the same nominal carbon content. (Modification of Callister, W. D.; Rethwisch, D. G. Applications and Processing of Metal Alloys. In *Fundamentals of Materials Science and Engineering, An Integrated Approach*, 3rd ed.; John Wiley & Sons Inc.: New York, NY, 2008; pp 358–413 (chapter 11).).

Table 11 Summary of data from Jominy example

AISI 4140 position	*Hardness (R_c)*	*Jominy distance (mm)*	*Jominy equivalent cooling rate (°C s^{-1})*	*Approximate % martensite*
Surface	50	16.3	13.3	80
Center	40	32.4	3.6	<50

used. Therefore, many steels are also available as H-grade, which possesses tighter compositional control and the control is specified by the maximum and minimum allowable hardenability.

One method of establishing the allowable hardenability variation for each steel grade is to provide minimum and maximum D_I – values for each grade of steel such as those shown in **Table 6**. Alternatively, the most common method used to establish the allowable hardenability variation for a range of steels is based on Jominy end-quench curve data. For each H-grade steel composition, there exists a maximum and minimum Jominy curve. Specifications such as SAE J1268 provide for the maximum and minimum Jominy curves corresponding to these compositional limits (*71*). Therefore, for each grade of steel, there exists an acceptable range of hardenabilities exemplified by a so-called 'Hardenability (H-) Band'. **Figures 21 and 22** illustrate the Jominy H-bands for AISI 1020 and 1040 carbon steels and AISI 4130 and 4140 low-alloy steels, respectively (*38*). Note that the H-bands become broader as steel hardenability increases.

Table 12 Rockwell hardness to tensile strength conversion

Hardness (R_c)	*Tensile strength (psi)*	*Hardness (R_c)*	*Tensile strength (psi)*
70	276 000	50	182 000
68	266 000	49	176 000
66	256 000	47	170 000
64	248 000	46	165 000
62	238 000	45	160 000
60	229 000	44	155 000
58	220 000	42	150 000
57	212 000	41	146 000
55	204 000	38	142 000
53	196 000	37	138 000
52	189 000	36	134 000

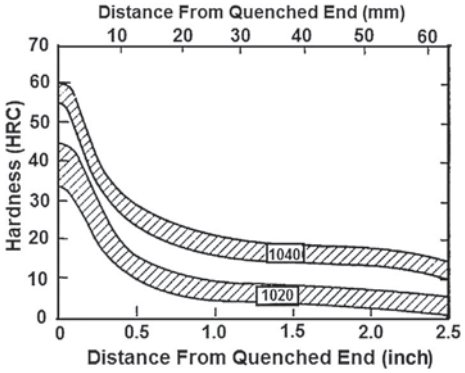

Figure 21 Illustration of Jominy H-bands for AISI 1020 and 1040 steels. Reproduced from *Steel Casting Handbook – Supplement 11: Hardenability and Heat Treatment*; Steel Founders Society of America: 780 Mcardle Dr # G Crystal Lake, IL 60014-8155, 1985; pp 3–20.

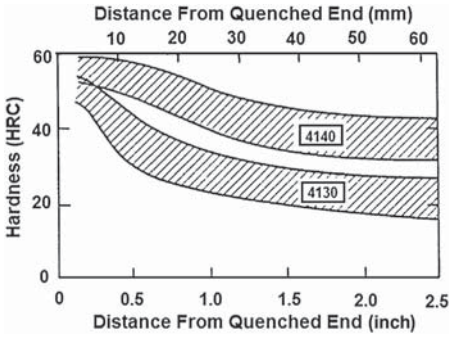

Figure 22 Illustration of Jominy H-bands for AISI 4130 and 4140 steels. Reproduced from *Steel Casting Handbook – Supplement 11: Hardenability and Heat Treatment*; Steel Founders Society of America: 780 Mcardle Dr # G Crystal Lake, IL 60014-8155, 1985; pp 3–20.

For the same composition, the Jominy H-bands for as-cast and wrought steel will be the same. However, the presence of residual elements that exhibit substantial effects on hardenability, such as chromium, may cause a significant broadening in the H-band. Therefore, the potential presence of such residual elements must be monitored carefully.

When even greater hardenability control is required beyond that afforded by the H-grade, to provide more controlled heat treatment response and dimensional control, then a special grade of steel with restricted hardenability (RH)-grade is typically specified. Generally, the hardness range for RH-grade steels will not exceed 5 HRC at the initial position on the end-quench hardenability bar ($J = 0$) and not greater than 65% of the hardness range for standard H-band steels according to SAE J1268 (*71*) in the 'inflection' region. The RH hardenability band usually follows the middle of the corresponding standard H-band (*72*).

12.03.2.6.2.1 Jominy hardenability to round-bar hardness transformation – Crafts-Lamont Jominy equivalence approach

One objective in conducting the Jominy end-quench test is to determine the adequacy of using a particular quenchant to harden a steel with a specific hardenability. Up until this point, this assessment has been done by immersion quenching of a steel bar into the quenching medium of interest. However, the Jominy end-quench test involves quenching only one end of a bar of steel with standardized dimensions and heating conditions with a stream of water at a specified temperature and flow conditions. To relate Jominy end-quench test data with round bar–quenching data, it is assumed that equal quenching histories will produce identical steel structures. This means that that any point within a round bar that exhibits the same cooling rate as the point on the surface of the Jominy bar will produce the same hardness. The Crafts-Lamont hardenability transformation is based on this assumption that the hardness at any position in a quenched bar can be predicted from the results of an end-quench test (*73*).

An alternative to the Jominy Equivalent Cooling Rate at 704 °C is the 'half-temperature time' (also designated as fractional temperature), which was originally defined by Russell and Williamson as:

$$U = \frac{T - T_2}{T_1 - T_2}$$

where T is the varying temperature of the Jominy bar during cooling, T_1 is the austenitizing temperature, and T_2 is the quenching temperature. The point where U equals 0.5 is the half-temperature cooling time (*70*). Asimow et al. used a simpler definition of half-temperature time, which was "the time occupied in the quench, in cooling from the quenching temperature (austenitizing temperature) to a temperature halfway down to that of the quenching medium" (*74*). **Figure 23** illustrates the correlation of half-

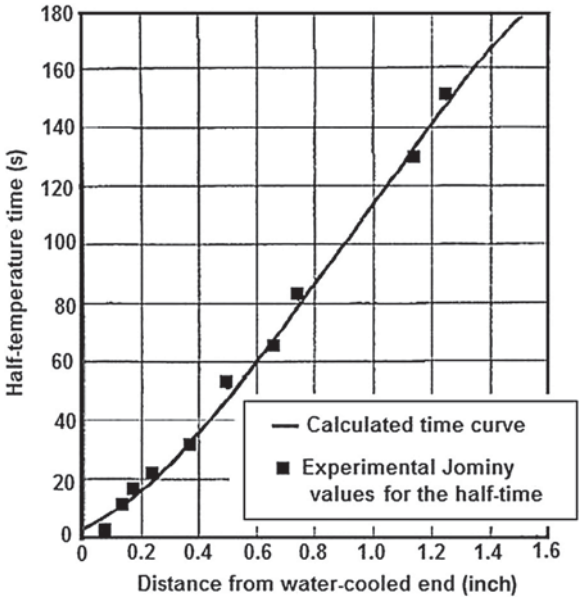

Figure 23 Half-temperature time versus distance from the water-cooled end of the Jominy bar. Reproduced from Asimow, M.; Craig, W. F.; Grossmann, M. A. Correlation between Jominy Test and Round Bars. *SAE Trans.* **1941,** *41* (1), 283–292.

temperature time at the surface of a Jominy bar with respect to the distance from the quenched end (*74*). (Compare to **Figure 18**.) Alternatively, half-temperature time results are shown in **Table 13** (*74*).

Half-temperature times have been used instead of Jominy equivalent cooling rates to correlate Jominy end-quench and immersion round bar–quenching results (*67,70,74*). Asimow et al. have derived an equation for calculating the D_I value for a round bar from Jominy bar data using half-temperature time (t_{htt}) and the value for thermal diffusivity (a), assuming that it is essentially temperature independent (*74*):

$$D_I = 4.458(at_{htt})^{0.5}$$

In Asimow's work on carbon and low-alloy steels, the value of thermal diffusivity (a) was assumed to be equal to 0.009 inch^2 s^{-1}, and the equation is then simplified to:

$$D_I^2 = 0.179t_{htt}$$

The value of D_I may also be determined from **Figure 24** when the complete Jominy curve has been determined (*74*).

Quench severity is related to the heat transfer coefficient (h) or cooling rate of the quenchant, which is dependent on the agitation of the quenchant in addition to fluid composition, viscosity-temperature properties, and so on. The depth of hardening is

Table 13 Variation of half-temperature time with distance from the water-quenched end of a Jominy bar[a]

Distance from the water-quenched end of the Jominy bar		*Time (sec) to cool to one-half temperature*
(inch)	*(mm)*	
1/16	0.0625	2.5
1/8	0.125	10.5
3/16	0.1875	15
1/4	0.250	22
3/8	0.375	33
1/2	0.500	52
5/8	0.625	66
3/4	0.750	81
1 1/8	1.125	130
1 1/4	1.250	150
2	2.00	224

[a]Reproduced from Asimow, M.; Craig, W. F.; Grossmann, M. A. Correlation between Jominy Test and Round Bars. *SAE Trans.* **1941,** *41* (1), 283–292.

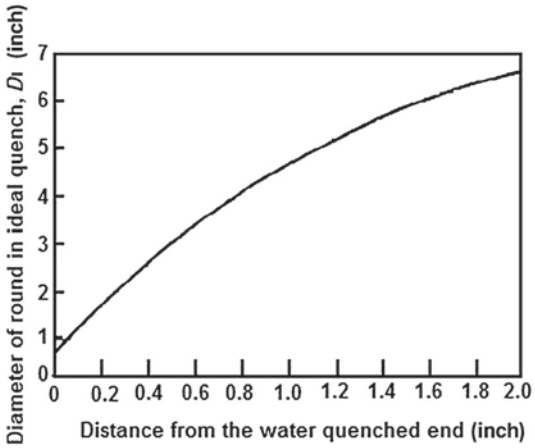

Figure 24 Correlation between the ideal diameter (D_I) for a round bar versus the distance from the water-quenched end of a Jominy bar. Reproduced from Asimow, M.; Craig, W. F.; Grossmann, M. A. Correlation between Jominy Test and Round Bars. *SAE Trans.* **1941,** *41* (1), 283–292.

the ratio (r/R) of the unhardened core (r) to the total radius (R) of the bar being quenched. The value of r/R is equal to 0 at the center of the bar and 1 at the surface. Each figure shown in **Figure 26(a–f)** represents a different ratio of r/R. Although it is possible to determine quench severity from the cooling rate, it is more common to measure the depth of hardening of round bars of different diameters as reported by Grossmann (*51*) and Jominy (*59*). Lamont developed a methodology based on the Jominy hardenability test and a fractionally hardened round bar (*75,76*).

It is assumed that equivalent cooling rates at two positions in a steel bar will exhibit the same hardness. Therefore, if a Jominy curve and the cross-sectional hardness U-curve for a steel alloy of interest as shown in **Figure 25** are available, it is possible to determine the Grossmann H-value (*75*). The process involves selecting a hardness, for example, $R_c = 45$, which in **Figure 25** occurs at $^3/_4$ inch from the quenched end of the Jominy bar and at a distance of 1 inch from the center of a 4-inch round bar ($r/R = 0.5$).

In **Figure 26(f)**, the point where the line intersects the Jominy distance of $^3/_4$ inch indicates that the Grossmann H-value is 2.0 (*76*). If the quenching conditions remain the same, this H-value ($H = 2.0$) may be used to determine the depth of hardening for a different section size or even a different steel.

The Jominy distance that produces the highest hardness is typically taken at the shoulder of the Jominy curve of interest. In **Figure 25(a)**, this occurs at approximately 9/16 inch. The question is: What is the maximum bar diameter that will produce the maximum hardness throughout when the steel is quenched in a petroleum oil with an H-value = 0.35? Through-hardening is determined from **Figure 26(a)**, where the fractional depth of hardening $r/R = 0.0$. The point where the H-value line for 0.35 intersects with the distance from the quenched end of 9/16 occurs at a round-bar diameter of 1.5 inch. Thus, the maximum bar diameter of the steel represented by the Jominy curve in **Figure 25(a)** that will be through-hardened when quenched in a petroleum oil with an H-value of 0.35 is 1.5 inch.

In some cases, it is desirable to quench a steel so that complete through-hardening ($r/R = 0$) does not occur. Instead, the objective may be to quench the steel so that there is a specific depth of hardening with an unhardened core. As an example, consider the steel represented by the Jominy curve in **Figure 25(a)**. Assume that the bar diameter is 4 inch, as illustrated in

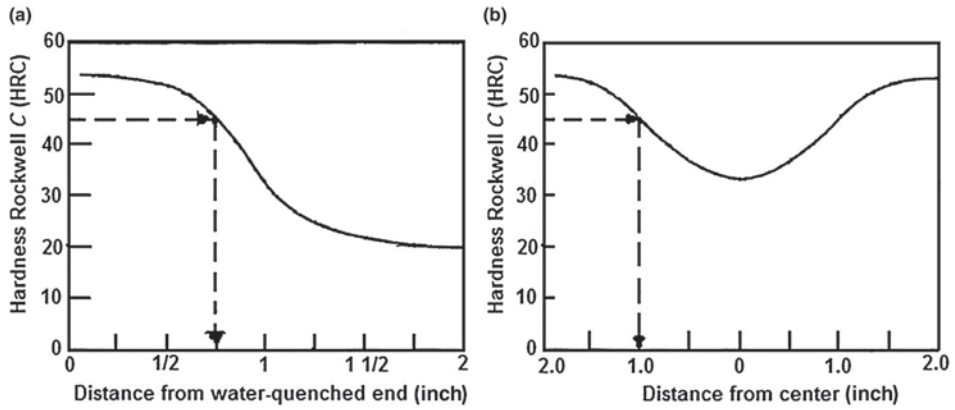

Figure 25 (a) Jominy hardenability curve and (b) cross-sectional hardness curve for a 4-inch diameter of a quenched round bar of the same steel and steel chemistry. Reproduced from Crafts, W.; Lamont, J. L. Quenching. In *Hardenability and Steel Selection*; Pittman Publishing: New York, NY, 1949; pp 53–83 (chapter 4).

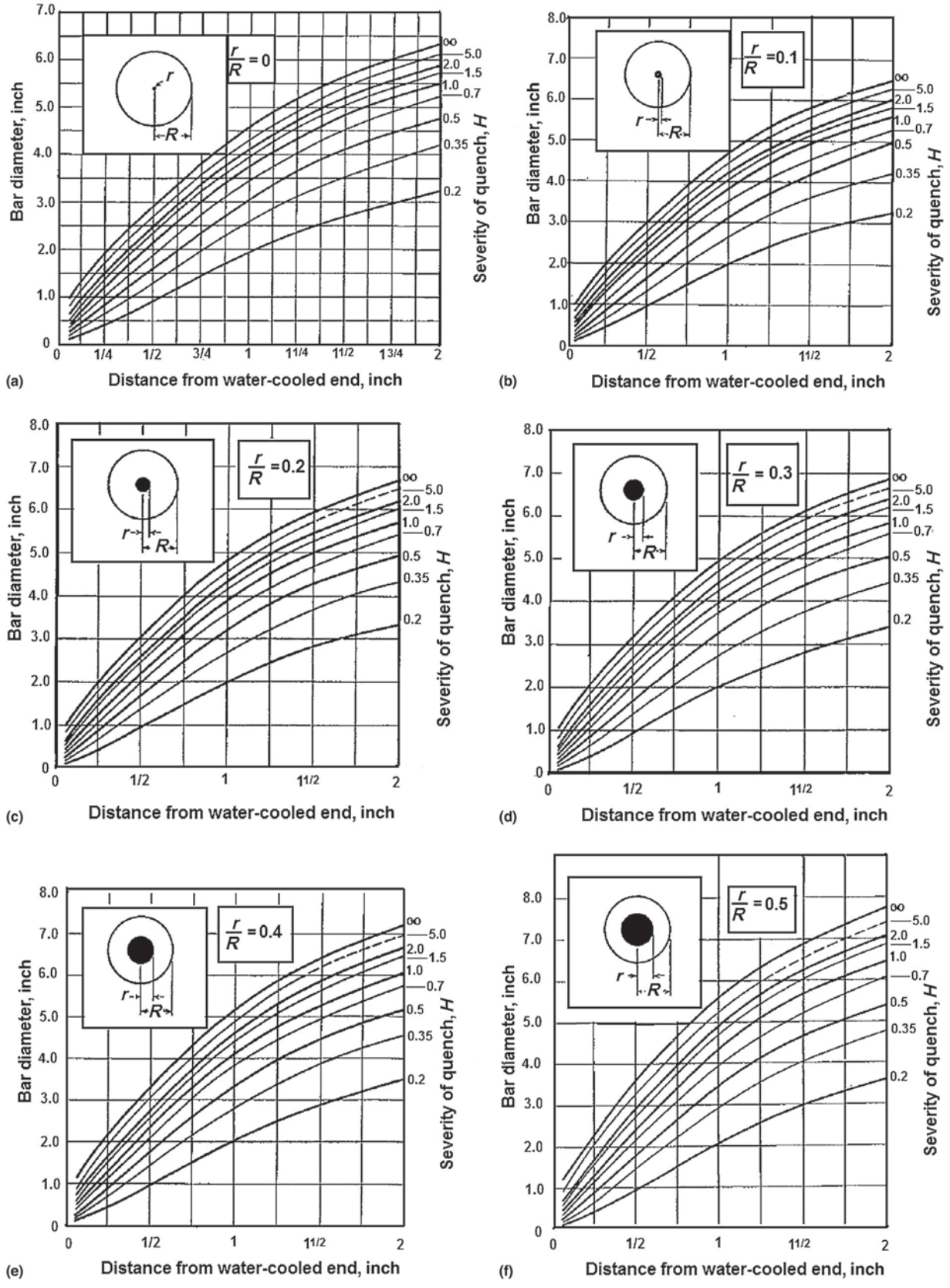

Figure 26 These figures illustrate the Lamont *H*-value correlation of Jominy end-quench distance and round-bar diameter at different locations in the round bar. *Note:* The value of '*r*/*R*' refers to the radius of the unhardened core '*r*' to the value of the total radius of the bar '*R*'. The value of *r*/*R* is '0' at the center and '1.0' at the surface. The round-bar diameter represents locations on the Jominy end-quenched bar: (a) corresponds to the center of a round bar; (b–k) represent locations on the end-quenched Jominy bar at: 10%, 20%, 30%, 40%, 50%, 60%, 70%, 80%, 90% from the center of a round bar; and (l) represents the surface of a round bar. Reproduced from Lamont, J. L. How to Estimate Hardening Depth in Bars. *Iron Age* **Oct 14, 1943,** *152*, 64–70.

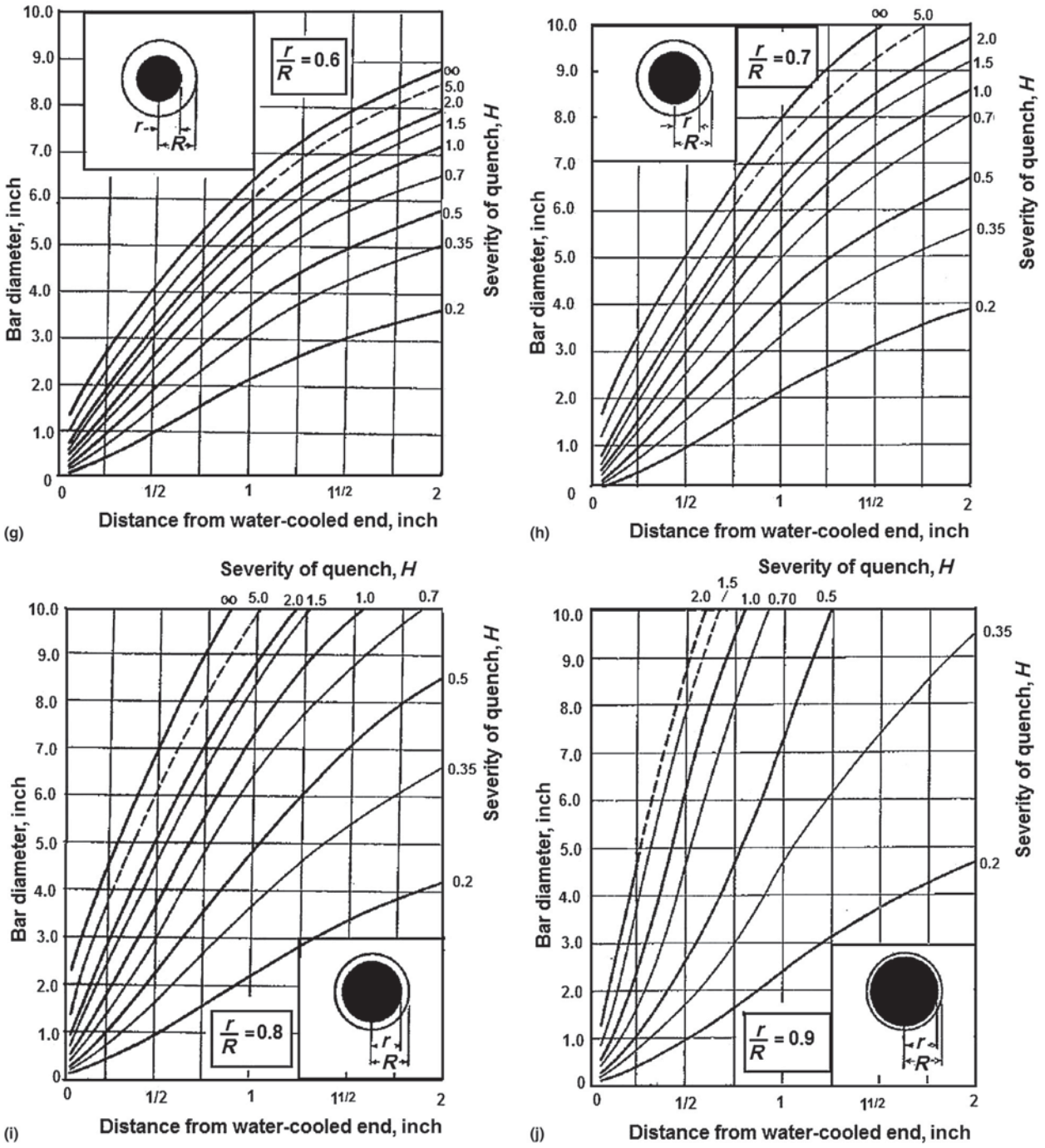

Figure 26 (*continued*).

Figure 25(b) ($R = 2$). In this example, it is desired to quench the bar to achieve a depth of hardening of 0.6 inch ($r = 1.4$). The value of $r/R = 1.4/2.0 = 0.7$, which corresponds to Figure 26(h). Since the same steel as represented by the Jominy curve in Figure 26(a) is used here, the shoulder of this curve, which represents the limit of maximum hardness, occurs at approximately 9/16 inch from the quenched end of the Jominy bar. Using Figure 26(h) for the depth of hardening of 0.6 inch, the intersection of the distance from the quenched end (9/16) and 4 inch (diameter of the round bar) corresponds to approximately $H = 1.5$. Table 5 shows that this quench severity can be achieved by a water quench with strong agitation. Thus, it is estimated that a 4-inch round bar of the steel represented by the Jominy curve in Figure 26(a) will be hardened to a depth of 0.6 inch when subjected to a strongly agitated water quench.

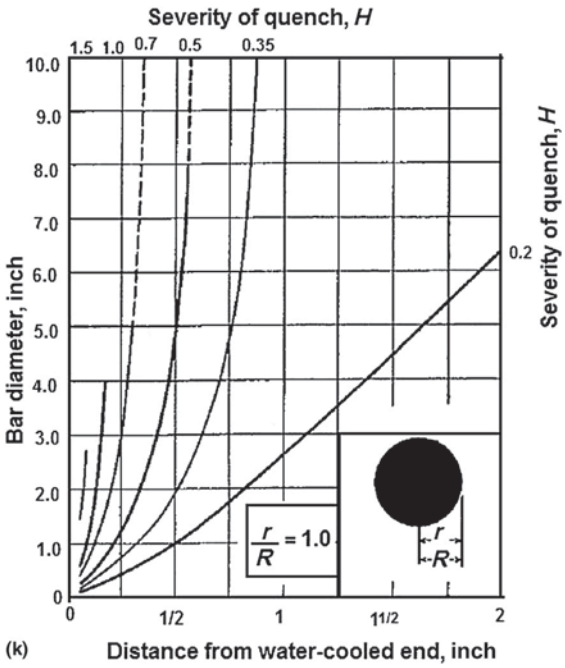

Figure 26 (*continued*).

As discussed previously, Aerospace Standard AS 1260 (*57*) or **Figure 10** (*56*) can be used to convert the diameter or thickness of square bars and plates to the equivalent diameter of a round bar. However, it is important to note that while it is possible to use these charts to approximate the size of a cross section that will provide equivalent hardness to another shape when quenched into a medium of known quench severity the difference decreases as the quench severity increases. Therefore, it is important to validate these approximations experimentally. Validation is also important because the effective *H*-value may vary somewhat with different-sized bars, steel compositional differences, in cases where very low depths of hardening are anticipated, if there may be scale on the bars, or if the thermal diffusivity varies significantly due to alloy content (*76*).

12.03.2.6.2.2 Jominy hardenability to round-bar hardness transformation – Rushman approach

Rushman developed an approach to predict the as-quenched hardness of a steel bar of known hardenability by using the Jominy diagram for the steel of interest, a two-diameter test bar shown in **Figure 27**, and a modified Grossmann chart shown in **Figure 28** (*74*). The two-diameter test bar is used to evaluate the quenchant under actual production conditions. The test bar is austenitized with the production load of parts, typically in the same basket with the parts being heat treated, and then quenched. Although the test bar may be machined from the same alloy as the parts being produced, more typically, to keep the size of the test bar small, it is machined from a low-hardenability steel. The largest diameter of the test bar is selected so that the as-quenched hardness will fall on the sloping portion of the Jominy curve for that steel. After austenitizing and quenching, the two-diameter bar is sectioned, and the hardnesses at the center are determined at three points: at the center of each diameter and at the 'common point'. These hardness values are used with **Figure 28**.

The Grossmann diagram relates the D_I value to Jominy distances (*74*). This well-known diagram may be modified by extending the lines indicating quench severity (*H*-values) to a common point as shown in **Figure 28** (*77*). This common point may be used to

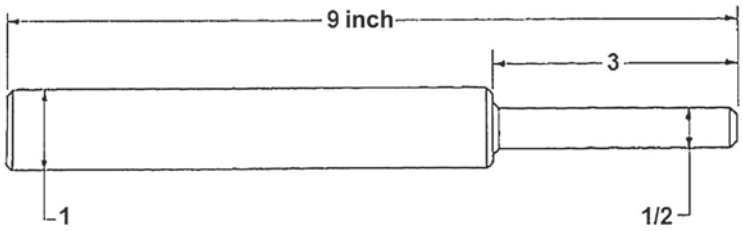

Figure 27 Two-diameter test bar used by Rushman. Reproduced from Rushman, W. F. How to Determine Quench Severity of Oil and Salt Baths. *Metal Prog.* **Dec 1963,** *84* (6), 91–92.

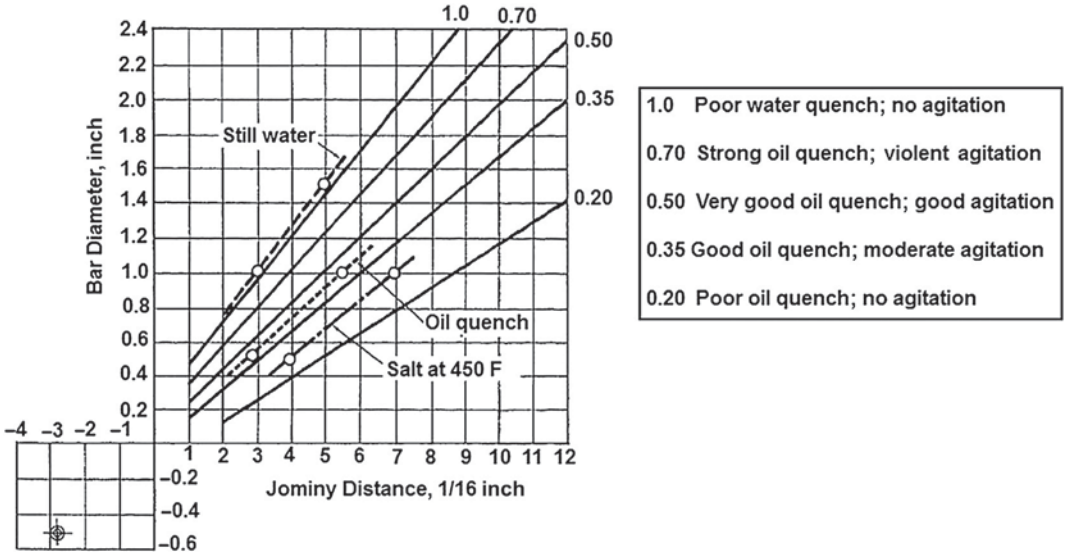

Figure 28 Modified Grossmann diagram to be used in conjunction with Rushman's two-diameter test bar illustrated in **Figure 27**. Reproduced from Rushman, W. F. How to Determine Quench Severity of Oil and Salt Baths. *Metal Prog.* **Dec 1963,** *84* (6), 91–92.

define specific quench severities of a quenchant in a tank in the heat-treating shop. The use of this approach to evaluate the quench severity will now be illustrated.

For the Rushman approach, the Jominy curve (hardenability) for the steel and the bar diameter are known. For example, assume that the hardness of the steel at 5/16 inch from the quenched end of a Jominy bar is $R_c = 45$. If a one-inch bar were quenched into the tank and the resulting hardness was $R_c = 45$, then $H = 0.5$. Since all of the H-value lines on the Grossmann chart converge at a common point, the measured hardness and the common point determine the line on the modified Grossmann chart. **Figure 29** illustrates the use of this approach to determine the quench severities of three commercial quench systems: still water, oil, and salt at 450 °F (*77*).

Boegehold also developed an approach that involves a series of cures that interrelates bar diameter, quench severity (H-value), and Jominy data for the prediction of round-bar hardness at the surface, mid-radius (1/2R), and center (R) (*78,79*). **Figure 29** is used by (*149*):

1. The family of curves for size of the round bar to be quenched is selected.
2. The curve most representative of the H-value of the quenching medium to be used is then identified.
3. From these data, the Jominy distance from the curve of the desired position on the selected round bar size is determined.

From the Jominy distance, the hardness is determined from the Jominy curve.

12.03.2.7 Hardenability of Shallow-Hardening Steels

Shallow-hardening steels include plain-carbon steels with low concentrations of Mn or Si as alloying elements. Neither the Grossmann hardenability test nor the conventional Jominy test is appropriate for use with these steels. This section provides an overview of various test methods that have been developed for use with shallow-hardening steels. Hardenability test procedures described under this subtitle are pertinent for tool steels with high hardenability.

12.03.2.7.1 Shepherd Disc Hardenability Test

The Shepherd Disc Hardenability Test was developed to determine the hardenability of carbon tool steels. A series of discs of at least 1 3/4 inch (4.4 cm) varying in thickness by 1/32 inch (0.79 mm) were heated for 20 min in a molten lead pot at 1420 °F (770 °C) and then quenched in a brine spray. After hardening, each disc was cut in half, polished, and etched to reveal the depth of hardening (*80*). Hardenability was reported as the thickness in 30-s of an inch of the thinnest test specimen that shows an unhardened core of 5/64 inch or greater (*79,81*).

12.03.2.7.2 The Cone Test

Post, Greene, and Fenstermacher developed a cone test for carbon tool steels with Shepherd disc hardenability numbers of 10–16 (*82*). The test involves heating the tapered test specimen schematically illustrated in **Figure 30** in a gas-fired laboratory muffle furnace with a controlled atmosphere (4% O_2 and 8.2% CO_2), usually to 1450 °F or 1600 °F for 10 min, and then quenching the test specimen into a spray of a 10% brine solution at room temperature through a 3-inch vertical pipe with a 1-inch overflow, with the small end of the tapered test specimen down (*83,84*). After hardening, the cone is sectioned longitudinally through the center, and the Rockwell hardness is determined along the centerline of the sectioned test specimen and along lines normal to the surface.

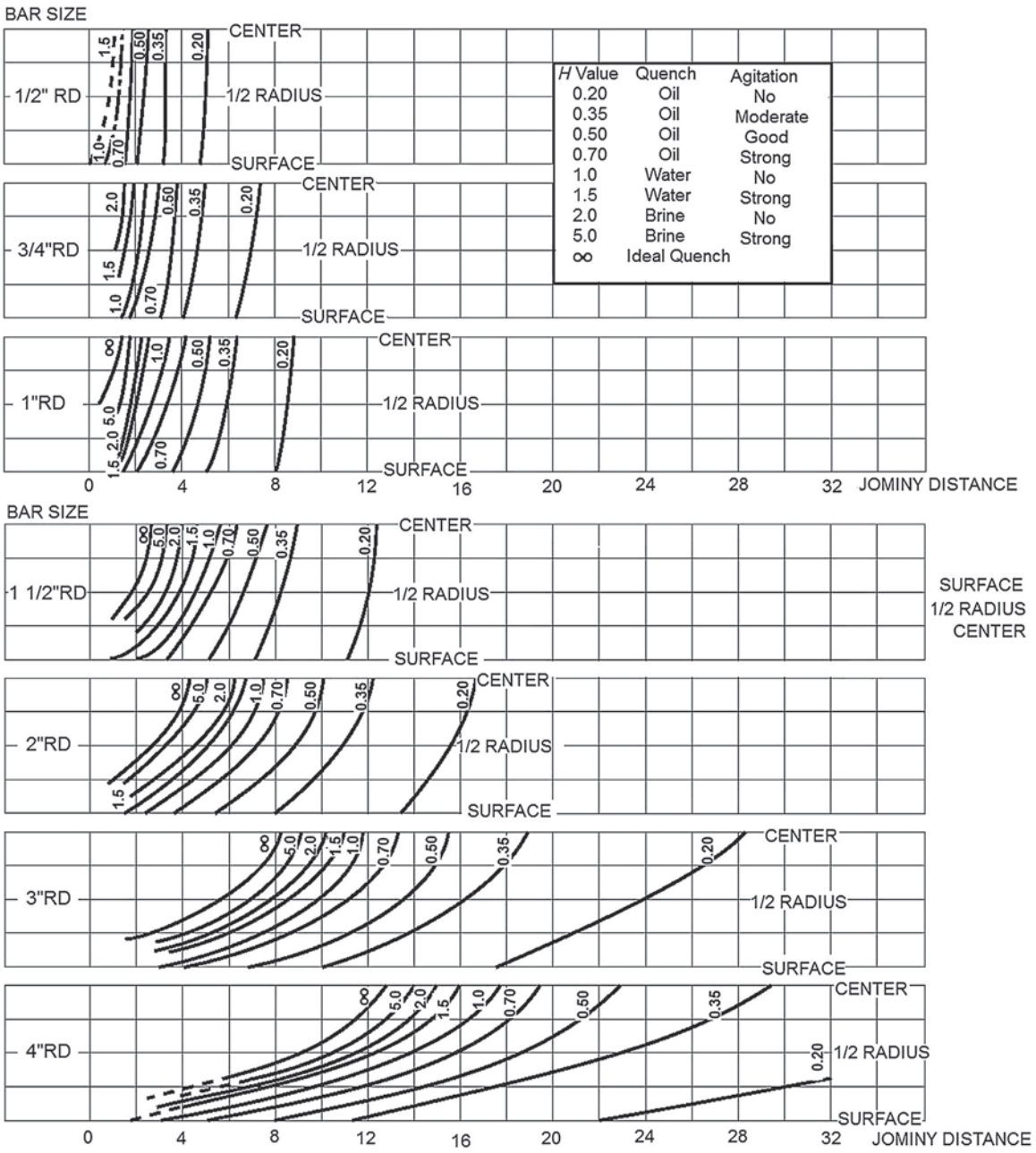

Figure 29 Chart for predicting approximate as-quenched cross-sectional hardness from Jominy curve data. Reproduced from Siebert, C. A.; Doane, D. V.; Breen, D. H. Utilization of Hardenability Concepts and Information. In *The Hardenability of Steels – Concepts, Metallurgical Influences and Industrial Applications*; American Society for Metals: Metals Park, OH, USA, 1977; pp 139–202.

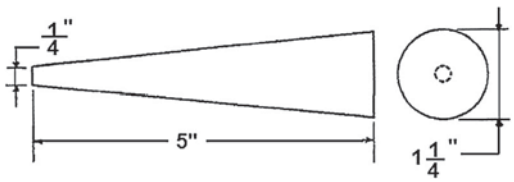

Figure 30 Schematic illustration of the cone test specimen. The degree of taper is 1 inch per 5 inch in length. Reproduced from Greene, O. V.; Post, C. B. Determination of Specific Hardenability of Shallow-Hardening Steels. *SAE Trans.* **July 1941,** *49* (1), 278–283.

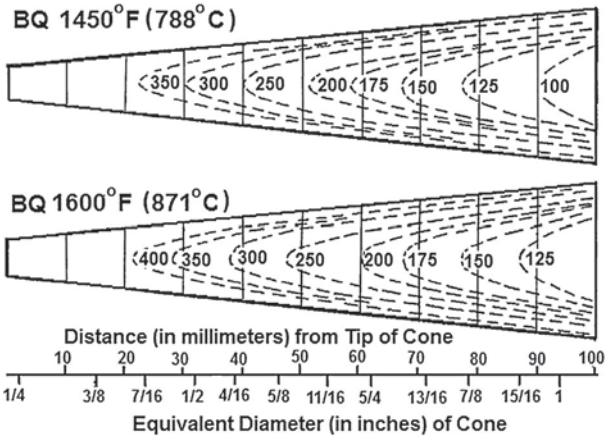

Figure 31 Iso-cooling rate (°F s^{-1} at 1300 °F) lines for the tapered test specimens. Reproduced from Greene, O. V.; Post, C. B. Determination of Specific Hardenability of Shallow-Hardening Steels. *SAE Trans.* **July 1941,** *49* (1), 278–283.

The tapered test specimen illustrated in **Figure 30** behaves like a series of round bars whose diameters are twice the perpendicular distance from the surface of the tapered test specimen at any point along the center axis (*84*).

The Jominy equivalent cooling rates (at 1300 °F) were calculated for two austenitizing temperatures of 1450 and 1600 °F, and the resulting cooling rate profiles are shown in **Figure 31** (*84*). These data permit the determination of specific hardenability in terms of a 'critical cooling rate' (in °F s^{-1} at 1300 °F).

In addition to critical cooling rates, the Grossmann critical bar diameter may be readily determined from the sectioned, ground and polished, and etched tapered test specimen by inspection for the tip of the case-core pattern, which represents the point where the hardness decreases most rapidly. The structure of the tip of this pattern contains 50% martensite. The depth of hardening may be observed by acid-etching a longitudinal section of the taped cone test specimen, as illustrated in **Figure 32** (*84*).

The ideal critical bar diameter (D_I) is defined as the bar diameter producing 50% martensite when subjected to an infinite quench. The brine quench used for this work approximates an infinite quench, so it is possible to obtain the D_I directly from the sectioned and etched tapered test specimen as the diameter of the test bar where the tip of the hardened/unhardened profile occurs. **Table 14** provides a correlation of the Shepherd disc hardenability rating, critical cooling velocity, Grossmann critical diameter, and D_I for shallow-hardening tool steels (*84*).

12.03.2.7.3 The Boegehold L-Bar Hardenability Test

Boegehold recognized that the Jominy test bar described thus far was not adequate for the complete range of steel hardenabilities and cooling rates. The so-called Type 'L' end-quench bar schematically illustrated in **Figure 33** was proposed by Boegehold to extend the cooling rates possible for a broader range of steels, including shallow-hardening steels (*85*). The 'L' refers to the L-shaped channel in the bar. The objective was to austenitize and quench the 'L-bar' in the normal way except that the stream of water rises to a height of 100 ± 5 mm above the orifice without the test specimen in position instead of the 63.5 mm used for the standard Jominy test. Boegehold proposed use of the L-bar as an alternative to the cone hardenability test discussed above for shallow-hardening steels (*82–84*).

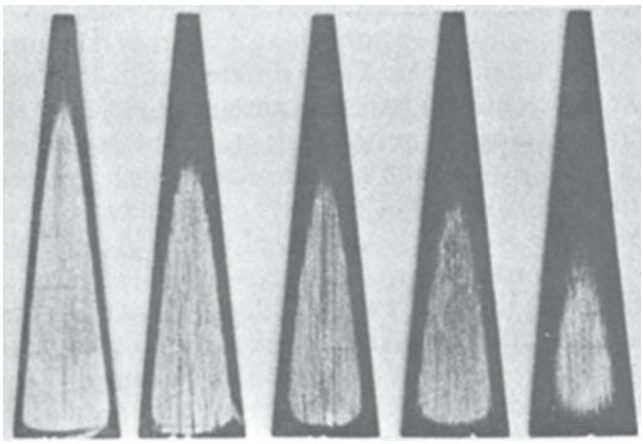

Figure 32 Light acid-etched longitudinal sections of tapered cone test specimens of Post, Green, and Fenstermacher which illustrate differences in depths of hardening. Reproduced from Post, C. B.; Greene, O. V.; Fenstermacher, W. H. Hardenability of Shallow-Hardenable Steels. *Trans. Am. Soc. Metals* **1942,** *30*, 1202–1254.

Table 14 Correlation between Shepherd disc number and specific hardenability obtained from taper test specimens[a]

Shepherd disc number	*Critical cooling velocity*[b] *(°F s^{-1}) at 1300°F*	*Critical bar diameter (inch) (H = 4.5)*	*Mean 'ideal' critical bar diameter*[c] *(inch)*
10	340/370	29/64–31/64	0.62
11	270/300	17/32–19/32	0.72
12	230/255	39/64–41/64	0.78
13	195/230	43/64–23/32	0.84
14	155/185	47/64–49/64	0.92
15	140/155	25/32–53/64	0.98
16	110/140	27/32–29/32	1.04

[a]Reproduced from Greene, O. V.; Post, C. B. Determination of Specific Hardenability of Shallow-Hardening Steels. *SAE Trans.* **July 1941,** *49* (1), 278–283.

[b]Cooling velocity necessary to yield Rockwell hardness at the inflection point of Rockwell contour curves; $R_c = 55$ for 1.10% carbon tool steels.

[c]The Grossmann *H*-value for 'ideal' bar diameter (D_I) is $H = \infty$.

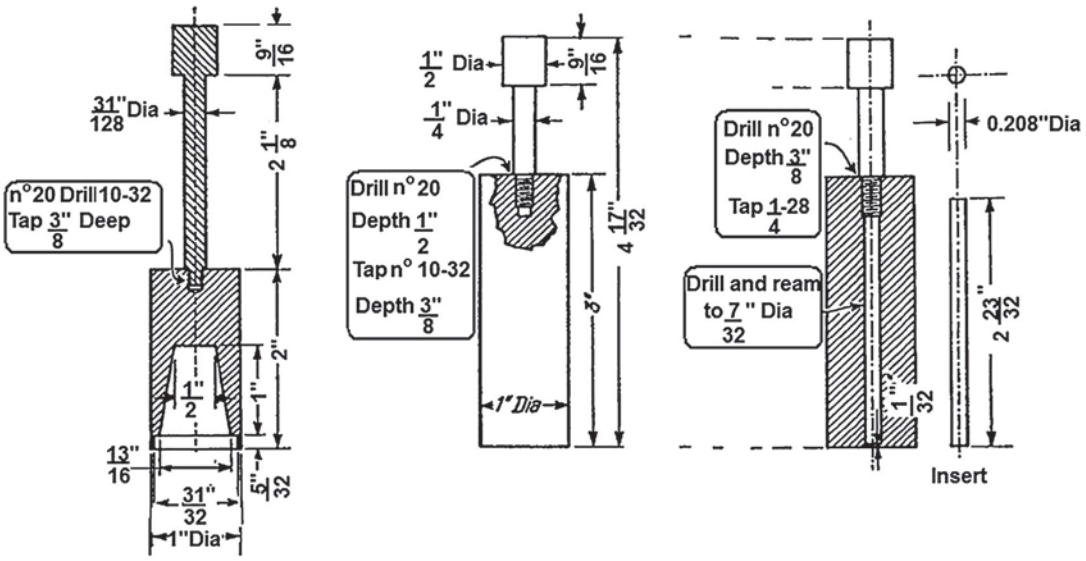

Figure 33 Schematic illustration of three different test bars reported by Boegehold for hardenability testing. The '*L*-' bar shown on the left was used for shallow-hardening steels; for comparison, the normal test bar is shown at the center, and the bar on the right was used for small sizes. Reproduced from Boegehold, A. L. Use of Hardenability Tests for Selection and Specification of Automotive Steels. *SAE Trans.* **1941,** *36–49*, 266–276.

12.03.2.7.4 The Wuerfel Bomb Hardenability Test

One limitation of the conventional immersion test and the Boegehold L-bar tests for shallow-hardening steels is that test specimens must be machined and that correlation of cooling rate and hardenability is fundamental to the interpretation of test data. Unfortunately, in some cases, the cross-sectional size of the test specimen may be insufficient to develop the desired cooling rates, such as those encountered for wires and slender rods. The conical-shaped, Wuerfel bomb illustrated in Figure 34 was developed to address these limitations (*86*).

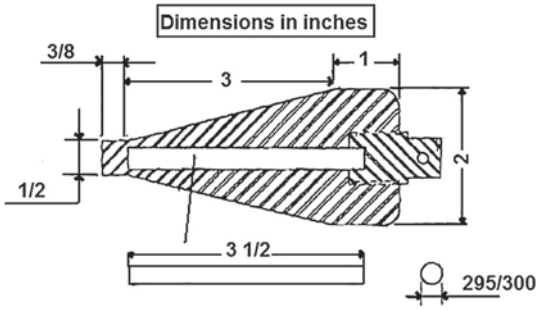

Figure 34 Schematic illustration of the Wuerfel bomb and test specimen. Reproduced from McCleary, F. E.; Wuerfel, R. Determining Hardenability on Small Sizes. *SAE Trans.* **1941,** *49*, 276–278.

As Figure 34 shows, there is a concentric hole that is slightly larger than the test piece in the Wuerfel bomb. The concentric hole is enlarged at the top with a threaded plug that acts as a handle. When the test specimen is inserted into the hole, it is filled with a low-melting alloy such as Wood's metal, which assures contact between the bomb and the test piece. *Note:* Wood's metal eutectic, fusible alloy has a melting point of approximately 70 °C (158 °F). It is a eutectic alloy of 50% bismuth, 26.7% lead, 13.3% tin, and 10% cadmium by weight. After the addition of Wood's metal, the threaded plug is screwed into the bomb and the assembly is heated to the desired austenitization temperature and then quenched into water. After warming the assembly to melt the Wood's metal, the test specimen is removed. Hardness measurements are taken along the test piece and the critical diameter is determined. The principal requirements of this test method are: (1) that the quenching process should be uniform and (2) the maximum hardness should be approximated at the small end of the Wuerfel bomb (*86*).

12.03.2.7.5 The SAC Test

The hardenability of shallow-hardening steels, those steels that will not through-harden bar sizes larger than 1.0 inch (25.4 mm), except for carbon tool steels, has traditionally been determined by the SAC hardenability test. Hardenability as quantified in this test is dependent on three numbers: surface hardness, area under the cross-sectional hardenability curve, and center hardness (SAC). These three numbers are obtained from a graphical representation of the hardness distribution curve (U-curve). The SAC test was proposed by Burns et al. as an alternative to the development of a CCT diagram (*87*).

The SAC test involves normalizing and then austenitizing a cylindrical test specimen with a length of 140 mm (5.5 inch) and a diameter of 25.4 mm (1 inch) and then quenching into a water bath at 24 ± 5 °C. A cylinder 25.4-mm (1-inch) long is cut from the middle of the test specimen, and the end faces are ground to remove any tempering effects induced by the cutting operation. Rockwell *C* hardness is determined at four positions, 90° to each other, on the surface, and the average of the hardness values provides the surface, or *S*-value. Rockwell hardnesses are then determined across the cross section of the test specimen at 1/16-inch (1.59-mm) intervals from the surface to the center to develop a hardness profile. The total area under the curve provides the area, or *A*-value, in units of 'Rockwell-inch', and the hardness at the center gives the *C*-value.

The traditional method to determine the area under the curve is illustrated in Figure 35 (*87*). The resulting SAC value is a set of three, two-digit numbers representing the average surface hardness (*S*), total Rockwell-inch area (*A*), and center hardness (*C*). For example, an SAC. rating of: 60-54-43 indicates a surface Rockwell hardness of 60, a total Rockwell-inch area of 50, and a center Rockwell hardness of 43 (*97*).

12.03.2.7.6 The Shepherd P–V Hardenability Test

Another hardenability test developed by Shepherd for shallow-hardening carbon tool steels is the P–V (Penetration–Velocity) test, which is conducted on a V-shaped test piece (*89,90*). This test utilizes 1 ⅛ inch test specimens with a 90° chisel-shaped point (Figure 36(b)) cut from a round bar as illustrated in Figure 36(a) (*79*). The entire wedge-shaped piece (Figure 36(b)) is austenitized and transferred rapidly to a quenching fixture with the chisel edge pointed down. The quenchant, usually brine, is sprayed onto the beveled edge. After quenching, a V-shaped slab section is then cut as illustrated by the dotted line in Figure 36(c). The test specimen is ground, if necessary, polished, and etched to indicate the depth of hardness. The depth of hardening (penetration) is determined on the face of the slab section from the tip along the axis of the original bar depicted in Figure 36(a) to the point where there is less than 50% martensite (*89*). A depth of hardening for a typical Shepherd P–V test specimen is shown by the shaded area in Figure 37 after simultaneously quenching edge faces AB and BC (*91*). The depth of hardening, BH, is measured by obtaining

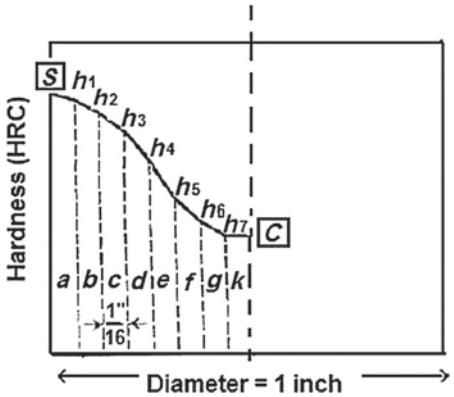

S = Average Surface Hardness
$h_1, h_2, h_3, \ldots h_i$ = Average hardness at the indicated depths from the surface
C = Average center hardness
Area of section $a = [(S+h_1)/2] \times 1/16$
Area of section $b = [(h_1 + h_2)/2] \times 1/16$
Total Area $(A) = 2 \times (a+b+c+d+e+f+g+h+i+j+k)$
$= 1/16 \times (S/2 + h_1 + h_2 + h_3 + h_4 + h_5 + h_6 + h_7 + C/2)$

Figure 35 Illustration of the graphical methodology for determining the 'Rockwell-in' area according to the SAC method. Reproduced from Burns, J. L.; Moore, T. L.; Archer, R. S. Quantitative Hardenability. *Trans. ASM* **1938,** *26*, 1–36.

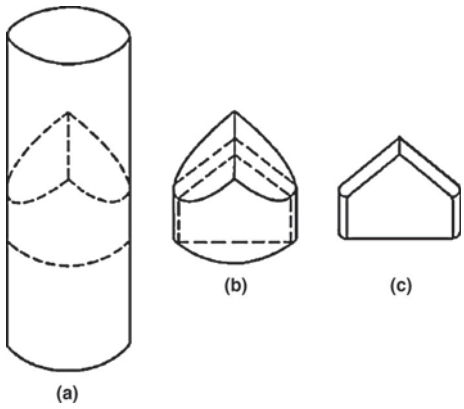

Figure 36 Illustration of the steps (a)–(c) involved in the preparation of a V-shaped test specimen used for Shepherd's P–V Hardenability test. Reproduced from Grossmann, M. A. Hardenability Tests. In *Elements of Hardenability*; American Society for Metals: Metals Park, OK, 1952; pp 1–42 (chapter 1).

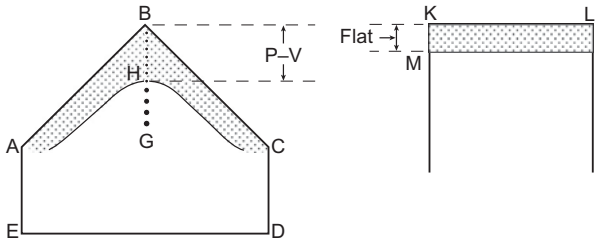

Figure 37 The shaded area of Shepherd P–V test specimen shown on the figure on the left illustrates the depth of hardening. The shaded area shown on the figure on the right illustrates the same depth of hardening for a standard Jominy test bar. Reproduced from Grossmann, M. A. Hardenability Tests. In *Elements of Hardenability*; American Society for Metals: Metals Park, OK, 1952; pp 1–42 (chapter 1).

hardnesses along the dotted line BG. Shepherd's data, shown in **Table 15** shows that the depth of hardening increases as the angle ABC decreases. However, the cracking susceptibility also increases significantly as the angle decreases below 90° (*91*).

The Shepperd P–V hardenability test is especially applicable for steels with a D_I-value of 1/2-3/4 inch (*79*). Shepperd found that the test was not significantly affected by minimal tempering that may occur during the cutting and grinding steps during test specimen preparation (*90*). The test has the added advantage that since the depth of hardening (depth to 50% martensite formation) is reasonably easy to detect, it can be conducted with hardness determination, if necessary.

The Shepherd P–V hardenability test was reported to be useful for steels with D_I values of 0.5–0.75 inch (*91*).

12.03.2.7.7 The McMullan Wedge Test

Another test that has been used to assess the hardenability of shallow-hardening steels is the McMullan wedge test illustrated in **Figure 38** (*91*,*92*). The 26.5° wedge-shaped test specimen is jet-quenched on the lower face as illustrated in **Figure 38** and the hardness is measured on the unquenched upper face. A distance versus hardness plot is prepared from the test data to illustrate the hardness distribution. Because of the wedge shape, a wide range of cooling rates and therefore hardnesses are obtained.

12.03.2.7.8 The 'Hot-Brine' Hardenability Test for Shallow-Hardening Steels

The use of Grossmann's D_I value, which is based on the 'ideal critical diameter' that produces 50% martensite at the center of a steel bar, is not suitable for many shallow-hardening ($D_I < 1$ inch) steels. For such steels, Grange found quenching to 90% martensite at the center was required in order to provide an adequate and quantitative discrimination of their hardenability (*19*). If less than 90% martensite is obtained, mechanical properties, either before or after tempering, degrade significantly.

Table 15 Correlation of depth of hardening with corner angle of the Shepherd P–V hardenability test specimen

*Angle of test specimen (°) (**Figure 37**)*	*Depth of hardening (inch)*
Flat (180)	0.165
90	0.373
60	0.515
45	0.665

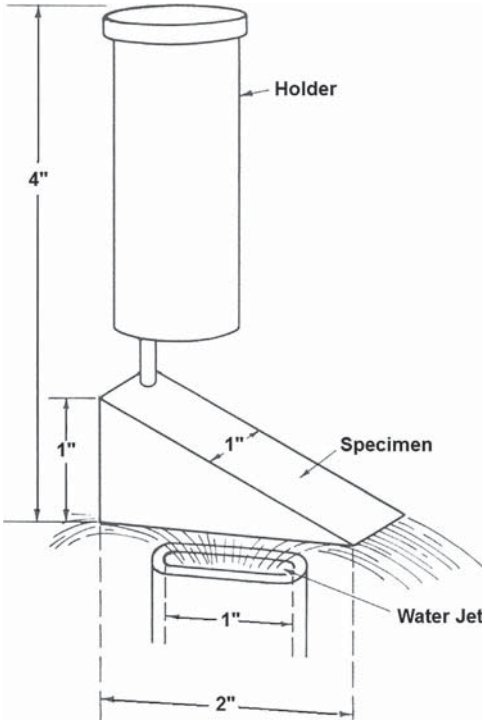

Figure 38 Schematic illustration of the McMullan wedge test. Reproduced from Grossmann, M. A. Hardenability Tests. In *Elements of Hardenability*; American Society for Metals: Metals Park, OK, 1952; pp 1–42 (chapter 1).

The 'hot-brine' hardenability test involves first normalizing the test bars at 1700 °F (925 °C). Each test specimen ($1 \times 1 \times 0.1$ inch) is then individually quenched in brine (6% NaCl in water) at the brine temperature that produces 90% martensite. Brine is used instead of hot water to provide a more uniform quench without soft-spotting even at temperatures approaching the boiling point of water. To prevent scaling, the small test specimen was heated in a cavity within a block of graphite.

The brine temperature that produces 90% martensite, by itself, was not considered to be an adequate quantitative hardenability criterion. Instead, these values were correlated with cylinder diameters (D_H) that produced 90% martensite at the center after quenching in water. Thus, the 'hardenability criterion is that diameter of a water-quenched cylinder which contains 90% martensite at its center' (*19*). Figure 8 is a nomogram for predicting hardenable diameter (90% martensite, water-quenched) for any grain size different from that at which hardenability was measured or estimated. Figure 39 is a nomogram that shows the variation in the hardenable diameter (ΔD) with respect to composition for shallow-hardening steels (*19*).

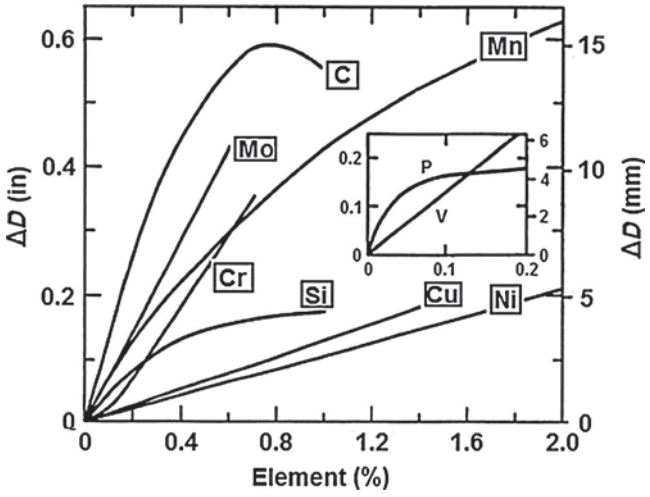

Figure 39 Variation in the hardenable diameter (ΔD) with respect to composition for shallow-hardening steels. The hardenable diameter (ΔD) is defined as the diameter of a cylinder that produces 90% martensite at the center when water quenched and the D_I is less than 25 mm (1 inch). Reproduced from Grange, R. A. Estimating the Hardenability of Carbon Steels. *Metall. Trans.* **Oct 1973,** *4*, 2231–2244.

Grange developed an equation that can be used to calculate the D_H value of shallow-hardening steels with different carbon content, alloying element composition, and grain size. It was assumed that the D_H value for pure iron was zero. The effect of carbon on hardenability was designated as ΔD_C and is determined from Figure 39 based on the total carbon content. The contribution to hardenability of other elements ΔD_X is similarly determined from their concentration using Figure 39 (19). The figure does not show the hardenability effects for S, Ti, and Zr since their contributions are typically very small. Once the ΔD values are determined, the D_H value is calculated from:

$$D_H(\text{inch}) = \Delta D_C + \Delta D_{Mn} + \Delta D_P + \Delta D_{Si} + \Delta D_{Cu} + \Delta D_{Ni} + \Delta D_{Cr} + \Delta D_{Mo} + \Delta D_V$$

The data in Figure 39 applies to ASTM grain size No. 4. To obtain parameters for other grain sizes, Figure 8 must be used as well (19).

12.03.2.8 Hardenability of Deep-Hardening Steels

Deep-hardening (D-Series) steels are characterized by a uniform depth of hardening that extends deep into the cross section. Typically, deep-hardening steels contain sufficient alloy content to facilitate hardening. An example of a D-Series tool steel contains 1.5–2.5% carbon and approximately 12% chromium. The pearlitic and bainitic transformation times of these steels are sufficiently long so that even heavy sections of these steels will fully harden. Therefore, the D-Series, except D-3, steels are conventionally quenched in molten salt or air (93).

In addition to D-series tool steels, there are the medium-alloy, air-hardening, (A-Series) tool steels that contain a wide range of carbon and alloy content. However, all of these steels are air-hardenable.

The cooling rate of a standard Jominy bar at 80 mm from the quenched end is 0.7 $K\,s^{-1}$. Therefore, the hardenability of all steel grades with a critical cooling rate greater than 0.7 $K\,s^{-1}$ can be determined by the standard Jominy test. However, when the critical cooling rate is less than 0.7 $K\,s^{-1}$, there will be no variation in the Jominy curve, and the entire bar will be fully transformed to martensite (88). This section will discuss various alternative methods that have been reported to date to experimentally assess the relative steel hardenability of deep-hardening and air-hardening steels.

12.03.2.8.1 The Modification of the Standard Jominy Test

Devries modified the standard Jominy test by end-quenching a 1 inch $\phi \times 6$ inch bar from the austenitizing temperature in a fixture that held the top of the bar in a furnace to maintain the temperature at the end of the bar at 1200 °F (650 °C) during the quench (94). The quenching fixture consisted of a large galvanized steel can with a hole at the bottom to allow the tap water at approximately 70 °F to drain. A quenching jet, which was 0.5 inch in diameter and 2.5 inch high, consisted of a pipe running upward at the center of the can. The furnace shown in Figure 40 was placed above the quenching fixture reservoir. The furnace held the top 2 inch of the test bar. Thermocouples were placed on the top and at the bottom of the core of the furnace as shown in Figure 40 to maintain the furnace temperature at 1200 °F (650 °C). The bottom end of the test bar was held 0.5 inch from the opening of the pipe forming the water jet. The temperature of the test bars was monitored at various positions during the test by thermocouples that were placed in 0.5-inch holes drilled 0.5 inch deep. The temperature distribution in the bars at different times during the test are shown in Figure 41 (94). After quenching under these conditions for 1 h, the bar was removed from the fixture and immersion quenched. Flats, 0.015 inch deep, were then ground along the bar, and the hardness and degree of transformation were determined at 1/16-inch intervals.

The greatest differences in hardness distribution were found to be at the top, heated end, of the bar since the steel achieves constant temperature slowly. In this way, the hardenabilities of deep hardenability steel alloys can be determined (94). However, a limitation of the Devries test is that it does not provide information during continuous cooling since it involves nearly isothermal austenitic transformation which may be potentially affected by transformational and nucleation effects during the initial cooling stage. The problem is that a principal reason for hardenability testing is that there is either no or limited knowledge of isothermal austenitic transformation and quenching (95).

12.03.2.8.2 The Wilson Hardenability Test

The Wilson hardenability test was developed to address some of the principal shortcomings of the Devries test, and it involved the use of an instrumented oversized Jominy test bar 1.25 inch in diameter and 11 inch long (95). The test bar had seven evenly spaced holes for thermocouples that were drilled through the bar to a depth of 1/16 inch from the opposite side of the bar. At the top of the test bar was an extension bar to support it when suspended in the quenching furnace-quenching fixture schematically illustrated in Figure 42 (95). In this position, the test bar is practically surrounded by the furnace during the test. At the bottom of the bar, there was a room temperature water jet from a 0.5-inch orifice rising to a vertical height of 3.5 inch. The thermocouples were extended from the test bar through the top of the furnace. After holding the test bar at the austenitizing temperature for 1 h, the power for the furnace is turned off and the following are simultaneously turned on: pump, cooling coils located in the furnace, and chart recorder. Cooling is a combination of end-quenching and cooling from the coils in the furnace walls. The total quenching time was 90 min.

After quenching, longitudinal flats were ground by removal of 0.030 inch per flat on opposite sides of the test bar. Hardness (R_c) measurements were taken along the bar at 0.5-inch intervals. In addition to hardness as a function of distance from the quenched end, time-temperature cooling curves were plotted as a function of distance from the quenched end as illustrated in Figure 43 (95). Wilson calculated the D_I – value from Asimov's equation: $D_I = 3.29\ t^{0.5}$ where t = half-temperature time in minutes (74).

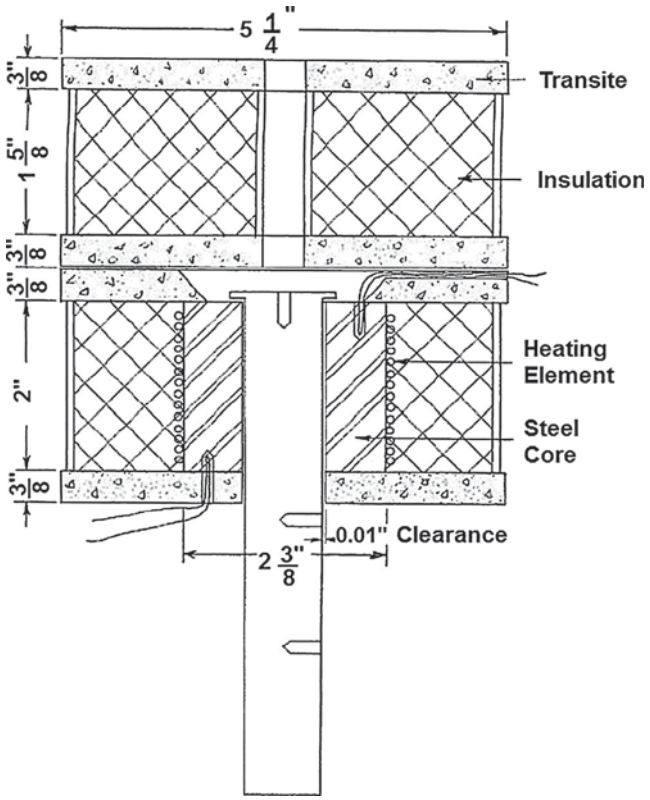

Figure 40 Schematic illustration of the Devries furnace used to keep the top of the standard Jominy end-quenched bar hot during the test to evaluate the hardenability of deep-hardening steels. Reproduced from DeVries, G. An End-Quenched Bar for Deep-Hardening Steels. *Trans. ASM* **1949,** *41*, 678–691.

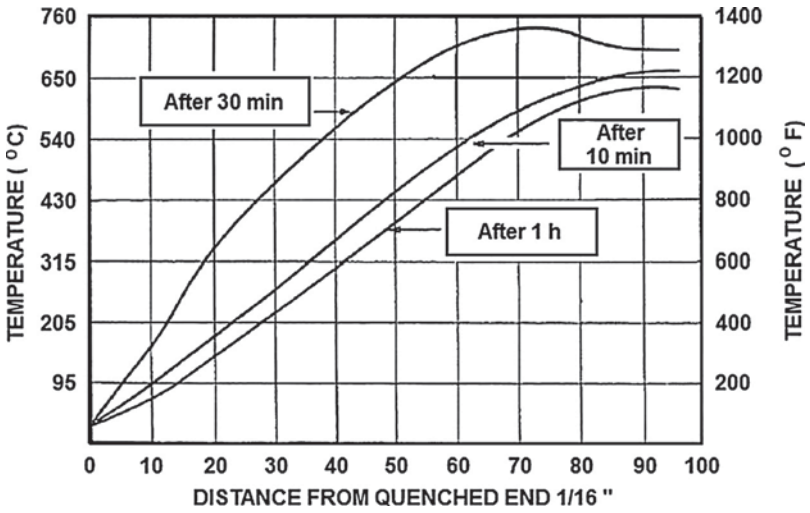

Figure 41 Temperature distribution in the Devries test bar after 3 min, 10 min, and 1 h after the start of the quenching process. Reproduced from DeVries, G. An End-Quenched Bar for Deep-Hardening Steels. *Trans. ASM* **1949,** *41*, 678–691.

Carman et al. used a simpler variation of the Wilson test to measure the hardenability of deep-hardening steels (*96*). The 1.5-inch ϕ by 11-inch test bar with seven thermocouple wells illustrated in Figure 44 was essentially the same as that used by Wilson (*95*). The furnace was a three-zone vertical tube furnace, with the temperature of each zone being controlled independently and which was placed above the quenching tank. In the 'open position' the top heater segment was tilted to one side. The thermocouple wires were extended through the top of the furnace. The test bar was placed inside a heavy tube located in the center zone of the furnace for austenitization for one hour. After austenitization, the power to the end heaters was turned off, and the bottom heating segment

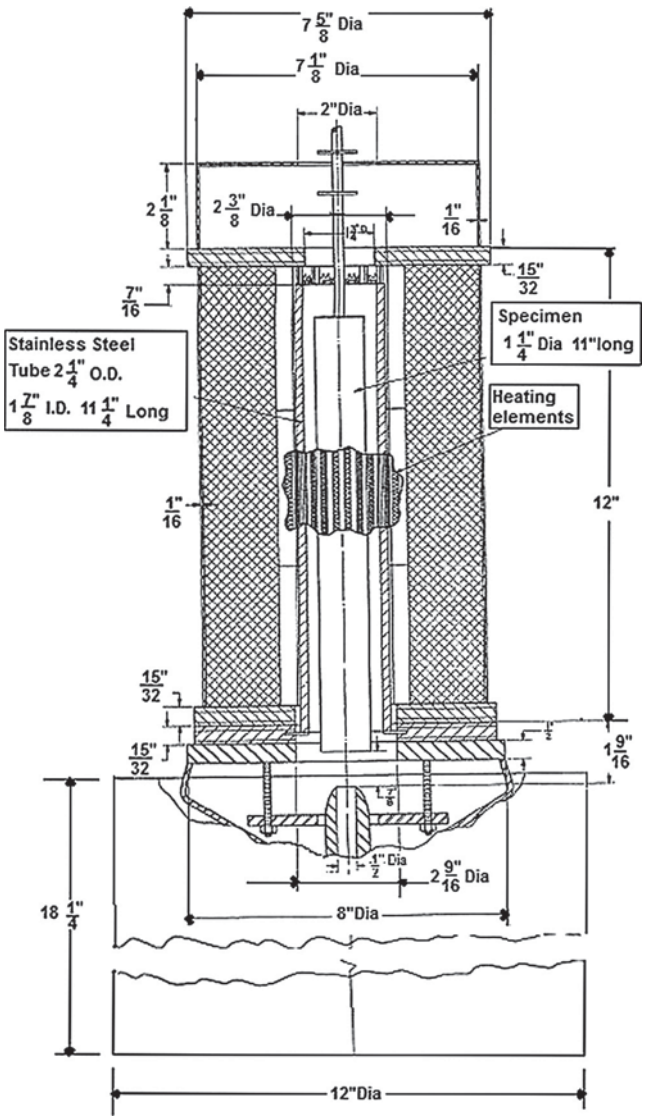

Figure 42 Quenching fixture for Wilson hardenability test. Reproduced from Wilson, W. A Hardenability Test for Deep-Hardening Steels. *Trans. ASM* **1951,** *43*, 454–479.

was removed. The test bar assembly was lowered 3 inch and then end-quenched. The center equalizer tube was also lowered to surround all except the bottom 1/8 to 1/4 inch of the test bar. The furnace was then cooled by using a programmed controller at a rate that corresponded to the water-quenching effect at the 3-inch position of the test bar. Cooling time-temperature profiles were recorded for all seven positions of the test bar. Two parallel flats 0.030 inch deep were ground on opposite faces of the test bar, and the hardness (R_c) was determined along the bar as reported by Wilson (*96*).

12.03.2.8.3 The Etienne and Sheepens Hardenability Test

In order to adequately differentiate the hardenabilities of deep-hardening steels, it is necessary to reduce the cooling rates relative to those normally observed along a standard Jominy hardenability bar. One of the principal means of accomplishing this objective is to increase the mass of the bar. This can be done by using a 'retarder block'. Although most research has involved the use of steel either as a cooling enclosure or simply to increase the mass of the test bar, Etienne and Sheepens utilized a concrete cone with a vertical, steel-lined hole illustrated in **Figure 45** (*97*). The test specimen is a thin steel rod that is austenitized for 30 min after it is inserted into the concrete block that was preheated for 3 h. The apparatus is placed on an insulating plate, and a cooling ring is fitted onto the end of the steel test bar and then end-quenched. Cooling is continued until the core of the concrete decreases to approximately 212 °F (100 °C), which typically requires about 3 h. As the cooling is complete, 0.12-inch (3-mm)-wide flats are ground on opposite faces of the test bar, and the hardness as a function of distance is determined.

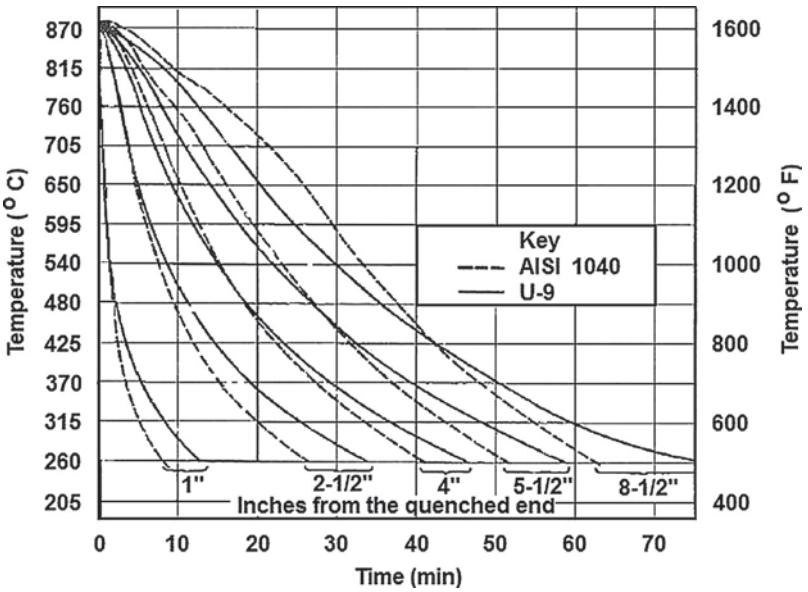

Figure 43 Wilson's hardenability bar cooling curves for AISI 1040 and steel U-9 (C, 0.49; Mn, 0.50; Si, 0.23; Cr, 0.78; Ni, 1.58; Mo, 0.35; Cu, 1.84) Reproduced from Wilson, W. A Hardenability Test for Deep-Hardening Steels. *Trans. ASM* **1951,** *43*, 454–479.

Although this test is relatively easy to perform and does provide excellent discrimination of the hardenability of deep-hardening steels, it does suffer from a number of important disadvantages. One disadvantage is that a retarder block of steel is much easier to prepare than one of concrete. Steel provides a much more reproducible heat transfer among different test bards. A steel retarder block was reported to be suitable for use for up to 40–50 measurements, whereas the concrete block can only be used for approximately 10 tests before replacement is necessary (*98*).

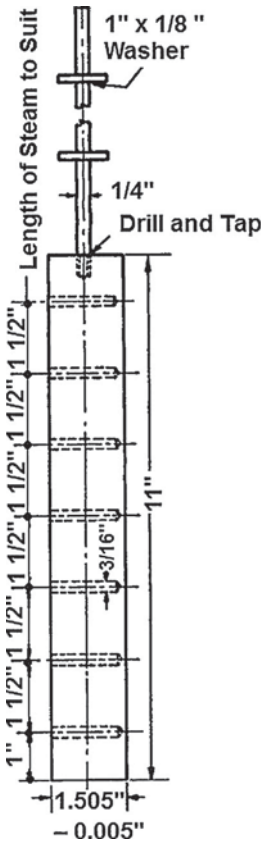

Figure 44 Carman, Armiento, and Markus instrumented, oversized, Jominy hardenability bar for determining hardenability of deep-hardening steels. Reproduced from Carman, C. M.; Armiento, D. F.; Markus, H. Hardenability Test for Deep Hardening Steel. *Metal Prog.* **May 1957,** *71*, 77–80.

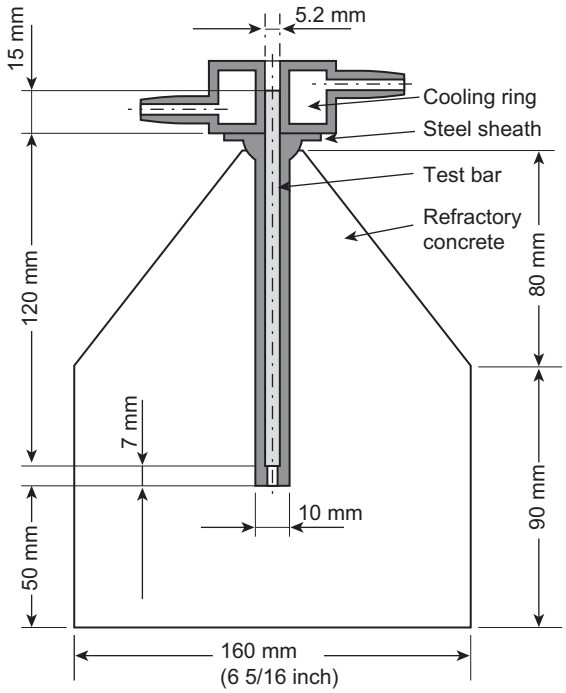

Figure 45 Schematic illustration of the Etienne and Sheepens device for measuring the hardenability of deep-hardening steels. Reproduced from Etienne, C. F.; Sheepens, C. P. A Hardenability Test for Deep-Hardening Steels. *Metal Prog.* **Dec 1965,** *88* (6), 77–81.

12.03.2.8.4 The Rose and Rademacher Jominy Test Modification

One method of using the standard Jominy test to assess the hardenability of air-hardening steels is to increase the mass. Rose and Rademacher developed a test modification that increases the mass by using a stainless steel conical device in which there is a hole for the Jominy test specimen, as illustrated in Figure 46 (*88*). This device contains an upper and lower enclosure to help equalize the austenitizing heating conditions of the entire test bar. The total heating time is 40 min in addition to 20 min holding time at temperature. At this time, the lower portion of the enclosure is removed, and the Jominy bar plus the conical upper portion are quenched together in the usual way. Figure 46 illustrates the effect of the conical upper portion on the cooling times to 500 °C from

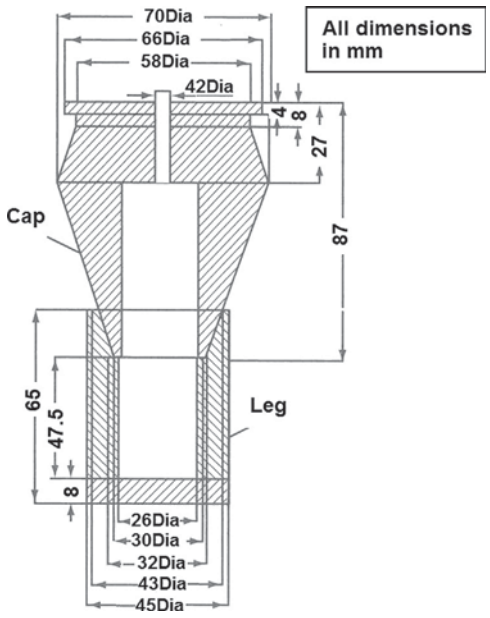

Figure 46 Illustration of the Rose and Rademacher modification of the standard Jominy test for use with assessment of the hardenability of deep-hardening steels. Reproduced from Liščič, B. Hardenability. Steel Heat Treatment Handbook. In *Steel Heat Treatment: Metallurgy and Technologies*; Totten, G. E., Ed., 2nd ed.; CRC Press Taylor & Francis Group: Boca Raton, FL, 2007; pp 213–276. ISBN: 978-0-8493-8455-4 (chapter 5).

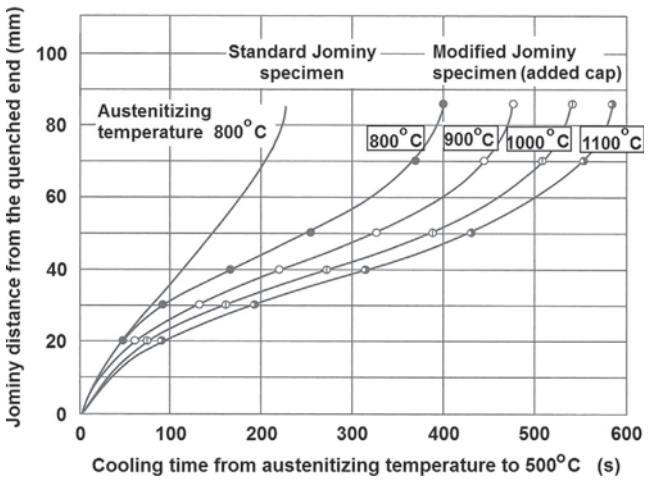

Figure 47 Cooling times to 500 °C for a standard Jominy test bar and for the Jominy test bar with the conical 'cap' from different austenitizing temperatures. Reproduced from Liščič, B. Hardenability. Steel Heat Treatment Handbook. In *Steel Heat Treatment: Metallurgy and Technologies*; Totten, G. E., Ed., 2nd ed.; CRC Press Taylor & Francis Group: Boca Raton, FL, 2007; pp 213–276. ISBN: 978-0-8493-8455-4 (chapter 5).

the austenitizing temperature with respect to the distance from the quenched end. When this conical addition to the standard Jominy test bar is used, the cooling rates of the upper part of the test specimen are decreased significantly, permitting use of the standard Jominy test bar for determining the hardenability of air-hardenable steels.

Figure 47 shows that when cooling from the austenitizing temperature of 800 °C to approximately 20 mm from the quenched end, the cooling-time curves and cooling rate of both the standard Jominy bar and the modified Jominy bar are similar. As the distance from the quenched end increases beyond 20 mm, the modified Jominy test specimen with the conical cap exhibits increasingly longer cooling times and slower cooling rates relative to the unmodified standard Jominy test specimen, which will facilitate the assessment of hardenability of air-hardenable steels (*88*).

12.03.2.8.5 The Post, Fetzer, Fenstermacher Air-Hardenability Test

Post, Fetzer, and Fenstermacher developed a test for measuring the hardenability of air-hardenable steels (*99*). This test utilizes a 6-inch (dia) × 6-inch round slug of a 32% nickel-iron alloy shown in Figure 48 into which a 0.858-inch hole is drilled through to the center. A 1-inch threaded hole is tapped at each end. The hardenability test specimen is 1 inch in diameter and 7 inch long. This 1-inch diameter portion of the test specimen illustrated in Figure 48 is threaded so that 4 inch of the bar extends from the 6-inch diameter slug, and the bar is machined so that 3 inch (0.856 including diameter) of the test specimen extends into the center of the slug. There are two test specimens, one each inserted into each end of the 6-inch slug. The two test specimens are screwed into the 6-inch slug and heated to the austenitizing temperature and soaked for the appropriate time to achieve uniform temperature throughout, and then the assembly is removed from the furnace and placed on an elevated screen to air cool. After cooling, the test specimens are unscrewed, flats are ground on two opposite sides, and hardnesses are obtained at locations corresponding to specific cooling rates past 1000 °F (540 °C).

Separate tests were run to determine cooling rates at 1/8, 5/8, 11/4, 2, 23/4, and 311/16 inch from the face of the 6-inch slug, at 1 inch below the face, and at the center with the test specimens in place. This was done by drilling 1/8 inch holes to the center of the

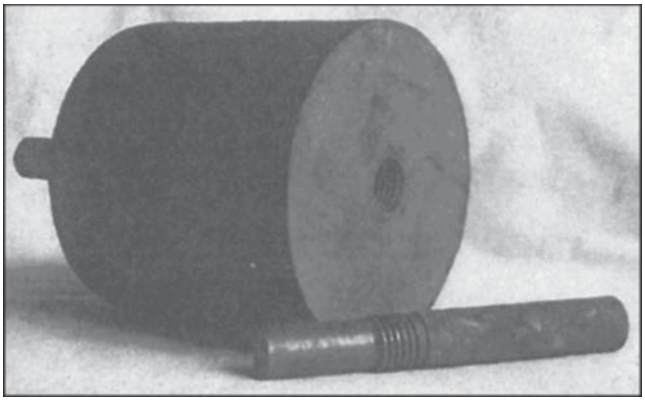

Figure 48 Post, Fetzer, Fenstermacher air-hardenability test device. Reproduced from Post, C. B.; Fetzer, M. B.; Fenstermacher, W. H. Air Hardenability of Steels. *Trans. ASM* **1945,** *35*, 85–111.

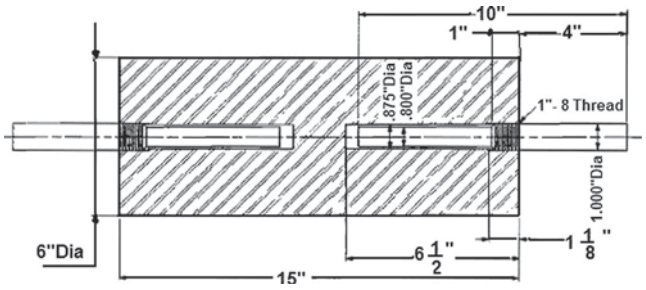

Figure 49 Jatczak steel air-hardenability test bar. (This is also known as the Timken air-hardenability test.) Reproduced from Jatczak, C. F. Assessment of Hardenability of Deep Hardening Steels. In *Hardenability Concepts with Application to Steel, Proceed. Symp.*, Oct 24–27, 1977, pp 334–347.

test specimens and a 22-gage iron constantan thermocouple inserted. This assembly was heated in the same manner as previously, removed to a wire screen, and air cooled (*99*). Hardenability is assessed as the cooling rate required to cool below 1000 °F to obtain a specific R_c value (*79*).

Jatczak developed a slightly modified form of the Post et al. test device shown in **Figure 48** (*98,99*). The Jatczak air-hardenability test bar is schematically illustrated in **Figure 49**. The test bar that is inserted into the larger steel block is a centrally threaded 1 inch ϕ × 10 inch long (25.4 mm ϕ × 254 mm), which is stepped down to 0.800 inch ϕ (20.3 mm ϕ) to facilitate insertion of the test bar into the 6-inch (152 mm) round steel block. Normally, two test bars that may be of the same, or different composition, are threaded into the large round leaving 4 inch (102 mm) exposed outside of the large mass. The total assembly is then heated to the desired austenitizing temperature (heating time is typically 3 h) and then equalized for 45 min, at which time it is removed and cooled in still air. The cooling rates are slow and decrease along the test bar. Jatczak reported these cooling rates to correspond to center cooling conditions in air-hardened bars from 1.25-inch (31.5 mm) to 6-inch (152 mm) diameter. This corresponds to a continuous decrease in cooling rates for air hardening of approximately 600 °F s^{-1} (330 °C s^{-1}) down to 0.2 °F s^{-1} (0.1 °C s^{-1}) (*98*).

After still-air cooling, 0.030-inch (1.2-mm)-deep flats are ground on each side of the stepped-down portion of the test bar, and a 0.130-inch (3.3-mm)-deep flat was ground on the 1-inch (25.4-mm)-diameter side of the test bar. The hardness and/or microstructure is then measured as a function of distance from the large end (*98*).

12.03.2.8.6 Jatczak's Controlled Furnace Cooling Hardenability Test Procedure

To further extend the sizes of steel test specimens on which hardenability was determined, Jatczak used a series of small test specimens of any convenient shape such as 1 inch ϕ (25.4 mm ϕ) × 1 inch (25.4 mm), which were cooled from the austenitization temperature at several specific furnace cooling rates between 1300 °F (704 °C) and 1000 °F (538 °C), at which point they were removed and still-air cooled to room temperature. The cooling rates used by Jatczak were: 9 °F min^{-1} (540 °F h^{-1}), 6 °F min^{-1} (360 °F h^{-1}), 1 °F min^{-1} (60 °F h^{-1}), and 0.33 °F min^{-1} (20 °F h^{-1}). These rates correspond to 5 °C min^{-1} (300 °C h^{-1}), 3.3 °C min^{-1} (200 °C h^{-1}), 1.66 °C min^{-1} (100 °C h^{-1}), and 0.18 °C min^{-1} (10 °C h^{-1}), respectively. Using Russell's tables (*49*), Jatczak determined that these cooling rates correspond to centerline cooling for 10-inch (254 mm), 15-inch (380 mm), 27.5-inch (700 mm), 38-inch (960 mm), and 75-inch (1905 mm) rounds, respectively. Hardness measurements are made on each furnace-cooled test specimen and recorded as a function of cooling rate (*98*).

12.03.2.9 Hardenability Tests for Gas-Quenched Steels

As indicated previously, air-hardening steels typically exhibit critical cooling rates less than 0.7 K s^{-1}, which is the approximate cooling rate at the air-cooled end of a standard water end-quenched Jominy bar. As with the air-hardened steels discussed above, high-alloy steels that are increasingly hardened by high-pressure gas-quenching in a vacuum furnace typically exhibit critical cooling of less than 0.7 K s^{-1}. Thus, the standard Jominy end-quench test is too severe, and an alternative test for gas-quenched steels must be utilized if the hardenabilities of these steels are to be differentiated (*101*). This section will provide an overview of a new, recently reported test developed by researchers at the Stiftung Institute für Werkstofftechnik at the University of Bremen in Bremen, Germany, and at the University of Zagreb in Zagreb, Croatia (*101–103*).

In this test, a modified Jominy test bar 20 mm ϕ by 100 mm in length is induction heated to the austenitizing temperature, 790–820 °C, for 3–5 min and then end-quenched in a stream of pressured gas such as nitrogen, using the apparatus schematically illustrated in **Figure 50**. The test bar has three thermocouples with one placed at the center axis at 3 mm below the quenched end; the second and third thermocouples are located at 50 and 90 mm from the quenched end at 3 mm below the surface. The test bar used for the work reported was EN-90MnCrV8 (C, 0.86; Mn, 2.06; Cr, 0.28; V, 0.079; Si, 0.24; S, 0.010; P, 0.023). Although any gas could be used, for this work, nitrogen at a constant pressure of 3 or 18 bar with a gas velocity of 10 or 70 m s^{-1} was selected. The nitrogen blows from a nozzle at a distance of 12 mm from the quenched end. Cooling times varied between 7 and 10 min. The cooling times from 800 to 500 °C and the distance from the quenched end were determined. After the test bars were quenched, flats were ground on opposing sides, and hardness as a function of distance from the quench end was determined.

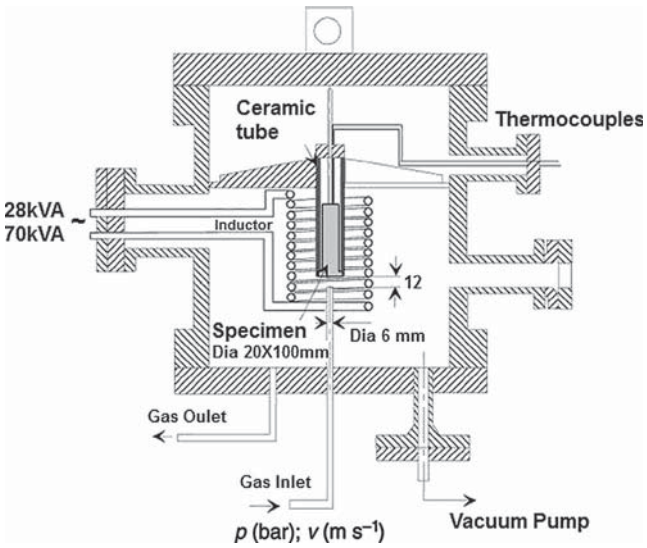

Figure 50 A schematic illustration of the high-pressure gas end-quenching apparatus used to determine hardenability of gas-quenched steel. Reproduced from Landek, D.; Liščič, B.; Filetin, T.; Lübben, T. End-Quench Hardenability Test for Gas-Quenched Steels. *Strojarstvo* **2011,** *53* (1), 33–37.

Figure 51 illustrates a comparison of the experimental and simulated cooling curves at 0.3 and 50 mm after nitrogen quenching (3 bar, 70 m s^{-1}) from the quenched end. The $t_{8/5}$ cooling times at different distances from the quenched end were also successfully simulated (*101*).

A comparison of the Jominy curves obtained by using the gas-quenching apparatus depicted in Figure 50 with different gas-quenching conditions are compared with the standard water-quench Jominy curve in Figure 52. These data illustrate that hardenability increases as the severity of the gas-quenching conditions is increased. For high-pressure gas quenching, these curves are dependent on the gas or gas composition used, pressure, and flow rate (*101–103*).

12.03.2.10 Hardenability of Carburized Steels

Steels are carburized to provide desirable high-surface compressive stresses by the formation of a high-hardness, high-carbon martensite containing case on a low-hardness/low-carbon containing core. Typically, the highest hardness is at, or near, the surface of the carburized case and is in the range of R_c 58–62. Because increasing carbon contents decrease the M_s temperature and because of the relatively high-carbon content in the case, it is not unusual to have retained austenite contents of 20–30% in many carburized

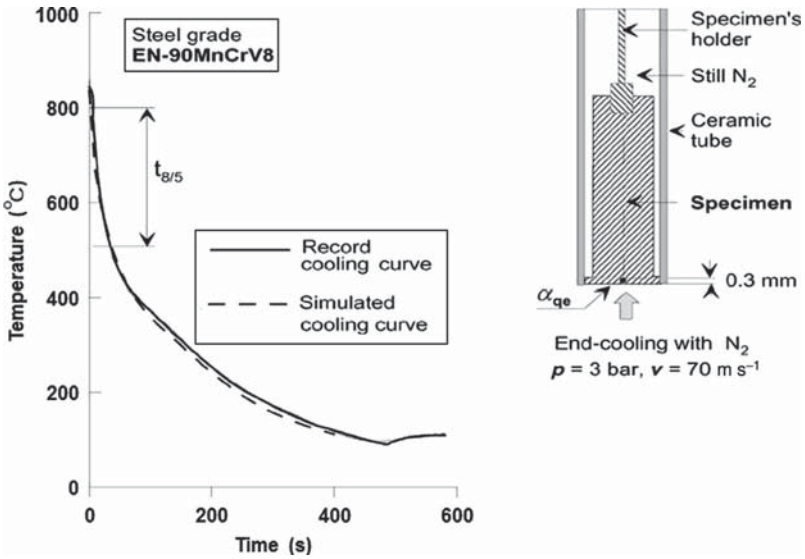

Figure 51 Model of thermodynamic finite element method used to calculate cooling curves at $t_{8/5}$ at 0.3 and 50 mm from the quenched end of the test bar. Reproduced from Landek, D.; Liščič, B.; Filetin, T.; Lübben, T. End-Quench Hardenability Test for Gas-Quenched Steels. In *Conf. Proceed. New Challenges in Heat Treating and Surface Engineering – Conference in Honor of Božidar Liščič, June 9–12, 2009, Cavtat Croatia*; Croatian Society for Heat Treatment and Surface Engineering: Zagreb, Croatia, 2009; pp 103–108.

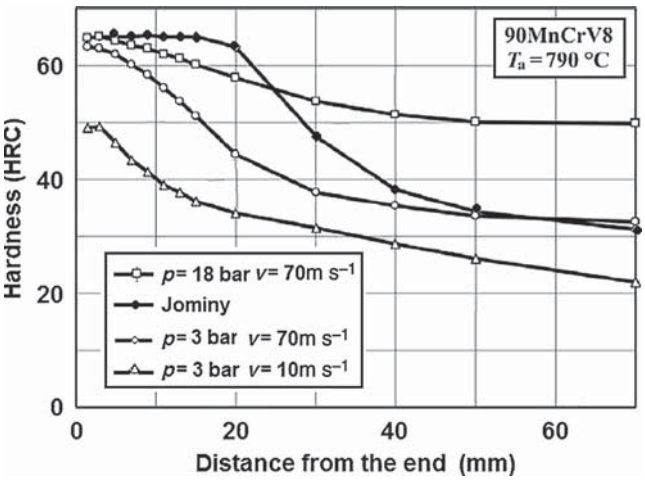

Figure 52 Hardenability curves for EN-90MnCrV8 steel obtained by the standard water-quenched Jominy bar and after gas quenching under three different conditions of increasing quench severity. Reproduced from Landek, D.; Liščič, B.; Filetin, T.; Lübben, T. End-Quench Hardenability Test for Gas-Quenched Steels. In *Conf. Proceed. New Challenges in Heat Treating and Surface Engineering – Conference in Honor of Božidar Liščič, June 9–12, 2009, Cavtat Croatia*; Croatian Society for Heat Treatment and Surface Engineering: Zagreb, Croatia, 2009; pp 103–108.

gear steels, which is detrimental to the total compressive residual stresses and fatigue strength (*104*). The hardness and strength of the core must be sufficient to support the case but not harder than necessary since excessive hardness will decrease fatigue strength (*105*). Therefore, the hardenability of BOTH the case and the core, core strength and hardness distribution, and depth in the case are important in order to optimize properties of a particular component (*106*).

Research on the hardenability of carburizing steels has been a major focus for more than 75 years, especially in the automotive industry for the production of hardened roller bearings and gears (*107*). One of the principal tests developed to study the hardenability of carburized automotive steel components was the Jominy Boegehold test, and it continues to be the primary method of studying the hardenability of carburized steels to this day (*59,78,85,107*).

Microstructure and residual stresses present in steel components are related to steel composition and therefore hardenability. The increasing hardenability of case-hardenable steels leads to more uniform distortion upon quench hardening and thus more reproducible production parts (*106,108*). For example, **Figure 53** illustrates the effect of distortion of opening of a Navy C-ring test specimen as a function of core hardness (or hardenability) of AISI 8620H carburizing grade of steel (*114*).

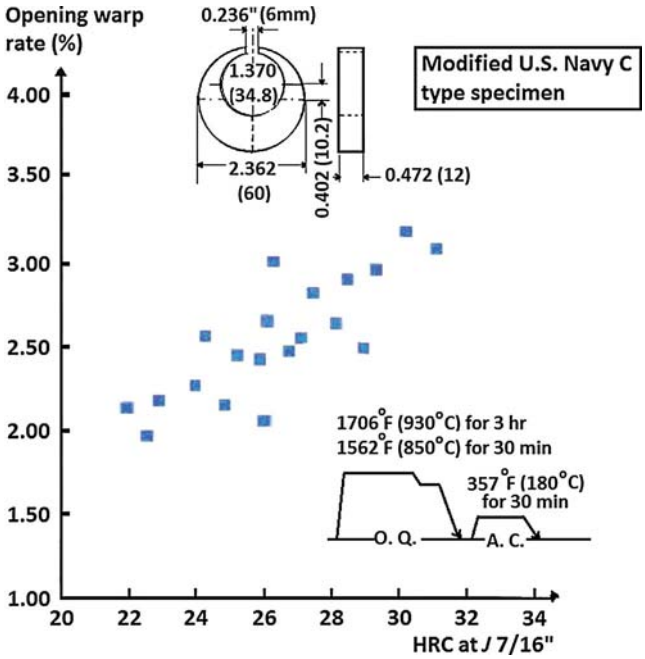

Figure 53 Distortion as a function of core hardness for carburized SAE 8620H steel. Reproduced from Lund, T.; Sabelström, U.; Johansson, G.; Leppänen, R.; Wulliman, C.; Ohlsson, P. Technical Report 7/1986 – The Measurement, Prediction and Control of Jominy – Hardenability of Carburizing Steels. Report by Ovako Steel AB, Box 5013, SE-194 05; Upplands, Väsby: Sweden, 1986. ISSN: 0282-9878.

The primary elements used to improve the hardenability of carburizing steel grades are manganese, chromium, nickel, and molybdenum (*109*). For example, increasing the nickel and/or molybdenum content may increase hardenability and fracture toughness. The effect of nickel isn't significant until a concentration of 1.5% is approached, although there is a strong positive molybdenum–nickel interaction on hardenability at nickel concentrations of 0.75% or higher (*109*). Vanadium may be used to reduce the molybdenum or molybdenum and nickel content to provide increased hardenability at lower cost. In some cases, an alloying combination of V–Mo–Ti may significantly increase the hardenability of a 0.4% C – 1% Cr steel, which would be more cost effective than Cr–Ni–Mo steel grades (*110*).

The remainder of this discussion will be divided into base material hardenability, core hardenability, and case hardenability of carburizing steels. It is important that the hardenability of both the case and the core be considered since the hardenability of the core determines the capability of a steel alloy to form high-strength martensite in the core, and the carbon content criterion in the core and transition region between the case and the core is typically chosen so that 50% martensite is formed, with the remainder being bainite (*111*). The hardenability of the case controls the hardness and microstructure as well as the formation and magnitude of compressive surface stresses. To adequately resist fatigue failure, a martensite level of 90%, with the remainder being retained austenite, is generally thought to be necessary (*112,113*).

12.03.2.10.1 Base Material Hardenability

Jominy end-quench hardenability curves are typically used to assess the hardenability of carburizing steels as they are for through-hardening steels. Experimentally, the Jominy curves are obtained using the conventional Jominy end-quench test described previously. In order to assure reasonable control of the hardenability of most carburizing grades of steel, one manufacturer has reported that the difference between the specified hardness and the value predicted or obtained for three points on the Jominy curve, 1.5, 5, and 11 mm from the quenched end, shall not exceed 10 HV units (approximately 1 R_c) (*114*).

However, since it is difficult to compare Jominy curves of carburized test bars, a point (7 mm, 0.27 inch) from the quenched end on the Jominy curve of the base steel composition has been reported to exhibit the greatest influence on the case depth (*115*). **Table 16** illustrates the variation in hardness at the $J = 7$ mm position, with variation of steel chemistry within the allowed H-band. (Note that $J = 7$ mm represents an inflection point on the Jominy curve previously identified by Grossmann, which is in the region of 50% martensite, sometimes $J = 6.5$ mm is used instead.) Alternatively, some authors use an alternative method called the 'hardness drop' method, which is the Jominy distance to a given drop in hardness reported to give lower uncertainty (*116*).

12.03.2.10.2 Core Hardenability

Typically, the tensile strength of the core is the mechanical property most often specified. However, although the microstructures of the core are rarely specified, they determine the strength and composition and therefore are hardenability dependent. Soft cores, $<750\ \mathrm{N\,mm^{-2}}$, suggest high ferrite content and hard cores, and $>1240\ \mathrm{N\,mm^{-2}}$, suggest primarily martensitic microstructure. However, the core may also contain a bainitic microstructure or mixed microstructures of ferrite, bainite, and martensite. Generally, as the strength and hardenability of a steel increase, elongation and reduction in area decrease. Also, as the tensile strength increases, impact strength decreases (*117*). Furthermore, it is important to note that core hardenability does not predict case hardenability (*112*).

Smith and Eldis reported that core hardenability is most strongly increased by molybdenum and manganese, although manganese may affect annealability and increase the difficulty in controlling the hardenability bandwidth (*109*). Excessive use of chromium can lead to surface oxidation and high carbide formation in the case and a decrease in toughness (*109,110*).

Multiplying factors developed by Grossmann for the calculation of D_I were based mostly on steels containing 0.35–0.65% carbon. De Ratana and Doane reported that if these values are used to calculate D_I for carburizing steels with carbon content of 0.15–0.25%, then different multiplying factors should be used (*118*). For these calculations, the multiplying factors provided by Climax Molybdenum Co. for carbon and grain size shown in **Figure 54** and those for alloying elements in **Figure 55** should be used

Table 16 Illustration of Jominy hardness variation at $J = 7$ mm with composition of two carburizing grades of steel[a]

		% Elemental composition						Jominy hardness (HV)
Grade	Heat	C	Si	Mn	Cr	Ni	Mo	at $J = 7$ mm
Ovako 146	Minimum	0.13	0.15	0.70	0.60	0.80	–	238
	R3130	0.14	0.22	0.83	0.74	0.85	0.04	285
	K9341	0.22	0.18	0.82	0.77	1.03	0.04	374
	R7230	0.20	0.25	1.04	0.94	0.97	0.10	418
	Maximum	0.25	0.40	1.10	1.20	1.40	0.20	550
Ovako 152	Minimum	0.18	0.20	0.70	0.40	0.40	0.15	256
	R9594	0.19	0.30	0.80	0.44	0.41	0.18	288
	R6120	0.21	0.22	0.89	0.58	0.47	0.18	340
	Maximum	0.23	0.35	0.90	0.60	0.70	0.25	379

Ovako 146 is a Mn–Cr–Ni steel.
Ovako 152 is equivalent to AISI 8620 and is a Mn–Cr–Ni–Mo steel.
[a]Reproduced from Tartaglia, J. M.; Eldis, G. T. Core Hardenability Calculations for Carburizing Steels. *Metall. Trans. A* **June 1984,** *15A*, 1173–1183.

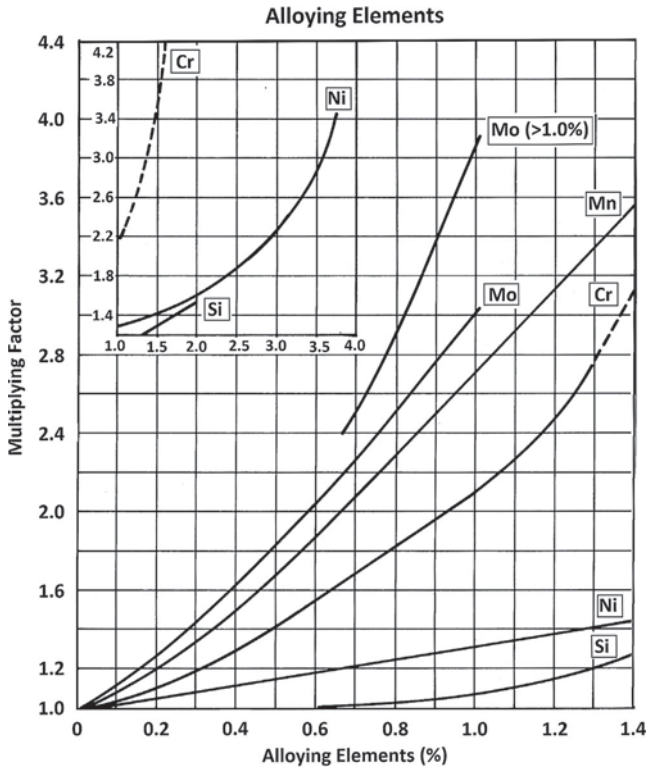

Figure 54 Elemental multiplying factors recommended by Climax Molybdenum Co. for steel alloys containing 0.15–0.25% carbon. Reproduced from de Retana, A. F.; Doane, D. V. Predicting Hardenability of Carburizing Steels. *Metal Prog. Sept* **1971,** 65–69.

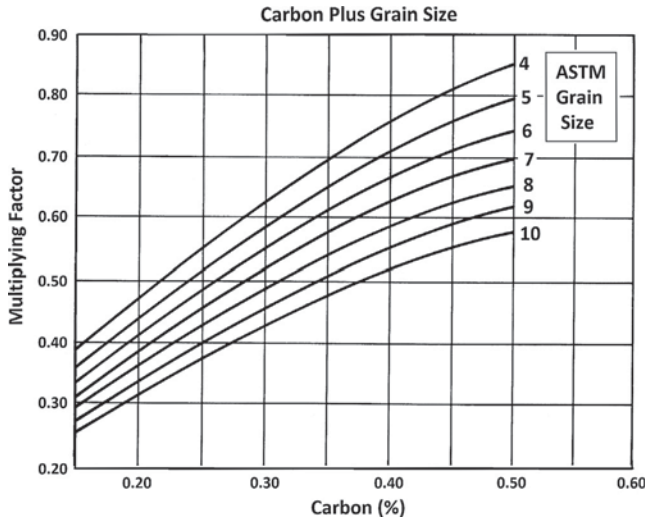

Figure 55 Multiplying factors for carbon and grain size recommended by Climax Molybdenum Co. for steel alloys containing 0.15–0.25% carbon. Reproduced from de Retana, A. F.; Doane, D. V. Predicting Hardenability of Carburizing Steels. *Metal Prog. Sept* **1971,** 65–69.

for calculating D_I. It is important to note that if the steel alloy contains >1% nickel, then line for the elemental multiplying factor designated as Mo(>1% Ni) (*48*) or for steels containing >0.75% Ni and no more than 0.20% Mo (*29*) should be used.

12.03.2.10.3 Case Hardenability

The standard definition of case depth, or thickness of the hardened layer, is that subsurface depth where the hardness is equal to 550 HV (*115*) or 50 R_c (*119*). Two factors that limit case depth are hardenability of the base material and the dimensions of the component. If the hardenability of the base material is low, the minimum case depth will be given by the amount of carbon diffused into the steel during carburizing. If the base material exhibits a hardness ≥550 HV, the case depth is defined as infinite. An increase in the component dimensions reduces the effective case depth. **Figures 56 and 57** illustrate the relationship between Jominy

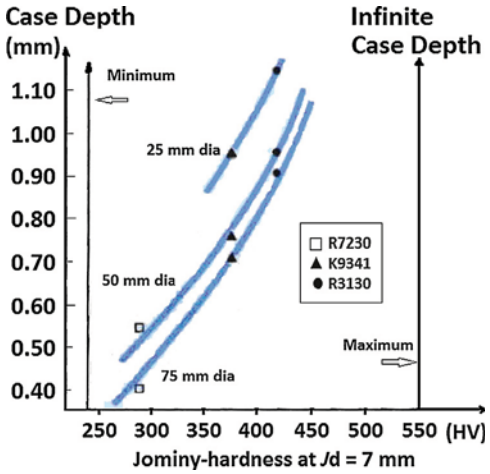

Figure 56 Case depth as a function of Jominy hardness at $J = 7$ mm and section size for Ovako 146, a Mn–Cr–Ni steel. Reproduced from Wretlind, J.; Sabelström, U.; Lund, T. *Technical Report 1/1989 – The Influence of Base Material Hardenability on the Case Depth after Case Hardening*. Report by Ovako Steel AB, Box 5013, SE-194 05; Upplands, Väsby: Sweden, 1989. ISSN: 0284-3366.

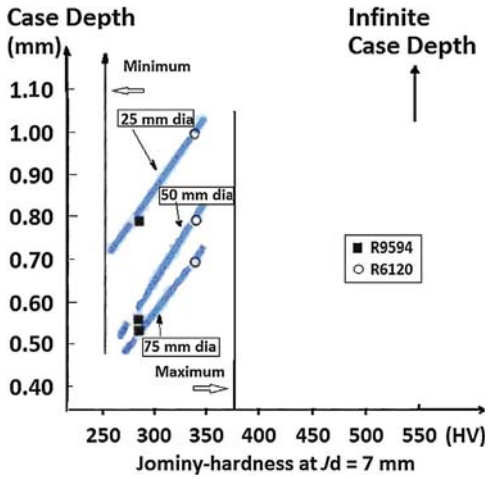

Figure 57 Case depth as a function of Jominy hardness at $J = 7$ mm and section size for Ovako 152, a Mn–Cr–Ni–Mo steel. Reproduced from Wretlind, J.; Sabelström, U.; Lund, T. *Technical Report 1/1989 – The Influence of Base Material Hardenability on the Case Depth after Case Hardening*. Report by Ovako Steel AB, Box 5013, SE-194 05; Upplands, Väsby: Sweden, 1989. ISSN: 0284-3366.

hardenability and case depth for Ovako 146, a Mn–Cr–Ni steel and Ovako 152 (AISI 8620), and a Mn–Cr–Ni–Mo steel. In both cases, although an increase in section size decreases hardenability, the effect of Jominy hardenability is unchanged (*115*).

It is possible to use the Jominy end-quench test to characterize the hardenability of the carburized case as a function of distance from the quenched end of the Jominy bar. Although this procedure works well with relatively low case hardenability, it is more difficult to apply for higher hardenability case structures since it is often difficult to be assured of complete martensite formation (*112*).

The experimental procedure for determining the case hardenability of carburized steels is detailed in Ref. (*111*). One example is described in Ref. (*88*). In this example, a standard Jominy end-quench test specimen was carburized at 925 °C for 4.5 h. In addition, 2 bars of the same steel, dimensions, surface condition, and chemistry (heat) are carburized under exactly the same conditions. These bars are used to plot the carbon gradient using chips obtained when machining the removal of the carburized layer at case depths (see **Figure 58(a)**). In the case of the steel represented in **Figure 58**, the carbon content as a function of case depth is shown in **Table 17**. In this example, one of the Jominy test bars was end-quenched directly from the carburizing temperature (925 °C) using the standard quenching procedure. A second Jominy test bar was cooled to room temperature and reheated and then quenched from 820 °C. After quenching, all of the Jominy test bars were ground on four sides at the depths d_1, d_2, d_3, and d_4 as shown in **Figure 58(b)**. HRC values were measured at standard distances from the quenched end, and Jominy curves were plotted. In the example illustrated in **Figure 58**, the carbon contents at increasing case depths were 1.0, 0.9, 0.8, and 0.7% C, and the carbon content in the core was 0.17% C.

The results of this experimental study showed that, as expected, the hardenability of the core was very different from that of the case, and the best hardenability of this particular steel was obtained at 0.9% C and with direct quenching or at 0.8% C and indirect quenching (*88*).

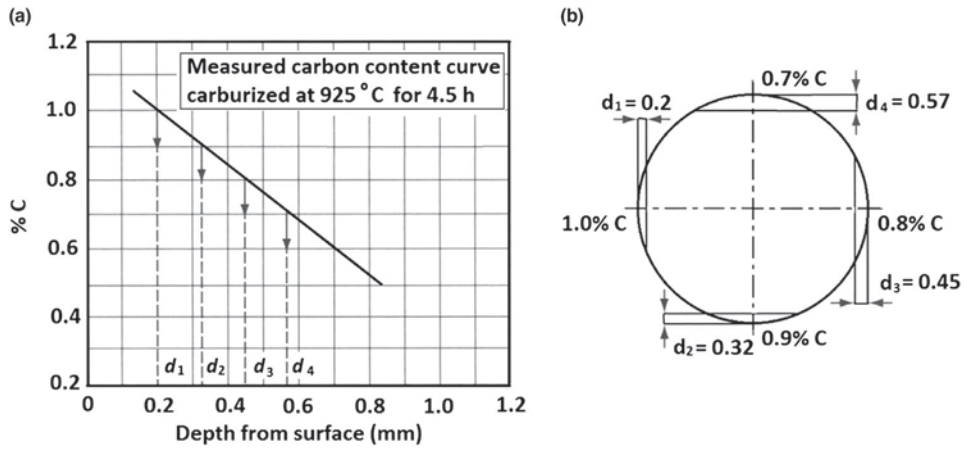

Figure 58 (a) Carbon gradient curve after gas carburizing 16MnCr5 steel (similar to AISI 5115) for 4.5 h at 925 °C (b) Grinding depths of the carburized Jominy end-quench test bar. The chemistry of the 16MnCr5 steel was 0.17% C, 0.25% Si, 1.04% Mn, 1.39% Cr. Reproduced from Liščič, B. Hardenability. Steel Heat Treatment Handbook. In *Steel Heat Treatment: Metallurgy and Technologies*; Totten, G. E., Ed., 2nd ed.; CRC Press Taylor – Francis Group: Boca Raton, FL, 2007; pp 213–276. ISBN: 978-0-8493-8455-4 (chapter 5).

Table 17 Carbon content at different case depths when a standard Jominy test bar of DIN 16MnCr5 steel is carburized at 925 °C[a]

d_n-*value (see Figure 59(b))*	*Case depth (mm)*	*Carbon content (%)*
$n = 1$	0.2	1.0
$n = 2$	0.32	0.9
$n = 3$	0.45	0.8
$n = 4$	0.57	0.7

[a]Reproduced from Liščič, B. Hardenability. Steel Heat Treatment Handbook. In *Steel Heat Treatment: Metallurgy and Technologies*; Totten, G. E., Ed., 2nd ed.; CRC Press Taylor – Francis Group: Boca Raton, FL, 2007; pp 213–276. ISBN: 978-0-8493-8455-4 (chapter 5).

The effects of alloying elements on case hardenability are dependent on the temperature from which the steel is quenched (*109*). When quenching from 1700 °F (925 °C), molybdenum exhibits the greatest effect on hardenability. However, when quenching from 1525 °F (830 °C), the effect of molybdenum on hardenability is reduced to a level more comparable to that exhibited by manganese and chromium, while nickel exhibits the weakest effect. Also, the susceptibility to bainite formation in the carburized case is reduced by the presence of molybdenum and chromium.

Jatczak redetermined multiplying factors used for calculating D_I for a wide range of steels, including multialloyed carburizing steels. This work was based on the determination of hardenability based on 10% transformation in the high-carbon region instead of the 50% transformation on which Grossmann based on pertinent multiplying factors (*108*). Jatczak's case hardenability calculations were developed for either reheating and quenching from 1475 to 1575 °F (802–857 °C) or direct quenching from the carburizing temperature of 1700 °F (925 °C). The accuracy of these calculations using Jatczak's revised multiplying factors was within ±10%. Extensive tabular summaries for a multiplying factor for a wide range of heating temperatures and times are available in Ref. (*100*). **Figures 59–61** provide a selected graphical summary of multiplying factors for calculating D_I for carburized cases containing 0.9–1.1% carbon and which have been reheated and quenched from 1475 °F (802 °C), 1525 °F (829 °C), and 1575 °F (857 °F), respectively (*118*). **Figure 62** is used for carburized cases that are direct quenched from 1700 °F (926 °C) (*118*).

Reduced hardenability has been observed for carburized steels where the case contains greater than 0.9% carbon. Electron microscopy revealed that this is due to the formation of a very fine network of carbides that were concentrated at the prior austenite grain boundaries, resulting in localized depletion of carbon adjacent to these networks in the same manner as when the formation of massive carbides depletes the carbon content in the surrounding matrix (*29*).

Walton has reported that high-molybdenum, high-hardenability carburizing grades of steel containing greater than 0.65%C exhibited what he called hardenability fade. At deeper levels in the case where the carbon content was <0.65%, the expected degree of hardenability returned (*120*).

Figures 59–61 are used as follows:

1. Select the appropriate chart for the hardening conditions being used; reheat and quench or direct quenching. The base D_I value for the calculation is provided in the figure caption;
2. Multiply the D_I value by the carbon correction factor shown in the upper right corner of the figure;
3. **Figures 59–61** may be used to determine the elemental multiplying factors if the total nickel content of the steel is less than 1.0%, or if the steel contains more than 2% manganese or nickel but molybdenum is less than 0.15% (*118*). Remember that the elemental contents of Mn, Si, Ni, and Cr that are less than 0.25% will exhibit multiplying factors of less than 1.0.

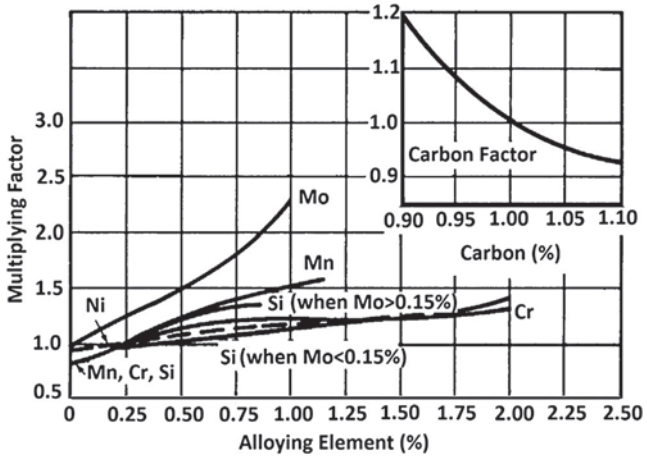

Figure 59 Use this figure for calculation of D_I for carburized cases containing 0.9–1.10% C where the austenitization temperature is 1475 °F (802 °C) – reheat and quench. The base D_I value is 1.05. Reproduced from de Retana, A. F.; Doane, D. V. Predicting Hardenability of Carburizing Steels. *Metal Prog. Sept* **1971,** 65–69.

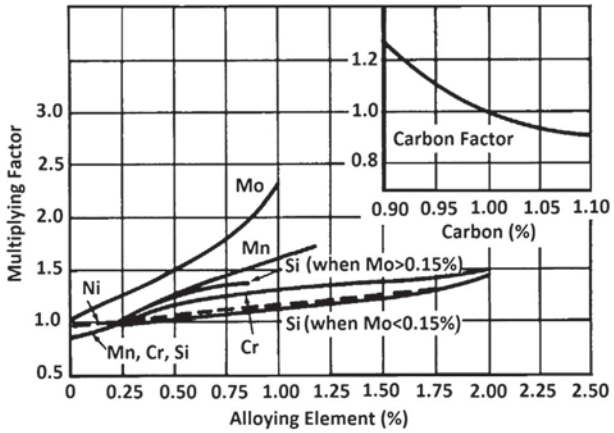

Figure 60 Use this figure for calculation of D_I for carburized cases containing 0.9–1.10% C where the austenitization temperature is 1525 °F (829 °C) – reheat and quench. The base D_I value is 1.13. Reproduced from de Retana, A. F.; Doane, D. V. Predicting Hardenability of Carburizing Steels. *Metal Prog.* **Sept 1971,** 65–69.

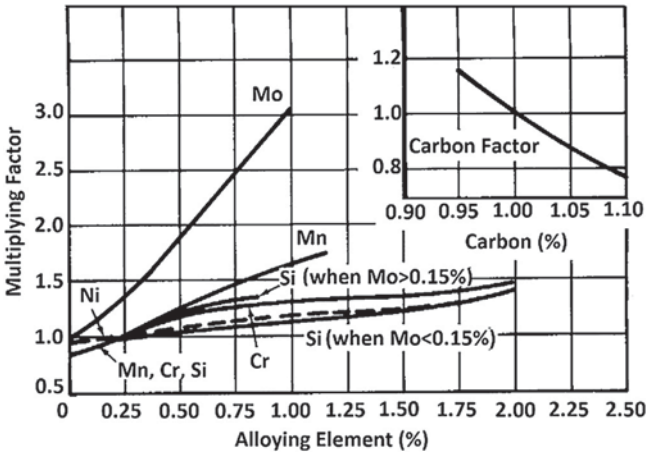

Figure 61 Use this figure for calculation of D_I for carburized cases containing 0.9–1.10% C where the austenitization temperature is 1575 °F (857 °C) – reheat and quench. The base D_I value is 1.35. Reproduced from de Retana, A. F.; Doane, D. V. Predicting Hardenability of Carburizing Steels. *Metal Prog.* **Sept 1971,** 65–69.

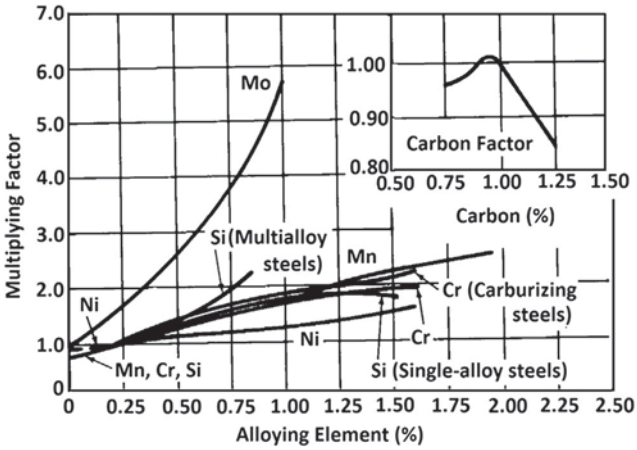

Figure 62 Use this figure for calculation of D_I for carburized cases containing 0.9–1.10% C where the carburized steel is direct quenched from 1700 °F (926 °C) and the soaking times are greater than 30–40 min. The base D_I value is 1.42. Reproduced from de Retana, A. F.; Doane, D. V. Predicting Hardenability of Carburizing Steels. *Metal Prog.* **Sept 1971,** 65–69.

For carburized cases that are direct hardened from 1700 °F (926 °C) with total soaking times of 30–40 min illustrated in Figure 62 (*118*), use the chromium factor labeled 'carburizing steels' and the other factors, as follows (*113*):

1. If the steel contains 0.15% or more of molybdenum, use the silicon factor labeled 'multialloy steels'.
2. If the steel contains less than 0.15% molybdenum, use the silicon factor labeled 'single-alloy' steels.
3. Use the Mn, Ni, Mo, and C factors up to the limit shown.

12.03.2.10.4 Case–Core Interface

It has been observed that a reduction in impact strength and increased potential for fracture occur in as-quenched microstructures containing upper bainite or pearlite in the carbon case. The presence of small amounts of bainite may also reduce fatigue resistance and case strength (*111*). In addition, the formation of bainite in the carburized case results in gear and bearing pitting (*121*). The presence of upper bainite is dependent on the quenching cooling rate, and therefore the amount of bainite formed is dependent on steel hardenability.

Preston reported that the residual stress distribution is affected when bainite is present at the case-core interface (*110*). One method of avoiding bainite formation is to increase steel hardenability by increasing the manganese or chromium content. However, this increases the potential for internal oxidation, and high chromium increases the potential for carbide formation and decreases toughness. Therefore, hardenability is usually increased by increasing the nickel and/or molybdenum content of the steel. In some cases, vanadium is used to replace some of the molybdenum or nickel content to reduce cost. Alternatively, it has been found that V–Mo–Ti steels containing 0.4% C–1% Cr have been used as increased hardenability alternatives to more expensive Cr–Ni–Mo grades of carburizing steel (*110*). In some cases, the amount of bainite formed did not affect the hardness, although it did affect fatigue (*110*). Thus, a better measure of hardenability in the case was proposed by Eldis and Smith, which involves the Distance to the First appearance of Bainite (DFB) based on the Jominy hardenability test (*110,112*). The determination of DFB is now included in SAE J1975 (*111*).

Kern proposed that the case hardenability be defined in terms of DFB (*121*). Kern described a test where a standard Jominy bar is carburized and end-quenched and the effect of different cooling rates on the formation of bainite can be determined. Simultaneously, a second bar of the same heat is quenched, and the carbon gradient from the surface to the core is determined, as discussed earlier for Jominy testing of carburized steels. To determine the highest cooling at which bainite is formed, the carburized bar was sectioned longitudinally. One face was polished, etched, and microscopically examined at 500X to determine how far from the distance to the Fist Bainite (DFB) formation.

The procedure for determining DFB as reported by Doane (*112*) and Eldis and Smith (*122*) is essentially the same procedure cited in SAE1975 (*111*). In their work, the Jominy bar was carburized at 1700 °F (926 °C), then cooled to 1550 °F (845 °F), and finally end-quenched. Flats were ground to a case depth corresponding to 0.9% C, which were then metallographically etched and polished. A schematic of the test specimen is illustrated in Figure 63 (*112*). The amount of bainite as a function of distance from the quenched end was determined, and the DFB was identified.

Eldis and Smith (*122*) and Doane (*112*) determined the DFB for a wide range of steel grades and chemistries and then used multiple linear regression analysis to obtain regression equations that permit the calculation of DFB as a function of steel chemistry. The DFB values in terms of mm and alloy content in wt.% may be calculated from:

$$\mathrm{DFB} = 54.72\ \mathrm{Mo}^2 + 6.39\ \mathrm{Cr}^2 - 76.07\mathrm{MoNi} + 118.80\mathrm{MnMoNi} + 106.12\mathrm{MnMoCr} + 15.48\mathrm{MnNiCr} + 52.93\mathrm{MoNiCr} + 1.18$$

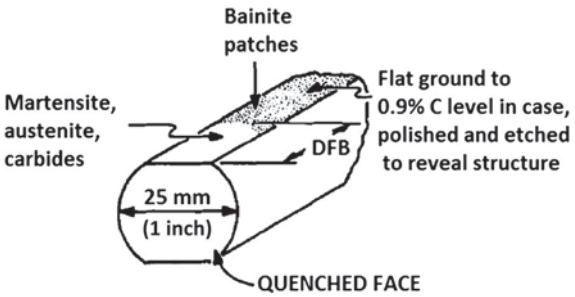

Figure 63 Schematic illustration of a carburized Jominy end-quenched test specimen on which flats have been ground. The DFB is determined along the centerline after grinding to a depth corresponding to 0.9% C and then etching and polishing before microscopic examination. Reproduced from Doane, D. V. Carburized Steel – Update on a Mature Composite. *J. Heat Treat.* **1990,** *8* (1), 33–53.

The DFB in 1/16 of an inch and using elemental content at wt.% yielded the regression equation:

$$DFB = 34.5Mo^2 + 4.0Cr^2 - 47.9MoNi + 74.8MnMoNi + 66.9MnMoCr + 9.8MnNiCr + 33.3MoNiCr + 0.7$$

12.03.2.11 Modeling Approaches to Hardenability of Steels

As suggested in the opening section of this chapter, the term *hardenability of a metal alloy* refers to the property that determines the depth and distribution of hardness when steel is heated to a given temperature and then quenched. It is also often referred to as the inverse measure of the severity of quenching conditions that produce the martensitic structure from steel that is initially austenitized so as to avoid transformation products such as pearlite and bainite. Chemical composition of the steel plays a key role in determining critical cooling rates; in general, the higher the carbon content, the higher the hardenability. Alloying elements such as nickel, manganese, chromium, and molybdenum tend to increase the hardness depth (*123*).

Hardness, on the other hand, is the materials' property or ability to resist indentation or scratching (*124–126*). Some applications benefit from superior hardness of alloys, for example, bearings, excavation tips, cutting tools, and the like. High-hardness materials usually create a challenge in metal joining processes such as welding because of the increased likelihood of hot and hydrogen-induced cold cracking. Weldability, which is a measure of the ease with which a metal can be welded, is inversely related to hardenability.

Hardenability of steels is a function of the carbon content and other alloying elements as well as the grain size of the austenite phase. The relative importance and influence of the various alloying elements are calculated by determining the equivalent carbon content of the steel. The fluid used to quench the material directly influences the cooling rate because the thermal conductivities and specific heats are dependent on the carbon content and other alloying elements. Liquids such as brine (salt solution in water) and water have a much higher cooling rate capability than air and oil. Additionally, when the fluid is agitated, its cooling rate capability increases quite significantly. The geometry of the part being quenched also affects the cooling rate, specifically, given two samples of equal volume; the one with higher surface area will cool faster. This concept can be extended to a load of components being quenched at the same time, for which it can be surmised that the smaller the load, the higher is the likelihood of even quenching for the load (*127,128*).

The hardenability of ferrous alloys is usually measured by the Jominy test: A round metal bar of standard size (ASTM A255) is heated in a furnace until it is transformed to 100% austenite, then quickly transferred to a Jominy quench tank, and it is quenched on one end with room-temperature water. A typical physical setup of the Jominy hardenability measurements is shown in Figure 15(a) (*147*).

Necessarily, the cooling rate will be highest at the end being quenched and will decrease with distance toward the end exposed to room-temperature air. Hardenability is then determined by measuring the hardness along the bar, and it can be surmised that the farther away from the quenched end that the hardness extends, the higher the hardenability for the alloy under study. The literature is rich with documentation of hardenability studies both experimentally and with computational modeling.

Considerations of the quantitative prediction of hardenability of steels need to take into account the fact that even though the Jominy testing procedure and data extraction are well established by an ASTM standard, significant spread of hardness versus depth has been recorded for an 8620 steel chemistry subjected to 'standard' identical test conditions as shown in Figure 64 (*132*).

Similar trends were reported for 4140 Steel (*129,131*). Such discrepancies, which are reported widely in the literature, may be attributed to several factors, including errors in reporting the correct steel chemistry, careless and erroneous test procedures, or process control.

Hardenability data extracted from Jominy test curves are closely related to CCT and IT curves. These curves are at the core knowledge of metallurgy. Hardness profiles of a Jominy test specimen, which are determined by microstructures that evolve from the differential cooling rates, can be constructed from CCT and IT curves superimposed on the same set of axes as shown in Figure 65 (*130*). This type of construction provides good insight into the ways to develop mechanisms for predicting the mechanical properties of arbitrarily shaped components.

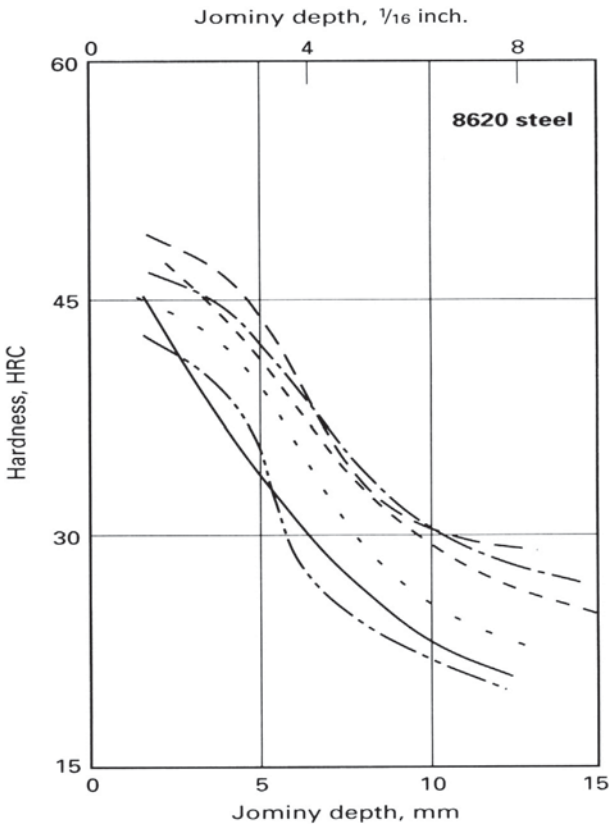

Figure 64 Summary of reported Jominy tests by several laboratories on SAE 8620 steel of approximately the same chemical composition and grain size. Reproduced from Kirkaldy, J. S.; Feldman, S. E. Optimization of Steel Hardenability Control. *J. Heat Treat.* **1989,** *1*, 57–64.

Prediction of hardenability in steels is a complicated process. It involves an interdisciplinary approach to quantifying fairly complex transient thermal fields that drive microstructure developments, mechanical response, and transformation behavior, as indicated by Figure 66 (*131*,*132*).

Several works can be cited in the literature for varying degrees of success in implementing models that predict steel alloy hardenability. The hardenability factors attributed to the work of Grossmann (*133*) were for a long time the de facto standard. Subsequent work by Kirkaldy (*134*) addressed several shortcomings of Grossmann's models and to date serves as the benchmark against which hardenability models are compared.

Finite element analysis (FEA) techniques have been embraced by many investigators as a tool for tackling the challenges of modeling the hardenability of alloy steels. Li et al. (*135*) developed a computational model for predicting steel hardenability. This model was formulated to predict the hardness distribution in end-quenched bars of heat-treatable steels by incorporating a thermodynamics model to compute phase equilibria in multicomponent Fe–C–M systems, a finite element model to simulate the heat transfer induced by end quenching Jominy bars, and a reaction kinetics model for austenite decomposition. This effort required writing several subroutines that were incorporated in a commercial FEA program, ABAQUS. This study concluded that their model was in good agreement and added some improvement and reliability to the work of Kirkaldy (*134*).

Malikizadi (*136*) used a FEA alongside MATLAB to simulate the cooling behavior and microstructure development of Powder Metallurgy Steels. A significant effort of this work focused on the comparison of predicted hardenability behavior to well-established experiment-based benchmarks.

Just (*137*) used the correlation of average carbon and alloy steel compositions to develop equations for computing hardenability profiles. To accomplish this predictive modeling tool, Just used multiple regression analysis to determine the effect of changing an individual alloying element at a time, while keeping all the other variables constant. This method is not reliable in predicting steel hardenability with good precision. The author recommends that this method is good largely for assisting the alloy designer select the steel for a particular application and for helping the metallurgist in ways to tweak the melt. Examples of hardnesses on the Rockwell C predicted by this method are:

$$J_1 = 52(\%C) + 1.4(\%Cr) + 1.9(\%Mn) + R_c33 \quad [1]$$

$$J_6 = 89(\%C) + 23(\%Cr) + 7.4(\%Ni) + 24(\%Mn) + 34(\%Mo) + 4.5(\%Si) - R_c30 \quad [2]$$

$$J_{22} = 74(\%C) + 18(\%Cr) + 5.2(\%Ni) + 16(\%Mn) + 21(\%V) + 4.5(\%Si) - R_c29 \quad [3]$$

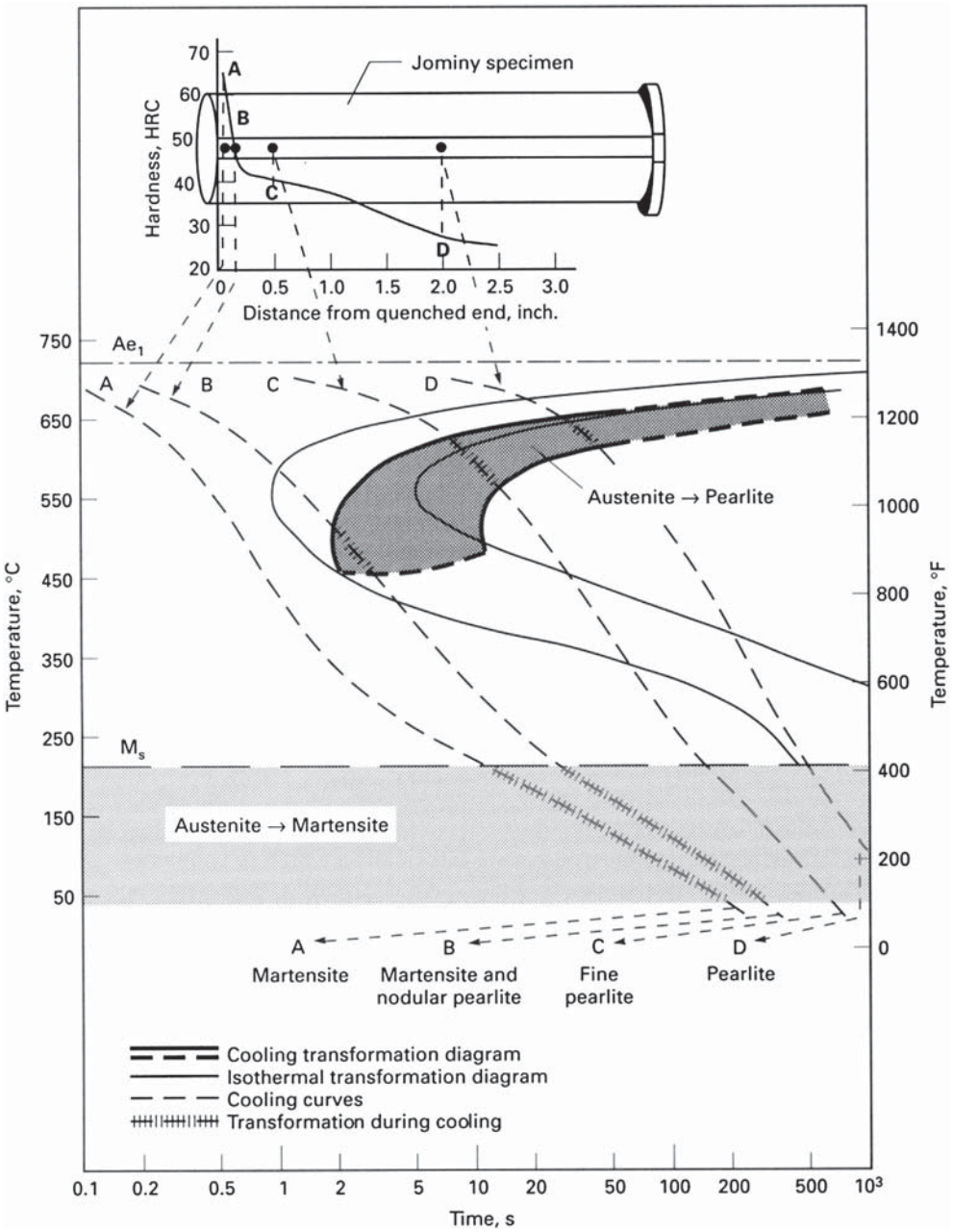

Figure 65 Relationship of CCT and IT curves of a eutectoid steel showing four cooling paths: A, B, C, and D. Reproduced from Krauss, G. *Steel, Heat Treatment and Processing Principles*; ASM International, 1990; p 94.

Subscripts 1, 6, and 22 in eqns [1]–[3] represent distances of 1/16, 6/16, and 22/16 inch, respectively, from the quenched end. Just's prediction models were modified in order to accommodate the nonlinear behavior of the chemical composition of steels, for which experiments indicated that as the content of the alloying element increased, their effect on hardenability decreased.

The results of Just's hardenability predictions were in good agreement with measurements for a wide variety of standard SAE-grade steels. Other investigators also implemented multiple regression algorithms. Sibert et al. (*138*) proposed a procedure for first establishing cooling rates for various locations along the Jominy bar, then transforming the time axis such that the time zero corresponded to the Ae_3 temperature. Corresponding cooling rate curves are related to proper CCT start curves. The critical cooling rate was taken to be the point at which hardness began to drop. The pearlite volume fraction associated with each cooling rate was converted to a percent martensite and then to a corresponding hardness. The results of this study involving a 4068 steel are shown in Figure 67 from which it is evident that experimental results (dashed curve) compared very favorably with predicted results in the range of 0–50% martensite for ASTM grain-size range of 4–12 (*138*).

Sarmiento et al. (*139*) applied several numerical prediction tools to improve the SAE J406 (*140*) hardenability predictor. To accomplish their hardenability prediction improvements, Sarmiento et al. used numerical codes IN-PHATRAN and INDUCTER-B

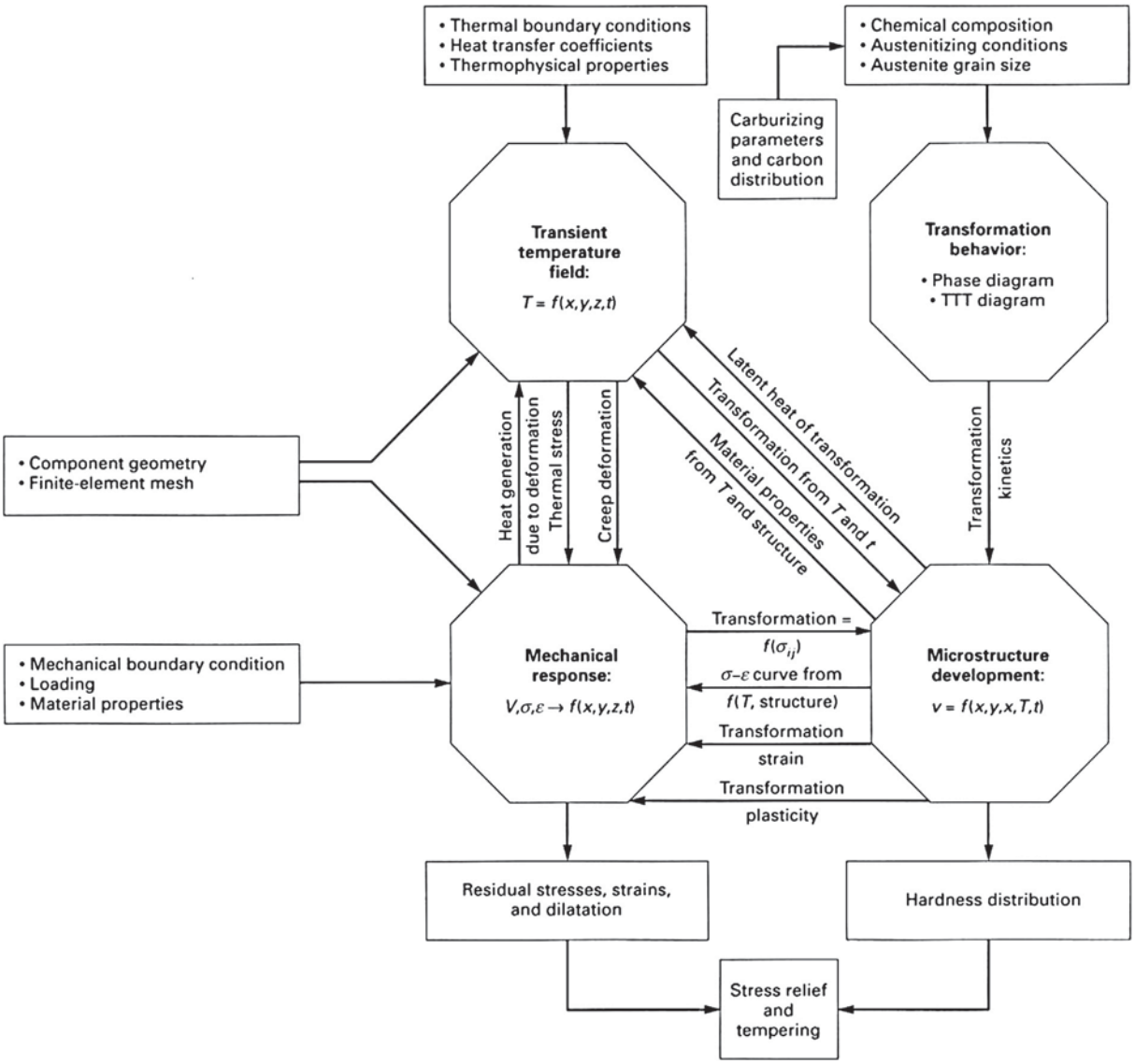

Figure 66 General system overview of a program for predicting the thermomechanical behavior of low-alloy steels. Reproduced from Buchmayr, B.; Kirkaldy, J. S. Modeling of the Temperature Field, Transformation Behavior Hardness, and Mechanical Response of Low Alloy Steels during cooling from the Austenite Region. *J. Heat Treat.* **1990**.

that were developed for modeling heat treatment processes duly modified to predict the spatial distribution of hardness in steel hardenability samples. Hardness prediction results initially did not fare well compared to other established predictors such as Cat, STECAL, AMAX, and Minitek. Upon applying least-squares fitting procedures on their predicted data, the result was a significant improvement of the J406 hardenability predictor. The improved J406 predictor effectively resulted in *J*-curves that tracked right between the J406 predicted results and experimentally determined results for a variety of steels.

Brooks (*141*) conducted analysis similar to Siebert et al. (*138*), which amounted to a refinement of Just's (*137*) original regression analysis. Brooks' equations for computing hardness at various Jominy distances as a function of steel chemical composition are summarized in Table 18 (*7*). The numbers beside the element symbols represent the amount of that element in weight percent.

Grain size was not included in the regression analysis, but it was in the range of ASTM 8–12. Ranges of chemistries in Brooks' work are summarized in Table 19.

Neural network application for the simulation of hardenability in steels is another modeling tool that has seen a fair amount of activity in the research literature. Dobranski et al. (*142*) developed a modeling technique for predicting the hardenability of steels based on the chemical composition of steels. Their work was based on multilayer feed-forward neural networks whose learning rule was based on the error propagation algorithm. Their technique employed more than 500 neural networks, with various numbers of hidden layers and hidden neutrons. They used a large number of iterations (100–10 000), resulting in a robust modeling tool that was used successfully to predict the hardenability of a wide range of steel chemistries as well as a large variation of heats of carburization.

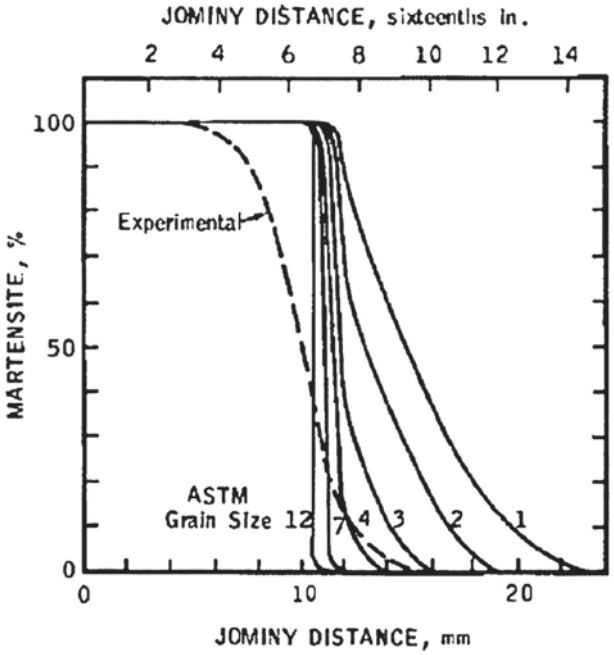

Figure 67 Predicted Jominy curves for Steel 4068 as a function of grain size. Reproduced from Siebert, C. A.; Doane, D. V.; Breen, D. H. *Recent Contributions to Hardenability Predictions, in the Hardenability of Steels – Concepts, Metallurgical Influences and Industrial Applications*; American Society for Metals.

Table 18 Brooks' equations for hardness prediction[a]

Jominy distance (1/16ths)	*Hardness* (R_c)
1	$204C+4.3Si+8.32Cu-241.3C^2 3+11.03$
2	$207.9C+7.06Cu-246.3C^2+400MnB+9.94$
3	$226.3C+2.28Mn+6.15Cu-281.7C^2+7.43\times10^3C^3B+4.176$
4	$7.02Ni-13.07+23.9\times10^3CB-9.01\times10^8CB^2+47.76$
5	$17.88Ni-11.76Cr+33.8\times10^3CB-19\times10^6CB^2+5.29\times10^3MnB+39.8$
6	$41.73Ni-80.32MnS+23.5\times10^3CB-23.1\times10^6CB^2+10.27\times10^3MnB+32.9$
7	$8.46Mn-115.6S+64.4Ni+26.7Cr-17.4\times10^6CB^2+12.47\times10^3Mn^2B+18.1$
8	$14.34Mn-80.34S+68.77Ni+36.84Cr-16.13\times10^6CB^2+9.89\times10^3Mn^2B+7.7$
9	$27.15Mn+136.9P+69.06Ni+33.6Cr+1.715Mn^2B-9.329$
12	$14.01Mn+87.59P+31.33.Ni+21.17Cr+70.76Mo+5.49$
16	$22.93C+9.173Mn+50.54P+16.36Ni+13.29Cr+57.44+1.696$
20	$29.11C+10.41Mn+1.02Ni+12.71Cr+50.43No-2.93$

[a]Reproduced from Brooks, C. R. Hardenability. In *Principles of the Heat Treatment of Plain Carbon and Low-Alloy Steels*; ASM International: Materials Park, OH, 1996; pp 43–86. ISBN: 978-0-87170-538-9 (chapter 3).

Table 19 Composition ranges for Brooks' equations[a]

Carbon	0.28–0.46%
Manganese	0.8–1.4%
Silicon	0.13–0.39%
Nickel	0.00–0.28%
Chromium	0.05–0.25
Molybdenum	0.01–0.06%
Copper	0.08–0.22%
Boron	0.0001–0.0019%

[a]Reproduced from Brooks, C. R. Hardenability. In *Principles of the Heat Treatment of Plain Carbon and Low-Alloy Steels*; ASM International: Materials Park, OH, 1996; pp 43–86. ISBN: 978-0-87170-538-9 (chapter 3).

12.03.3 Conclusions

Steel hardenability is dependent on steel composition. An overview of a wide range of testing procedures used to determine and quantify steel hardenability ranging from classical fracture and etching, Grossmann hardenability, Jominy end-quench testing, and manual and computerized computational methods were discussed. The application of these procedures on steels ranging from shallow-hardening to air-hardening steels was discussed as well as methods of quantifying the case and core hardenabilities for carburized steels. Taken together, the information in this review provides the reader with a historical and current reference on the general topic of steel hardenability and testing procedures.

Acknowledgments

The authors acknowledge their appreciation to CAPES (Coordenação de Aperfeiçoamento de Pessoal de Nível Superior) for the financial support for this work.

References

1. Totten, G. E.; Bates, C. E.; Clinton, N. A. Measuring Hardenability and Quench Severity. In *Quenchants and Quenching Technology;* ASM International: Materials Park, OH, USA, 1993; pp 35–68. ISBN: 978-0-8717-0448-1 (chapter 2).
2. Davenport, E. S. Isothermal Transformation in Steels. *Trans. ASM* **1939,** *27,* 837–886.
3. Davenport, E. S.; Bain, E. C. Transformation of Austenite at Constant Subcritical Temperatures. *Trans. AIME* **1930,** *90,* 117–154.
4. Wever, P.; Rose, A. On the Question of Heat Treatment of Steels on the Basis of Time-Temperature-Transformation Diagrams (Zur Frage der Wärmbehandlung der Stähle auf Grund ihrer Zeit-Temperatur-Umwandlungs-Schaubilder). *Stahl und Eisen* **1954,** *74* (12), 749–760.
5. Krauss, G. *Steels: Heat Treatment and Processing Principles;* ASM International: Materials Park, OH, 1990. ISBN: 0-87170-370-X, p 457.
6. Weinberg, M. C.; Uhlmann, D. R.; Zanotto, E. D. Nose Method of Calculating Critical Cooling Rates for Glass Formation. *J. Am. Ceram. Soc.* **Nov 1989,** *72* (11), 2054–2058.
7. Brooks, C. R. Hardenability. In *Principles of the Heat Treatment of Plain Carbon and Low-Alloy Steels;* ASM International: Materials Park, OH, 1996; pp 43–86. ISBN: 978-0-87170-538-9 (chapter 3).
8. Sverdlin, A. V.; Ness, A. R. Fundamental Concepts in Steel Heat Treatment. Steel Heat Treatment Handbook. In *Steel Heat Treatment: Metallurgy and Technologies;* Totten, G. E., Ed., 2nd ed.; CRC Press Taylor & Francis Group: Boca Raton, FL, 2007; pp 121–163. ISBN: 978-0-8493-8455-4 (chapter 3).
9. Zeng, Q. Y.; Xu, K. Y. Predicting the Hardenability of Steel Using the Critical Cooling Rate. *Mémoires et Études Scientifiques Revue de Métallurgie* **Feb 1988,** 105–110.
10. Fu, T-l; Wang, R-q; Wang, Z-d; Wang, G-d; Wang, M-t Construction and Application of Quenching Critical Cooling Rate Model. *J. Iron Steel Res. Int.* **2010,** *17* (3), 40–45.
11. Shepherd, B. F. The P-F Characteristic of Steel. *Trans. Am. Soc. Metals* **1934,** *22,* 979–1016.
12. Wadhwa, A. S.; Dhaliwad, H. S. Hardenability. In *A Textbook of Engineering Materials and Metallurgy;* Firewall Media, Laxmi Publications Ltd: New Delhi, India, 2008; pp 417–426. ISBN: 978-81-318-0357-8 (chapter 5).
13. Sharma, R. C. Hardenability of Steels: Concepts and Characterization. In *Principles of Heat Treatment of Steel;* New Age International Publishers: New Delhi, India, 1996; pp 160–176. ISBN: 978-81-224-0869-0 (chapter 9).
14. Kramarov, M. A.; Orlov, E. D.; Rybakov, A. B. Work of Fracture as a Criterion for Determining the Hardenability of Steel. *Met. Sci. Heat Treat.* **1980,** *22* (1), 42–44.
15. Davis, J. R. Classification and Properties of Tool and Die Steels. In *ASM Specialty Handbook – Tool Materials;* ASM International: Materials Park, OH, USA, 1995; pp 119–153.
16. Holloman, J. H.; Jaffe, L. D. Hardenability. In *Ferrous Metallurgical Design: Design Principles for Fully Hardened Steel;* John Wiley & Sons: New York, NY, USA, 1947; pp 196–214 (chapter 6).
17. Crafts, W.; Lamont, J. L. Hardness and Hardenability. In *Hardenability and Steel Selection;* Pittman Publishing: New York, NY, 1949; pp 84–110 (chapter 5).
18. Hodge, J. M.; Orchoski, M. A. Relationship between Hardenability and Percentage of Martensite in Some Low-Alloy Steels. *Trans. Am. Inst. Min. Metall. Eng.* **1946,** *107,* 627–642.
19. Grange, R. A. Estimating the Hardenability of Carbon Steels. *Metall. Trans.* **Oct 1973,** *4,* 2231–2244.
20. Hwang, B.; Suh, D.-W.; Kim, S.-J. Austenitizing Temperature and Hardenability of Low-Carbon Boron Steels. *Scr. Mater.* **2011,** *64,* 1–12.
21. Rajan, T. V.; Sharma, C. P.; Sharma, A. Hardenability. In *Heat Treatment Principles and Techniques,* 2nd ed.; PHI Learning Private Ltd: New Delhi, India, 2011; pp 124–141 (chapter 6).
22. Sharma, R. C. Hardenability of Steels II. In *Principles of Heat Treatment of Steel;* New Age International: New Delhi, India, 1996; pp 177–208 (chapter 10).
23. Anon. Alloying Elements and Their Effects and Hardenability. In *Reprint from "Republic Alloy Steels" Handbook Adv. 1099;* Republic Steel: Cleveland, OH, 1961.
24. Heine, H. J. Understanding the Hardenability of Steel. *Heat Treat.* **March/April 1994,** 31–34.
25. Hollomon, J. H.; Jaffe, L. D. The Hardenability Concept. Technical Publication 1926, Metals Tech. *Trans. Am. Inst. Min. Metall. Eng.* **1946,** *13* (1), 1–12.
26. Whittenberger, E. J.; Burt, R. R.; Carney, D. J. Hardenability Factors for Hypereutectoid Low-Alloy Steels. *Trans. AIME J. Metals* **Aug 1956,** *206,* 1008–1016.
27. Grossmann, M. A. Hardenability Calculated from Chemical Composition. *AIME Trans.* **1942,** *150,* 227–259.
28. Doane, D. V. Applicability of Hardenability Concepts in Heat Treatment of Steel. *J. Heat Treat.* **1979,** *1* (1), 5–30.
29. Siebert, C. A.; Doane, D. V.; Breen, D. H. Metallurgical Factors Influencing Hardenability of Steel. In *The Hardenability of Steels – Concepts, Metallurgical Influences and Industrial Applications;* American Society for Metals: Metals Park, OH, USA, 1977; pp 65–138.
30. Jatczak, C. F. Hardenability of High Carbon Steels. *Metall. Trans.* **1973,** *4,* 2267–2277.
31. Hewitt, W. Hardenability – Its Prediction from Composition. *Heat Treat. Met.* **1981,** *8* (2), 33–38.
32. Davenport, E. S.; Grange, R. A.; Hafsten, R. J. Influence of Austenite Grain Size upon Isothermal Transformation Behavior of S.A.E. 4140. *Trans. AIME* **1941,** *145,* 301–314.
33. Bain, E. C. Factors Affecting the Inherent Hardenability of Steel. *Trans. Am. Soc. Steel Treat.* **1932,** *20,* 385–428.
34. ASTM E112-10 – *Standard Test Methods for Determining Average Grain Size*; ASTM International; 100 Barr Harbor Drive, West Conshohocken, PA 19429-2959 USA.

35. Woodhead, J. H. The Physical Metallurgy of Vanadium Steels. In *Vanadium in High Strength Steel, Proceedings of VANITEC Seminar, Chicago;* The Vanadium International Technical Committee, Vanitec Limited: Westerham Kent, England, Nov 1979; pp 3–10.
36. Pacyna, J.; Dabrowski, R.; Skrzypek, T. The Effect of Vanadium on the Kinetics of Phase Transformations of Undercooled Austenite in the Steels of Low Content of Other Elements. *Adv. Mater. Sci.* **Nov 2001,** *1* (1), 74–78.
37. Maalekian, M. *Christian Doppler Laboratory for Early Stages of Precipitation – The Effects of Alloying Elements on Steels – I.* Report CDL/ESOP Report; Technical Universität Graz, Institut für Werkstoffkunde, Schweißtechnik und Spanlose Formgebungsverfahren: Graz, Austria, Oct 2007; pp 1–36.
38. *Steel Casting Handbook – Supplement 11: Hardenability and Heat Treatment;* Steel Founders Society of America: 780 Mcardle Dr # G Crystal Lake, IL 60014-8155, 1985; pp 3–20.
39. Kapadia, B. M.; Brown, R. M.; Murphy, W. J. The Influence of Nitrogen, Titanium and Zirconium on the Boron Hardenability Effect in Constructional Alloy Steel. *Trans. Metall. Soc. AIME* **1968,** *242,* 1689–1694.
40. Krauss, G. Hardness and Hardenability. In *Steels: Heat Treatment and Processing Principles;* ASM International: Materials Park, OH, 1990; pp 145–178. ISBN: 0-87170-370-X (chapter 6).
41. SAE J1268 Feb88 – *Hardenability Bands for Carbon and Alloy H Steels*; SAE International; 400 Commonwealth Drive, Warrendale, PA, 15096–0001, USA.
42. Fourier, J. B. J. *The Analytical Theory of Heat.* Translated by Alexander Freeman, 1878; Cambridge University Press: London, UK, 1822.
43. Carney, D. J.; Janulionis, A. D. Examination of the Quenching Constant H. *Trans. ASM* **1951,** *43,* 480–496.
44. Heindlhofer, K. Quenching: A Mathematical Study of Various Hypotheses on Rapid Cooling. *Phys. Rev.* **1922,** *XX* (3), 221–243.
45. Russell, T. F. *Some Mathematical Considerations of the Heating and Cooling of Steel.* Special Report No. 14; Iron and Steel Institute, 1936; pp 149–187.
46. Russell, T. F. *Some Theoretical Considerations of the Jominy Hardenability Test.* Special Report No. 36; Iron and Steel Institute, 1936; pp 25–33.
47. Russell, T. F. *Surface Temperature Measurements during the Cooling of a Jominy Test Piece.* Special Report No. 36; Iron and Steel Institute, 1936; pp 34–46.
48. Grossmann, M. A.; Asimow, M.; Urban, S. F. *The Hardenability of Alloy Steel;* American Society for Metals: Cleveland, OH, 1939; p 124.
49. Russell, T. F. *Section IX (Continued) – C. Some Mathematical Considerations on the Heating and Cooling of Steel.* Special Report No. 14; Iron and Steel Institute, 1936; pp 149–187.
50. Tensi, H. M.; Lišči&cacute, B. Determination of Quenching Power of Various Fluids. In *Quenching Theory and Technology,* 2nd ed.; CRC Press: Boca Raton, FL, 2010; pp 315–358. ISBN: 978-0-8493-9279-5 (chapter 11).
51. Grossmann, M. A.; Asimov, M.; Urban, S. F. Hardenability, Its Relation to Quenching and Some Quantitative Data. In *Hardenability of Alloy Steels;* American Society for Metals: Cleveland, OH, 1939; pp 124–190.
52. Aronov, M. A.; Kobasko, N. I.; Powell, J. A.; Hernandez-Morales, J. B. Correlation between Grossmann H-Factor and Generalized Biot Number BiV. In *5th WSEAS Int. Conf. on Heat and Mass Transfer (HMT'08),* Acapulco, Mexico, Jan 25–27, 2008, ISBN: 978-960-6766-31-2, pp 122–126.
53. Grossmann, M. A. The Nature of the Quenching Process. In *Elements of Hardenability;* American Society for Metals: Metals Park, OK, USA, 1952; pp 61–91 (chapter 3).
54. Monroe, R. W.; Bates, C. E. Evaluating Quenchants and Facilities for Hardening Steel. *J. Heat Treat.* **Dec 1983,** *3* (2), 83–89.
55. Dakins, M. E.; Bates, C. E.; Totten, G. E. Estimating Quench Severity with Cooling Curves. *Heat Treat.* **April 1992,** 24–26.
56. Jackson, C. R.; Christenson, A. L. The Effect of Quenching Temperature on the Results of the End-Quench Hardenability Test. *Trans. Am. Inst. Min. Metall. Eng.* **1944,** *158,* 125–137.
57. Aerospace Standard AS 1260. *Equivalent Sections of Certain Shapes to Round Bars;* SAE International: 400 Commonwealth Drive, Warrendale, PA 15096–0001 USA, 1972.
58. Grossmann, M. A.; Bain, E. C. Quantitative Hardenability. In *Principles of Heat Treatment,* 5th ed.; American Society for Metals: Metals Park, OH, 1964; pp 92–112
59. Jominy, W. E.; Boegehold, A. L. A Hardenability Test for Carburizing Steel. *Trans. Am. Soc. Metals* **1938,** *26,* 575–606.
60. ASTM A255-10 – *Standard Test Methods for Determining Hardenability of Steel*; ASTM International; 100 Barr Harbor Drive, West Conshohocken, PA 19428-2959 USA.
61. SAE J406. *Methods of Determining Hardenability of Steels;* SAE International: 400 Commonwealth Drive, Warrendale, PA 15096–0001 USA, 2009.
62. JIS G 0561. *Method of Hardenability Test for Steel (End Quenching Method);* Japanese Standards Association: 4-1-24 Akasaka Minato-ku, Tokyo, 107-8440, Japan, 2006.
63. DIN 50191 (1987–09) – *Hardenability Test by End-Quenching*; VDE Verlag; Bismark str. 33, 10625 Berlin, Germany.
64. ISO 642:1999 – *Steel – Hardenability Test by End Quenching (Jominy Test)*; International Organization for Standardization; 1, ch. de la Voie Creuse, CP 56, CH-1211, Geneva 20, Switzerland.
65. Morrow, J. Understanding the Jominy End-Quench Test. *Ind. Heat.* **Sept 2001,** *68* (9), 57–60.
66. Fong, H. S. Further Observations on the Jominy End-Quench Test. *J. Mater. Process. Technol.* **1993,** *38,* 221–226.
67. Weinman, E. W.; Thomson, R. F.; Boegehold, A. L. A Correlation of End-Quenched Test Bars and Rounds in Terms of Hardness and Cooling Characteristics. *Trans. ASM* **1952,** *44,* 803–844.
68. Gulden, H.; Krieger, K.; Lepper, D.; übben, A. L.; Rohloff, H.; Schüler, P.; Wieland, H.-J. Calculation of the Hardenability in the End-Quench Test of Case-Hardening ad Quenched and Tempered Steels. *Stahl und Eisen* **1991,** *111* (7), 103–110.
69. Vander Voort, G. F. Hardenability. In *Atlas of Time-Temperature Diagrams for Irons and Steels;* ASM International: Materials Park, OH, USA, 1991; pp 73–77. ISBN: 13-9780871704153.
70. Russell, T. F.; Williamson, J. G. *Section IV B. – Surface Temperature Measurements During the Cooling of a Jominy Test Piece.* Special Report No. 36; Iron and Steel Institute, 1946; pp 34–46.
71. SAE J1268. *Hardenability Bands for Carbon and Alloy H-Steels;* SAE International: 400 Commonwealth Drive, Warrendale, PA 15096–0001 USA, May 2010.
72. SAE J1868. *Restricted Hardenability Bands for Selected Alloy Steels;* SAE International: 400 Commonwealth Drive, Warrendale, PA 15096–0001 USA, Feb 2010.
73. Russell, T. F. *Section IVa – Some Theoretical Considerations of the Jominy Hardenability Tests.* Special Report No. 36; Iron and Steel Institute, 1946; pp 25–33.
74. Asimow, M.; Craig, W. F.; Grossmann, M. A. Correlation between Jominy Test and Round Bars. *SAE Trans.* **1941,** *41* (1), 283–292.
75. Crafts, W.; Lamont, J. L. Quenching. In *Hardenability and Steel Selection;* Pittman Publishing: New York, NY, 1949; pp 53–83 (chapter 4).
76. Lamont, J. L. How to Estimate Hardening Depth in Bars. *Iron Age* **Oct 14, 1943,** *152,* 64–70.
77. Rushman, W. F. How to Determine Quench Severity of Oil and Salt Baths. *Metal Prog.* **Dec 1963,** *84* (6), 91–92.
78. Boegehold, A. L. Hardenability Control for Alloy Steel Parts. *Metal Prog.* **May 1948,** *53,* 697–709.
79. Crafts, W.; Lamont, J. L. Hardenability Test Methods. In *Hardenability and Steel Selection;* Pittman Publishing: New York, NY, 1949; pp 111–127 (chapter 6).
80. Bucknall, E. H.; Steven, W. Hardening Response of Steels. In *Progress in Metal Physics I;* Chalmers, B., Ed.; Butterworths Scientific Publishers: London, UK, 1949; pp 235–280 (chapter 5).
81. Shepherd, B. F. Inherent Hardenability Characteristics of Tool Steels. *Trans. Am. Soc. Steel Treat.* **1930,** *17,* 90–110.
82. Post, C. B.; Greene, O. V.; Fenstermacher, W. H. Hardenability of Shallow-Hardenable Steels. *Trans. Am. Soc. Metals* **1942,** *30,* 1202–1254.
83. Greene, O. V.; Post, C. B. Hardenability of Shallow-Hardenable Steels. *Heat Treat. Forg.* **March 1941,** 120–121.
84. Greene, O. V.; Post, C. B. Determination of Specific Hardenability of Shallow-Hardening Steels. *SAE Trans.* **July 1941,** *49* (1), 278–283.
85. Boegehold, A. L. Use of Hardenability Tests for Selection and Specification of Automotive Steels. *SAE Trans.* **1941,** *36–49,* 266–276.
86. McCleary, F. E.; Wuerfel, R. Determining Hardenability on Small Sizes. *SAE Trans.* **1941,** *49,* 276–278.
87. Burns, J. L.; Moore, T. L.; Archer, R. S. Quantitative Hardenability. *Trans. ASM* **1938,** *26,* 1–36.

88. Liščić, B. Hardenability. Steel Heat Treatment Handbook. In *Steel Heat Treatment: Metallurgy and Technologies;* Totten, G. E., Ed., 2nd ed.; CRC Press Taylor & Francis Group: Boca Raton, FL, 2007; pp 213–276. ISBN: 978-0-8493-8455-4 (chapter 5).
89. Grossmann, M. A. *Principles of Heat Treatment;* ASM: Metals Park, OH, 1962; pp 120–121.
90. Shepperd, B. F. Hardenability of Shallow-Hardening Steels Determined by the P-V Test. *Trans. ASM* **1947,** *38,* 354–397.
91. Grossmann, M. A. Hardenability Tests. In *Elements of Hardenability;* American Society for Metals: Metals Park, OK, 1952; pp 1–42 (chapter 1).
92. McMullan, O. W. A Hardenability Test for Low-Carbon and Shallow-Hardening Steel. *Trans. ASM* **1945,** *35,* 584–608.
93. Chandler, H. *Heat Treaters Guide: Practices and Procedures for Irons and Steels,* 2nd ed.; ASM International: Materials Park, OH, 1995. ISBN: 978-0-87170-520-4, p 560.
94. DeVries, G. An End-Quenched Bar for Deep-Hardening Steels. *Trans. ASM* **1949,** *41,* 678–691.
95. Wilson, W. A Hardenability Test for Deep-Hardening Steels. *Trans. ASM* **1951,** *43,* 454–479.
96. Carman, C. M.; Armiento, D. F.; Markus, H. Hardenability Test for Deep Hardening Steel. *Metal Prog.* **May 1957,** *71,* 77–80.
97. Etienne, C. F.; Sheepens, C. P. A Hardenability Test for Deep-Hardening Steels. *Metal Prog.* **Dec 1965,** *88* (6), 77–81.
98. Jatczak, C. F. Assessment of Hardenability of Deep Hardening Steels. In *Hardenability Concepts with Application to Steel, Proceed. Symp.*, Oct 24–27, 1977, pp 334–347.
99. Post, C. B.; Fetzer, M. B.; Fenstermacher, W. H. Air Hardenability of Steels. *Trans. ASM* **1945,** *35,* 85–111.
100. Jatczak, C. F. Hardenability in High Carbon Steels. *Metall. Trans.* **Oct 1973,** *4,* 2267–2277.
101. Landek, D.; Liščić, B.; Filetin, T.; Lübben, T. End-Quench Hardenability Test for Gas-Quenched Steels. In *Conf. Proceed. New Challenges in Heat Treating and Surface Engineering – Conference in Honor of Božidar Liščić, June 9–12, 2009, Cavtat Croatia;* Croatian Society for Heat Treatment and Surface Engineering: Zagreb, Croatia, 2009; pp 103–108.
102. Landek, D.; Liščić, B.; Filetin, T.; Lübben, T.; Lisjak, D. Hardenability Testing and Simulation of Gas-Quenched Steel. *Mater. Manuf. Process.* **2009,** *24,* 868–872.
103. Landek, D.; Liščić, B.; Filetin, T.; Lübben, T. End-Quench Hardenability Test for Gas-Quenched Steels. *Strojarstvo* **2011,** *53* (1), 33–37.
104. Wise, J. P.; Krauss, G.; Matlock, D. K. Microstructure and Fatigue Resistance of Carburized Steels. In *Heat Treating – Proceedings of the 20th Conference*, Funatani, K., Totten, G. E., Eds.; ASM International: Materials Park, OH, October 9–12, 2000; Vol. 2, pp 1152–1161.
105. Anon. *Atlas: Hardenability of Carburized Steels;* Climax Molybdenum Company: New York, NY, 1960; p 136.
106. Hock, S.; Kellermann, I.; Kleff, J.; Mallener, H.; Wiedmann, D. Relevance of Hardenability for the Machining and Application of Case-Hardening Steels. *Drive System Technique* **2005,** *19* (1), 1–18.
107. Bruckner, W. H. *The Hardenability of Carburizing Steels.* Bulletin Series, No. 320, Vol. XXXVII, No. 13; University of Illinois, Engineering Experiment Station: Urbana, IL, USA, Nov 21, 1939; p 64.
108. Cristinacce, M. Heat Treatment of Metals: Distortion in Case Carburized Components – The Steel Maker's View. In *18th Heat Treating Society Conference Proceedings;* Walton, H., Wallis, R., Eds.; ASM International: Materials Park, OH, 1998; pp 5–11. ISBN: 0-87170-626-1.
109. Smith, Y. E.; Eldis, G. T. New Developments in Carburizing Steels. *Metals Eng. Q.* **1976,** *16* (2), 13–20.
110. Preston, S. Influence of Vanadium on the Hardenability of a Carburizing Steel. *J. Heat Treat.* **1990,** *8,* 93–99.
111. SAE J1975. *Case Hardenability of Carburized Steels;* SAE International: 400 Commonwealth Drive, Warrendale, PA 15096–0001 USA, 1997.
112. Doane, D. V. Carburized Steel – Update on a Mature Composite. *J. Heat Treat.* **1990,** *8* (1), 33–53.
113. Jatczak, C. F. Determining Hardenability from Composition. *Metal Prog.* **Sept 1971,** 60–69.
114. Lund, T.; Sabelström, U.; Johansson, G.; Leppänen, R.; Wulliman, C.; Ohlsson, P. *Technical Report 7/1986 – The Measurement, Prediction and Control of Jominy – Hardenability of Carburizing Steels.* Report by Ovako Steel AB, Box 5013, SE-194 05; Upplands, Väsby: Sweden, 1986. ISSN: 0282-9878.
115. Wretlind, J.; Sabelström, U.; Lund, T. *Technical Report 1/1989 – The Influence of Base Material Hardenability on the Case Depth after Case Hardening.* Report by Ovako Steel AB, Box 5013, SE-194 05; Upplands, Väsby: Sweden, 1989. ISSN: 0284-3366.
116. Tartaglia, J. M.; Eldis, G. T. Core Hardenability Calculations for Carburizing Steels. *Metall. Trans. A* **June 1984,** *15A,* 1173–1183.
117. Boyle, E.; Northwood, D. O.; Bowers, R.; Sun, X.; Bauerle, P. The Effects of Initial Microstructure and Heat Treatment on the Core Mechanical Properties of Carburized Automotive Steels. *Mater. Forum* **2008,** *32,* 44–54.
118. de Retana, A. F.; Doane, D. V. Predicting Hardenability of Carburizing Steels. *Metal Prog.* **Sept 1971,** *100,* 65–69.
119. SAE J423. *Methods of Measuring Case Depth;* SAE International: 400 Commonwealth Drive, Warrendale, PA, 15096–0001, USA, Dec 1983.
120. Walton, H. Case Hardenability at High Carbon Levels. *J. Mater. Eng. Perform.* **1995,** *4,* 106–110.
121. Kern, R. F. New Dimension in Selecting Carburized Steels. *Metal Prog.* **Oct 1972,** 127–128.
122. Eldis, G. T.; Smith, Y. E. Effect of Composition on Distance to First Bainite in Carburized Steels. *J. Heat Treat.* **1980,** *2* (1), 62–72.
123. www.aboutmetals.com, Dec 24, 2011.
124. Callister, W. D.; Rethwisch, D. G. *Fundamentals of Materials Science and Engineering, An Integrated Approach,* 3rd ed.; John Wiley: Hoboken, NJ, 2008.
125. Shackelford, J. F. *Introduction to Materials Science for Engineers,* 7th ed.; Pearson, Prentice Hall: Upper Saddle River, NJ, 2009.
126. Kalpakjian, S.; Schmid, S. *Manufacturing Engineering and Technology;* Prentice Hall: Upper Saddle River, NJ, 2009.
127. Ericsson, T. Principles of Heat Treating of Steels. In *ASM Handbook*; 2004, Vol. 4, pp 1–19.
128. Bruce, R. G.; Dalton, W.; Kibbe, R. *Modern Materials and Manufacturing Processes,* 3rd ed.; Pearson, 2004.
129. Tanaka, T. In *High Strength Low Alloy Steels;* Dunne, D. P., Chandra, T., Eds.; South Coast Printers: Port Kembla, Australia, 1985; p 7.
130. Krauss, G. *Steel, Heat Treatment and Processing Principles;* ASM International, 1990; p 94.
131. Buchmayr, B.; Kirkaldy, J. S. Modeling of the Temperature Field, Transformation Behavior Hardness, and Mechanical Response of Low Alloy Steels during cooling from the Austenite Region. *J. Heat Treat.* **1990,** *8,* 127–136.
132. Kirkaldy, J. S.; Feldman, S. E. Optimization of Steel Hardenability Control. *J. Heat Treat.* **1989,** *1,* 57–64.
133. Grossmann, M. A.; Bain, E. C. *Principles of Heat Treatment,* 5th ed.; American Society for Metals: Metals Park, Ohio, 1964.
134. Kirkaldy, J. S. Prediction of Alloy Hardenability from Thermodynamic and Kinetic Data. *Metall. Trans.* **1973,** *4,* 1973–2333.
135. Li, M. V.; Nieuhr, D.,V.; Meekisho, L. L.; Atteridge, D. G. A Computational Model for the Prediction of Steel Hardenability. *Metall. Mater. Trans. B* **1998,** *29B,* 627.
136. Malikizadi, A. Simulation of Cooling Behavior and Microstructure Development of Powder Metallurgy Steels. MSc Diploma, Department of Materials and Manufacturing, Chalmers University of Technology, Gothenburg, Sweden, 2010.
137. Just., E. New Formulas for Calculating Hardenability Curves. *Metal Prog.* **Nov 1969,** 87–88.
138. Siebert, C. A.; Doane, D. V.; Breen, D. H. *Recent Contributions to Hardenability Predictions, in the Hardenability of Steels – Concepts, Metallurgical Influences and Industrial Applications*; American Society for Metals.
139. Sanchez Sarmiento, G.; Morelli, M. A.; Vega, J. Improvements to the SAE J406 Hardenability Predictor. In *The 1st International Automotive Heat Treating Conference;* Colas, R., Funatani, K., Stickels, C. A., Eds.; ASM International: Materials Park, OH, 1998; pp 401–414.
140. SAE Iron and Steel Division. Methods of Determine Hardenability of Steels SAE Standard J406, *Hardenability of Carbon and alloy Steels;* Iron and Steel Technical Committee – Division 8, Last Rev. June 1993; pp 1.23–1.48.
141. Brooks, C. *Principles of Heat Treatment of Plain Carbon Steels and Low Alloy Steels;* ASM International, 1996, 06456G.
142. Dobranski, L. A.; Sitek, W. *Computer Simulation of Heat Treatable Steel;* International Conference on Heat Treatment and Surface Engineering (IFHTSE) of Tools and Dies: Pula Croatia, June 8–11, 2005.

143. Boyer, H. E.; Gray, A. G. *Atlas of Isothermal Transformation and Cooling Transformation Diagrams;* ASM International: Metals Park, OH, 1977.
144. Atkins, M. *Atlas of Continuous Cooling Transformation Diagrams for Engineering Steels;* ASM International: Metals Park, OH, 1980.
145. Diggs, T. G.; Rosenberg, S. J.; Geil, G. W. *Heat Treatment and Properties of Iron and Steel;* National Bureau of Standards Monograph 88, Nov 1, 1966.
146. Grossmann, M. A.; Asimow, M. Hardenability and Quenching. *Iron Age* **April 25, 1940,** *36,* 25–29.
147. Dorivaldo Batista Nogueira Junior, Universidade São Francisco, Internet: http://amigonerd.net/trabalho/2320-ensaio-jominy.
148. Callister, W. D.; Rethwisch, D. G. Applications and Processing of Metal Alloys. In *Fundamentals of Materials Science and Engineering, An Integrated Approach,* 3rd ed.; John Wiley & Sons Inc.: New York, NY, 2008; pp 358–413 (chapter 11).
149. Siebert, C. A.; Doane, D. V.; Breen, D. H. Utilization of Hardenability Concepts and Information. In *The Hardenability of Steels – Concepts, Metallurgical Influences and Industrial Applications;* American Society for Metals: Metals Park, OH, USA, 1977; pp 139–202.
150. Grossmann, M. A. *Principles of Heat Treatment;* American Society for Metals: Metals Park, OH, 1962; p 94.

This page intentionally left blank

12.04 Controlling the Cooling Process – Measurement, Analysis, and Quality Assurance

E Troell, H Kristoffersen, and J Bodin, Swerea IVF, Mölndal, Sweden
S Segerberg, Heattec Värmebehandling, Halmstad, Sweden

12.04.1	**Introduction**	99
12.04.1.1	Overview	99
12.04.1.2	Selecting Quenchants	99
12.04.1.3	Cooling Curves	102
12.04.2	**A Short Historical Overview of Test Methods**	103
12.04.3	**Standards for Testing Quenching Media**	104
12.04.4	**Procedure to Record Cooling Curves**	105
12.04.5	**Different Types of Test Probe**	109
12.04.6	**Cooling Curve Analysis**	110
12.04.6.1	Calculation of Heat Transfer Coefficient	112
12.04.6.2	Prediction of Hardening Results Using Calculated Heat Transfer Coefficients	113
12.04.7	**Influence of Process Parameters, Aging, and Contaminations on Cooling Characteristics for Oils and Polymers**	114
12.04.8	**Maintenance and Quality Assurance (Flame Point, Water Content, etc., ref to CQI-9)**	115
12.04.9	**Outlook**	119
References		120

12.04.1 Introduction

12.04.1.1 Overview

Quenching is the process to cool a heated steel workpiece from the austenite temperature region to obtain certain material properties. The thermal process entails heating the steel to hardening temperature (austenitizing), during which a variety of thermochemical treatments may be applied, followed by quenching in a suitable quenchant.

The cooling sequence has considerable influence on properties such as microstructure, hardness uniformity, residual stresses, and the strength of the hardened part as well as on the distortion caused by the hardening. Different quenchants provide different cooling sequences and the character of the quenchant and its cooling capacity may change over time. For this reason, it is essential to monitor and control the cooling process. Methods and procedures to evaluate and assess quenchants before and during use are therefore most important.

12.04.1.2 Selecting Quenchants

The quenching operation is one of the most critical, and usually the least controllable, part of the heat treatment process. Improper selection or application of a quenching medium, or a drift in its cooling characteristics during its lifetime will result in large, unexpected costs and delays due to the heat-treated components not meeting specifications. This will result in the need for, e.g., straightening the distorted workpiece, rework, or even face rejection of the product as well as delayed deliveries.

Selection of a proper quenchant for a particular case is determined mainly by the hardenability of the steel, the dimensions of the workpiece, and the desired properties. Quenching normally takes place in hardening oils, polymers, water, gas, or salt but other quenching media are also used, e.g., brine and fluidized beds. The quenchant can be applied by different methods, e.g., dipping the workpiece or load in a bath or applying the quenchant by spraying as for induction hardening.

Figure 1 shows an overview of the most common quenchants and their cooling capacities (*1,2*). The figure also indicates the normal application ranges as regards hardenability of the steel and the part dimension.

The most commonly used quenchants today are quenching oils, polymer quenchants, salt baths, and certain gases. Figure 2 shows cooling curves for different quenchants (see also Section 12.04.1.3). It should be emphasized that these are only examples of cooling characteristics for the different quenchants. Cooling curves for oils and polymers may vary in a great range depending on, e.g., type, temperature, concentration, and agitation. A higher pressure or use of helium instead of nitrogen during gas quenching will result in faster cooling.

The most common *quenching oils* are refined mineral oils, but there is extensive research and development (2012) to facilitate increased use of vegetable oils. Additives are used to improve functionality properties such as increased wetting capacity, increased cooling capacity, vapor film dissipation properties, and improved washing properties, as well as greater oxidation stability for increased service life. The application temperatures range from about 40 to 200 °C. The choice of oil depends on the intended use.

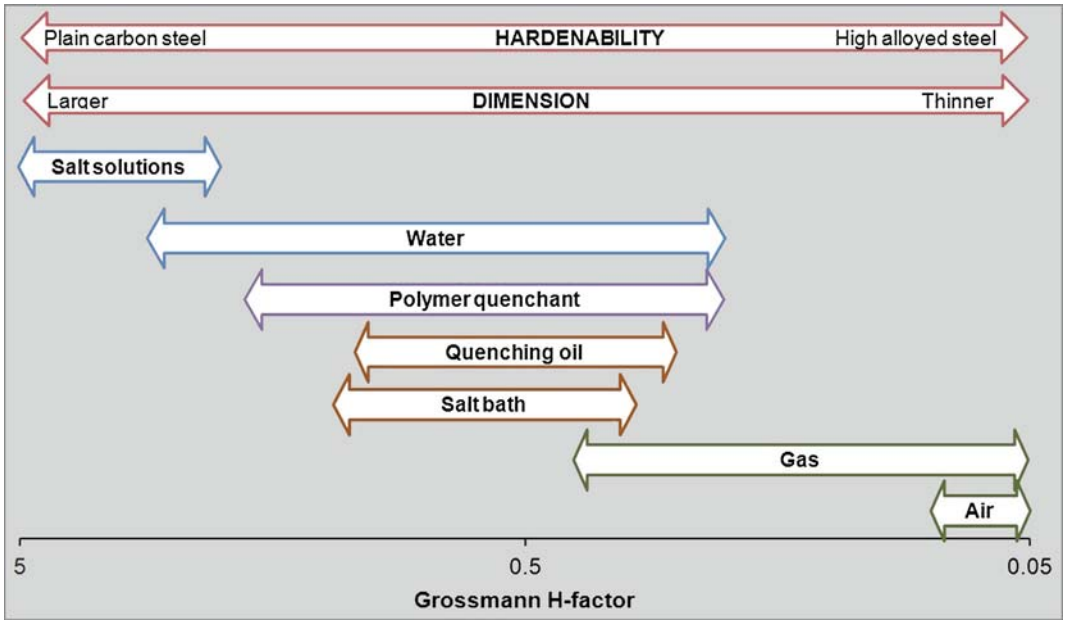

Figure 1 Cooling capacity, expressed as the Grossmann H-factor, for different quenchants. The Grossmann H-Factor is defined as the ratio of the heat transfer coefficient at the surface of the steel specimen divided by twice the heat conductivity of the steel. Reproduced from Holm, T.; Olsson, P.; Troell, E. *Steel and Its Heat Treatment*. ISBN: 978-91-86401-11-5, 2012, www.swereaivf.se; MacKenzie, S. *Houghton on Quenching*, 2010.

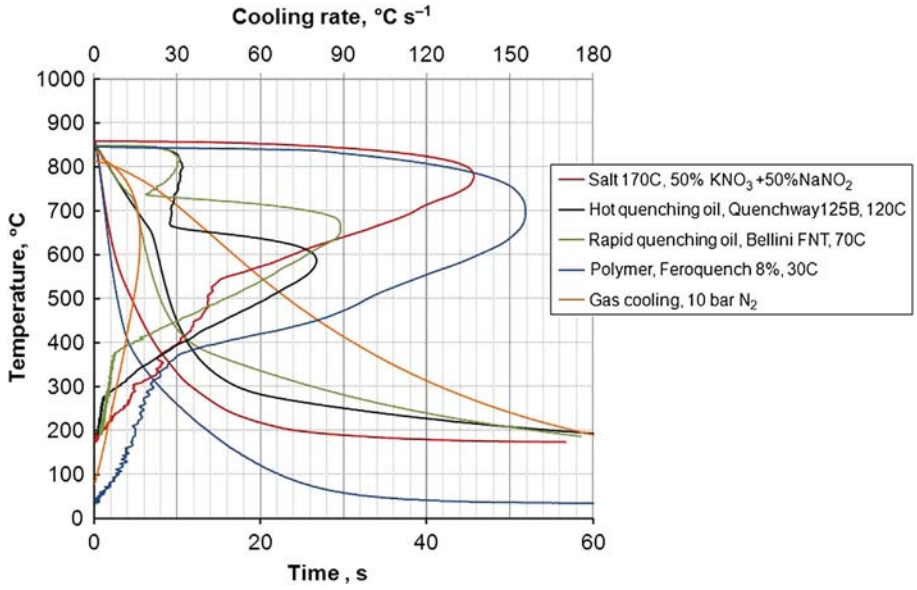

Figure 2 Cooling curves for different quenchants. The cooling curves have been recorded using a test probe in Inconel 600, ø12.5 × 60 mm, according to ISO 9950. Reproduced from Holm, T.; Olsson, P.; Troell, E. *Steel and Its Heat Treatment*. ISBN: 978-91-86401-11-5, 2012, www.swereaivf.se.

The terms 'Rapid quenching oils' (applied at about 60 °C), 'General quenching oils' (applied at about 60–130 °C), and 'Hot quenching oils' (applied at about 120–200 °C) are used.

The cooling rates of mineral quenching oils are generally highest at about 550–650 °C and are low at temperatures close to those at which martensite forms in low alloy steels which is beneficial regarding distortion. The cooling capacity of a quenching oil is affected by its temperature and the agitation rate. The higher the temperature, the lower the viscosity. The temperature affects the cooling sequence mainly at lower temperatures, but even the maximum cooling rate becomes somewhat lower when the oil is at a higher temperature. The greater the agitation, the faster is the cooling.

Polymer quenchants are water-based solutions and are used as quenchants for baths and sprays (mainly with induction hardening). The most common polymer quenchants are based on acrylates and glycols. Additives are used to reduce foam, inhibit

corrosion, and reduce bacteria growth. The application temperature is about 30–60 °C (or even 70 °C). Concentrations used are about 5–30% in baths and about 5–15% for spray in induction hardening.

The cooling capacity of polymers is generally between those of water and oil, but there are polymers with similar cooling characteristics as oil. The cooling capacity of polymer quenchants is affected by the type of polymer, the concentration, temperature, and degree of agitation. Polymers are much more sensitive to temperature variation than oils, which places high demands on the volume and shape of quenching baths. It also entails having careful control of the process to avoid undesirable variation, but, on the other hand, good cooling capacity control is possible.

The advantages of polymers over quenching oils are that no oil mist or soot forms and there is no risk of fire. They are also relatively easy to wash off. Polymers can be used to replace quench oils in open bath applications. However, they are not really suitable for use in protective atmosphere furnaces, where the quenching bath is integrated in the furnace, as the water vapor emitted would spoil the furnace atmosphere.

Salt bath quenchants are molten salts, normally comprising a combination of nitrite and nitrate salts, which melt at about 150–180 °C. Salt baths usually comprise equal amounts of sodium nitrite and potassium nitrate. The heat transfer takes place through convection. This, in combination with that the temperature of the salt causes a slow cooling rate in the martensite transformation region that results in a cooling sequence that facilitates minimal distortion. Quenching is normally applied at 180–200 °C, but temperatures up to 500 °C are also used. The cooling capacity is affected by added water, using special equipment (about 0.2–1.0% water), and temperature as well as the degree of agitation. Modern technology consists of closed systems in which salt is reused and no wastewater is released.

Gas quenching is used primarily in connection with hardening in vacuum furnaces, but it can also be used with the gas applied by nozzles or fans at a high flow rate and a relatively low pressure. The gases most commonly used today in connection with hardening are air and nitrogen. Also helium can be used but then gas recycling is necessary to minimize consumption and make the process cost effective. The cooling capacity depends on choice of the gas, its flow rate and pressure. In vacuum furnaces, gas quenching is normally applied using nitrogen at pressures up to 20 bars, but higher pressures are also used. Cooling capacity can be increased by quenching in a separate cold chamber instead of in the furnace. A major advantage of gas quenching is that the parts leave the process clean, eliminating the need for a subsequent washing operation.

During gas quenching, all heat transfer takes place through convection, which means that the heat transfer coefficient is relatively constant compared with oil- and water-based quenchings, where there can be extreme variation during the cooling sequence. With gas quenching at high pressure and high flow rate the average heat transfer coefficient can be as high as for quenching in oil. At lower temperatures, gas quenching is often faster than oil quenching, which can be negative as it is beneficial to quench slowly through the martensite transformation range. However, the cooling sequence during gas quenching can be adjusted by adjustment of gas pressure and flow rate.

A guiding principle is that a quenchant must have sufficient cooling capacity for the steel to achieve the desired hardness but must not quench so rapidly that quench cracks or undesirable distortion occur.

It is often necessary for practical and economical reasons to use the same quenchant for several types of parts. The cooling sequence then becomes a compromise between, e.g., achieving best possible fatigue strength and the result that can be achieved using the available quenchant.

By varying the quenching cycle, different properties, depending on microstructural changes, can be achieved. Variation of the quenching cycle for a quenchant can be effected by varying its temperature or degree of agitation. Some typical quenching cycles are direct hardening, martempering, and austempering, which are illustrated schematically in **Figure 3**.

To obtain the desired result of martensite from the surface to a specific depth, quenching must be rapid enough to transform austenite to martensite. An appreciation of the time available can be gained from CCT curves, as illustrated in **Figure 3**. The important thing is that quenching is rapid enough to ensure that the cooling curve for the austenitized volume goes past the pearlite/ferrite and bainite noses.

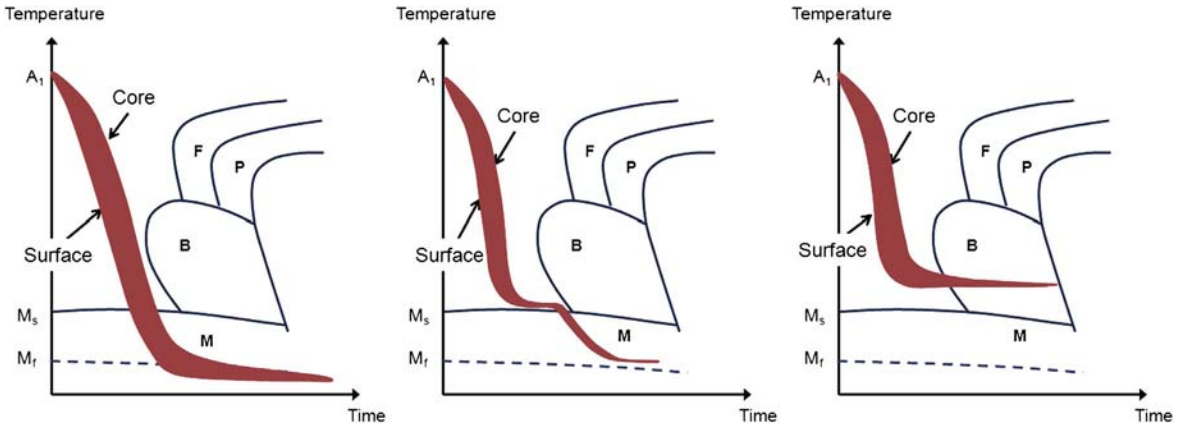

Figure 3 Quenching cycles. Left: direct hardening (conventional quenching), middle: martempering, right: austempering.

12.04.1.3 Cooling Curves

Cooling curves are used for illustration and evaluation of the quenching characteristics of a quenchant. A cooling curve is obtained using a thermocouple inserted in a workpiece or test probe. The part is heated and then quenched in the cooling medium. During the cooling, the temperature sequence is monitored by a data acquisition system. Both the temperature path and the cooling rate versus temperature are used for the evaluation. The cooling rate curve is the graph of the cooling rate in $^{\circ}C\,s^{-1}$, which is derived from the temperature-time sequence at each temperature/time measurement point. The two curves provide a 'fingerprint' for the quenchant.

Three stages of heat transfer (phases) appear when a piece of metal is quenched in the majority of liquids. The phases appear at different temperature ranges through three different mechanisms. The three stages and mechanisms are, see Figures 4 and 5:

- The *vapor film phase.* In this stage, the surface temperature is so high that the quenchant evaporates and a vapor film, more or less stable, is formed around the part. At this stage, the heat transfer is quite low as it mainly occurs by radiation. The main parameters that affect the duration of the vapor film phase are the surface condition, the geometry of the part, and the loading pattern of the charge.
- The *nucleate boiling phase.* When the temperature drops, there is not sufficient heat to maintain a stable vapor film. This allows the quenchant to come in contact with the hot surface and the quenchant starts to boil at the part, surface. This provides a high heat transfer rate. Boiling usually starts at corners and sharp edges.
- The *convection phase.* When the surface temperature has decreased below the quenchant's boiling point, boiling stops and the heat transfer continues by convection. At this stage, the heat transfer is low and is affected mainly by the viscosity and the agitation of the quenchant.

When quenching in salt and gas, only convection and radiation apply.

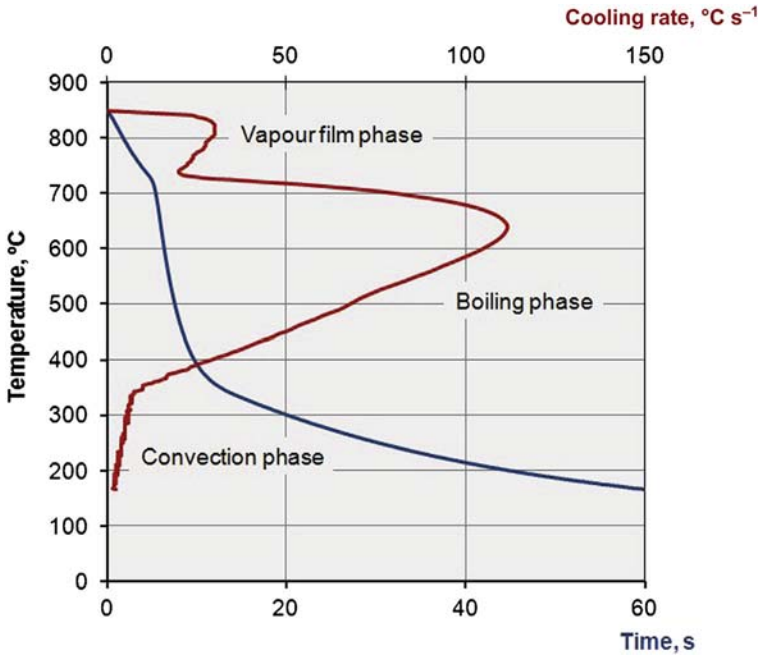

Figure 4 Cooling curve and cooling rate curve showing the three stages; vapor film phase, boiling phase, and convection phase.

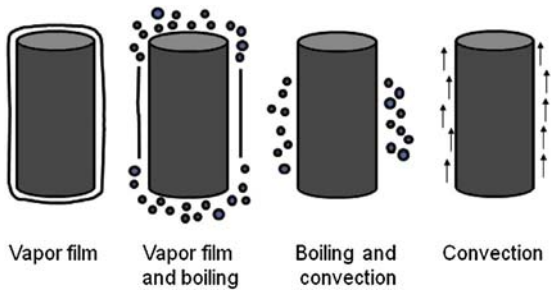

Figure 5 Schematic illustration of the cooling mechanisms in a stationary quenchant.

12.04.2 A Short Historical Overview of Test Methods

Before entering into details about methods of testing and evaluation of quenchants, it is essential to make a distinction between the two concepts: *cooling power* and *hardening power* of quenchants. According to Metals Handbook (3), the cooling power is the thermal response of the quenchant or the rate of the heat removal from a specimen, usually instrumented, while the hardening power is the metallurgical response of steel specimens or the ability of the quenchant to develop a specified hardness in a given material/section size combination (4).

Methods for evaluation of a quenchant's capability to extract heat can be divided into mechanical and thermal methods (5). Mechanical methods are usually based on hardening power and examination of hardness or microstructure on hardened parts or specimens, under standardized conditions. Thermal methods involve recording and evaluation of cooling curves and the cooling power. Terms to be evaluated can be, e.g., the cooling rate or the time to a certain temperature.

Grossmann et al. (6) introduced in the late 1930s the H value, the 'heat transfer equivalent' (also called the 'Grossmann's hardenability constant' or the 'quench severity factor') for the cooling power of quenching media. The H value is defined as:

$$H = h/2k$$

where

h = the mean value of the heat transfer coefficient throughout the entire quench process
k = the thermal conductivity of the material

The H value is a measure of the quenching agent's average cooling ability throughout the entire cooling process. The H value for stationary water at room temperature is 1.0 (cm^{-1}), while slower-cooling quenchants have values less than 1. The H value takes little or no consideration of the fact that both the heat transfer coefficient and the thermal conductivity vary with temperature. Therefore, a quenchant with a higher H value will not always produce a higher hardness when real steel workpieces are quenched.

The Grossmann method is used to determine the hardenability of steel. In the method a number of steel rods of different diameters are hardened in a quenchant with a known H value. By means of metallographic examination, the rod that has 50% martensite in the center is chosen. The diameter of this rod is called the *critical diameter*, D0. Based on the H value for the quenching agent the D0 value can be converted to the critical diameter, Di, which indicates that dimension which on cooling of the specimen surface at an infinitely rapid rate would produce 50% martensite in the center. The Di value obtained is thus a measure of the steel's hardenability, regardless of which quenching agent is used. In practice, the Di values are then used for determination of D0 values for different quenching agents.

Cooling curve testing is the most useful method for testing the cooling power of quenching media and quenching systems, as the complete cooling process is recorded. Cooling curves can be recorded using a test-piece (probe) with a thermocouple embedded at some point, usually at its geometric center or near the surface, and monitoring the cooling process with a data acquisition system. Cooling curves have been recorded and analyzed at least since the 1930s. The geometry of the probes has had many shapes, including cylinders, spheres, square bars, plates, rings, and coils (5).

One of the earliest methods was the 'Silver ball' method. In this, a heated silver ball instrumented with a thermocouple at its center was lowered into the quenchant (**Figure 6**,7).

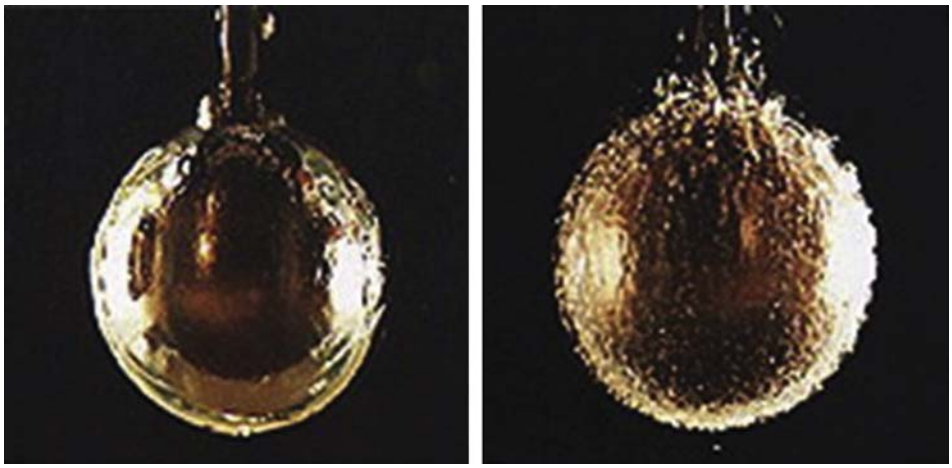

Figure 6 The 'Silver ball' test. Reproduced from *Quenchants for the Heat-treatment of Steel, Cast Iron and Aluminium Alloys*; Petrofer Chemie GmbH, 2012, www.petrofer.com.

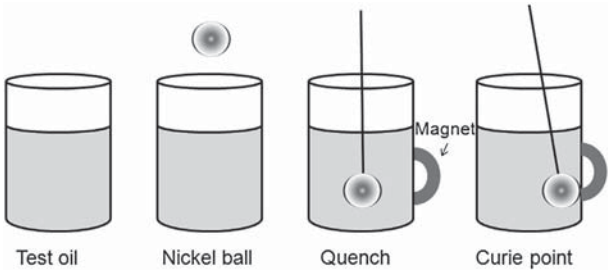

Figure 7 Principle of the 'Nickel ball' test.

Another of the older test methods is the Magnetic test, or the GM Quenchometer test, also known as the 'nickel ball test,' which is conducted according to ASTM D3520 (*8*). The method is of limited value today and the standard is now withdrawn. This method determines the time for cooling a chromized 22-mm-diameter nickel ball between two temperatures. The principle is illustrated in Figure 7. The ball is heated to 885 °C and quenched in a 200 ml beaker with the test fluid. The quenching time is recorded by a digital timer which is energized by a photoelectric cell from light produced by the ball at 885 °C and which is stopped when the ball becomes magnetic (at the Curie point, approximately 354 °C for pure nickel). At this point, the ball is attracted to a magnet to the side of the beaker, activating a sensor that stops the timer. By varying the nickel content of the ball, the Curie temperature can be altered, providing alternative finish temperatures for the cooling process. One limitation with the method is that it does not provide any information regarding the cooling pathway, which must be known if the quenchant's ability to harden steel is to be determined.

Another test system is the Houghton quench test (system Meinhardt). This method is a simplified version of the cooling curve test. A test-piece of carbon steel, normally with thermocouple wire, which together with the steel probe and support tube forms the thermocouple, is immersed in the quenchant. The time to cool within a certain temperature interval is determined with a built-in stopwatch. Thus, two points on the cooling curve can be determined in each test. The result is expressed as the time to cool between two fixed temperatures, normally from 700 to 400 °C (or 300 °C) (*4*).

In the 'Hot wire test,' a resistance wire is heated by means of an electric current in a sample of the quenchant. The current is increased steadily and the cooling power is indicated by the maximum steady current reading as measured by an ammeter (*4*).

In the 'Interval test,' also known as the 5-s test, a heated bar of metal (usually stainless steel) is immersed for 5 s in a sample of the quenchant which is contained in an insulated container. The increase in temperature is noted. The process is repeated for a series of bars. Finally, a bar of identical size and material is fully quenched in a new sample of quenchant of the same volume. The cooling power is expressed as the rate between the average rise in temperature for the 5-s quench bars and the rise for the fully quenched bar (*4*).

12.04.3 Standards for Testing Quenching Media

In order to avoid a drift in cooling capacity – e.g., due to thermal/oxidative degradation, contamination of the quenchant, and additive depletion in the quenchant – the entire cooling process should be checked on a regular basis. Advancement in awareness of the importance of the quenching process came with the introduction of new ISO and ASTM standards for testing cooling media (hardening oils and polymers) in the 1980s and 1990s.

The standard CQI-9 (*9*) applies to automotive industry suppliers' purchases of heat-treated material and to companies that heat treat parts for the automotive industry. It has been prepared by AIAG (The Automotive Industry Action Group). For a polymer quenchant, a quenchability check – e.g., cooling curve, viscosity, or titration – should be performed every 6 months according to CQI-9 (Special Process: Heat Treatment System Assessment). Concentration should be checked daily. Oil quench media should be checked quarterly regarding water content, suspended solids, viscosity, cooling curve, total acid, and flash point.

Analysis of cooling curves provides an excellent method to get a picture of the cooling characteristics of a quenchant. It is also a useful tool for quenchant selection as well as for comparing a used quenchant with a new one to identify any changes in the cooling characteristics.

It is relatively easy to record cooling curves experimentally by using a thermocouple, a test probe, and a data acquisition system. Systems for this can be constructed at home, but there are also commercial systems available for purchase. Regardless of whichever way the system is installed, it is important that the user understands how they operate and how to analyze the result.

The quenching characteristics can be determined by a number of methods. However, it is difficult to compare results received with different types of equipment. A number of standards have been developed to determine how the testing should be conducted. The procedure differs depending on quenchant to be tested, whether the quenchant is oil or

Table 1 Standards for determination of cooling curves

Type of quenchant to be analyzed	*Probe*	*Sample container*	*Reference fluid*
ISO 9950 Industrial Quenching Oils – Determination of cooling characteristics – Nickel-alloy probe test method			
ASTM D 6200 Determination of Cooling Characteristics of Quench Oils by Cooling Curve Analysis (*10*)			
Quench oils	Made of Inconel 600. Cylindrical, having a diameter of 12.5 mm and a length of 60 mm with a 1.5 mm sheathed Type K thermocouple, see **Figure 8**.	Shall be selected to provide 50 ml of fluid above and below the probe when quenched. It is recommended that 2000 ml of oil be used.	Mineral oil
ASTM D 6482 Standard Test Method for Determination of Cooling Characteristics of Aqueous Polymer Quenchants by Cooling Curve Analysis with Agitation (Tensi Method) (*11*)			
Aqueous polymer quenchants	According to ISO 9950 above	See **Figure 9** (*13*). The volume of the assembly is approximately 1500 ml. Quenchant agitation is provided by an impeller.	
ASTM D 6549 Standard Test Method for Determination of Cooling Characteristics of Quenchants by Cooling Curve Analysis with Agitation (Drayton Unit) (*12*)			
Aqueous polymer quenchants	According to ISO 9950 above	See **Figure 10**. A stainless steel beaker, 2000 ml, according to the container in ISO 9950, has been modified to provide upward or axial flow of the quenchant past the probe.	
JIS K 2242 Heat Treating oils (*14*)			
Quench oils	Silver rod having a diameter of 10 mm and length 30 mm. Thermocouple located at the surface (see **Figure 11**, left).	A 300 ml beaker and a fluid volume of 300 ml, specified in JIS R 3503.	Dioctylphthalate
JIS K 2242 – B method			
Water and polymer quenchants	Silver rod having a diameter of 10 mm and length 30 mm. Thermocouple located at the center (see **Figure 11**, right).	–	–
AFNOR NFT 60178 Cooling characteristics of hardening oils. Silver probe test method			
Quench oils	Silver cylinder, diameter 16 mm and length 48 mm. Thermocouple located at the center.	A volume of 800 ml	Mineral oil
Chinese standard ZB E 45003-88			
Quench oils	Silver cylinder, 99.96% pure. Diameter 10 mm and length 30 mm	300 ml beaker and oil volume 250 ml	Dioctylphthalate

polymer, and they are not the same for all countries. The main difference between the standards for different countries is the probe, both probe material and dimension and the design of the container for the quenchant. The most common probe material is austenitic nickel–chromium-based superalloys, but silver is also used. They are suitable for this application because they have no phase transformations during cooling that would affect the temperature curve, and are slow to oxidize.

Oils are tested without agitation (forced convection). The reason for this is to secure a stable and repeatable test procedure. However, it means that the results are not directly comparable with the conditions of a commercial quench bath, in which agitation is always applied.

Polymer quenchants are not capable of being evaluated reproducibly without agitation, so in this case, containers with agitation are used.

Some different standards and their characteristics are summarized in **Table 1**.

12.04.4 Procedure to Record Cooling Curves

As mentioned above, the cooling capacity of quenching oils and polymers can be characterized by deriving cooling curves according to a certain standard. As also mentioned, the cooling curve is obtained using a probe with an inserted thermocouple that is heated and lowed into a sample of the quenchant being tested. The temperature versus time is recorded by a data acquisition system. From the temperature versus time data, the cooling rate is determined by derivation. **Figure 12** shows an overview of a system for recording and analyzing cooling curves. An example of a commercial system for this is shown in **Figure 13**.

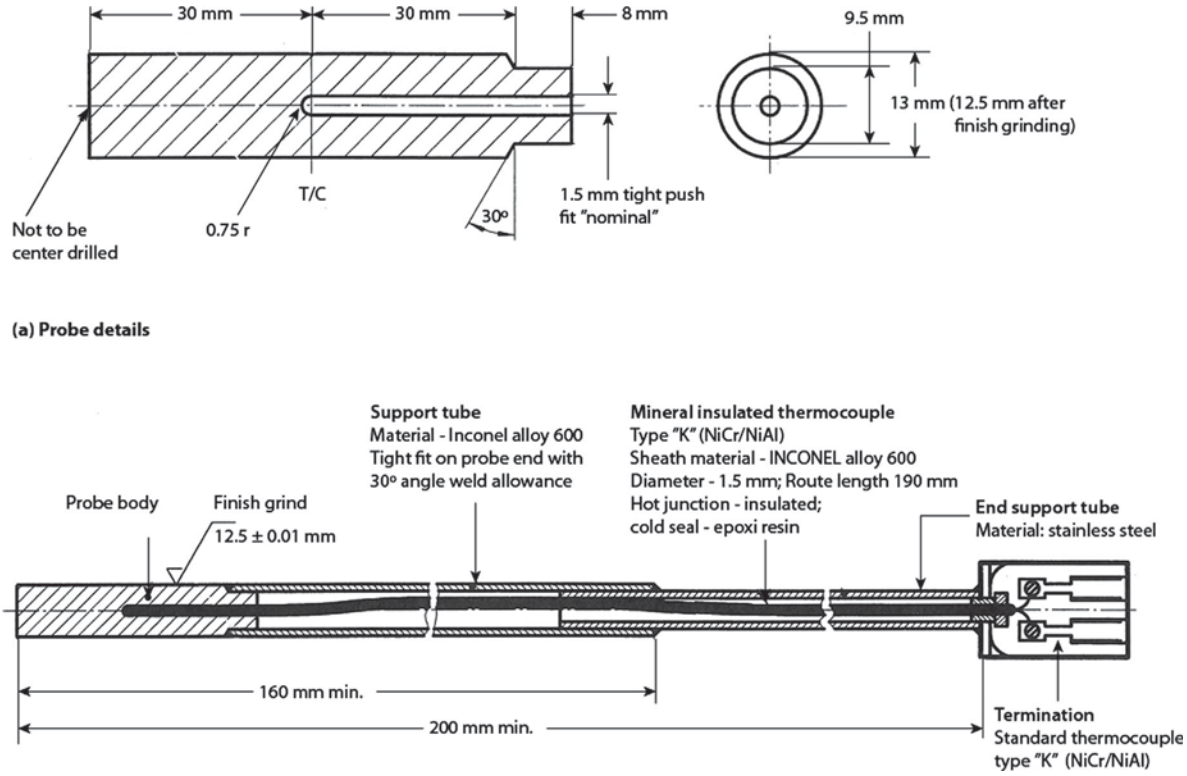

Figure 8 Test probe used in the standards ISO 9950, ASTM D 6200, ASTM D 6482, and ASTM D 6549. Reproduced from ASTM D 6549-06 Standard Test Method for Determination of Cooling Characteristics of Quenchants by Cooling Curve Analysis with Agitation (Drayton Unit), 2006.

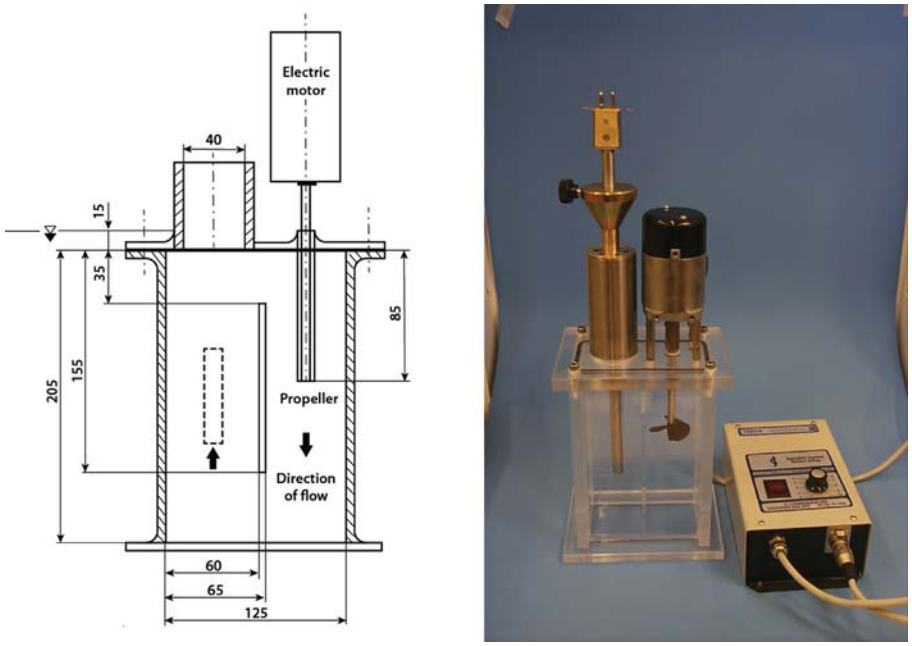

Figure 9 Tensi agitation assembly used in ASTM D 6482. Left: schematic (reproduced from ASTM D 6200-01 Standard Test Method for Determination of Cooling Characteristics of Quench Oils by Cooling Curve Analysis, 2012), right: container made of PVC (reproduced from Web page IVF SmartQuench, www.ivfsmartquench.com, Nov 2012).

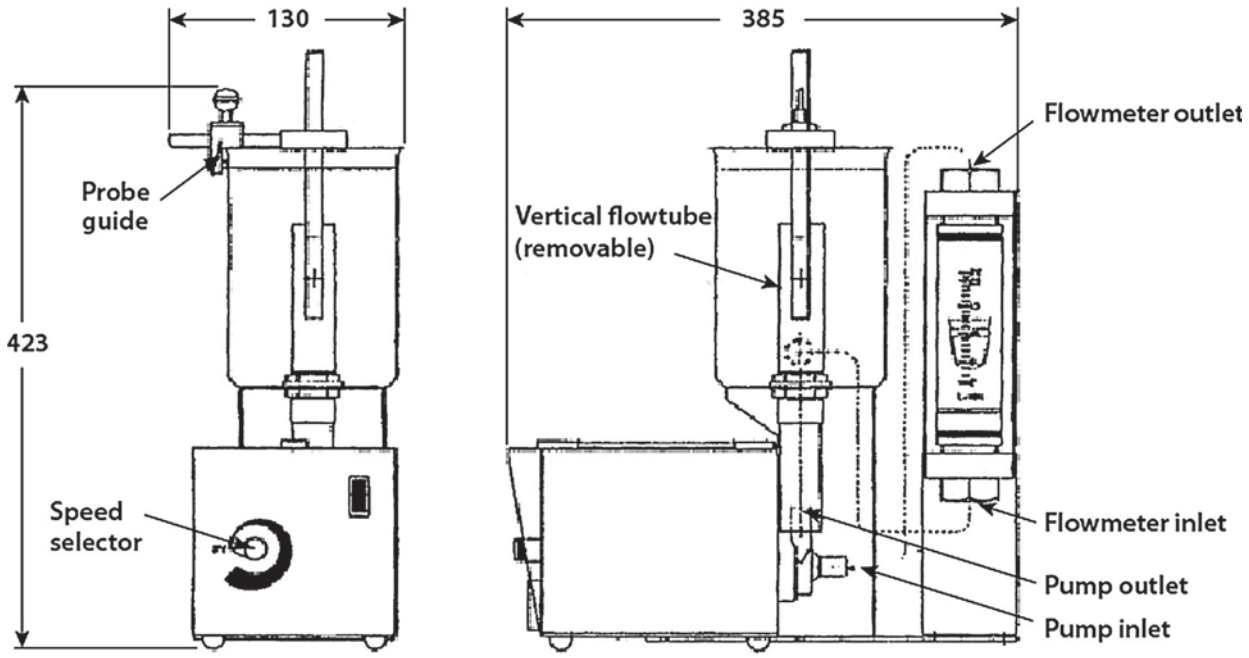

Figure 10 Drayton agitation unit. Reproduced from ASTM D6482-06 Standard Test Method for Determination of Cooling Characteristics of Aqueous Polymer Quenchants by Cooling Curve Analysis with Agitation (Tensi Method), 2006.

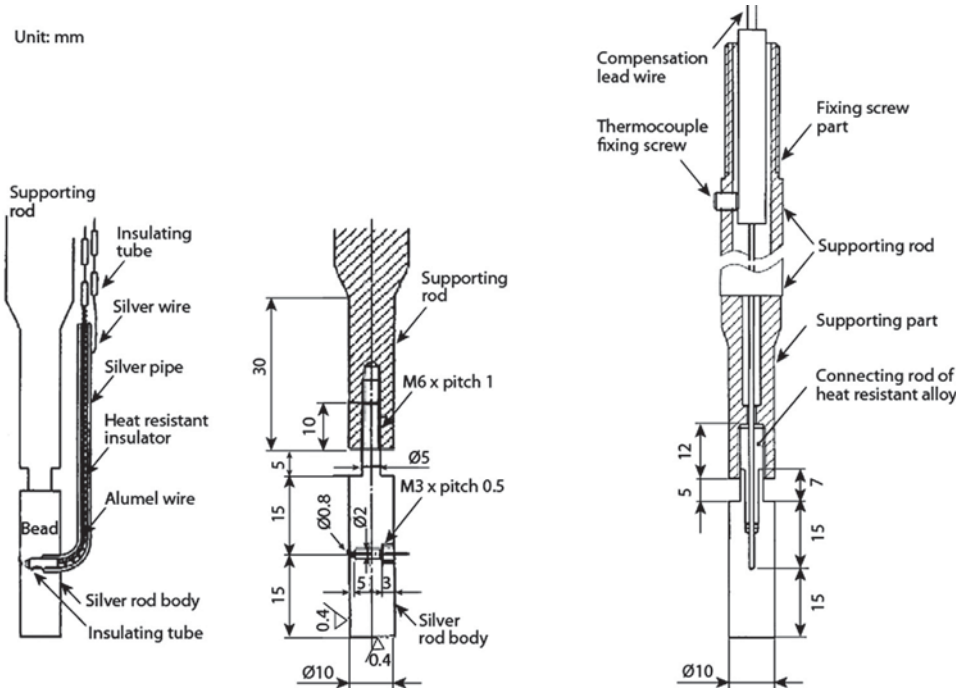

Figure 11 Silver rod probes used in JIS K 2242. Left: surface temperature measuring method, right: center temperature measuring method. Reproduced from JIS K 2242:2006 (E) JMFA/JSA *Heat Treating Oils*; Translated and Published by Japanese Standards Association, 2006.

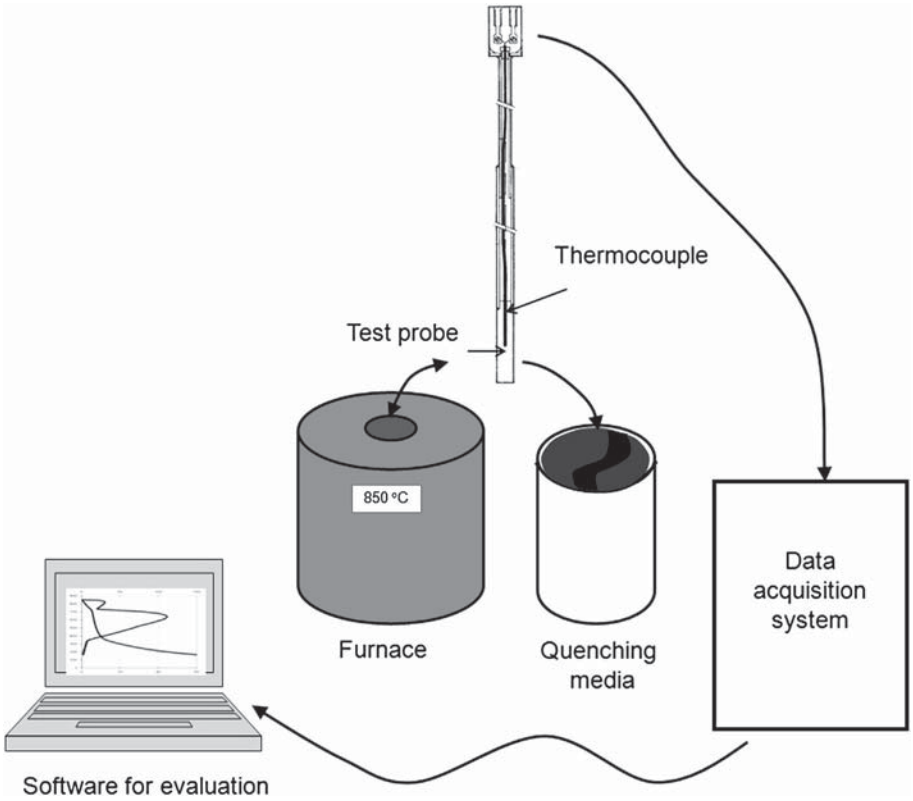

Figure 12 Overview of system for recording and analyzing cooling curves including furnace, test probe with thermocouple, data acquisition system, and computer with software for evaluation of the cooling curves.

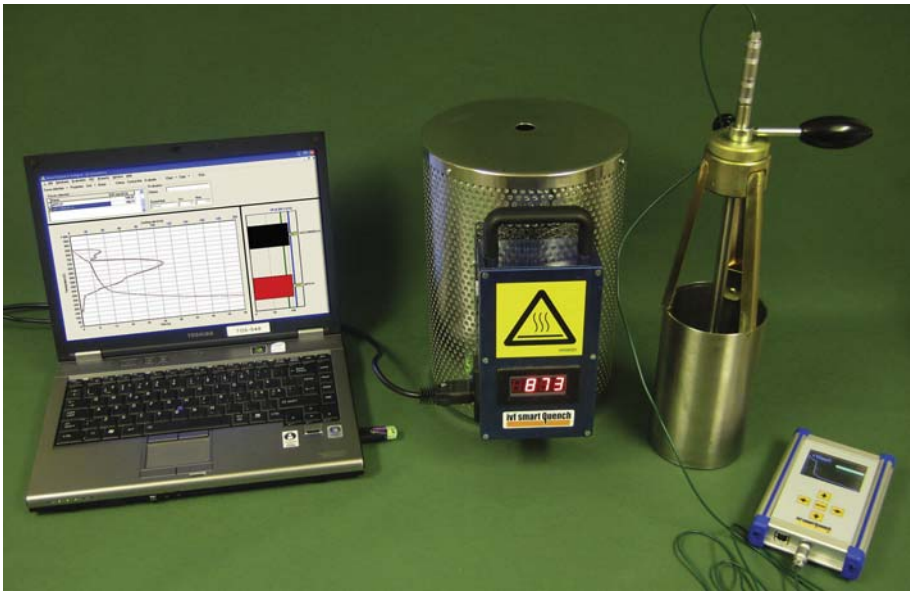

Figure 13 Equipment for standardized testing of quenchants (ivf SmartQuench). Reproduced from ivf SmartQuench, Users' Manual., Swerea IVF AB, 2009.

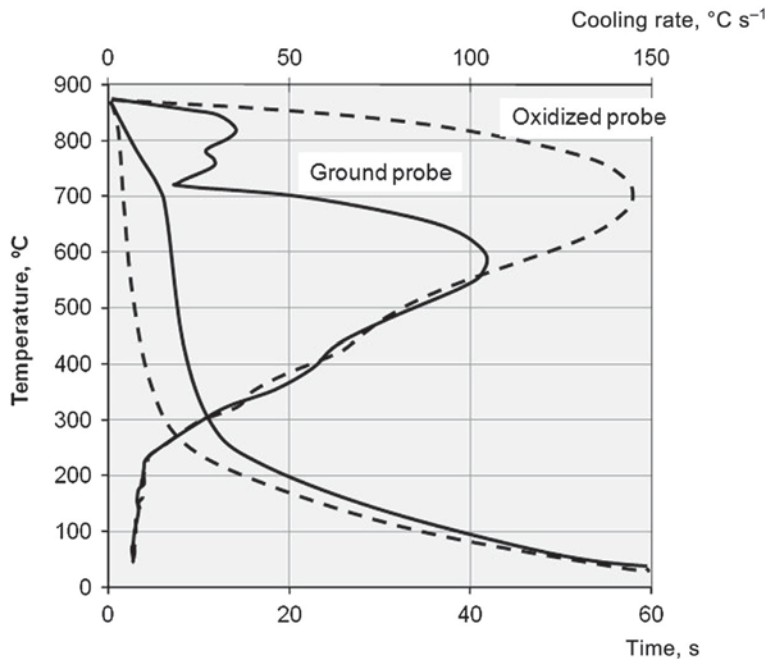

Figure 14 Cooling curves recorded with ground as well as oxidized probes.

The procedure to record and analyze a cooling curve includes the following:

- Preparing the test probe by grinding and/or conditioning,
- Heating the probe in the furnace,
- Quenching the probe in the sample container (or quench tank, see below), and
- Analyzing the cooling curve.

The condition of the probe before testing is of vital importance in order to receive a reliable and repeatable cooling curve. Oxide or residues on the probe surface may influence the test result to a considerable extent. Probe preparation prior to testing is critical to facilitate a repeatable test procedure. It is important to have a stable condition of the probe surface before each test. Figure 14 shows how the cooling curve is influenced if oxide is present on the test probe. In this case, no vapor film appears. Probe preparation can either be done by cleaning the probe surface with emery paper before each test or by conditioning the probe by making a number of dummy quenchings (at least six according to the ISO and ASTM standards) in oil resulting in a thin but stable oxide layer. If conditioning is used, make sure that the probe surface is free from residual traces of the quenchant and that its oxide coating is uniform and free from loose scale.

The sample container (beaker) must be clean and dry. Make sure that the test sample is representative of the fluid to be tested. The sample is poured into the beaker and brought up to the test temperature. During heating, the fluid should be agitated. The stirrer is removed prior to start of test. For testing with no agitation, enough time is needed for the fluid to get still.

Before transport of the probe for quenching in the beaker, the measurement system should be connected and started.

When the probe has reached the heating temperature, about 850 °C, the measurement should be started. The probe is moved from the furnace and immersed into the quenchant to be tested. This must be done as a fast, and repeatable, movement without letting the probe cool down more than absolutely necessary. During the transfer, which takes about 2 s, the temperature drops about 5 °C, so some excess temperature may be needed. According to ISO 9950, the movement should be done not in more than 2 s, preferably with an automated mechanism.

To ensure a consistent test result, the test may be repeated once or twice.

12.04.5 Different Types of Test Probe

A number of different test probe designs exist; some of them are standardized as noted in Section 12.04.3 and some probes are manufactured for certain purposes. The test probe design and the position of the thermocouple influence greatly the recorded cooling curve. Choice of test probe and thermocouple position depend on the purpose of recording a cooling curve. In order to control and monitor the quality of a quenching medium, use of standardized probes are recommended. The advantages of these

are that the probe material, dimensions, and location of thermocouple is defined securing a consistent measurement from time to time.

In order to record cooling curves for a specific component, e.g., a shaft or a gear, other probes could be more useful, such as other dimensions or geometries. Regarding the choice of material, it is an advantage to avoid heat generated from phase transformations; this means that hardenable steels should be avoided. More component-like probes or test pieces could be beneficial for, the e.g., determination of heat transfer coefficients around the component.

To illustrate the influence of probe material, dimension, and placement of thermocouple, Figure 15 shows cooling curves for three different probes that have been quenched in the same hot quenching oil at 120 °C.

12.04.6 Cooling Curve Analysis

By analyzing the cooling curve, it is possible to get an impression of the cooling capacity of the quenching medium, the tendency for vapor film appearance and the cooling rate at lower temperatures, during the formation of martensite. The cooling curve gives an immediate picture of the characteristics of the quenchant and makes it easy to compare the quenchant in use with a newly mixed quenchant to identify possible changes in cooling capacity.

Depending on system or procedure used for recording the cooling curve, different analyses are possible. A large number of characteristics can be recorded or calculated, such as maximum cooling rate, temperature at which the maximum cooling rate occurs, cooling rate at 300 °C and cooling times to certain temperatures (e.g., 600, 400, and 200 °C). Some characteristics used for the evaluation of quench oils and polymers are shown in Figure 16.

In this context, the features available in the commercial *ivf SmartQuench* system are used as an example. The software for this system contains functions for evaluation and analysis that makes it possible to interpret cooling curves from several different viewpoints (*15*).

The cooling curves recorded and calculated cooling rate curves are presented in diagrams. All parameters, e.g., the maximum cooling rate, the cooling time to a certain temperature, or the cooling rate at a certain temperature, can be shown in bar charts, see Figure 17. By choosing the critical parameters in combination with, e.g., statistical process control (SPC), it is possible to implement a proactive preventive maintenance of the quenchant and the system.

The cooling sequence in interaction with the hardenability of the steel and the part dimension determines the microstructure and residual stress conditions after hardening. During quenching of a component, different parts of the component will experience different temperature sequences. The effect on the microstructure can be illustrated through a CCT diagram, see Figure 18. In this case, the surface will be martensitic and the core will contain bainite and martensite.

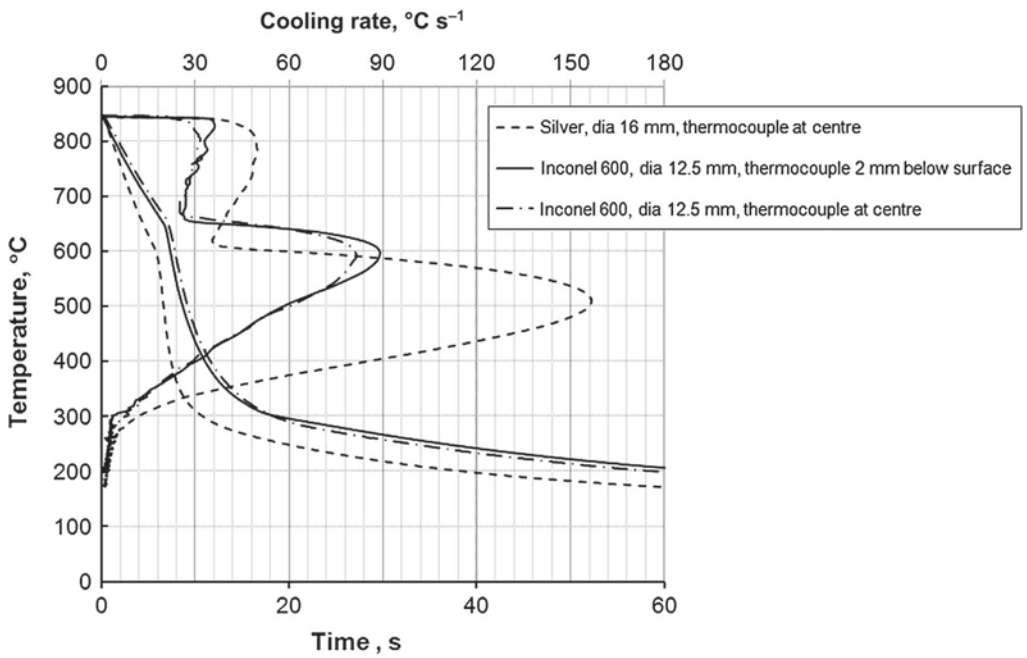

Figure 15 Influence of probe dimension, material, and placement of thermocouple on the cooling curve. All cooling curves are recorded with the oil Quenchway 125B at 120 °C, no agitation.

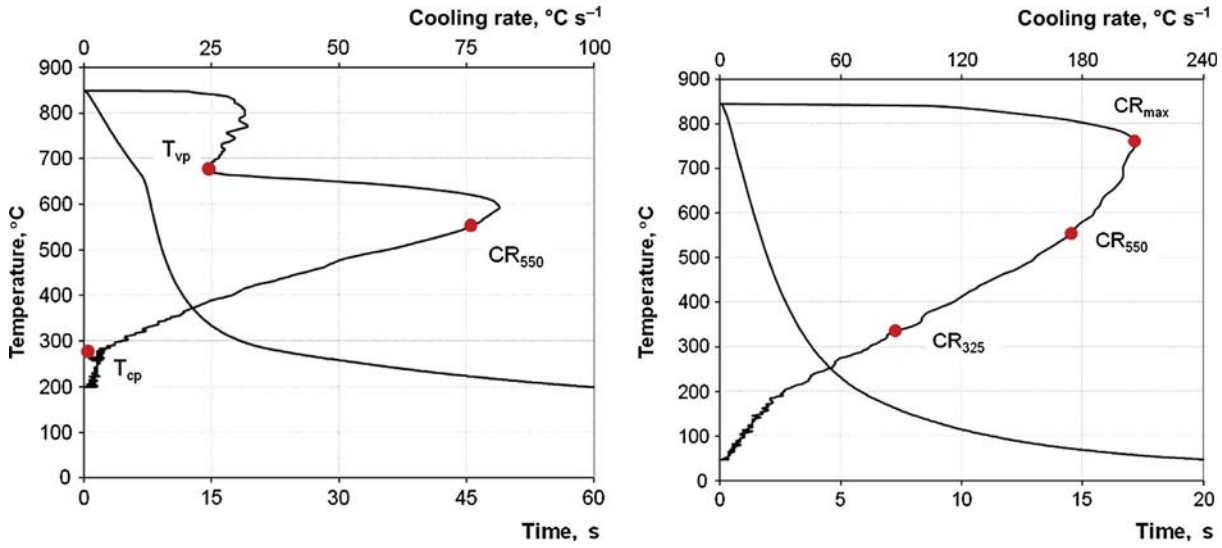

Figure 16 Cooling sequence for left: an oil and right: a polymer with some characteristic features that are used for evaluation of the cooling characteristics.

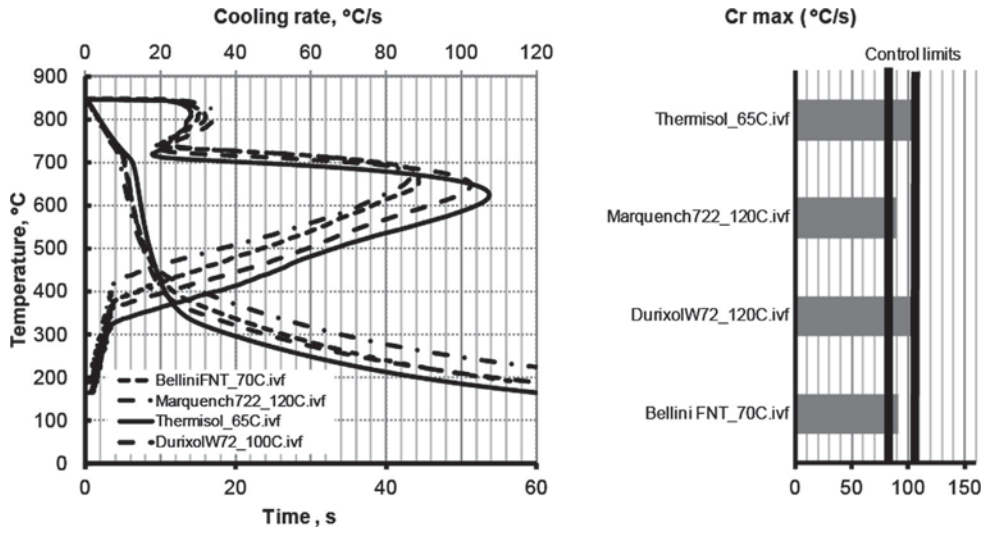

Figure 17 Evaluation diagram (right) showing the cooling rate and the minimum and maximum levels chosen for the selected characteristic. Reproduced from ivf SmartQuench, Users' Manual., Swerea IVF AB, 2009.

It is difficult to define an ideal cooling sequence. It depends on the steel grade, the part geometry, the charge pattern, the quenching equipment, etc. The cooling must be fast enough for the steel to achieve the desired hardness and microstructure but not faster than necessary in order to avoid quench cracks or excessive distortion.

Some important characteristics when analyzing a cooling curve are (see also **Figure 16**):

- The length of the vapor phase, e.g., T_{vp}. Presence of a vapor film may cause uneven cooling around the component, which may cause distortion.
- Maximum cooling rate and cooling rate at 550 °C (to avoid formation of ferrite/pearlite).
- Cooling rate at the range for martensite formation start. In this range, the cooling rate should be low in order to minimize distortion and the risk for quench cracking.

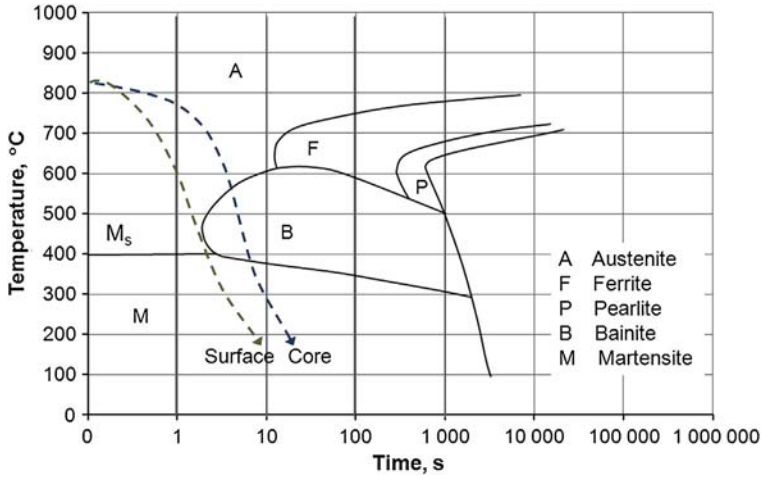

Figure 18 Cooling sequences for the core and the surface of a quenched part. Reproduced from Holm, T.; Olsson, P.; Troell, E. *Steel and Its Heat Treatment*. ISBN: 978-91-86401-11-5, 2012, www.swereaivf.se.

12.04.6.1 Calculation of Heat Transfer Coefficient

During quenching, heat transfer can occur through radiation, convection, and conduction. Heat transfer around a quenched part normally occurs through several means simultaneously. The heat transfer coefficient is a measure of the quenchant's capacity to transfer heat from the surface of the quenched component. The dimension is $W/(m^2 \cdot °C)$.

The heat transfer coefficient is governed by the physical properties of the quenchant, its pressure (in gas quenching), its flow rate and the local flow pattern as well as the geometry and size of the part. It is possible to predict the heat transfer coefficient by simulation in simple fluid flow situations, e.g., a cylinder where the cooling gas is flowing in axial direction. It is more difficult for parts with more complicated geometry that are cooled in liquid quenching media. This is due to the fact that the heat transfer is strongly dependent on the three different stages during cooling described above, i.e., the vapor, boiling, and convection phases, which all are highly surface-temperature dependent. This means that all three stages may exist simultaneously at different places on the part's surface during quenching and that the estimation of heat transfer coefficients can be very complex.

A practical way of determining the heat transfer coefficient of a quenchant is to record a cooling curve, valid for a test piece that was quenched using the quenchant in question, from which the variation in the heat transfer coefficient during the cooling sequence can be calculated, see **Figure 19**. For determining the heat transfer coefficient, austenitic nickel–chromium-based superalloys or stainless steels are common materials for recording the cooling curve. Silver may also be used. This is because they show no phase transformation, that would otherwise affect the cooling curve due to phase transformation heat, and because they are slow to oxidize.

For the calculation process, it is necessary to know, among other things, the temperature-dependent material data for the test probe, such as specific heat and conductivity, as well as the temperature of the quenchant. The mathematical part of the problem must be solved using an inverse method, which means that the 'answer' is known but an iterative mathematical procedure must be

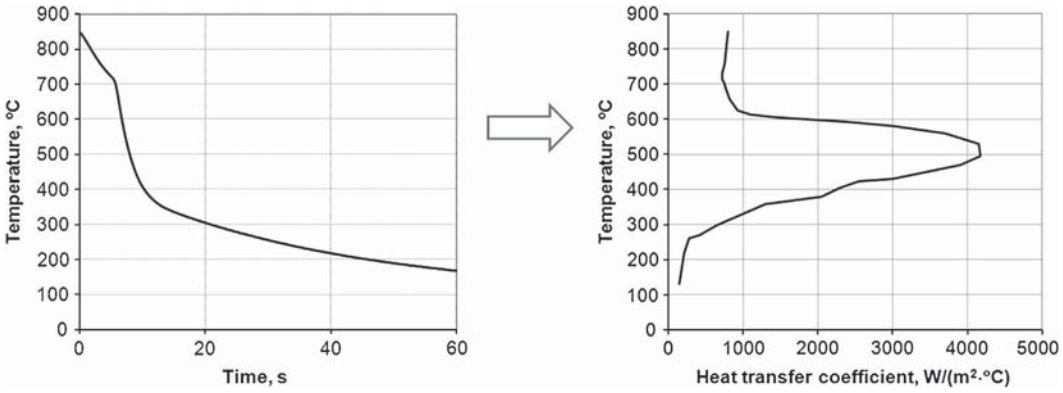

Figure 19 Heat transfer coefficient at the surface (right) calculated from a cooling curve (left) for a rapid quenching oil. Test probe in Inconel 600, ø12.5 × 60 mm, with thermocouple placed in the center (according to ISO 9950).

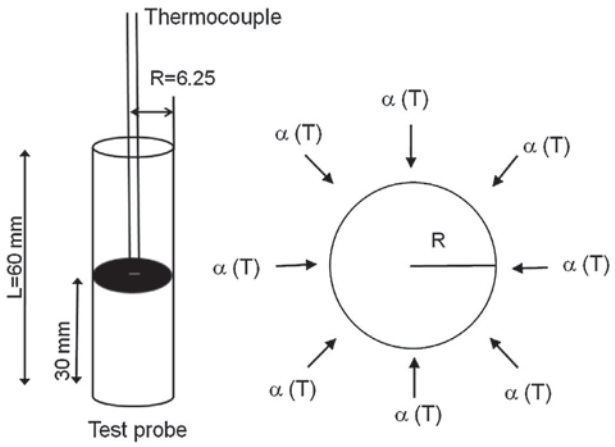

Figure 20 The heat transfer coefficient can be calculated by recording a cooling curve and calculating the heat transfer coefficient around the periphery of the test piece. Test piece according to ISO 9950 (Inconel test piece with dimensions ø12.5 × 60 mm). Reproduced from Felde, I. Determination of Thermal Boundary Conditions during Immersion Quenching by Optimization Algorithms. *Mater. Perform. Charact.* **2012**, *1* (1), 1–11, http://dx.doi.org/10.1520/MPC104417. ISSN: 2165-3992.

employed (several calculations made until the unknown factor is found) until the boundary conditions are determined, which, in this case, is the heat transfer coefficient, see Figure 20 (*16*).

12.04.6.2 Prediction of Hardening Results Using Calculated Heat Transfer Coefficients

If the heat transfer coefficient is known, microstructure and hardness can be calculated. By using different calculation programs, it is possible to predict parts of or entire hardening processes, applying basic calculations such as temperature change sequences in just one dimension (1D) through to total predictions of distortion, and residual stresses for a part with complex geometry in three dimensions (3D).

Here, this is illustrated using the commercial software SQIntegra (*13*), in which calculation of microstructure and hardness of cylindrical samples can be performed in 1D. These, in this context rather simple calculations, make it possible to get an impression of the quenchant's hardening power. It should be noted that the quality of the calculations are strongly dependent on the quality of input data used such as material data, temperatures of the quenchant, and the calculated heat transfer coefficient. Necessary material data are temperatures for A_1, M_S, B_S, and A_3 in the CCT diagram, as well as the data for isothermal transformation and ISO hardness values. Figure 21 shows the results of such calculations for C45E grade steel, in three diameters, after quenching in a rapid quenching oil at 70 °C.

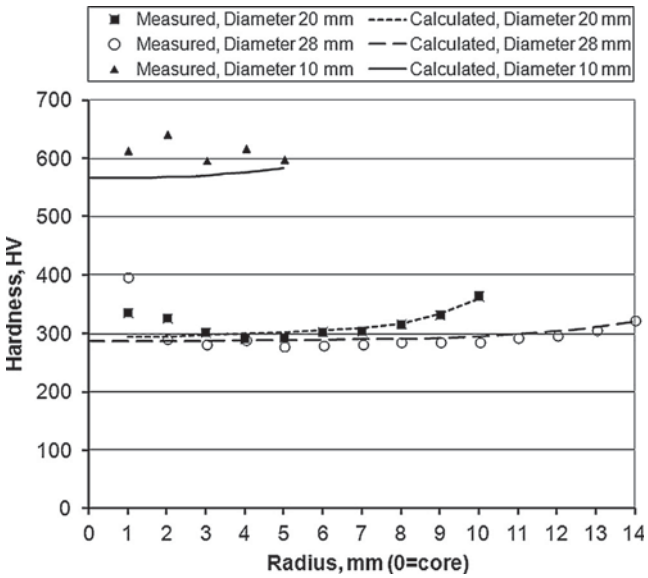

Figure 21 Measured and calculated hardness for steel C45E, diameter 10, 20, and 28 mm, quenched in a rapid quenching oil at 70 °C. Reproduced from Holm, T.; Olsson, P.; Troell, E. *Steel and Its Heat Treatment.* ISBN: 978-91-86401-11-5, 2012, www.swereaivf.se.

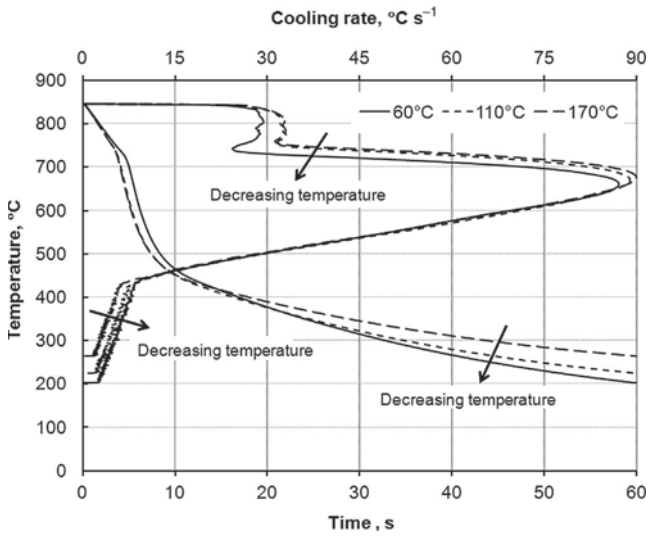

Figure 22 Influence of oil temperature on the cooling curve for a quenching oil, Thermisol QH120.

12.04.7 Influence of Process Parameters, Aging, and Contaminations on Cooling Characteristics for Oils and Polymers

This section addresses how process parameters such as agitation and temperature influences on the cooling characteristics for quenching oils and polymers. In the latter case, concentration is also dealt with. The cooling performance of quenchants are also affected by contaminants as well as change in cooling characteristics due to degradation and changes in chemistry of the quenchant during use, which is also covered. Corresponding changes may also occur for other quenchants such as salts and brine, but these are not addressed in this chapter.

The cooling capacity of a quenching oil is affected by its temperature and the agitation rate. The temperature affects the viscosity – the higher the temperature, the lower the viscosity. Above all, the temperature affects the cooling sequence at lower temperatures, but also at the beginning of the cooling sequence, see Figure 22. Figure 23 shows the influence of agitation on the cooling capacity. The greater the agitation, the faster is the cooling.

The cooling performance of quenching oils is affected by contaminants such as water, hydraulic fluids, sludge, additive loss, and oil degradation. Figure 24 shows cooling curves for a hot quenching oil, used at two different sites, in new and used condition. The reason for the change in cooling characteristics has not been evaluated, but in the case shown on the left, it could be due to the presence of water.

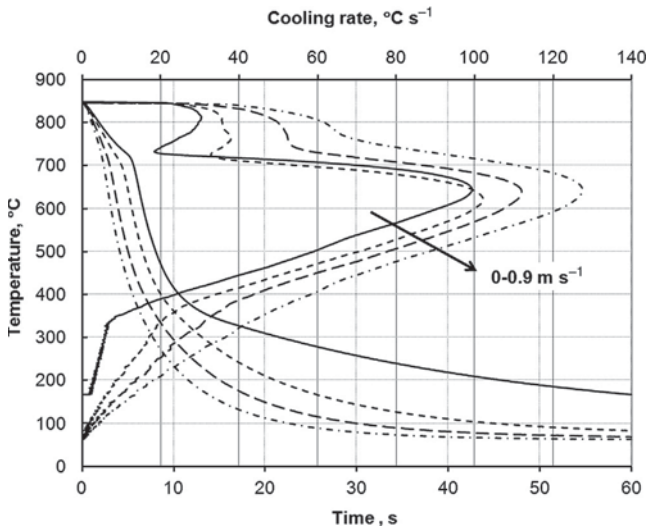

Figure 23 Influence of agitation on the cooling curve for a quenching oil, Bellini FN at 70 °C.

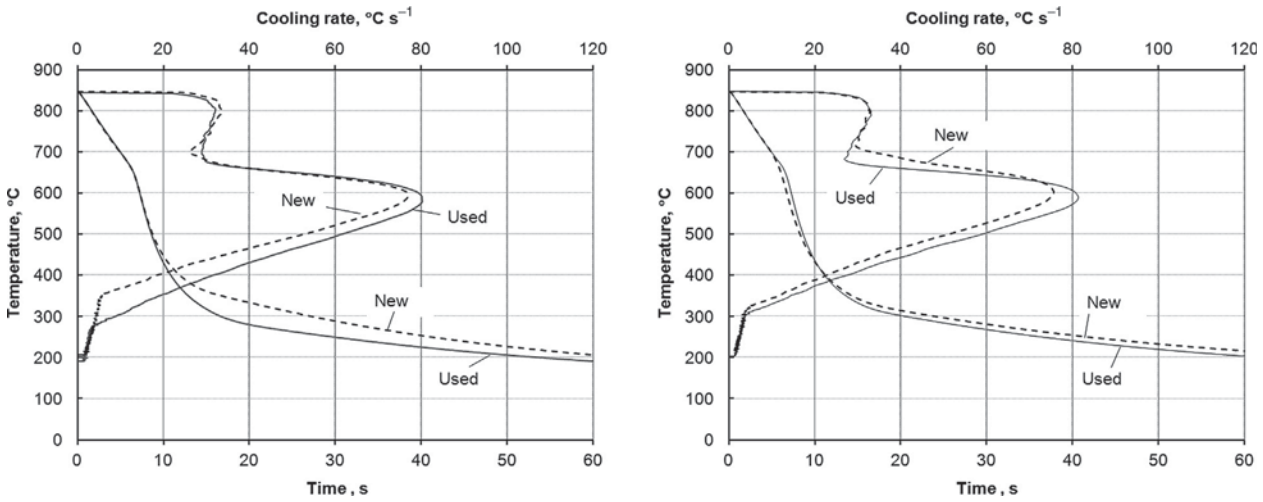

Figure 24 Cooling curves for new and used hot quenching oils, left: 120 °C, right: 130 °C, no agitation.

The cooling capacity of a polymer quenchant is affected by the type of polymer the quenchant is constituted, concentration, temperature, and agitation, see **Figure 25**. Polymers are sensitive regarding temperature variations as well as changes in concentration, which entails a careful control and maintenance of the quenchant. Concentration will change over time, e.g., due to drag-out and evaporation. Also the presence of contaminants in polymers, such as oil, salt, metalworking fluids, forging lubricants, as well as thermal and mechanical degradation of polymer, is affecting the cooling performance and thus the cooling curves.

Figure 26 shows cooling curves measured in polymers that have been used in heat treatment workshops for different running times. In all these cases, measurement of concentration by refractometer indicated the concentration desired, which could be incorrectly interpreted the bath works as it should, if not other measures are taken to control the bath. The cooling curves show clearly that the cooling characteristics have changed over time in all the studied polymer solutions.

It should be noted that in some cases, the cooling capacity has increased and in some cases it has decreased. This is due to different mechanisms that have influence on the cooling characteristics of the polymer solution. **Figure 27** shows how a 15% Aquatensid solution is influenced by addition of detergent and cutting fluid. In the presence of 5% of the washing agent, the maximum cooling rate tends to decrease somewhat. The presence of 5% cutting fluid is greater and also has an effect by increasing cooling capacity at lower temperatures, below 300 °C.

During use in production, the polymer bath is exposed for large temperature changes which affect the polymer chains. This has been illustrated by an accelerated aging test. In this test, an Inconel probe, ø25 × 75 mm, was induction heated and quenched in a polymer bath of 10% Aquatensid at 20 °C. The heating and quenching procedures were repeated up to 400 cycles and cooling curves were recorded after certain intervals, see **Figure 28**. In this case, the viscosity had decreased over time indicating a breakdown of the polymer chains resulting in an increased heat transfer rate.

12.04.8 Maintenance and Quality Assurance (Flame Point, Water Content, etc., ref to CQI-9)

As the cooling capacity of a quenchant always changes over time, maintenance and quality assurance is of vital importance in order to maintain high quality production with high throughput. As mentioned earlier, the cooling capacity is influenced by contamination, e.g., by cutting fluids, washing agents, impurities, bacteria, and oxide scale, as well as by thermal loading and mechanical agitation. Consequently, it is important to check quenchant quality on a regular basis.

When it comes to maintenance also the equipment needs to be checked on a regularly basis. The quenchant's flow conditions can change through, e.g., an agitator malfunctioning or a propeller blade bending or breaking off. Problems in the equipment may also cause contamination or dilution with oil or water in the quenchant. The latter can, besides causing quality problems with the quenched parts, also cause fire hazards, e.g., caused by water in oil.

Examining cooling capacity using cooling curves gives an immediate picture of the characteristics of the quenchant and makes it easy to monitor any changes over time.

Procedures for this have been described earlier in this chapter. For oils and polymers, standards exist, see **Table 1**, but the same approach can also be used for other quenchants.

According to CQI-9, quenchants must be checked as follows (9):

- Polymers
  - Concentration (daily)
  - Quenchability check: e.g., cooling curve, viscosity, or titration (every 6 months)

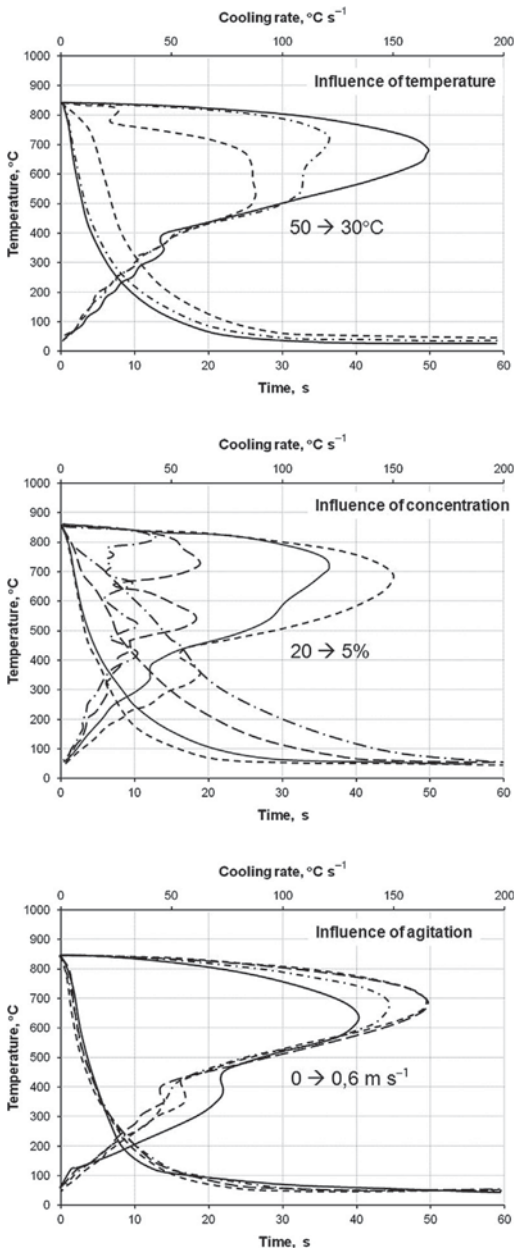

Figure 25 Influence of temperature, concentration, and agitation on the cooling capacity of Polyquench VP65. Upper: Concentration 5%, 0.4 m s^{-1}, middle: 30 °C, 0.4 m s^{-1}, and lower: 30 °C, concentration 5%. Reproduced from Holm, T.; Olsson, P.; Troell, E. S *Steel and Its Heat Treatment*. ISBN: 978-91-86401-11-5, 2012, www.swereaivf.se.

- Oil quench media
  - Water content, suspended solids, viscosity, cooling curve, total acid, and flash point (quarterly)
- Water quench media
  - Suspended solids (every 6 months)
- Salt quench media
  - Analysis and contaminants (every 6 months)
- Brine or caustic quench media
  - Concentration and/or specific gravity (daily)

In production, quenching oils are tested in several ways to determine and evaluate its characteristics and quality (*1*):

- Cooling capacity: Cooling curves give a direct indication of any changes that may have occurred in the cooling capacity of an oil.
- Appearance: The oil darkens over time.

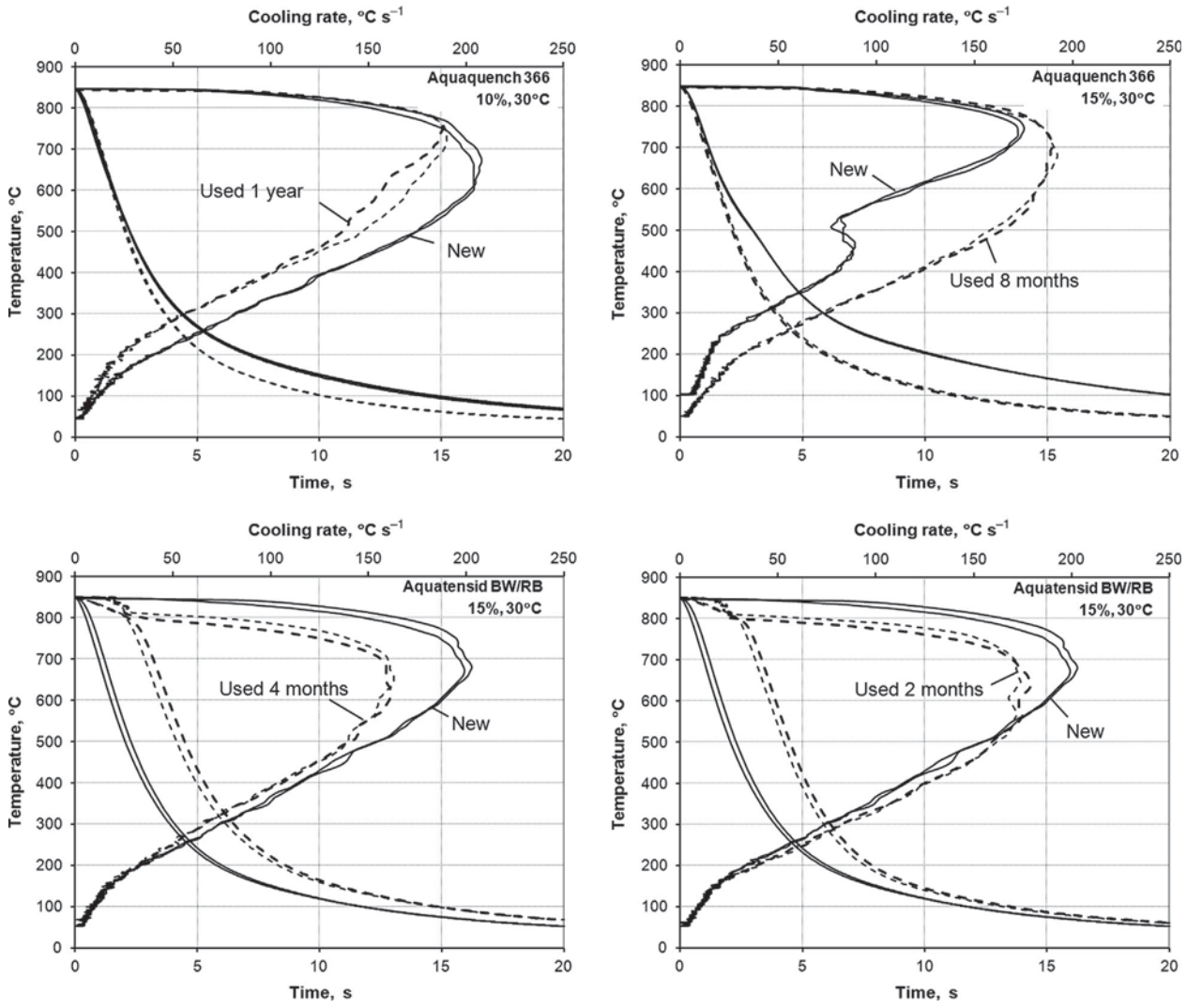

Figure 26 Cooling curves for new and used, 2–12 months, polymer baths. Top: Aquaquench 366, 15%, 30 °C. Bottom: Aquatensid BW/RB, 15%, 30 °C.

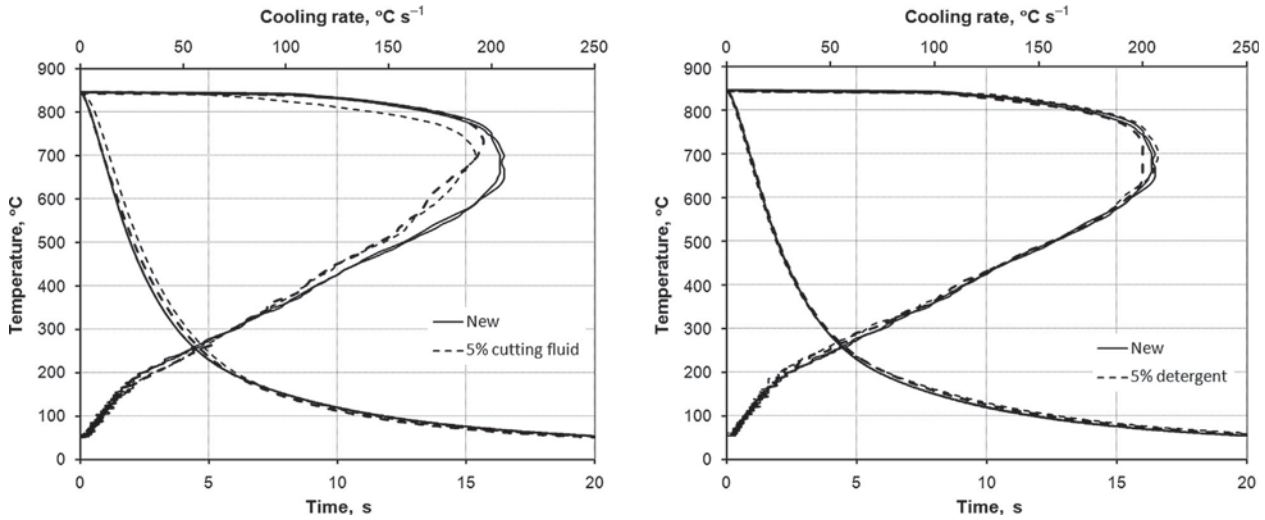

Figure 27 Influence of contamination on the cooling capacity for Aquatensid, 15%, 30 °C. Left: contaminated with 5% cutting fluid. Right: contaminated with 5% washing agent.

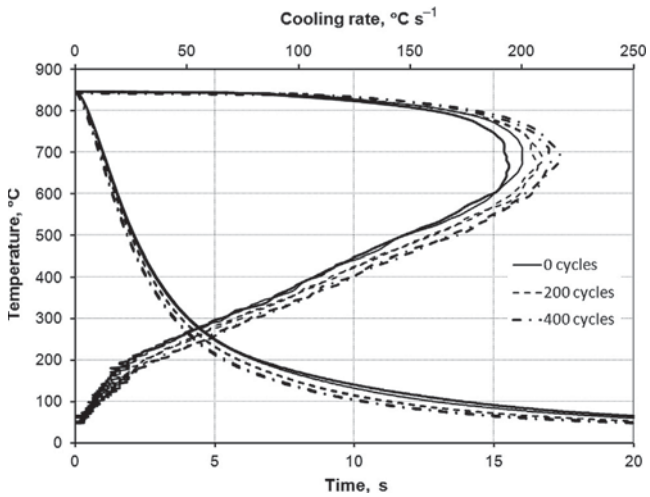

Figure 28 Cooling curves after accelerated aging test of polymer quenchant. Aquatensid, 10%, 20 °C.

- Sludge: Oxidation products sink to the bottom of the quench tank, the amount of sludge gives an indication of the degree of oxidation.
- Flash point: Due to oxidation, the flash point can either increase or decrease depending on the base oil. Each oil has a given flash point, which should not be exceeded. The quenching oil temperature should always be at least about 60 °C below the flash point. To avoid overheating, the output of the oil heaters should not exceed 1 W m^{-2}. Flash points can be tested according to ASTM D93-96.
- Viscosity: This increases with increase in oxidation. A low viscosity gives a higher flow rate and thus an increased cooling capacity. A lower viscosity entails a more uniform flow. Viscosity can be measured according to ASTM D445-96.
- Acid number: This increases with increase in oxidation, and each oil has a threshold value. It is measured according to ASTM D664-95, as per which the oil sample is dissolved in toluene and 2-propanol and titrated into potassium hydroxide.
- Water content: Even small quantities of water can affect quenching oils in different ways depending on the working temperature, agitation, and additives. Zero water content is preferable for the best results. More than half of all fires in hardening workshops are caused by water in the quenching oil. Oil fires should be extinguished using CO_2. The simplest way of checking for water in the oil is to heat up a small quantity of oil in a beaker or test tube and listen for a clicking sound, which would indicate the presence of water. Other ways are through cooling curves, see Figure 29, and electrolytic titration according to ASTM D4928-89

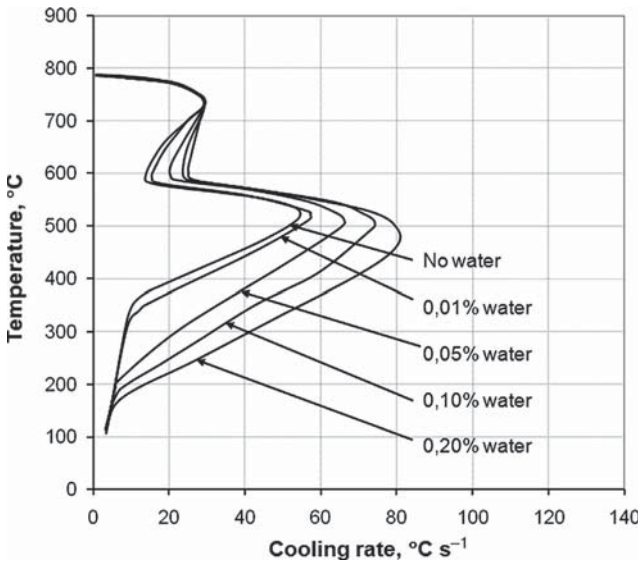

Figure 29 Influence of water content on the cooling curve for a typical oil. Reproduced from Holm, T.; Olsson, P.; Troell, E. *Steel and Its Heat Treatment.* ISBN: 978-91-86401-11-5, 2012, www.swereaivf.se.

using coulometric Karl Fischer titration. Water can be removed by heating up the oil to, e.g., 120 °C while agitating. If water is detected, the source, e.g., a leaking oil cooler, must be investigated and eliminated.

- There are also methods for detecting solid impurities. According to ASTM D893-92, a sample of the oil is dissolved in pentane and toluene and centrifuged three times.

Polymer quenchants are in many ways more sensitive to variation in the process parameters and demand more maintenance than oils. The quench bath must be checked every day when operational. Polymers are tested in several ways to determine and evaluate its characteristics and quality (*1*):

- Cooling capacity: Cooling curves give a direct indication of any changes that may have occurred in the cooling capacity of a polymer. Polymer concentrations can be measured using a refractometer or a viscosimeter. Measuring the concentration is an adequate way of monitoring day-to-day changes, but cooling curves should also be derived on a regular basis, as refractometer readings can be misleading. The relationship between the refractometer index and the concentration depends on the type of polymer.
- Bacteria control: Bacteria are caused by pollutants such as oils, corrosion inhibitors, lubricants, cutting fluids, and penetrants for crack indication. It is analyzed through cultivation in a nutrient solution, which also indicates the possible presence of fungus in the system.
- To avoid problems with corrosion, the pH-value must be checked regularly and additives provided as necessary to maintain the correct value.

In some cases, cooling curve measurements on site in quench tanks may provide useful data. The measurement procedure is more or less the same as when testing quenchants in a laboratory but it can sometimes be necessary to have an extended test probe in order to measure at the desired depth in the tank.

As the main local difference in the quenching performance is due to variation of the agitation, it is always a good idea to also make measurements of the flow rate in approximately the same positions as where the cooling curves are recorded. These instruments are in its simplest form mainly a unit consisting of a calibrated propeller coupled to a counting apparatus. The measuring is performed during a fixed time interval and the number of counts is then converted to the flow rate using a simple formula.

In Figure 30, results are presented from cooling curve and flow rate measurements in five different positions in a pusher furnace quench tank (*17*). It can be seen that the different flow rates seems to have a strong impact on the appearance of the cooling curves.

12.04.9 Outlook

The trend is toward reduced energy consumption, less consumption of chemicals, and consumables, as well as reduced scrap and rework and improved product performance. Examples of chemicals that are consumed in a heat treatment process are the quenchants and detergents that are used both before and after the heat treatment process. Quenchants that do not require any, or very

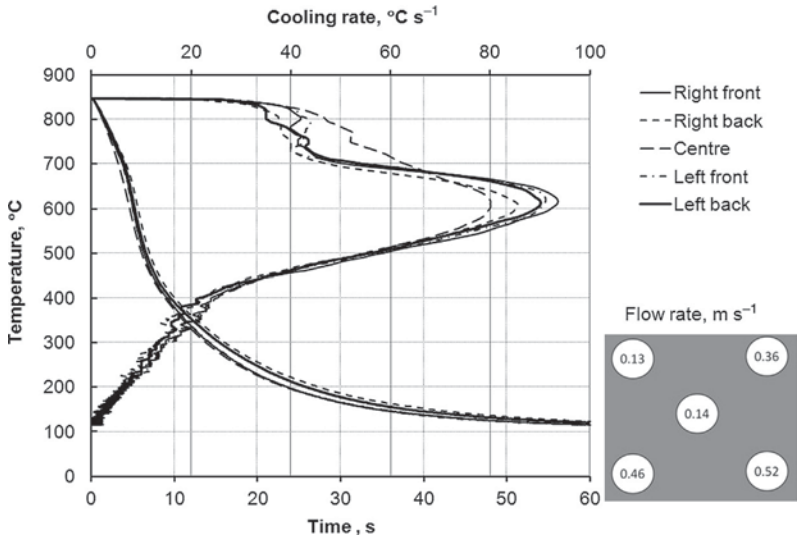

Figure 30 The variation of flow rate and the impact on cooling curve appearance at different positions in a pusher furnace quench tank. Reproduced from Werke, M.; Kristoffersen, H.; Andersson, J.; Johansson, K.; Thoors, H. Virtual Verification of the Shape Accuracy of a Powertrain Component, 2008.

little, washing of the details before and after heat treatment are an advantage because the detergent consumption as well as energy consumption can be reduced.

One of the most common quenchants is the group of hardening oils. Some disadvantages of these are that they are based on mineral oils, are difficult to wash off, and that they constitute a fire hazard. There is ongoing research and development regarding vegetable oils to replace mineral oils as quenchants (*18*,*19*). Vegetable oils are identified as renewable, biodegradable, and nontoxic. Another advantage of these is that they exhibit no vapor phase, which is beneficial in terms of shape change. However, in the current form they exhibit considerably lower thermal-oxidative stability compared with mineral oils, which has inhibited their use (*20*,*21*).

Gas cooling is used to an increasing extent, particularly in combination with vacuum carburizing. The main advantage of gas cooling is that the details are clean and do not require washing after cooling. During cooling, the cooling sequence can also be adjusted by regulating pressure and flow rate/fan speed.

Water-based quenchants, including, e.g., brine and polymers, are easy to wash off but require closer monitoring and more follow-up during use than, e.g., hardening oils. With the use of polymers, plant and equipment are cleaner as soot, smoke, and residues from oil quenchants are eliminated and there is no risk of fire hazards. Compared with oils, polymer quenchants are more sensitive to variations in concentration, temperature, agitation, and contamination, thus demanding frequent and careful monitoring. For all liquid quenchants, there is also an aging effect that influences their performance and must be observed. Polymers stick to the surface after quenching so washing is still needed. Less sticky polymers would decrease the need for washing or facilitate washing, and thus reduce the need of equipment maintenance.

Single-piece-based manufacturing with heat treatment integrated in production lines, which is used to an increasing extent, means heating and cooling the components individually, which enables increased use of methods where the cooling is optimized for a particular component. In this case, controlled spray cooling with water can be used.

Through better control and monitoring of the function of the quenchant it should be possible to increase the interval for replacing the quenching bath, which would be an advantage both in economic terms and with regard to the environment.

By minimizing distortion, rework, and scrapping can be reduced. The cause of distortion can be tracked throughout the total manufacturing chain, but the quenching process is a major contributing part (*22*). To minimize distortion, better control, and management of the quenching bath, e.g., regarding flow and agitation rate is needed. To ensure that the cooling is consistent, adequate sensors are needed to control variation in the cooling bath and in a load.

Finite element method (FEM) calculations are used increasingly to predict the development of microstructures, stresses, strains, and distortions during quenching and is very helpful for better understanding, optimizing, and developing the quenching operation. Fluid dynamics calculations (CFD) are used to calculate fluid flow (gases and liquids) in a quench bath, around a part or for complex loads. Such calculations makes it possible to design a quench bath and the cooling sequence in order to produce components with desired properties as well as minimizing distortion. For increased precision from FEM calculations, better knowledge is required of how the heat transfer coefficient varies during cooling around the components, particularly in a charge.

The impressive development of computer hardware in the last decade has opened up opportunities to 'run the heat treatment process' in the computer. However, for more accurate predictions of properties and distortion, better models of the processes and material behavior are needed as well as more precise data regarding heat transfer around components being quenched.

See also: Introduction to Steel Heat Treatment; Calculation of the Heat Transfer Coefficient Based on Experiments by the Liscic Probes; Metallo-Thermo-Mechanical Coupling in Quenching; Hardenability of Steel.

References

1. Holm, T.; Olsson, P.; Troell, E. *Steel and Its Heat Treatment*. ISBN: 978-91-86401-11-5, 2012, www.swereaivf.se.
2. MacKenzie, S. *Houghton on Quenching*, 2010.
3. *Metals Handbook*; *Heat Treating*. 9th ed. ASM International: USA, 1981; Vol. 4.
4. Bodin, J.; Segerberg, S. Measurement and Evaluation of the Quenching Power of Quenching Media for Hardening. In *Proceedings of the First International Conference on Quenching & Control of Distortion;* Chicago, IL, 1992.
5. Totten, G. E.; Bates, C. E.; Clinton, N. A. *Handbook of Quenchants and Quenching Technology;* ASM International: Materials Park, OH, 1993.
6. Grossmann, M. A.; Asimov, M.; Urban, S. F. *Hardenability of Alloy Steels;* American Society for Metals: Cleveland, OH, 1939.
7. *Quenchants for the Heat-Treatment of Steel, Cast Iron and Aluminium Alloys;* Petrofer Chemie GmbH, 2012, www.petrofer.com.
8. ASTM D3520-04 Standard Test Method for Quenching Time of Heat-Treating Fluids (Magnetic Quenchometer Method) www.astm.org (withdrawn 2008).
9. (CQI-9)*Special Process: Heat Treat System Assessment,* 2nd ed.; Automotive Industry Action Group (AIAG), 2007, www.aiag.org.
10. *ASTM D 6200-01 Standard Test Method for Determination of Cooling Characteristics of Quench Oils by Cooling Curve Analysis,* 2012.
11. *ASTM D6482-06 Standard Test Method for Determination of Cooling Characteristics of Aqueous Polymer Quenchants by Cooling Curve Analysis with Agitation (Tensi Method),* 2006.
12. *ASTM D 6549-06 Standard Test Method for Determination of Cooling Characteristics of Quenchants by Cooling Curve Analysis with Agitation (Drayton Unit),* 2006.
13. Web page IVF SmartQuench, www.ivfsmartquench.com, Nov 2012.
14. *JIS K 2242:2006 (E) JMFA/JSA Heat Treating Oils;* Translated and Published by Japanese Standards Association, 2006.
15. ivf SmartQuench, Users' Manual., Swerea IVF AB, 2009.

16. Felde, I. Determination of Thermal Boundary Conditions during Immersion Quenching by Optimization Algorithms. *Mater. Perform. Charact.* 2012, *1* (1), 1–11, http://dx.doi.org/10.1520/MPC104417. ISSN: 2165-3992.
17. Werke, M.; Kristoffersen, H.; Andersson, J.; Johansson, K.; Thoors, H. *Virtual Verification of the Shape Accuracy of a Powertrain Component,* 2008.
18. Schicchi, D.; Carvalho de Souza, E.; Gaston, A., et al. Effect of Vegetable Oil Oxidation on Heat Transfer and Residual Stress during Quenching. In *6th International Quenching and Control of Distortion Conference Including the 4th International Distortion Engineering Conference;* Chicago, 2012.
19. Schicchi, D.; Belinato, G.; Sarmiento, G. Effect of Soybean Oil and Palm Oil Oxidation Stability on the Variation of Heat Transfer Coefficients and Residual Stress. In *6th International Quenching and Control of Distortion Conference Including the 4th International Distortion Engineering Conference;* Chicago, 2012.
20. Lauralice, C. F.; Canale, E.; Carvalho, de Souza; Totten, G. E. Quenchants Derived from Vegetable Oils as Alternatives to Petroleum Oil. *Ind. Heat.* Aug 2011.
21. Andriollo, J. P.; Parodi, A.; Baglietto, L.; Bianchi, S. Vegetable Oil vs Mineral Oil in Quenching Applications. In *6th International Quenching and Control of Distortion Conference Including the 4th International Distortion Engineering Conference;* Chicago, 2012.
22. Zoch, H.-W. Distortion Engineering – Interim Results after One Decade Research within the Collaborative Research Center. In *3rd International Conference on Distortion Engineering;* Bremen, 2011.

This page intentionally left blank

12.05 Calculation of the Heat Transfer Coefficient Based on Experiments by the Liscic Probes

B Liščić (retired), University of Zagreb, Zagreb, Croatia
S Singer, University of Zagreb, Zagreb, Croatia

12.05.1	**Characteristics of the Heat Transfer at Quenching**	123
12.05.1.1	Heat Transfer When Using Vaporizable Liquid Quenchants	123
12.05.1.1.1	Film Boiling	124
12.05.1.1.2	Nucleate Boiling (Transient Nucleate Boiling Process)	125
12.05.1.1.3	Convection Cooling	125
12.05.1.2	Heat Transfer at High-Pressure Gas Quenching in Vacuum Furnaces	130
12.05.1.2.1	Cold Chamber Gas Quenching	132
12.05.1.2.2	Nozzle Field Gas Quenching	133
12.05.2	**Laboratory Tests to Evaluate the Cooling Intensity of Liquid Quenchants**	133
12.05.3	**Requirement for a Workshop Designed Test to Evaluate the Cooling Intensity of Liquid Quenchants**	140
12.05.4	**Temperature Gradient Method for Evaluation of Cooling Intensity When Quenching in Workshop Conditions**	141
12.05.4.1	Theoretical Principles	141
12.05.5	**Temperature Measurement and Unavoidable Physical Phenomena When Measuring Transient Temperatures at Quenching**	143
12.05.5.1	Damping Effect	144
12.05.5.2	Time Lag	144
12.05.5.3	Thermocouple Response Time	144
12.05.6	**Design and Characteristics of the Liscic Probes**	146
12.05.6.1	The Liscic/Petrofer Probe for Industrial Application When Liquid Quenchants are Used	146
12.05.6.2	The Ipsen–Liscic Flux Sensor for High-Pressure Gas Quenching in Vacuum Furnaces	147
12.05.6.3	The Liscic/Nanmac Probe for Scientific Investigation and Quenching Process Analysis	150
12.05.7	**Influence of Wetting Kinematics on the Heat Transfer Coefficient**	153
12.05.8	**Inverse Heat Conduction Problem**	156
12.05.8.1	Temperature Distribution Model	156
12.05.8.2	Numerical Solution of the Inverse Problem	157
12.05.8.3	Simplified 1-D Model for Standard Probes	158
12.05.8.4	Outline of the Heat Transfer Coefficient Calculation	158
12.05.8.4.1	Ipsen–Liscic Flux Sensor	159
12.05.8.4.2	Liscic/Petrofer Probe	160
12.05.9	**Finite Differences and Finite Volumes for the HCE**	161
12.05.9.1	Time and Space Discretizations	161
12.05.9.2	Implicit Methods	162
12.05.9.3	Finite Difference Method	163
12.05.9.4	Finite Volume Method	164
12.05.10	**Smoothing of Measured Temperatures**	166
12.05.10.1	Ordinary Smoothing without Constraints	166
12.05.10.2	Monotone Smoothing	167
12.05.11	**Numerical Examples**	169
12.05.11.1	Ipsen–Liscic Flux Sensor – Gas Quenching	169
12.05.11.2	Liscic/Petrofer Probe – Oil Quenching	170
12.05.11.3	Liscic/Petrofer Probe – Polymer Quenching	173
References		175

12.05.1 Characteristics of the Heat Transfer at Quenching

12.05.1.1 Heat Transfer When Using Vaporizable Liquid Quenchants

Quenching is a nonstationary thermodynamic process, the aim of which is to attain the required level of superficial hardness, as well as adequate hardness distribution on the cross section of a hardened workpiece, with minimum deformation and size change. These two requirements are opposite to each other. A higher quenching intensity to achieve greater depth of hardening increases deformation and size change. This shows the complexity of the quenching process and the need to optimize quenching parameters

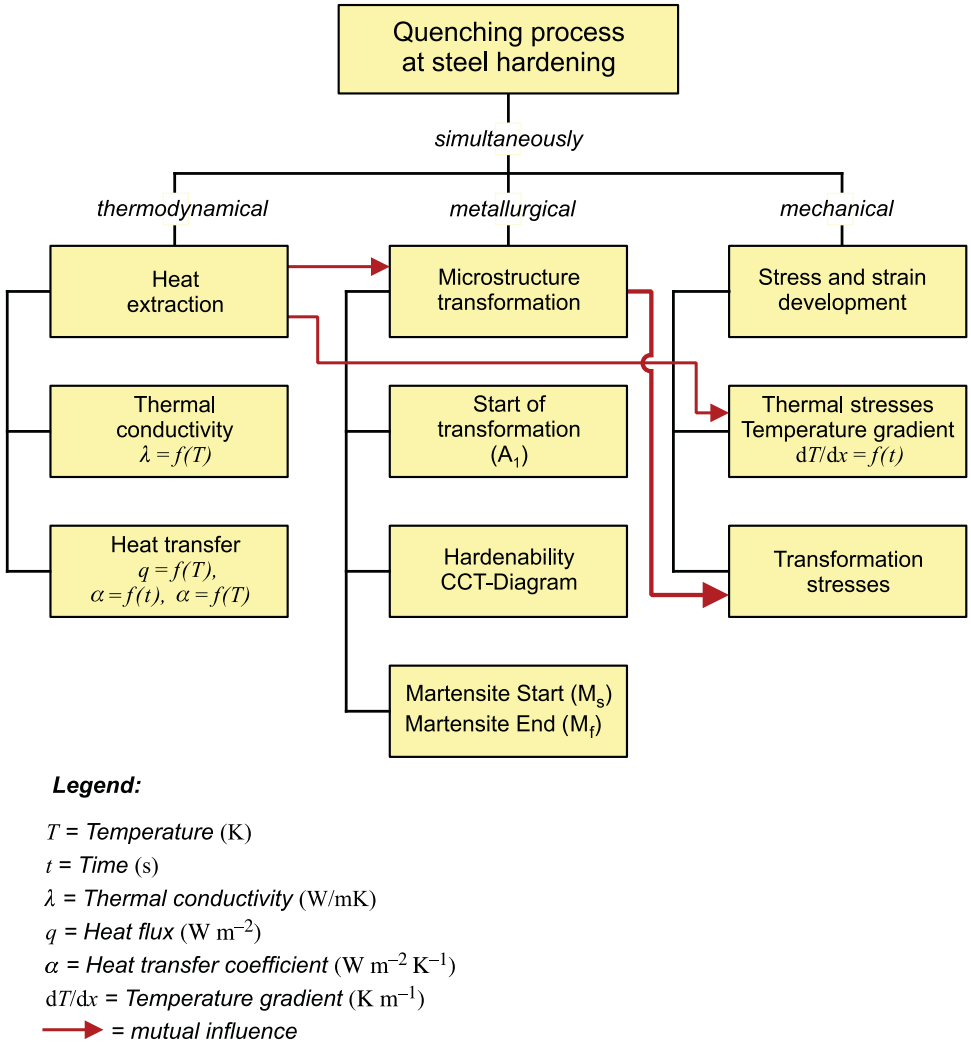

Figure 1 Simultaneous mutually dependent processes during quenching. Reproduced from Liscic, B. Heat Transfer Control during Quenching. *Mater. Manuf. Process.* **2009,** *24* (7–8), 879–883.

and control the quenching intensity as far as possible. To do this one has to know, from one side, the hardenability of the steel grade in question and, from the other side, the dynamic of heat extraction from the workpiece.

From the first moment when a workpiece is immersed in a quenchant, three different processes start and develop simultaneously, as shown in Figure 1. Each of these three processes has its own dynamic (*1*).

It is especially important to know that the transformation of the microstructure does not start on the whole cross section simultaneously, but gradually from the surface to the core, only then when a particular point attains the temperature A_1, because in the temperature region from the austenitizing temperature to A_1 there is no transformation of the microstructure, as shown in Figure 2. This fact makes it possible (at least for bigger cross sections) to intentionally change the heat extraction dynamic, i.e., to control the quenching process.

The three main heat transfer mechanisms at quenching are film boiling, nucleate boiling, and convection, as shown in Figure 3 (*2*).

12.05.1.1.1 Film Boiling

Film boiling surrounds the part surface with a vapor blanket. During this stage the heat flux from the part surface, due to this isolating blanket, is considerably reduced and occurs mainly by radiation. When the part surface and core cool so much that the heat flux is not enough to support film boiling, the vapor blanket begins to collapse in some areas of the part. Sporadically, the vapor blanket will collapse and may re-form in certain areas of the part. The duration of film boiling depends on many factors such as the mass and shape of the part, physical properties of the quenchant, its temperature, and agitation rate. Film boiling can last from a few seconds to tens of seconds, on the same part. For example, in a blind hole the film boiling will go on for a longer time than at the area on the outer diameter of the part, where the agitation is greater. Also, there is likely to be more film boiling at the bottom of a part, since the bubbles have a difficult time leaving the surface and rising to the top of the tank. As the sporadic film blanket collapses and re-forms in different areas of the part, the film boiling becomes unstable and transitions to nucleate boiling. This

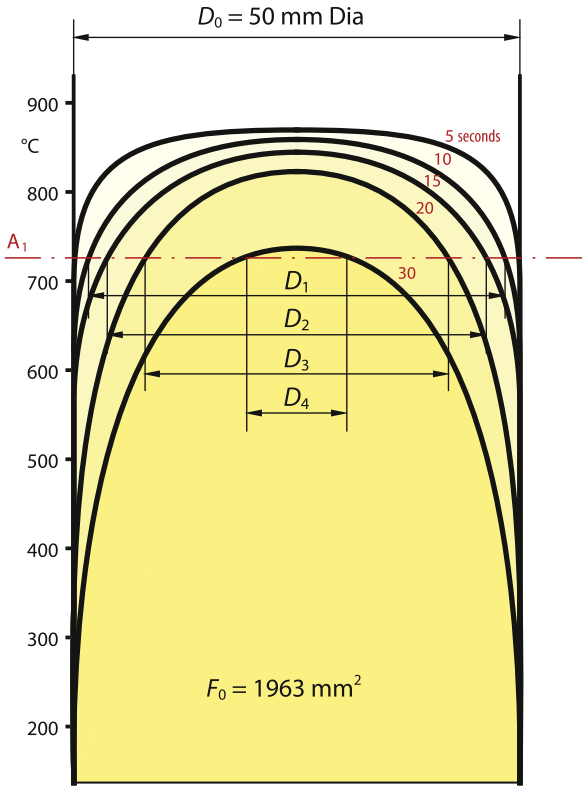

The nontransformed part of the cross-section after:

10 Seconds	D_1 = 47.5 mm	F = 1771 mm^2	90% of F_0
15 Seconds	D_2 = 42.5 mm	F = 1418 mm^2	72% of F_0
20 Seconds	D_3 = 35.0 mm	F = 962 mm^2	49% of F_0
30 Seconds	D_4 = 14.5 mm	F = 165 mm^2	8% of F_0

Figure 2 Gradual transformation of the microstructure on the cross section of a steel cylinder of 50 mm diameter quenched in still mineral oil at 20 °C. Reproduced from Liscic, B. Heat Transfer Control during Quenching. *Mater. Manuf. Process.* **2009,** *24* (7–8), 879–883.

period is called transition boiling. Because of the nonuniformity of the film boiling process, this heat transfer mechanism causes much of distortion in the part during quenching, and therefore should be avoided.

12.05.1.1.2 Nucleate Boiling (Transient Nucleate Boiling Process)

Nucleate boiling is characterized by a very high rate of heat extraction at the surface of the part, due to formation, in each second, of hundreds of tiny bubbles over the part surface, which grow and detach from the surface. The end of film boiling and the start of nucleate boiling is the critical heat flux density two (q_{cr2}).

As soon as nucleate boiling starts, the heat flux from the part surface begins increasing, and during nucleate boiling the heat transfer coefficient (HTC) attains its maximum. Nucleate boiling is a more stable and uniform mode of cooling. Unlike film boiling, there is usually less part distortion associated with nucleate boiling mode. Duration of this transient nucleate boiling process is directly proportional to the square of the thickness of a part, and inversely proportional to the thermal diffusivity of its material. It depends on the configuration of the part, its initial temperature, velocity of the quenchant, and its thermal properties. During nucleate boiling, the part surface temperature drops to slightly above the liquid's boiling temperature, and remains at this plateau during almost the entire nucleate boiling mode. As the nucleate boiling continues, the part is getting colder; the heat flux from the surface stops increasing and then begins reducing. At some point in time, when the surface temperature is close to the liquid's boiling temperature, the heat flux from the part cannot support the nucleate boiling mode any more, and then convection, as the last stage of quenching, begins.

12.05.1.1.3 Convection Cooling

After the nucleate boiling process stops, the part surface temperature starts dropping from slightly above the quenchant boiling temperature down to the quenchant temperature. Convection cooling is characterized by a much slower cooling rate than either the film boiling or nucleate boiling, and is also very uniform in its cooling around the part surface. Its cooling rate depends primarily on the agitation of the quenchant. The good uniformity of part cooling during convection limits the amount of

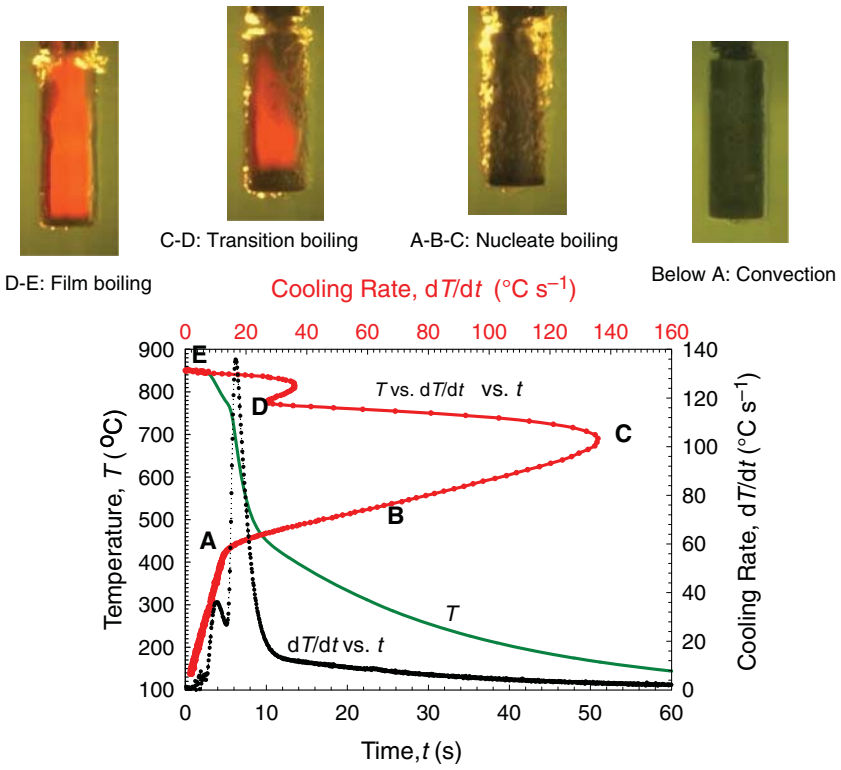

Figure 3 Cooling mechanisms, Center for Heat Treating Excellence (CHTE). Reproduced from Rondeau, D. The Effects of Part Orientation and Fluid Flow on Heat Transfer Around a Cylinder. MSc Thesis, Worcester Polytechnic Institute, 2004.

distortion in the part being quenched. This is why the gas quenching usually provides less distortion than a vaporizable liquid quenchant.

The complexity of the quenching process in evaporable liquid quenchants, as can be seen in colored small pictures at the top of Figure 3, confirms the fact that film boiling, nucleate (bubble) boiling, and convection can be present simultaneously on the surface of the same part. As a consequence, the HTC, the temperature distribution fields, and gradients in a particular moment look like as shown in Figure 4 (3). This is the cause of residual stresses and distortion. The real situation is even more complicated, because the boundary between nucleate boiling and convection, called 'the wetting front,' moves with a certain speed from the lower to the upper end of the part.

Experimental studies (4) have shown that the cooling potential of a liquid is primarily characterized by the first and second critical heat flux density. The first critical heat flux density (q_{cr1}) is the maximum heat flux density that causes film boiling (vapor

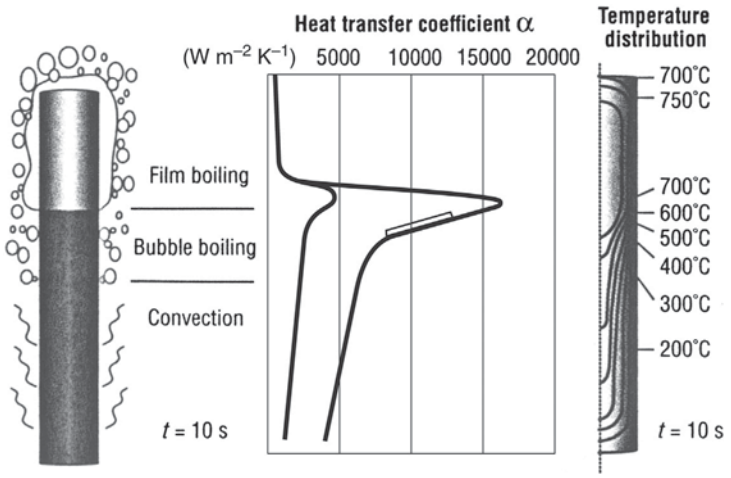

Figure 4 Heat transfer coefficient, temperature fields, and gradients at a cylinder when all three heat transfer mechanisms are present simultaneously. Reproduced from Stich, A.; Tensi, H. M. Wärmeübetragung und Temperaturverteilung mit Benetzungsablauf beim Tauchkühlen. *HTM Härterei–Techn. Mitt.* **1995,** *50* (1), 31–35.

blanket) at the very beginning of the quenching process. It occurs typically within approximately 0.1 s after initial immersion of the hot metal. This short period, which precedes the film boiling mode, is called 'shock-film boiling.' This is the point where vapor bubbles first depart from the hot metal surface upon their formation to make the vapor blanket. Because of its very short period it is seldom detected in published quenching data.

The second critical heat flux density (q_{cr2}) is the minimum heat flux necessary to support film boiling. This is the point at which the surface of a hot part has cooled enough to allow the collapse of the vapor blanket (end of film boiling) and nucleate boiling begins. **Figure 5** shows schematically how the HTC and the heat flux density develop during all modes of cooling during quenching.

According to Tolubinski (see Ref. (4)), the first critical heat flux density can be calculated as:

$$q_{cr1} = 7r(af\rho'\rho'')^{0.5}$$

where r = heat of evaporation; $a = \lambda/\rho c$ = thermal diffusivity; f = frequency of vapor bubbles detachment; ρ' = density of the liquid; and ρ'' = density of the liquid's vapor. The only variable in this equation on which the q_{cr1} depends is f; i.e., the frequency of vapor bubble detachment. In other words, a compact vapor blanket around the part will be formed only if the critical heat flux density q_{cr1} is attained, which depends on the number of vapor bubbles and the frequency of their detachment from the part's surface.

Both critical heat flux densities q_{cr1} and q_{cr2} are inherent properties of any vaporizable liquid. They do not change because of a change in part geometry or the mass of the part being quenched. There is also a universal correlation between q_{cr1} and q_{cr2} that is true for all vaporizable liquids:

$$q_{cr1} = 5 \times q_{cr2}.$$

From the other side, in every quenching process there is an initial heat flux density (q_{in}) that depends on the part to be quenched. This initial heat flux density depends on the ratio between the volume (heat capacity) and the surface area of the body. At the very beginning after immersion the heat flux density depends on the temperature gradient at the surface. Bodies having a relatively small volume and a large surface area will have a larger temperature gradient; i.e., a greater initial heat flux density (q_{in}) than bodies having a relatively large volume and a small surface area, as shown in **Figure 6**.

According to Ref. (7), upon immersion of a hot steel part into the quenchant, the initial heat flux density (q_{in}) can be:

$$q_{in} > q_{cr1}; \quad q_{in} = q_{cr1}; \quad q_{in} < q_{cr1}.$$

When $q_{in} > q_{cr1}$ full film boiling (vapor blanket) will appear. When $q_{in} = q_{cr1}$ transition boiling is observed. In the case of $q_{in} < q_{cr1}$ film boiling stage is absent; i.e., nucleate boiling starts from the beginning, as shown schematically in **Figure 7**.

This has been confirmed by the following investigation in Ref. (6). Cylindrical specimens of 20, 50, and 80 mm diameter have been quenched in a low viscous accelerated oil at 50 °C, and the HTC values have been calculated. All specimens have the length of 4 × diameter, so the specimen 20 mm diameter × 80 mm has a mass of 0.2 kg and the specimen 80 mm

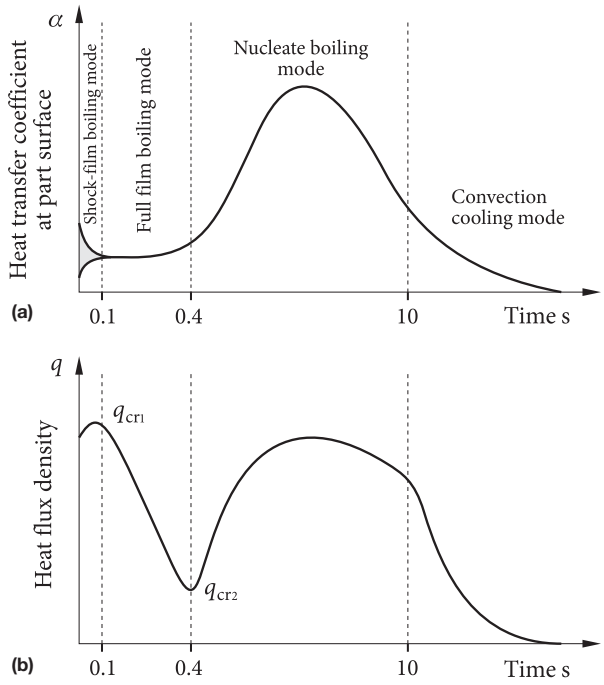

Figure 5 Four modes of cooling at quenching (a), and critical heat flux densities (b), according to Kobasko, N. I. Private Communication (with permission of N. I. Kobasko). Reproduced from Liscic, B.; Singer, S.; Beitz, H. Dependence of the Heat Transfer Coefficient at Quenching on Diameter of Cylindrical Workpieces. *J. ASTM Int.* **2011,** *8* (7).

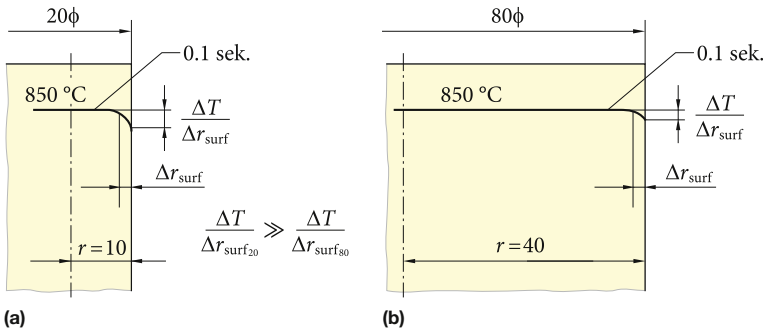

Figure 6 Schematic presentation of cooling at quenching (a) for a cylinder of 20 mm diameter and (b) for a cylinder of 80 mm diameter. Reproduced from Liščić, B.; Singer, S.; Beitz, H. Dependence of the Heat Transfer Coefficient at Quenching on Diameter of Cylindrical Workpieces. *J. ASTM Int.* **2011**, *8* (7). Reprinted, with permission from *Journal of ASTM Intl.*, copyright ASTM International, 100 Barr Harbor Drive, West Conshohocken, PA 19482.

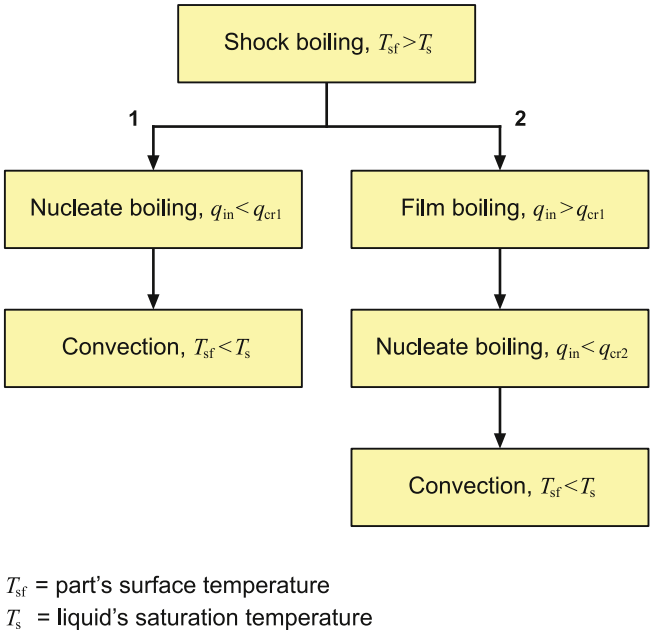

Figure 7 Schematic presentation (from N. I. Kobasko's presentation at WSEAS HMT' 11, Puerto Morelos, Mexico, with permission of N. I. Kobasko), whether or not the film boiling stage will occur during quenching.

diameter × 320 mm has a mass of 13.6 kg. The volume to surface ratio of the bigger specimen is 4 times greater than that of the smaller one. In other words, the specimen 20 mm diameter × 80 mm is a case of small volume and relatively large surface area, while the specimen 80 mm diameter × 320 mm is a case of large volume and relatively small surface area. Cooling the larger cylinder is slower than cooling the smaller one, i.e., the initial heat flux q_{in} in the case of the larger specimen is smaller than the initial heat flux (q_{in}) of the smaller specimen. The q_{in} for specimen of 20 mm diameter was greater than $q_{cr1,}$ therefore full film boiling mode has developed, as shown in Figure 8. For the specimen of 80 mm diameter, the q_{in} was smaller than q_{cr1}, so there was no film boiling, but instead nucleate boiling started from the beginning of cooling, as Figure 8 shows.

The first critical heat flux density determines whether or not full film boiling will develop and as such has a great effect on the cooling rate of steel parts and their distortion. It depends on the saturation temperature of the liquid, and the difference between the saturation temperature and the actual temperature of the quenchant. The more resistant a liquid is to boiling, the higher is its q_{cr1}. The more resistant a quenchant is to boiling, the more uniformly the part will be quenched (without film boiling), thus yielding less distortion.

When water is applied as quenchant, the q_{cr1} value depends on the water flow rate and the water temperature. It can be increased by increasing the agitation rate. Besides, a small amount (e.g., 0.1%) of certain chemical additive can increase q_{cr1} by 2–3 times. The knowledge of the additive, its concentration, and adequate water flow velocity are parameters that constitute the know-how for the intensive quenching technology.

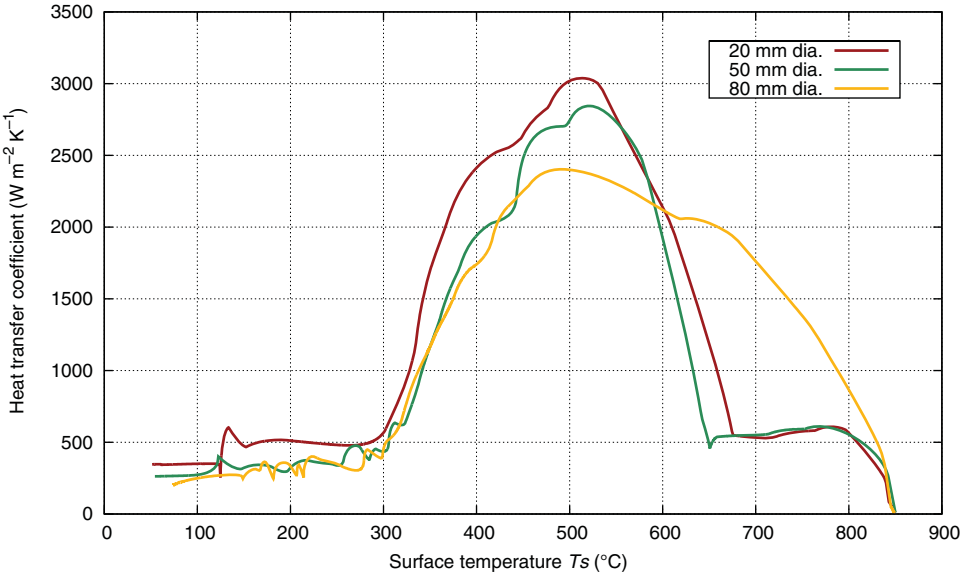

Figure 8 Heat transfer coefficients as function of surface temperature for cylinders of 20, 50, and 80 mm diameter, quenched in low viscous accelerated oil at 50 °C. Data courtesy of PetroFer GmbH.

Finally, there are two following important facts that should be always taken into account when dealing with HTC at quenching:

- Dependence of the HTC on diameter of the specimen. In 1968 Kobasko (*8*) published the diagram showing the influence of a specimen's diameter on the HTC at nucleate boiling stage, when quenching in water and in 12% water solution of NaOH, see Figure 9. As can be seen, the smaller the specimen's diameter, the higher is the HTC. For diameters less than 40 mm, this dependence is exponential.
- Variation of the HTC around the part's surface. One should be aware that the HTC varies around the surface of the quenched part. Within the frame of the Small Business Innovation Program, Techxperts Inc. (run by Dr. Robert W. Bass) in 1998 undertook an investigation project for the US National Aeronautics and Space Administration (NASA) to find out the HTC variation around a turbine disc (which is a quite simple shape), quenching it in still mineral oil. Temperature was measured by 16 thermocouples at different points near the surface. Using the finite elements software ANSYS, local HTC were calculated for 9 points. As can be seen in Figure 10, substantial differences in HTC were found not only between points at upper and lower surface but also between different points at the lower surface.

When evaluating the HTC in usual practice, it is impossible to use so many thermocouples at different points of a real workpiece of complex shape. This investigation shows how much compromise we have to make when evaluating the HTC, using specimens, or probes that measure the temperature usually in one point only.

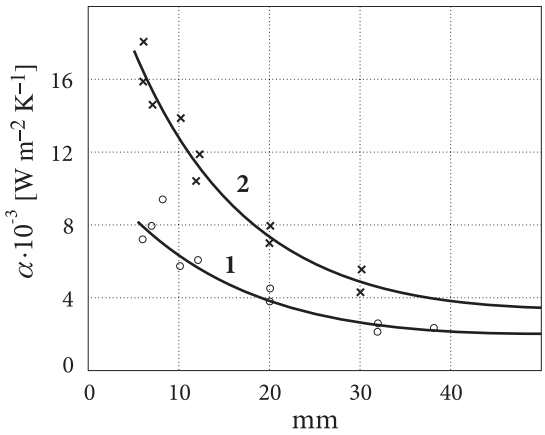

Figure 9 Influence of a specimen's diameter on the heat transfer coefficient at nucleate boiling phase. 1 – quenching in water of 25–40 °C; 2 – quenching in 12% water solution of NaOH at 25–30 °C. Reproduced from Kobasko, N. I. Thermal Processes in Quenching of Steel (in Russian). *Metallovedenie i Termicheskaya Obrabotka Metallov* **1968,** (3), 2–6; Liscic, B.; Singer, S.; Beitz, H. Dependence of the Heat Transfer Coefficient at Quenching on Diameter of Cylindrical Workpieces. *J. ASTM Int.* **2011,** *8* (7).

12.05.1.2 Heat Transfer at High-Pressure Gas Quenching in Vacuum Furnaces

At gas quenching, the quenching medium remains gaseous throughout, and there are no phase transitions as with liquid quenchants. The only cooling mechanism is convection. The axial distribution of the HTC is therefore highly uniform, resulting in smaller and uniform temperature gradients within a cylinder, as shown in Figure 11. This is a favorable condition for avoiding component distortion in the quenching process.

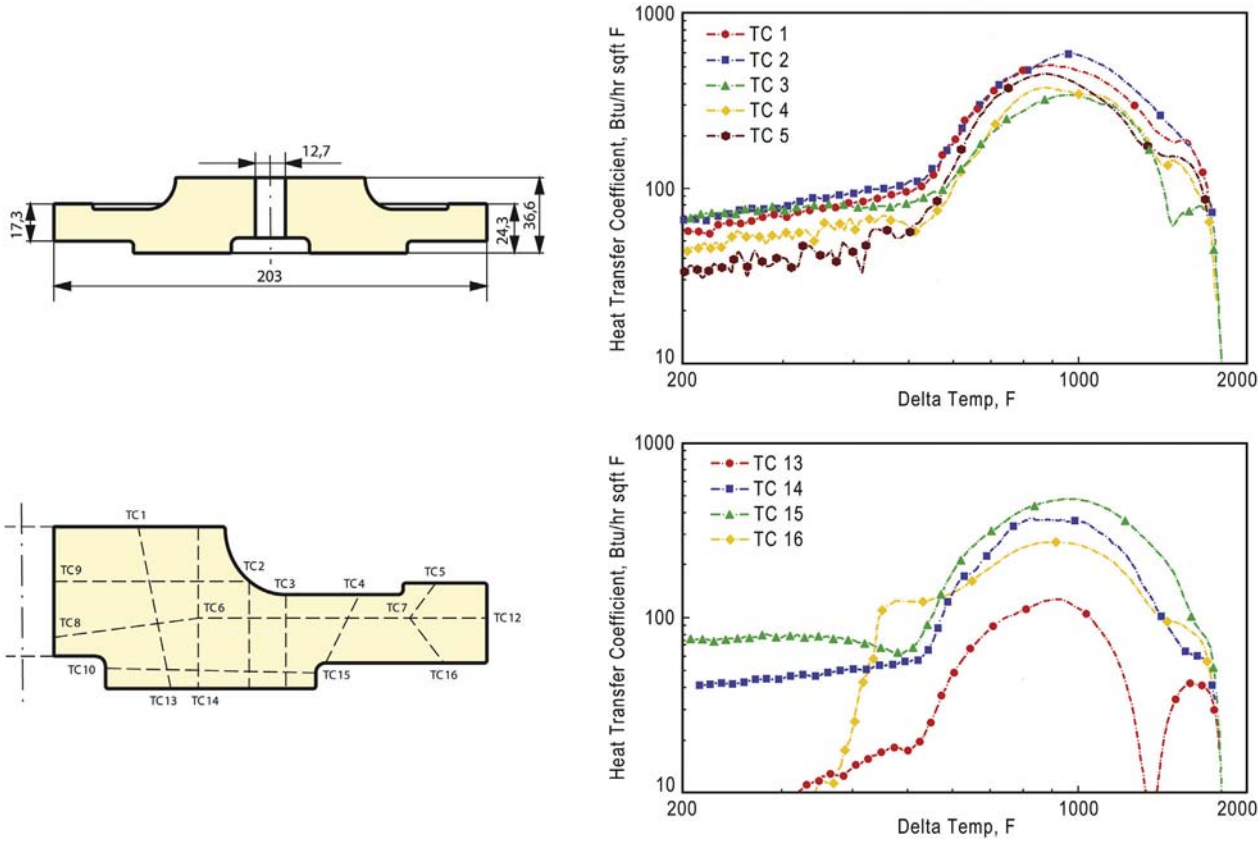

Figure 10 Local heat transfer coefficients at quenching a turbine disc in still mineral oil – data generated by Techxperts Inc. for the NASA Small Business Innovation Program, 1998.

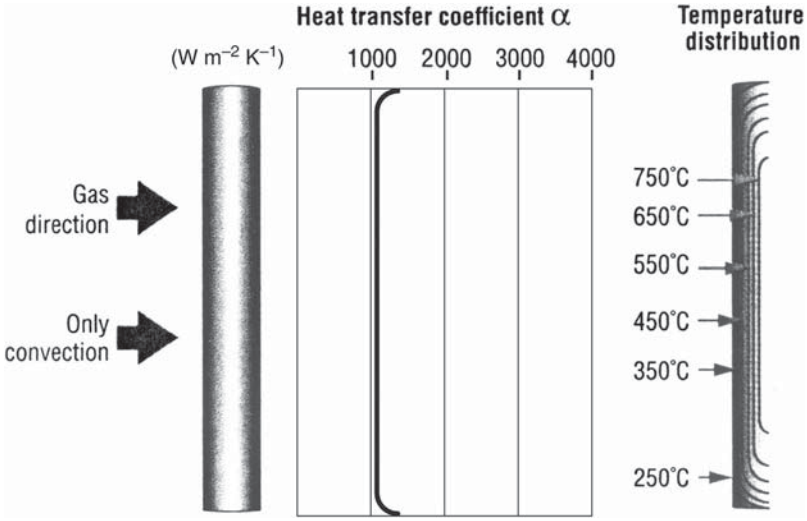

Figure 11 Heat transfer coefficient and temperature distribution within a cylinder which is cooled by transversal gas flow. Reproduced from Liscic, B. Heat Transfer Control during Quenching. *Mater. Manuf. Process.* **2009,** *24* (7–8), 879–883.

Quenching gases such as nitrogen and helium are absolutely inert and ecologically benign. They leave behind no residues on workpieces or in a hardening system. These properties make it unnecessary to invest in washing facilities and fire monitors, and lower the operating cost, since maintenance procedures and disposal of quenching media are eliminated.

However, gases have a fundamental disadvantage in comparison to fluids, which is that they have poor heat transfer characteristics under normal condition. For their use as cooling media in vacuum furnaces, they have to be optimized by proper adjustment of the gas pressure and flow speed. **Figure 12** shows an approximate comparison of average HTCs between liquid quenchants and high-pressure gas quenching (HPGQ) technology used in vacuum furnaces (*9*). A big difference is to be observed between densely packed batch loading and single component cooling in the vacuum furnace.

Four types of gases are considered for HPGQ in vacuum furnaces: argon (Ar), nitrogen (N_2), helium (He), and hydrogen (H_2). Their physical properties are presented in **Table 1**. The most important properties are specific heat capacity c_p (kJ kg^{-1} K^{-1}) and thermal conductivity λ (W m^{-1} K^{-1}). Both of them increase in inverse proportion to their density, i.e., the lighter the gas, the greater is its specific heat capacity and its thermal conductivity, which greatly contribute to better cooling rate at quenching.

Argon has the poorest characteristics, and is very seldom used. The ideal quench gas is hydrogen, but it is explosive in contact with oxygen. Because of safety reasons it is used only exceptionally (for scientific reasons) in special facilities, but not in common HPGQ practice. The other two gases, nitrogen and helium, are currently used in vacuum furnaces. In terms of cost per unit volume, helium is much more expensive; therefore it is used usually when adequate recycling facilities exist.

The main technological parameters at HPGQ are shown in **Figure 13** (*10*). All temperature versus time diagrams in this figure are valid for metal pieces (slugs) of 25 mm diameter. **Figure 13(a)** shows the effect of different gases on the cooling time. **Figure 13(b)** shows the effect of gas pressure, and **Figure 13(c)** shows the effect of gas velocity (expressed in amount of circulated gas in m^3 s^{-1}).

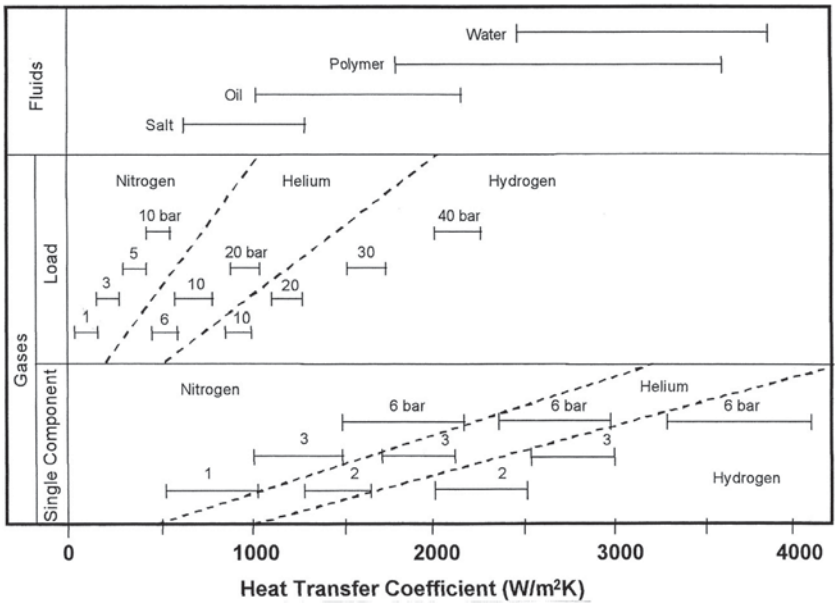

Figure 12 Approximate comparison of average heat transfer coefficients between liquid quenchants and high-pressure gas quenching (HPGQ) in vacuum furnaces. Edenhofer, B. An Overview of Advances in Atmosphere and Vacuum Heat Treatment. *Heat Treat. Met.* **1999**, *26* (1), 1–5. Reprinted with permission, from *Heat Treatment of Metals*, publisher Wolfson Heat Treatment Centre. The journal is now incorporated as a part of *International Heat Treatment and Surface Engineering Journal*, publisher W. S. Maney & Son Ltd. Copyright holder of the figure: The Institute of Materials, Minerals and Mining (Institute's web site: http://www.iom3.org/).

Table 1 Physical properties of quenching gases

	Argon	*Nitrogen*	*Helium*	*Hydrogen*
Chemical symbol	Ar	N_2	He	H_2
Density at 15 °C and 1 bar, (kg m^{-3})	1.6687	1.170	0.167	0.0841
Density ratio to air	1.3797	0.967	0.138	0.0695
Molar mass, (kg kmol^{-1})	39.948	28.0	4.0026	2.0158
Specific heat capacity c_p, (kJ kg^{-1} K^{-1})	0.5024	1.041	5.1931	14.3
Thermal conductivity λ, (W m^{-1} K^{-1})	177×10^{-4}	259×10^{-4}	1500×10^{-4}	1869×10^{-4}
Dynamic viscosity η, (Ns m^{-2})	22.6×10^{-6}	17.74×10^{-6}	19.68×10^{-6}	8.92×10^{-6}

Source: Vacuum Quenching, In *Heat Treater's Guide: Practices and Procedures for Irons and Steels*, 2nd ed.; Chandler, H., Ed.; ASM International, 1995; pp. 88–89. Reprinted with permission of ASM International.

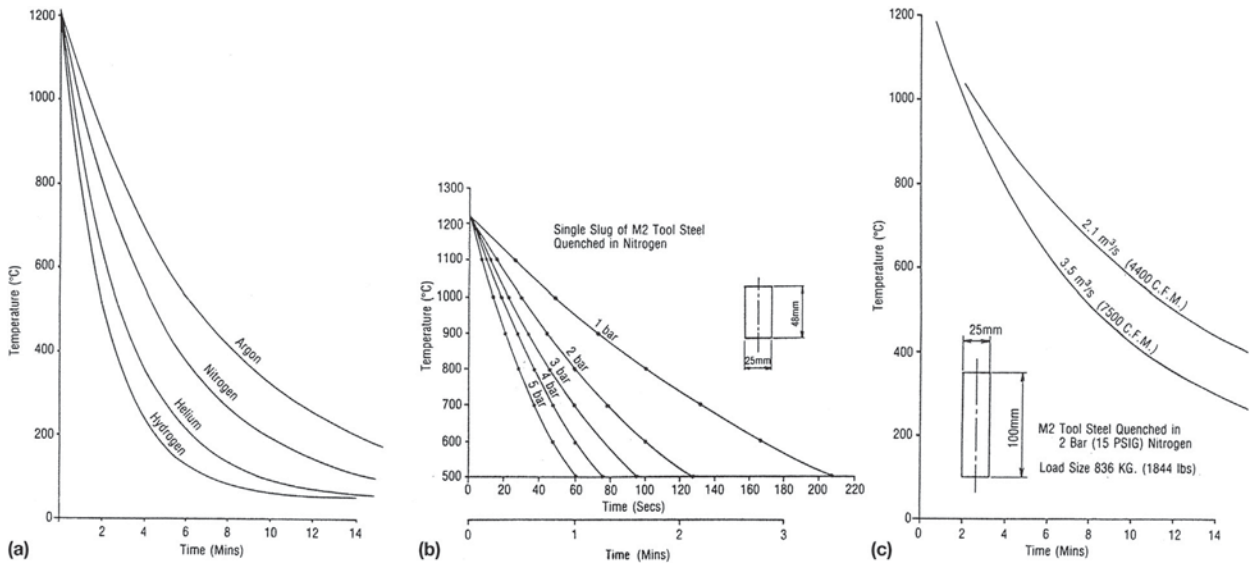

Figure 13 The main technological parameters at high-pressure gas quenching (HPGQ) in vacuum furnaces. Reproduced from Radcliffe, E. J. Gas Quenching in Vacuum Furnaces – A Review of Fundamentals. *Ind. Heat.* **1987,** *54* (11), 34–39.

The following influential factors can have great effect on the cooling process in vacuum furnaces:

- The size of the workpiece. The cooling rate at the surface is inversely proportional to the component diameter. Increasing the diameter by a factor of two decreases the cooling rate by a factor of two.
- Loading arrangement of workpieces. Gas circulation velocities within a batch of workpieces may differ because of different loading arrangements. This can, of course, change the heat transfer among different workpieces in a batch. By different positions of workpieces (horizontal or vertical) with respect to the gas flow direction, different parts of the workpiece's surface are exposed to the gas flow.
- Furnace design. Furnaces of different design use different directions of the gas flow (radial; up-down; or reversible up-down down-up). This has a consequence that in different furnaces at same pressure, with the same kind of gas, for same batches of workpieces, different values of gas flow velocity and therefore different heat transfer rates occur.

When HPGQ is applied, the HTC can be calculated as follows:

$$\alpha = Cp^{0.7} v^{0.7} d^{-0.3} \eta^{-0.39} c_p^{0.31} \lambda^{0.69}, \qquad [1]$$

where:

C = constant dependent on quench vessel design and load configuration
p = pressure (bar)
v = gas velocity (m s^{-1})
d = workpiece's characteristic dimension (m)
η = dynamic viscosity of the gas (Ns m^{-2})
c_p = specific heat capacity (kJ kg^{-1} K^{-1})
c = Specific heat (J kg^{-1} K^{-1})
λ = thermal conductivity of the gas (W m^{-1} K^{-1})

According to eqn [1], gas pressure and gas velocity (having exponents 0.7) are the most significant parameters in every HPGQ process. Equal increase in either pressure or gas velocity has the same effect on the HTC, and hence on the cooling rate of a component. Practical consequences, however, when increasing either pressure or gas velocity are not the same. Doubling the gas velocity increases the necessary blower power by a factor of eight, while doubling the gas pressure increases the blower power by only a factor of two. Therefore, in the course of vacuum furnace development, pressure of the quenching gas has been gradually increased.

12.05.1.2.1 Cold Chamber Gas Quenching

The majority of single chamber vacuum furnaces are of 'hot chamber' design. When quenching in a hot chamber, not only the load with the workpieces and the batch carriers have to be cooled, but also the whole of the hot chamber system like hearth, insulation, and heating elements. Quenching the load in a cold chamber requires transferring it into a separate cold quench chamber, but the exceptional advantage of this is that only the load itself is cooled, thus lowering the total amount of heat to be extracted by at least 50%. The additional advantage is that the cold chamber can be designed in such a way that the gas flow through the load is optimized, leaving the gas flow almost no side passage around the load, but forcing it totally through the load. The gas velocities through the load are increased from 10 to 20 m s^{-1} in a single hot chamber furnace to 30 m s^{-1} and more in a cold chamber. Using

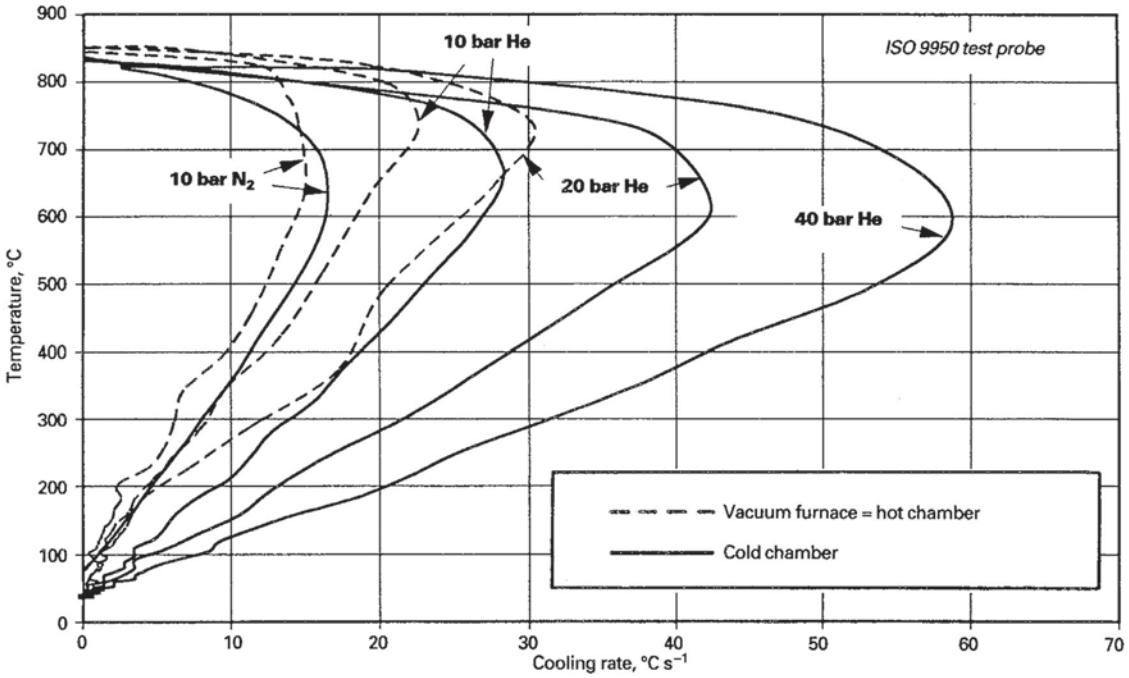

Figure 14 Cooling rate curves from the cold gas quenching chamber compared with those from a hot chamber vacuum furnace. Reprinted with permission, from *Heat Treatment of Metals*, publisher Wolfson Heat Treatment Centre. The journal is now incorporated as a part of *International Heat Treatment and Surface Engineering* Journal, publisher W.S. Maney & Son Ltd. Copyright holder of the figure: The Institute of Materials, Minerals and Mining (Institute's web site: http://www.iom3.org/). Reproduced from Segerberg, S.; Troell, E. High-pressure Gas Quenching Using a Cold Chamber to Increase Cooling Capacity. *Heat Treat. Met.* **1997,** *24* (1), 21–24.

such a cold chamber with increased gas volume flow and reduced flow section area, HTCs attainable in single hot chamber vacuum furnace of 300–400 W m^{-2} K^{-1} (using 6 bar nitrogen) can be increased up to 700–800 W m^{-2} K^{-1} using the same gas and the same gas pressure. Figure 14 shows the comparison of the cooling rate curves, measured by the laboratory test specimen of 12.5 mm diameter × 60 mm according to ISO 9950 (this standard has originally been developed for oil quenching) between quenching it in a hot chamber vacuum furnace and a cold chamber, for different gases and gas pressures.

12.05.1.2.2 Nozzle Field Gas Quenching

Further increase of gas velocities impinging the surface of the workpieces can be realized by using a gas nozzle field. Depending on the nozzle diameter and the pressure difference produced, gas velocities at the nozzle exit of 100 m s^{-1} and even 200 m s^{-1} are obtainable. Figure 15 gives a schematic presentation of a cold gas quench chamber with a nozzle field for quenching single-layer loads (*12*).

Because the velocity of the gas exiting from the nozzles decreases rapidly with increasing distance from the nozzle exit, the utilization of such a nozzle field gas quenching system is limited to single-layer load arrangements with not too high workpieces. The quenching capability of such a nozzle field is extremely high. Figure 16 shows that using nitrogen of 5 bar pressure with the nozzle field has considerably shortened the cooling time from 1050 to 500 °C of 120 s, when using only gas volume flow, to only 38 s when using the nozzle field. This corresponds to a maximal HTC of about 2600 W m^{-2} K^{-1} within the first 30 s, which later stabilizes at about 2100 W m^{-2} K^{-1}.

12.05.2 Laboratory Tests to Evaluate the Cooling Intensity of Liquid Quenchants

Cooling curve analyses have been performed for many years, but standardized test procedures were established much later. In 1982, the Wolfson Heat Treatment Centre Engineering Group in Birmingham, United Kingdom, issued the 'Laboratory Test for Assessing the Cooling Curve Characteristics of Industrial Quenching Media,' which served as the basis for the first international standard ISO 9950–1995, entitled "Industrial quenching oils – Determination of cooling characteristics – Nickel-alloy probe test method." According to this standard, the probe shall have a diameter of 12.5 mm and a length of 60 mm, and shall be manufactured from INCONEL 600, a nickel-chromium alloy that does not undergo phase transformations and is oxidation resistant. A thermocouple type K (NiCr/NiAl) of 1.5 mm OD is placed with its tip at the geometrical center of the probe. The assembly of the probe is shown in Figure 17. A reference quenching fluid is recommended for initial calibration and regular reconditioning of the probe. This fluid shall be an unblended, high viscosity-index paraffinic mineral oil, completely free of any additive treatment, with prescribed physical characteristics. The surface of the probe must be passivated in an unprotected furnace atmosphere. The quantity of tested

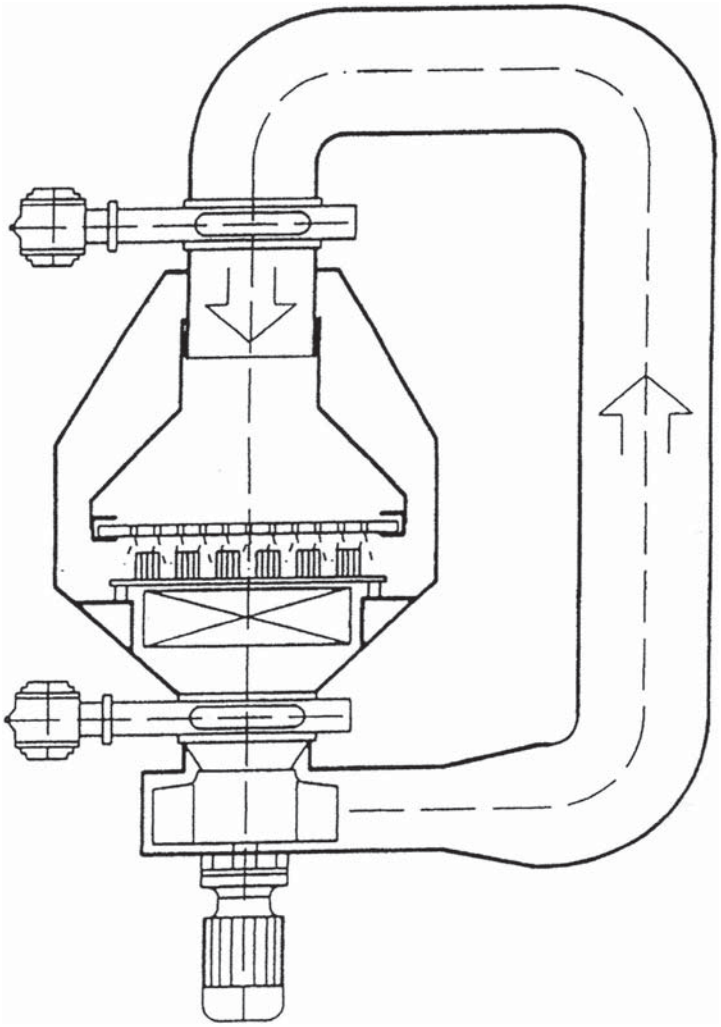

Figure 15 Schematic of a cold gas quench chamber with a nozzle field for quenching single-layer loads – IPSEN Jet–Haerter. Reproduced from Edenhofer, B.; Bouwman, J. W.; Peter, W.; Bless, F. Erfahrungen und Ergebnisse beim Gasabschrecken in einer kalten Kammer mit und ohne Düsenfeld. *HTM Härterei–Techn. Mitt.* **1997**, *52* (3), 138–143. Reprinted from *HTM Härterei–Techn. Mitt.*, with permission of Carl Hanser Verlag.

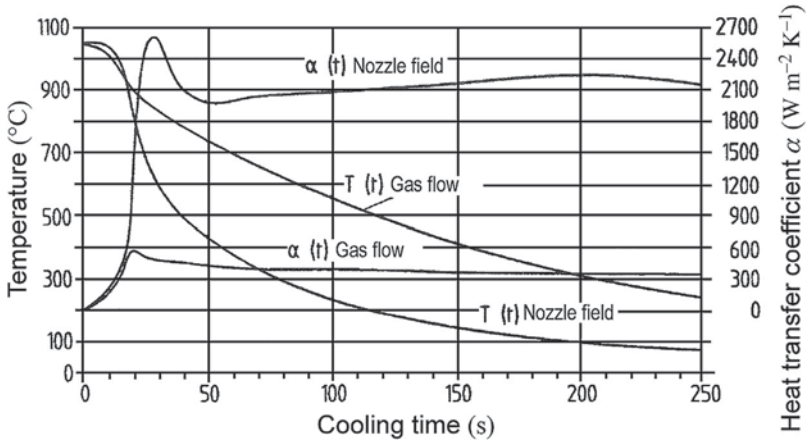

Figure 16 Comparison of cooling curves and heat transfer coefficients for quenching with 5 bar nitrogen in a cold chamber with and without a nozzle field. Reproduced from Edenhofer, B.; Bouwman, J. W.; Peter, W.; Bless, F. Erfahrungen und Ergebnisse beim Gasabschrecken in einer kalten Kammer mit und ohne Düsenfeld. *HTM Härterei–Techn. Mitt.* **1997**, *52* (3), 138–143. Reprinted from *HTM Härterei–Techn. Mitt.*, with permission of Carl Hanser Verlag.

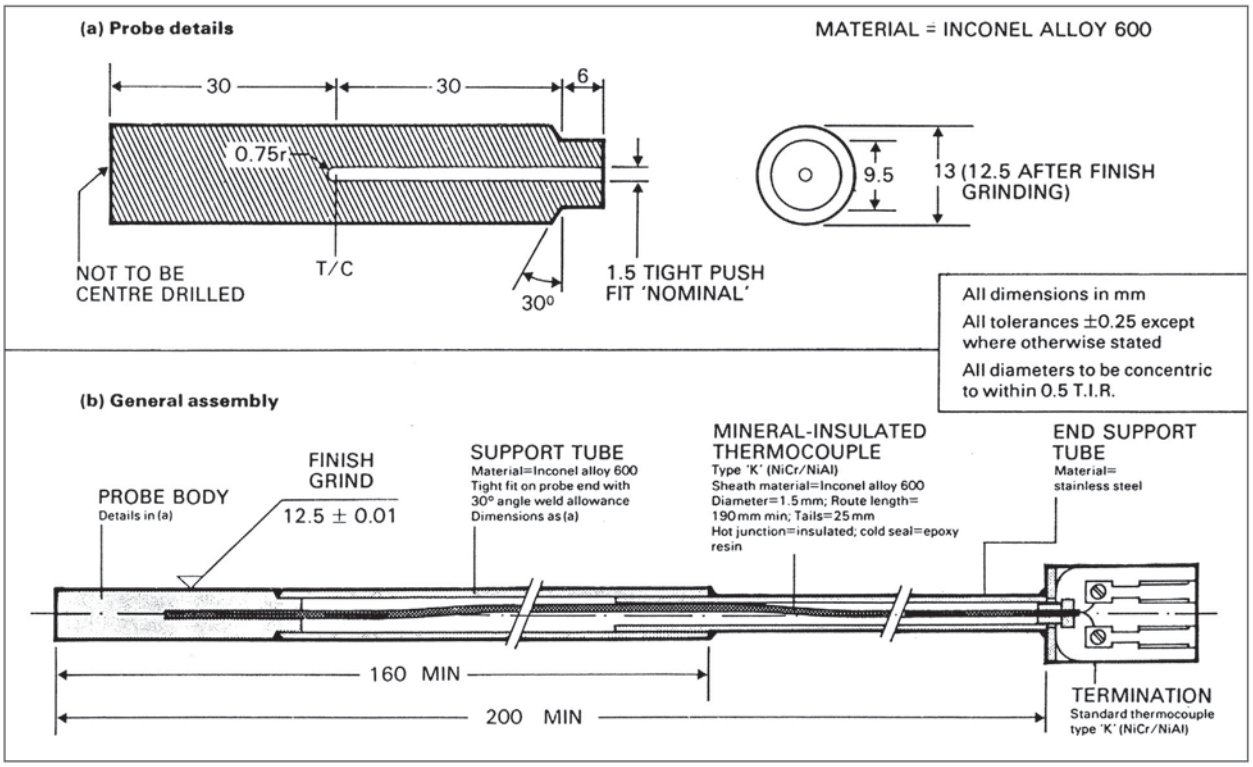

Figure 17 The assembly of the ISO 9950 probe.

quenching fluid is 2 l. The starting probe temperature is 850 °C. The quenching oil temperatures may be chosen to suit individual requirements, but to facilitate comparisons, it is recommended that tests be carried out with oil at 40 °C.

Test results are represented by the cooling curve, i.e., the temperature as a function of time, and the cooling rate as a function of the surface temperature, as shown in Figure 18. From the plot temperature versus time the following data are important: time required for the probe temperature to drop from immersion temperature to 600, 400, and 200 °C. From the plot of cooling rate, the important data are the maximum cooling rate, temperature at which the maximum cooling rate occurs, and the cooling rate at 300 °C. In the case of digital measuring, frequencies of $>20\ s^{-1}$ are recommended. It should be particularly emphasized that this test is carried out in still oil, i.e., without any agitation.

Later, in the United States, a series of relevant testing standards were issued by the ASTM:

- ASTM D 6200 (Reapproved 2007): Standard Test Method for Determination of Cooling Characteristics of Quench Oils by Cooling Curve Analysis. This standard is based on ISO 9950, uses the same probe of 12.5 mm diameter × 60 mm made of

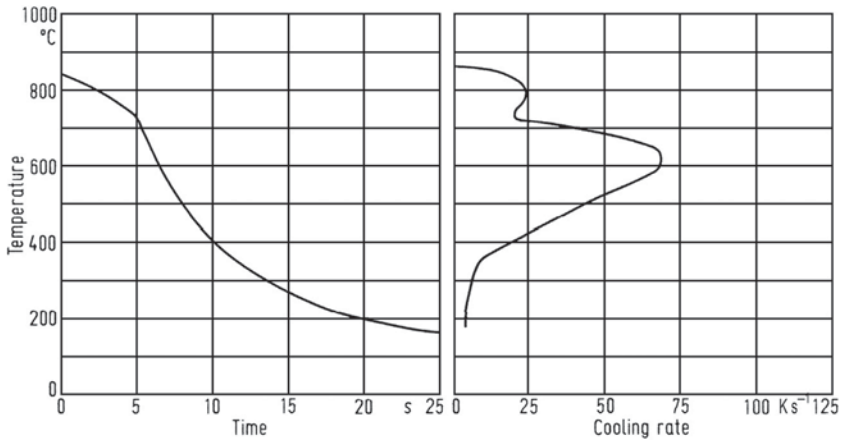

Figure 18 Typical temperature/time (a) and temperature/cooling rate (b) plots for the test probe cooled in quenching oil.

INCONEL 600, and uses the same amount of the still oil sample, 2000 ml. The starting test temperature is also 850 °C, and temperature of the oil sample is 40 °C. Interpretation of results is the same as with ISO 9950.

- ASTM D 6482–06: Standard Test Method for Determination of Cooling Characteristics of Aqueous Polymer Quenchants by Cooling Curve Analysis with Agitation (Tensi Method). Aqueous polymer solutions are subject to much greater influences by variation of physical and chemical parameters than oils, and polymeric quenching media exhibit extremely great differences in their wetting behavior. Quench severity of aqueous polymer quenchants is dependent on the concentration and molecular weight of the specific polymer, quenchant temperature, and agitation rate. Therefore, forced bath convection is always used when testing polymer solutions. The above-mentioned standard uses the agitation device developed by Prof. H. M. Tensi, see **Figure 19**. The probe and its assembly are the same as with ISO 9950. The starting test temperature is also 850 °C, and the aqueous polymer quenchant shall be heated to the desired temperature, if production testing is being performed, or to 40 °C if the reference quenching fluid is being tested. Interpretation of results is essentially the same as with ISO 9950.
- ASTM D 6549–06: Standard Test Method for Determination of Cooling Characteristics of Quenchants by Cooling Curve Analysis with Agitation (Drayton Unit). This standard is the same as ASTM D 6482, with another agitation device. Instead of Tensi's agitation device with rotating impeller, the Drayton agitation unit using a pump, see **Figure 20**, has been applied.
- ASTM D 7646–10: Standard Test Method for Determination of Cooling Characteristics of Aqueous Polymer Quenchants for Aluminum Alloys, by Cooling Curve Analysis. This test method is designed to evaluate aqueous polymer quenchants for

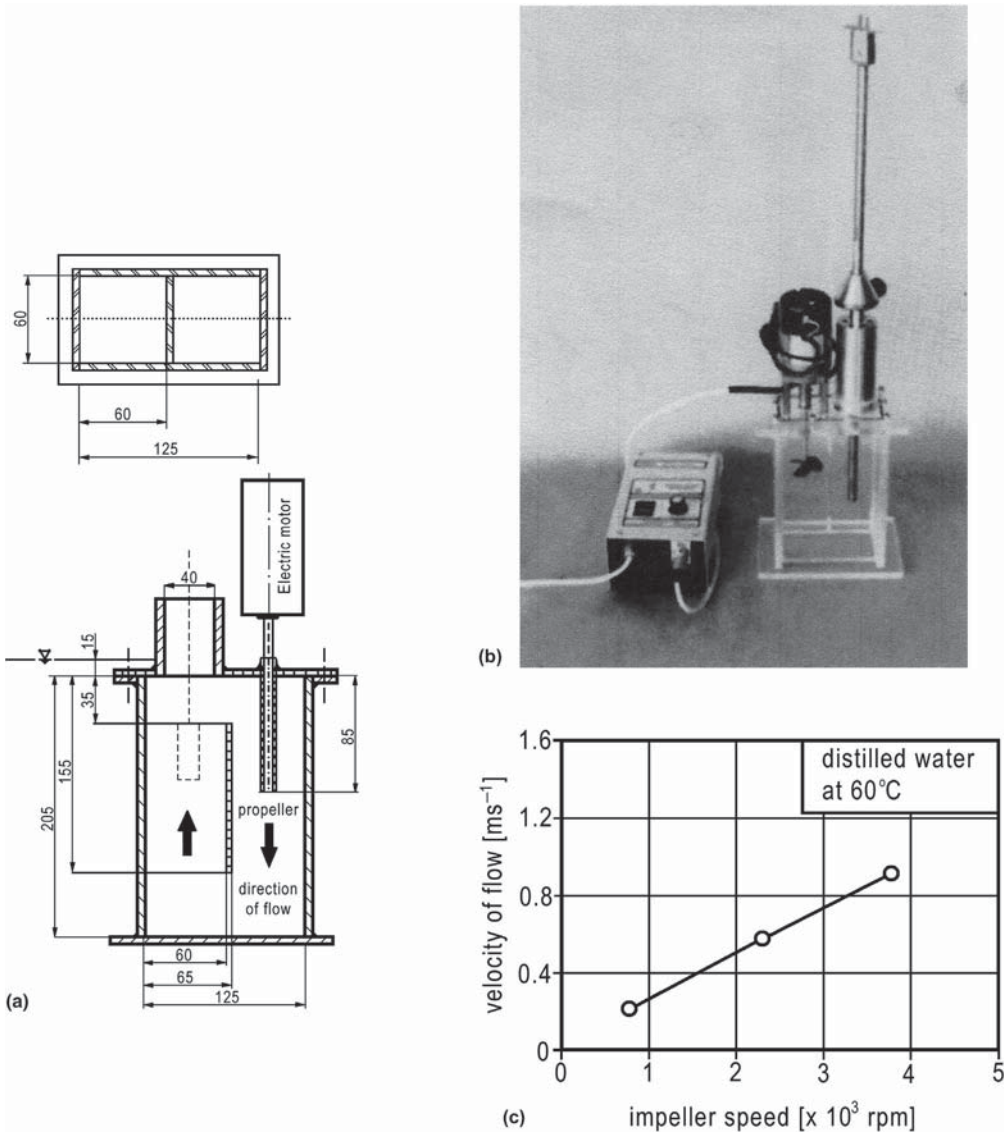

Figure 19 Schematic drawing of Tensi agitation device (a), Tensi agitation assembly (b), and correlation of flow velocity through quenching chamber and impeller rotational speed for water (c) (ASTM D 6482-06).

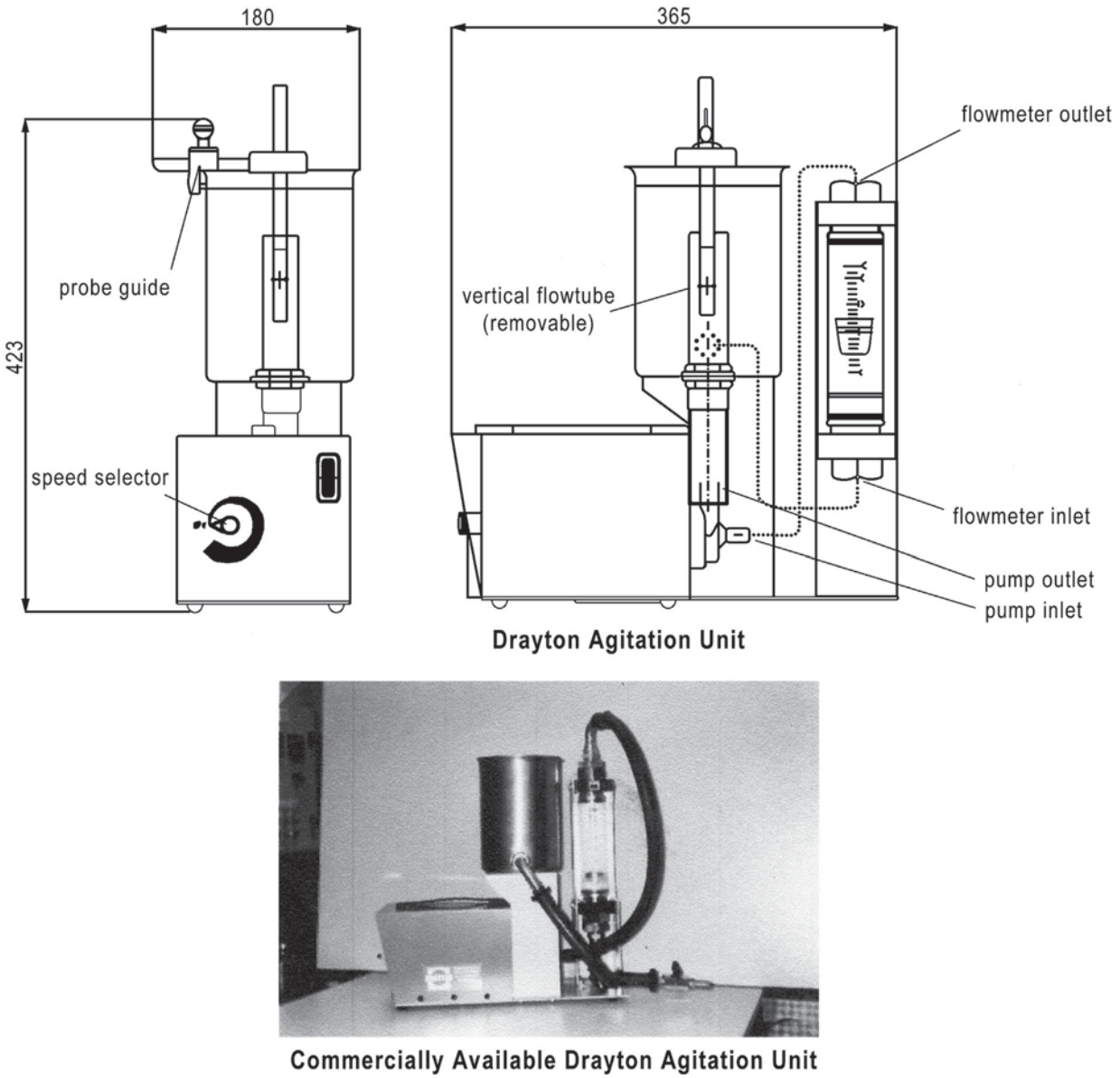

Figure 20 Drayton agitation unit (ASTM D 6549-06).

aluminum alloys in a non-agitated system. There is no correlation between these test results and the results obtained in agitated systems. The probe shall be made of pure silver having dimensions 10 mm diameter × 30 mm, as shown in Figure 21. In this case the starting test temperature is significantly lower, i.e., 500 °C, and the amount of the sample tested is only 300 ml. The aqueous polymer quenchant shall be heated or cooled to the desired temperature if production testing is being performed, or to 80 °C if the reference fluid (dioctyl phthalate) is being tested. Interpretation of results is also by cooling curves and cooling rate curves. The cooling time in seconds from 350 to 150 °C is considered the cooling performance.

There are, of course, national standards for laboratory tests in some other countries like France, Japan, China, as shown in Table 2. They use silver probes of different dimensions. Because the thermal conductivity (W m^{-1} K^{-1}) of silver is 16 times higher than for INCONEL or for stainless steel, the cooling curves measured by probes made of INCONEL or stainless steel are not comparable with those measured by silver probes.

Figure 22 shows the Japanese new silver probe, according to JIS K 2242 – method B, and some examples of cooling curves measured by this probe. Due to the small size of this probe, and the very high heat conductivity of silver, when quenched in oil this probe cools down to 200 °C in about 15–20 s, and when quenched in water, brine, or polymer solution of low concentration, in less

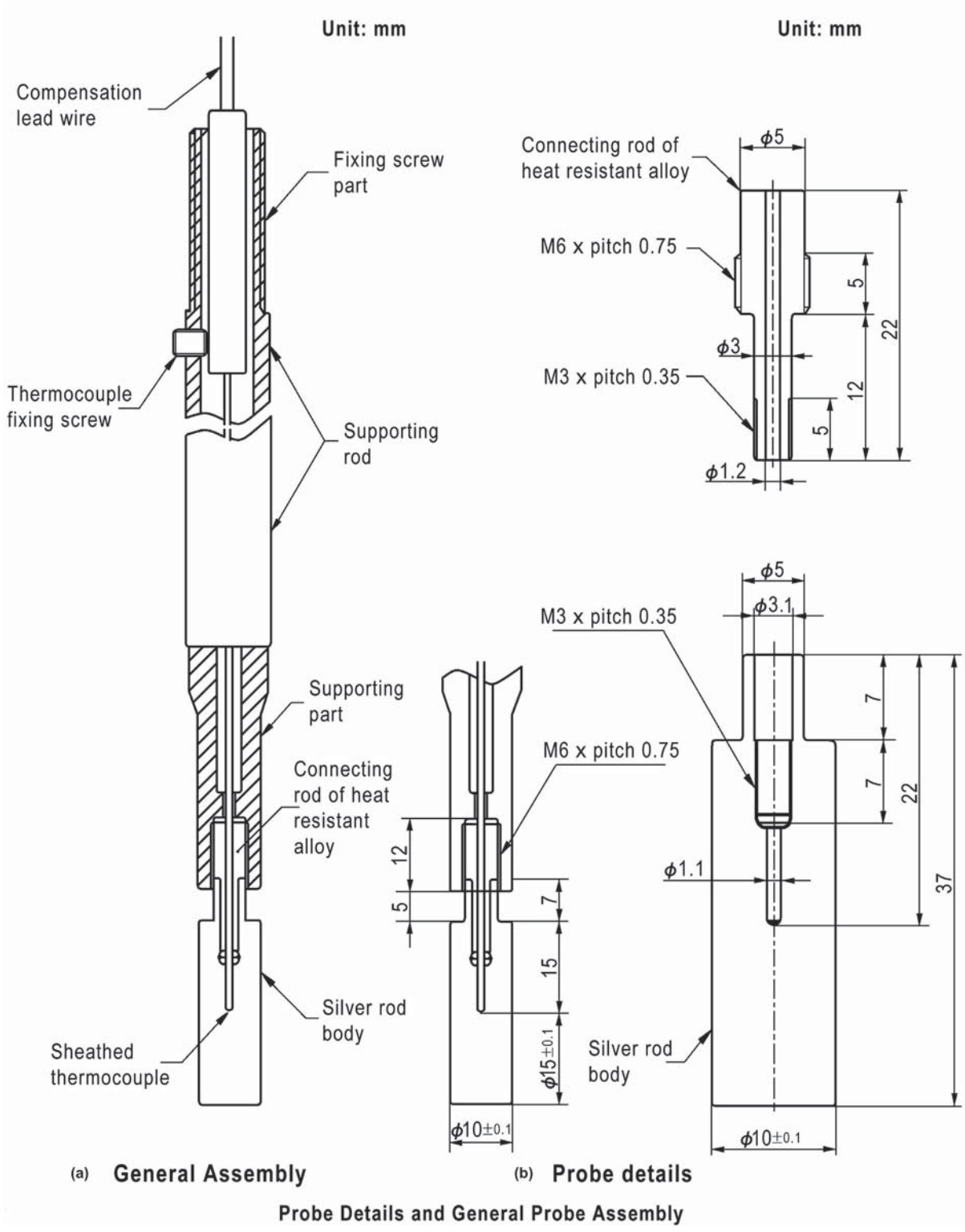

Figure 21 The probe according to ASTM D 7646-10 when testing aqueous polymer quenchants for aluminum alloys.

than 2 s. Such a probe is well suited for laboratory evaluation of the critical heat flux density of a quenching fluid in the very beginning of the cooling process.

Generally, the laboratory tests for evaluation of cooling intensity of liquid quenchants are used for the following:

- Comparison of cooling intensity among different kinds of oils, different polymer solutions, or other water-based solutions, under different conditions, with the purpose to select the optimal quenchant and its condition in the concrete case.

Table 2 Comparison of cooling curve standards

Variable	*ISO 9950:1995(E) (International)*	*AFNOR NFT–60778 (France)*	*JIS K 2242 (Japan)*	*ZB E 45003–88 (China)*
Probe alloy	Alloy 600	Silver, 99.999% Pure	Silver, 99.999% pure	Silver, 99.999% pure
Probe dimensions, (mm)	12.5 × 60	16 × 48	10 × 30	10 × 30
Standard reference oil	Reference quenching fluid[a]	Reference quenching fluid[a]	Dioctyl phthalate	Dioctyl phthalate
Vessel dimensions	115 ± 5 mm Dia.	138 mm high × 99 mm Dia.	300 ml beaker	300 ml beaker
Oil volume, (ml)	2000	800	250	250
Oil temperature, (°C)	40 ± 2	50 ± 2	80, 120, 160	80 ± 2
Probe temperature, (°C)	850 ± 5	800 ± 5	810 ± 5	810 ± 5

[a]The oil's physical properties are summarized in Table 2 in Advanced Materials & Processes **1997,** *151* (6).
Source: Table 1 in Totten, G. E.; Webster, G. M.; Tensi, H. M.; Liščić, B. Standards for Cooling Curve Analysis. *Advanced Materials & Processes* **1997,** *151* (6), 68LL–68OO. Reprinted with permission of ASM International.

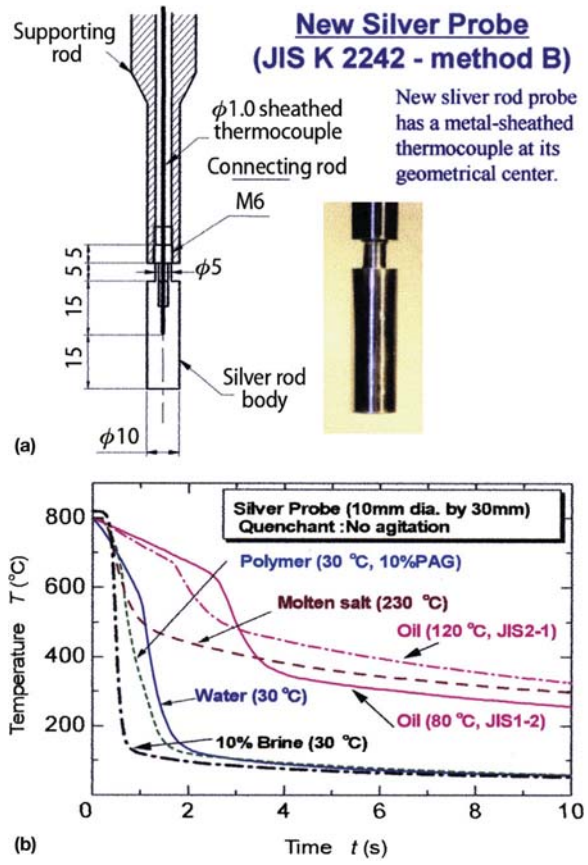

Figure 22 Japanese new silver probe according to JIS K 2242 – method B (a) and examples of cooling curves measured by this probe (b) (from M. Narazaki's lecture at the Workshop on Quenching, Karnataka Institute of Technology, Mangalore, India, 2008, with permission of M. Narazaki).

- Checking the quenching effect of currently used quenching fluids, or at developing a new type of quenchant, when adding some new component of the liquid's composition.
- Monitoring the condition of a liquid quenching bath in regular intervals, in order to prevent its deterioration.
- Computer-aided calculation of the HTC for small cylindrical pieces.

Comparing the cooling of laboratory test specimens with the cooling of real workpieces of bigger dimensions and mass, the following differences are apparent:

1. A big difference in the cooling time (while the small laboratory specimen cools to 200 °C, when quenched in still oil, in about 20–25 s, a real cylindrical workpiece of 50 mm diameter cools in equal conditions within 500–600 s).

2. As already shown in Figure 9, there is a big difference in HTC during nucleate boiling between a specimen of 12.5 mm diameter and a cylindrical workpiece of, e.g., 50 mm diameter. The smaller the specimen's diameter, the bigger are the HTC values, especially below 50 mm diameter.
3. Small laboratory test probes have small volume and relatively big surface area. They cool from the beginning so fast that the initial heat flux (q_{in}) is usually greater than the first critical heat flux density (q_{cr1}), so the film boiling is always present, which is not always the case with real workpieces.
4. The cooling time of laboratory test probes is too short to analyze and measure the wetting front advancement. For this purpose cylinders of larger diameters are used.
5. Technological conditions in a workshop (bath temperature, agitation rate, and direction) differ substantially from those in a laboratory test.

These are the reasons why the experimental results obtained with a small laboratory specimen cannot be directly transferred to the real workpieces.

12.05.3 Requirement for a Workshop Designed Test to Evaluate the Cooling Intensity of Liquid Quenchants

There are two main reasons why a generally recognized workshop designed test to evaluate the cooling intensity of all liquid quenchants, quenching conditions, and quenching techniques is necessary:

1. To compare the cooling intensity, i.e., the heat extraction dynamic of real engineering components among very many different kinds, grades, and provenance of quenchants in different conditions worldwide. Such a test method does not exist; therefore, in respect of the cooling intensity nobody can tell whether, for a concrete case, it is better to use a still mineral oil of 60 °C, a 20% concentration of a polyalkylene glycol (PAG) polymer solution of 40 °C and 0.5 m s^{-1} agitation rate, or a salt bath of 200 °C.
2. To make sure that such tests will be performed worldwide by the probe of the same shape, size, and material, under the same specified conditions, so that the comparison can be as exact as possible.

These two reasons constitute an important task of the International Federation for Heat Treatment and Surface Engineering (IFHTSE) 'Liquid Quenchants Database' project, Phase 1, as adopted at the 19th Congress of IFHTSE in 2011 in Glasgow, United Kingdom.

Once such a database exists, containing an adequate number of test results, the following will be possible:

1. Virtual comparison among different liquid quenchants and quenching conditions, in order to select the optimal one for the concrete case.
2. Use of the heat transfer data, which are similar to real engineering components, when needed as an input for computer simulation of microstructure transformations, quenched hardness, stresses, and distortion.

For modeling real engineering components, the probe for measuring and recording cooling curves should be of similar shape, mass, and dimensions (a cylinder-like probe, plate-like probe, and ring-like probe). This is important in order to follow the real heat extraction dynamic, and show the real initial heat flux density (q_{in}). All three kinds of the Liscic probe – described later, are cylindrical probes of 50 mm diameter and 200 mm length, having a ratio of length to diameter of 4:1, which ideally suits representing axially symmetric workpieces. It is particularly important to emphasize that using the Liscic probe, although having a large volume, the measured cooling curves and calculated heat flux densities are sufficiently sensitive to reflect changes in each of important quenching factors, as, e.g., the change of only the concentration of a polymer solution, as shown in Figure 23 (*13*).

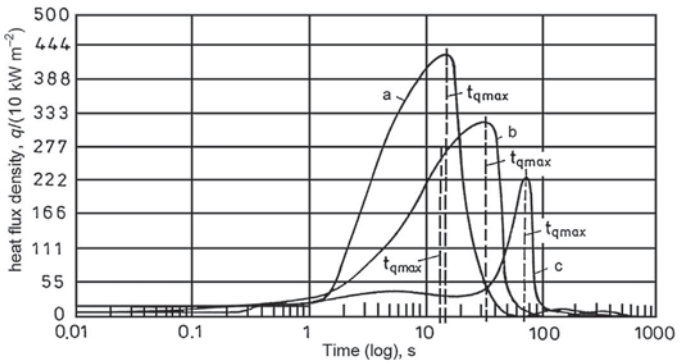

Figure 23 Quenching in PAG polymer solution of 40 °C bath temperature and 0.8 m s^{-1} agitation rate for concentrations: (a) 5%; (b) 15%; (c) 25%. Time-dependent heat flux densities are calculated from cooling curves recorded by the Liscic/Nanmac probe. Reproduced from Liščić, B. Der Wärmeentzug beim Härten – Vom unbestimmten Abschrecken in flüssigen Mitteln hin zum geregelten Wärmeentzug beim Gasabschrecken. *HTM – J. Heat Treat. Mater.* **2007**, *62* (6), 250–259. Reprinted from *Journal of Heat Treatment and Materials*, with permission of Carl Hanser Verlag.

12.05.4 Temperature Gradient Method for Evaluation of Cooling Intensity When Quenching in Workshop Conditions

The first paper on the temperature gradient method (*14*) was published by B. Liščić in 1978. The method is designed for practical measurement and recording of the cooling intensity when real engineering components are quenched under workshop conditions. It expresses the quenching intensity by continuous change in relevant thermodynamic functions, based on the heat flux density during the entire quenching process. The method is applicable to all liquid-quenching media (water, oils, brine, aqueous polymer solutions, salt baths, and fluidized beds) as well as to different quenching conditions (different bath temperatures, agitation rates, and fluid pressures). All quenching techniques, including direct immersion quenching, interrupted quenching, martempering, and austempering, can be evaluated by this method. The main aims of the method are as follows:

- It should enable a real comparison of the quenching intensity among different quenchants, quenching conditions, and quenching techniques.
- It should provide an unambiguous relation between the evaluated quenching intensity and the resulting depth of hardening.
- It should furnish as much information as possible about thermal stresses.

The tool that is used with this method in industrial practice is the Liscic/Petrofer probe, the design of which is described later. It is a cylindrical probe of 50 mm diameter and 200 mm length, instrumented with three thermocouples placed within the same radius at the half length cross section.

12.05.4.1 Theoretical Principles

The method itself known in the literature as the temperature gradient method is based on the known physical rule that the heat flux at the surface of a body is directly proportional to the temperature gradient at the surface multiplied by the thermal conductivity of the material of the body being cooled:

$$q = \lambda \frac{\partial T}{\partial x},$$

q = heat flux density (W m^{-2}),
λ = thermal conductivity of the body material (W m^{-1} K^{-1}),
$\frac{\partial T}{\partial x}$ = temperature gradient inside the body at the body surface perpendicular to it (K m^{-1}).

One thermocouple is placed 1 mm below the surface, the second one 4.5 mm below the surface, and the third one at the center of the cross section. The probe is made of INCONEL 600, the microstructure of which does not change during heating and cooling, so there is no latent heat because of microstructure changes.

For the test, the probe is heated to 850 °C until the central thermocouple reaches this value, then transferred quickly to the quenching bath and immersed vertically. The probe is connected to a data acquisition system including a personal computer. The data acquisition card contains three A/D converters and amplifiers, with a program enabling digital recording of all three thermocouple signal outputs and simultaneously drawing in real time three cooling curves, as shown in **Figure 24** (*15*).

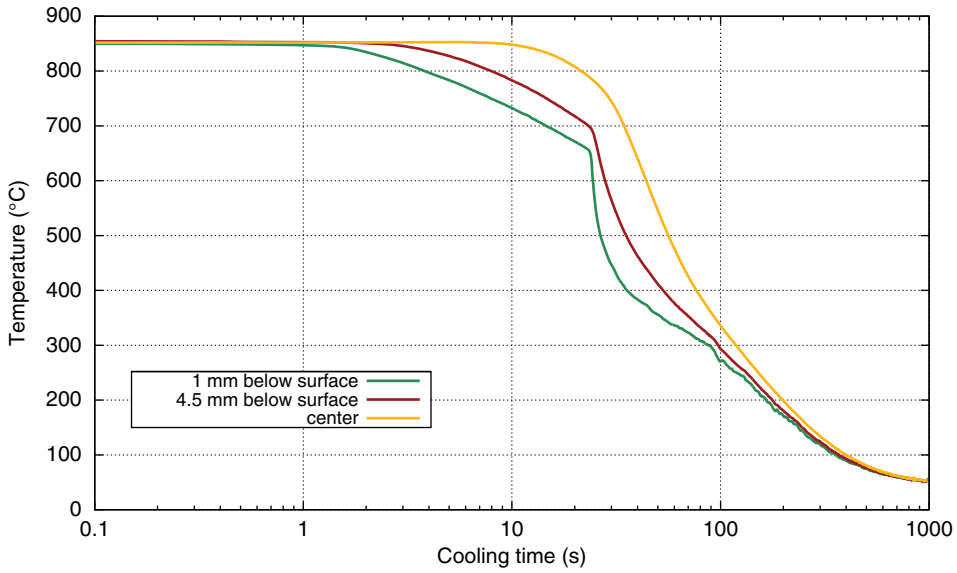

Figure 24 Cooling curves measured by the Liscic/Petrofer probe quenched in low viscous accelerated oil of 50 °C with medium agitation (data courtesy of PetroFer GmbH). Reproduced from Liscic, B.; Filetin, T. Measurement of Quenching Intensity, Calculation of Heat Transfer Coefficient and Global Database of Liquid Quenchants. *Mater. Eng. – Materialove inz inierstvo 2012, 19*, 52–63.

The temperature gradient method can be used also with probes of same design (with the ratio $L/D = 4{:}1$) having different diameters. Figure 25 shows results with probes of (a) 20 mm diameter × 80 mm and (b) 80 mm diameter × 320 mm, quenched in low viscous accelerated oil of 50 °C with medium agitation.

Irrespective of the probe diameter and mass of the probe, the temperature gradient method exhibits two very important features:

a. It displays clearly the dynamic of heat extraction during the whole quenching process.
b. It shows the initial heat flux density (q_{in}) at the beginning of cooling.

Let us discuss these features:

a. The probe of 80 mm diameter × 320 mm has a mass of 13.6 kg, a surface area/volume ratio of only 56 m^{-1}, and a heat capacity of 6045 J K^{-1}, representing a case of great volume (and heat capacity) and relatively small surface area.

   The probe of 20 mm diameter × 80 mm has a mass of only 0.2 kg, a surface area/volume ratio of 225 m^{-1}, and a heat capacity of only 94 J K^{-1}, representing a case of small volume (and heat capacity) and relatively big surface area. The heat capacity of the larger probe is 64 times greater than the heat capacity of the smaller probe!

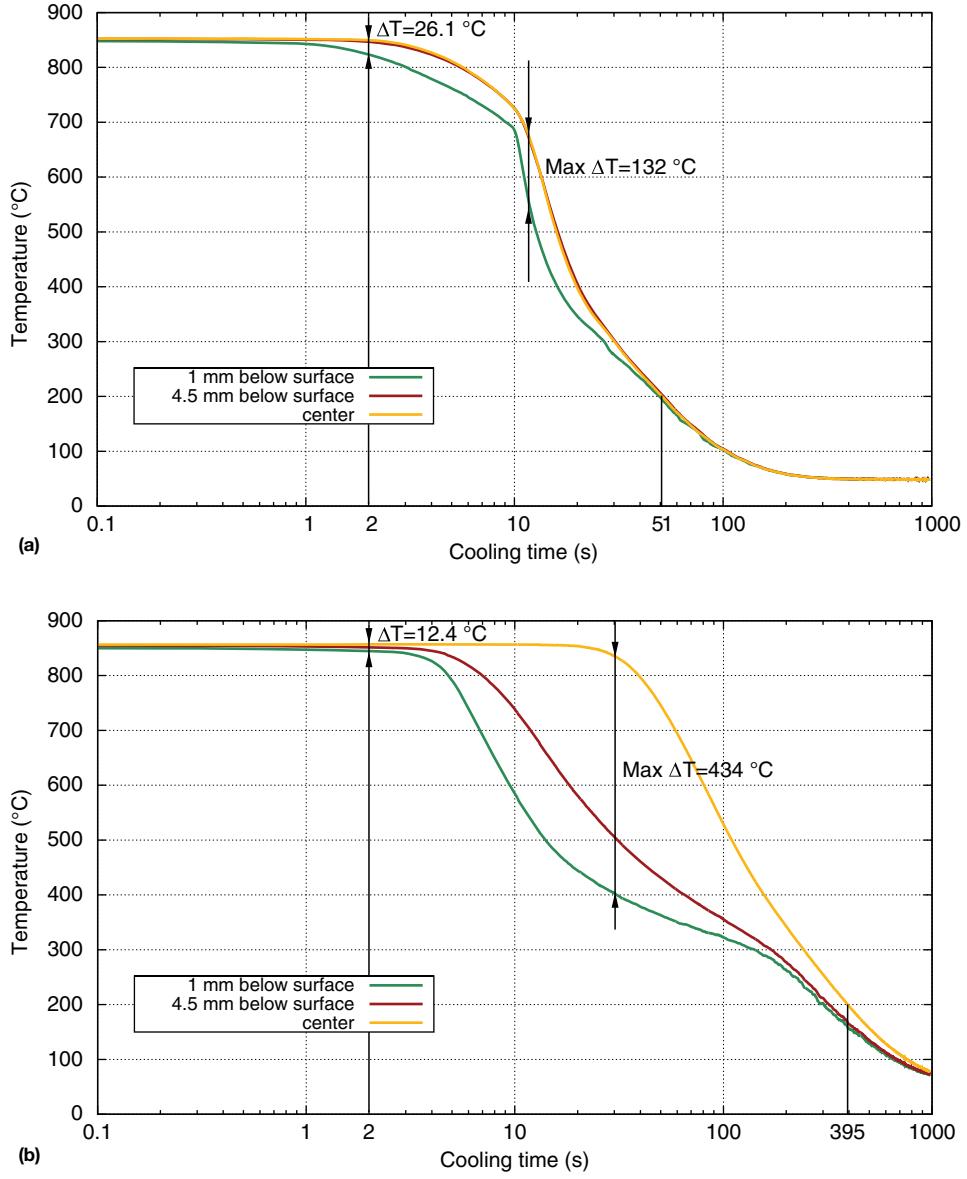

Figure 25 Cooling curves measured by the probes of (a) 20 mm diameter × 80 mm and (b) 80 mm diameter × 320 mm, of the same design as the Liscic/Petrofer probe, quenched in low viscous accelerated oil of 50 °C with medium agitation (data courtesy of PetroFer GmbH). Reproduced from Liscic, B.; Filetin, T. Measurement of Quenching Intensity, Calculation of Heat Transfer Coefficient and Global Database of Liquid Quenchants. *Mater. Eng. – Materialove inz inierstvo 2012, 19*, 52–63.

One would expect that the cooling time to 200 °C of the larger probe would be several tens of times longer than that of the smaller probe, but it is only 7.7 times longer, as can be seen on **Figure 25(a)** and **25(b)** (395 s for the larger probe, against 51 s for the smaller probe). The reason why it is so can be explained by comparing the temperature gradients during quenching of both probes. The smaller probe cools from the beginning faster than the larger one, but later the maximal temperature gradient within the larger probe (434 °C) is much greater than within the smaller probe (132 °C), which causes greater heat fluxes within the larger probe. This is the reason why the cooling time of the larger probe is only 7.7 times longer, although its heat capacity is 64 times greater.

b. Regarding the initial heat flux density q_{in}, one can compare it in the beginning of cooling. For instance, 2 s after immersion of the smaller probe, see **Figure 25(a)**, the temperature gradient between 1 mm below the surface and the center was already 26.1 °C. For larger probe at the same time, the temperature gradient between 1 mm below the surface and the center was only 12.4 °C, as shown in **Figure 25(b)**, making a big difference in the initial heat flux density q_{in}.

This analysis shows how the Liscic/Petrofer probe, based on the temperature gradient method, can precisely describe the dynamic of heat extraction during the whole quenching process, as well as determine the real initial heat flux density, depending on the volume (mass) of the workpiece. To calculate the HTC based on experiments with the Liscic/Petrofer probe, the one-dimensional (1D) inverse heat conduction method is used.

12.05.5 Temperature Measurement and Unavoidable Physical Phenomena When Measuring Transient Temperatures at Quenching

The accuracy of temperature measurement depends on how precisely thermocouples (TC) are instrumented into metallic specimens and how perfect the contact is between the TC and the specimen material (*16*). It is shown that the errors of temperature measurement can be large. The differences can be explained by the use of a ceramic sheath and a not-welded TC junction.

Figure 26 shows four types of TCs instrumented differently into metal used for investigation by Tensi, Totten, and Stich (*17*). The TC response in this case is represented by the cooling curves and by the cooling rate curves. In **Figure 27(a)**, 1 refers to a sheathed TC with insulated measuring junction (see **Figure 26(a)**); 2 refers to a sheathed TC with a measuring junction welded to the probe (see **Figure 26(b)**). In **Figure 27(b)**, 3 denotes a TC with separated wires, a ceramic tube, and a welded junction to the probe. It is evident that welded junction substantially improves the sensitivity of the TC. Despite the welded tip, the TC placed within a ceramic sheath shows almost 2 times less the cooling rate as compared with the TC without the ceramic sheath, as **Figure 27(b)** (curves 2 and 3) shows.

In order to obtain a good sensitivity and undistorted cooling curve temperature measurement, the following conditions, according to Ref. (*17*), are necessary:

- Good thermal contact between the TC tip and the volume of the probe.
- The amount of material removed to make TC holes should be minimized (the smaller the hole, the better the thermal contact between the probe and the TC).
- Similar thermal properties of probe material and material used to construct the TC.

While the described problem can be intentionally avoided or at least minimized, by the precise manufacturing of the probe, there are three following unavoidable physical phenomena when measuring transient temperature at quenching.

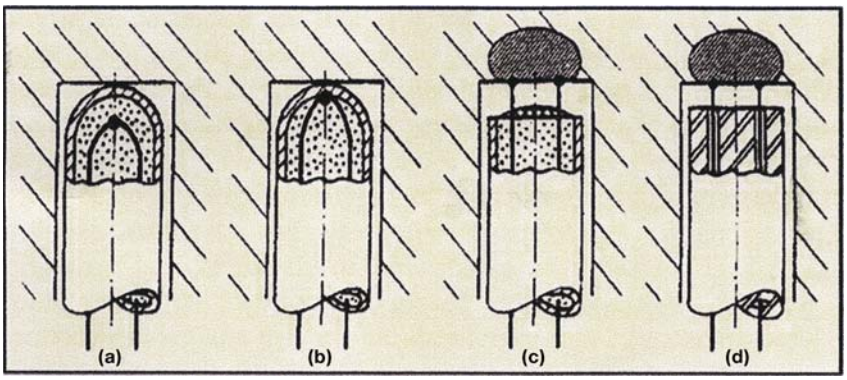

Figure 26 Four types of thermocouples differently instrumented into metal for investigation. Reproduced from Kobasko, N. I. Effect of Accuracy of Temperature Measurement on Determination of Heat Transfer Coefficient during Quenching in Liquid Media. *J. ASTM Int.* **2012**, *9* (2). Reprinted, with permission, from *Journal of ASTM Intl.*, copyright ASTM International, 100 Barr Harbor Drive, West Conshohocken, PA 19428.

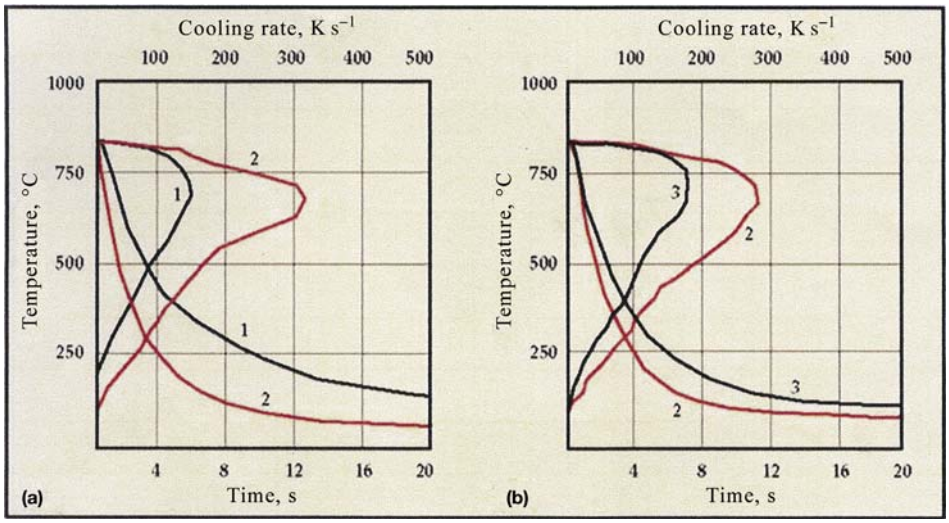

Figure 27 Comparison of the response sensitivity of thermocouples having the same outer diameter (2 mm). Reproduced from Kobasko, N. I. Effect of Accuracy of Temperature Measurement on Determination of Heat Transfer Coefficient during Quenching in Liquid Media. *J. ASTM Int.* **2012**, *9* (2). Reprinted, with permission, from *Journal of ASTM Intl.*, copyright ASTM International, 100 Barr Harbor Drive, West Conshohocken, PA 19428.

12.05.5.1 Damping Effect

In the case of very fast-changing temperatures at the surface of a body, the maximum values will not be recorded, if temperature is measured below the surface. The greater the distance from the surface, the greater is the damping effect, as shown in Figure 28. As is known, quenching in a polymer solution provokes very turbulent events on the surface, which are damped at 1 mm below the surface and even more damped at 4.5 mm below the surface.

12.05.5.2 Time Lag

This is the time required for a sensor at a distance l below the surface to sense changes in surface conditions, which are delayed because of thermal diffusivity. It can be calculated as follows:

$$\frac{a\,\delta t}{l^2} = 0.06,$$

i.e.,

$$\delta t = \frac{0.06\,l^2}{k/\rho c},$$

δt = Time lag (s)
l = Distance from surface (m)
a = Thermal diffusivity (W m^2 J^{-1})
k = Thermal conductivity (W m^{-1} K^{-1})
c = Specific heat (J kg^{-1} K^{-1})
ρ = Density (kg m^{-3})

12.05.5.3 Thermocouple Response Time

During very fast temperature changes on the surface, the conventional sheathed TC below the surface may not follow the real-time temperature changes because of its slow response time.

A TC of, e.g., 3.175 mm outer diameter, has two round wires of 0.5 mm diameter insulated from each other by about 0.38 mm of alumina oxide (Al_2O_3), as shown in Figure 29(a) (*18*). The Al_2O_3 is an insulator having very low thermal conductivity. Once it is heated up, it cools relatively slowly (it acts as a heat reservoir). As a result, at any instant of time during the rapid cool-down phase, the Al_2O_3 is hotter than the thermal junction. It then tends to inhibit the cool-down of the junction, and hence this TC indicates a temperature that is higher than the real temperature at that instant of time.

According to definition, the time constant of a TC (63.2% of the total output signal, when subjected to a step change in temperature) for the TC described is 3.5 s. In order to reach 99% of its full output, the time constant has to be multiplied by 5, which makes 17.5 s, as shown in Figure 29(b). Therefore, any temperature change that occurs in less than 17.5 s will not be read accurately; i.e., it will be delayed in time. It should be mentioned, however, that the time constant is determined by rapid immersion of the TC alone into hot oil bath, while in the case of a quench probe, the TC is embedded in the probe's body and cools down together with it. Therefore, it is questionable whether or not the time constant described is fully applicable in this case.

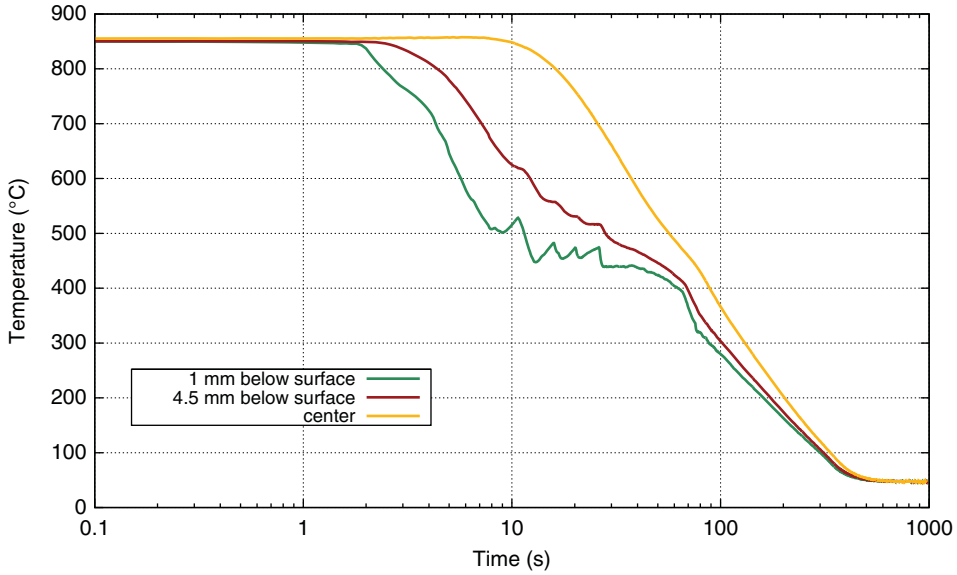

Figure 28 Damping effect when a Liscic/Petrofer probe of 50 mm diameter was quenched in a polymer solution of 35 °C with agitation. Data courtesy of PetroFer GmbH.

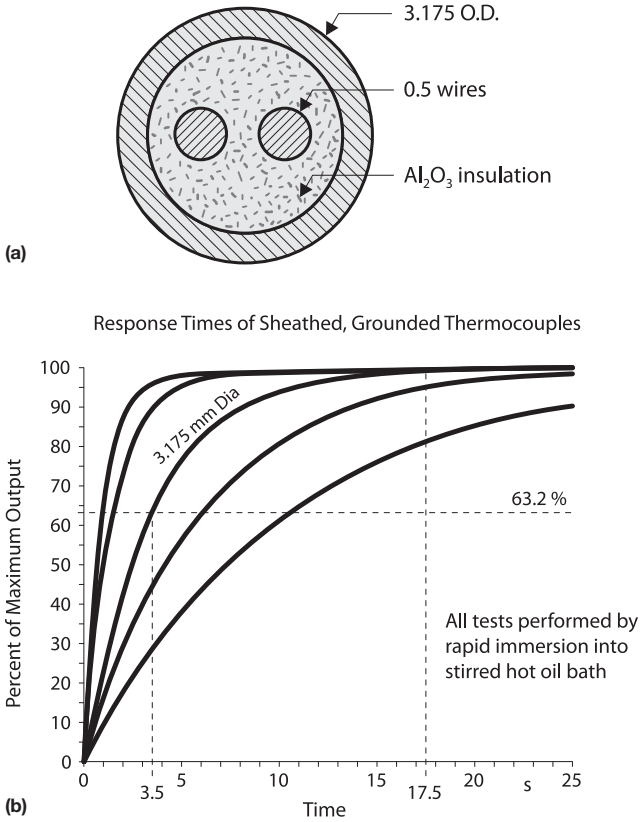

Figure 29 Cross section of the 3.175 mm outer diameter stainless-steel sheathed thermocouple (a); response times of sheathed grounded thermocouples having different outer diameters (b), according to Nanigian, J. Improving Accuracy and Response of Thermocouples in Ovens and Furnaces. In *Proc. of Intl. Heat Treating Conference: Equipment and Processes, Schaumburg, Ill.*; Totten, G. E.; Wallis, R. A., Eds., 1994, pp 171–174. Reprinted, with permission of ASM International. Reproduced from Liscic, B.; Singer, S.; Smoljan, B. Prediction of Quench-Hardness within the Whole Volume of Axially Symmetric Workpieces of Any Shape. *J. ASTM Int.* **2010,** *7* (2).

In any case, the position of the TC should be as close as possible to the surface, and to minimize the response time, the shielded and grounded TC of the smallest possible outer diameter (see Figure 29(b)) should be used, for measuring fast-changing temperatures (*19*).

12.05.6 Design and Characteristics of the Liscic Probes

There are three different Liscic probes, all of them having the same dimension, 50 mm diameter × 200 mm, instrumented with thermocouples at half the length of the probe. All are based on the temperature gradient method, but every one of them has been designed specifically for a concrete purpose.

12.05.6.1 The Liscic/Petrofer Probe for Industrial Application When Liquid Quenchants are Used

This probe is used within a program called temperature gradient system (TGS) for hardness prediction in quenched axially symmetrical workpieces of any shape.' Figure 30 shows the Liscic/Petrofer probe made of INCONEL 600, produced by the German company PetroFer Chemie H. R. Fischer GmbH + Co. KG, Hildesheim. It is instrumented with three TCs along the same radius at half the length of the cross section, at 1 mm below the surface, 4.5 mm below the surface, and in the center. The acquisition software allows measuring temperatures of all three TCs with a frequency of 0.02 s (50 measurements per second) during the whole quenching process, and drawing simultaneously in real time three cooling curves, as shown in Figure 24.

For calculation of the HTC, the measured temperatures at 1 mm below the surface are used as an input for the 1-D inverse heat conduction finite volume (FV) calculation.

After calculation of the HTC and the surface temperature of the probe, the TGS program enables a comprehensive analysis of the quenching process using the following thermodynamic functions:

- Comparison between the calculated surface temperature (T_s) and the measured temperatures at 1 mm below the surface, 4.5 mm below the surface, and the center (Figure 31(a)).
- Temperature differences versus time between the center and the surface, between the center and 1 mm below the surface, and between the center and 4.5 mm below the surface (Figure 31(b)). These graphs are very important when thermal stresses are to be calculated.

The third module of the TGS program enables prediction of the achieved hardness after quenching in every point of the longitudinal section of an axially symmetrical workpiece of any shape. The prerequisites for using this module are the following steps:

- A half of the contour of the workpiece has to be drawn on a computer screen.
- The steel grade has to be selected, which automatically determines its hardenability by relevant Jominy test results.
- The HTC has to be calculated for the selected quenching test performed by the Liscic/Petrofer probe.

Figure 32 shows the results of hardness prediction across half of the whole longitudinal section of a complex axially symmetric workpiece made of steel grade AISI 5140, quenched in oil, (a) when the workpiece is without a central hole, and (b) when the workpiece has a central hole of 20 mm diameter (*20*). The prediction of the quenched hardness, using colors to denote the quenched hardness (HRC) index, which is a unique method, shows hardness differences exactly between slim and thick sections and especially sharp corners, as well as areas of insufficient hardness. Note that the area of insufficient hardness is much smaller at the workpiece with a central hole, because also the cooling from inside the hole has been accounted for.

The customer who possesses the Liscic/Petrofer probe and TGS program can perform tests under practical workshop conditions, calculate relevant HTCs, and create his/her own database. The TGS program incorporates a database for a large number of structural

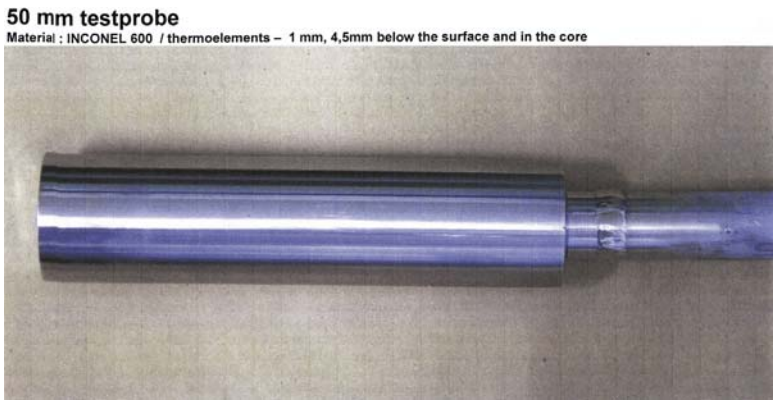

Figure 30 The Liscic/Petrofer probe. Courtesy of PetroFer GmbH.

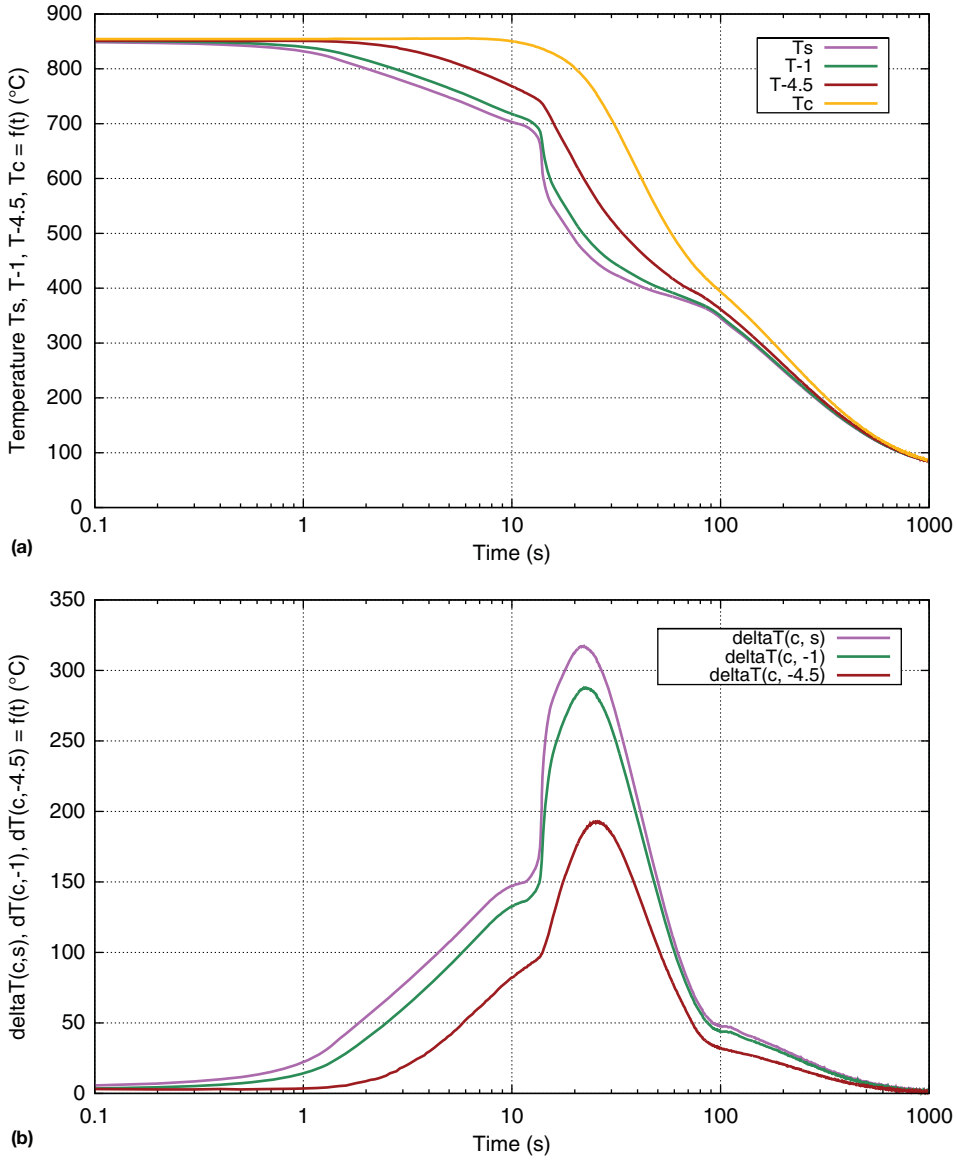

Figure 31 Thermodynamic functions between calculated surface temperatures and other calculated functions at 1 mm below the surface, 4.5 mm below the surface, and the center, as described in the text. By courtesy of PetroFer GmbH.

steel grades with relevant Jominy hardenability data. This enables one to predict and compare quenched hardness for different quenchants, quenching conditions, and different steel grades.

12.05.6.2 The Ipsen–Liscic Flux Sensor for High-Pressure Gas Quenching in Vacuum Furnaces

The Ipsen–Liscic flux sensor was developed in cooperation with the German company Ipsen International GmbH, 47514 Kleve, in order to calculate the HTC during cooling in vacuum furnaces at HPGQ directly in a batch of workpieces. Figure 33 shows the scheme of the sensor, which is a cylinder of 50 mm diameter and 200 mm length instrumented with three TCs at the half length cross section. It is made of an austenitic stainless steel. The ratio L/D of 4:1 ensures that the heat loss through the sensor's ends is negligible. By measuring the temperature at a point near the surface of the sensor, the heat flux density that passes through the sensor's surface can be calculated without any further measurement.

This was the reason that this sensor is called 'Heat Flux Sensor' (Wärmefluss–Sensor in German).

Two TCs are placed 2.4 mm below the surface at opposite sides, and the third TC is in the center. Because the cooling in vacuum furnaces by convection only is much slower than in liquid quenchants, the response time of the TCs was not critical, so all TCs have an outer diameter of 3.2 mm. All three temperatures are measured and stored in a data-logger, shown in Figure 34.

The opposite position of temperature measuring points enables the sensor to be used, not only in the standing position, but also in the lying position.

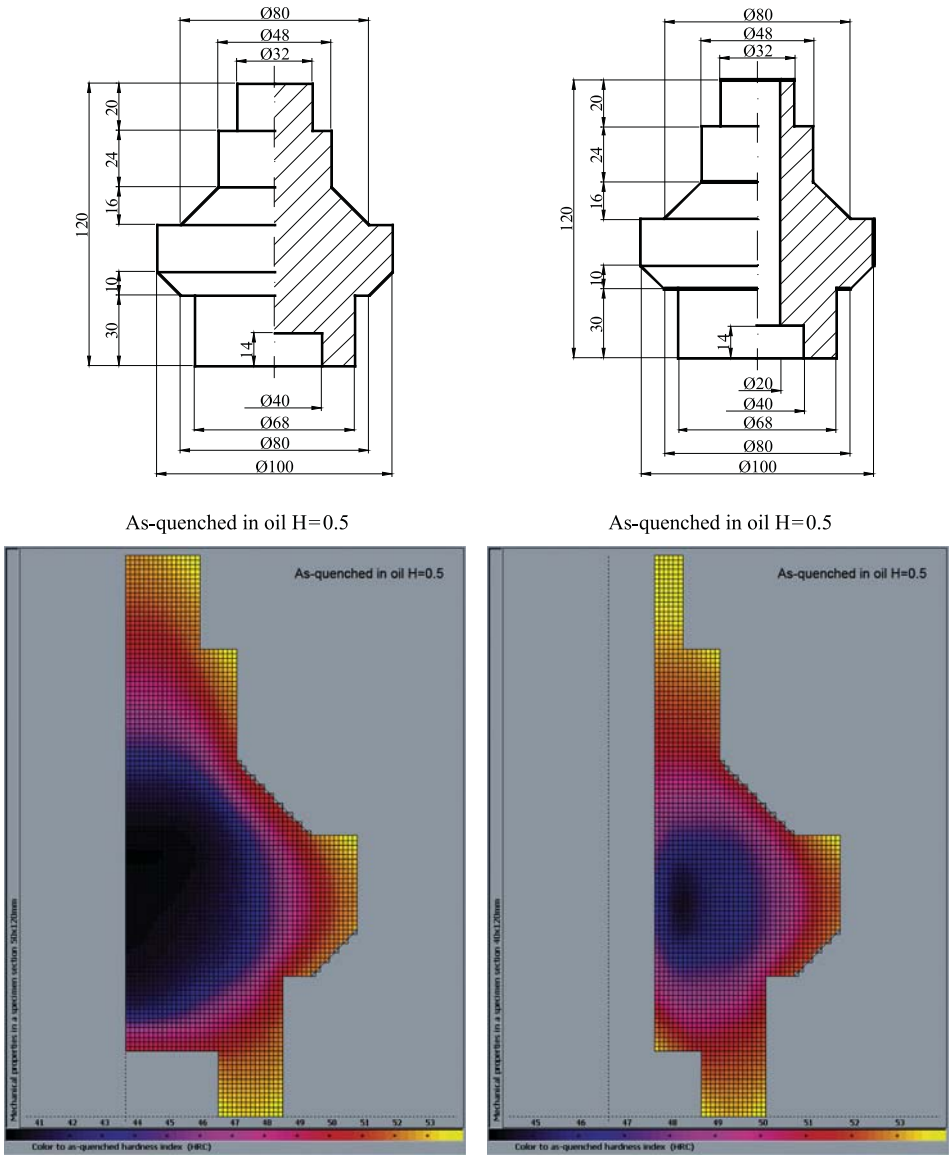

Figure 32 Result of hardness prediction across a half of the axial section of a complex axially symmetric workpiece. Reproduced from Liščić, B. System for Process Analysis and Hardness Prediction When Quenching Axially-symmetrical Workpieces of Any Shape in Liquid Quenchants. In *Materials Science Forum*, Vols. 638–642, Chandra, T.; Wanderka, N.; Reimers, W.; Ionescu, M., Eds.; *THERMEC 2009, 6th International Conference on Processing & Manufacturing of Advanced Materials*, Berlin, Germany, *Aug. 25–29, 2009*; Trans Tech Publications, 2010, pp 3966–3974. Reprinted with permission of Trans Tech Publications.

Figure 35 is a schematic presentation of a hot chamber vacuum furnace with the flux sensor in the middle of the heating/cooling chamber showing the system of measuring the cooling gas temperature.

To calculate the HTC it is necessary to determine the gas temperature in the vacuum furnace. If the gas temperature is measured inside the heating chamber in the vicinity of the flux sensor, the measured temperature in the beginning of cooling is influenced by the radiation heat from surrounding workpieces, and for the first 50–100 s would be substantially higher than the real gas temperature. Therefore, the gas temperature is measured by a fixed TC before the cooled gas enters the heating chamber (T_{ge}) and by another fixed TC when the hot gas exits from the heating chamber (T_{ga}). The value $(T_{ga} + T_{ge})/2$ is in practice considered the real gas temperature.

Figure 36 shows the HTCs based on measurements with the Ipsen–Liscic flux sensor in an empty Ipsen vacuum furnace for different gases and gas pressures. The experiments have been done at the cooling gas velocity of 25 m s^{-1} and the results are in good agreement with theoretical formulas. Further experiments have shown that the weight of a batch has influence on the calculated HTC.

At the same cooling conditions the increase of the batch weight lowers the HTC values. An important factor is the position of the flux sensor with respect to the gas flow direction. In the lying position of the sensor, the HTC value is greater on the surface, which is

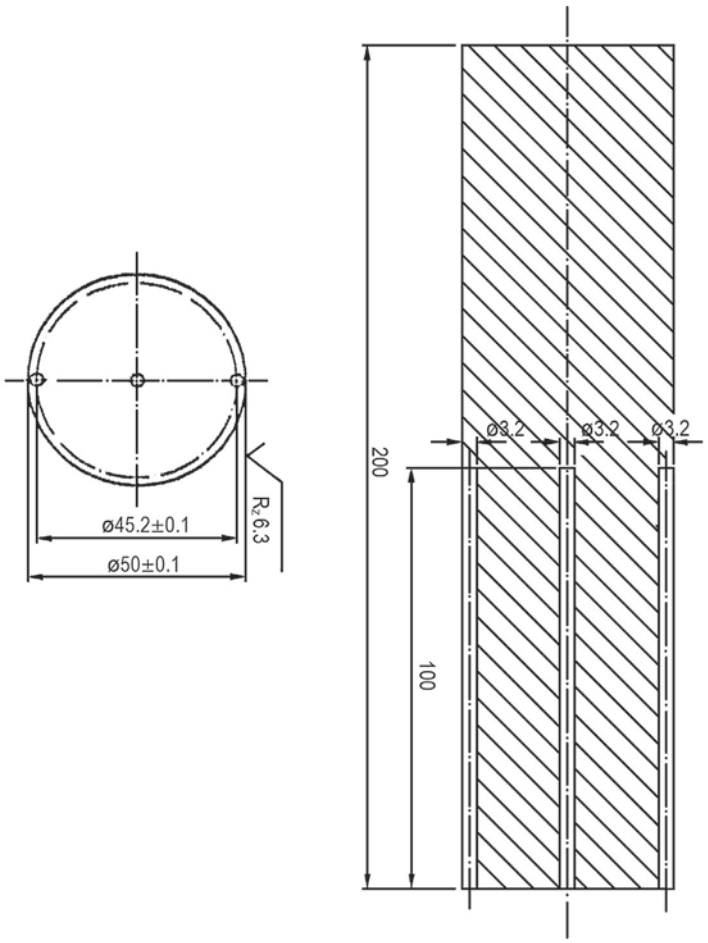

Figure 33 Schematic of the Ipsen–Liscic sensor. Reproduced from Edenhofer, B. Steuerung der Hochdruckgasabschreckung mittels Wärmestromsensor. *HTM Härterei–Techn. Mitt.* **1996**, *51* (5), 314–318. Reprinted from *HTM Härterei–Techn. Mitt.*, with permission of Carl Hanser Verlag.

Figure 34 The data-logger with the Ipsen–Liscic sensor. By courtesy of Ipsen, GmbH, Kleve.

exposed to the direct gas flow, than on the other surface, which is in shadow. In the standing position, both near-surface TCs show the same HTC.

By using the calculated HTC for the flux sensor, the temperature profiles in other workpieces in a batch can be calculated if two following conditions are met:

- The HTC values of the flux sensor must be measured and calculated near the respective workpiece.
- The geometry of the workpiece must be similar to the shape of the flux sensor. Regarding the mass of the workpiece, experiments have shown good agreement at workpieces having cross sections smaller than the flux sensor, while for workpieces with much larger cross sections an HTC correction is necessary.

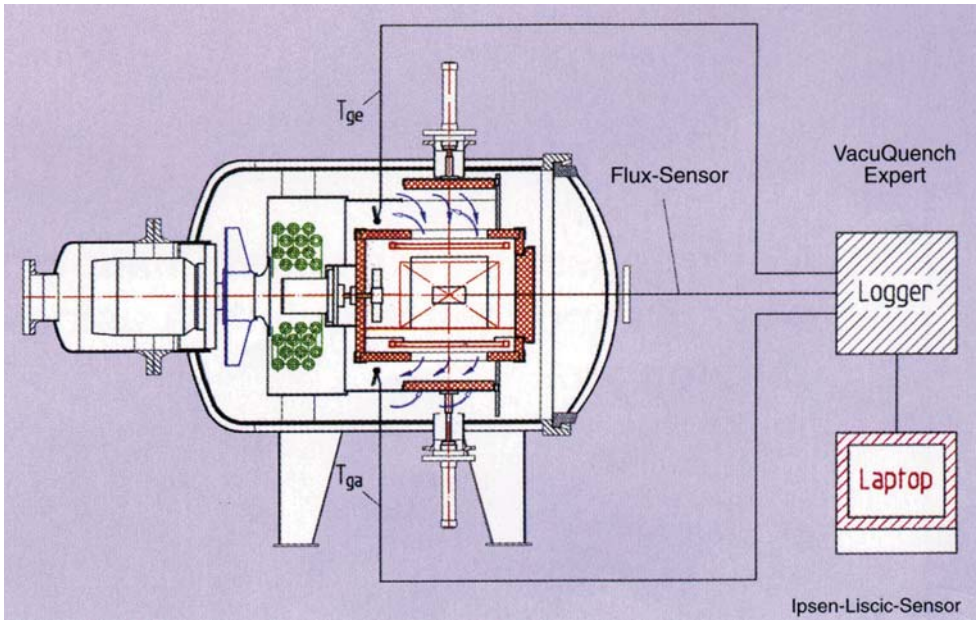

Figure 35 Measuring of the cooling gas temperature in a hot chamber vacuum furnace. Reproduced from Edenhofer, B. Steuerung der Hochdruckgasabschreckung mittels Wärmestromsensor. *HTM Härterei–Techn. Mitt.* **1996**, *51* (5), 314–318. Reprinted from *HTM Härterei–Techn. Mitt.*, with permission of Carl Hanser Verlag.

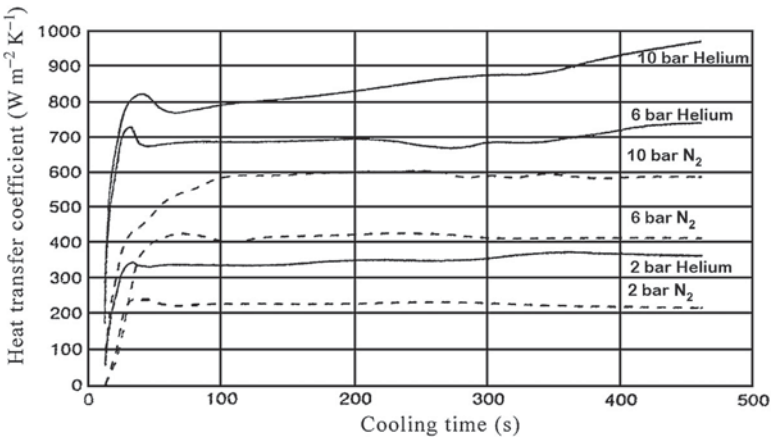

Figure 36 Heat transfer coefficients calculated from measurements by the Ipsen–Liscic Flux-Sensor, in an empty vacuum furnace for different gases and gas pressures. Reproduced from Edenhofer, B. Steuerung der Hochdruckgasabschreckung mittels Wärmestromsensor. *HTM Härterei–Techn. Mitt.* **1996**, *51* (5), 314–318. Reprinted from *HTM Härterei–Techn. Mitt.*, with permission of Carl Hanser Verlag.

Relatively good agreement between HTC values calculated based on the measurement by the flux sensor and the temperature profiles calculated in relevant workpieces proves the possibility to use this method for prediction of the cooling parameters when a new batch of workpieces has to be quenched, enabling the control of the quenching process.

The company Ipsen has developed a program called 'Vacu-Quench Expert' (*21*), the algorithm of which is shown in **Figure 37**.

Following the details described in this algorithm, the quenching parameters can be determined for a new batch by selecting these parameters from a data file of previously quenched batches, if a new batch is of a similar weight and is quenched with a similar HTC as the batch selected from the data file.

12.05.6.3 The Liscic/Nanmac Probe for Scientific Investigation and Quenching Process Analysis

The Liscic/Nanmac probe was developed in cooperation with the American company Nanmac Corp., Framingham, Massachusetts. The main difference of this probe, which is unique, is that the temperature at the very surface is not calculated, but measured. In this way all the phenomena unavoidable with probes having thermocouples embedded below the surface have been avoided. There is neither damping effect nor time lag. Because the TC at the very surface is of special design (US Patent 2,829,185) it has an extremely

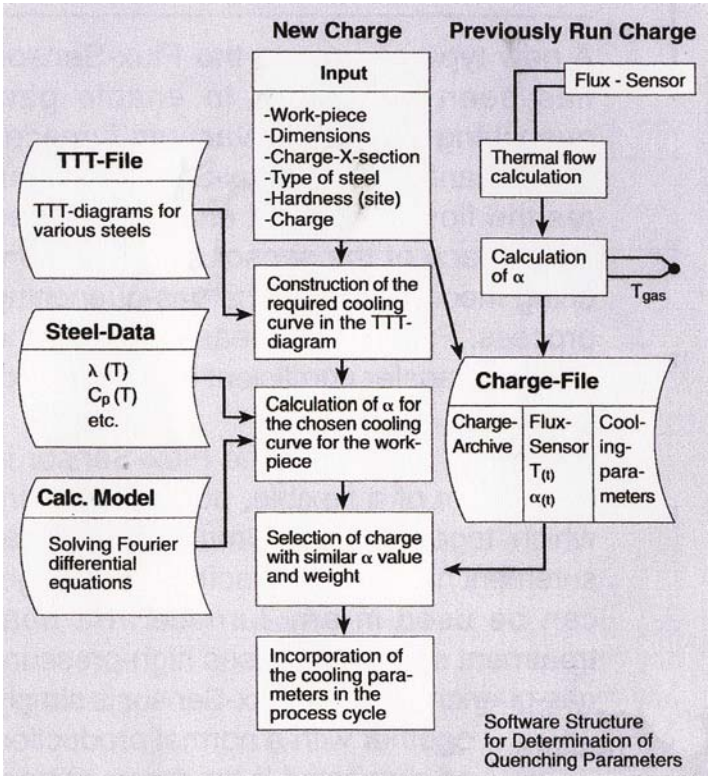

Figure 37 The algorithm of the Ipsen's 'Vacu-Quench Expert' program. By courtesy of Ipsen GmbH, Kleve.

fast response time of about 10 μs. The application of this probe is primarily for scientific experiments and a detailed analysis of the quenching process. It is constructed from AISI 304 stainless steel having 50 mm diameter and 200 mm length, instrumented with three TC's at the half length cross section, as shown in **Figure 38**. One TC measures the actual surface temperature (T_n), another measures the temperature at a point 1.5 mm below the surface (T_i), and the third one at the center (T_c). The TCs inside the body are standard grounded sheath-type TCs.

There are two important requirements for a TC used for measuring surface temperature:

1. Its thermal junction must be two-dimensional (2-D, instead of three-dimensional (3-D) geometry).
2. It should be flush with the surface.

The unique details of the sensing tip of the surface TC, shown enlarged in **Figure 38**, are as follows.

In the vicinity of the hot measuring junction, the round TC wires are flattened into ribbons and are electrically insulated from each other and from the thermowell by sheets of mica only 5 μm thick. This 'sandwich' of 90 μm total thickness is placed between a split-tapered insert and pressed into the thermowell (body). The thermal junction is formed by grinding and polishing across the sensing tip. The mica isolation is so thin that the metallic whiskers of one ribbon element bridges across the mica to the other ribbon element and makes hundreds of microscopic friction welded junctions that are parallel to one another, thus forming one composite measuring junction. Any subsequent erosion on the surface of the body simply forms new junctions while removing the old junctions, hence its name 'self-renewing TC.' Due to this unique characteristic, this is the best type of thermal junction to be used for heat transfer calculations, because it registers all the phenomena occurring at the surface in real time. The temperatures recorded at the surface (T_n) and at 1.5 mm below the surface (T_i) permit calculation of the temperature gradient within this surface layer through the quenching process.

Specific characteristics of the Liscic/Nanmac probe among others are as follows:

- The surface condition of the probe can be maintained for each test by polishing the sensing tip of the surface TC before each measurement.
- Extremely fast response time of the surface TC and the absence of damping and lagging effects allow any transient temperature at the surface to be measured and recorded exactly and in real time. In each test three cooling curves are obtained: T_n for the surface, T_i for the point 1.5 mm below the surface, and T_c for the center.

Figure 39 shows a graphical display of different functions when quenching the probe into a 20 °C mineral oil bath without agitation (left row vertically), and a 25% PAG polymer solution at 40 °C bath temperature and 0.8 m s^{-1} agitation rate (right row vertically) (*23*):

(a) measured and recorded temperatures versus time $T = f(t)$;
(b) calculated heat flux density versus time $q = f(t)$;

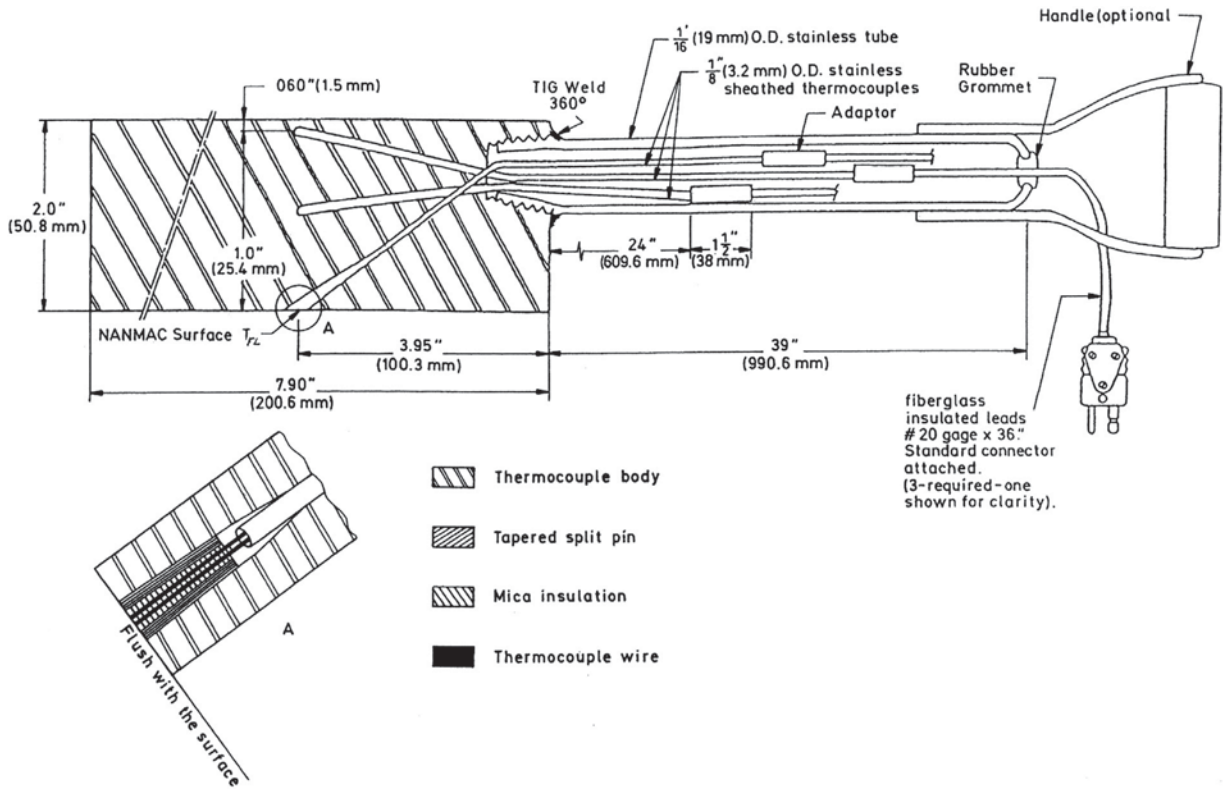

Figure 38 The Liscic/Nanmac quench probe. See for example In *Fuels and Lubricants Handbook: Technology, Properties, Performance, and Testing*; Totten, G. E., Ed.; ASTM International: West Conshohocken, 2003, p 624. Reprinted, with permission, from *Fuels and Lubricants Handbook: Technology, Properties, Performance, and Testing*, copyright ASTM International, 100 Barr Harbor Drive, West Conshohocken, PA 19428.

(c) calculated heat flux density versus surface temperature $q = f(T_s)$.

Figure 40 shows a graphical display of the following functions when quenching the probe into a 20 °C mineral oil bath without agitation (left row vertically), and a 25% PAG polymer solution at 40 °C bath temperature and 0.8 m s^{-1} agitation rate (right row vertically):

(d) calculated temperature difference versus time $\Delta T = f(t)$;
(e) calculated integral of the heat flux (heat extracted) versus time $\int q\mathrm{d}t = f(t)$;
(f) calculated cooling rate versus surface temperature $\partial T/\partial t = f(T_s)$.

The diagrams in Figures 39 and 40 enable a detailed process analysis. They show the possibility of comparing two different quenching cases:

Case A (diagrams on both left vertical rows) is a quenching process in a mineral oil at 20 °C without agitation. Case B (diagrams on both right vertical rows) is a quenching process in a 25% PAG polymer solution at 40 °C bath temperature and 0.8 m s^{-1} agitation rate.

Let us discuss only three examples of what can be concluded from a detailed analysis of their comparison:

1. By comparing the diagrams (b), i.e., the heat flux density versus time, it is clear that the case B exhibits delayed quenching, because in case A the time required for the maximum heat flux to occur (t_{qmax}) is only 15 s, where in case B it is 72 s.
2. Another analysis with respect to thermal stresses during quenching (on which residual stresses and possible distortion depend), see diagrams (d), shows in case B a 27% lower maximum temperature difference between the center and the surface of the probe (○). It is also worthy to note that the maximum temperature difference between the center and the point 1.5 mm below surface (Δ), although a little higher in case A, appears at 30 s, while in case B appears much later (at 100 s), showing a delayed abrupt heat extraction after the polymer film bursts.
3. Comparing the diagrams (e), i.e., the $\int q\mathrm{d}t$ versus time, one can follow exactly the dynamic of heat extraction. In case A, the heat extracted between 1.5 mm below surface and the surface itself (□) shows that at 20 s after immersion 34 MJ m^{-2} has already been extracted, and by 50 s, 50 MJ m^{-2}. In the case B, at 20 s after immersion, only 5 MJ m^{-2}, and by 50 s, only 20 MJ m^{-2} has been extracted. However, immediately after that period, between 50 s and 100 s the heat extracted in case A has increased very little (from 50 to 55 MJ m^{-2}), whereas in case B the heat extracted has increased from 20 to 86 MJ m^{-2}. This shows that in case B the thick polymer film has prevented the heat extraction for a relatively long time until insulating polymer film surrounding the probe burst, and a sudden increase in heat extraction occurred.

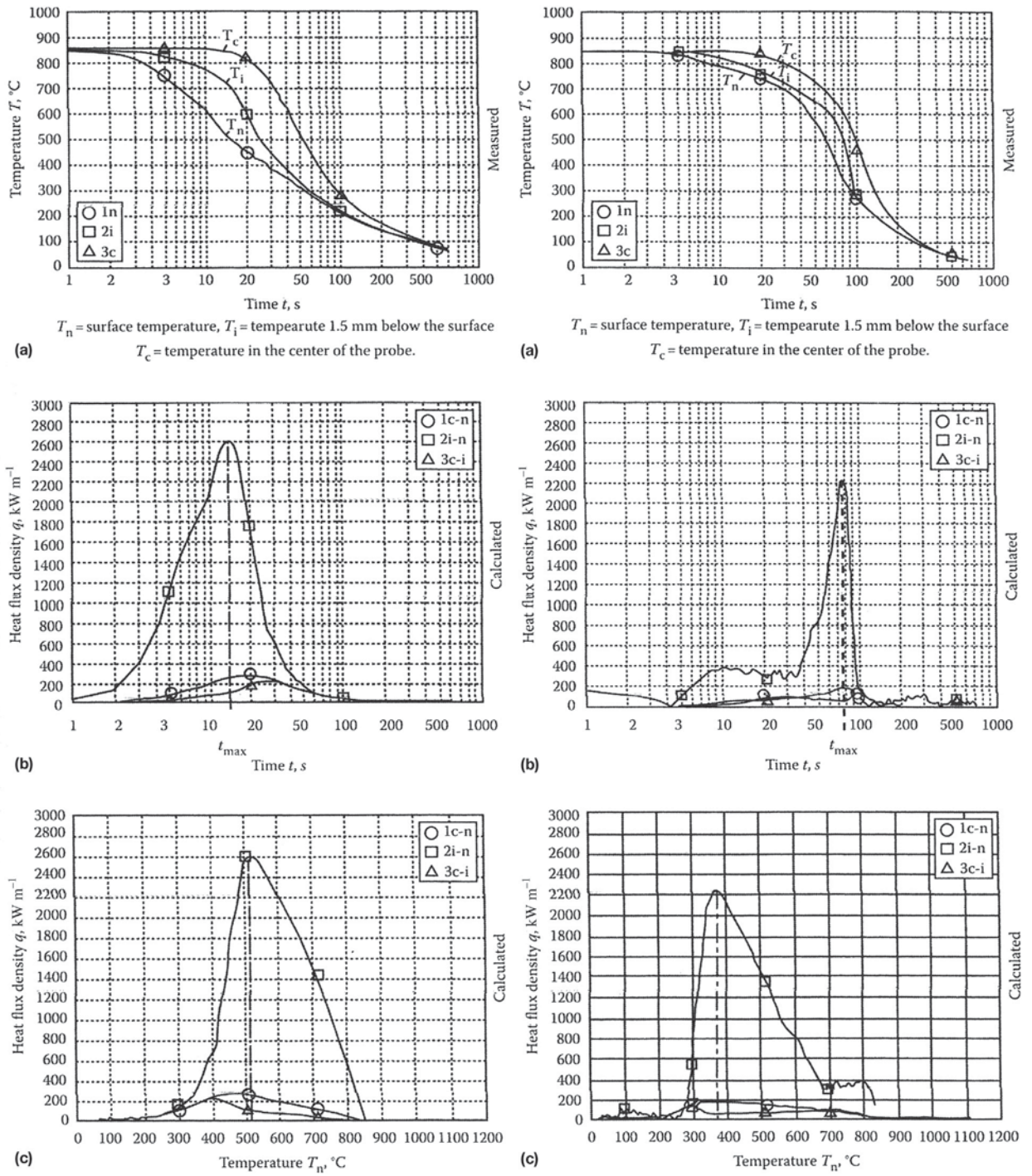

Figure 39 Graphic display of thermodynamic functions (a), (b), and (c) calculated after measurement by the Liscic/Nanmac probe. Reproduced from Liscic, B., Tensi, H. M., Canale, L. C. F., Totten, G. E., Eds. *Quenching Theory and Technology*; CRC Press, Taylor & Francis: Boca Raton, 2010.

12.05.7 Influence of Wetting Kinematics on the Heat Transfer Coefficient

At every quenching process in evaporable liquids there is a phenomenon called wetting kinematics (*24*). It can be best followed at immersion cooling of cylinders. As shown in Figure 41, rewetting starts in those places on the workpiece's surface where the film boiling collapses and nucleate boiling starts. At each of these places, at this moment, a sudden increase of the HTC occurs. When cylinders with smooth surface are involved, rewetting starts usually at the lower end and moves gradually as a wetting front toward the upper end, as is shown on the left side of Figure 42 (*25*). Temperature inside the cylinder changes, not only radially but also

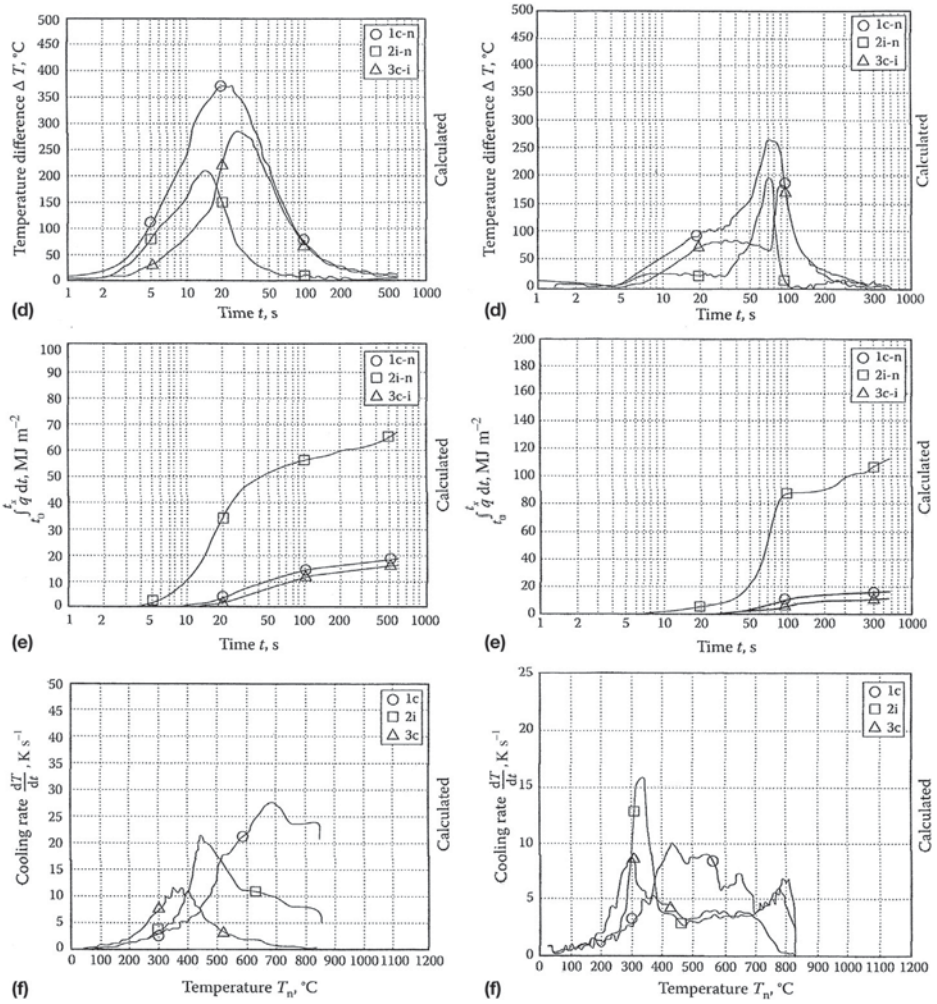

Figure 40 Graphic display of thermodynamic functions (d), (e), and (f) calculated after measurement by the Liscic/Nanmac probe. Reproduced from Liscic, B., Tensi, H. M., Canale, L. C. F., Totten, G. E., Eds. *Quenching Theory and Technology*, CRC Press, Taylor & Francis: Boca Raton, 2010.

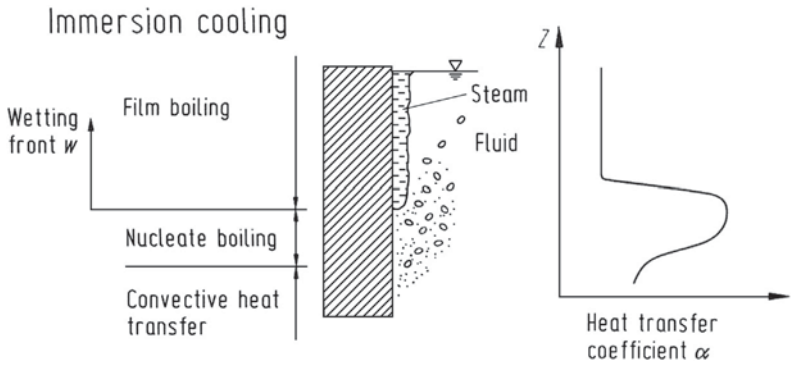

Figure 41 Change in the HTC at immersion cooling due to wetting kinematics. Reproduced from Tensi, H. M. Wetting Kinematics. In *Theory and Technology of Quenching*; Liščić, B.; Tensi, H. M.; Luty, W., Eds.; Springer Verlag, 1992. With kind permission of Springer Science + Business Media.

along the cylinder, as is shown on the right side of the same figure. This case relates to immersion cooling of an AISI 4140 steel cylinder of 40 mm diameter × 120 mm quenched in water at 80 °C, which certainly are not conditions used in practice.

The rewetting process can have different forms and durations (from slowly moving wetting front at, e.g., a quenching oil of high temperature, to abrupt explosion at some polymer solutions), so it can have a smaller or larger influence on the local HTC. This phenomenon is today an object of scientific research in laboratory conditions, but it is not as yet been taken into consideration when calculating the HTC of real workpieces.

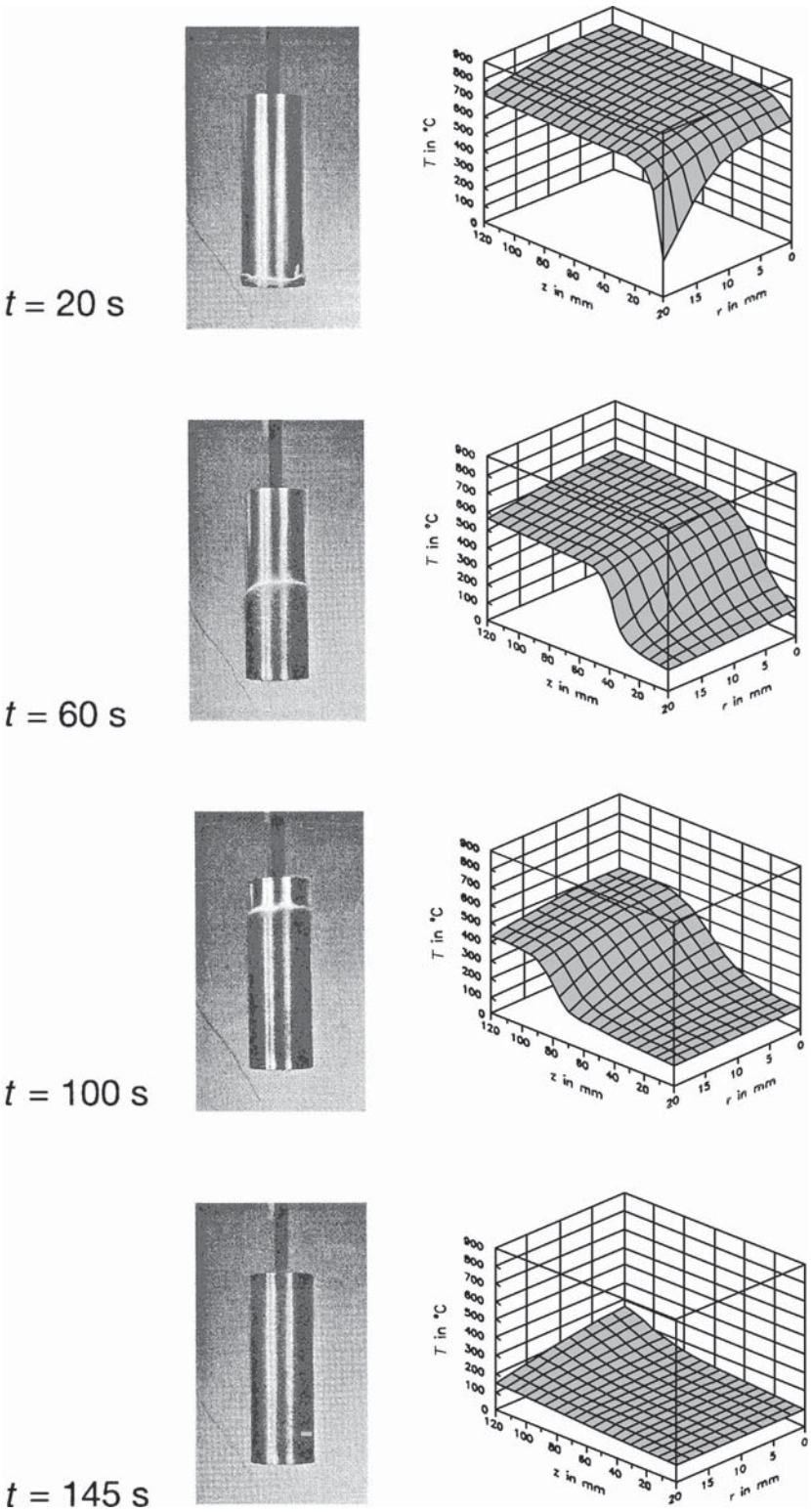

Figure 42 Observed wetting kinematics (left) and temperature distribution (right), calculated using local HTC when immersion cooling AISI 4140 steel cylinders of 40 mm diameter × 120 mm in water of 80 °C. Reproduced from Majorek, A.; Müller, H.; Macherauch, E. Computersimulation des Tauchkühlens von Stahlzylindern in verdampfenden Flüssigkeiten (in German). *HTM Härterei–Techn. Mitt.* **1996,** *51* (1), 11–17.

It is important to know that the calculated HTC, based on a temperature measurement in one point under the surface represents the HTC only exactly at the corresponding point at the surface, but at the same moment, other points on the surface have different local HTC values due to influence of wetting kinematics.

12.05.8 Inverse Heat Conduction Problem

12.05.8.1 Temperature Distribution Model

A workpiece being quenched is represented as a body Ω in the standard 3-D space. The temperature distribution inside this body throughout the quenching process is determined by the heat conduction equation (HCE) (*26*).

$$c\rho\frac{\partial T}{\partial t} = \mathrm{div}(\lambda\ \mathrm{grad}\ T), \qquad [2]$$

where we use the following notation:

x = a point in Ω, given as a triplet of space coordinates, each in meters,
t = time (s), with $t \geq 0$, assuming that the quenching process starts at $t = 0$,
$T = T(x, t)$ = temperature (K) or (°C), at point x and time t.

Physical properties of the material composing the workpiece are:

c = specific heat (J kg^{-1} K^{-1}),
ρ = density (kg m^{-3}),
λ = thermal conductivity (W m^{-1} K^{-1}).

Regardless of the eventual heat treatment before quenching, we assume that the temperature of the whole body at the start of the quenching process ($t = 0$) is a known function T_0 of x, and it is taken as the initial condition for the heat conduction problem

$$T(x, 0) = T_0(x), \quad x \in \Omega.$$

In practice, T_0 is computed as a simple global approximation of the initial measured temperatures, depending on the number of measurement devices inside the workpiece and their positions. Quite often, we simply assume that the quenching starts with a uniform temperature distribution, so T_0 is just a given constant

$$T(x, 0) = T_0, \quad x \in \Omega.$$

The values of T_0 for high-pressure gas quenching in vacuum furnaces can be as high as 1320 °C, while the standard starting temperature for liquid quenchants is 850 °C.

Because of the temperature range involved in the problem, all physical properties c, ρ, and λ have to be considered as temperature dependent (see Refs. (*27–29*)). Since they cannot be taken as constants, the heat conduction problem [2] becomes a nonlinear problem.

We assume that all physical properties are reasonably smooth functions of T over the whole temperature range – at least continuous and, therefore, bounded. Since we are dealing only with metal alloys, these assumptions are certainly valid for ρ and λ. In fact, both functions are almost linear in T for most alloys.

But specific heat c requires a more careful consideration. Note that c in eqn [2] represents the so-called 'true' specific heat, and not the 'mean' one, where the mean is taken over some temperature range. Some alloys have complicated phase transitions (changes in structure), which are reflected as irregularities in c, and c may even become unbounded (when the latent heat is involved in a phase transition). For alloys that do not have such phase transitions and remain in the austenitic condition throughout the whole quenching temperature range, c is also almost linear in T.

Essentially the same model can be applied in all cases, but great care must be taken to ensure that c correctly represents the actual thermal behavior in the workpiece during the quenching period. In fact, this model has also been used to simulate the freezing of strawberries in the food industry, with reasonably accurate phase transition data for all physical properties, including the latent heat for freezing.

The actual thermal properties c, ρ, and λ for a particular material are usually given as tables of values for a small number of temperatures, such as Ref. (*29*) for INCONEL 600. For numerical solution of the heat conduction problem, these tables first have to be 'converted' into functions, by computing a suitable approximation over the whole temperature range involved in the quenching process. As a general guideline, global polynomial approximations should be avoided, even though they are sometimes given along with tables or graphs of thermal properties. It is usually better to use a local (piecewise) approximation, or even interpolation of given values. For most purposes, a simple piecewise linear interpolation in the table is sufficient. If a smoother function is required, then cubic or quadratic splines can be used (see Ref. (*30*) or (*31*), where the algorithms for computing such functions are also given).

Finally, the boundary conditions for the heat conduction problem represent the flow of thermal energy between the surface of the workpiece, denoted by $\partial\Omega$, and the quenching medium, which can be a cooling gas blown at high velocity and pressure, or a liquid quenchant. An appropriate model is the Newton law of cooling on the boundary $\partial\Omega$, which says that the heat flux density

on the surface is 'proportional' to the difference between the surface temperature and the external quenching medium temperature

$$q = \lambda \frac{\partial T}{\partial \vec{n}} = -\alpha(T - T_x), \qquad [3]$$

where:

q = heat flux density at the surface (W m^{-2}), with $q < 0$, if the temperature drops,
$\vec{n}$ = unit outer vector perpendicular to $\partial\Omega$,
T_x = external temperature of the quenchant (K) or (°C),
α = surface HTC (W m^{-2} K^{-1}).

Generally, both T_x and α depend on (x, t) on $\partial\Omega$. While T_x can be regarded as known (say, measured), α is unknown. Therefore, to use this model, we first have to find α. In other words, we have to solve the inverse heat conduction problem.

In principle, the external quenchant temperature and the HTC can be calculated by using sophisticated computational fluid dynamics (CFD) models of the quenchant flow around the workpiece. Unfortunately, these models require many measured input data, and still demand very high computing resources, so their use is almost exclusively limited to scientific and experimental environments. For everyday industrial applications, such models are simply not feasible.

To facilitate extensive data gathering by standard probes in workshop environments, we need a highly efficient and reasonably accurate procedure for α calculation. This practical goal immediately rules out all CFD-based methods, as they require too much computing time. For the same reason, it also prohibits the use of methods that are based on standard regularization or statistical model parameter/function estimation (see Ref. (*32*)).

For efficiency reasons, the HTC needs to be computed by a more direct approach. We use a simplified model that does not even try to simulate the actual flow of the quenchant around the workpiece. Instead, we concentrate on the temperature distribution inside it, as described by eqn [2]. The workpiece is equipped with a certain (small) number of temperature measurement devices, which are placed at selected positions inside the workpiece. Likewise, the quenchant temperature is also measured at some points, since it is required in eqn [3]. The measured temperature curves in time are the only input data to this model.

12.05.8.2 Numerical Solution of the Inverse Problem

With these data, the HTC can be computed by global fitting or by using only local information. The choice between these two approaches depends on the intended use of the HTC and on available computational resources.

In global fitting, a form of the function $\alpha(x, t)$ is prescribed, with a certain number of 'free' parameters. These parameters are then computed iteratively, by repeatedly solving the heat conduction eqn [2] with boundary conditions [3], until a good fit to the measured temperature data is obtained. This procedure is equivalent to statistical parameter estimation and might require too much time to compute a reasonably good fit. Another disadvantage of this approach lies in the fact that the globally fitted HTC may be a poor approximation of the cooling intensity at some points.

The purpose of all Liščić probes is to provide further insight into the actual local quenching conditions at particular points at the surface. Then the HTC should be calculated from local information, even though it may give somewhat poorer results far away from the surface. This is why the 'main' thermocouples are located near or at the surface of the probe, while the others serve mainly as 'control' points.

Quite generally, this approach requires a sufficient number of measurement points near or at the surface of the workpiece, and these points should be spread across the workpiece in such a way to approximate the boundary $\partial\Omega$ reasonably well. The HTC can then be calculated by the following global numerical procedure:

- use these measured temperature curves as fixed (Dirichlet) boundary conditions and solve the heat conduction equation, eqn [2],
- if necessary, extend or extrapolate the solution toward the boundary, to get the surface temperature,
- calculate α from eqn [3] by using measured external temperature T_x and numerical differentiation.

An alternate and more time-consuming procedure is:

- use a space integrated formulation of eqn [2] in terms of control volumes, with (unknown) surface heat flux density as the 'boundary' condition,
- in each time step, solve the equation for the surface heat flux density to reproduce the measured temperatures at that time, and then calculate α from eqn [3].

Unfortunately, this approach is useless in the 3-D space. For, in practice, it is technically impossible to put enough thermocouples in the workpiece to approximate its boundary reasonably well – even when its geometry is a very simple one, with much symmetry, like a cylinder or a plate.

The number of dimensions in the model has to be reduced, and only a 1-D model is currently feasible for standard workshop environments. Two basic geometries that allow 1-D models are infinite plates and infinite cylinders with radial symmetry.

The procedures for HTC calculation, based on the 1-D model for 'infinite' cylinders, have been used for two of the Liščić probes, and are described here in more detail. A similar procedure for infinite plates is given in Ref. (33).

12.05.8.3 Simplified 1-D Model for Standard Probes

The standard probe is treated as a long radially symmetric cylinder of a given radius $R = 25$ mm. Asymmetries and changes in the material introduced by the thermocouples are simply ignored. Furthermore, we assume that the heat loss during the quenching process occurs only through the 'curved' side of the cylinder, and ignore the 'flat' top and bottom sides, as if the cylinder is of infinite length. Since the ratio of the radius R and the true length L of the probe is 1:8, the ratio of the ignored surface area and the 'active' surface area is the same. This is not negligible, but there is no other choice, if we want to use the simplified infinite cylinder model. To cope with this problem, additional thermocouples, placed far away from the surface of the probe, are used as control points.

Finally, in a simplified 1-D model, the temperature distribution inside the cylinder, for all times $t \geq 0$, depends only on the radial distance $r \in [0,R]$ from the center of the cylinder. In other words, the temperature T depends only on one (radial) space coordinate r, and can be written as $T = T(r, t)$. This assumption poses severe restrictions in practical applications. Great care must be taken when using the probe, to ensure that this is valid as much as possible. For example, the probe should be immersed vertically into the liquid quenchant, and eventual quenchant agitation must be vertical as well.

With all these assumptions, the temperature inside the cylinder is determined by the 1-D heat conduction equation, eqn [2], written in polar coordinates (without the angular component)

$$c\rho\frac{\partial T}{\partial t} = \frac{1}{r}\cdot\frac{\partial}{\partial r}\left(r\lambda\frac{\partial T}{\partial r}\right). \qquad [4]$$

All physical properties c, ρ, and λ of the material in eqn [4] are temperature dependent, so the whole problem is nonlinear.

- The thermal properties for the Ipsen–Liscic flux sensor are taken from Refs. (27,28), and piecewise linear interpolation in the corresponding table is used to convert them into functions of temperature, simply to speed up the calculation.
- For the Liscic/Petrofer probe made of INCONEL 600, the thermal properties are taken from Ref. (29). Since computers are much faster nowadays, Akima's piecewise cubic interpolation (30,34) in the table is used to compute the required thermal property for a given temperature. This method is chosen because it produces a smoother function (the first derivative is continuous), and also avoids wiggles in it.

The probe is initially heated up to a certain temperature before quenching, so the initial condition $T(r, 0) = T_0(r)$ at the start of the quenching process is known. Usually, we assume that the probe is uniformly heated and T_0 is constant.

Due to symmetry, the boundary condition at the center of the cylinder ($r = 0$) must be

$$\frac{\partial T}{\partial r} = 0. \qquad [5]$$

By the infinity assumption, the probe has only one cooling surface and radial symmetry implies that the surface HTC α depends only on time t. The boundary condition, eqn [3], for $r = R$ can then be written as

$$q_s = -\lambda\frac{\partial T}{\partial r} = \alpha(T_s - T_x), \qquad [6]$$

where $T_s(t) = T(R, t)$ is the surface temperature of the cylinder, and $T_x(t)$ is the measured external temperature of the quenchant. Here, the surface heat flux density $q_s(t)$ is considered to be positive when the probe cools (as if looked at from the quenchant's perspective), which is customary in industrial applications.

To determine α as a function of time in eqn [6], an additional temperature curve $T_n(t)$ is measured by a thermocouple located at a point $r = r_n$, near or at the surface of the cylinder.

Before we describe the actual HTC calculation, note that the model itself requires only two measured temperature curves in time, $T_n(t)$ and $T_x(t)$. No other input is needed, which makes it simple, but fast in practice. In particular, the quenching conditions (type of quenchant, direction and speed of flow around the probe) are reflected only in these two measured temperatures, and there is no other input of quenching conditions into the model.

All standard probes have additional thermocouples. One of them measures the core temperature T_c at $r = 0$, and there may be others closer to the surface. These measured temperatures are sometimes used to calculate an approximation of the initial temperature distribution $T_0(r)$. Apart from that, they are used only as a reference to check the results.

12.05.8.4 Outline of the Heat Transfer Coefficient Calculation

The input temperatures T_n and T_x are measured at discrete times by a data acquisition device, until some final time t_{final}. The values recorded are rounded to a small number of decimal digits (no more than two, and sometimes even to the nearest integer value). They may also be affected by measurement errors. Finally, the HTC α is obtained by numerical differentiation, and any 'jumps' in measured temperatures will be greatly amplified in the computed α. So, before any use, these measured temperatures have to be smoothed in time over the measured range.

The primary goal of smoothing is to get rid of random measurement errors and convert discrete tables into true functions of time, for all values $t \in [0,t_{\text{final}}]$. Depending on the application, there may be additional goals (or constraints) in smoothing, such as the monotonicity of the smoothed temperature functions. The smoothing procedure is described later in more detail, but for now, we assume that the original discrete values have already been replaced by smoothed functions of time, also denoted by $T_n(t)$ and $T_x(t)$, respectively.

Ideally, T_n would be measured at the surface of the cylinder, i.e., at $r_n = R$ (as in the Liscic/Nanmac probe), and simply substituted as the surface temperature T_s into eqn [6] to calculate α. The left-hand side in eqn [6] can be calculated by solving the heat conduction eqn [4] on $[0,R]$, with $T_s(t) = T_n(t)$ as the Dirichlet boundary condition. For example, the solution can be computed by the implicit finite difference method (35,36) (also, see the next section).

However, accurate measurement of the surface temperature is not feasible in everyday workshop environments. In two other probes, T_n is measured at a point r_n beneath the surface, so $r_n < R$. We can still solve eqn [4] with $T_n(t)$ as the Dirichlet boundary condition, but only on $[0,r_n]$. To calculate α at the boundary, the solution has to be extended from $[0,r_n]$ to $[0,R]$ in order to find the surface temperature T_s. This extension can be accomplished by two methods:

- the quasi-reversibility method of Lattès and Lions (see Ref. (37), Chapter 5), or
- simple extrapolation of the computed solution, if the depth $d = R - r_n$ is sufficiently small with respect to the whole radius of the probe.

From the theoretical point of view, the quasi-reversibility method would be the correct algorithm to compute the solution extension on $[0,R]$. On the other hand, it is far more demanding in terms of computing time and space. Moreover, it also requires some extrapolation, even though it is over a very small space gap near the surface.

We have compared these two methods in a series of numerical experiments during the design of the Ipsen–Liscic flux sensor. The results show that simple extrapolation is quite sufficient for all depths up to 10% of the radius. It works reasonably well even for 20%, which is the largest depth-to-radius ratio that has been used in prototype measurements.

12.05.8.4.1 Ipsen–Liscic Flux Sensor

In the Ipsen–Liscic flux sensor, T_n is measured at the depth of 2.4 mm, which is just below 10% of the radius, so simple extrapolation is used for the solution extension. The whole computation is divided into two phases. The first one computes the HTC α as a function of time by solving the inverse problem. The computed α is then smoothed in time and stored for future use in other calculations. Because of this smoothing, the second phase 'verifies' the final α by solving the direct problem.

In each phase, the computation is performed in a series of discrete time levels t_i until the final time is reached, which is the standard procedure for solving the heat conduction equation. The time steps between levels (usually 1 s) are chosen in accordance with the relatively small temperature gradients in gas quenching, to provide sufficient accuracy at reasonable speed. A brief description of main steps in each phase is given next.

Phase 1. HTC α calculation (inverse problem), for discrete times $t_i \in [0,t_{\text{final}}]$:

1.1. Solve the heat conduction eqn [4] on $[0,r_n]$, with the smoothed temperature $T_n(t)$ as Dirichlet's boundary condition;
1.2. Extend the solution from $[0,r_n]$ to $[0,R]$ by simple extrapolation to get the surface temperature $T_s(t)$;
1.3. Calculate α from eqn [6] by numerical differentiation of the computed solution, using the smoothed external temperature $T_x(t)$;
1.4. Check the errors in the calculated core temperature with respect to the measured $T_c(t)$ curve (one reference point).

At the very end of Phase 1, the calculated α is smoothed in time. This step also converts the discrete $\alpha(t_i)$ table into a function over the whole time range $[0,t_{\text{final}}]$.

Phase 2. Model verification (direct problem with known α), for discrete times $t_i \in [0,t_{\text{final}}]$:

2.1. Solve the heat conduction eqn [4] on $[0,R]$, with Newton's law of cooling [6] as the boundary condition, using the final smoothed α from Phase 1;
2.2. Check the errors in the calculated temperatures at r_n and the core ($r = 0$), with respect to the original measured $T_n(t)$ and $T_c(t)$, respectively (two reference points).

Due to memory limitations (at the time when the Ipsen–Liscic flux sensor was built), the computation in both phases is organized in such a way that each of the steps advances only by one time level t_i in a global time-step loop, so only the information from the previous time level t_{i-1} needs to be stored.

The implementation of these steps involves several numerical problems that have to be adequately solved to achieve the desired efficiency and accuracy:

- Numerical solution of the heat conduction eqn [4] in both phases, with different boundary conditions, is done by the nonlinear implicit finite difference method (FDM). In each time step, simple iterations are used to adjust all thermal properties to new temperatures. The actual algorithm is given in the next section.
- At each time level, the solution extension in step 1.2 is calculated by local extrapolation. First, two low degree polynomial (parabolic and cubic) least-squares approximations of the solution on $[r_n - d, r_n]$ are computed, and then the average of these

two approximations is evaluated at $r_n + d = R$ to get the surface temperature. The same approximation is also used for numerical differentiation of the surface temperature, needed to compute α in step 1.3.

- Finally, the smoothing of α at the end of Phase 1 is done by the so-called smoothing cubic spline approximation (*31*). The whole software package FITPACK described therein is publically available from Netlib. Based on an example in Ref. (*31*), the curve fitting routine CURFIT gives a sufficiently accurate approximation of α for all times in only 3 steps, and the computed cubic B-spline coefficients are stored for future evaluations. Actually, the same algorithm is also used for global smoothing of both measured temperatures T_n and T_x.

As a result, the whole computation lasted less than a minute in 1994.

12.05.8.4.2 Liscic/Petrofer Probe

In the Liscic/Petrofer probe, T_n is measured at the depth of only 1 mm below the surface, so one might expect that the same procedure is even more applicable in this case. However, with standard liquid quenchants (mineral oils, polymer solutions, water), the temperature gradient at the surface and the HTC in eqn [6] are, usually, much higher than in gas quenching (as is illustrated by examples given in the last section).

Because of this, the errors introduced by numerical differentiation in step 1.3 can be much higher as well, regardless of the fact that the solution extension in step 1.2 needs to be performed over a smaller space gap. Therefore, the HTC α in eqn [6] is computed by an alternate and more accurate procedure that avoids explicit numerical differentiation of calculated temperatures.

The whole model [4] is written in a space integrated form, as a heat conservation law for the cylinder, in terms of the surface heat flux density q_s (see Ref. (*26*))

$$\int_0^R \left(c\rho \frac{\partial T}{\partial t}\right)(r,t)\cdot r \ \mathrm{d}r = R\cdot\left(\lambda\frac{\partial T}{\partial r}\right)(R,t) = -R\cdot q_s(t). \qquad [7]$$

This is valid for all times t, and already includes the symmetry boundary condition [5]. The surface boundary condition [6] is represented here as the right-hand side in eqn [7], with unknown q_s as a function of time. Once we find q_s, the HTC α can be computed directly from eqn [6], as

$$\alpha = \frac{q_s}{T_s - T_x} \qquad [8]$$

The actual HTC calculation is done as a part of Module 1 in the TGS software that accompanies the probe. In accordance with eqn [7], the inverse heat conduction problem is now solved by the finite volume method (*36,38*). Like before, the whole computation progresses by one time level in a global time-step loop, and contains the following main steps.

Module 1. HTC α calculation (inverse problem), for discrete times $t_i \in [0,t_{\text{final}}]$:

1.1. Solve the heat conduction eqn [4] on $[0,R]$ to calculate the surface heat flux density $q_s(t)$ and the surface temperature $T_s(t)$;
1.2. Calculate α from eqn [8], using the smoothed external temperature $T_x(t)$;
1.3. Check the errors in the calculated temperatures, with respect to the original measured temperatures $T_n(t)$, $T_i(t)$ (measured at 4.5 mm below the surface) and $T_c(t)$, respectively (three reference points).

To provide as much accuracy as possible, the implementation of step 1.1 is composed of two numerical tasks.

- At each time level t_i, the surface heat flux density $q_s(t_i)$ is calculated iteratively, until the resulting temperature at the position r_n is exactly equal to the smoothed near-surface temperature $T_n(t_i)$. The numerical solution of this equation $T(r_n, t_i) = T_n(t_i)$ is done by the Brent–Dekker method (*39*), because it requires no derivatives and is also reasonably fast.
- Throughout these iterations, for each 'trial value' of the surface heat flux density, the heat conduction equation on $[0,R]$ is solved by the nonlinear implicit finite volume method (FVM). This algorithm is very similar to the previous one, and will be given in the next section.

This procedure for the HTC calculation is more demanding in time. But, nowadays, even with the time steps of only 0.02 s (to match the measurements), the whole computation takes only a few seconds.

In contrast to the gas quenching, where the gas pressure and velocity can be changed during the process to control the quenching conditions, the liquid quenching is far less controllable in time, once the process starts. Furthermore, in the TGS software, the calculated HTC is used primarily in the hardness prediction module, to simulate the behavior of workpieces in various quenching conditions. Here, the simulated workpiece can be of any dimensions, and experience shows that much better results are obtained if α is treated as a function of the surface temperature T_s rather than the time t. Thus, it is an additional duty of Module 1 to deliver α, not only as a function of time but also as a function of T_s.

Note that the change of the independent variable in α, from t to T_s, is possible only if the calculated $T_s(t)$ is a monotone decreasing function of time. For, otherwise, we may have two different values of α for different times, that correspond to the same value of the surface temperature at these times, so α cannot be a function of T_s.

However, in practice, the surface temperature of the probe may increase at times, due to chaotic behavior of the quenchant near the surface, even though the probe cools 'globally' in time. This phenomenon is clearly demonstrated by the polymer quenching example in the last section. In that example, the measured near-surface temperature T_n also increases over some time intervals,

despite the damping effect. These jumps in T_n would be even more visible in the calculated surface temperature, and greatly magnified in the $\alpha(t)$ curve.

A simple and blunt numerical approach would be to compute a monotone approximation to the calculated surface temperature $T_s(t)$ over the whole time interval $[0,t_{final}]$, and then substitute it into the computed $\alpha(t)$ curve. The algorithms for computing such an approximation will be described later in more detail. Unfortunately, the resulting $\alpha(T_s)$ curve would still be extremely jumpy, and almost useless for further computation, without additional smoothing.

Before that, it is worth considering the problem from a more global perspective. Since the jumps in temperature (either T_n or T_s) usually occur over relatively small periods of time, a monotone approximation of the temperature over such an interval should be interpreted as local averaging (in time) of the cooling conditions at the surface of the probe. In other words, this introduces yet another approximation into the simplified model, which now 'insists' on constant cooling of the probe.

As a compromise, to retain some insight into the actual surface conditions, this averaging of the heat extraction at the boundary is performed in two stages, and only one of them is done before the HTC calculation.

- At the very beginning, the measured near-surface temperature T_n is smoothed by a monotone decreasing function. The aim of this is to initially damp any chaotic surface effects, including the most violent jumps in α.
- The calculated $\alpha(t)$ is smoothed locally in time, to avoid sudden big jumps over very short time periods, which still may be present. This provides a visually more pleasing curve, and introduces only negligible errors in any further calculations.
- If the computed surface temperature $T_s(t)$ does not decrease in time over the whole time interval, a monotone decreasing approximation is computed by the same algorithm as in the initial monotone smoothing of T_n.
- Finally, the monotone decreasing $T_s(t)$ function is simply substituted in the calculated $\alpha(t)$ to obtain the $\alpha(T_s)$ function for other calculations.

Instead of the last step, a more conservative approach would be to use the monotone surface temperature $T_s(t)$ as the boundary condition for the second HTC calculation, and then use this 'more damped' α in subsequent calculations.

Due to the number of values involved, it turns out that the monotone smoothing of (possibly two) temperatures is the most time-consuming part of Module 1. Typically, for 7000 values, it takes about a minute per each smoothing.

12.05.9 Finite Differences and Finite Volumes for the HCE

In the numerical solution of the heat conduction problem, both time and space coordinates are discretized by finite grids, and an approximation of the solution is computed only at these grid points. Quite generally, in a chosen formulation of the problem, regardless of the particular method, all time and space derivatives are approximated by finite (or, more precisely, divided) differences with respect to the chosen grid points, and the resulting system of equations for unknown values at grid points is then solved numerically. The computation is organized to advance in time, in a global time-step loop that corresponds to the chosen time grid.

The only difference between the FDM and FVM lies in the initial formulation of the heat conduction problem, which is then discretized. In the FDM, the original formulation is the heat conduction eqn [4], with the appropriate boundary conditions [5] and [6] (or the Dirichlet boundary condition in Phase 1); i.e., the partial differential equation is discretized as it is.

In the FVM, the problem is first rewritten in its integral form, as a conservation law for a certain volume, similarly to eqn [7]. This law is then applied in a semidiscretized form, for a discrete set of control volumes. Finally, these equations are fully discretized in time and space.

12.05.9.1 Time and Space Discretizations

The whole time interval $[0,t_{final}]$ is divided into a discrete sequence of increasing time levels

$$0 = t_0 < t_1 < \ldots < t_{n_t-1} < t_{n_t} = t_{final},$$

with time steps

$$\tau_i = t_i - t_{i-1}, \quad i = 1, \ldots, n_t. \qquad [9]$$

These time steps have to be chosen in accordance with the thermal behavior of the probe in a particular quenchant, to avoid extreme temperature gradients in a single time step, which may result in a loss of accuracy.

- With the Ipsen–Liscic flux sensor, the temperatures are usually measured with a time step $\Delta t = 1$ s for a period of $t_{final} \approx 1800$ s. In gas quenching, there are no chaotic changes of the quenching conditions, but they can be controlled in time. Therefore, the time steps τ_i in eqn [9] are all equal, with $\tau_i = 1$ s.
- With the Liscic/Petrofer probe, the finest temperature measurements are taken with a time step $\Delta t = 0.02$ s throughout the whole quenching period, with $t_{final} \approx 1000$ s.

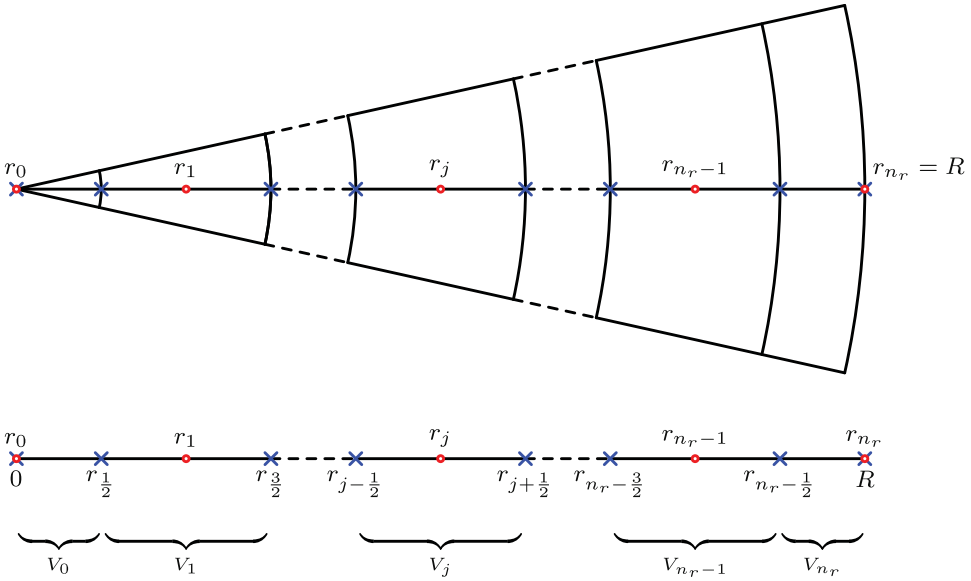

Figure 43 Finite control volumes for the one-dimensional heat conduction problem.

Such a fine time step provides very accurate data during the first intensive part of the quenching process, but is quite unnecessary later on, when the temperature drops. Hence, three different time steps are used in eqn [9], to speed up the calculation:
$\tau_i = 0.02$ s, for the first 100 s,
$\tau_i = 0.1$ s, from 100 s up to 200 s,
$\tau_i = 1$ s, from 200 s until the final time.

This gives about 6800 time levels in total, instead of 50 000.

In the simplified 1-D model of the probe, only the radial space coordinate needs to be discretized. This is always accomplished by a uniform grid on the interval $[0,R]$, where R represents the active radius or boundary of the probe. Note that in Phase 1 for the Ipsen–Liscic flux sensor, the active boundary condition is given at r_n, so r_n should be substituted as R in everything below, to simplify the presentation.

A uniform grid on $[0,R]$ is generated by prescribing a number of subintervals n_r, which determines the space step h

$$h = \frac{R}{n_r}, \qquad [10]$$

and the corresponding grid points r_j (illustrated in **Figure 43**) are given by

$$r_j = j \cdot h, \quad j = 0, \ldots, n_r. \qquad [11]$$

Here again, the number of subintervals n_r has to be sufficiently large (i.e., the space step h in eqn [10] has to be sufficiently small) for an accurate solution of the problem. The standard values are $n_r = 100$ (or $h = 0.25$ mm) for the Ipsen–Liscic flux sensor, and $n_r = 200$ (or $h = 0.125$ mm) for the Liscic/Petrofer probe.

12.05.9.2 Implicit Methods

As described before, the numerical algorithm advances by one time level per step in a global time-step loop. So, in step i, approximate values for temperatures at time level t_i are computed at all grid points r_j. These approximate values will be denoted by T_j^i, to be distinguished from the unknown true values $T(r_j, t_i)$.

The actual discretization of the problem is done by the so-called implicit approach (35,36). In implicit methods, the space discretization of the problem formulation is always performed at the new time level t_i, where the approximate solution is yet to be calculated, and time derivatives are approximated by the backward difference, in terms of the previous time level t_{i-1}, where the approximate solution is already known. At the first step, when $i = 1$, the previous time level $t_0 = 0$ corresponds to the known initial condition T_0 for the heat conduction problem.

For example, if f is a function that appears in the problem formulation, then the backward difference approximation of its time derivative at (r_j, t_i) is given by

$$\frac{\partial f}{\partial t}(r_j, t_i) \approx \frac{f(r_j, t_i) - f(r_j, t_{i-1})}{\tau_i} \approx \frac{1}{\tau_i}\left(f_j^i - f_j^{i-1}\right). \qquad [12]$$

This approximation is not restricted to the grid points r_j from eqn [11]. If we write $r_j = j \cdot h$, as in eqn [11], but allow j to take any real value, then eqn [12] can be used at any point r_j. The grid points from eqn [11] are specified by the integral values of j between 0 and n_r. With this convention, the notation introduced on the right-hand side of eqn [12] will be used to describe the algorithms.

The implicit approach to discretization generally leads to a more complicated numerical problem than the so-called explicit approach, where the discretization is performed at the previous time level t_{i-1}. Nevertheless, the implicit methods are preferable in practice, as they are unconditionally stable, at least in the linear case, which means that the artificial oscillations produced by the numerical solution are quickly damped. As a consequence, the time and space steps in eqns [9] and [10] can be chosen with some freedom, as above, to match the actual dynamics of the problem, without severe additional constraints regarding the numerical stability of the method. On the contrary, in all explicit methods, for a given space step h in eqn [10], there is a strict upper limit on the time step τ_i that guarantees the stability of the method. In fact, for quenching problems, the required time steps are too small, and the whole computation lasts much longer than with the implicit methods.

12.05.9.3 Finite Difference Method

In the implicit FDM, the heat conduction eqn [4]

$$c\rho \frac{\partial T}{\partial t} = \frac{1}{r} \cdot \frac{\partial}{\partial r}\left(r\lambda \frac{\partial T}{\partial r}\right)$$

is discretized at time level t_i at all internal grid points r_j, for $j = 1, \ldots, n_r - 1$. The left-hand side is discretized by the backward difference, as in eqn [12], with accuracy of the first order in terms of the time step τ_i. The right-hand side is discretized by a repeated usage of central differences (see Ref. (36), equation (5.32b), p 80), to obtain the second-order accuracy in the space step h. After some manipulation, this gives the following system of equations

$$-\left[\left(1-\frac{1}{2j}\right)\lambda^i_{j-1/2}\right]T^i_{j-1} + \left[\left(1-\frac{1}{2j}\right)\lambda^i_{j-1/2} + \left(1+\frac{1}{2j}\right)\lambda^i_{j+1/2} + \frac{h^2}{\tau_i}(c\rho)^i_j\right]T^i_j - \left[\left(1+\frac{1}{2j}\right)\lambda^i_{j+1/2}\right]T^i_{j+1} = \left[\frac{h^2}{\tau_i}(c\rho)^i_j\right]T^{i-1}_j, \qquad [13]$$

for $j = 1, \ldots, n_r - 1$. Note that the thermal properties with 'indices' in eqn [13] refer to the values that correspond to the temperatures at these points,

$$\lambda^i_{j\pm 1/2} = \lambda\left(T^i_{j\pm 1/2}\right), \quad (c\rho)^i_j = c\left(T^i_j\right) \cdot \rho\left(T^i_j\right).$$

Once we have even very crude approximate values for temperatures T^i_j at all grid points, then $(c\rho)^i_j$ is calculated directly from T^i_j. The approximate temperatures required for λ are computed by using linear interpolation from the nearest grid point values,

$$T^i_{j\pm 1/2} = \frac{1}{2}\left(T^i_j + T^i_{j\pm 1}\right),$$

or λ itself is calculated by linear interpolation from the values at the nearest grid point temperatures

$$\lambda^i_{j\pm 1/2} = \frac{1}{2}\left(\lambda^i_j + \lambda^i_{j\pm 1}\right).$$

The final two equations are obtained by discretization of the boundary conditions [5] and [6]. Since both of them contain the first spatial derivative of the temperature, we use a standard procedure that preserves the space discretization accuracy. The whole problem is considered on a slightly larger domain that contains two virtual grid points $r_{-1} = -h$ and $r_{n_r+1} = R + h$, which lie beyond the regular boundaries of the cylinder. The HCE is now discretized in the same way as before, but at the boundary points $r_0 = 0$ and $r_{n_r} = R$. Finally, the unknown 'virtual' values are eliminated by a finite difference approximation of the corresponding boundary condition.

At the center of the cylinder ($r = 0$), the symmetry boundary condition [5] implies the following special form of the HCE

$$c\rho \frac{\partial T}{\partial t} = 2\frac{\partial}{\partial r}\left(\lambda \frac{\partial T}{\partial r}\right).$$

The corresponding discretized equation is

$$-\left[2\lambda^i_{-1/2}\right]T^i_{-1} + \left[2\lambda^i_{-1/2} + 2\lambda^i_{1/2} + \frac{h^2}{\tau_i}(c\rho)^i_0\right]T^i_0 - \left[2\lambda^i_{1/2}\right]T^i_1 = \left[\frac{h^2}{\tau_i}(c\rho)^i_0\right]T^{i-1}_0.$$

The boundary condition [5] is discretized by the central difference approximation

$$\frac{T^i_1 - T^i_{-1}}{2h} = 0,$$

giving $T^i_{-1} = T^i_1$. Also, due to symmetry, we must have $\lambda^i_{-½} = \lambda^i_{½}$. By substituting these values into the discretized HCE, we obtain the central or the inner boundary equation

$$\left[4\lambda^i_{½} + \frac{h^2}{\tau_i}(c\rho)^i_0\right]T^i_0 - \left[4\lambda^i_{½}\right]T^i_1 = \left[\frac{h^2}{\tau_i}(c\rho)^i_0\right]T^{i-1}_0. \qquad [14]$$

This equation is added as the first equation (for $j = 0$) into the system [13].

At the surface of the cylinder ($r = R$), the discretized HCE gives an equation of the same form as in eqn [13], but for $j = n_r$. The boundary condition [6] is discretized by the central difference approximation

$$\lambda^i_{n_r}\frac{T^i_{n_r+1} - T^i_{n_r-1}}{2h} = -q_s(t_i).$$

In Phase 2 for the Ipsen–Liscic flux sensor, the HTC α is already calculated (and smoothed) as a function of time. An approximate value of the heat flux density q^i_s can then be calculated from a previous surface temperature approximation, denoted by T^i_s, and the external quenchant temperature $T_x(t_i)$

$$q^i_s = \alpha(t_i)\left(T^i_s - T_x(t_i)\right).$$

This approach is consistent with the iterative adjustment of all thermal properties (described below), which is used throughout the whole computation. An approximate value T^i_s is always available, either from the previous time level (as a crude initial approximation) or from the previous iteration.

From these two equations, the virtual value $T^i_{n_r+1}$ can be expressed as

$$T^i_{n_r+1} = T^i_{n_r-1} - \frac{2hq^i_s}{\lambda^i_{n_r}},$$

and eliminated from the discretized HCE [13] for $j = n_r$. This gives the surface or the outer boundary equation

$$\begin{aligned} &-\left[\left(1 - \frac{1}{2n_r}\right)\lambda^i_{n_r-1/2} + \left(1 + \frac{1}{2n_r}\right)\lambda^i_{n_r+1/2}\right]T^i_{n_r-1} + \left[\left(1 - \frac{1}{2n_r}\right)\lambda^i_{n_r-1/2} + \left(1 + \frac{1}{2n_r}\right)\lambda^i_{n_r+1/2} + \frac{h^2}{\tau_i}(c\rho)^i_{n_r}\right]T^i_{n_r} \\ &= \left[\frac{h^2}{\tau_i}(c\rho)^i_{n_r}\right]T^{i-1}_{n_r} - 2\left[\left(1 + \frac{1}{2n_r}\right)\lambda^i_{n_r+1/2}\right]\frac{hq^i_s}{\lambda^i_{n_r}}, \end{aligned} \qquad [15]$$

which is added as the last equation into the system [13]. Here, $\lambda^i_{n_r+½}$ can be evaluated from $T^i_{n_r+½}$, which is obtained by linear extrapolation

$$T^i_{n_r+½} = \frac{3}{2}T^i_{n_r} - \frac{1}{2}T^i_{n_r-1}.$$

In Phase 1 for the Ipsen–Liscic flux sensor, we have the Dirichlet boundary condition $T(R, t) = T_n(t)$ at $R = r_n$. In this case, there is no need for an additional discretized equation at the outer boundary. The known values $T_n(t_i)$ at the boundary can be substituted for $T^i_{n_r}$ into the last equation $j = n_r - 1$ in eqn [13].

Generally, the discretization procedure gives a system of $n_r + 1$ eqns [13]–[15], for $n_r + 1$ unknown temperatures T^i_j at all grid points r_j, $j = 0, \ldots, n_r$. In fact, because the whole problem is nonlinear, in the implicit formulation, this system has many more unknown values. The coefficients in brackets contain thermal properties that depend on the unknown temperatures at the same time level.

However, since all thermal properties vary quite slowly with the temperature, the whole system is solved by a simple iterative adjustment of thermal properties to new calculated temperatures.

- The initial approximations for thermal properties at time level t_i are computed from the already calculated temperatures at the previous time level t_{i-1}. If time steps τ_i are not too large, this gives a very good approximation for all thermal properties.
- The thermal properties are then considered as known, as if they are constant at the corresponding spatial points. Since all coefficients in the system [13]–[15] are treated as constants, the system now becomes a tridiagonal linear system for unknown temperatures at time t_i, which is solved very quickly and accurately.
- The newly computed temperatures are used to compute better approximations for thermal properties, and the system is solved again.
- The whole process is iterated until all computed temperatures at grid points are stabilized to within a prescribed accuracy.

This algorithm is, actually, very fast in practice. For example, with the Ipsen–Liscic flux sensor, for standard time steps $\tau_i = 1$ s, only 3–4 iterations per time step are needed to get the required accuracy of 10^{-4} in all computed temperatures.

12.05.9.4 Finite Volume Method

The FVM (38) differs from the FDM only in that the finite difference approximation is used for the heat flux (or the heat flux density in 1-D models) rather than for the partial differential equation itself.

To begin with, the spatial coordinate is discretized in the same way as before, by a uniform grid on $[0,R]$, with grid points r_j given by eqns [10] and [11]. The probe is radially divided into $n_r + 1$ annular finite control volumes, as shown in Figure 43.

Due to symmetry, only the radial component is significant, and in the simplified 1-D model of the probe, these volumes collapse into ordinary intervals V_j, shown at the bottom of Figure 43.

The internal volumes V_j, for $j = 1, \ldots, n_r - 1$, are cell-centered at grid points r_j,

$$V_j = \left[r_j - \frac{h}{2}, r_j + \frac{h}{2}\right], \quad j = 1, \ldots, n_r - 1,$$

and their length is equal to the space step h. The two boundary volumes V_0 and V_{n_r} cover the remaining portion of the whole radius of the probe

$$V_0 = \left[0, \frac{h}{2}\right], \quad V_{n_r} = \left[R - \frac{h}{2}, R\right],$$

They are neither vertex-centered, nor cell-centered, and their length is halved. This somewhat unusual choice of control volumes is particularly well suited for the problem, since it is easy to discretize the equations with high accuracy.

In the FVM, the problem is first rewritten in its space integrated form for each control volume, to obtain the so-called semi-discretized system of equations. Space integration of the heat conduction eqn [4] over the control volume V_j with the inner radius r_-, and the outer radius r_+ gives

$$\int_{r_-}^{r_+} \left(c\rho \frac{\partial T}{\partial t}\right)(r,t) \cdot r \, \mathrm{d}r = r_+ \cdot \left(\lambda \frac{\partial T}{\partial r}\right)(r_+,t) - r_- \cdot \left(\lambda \frac{\partial T}{\partial r}\right)(r_-,t). \qquad [16]$$

This equation is valid for all times t, and can be interpreted as the heat conservation law for the volume V_j, in terms of the heat flow through the boundaries at r_- and r_+. Note that the parentheses on the right-hand side in eqn [16] contain exactly the heat flux densities at both surfaces. In fact, this is the natural formulation of the heat conduction problem. Here it is easy to incorporate both boundary conditions [5] and [6], which are already given in terms of the heat flux density, thus avoiding explicit numerical differentiation at the boundary, which was necessary in the FDM.

In the implicit FVM, the semidiscretized system of equations in eqn [16] is further discretized at the current time level t_i. Because of the choice of control volumes, the right-hand side is easily discretized by the central differences in terms of the temperatures T_j^i at grid points r_j, which gives the second-order accuracy in h.

The integral on the left-hand side is approximated by a quadrature formula, which is based on a suitably chosen interpolation of the integrand. The midpoint formula, based on the interpolation by a constant function at the midpoint of the interval (see Ref. (40)), turns out to be the optimal choice. It is the easiest one to implement and is also second order accurate in h. If necessary, this approximation is combined with the linear interpolation in terms of the grid-point values. Finally, the backward difference approximation [12] is used for all time derivatives.

For all internal volumes V_j, with $r_- = r_{j-½}$ and $r_+ = r_{j+½}$, this gives exactly the same set of discretized equations [13], as in the FDM.

The equations in eqn [16] for the boundary volumes V_0 and V_{n_r} are discretized after the substitution of boundary conditions [5] and [6], respectively.

For the innermost (central) volume V_0, with $r_- = 0$ and $r_+ = r_{½} = h/2$, the midpoint formula is used at the point $r_{1/4}$, and the resulting value is approximated by the linear interpolation in terms of values at grid points r_0 and r_1. This gives the following central or the inner boundary equation

$$\left[4\lambda_{½}^i + \frac{3h^2}{4\tau_i}(c\rho)_0^i\right] T_0^i + \left[-4\lambda_{½}^i + \frac{h^2}{4\tau_i}(c\rho)_1^i\right] T_1^i = \left[\frac{3h^2}{4\tau_i}(c\rho)_0^i\right] T_0^{i-1} + \left[\frac{h^2}{4\tau_i}(c\rho)_1^i\right] T_1^{i-1}. \qquad [17]$$

Analogously, for the outermost (surface) volume V_{n_r}, with $r_- = r_{n_r-1/2} = R - h/2$ and $r_+ = r_{n_r} = R$, the midpoint formula is used at the point $r_{n_r-1/4}$, and the resulting value is approximated by the linear interpolation in terms of values at grid points r_{n_r-1} and r_{n_r}. This gives the surface or the outer boundary equation

$$\begin{aligned}\left[-2\left(1 - \frac{1}{4n_r - 1}\right)\lambda_{n_r-1/2}^i + \frac{h^2}{4\tau_i}(c\rho)_{n_r-1}^i\right] T_{n_r-1}^i + \left[2\left(1 - \frac{1}{4n_r - 1}\right)\lambda_{n_r-1/2}^i + \frac{3h^2}{4\tau_i}(c\rho)_{n_r}^i\right] T_{n_r}^i \\ = \left[\frac{h^2}{4\tau_i}(c\rho)_{n_r-1}^i\right] T_{n_r-1}^{i-1} + \left[\frac{3h^2}{4\tau_i}(c\rho)_{n_r}^i\right] T_{n_r}^{i-1} - 2\left(1 + \frac{1}{4n_r - 1}\right) h q_s^i,\end{aligned} \qquad [18]$$

where q_s^i is an approximate value of the surface heat flux density, as before.

Remember that, at each time level t_i, the surface heat flux is calculated iteratively, until it reproduces the smoothed near-surface temperature of the probe at that time. So, the trial values q_s^i are generated by the surrounding Brent–Dekker algorithm for iterative solution of this nonlinear equation. In each iteration of the Brent–Dekker algorithm, the approximate value of q_s^i is considered as known.

- The resulting system of $n_r + 1$ eqns [13], [17], and [18] for unknown temperatures T_j^i at all grid points r_j, $j = 0, \ldots, n_r$, is solved in exactly the same way as in the FDM, by a simple iterative adjustment of thermal properties to new calculated temperatures.
- Unlike before, because of the surrounding Brent–Dekker algorithm, the required accuracy is much stronger here. These simple iterations are terminated when all computed temperatures at grid points are stabilized almost to full machine relative precision. Despite that, the average number of simple iterations is only about seven.

The Brent–Dekker iterations are terminated with a similar accuracy requirement for the calculated surface heat flux density in each time step. With the standard time steps for the Liscic/Petrofer probe, the average number of these iterations is three, and very rarely rises to seven.

12.05.10 Smoothing of Measured Temperatures

The calculation of the surface HTC involves either explicit (FDM) or implicit (FVM) numerical differentiation for the surface heat flux density. Hence, before any further processing, the measured temperatures have to be smoothed in time. The type of smoothing very much depends on the intended application of the finally computed HTC.

If it will be used only as verifier of the quenching conditions, i.e., as a function of time, to calculate the temperature distribution in the probe itself, then ordinary smoothing of input temperatures is sufficient. It only has to remove the so-called noise in the data that is caused by random measurement errors. On the other hand, if the surface HTC is to be used for other geometries, then it is taken as a function of the surface temperature instead of time. Here, the smoothing includes an additional task. Besides removing the noise, it also has to produce a function that is monotone decreasing in time, to eventually ensure the monotonicity of the surface temperature.

12.05.10.1 Ordinary Smoothing without Constraints

For temperatures measured in quenching, the noise introduced by random measurement errors contains only high frequency oscillations, which are, usually, small in amplitude. So, the main goal of smoothing is to filter this type of noise, but the overall shape of the data should remain unchanged. Quite generally, such a smoothing of data can be done locally or globally in time by several standard algorithms.

Immediately, it should be said that standard local algorithms (see Ref. (*41*)) are not adequate for smoothing of measured temperatures. In local smoothing, the smoothed value at a given point in time is calculated as a weighted average of a small number of nearby measurements. Very often, it is computed from a low-degree polynomial least-squares approximation. When applied through the whole data set, this provides a quick and simple way to obtain a locally smoothed table of values. Unfortunately, this procedure is frequently misused in practice as a substitute for global smoothing. Due to its local nature, it removes only the 'local noise,' and simply damps all other oscillations in the data. To achieve a more global damping, the procedure is then bluntly repeated several times. As a result, we may get an oversmoothed data set in which the true shape of the curve is lost. In the so-smoothed near-surface temperature, all local variations are overdamped, and this gives unrealistically small peaks in the calculated HTC.

To circumvent these problems, the measured temperatures are smoothed globally, over the whole time range. In order to provide a freedom of choice for time levels in the HCE solution algorithm, an output of smoothing needs to be a smoothing function f, which can be evaluated at any time point in the range. Moreover, this function f has to be sufficiently smooth for numerical differentiation – at least continuously differentiable (C^1 smoothness), to avoid sudden jumps or discontinuities in the calculated α.

The smoothing function f is obtained by finding a suitable approximation of the measured data, i.e., by solving an appropriate optimization problem. Usually, the function $f(t)$ is assumed to have a prescribed form, with a certain number of 'free' parameters, as in global fitting. For statistical reasons that justify the noise removal from the original data, these unknown parameters are computed by solving the corresponding least squares (LSQ) approximation problem. Sometimes, this problem is extended by introducing additional parameters, which are then optimized to provide a visually more pleasing curve (as in Ref. (*31*), for smoothing splines).

The following three forms of functions are often used in practice for global approximation: piecewise polynomials (splines), trigonometric polynomials (Fourier sums), and exponential sums. In our experience, when there are no additional shape constraints on the smoothing function, the best way for global smoothing of measured temperatures is to take f as a low-degree polynomial spline. Trigonometric polynomials are more suited for approximation of periodic functions, and the so-called Fourier filtering would be unnatural here, because there is no inherent periodicity in measured temperatures. Finally, exponential sums are somewhat harder to compute, as we have to solve a nonlinear LSQ problem to get the so-called decay exponents.

Algorithms for global smoothing by polynomial splines are given in Refs. (*30,31*). In addition, the accompanying software is publically available and free to use. So, all measured temperatures can be smoothed by using the curve-fitting routine CURFIT from FITPACK (*31*), which is perfectly suited for this purpose.

- CURFIT computes a smoothing spline approximation of a given data set, as a compromise between global goodness and local smoothness of fit. The smoothing function f is represented as a linear combination of polynomial B-splines, and the computed coefficients are used for future evaluations of f.

- Since all temperature curves have a similar overall shape (they are measured by the same type of probe, and only the quenching conditions are different), it is quite easy to incorporate CURFIT into an automatic smoothing routine for all data sets.

This procedure is used with the Ipsen–Liscic flux sensor for smoothing of both measured temperatures and the calculated α curve. Because the cooling process is relatively slow in gas quenching, all approximations are computed as cubic splines, which are twice continuously differentiable (C^2). For liquid quenchants, such approximations are simply too smooth, and this is clearly visible in both examples given in the last section. Here, parabolic splines (with C^1 smoothness) are more adequate for global smoothing without constraints.

12.05.10.2 Monotone Smoothing

In the TGS software that comes with the Liscic/Petrofer probe, we have an additional shape constraint on the smoothing function f – it has to be monotone decreasing in time. Accordingly, a global numerical procedure for finding f is to compute a least squares approximation of the measured data, except that f is restricted to be monotone. Any decent fit should observe a descending trend in the data, and this fact may be used to check the data. Depending on the chosen form of f, this usually leads to a constrained optimization problem, which is more difficult to solve than the corresponding unconstrained problem.

For example, monotone smoothing can done by using low-degree polynomial splines (*31*), and this leads to a constrained optimization problem, with linear inequality constraints on coefficients in the B-spline representation of f. Note that FITPACK already contains the routine CONCON for convex smoothing of data. It can be modified into a monotone decreasing smoother by changing the built-in constraints. Unfortunately, while CURFIT works with splines of any given degree, CONCON is designed to compute only with cubic splines. So, even more changes are needed to make it work with parabolic splines, which are better suited for temperatures measured in liquid quenchants.

For these reasons, we take a different approach. Instead of polynomial splines, we use continuously differentiable (C^1) exponential splines for monotone smoothing. These splines are more difficult to calculate, but in the end, we obtain an unconstrained LSQ optimization problem, which is then easier to solve. Moreover, for smoothing of temperatures, this form of the smoothing function f offers some extra advantages.

Informally speaking, exponential C^1 splines are functions that are piecewise composed of ordinary exponential functions $a + be^{d \cdot t}$, where the parameters a, b, d may be different for each piece (on its subinterval), and these pieces have to be joined in such a way to give the global C^1 smoothness of the function.

More precisely, as with all splines, the construction of exponential C^1 splines begins by specifying the so-called spline mesh. It is given as an ascending sequence of $m + 1$ knots

$$\xi_0 < \ldots < \xi_m,$$

and divides the whole interval $[\xi_0,\xi_m]$ into m subintervals $[\xi_{j-1},\xi_j]$, for $j = 1,\ldots, m$. An exponential C^1 spline f on the interval $[\xi_0,\xi_m]$ is then constructed as follows. The restriction of f on each subinterval $[\xi_{j-1},\xi_j]$ is equal to some exponential function p_j, i.e.,

$$f(t) = p_j(t), \quad t \in [\xi_{j-1}, \xi_j], \quad j = 1, \ldots, m, \qquad [19]$$

where the exponential 'piece' p_j is defined by

$$p_j(t) = \begin{cases} a_j + b_j e^{d_j t}, & \text{for } d_j \neq 0, \\ a_j + b_j t, & \text{for } d_j = 0, \end{cases} \qquad [20]$$

Note that each piece p_j is determined by three parameters a_j, b_j, and d_j. When $d_j = 0$, the first form in eqn [20] would give p_j as the constant $a_j + b_j$, despite the fact that it is specified by two remaining parameters, and only one is sufficient. To retain consistency in this case, p_j is taken as a linear function, which has two degrees of freedom.

The requirements [19] and [20] impose the following continuity conditions at all interior knots $\xi_1, \ldots, \xi_{m-1}$ of the spline mesh

$$f(\xi_j) = p_j(\xi_j) = p_{j+1}(\xi_j), \quad 1, \ldots, m-1. \qquad [21]$$

Finally, to make f continuously differentiable on the whole interval $[\xi_0,\xi_m]$, similar continuity conditions are imposed on the first derivatives of pieces at all interior knots

$$f'(\xi_j) = p_j'(\xi_j) = p_{j+1}'(\xi_j), \quad j = 1, \ldots, m-1. \qquad [22]$$

The interior knots are also known as the breakpoints of f, since the second derivative f'' has jumps at these points.

From eqn [20] it is obvious that each piece p_j has three degrees of freedom. It can also be given by its endpoint values $p_j(\xi_{j-1})$, $p_j(\xi_j)$, and d_j then determines the essential shape of p_j between these two values. This initially gives $3m$ degrees of freedom, but $2m - 2$ continuity conditions [21,22] imply that only $m + 2$ degrees of freedom are left for f. In fact, the exponential C^1 spline f is uniquely determined by the following $m + 2$ parameters:

- two global endpoint values $f_0 = f(\xi_0)$ and $f_m = f(\xi_m)$, which can be viewed as the boundary conditions for f,
- m values of local shape parameters $d_1, \ldots, d_m$ – one value for each subinterval of the spline mesh.

It is easy to see that such a function is always monotone on the interval $[\xi_0,\xi_m]$. The trend of f is determined solely by the boundary conditions, and $f_0 > f_m$ makes f monotonically decreasing. Therefore, no additional monotonicity constraints are required for monotone smoothing.

For a given set of parameter values, in the above form of f, the continuity eqns [21] and [22] become a linear system for the remaining local parameters of all pieces. This system is quite easy to solve, either numerically, or even analytically, to obtain the local form [20] of each piece. Then p_j can be evaluated at each point t in its subinterval.

Exponential C^1 splines can also be constructed by using the so-called monotonicity operator (see Ref. (*42*)), which gives the following alternate form of f

$$f(t) = f(\xi_0) + f'(\xi_0) \cdot \int_{\xi_0}^{t} \exp\left(\int_{\xi_0}^{\xi} B_0(\eta) \mathrm{d}\eta \right) \mathrm{d}\xi, \qquad [23]$$

where B_0 is a piecewise constant function on the same spline mesh, and its value is equal to the shape parameter d_j on the half-open subinterval $[\xi_{j-1},\xi_j]$, for $j = 1,\ldots, m$ (the value at ξ_0 is not important, and may be taken as zero).

After some manipulation, this form gives somewhat different, numerically more stable expressions for pieces p_j than those in eqn [20], and they are used in the actual computation.

Finally, from eqn [23] it follows that the shape parameters d_j control the second derivative of f, i.e., determine the local convexity or concavity of each piece, which justifies their name.

Suppose that the measured data set consists of $n_d + 1$ points (t_k, T_k), for $k = 0,\ldots, n_d$, where t_k now denote the times at which the temperatures are measured (and not the time levels, as before), and $T_k = T_n(t_k)$ are the measured near-surface temperatures. In addition, we assume that the whole set is sorted increasingly in time

$$0 = t_0 < t_1 < \ldots < t_{n_d-1} < t_{n_d},$$

and that the first measurement is taken at the time $t_0 = 0$. If the original measurement starts at a time $t_1 > 0$, the point $(0, T_1)$ is added at the beginning of the data set.

For simplicity, the spline mesh is taken as a suitable subset of all measured times; i.e., the spline knots coincide with some of the data sites t_k. Regardless of the number of knots in the mesh (which may vary), the boundary knots are always placed as

$$\xi_0 = t_0 = 0, \quad \xi_m = t_{n_d}.$$

This choice makes it easier to manipulate with the boundary conditions f_0 and f_m throughout the smoothing process.

The calculation is organized in several stages, as an iterative refinement of the spline mesh, to obtain better and better approximations. In each stage, the spline mesh is fixed, and the corresponding exponential C^1 spline f is computed to fit the data. Remember that f is determined by $m + 2$ parameters f_0, f_m, $d_1,\ldots, d_m$. At a particular stage, some of them may have fixed values (mainly to speed up the process), and the remaining free parameters are computed by solving the least squares problem

$$\sum_{k=0}^{n_d} (T_k - f(t_k))^2 \to \min, \qquad [24]$$

to obtain the best possible fit and remove the noise in the data as well.

This is a nonlinear unconstrained optimization problem, which can be solved by various iterative methods. However, the derivatives of f with respect to the free parameters are quite hard to compute here. To avoid that, eqn [24] is actually solved by the Nelder–Mead simplex search algorithm (*43*), because it uses only function values of f.

- In the first stage, the spline mesh consists of only four subintervals, and the interior knots are positioned in accordance with the temperature range, as uniformly as possible. The initial approximation is computed with fixed boundary conditions, which are taken from the measurements. This very crude approximation is then iteratively refined.
- In each subsequent stage, the number of subintervals in the mesh is doubled, and new interior knots are inserted between the old ones, halfway in temperature. The initial values of all parameters are taken from the previous approximation.
- This refinement is repeated until a sufficiently good approximation is found, or until a prescribed maximum of subintervals is reached (this limit is 64 in Module 1).
- In the last stage, the spline mesh is not changed, but all parameters, including the boundary conditions f_0 and f_m, are allowed to be free. This gives the final monotone approximation f of measured temperatures.

As can be expected, monotone smoothing with exponential C^1 splines is much slower than smoothing or monotone smoothing with polynomial splines. Still, it is not prohibitively slow for measured data sets encountered in practice. It can also be used to provide additional information about the quenching process, which may be missing or inaccurate.

An exponentially decaying function in time matches the form of the exact solution of the HCE for slowly varying boundary conditions. This is the case at the end of the quenching process, when the difference between the probe temperature and the surrounding quenchant temperature becomes sufficiently small. If the temperatures are measured until the probe is properly cooled, and the tail end temperatures are approximated by an exponential function, the time limit $t \to \infty$ of such an approximation provides a very good approximation of the final stationary temperature T_∞ of the whole system.

- If T_∞ is required, we can use the time limit of the last piece p_m in the final monotone approximation f.
- As an alternative, only a selected final portion of the temperature data (for example, the last 25 °C) is approximated as in eqn [24], with only one subinterval. The time limit is then given by a_1 from eqn [20].

This is very useful in practice, when the quenchant temperature T_x is given only as a constant value, which is, usually, the initial temperature of the bath.

12.05.11 Numerical Examples

12.05.11.1 Ipsen–Liscic Flux Sensor – Gas Quenching

The cooling process in gas quenching is relatively slow, but the quenching conditions can be changed in time. The example given here is chosen specifically in order to demonstrate that such changes are well reflected in the calculated HTC, based on the data gathered by the Ipsen–Liscic flux sensor. (Data used by permission from Ipsen International GmbH, Kleve, Germany.)

In this particular experiment, the probe is put in a standing position inside a high-pressure vacuum furnace. It is initially heated to $T_0 = 1101$ °C, and then quenched by nitrogen N_2, blown from above the probe, at fan speed of 3000 rotations per minute, with varying pressure: 600 kPa for the first 900 s, and 320 kPa later on. This change in pressure should be reflected as a drop in α.

Two near-surface temperatures T_{n_1} and T_{n_2} are measured at the opposite sides of the probe, both at the depth of 2.4 mm. Since the probe is standing and the gas is blown along the probe, to apply the 1-D model [4] with radial symmetry, the near-surface temperature T_n is taken as the average $T_n = (T_{n_1} + T_{n_2})/2$. It is considered as if measured at the depth $d = 2.4$ mm, so its position is $r_n = 0.0226$ m. The difference between T_{n_1} and T_{n_2} is always less than 4 °C, which indicates only a small departure from radial symmetry. Henceforward, T_n will be denoted by $T- 2.4$ to indicate the depth.

The external gas temperature T_x is also taken as the average of temperatures measured before and after the heat exchanger, and here we have only one additional thermocouple that measures the core temperature T_c.

All temperatures are measured until $t_{\text{final}} = 1871$ s, but each data set has only 184 points, with the time step $\Delta t \approx 10$ s. This time step is much larger than usual, due to an error in calibration of the data gathering device. Despite that, we use these data here to illustrate the robustness of the smoothing procedure, which has to cope with such events in practice.

The original unsmoothed measured temperatures T_c, $T- 2.4$, and T_x are given in Figure 44 (in that order, from the top of the figure).

The calculated HTC α is shown in Figure 45 as a function of time, and in Figure 46 as a function of the calculated surface temperature T_s.

The change of pressure at $t = 900$ s is clearly visible in α. Note that the smoothed $\alpha(t)$ curve has a small wiggle around $t = 900$ s, just before the drop, which is an actual phenomenon, only slightly exaggerated by the cubic spline approximation.

This example shows that α in gas quenching has to be treated as a function of time, to represent the quenching conditions correctly. Therefore, no attempt is made to convert α into a function of T_s for practical purposes, even though it is shown here.

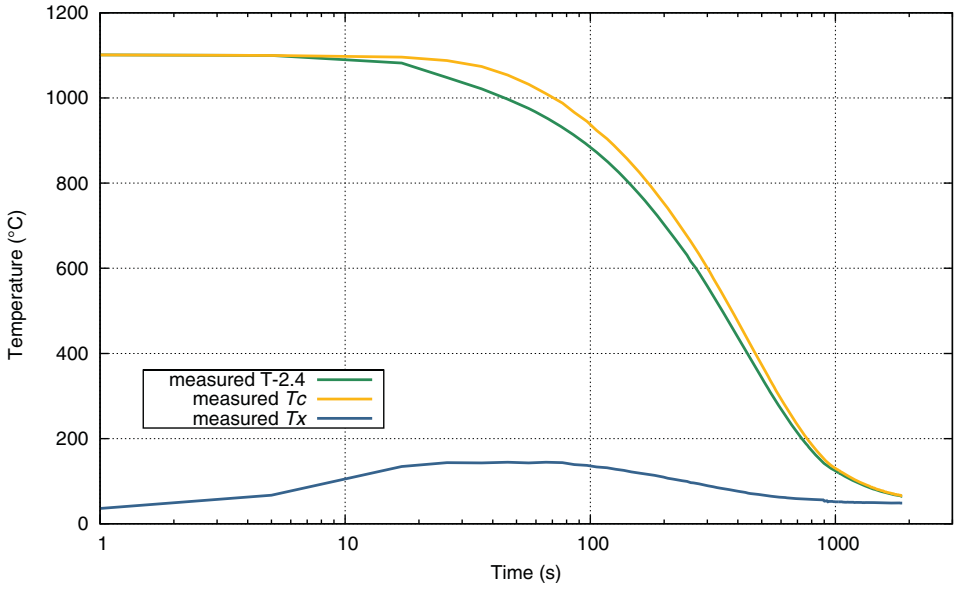

Figure 44 Gas quenching: measured core, near-surface, and external temperatures.

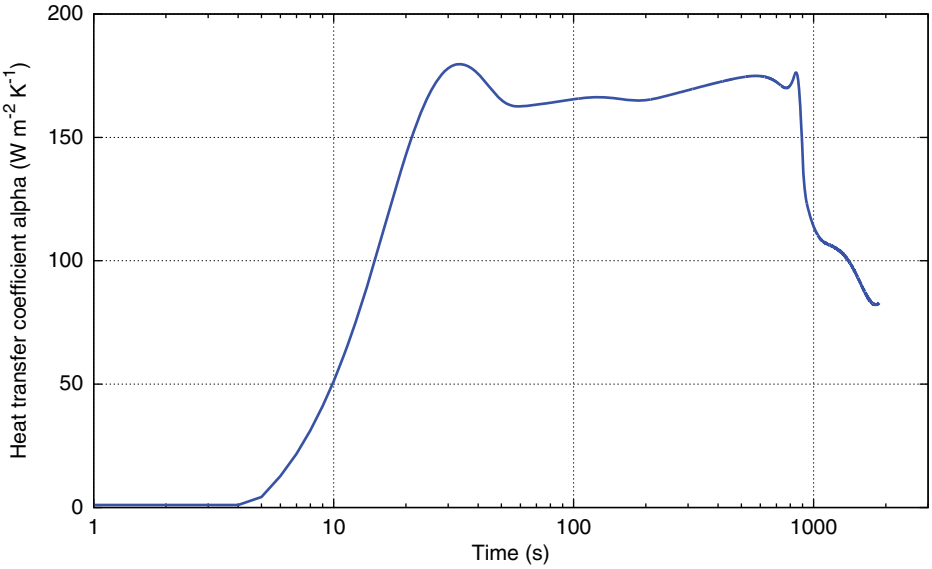

Figure 45 Gas quenching: calculated HTC α as a function of time.

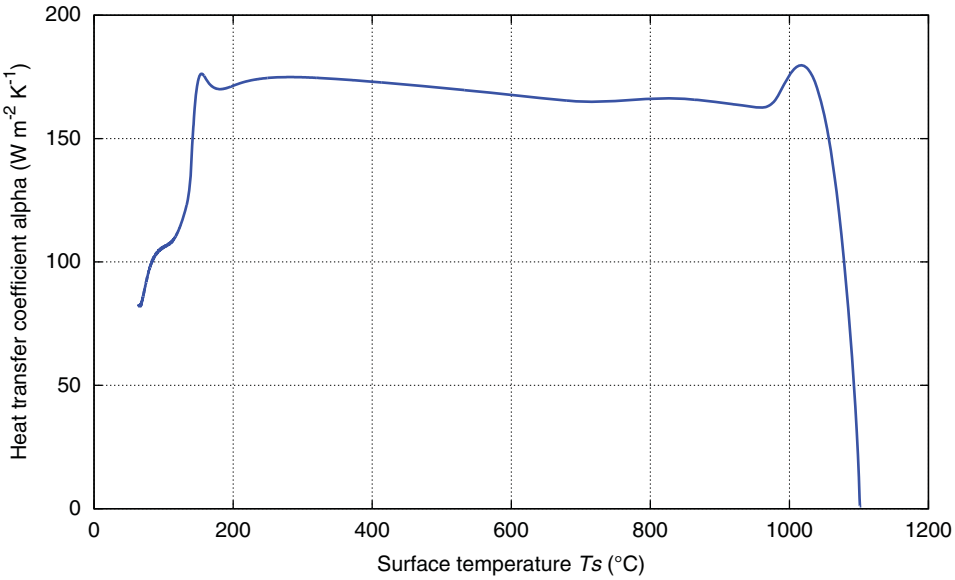

Figure 46 Gas quenching: calculated HTC α as a function of the surface temperature.

The differences between measured and calculated temperatures at reference points are given in Figure 47.

These errors are calculated in Phase 2 (model verification), and refer to the original measured temperatures, so they include the initial smoothing of measured near-surface temperatures, numerical solution of the HCE [4], and the final smoothing of calculated α.

The errors in near-surface temperature $T-$ 2.4 are almost entirely caused by the initial smoothing, i.e., they represent the noise in the data. We may conclude that the HTC calculation in Phase 1 is quite accurate, and the smoothing errors in α are really negligible. Finally, the errors in core temperature T_c are reasonably small, and well within acceptable limits for all applications.

12.05.11.2 Liscic/Petrofer Probe – Oil Quenching

The cooling process in liquid quenchants is less controllable in time. On the other hand, there is a wide variety of quenchants that can be selected for the process, and the choice depends on a particular purpose. Here, different quenchants may cause very different effects near the surface. This point will be illustrated by two examples, where the Liscic/Petrofer probe is used in different

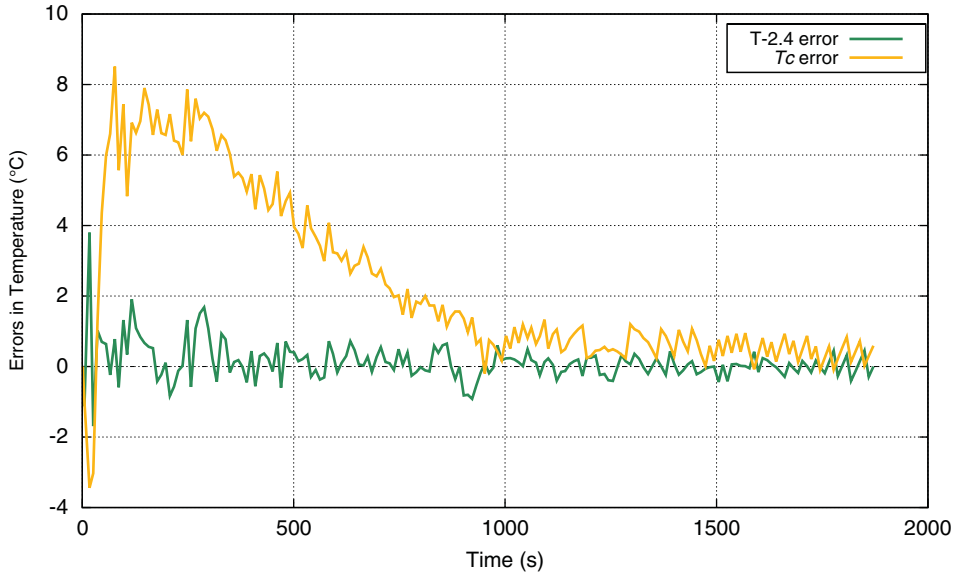

Figure 47 Gas quenching: errors in calculated core and near-surface temperatures.

quenchants – a mineral oil and a polymer solution. (Data used by permission from PetroFer Chemie H. R. Fischer GmbH + Co. KG, Hildesheim, Germany.)

The near-surface temperature T_n is measured at the depth $d = 1$ mm, so its position is $r_n = 0.024$ m. The probe is equipped with two additional thermocouples. One measures the core temperature T_c, and the other one is located at the depth of 4.5 mm and measures the intermediate temperature T_i. From now on, to indicate the depths, T_n and T_i will be denoted by $T-$ 1.0 and $T-$ 4.5, respectively.

All three temperatures are measured until $t_{\text{final}} = 981$ s, with nonuniform time steps. At the beginning, the time step is $\Delta t = 0.1$ s, while at the end, it is much larger, $\Delta t = 1$ s. Each data set has 1461 points.

Unlike before, the external temperature T_x is not measured in time. Here, it is given as the initial temperature of the quenching bath. In both cases below, we have $T_x = 50\ ^\circ$C.

In the first example, the probe is quenched in a medium viscosity accelerated quenching oil, and the initial temperature of the probe is $T_0 = 854\ ^\circ$C.

The original unsmoothed measured temperatures T_c, $T-$ 4.5, $T-$ 1.0, and T_x are given in Figure 48 (in that order, from the top of the figure).

Note that there is a very sharp change (or drop) in the near-surface temperature at about $t = 14$ s, when nucleate boiling begins. This change is slightly less visible in the intermediate temperature, because of the damping effect.

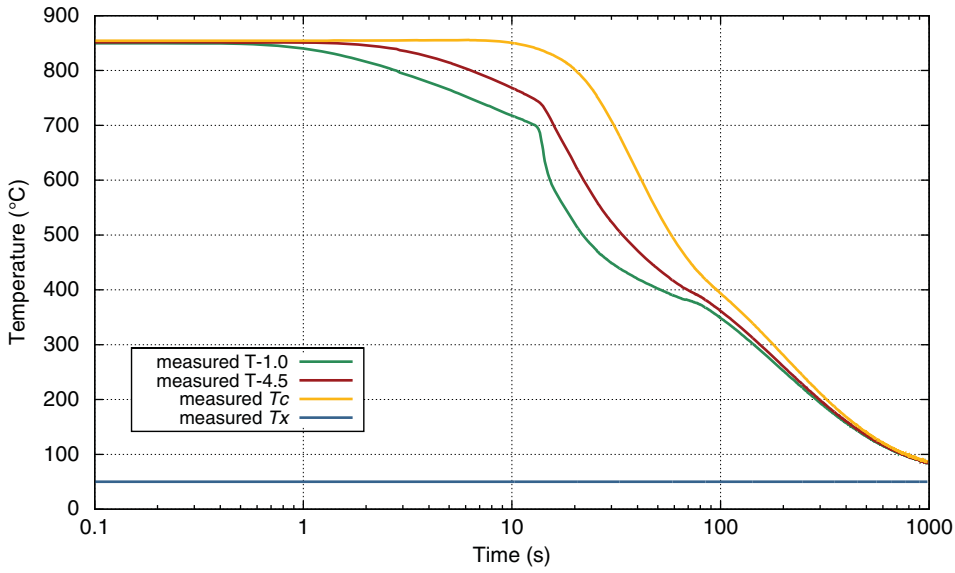

Figure 48 Oil quenching: measured core, intermediate, near-surface, and external temperatures.

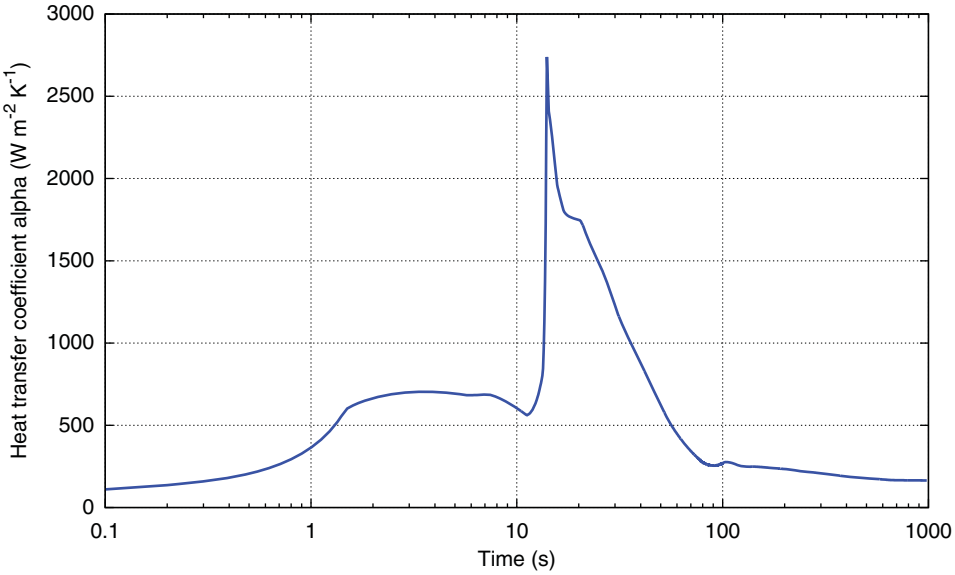

Figure 49 Oil quenching: calculated HTC α as a function of time.

Apart from that, all temperatures appear to be very smooth, even without smoothing, since the noise is very small in magnitude. However, this single sharp change in $T-1.0$ shows that C^1 smoothness is the highest reasonable smoothness that should be used for approximating functions.

Since there are no other abrupt changes of quenching conditions, the calculated surface temperature T_s also decreases in time, and there is no need for an additional monotone approximation to make α a function of T_s.

The calculated HTC α is shown in **Figure 49** as a function of time, and in **Figure 50** as a function of the calculated surface temperature T_s.

As expected, the HTC values are much higher here than in the gas quenching example. Because the quenching is done in oil, there are no chaotic effects on the surface of the probe, and both HTC curves are fairly regular in shape. In fact, all three phases of the heat extraction are nicely visible.

The differences between measured and calculated temperatures at reference points are given in **Figure 51**.

Like before, the errors refer to the original measured temperatures. It should be noted that all errors in $T-1.0$ are now entirely due to the initial monotone smoothing, since the HTC calculation exactly reproduces the smoothed near-surface temperature. Most of these errors come from random noise in the data, and only a small 'regular' part reflects the monotone approximation errors.

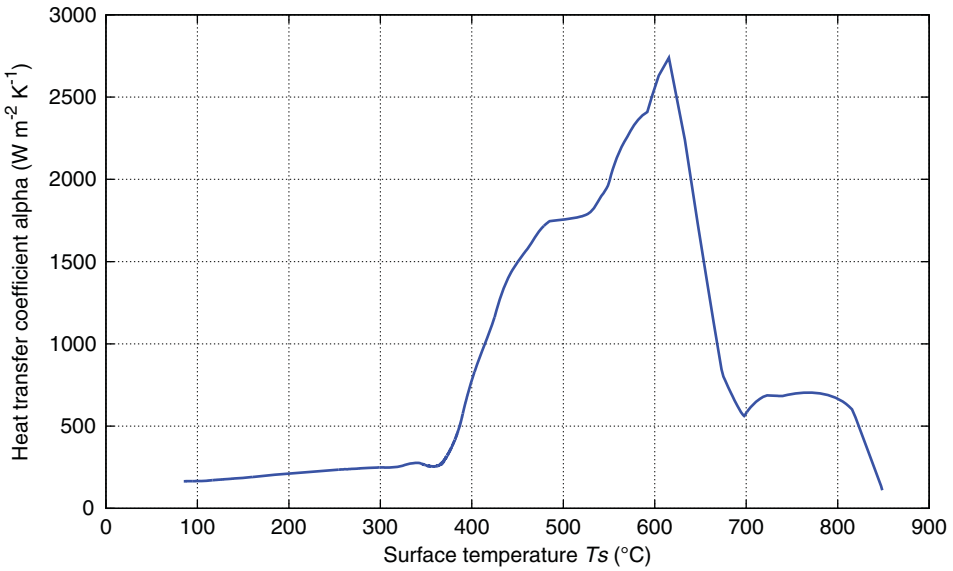

Figure 50 Oil quenching: calculated HTC α as a function of the surface temperature.

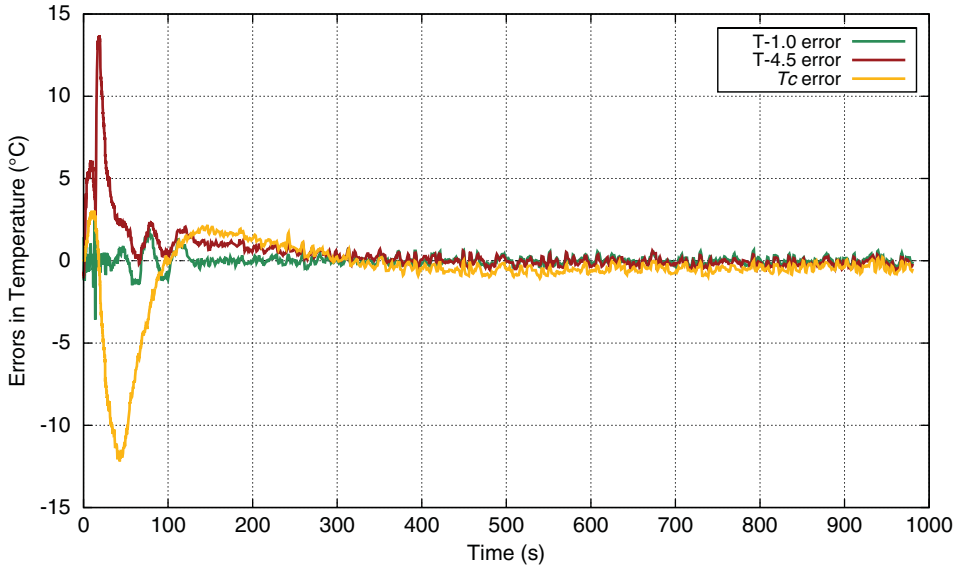

Figure 51 Oil quenching: errors in calculated core, intermediate, and near-surface temperatures.

The errors in core and intermediate temperatures are somewhat larger than before. This is nothing unusual, as the temperature gradients are much higher here. In addition, the strict radial symmetry of temperatures in the probe is almost impossible to achieve in practice, and these errors may be caused by slightly slanted immersion of the probe into the quenchant, or small variations in the fluid flow around the probe.

12.05.11.3 Liscic/Petrofer Probe – Polymer Quenching

It is well known that polymer quenching is likely to cause chaotic violent changes in local quenching conditions near a particular point at the surface, so that the symmetry assumption is almost certainly not valid in this case. However, in most cases, these irregularities are very local, both in time and space, and the 1-D radial symmetry model may still be sufficiently accurate 'on the average' to calculate the temperature distribution in the probe.

To demonstrate this, in the second and final example, the probe is quenched in a 10% polymer solution, and the initial temperature of the probe is $T_0 = 855\ ^\circ\text{C}$.

The original unsmoothed measured temperatures T_c, $T-4.5$, $T-1.0$, and T_x are given in Figure 52 (in that order, from the top of the figure).

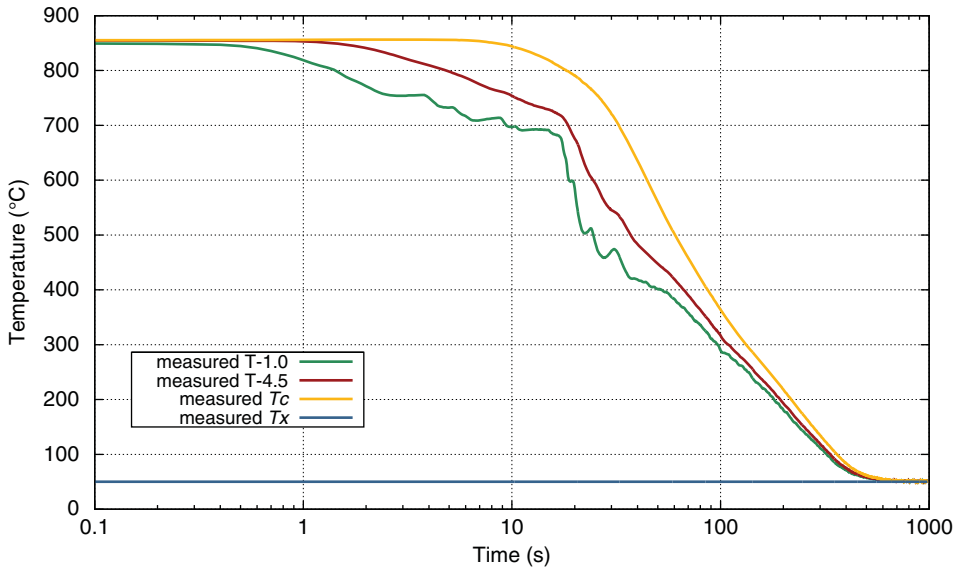

Figure 52 Polymer quenching: measured core, intermediate, near-surface, and external temperatures.

The measured near-surface temperature is very rough for the first 35 s. Moreover, it increases significantly for some periods of time, reflecting the violent conditions at the surface. In fact, these conditions are so irregular, that the monotone smoothing of $T-1.0$ does not help, and the calculated surface temperature T_s is not strictly decreasing in time. As a consequence, an additional monotone approximation of T_s is necessary to express α as a function of T_s.

The calculated HTC α is shown in **Figure 53** as a function of time, and in **Figure 54** as a function of the monotone surface temperature T_s.

In contrast to the previous example, both HTC curves are very irregular. So, despite all monotone smoothing efforts, they still reflect the quenching conditions at the surface.

The differences between measured and calculated temperatures at reference points are given in **Figure 55**.

High errors in $T-1.0$ for the first 35 s are now caused by the monotone approximation of $T-1.0$, and reflect the non-monotonicity in the original data.

Finally, regardless of all chaotic phenomena at the surface, the errors in core and intermediate temperatures are not much higher than in oil quenching.

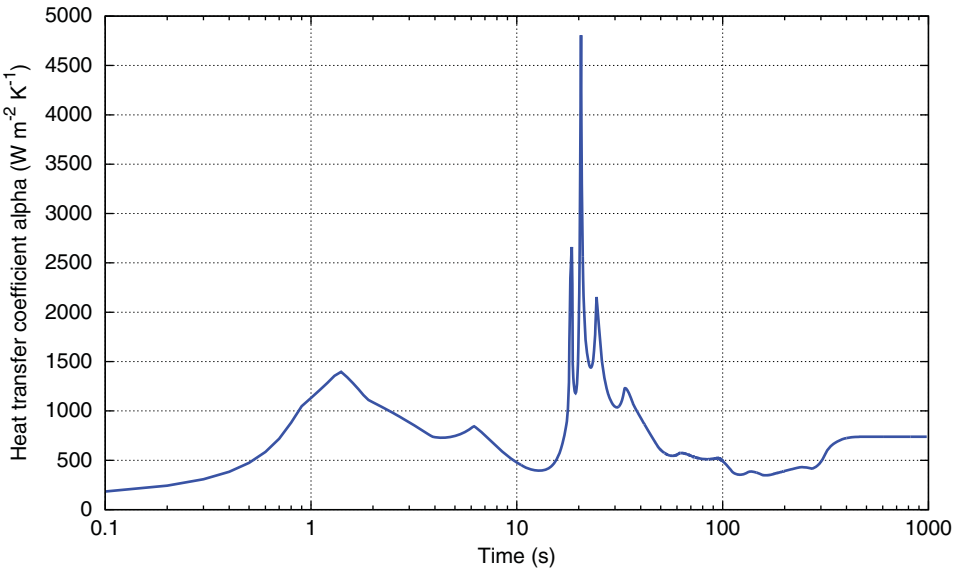

Figure 53 Polymer quenching: calculated HTC α as a function of time.

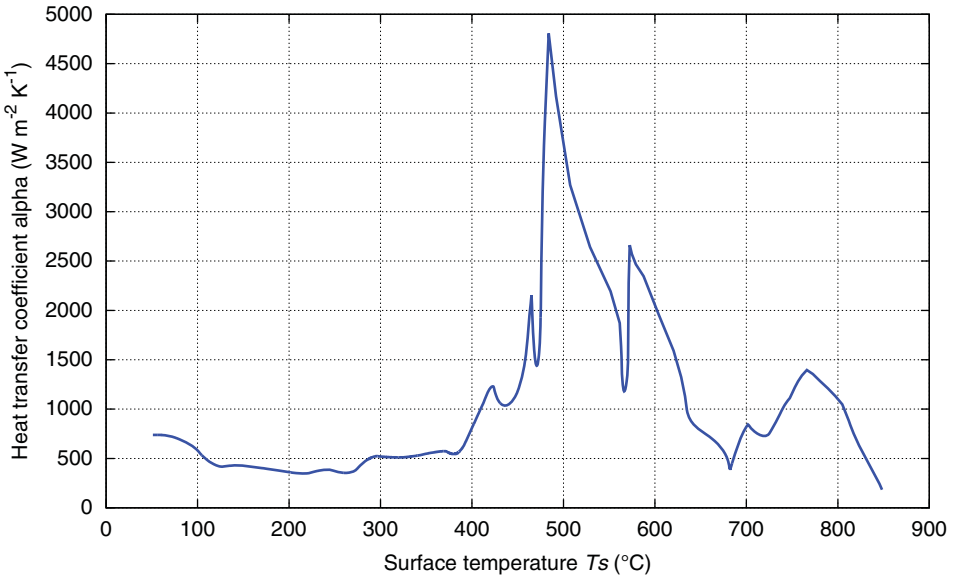

Figure 54 Polymer quenching: calculated HTC α as a function of the surface temperature.

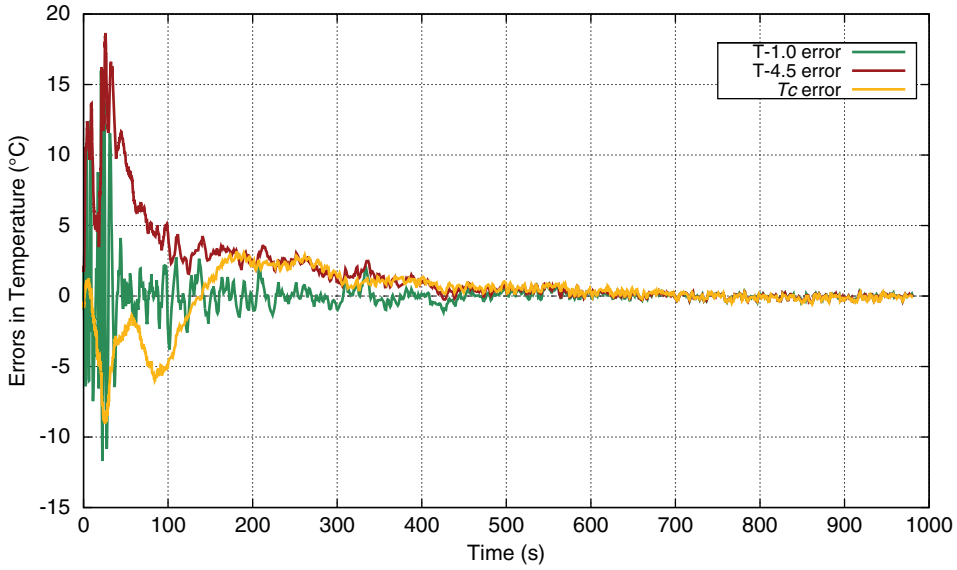

Figure 55 Polymer quenching: errors in calculated core, intermediate, and near-surface temperatures.

See also: Material Properties for Numerical Calculations; Introduction to Steel Heat Treatment; Controlling the Cooling Process – Measurement, Analysis, and Quality Assurance; Hardenability of Steel.

References

1. Liščić, B. Heat Transfer Control during Quenching. *Mater. Manuf. Process.* **2009,** *24* (7–8), 879–883.
2. Rondeau, D. The Effects of Part Orientation and Fluid Flow on Heat Transfer Around a Cylinder. MSc Thesis, Worcester Polytechnic Institute, 2004.
3. Stich, A.; Tensi, H. M. Wärmeübetragung und Temperaturverteilung mit Benetzungsablauf beim Tauchkühlen. *HTM Härterei–Techn. Mitt.* **1995,** *50* (1), 31–35.
4. Kobasko, N. I.; Moskalenko, A. A.; Totten, G. E.; Webster, G. M. Experimental Determination of the First and Second Critical Heat Flux Densities and Quench Process Characterization. *ASM Int. JMEPEG* **1997,** *6* (1), 93–101.
5. Kobasko, N. I. Private Communication.
6. Liščić, B.; Singer, S.; Beitz, H. Dependence of the Heat Transfer Coefficient at Quenching on Diameter of Cylindrical Workpieces. *J. ASTM Int.* **2011,** *8* (7).
7. Kobasko, N. I. Why Database for Cooling Capacity of Various Quenchants Should be Developed?. In *Proc. 8th IASME/WSEAS Intl. Conf. on Heat Transfer, Thermal Engineering and Environment, August 20–22, 2010,* Taipei, Taiwan; pp 304–309.
8. Kobasko, N. I. Thermal Processes in Quenching of Steel (in Russian). *Metallovedenie i Termicheskaya Obrabotka Metallov* **1968**, 3, 2–6.
9. Edenhofer, B. An Overview of Advances in Atmosphere and Vacuum Heat Treatment. *Heat Treat. Met.* **1999,** *26* (1), 1–5.
10. Radcliffe, E. J. Gas Quenching in Vacuum Furnaces – A Review of Fundamentals. *Ind. Heat.* **1987,** *54* (11), 34–39.
11. Segerberg, S.; Troell, E. High-pressure Gas Quenching Using a Cold Chamber to Increase Cooling Capacity. *Heat Treat. Met.* **1997,** *24* (1), 21–24.
12. Edenhofer, B.; Bouwman, J. W.; Peter, W.; Bless, F. Erfahrungen und Ergebnisse beim Gasabschrecken in einer kalten Kammer mit und ohne Düsenfeld. *HTM Härterei–Techn. Mitt.* **1997,** *52* (3), 138–143.
13. Liščić, B. Der Wärmeentzug beim Härten – Vom unbestimmten Abschrecken in flüssigen Mitteln hin zum geregelten Wärmeentzug beim Gasabschrecken. *HTM – J. Heat Treat. Mater.* **2007,** *62* (6), 250–259.
14. Liščić, B. Der Temperaturgradient auf der Oberfläche als Kenngröße für die reale Abschreckintensität beim Härten. *HTM Härterei–Techn. Mitt.* **1978,** *33* (4), 179–191.
15. Liščić, B.; Filetin, T. Measurement of Quenching Intensity, Calculation of Heat Transfer Coefficient and Global Database of Liquid Quenchants. *Mater. Eng. – Materialove inžinierstvo* **2012,** *19,* 52–63.
16. Kobasko, N. I. Effect of Accuracy of Temperature Measurement on Determination of Heat Transfer Coefficient during Quenching in Liquid Media. *J. ASTM Int.* **2012,** *9* (2).
17. Tensi, H. M.; Totten, G. E.; Stich, A. Temperature Measurement Accuracy in Cooling Curve Analysis. *Heat Treat. Prog.* **Jun 2002,** *2*.
18. Nanigian, J. Improving Accuracy and Response of Thermocouples in Ovens and Furnaces. In *Proc. of Intl. Heat Treating Conference: Equipment and Processes,* Schaumburg, *Ill.;* Totten, G. E., Wallis, R. A., Eds.; 1994; pp 171–174.
19. Liščić, B.; Singer, S.; Smoljan, B. Prediction of Quench-Hardness within the Whole Volume of Axially Symmetric Workpieces of Any Shape. *J. ASTM Int.* **2010,** *7* (2).
20. Liščić, B. System for Process Analysis and Hardness Prediction When Quenching Axially-symmetrical Workpieces of Any Shape in Liquid Quenchants. In *Materials Science Forum*, Vols. 638–642, Chandra, T.; Wanderka, N.; Reimers, W.; Ionescu, M., Eds.; *THERMEC 2009, 6th International Conference on Processing & Manufacturing of Advanced Materials*, Berlin, Germany, *Aug. 25–29, 2009*; Trans Tech Publications, 2010, pp 3966–3974.
21. Edenhofer, B. Steuerung der Hochdruckgasabschreckung mittels Wärmestromsensor. *HTM Härterei–Techn. Mitt.* **1996,** *51* (5), 314–318.
22. Totten, G. E., Ed. *Fuels and Lubricants Handbook: Technology, Properties, Performance, and Testing;* ASTM International: West Conshohocken, 2003.
23. Liščić, B., Tensi, H. M., Canale, L. C. F., Totten, G. E., Eds. *Quenching Theory and Technology;* CRC Press, Taylor & Francis: Boca Raton, 2010.
24. Tensi, H. M. Wetting Kinematics. In *Theory and Technology of Quenching;* Liščić, B., Tensi, H. M., Luty, W., Eds.; Springer Verlag: London, 1992.
25. Majorek, A.; Müller, H.; Macherauch, E. Computersimulation des Tauchkühlens von Stahlzylindern in verdampfenden Flüssigkeiten (in German). *HTM Härterei–Techn. Mitt.* **1996,** *51* (1), 11–17.
26. Jeffrey, A. *Applied Partial Differential Equations: An Introduction;* Academic Press, An imprint of Elsevier Science: San Diego, 2003.

27. The British Iron and Steel Research Association. *Physical Constants of Some Commercial Steels at Elevated Temperatures;* Butterworths Scientific Publications: London, 1953.
28. Richter, F. *Die wichtigsten physikalischen Eigenschaften von 52 Eisenwerkstoffen.* Stahleisen-Sonderberichte, Heft 8; Verlag Stahleisen m. b. H., Düsseldorf, 1973.
29. INCONEL Alloy 600, Publication Number SMC–027, Special Metals Corporation, 2008.
30. de Boor, C. *A Practical Guide to Splines,* rev. ed.; Springer: New York, 2001.
31. Dierckx, P. *Curve and Surface Fitting with Splines;* Clarendon Press: Oxford, 1993.
32. Tarantola, A. *Inverse Problem Theory and Methods for Model Parameter Estimation;* SIAM: Philadelphia, 2005.
33. Singer, S. Determination of the Heat Transfer Coefficient in the Law of Cooling for Gas-quenching Systems. *J. Numer. Anal. Ind. Appl. Math.* **2007,** *2,* 103–114.
34. Akima, H. A New Method of Interpolation and Smooth Curve Fitting Based on Local Procedures. *J. Assoc. Comput. Mach.* **1970,** *17* (4), 589–602.
35. Mitchell, A. R.; Griffiths, D. F. *The Finite Difference Method in Partial Differential Equations;* John Wiley & Sons Ltd.: Chichester, 1980.
36. Mattheij, R. M. M.; Rienstra, S. W.; ten Thije Boonkkamp, J. H. M. *Partial Differential Equations: Modeling, Analysis, Computation;* SIAM: Philadelphia, 2005.
37. Lattès, R.; Lions, J.-L. *Mèthode de Quasi-Reversibilitê et Applications;* Dunod: Paris, 1967.
38. Eymard, R.; Gallouët, T.; Herbin, R. Finite Volume Methods. In *Handbook for Numerical Analysis*; Ciarlet, P. G., Lions, J. L., Eds.; Elsevier Science: Amsterdam, 2000; Vol. VII, pp 713–1018.
39. Brent, R. P. *Algorithms for Minimization without Derivatives;* Prentice-Hall: Englewood Cliffs, 1973.
40. Gautschi, W. *Numerical Analysis,* 2nd ed.; Birkhäuser: New York, 2012.
41. Scheid, F. J. *Schaum's Outline of Theory and Problems of Numerical Analysis,* 2nd ed.; McGraw-Hill: New York, 1989.
42. Ramsey, J. O. Estimating Smooth Monotone Functions. *J. R. Statist. Soc. B* **1998,** *60,* 365–375.
43. Singer, S.; Singer, S. Efficient Implementation of the Nelder–Mead Search Algorithm. *Appl. Num. Anal. Comp. Math.* **2004,** *1* (3), 524–534.

12.06 Metallo-Thermo-Mechanical Coupling in Quenching

T Inoue, Saitama Institute of Technology, Fukaya, Japan

12.06.1	**Introduction**	178
12.06.1.1	Overview of the History of Modeling and Simulation up to 2000	178
12.06.1.2	What Is Metallo-Thermo-Mechanics?	179
12.06.2	**Kinetics of Phase Transformation and Structures in Solids**	181
12.06.2.1	Phase Transformation in Solids	181
12.06.2.2	Kinetics of Diffusion Transformation	181
12.06.2.3	Kinetics of Diffusionless Transformation	183
12.06.3	**Basic Theory and Governing Equations**	183
12.06.3.1	Mixture Rule and Basic Theory Based on Thermodynamics	183
12.06.3.2	Heat Conduction Equation and the Boundary Condition	185
12.06.3.3	Diffusion Equation of Carbon and/or Nitrogen and the Boundary Condition	185
12.06.3.4	Equation of Motion, Kinematics, and the Boundary Condition	186
12.06.4	**Inelastic Constitutive Equation**	186
12.06.4.1	Elastic Strain	186
12.06.4.2	Plastic Strain	187
12.06.4.3	Viscoplastic Strain	188
12.06.4.4	Creep Strain	188
12.06.4.5	Transformation Plastic Strain	188
12.06.4.6	Strain Induced by Diffusion of Chemical Components	190
12.06.5	**Material Data and the Database**	190
12.06.5.1	Outline of the Material Database MATEQ	191
12.06.5.1.1	Structure of the Database	191
12.06.5.2	Search Engine	192
12.06.5.3	Accumulated Data of Material Properties	193
12.06.5.3.1	Description of Data	193
12.06.5.4	Steel Grade Covered in the Database	195
12.06.6	**Computer Code Relevant to Metallo-Thermo-Mechanical Simulation – COSMAP**	197
12.06.6.1	Under Releasing Software	197
12.06.6.2	Development of New Code	197
12.06.6.3	Overview of the COSMAP System	197
12.06.6.3.1	COSMAP System	198
12.06.6.4	Development of New Simulation Code	198
12.06.6.5	Simulated Examples by the COSMAP System	200
12.06.7	**Jominy End Quenching**	201
12.06.7.1	Jominy Test	201
12.06.7.2	Identification of Heat Transfer Coefficient	202
12.06.7.3	Materials and the Data, Test Condition, and Simulation Technique	204
12.06.7.4	Experimental and Simulated Results and Discussions	204
12.06.7.5	Discussion from the Viewpoint of Hardenability	207
12.06.8	**Carburized Quenching**	207
12.06.8.1	Experimental Method	208
12.06.8.2	Simulation Method	208
12.06.8.2.1	Finite Element Model	208
12.06.8.2.2	Diffusion Analysis of Carbon	209
12.06.8.2.3	Heat Conduction Analysis	209
12.06.8.2.4	Transformation Plasticity	210
12.06.8.3	Results of Simulation and Experiment	210
12.06.8.3.1	Temperature, Carbon Content, and Phase Change	210
12.06.8.3.2	Distortion	211
12.06.8.3.3	Stress	212
12.06.8.4	Discussion on the Effect of Transformation Plasticity	212
12.06.9	**Dual Frequency Induction Hardening**	216
12.06.9.1	The Procedure for Electromagnetic and Metallo-Thermo-Mechanical Coupling Analyses	216
12.06.9.2	Joule Heat Induced by Eddy Current	217

12.06.9.3 Simulation Models 218
12.06.9.4 Experimental Details 218
12.06.9.5 Simulated Results and Comparison with Experiments 219
12.06.9.5.1 Temperature Variation 219
12.06.9.5.2 Metallic Structure 221
12.06.9.5.3 Residual Stresses 221
12.06.9.5.4 Distortion 224
12.06.9.6 Discussion on the Mechanism of Contour Hardening 224
12.06.10 Laser – Hardening 225
12.06.10.1 Experimental Conditions and the Results 226
12.06.10.1.1 Experimental Condition of YAG and CO_2 Laser Beam Irradiation 226
12.06.10.1.2 Observed Pattern of Irradiated Zone and the Microstructure 226
12.06.10.2 Simulation Condition of Laser Hardening 227
12.06.10.2.1 Pulsed YAG Laser Spot Hardening 227
12.06.10.2.2 CO_2 Laser Line-Hardening 227
12.06.10.3 Simulated Results and Discussions 228
12.06.10.3.1 Pulsed YAG Laser Spot Hardening 228
12.06.10.3.2 Traveling CO_2 Laser Hardening 230
12.06.11 Japanese Sword 232
12.06.11.1 Identification of Heat Transfer Characteristics Depending on Clay Pasting 234
12.06.11.2 Simulated Results of the Quenching Process 235
12.06.11.2.1 Sword Simulated and the Condition of Simulation 236
12.06.11.3 Simulation of Short Swords Made of Several Kinds of Steels 237
12.06.12 Benchmark Results on Heat Treating Simulation 240
12.06.12.1 Introduction 240
12.06.12.2 Benchmark Project and the Problems 241
12.06.12.2.1 Benchmark Problems 241
12.06.12.2.2 Material Data 242
12.06.12.2.3 Heat Transfer Coefficient 242
12.06.12.3 Results of Simulation and Verification 245
12.06.12.3.1 Cylinder 245
12.06.12.3.2 Ring in Gear Shape without Teeth 245
12.06.12.3.3 Helical Gear 246
12.06.12.4 Concluding Remarks on This Section and Future Works 247
12.06.13 Concluding Remarks on This Chapter 248
Acknowledgments 248
References 249

12.06.1 Introduction

12.06.1.1 Overview of the History of Modeling and Simulation up to 2000

Heat treatment is one of the core industrial technologies in the automobile, aerospace, transportation, construction, and other manufacturing industries. To remain competitive, participants in these industries must continually optimize their processes to reduce cost, improve quality, and reduce environmental problems. A number of studies have been conducted to determine what it will take for developed countries to remain competitive in the heat-treating industry (*1–5*). In addition to these studies, a number of international conferences have been held to provide a continual assessment of technology developments in process modeling and simulation in the global heat treating industry (*6–8*).

A historical overview of the theoretical analysis of quenching stress, which occurs with a change in volumetric dilatation due to phase transformation, is provided in **Table 1** (*9*). Various events and publications relating to modeling and simulation are summarized in **Table 2** (*10*).

One of the subject areas reviewed was "Research/Action Needed to Overcome Barriers to Improved Processes and Materials." A summary of the developments that are needed is provided in **Table 3** (*10*). From the listing shown in **Table 3**, it is clear that Process and Simulation (Predictive) Modeling is perceived to be an extremely important research area. The application of this and other programs to solve problems in quenching, carburizing, induction heat treating, and fluid flow simulation will be discussed. Finally, there will be a brief discussion of the future challenges that must be addressed before process modeling and simulation in the heat treating process industries becomes widely accepted.

In 1997, ASM International conducted a workshop to identify critical technology developments that will be necessary for the US heat treating industry to remain competitive in the twenty-first century (Vision 2020) (*3,4*).

Table 1 Summary of references with respect to aims and phenomena

	Aims		*Phenomena attributed to*		
References	*Residual stress*	*Transient stress*	*Thermal expansion*	*Elasticity*	*Plasticity*
Maurer (1972,1928) (*11,12*)	Yes	No	Yes	Yes	Yes
Bielenov (1953) (*13*)	Yes	Yes	Yes	Yes	No
Hirone (1936, 1937) (*14,15*)	Yes	Yes	Yes	Yes	No
Hirone and Tsuya (1949) (*16,17*)	Yes	Yes	Yes	Yes	No
Mura (1956) (*18*)	Yes	Yes	Yes	Yes	No
Zukievich-Stocha (1940) (*19*)	Yes	Yes	Yes	Yes	No
Bielenov (1952, 1953) (*20,21*)	No	Yes	Yes	Yes	No
Weiner and Huddleston (I959) (*22*)	Yes	Yes	No	Yes	Yes
Landau and Weiner (1964) (*23*)	Yes	Yes	No	Yes	Yes
Landau (1963) (*24*)	Yes	Yes	No	Yes	Yes
Lomakin (1959) (*25*)	Yes	Yes	Yes	Yes	Yes
Inoue and Tanaka (1975) (*26*)	Yes	Yes	Yes	Yes	Yes
Raniecki and Inoue (1977) (*9*)	Yes	Yes	Yes	Yes	Yes
Inoue et al. (1982) (*27–30*)	Yes	Yes	Yes	Yes	Yes

Table 2 Historical Background of modeling and simulation

1960	Quenching and related factors identified
1961	Handbook for heat treatment JSHT. Estimation of residual stress. Manual calculator
1960, 1972	NATSTR.AN. ANSYS. MARC → CAE Tech. 90s
1982	Simulation of transformation kinetics by Prof. I. Tamura and Umemoto
	Proposal of theory of metallo-thermo-mechanics, T. Inoue, S. Nagaki et al.
	Presymposium for quenching simulation in Nancy, Beck, Inoue, Erickson, Simon, and Dennis
1984	First conference on simulation in Sweden, T. Inoue; Richmond: Beck: Erickssen: Raniecki
1984	Sysweld commercialized for welding simulation
1990–93	HEARTS: 3D
1991	ASM Europe modeling & simulation: 10 papers (not full model)
1991	Inoue, Arimoto, and Ju developed 1st program HEARTS for quenching and released by CRC
1992	ASM 1st conference on quenching and the control of distortion, Chicago
	Modeling and simulation 15 papers (2 full models) by Inoue and Henridsen
1992	IFHT 92 in Kyoto-modeling: 13 papers
	Inoue et al. Gear distortion – HEARTS
	Shichino from Komatsu, Gear distortion simulation and validation
1993	ASM Europe modeling 16 papers (process and partial model)
1993	ASM carburizing and nitrizing: quench process model. 5 papers (partial model)
1994	ASM Conf.: Modeling and control: 10 papers
1995	ASM 16th Conf.: Quench process model: 5 papers (partial model)
1996	ASM 2nd Conf.: Control and distortion. HEARTS(3). NCMS(4) and Mingjam (total 13 papers)
1996	ASM-HTS I7th Conf.: Modeling (modeling prediction carburizing, nitriding): 19 papers
1998	ASM 18th HT Conf.: Modeling: 5 papers
1998	11th IFHT & ASM HTSE in Europe: 2 Modeling sessions: 18 papers
1999	ASM Europe-3rd WCD; Modeling. Simulation distortion: 26 papers
1999	HEARTS. SYSWELD. NCMS. DEFORM-HT GRANTAS CspisI
1999	7th IFHT Seminar: Modeling: 17 papers, Pan, Bergheau etc.
1999	ASM, HTS-OD Modeling 2 sessions· 7 papers (NCMS, SFTC + IH: 2 papers)
2000	So many simulation softwares have been developed, COSMAP, FIMAS-TPS, MUSIMAP, and others, adopting users subroutine to general-purpose program

12.06.1.2 What Is Metallo-Thermo-Mechanics?

The characteristics of material can be improved by controlling the internal structure due to phase transformation, such as quenching, tempering, and so on. However, such phase transformations are essentially coupled with temperature and mechanical fields. Considering the case of quenching of steels with an initial structure of pearlite and ferrite, if the steel is heated up beyond A_{C1} temperature to become austenite and cooled moderately to room temperature, it will return to the original pearlite and ferrite

Table 3 Selected topics for research/action needed to overcome barriers to improved processes and materials

1.	Induction coil design. Electromagnetic field distribution for heating.
2.	Knowledge-based database. Alloy vs. process vs. performance.
3.	Improve predictive capability/understanding of heat transfer behavior in quench baths.
4.	Modeling of nonhomogeneous microstructures and nonisothermal conditions.
5.	Thermochemical modeling (atmosphere, material interactions).
6.	Thermomechanical models to predict residual stress and distortion.
7.	Transformation plasticity (identification of TP coefficient).
8.	Modeling of phase transformations (volume strains on heating and cooling).
9.	Predictive models that can equate material characteristics to failure performance.
10.	Software for designers that enables specification of materials. Design and processes.
11.	Relationship between structure/performance. Define performance characteristics, determine mechanisms that raise performance.
12.	Develop nondestructive model to measure residual stress.
13.	Modeling of fluid flow in furnace atmospheres and Quench tanks.

structure. On the contrary, when the cooling rate is high enough in the cooling process by water, oil, or polymer solution, martensite or bainite structure in addition to pearlite is developed depending on the difference in the cooling rate at each location of the work.

As seen in a schematic *temperature–elongation* diagram in Figure 1, such structure changes lead to dilation, also resulting in the stresses that are summarized in the following manner:

Three kinds of field play an important role: a temperature field, phases of the metallic structures, and an elastic – or in most cases, inelastic – stress and strain field. A variation in any of the three parameters will have an effect on the others, and the interaction is properly termed metallo-thermo-mechanics (*27–32*).

The triangle in Figure 2 shows a schematic representation of these parameters and the effect of their interaction. When the temperature distribution in a material (and in some cases the heating and cooling rate) is unequal, *thermal stress* ① is caused in the solid, and the *temperature-dependent phase transformation* ② leads to alterations in structure (i.e., melting or solidification in solid–liquid transition, and austenite–pearlite and austenite–martensite transformation in the solid phase). Local dilatation due to phase changes in the solid brings about *transformation stress*, and in some cases, *transformation plasticity strain* ③ induces the stress or strain field of the body.

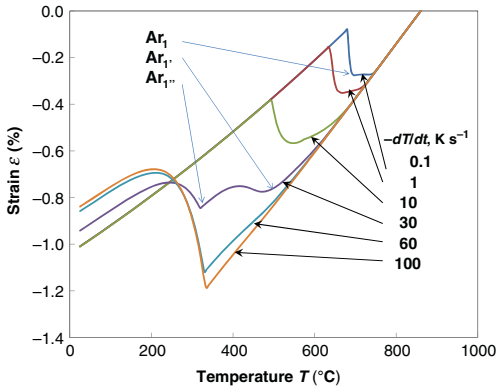

Figure 1 Temperature–dilatation diagram depending on cooling rate.

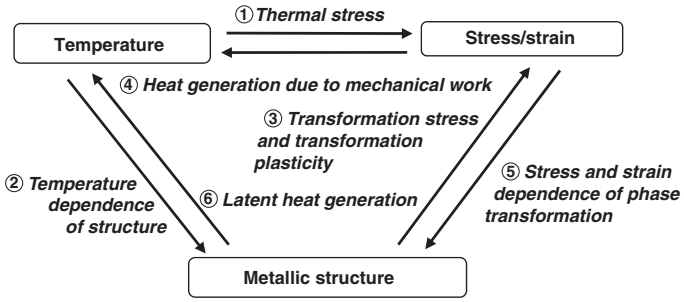

Figure 2 Metallo-thermo-mechanical coupling.

Contrary to these effects, which are taken into account in ordinal stress analyses, arrows facing the opposite direction indicate different coupling modes. Part of the mechanical work done by existing stress in the material converts into *heat* ④, which is sometimes predominant in plastic deformation, thus the temperature is affected. The acceleration of phase transformation by stress or strain, called *stress- (or strain-) induced transformation* ⑤, is sometimes applied to improve the mechanical properties of metallic materials. Arrow number ⑥ corresponds to the *latent heat generation* due to phase transformation, which affects the temperature distribution.

Suppose that no interaction or coupling exists, or the effect is negligibly small. Then, the three fields can be solved with use of a simple *heat conduction equation* for temperature, an *equation of motion* (stress equilibrium equation) combined with a kinematic relation and a material constitutive equation for stress analysis, and a simple *kinetic equation for phase transformation*. This kind of simulation is normally carried out in most cases even in the process incorporating phase change: The heat conduction equation is solved to determine the temperature distribution in the first step, followed by determining the phase distributions. By use of the data, it may be possible to analyze the stress/strain field by considering the thermal stress and phase transformation stress.

In the general situation when the coupling effect plays an important role, as seen in **Figure 2**, it seems to be necessary to consider thermodynamics of continua to derive the governing equations for temperature, stress/strain, and structure fields. Such a general theoretical framework that can describe the governing equations when incorporating phase transformation is termed *metallo-thermo-mechanics*.

12.06.2 Kinetics of Phase Transformation and Structures in Solids

12.06.2.1 Phase Transformation in Solids

Phase transformation of material, such as transformation between solid and liquid (from ice to water, for example) and transformation between liquid and gas (from water to vapor) is well understood. Nevertheless, phase transformation also occurs in solids themselves. As for metal, alloy, and ceramics used as industrial materials, various types of phase appear in the solid state depending on the composition of material and temperature. Phase transformation occurs due to temperature and variation, and it is also affected by stress or strain (*27–33*), for example, as seen in a shape memory alloy. Another example is observed in transformation-induced plasticity (TRIP) steel, which is a case utilizing phase transformation. Phase transformation occurring in such a solid is called solid–solid phase transformation, and it sometimes strengthens structural materials. *Phase transformation* is an important key word in the field of material science, as well as other physical and chemical phenomena.

Moreover, a change of the various characteristics due to the solid–solid phase transformation is widely used for functional materials. For example, there is the dominating function of the shape memory effect and also superelasticity related to the thermoelasticity-type martensite transformation in titanium–nickel alloy, as with phase transformation in metals and alloys. Also, phenomena such as a paraelectric–ferroelectric phase transition in barium titanate are studied in the materials science field.

When developing new engineering materials, on the other hand, it is important to construct a useful theory to systematically understand the major characteristics of various materials and to recognize a coupled problem based on thermodynamics, since both macroscopic issues of phase transformation and also the microscopic change in atomic scale are closely related to each other, and it is affected by the change of the temperature field and the stress/pressure field in solids. Therefore, *metallo-thermo-mechanics* theory is expected to provide a useful tool both in a theoretical aspect and also for engineering purposes.

12.06.2.2 Kinetics of Diffusion Transformation

In the process of heat treatment of steel, the identification of various kinds of transformed structure and the start-end points of phase transformation can be estimated by using a time temperature transformation (TTT) diagram and/or a continuous cooling transformation (CCT) diagram as shown, respectively, in **Figure 3(a) and 3(b)**. The amount of pearlite or bainite transformation at time t in each material point can be calculated using the modified formula when taking into account the stress effect (*34–38*) (see **Figures 4 and 5**, for example) originally proposed by Johnson–Mehl–Abrami (*39*): The amount of transformation ξ_I represented by the volume fraction is given as

$$\xi_I = 1 - \exp\left\{ -\int_0^t f_1(T) f_2(\sigma_{ij}) (t-\tau)^3 \mathrm{d}\tau \right\} \quad [1]$$

When using this formula, temperature T and stress σ_{ij} must be given as a function of time and position like $T = T(x,t)$, $\sigma_{ij} = \sigma_{ij}(x,t)$. However, a modified approach is used to calculate as follows, since it is not desirable for numerical computation to save all data of the past time history. Equation [1] for the amount of transformations $\xi_I (I = P,B)$ is rewritten as

$$\xi_1 = 1 - \exp\left\{ -t^3 \int_0^t f_1(T) f_2(\sigma) \mathrm{d}\tau + 3t^2 \int_0^t f_1(T) f_2(\sigma) \tau \mathrm{d}\tau - 3t^2 \int_0^t f_1(T) f_2(\sigma) \tau^2 \mathrm{d}\tau + \int_0^t f_1(T) f_2(\sigma) \tau^3 \mathrm{d}\tau \right\} \quad [2]$$

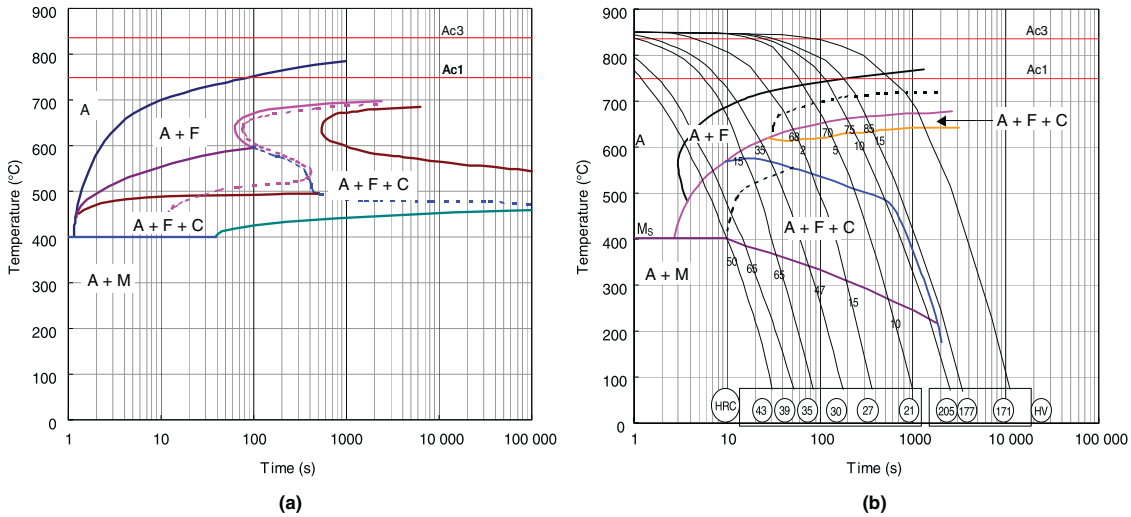

Figure 3 (a) TTT and (b) CCT diagrams of chromium steel SCr415.

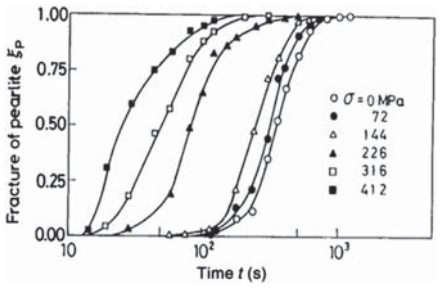

Figure 4 Dependence of applied stress on pearlite reaction.

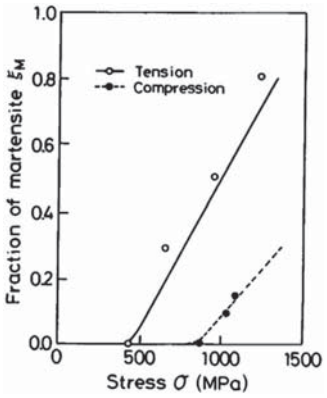

Figure 5 Dependence of applied stress on martensite reaction.

Replacing each integration terms in the right-hand side by

$$a_k = \int_0^t f_1(T) f_2(\sigma) \tau^{k-1} \mathrm{d}\tau \quad (k = 1, 2, 3, 4) \qquad [3]$$

we have

$$\xi_1 = 1 - \exp\left(- t^3 a_1 + 3t^2 a_2 - 3t a_3 + a_4 \right) \qquad [4]$$

The rate forms of eqn [3], which will be used in practical calculation, are given as follows:

$$\dot{a}_k = f_1(T) f_2(\sigma) t^{k-1} \quad (k = 1, 2, 3, 4) \tag{5}$$

or

$$\Delta a_k = f_1(T) f_2(\sigma) t^{k-1} \Delta t \quad (k = 1, 2, 3, 4) \tag{6}$$

Therefore, the value of a_i ($i = 1, \ldots, 4$) at time t is given as follows:

$$a_{i\,t} = a_{i\,t-\Delta t} + \Delta a_i \tag{7}$$

If the initial condition at time $t = 0$ is $a_i = 0$, then a_i in arbitrary time t is obtained by the recurrence equation of eqn [7], and the amount of transformations ξ_1 is calculated from the eqn [4].

In the case of the surface hardening treatment process by diffusion of carbon and/or nitrogen, such as carburizing, nitrizing, and carburizing-nitrizing, the kinetic eqn [1] for the diffuse type transformation is to be modified by taking into consideration the change of carbon and/or nitrogen content (*40–42*):

$$\xi_J = 1 - \exp\left\{ -\int_0^t f_1(T) f_2(C, N) f_3(\sigma) (t - \tau)^3 \mathrm{d}\tau \right\} \tag{8}$$

$$f_1(T) = a_0 \left(\frac{T - a_1}{a_2} \right)^{a_3} \left(\frac{a_4 - T}{a_5} \right)^{a_6} \tag{9}$$

$$f_2(C, N) = \exp\{ -a_7 (C - C_0) - a_8 (N - N_0) \} \tag{10}$$

$$f_3(\sigma) = \exp(a_9 \sigma_m) \tag{11}$$

Here, a_7 and a_8 are the parameters depending on the change of carbon and nitrogen, respectively.

12.06.2.3 Kinetics of Diffusionless Transformation

By CCT, as shown in the diagram in **Figure 3(b)**, the almost straight lines Ms and Mf, respectively, show the start and finish temperature of martensitic transformation. Since the martensite transformation is a *diffusionless transformation* (or martensite transformation), the start and finish temperature of transformation does not depend on time, and the start and finish lines turn into parallel lines. And the amount ξ_M, i.e., the change of martensite volume fraction, is evaluated by using the formula (*33*), when considering the effect of stress on the kinetics as seen in **Figure 5**.

$$\xi_M = 1 - \exp\left[\varphi(M_S - T) + \phi(\sigma_{ij}) \right] \tag{12}$$

Here, the kinetics of Magee (*43*) is adopted to consider stress dependency from thermodynamics. The material parameter φ is related to thermodynamic free energy, and is determined from the experiments on the stress-dependent start condition of martensite transformation, and $\varphi(\sigma_{ij})$ is some function of stress.

In the carburizing–nitrizing–quenching case, the effect of diffused carbon and/or nitrogen is to be considered in the form

$$\xi_M = 1 - \exp\{ \phi_1 T + \phi_2 (C - C_0) + \phi_3 (N - N_0) + \phi_4 \sigma_m + \phi_5 \sigma_e + \phi_6 \} \tag{13}$$

Here, σ_m and σ_e are mean and equivalent stresses, and φ_1–φ_6 are the parameters determined by experiment.

12.06.3 Basic Theory and Governing Equations

A theoretical framework to describe thermal and mechanical behaviors of materials incorporating phase transformation is introduced in this section from the viewpoint of continuum mechanics, and coupled equations for heat conduction, inelastic stress analysis, and kinetics of phase transformation are presented.

12.06.3.1 Mixture Rule and Basic Theory Based on Thermodynamics

A material point undergoing structural change due to phase transformation is assumed to consist of a mixture of N constituents (*44*), say pearlite, austenite, martensite, and liquid phase, as schematically shown in **Figure 6**. It is well known that such changes in microstructure are really observed on a microscopic level. For the analysis based on the continuum mechanics level, however, any material point with some volume is assumed to consist of N kinds of some constituents: Denoting the volume fraction of the Ith constituent as ξ_I, the mechanical and physical properties χ of the material may be expressed as a linear combination of the properties χ_I of the constituents.

$$\chi = \sum_{I=1}^{N} \chi_I \xi_I \tag{14}$$

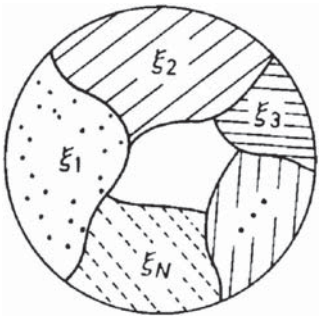

Figure 6 A material point composed of *N*-constituents.

where

$$\sum_{I=1}^{N} \xi_I = 1 \qquad [15]$$

The thermodynamic state of the material is assumed to be determined by stress σ_{ij}, temperature T, temperature gradient $g_i = \partial T/\partial x_i$, a set of *internal variables* of inelastic strain ε^i_{ij}, and hardening parameter κ related to inelastic deformation, and the volume fractions of the constituents $\xi_I (I = 1, 2, \ldots, N)$. The general forms of the constitutive equation for Gibbs free energy G, entropy η, heat flux vector q_i, and elastic strain ε^e_{ij} are expressed as

$$\begin{aligned} G &= G(\sigma_{ij},\ T,\ g_i,\ \varepsilon^i_{ij},\ \kappa,\ \xi_I) \\ \eta &= \eta(\sigma_{ij},\ T,\ g_i,\ \varepsilon^i_{ij},\ \kappa,\ \xi_I) \\ q_i &= q_i(\sigma_{ij},\ T,\ g_i,\ \varepsilon^i_{ij},\ \kappa,\ \xi_I) \\ \varepsilon^e_{ij} &= \varepsilon^e_{ij}(\sigma_{ij},\ T,\ g_i,\ \varepsilon^i_{ij},\ \kappa,\ \xi_I) \end{aligned} \qquad [16]$$

Here, elastic strain ε^e_{ij} is given as the remainder of total strain ε_{ij} subtracted by inelastic strain ε^i_{ij}. The evolutional equations of the internal variables ε^i_{ij}, α_{ij}, κ, and ξ_I can be defined in the same form as eqn [16]:

$$\begin{aligned} \dot{\varepsilon}^i_{ij} &= \dot{\varepsilon}^i_{ij}(\sigma_{ij},\ T,\ g_i,\ \varepsilon^i_{ij},\ \kappa,\ \xi_I) \\ \dot{\alpha}_{ij} &= \dot{\alpha}_{ij}(\sigma_{ij},\ T,\ g_i,\ \varepsilon^i_{ij},\ \kappa,\ \xi_I) \\ \dot{\kappa} &= \dot{\kappa}(\sigma_{ij},\ T,\ g_i,\ \varepsilon^i_{ij},\ \kappa,\ \xi_I) \\ \dot{\xi}_I &= \dot{\xi}_I(\sigma_{ij},\ T,\ g_i,\ \varepsilon^i_{ij},\ \kappa,\ \xi_I) \end{aligned} \qquad [17]$$

When the *Clausius–Duhem inequality* representing the second law of thermodynamics,

$$-\rho\left(\dot{G} + \eta\dot{T}\right) - \dot{\sigma}_{ij}\varepsilon^e_{ij} + \sigma_{ij}\dot{\varepsilon}^i_{ij} - g_i q_i \ \geq\ 0 \qquad [18]$$

is applied, we have

$$\begin{aligned} &-\left(\varepsilon^e_{ij} + \rho\frac{\partial G}{\partial \sigma_{ij}}\right)\dot{\sigma}_{ij} - \rho\left(\eta + \frac{\partial G}{\partial T}\right)\dot{T} + \left(\sigma_{ij} - \rho\frac{\partial G}{\partial \varepsilon^e_{ij}}\right)\dot{\varepsilon}^i_{ij} \\ &-\rho\frac{\partial G}{\partial \kappa}\dot{\kappa} - \rho\sum_{x=1}^{N}\frac{\partial G}{\partial \xi_I}\dot{\xi}_I - \frac{1}{T}q_i g_i \geq 0 \end{aligned} \qquad [19]$$

The fact that eqn [19] must hold for every change in stress and temperature necessitates giving the constitutive relations instead of eqn [16],

$$\begin{aligned} G &= G(\sigma_{ij},\ T,\ g_i,\ \varepsilon^i_{ij},\ \kappa,\ \xi_I) \\ \varepsilon^e_{ij} &= \rho\frac{\partial}{\partial \sigma_{ij}}G(\sigma_{ij},\ T,\ g_i,\ \varepsilon^i_{ij},\ \kappa,\ \xi_I) \\ \eta &= -\frac{\partial}{\partial T}G(\sigma_{ij},\ T,\ g_i,\ \varepsilon^i_{ij},\ \kappa,\ \xi_I) \\ q_i &= -k(\sigma_{ij},\ T,\ g_i,\ \varepsilon^i_{ij},\ \kappa,\ \xi_I) \end{aligned} \qquad [20]$$

Here, low density ρ and heat conductivity k are expressed in the same manner ξ_I in eqn [14].

12.06.3.2 Heat Conduction Equation and the Boundary Condition

The local energy balance or the first law of thermodynamics is usually given in terms of internal energy $U = G + T\eta + 1/\rho\ \sigma_{ij}\varepsilon^e_{ij}$ as

$$\rho\dot{U} - \sigma_{ij}\dot{\varepsilon}^e_{ij} + \frac{\partial q_i}{\partial x_i} = 0 \quad [21]$$

with Gibbs free energy G, entropy η, stress σ_{ij}, and elastic strain ε^e_{ij}. Introducing expressions for the specific heat c $(=T\partial\eta/\partial T)$ and enthalpy density H $(=g + T\eta)$, eqn [21] is reduced to the general form of the heat conduction equation,

$$\rho c\dot{T} + T\frac{\partial\varepsilon^e_{ij}}{\partial T}\dot{\sigma}_{ij} - \left(\sigma_{ij}\dot{\varepsilon}^i_{ij} - \rho\frac{\partial H}{\partial\varepsilon^i_{ij}}\dot{\varepsilon}^i_{ij} - \rho\frac{\partial H}{\partial\kappa}\dot{\kappa}\right) + \rho\sum_{I=1}^{N} l_I\dot{\xi}_I = k\frac{\partial^2 T}{\partial x_i\partial x_i} \quad [22]$$

Here, Fourier's heat conduction law

$$q_i = -k\frac{\partial T}{\partial x_i} \quad [23]$$

with heat conductivity k, is adopted, and the latent heat l_I when producing the Ith constituent

$$l_I = \frac{\partial H}{\partial\xi_I} \quad [24]$$

is introduced.

The third term on the left-hand side of eqn [22] denotes the heat generated by inelastic dissipation, which is significant when compared with the elastic work represented by the second term, and the fourth term arises from the latent heat through structural changes. Hence, it can be seen that eqn [22] corresponds to the ordinal equation of heat conduction, provided these terms are neglected. (Ordinal heat conduction equation $\rho c\dot{T} = k\frac{\partial^2 T}{\partial x_i\partial_i}$, is known to be derived from an assumption that only thermal energy is considered by neglecting mechanical work. However, if a temperature gradient is in a body, induced thermal stress essentially acts to thermal strain to produce mechanical work, which is converted to heat generation.)

As for the case of carburized and nitrided quenching, we need the distribution of carbon and/or nitrogen content diffused from the surface of the body. This process is generally operated in advance of the quenching, so the coupling with stress and structural change does not need to be considered here. When neglecting trivial terms of elastic strain and enthalpy-related ones, we have

$$\rho c\dot{T} - \frac{\partial}{\partial x_i}\left(k\frac{\partial T}{\partial x_i}\right) - r_v = 0 \quad [25]$$

$$r_v = \sigma_{ij}\dot{\varepsilon}^p_{ij} + \sum\rho_I\ell_I\dot{\xi}_I \quad [26]$$

The *general heat conduction equation* [25] can be solved by adopting the *boundary condition:*

Convection boundary condition

$$-k\frac{\partial T}{\partial n} = h(T)(T - T_w) \quad [27]$$

Radiation boundary condition

$$-k\frac{\partial T}{\partial n} = \Gamma(T)\lambda\left(T^4 - T_w^4\right) \quad [28]$$

Here, n is the normal to the surface, T_w is the temperature of ambient, and $h(T)$ and $\Gamma(T)$, respectively, denote the heat transfer coefficient and radiation parameter with Boltzmann constant λ.

12.06.3.3 Diffusion Equation of Carbon and/or Nitrogen and the Boundary Condition

When taking the diffusion processes of carbon and/or nitrogen into consideration, such as carburizing and nitrizing, the diffusion equation based on Fick's law can describe the phenomenon (*40–42*).

Carburizing process:

$$\frac{\partial C}{\partial t} - \frac{\partial}{\partial x_i}\left(D_C\frac{\partial C}{\partial x_i}\right) - r_C = 0 \quad [29]$$

$$-D\frac{\partial C}{\partial x_i}n_i = \beta_C(C - C_W) \quad [30]$$

Nitrizing process:

$$\frac{\partial N}{\partial t} - \frac{\partial}{\partial x_i}\left(D_N\frac{\partial N}{\partial x_i}\right) - r_N = 0 \quad [31]$$

$$-D_N\frac{\partial N}{\partial x_i}n_i = \beta_N(N - N_w) \quad [32]$$

$$\beta_N = \beta_0 p_{H_2}\exp\left(-\frac{Q_N}{RT}\right) \quad [33]$$

$$D_N = \sum D_{NI}(N)\xi_I \quad [34]$$

In the process of combined carburizing and nitrizing, the effect of interaction of carbon and nitrogen is to be considered in the diffusion coefficient, which is influenced by the gradient and the distribution of the chemical composition in the form

$$D_{NI}(N) = D_{NI,0}f(C,\ N)h(\text{grad } C,\ \text{grad } N)\exp\left(-\frac{Q_N}{RT}\right) \quad [35]$$

12.06.3.4 Equation of Motion, Kinematics, and the Boundary Condition

The inelastic body under a heat treatment process is treated as a boundary value problem of an infinitesimal strain framework, and the rate type governing equation of the stress and strain fields is given as follows.

$$\frac{\partial\dot{\sigma}_{ij}}{\partial x_j} + \dot{f}_i = 0 \quad [36]$$

$$\dot{\varepsilon}_{ij} = \frac{1}{2}\left(\frac{\partial\dot{u}_i}{\partial x_j} + \frac{\partial\dot{u}_j}{\partial x_i}\right) \quad [37]$$

Here, f_i is body force and u_i is a displacement vector, and the boundary condition reads

$$u_i = \overline{u}_i \quad \text{on } S_u \quad [38]$$

$$\sigma_{ij}n_j = \overline{T}_i \quad \text{on } S_\sigma \quad [39]$$

for subscribed values of displacement $\overline{u}_i$ and surface traction $\overline{T}_i$.

The inelastic constitutive equation, including elastic, plastic, and thermal strains, transformation plasticity strain, as well as chemically diffused strain, in some cases is needed in addition to the above equilibrium equation and kinematic relation. Details of such an inelastic constitutive formula in consideration of a phase transformation will be discussed in Section 12.06.4.

12.06.4 Inelastic Constitutive Equation

12.06.4.1 Elastic Strain

An explicit expression of the elastic stress–strain relation can be obtained when a form of the Gibbs free energy function G is given. To do so, let us assume that G follows the mixture law, eqn [14] as (*29*,*30*)

$$G\left(\sigma_{ij}, T, \varepsilon^p_{ij}, \kappa, \xi_I\right) = \sum_{I=1}^{N}\xi_I G_I\left(\sigma_{ij}, T, \varepsilon^p_{ij}, \kappa\right) \quad [40]$$

with Gibbs energy G_I for the Ith constituent being divided into elastic and inelastic parts

$$G_I\left(\sigma_{ij}, T, \varepsilon^p_{ij}, \kappa\right) = G^e_I\left(\sigma_{ij}, T\right) + G^p_I\left(T, \varepsilon^p_{ij}, \kappa\right) \quad [41]$$

Substituting eqns [40] and [41] into eqn [20], we have

$$\varepsilon^e_{ij} = -\rho\sum_{I=1}^{N}\xi_I\frac{\partial G^e_I\left(\sigma_{ij}, T\right)}{\partial\ \sigma_{ij}} \quad [42]$$

Expansion of $G_I(\sigma_{kl}, T)$ around the natural state $\sigma_{kl} = 0$ and $T = T_0$ with the assumption of isotropy leads to

$$G^e_I(\sigma_{kl}, T) = -\rho\left[\phi_{I0} + \phi_{I1}\sigma_{kk} + \phi_{I2}(\sigma_{kk})^2 + \phi_{I3}\sigma_{kl}\sigma_{kl} + \phi_{I4}(T - T_0)\sigma_{kk} + f_I(T - T_0)\right] \quad [43]$$

where ϕ_{I0}, ϕ_{I1}, ϕ_{I2}, ϕ_{I3}, and ϕ_{I4} are the polynomial function of stress invariants and temperature and $f_I(T - T_0)$ is the function of temperature rise. Then, eqn [42] reads

$$\varepsilon^e_{ij} = \sum_{I=1}^{N}\xi_I\varepsilon^e_{Iij} \quad [44]$$

with

$$\varepsilon^e_{Iij} = 2\phi_{I3}\sigma_{ij} + 2\phi_{I2}\sigma_{kk}\delta_{ij} + \phi_{I4}(T - T_0)\delta_{ij} + \phi_{I1}\delta_{ij} \quad [45]$$

Since the first two terms of eqn [45] mean Hooke's law, the third is thermal strain, and the fourth corresponds to isotropic strain of the Ith constituent provided that the parameters are constant, we can put

$$2\phi_{I3} = \frac{1+\nu_I}{E_I}, \quad 2\phi_{I2} = -\frac{\nu_I}{E_I}, \quad \phi_{I4} = \alpha_I, \quad \phi_{I1} = \beta_I \quad [46]$$

when E_I and ν_I are Young's modulus, Poisson's ratio, and the thermal expansion coefficient of the constituent, respectively, and $3\beta_I$ is volumetric dilatation due to phase change in this case. Then, we have

$$\varepsilon^e_{Iij} = \frac{1+\nu_I}{E_I}\sigma_{ij} - \frac{\nu_I}{E_I}\sigma_{kk}\delta_{ij} + \alpha_I(T - T_0)\delta_{ij} + \beta_I\delta_{ij} \quad [47]$$

Finally, the elastic stress–strain relation of the mixture takes

$$\varepsilon^e_{ij} = \sum \varepsilon^e_{Iij} \quad [48]$$

or, in the other form,

$$\varepsilon^e_{ij} = \frac{1+\nu}{E}\sigma_{ij} - \frac{\nu}{E}\sigma_{kk}\delta_{ij} + \alpha(T - T_0)\delta_{ij} + \beta\xi\delta_{ij} \quad [49]$$

with the global form of material parameters

$$E = \frac{1}{\sum_{I=1}^{N}\frac{\xi_I}{E_I}}, \quad \nu = \frac{\sum_{I=1}^{N}\frac{\xi_I\nu_I}{E_I}}{\sum_{I=1}^{N}\frac{\xi_I}{E_I}}, \quad \alpha = \sum_{I=1}^{N}\xi_I\alpha_I, \quad \beta\xi = \sum_{I=1}^{N}\xi_I\beta_I \quad [50]$$

12.06.4.2 Plastic Strain

For an elastic–plastic material, the evolutional equation of the plastic strain is derived by normality law,

$$\dot{\varepsilon}^p_{ij} = \Lambda\frac{\partial F}{\partial\sigma_{ij}} \quad [51]$$

with the yield function (*26*)

$$F = F\left(\sigma_{ij}, \varepsilon^p_{ij}, \kappa, T, \xi_I\right) = 0 \quad [52]$$

including the effect of structures represented by the volume fraction ξ_I in addition to the hardening parameter κ.

The parameter Λ in eqn [51] is a function depending on stress, stress rate, strain, and its history. When introducing Prager's consistency relation:

$$\dot{F} = \frac{\partial F}{\partial\sigma_{ij}}\dot{\sigma}_{ij} + \frac{\partial F}{\partial\varepsilon^p_{ij}}\dot{\varepsilon}^p_{ij} + \frac{\partial F}{\partial\kappa}\dot{\kappa} + \frac{\partial F}{\partial T}\dot{T} + \sum_{I=1}^{N}\frac{\partial F}{\partial\xi_I}\dot{\xi}_I = 0 \quad [53]$$

the parameter Λ is easily determined as

$$\Lambda = \widehat{G}\left(\frac{\partial F}{\partial\sigma_{mn}}\dot{\sigma}_{mn} + \frac{\partial F}{\partial T}\dot{T} + \sum_{I=1}^{N}\frac{\partial F}{\partial\xi_I}\dot{\xi}_I\right) \quad [54]$$

And finally we have

$$\dot{\varepsilon}^p_{ij} = \widehat{G}\left(\frac{\partial F}{\partial s_{kl}}\dot{s}_{kl} + \frac{\partial F}{\partial T}\dot{T} + \sum_{I=1}^{N}\frac{\partial F}{\partial x_I}\dot{x}_I\right)\frac{\partial F}{\partial\sigma_{ij}} \quad [55]$$

Here, $\widehat{G}$ is termed as the hardening function and takes the form

$$\frac{1}{\widehat{G}} = -\left(\frac{\partial F}{\partial\varepsilon^p_{mn}} + \frac{\partial F}{\partial\kappa}\sigma_{mn}\right)\frac{\partial F}{\partial\sigma_{mn}} \quad [56]$$

for the work hardening parameter $\dot{\kappa} = \sigma_{ij}\dot{\varepsilon}^p_{ij}$, and

$$\frac{1}{\widehat{G}} = -\frac{\partial F}{\partial s_{mn}}\frac{\partial F}{\partial e^p_{mn}} - \left(\frac{2}{3}\frac{\partial F}{\partial s_{mn}}\frac{\partial F}{\partial s_{mn}}\right)^{1/2}\frac{\partial F}{\partial k} \quad [57]$$

for the strain hardening parameter $\dot{\kappa} = \overline{\dot{\varepsilon}}^p = \sqrt{2/3\dot{\varepsilon}^p_{ij}\dot{\varepsilon}^p_{ij}}$.

12.06.4.3 Viscoplastic Strain

When the operation time of quenching is so long, as in the case of a machine component with a large dimension, or when the temperature is so high, as in the case of welding and casting, the effect of time on inelasticity is not negligible. Such time-dependent (or rate-dependent) inelasticity, sometimes termed viscoplasticity, has been developed to formulate proper but sophisticated constitutive equations, under the plasticity–creep interaction condition.

A detailed discussion will be provided elsewhere, where we will employ a simple form of time-dependent plasticity, or viscoplasticity in a narrow sense.

The theory is essentially based on the concept that the stress beyond the pseudostatic yield surface $F = 0$, called the excess stress, provides the viscosity η, and the viscoplastic strain rate is given as (45)

$$\dot{\varepsilon}^{vp}_{ij} = \eta\langle\Phi(F)\rangle\frac{\partial F}{\partial\sigma_{ij}} \quad [58]$$

where

$$\langle\Phi(F)\rangle = \begin{cases}\Phi(F) & \text{if } F \geq 0\\ 0 & \text{if } F < 0\end{cases} \quad [59]$$

and the stress point under the nonzero strain rate satisfies the inequality $F > 0$. This is different from the ordinary plasticity theory.

12.06.4.4 Creep Strain

The creep strain rate $\dot{\varepsilon}^c_{ij}$ is given in a similar form to the plastic strain rate,

$$\dot{\varepsilon}^c_{ij} = \Lambda^c\frac{\partial G}{\partial\sigma_{ij}} \quad [60]$$

by use of the creep function

$$G = G\left(\sigma_{ij}, \varepsilon^c_{ij}, \kappa^c, T, \xi_I\right) \quad [61]$$

equivalent to the yield function, with a creep hardening parameter κ^c.

The consistency relation held during creep loading leads to the final form for the creep constitutive equation,

$$\dot{\varepsilon}^c_{ij} = \widehat{G}^c\left(\frac{\partial G}{\partial\sigma_{kjl}}\dot{\sigma}_{jkl} + \frac{\partial G}{\partial T}\dot{T} + \sum_{I=1}^{N}\frac{\partial G}{\partial\xi_I}\dot{\xi}_I\right)\frac{\partial F}{\partial\sigma_{ij}} \quad [62]$$

Mises or Tresca type is also employed for the creep function, being similar to the yield function.

12.06.4.5 Transformation Plastic Strain

Large inelastic deformation is induced under relatively low stress even lower than yield stress during phase transformation, which is called *transformation superplasticity*. Figure 7 presents an example of an elongation–temperature diagram under phase transformation depending on applied stress. Transformation plastic strain is defined as the difference in strain with and without stress. As is observed in some alloys, such an inelastic strain is sometimes very large, thus it is called transformation superplastic strain. The strain-induced during quenching is, however, mostly small since the operation time is relatively short, and the phenomenon is called as *transformation plasticity* (46–51).

In order to formulate a constitutive equation of a body under phase transformation, we again assume that the material point in question is composed of N kinds of phases, which include all phases with the volume fraction ξ_I (I = 1,2,3, …, N), as is shown in Figure 8(a), and that the mechanical and hermophysical property χ is represented by the *mixture law* (44) in the same form of eqn [14].

$$\chi = \sum_{I=1}^{N}\xi_I\chi_I, \quad \text{with} \quad \sum_{I=1}^{N}\xi_I = 1 \quad [63]$$

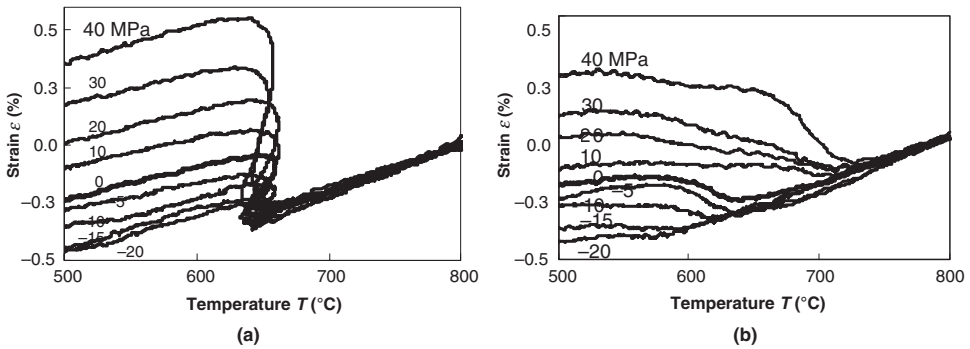

Figure 7 Experimental temperature–elongation diagram under some applied stress. (a) S45C and (b) FR-490.

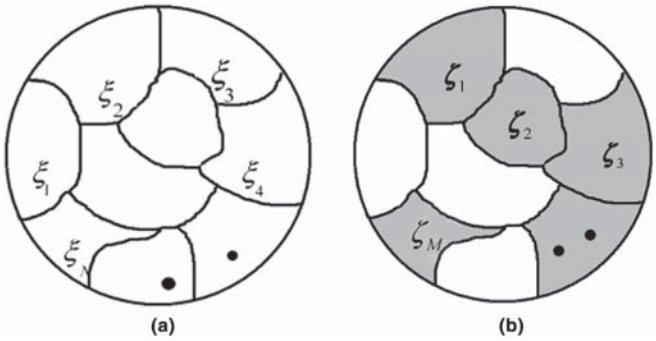

Figure 8 Volume fraction of phases consisting of a material point. (a) All phases and (b) some phases associating plastic deformation.

Here, the stress state related to the yielding of the Ith phase (say, the mother phase) is assumed to be affected by other phases (new phase) with the volume fraction ζ_J ($J = 1,2,3, \ldots, M$) as indicated in Figure 8(b). Then, the plasticity of the Ith phase is controlled by the yield function in the form

$$F_I = F_I\left(\sigma_{ij}, T, \varepsilon^p_{Iij}, \kappa_I, \zeta_J\right), \quad (I = 1,2,\ldots,N\,;\; J = 1,2,\ldots,M) \tag{64}$$

Here, σ_{ij}, T, and κ_I, respectively, stand for uniform stress and temperature and the plastic hardening parameter.

Applying the consistency relation and the normality law, we have the form of the plastic strain rate of the Ith phase as

$$\dot{\varepsilon}^p_{Iij} = \Lambda_I \frac{\partial F_I}{\partial \sigma_{ij}} = \widehat{G}_I \left[\left(\frac{\partial F_I}{\partial \sigma_{kl}} \dot{\sigma}_{kl} + \frac{\partial F_I}{\partial T} \dot{T} \right) + \sum_{J=1}^{M} \frac{\partial F_I}{\partial \zeta_J} \dot{\zeta}_J \right] \frac{\partial F_I}{\partial \sigma_{ij}} \tag{65}$$

with the hardening modulus $\widehat{G}_I$.

The first term in eqn [65] is the ordinal thermo-mechanical plastic strain rate in the Ith phase, which is a summation of the mechanical and thermal parts. It is noted that the second term in eqn [65] occurring in the Ith phase originates from the new Jth phase ζ_J, which is found to be the so-called *transformation plastic strain rate*,

$$\dot{\varepsilon}^{tp}_{Iij} = \widehat{G}_I \left(\sum_{J=1}^{M} \frac{\partial F_I}{\partial \zeta_J} \dot{\zeta}_J \right) \frac{\partial F_I}{\partial \sigma_{ij}} \tag{66}$$

Adopting the mixture law, we finally have the global strain rate in the form

$$\dot{\varepsilon}_{ij} = \dot{\varepsilon}^e_{ij} + \dot{\varepsilon}^{th}_{ij} + \dot{\varepsilon}^m_{ij} + \dot{\varepsilon}^p_{ij} \tag{67}$$

Attention is focused on the unified plastic strain rate

$$\dot{\varepsilon}^p_{ij} = \sum_{I=1}^{N} \xi_I \dot{\varepsilon}^p_{Iij} = \sum_{I=1}^{N} \widehat{G}_I \left[\left(\frac{\partial F_I}{\partial \sigma_{kl}} \xi_I \dot{\sigma}_{kl} + \frac{\partial F_I}{\partial T} \xi_I \dot{T} \right) + \xi_I \left(\sum_{J=1}^{M} \frac{\partial F_I}{\partial \zeta_J} \dot{\zeta}_J \right) \right] \frac{\partial F_I}{\partial \sigma_{ij}} \tag{68}$$

as the sum of thermo-mechanical and transformation plastic parts. The result indicates that both plastic strain rates related to thermo-mechanical and phase transformation effects are automatically derived from the yield function in the form of eqn [64] and that eqn [68] is the *unified plastic strain rate*.

Now, consider a special case when uniaxial stress σ is applied. Then we have the transformation plastic strain rate,

$$\dot{\varepsilon}^{tp} = \sum_{I=1}^{N} \frac{1}{H'_I} \left[\sum_{J=1}^{M} \frac{H^{\zeta}_{IJ} \dot{\zeta}_J}{\overline{\sigma}_I} \xi_I \right] \sigma \qquad [69]$$

Here, hardening parameters are defined with the flow stress of the Ith phase $\overline{\sigma}_I$,

$$H'_I = \frac{\partial \overline{\sigma}_I}{\partial \overline{\varepsilon}^p_I} \quad : \quad \text{Strain hardening parameter of the } I\text{th phase} \qquad [70]$$

$$H^{\zeta}_{IJ} = \frac{\partial \overline{\sigma}_I}{\partial \zeta_J} \quad : \quad \text{Dependence of flow stress in the } I\text{th phase} \qquad [71]$$

And the constitutive equation for TP strain in the case between the mother and new phase reads

$$\dot{\varepsilon}^{tp} = \frac{1}{H'_m} \left[\left(\frac{H^{\zeta}_{mm} \dot{\zeta}_m}{\overline{\sigma}_m} + \frac{H^{\zeta}_{mn} \dot{\zeta}_n}{\overline{\sigma}_m} \right) \xi_m \right] \sigma + \frac{1}{H'_n} \left[\left(\frac{H^{\zeta}_{nm} \dot{\zeta}_m}{\overline{\sigma}_n} + \frac{H^{\zeta}_{nn} \dot{\zeta}_n}{\overline{\sigma}_n} \right) \xi_n \right] \sigma \qquad [72]$$

with the flow stress $\overline{\sigma}_m$, $\overline{\sigma}_n$ of the mother and new phase. Since the effect of structure on flow stress is possible,

$$H^{\zeta}_{mn} \neq 0, \quad \text{and} \quad H^{\zeta}_{mm} = H^{\zeta}_{nm} = H^{\zeta}_{nn} = 0 \qquad [73]$$

And putting

$$\xi_m = 1 - \xi_n \equiv 1 - \xi, \quad \text{and} \quad \zeta_n \equiv \xi, \qquad [74]$$

then we have

$$\dot{\varepsilon}^{tp} = \frac{1}{H'_m} \frac{H^{\zeta}_{mn} \dot{\xi}}{\overline{\sigma}_m} (1 - \xi) \sigma \equiv 3K(1 - \xi) \dot{\xi} \sigma \qquad [75]$$

This is the well-known formula of Greenwood–Johnson for TP (*47–51*).

To know how the TP strain is induced, the value of the TP coefficient in eqn [75] must be identified. Some experimental methods are proposed. The simplest way is to measure the strain occurring during the phase transformation depending on applied stress σ as shown in **Figure 7**. Note that the TP strain is given as the difference between strain with nonzero applied stress subtracted by that without stress.

Integration of eqn [75] from $\xi = 0$ at the transformation start time to $\xi = 1$ at the finish time reads

$$\varepsilon^{tp} = \int_0^1 3K(1 - \xi) \sigma \mathrm{d}\xi = K\sigma, \quad \text{or} \quad K = \frac{\varepsilon^{tp}}{\sigma} \qquad [76]$$

Then the TP coefficient K is identified by the ratio of ε^{tp} to stress σ.

12.06.4.6 Strain Induced by Diffusion of Chemical Components

Carburizing, nitrizing, or carburizing–nitrizing is known to improve the mechanical properties on the work surface, such as surface hardness, fatigue strength, and wear resistance, since the diffused atoms change lattice parameters and give volumetric dilation to cause a strain rate termed $\dot{\varepsilon}^{df}_{ij}$. If no transformation occurs during diffusion of carbon and/or nitrogen, the microstructure remains austenite at high operating temperature. Thus, the strain rate $\dot{\varepsilon}^{df}_{ij}$ simply depends on the diffusion rate of carbon and/or nitrogen in the form (*42*):

$$\dot{\varepsilon}^{df}_{ij} = \frac{1}{3} \left\{ \frac{a^3(C_{t_1}, N_{t_1})}{a^3(C_{t_0}, N_{t_0})} - 1 \right\} \left(\frac{1}{C_{t_1} - C_{t_0}} \dot{C} + \frac{1}{N_{t_1} - N_{t_0}} \dot{N} \right) \delta_{ij} \qquad [77]$$

where a is the lattice parameter of austenite, which is a function of current carbon and nitrogen contents.

12.06.5 Material Data and the Database

So much data must be propounded for the practical simulation of some machine parts made of different material depending on temperature, and the transfer of these data to a simulation code is laborious and time-consuming. In our cases of quenching and other metallo-thermo-mechanical process simulation, the temperature dependence and sometimes stress/strain dependence of the data must be taken into account for the data on phase transformation, heat conduction, and inelastic stress analysis; they are the TTT and/or CCT diagram and other transformation kinetics data for phase change, heat conductivity, density, heat capacity, heat generation, and heat conduction, and the thermal expansion coefficient, the stress–strain diagram including Young's modulus and Poisson's ratio and the yield stress and hardening coefficient, and transformation plasticity characteristics for the mechanical field.

From such a background, the Sub-committee on Material Database under the Committee on Engineering Plasticity, the Society of Material Science, Japan (JSMS), has conducted a joint project to construct a database relevant to such simulations. The developed database contains the stress–strain constitutive data in the elastic and inelastic range, the thermal expansion or the temperature-dilatation diagrams, thermal conductivity, specific heat, and isothermal and continuous cooling diagrams and recently collected data for the transformation plastic coefficient. The platform of the database is based on the commercial spreadsheet software Microsoft Excel. The database has two types of search engines, which are built by macro programming of a spreadsheet: One is a search based on the chemical components of the target steel, and the other is a search based on the steel name. Here, the structure, function, and variety of recorded data of the developed database "MATEQ" (MATErial database for Quenching) are developed (see Figure 9) (52).

12.06.5.1 Outline of the Material Database MATEQ

12.06.5.1.1 Structure of the Database

Strategies to construct the database are based on the following four points:

1. Being able to run on commonly used software, or easy and low-cost renewal of the system for the database.
2. Easy recording and managing of the data.
3. Portability to transform to other database frames or operating systems.
4. Target materials used for heat treatments in the primary stage.

According to the above strategies, the frame of the database was constructed with use of the commercial spreadsheet software Microsoft EXCEL to develop the system running on personal computers.

The developed database is roughly divided into two parts. One is the main part provided by a search engine. The other is a data file including the material property data as a numerical value and the information of the test piece such as the chemical compositions, shape of the test piece, thermal history of material, and so on. The main part and the data files are administrated as different files, and they form the structure of files and directories shown in Figure 9. Under the home directory of the database, there are subdirectories, IT-CCT storing files of isothermal and CCT diagrams, CONDUCT files of thermal conductivity, SHEAT for specific heat, EXPAN for temperature-dilatation diagrams, S–S for stress–strain curves, and ELAST for elastic modulus. Recently, the data of transformation plasticity or TP coefficients were also collected as TP in MATEQ Ver.3. One data file is made for each material and each property. Both the main part and the data files are made with use of EXCEL.

The database is started up by opening the main part from EXCEL. Users can access three screens, such as a title screen and two types of search screens. The function of a search is explained in a later section. All of these three screens are formed on work sheets of EXCEL. The main part contains seven other hidden work sheets and three accessible sheets. These seven hidden sheets include lists of materials recorded in the database. These sheets are used for managing data and data search.

One sheet corresponds to one of six kinds of material properties in Figure 10. An example of this sheet is shown in Figure 11. Steel name, chemical composition, and name of the data file are included in this sheet, and all data files recorded in a subdirectory are listed in this sheet. When intending to add new data into the database, the operator must insert these three pieces of information

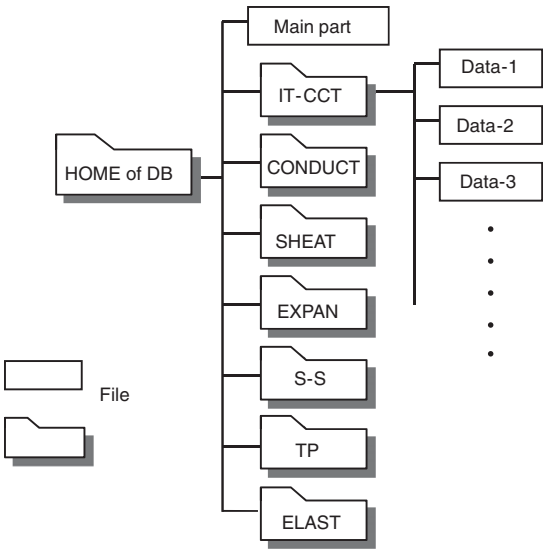

Figure 9 Structure of materials database MATEQ.

No.	Steel name	C	Si	Mn	P	S	Ni	Cr	Mo	Cu	V	Al	Nb	B	Ti	N	W	File name
1	S10C	0.06		0.43														itcct\S10C-TTT
2	S15C	0.15	0.22	0.41	0.021	0.024	0.06	0.06		0.150		0.005						itcct\S15C-CCT
3	S15C Mod(0.30%C)	0.30	0.29	0.39	0.012	0.026		0.12		0.215		0.003				0.006		itcct\S15C-Mod1-CCT
4	S15C Mod(0.46%C)	0.46	0.29	0.39	0.012	0.026		0.12		0.215		0.003				0.006		itcct\S15C-Mod2-CCT
5	S15C Mod(0.90%C)	0.90	0.29	0.39	0.012	0.026		0.12		0.215		0.003				0.006		itcct\S15C-Mod3-CCT
6	S15C Mod(0.98%C)	0.98	0.29	0.39	0.012	0.026		0.12		0.215		0.003				0.006		itcct\S15C-Mod4-CCT
7	S20C	0.17		0.92														itcct\S20C-TTT
8	S38C	0.36	0.27	0.66	0.020	0.016	0.02	0.21	0.22	0.22		0.060						itcct\S38C-TTT
9	S38C	0.37	0.28	0.60	0.027	0.027		0.06		0.13								itcct\S38C-CCT
10	S45C	0.44	0.22	0.66	0.022	0.029		0.15			0.020							itcct\S45C

Figure 10 Example of data managing sheet included in the main part of the database.

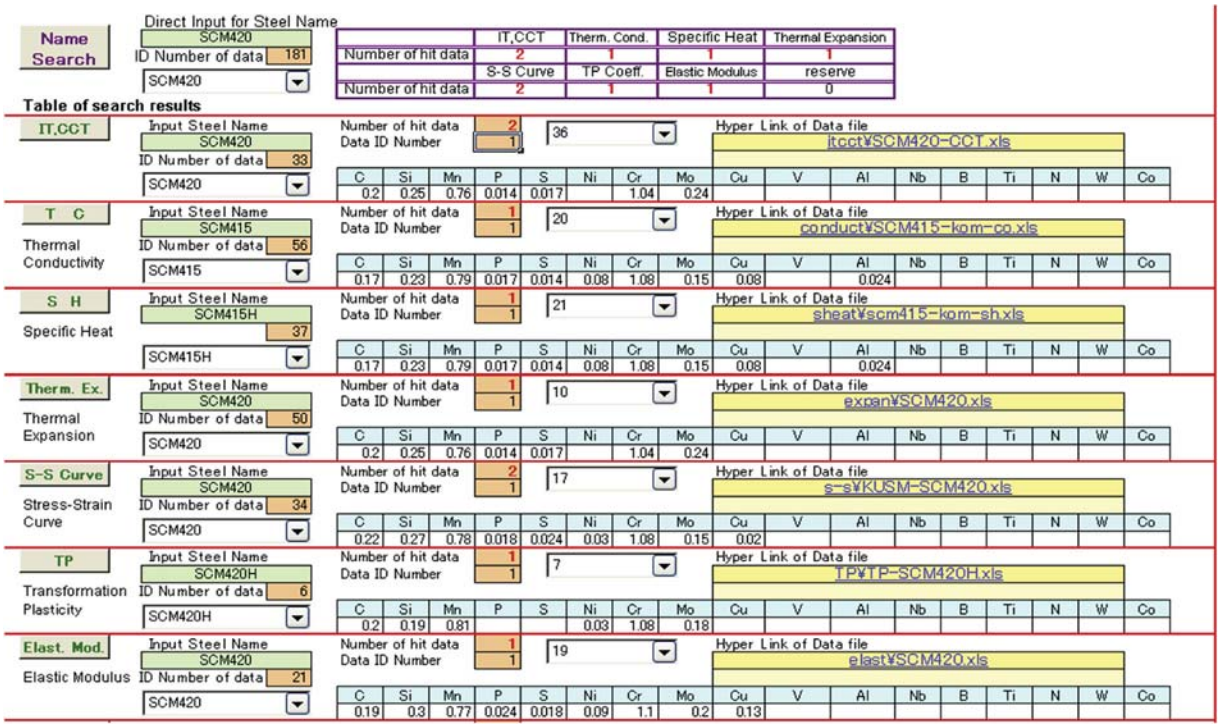

Figure 11 Screen image for data file from name of material.

(steel name, chemical composition, and file name) into the data managing sheet and put a new data file into the corresponding subdirectory.

12.06.5.2 Search Engine

The database has two types of search methods. One is a search using the *steel name*, the other is a search using the *chemical compositions* of the steel. Figures 11 and 12 illustrate the images of these search screens. In Figure 12, the state of the screen is shown when searching for SCM420 steel in JIS grade. Users can adopt the dropdown menu to select the steel name, or they can write the name directly into the input cell. After selecting the steel, data files can be searched by pushing the Name Search button.

Figure 12 indicates that there are two files corresponding to SCM420 in the transformation diagram directory, two files in the S–S curve directory; one file in the temperature–dilatation diagram directory, and the other file in the elastic modulus directory. Users can select the file number by the dropdown menu located on the left side of the cell indicating the data file path. When the file number is selected, the data file path appears in the cell. As seen in Figure 12, for example, the path itcct\SCM420-CCT.xls is printed in the cell for IT-CCT. The path in the cell links to the target file, and users can move to the target file immediately by clicking the

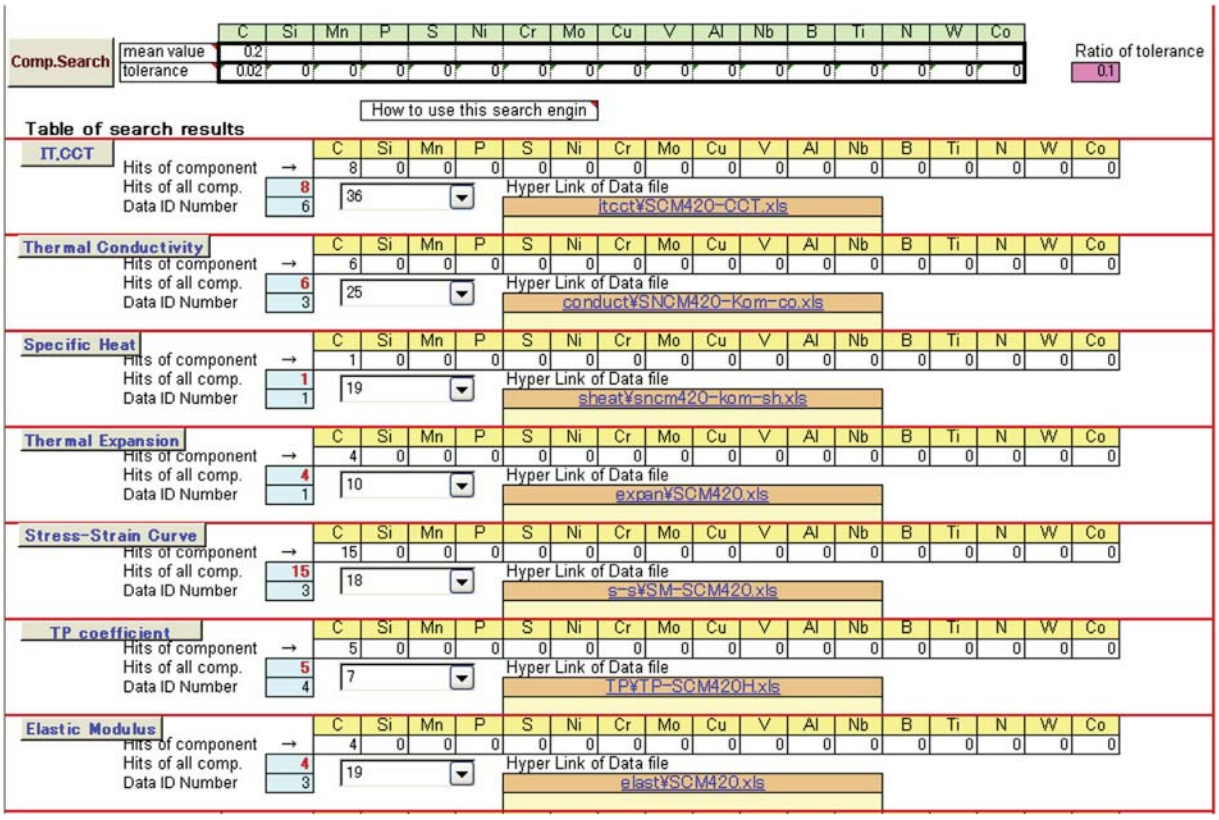

Figure 12 Screen image of search for data file from chemical compositions.

path name. The link is defined by use of a relative address. Data searching is available both simultaneously for all properties and also individually for each property. The dropdown menu of the steel name is prepared for each property. By use of the individual dropdown menu and pushing the property button, the individual search is executed.

Figure 13 explains the state of search based on the chemical composition of steels. Users must input the content to be searched and its tolerance in the cells enclosed by bold lines. The tolerance means the deviation from the input value to be searched. Users need not specify all contents. The unspecified compositions are ignored in searching. In the example in Figure 13, the contents of carbon and molybdenum are specified in mass % unit. The default value of the tolerance can be modified by typing the number in the cell of 'Ratio of tolerance.' Direct input into the cell of tolerance is also available. This search method enables users to choose steels with different content in a specified element. By setting the large digit number in cells for the content and tolerance of carbon content C, for example, users can accumulate the data files to investigate the dependency of carbon content on properties.

The results of a search are indicated by the number of files, which have contents in the searching rage. For example, there are eight material data that have carbon content from 0.18 to 0.22% in the IT-CCT diagrams directory. The number of materials with compositions satisfying all searching conditions is reported in the cell 'Hits of all comp.' Users can select the data number from the dropdown menu to get the data file path. Both simultaneous and individual searches are also available in composition search. These name search and composition search functions are programmed by VISUAL BASIC provided in EXCEL.

12.06.5.3 Accumulated Data of Material Properties

12.06.5.3.1 Description of Data

All data of material property are recorded as a numerical value with graphs in a data file. The data file contains an information sheet and data sheets as a work sheet of EXCEL. The information sheet is at the head of the data file. Figure 14 shows the information sheet of SCM420 about the stress–strain curves. Information about the test piece and testing conditions are described here in as much detail as possible. In the lower half of the information sheet, the testing conditions are described. Each row of the testing conditions links to another sheet in the same data file where material properties are listed in numerical value. Some examples of data sheets are shown in Figures 15 and 16. Figure 15 is the data sheet of stress-strain curve of SCM420 steel. After some comments about testing conditions, numerical data are listed accompanied with a diagram. The stress–strain relation is recorded in detail up to several percent of strain range, but not for large strain. The reason why relatively small strain is focused upon is the necessity of

Material

Material name	SCM420
Production process	
Shape	Cylinder (f30)

Chemical composition(mass %)

C	Si	Mn	P	S	Ni	Cr	Mo	Cu	V	Al	Nb	B	Ti	N	W	Co
0.22	0.27	0.78	0.018	0.024	0.03	1.08	0.15	0.02								

Heat treatment

Diameter or thickness (mm): 20

	1st	2nd	3rd	4th
Temperature (°C)	925 (925)*			
Time (h)	1hr (30min)			
Cooling	FC (WQ)			

*Pearlite/ferrite(martensite/bainite)

Grain size:
Hardness: Unit of hardness
Note:

Tensile test

Direction:
Specimen diameter (mm): 10 (8)* *Pearlite/ferrite(martensite/bainite)
Specimen thickness (mm):
Specimen width (mm):
Gage length (mm): 50(30)
Yield stress (MPa):
Tensile strength (MPa): 1059
Elongation (%): 18
Reduction of area (%): 43

Contents of digital data	Linked destination	Note (data provider or reference, testing condition etc.)
S–S curve (1)	Sheet2!A1	R.T., pearlite/ferrite, strain rate 0.15 mm min^{-1} before 5%, 3.75 mm min^{-1} after 5%
S–S curve (2)	Sheet3!A1	200 degC, pearlite/ferrite, strain rate 0.15 mm min^{-1} before 5%, 3.75 mm min^{-1} after 5%
S–S curve (3)	Sheet4!A1	300 degC, pearlite/ferrite, strain rate 0.15 mm min^{-1} before 5%, 3.75 mm min^{-1} after 5%
S–S curve (4)	Sheet5!A1	400 degC, pearlite/ferrite, strain rate 0.15 mm min^{-1} before 5%, 3.75 mm min^{-1} after 5%
S–S curve (5)	Sheet6!A1	500 degC, pearlite/ferrite, strain rate 0.15 mm min^{-1} before 5%, 3.75 mm min^{-1} after 5%
S–S curve (6)	Sheet7!A1	600 degC, pearlite/ferrite, strain rate 0.15 mm min^{-1} before 5%, 3.75 mm min^{-1} after 5%
S–S curve (7)	Sheet8!A1	700 degC, Pearlite/Ferrite, strain rate 0.15 mm min^{-1} before 5%, 3.75 mm min^{-1} after 5%
S–S curve (8)	Sheet9!A1	850 degC, pearlite/ferrite, strain rate 0.15 mm min^{-1} before 5%, 3.75 mm min^{-1} after 5%
S–S curve (9)	Sheet10!A1	950 degC, pearlite/ferrite, strain rate 0.15 mm min^{-1} before 5%, 3.75 mm min^{-1} after 5%
S–S curve (10)	Sheet11!A1	R.T., martensite/bainite, strain rate 0.15 mm min^{-1} before 5%, 3.75 mm min^{-1} after 5%
S–S curve (11)	Sheet12!A1	200 degC, martensite/bainite, strain rate 0.15 mm min^{-1} before 5%, 3.75 mm min^{-1} after 5%
S–S curve (12)	Sheet13!A1	300 degC, martensite/bainite, strain rate 0.15 mm min^{-1} before 5%, 3.75 mm min^{-1} after 5%
S–S curve (13)	Sheet14!A1	400 degC, martensite/bainite, strain rate 0.15 mm min^{-1} before 5%, 3.75 mm min^{-1} after 5%
S–S curve (14)	Sheet15!A1	500 degC, martensite/bainite, strain rate 0.15 mm min^{-1} before 5%, 3.75 mm min^{-1} after 5%
S–S curve (15)	Sheet16!A1	600 degC, martensite/bainite, strain rate 0.15 mm min^{-1} before 5%, 3.75 mm min^{-1} after 5%
S–S curve (16)	Sheet17!A1	700 degC, martensite/bainite, strain rate 0.15 mm min^{-1} before 5%, 3.75 mm min^{-1} after 5%
S–S curve (17)	Sheet18!A1	850 degC, martensite/bainite, strain rate 0.15 mm min^{-1} before 5%, 3.75 mm min^{-1} after 5%
S–S curve (18)	Sheet19!A1	950 degC, martensite/bainite, strain rate 0.15 mm min^{-1} before 5%, 3.75 mm min^{-1} after 5%

Figure 13 Example of information sheet of data file.

R.T.
Pearlite/Ferrite
Strain rate 0.15 mm min^{-1} before 5%, 3.75 mm min^{-1} after 5%

Strain (%)	Stress (MPa)
0.033	7.51
0.167	318.38
0.180	332.12
0.207	333.39
0.274	319.71
0.314	306.01
0.375	289.83
0.415	299.85
0.455	294.89
0.522	299.93
0.595	298.74
0.655	298.78
0.736	292.60
0.802	298.89
0.883	297.70

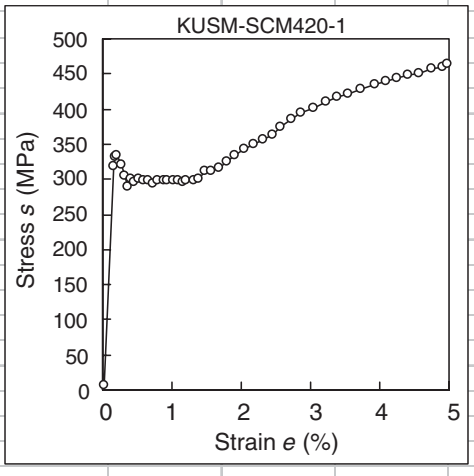

Figure 14 Stress–strain diagram.

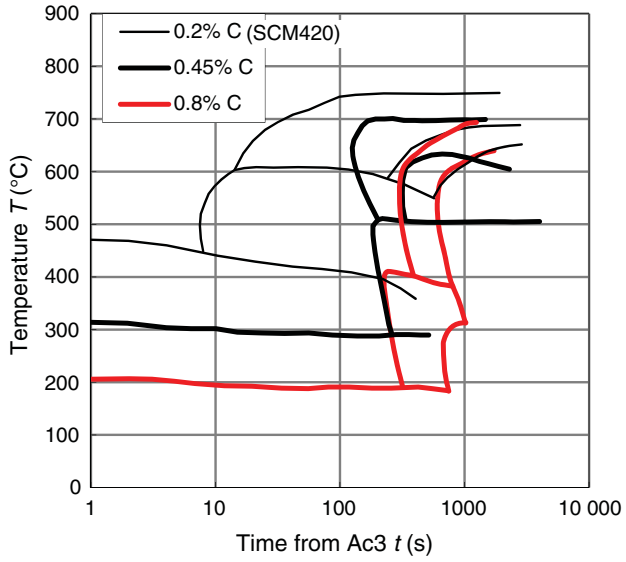

Figure 15 TTT diagram.

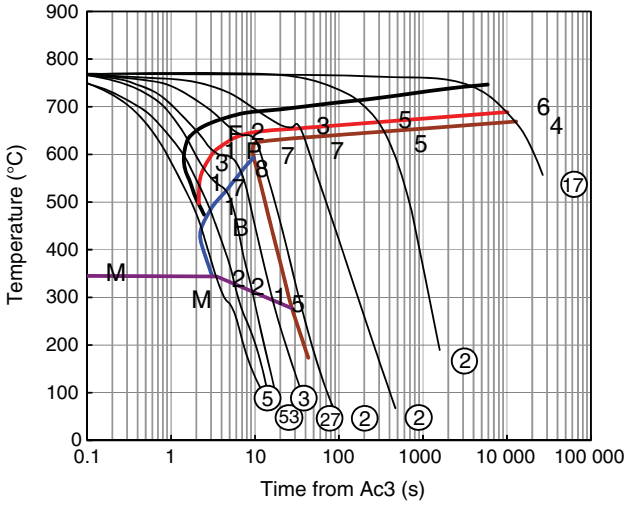

Figure 16 CCT diagram.

detailed stress–strain diagrams for the quenching simulation. Figure 14 is the continuous cooling diagram extracted from the data sheet of phase transformation data of S45C steel. In the CCT diagram, the start and end lines of transformation, the volume fraction of the transformed phase, cooling curves, and hardness are recorded. Since the data are recorded by a digital value, it is easy to plot different data in the same graph. Figure 15 is the multiplex plot of the CCT diagram to compare the start and end lines of CCT in different carbon content. In the modeling of the transformation kinetics, the time at the start and finish points during isothermal or CCT is often required to be formulated as a function of temperature and/or cooling rate. The approximate equation of the transformation curve is immediately solved by the use of the graph tool provided by EXCEL. The data sheet formed on the work sheet of EXCEL may provide such benefits to users. For more practical use of the data sheet, the application to create an input data file for major simulation codes remains for future work.

12.06.5.4 Steel Grade Covered in the Database

The developed database contains the number of data listed in Table 1 at present. Here the number of data is counted by the data series newly defined in the following way. For the data related to the phase transformation, all data included in one CCT or IT diagram are counted as one data series. The data of specific heat, thermal conductivity, or elastic modulus at some temperature levels are, respectively, classified into different data series, and the dilatation–temperature curves

under some cooling rates as well as the stress-strain curve at different temperature is defined as one data series. Steels for machine structural use are composed of carbon steels or low alloy steels. The category of other steels contains nonstandard carbon and low alloy steels, high alloy steels, cast irons, and aluminum alloys. Most of the data are included in these categories. Approximately 1000 stress–strain curves are included in the database, depending on temperature and strain rate.

Table 4 shows the consistency of data through each material property for the material widely used in practice. Solid marks denote the existing data in the database, while open marks denote the data not included, but they can be substituted by other existing data. In the category of carbon steels, there are some lacking data, but it may be possible to substitute other material data. In the low alloy steels, some data are not completed in thermophysical properties and elastic modulus. Most of the properties are included for popular austenitic stainless steels, even though the steel menu does not change.

Commonly used database software is employed as a tool, but the commercial spreadsheet software is easily adopted to reconstruct the database. The developed database has the necessary functions, such as easy search and access to the target data. And the supplement and the deletion of data are easily available by editing the spreadsheet.

The database contains about 1000 curves for the stress–strain relation and 50–100 data series for the other material properties, and is able to be in practical use.

The way to release the database is under discussion after verifying the quality of accumulated data. For some materials, the property data necessary for numerical simulation have not been completely provided. Both the supplement of incomplete data and the newly added data for transformation plasticity are imported to the database.

Some useful commercial codes for the simulation of heat treatment have been used popularly. However, the quality of material property data will dominate the accuracy of the simulation. Moreover, the quality of such simulation codes may depend on the reliable database for material properties.

Table 4 Consistency of data through each material property for the material

JIS steel grade		*TTT*	*CCT*	*Thermal conductivity*	*Specific heat*	*Thermal expansion*	*Stress–strain curve*	*Transformation plasticity*
Carbon and low alloy steel for machine structural use	S10C	●		●	●	●	○	
	S15C		●	○	●	○	●	
	S25C		○	○	●	●	●	
	S38C	●	●	○	●	○	○	
	S45C	●	●	●	○	○	●	●
	S50C	●		○	●	○	●	
	S58C	●		○	○	●	○	
	SCM415			●	●	●	●	○
	SCM420	●	●	●	●	●	●	●
	SCN430	●	●	●	●	●	●	
	SCM440	●	●	●	●	●	●	
	SCr415	●	●				●	
	SCr420					●	●	●
	SCr430	●	●	●	●	●	●	
	SCr440	●	●			●	●	
	SCr460					●	●	
	SCr480					●	●	
	SMn438	●	●					
	SNC815	●	●				●	
	SNC836	●	●	●	●			
	SNCM220	●	●					
	SNCM420	●		●	●	●	●	
Tool steel	SK3	●	●	●	○			
	SKD6	●	●	●	●		●	
	SKD61		●				●	
Bearing steel	SUJ1						●	
	SUJ2	●	●	●				●
Stainless steel	SUS304	–	–	●	●	●	●	
	SUS316	–	–	●	●	●	●	
	SUS321	–	–	●	●	●	●	
	SUS347	–	–	●	●	●		
	SUS430			●			●	
Ferrite heat-resisting steel	2.1/4Cr–1Mo		●	●		●	●	
	Mod.9Cr–1Mo		●		○	●	●	

The authors emphasize, in this section, the importance of constructing the material database for such simulations of some processes incorporating phase transformation in addition to the heat treating process, and international cooperation in further developments of a larger scaled database is expected.

12.06.6 Computer Code Relevant to Metallo-Thermo-Mechanical Simulation – COSMAP

The strategy and function of a newly developed FEM code called COSMAP (COmputer Simulation of Material Process) (*53–55*) for surface hardening during thermal processing, including heat treatment, carbonizing, and nitriding, are briefly introduced in this section. The simulation code is developed based on the metallo-thermo-mechanical theory (*27–30*) considering the coupled equations of diffusion, heat conduction, inelastic stresses, and kinetics of phase transformation. Some examples of simulation and the experimental verification for carbonized quenching, the carbonized-nitrided-quenching process of a cylinder and ring as well as a gear, are illustrated, and a comparison of the simulated values of distortion, residual stresses, and the profile of induced phases with experimental data is made with some discussions.

12.06.6.1 Under Releasing Software

As seen in Sections 12.06.2–12.06.4, the evaluation of metallic structures, temperature, and mechanical fields occurring during quenching and other processes incorporating phase transformation is complicated since the governing equation governing these three fields are given by the nonlinear equation of high order and since the fields are coupled to each other. This is more sophisticated in the case of carburizing, nitriding, and carbo-nitriding followed by quenching.

The first computer program to approach such a coupled metallo-thermo-mechanical problem was developed in 1990 by the present author and coworkers (*31*,*32*). It was termed HEARTS, and was based on the theory of metallo-thermo-mechanics also developed by the authors with some application of practical engineering problems.

After that, some codes were developed based on the consideration of coupling between temperature, metallic structure, and mechanical field, in the sense of metallo-thermo-mechanics termed by the present author.

They are as follows:

COSMAP (*53–55*) – http://www.ideamap.co.jp/cosmap/e_product_cosmap010_outline.html
DANTE (*56*) – http://deformationcontrol.com/dct_products.htm
DEFORM-HT (*57*) – http://www.deform.com/products/deform-ht/
SYSWELD (58) – http://www.esi-group.com/products/welding-old/sysweld
GRANTAS (*59*) – http://www.eonet.ne.jp/~smiling/SOFT/GRANTAS/grantas-eng.htm
FINAS-TPS (*60*) – CRC http://www.engineering-eye.com/FINAS/FINAS_TPS/index.html
MUSIMAP (*61*) – http://www.arimotech.com/Pages/EnglishMUSIMAP.aspx

as stand-alone type codes, while

QUESS (*62*)
K-TRA (*63*)

and so on. They are developed as user's subroutines connected with programs for nonlinear problems such as ABAQUS and others.

12.06.6.2 Development of New Code

COSMAP was born in the cooperative research project in Japan as a part of the international VHT (Virtual Heat Treatment tool for monitoring and optimizing HT process) project, organized by Intelligent Manufacturing Systems (IMS). Note that COSMAP is also based on our theory of metallo-thermo-mechanics, but quite a different code from HEARTS.

12.06.6.3 Overview of the COSMAP System (*53–55*)

The code COSMAP is constructed by multiple solvers of the direct method and the ICCG method. It is possible to select an analytical technique flexibly depending on the problems based on the user's requirement. Pre- or post-processor FEMAP or GiD is adequately employed as GUI. The interface is equipped for easier accessibility to a heat transfer coefficient identification program and the material database, MATEQ, developed by Materials Database Subcommittee of Engineering Plasticity Committee, the Society of Materials Science, Japan. Users can also adopt an individual program to identify the heat transfer coefficient.

12.06.6.3.1 COSMAP System

12.06.6.3.1.1 Input Data Type and Format

Input data for COSMAP consist of three parts as follows: analysis model data, control data for process and analysis, and material property data.

1	Analysis model file: *.nas; MSC-NASTRAN format
2	Control data files for process and analysis: *.pos; data in file are free format
3	Material property file: *.dat; data in file are free format

12.06.6.3.1.2 Analysis Function

COSMAP simulates temperature distribution, progressing phase transformation, stress/strain (distortion) profiles in the manner of the coupling between each other, and chemical composition of carbon and nitrogen in the case of carburizing and nitriding. The function of COSMAP consists of three parts: problem type (geometric type of analysis model), analysis function, and process function as indicated in Tables 5 and 6.

In addition, since all the boundary conditions in diffusion analysis, heat transfer analysis, and inelastic analysis can be set up using the variables depending on time, which are temperature, outside load (e.g., pressure), etc., COSMAP can be applied to other analyses if boundary conditions are taken into consideration.

12.06.6.3.1.3 Unit System

An SI unit system is fundamentally used for COSMAP.

Note: An engineering unit system cannot be used for COSMAP (Table 7).

12.06.6.4 Development of New Simulation Code

One of the main objectives of VHT is to improve proper functions and the numerical modeling method to the theory and practice of metallo-thermo-mechanical behavior involving carbonitrided quenching when developing a new FEM code. The purpose of the modeling is to enable us not only to simulate the diffusion process of carbon during the carbonized HT process, but also to describe the evolution of microstructure, stress, and distortion during carbonitrided quenching by considering the effects of C/N diffusion on distortion and phase transformation kinetics. In developing the simulation code COSMAP, some types of kinetic equations of diffusing elements for simulating the carbonitrided quenching process are proposed. Thus developed models can be used to predict the coupling behavior, including temperature, microstructure, stress/distortion, and diffusion of elements such as carbon and nitrogen and so on, during thermo-chemical processes (Tables 5–7). The models involved in the FEM procedure are divided into four categories: heat conduction, diffusion of C/N, transformation, and stress/strain analysis by use of elasto-plastic constitutive equations. The heat transfer coefficient identification program to be used as a cooling boundary condition, and the material

Table 5 Analysis function

Type of function	*Function*
Problem type	2D problems (plane strain, plane stress, axisymmetric)
(Geometric type)	3D problems
Analysis function	Heat transfer analysis, diffusion analysis of multielement, thermoplastic analysis, inelastic analysis (thermo-elastoplastic analysis, creep, transformation plasticity, induced strain by diffusion)
Process functions	Carburizing, nitriding, quenching, combination of carburizing, nitriding, and quenching, localized heating and cooling)

Table 6 Finite element library

Problem type	*Element type*
2D, axisymmetric problem	Quadrilateral element with 4 nodes or 8 nodes Triangular element with 6 nodes
3D problems	Hexahedron element with 8 nodes or 20 nodes Pentahedron element with 6 nodes or 12 nodes

Table 7 List of unit system used in COSMAP

Category	*Physical quantity*	*SI unit*	*Note*
Analysis model	Length	mm	Millimeter
	Time	s	Second
Heat transfer analysis, thermo-physical properties	Temperature	K	
	Thermal flux of surface	W m^{-2}	
	Internal heat generation	W m^{-3}	
	Thermal conductivity	W (mm^{-1} K^{-1})	
	Specific heat	kJ (kg^{-1} K^{-1})	Note 1
	Density	kg m^{-3}	
	Latent heat	kJ kg^{-1}	Note 1
Diffusion analysis, diffusion properties	Carbon concentration	wt%	
	Nitrogen concentration	wt%	
	Diffusion coefficient	m^2 s^{-1}	
Metallic structure analysis and structure property	Volume fraction	(Nondimensional)	
	Temperature	K	
	Concentration of chemical content	wt%	
Stress analysis and mechanical property	Longitudinal elastic modulus	GPa	
	Poisson ratio	(Nondimensional)	
	Linear expansion coefficient	K^{-1}	
	Initial yield stress	MPa	
	Work hardening coefficient	GPa	
	Transformation expansion coefficient	(Nondimensional)	
	Transformation plasticity coefficient	MPa^{-1}	
Property data of boundary	Heat transfer coefficient	W (mm^{-2} K^{-1})	
	Concentration transfer coefficient	mm s^{-1}	
	Radiation factor	(Nondimensional)	
	Radiation view factor	(Nondimensional)	
	Displacement	mm	
	Force	N	
	Stress	MPa	$=1.0 \times 10^6$ Pa
	Temperature	K	

Note 1: Within a program, this is multiplied by 10^3 for unit conversion. Here, kJ is a kilo joule.

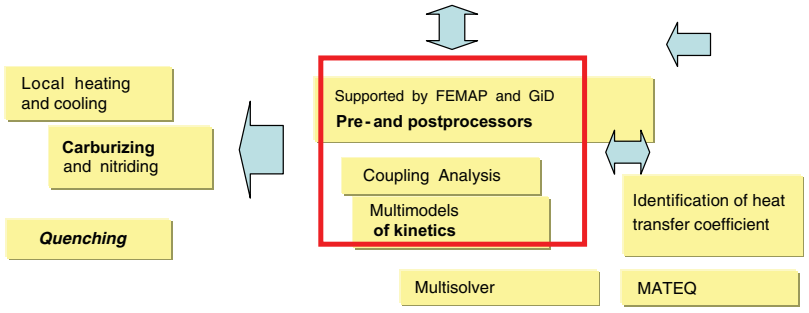

Figure 17 Framework of COSMAP system.

database, MATEQ (*48*), are also possible to be employed for the system. The system is constructed by several parts with characteristic functions as depicted in Figure 17.

As one of the activities of the Japanese VHT project, a benchmark simulation project was carried out by adopting COSMAP and other codes in cooperation with both societies of JSMS and JSHT. In the benchmark research, the calculation accuracy of COSMAP is verified with experimental data involving temperature, distortion, and residual stresses. To do so, the authors also have been working to amass material property data and construction of the database of thermophysical and mechanical properties, and to identify the heat transfer property, data of some kinds of quenchants are collected using benchmarked specimens.

12.06.6.5 Simulated Examples by the COSMAP System

a. Simulation of the carburizing quenching process

The simulation of the carburizing quenching process for a cylinder, ring, and helical gear made of SCr420H is executed by the use of the developed COSMAP system. The works are heated up to 950 °C for carburization at a carbon potential (C_p) of 1.1% for 120 min and diffusing at a C_p of 0.85% for 170 min followed by quenching into oil at 100 °C. Figure 18(a1)–(a3) represents the simulated results of distortion, microstructure, and axial residual stress σ_y of the cylinder. Figure 18(b1)–(b3) depicts the calculated profiles of distortion and the residual stress on the side and at the top of the ring. The results of carbon contents, martensite, and

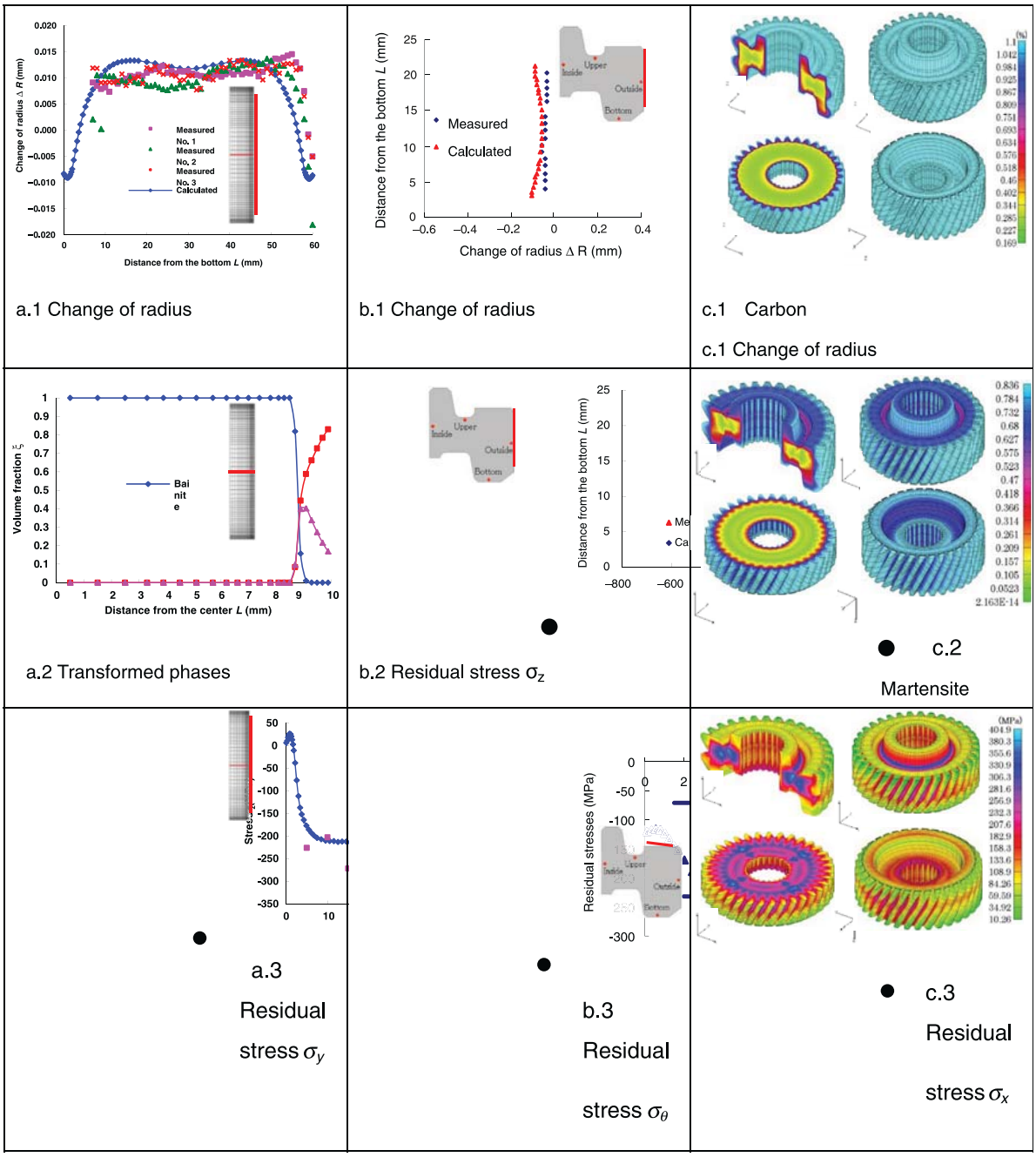

Figure 18 Simulation results of three models during carburizing quenching process. (a) Cylinder model; (b) Ring model; (c) Gear model.

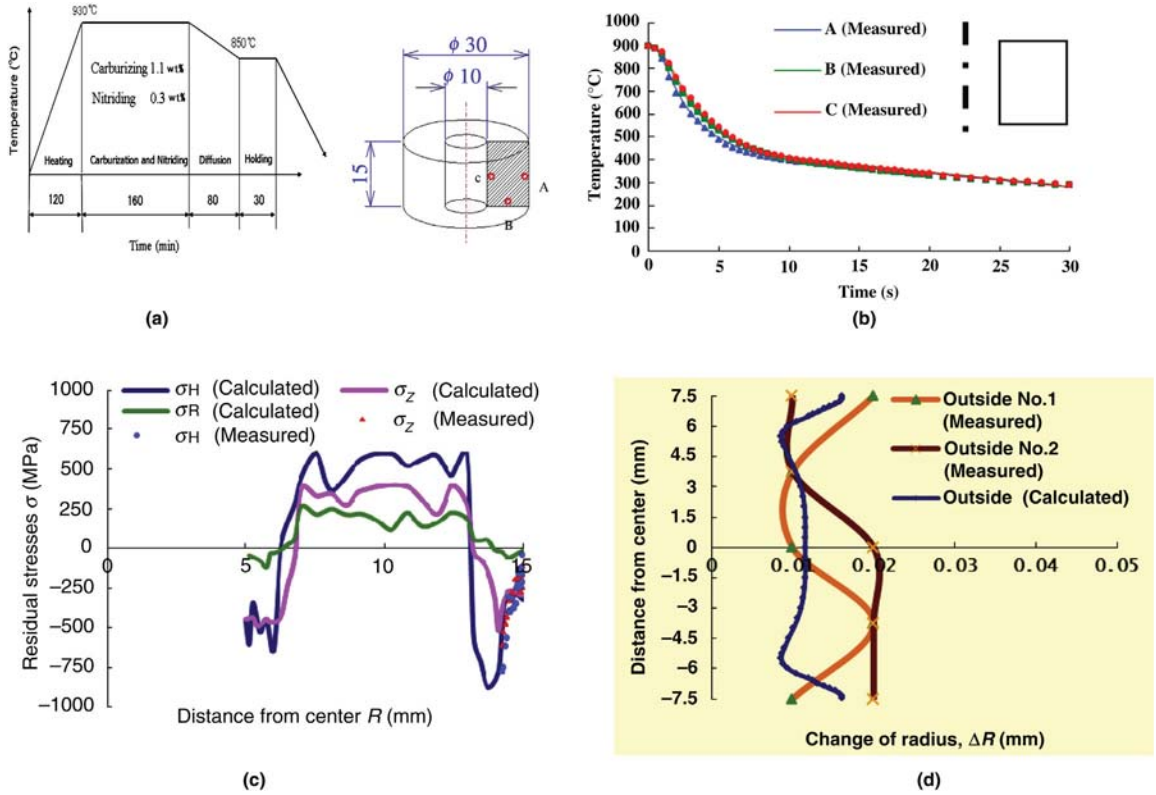

Figure 19 Simulated results of carburizing–nitriding quenching process. (a) Heat pattern and experimental model; (b) cooling curves of quenching process; (c) residual stresses in quenched ring; and (d) distortion of quenched ring.

residual stress in 3D helical gear are shown in Figure 19(c1)–(c3). Some data of experimentally measured distortion and residual stress are also overplotted to verify the simulated results and to confirm the reliability of the developed code.

b. Simulation of the carburizing–nitriding quenching process

The steel used in this chapter is carbon steel (JIS-SCM420). The heat pattern is composed of five steps, as shown in Figure 19(a). The cooling curves of the ring specimen are shown in Figure 19(b), in which the holes (A–C) are drilled to insert thermocouples for temperature measurement during quenching. The thermal and diffusion boundary conditions are both the flux type, and hardness and residual stresses are measured after experiments, the results of which are used to compare with the calculated ones. Figure 19(c) represents the profile of residual stresses on the middle section of the specimen. The data on the surface agree qualitatively with the measured values by the X-ray diffraction method on the surface. The value of axial stress almost equals that of tangential stress. Figure 19 displays the calculated results of final distortion, which also agree well with the measured displacements in the radial direction. The small discrepancy between the measured and calculated values may be caused by the following factors: Constitutive equations should be functions of carbon and nitrogen content, and transformation plasticity should be added while both effects are neglected at present in the first approximation. But due to the lack of related experimental results about the effects of carbon and nitrogen content on the related parameters used in the constitutive equations, they are neglected at present. These factors will be considered in future research and calculations.

Application of the fundamental theory and the governing equations developed in the previous sections to some kinds of engineering problems incorporating phase transformation is made in the following sections.

12.06.7 Jominy End Quenching

12.06.7.1 Jominy Test

The Jominy test, or Jominy end quench test, is known to evaluate the hardenability of steel in a simple way (*64*). The basic idea of the test and also the data obtained are used to understand the effects of alloying elements and microstructure.

The test specimen is a cylinder with a length of 100 mm (4 inches) and a diameter of 25.4 mm (1 inch) with a thin head. The steel sample is heated up to austenite temperature depending on the chemical component, usually between 800 and

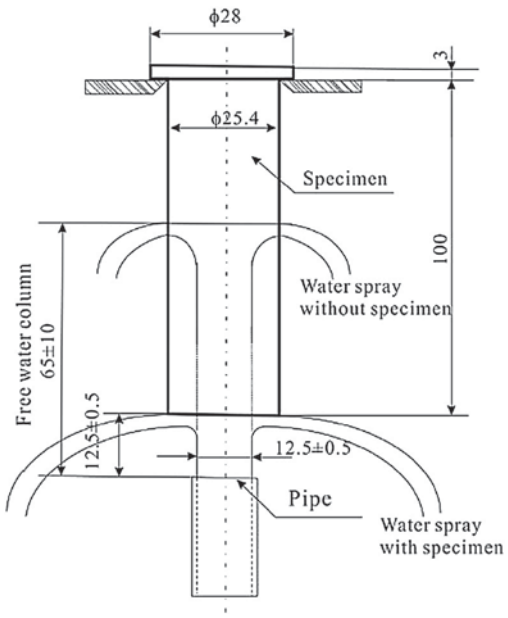

Figure 20 Jominy end quench fixture.

900 °C. The test specimen is quickly transferred to the test system that sprays a controlled flow of water onto the lower end of the specimen. The cooling velocity varies along the length of the sample from very rapid at the quenched end, to rates equivalent to air cooling at the other end and the surface of the cylinder (see **Figure 20**) (*65*).

The hardenability is defined as the ability of the steel to partially transform from austenite to martensite at a given depth below the end surface, when cooled under a given condition. To evaluate the hardenability, the hardness is measured at a grounded flat portion on the cylinder along the length from the quenched end to know the profile of hardness. The Jominy distance is defined as the length where 50% martensite occurs, which is estimated by the profile.

In the standard case of the test, the effect of thermal and transformation stress or strain is ignored; these are essentially induced during the course. The discussion on the effect is also described, and the effect of alloying elements is investigated.

12.06.7.2 Identification of Heat Transfer Coefficient

As one of the fundamental data necessary for the simulation, we tried to evaluate the heat transfer coefficient on the end surface when cooled by water spray. **Figure 21** indicates an example of the cooling curve for SCr420 steel detected by a thermocouple inserted from the upper part and welded close to the end surface of a circular plate with the same diameter (1 inch) but a thickness of $l = 5$ mm. If the heat transfer coefficient of the other end surface facing the air is small enough compared to the end surface, an

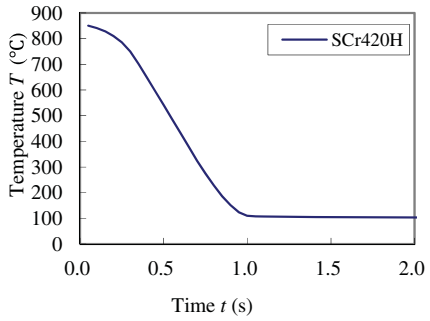

Figure 21 Cooling curve on the end surface for SCR420.

inverse calculation is made for the infinite half-space, for simplicity. The temperature $T(x, t)$ at time t at the distance x from the end is now given in terms of $T(x, t - \Delta t)$,

$$T(x,t) = \sum_{i=1}^{\infty} \frac{2\int_0^l T(x, t-\Delta t)\cos\lambda_i x \mathrm{d}x}{l + \dfrac{\sin 2\lambda_i l}{2\lambda_i}} e^{-k\lambda_i^2 \Delta t} \cos\lambda_i l + T_w \quad [78]$$

with the temperature T_w of the water and heat transfer coefficient $h(T_s)$ of the end surface. Here the λ_i is the ith solution of the equation

$$\lambda_i \tan\lambda_i l = \frac{h}{k} \quad [79]$$

The heat transfer coefficient versus temperature by inverse calculation with regression analysis is shown in Figure 22. The data of Figure 21 taken for SCr420 steel may include the small perturbation in the cooling curve due to heat generation by martensite transformation. As is done in other normal cases to identify the h value, we tried to use stainless steel without oxidation. The data are represented in Figures 23 and 24, which show that the cooling rate is much smaller than the one in Figure 21 and that the maximum value of the heat transfer coefficient is quite different from one in Figure 22. Actually,

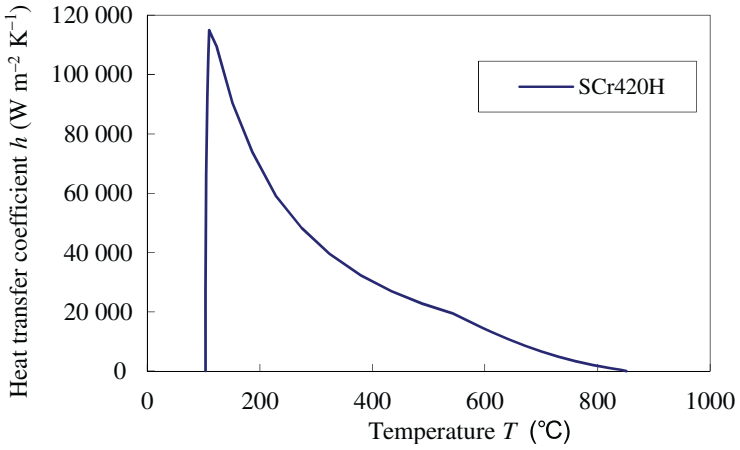

Figure 22 Heat transfer coefficient depending on surface temperature for SCR420.

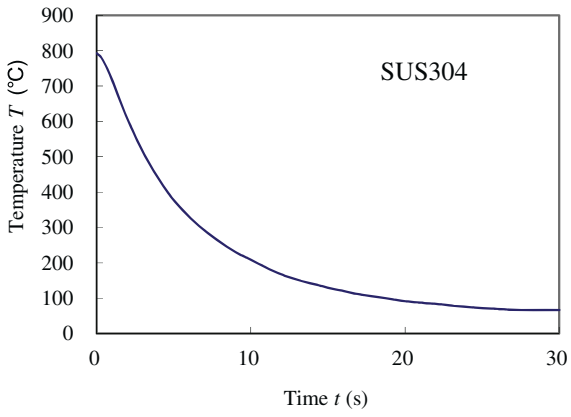

Figure 23 Cooling curve on the end surface for SUS304.

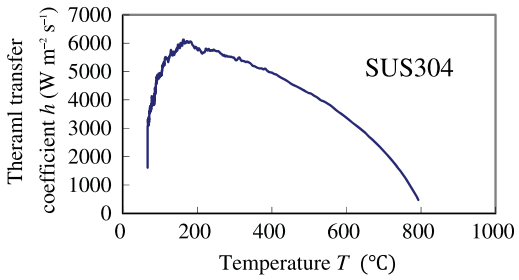

Figure 24 Heat transfer coefficient depending on surface temperature for SUS304.

Table 8 Chemical compositions of materials employed

Material	*C*	*Si*	*Mn*	*P*	*S*	*Cr*	*Mo*
S45C	0.43	0.27	0.84	0.018	0.01	0.16	0.02
SCM420	0.21	0.24	0.89	0.013	0.016	1.25	0.18
SCM440	0.40	0.22	0.82	0.014	0.014	1.12	0.2
SCr420	0.21	0.16	0.85	0.014	0.017	1.15	0.01

the end surface of the normal steel is found to be covered by oxidized film. This is the reason why the data for normal steel take larger values as pointed out in the similar case of mounted clay on the Japanese sword, to be discussed in Section 12.06.11.

12.06.7.3 Materials and the Data, Test Condition, and Simulation Technique

The materials treated here are normal carbon steel S45C, Cr–Mo steels SCM420, SCM440H, and Cr steel SCr420, being used for quenching practice. The chemical compositions are listed in Table 8.

So many material parameters are needed for the metallo-thermo-mechanical simulation during quenching, such as the stress–strain relation and other mechanical, thermo-physical, and metallurgical data in a wide range of temperature level, also depending on metallic structure. It may not be uncommon that the experimental measurement of all necessary material properties costs so much and is so time-consuming. And, the translation of material property data to prepare input data for the simulation code is also difficult to do well. The materials data necessary for the present simulation are employed from the database MATEQ stated in Section 12.06.5.

The specimen as shown in Figure 20 is prepared and heated up to 845 or 925 °C (depending on material composition), staying in the furnace for 30 min. Hardness profile is measured by a Rockwell C-scale hardness tester at a 0.4 mm grounded flat portion on the cylinder along the length from the quenched end, and residual stresses on the surface at some characteristic portions are measured by X-ray diffraction technique (beam, Cr-Kα_1, diffraction area: 0.5 × 2 mm^2 for axial direction, 1 × 1 mm^2 for circumferential direction).

Computer simulation is carried out by use of the developed code HEARTS based on metallo-thermo-mechanical theory to evaluate coupled fields of temperature, microstructure, and stresses (see Section 12.06.2). The substantially induced stress is ignored for consideration in the Jominy test, while the effect of induced stress is considered for simulation. The data of heat transfer in Figure 22 for cooling from the end surface are employed for the simulation while other surfaces are assumed as a heat insulated boundary.

12.06.7.4 Experimental and Simulated Results and Discussions

Figure 25 demonstrates the measured profile of Rockwell-C scale hardness for each material. It is seen that the profiles for three steels, SCM420, SCM440 and SCr420 used for quenching are smoothly decreasing from quenched end to be the steady value of the virginal hardness; while the plain carbon steel, S45C is hardened only near the end surface. The Jominy distance is defined as the distance from the end to the portion in which the martensite fraction is 50%, which conventionally corresponds to the inflection point of the curve. The Jominy distance measured by this way is listed in the first column of Table 9.

Since the coupled simulation provides the time variation and spatial distribution of temperature in the specimen, we can estimate the cooling rate at every portion. When compared with the CTT diagram of each steel including harness data for a given

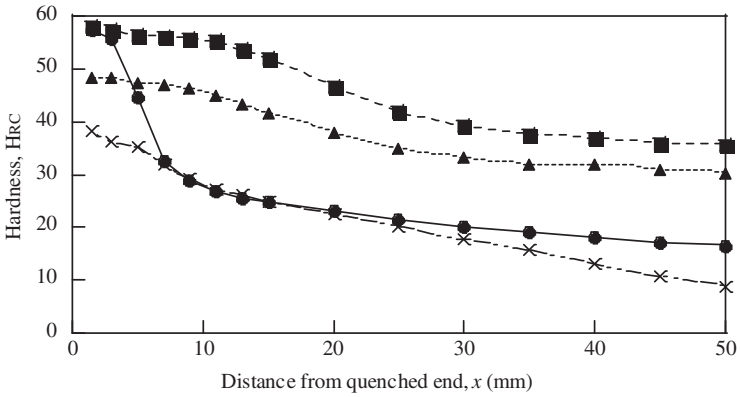

Figure 25 Measured hardness profile.

Table 9 Jominy distances evaluated by several methods, mm

Evaluated from	*S45C*	*SCM420H*	*SCM440H*	*SCr420H*
Measured hardness	5–8	15–20	20–25	5–8
Calculated from cooling rate with TTT diagram	4–5	15–18	20–23	4–6
Simulated portion of 50% martensite coupled with stress	4.3	14.7	19.0	4.2
Similar, but uncoupled	4.2	14.7	18.7	41.5

cooling rate, the hardness distribution is also determined shown in Figure 26, so to identify the Jominy distance. The results are listed in the second column in Table 9.

The simulated pattern of volume fraction of martensite in the cross section of Jominy bar is represented by a dark color in Figure 27, while the white part represents the combined pearlite and bainite (and ferrite) fractions. It is noted that a little gradient in the martensite is seen in the radial direction, which results from the coupled effect of existing stress even when there is an assumed insulation boundary on the cylindrical surface. Upper and lower figures in Figure 28, respectively, represent the axial and circumferential residual stress pattern in the cross section on four materials, and both stress distributions on the surface of the cylinder surface are shown in Figure 29. Here, the lines denote the simulated results and the marks are the measured data using the X-ray diffraction technique. In spite of some scatters in measurement, the simulated curves are confirmed to correspond satisfactorily to the experimental values. It is seen that the tensile stress is induced in the martensite (see Figure 28), and high compressive stress is seen at the Jominy distance.

The Jominy distance is defined as from the end to the portion with 50% transformed martensite. The determined distance for four steels is written in the third column of Table 9. The practical evaluation of the distance is, however, made by neglecting the effect of stresses. However, induced martensite is known to depend on the existing stress and it follows that there may be some difference in the Jominy distance evaluated by the martensite fraction when considering or neglecting the coupling effect of stress. The distance shown in the fourth column in Table 9 is thus determined data.

There are some data of H-band for many kinds of steel used for quenching, which represents the upper and lower limits of hardness variation. The Jominy distance can be estimated from the data (66), which are listed in the bottom of Table 9.

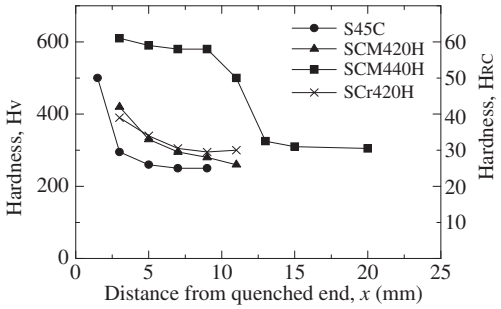

Figure 26 Hardness distribution evaluated from calculated cooling rate with CCT diagram.

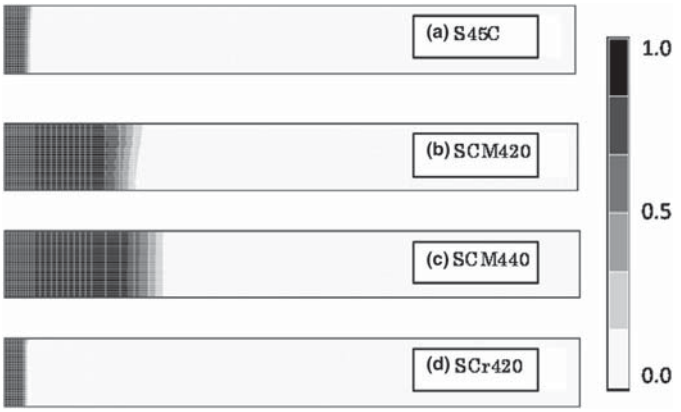

Figure 27 Volume fraction of martensite phase in the half section of Jominy bar.

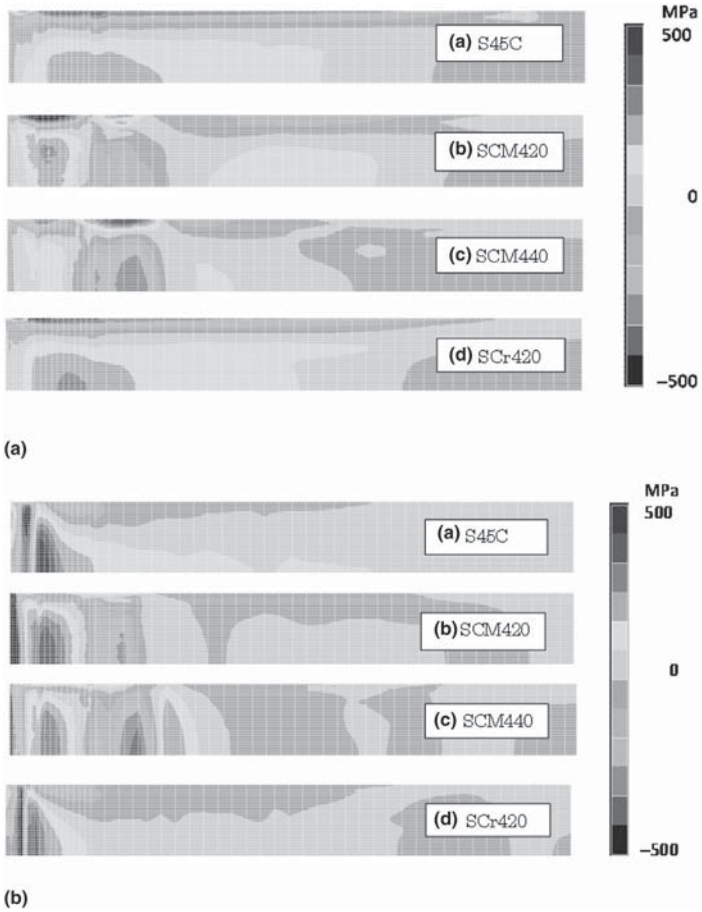

Figure 28 Residual stress in the half section of Jominy bar. (a) Axial stress and (b) circumferential stress.

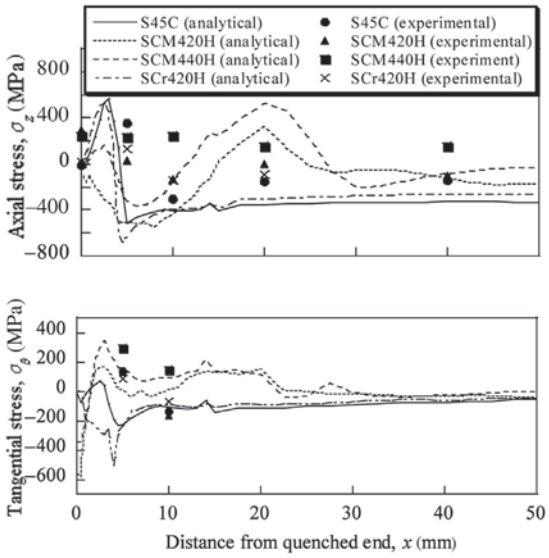

Figure 29 Simulated and experimental residual stress distributions.

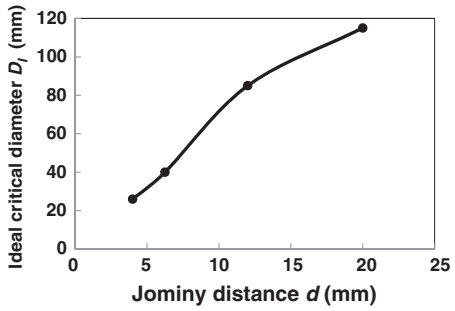

Figure 30 Relation between ideal critical diameter and thickness of the sword with 50% martensite transformed.

12.06.7.5 Discussion from the Viewpoint of Hardenability

The concept of hardenability (*64*) is introduced to discuss the simulated martensite distribution depending on the kind of steel in this section. The ideal critical diameter D_I of a solid bar representing the diameter with 50% martensite transformed at its center is represented as

$$D_I = D_{I\,\text{base}}(\text{carbon and grain size}) \cdot f_{\text{Mn}} \cdot f_{\text{Si}} \cdot f_{\text{Cr}} \cdot f_{\text{Mo}} \cdot f_{\text{V}} \cdot f_{\text{Cu}} \quad [80]$$

Here, $D_{I\text{base}}$ denotes the ideal base critical diameter depending on carbon content and grain size for plain carbon steel, and f_x is the multiplicative factor for the particular alloying element x, where 'ideal' quenching means the particular alloying element x, and that the surface temperature of an austenized steel is supposed to be cooled down to the temperature of a quenchant instantaneously. Since the data for both kinds of parameters $D_{I\text{base}}$ and f_x are identified by Jominy tests and represented by some chart, it is easy to evaluate the value D_I from the chemical composition of each steel. In the present case, the effect of grain size is neglected for simplicity.

Figure 30 depicts the Jominy distance at which 50% martensite is induced at the center with respect to the ideal critical diameter D_I. The critical diameter is for the round bar, and the sword is a rather flat plate. Nevertheless, one-to-one correspondence is seen between the parameters, as is shown in the figure.

12.06.8 Carburized Quenching

The ring-shaped model widely used in the fundamental heat treatment study is employed throughout the project. Calculation of diffused carbon by carrier gas is executed, followed by the process of oil-quenching from 850 °C to estimate the distortion, residual stress, and strain as well as structure distribution (*67*). The calculated results under the different conditions of intensity of the effect of transformation plasticity are compared with the experimental data (*66,67*).

Discussions are also presented on the simulated results of normal quenching without carburizing under the same condition of quenching to examine the influence of transformation plasticity.

12.06.8.1 Experimental Method

Material and specimen. A Cr–Mo steel (JIS-SCM420), being popular for carburized quenching with chemical compositions as listed in Table 10, was employed. The ting-shaped specimen shown in Figure 31, widely used as a simplified model for gears or bearing races, was processed for the experiments. The dimension of the specimen is 75 and 25 mm in outer and inner diameter, respectively, with a height of 10 mm.

Carburizing and diffusion were performed in the atmosphere of controlled butane gas keeping the carbon potential C_p as 1.2% for 4 h and 0.85% for 1 h at 930 °C, respectively, followed by an intermediate period for 1 h and a steady temperature stage of 850 °C for 30 min with $C_p = 0.85\%$ (see Figure 32). Consequently, quenching was carried out with use of a hot oil quenchant of 130 °C and the specimen was kept in an oil bath for 10 min. The flat surface of the specimen was held horizontally during both carburizing and quenching.

Normal quenching is also conducted under the same cooling condition as that of carburized quenching, controlling the gas atmosphere so as not to bring about decarburizing in the heating and holding periods. An electron probe micro analyzer (EPMA) was employed to measure the profile of carbon content from the top surface to the inside after carburized quenching.

Modes of a distorted profile of specimens for both cases of carburized and normal quenching were measured by the 3-D shape inspection instrument. Dimensional changes of specimens before and after the treatments will be represented as axial and radial displacements in the following figures. The X-ray diffraction method was employed to measure the residual stresses on the surface of the specimen, and retained austenite was identified by an X-ray analyzer equipped in the same system.

12.06.8.2 Simulation Method

Finite element calculation for temperature, stress/strain, distortion, and structural evolution in the course of quenching was implemented by the heat treatment simulation code HEARTS based on coupled metallo-thermo-mechanical governing equations, also including carburizing analysis in advance. The program is so designed that users can introduce the effects of transformation plasticity, which affects the stress/strain field in addition to the transformation stress (see Figure 33).

12.06.8.2.1 Finite Element Model

Axisymmetric finite element analysis is implemented with use of quadratic elements in the entire cross-sectional area. Here, no symmetry assumption is placed for the middle plane since the heat transfer coefficient on the upper and lower surfaces takes a different value. The number of nodes and elements in the cross section is, respectively, 3723 and 3600. Bearing in mind that the

Table 10 Chemical composition of SCM420 (wt%)

C	*Si*	*Mn*	*P*	*S*	*Cr*	*Mo*
0.20	0.21	0.80	0.009	0.016	1.06	0.15

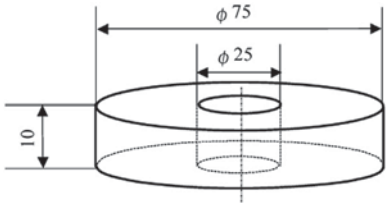

Figure 31 Ring-shaped specimen.

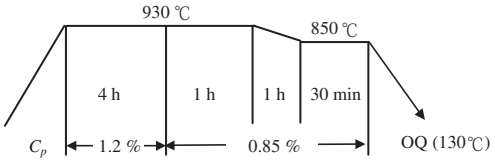

Figure 32 Heat pattern.

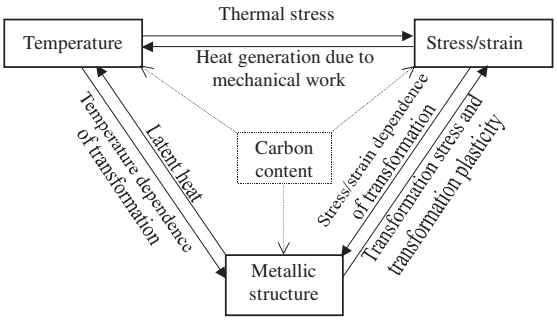

Figure 33 Metallo-thermo-coupling with carbon content.

diffused carbon is limited on the surface of the ring, a finite mesh pattern is prepared near the surface as partly illustrated in Figure 34.

12.06.8.2.2 Diffusion Analysis of Carbon

The diffusion equation

$$\frac{\partial C}{\partial t} = D\frac{\partial^2 C}{\partial x^2} \qquad [81]$$

for carbon content C was solved under such a boundary condition that the carbon intrusion rate h_c, related to the surface reaction coefficient, is given on all surfaces, i.e.,

$$q = D\frac{\partial C}{\partial x} = -h_c(C - C_p) \qquad [82]$$

where q and D are the carbon flux and the diffusion coefficient, respectively, and C_p represents the carbon potential of the atmosphere. An assumption is made here that the diffusion coefficient D is a linear function of carbon content.

12.06.8.2.3 Heat Conduction Analysis

In the heating process before carburizing, temperature in the entire domain of the ring is assumed to increase uniformly due to low heating rate to austenitizing temperature for uniform γ transformation. Coupled heat conduction analysis was carried out during quenching from 850 °C into quenchant oil of $T_q = 130$ °C for 10 min with the boundary condition

$$k\frac{\partial T}{\partial n} = -h_t(T - T_q) \qquad [83]$$

with thermal conductivity k and heat transfer coefficient h_t.

A different value of heat transfer coefficient shown in Figure 35 was employed on each surface according to the experimental data by Bodin and Segerberg (68). After 10 min elapsed, air cooling was executed until complete cooling with a steady heat transfer coefficient of 200 W m^{-2} K^{-1}.

As illustrated in Figure 33, diffused carbon content affects the material property. To accumulate the data of mechanical and physical properties, special types of Cr–Mo steel containing 0.4 and 0.6% carbon, with the same value as other elements, as well as original steel with 0.2% C were propounded to obtain data of the stress–strain curve, the temperature–elongation curve, and the TTT-diagram. Other data which are indispensable for calculation were quoted from experimental data (69) investigated by Inoue et al.

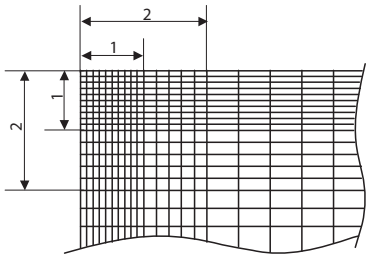

Figure 34 Mesh division near edge.

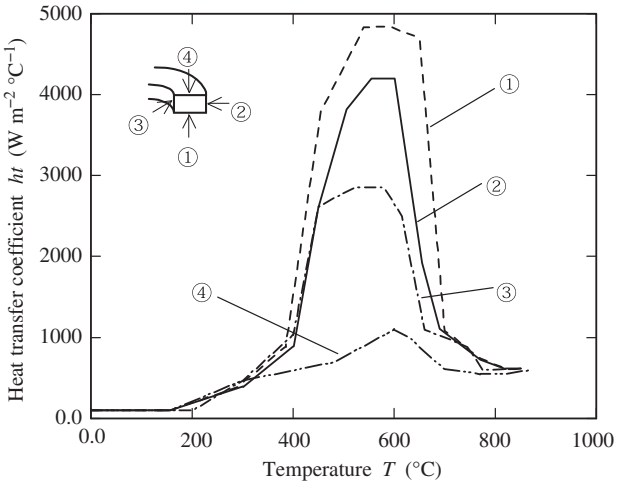

Figure 35 Hear transfer coefficient depending on temperature and location.

12.06.8.2.4 Transformation Plasticity

When transformation from austenite to martensite or pearlite occurs under relatively small stress, irreversible strain called transformation plastic strain is introduced (*47–51*). Such plasticity due to martensitic transformation being essential in this case of Cr–Mo steel is characterized by a crystallographic feature, bringing about the preference of the variant during transformation even under such a low stress as 30 MPa.

Here, the equation of transformation plasticity is employed based on the theory of Greenwood and Johnson (*47*). Namely, the transformation plastic strain rate is proportional to the martensitic transformation rate $\dot{\xi}$ and deviatoric stress s_{ij}

$$\dot{\varepsilon}_{ij}^{tp} = \frac{3}{2} Kh(\xi)\dot{\xi}s_{ij} \qquad [84]$$

$$h(\xi) = 2(1-\xi) \qquad [85]$$

In this study, the transformation coefficient K is assumed to be constant to be characterized by experiment data measured by Inoue et al. (*69*).

12.06.8.3 Results of Simulation and Experiment

12.06.8.3.1 Temperature, Carbon Content, and Phase Change

Figure 36 represents the calculated time-dependent distribution of diffused carbon content with the experimental data by means of EPMA from a flat surface to 2.5 mm in depth. Carbon seems to diffuse beneath the surface with carburizing time and the gradient

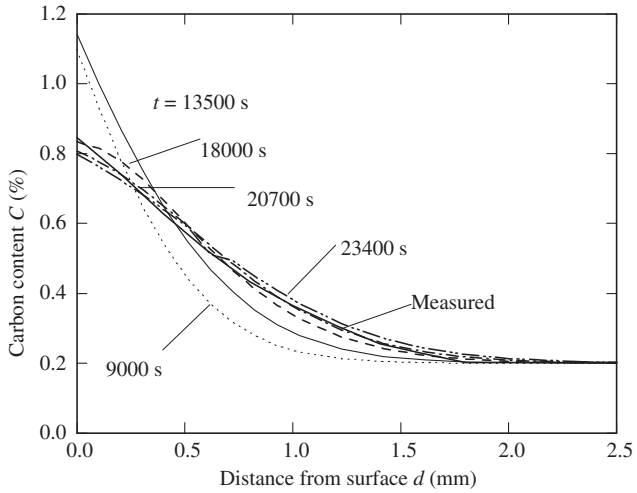

Figure 36 Simulated distribution of carbon content in the course of carburizing with measured data by EPMA.

becomes lower with diffusion time. Experimental data measured by EPMA after the process of 23 400 s shows good agreement with calculated results.

Calculated cooling curves, considering coupled effect of both stress/strain and structure, at three typical positions of the ring are shown in Figure 37. Difference in the heat transfer coefficient on the top and bottom surfaces as indicated in Figure 35, i.e., smaller coefficient on the top and larger on the bottom, give the temperature difference of approximately 30 °C higher before 20 s.

Rates of cooling on both surfaces abruptly change at about 650 and 450 °C, which are due to the starting points of nucleation boiling and convection stages, respectively. The effect of transformation plasticity on the cooling curve is so small as to be neglected.

The normal quenching process without carburizing is also simulated to distinguish from carburized quenching. Figure 38(a) and 38(b) indicate the time change in the distribution of the martensite fraction from the flat surface at the center of the ring at a completely cooled stage for carburized and normal quenching. Since martensite starting temperature M_s on the CCT-diagram decreases with higher carbon content, martensite initiates from inside of the ring in the case of carburized quenching, while an almost even distribution is seen in normal quenching.

Measured data of retained austenite by X-ray analyzer in this case is 20% on the surface, being 18% by simulation calculated by the data of martensite at $t = 2400$ s in Figure 38(a), since the volume fraction of bainite is revealed to be less than 0.1% in calculation, which also corresponds to the hardness data.

12.06.8.3.2 Distortion

The simulated radial displacement variation with respect to time on the outer and inner faces of carburized quenched ring in both conditions with and without consideration of transformation plasticity is depicted in Figure 39(a) and 39(b) for carburized and normal quenching, respectively.

Figure 39(a) shows that, in the case of carburized quenching, radial displacement both at the outer and inner faces, when considering the effect of transformation plasticity, is obviously moderate compared with that in the case without transformation

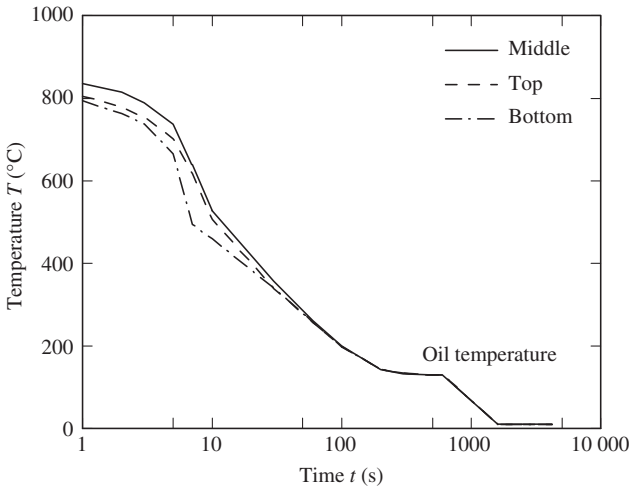

Figure 37 Simulated cooling curve.

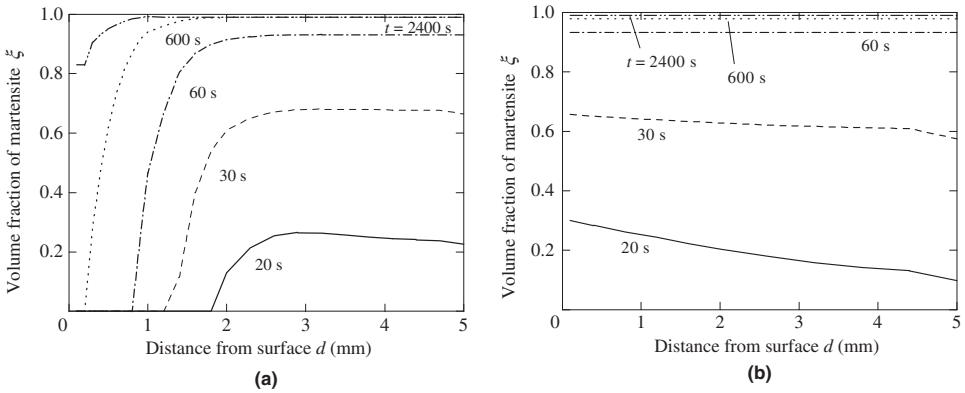

Figure 38 Simulated volume fraction of martensite. (a) Carburized quenching and (b) normal quenching.

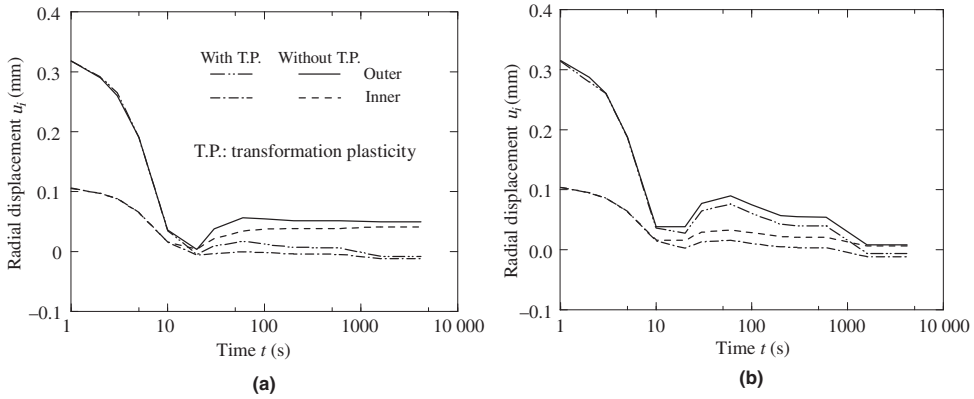

Figure 39 Distortion of middle plane. (a) Carburized quenching and (b) normal quenching.

plasticity. In the case of normal quenching, on the other hand, the effect on radial displacement is smaller, as shown in Figure 39(b).

Figure 40 illustrates the simulated distortion of the cross section of the ring at the final step of both conditions. Solid lines in Figure 40(a) and 40(b) represent the estimated pattern of distortion from initial shape shown in the thin dotted line when considering transformation plasticity. Experimental results of distortion are plotted by solid marks in the figure to compare with simulated patterns. Changes in the distortion with time from the beginning of quenching with and without the effect are shown in Figure 41.

The most remarkable difference between carburized quenching with and without the effects of transformation plasticity lies in the mode of distortion, as depicted in Figures 40 and 41. Transformation plasticity gives a convex shape on all surfaces, but concave without the effect. Experimental data agree well with simulated distortion with the effect in both cases of carburized and normal quenching.

12.06.8.3.3 Stress

Figure 42(a) and (b) show the simulated stress distribution at 30 and 2400 s with residual tangential stress after carburized and normal quenching by the solid marks corresponding well with the simulation. This denotes that simulated radial and tangential stresses in the case of carburizing quenching at 2400 s by considering transformation plasticity take approximately half the time of that without the effect.

12.06.8.4 Discussion on the Effect of Transformation Plasticity

As stated above, transformation plasticity is shown to play an important role in distortion, especially of a carburized quenched ring. Figure 39(a) demonstrates that two characteristic points are found in the displacement–time diagram for carburized quenching. One is at about 30 s when martensitic transformation starts inside of the ring (see Figure 38(a)). The other is at 2400 s when it finishes near the surface as shown in the figure. Compared with carburized quenching, two curves on normal quenching show little difference, giving a small discrepancy at around 30 s as is shown in Figure 39(b).

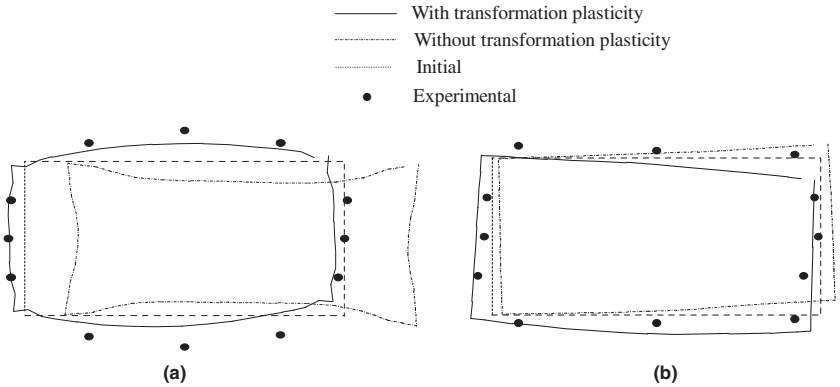

Figure 40 Simulated distortion after quenching with measured data – 100 times enlarged and central line on the left. (a) Carburized quenching and (b) normal quenching.

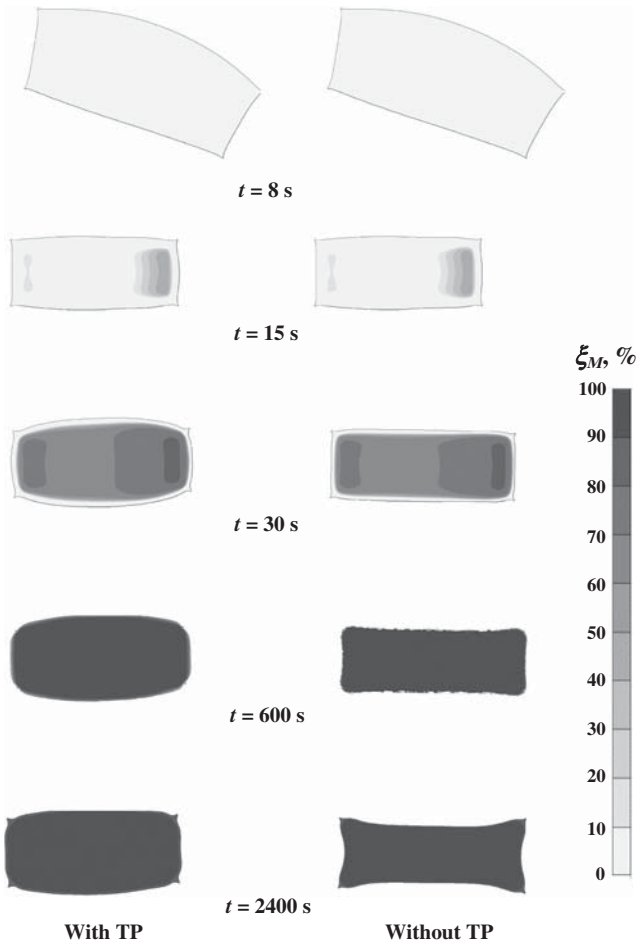

Figure 41 Comparison of distortion with and without considering the TP effect.

In order to know more detail about the effect of transformation plasticity on displacement and distortion, stresses at 30 and 2400 s for carburized and normal quenching are depicted in Figure 42(a) and 42(b), respectively. Transformation plastic strain and total strain in the tangential direction, which is closely connected with the radial displacement of the ring, are represented in Figure 43.

Martensite transformation of carburized quenching occurs rapidly from the inside of the ring to cause compressive radial and tangential stresses due to the dilatation by martensite formation, and to induce compressive transformation plastic strain in the radial direction and tensile in the axial direction, respectively. Stresses of opposite direction occur at the same time near the surface

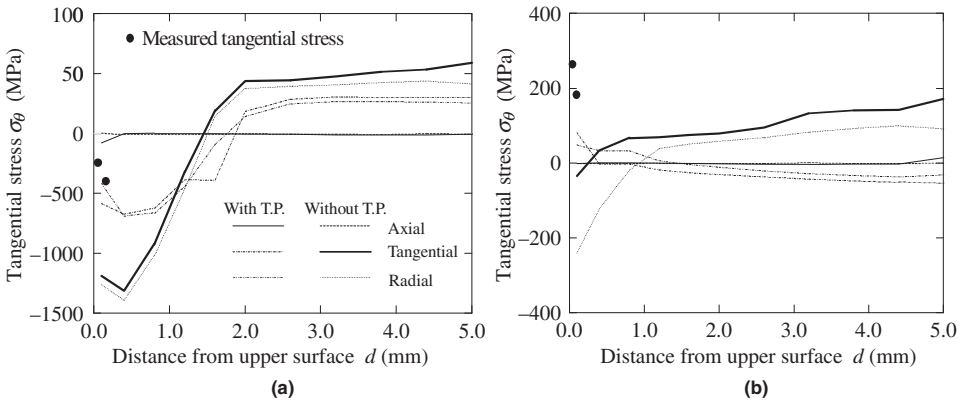

Figure 42 Variation of stress distribution at $r = 25$ mm. (a) Carburized quenching and (b) normal quenching.

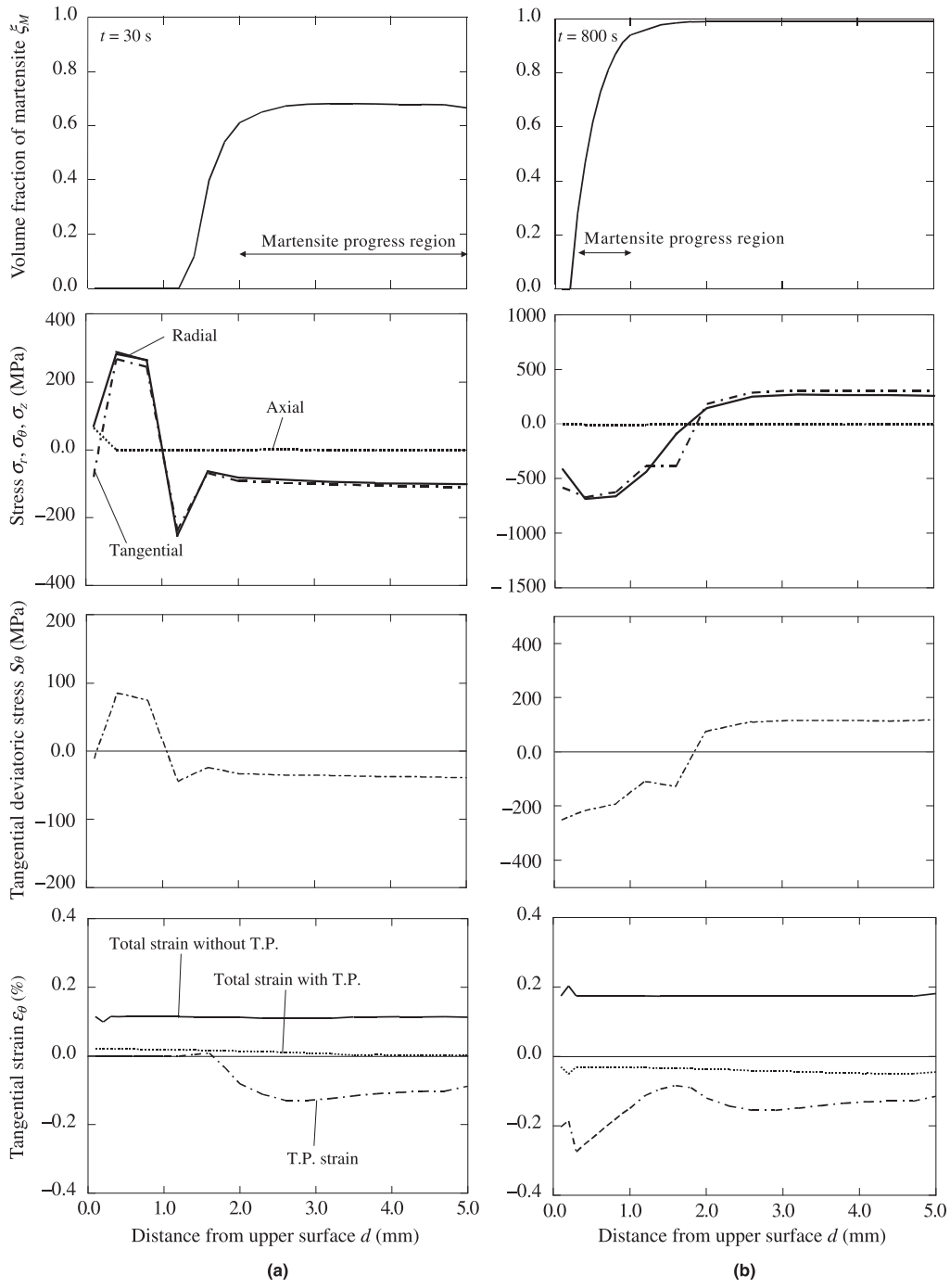

Figure 43 Distribution of simulated martensite fraction and stresses. (a) 30 s after quenching and (b) 800 s after quenching.

and inside the body, and no transformation plastic strain arises in the former region because of the delay of martensite transformation.

At 2400 s when martensitic transformation occurs, compressive strain is induced in both radial and tangential directions near the surface with higher carbon content compared with the inside. As a result, the transformation plastic strain in the same direction as at 30 s is induced. In the case of normal quenching, however, distribution of martensite starting at 30 s is almost flat, as shown in Figure 38(b). Consequently, transformation plastic strain with opposite sign simultaneously occurs near the surface and inside of the ring, as shown in Figure 44. This is the reason why only a little effect of transformation plasticity during normal quenching appears.

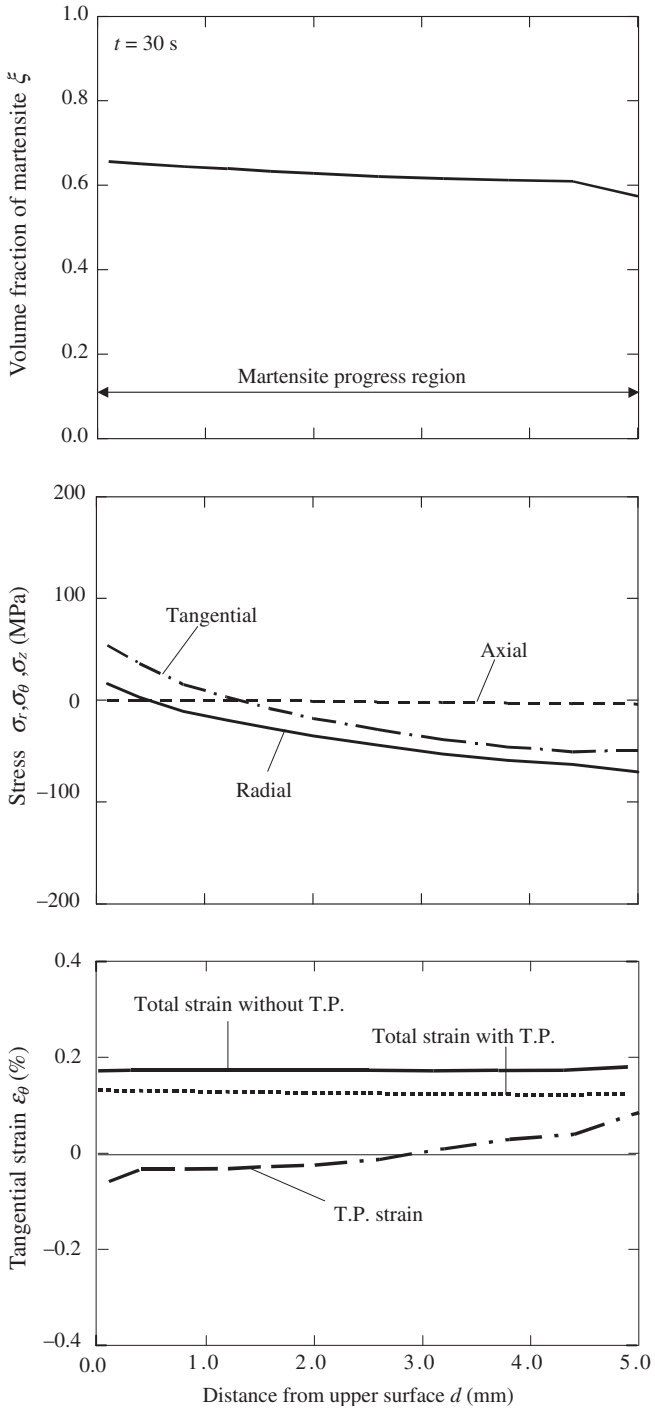

Figure 44 Formation of TP strain.

To examine the intensity of the transformation plasticity effect especially on the distortion, several hypothetical calculations with use of different coefficients K in eqn [76] are carried out as illustrated in Figure 44. The results indicate that cross-sectional shape is concave for the lower K than 3×10^{-5} MPa^{-1}, while convex for larger K value.

In summary, the reason why the transformation plasticity intensively affects only the carburized quenching process is from the induced stress in the course of transformation. Since the stress distribution mainly depends on carbon content, phase change, heat transfer coefficient, and shape of the workpiece, transformation plasticity is concluded to be indispensable for heat treatment simulation to obtain accurate information about distortion, even in the case of normal quenching.

12.06.9 Dual Frequency Induction Hardening

Mechanical components such as a gear wheel are usually required to hold necessary hardness and toughness by surface hardening processes such as induction hardening, carburizing, nitriding, and so on. In this section, an induction hardening process with dual frequency (70–72) is simulated to evaluate how such hardening is achieved with the consideration of the distortion.

The dual frequency induction hardening is conducted for a suitable appropriate preheating period by medium frequency (3–10 kHz) and a rapid subsequent heating by high frequency (100–250 kHz) followed by spray quenching. This process makes it possible to achieve contour hardening, and the advantage of the process is to provide high hardness, high residual compressive stresses on the surface compared to small distortion with enough toughness in the core part.

In the case of the induction hardening process, however, it is necessary to analyze the magnetic field to evaluate heat generation in the workpiece due to eddy current in combination with coupled analysis on mechanical fields and structural change. This is due to the fact that Jouel heat resulting from eddy current by induction heating is affected by not only the coil current but also the temperature-dependent permeability and the conductivity of the workpiece.

Since the numerical calculation of fully coupled magnetic analysis with metallo-thermo-mechanical fields is too complicated, magnetic field analysis is conducted coupled with temperature in the first approximation to consider temperature dependency on magnetic properties, and the calculated temperature distribution is taken into account to the coupled simulation of metallurgical structure and stress/distortion (see **Figure 45**).

Magnetic field simulation is conducted for relatively long time steps except for the region of Curie temperature (770 °C) where smaller time steps are applied since the magnetic properties change drastically around the temperature range. Metallo-thermo-mechanical calculation is performed with use of smaller time steps compared to magnetic field calculation.

A spur gear wheel is focused in the present chapter, where the 3-D simulation of the dual frequency induction hardening process is made using the above mentioned pseudocoupled approximation. The conventional quenching process heated by a single frequency is also simulated for comparison. Temperature variations, hardened pattern and residual stresses/distortion are compared with the experimental data.

12.06.9.1 The Procedure for Electromagnetic and Metallo-Thermo-Mechanical Coupling Analyses

The technique of combining two kinds of coupling analyses, metallo-thermo-mechanical and electromagnetic ones, to evaluate heat generation during heating and to introduce the result into the calculation of metallo-thermo-mechanical fields is given in the following (see **Figure 46**).

The heat generation increment in the workpiece is simulated by electromagnetic field analysis by the code MAGNA for each step, and the permeability and conductivity in the finite elements are modified for several steps according to the calculated temperature. The result is transferred into the coupled analysis of metallurgical change due to phase transformation, and also stress/strain by use of the code HEARTS. The procedure is iterated from the initial state of the workpiece at room temperature to the end of induction heating followed by the quenching process in terms of simple metallo-thermo-mechanical analysis.

The magnetic permeability generally depends on the magnetic field as well as temperature. We assume, however, in the first approximation of practical calculation, that permeability is constant in the workpiece during heating since the magnetic field is almost steady, but that the magnetic permeability and conductivity are functions of temperature.

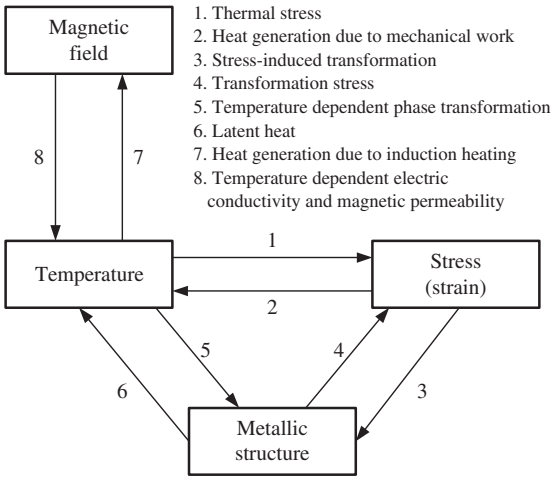

Figure 45 Coupling between metallic structure, stress (strain), and temperature, also coupled with magnetic field.

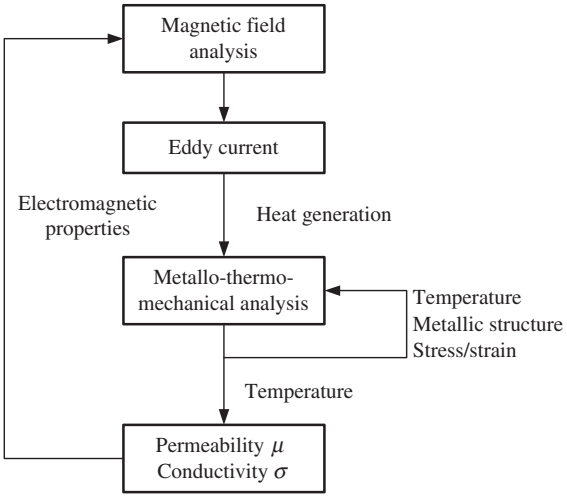

Figure 46 Flowchart of the numerical calculation.

12.06.9.2 Joule Heat Induced by Eddy Current

This section briefly treats the fundamental theory governing electromagnetic field since the theory of metallo-thermo-mechanics is already stated in Section 12.06.3.4. The series of Maxwell equations are summarized as follows:

$$\text{Ampere's law}: \nabla \times H = J + \frac{\partial D}{\partial t} \quad [86]$$

with intensity of magnetic field H, electric current density J, and electric displacement D, where $\nabla \times H$ represents the rotation of a vector H.

$$\text{Faraday's law}: \nabla \times E = -\frac{\partial B}{\partial t} \quad [87]$$

with intensity of electric field E and magnetic flux density B. Here, the conditions for B and D hold such that

$$\text{Gauss' law for magnetic field} \quad \nabla \cdot B = 0 \quad [88]$$

$$\text{Gauss' law for electric field} \quad \nabla \cdot D = \rho_e \quad [89]$$

with the density of electric charge ρ_e.

The constitutive relations are, on the other hand, expressed with use of material parameters of permittivity ε, permeability μ, and conductivity σ,

$$D = \varepsilon E \quad [90]$$

$$B = \mu H \quad [91]$$

$$J = \sigma E \quad [92]$$

The magnetic field B satisfying eqn [88] is generally expressed in the following form by use of a magnetic vector potential A.

$$B = \nabla \times A \quad [93]$$

The displacement current, $\partial D/\partial t$, on the right side of eqn [86], can be neglected in a solid material such as metals and alloys. Then, we have the equation for A in relation with the external current distribution J by substituting eqns [91] and [93] into

$$\text{Ampere's law}: \nabla \times \left(\frac{1}{\mu}\nabla \times A\right) = J \quad [94]$$

Once a solution for A is obtained by solving this eqn [94], it is possible to determine B, H, and E from eqns [87], [91], and [93].

Since the electric field E induced in the body is equivalent to the field E_e resulting the eddy current by electromagnetic induction, the density of the eddy current J_e is given as

$$J_e = \sigma E_e \quad [95]$$

The eddy current is normally limited on the surface of the body due to the skin effect, and the depth of the current penetration δ, in the case of a simple-shaped body such as a cylinder and a slab, gives (75)

$$\delta = \sqrt{\frac{1}{\pi \mu f \cdot \sigma}} \qquad [96]$$

where f is the frequency of the current. Joule heat generated by eddy current is now expressed as

$$P = \frac{J_e^2}{\sigma} \qquad [97]$$

12.06.9.3 Simulation Models

The workpiece treated throughout the study is a spur gear of 0.45% carbon steel (JIS-S45C). The dimension is 126 mm in OD, 120 mm in PCD (or module 3), 66 mm in boss hole diameter, and 20 mm in tooth width with 40 teeth.

A one-turn coil with an inner diameter of 130 mm and a cross-sectional area of 22 by 35 mm^2 is equipped outside of the gear wheel. Figure 47(a) shows finite element division of a gear and coil. The part of the gear is zoomed in Figure 47(b).

Finite element calculation is made for one fourth of a tooth and the coil by introducing the symmetric boundary conditions in x–z and x'–z' planes and also the x–y plane as indicated in Figure 47. The numbers of elements and nodes are 378 and 574 for the gear, and those of the coil are 1382 and 1604, or totally 1760 elements and 2178 nodes.

The outer surface of the tooth cooled by water spray is regarded as the convection boundary and other surfaces as an adiabatic one. The heat transfer coefficient during cooling is assumed to be constant as 20 000 W m^{-2} K^{-1}, which is verified by the coincidence between the calculated and measured temperatures.

The electro-magnetic boundary condition of the x–z and x'–z' planes (including space between the workpiece and coil) for the bottom and tip of the tooth are assumed to be the symmetric boundary for magnetic field ($A_x = A_{x'} = A_z = 0$). The condition of the x–z plane for the upper and lower sides is assumed to be the antisymmetric boundary for magnetic field ($A_z = 0$), while the finite integral equation method is applied to the asymmetrical ($A_i = -A_i$).

12.06.9.4 Experimental Details

The heat pattern applied in the present dual frequency induction hardening is 293 kW with 3 kHz for 1.8 s in preheating and 339 kW with 150 kHz for 0.18 s in subsequent heating. The maximum temperature measured at the central part of the tooth bottom is 740 °C in preheating, and 858 °C in subsequent heating after soaking for 0.9 s. In the cooling process, the outer surface of the gear is quenched by water spray.

On the other hand, the heat pattern for the conventional one with a single frequency of 25 kHz for 2.8 s is 165 kW during heating. The maximum temperature measured at the same point is 970 °C. Cooling is carried out as in the case of dual frequency induction hardening. These heat patterns are shown in Figure 48(a) and 48(b), respectively.

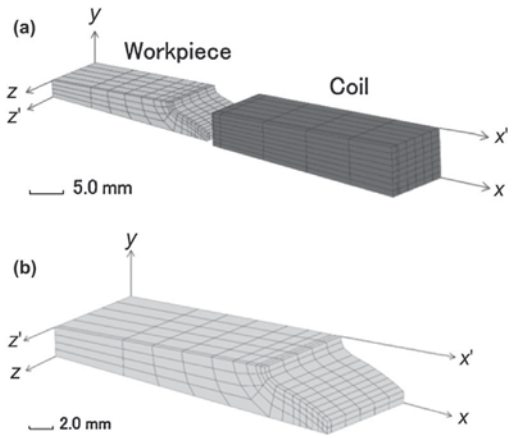

Figure 47 Finite element division of a quarter part of a gear tooth. (a) Workpiece and coil and (b) workpiece.

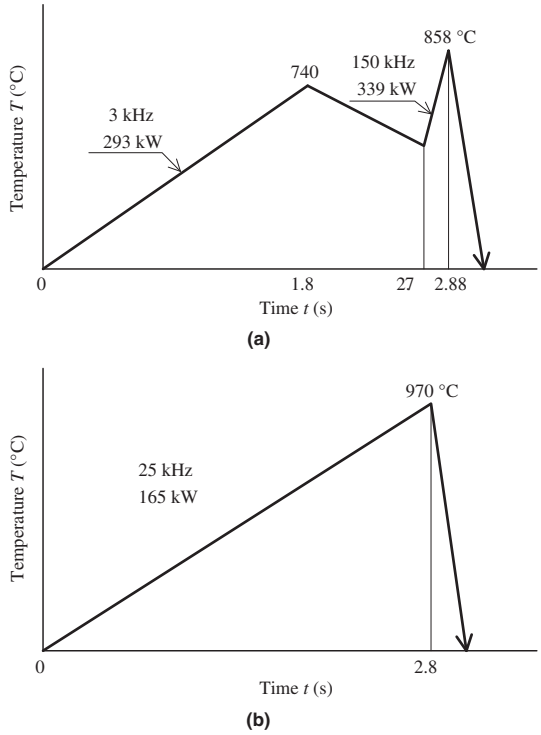

Figure 48 Heat patterns. (a) Dual frequency and (b) single frequency.

12.06.9.5 Simulated Results and Comparison with Experiments

The electric current in the coil as well as the frequency are altered in both heating stages while the output power of the high-frequency generator is automatically controlled to be constant in each stage. In the practical process of the present calculation, the current distribution in the coil is assumed to be steady during heating in each stage. The total power induced in the workpiece is as 96 kW for preheating and 176 kW for the subsequent stage in dual heating, while the power in the conventional case is 49.6 kW.

12.06.9.5.1 Temperature Variation

a. Dual Frequency Induction Hardening

The simulated and experimental temperature variations at three typical locations such as the tooth tip, PCD, and the bottom in dual frequency induction hardening are depicted in Figure 49. The simulated distribution of heat generation at the beginning of heating $t = 0.0$ s and the end of heating at $t = 1.8$ s in the preheating are shown in Figure 50(a) and 50(b), respectively. Figure 50(c) and 50(d) represent the ones at the beginning of heating $t = 2.7$ s and the end of heating $t = 2.88$ s in the subsequent heating.

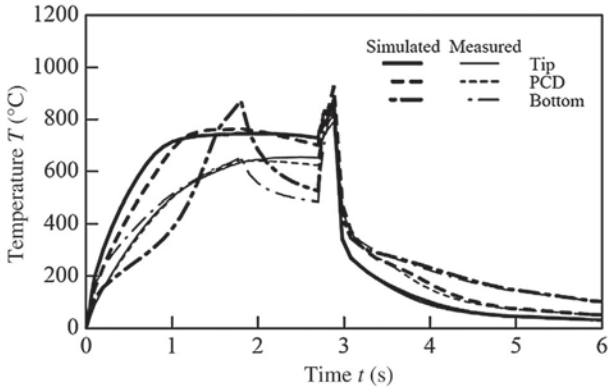

Figure 49 Simulated and measured temperature variations (dual frequency).

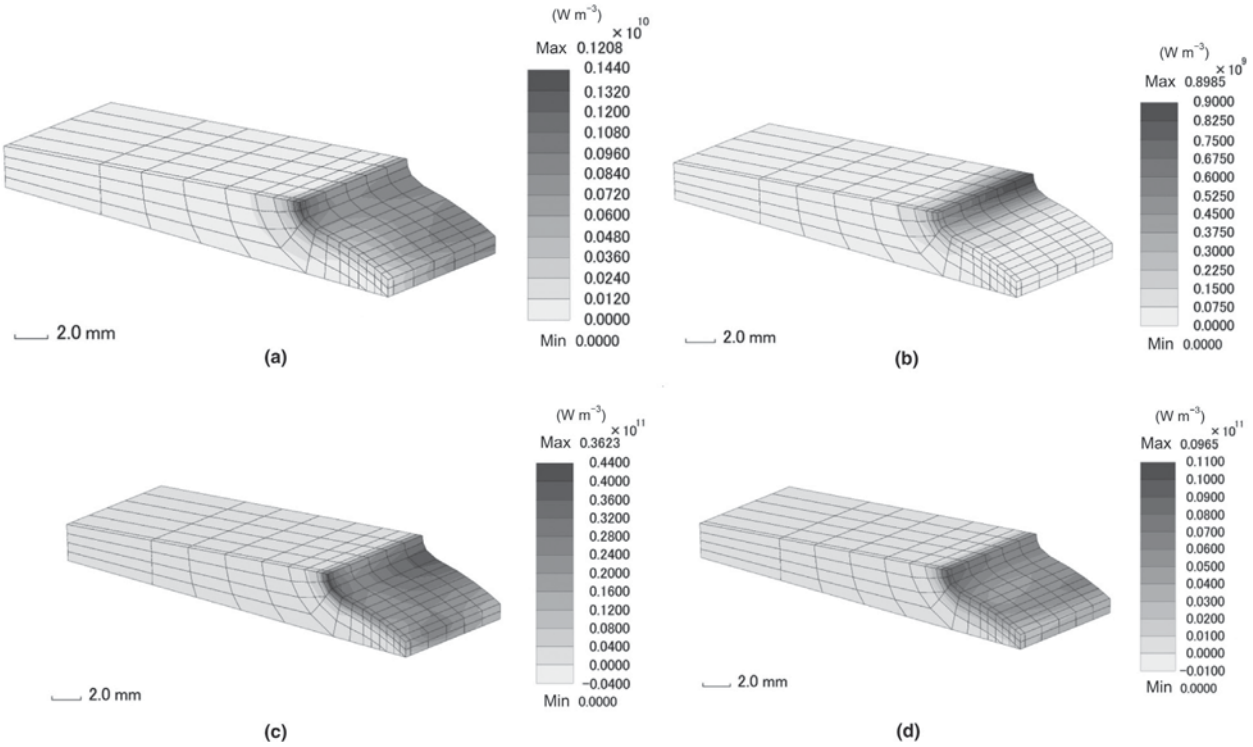

Figure 50 Generated heat distributions (dual frequency). (a) $t = 0.0$ s; (b) $t = 1.8$ s; (c) $t = 2.7$ s; and (d) $t = 2.88$ s.

The frequency used in preheating is relatively low at 3 kHz so that the heat is generated in a thick layer to current penetrated depth and is distributed uniformly. When the relative permeability at the tooth tip became unity after the temperature rises beyond the Curie point, heat generation in the gear by induction heating seems to distribute in a similar pattern as in a ring with the same radius of tooth bottom.

The simulated temperature variation at the tooth bottom is delayed, but the maximum temperature is higher compared to the measured one in preheating. In the subsequent heating stage, the temperature variations agree well with measured data except at the tooth bottom saturating to around 800 °C. One of the reasons for this disagreement may come from the rough mesh division in the depth direction.

b. Conventional Induction Hardening

Figure 51 represents the simulated and measured temperature variations in the case of conventional heating by a single frequency at the same three locations as dual frequency hardening.

The temperature at the tooth tip rises so fast in the beginning, while the PCD and bottom are heated with some time delay. Calculated temperature rise and the pattern show good coincidence with measured data until $t = 1.8$ s, and the mode of variation at

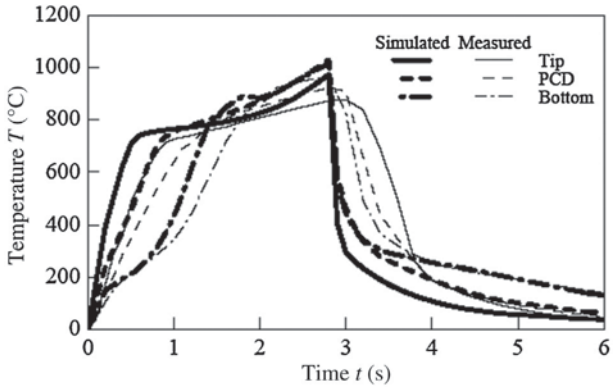

Figure 51 Simulated and measured temperature variations (single frequency).

the characteristic three points shows a similar tendency. The simulated distributions of heat generation at the beginning and the end of heating are illustrated in Figure 52(a) and 52(b), respectively, which indicate that the peak area of heat generation moves from the tooth tip to the bottom direction according to the appearance of a high-temperature area beyond the Curie point in tooth tip. These movements of the peak area of heat generation cause the phenomena of the temperature inversion of the tooth tip and bottom as is seen from Figure 51.

12.06.9.5.2 Metallic Structure

Simulated results of temperature distribution at the end of the preheating and the subsequent heating in dual frequency process are, respectively, illustrated in Figure 53(a) and 53(b). The volume fraction of martensite after quenching completed is also presented in Figure 54. Figures 55 and 56 are, on the other hand, the simulated temperature pattern and the martensite fraction in conventional induction hardening. The simulated distributions of the martensite fraction give a similar pattern as the measured value of Vickers hardness near three typical surfaces of the tip, PCD, and bottom in dual frequency induction hardening, as illustrated in Figures 57 and 58 respectively, while the data for the conventional method are in Figures 59 and 60. The reason why the high-temperature pattern at the end of heating and the distribution of martensite after quenching are almost similar in both heating methods may come from the fact that the region once transformed into austenite is changed into martensite due to the spray cooling with such a high heat transfer coefficient. Simulated hardened layers are a little deeper than the measured ones.

12.06.9.5.3 Residual Stresses

The residual stress distribution of the tangential component near the surface at the tooth root in dual frequency induction hardening is given in Figure 61(a), and that in the conventional case is in Figure 61(b). The residual stresses measured by

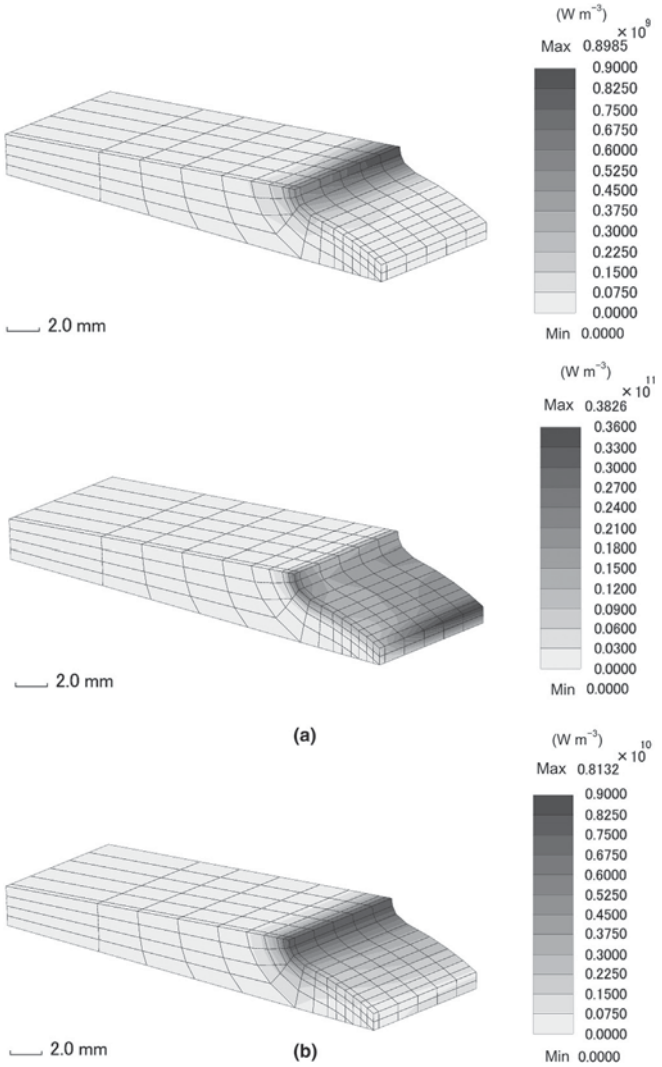

Figure 52 Generated heat distributions (single frequency) (W m^{-2}). (a) $t = 0.0$ s and (b) $t = 2.8$ s.

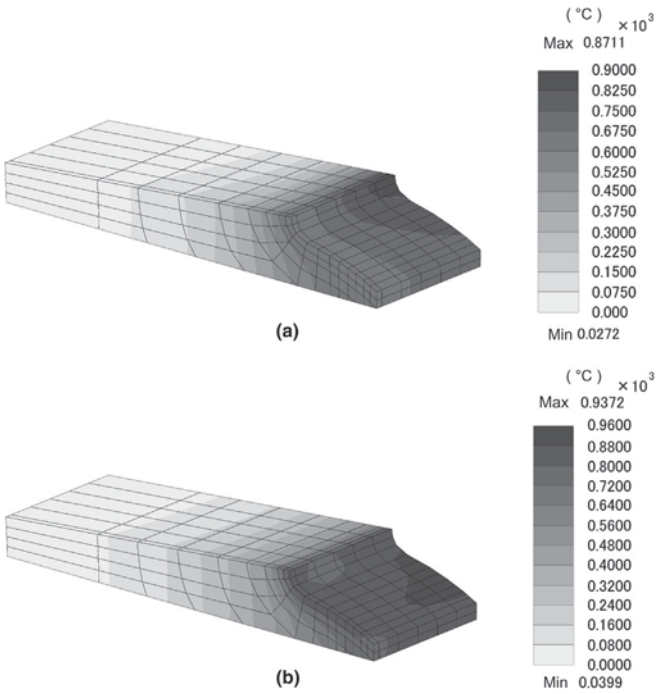

Figure 53 Temperature distributions (dual frequency) (°C). (a) $t = 1.8$ s and (b) $t = 2.88$ s.

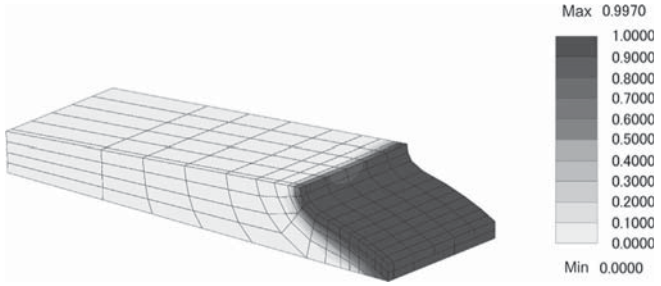

Figure 54 Volume fractions of martensite retained (dual frequency).

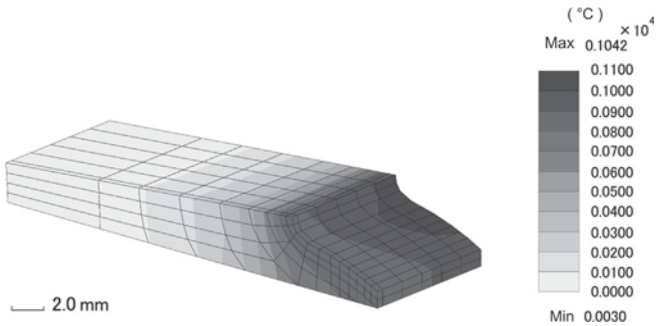

Figure 55 Temperature distribution at $t = 0$ (single frequency) (°C).

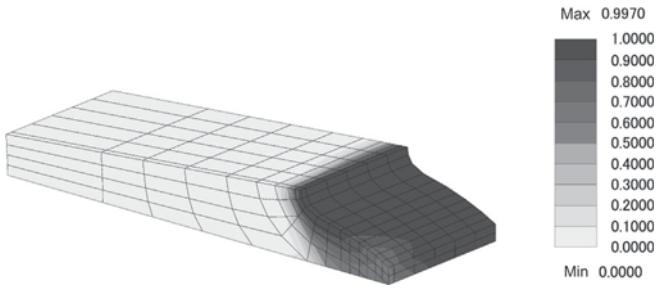

Figure 56 Volume fractions of martensite retained (single frequency).

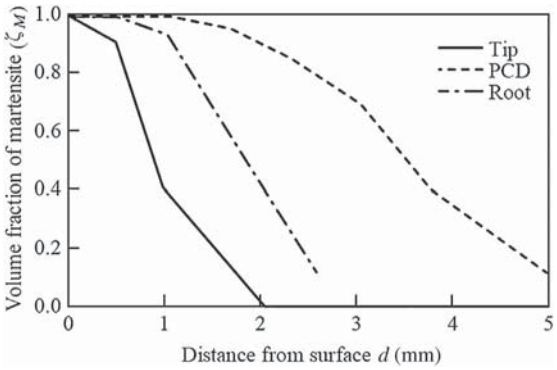

Figure 57 Simulated volume fraction of martensite (dual frequency).

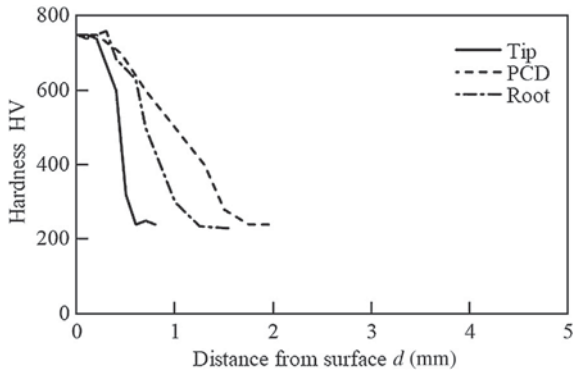

Figure 58 Measured hardness (dual frequency).

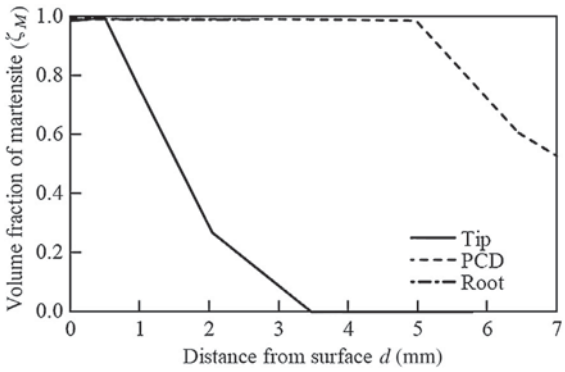

Figure 59 Simulated volume fraction of martensite (single frequency).

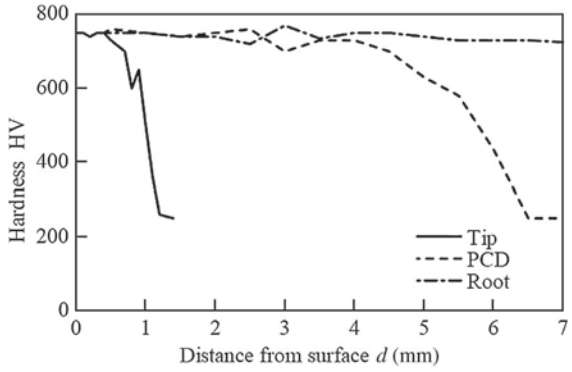

Figure 60 Measured hardness (single frequency).

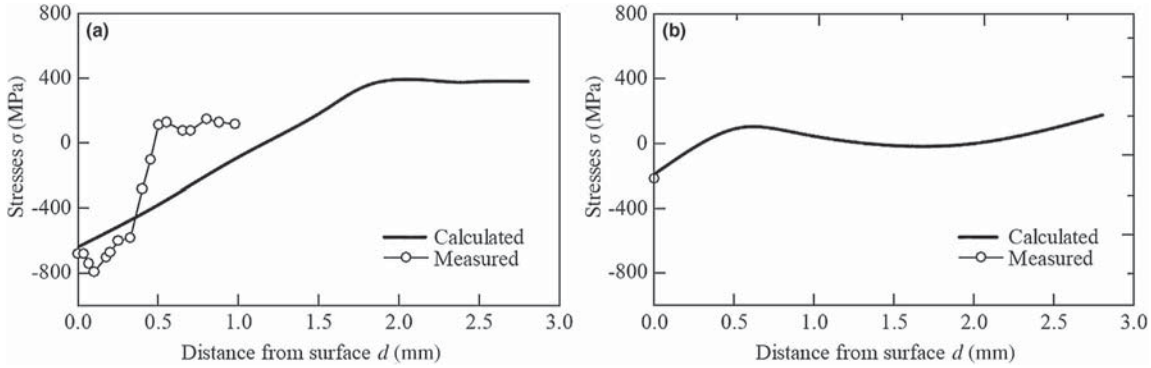

Figure 61 Comparison of simulated residual stress with experimental data. (a) Dual frequency and (b) single frequency.

the X-ray diffraction method are also depicted in both figures. As shown in these figures, the simulated residual stresses at the surface are coincident with the experimental ones, and the residual stress in dual frequency induction hardening is two or three times as much as the one in conventional induction hardening. This is the confidence of high fatigue strength achieved by dual frequency induction hardening due to such high compressive residual stresses.

12.06.9.5.4 Distortion

Figure 62(a) and 62(b) represent the comparison of simulated distortion for the induction hardening of dual frequency and the conventional one. The actual distortion of 5 μm is expressed by 2.0 mm in the geometry scale. When comparing the two cases, the distortion of conventional induction hardening in the tooth width direction is about two times as much as that of dual frequency induction hardening. The typical characteristic of dual frequency induction hardening that the distortion and the deformation are less due to the hardening-only contour zone is confirmed by these results.

12.06.9.6 Discussion on the Mechanism of Contour Hardening

The important factors needed to accomplish contour hardening by dual frequency induction hardening are closely connected to the selection of frequency and the temperature dependence of permeability. For the conventional case, the temperature difference between the tooth tip and the bottom is fairly large, as seen in Figure 51, since the heat generation is concentrated on the tooth tip area and the generated heat is stored in the part depending on the geometrical shape.

As a result, the tooth tip region is heated to the Curie temperature in the beginning, and the reduction in magnetic property occurs due to its temperature dependence. At the same time, there will be a redistribution of magnetic flux, and so the heat generation region moves toward the tooth bottom. Although the temperature difference between the surfaces of the tooth tip and the bottom will be reversed after a while, the heat in the part near the tooth tip will be transferred deeper than that of the tooth bottom. Consequently, the case depth of the tooth tip is deeper than that of the bottom.

On the other hand, in preheating of the dual frequency case, the heat generated region is enlarged from the tooth tip to the bottom with relatively low frequency, and those areas are heated almost uniformly to the Curie temperature as seen in Figure 55. By the subsequent high-frequency heating, the magnetic flux and the temperature are distributed uniformly from the tooth tip to the bottom, as in the case of the preheating by low frequency. This is the reason why the contour hardening is accomplished. There are

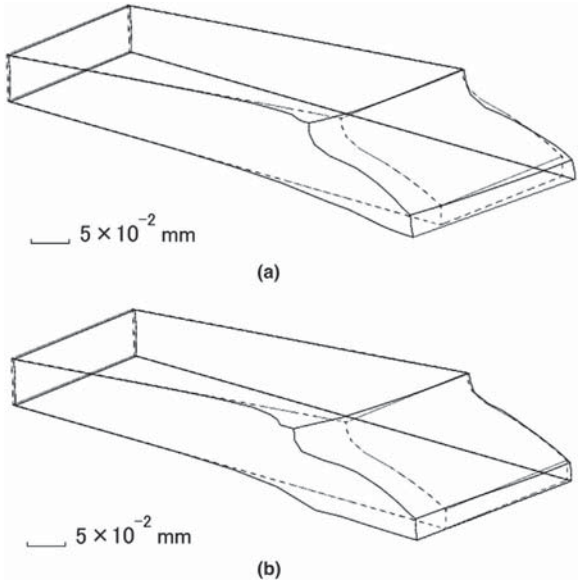

Figure 62 Distortion after hardening. (a) Dual frequency and (b) single frequency.

some areas in the tooth bottom at which temperature falls down during the soaking period. The temperature at the tooth bottom rises soon to the temperature of the tooth tip at the beginning of the subsequent heating with high frequency due to the temperature dependence of permeability.

12.06.10 Laser – Hardening

Pulsed YAG and CO_2 lasers have excellent properties of concentration of energy in the extremely small region, and so they are effectively applied to laser hardening, as one of the surface hardening technologies for metals and steels (*76–81*).

The characteristics of the laser hardening compared with normal quenching cooled by water or oil are summarized as follows:

1. The laser beam can be adequately irradiated to a focused spot, and irradiating energy input can easily be controlled depending on the user's requirement, which follows to generate very small residual stresses and strain after operation in a localized region.
2. Laser hardening is available on a small spot even inside a hole or ditch with complex shape.
3. Coolants such as water and oil are not necessarily used since the heated spot is naturally cooled by the chilled surrounding.

When comparing laser hardening cooled by heat conduction to surroundings with normal hardened body cooled from the surface by heat transfer from the surface, there are some differences in the martensite-generating mechanism and induced stress and distortion. Then, characteristics necessary to obtain the high-quality hardened zone are expected as follows:

1. Intensity of irradiated energy on the focused area of hardening should appropriately be controlled by the laser beam system.
2. The temperature of the spot should exceed the austenite transformation temperature, and the temperature difference between the irradiated zone and the parent metal must be necessary.
3. Carbon contained in the steel within the heated region is necessary to diffuse into the transformed homogeneous austenite.
4. Mass of the heat-treating body must be large enough to overcome the cooling by thermal diffusion to induce martensitic transformation.
5. The difference in generated stress and distortion between the parent metal and the irradiated zone is preferable to be as small as possible.

Difficulty arises in measuring the change in metallic structure, temperature, and distribution of transient and residual stress by the experiment due to the too small spot and the short operation time, and the development of the simulation method for such three coupled fields of temperature, metallic structure, and stress/strain as shown in Figure 2 is required to evaluate the proper operating condition.

The present authors have reported some results of simulation for spot hardening by a YAG laser and line-hardening by a CO_2 laser beam by use of CAE simulation code HEARTS (*81,82*). This section summarizes the results and compares the simulated results with experiments.

12.06.10.1 Experimental Conditions and the Results

12.06.10.1.1 Experimental Condition of YAG and CO_2 Laser Beam Irradiation

A cylinder of 12 mm diameter and 8 mm height of normal 0.48% carbon steel with 0.24% Si and 0.76% Mn is employed for pulsed YAG laser hardening. Use is made of an Nd-YAG laser system with an opticalwave length of 1.06 μm and irradiation energy of 3.3 J. And the operating condition are as follows: 75 mm lens focal distance and 12 ms irradiation time. A shot of the beam is irradiated to the center of the flat surface of the specimen. Here, the focal position is artificially shifted by 9 mm for mild heating without melting.

In the other case of traveling CO_2 laser hardening, the beam oscillating system is used with an optical wavelength of 10.6 μm and irradiation power of 1100 W by single oscillation mode. As shown in **Figure 63**, a block of 20 × 20 × 70 mm of 0.44% carbon steel with 0.20% Si and 0.71% Mn is prepared, on which a beam of 127 mm focal distance with a defocus distance of 50 mm is irradiated and travels for the central 30 mm part with a traverse rate of 30 mm s^{-1}.

12.06.10.1.2 Observed Pattern of Irradiated Zone and the Microstructure

The central cross section of the irradiated cylinder and block are polished and chemically etched by 3% nital for microscopic observation. Micrographs of the cross section of the irradiated material by pulsed YAG and CO_2 laser are, respectively, shown in **Figures 64** and **65**. The diameter and depth of the pulsed YAG laser irradiated zone are, respectively, evaluated as 0.65 and 0.28 mm from **Figure 64**, while the width and depth of the traveling CO_2 laser–irradiated zone are 6.5 and 1.2 mm from by **Figure 65**. These figures depict the microstructure of base carbon steel of the hypo-eutectoid steel for laser beam irradiation with pro-eutectoid ferrite and pearlite.

It can be confirmed that the pulsed YAG laser–irradiated zone is composed of the hardened zone of the pure martensite structure near the center of the optical axis and the intermediate zone with pro-eutectoid ferrite and pearlite mixed by martensite as seen in **Figure 64**. The martensite structure in the hardened zone presumes that the focused spot is heated up beyond the A_3 transformation temperature and changes into austenite completely. That part is followed by rapid cooling by thermal diffusion into the inner part of the cylinder and transformed into martensite structure. The intermediate zone between the hardened zone and the parent metal is found to be moderately heated up to the temperature lower than the A_3 point and cooled rapidly from imperfect austenite. In the case of pulsed YAG laser hardening, however, the boundary of the hardened zone, the intermediate zone, and the virgin structure appears clearly.

It is found that the hardened zone with perfect martensite near the surface is very narrow, while the intermediate zone composed of pro-eutectoid ferrite, pearlite, and martensite is so wide, as observed in **Figure 65**. In the intermediate zone, the ratio of pro-eutectoid ferrite and pearlite to martensite increases from the center to the virgin material. In case of CO_2 laser hardening, such variation is continuous, and the boundary of the hardened zone, the intermediate zone and the the virgin structure is not clearly detected.

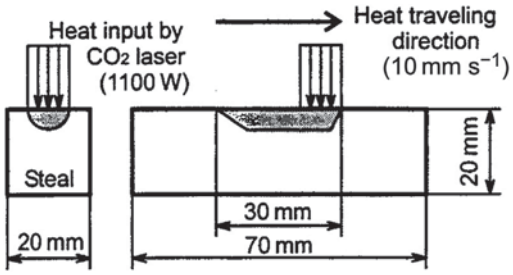

Figure 63 CO_2 laser beam irradiation condition.

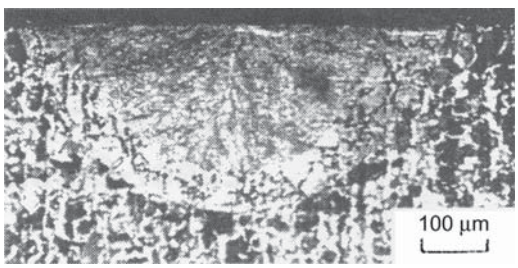

Figure 64 Micrograph of cross section of pulsed YAG laser–irradiated material.

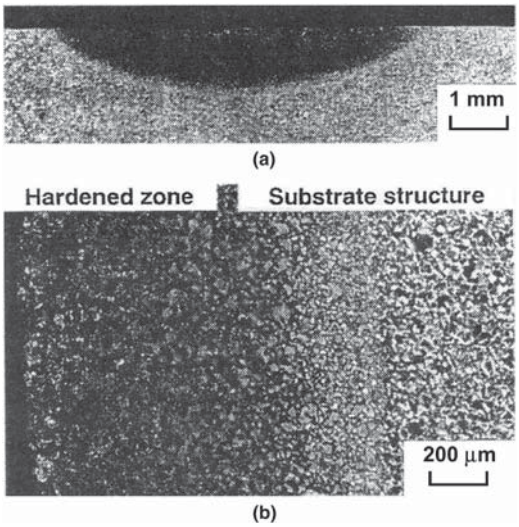

Figure 65 Micrograph of cross section of CO_2 laser–irradiated material. (a) Global view and (b) near the center.

12.06.10.2 Simulation Condition of Laser Hardening

In this chapter, the CAE code HEARTS developed by one of the authors using the finite element method is applied to the simulations of heat treatment processes of carbon steel, while the system has been used for analysis of normal and carburized quenching.

12.06.10.2.1 Pulsed YAG Laser Spot Hardening

A cylindrical simulation model is propounded with 2 mm in radius and 2 mm in depth, as shown in Figure 66. Here, the domain is large enough compared with laser-irradiated zone as seen from photograph in Figure 64. The irradiated and nonirradiated surfaces are regarded as heat flux boundary and heat transfer boundary to air, respectively, for heat conduction analysis, and the free displacement boundary condition is applied for stress analysis. Moreover, a simplified condition is applied on the internal boundary shown by a dashed line in Figure 66 with a constant temperature of $T = 293$ K and prescribed displacement.

Calculation is made as an axisymmetric problem using quadrangle ring elements with four nodes, and the total numbers of elements and nodes are, respectively, 729 and 676. Fine discretization is made near the laser-irradiated zone, while the element near the position where the model is simplified is divided roughly. The heat pattern of the process is such that the laser irradiation is operated for $t = 0$–12 ms followed by the cooling process for $t = 2$–1000 ms based on the experiment.

12.06.10.2.2 CO_2 Laser Line-Hardening

Since the hardened region is symmetric, as is seen from the photograph in Figure 65, only half of the model in Figure 67 is treated for analysis, where the length of the block is 70 mm, while the beam traveling distance is 30 mm, with 10 mm in width and 20 mm in height.

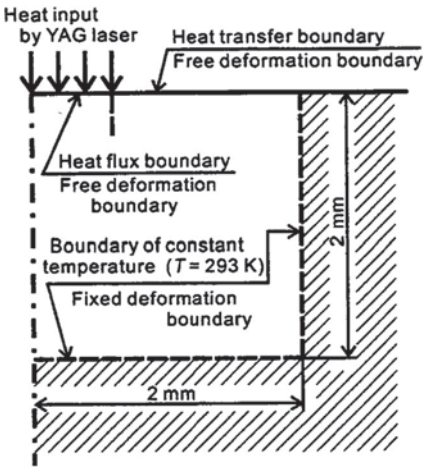

Figure 66 Simulation model of pulsed YAG laser hardening process for temperature and stress/strain.

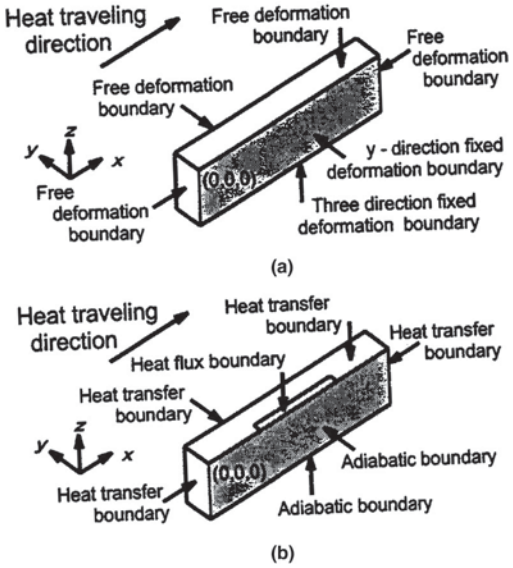

Figure 67 Simulation model of CO_2 laser hardening for temperature and stress/strain. (a) Mechanical boundary condition and (b) thermal boundary condition.

The imposed mechanical boundary condition is shown in Figure 67(a): the lower face is regarded as a fixed displacement boundary in three directions considering the small enough irradiation zone near the upper side. On the symmetry face, the *y*-direction is a fixed displacement boundary and the *x* and *z* directions are free displacement boundaries, while other planes are a free displacement boundary. A part of the upper face where laser irradiation is applied (see Figure 67(b)) is taken as the heat flux boundary, and the other upper part and surfaces are a heat transfer boundary, while adiabatic boundary condition is applied to the lower and symmetry faces.

Three-dimensional calculation is made with use of a hexahedral element with eight nodes, and the total number of nodes and elements is 2706 and 2080, respectively. Since the base structure of parent hypo-eutectoid steel is ferrite and pearlite, bainite and other structures are expected to be produced in the hardening processes. However, in this chapter, the produced structure from austenite by the carbon diffusion mechanism is called as pearlite.

12.06.10.3 Simulated Results and Discussions

12.06.10.3.1 Pulsed YAG Laser Spot Hardening

Simulated results of temperature, structure, and stress/strain distribution in the pulsed YAG laser hardening process on the cylinder are shown in Figures 68–71. Here, the display of deformation is enlarged by two times comparing with the size of region.

12.06.10.3.1.1 Temperature Distribution

Dark parts in Figure 68 represent the heated region over 1000 K being achieved intensively and rapidly until the end of irradiation. The temperature is almost 1000 K where pro-eutectoid ferrite and pearlite structure transforms into austenite as shown in Figure 69. The size of the surface with such high temperature is so small compared with the entire model, which follows that the pulsed YAG laser is able to heat very small part in the specimen for short time.

Until the time $t = 15$ ms being 3 ms after the end of laser irradiation, the heat intensively diffuses to the entire domain to become homogeneous. Since the heated part is very small compared with the size of the specimen, the effect of self-cooling can be actually confirmed. At $t = 1000$ ms when the simulation ceased, the temperature distribution in entire domain disappeared to initial homogeneous temperature of $T = 293$ K.

12.06.10.3.1.2 Structure Distribution

Before the time $t = 2$ ms, the pro-eutectoid ferrite and pearlite as the base structure of the material is heated up over A_3 transformation temperature by the laser irradiation as seen in Figure 69(a). Moreover, the intermediate structure between austenite and virgin structure is not observed to transform into complete austenite with nonuniform mixture of pro-eutectoid ferrite and pearlite. The volume fraction of the austenite increases on the irradiated surface near optical axis. The induced austenite transformed area gives a slight dilatation of the upper surface with progressive heating to be the maximum at $t = 12$ ms at the end of heating.

After $t = 12$ ms when the irradiation is terminated, the thermal dilatation decreases as shown in Figure 68, and self-cooling makes the austenite structure transform into martensite (see Figure 70): Martensitic transformation starts from the vicinity of specimen surface at $t = 15$ ms. When time is $t = 16$ ms, the martensite-rich region is expanded to the whole area of the intermediate structure on the contrary to the decrease in austenite. The progress of the martensitic transformation until $t = 20$ ms from the vicinity

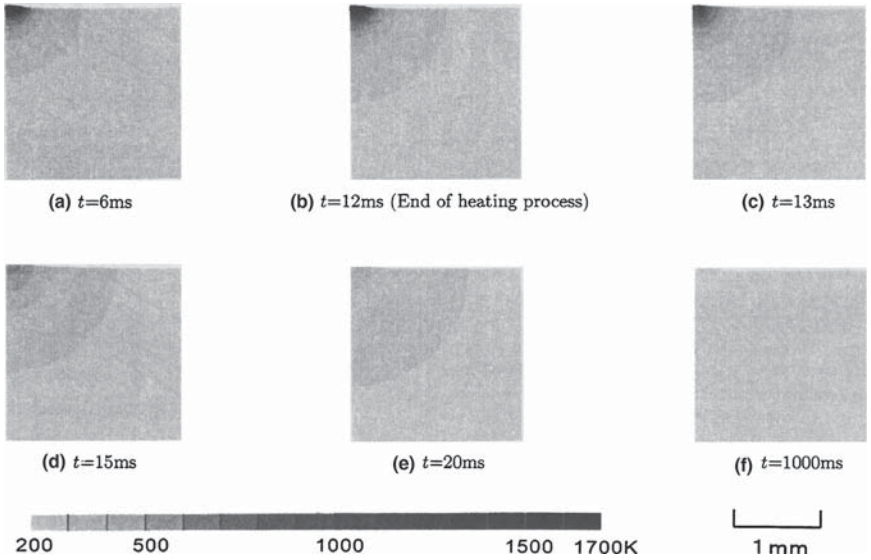

Figure 68 Temperature and deformation – pulsed YAG laser hardening process. (a) $t = 6$ ms; (b) $t = 12$ ms (end of heating process); (c) $t = 13$ ms; (d) $t = 15$ ms; (e) $t = 20$ ms; and (f) $t = 100$ ms.

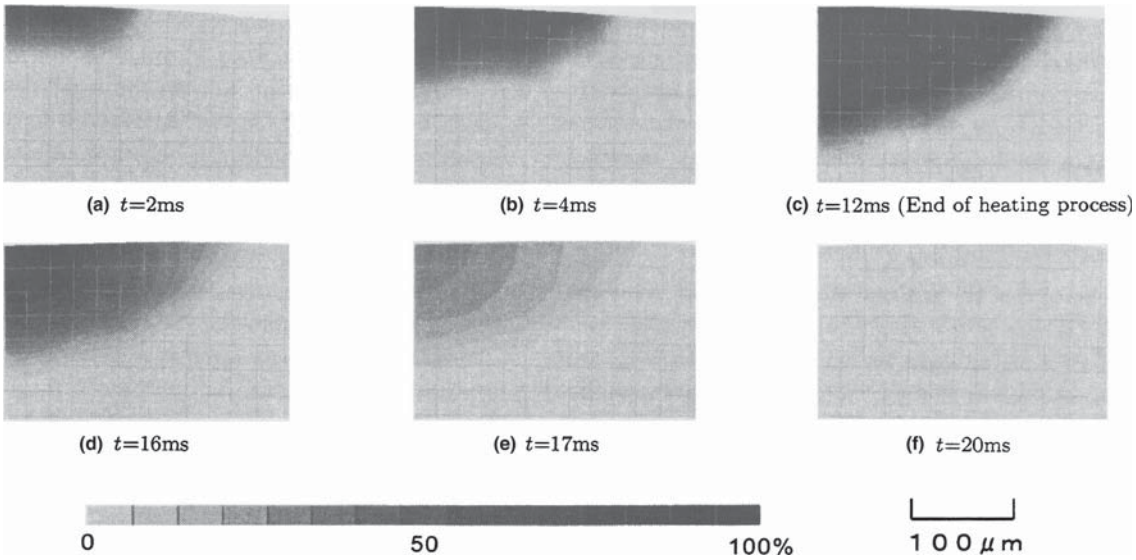

Figure 69 Austenite distribution – pulsed YAG laser hardening process. (a) $t = 2$ ms; (b) $t = 4$ ms; (c) $t = 12$ ms (end of heating process); (d) $t = 16$ ms; (e) $t = 17$ ms; and (f) $t = 20$ ms.

of the specimen surface is confirmed in the region with over 90% austenite at $t = 17$ ms. Above results proves that the cooling rate in the pulsed YAG laser hardening process of carbon steel is very high: Martensite starts to transform 3 ms after the termination of irradiation and finishes after 8 ms.

12.06.10.3.1.3 Induced and Residual Stresses

Figure 71 represents the variation of shear stress distribution. The generation of low shear stress is observed in the inner part near laser-irradiated surface even at $t = 1$ ms. This kind of shear stress increases in the material until $t = 6$ ms, and another high shear stress in the opposite direction is induced at the upper position near the surface at the end of irradiation. This kind of shear stress generation in the periphery of transformed region is partly due to the transformation as well as thermal dilatation.

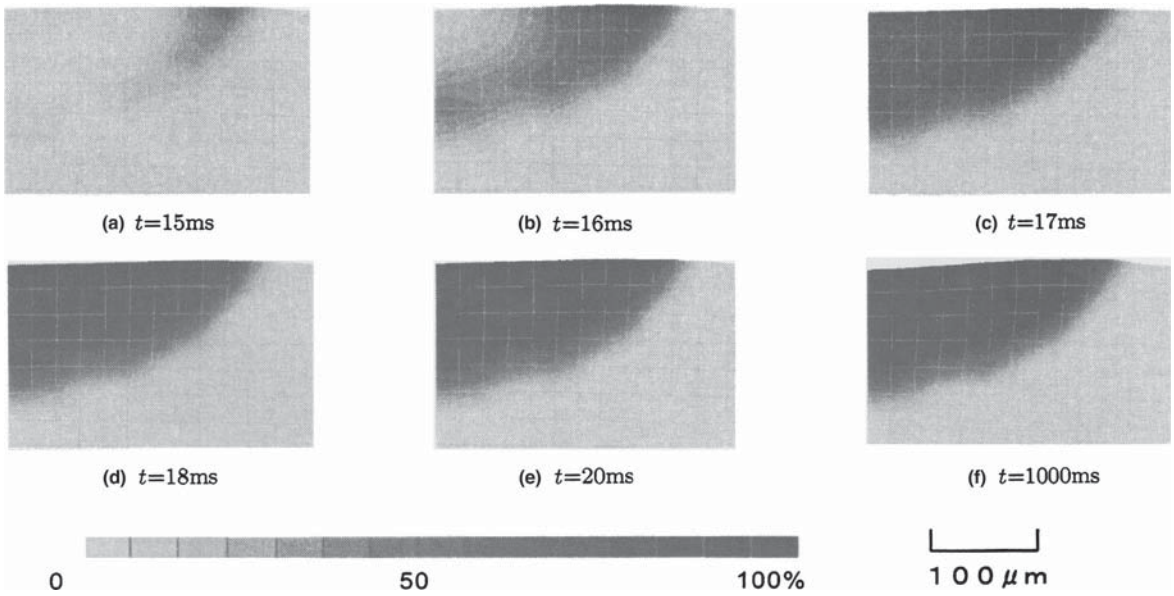

Figure 70 Martensite distribution – pulsed YAG laser hardening process. (a) $t = 15$ ms; (b) $t = 16$ ms; (c) $t = 17$ ms; (d) $t = 18$ ms; (e) $t = 20$ ms; and (f) $t = 1000$ ms.

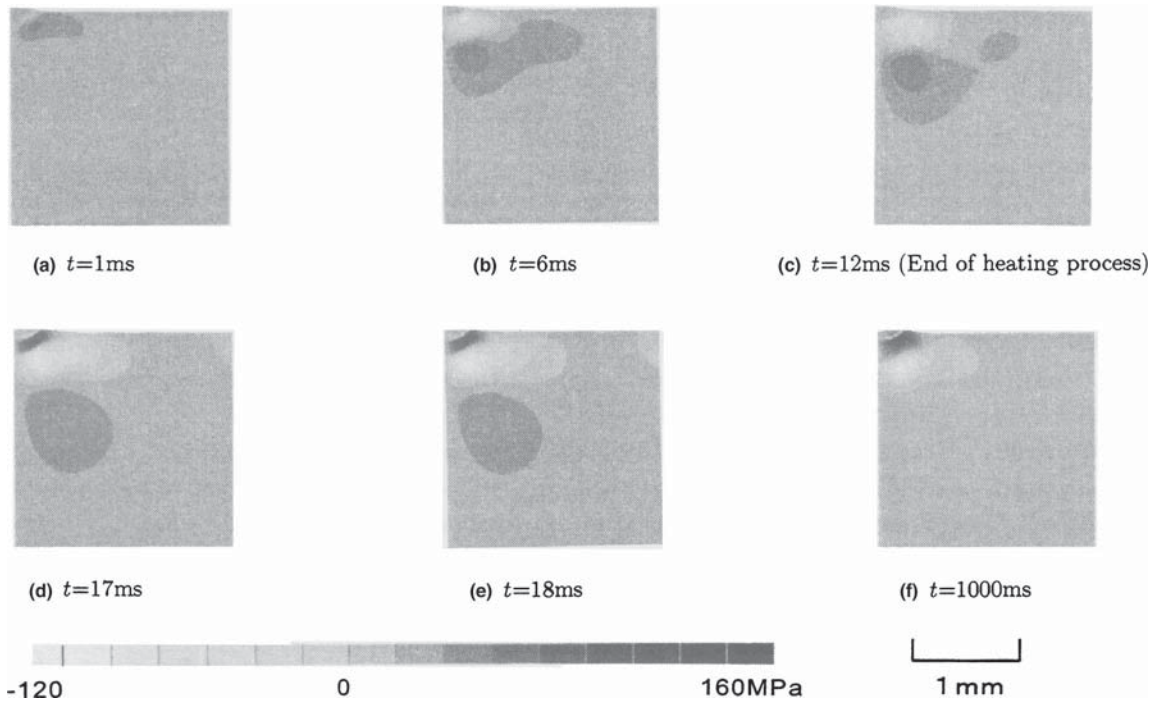

Figure 71 Shear stress and deformation – pulsed YAG laser hardening process. (a) $t = 1$ ms; (b) $t = 6$ ms; (c) $t = 12$ ms (end of heating process); (d) $t = 17$ ms; (e) $t = 18$ ms; and (f) $t = 1000$ ms.

At $t = 17$ ms when the martensite structure is generated as seen in Figure 71(d), the shear stress appears continuously at the upper part. The location for the third shear stress corresponds to the intermediate zone shown by Figures 69 and 70, and the residual stress at $t = 1000$ ms reaches 150 MPa. The intermediate zone of the virgin structure and martensite produces the highest value residual shear stress at the end of cooling process.

12.06.10.3.2 Traveling CO_2 Laser Hardening

Simulated results of the CO_2 laser hardening process in heat traveling condition are shown in Figures 72–76.

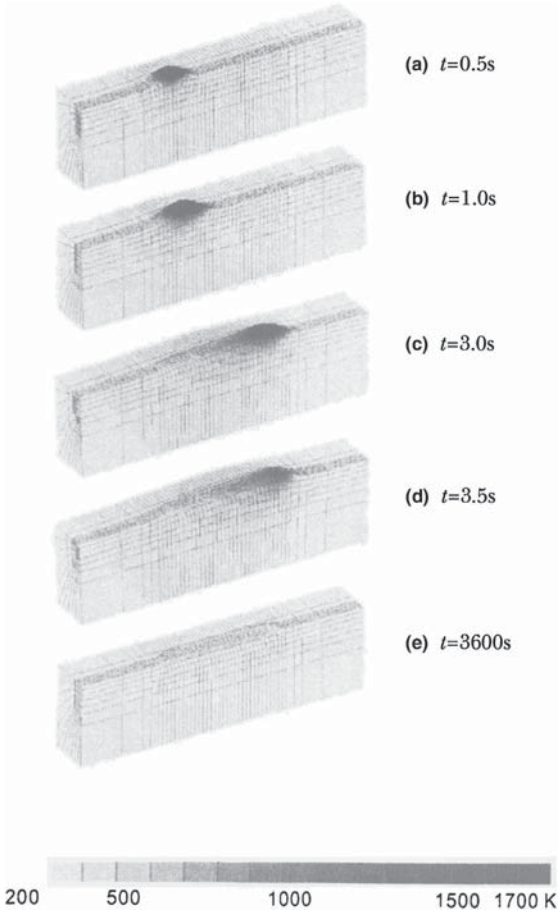

Figure 72 Temperature and deformation – CO_2 laser hardening process. (a) $t = 0.5$ s; (b) $t = 1$ s; (c) $t = 3$ s; (d) $t = 3.5$ s; and (e) $t = 3600$ s.

12.06.10.3.2.1 Temperature Distribution

Figure 72 depicts the variation of temperature distribution with the traveling laser irradiation. The deformation in this figure is enlarged five times compared with the region size. It is confirmed that the vicinity of the irradiated surface is heated intensively and rapidly. The irradiated small part is heated up over 1000 K, which is the transformation temperature from pro-eutectoid ferrite and pearlite to austenite, and expands much more than surrounding. This phenomenon appears at $t = 1.0$ s, and high temperature spot is moved with heat traveling from initial to final point of irradiation until $t = 3.0$ s. After laser passing the heated area is chilled by self-cooling, and the entire carbon block comes to room temperature of $T = 293$ K at $t = 3600$ s.

12.06.10.3.2.2 Structure Distribution

Variation of volume fraction of austenite and martensite is illustrated in Figures 73 and 74, and the maximum values are plotted in Figure 75. In this figure, each maximum value of austenite and martensite does not have the correlation, and change independently with the passage of operation time. The initial austenite generation is confirmed at $t = 0.7$ s from Figures 73 and 75(a). The volume fraction of austenite increases with time, and reaches $\xi_a = 100\%$ at $t = 1.0$ s until $t = 3.6$ s by the remaining heating and other factors. However, the austenite decreases rapidly after that, and $\xi_a = 0.8\%$ exists as a retained austenite at the simulation terminated time.

Martensite generation is observed from Figures 73 and 75(b) for the first time in the vicinity of irradiation starting point $x = 30$ mm at $t = 1.2$ s. The volume fraction increases with time, and the transformation progresses slightly after the end of laser irradiation, and volume fraction becomes $\xi_m = 98.2\%$ at $t = 3600$ s. This is due to the fact that enough time has passed after the end of irradiation, and therefore that the self-cooling is done by thermal diffusion.

12.06.10.3.2.3 Induced and Residual Stresses

Figure 76 represents that the highest compressive stress occurs in the vicinity of $x = 25$ mm at $t = 0.5$ s, and that it moves with heat traveling. This corresponds to the austenite development until irradiation finish time at $t = 3.0$ s shown in Figure 73. However, the compressive stress is seen to be released at $t = 3.5$ s after 0.5 s of irradiation end due to the increase in austenite. This comes from a thermal expansion of the material: The material is heated and dilated partially by laser, while the nonheated surrounding part remains as it is. Then, such highest compressive stress is induced by reaction of thermal expansion.

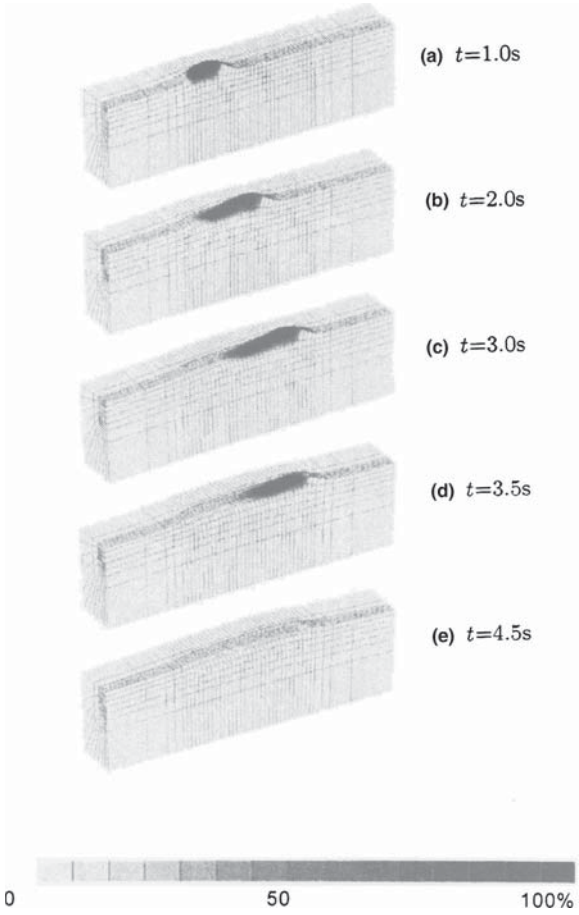

Figure 73 Austenite distribution – CO_2 laser hardening process. 12 ms at the end of heating. (a) $t = 1$ s; (b) $t = 2$ s; (c) $t = 3$ s; (d) $t = 3.5$ s; and (e) $t = 4.5$ s.

On the other hand, at $t = 1.0$ s, the maximum tensile stress generates in the vicinity of $x = 20$ mm, where compressive stress disappears. The region of such a part is expanded with the movement of the laser. When all the material is cooled down at $t = 3.5$ s, the maximum tensile stress appears within the range of $x = 20$–50 mm at the center of irradiated zone. Residual stress finally corresponds to martensitic hardened zone as shown in **Figure 74**.

In addition, another compressive stress generates in vicinity of $x = 20$ mm at $t = 3.0$ s. This zone enlarges so as to enclose the part with tensile stress in hardened zone until $t = 3600$ s. This stress becomes final residual stress near the virgin material in intermediate zone with little martensite.

Since the cooling in laser hardening is achieved by the self-cooling mechanism, the austenite structure of material is cooled and martensite is developed near the virgin structure. Afterward, the growth of the martensite advances toward the laser irradiation surface. In other words, the dilated austenite by laser is cooled and shrinks rapidly, at the primary stage of cooling process, and the tensile stress causes in the hardened zone. In the next stage, cooling ceased completely near the virgin structure and the martensitic transformation has terminated. However, cooling does not progressed near the surface, and the transformation does not finish completely. This is the reason why the residual tensile stress causes near the virgin structure due to the thermal and phase change stresses.

12.06.11 Japanese Sword

So many monographs on Japanese swords have been published in English (*83–85*) in addition to Japanese (*86–89*), from the viewpoint of typical traditional crafts of arts. The sword is also interesting from the aspect of modern science and technology since the way of making the sword is really consistent with science as with other surviving traditional products.

Most Japanese swords are made of characteristic and traditional Japanese steel, so-called *tamahagane*, but not of modern steel, produced by *tatara* system with use of iron sand. The author has so enjoyed devoting himself to accumulate information on the

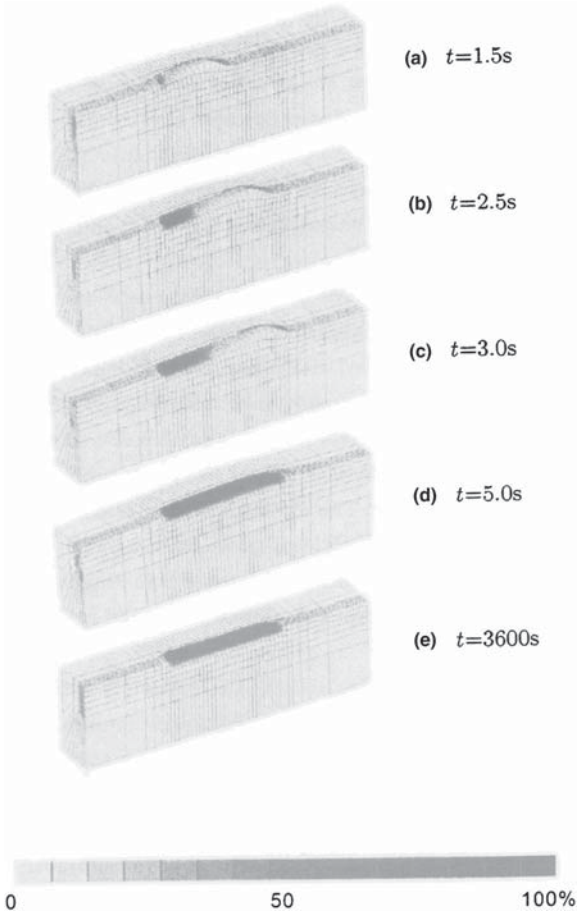

Figure 74 Martensite distribution – CO_2 laser hardening process. (a) $t = 1.5$ s; (b) $t = 2.5$ s; (c) $t = 3$ s; (d) $t = 5$ s; and (e) $t = 3600$ s.

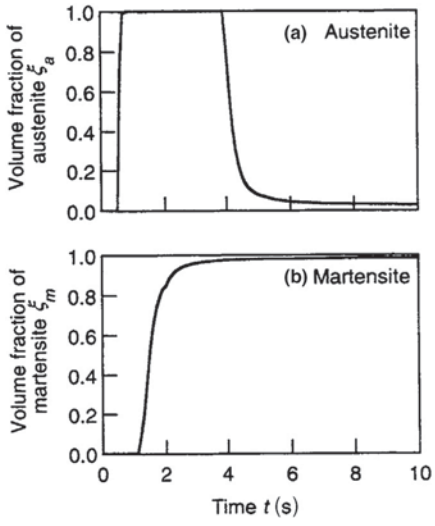

Figure 75 Variation of maximum volume fraction of austenite and martensite – CO_2 laser hardening process. (a) Austenite; and (b) martensite.

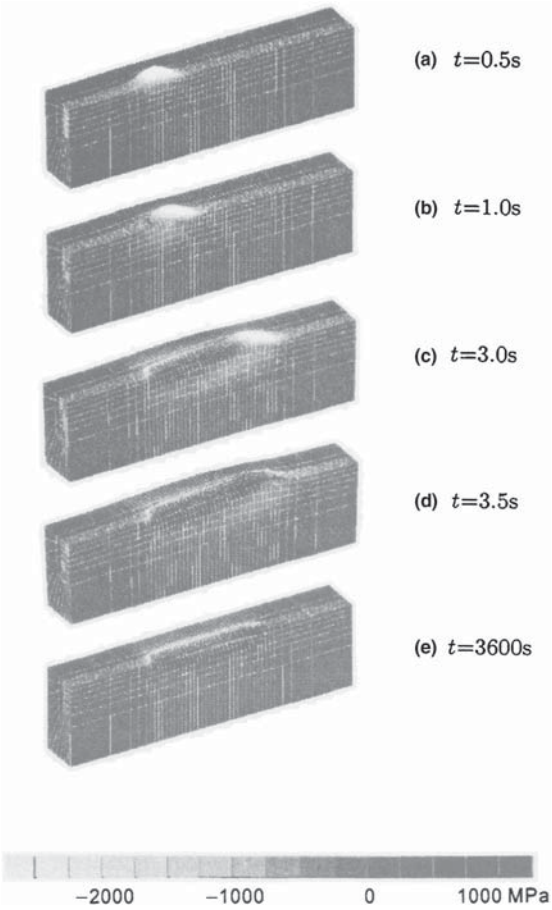

Figure 76 Stress σ_x and deformation – CO_2 laser hardening process. (a) $t = 0.5$ s; (b) $t = 1$ s; (c) $t = 3$ s; (d) $t = 3.5$ s; and (e) $t = 3600$ s.

science of the Japanese sword making and the *tatara* (*85,86*), and carried out some computer simulations during quenching of the sword (*90–99*).

In this section, a special emphasis is placed on the computer simulation of quenching, or hardening, applied in the final stage of the manufacturing the sword in the framework of continuum metallo-thermo-mechanics representing the modes of bending and the formation of blade simulated mainly by a developed computer code COSMAP.

12.06.11.1 Identification of Heat Transfer Characteristics Depending on Clay Pasting

Before quenching the Japanese sword into water, the *yakiba-tsuchi* clay is coated on the surface as shown in **Figure 77** to control the cooling condition of the surface of the steel. This kind of process to accelerate the cooling rate had been known by the sword smith

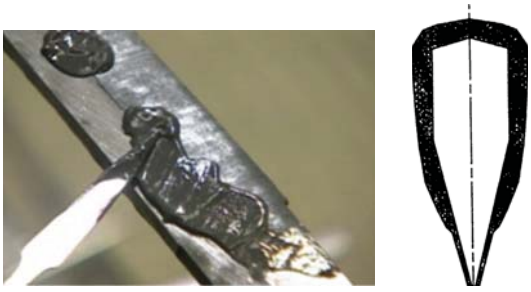

Figure 77 Clay pasting on the surface of the Japanese sword before quenching. (a) *Yakiba-tsuchi* on the sword and (b) clay thickness.

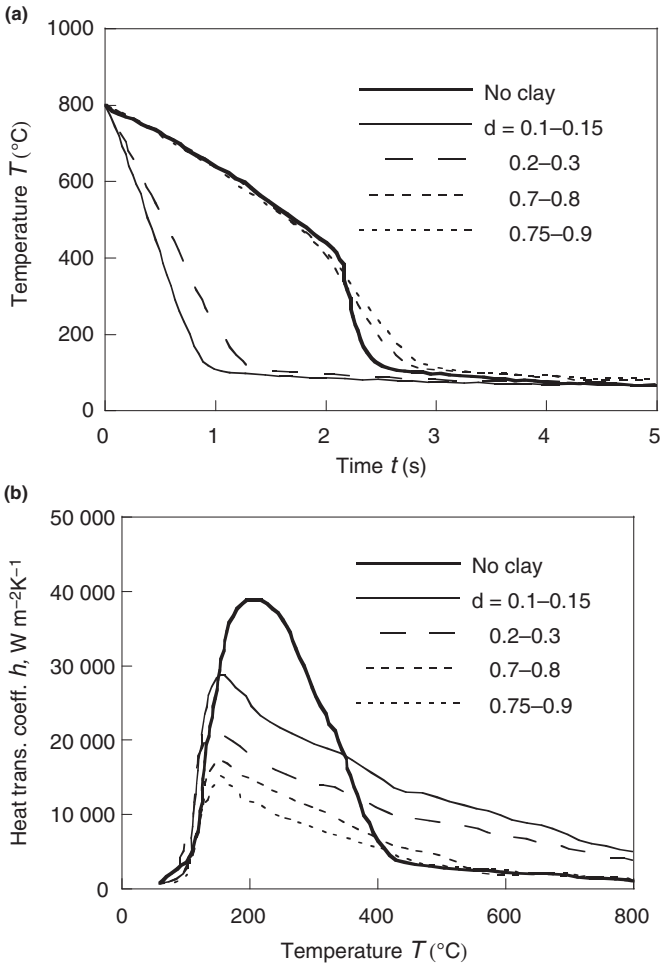

Figure 78 Cooling curves depending on coated clay thickness. (a) Cooling curves depending on the thickness of clay and (b) identified heat transfer coefficient.

since the method of manufacturing Japanese sword was established in the fifth or sixth century, and is also applied to harden the blade of knives and other cutting tools. As far as the author knows, this kind of technique is specially developed in Japan.

Since the temperature distribution is to be calculated in the body of the sword, it is necessary to identify the relative heat transfer coefficient on the metal surface as the function of the thickness of the clay. Series of experiments based on Japan Industrial Standard, JIS-K2242, were made to measure the cooling curve of a cylinder made of silver coated by the clay with different thickness. A thermocouple is mounted on the surface. The cylinder is heated up to 800 °C by a reflection-type electric furnace, and cooled in the water.

Obtained cooling curves are demonstrated in **Figure 78(a)** as the parameter of thickness of the pasted clay (*99*). It is so interesting that the curves for thick clay ($t = 0.7$–0.8 and 0.75–0.9 mm) show typical mode with moderate cooling rate due to film boiling followed by severe cooling stage by nuclear boiling, the shape of which are similar to the case without the clay. When the thickness is small ($t = 0.1$–0.15 and 0.2–0.3 mm), on the other hand, no film boiling stage is observed, which means that the cylinder is cooled severely from the beginning. This is also confirmed by the observation of bubble nucleation by video camera. Inverse calculation is carried out by perturbation method to identify the heat transfer coefficient on the surface of the cylinder. It is a paradox to note from **Figure 78(b)** that the coefficient in the case with thin clay gives higher value than the one without clay during 800–400 °C being most important temperature range for quenching. The mechanism of such paradox is discussed by Kikuchi (*101*). This data will be employed as the boundary condition when solving the coupled heat conduction equation.

12.06.11.2 Simulated Results of the Quenching Process

Simulation of a sword during the quenching process mainly by the code is carried out by the developed code COSMAP. The data of the material are employed mainly from the database MATEQ, and sometimes from JMatPro (*102*).

12.06.11.2.1 Sword Simulated and the Condition of Simulation

The sword simulated in this work is 500 mm in length with 7 mm in maximum width, which is a model of the author's classical sword made in Houki region. Three-dimensional finite element mesh division of the sword is represented in Figure 79, where the division is made for a half part in the width direction due to symmetry, and Figure 79(a) and 79(b), respectively, denotes the whole region and the enlarged part near *kissaki*, or tip. Total number of the elements is 3904, and that of the nodes is 5205. This model is supposed to consist of two regions, core steel with 0.2% carbon content and skin steel with 0.65% C to which different material data are applied. To differentiate the relative heat transfer coefficient depending on the thickness of the *yakiba-tsuchi* clay, the surface of the sword is divided into two layers with different value as are evaluated by use of the cooling curves, also depending on temperature.

The sword is uniformly heated up to 850 °C, at which temperature the whole region is changed into austenitic structure, and the sword is quenched into the water of 40 °C.

12.06.11.2.1.1 *The Effect of the Thickness of Pasted Clay on the Formation of* Hamon

To know the effect of the thickness of the clay on the induced *hamon* and the hardenability, simulation of quenching by use of different conditions of heat transfer coefficient, actually depending on the way of pasting of the clay, are carried out. The dark part of Figure 80 represents the martensite rich area while the white part is the pearlite. Figure 80(a) is the simulated result when pasting thick clay on an entire region of the sword, which follows that only a thin blade is induced. On the contrary, the whole region is covered by martensite when pasting thin clay as seen in Figure 80(b). The former sword might be ductile, but too soft on the edge not good enough for cutting, and the latter is too brittle. Figure 80(c) shows the proper distribution of martensite, or edge with thick clay on the ridge and thin on the edge. It is surprising that old sword smith knew such a way to control the clay thickness to obtain proper distribution of *hamon*.

12.06.11.2.1.2 *Variation of Temperature, Metallic Structures, and Induced Stress Associated with Deformation*

The color demonstrates the temperature distribution of the surface of the sword with successive time from the beginning of quenching, and the mode of deformation is also depicted in the figure. Here, the clay is supposed to be pasted in the manner of Figure 80(c); thick on the ridge and thin on the edge.

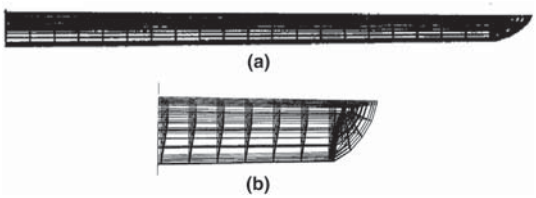

Figure 79 Finite element division of the sword. (a) Entire region and (b) near the tip.

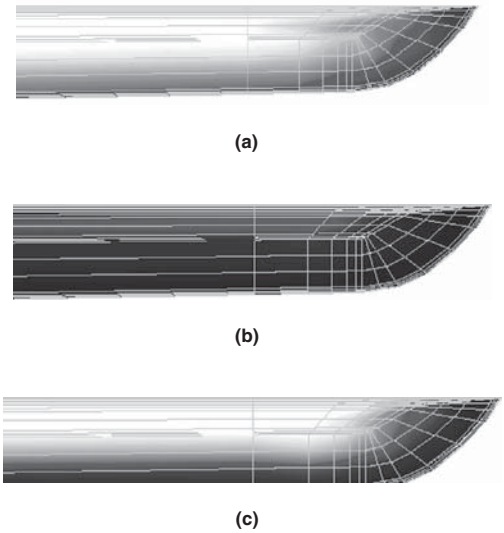

Figure 80 Formation of *hamon* depending on the way of pasting clay. (a) Thick clay pasted; (b) thin clay pasted; and (c) thick clay on the ridge and thin on the edge pasted.

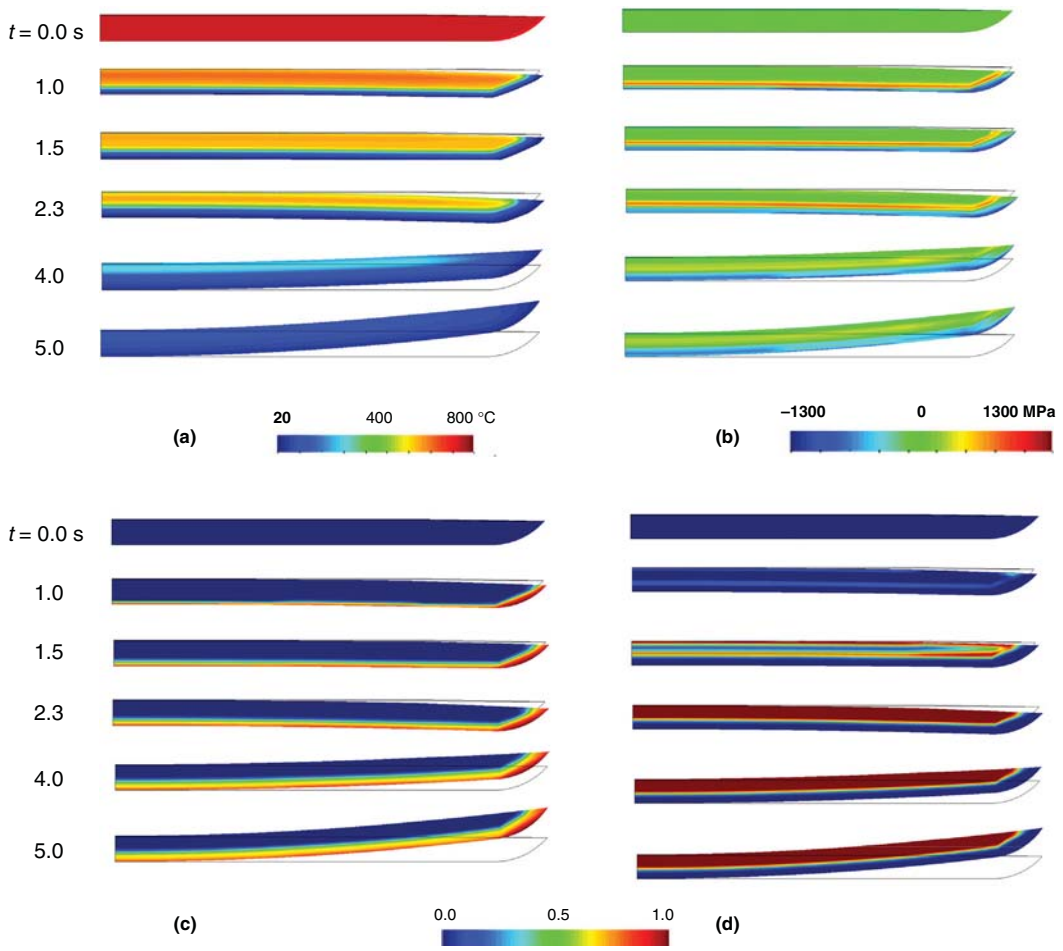

Figure 81 Summary of the simulation. (a) Temperature; (b) longitudinal stress; (c) martensite fraction; and (d) pearlite fraction.

The edge part of the sword with thin thickness shrinks due to thermal contraction by severe cooing, which leads to the bending to the downward termed as *gyaku-sori* or reverse bending at $t = 1$ s. As seen in **Figure 81(c)**, martensite start to induce in the part, details of which are illustrated in **Figure 82(a)**, and volumetric dilatation causes the upward bending at 2 s, termed as *sori*. The second *gyaku-sori* is again observed at time $t = 1.5$ s since the ridge is converted from austenite to pealite to cause the volumetric dilatation as represented in **Figure 81(d)**. In the successive stage of cooling, hot ridge side shrinks gradually because of thermal contraction, and finally, the normal bending is obtained. Thus simulated deformation gives the good agreement with the actual bending mode of *sori*.

Mode of stress distribution along longitudinal direction is also depicted in **Figure 83(b)**. In the mean time of quenching operation, so high tensile stress occurs which sometimes may lead to the cracking or fracture of the sword. Residual stress in the final stage is in tension on the ridge while in compression on the edge, which is so beneficial for reducing the bending stress during cutting operation. The data of simulated residual stresses after complete cooling are compared with measured data by X-ray diffraction technique, and satisfactory coincidence is obtained.

12.06.11.3 Simulation of Short Swords Made of Several Kinds of Steels

A group of people mainly related to Hitachi Metals, Ltd. and Wako Musium organized so interesting project in 1997 on the short sword making process by use of several kinds of steel (*101*). Prepared materials include traditional Japanese steels taken from *kera*, a block of ingot processed by *tatara* system as well as modern steels for comparison. The name of these steels and the chemical compositions are listed in **Table 11**. Note that this data is not the chemical composition of virgin raw material, but the ones after forging and before quenching.

The cross section of *kera* can be seen in **Figure 84**. As stated before, higher deoxidation with less impurities is possible in the outer parts of the *kera* due to the strong blow of air from *kirokan*, so as to get high grade steel called *tamahagane*, a noble steel. Other parts containing impurities are divided to *wazuku*, a pig iron, *ohkaji-sozai* and *ohkaji-shita*. Old Japanese steel taken from old temple also made by *tatara* system is prepared. Electrolytic iron and cutlery steel made by modern technology are also propounded for

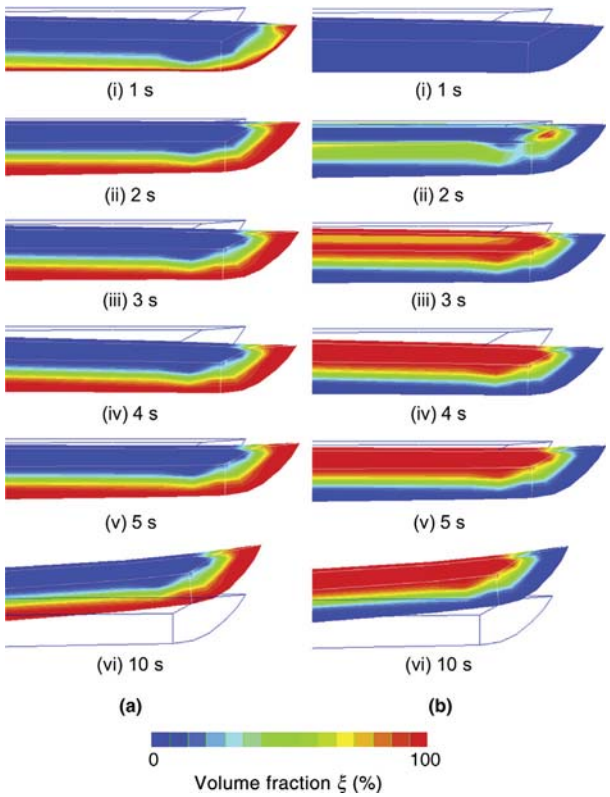

Figure 82 Structure change. (a) Martensite and (b) pearlite.

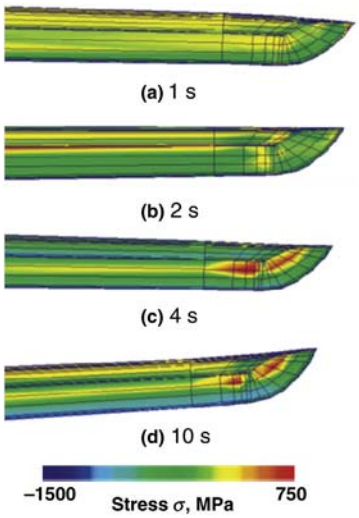

Figure 83 Longitudinal stress change. (a) 1 s; (b) 2 s; (c) 4 s; and (d) 10 s.

Table 11 Name of steels employed and the chemical composition (wt%)

Material	*C*	*Si*	*Mn*	*P*	*S*	*V*	*Al*	*Ti*	*Sn*	*As*	*Cu*
Tamahagane	0.69	0.011	0.005	0.057	0.0030	0.009	0.010	0.002	0.001	0.003	0.005
Wazuku	0.57	0.030	0.006	0.088	0.0054	0.009	0.011	0.003	0.001	0.003	0.004
Ohkaji-sozai ①	0.37	0.012	0.003	0.048	0.0020	0.003	0.011	0.002	0.001	0.002	0.004
Ohkaji-sozai ②	0.63	0.015	0.004	0.055	0.0030	0.007	0.015	0.010	0.001	0.001	0.004
Ohwari-shita	0.45	0.038	0.005	0.037	0.0020	0.008	0.025	0.006	0.001	0.002	0.004
Old steel	0.37	0.014	0.003	0.018	0.0019	0.002	0.012	0.004	0.003	0.004	0.010
Electrolytic iron ①	0.35	0.009	0.003	0.013	0.0010	0.002	0.011	0.001	0.001	0.003	0.001
Electrolytic iron ②	0.50	0.002	0.002	0.017	0.0020	0.001	0.012	0.001	0.001	0.002	0.001
Cutlery steel	0.89	0.063	0.024	0.016	0.0035	0.003	0.006	0.002	0.001	0.001	0.007

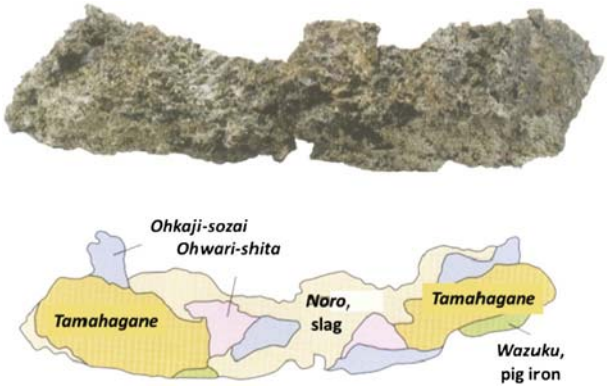

Figure 84 Cross section of *kera*.

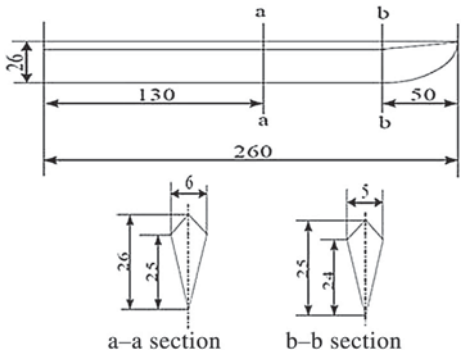

Figure 85 Dimension of short sword.

comparison. A sword master made nine short swords, *tanto* in same dimension (see Figure 85) by use of the materials by almost similar forging method and quenched into water. Figure 86 shows the photos of these swords, where *hamon*, pattern of martensite transformed region are different.

By using the FE mesh pattern in Figure 87, quenching simulation was carried out for these swords, where different patterns of *hamon* on the surface of the swords depending on the material property are presented in Figure 88. Here, material data were employed from the database, MATEQ (*53*) accumulated by the Sub-committee of Database, the Society of Materials Science, Japan (JSMS) and the Thermophysical and Mechanical Properties Simulation Software, JMatPro (*102*), a Practical Software for Materials Properties. Thicker *hamon* is observed for the swords mainly with higher carbon content.

Figure 89 depicts the simulated results of residual stresses in longitudinal direction on the surface along the line shown by arrow in Figure 89(a). The data measured by X-ray diffraction technique (Cr-Kα) are also plotted in the figure by solid circles. As seen in the figures, some scatters are visible from sword to sword. Nevertheless, the simulation is found to roughly correlate with the measured data.

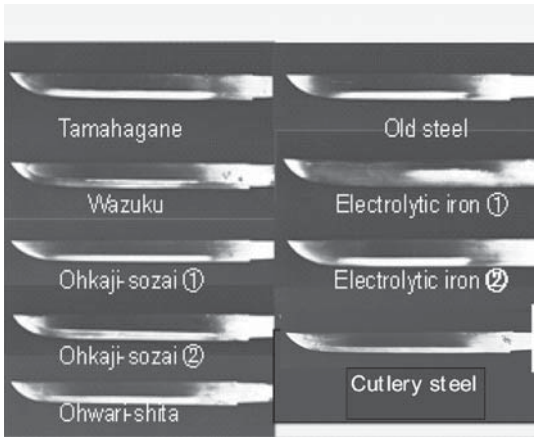

Figure 86 Photos of quenched sword.

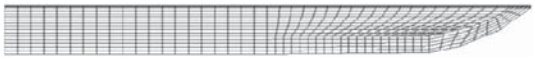

Figure 87 Finite element mesh pattern.

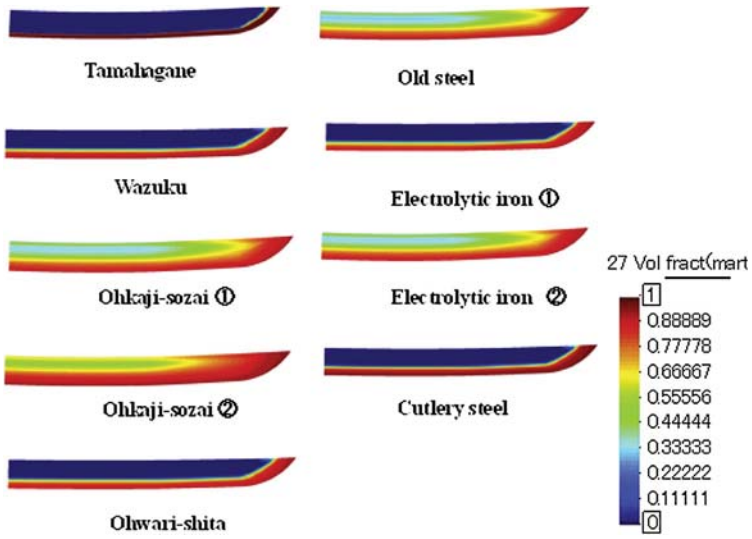

Figure 88 *Hamon* indicating martensite transformed portion depending on materials.

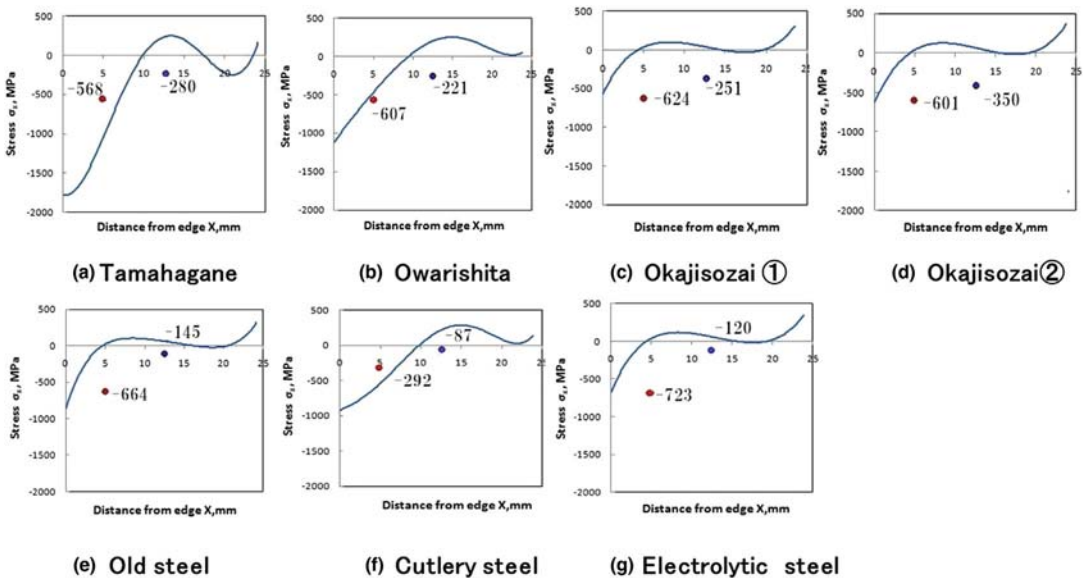

Figure 89 Simulated distribution of longitudinal residual stress from edge to ridge along a-a line on the surface of swords in comparison with measured data.

12.06.12 Benchmark Results on Heat Treating Simulation

12.06.12.1 Introduction

Intelligent Manufacturing Systems, IMS, is an industry-led, international research and development program established to develop the next generation of manufacturing and processing technologies (IMS International). Companies and research institutions from the European Union, Japan, Korea, Canada, USA, Switzerland, and Norway participate in this program. The next generation of advanced manufacturing and processing technologies will be expensive to produce, expertise needed. Cooperative R&D to share costs, risks, and expertise is the order of the day. Properly managed international cooperation in advanced manufacturing R&D can

help improve manufacturing operations, enhance international competitiveness, and lead to technology breakthroughs via market-driven R&D. Nearly 300 companies and 200 research institutions currently active in IMS research consortia.

The author and his group as well as their organizations of the present section are the partners of a project termed as VHT (Virtual Heat Treatment tool for monitoring and optimizing HT process) and also carrying out domestic activity in Japan (IMS Japan).

The purpose of this project is to predict distortion qualitatively, and to optimize time and operating condition of heat treatments. The final goal is to evaluate and decide optimum HT process virtually by using computer. The work plan is divided into several work packages such as databases development (material and generic databases as well as cooling characteristics), FEM adaptation (modification of the physical models in developed codes), design of the KBS (Knowledge-Based System), KBS development (collection of knowledge, real industrial cases and FEM input), integration in the DSS (Decision Support System) of the KBS, databases and FEM controls, and industrial validation of the DSS.

To do so, the authors have worked to compile material property data and to construct the database of thermophysical and mechanical properties, for four kinds of typical steels, in cooperation with the Subdivision of the Society of Materials Science, Japan. Special attention is paid to collect the data at high-temperature levels and for each phases induced during heat treatment.

Heat transfer property of quenchants is another substantial data necessary to simulate the HT process, and through collaboration with the Division of Quenching and Simulation, the Japan Society of Heat Treating Technology, standard heat transfer properties data of some kinds of quenchants are collected using cylindrical silver specimens. Heat transfer coefficients of several kinds of typical quenching oils used for industry are also accumulated as the database.

12.06.12.2 Benchmark Project and the Problems

As one of the activities of the Japanese VHT project, the authors proposed to organize a benchmark simulation with other people in the cooperation with both societies of JSMS and JSHT. The summary is as follows (*103,104*);

1. Carburized quenching process is focused.
2. Material treated is a Chromium steel (JIS-SCr420H).
3. Works treated are a cylinder, disc, ring for a gear and helical gear.
4. Common data of the material and cooling characteristics are propounded.
5. Programs to solve the problems are at the disposal of each member. Finally, HEARTS, GRANTAS, QUESS, SYSWELD, DEFORM-HT, and COSMAP joined in the project. All programs are available for coupled metallo-thermo-mechanical simulation.
6. Experimental data for temperature change, residual stresses, distortion, and hardness are presented to verify the results of simulation.

12.06.12.2.1 Benchmark Problems

The works for simulation and experiment are

1. Cylinder with diameter $D = 20$ mm and length $L = 60$ mm.
2. Disc with diameter $D = 30$ mm and thickness $t = 10$ mm.
3. Ring to be used for helical gear but without teeth, so in a complicated shape shown later in **Figure 8**; outer diameter $D = 76.6$ mm, inner diameter $d = 26$ mm, face width $w = 22.2$ mm.
4. Helical gear; same dimension as the ring, but with teeth of module $m = 1.77$.

Heat pattern including carburizing is depicted in **Figure 90**. Here, the chemical potential of carbon environment in carburizing period is kept constant as $C_p = 1.1$ and 0.85% respectively in carburizing and diffusing/keeping period.

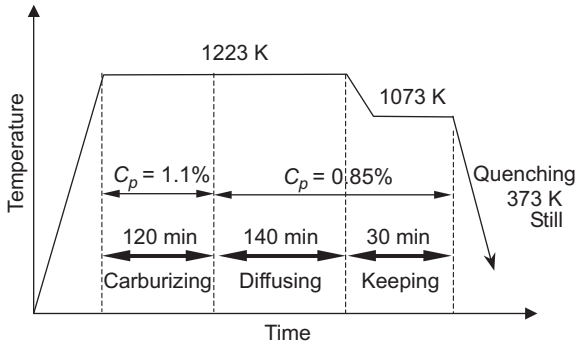

Figure 90 Heat pattern for carburized quenching process.

12.06.12.2.2 Material Data

A chromium steel (JIS-SCr420H; 0.21% C, 0.2% Si, 0.2% Mn, 0.016% P, 0.017% S, 0.02% Ni, 1.15% Cr, 0.01% Mo) is focused. The material characteristics data employed for the simulation are basically quoted from the database MATEQ (MATErial database for Quenching) accumulated by the Subcommittee of Material Database, JSMS (*62*). They are Young's modulus, Poisson's ratio, and stress-strain curves including yield stress and hardening modulus as temperature-dependent mechanical properties, thermal conductivity, specific heat and latent heat as thermophysical properties, and TTT/CCT diagrams and temperature–dilatation curves as phase change characteristics. However, some data are still needed for more sophisticated simulation, and so some experiments are carried out to identify the material data in this project. Considering that the carbon content closed to the surface increases in the carburizing process, other series of experiments for other materials with different carbon content are carried out to know the carbon dependent material data. Some examples of the data provided are depicted in **Figures 91–95** and **Tables 11–14**.

12.06.12.2.3 Heat Transfer Coefficient

Coolant used for the quenching process after carburization is a cooling oil HI-TEMPOIL A (Idemitsu). By applying the lumped-heat-capacity or inverse calculation method to the cooling curves measured by silver rod probe based on JIS-K2242 and the improved method, the heat transfer coefficient is identified as the function of temperature of the surface of the body (*105*). As is well known, however, the cooling characteristics depend on the location of a body in the case of immersion quenching, especially upper and lower surfaces. Then modifying the identified heat transfer coefficient, the data presented in **Figures 96** and **97** are, respectively, used in the case of cylinder and ring. The availability of the data is confirmed by conducting the simulation of Jominy end quench process compared with the experiments.

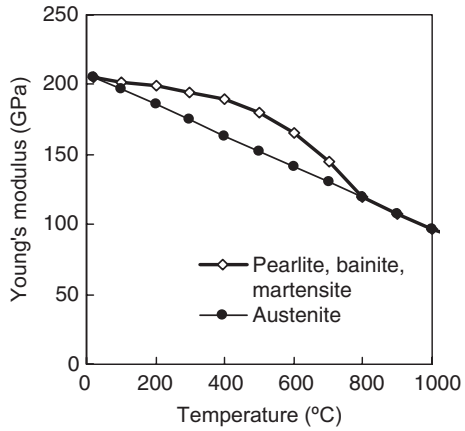

Figure 91 Young's modulus.

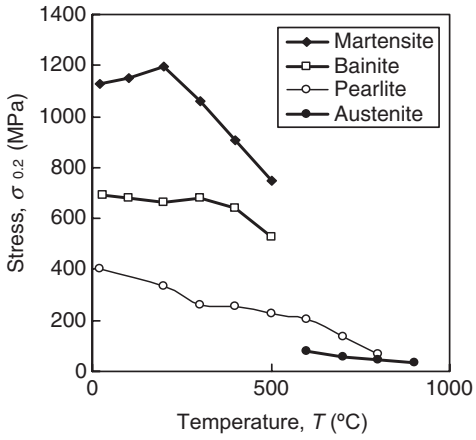

Figure 92 0.2% proof stress.

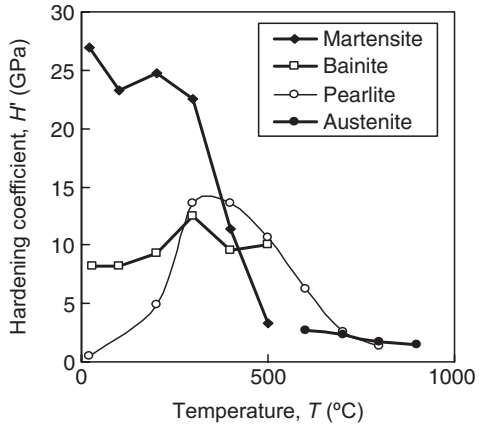

Figure 93 Hardening coefficient.

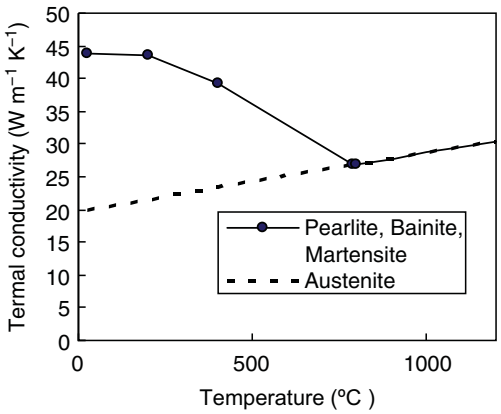

Figure 94 Thermal conductivity.

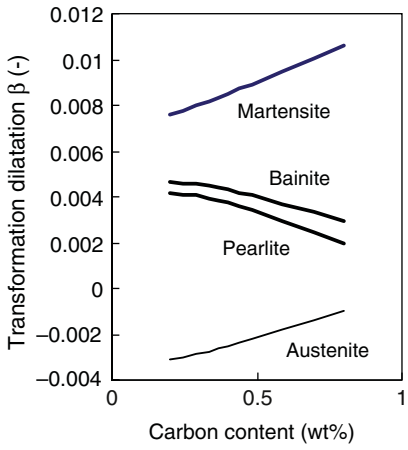

Figure 95 Dilatation due to transformation as example of material data depending on carbon content.

Table 12 Linear thermal expansion coefficient α defined as $\alpha = a \cdot T + b$ ($^{\circ}C^{-1}$)

		Carbon content (wt%)			
Phase	*Coefficient*	*0.2*	*0.4*	*0.6*	*0.8*
Pearlite, bainite, martensite	a ($\times 10^{-9}$)	6.56	6.89	7.22	7.59
	b ($\times 10^{-6}$)	12.2	11.9	11.7	11.3
Austenite	a ($\times 10^{-9}$)	1.42	1.42	1.42	1.41
	b ($\times 10^{-6}$)	20.7	20.7	20.7	20.7

Table 13 Transformation plasticity coefficient from austenite (MPa^{-1})

Ferrite–pearlite K_p	13×10^{-5}
Bainite K_b	8.5×10^{-5}
Martensite K_m	7.4×10^{-5}

Table 14 Latent heat from austenite ($kJ\ kg^{-1}$)

Ferrite–pearlite	36
Bainite	75
Martensite	84

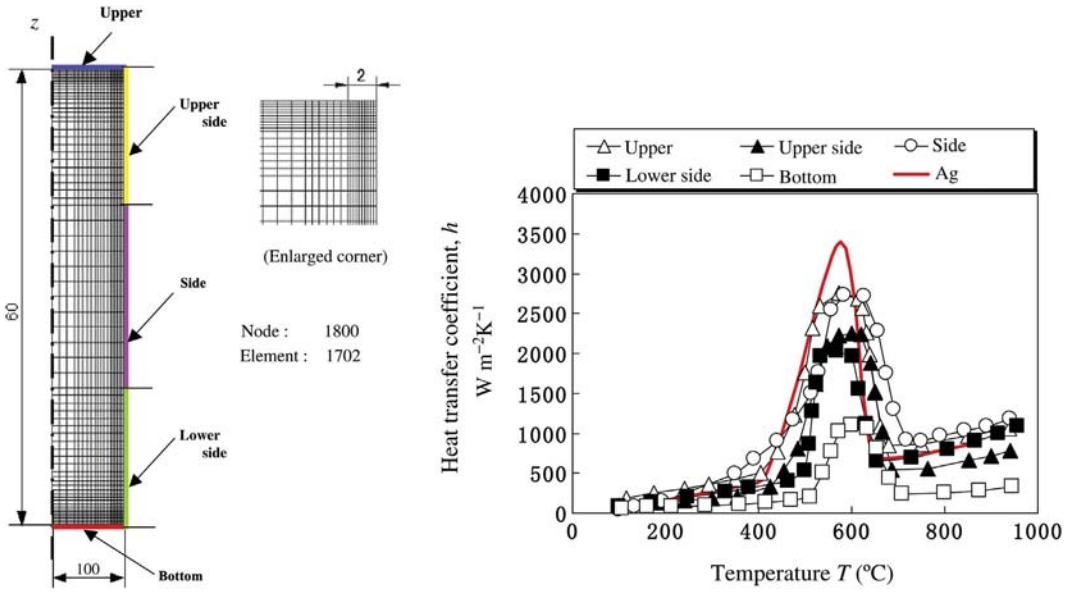

Figure 96 Temperature and location dependent heat transfer coefficient – cylinder.

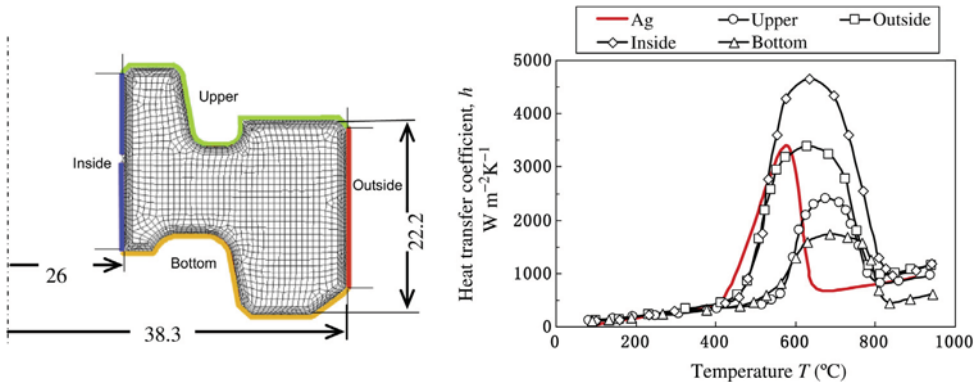

Figure 97 Temperature and location dependent heat transfer coefficient – ring.

12.06.12.3 Results of Simulation and Verification

Solution to the benchmark problems of No. 1, 3, and 4 for a cylinder, ring, and helical gear are attempted by several programs; HEARTS (*31*,*32*), GRANTAS (*59*), QUESS (*62*), SYSWELD (*58*), DEFORM-HT (*56*), COSMAP (*53*), and another software by cooperating member. Some results are illustrated in the followings (*103*,*104*).

12.06.12.3.1 Cylinder

Figure 98(a) represents an example of simulated pattern of carbon content in the cylinder in the final stage. In spite of member's disposal to introducing boundary condition for carbon absorption, the results by several programs give the similar pattern. Typical mode of quenched distortion is illustrated in Figure 98(b). Martensite fraction after quenching calculated by several programs, named as A, B, C, and D is overplotted in Figure 99, and distortion along outer surface with measured data is summarized in Figure 100. There are some scatters among the employed programs, which is to be carefully discussed in the future.

12.06.12.3.2 Ring in Gear Shape without Teeth

Another axisymmetric problem is for a ring shaped body before rough cutting teeth of helical gear, shown in Figure 97. Figure 101 depicts the results of simulation of distortion (a), carbon content (b) and martensite fraction (c) and residual stress in tangential

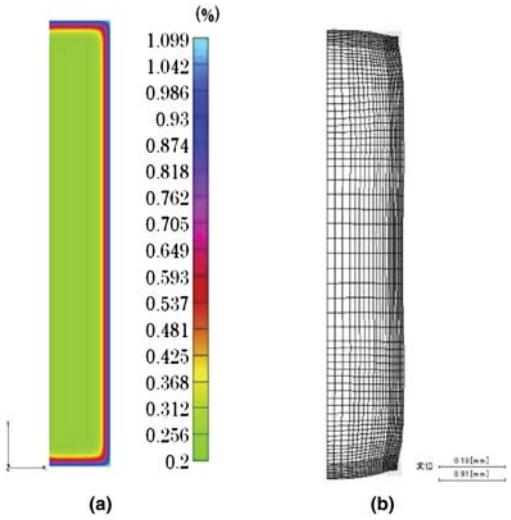

Figure 98 Distribution of diffused carbon and distortion – cylinder. (a) Carbon profile and (b) distortion.

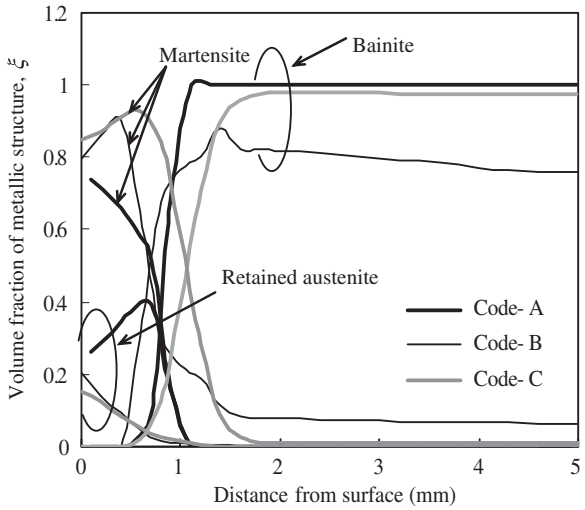

Figure 99 Martensite fraction from surface on the middle section – cylinder.

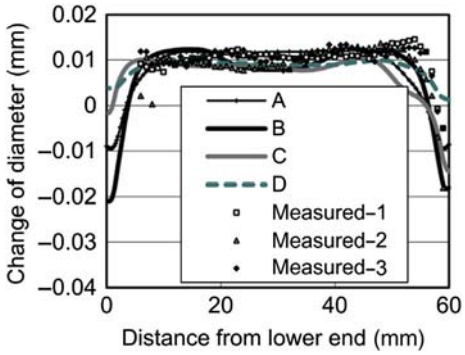

Figure 100 Comparison of quenched distortion with experiment – cylinder.

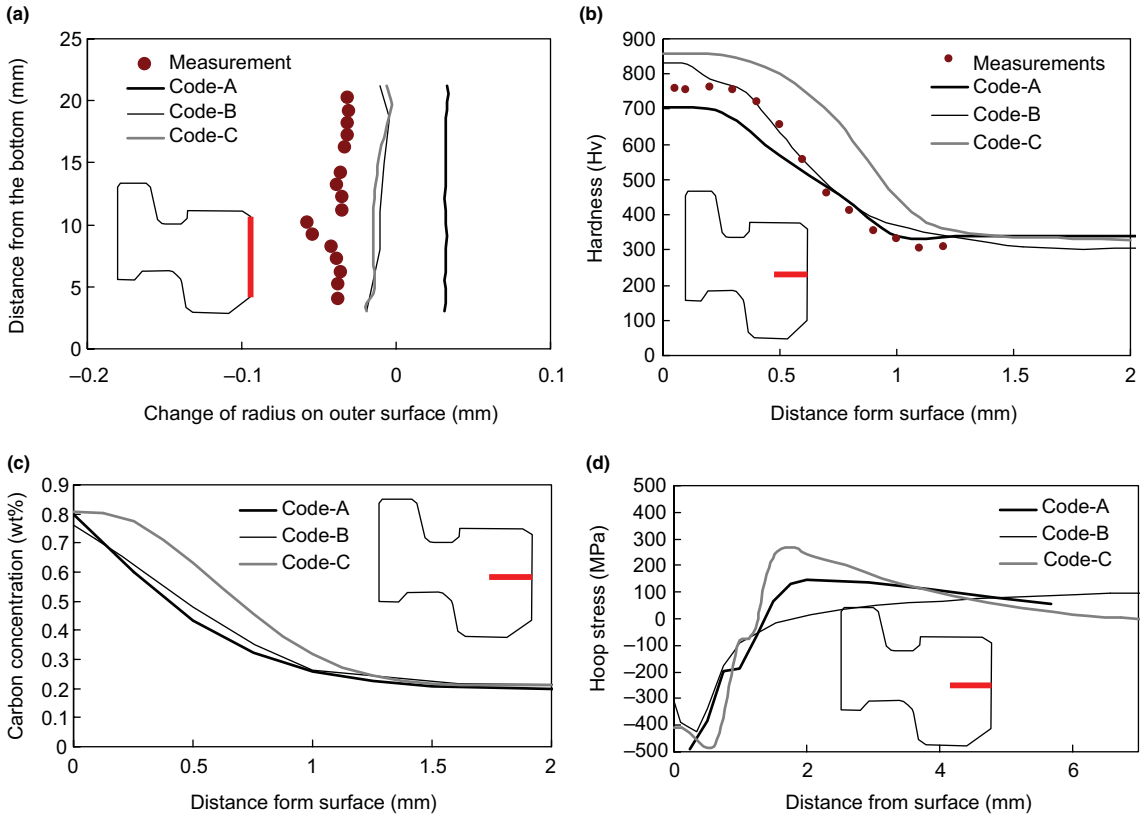

Figure 101 Comparison of simulated results by some codes – ring. (a) Variation in the change of radius; (b) Hardness distribution; (c) Carbon profile; (d) Distribution of hoop stress.

direction (d) by use of the boundary condition and heat transfer coefficient stated in Figure 97. Comparison of the distortion with measured profile is also shown in Figure 102.

12.06.12.3.3 Helical Gear

Since this helical gear is not in axisymmetric shape, full 3-D simulation or pseudo 3-D approximation with periodical boundary condition is to be applied. The results shown in Figures 103 and 104 are examples of simulation using over 21 000 nodes and 16 000 elements (computing time for coupled calculation is approximately 100 h by PC with 2.8 GHz processor). In these figures, left illustrations correspond to the vertical cross section, while the right corresponds to horizontal. Figure 105 depicts a simulated result of residual stress.

From these results one can conclude that the simulation gives fairly reasonable results in practical sense.

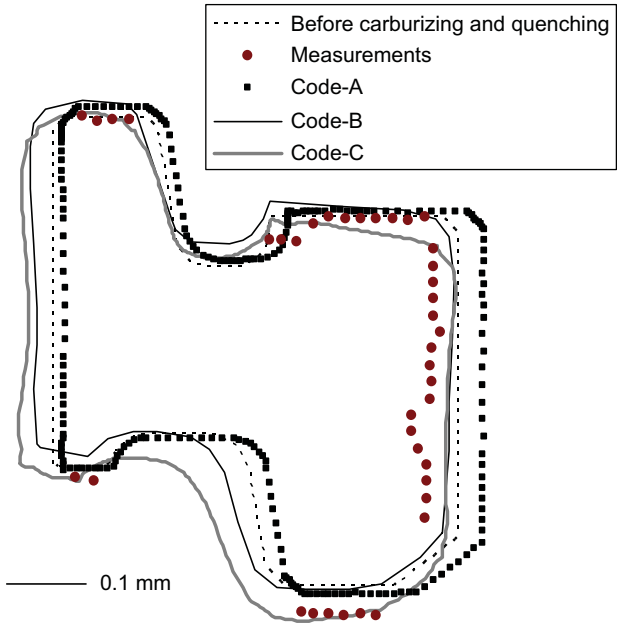

Figure 102 Comparison of simulated data of distortion with experimental result – ring.

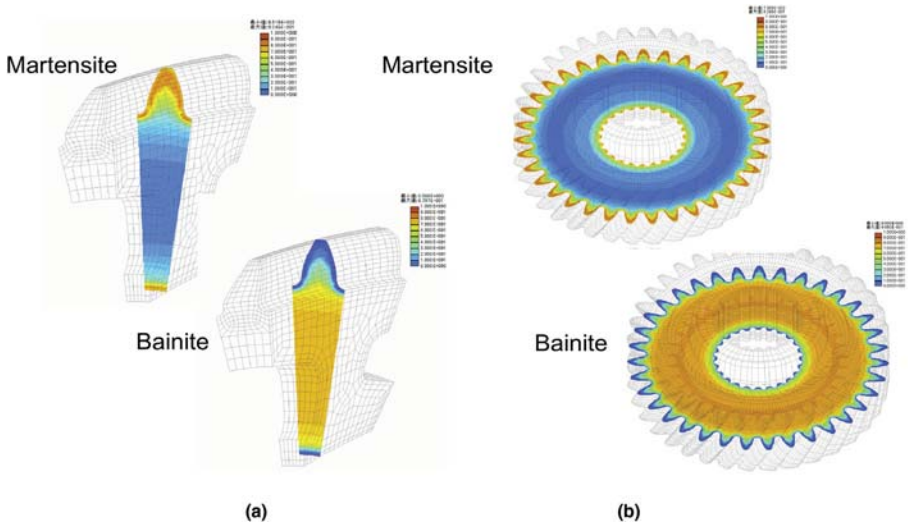

Figure 103 Calculated microstructure after carburized quenching. (a) A tooth model, CPU time: 255 min and (b) entire gear model, CPU time: 2562 min.

12.06.12.4 Concluding Remarks on This Section and Future Works

Current progress of our project on IMS-VHT project is briefly introduced, and the interim situation of the benchmark project of carburized quenching process is reported. The project examines the applicability of available programs for quenching simulation by use of common data.

The results obtained in this stage are rather limited; all problems have not been solved by all participating programs, and focused material is only SCr420. Further works are expected to solve the problems in a wider range.

The results will be open for other cooperating members from JSMS and JHTS, and they are asked to join in this project.

Future works are also expected for international cooperation. The authors will willingly provide their data and problems to potential researchers who want to simulate the problems using other programs.

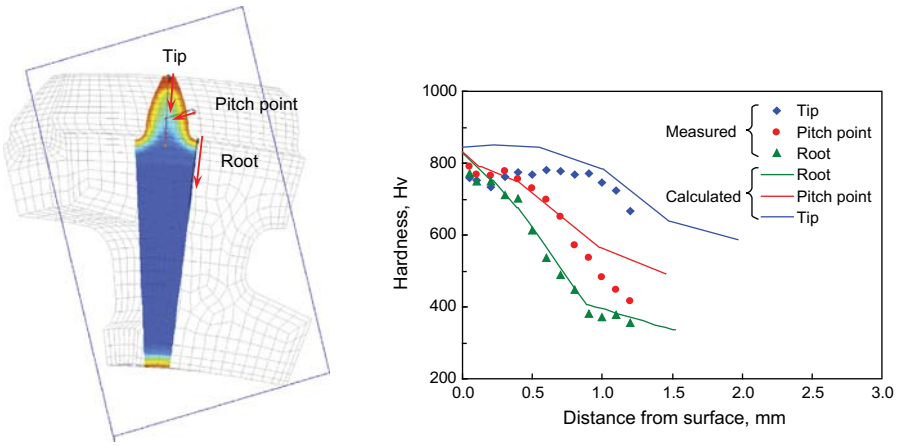

Figure 104 Measured and calculated hardness distribution after carburized quenching.

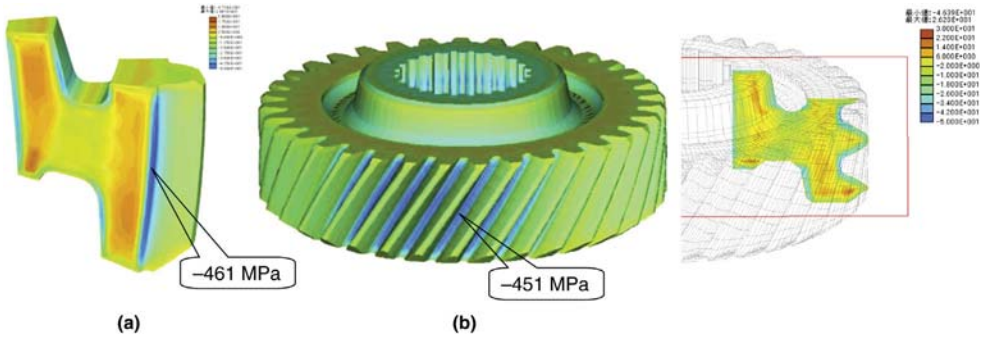

Figure 105 Calculated residual stress after carburized quenching. (a) A tooth model, axial (σ_z) and (b) entire gear model, axial (σ_z).

12.06.13 Concluding Remarks on This Chapter

This chapter introduces the concept of metallo-thermo-mechanics, proposed by the present author, which is relevant to describing the coupled structure change, temperature, and mechanical fields in the course of quenching processes. After reviewing a brief summary of the history of numerical analysis up to the year 2000, fundamental governing equations for three fields are explained. Database MATEQ necessary for the quenching simulation for many kinds of materials are introduced in Section 12.06, and the brief summary of the existing quenching simulation softwares followed by developed cord COSMAP in cooperation with the author group are stated in Section 12.07.

As practical applications of the theory with use of developed software, several kinds of quenching processes, including Jominy end quenching, carburized quenching, induction hardening, and laser hardening with quenching of Japanese swords, are presented. The results of a benchmark project carried out by the author's group are summarized in the final section.

Phase transformation occurring in solids is predominant in quenching. Melting and/or solidification are another mode of phase transformation, which are so important in welding and casting, and the concept of metallo-thermo-mechanics is also useful in these cases. Readers interested in this area should refer to Refs. (*28,29,106–112*).

Acknowledgments

This series of projects on computer simulation for quenching have been conducted by the author for over 40 years. Many graduate students and research staff, mainly from Kyoto University, cooperated with me. Following are a number of people to whom the author wishes to express his gratitude.

Professor K. Tanaka for inelastic constitutive equations, Professor S. Nagaki for metallo-thermo-mechanics, Professor D. Ju, for software COMAP, Dr K. Arimoto for the code HEARTS, and Dr K. Okamura for the database MATEQ.

Practical simulations in each section were carried out with the cooperation of Dr Z. Wang and Mr. Y. Morimoto for Jominy end quenching, Dr S. Yamanaka, T. Sakanoue, and T. Yoshii for carburized quenching, Dr F, Ikuta for induction hardening, Dr K. Nakasaki for laser hardening, and Professor T. Uehara for Japanese swords.

Instructive discussions with Professor B. Raniecki, IPPT-PAN, especially on theoretical aspects, have been ongoing for these long years.

References

1. *Materials Science and Engineering for the 1990s;* Report by the National Research, Council National Academy Press, 1989; pp 35–73.
2. *Enabling the Future – Linking Science and Technology to Societal Goals,* 1992. Report by the Carnegie Commission on Science, Technology, and Government.
3. *VISION 2020: Heat Treating Industry of the Future;* Report by the ASM Heat Treating Society, ASM International: Materials Park OH, 1997.
4. *Report on the Heat Treating Technology Roadmap Workshop;* Report by the ASM Heat Treating Society, ASM International: Materials Park, OH, 1997.
5. Clements, T. E.; Chuzoy, L.; Shared, I. Application of Heat Treatment Simulation of Production Environment. In *Proc. 2nd Int. Conf., on Quenching and Control of Distortion;* Totten, G. E., Howes, M. A. H., Sjostrom, S. J., Funatani, K., Eds.; ASM International: Materials Park, OH, 1996; pp 235–238.
6. Totten, G. E., Ed. *Conf. Proc. Quenching and Distortion Control;* ASM International: Materials Park, OH, 1992.
7. Totten, G. E., Howes, M. A. H., Sjostrom, S. J., Funatani, K., Eds. *Proc. 2nd Int. Conf. on Quenching and Control of Distortion;* ASM International: Materials Park, OH, 1996.
8. Totten, G. E.; Tensi, H. M.; Liscic, B. *Proc. 34 Int. Conf. on Quenching and Control of Distortion;* ASM International: Materials Park, OH, 1999.
9. Inoue, T.; Raniecki, B. Determination of Thermal-Hardening Stresses in Steels by Use of Thermoplasticity Theory. *J. Mech. Phys. Solids* **1978,** *26,* 187–212. Pergamon Press Lid. Printed in Great Britain.
10. Inoue, T.; Funatani, K.; Totten, G. Process Modeling for Heat Treatment: Current Status and Future Developments. In *Proc. 1st Int. Conf. Thermal Process Modeling and Computer Simulation, Shanghai, March 28–30;* 2000; pp 14–25.
11. Maurer, E. Wärmespannungen Beim Abkühlen Großer Güsse bzw. Beim Vergüten Großer Schmiedestücke in Form Von Vollzylindern. *Stahl Eisen* **1927,** *47,* 1323–1327.
12. Maurer, E. Wärmespannungen Beim Abkühlen Bzw. Vergüten Großer, Hohlgebohrter Zylinder. *Stahl Eisen* **1928,** *48,* 225–228.
13. Bielenov, O. S. On Approximate Evaluation of Residual Stresses Due to Thermal Hardening. *J. Tech. Phys.* **1953,** *23,* 2048–2055.
14. Hirano, T. *Bull. Inst. Phys. Chem. Res.* **1936,** *15,* 243.
15. Hirone, T. *Bull. Inst. Phys. Chem. Res.* **1937,** *16,* 1229.
16. Hirone, T.; Tsuya, N. *Sci. Rep. Res. Inst., Tohoku University (Set. A)* **1949,** *1,* 169.
17. Hirono, T.; Tsuye, N. *Sci. Rep. Res. Inst., Tohoku University (Set. A)* **1949,** *1,* 111.
18. Mura, T. *Residual Stresses Due to Thermal Treatments,* **10**; Faculty of Engineering, Meiji University, 1957, 14–27.
19. Zukievich-Stocha, A. V. Quenching Process and Method for Numerical Calculation of Stresses. *J. Tech. Phys.* **1940,** *16,* 478–490.
20. Bielenov, O. S. *J. Tech. Phys* **1952,** *22,* I11 (in Russian).
21. Bielenov, O. S. On Approximate Evaluation of Residual Stresses Due to Thermal Hardening. *J. Tech. Phys.* **1953,** *23,* 2048–2055.
22. Weiner, J.,H.; Huddleston, J. V.. Trans. ASME 81, Ser. E. *J. Appl. Mech.* **1959,** *26,* 31.
23. Landau, H. G.; Weiner, J. H. Stresses in an Elastic-Plastic Cylinder Due to a Dilatational Phase Transformation. *J. Appl. Mech.* **1964,** *31,* 148–150. ASME, Ser. E.
24. Landau, H. G. *J. Mech. Phys. Solids* **1963,** *11,* 97.
25. Lomakin, V. A. Transformation of Austenite under Nonisothermal Cooling. *Izv. Ak. Nauk CCCP, Pd. T. N., Mech. and Machine* **1958,** *2,* 20–25. Problems of Evaluation of Stresses and Deformations due to Thermal Treatment. Izv. Ak. Nauk CCCR. Od. T. N., Mech. and Machine 1 (1959) 103–110.
26. Inoue, T.; Tanaka, K. An Elastic-Plastic Stress Analysis of Quenching when Considering a Transformation. *Int. J. Mech. Sci.* **1975,** *17,* 361.
27. Inoue, T.; Nagaki, S.; Kishino, T.; Monkawa, M. Description of Transformation Kinetics, Heat Conduction and Elastic-Plastic Stresses in the Course of Quenching and Tempering of Some Steels. *Ing.-Arch.* **1981,** *50* (5), 315–327.
28. Inoue, T. Metallo-Thermo-Mechanical Coupling – Application to the Analysis of Quenching, Welding and Continuous Casting Processes. *Berg- und Huttenmannische Monatshefte* **1987,** *132* (3), 63–71.
29. Inoue, T. In *Inelastic Constitutive Relationships and Applications to Some Thermo-Mechanical Processes Involving Phase Transformation, Thermal Stresses III;* Hetnarski, R. B., Ed.; North Holland, 1988.
30. Inoue, T. Macro-, Meso- and Micro-Scopic Metallo-thermo-mechanics – Application to Phase Transformation Incorporating Process Simulation. *Mater. Sci. Res. Int.* **2004,** *10,* 1–11.
31. Inoue, T.; Arimoto, K.; Ju, D.-Y. Metallo-Thermo-Mechanical Simulation of Quenching Process – Theory, and Implementation of Computer Code "HEARTS". In *Proc. of the First Int. Conf. on Quenching and Control of Distorsion, Chicago, September 22–25;* 1992; pp 205–212.
32. Inoue, T.; Arimoto, K. Development and Implementation of CAE System "HEARTS" for Heat Treatment Simulation Based on Metallo-Thermo-Mechanics. ASM International. *J. Mater. Eng. Perform.* **1997,** *6* (1), 51–60.
33. Inoue, T.; Yamaguchi, T.; Wang, Z. G. Stresses and Phase Transformations Occurring in Quenching of Carburized Steel Gear Wheel. *Mater. Sci. Technol.* **1985-10,** Vol. 1, 872–876.
34. Bhattacharya, S.; Kehl, G. L. Isothermal Transformation of Austenite under Externally Applied Tensile Stress. *Trans. ASM* **1955,** *47,* 351–379.
35. Onodera, H.; Gotoh, H.; Tamura, I. Effect of Volume Change on Martensitic Transformation Induced by Tensile or Compressive Stress in Polycrystalline Iron Alloys. In *Proc. 1st JIM Int. Symp. New Aspects of Martensitic Transformation;* 1976; pp 327–332.
36. Patel, J. P.; Cohen, M. Criterion for the Action of Applied Stress in the Martensitic Transformation. *Acta Metal.* **1953,** *1,* 531–538.
37. Radcliffe, S. V.; Schatz, M. The Effect of High Pressure on the Martensitic Reaction in Iron–Carbon Alloys. *Acta Metal* **1962,** *10,* 201–207.
38. Barbe, F.; Quer, R.; Taleb, L.; Cursi, E. S. FE Determination of the Effective TRIP during Diffusive Transformation in a Volume with Randomly Positioned Nuclei. In *Proc. 1st Int. Conf. on Distortion Engineering, Bremen;* 2005, pp 149–148.
39. Johnson, W. A.; Mehl, R. F. Reaction Kinetics in Processes of Nucleation and Growth. *Trans. AIME* **1939,** *135,* 416–458.
40. Ju, D. Y.; Liu, C. C. Numerical Modeling and Simulation of Carburized and Nitrided Quenching. In *Proc. of Int. Conf. on Advances in Materials and Processing Technologies,* Vol. 3; Spain, September, 18–21, 2001; pp 1025–1032.
41. Ju, D. Y.; Mukai, R. Simulation and Experimental Verification of Metallo-Thermo-Mechanical Behavior in Stirring Quenching Process. In *Proc. of 8th Seminar of Int. Federation for Heat Treatment and Surface Engineering, 12–14 September, Dubrovnik-Cavtat, Croatia;* 2001; pp 317–324.
42. Liu, C.; Ju, D.-Y.; Inoue, T. Numerical Modeling for Simulating Metallo-Thermal-Mechanical Behavior during Carburized and Nitrided Quenching. *Mater. Sci. Res. Int.* **2001,** *2,* 469–474. Special Publications.
43. Magee, C. L. *The Nucleation of Martensite;* ASM: New York, 1968. Chapter 3.
44. Bowen, R. M. Theory of Mixture. In *Continuum Physics,* Vol. 3; Eringen, A. C., Ed.; Academic Press: New York, 1976; pp 2–129.
45. Wang, Z. G.; Inoue, T. Viscoplastic Constitutive Relation Incorporating Phase Transformation – Application to Welding. *Mater. Sci. Technol.* **1985,** *1,* 899–903.
46. Fischer, D. D.; Reisner, G. E.; Werner, G.; Tanaka, K.; Gailletand, G.; Antretter, G. A New View on Transformation Induced Plasticity. *Int. J. Plast.* **2000,** *16,* 723–740.

47. Greenwood, G. W.; Johnson, R. H. The Deformation of Metals under Small Stresses during Phase Transformations. *Proc. Roy. Soc.* **1965,** *283A,* 403–422.
48. Leblond, J. B. Mathematical Modelling of Transformation Plasticity in Steels, II Coupling with Train Hardening Phenomena. *Int. J. Plast.* **1989,** *5,* 1371–1391.
49. Inoue, T. Unified Transformation-Thermoplasticity and the Application. *J. Soc. Mater. Sci., Japan* **2007,** *56,* 354–355.
50. Inoue, T. On Phenomenological Mechanism of Transformation Plasticity and Inelastic Behavior of a Steel Subjected to Varying Temperature and Stress – Application of Unified Transformation-Thermoplasticity Theory. *Soc. Mater. Sci., Japan* **2008,** *57*, 255–230.
51. Otsuka, T.; Wakasu, Y.; Inoue, T. A Simple Identification of Transformation Plastic Behavior and Some Data for Heat Treating Materials. *Int. J. Mat. Prod. Technol.* **2005,** 298–311.
52. Inoue, T.; Okamura, K. Material Database for Simulation of Metallo-Thermo-Mechanical Fields. In *Proc. of 5th Int. Symp. on Quenching and Distortion Control;* ASM: St Louis, October, 2000; pp 753–760.
53. http://www.ideamap.co.jp/cosmap/e_product_cosmap010_outline.html.
54. Ju, D.-Y.; Inoue, T. On the Material Process Simulation Code COSMAP Simulation Examples and Its Experimental Verification for Heat Treatment Process. *Key Eng. Mater.* **2007,** *345–346,* 955–958 (CD-Published), Proceedings of 10th International Conference on Mechanical Behaviour of Materials.
55. Ju, D. Y.; Inoue, T. In Simulation and Its Experimental Verification by a Material Process CAE Code COSMAP. *Proc. of 2nd Int. Conf. on Distortion Engineering,* Bremen, Germany **September 2008,** *17–19,* 441–448.
56. http://www.deform.com/products/deform-ht/.
57. http://deformationcontrol.com/dct_products.htm.
58. http://www.esi-group.com/products/welding-old/sysweld.
59. http://www.eonet.ne.jp/~smiling/SOFT/GRANTAS/grantas-eng.htm.
60. http://www.engineering-eye.com/FINAS/FINAS_TPS/index.html.
61. http://www.arimotech.com/Pages/EnglishMUSIMAP.aspx.
62. Inoue, T.; Okamura, K. Material Database for Simulation of Metallo-Thermo-Mechanical Fields. In *Proc. of 5th Int. Symp. on Quenching and Distortion Control;* ASM: St Louis, 2000; pp 753–760.
63. Fukumoto, M.; Kizawa, K.; Okamura, K.; Ohta, A. *Finite Element Analysis of a Steering Rack Shaft Subjected to High-Frequency Induction Hardening Process.* 49-Special Issue; Netsu-shori, 2009, 689–692.
64. Kraus, G. *Principles of Heat Treatment;* ASM International, 1980.
65. Shigeru, Y.; Takayuki, S.; Souichi, Y.; Kozuka, T.; Inoue, T. Influence of Transformation Plasticity on the Distortion of Caburized Quenching Process of Cr-Mo Steel Ring. In *Proceedings of the 18th Conference on Heat Treating, 12–15 October, ASM International;* 1998; pp 657–664.
66. Shigeru, Y.; Takayuki, S.; Toshikazu, Y.; Inoue, T. Transformation Plasticity – The Effect an Metallo-Thermo-Mechanical Simulation of Carburized Quenching Process. In *Proceedings of 1st International Conference on Thermal Process Modeling and Computer Simulation, 28–30 March, Shanghai;* 2000; pp 185–195.
67. Inoue, T.; Morimoto, Y. Metallo-Thermo-Mechanical Simulation of Jominy End Quench Tests Introducing Developed Material Database "MATEQ". In *Proc. of the Fifth World Congress on Computational Mechanics (WCCM-V);* 2002. Web-publishing.
68. Bodin, J.; Segerberg, S. In *Proc. 9th Int. Conf. Heat Treatment and Surface Engineering;* 1994.
69. Miyao, M.; Wang, Z. G.; Inoue, T. J. *Soc. Mat. Sci* **1986,** *35,* 1352 (in Japanese).
70. Ikuta, F.; Arimoto, K.; Inoue, T. In *Proc. 2nd Int. Conf. Quenching and Distortion;* ASM, 1996; pp 259–266.
71. Ikuta, F.; Inoue, T. In *Proc. 1st Int. Induction Heat Treating Symposium;* ASM, 1997; pp 541–550.
72. Arimto, K.; Ikuta, F.; Inoue, T. *J. Jpn Soc. Heat Treat.* **1994,** *34,* 332–338 (in Japanese).
73. Melander, M. *J. Heat Treat.* **1985,** *4,* 145–166.
74. Melander, M. *Mat. Sci. Tech.* **1985,** *1,* 877–882.
75. Wang, K. F.; Chandrasekar, S.; Yang, H. T. Y. *J. Mat. Eng. Perf.* **1995,** *4,* 460–473.
76. Davies, J.; Simpson, P. *Induction Heating Handbook;* McGraw-Hill B. C. Ltd., 1979; pp 307–340.
77. Fan, G.; Guan, Y.; Chen, T.; Wang, H. *J. Shanghai Hiaotong Univ.* **2000,** *E-5* (1), 58–62.
78. Zhang, J.; Fan, G.; Gun, G.; Sun, J. *J. Shanghai Hiaotong Univ.* **2000,** *E-5* (1), 76–81.
79. Kim, T. H.; Chong, K. C.; Yoo, B. Y. *J. Mater. Sci.* **1995,** *30,* 784–792.
80. Stamm, H.; Holzwarth, U.; Boerman, D. J.; Dos Santos Marques, F.; Olchini, A.; Zausch, R. *Fatigue Fract. Eng. Mater. Struct.* **1996,** *19,* 985–995.
81. Nakasaki, K.; Inoue, T. Metallo Thermo-Mechanical Simulation of Laser – Quenching Process of Some Steels. In *Proc. of 5th Int. Symp. on Quenching and Distortion Control*, ASM, St Louis, October, 2000, pp 129–137 Nakasaki, K.; Inoue, T. *J. Soc. Mat. Sci., Jpn.* **1997,** *46,* 268–275.
82. Nakasaki, K.; Inoue, T. Effect of Carbon Content on Hardened Structure of Laser Beam Irradiated Cr–Mo Steels – Experiment and Simulation. In *Proc. of 7th Asia Foundry Congress, Taipei, October 12–14;* 2001; pp 235–245.
83. Tawara, K. *Scientific Research on Japanese Swords* (in Japanese); Hitachi-Hyoronsha: Tokyo, 1953.
84. Kozuka, J. Tatara Process – A Pig Iron- and Steel Making Process, Transmitted from Ancient Times. In *Change in Carbon Content of Materials of the Japanese Sword under Traditional Forging Process;* Sasaki, N., Momono, T., Eds.; *ISIJ International.* 2007, Vol. 93; pp 792–798.
85. Bain, B. C. Nippon-to, an Introduction of Old Swords of Japan. *J. Iron Steel Inst. Jpn.* **1962,** 265–282.
86. Fujiwara, H.; Hanabusa, T.; Tanaka, K. Scientific Research of Japanese Sword – Its Curvature (Sori) and Residual Stresses. In *Proc. 3rd Int. Conf. Residual Stresses* **1991,** *2*; pp 1537–1542.
87. Matsushita, Y. Restoration of the Tatara Ironmaking Process, an Ancient Ironmaking Process of Japan. In *Proceedings of International Conference Science and Technology of Iron and Steel, Trans. ISIJ* **1971,** Vol. 11; pp 212–218.
88. Williams, A. R. Seven Swords of the Renaissance from an Analytical Point of View. *Glaudius* **1978,** *14,* 97–127.
89. Park, J. S. Traditional Japanese Sword Making from a Tatara Ingot from Microstructural Examination. *ISIJ Int.* **2004,** *44-6,* 1040–1048.
90. Inoue, T. Japanese Sword in Science and Technology – Computer Simulation of Quenching Process. *Boundary* **1995,** *11,* 36–41 (in Japanese).
91. Inoue, T. The Japanese Sword – the Material, Manufacturing and Computer Simulation of Quenching Process. *Mater. Sci. Res. Int.* **1997,** *3–4,* 193–203.
92. Inoue, T. The Japanese Sword – the Material, Manufacturing and Computer Simulation of Quenching Process. *J. S. Afr. Arms Armour Soc.* **2002,** 108–142.
93. Inoue, T. Japanese Sword in Comparison with Others. In *Proc. of 8th Int. Conf. on Mechanical Behaviour of Materials;* Canada: Victoria, 1999; pp 458–468.
94. Inoue, T. Science of Tatara and Japanese Sword – Traditional Technology Viewed from Modern Science. In *Proc. of 1st Int. Conf. on Business and Technology Transfer;* 2002; pp 131–138.
95. Inoue, T. Scientific Rationality in the Japanese Sword. *J. Jpn. Soc. Mech. Eng.* **2004,** *107–1027,* 132–135 (in Japanese).
96. Inoue, T. The Japanese Sword – the Material, Manufacturing and Computer Simulation of Quenching Process. *Mater. Sci. Res. Int.* **1997,** *3* (4), 193–203.
97. Inoue, T. Tatara and the Japanese Sword – the Science and Technology. *Acta Mech.* **2011,** *214,* 17–30.
98. Inoue, T. Simulation of Quenched Japanese Short Swords Made of Several Kinds of Materials. In *Proceedings of the 6th International Quenching and Control of Distortion Conference, Chicago;* 2012; pp 575–588.
99. Uehara, T.; Inoue, T. Quenching Process Simulation of Japanese Sword Covered with Clay. *J. Soc. Mater. Sci., Jpn.* **1995,** *44,* 309–315 (in Japanese).
100. Kikuchi, Y. The Effect of Thin Coating Material o Rapid Cooling of Hot Metal in Boiling Liquid. *Netsushori.* **2006,** *46,* 359–366.
101. Murakawa, Y.; Kishida, T.; Sato, Y.; Miyake, H.; Suzuki, T.; Kihara, A.; Kubo, Y. Variation of Metallurgical Properties of Several Kinds of Raw Material in the Course of Swordmaking Process. In *Proc. of Fall Symp., JISI;* 1988; pp 1–12 (in Japanese).

102. http://www.sentesoftware.co.uk/.
103. Inoue, T.; Watanabe, Y.; Okamura, K.; Narazaki, M.; Shichino, H.; Ju, D.-Y.; Kanamori, H.; Ichitani, K. A Cooperative Activity on Quenching Process Simulation – Japanese IMS-VHT Project on the Benchmark Analysis and Experiment. *Trans. Mater. Heat Treat.* **2004-5,** *25* (5), 28–34.
104. Inoue, T.; Watanabe, Y.; Okamura, K.; Narazaki, M.; Shichino, H.; Ju, D.-Y.; Kanamori, H.; Ichitani, K. Recent Development of Heat Treating Simulation in Japan. In *Proc. of 1st Int. Conf. on Distortion Engineering, Bremen;* 2005-9; pp 133–140.
105. Narazaki, M. *Estimation of Heat Transfer Coefficients in Quenching*. Reports in Joint Meeting of JSMS and JSHT on Benchmark Project on Quenching Simulation (in Japanese), July, 2004, 9–14.
106. Inoue, T. Welding and Casting. In *Encyclopaedia of Thermal Stresses;* Hetraski, R., Ed.; Pergamon, 2013.
107. Wang, Z. G.; Inoue, T. Viscoplastic Constitutive Relation Incorporating Phase Transformation – Application to Welding. *Mater. Sci. Technol.* **1985,** *1* (10), 899–903.
108. Wang, Z. G.; Inoue, T. Analysis of Temperature and Elastic-Viscoplastic Stresses during Continuous Casting Process. In *Proc. of the Int. Conf. on Computational Mechanics;* 1986-5; pp 103–108.
109. Inoue, T.; Wang, Z. G. Thermal and Mechanical Fields in Continuous Casting Slab – a Steady State Analysis Incorporating Solidification. *Ing.-Arch.* **1988,** *58* (4), 265–275.
110. Inoue, T.; Ju, D. Y.; Yoshihara, N. Temperature and Viscoplastic Stresses during Vertical Semi-Continuous Direct Chill Casting of Aluminum Alloy. In *Proc. of the 2nd Int. Conf. on Residual Stresses, Nancy;* Elsevier, 1988-11; pp 523–528.
111. Inoue, T.; Ju, D. Y. Simulation of Solidification and Viscoplastic Stresses during Vertical Semi-Continuous Direct Chill Casting of Aluminum Alloy. *Int. J. Plast.* **1992,** *8* (2), 161–183.
112. Mizuno, M.; Matsuoka, T.; Inoue, T. Simulation of Centrifugal Casting Process of Metal Matrix Composite. In *Proc. of Int. Conf. on Computer-Assisted Materials Design and Process Simulation;* 1993-9; pp 30–35, Tokyo.
113. Okita, K.; Tsutsumi, K.; Iwasaki, K.; Fujita, M.; Hadano, H.; Yaguchi, H. Heat Treatment Simulation of Carburized Gears and Its Verification. In *Proc. of 2nd Int. Conf. on Distortion Engineering, Bremen;* 2008; pp 285–291.

This page intentionally left blank

12.07 Intensive Quenching

NI Kobasko and MA Aronov, IQ Technologies Inc., Akron, OH, USA

11.18.1	**Introduction**	483
11.18.2	**Nano-Surface Generation by Grinding**	483
11.18.3	**In-Process Dressing of Super Abrasive Wheel**	484
11.18.4	**History of ELID Grinding**	486
11.18.5	**Classifications of ELID Grinding**	488
11.18.5.1	Electrolytic In-Process Dressing	488
11.18.5.2	Electrolytic Interval Dressing	489
11.18.5.3	Electrodeless ELID	491
11.18.5.4	Electrodeless ELID	491
11.18.5.5	Ion Shot ELID	491
11.18.6	**Fundamental Study on ELID Grinding**	492
11.18.7	**Study Related to Control of ELID Grinding Process**	499
11.18.8	**Study Related to ELID Grinding Machine Development**	504
11.18.9	**Study Related to Application of ELID Grinding**	508
11.18.9.1	ELID on Ceramics	508
11.18.9.2	ELID on Coated Film	510
11.18.9.3	ELID on Metal	511
11.18.9.4	ELID on Optical Glasses	514
11.18.9.5	ELID on Silicon Wafer	517
11.18.10	**Conclusions**	520
References		520

12.07.1 Introduction

In this chapter, different applications of intensive quenching (IQ) techniques to actual steel products and test samples provided by parts manufacturers are discussed (*1–6*). Two intensive water-quenching methods are considered: an IQ-2 technique (a two- or three-step quenching process that initially cools parts under the nucleate boiling mode of heat transfer and then by convection) and an IQ-3 technique, also known as direct convection cooling (*6*).

The first step of the IQ-2 process involves intensive cooling without film boiling until a superficial layer of the part being quenched contains 50% martensite. At this point, the intensive cooling process is interrupted, and steel parts are removed from the quench and cooled in the air. During this period of time, the temperature is equalized throughout the part cross sections, and self-tempering of the newly formed martensite in the superficial layer occurs. Then the parts are moved back to the quench, and intensive cooling continues until the martensite transformation is completed, or until parts are cooled completely to the room temperature in the air.

In contrast to the IQ-2 method, the IQ-3 technique fully eliminates a boiling mode of heat transfer (both the film boiling process and the nucleate boiling process). This is accomplished by using powerful water jets or streams of water to lower the part surface temperature of the steel almost immediately to the temperature of the quenchant. In this case, a maximum thermal gradient between the part superficial layer and the core is created. The process of intensive cooling is performed until maximum surface compressive stresses are formed. Then, the parts are removed from the quench chamber, and the cooling process continues in the air.

Both the IQ-2 quench method and the IQ-3 method are suitable for a variety of steel products, including automotive and off-highway equipment components (coil springs, kingpins, torsion bars, bearing products, ball studs, gears, etc.), fasteners of different types, tool products (punches, dies, die components), and the like. For intensive quenching of steel parts, different IQ systems were designed and built. These systems are installed at the Center for Intensive Quenching in Cleveland, Ohio, at three commercial heat-treating shops and at one captive heat-treating shop. The data obtained during the last several years are presented in numerous papers and books and were discussed at different heat-treating conferences and forums (*5–11*). Prior to discussing these results, let us review the relationship between the quench cooling rate and hardened part mechanical properties.

Figure 1 shows a correlation between the part properties and part cooling rate for both conventional quenching and intensive quenching. The curve 'breaks' between the conventional and intensive quenching zones. This break illustrates that, in conventional quenching, the part starts experiencing severe distortion (or the ultimate in distortion: cracking) above a certain cooling rate. At that point, it is useless to quench faster in an attempt to obtain any further 'improvements' in the steel's mechanical properties on a distorted or broken part. As also shown in **Figure 1**, in the IQ zone, the part's mechanical properties are not only greater compared

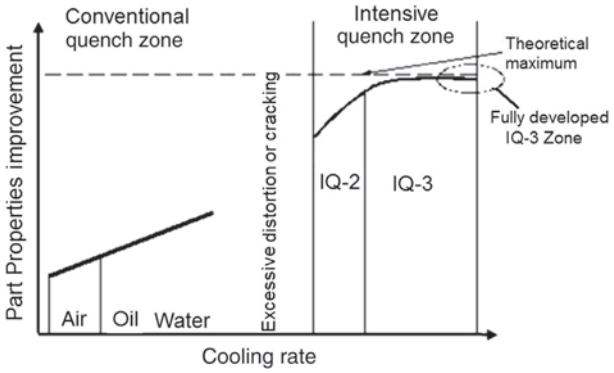

Figure 1 Steel part properties versus cooling rate.

to the conventional quench zone, but they continuously increase up to a certain 'ultimate' level for the given steel type. Once in the intensive quench zone, a faster quench rate on the part surface does not improve the part's properties. This is because at the initiation of the intensive quench, the part's surface temperature almost instantaneously becomes the same as the quenchant temperature. After a certain intensity of quench heat extraction, the part cannot give up its heat any faster than the rate of heat conduction through the part. This is why one cannot quench 'too fast' during the intensive portion of the quench. Once the part surface layer has reached the temperature of the quenchant, conduction within the part sets a natural limit on the rate of cooling in the subsurface layers and the core of the part. Since conduction is also a very rapid and very uniform form of heat removal, intensive quenching is able to reach the ultimate goal of any quench – the most uniformly rapid removal of heat that yields the less part distortion.

IQ-2 and IQ-3 processes provide the following proven benefits:

- Increases the depth of hardness.
- Eliminates surface cracking.
- Minimizes part distortion.
- Achieves the same or better metallurgical properties while using lower alloy, less costly steel.
- Provides an optimum combination of high-surface compressive stresses; high-strength, wear-resistant quenched layer; and relatively soft but properly strengthened core resulting in longer part life.
- Uses less costly, environmentally friendly quenchant (usually plain water), instead of expensive, hazardous oil.
- Shortens the duration, or fully eliminates, the carburizing cycle.
- Achieves a greater productivity of the quenching equipment due to a much faster cooling rate.

12.07.2 Basics of Intensive Quenching

12.07.2.1 A Bell-Shaped Curve

In 1964, a phenomenon was discovered (see **Figure 2**) that now is positioned to transform the quenching process (*1–4*). The essence of the IQ process is to quench the steel part uniformly and with a very high cooling rate (several times greater than that in the current, conventional quench process). With this IQ process, beneficial high residual compressive stresses develop on the part

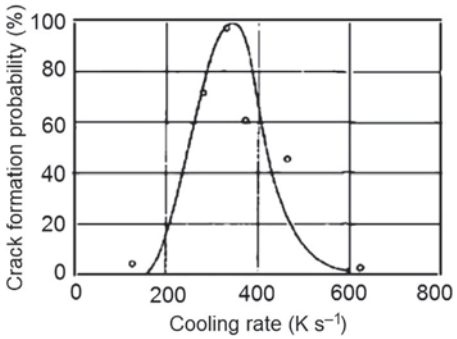

Figure 2 Effect of cooling rate within the martensite range on cracking in cylindrical samples of 6-mm diameter made of 40Kh steel (0.42% C, 0.60% Mn, 0.28% Si, 0.95% Cr, 0.25% Ni). Reproduced from Kobasko, N. I. *Steel Quenching in Liquid Media under Pressure*; Naukova Dumka: Kyiv, 1980; pp 206.

surface layer, resulting in the reduction of part distortion while concurrently reducing the probability of part cracking. This is in contrast to conventional quenching where there are usually tensile or neutral surface stresses at the end of quench.

In current heat-treating practice, when residual compressive stresses are required on a part surface, carburizing, induction hardening, or shot peening may be used. The IQ method, in many cases, can fully eliminate or significantly shorten the carburizing cycle, or it can fully eliminate shot peening operations. Both of these benefits result in tremendous energy savings, in an increase of heat-treating equipment productivity, and in reduction of heat-treating furnaces emissions.

An additional enhancement is that the IQ process provides superior performance characteristics in the hardened part. A significant added benefit is that the IQ process is environmentally friendly, as intensive quenching is conducted in plain water compared to conventional quenching, which usually uses environmentally unfriendly hazardous oil.

Figure 2 illustrates this new IQ paradigm. As seen from Figure 2, a bell-shaped curve characterizes the probability of cracking (or part distortion) as it relates to the quench cooling rate. The left side of the bell-shaped curve presents the conventional quenching zone, while the right side of the curve presents the previously unknown paradigm of the intensive quenching zone. The part's mechanical properties obtained by conventional quenching can be further improved (super-strengthened) by quenching the part in the IQ zone (see Figures 1 and 2). The discovered IQ phenomenon contradicts the common heat-treating practice and is so revolutionary in concept that multiple development demonstrations have been required to generate enough data to confirm to metallurgists that this alternative method of quenching steel products can dramatically transform conventional heat-treating approaches.

12.07.3 Intensive Quenching IQ-2 and IQ-3 Technologies

12.07.3.1 IQ-2 Technology

For an understanding of the IQ-2 process, let's consider a continuous cooling transformation (CCT) diagram presented in Figure 3. The CCT diagram shows a martensite start temperature M_s, which is about 180 °C. The same diagram presents experimental data on the measurement of the surface temperature of a cylindrical specimen of 20-mm diameter, made of stainless steel Kh18N9T (AISI 304). The specimen was quenched at various pressures: 0.1 and 0.7 MPa. Curve 1 is related to the pressure of 0.7 MPa, and curve 2 to normal atmospheric pressure, that is, 0.1 MPa.

During nucleate boiling, the temperature at the surface of the specimen is maintained approximately at the same level, which corresponds to the temperature of the boiling point of liquid (*11,12*). By changing a pressure above the quench bath, or by changing the concentration of special salt solutions, one can adjust the temperature at the surface of the specimen during nucleate boiling process to prevent crack formation. For the considered CCT diagram (Figure 3), the process can be performed with quenching parts in usual water at the atmospheric pressure. As shown in Figure 3, it is obvious that, at the atmospheric pressure (curve 2), the surface temperature of the cylindrical specimen reaches the martensite start temperature M_s in 1 s. The surface temperature maintains at the level of approximately 100 °C from about 2 s till 12 s. Note that no more than 50% of martensite is formed in the part surface layer during this time period. As it is known, the quenching cracks appear when there is more than 50% martensite in the surface layer of the part.

When nucleate boiling is completed, it is necessary to interrupt the intensive cooling and to keep the part in the air to equalize the temperature through the part cross section (*5,6*). This procedure will also result in a self-tempering of the newly formed martensite in the superficial layers. As a result of the self-tempering, mechanical properties of steel improve. Therefore, after keeping parts in the air and self-tempering of the superficial layer, it is possible to continue intensive cooling until the steel part is completely

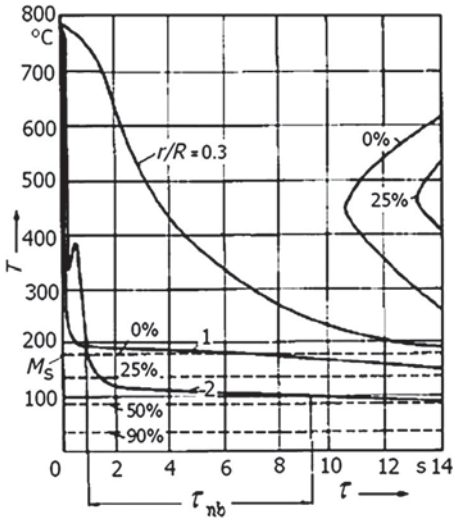

Figure 3 Pressure adjustment of the cylindrical part's (diameter 20 mm) surface temperature with water cooling at 20 °C Kobasko, N. I. Thermal Processes at Steel Quenching. *MiTOM* **1968**, 3, 3–8: 1, quenching under pressure 0.7 MPa; 2, quenching under pressure 0.1 MPa.

cooled without a quench crack formation. This technology is easily implemented for high-carbon steels with a low martensite start temperature (see Figure 3). The duration of the nucleate boiling process τ_{nb} (see Figure 3) can be calculated from eqn [1] (6):

$$\tau = \left[\Omega + f \ln \frac{\vartheta_I}{\vartheta_{II}}\right] \frac{K}{a} \quad [1]$$

where $\Omega = 0.48$; $f = 3.21$; $K = \dfrac{R^2}{5.783} = 108.1 \cdot 10^{-6} \text{m}^2$; $a = 5.36 \times 10^{-6}\ \text{m}^2\ \text{s}^{-1}$.

Values ϑ_I and ϑ_{II} can be calculated by eqn [2] and eqn [3]:

$$\vartheta_I = \frac{1}{\beta}\left[\frac{2\lambda(\vartheta_0 - \vartheta_I)}{R}\right]^{0.3} \quad [2]$$

$$\vartheta_{II} = \frac{1}{\beta}[\alpha_{\text{conv}}(\vartheta_{II} + \vartheta_{\text{uh}})]^{0.3} \quad [3]$$

According to the theory of similarity, one can calculate the heat-transfer coefficient (HTC) for natural convection (10):

$$Nu = 0.13(Gr \cdot Pr)^{1/3} \quad [4]$$

where $Nu = \dfrac{\alpha \ell}{\lambda}$;

$$Gr = g\beta' \Delta T \frac{\ell^3}{\nu^2};$$

$$Pr = \frac{\nu}{a}.$$

Here the temperature volumetric expansion β' characterizes a relative change in volume with the change of the temperature by 1°:

$$\beta' = \frac{1}{V}\left(\frac{\partial V}{\partial T}\right)_{p=\text{const}}$$

α is a heat-transfer coefficient ($\text{W m}^{-2}\text{K}^{-1}$); ℓ is a characteristic geometrical size (m); λ is the heat conductivity of liquid (W m K^{-1}); g is a gravitational acceleration (m s^{-2}); ΔT is a temperature difference; ν is a kinematic viscosity ($\text{m}^2\ \text{s}^{-1}$); and a is a thermal diffusivity of a liquid ($\text{m}^2\ \text{s}^{-1}$).

Equation [4] can be reduced to the following:

$$\alpha_{conv} \approx 0.13\lambda' \left(\frac{g\beta\Delta T'}{a\nu}\right)^{1/3} \quad [5]$$

Let's calculate the HTC at a time of the transition from nucleate boiling to natural convection. It occurs when the part surface temperature is equal to 100 °C. As an example, let's consider cylindrical samples of different diameters and heights which are cooled from the temperature of 860 °C in the water having a temperature of 20 °C. Physical properties of water at 20 °C are provided below:

$\lambda' = 0.597\ \text{W m}^{-1}\ \text{K}^{-1}$;
$\beta' = 1.82 \times 10^{-4}\ \text{K}^{-1}$;
$\nu = 1.996 \times 10^{-6}\ \text{m}^2\ \text{s}^{-1}$;
$g = 9.81\ \text{m s}^{-2}$;
$a = 14.3 \times 10^{-6}\ \text{m}^2\ \text{s}^{-1}$;
$\Delta T = 100 - 20\ °\text{C} = 80\ °\text{C}$.

Substituting these values into eqn [5], we obtain the following value for the HTC:

$$\alpha_{conv} \approx 0.13 \times 0.597\left(\frac{9.81 \times 1.82 \times 10^{-4} \times 80}{14.3 \times 10^{-6} \times 1.996 \times 10^{-6}}\right)^{1/3} \approx 1020\ \text{W m}^{-2}\text{K}^{-1}$$

To calculate the duration of the nucleate boiling process, eqns [1]–[3] can be used.

Table 1 Heat conductivity of supercooled austenite versus temperature

T, °C	100	200	300	400	500	600	700	800	900
λ, $\text{W m}^{-1}\text{K}^{-1}$	17.5	18	19.6	21	23	24.8	26.3	27.8	29.3
$\bar{\lambda}$, $\text{W m}^{-1}\text{K}^{-1}$	17.5	17.75	18.55	19.25	20.25	21.15	21.90	22.65	23.4

Note: $\bar{\lambda}$ at 500 °C is the mean average value for the range of 100–500 °C (analogously at other temperatures).

Table 2 Thermal diffusivity *a* of supercooled austenite versus temperature

T, °C	100	200	300	400	500	600	700	800	900
$a \cdot 10^6$, $m^2 s^{-1}$	4.55	4.63	4.70	4.95	5.34	5.65	5.83	6.19	6.55
$\bar{a} \cdot 10^6$, $m^2 s^{-1}$	4.55	4.59	4.625	4.75	4.95	5.10	5.19	5.37	5.55

Note: $\bar{a}$ at 500 °C is the mean average value for the range of 100–500 °C (analogously at other temperatures).

Table 3 Kondratjev form factors and duration of nucleate boiling process depending on size of finite cylinders

Cylindrical sample D × H (mm)	ϑ_I, °C	ϑ_{II}, °C	K × 10^6, m^2	τ_{nb}, s
10 × 50	26	7.1	4.32	3.65
14 × 60	23.6	7.1	8.47	6.68
20 × 40	21.2	7.1	15.62	11.3
20 × 80	21.2	7.1	16.84	12.2
30 × 60	18.8	7.1	35.16	23
30 × 120	18.8	7.1	37.90	24.8
40 × 40	17.2	7.1	48.48	29.3
40 × 160	17.2	7.1	67.37	40.7
50 × 50	16.1	7.1	75.75	42.8
50 × 100	16.12	7.1	97.66	55.3
50 × 200	16.12	7.1	105.3	59.6

Table 4 Experimental data on duration of nucleate boiling process depending on size of cylindrical specimens according to Ref. (*10*)[a]

Cylindrical specimen, D × H, mm	Duration, s (experiment)	Duration, s (calculation)
10 × 50	3.8	3.65
50 × 100	50	55.3

[a]*Kobasko, N. I.; Aronov, M. A.; Powell, J. A.; Totten, G. E. Intensive Quenching Systems: Engineering and Design; ASTM International: West Conshohocken, 2010; pp 252.*

Equations [2] and [3] require knowing the value of β and HTC at natural convection. According to Kutateladze, $\beta = 4.3$ (*12,13*), and, at the time of transition from nucleate boiling to a natural convection, the HTC during cooling in still water at 20 °C is approximately equal to 1020 $W m^{-2} K^{-1}$.

Thermal properties of steel depending on temperature are provided in **Table 1** and **Table 2**.

To calculate the duration of the nucleate boiling process, one needs to calculate $\vartheta_I, \vartheta_{II}$ values using eqn [2] and eqn [3]:

$$\vartheta_I = \frac{1}{4.3}\left[\frac{2 \times 23 \times (760 - \vartheta_I)}{0.005}\right]^{0.3} = 26\ ^\circ\mathrm{C}$$

The Kondratjev form factor (K) for a finite cylinder is equal to (*10*):

$$K = \frac{1}{\frac{5.783}{R^2} + \frac{9.87}{H^2}}$$

Kondratjev form factors for different cylinders are provided in **Table 3**.

The average thermal diffusivity of steel is equal to 5.5×10^{-6} $m^2 s^{-1}$.

Knowing these data, we can easily calculate the duration of the nucleate boiling process for different cylinders.

A continuous line presented in **Figure 4** can be used for implementing the IQ-2 process (*10*) (**Tables 4 and 5**).

The industrial continuous line presented in **Figure 4** operates in the following way. A conveyor furnace HT1 is loaded automatically in section I. The furnace HT1 is connected to a computer control device, which is schematically shown at the top in **Figure 4**. A speed of the furnace conveyor movement is set by a computer, depending on the shape and sizes of the steel parts and the chemical composition of the material. The parts being heated to the austenitization temperature are delivered to the shoot II, where an intensive circulation of the quenchant is provided. The quenchant may be an aqueous solution of neutral salts of optimal concentration. The quenchant provides a maximal value of the first critical heat flux density q_{cr1}. In addition, aqueous solutions of salts prevent corrosion of metal surfaces. An intensive circulation of the quenchant at section II and an optimal concentration of the aqueous solution eliminate film boiling or make it practically vanish.

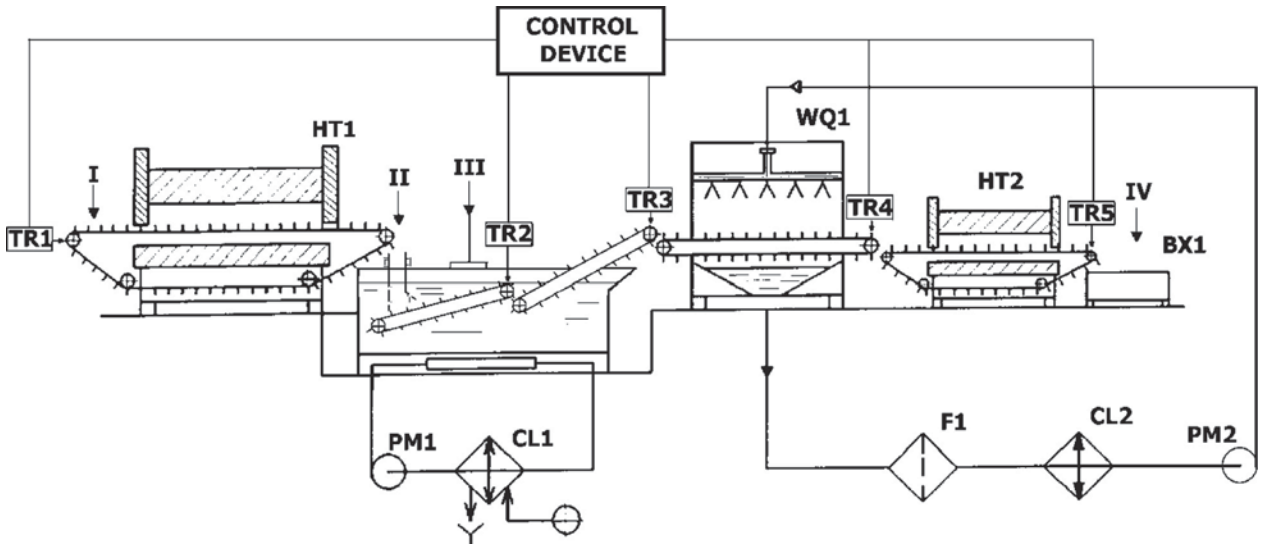

Figure 4 Schematic explaining IQ-2 technology implementation: I, loading point for steel parts onto the conveyor for heating in furnace HT1; II, chute with intensive cooling devices; III, quenching tank with two conveyors; IV, unloading point of steel parts from furnace HT2; TR1–TR5, speed control units for conveyor belts 1, 2, 3, 4, and 5 operated by the control device; HT1 and HT2, furnaces 1 and 2; WQ1, washing and quenching device; PM1 and PM2, pumps 1 and 2; CL1 and CL2, chillers 1 and 2; F1, filter; BX1, container for heat treated parts.

When hot parts fall through shoot II onto the first conveyor, they are cooled very intensively since there is no film boiling and since the part surface temperature is kept at the level of the quenchant boiling temperature. For pure water, this level is equal to 100 °C. Depending on the shape and sizes of parts being quenched, the furnace control system sets a certain speed of the movement of the first conveyor in the quench tank. The first conveyor speed is calculated using eqn [1]. The parts are removed from the quench when the nucleate boiling process is completed, or when the current compressive stresses in superficial layers reach their maximum value. The first conveyor delivers the quenched parts to the second conveyor, where the temperature through the part cross sections equalizes in the air and the formed martensite layer at the surface of the parts is self-tempered.

The speed of the second conveyor is also regulated by the control system through drive TP3. Equalizing the temperature through the part cross section during cooling in the air may be checked by means of a special semiconductor sensor (like a barometer), which determines the time of reaching the maximal temperature on the part surface during the self-tempering process. The quenchant temperature is kept at the constant level by means of chiller TX1. To maintain an optimal concentration of the solution, it is necessary to check it from time to time. The self-tempered parts get to the next conveyor (see UD1), where they are washed and further cooled intensively. The speed of the conveyor is regulated by the control system through drive TP4. The water temperature in a washing tank is also kept at the constant level by means of chiller TH2. The washed out parts then get to the tempering furnace EP2, where they are finally tempered. The speed of the conveyor of the tempering furnace is regulated by the control system through drive TP5. The fully processed parts are collected in store JAN1.

Table 5 Martensite start temperature M_S and temperature M_{50} at which 50% of martensite for some tool steels is formed

Steel grade	*Austenization temperature, °C*	*Carbon content, %*	*°C*	
			M_s	M_{50}
R18 (AISI M41)	1230	0.81	160	80
	1290	0.81	140	60
R12 (AISI M41)	1210	0.87	210	120
	1270	0.87	155	77
Kh12 (AISI D3)	950	2.07	210	115
	970	2.08	184	110
	1050	2.08	70	–
	1180	2.07	−85	–
U12 (AISI W1)	800	1.15–1.24	200	–
ShKh15 (AISI 52100)	860	0.95–1.10	245	–

Figure 5 Production IQ system installed at Akron Steel Treating Co.

Figure 6 Picture of production IQ system installed at Euclid Heat Treating Co.

Considering the above basic schematic of the industrial line for implementing the IQ-2 process, one can see that designing and running this line require knowledge of the regularities of part heating and cooling processes and ways of optimizing these processes (*13–18*).

Let's consider a specific example of the implementation of the IQ-2 process in the industrial line described above. Certainly, the simplified engineering calculations require more accurate computations through the computer simulation. Such a computer simulation may not produce effective results, if there are no correct initial data (*10*).

Further developments of IQ-2 processes were made by IQ Technologies Inc. and implemented in the heat-treating practice, and their optimization by computer simulation was provided by authors (*10,19–28*). For example, the Akron Steel Treating Co. (AST) of Akron, Ohio, has one production 6000-gallon IQ water tank that is equipped with an atmosphere surface combustion furnace (**Figure 5**).

The furnace is located across the aisle from the IQ tank. The IQ water tank is fully automated. It is equipped with a fast moving load-lifting mechanism to reduce the time required for loading/unloading the parts during intensive quench. AST has also developed a standard procedure for controlling a concentration of the sodium nitrite in the IQ water tank, water temperature, and rate of the quenchant agitation. Full automation of the IQ water tank and precise control of the quench parameters allow intensive quenching of a variety of steel products. These products include gear blanks made of alloy 4140 and 4340 steels used for manufacturing rack and pinion gears for different actuators, a variety of cast products made of 8630 steel, fasteners, and so on.

The Euclid Heat Treating Co. (EHT) of Cleveland, Ohio, acquired its first IQ production unit (see **Figure 6**) from AFC-Holcroft, Inc. in 2004. It is a three-chamber, integral quench, batch-type furnace with working dimensions of $91 \times 91 \times 183$ cm ($36'' \times 36'' \times 72''$) for implementing the batch IQ process. Note that when using an integral quench-type furnace with the water quench tanks, one of the major issues is the possible contamination of the furnace's protective atmosphere by water vapors coming from the quench tank into the furnace heating chamber. This may happen while the inner furnace door is open and the

Figure 7 UJ crosses.

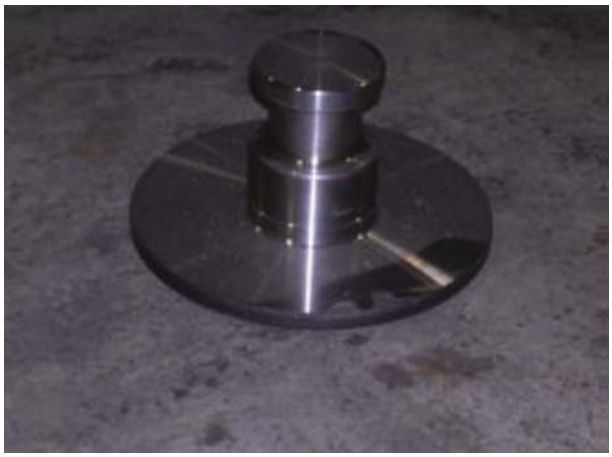

Figure 8 Kingpin.

Figure 9 Base key.

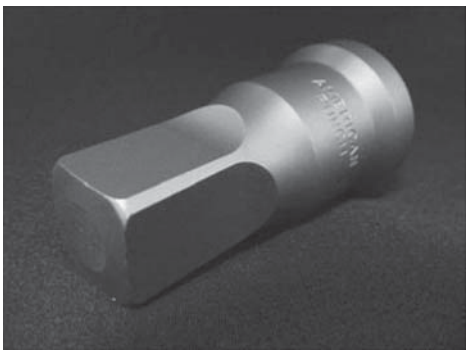

Figure 10 S5 punch intensively quenched by use IQ-2 process.

Figure 11 AISI 8630 steel casting, 4″ × 4″ × 9″.

load is moved from the furnace to the quench tank, or even when the door is closed by migration around the door. To solve this problem, the AFC-Holcroft Co. proposed a three-chamber design approach similar to the integral atmosphere furnaces using melted salts.

Some examples of steel parts processed in batches in the above two industrial IQ systems are shown in Figures 7–11.

The service life of punches after intensive quenching (IQ-2 processing) increases 2–8 times as compared with oil quenching (*10*). Customers indicate that in average service life of punches increases 5 times as compared with oil quenching. The mechanical properties of AISI 8630 steel after IQ-2 processing are provided in Table 6.

12.07.3.2 IQ-3 Technology, Quenching in High-Velocity Water Flow

The quenching of steel parts in a high-velocity water flow (of 8–10 m s^{-1}) was used for the first time in 1967 for truck semiaxles produced by the automotive plant ZIL of Moscow, Russia (*2,3*). The metallurgists of ZIL were the first heat treaters who have paid a special attention to intensive methods of quenching (*2,3,6*). A schematic of the automated production-intensive quenching (IQ) unit used for processing semiaxles is shown in Figure 12. The IQ unit was equipped with a set of sensors for controlling the nucleate and film boiling process and for analyzing the steel microstructure (a percent of transformed austenite) (*8*).

A configuration of the quench chamber 2 (Figure 12) was of two types (see Figure 13).

A water-flow velocity in the quench chamber required for realizing the IQ-3 process depends on the semiaxles diameter and is calculated from the following equation (*10*):

Table 6 Mechanical properties of cast steel AISI 8630 after oil quenching and after IQ-2 process

	Oil quenching				*IQ process*			
Steel after casting	R_m, *ksi*	$R_{p0.2}$, *ksi*	A, *%*	Z, *%*	R_m, *ksi*	$R_{p0.2}$, *ksi*	A, *%*	Z, *%*
AISI 8630	120	95	12	25	132	110	16	38

R_m , ultimate strength; $R_{p0.2}$, yield strength; A, elongation; Z, reduction area.

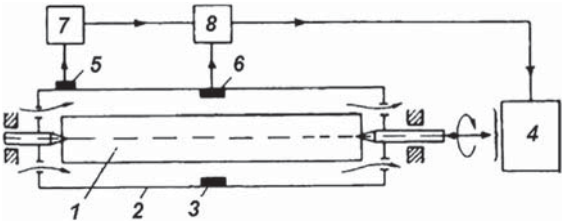

Figure 12 Detailed scheme of quench chamber with automatic control Kobasko, N. I. Intensive Steel Quenching Methods. In *Handbook: Theory and Technology of Quenching*; Liscic, B., Tensi, H. M., Luty, W., Eds.; Springer -Verlag: Berlin, 1992; pp 367–389; Kobasko, N. I. Thermal Processes at Steel Quenching. *MiTOM* **1968**, 3, 3–8 and Kobasko, N. I.; Aronov, M. A.; Powell, J. A.; Totten, G. E. *Intensive Quenching Systems: Engineering and Design*; ASTM International: West Conshohocken, 2010; pp 252. 1, semiaxle; 2, quench chamber; 3, pressurized water flow; 4, mechanical drive for semiaxles; 5, sensor for analyzing the process of nucleate and film boiling; 6, sensor for analyzing the portion of transformed structures by the changing ferromagnetic state; 7, electronic device (amplifier and microprocessor); 8, amplifier.

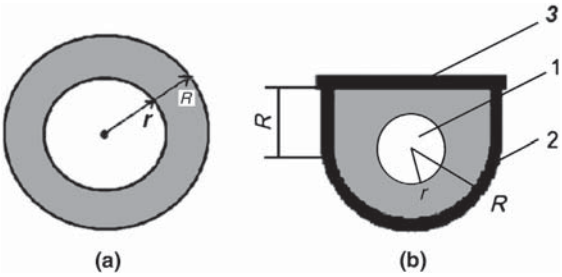

Figure 13 Cross section of round (a) and U-shaped (b) quench chambers used for truck semiaxles Kobasko, N. I.; Aronov, M. A.; Powell, J. A.; Totten, G. E. *Intensive Quenching Systems: Engineering and Design*; ASTM International: West Conshohocken, 2010; pp 252.: 1, semiaxle of 60-mm diameter; 2, U-shaped chamber consisting of a half-cylinder of 40-mm radius and additional side walls *R* of 40-mm height; 3, cover of the chamber.

$$Bi = \frac{2(\vartheta_0 - \vartheta_I)}{\vartheta_I + \vartheta_{\text{uh}}} \qquad [6]$$

where $\vartheta_0 = T_0 - T_S$; $\vartheta_{\text{uh}} = T_S - T_m$; ϑ_I is calculated from eqn [2].

Knowing the heat-transfer coefficient (HTC) from eqn [6], we can easily calculate a Nusselt number *Nu*, which, in turn, allows calculating a Reynolds number *Re* from eqn [7] and consequently the water flow velocity. A characteristic size d_{eq} used for calculating the Nusselt number depends on the configuration of the quench chamber (see **Figure 13**) and is discussed in more detail below.

For the forced convection, a general expression for the Nusselt number is the following (*10*):

$$Nu = f(Re, Pr). \qquad [7]$$

where a criterion of Reynolds is equal to $Re = \frac{wD}{\nu}$ and a criterion of Prandtl is equal to $Pr = \frac{\nu}{a}$. Let's consider in more detail a cooling process of parts in ring channels since such systems are most often used in practice and have a direct relation to the IQ process.

A generalized similarity equation for a forced stream of a liquid in ring channels of any cross section shape is the following (*17,18*):

$$\overline{Nu} = 0.021 \ Re^{0.8} \cdot Pr^{0.43} \left(Pr_m / Pr_{sf}\right)^{0.25} \cdot \varepsilon_e \qquad [8]$$

For quenching, the liquid (quenchant) properties used for calculating *Nu*, *Re*, Pr_m, and Pr_{sf} numbers are determined at an average quenchant temperature in the quench chamber. A characteristic size d_{eq} (used for calculating *Nu* and *Re* numbers) is equal to:

$$d_{\text{eq}} = \frac{4S}{u} \qquad [9]$$

where *S* is the area of the channel cross section (see **Figure 13**) and *u* is a full perimeter of the channel (**Figure 13**).

For pipes of a round cross section, the equivalent diameter d_{eq} is equal to a geometrical diameter *d*.

The factor ε_e takes into account the change in the average heat-transfer coefficient depending on the ratio $\frac{L}{d_{\text{eq}}}$ and Reynolds number (*14*) (here *L* is the length of the steel part).

If $\ell/d > 50$, $\varepsilon_e = 1$. At $\ell/d < 50$, it is necessary to take into account the effect of the ratio $\frac{L}{d_{\text{eq}}}$ (*10*). The multiplier $(Pr_m/Pr_{sf})^{0.25}$ represents a correction that takes into account a dependence of the quenchant physical properties (mainly viscosity) on the temperature. Depending on a direction of the heat flux, this correction factor can be either greater or less than 1. More particulars on the single-phase convection are presented in Refs. (*10,13*).

Let's consider a concrete example. The task is to determine a convection heat-transfer coefficient at the time of transition from nucleate boiling to a single-phase convection for the truck semiaxles of 0.060 m diameter and 0.8 m length. The semiaxle is

quenched by a water flow of 8 m s^{-1} in the U-shaped chamber shown in Figure 13. The average pressure in the quench chamber is 0.143 MPa. First, one should calculate an equivalent diameter of the cross section of the quench chamber using eqn [9].

A fourfold area of the cross section of the quench chamber is equal to:

$$4S = 2(\pi + 4)R^2 - 4\pi r^2 = 1.95 \cdot 10^{-3}\ \mathrm{m}^2$$

A full wetted perimeter U is equal to:

$$U = (\pi + 4)R - 2\pi r^2 = 0.474\ \mathrm{m};$$

Therefore, the equivalent diameter d_{eq} is equal to $d_{eq} = \frac{4S}{U} = \frac{1.95 \cdot 10^{-3}\ \mathrm{m}^2}{0.474\ \mathrm{m}} = 4.11 \cdot 10^{-3}\mathrm{m}$.

A ratio of the length of the chamber ℓ to the equivalent diameter d_{eq} is equal to $\varepsilon_\ell = \ell/d_{eq} = \frac{0.8}{0.00411} \approx 195$; therefore, ℓ/d_{eq} is much greater than 50.

Let us calculate a temperature factor $\left(\frac{Pr_m}{Pr_{sf}}\right)^{0.25}$. Assuming that the water temperature in the quench chamber is 20 °C, the wall temperature at the pressure of 0.143 MPa is equal approximately to 110 °C. At the specified temperatures, $Pr_m = 7.03$; $Pr_{sf} = 1.60$ (*10,18*). Therefore $\left(\frac{Pr_m}{Pr_{sf}}\right)^{0.25} = 1.45$.

Based on the above calculations, dimensionless dependence eqn [9] can now be written as follows:

$$\overline{N}u = 0.03Re^{0.8} \cdot Pr^{0.43} \qquad [10]$$

For the water temperature of 20 °C, $Pr^{0.43} = 2.31$ and $Re^{0.8} = \frac{8\ \mathrm{m\ s^{-1}} \cdot 4.11 \cdot 10^{-3}\mathrm{m}}{1.006 \cdot 10^{-6}\ \mathrm{m^2\ s^{-1}}} = (32684)^{0.8} = 4088$.
Thus,

$$\overline{N}u = 0.03 \times 4088 \times 2.31 = 283.3$$

$$\overline{N}u = \frac{\alpha}{\lambda} d_{eq} \text{ or } \alpha_{conv} = \frac{Nu\lambda}{d_{eq}}$$

Therefore $\alpha_{conv} = \frac{283.3 \cdot 0.597\ \mathrm{W\ m^{-1}\ K^{-1}}}{0.00411\ \mathrm{m}} = 41150\ \mathrm{W\ m^{-2}K^{-1}}$.

A described process of cooling of the semiaxle is, in fact, an intensive quenching process since the Bi number for the semiaxle of 60-mm diameter is equal:

$$Bi = \frac{41150\ \mathrm{W\ m^{-2}K^{-1}} \times 0.03}{22\ \mathrm{W\ m^{-1}K^{-1}}} = 56, \text{ which is equivalent to } Bi \to \infty.$$

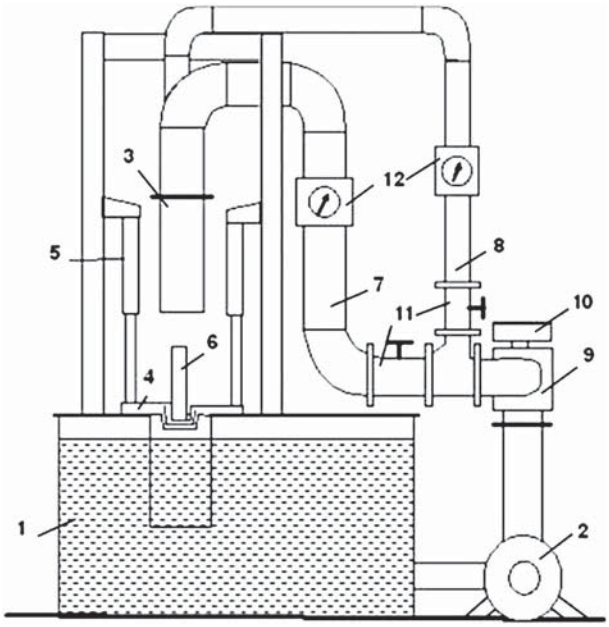

Figure 14 General schematic of high-velocity IQ unit. Kobasko, N. I.; Aronov, M. A.; Powell, J. A.; Totten, G. E. *Intensive Quenching Systems: Engineering and Design*; ASTM International: West Conshohocken, 2010; pp 252.

Figure 15 High-velocity IQ system for processing parts of up to 200 mm diameter and 500 mm length installed at Euclid Heat Treating Co.

Figure 16 High-velocity IQ system for processing shafts of up to 50 mm diameter and 910 mm length installed at Euclid Heat Treating Co.

Over the last several years, IQ Technologies Inc. has designed and manufactured several production IQ systems for implementing an IQ-3 process in a high-velocity water flow (*21–31*). A general schematic of a high-velocity IQ unit is presented in **Figure 14** (*10*).

The IQ-3 system consists of the following major components:

- Water tank, 1
- Pump, 2
- Vertical quench chamber that consists of two sections: the stationary upper section, 3, and the movable loading lower section, 4.
- Four air cylinders, 5, that move up and down the lower section, 4, with the part, 6, to be quenched.
- Three water lines: two lines, 7 and 8, that provide the water flow through the quench chamber and one 'bypass' water line (not shown on the sketch) that is used in 'idle' conditions immediately before or after the intensive quenching is done.
- Three-way valve, 9, with actuator, 10, that provides water flow from the pump either through the quench chamber or through the bypass line.
- Two control valves, 11, and two flow meters, 12, installed on the water lines leading to the quench chamber and used for controlling the water flow.

The IQ-3 quench sequence is as follows. With the pump operating and the three-way valve in the bypass position, an austenitized part is placed in the lower section of the quench chamber. The air cylinders move the lower section up to the stationary upper section and lock (seal) the quench chamber in place. The three-way valve switches from the 'bypass' to the 'quench' position, and high-velocity water starts flowing through the quench chamber and over the part. When intensive quenching is completed, the

Figure 17 High-velocity IQ system for processing torsion bars.

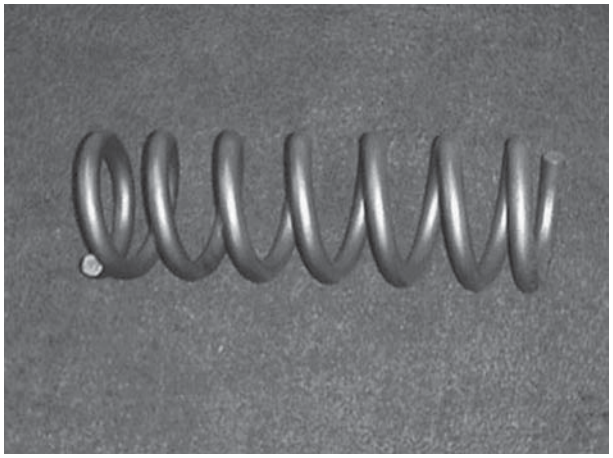

Figure 18 Coil spring.

Figure 19 Output shaft.

three-way valve switches back to the bypass position and the water stops flowing through the quench chamber and flows through the bypass line. The air cylinders open the quench chamber by moving the lower section down. The part is removed from the lower section of the quench chamber.

Figures 15–17 present pictures of production high-velocity IQ systems.

Figure 20 Bearing roll.

Figure 21 Side pinion.

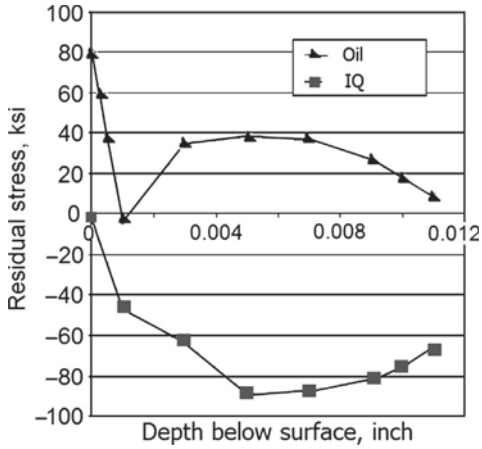

Figure 22 Coil spring surface residual stress for as-quenched conditions.

The high-velocity IQ system (Figure 15) is installed at Euclid Heat Treating Co. (EHT) in Cleveland, Ohio. This unit is designed for processing parts of up to 200 mm diameter and 500 mm length. These parts include gears, shafts, and bearing rings. The IQ system is equipped with a chiller for maintaining the water temperature and with an atmosphere box furnace for austenitizing the parts prior to quenching.

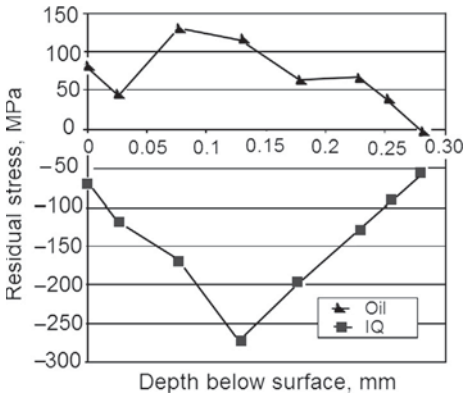

Figure 23 Coil spring surface residual stresses for as-tempered conditions.

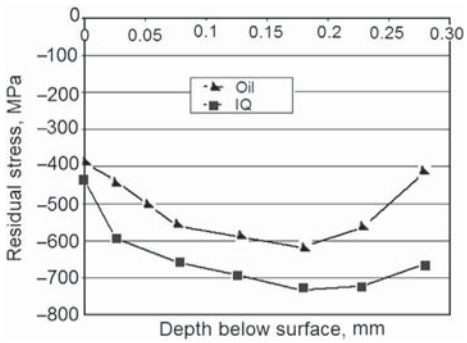

Figure 24 Coil spring surface residual stresses for as-shot peened conditions.

Table 7 Torsion bar microstructure improvement (% of bainite)

Quench	*Oil*	*IQ*
Surface	3	0
½ radius	12	2
Center	29	2.5

The high-velocity IQ system presented in Figure 21 is also installed at the EHT Company. It is designed for processing long shafts of up to 50 mm diameter and up to 910 mm length. The IQ unit is equipped with a chiller and with an induction heating station for austenitizing the shafts. Induction heating of the parts can be conducted in a protective atmosphere.

The high-velocity IQ system shown in Figure 22 is installed in one of the automotive plants in Canada and is designed for processing torsion bars of up to 50 mm diameter and 1520 mm length. In contrast to the above high-velocity IQ units, torsion bars are quenched in horizontal orientation.

Figures 18–21 present pictures of some parts processed in high-velocity IQ-3 systems.

The IQ-3 process provides steel parts with superior mechanical properties and performance characteristics (*22–28*). For example, an extensive IQ demonstration study for automotive coil springs conducted together with ArvinMeritor Automotive, Inc. of Detroit, Michigan, showed greater residual surface compressive stresses, resulting in a better spring fatigue life (*10*).

Figures 22–24 present the surface residual stresses in the intensively quenched springs and oil-quenched springs at the as-quenched condition and as-tempered condition, as well as after shot peening. As seen in Figure 22, the oil-quenched coil spring generally exhibits tensile residual stresses, whereas the intensively quenched spring exhibits compressive residual stresses that increase from −18 MPa on the very spring surface to −613 MPa at the depth of 0.13 mm. (The lower values of the residual stresses in the thin surface layer of the intensively quenched springs are due to slight decarburization of the spring-wire material during heating in the neutral salt bath furnace prior to quenching.) After tempering, the compressive residual stresses decrease on the intensively quenched coil springs; however, the stresses are still compressive (up to −276 MPa) and not tensile, as shown in Figure 23. The shot peening provides compressive stresses on the oil-quenched springs (Figure 24); however, they are less than the compressive stresses on the intensively quenched springs after shot peening, generally by about 138–276 MPa in the measured surface layer of 0.28 mm in depth. Note that residual stress distribution can be calculated using existing software (*10,26–29*).

The fatigue test results revealed that, on average, the intensively quenched coil springs completed approximately 33% more cycles than the oil-quenched springs. The Weibull statistical analysis showed that the B10 and B50 life was higher for the intensively quenched springs by about 27%.

An IQ study conducted for torsion bars of Ø36 mm made of 5160 steel demonstrated a significant improvement of the part microstructure (**Table 7**).

An IQ demonstration study conducted for the output shaft (see **Figure 19**) showed that the currently used alloy steel can be substituted by plain carbon AISI 1050 steel for the same part fatigue life. Very important experiments and calculations concerning the intensive quenching of cylindrical samples were made recently also by authors (*30,31*).

12.07.4 Discussion

Over the last several years, IQ Technologies Inc. and its customers have conducted numerous studies of mechanical properties of actual parts that were intensively quenched (*26–28*). The data were compared to the same parts quenched in oil. In all instances, the oil-quenched parts and intensively quenched parts were made from the same steel heat and were tempered to the same surface hardness. The intensively quenched parts have shown superior mechanical properties.

The data presented in this work clearly demonstrates that the IQ process significantly improves the mechanical properties of steel. Another important benefit of the IQ process is that it improves both the part strength and the part toughness at the same time. In addition, the environmental and cost benefits from the elimination of quench oils or quench polymers when using IQ should be noted.

The IQ technology provides the following benefits:

- Reduced energy consumption in heat-treating and forging operations due to a significant reduction or full elimination of the energy-consuming carburization cycle.
- Higher production rates of heating and quenching equipment, shorter cycle times, and reduced lead times.
- Reduced part distortion and less post-heat-treat processing as compared with conventional water quenching.
- Cleaner and safer working environment; reduced hazardous waste generation in heat-treating operations (no oil).
- Improved market competitiveness for the United States' equipment manufacturers, parts suppliers, and heat treaters.
- Products with improved quality and performance characteristics (better metal hardness, strength, wear resistance, and service life, lighter yet stronger product, etc.).

12.07.5 Summary

1. IQ process is a computer-controlled, interrupted water-quenching method. It differs from standard water quenching by an extremely high water agitation rate that completely eliminates *noncontrollable* film boiling during the quenching process, resulting in more uniform and faster part cooling, no part cracking, and better part performance.
2. IQ-2 and IQ-3 processes can provide higher power density parts (lighter yet stronger steel parts with improved mechanical properties, residual surface compressive stresses, and wear and fatigue resistance) (*12*).
3. IQ technology is a clean, environmentally friendly quenching process: No hazardous oils or environmentally unfriendly polymers are used.
4. Part cost reduction by substitution of plain carbon steels for more expensive alloy steels is achieved by use IQ technologies.
5. IQ technology allows reduction of process cost by saving energy: It significantly reduces the carburization cycle or completely eliminates carburization.
6. Heat-treatment operations can be integrated or embedded in the part manufacturing cell for in-line, single-part processing.

References

1. Kobasko, N. I.; Prokhorenko, N. I. Effect of Cooling Rate during Quenching upon Crack Formation in Steel 45. *Metallovedeniye I Termicheskaya Obrabotka Metallov (MiTOM)* **1964,** *2,* 53–54.
2. Correspondence Reader's Conference at Lichachev Plant. *MiTOM* **1965,** *6,* 72.
3. Bogatyrev, Ju. M.; Shepelyakovskii, K. Z.; Shklyarov, I. N. Cooling Rate Effect on Crack Formation at Steel Quenching. *MiTOM* **1967,** 15–22.
4. Kobasko, N. I. Crack Formation at Steel Quenching. *MiTOM* **1970,** *11,* 5–8.
5. Kobasko, N. I. *Steel Quenching in Liquid Media under Pressure;* Naukova Dumka: Kyiv, 1980; pp 206.
6. Kobasko, N. I. Intensive Steel Quenching Methods. In *Handbook: Theory and Technology of Quenching;* Liscic, B., Tensi, H. M., Luty, W., Eds.; Springer–Verlag: Berlin, 1992; pp 367–389.
7. Kobasko, N. I. Thermal Processes at Steel Quenching. *MiTOM* **1968,** *3,* 3–8.
8. Kobasko, N. I. Self-Regulated Thermal Process during Part Quenching. *Promteplotekhnika* **1998,** *20* (5), 10–14.
9. Kobasko, N. I. Increase in Service Life and Durability of Steel Parts for the Account of Use the New Steel Quenching Methods. *MiTOM* **1989,** *9,* 7–14.
10. Kobasko, N. I.; Aronov, M. A.; Powell, J. A.; Totten, G. E. *Intensive Quenching Systems: Engineering and Design;* ASTM International: West Conshohocken, 2010; pp 252.
11. Kutateladze, S. S. *Heat Transfer at Condensation and Boiling;* Mashgiz: Moscow, 1952.
12. Tolubinsky, V. I. *Heat Transfer at Boiling;* Naukova Dumka: Kyiv, 1980.

13. Ganiev, R. F.; Kobasko, N. I.; Kulik, V. V., et al. *Oscillation Phenomena in Multi-Phase Media and Their Use in Technology;* Tekhnika: Kyiv, 1980; pp 142.
14. Kobasko, N. I.; Morganyuk, V. S. Numerical Study of Phase Changes, Current and Residual Stresses at Quenching Parts of Complex Configuration. In *Proceedings of the 4th International Congress of Heat Treatment Materials, Berlin*, 1985; Vol. 1, pp 465–486.
15. Kobasko, N. I.; Morganyuk, V. S. *Investigation of Thermal and Stress-State in the Process of Heat Treatment;* Znanie: Kyiv, 1981.
16. Kobasko, N. I.; Morhuniuk, W. S. *Issledovanie teplovogo I napriazhenno- eformirovannogo sostoyaniya pri termicheskoy obrabotke izdeliy mashinostroeniya (Study of Thermal and Stress-Strain State at Heat Treatment of Machine Parts);* Znanie: Kyiv, 1983.
17. Lienhard, J. H., IV; Lienhard, VJ. H. *A Heat Transfer Textbook,* 3rd ed.; Phlogiston Press: Cambridge, Massachusetts, 2005.
18. Isachenko, V. P.; Osipova, V. A.; Sukomel, A. S. *Teploperedacha (Heat Transfer);* Energomash: Moscow, 1981; pp 417.
19. Freborg, A. M.; Ferguson, B. L.; Aronov, M. A.; Kobasko, N. I.; Powell, J. A. Intensive Quenching Theory and Application for Imparting High Residual Surface Compressive Stresses in Pressure Vessel Components. *SAE J. Pressure Vessel Technol.* **2003,** *125,* 188–194.
20. Freborg, A. M.; Li, Z.; Ferguson, B. L.; Schwann, D. *Improving the Bend Fatigue Strength of Carburized Gears, MS&T '04,* Vol. 4; ASM International: Materials Park, OH, 2004; pp. 227–234.
21. Inoue, T.; Arimoto, K. Development and Implementation of CAE System "Hearts" for Heat Treatment Simulation Based on Metallo-thermo-mechanics. *J. Mater. Eng. Perform.* **1997,** *6* (1), 51–60.
22. Kobasko, N. I. Basics of Intensive Quenching. *Adv. Mater. Process.* **Sept 1995,** *9*, 42W-42Y.
23. Kobasko, N. I. Part II: Basics of Intensive Quenching. *Adv. Mater. Process.* **Aug 1996,** *8*, 40CC-4EE.
24. Kobasko, N. I. Part III: Basics of Intensive Quenching. *Adv. Mater. Process.* **Feb 1998,** *2.*
25. Kobasko, N. I. Part IV: Basics of Intensive Quenching. *Adv. Mater. Process.* **Dec 1999,** *12*, H31- H33.
26. Aronov, M. A.; Kobasko, N. I.; Powell, J. A.; Wallace, J. F.; Schwam, D. Practical Application of the Intensive Quenching Technology for Steel Parts. *J. Heat Treat. Met. England* **2000,** *1.*
27. Aronov, M. A.; Kobasko, N. I.; Powell, J. A.; Wallace, J. F.; Zhu, Y. Effect of Intensive Quenching on Mechanical Properties of Carbon and Alloy Steels. In *Proceedings of 23rd ASM Heat Treating Conference*, Pittsburgh, Pennsylvania, 2005.
28. Aronov, M. A.; Kobasko, N. I.; Powell, J. A.; Hubbard, C.; Tang, F. Intensively Quenched Rod Residual Stress Mapping. In *Proceedings of 23rd ASM Heat Treating Conference*, Pittsburgh, Pennsylvania, 2005.
29. Kobasko, N. I.; Moskalenko, A. A.; Mazurenko, E. A.; Medvedev, A. M. Intensive Quenching of Tools in Water Salt Solutions, New Aspects of Fluid Mechanics. In *Heat Transfer & Environment;* Mastorakis, N., Mladenov, V., Bojkovich, Z., Eds.; WSEAS Press: Athens, 2010; p 385. ISSN: 1792-4596 and ISBN: 978-960-474-215-8.
30. Rath, J.; Luebben, Th.; Hunkel, M.; Hoffman, F.; Zoch, H.-W. Basic Researches about the Generation of Compressive Stresses by High Speed Quenching. *HTM J. Heat Treat. Mat.* **2009,** *64* (6), 338–350 (in German).
31. Rath, J.; Luebben, Th.; Hoffman, F.; Zoch, H.-W. Generation of Compressive Residual Stresses by High-Speed Water Quenching. In *The 4th International Conference on Thermal Process Modeling and Computer Simulation*, Shanghai, China, June 2010.

This page intentionally left blank

12.08 Residual Stresses Produced by Quenching of Martensitic Steels

T Ericsson, Linköping University, Linköping, Sweden

12.08.1	**Introduction**	271
12.08.2	**Definitions of Residual Stresses**	271
12.08.3	**Qualitative Discussion of Residual Stress Formation in Steel**	272
12.08.4	**Methods to Measure Residual Stresses in Steel**	273
12.08.5	**Modeling of Heat Treatment Stresses**	276
12.08.5.1	Principles	276
12.08.5.2	Temperature Field Calculation	277
12.08.5.3	Phase Transformation Calculation	277
12.08.5.4	Thermomechanical Calculation	278
12.08.6	**Through Hardening**	278
12.08.7	**Surface Hardening**	280
12.08.7.1	Definitions	280
12.08.7.2	Induction Hardening	281
12.08.7.3	Laser Hardening	284
12.08.7.4	Carburizing	287
12.08.8	**Effect of Tempering on Residual Hardening Stresses**	290
12.08.9	**Effect of Fatigue on Residual Hardening Stresses**	293
12.08.10	**Examples of Commercial Codes for Calculation of Residual Stresses due to Martensite Hardening**	296
References		296

12.08.1 Introduction

Rapid cooling or quenching of a part from high temperature can cause large thermal gradients and thus thermal stresses. If a phase transformation such as martensite transformation occurs simultaneously, phase transformation dilatations will add to the thermal dilatations and contribute to the internal stress distribution. The effect can be that local nonelastic deformations occur which will cause residual stresses when the part has attained its final temperature. The thermal and transformation processes are normally very rapid, and it is not possible to follow the stress buildup experimentally. Therefore computer modeling has been very important in increasing the understanding of the physical processes. The computed residual stresses can be verified experimentally. Due to the complexity of the calculations, most models handle only simple geometries such as long cylinders or large plates, but in later years complicated geometries such as gears have been treated (*1*,*2*,*3*). The present text is laid out so that first a qualitative treatment of the residual stress buildup after martensite hardening is given. Residual stress distributions after different hardening procedures, sometimes completed with quantitative computer modeling, are then presented as well as the effect of tempering and fatigue loading.

12.08.2 Definitions of Residual Stresses

It is appropriate to remind the reader of some definitions. Residual stresses are stresses that remain in a mechanical part after it has attained its final homogeneous temperature and when there are no external stresses acting on the part. So the stresses generated during a cooling process are not residual stresses strictly speaking, although they are internal stresses. One distinguishes between residual macro-, pseudomacro, and microstresses (*4*). A more elaborate classification distinguishes between residual stresses of the first, second, and third order (*5*,*6*). The macro- and first-order residual stresses are equivalent. A residual macrostress is the average of the residual stresses in many adjacent grains of the material. If a workpiece is cut or material is removed, the presence of residual macrostresses will cause a distortion of the workpiece. In a multiphase structure such as martensitic steel with retained austenite, the residual stresses within each phase are usually different. The pseudomacro (the second-order stresses) are the averages within each phase. They are sometimes called phase stresses. The relation between the macro- and pseudomacro stresses (second-order stresses) in a restricted volume in a two-phase material can be written as

$$\sigma_{\text{macro}} = (1 - f) \times \sigma_1 + f \times \sigma_2$$

where σ_1 is the average stress in phase 1, σ_2 is the average stress in phase 2, and f is the volume fraction of phase 2. In the general case, the stresses are three-dimensional (3D) tensors. If the volume considered is the total volume, then

$$\int \sigma \cdot \mathrm{d}V = 0$$

It is important to remember that compressive residual stresses in one subvolume of a workpiece must always be compensated by tensile residual stresses in another subvolume. A change in residual stress in one subvolume due to, for example, metallurgical transformation or fatigue loading will therefore affect residual stress in another subvolume. This will be illustrated later in this chapter.

The residual microstress (third-order stress) is inhomogeneous on a macroscopic scale and can be caused by dislocation pile-ups within a grain or elastic stresses around precipitates. They do not give rise to distortions if the workpiece is cut. The relation between the different kinds of residual stress is illustrated in **Figure 1** (*6*). The figure shows the residual stress along an axis in a plane cut through a workpiece. The following equations can be written

$$\sigma = \sigma^{\mathrm{I}}(\mathrm{X},\mathrm{Y}) + \sigma^{\mathrm{II}}(\mathrm{X},\mathrm{Y}) + \sigma^{\mathrm{III}}(\mathrm{X},\mathrm{Y})$$

where

$$\sigma^{\mathrm{I}} = \left(\int \sigma \, \mathrm{d}f \Big/ \int \mathrm{d}f \right)_{\text{several grains}}$$

$$\sigma^{\mathrm{II}} = \left(\int \sigma \, \mathrm{d}f \Big/ \int \mathrm{d}f \right)_{\text{one grain}} - \sigma^{\mathrm{I}}$$

$$\sigma^{\mathrm{III}} = (\sigma - \sigma^{\mathrm{I}} - \sigma^{\mathrm{II}})_{\text{at point } x,y}$$

The present chapter will only discuss macro and pseudomacro residual stresses in steel and not microstresses.

12.08.3 Qualitative Discussion of Residual Stress Formation in Steel

The subject of residual stresses after heat treatment of steel has been studied extensively in the recent literature (*7–13*). The principle for the creation of thermal stresses on cooling is shown in **Figure 2** for a 100-mm (4-in.)-diameter bar that was water quenched from the austenitizing temperature of 850 °C (1560 °F). The surface temperature (*S*) decreases more rapidly than the core temperature (*C*), and at time *w* the temperature difference between the surface and the core is at a maximum of about 550 °C (1020 °F). This means that the specific volume is greater in the core than in the surface. The volume contraction in the surface is prevented by the higher specific volume in the core. The thermal stress is approximately proportional to the temperature difference and is tensile in the surface and compressive in the core. Large thermal stresses are favored by low thermal conductivity, high heat capacity, and a high thermal expansion coefficient. Other factors increasing the temperature difference and thermal stresses are large-thickness dimensions and high cooling intensity of the cooling medium. If the stress during the cooling exceeds the yield stress, plastic deformation will occur. Therefore, the surface will become 'larger' than the core, and when the temperature difference between the surface and the core decreases, the stress will be reversed at a certain time *u*, resulting in compressive residual stresses in the surface, and tensile residual stresses in the core. A large yield stress at elevated temperatures will decrease the degree of plastic flow and thus the residual stress, while the yield stress at the ambient temperature puts an upper limit on the residual stress. If the thermal stress never exceeds the yield stress, the residual stress after finished cooling is zero.

A well-known case of phase transformation that induces residual stresses is the transformation of austenite to martensite, bainite, ferrite, or pearlite in steel. It is accompanied by a volume expansion whose value depends on the transformation product and alloy carbon content, including the degree of carbide dissolution (see **Table 1**). The expansion can also be expressed as a linear expansion, which is usually assumed to be equal to the volume expansion divided by three.

The added effect of transformation of austenite to martensite in steel is demonstrated in **Figure 3**. At time t_1, the surface temperature falls below the M_s temperature, and the surface starts to transform. The surface expands, and the thermal tensile stresses are counteracted. The stress reversal takes place earlier than when transformation stresses are not taken into consideration. At time t_2, the core transforms, causing another stress reversal. After cooling, transformation-induced tensile stresses at the surface dominate over the thermally induced compressive stresses. Rose (*14*) points out that it is very important to recognize whether the core and surface transform before or after the stress reversal. The highest surface compressive stresses are obtained when the core transform

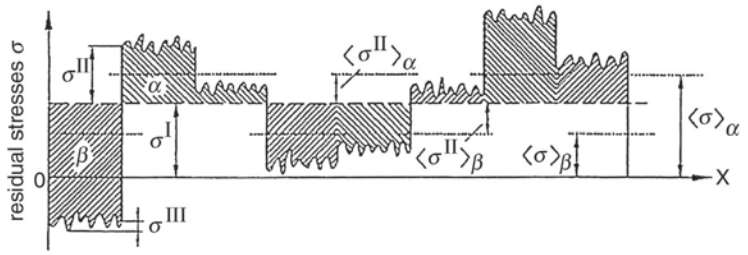

Figure 1 To the definition of residual stresses of the first, second, and third kinds. Reproduced from Hauk, V. *Structural and Residual Stress Analysis by Nondestructive Measures*; Elsevier Science BV: Amsterdam, New York, Oxford, 1997.

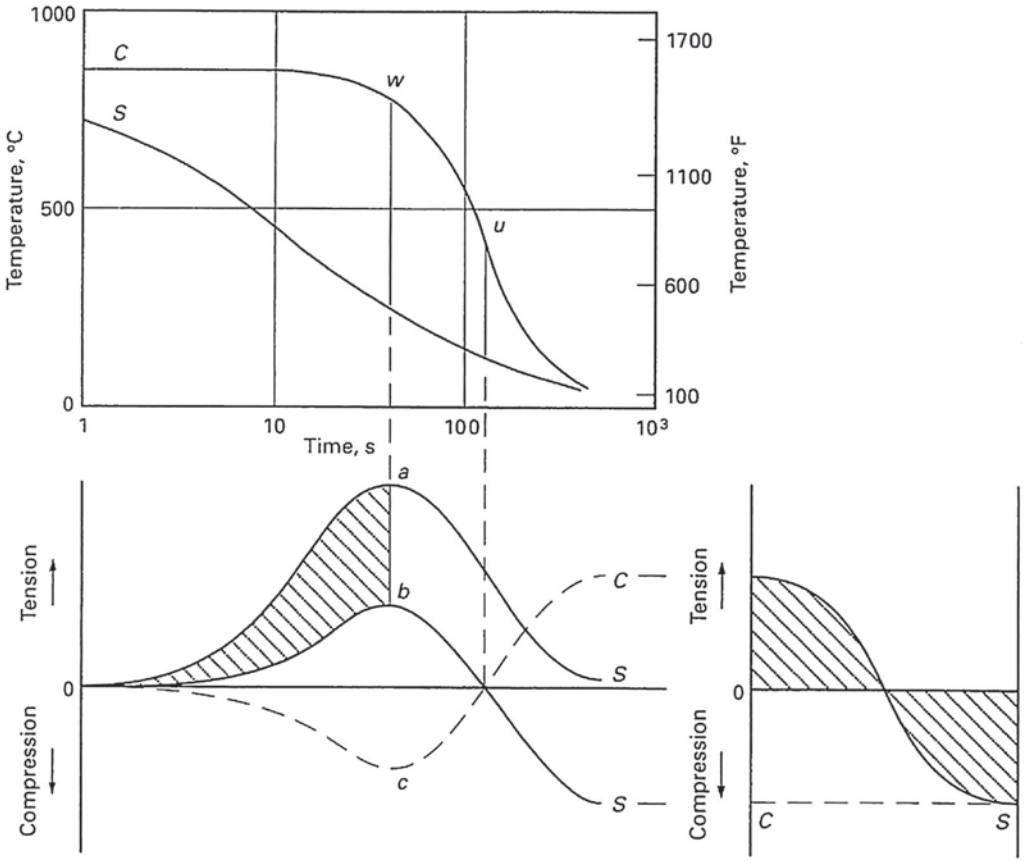

Figure 2 Formation of thermal stresses on cooling in a 100 mm steel specimen. *C* designates the core, *S* the surface, *u* the stress reversal time instant, and *w* the time instant of maximum temperature difference. The top graph shows the temperature variation with time at the surface and in the core; the graph below shows hypothetical thermal stress, *a*, which is proportional to the temperature difference between the surface and the core, the actual stress at the surface, and, *b*, which can never exceed the yield stress, and the actual stress in the core, *c*. To the right is shown the residual stress distribution after completed cooling as a function of the specimen radius. Reproduced from Rose, A.; Hougardy, H. Transformation Characteristics and Hardenability of Carburizing Steels. In *Transformation and Hardenability in Steels*; Climax Molybdenum Company of Michigan, 1967; pp. 155–167.

Table 1 Volume changes due to different transformations

Transformation	*Volume change, % (a)*
Spheroidized pearlite–austenite	4.64–2.21 × (%C)
Austenite–martensite	4.64–0.53 × (%C)
Austenite–lower bainite	4.64–1.43 × (%C)
Austenite–upper bainite	4.64–2.21 × (%C)

before, and the surface after, the stress reversal, while tensile residual stresses result when the core transforms after, and the surface before, the stress reversal, as in Figure 3.

A third situation when only the surface forms martensite is shown in Figure 4. Up to time t_1, tensile stresses are formed in the surface and compressive stresses in the core. When pearlite formation starts at time t_1, it causes a volume increase in the core, at the same time as the temperature decrease causes a volume shrinkage. Which factor will dominate is of less importance as the yield stress at the surface will determine the stress there. At time t_2, the pearlite formation in the core is just finished, and the martensite formation will start at the surface. The volume expansion in the surface and the shrinkage in the core both contribute to a rapid stress reversal. The compressive stresses in the martensitic surface layer can become quite high. The yield stress in the core is relatively low. With increased thickness of the martensitic surface zone, the tensile stress in the center increases and may even attain a critical value for fracture.

12.08.4 Methods to Measure Residual Stresses in Steel

A number of methods are available to measure residual stresses in steel and other metallic materials. Table 2 lists the most important techniques. There are handbooks that present detailed descriptions of measurement methods (*4,6,8*).

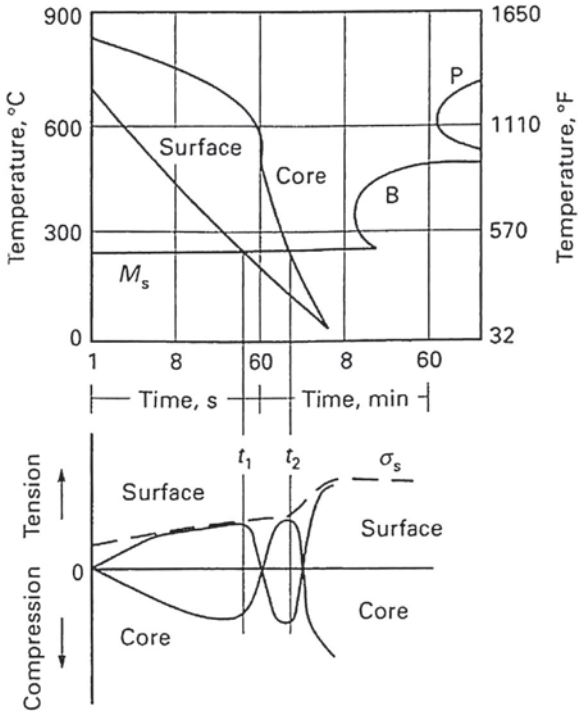

Figure 3 Formation of residual stress on cooling considering thermal expansion and the austenite to martensite transformation. The dashed line is the yield stress, σ_s, at the surface. Reproduced from Chatterjee-Fischer, R. Beispiele fuer durch Waermebehandlung bedingte Eigenspannungen undIhre Auswirkungen. *Härterei-Technische Mitteilungen* **Nov 1973**, *28*, 276–288.

The mechanical methods are based on the measurements of strains released when the workpiece is cut or slitted or material is removed, for instance, by hole drilling. Most often the strain is measured with strain gages. Some methods are only applicable on special geometries such as slitting of bars or rails. A more generally applicable method is the hole drilling method. A hole is drilled in incremental steps down to a depth roughly equal to the drill diameter. The strains in several directions (often three) around the hole are measured after each step with a rosette strain gage. Contact-free methods, such as electronic speckle pattern interferometry, have also been developed (*15*). The strain data is fed into a computer program, and with the knowledge of the elastic constants, the residual stress profile from the surface into the depth of the hole can be calculated. The measured residual stress is the macrostress (the first-order stress). The mechanical methods are destructive, but the holes after the hole drilling method can sometimes be disregarded or removed by grinding. In such a case, it is a semidestructive method. Portable hole drilling equipment is available for doing in-field measurements.

The diffraction methods measure residual lattice strain distribution in a crystalline microstructure. It cannot be used on amorphous metals. The X-ray diffraction method has mainly become used for research studies, but equipment for in-line production control has also been developed. There are several good textbooks about the X-ray diffraction method (*4*,*6*,*8*). The X-ray is generated in an X-ray tube in which high-energy electrons hit a target of a pure metal. Then X-rays with wave lengths characteristic for the target material are generated. For studies on steel, Cr Kα radiation with a V filter has normally been used. It gives fewer problems with Fe-fluorescens than the more intense Cu Kα radiation. Modern solid-state X-ray detectors exist nowadays that can suppress the Fe fluorescens so that Cu Kα radiation can be used. In a typical laboratory diffractometer, the specimen is mounted in the center of a circle. An X-ray detector can be moved around the periferi to scan and record the X-ray diffraction profile. The peak position is then determined from the shape of the peak. Then the specimen is turned a certain angle, ψ-angle, around the diffractometer axis. The important information is the peak shift as a function of the ψ-angle. Knowing the so-called X-ray elastic constants, one can calculate the residual stress, and there is ample commercial software that can perform this function. Large samples such as engineering parts may be impossible to mount on a diffractometer. Then portable equipment often using so-called parallel beam geometry is more suited in which only a parallel beam of X-rays is permitted using a long parallel beam collimator. Much X-ray intensity is lost, but the setup is rather insensitive to the exact specimen surface position.

With X-ray diffraction, residual stresses in a surface layer are measured in a nondestructive manner. It is important to emphasize that no stress-free standard specimen is needed with the commonly used $\sin^2\psi$ method. The penetrating depth of Cr Kα radiation in steel is about 5 μm. If a depth profile is required, surface material has to be removed, usually by electropolishing, in order not to introduce machining stresses. Then the X-ray method is destructive or semidestructive depending on circumstances. The accuracy of residual stress measurements by X-ray diffraction is typically about 10 MPa. A good evaluation software calculates a value for the uncertainty in a measurement based on counting statistics, and it is important to report it together with the residual stress value.

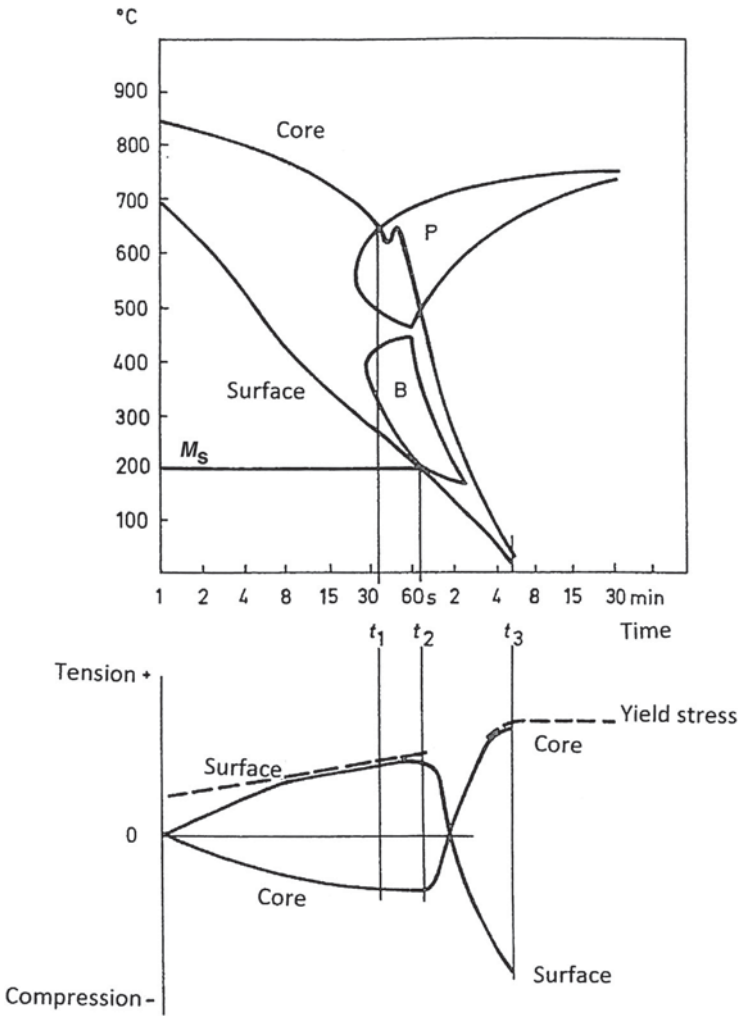

Figure 4 Stress buildup during cooling when a mixed structure of martensite, bainite, and pearlite is formed in a steel specimen with diameter 100 mm. Reproduced from Thelning, K.-E. *Steel and Its Heat Treatment, Bofors Handbook*; Butterworth and Co.: London, 1975.

Table 2 Techniques to measure residual stress in steels

Type	*Techniques*	*Measured quantities*	*Evaluated stress*	*Accuracy*
Mechanic	Sectioning, hole drilling	Released strain	Macro	10 MPa
Diffraction	X-rays and neutrons	Diffraction angles	Macro and pseudomacro	10 MPa
Ultrasonic	Acousto-elasticity	Velocities	Macro	10 MPa
Magnetic	Barkhausen noise		Macro and micro	10 MPa

The X-ray diffraction method is rather general, but there are certain limitations. Very large grain-size materials and heavily crystallographically textured materials can be impossible to measure, or at least they require rather sophisticated data treatments. Luckily enough, martensitic steels do not normally belong to these categories.

The limitations of surface measurements can be circumvented by using X-ray synchrotron radiation. Then a very intense X-ray is generated by extremely high-speed electrons traveling in a closed circuit. By using a monochromator, only a narrow beam of a well-defined wavelength hits the specimen. One can avoid the effects of fluorescens by choosing a suitable wavelength. Due to the high-beam intensity, radiation can be diffracted from large depths. Thus one can carry out residual stress measurements in the interior without removing material from the surface zone. In this case, the residual stress state can be three-dimensional instead of two-dimensional (surface stress). Synchrotron X-rays have become a popular research tool in the last few years.

The X-ray method can measure macro residual stresses (first-order stresses) and pseudomacro residual stresses (second-order stresses). The diffraction peak width also gives some information about third-order residual stresses. Diffraction peaks from martensitic steel are usually very broad, which indicates large amounts of microresidual stresses (third-order residual stresses). An

important feature of X-ray stress analysis is the possibility of determining the residual stress state in very small volumes of surface material. Hence stresses ahead of cracks or in small second-phase particles can be measured.

The neutron diffraction method is similar to the X-ray diffraction method, but it also has some different features (*6,8*). The X-ray beam is replaced by neutron beams, which will penetrate much deeper into the material. Neutron diffraction is therefore not well suited for surface residual stress measurements. The X-ray and neutron diffraction methods complement each other. The neutron source has typically been nuclear reactors, from which a beam of thermal energy neutrons are allowed into a monochromator before hitting the specimen in the center of a diffractometer. More intense neutron beams can be obtained from so-called spallation sources where a target is hit by high-energy protons, which then generate neutrons. It is important with neutron diffraction to have a stress-free calibration specimen. Strain and hence residual stress are calculated from the difference in peak position between specimen and standard specimen. A 3D stress analysis is required because residual stress in the interior is measured.

The ultrasonic stress measurement is based on the stress dependence of the velocities of ultrasonic waves in solid materials (*6,8*). Longitudinal waves, polarized shear waves, and Rayleigh surface waves can be used. Knowledge of higher order elastic constants in the actual state of the material is required. The instruments are often portable and can be moved to the part being analyzed. An example is measurements in rails using surface waves. A problem with the ultrasonic method is that it is sensitive to both macro- and microresidual stresses (first, second, and third kind of stress), and hence it is very sensitive to the microstructure of the material.

The magnetic method that is used is based on the Barkhausen noise phenomenon (*6,8*). It is well suited for routine measurements of magnetic steels after calibration. It is for instance used for production control of heat-treated steel parts in the truck industry.

12.08.5 Modeling of Heat Treatment Stresses

12.08.5.1 Principles

Before discussing various hardening processes, it can be helpful to present principles for modeling residual stress creation. It is necessary to consider interactions among various factors. As shown in **Figure 5**, these include (1) phase transformations, (2) latent heat, (3) thermal stress, (4) transformation stress and plasticity, (5) heat generation due to deformation, and (6) mechanically induced transformation. The most important of these are interactions 1, 3, and 5. Interaction 6, however, is also a very important factor. When discussing mechanically induced transformations, at least three different effects should be mentioned (*16*). The first is that the M_s temperature is decreased by hydrostatic pressure and slightly raised by tensile stress. An increase of about 15 °C for a high-carbon steel submitted to 285 MPa has been reported (*16*). The second effect is the transformation plasticity which is a permanent strain that occurs during an ongoing phase transformation under applied stress lower than the yield stress. Several mechanisms for transformation plasticity have been proposed. The original and most frequently used considers that transformation plasticity strain results from plastic deformation of the weaker phase, and its magnitude is related to the yield strength of the weaker phase and the volume expansion of transformation (*17*). The third effect is the incubation time of nonmartensitic transformations, which is prolonged by hydrostatic stress (*18*) and shortened by tensile stress (*19*). This is particularly important for large dimensions.

The mathematical modeling starts with calculation of the temperature field, including heat of transformation, heat generated by eddy currents in induction hardening, and laser light illumination in laser hardening. Usually of less importance is heat generated by plastic deformation. Then one calculates the phase transformation caused by the temperature change. Finally, the mechanical stresses and deformations are calculated. One has to go through several computation loops before reaching a stable final stress distribution because the phenomena are coupled. Implicit in the scheme is that the dimensions and shape (the presence of notches, thickness variations, etc.) are important because they affect the temperature field and the stresses. Obviously, the cooling medium is also important, as it influences the temperature field.

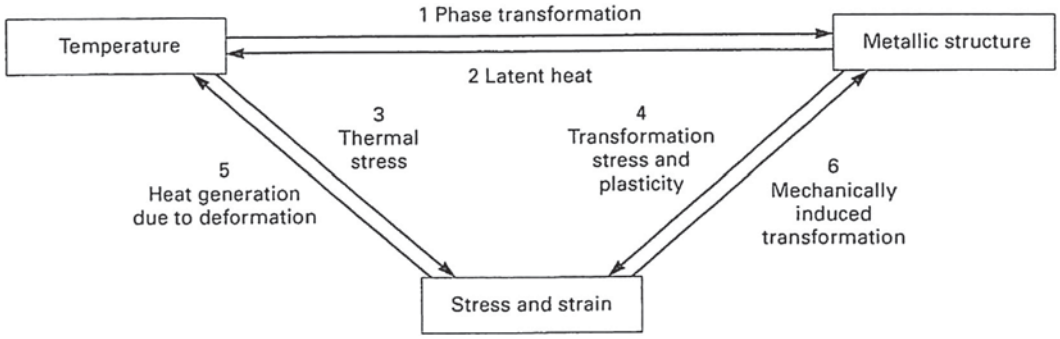

Figure 5 The interactions between various factors of importance for residual stress generation. Reproduced from *Heat Treating*; ASM Handbook, ASM International: Metals Park, Ohio, 1991; Vol. 4.

12.08.5.2 Temperature Field Calculation

The equation for calculating the temperature field can be written as

$$\nabla(k \cdot \nabla T) = \rho C_p \cdot \dot{T} - \dot{Q}$$

where ∇ denotes the gradient operator, T is the temperature, and $\dot{T}$ is the time derivative of the temperature; $\dot{Q}$ is the heat generated per unit volume and unit time due to latent heat from phase transformations, heat sources for induction or laser hardening, and heat generated by deformation. The thermal conductivity is k, the density is ρ, and the specific heat is C_p. These quantities depend on the temperature and the type of phase; usually, a volume average over the phases present is assumed.

Heat conduction in the interior depends on the heat conductivity of the phases present, and that in the surface depends on the heat transfer to surrounding. The latter is quite complicated when the cooling is carried out in a vaporizing liquid, where one can distinguish three stages: vapor blanket, boiling, and convection (see **Figure 6**). How to treat this in an approximate but still sufficient manner is discussed by Majorek et al. (*20*). Gas cooling is simpler, but if one considers the gas flow in a blowing gas, shadow effects must be dealt with. This has been done in some recent work (*21*).

To calculate the heating during induction hardening, the magnetic permeability is needed. Static induction heating is easier to handle than progressive induction heating (*22*). The depth of the eddy-current layer (skin depth) is mainly determined by the frequency of the current in the coil and is given by the equation

$$\delta = \sqrt{\rho/\mu\pi f}$$

where ρ is the resistivity, f the frequency, and μ the permeability. As is well known, the skin depth decreases with increasing frequency.

12.08.5.3 Phase Transformation Calculation

Phase transformations in steel are of both the diffusional and nondiffusional type (martensitic). Diffusional transformations are the formation of ferrite, pearlite, and bainite from austenite during cooling and the formation of austenite during heating, and for these the so-called Johnson-Mehl-Avrami (J-M-A) exponential model is used:

$$v_k = v_{\max,k}(1 - \exp(-b_k t_k^n))$$

where v is volume fraction, $v_{\max}$ is the maximum possible volume fraction, b and n are temperature-dependent quantities, and the subscript k indicates the phase.

It has been shown that in some cases better agreement with observations can be obtained if an incubation period preceded the J-M-A transformation (*23*). The input data used are most often isothermal transformation diagrams (TTT-diagrams), but continuous transformation diagrams (CCT-diagrams) can also be used (*24*). Denis (*25*) has pointed out that the use of TTT-diagrams is more general, but better agreement can be obtained by using continuous cooling diagrams with a cooling function close to the actual. To simulate the induction or laser heating, transformation diagrams for heating are needed (*24*). The martensitic transformation during quenching is usually described by the Koistinen-Marburger expression

$$v_m = v_{\max,m}(1 - \exp(-(M_s - T))$$

where v_m is the volume fraction of martensite, $v_{\max,m}$ is the maximum possible volume fraction of martensite, T is a constant (often assumed to be 0.011), and M_s is the martensite start temperature.

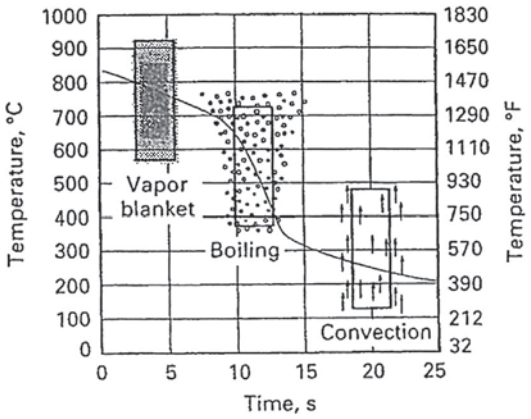

Figure 6 The three stages of quenching in a liquid such as oil or water.

12.08.5.4 Thermomechanical Calculation

The thermomechanical part includes the elastic strain, the thermal strain, the density changes due to phase transformations, the transformation plasticity, and (usually neglected) the creep strain. The mechanical model is usually written in terms of the strain rate tensor

$$\dot{\varepsilon}_{ij}^{tot} = \dot{\varepsilon}_{ij}^{el} + \dot{\varepsilon}_{ij}^{th} + \dot{\varepsilon}_{ij}^{pl} + \dot{\varepsilon}_{ij}^{tr} + \dot{\varepsilon}_{ij}^{tp}$$

where the superscript 'tot' indicates total, 'el' elastic, 'th' thermal, 'pl' plastic, 'tr' transformation, and 'tp' transformation plasticity. The material data needed are Young's modulus, the Poisson ratio, the thermal expansion coefficient, the yield (flow) stress, the strain hardening coefficient, and sometimes the deformation rate dependence of the yield stress. All these quantities are usually functions of the type of phase, composition, and temperature.

The modeling of steel hardening has so far concentrated on the calculation of macrostresses and not phase stresses, and then one can simplify the situation by using phase averages of thermal and mechanical properties. The macroscopic stress at each time instant is obtained by an iterative procedure.

When chemical composition gradients exist, as is the case for carburizing, the models may include calculations of the chemical diffusion, which necessitates knowledge of diffusion coefficients in the phases present.

12.08.6 Through Hardening

The most important case of residual stress generation during quenching when a phase transformation takes place is martensite hardening of steel. There are numerous treatments in the literature about this phenomenon (*2*,*11*,*13*,*23*,*25–27*). Here some examples partly based on computer simulations are chosen to illustrate important aspects. The text accompanying **Figure 7** is borrowed from Denis (*28*).

Figure 7 shows the calculated stress (a) and the plastic strain (b) development during martensitic quenching in cold water of a cylinder made of the steel 60NCD11 with 0.6%C. In the first stage of cooling, the surface is under tension, and the center under compression due to thermal gradients alone and plastic strains occur in austenite. As martensitic transformation takes place at the surface when the temperature passes below M_s, very rapid unloading occurs due to the volume increase. Transformation plasticity

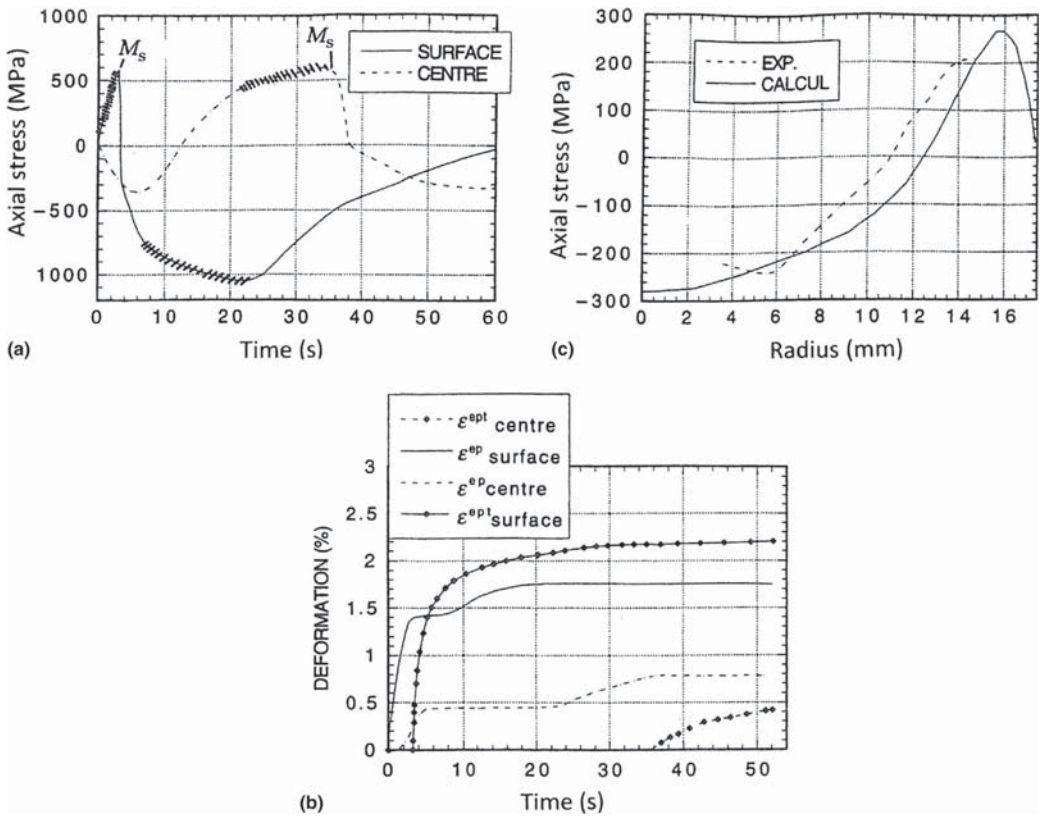

Figure 7 Quenching in cold water of a 60NCD11 steel cylinder with 35 mm diameter: (a) Calculated stress evolution over time at the surface and in the center. The hatching indicates domains where plastic strains occur. (b) Evolutions of the equivalent plastic strain and equivalent transformation plasticity strain versus time. (c) Residual axial stress profiles. Reproduced from Denis, S. Prévision des contraintes résiduelles induites par traitement thermique et thermochimique. *La Revue de Métallurgie* **1997**, *77*, 164.

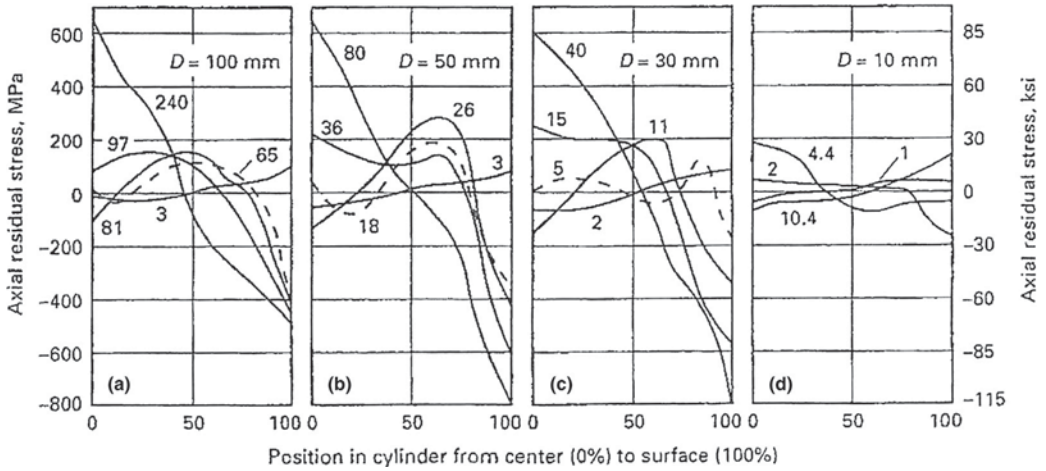

Figure 8 Axial residual stress distributions for various AISI 1045 steel cylinders with diameters, *D*, at selected times (in seconds) after the start of quenching from 850 °C in 20 °C water. The final microstructure of the 10-mm-diameter cylinder is completely martensitic, while the others have a ferritic-pearlitic core. Reproduced from Yu, H.; Schröder, R.; Graja, P.; Besserdich, G.; Majorek, A.; Hoferer, M. Zur modellierung und Simulation der Wärmebehandlung metallischer Werkstoffe. *Härterei-technische Mitteilungen* **1996**, *51*, 48–55.

strains accompany the transformation, and new plastic strains only occur as the material is submitted to high compressive stresses. When the transformation continues in the cylinder, the center is deformed plastically in tension until the center temperature reaches M_s. Then the last stage of unloading due to the martensitic transformation in the center can be observed. The final residual stress distribution over the cross section is shown in Figure 7(c). Notice that the maximum tensile stress is not attained at the surface but slightly below.

In other works (*29,30*), series of calculations were made to study the influence of cylinder diameter and cooling medium on residual stresses in 1045 steel. In the case of oil, ferrite–pearlite mixtures are formed during water quenching, martensite and bainite are also formed. Figure 8 shows the stress development during water quenching. The 10 (0.4 in.)-mm-diameter cylinder starts to transform to martensite at the surface, and the transformation front moves gradually inward, resulting in a typical tensile stress at the surface. The large-diameter cylinders first transform to ferrite–pearlite at intermediate radii and then to martensite at the surface. This causes the two-stress minima seen in the dashed curves in Figure 8(a)–8(c). The final residual stress is compressive at the top surface and tensile in the core. In several cases, good agreement was obtained with X-ray stress measurements, as well as with older mechanically measured data. The dependence on specimen diameter and quenching medium is summarized in Figure 9. The difference between oil and water quenchings decreases with increasing diameter.

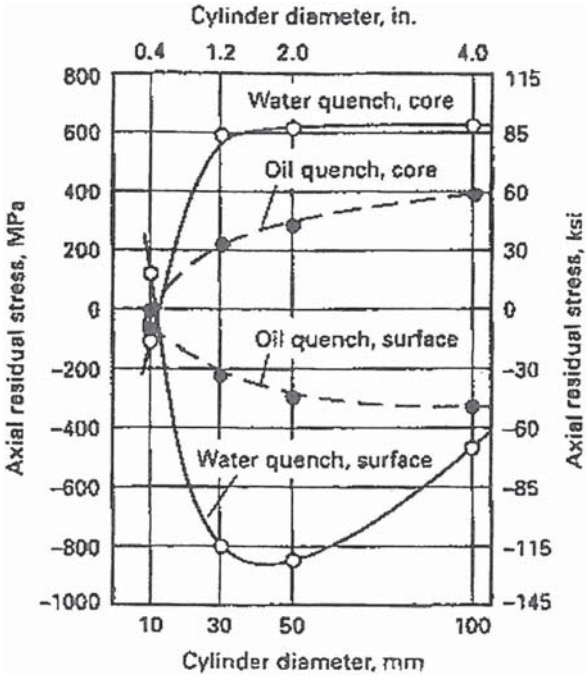

Figure 9 Dependence of axial residual stresses on the cylinder diameter. Same steel as in Figure 8. The core is martensitic for 10 mm diameter but pearlitic for larger diameters. Reproduced from Yu, H.; Schröder, R.; Graja, P.; Besserdich, G.; Majorek, A.; Hoferer, M. Zur modellierung und Simulation der Wärmebehandlung metallischer Werkstoffe. *Härterei-technische Mitteilungen* **1996**, *51*, 48–55.

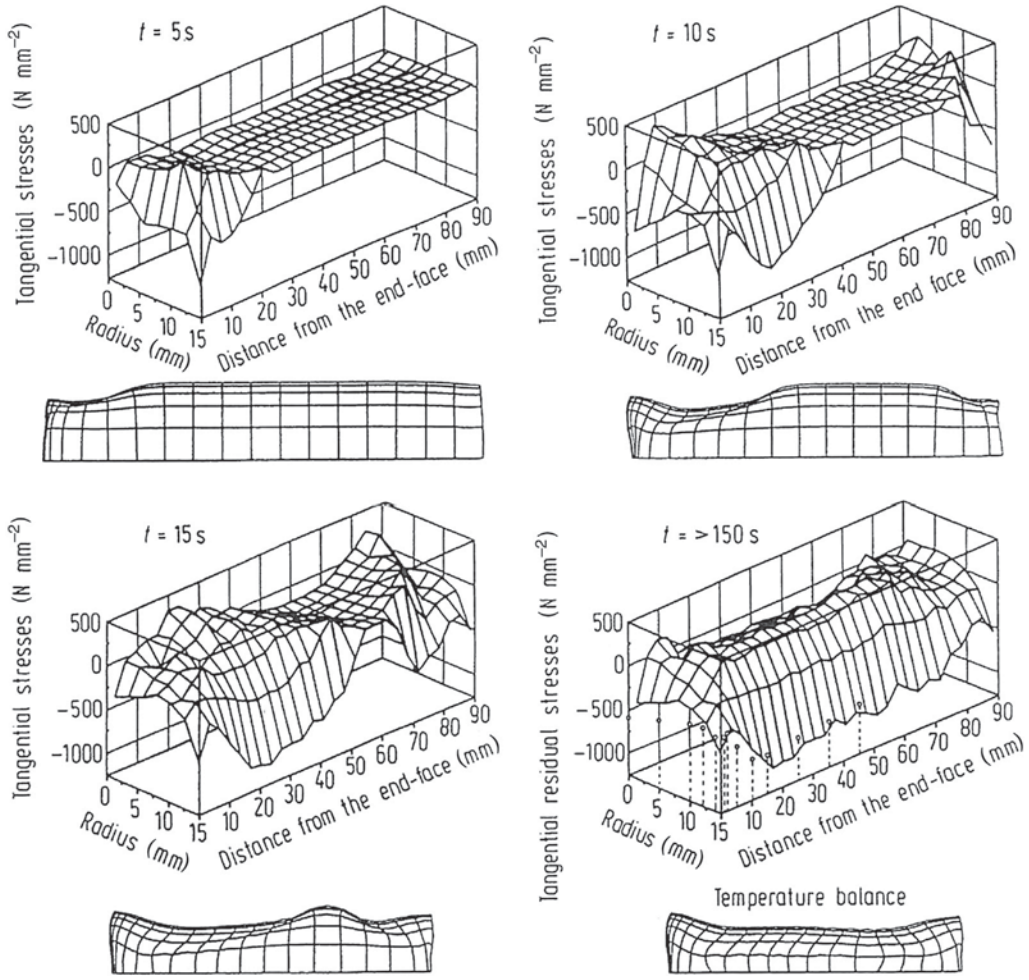

Figure 10 Distributions of tangential stresses and of 50-fold enlarged nodal displacements in an end-face immersion cylinder at different times after the starting of quenching (°) experimentally determined values. Reproduced from Yu, H.; Schröder, R.; Graja, P.; Besserdich, G.; Majorek, A.; Hoferer, M. Zur modellierung und Simulation der Wärmebehandlung metallischer Werkstoffe. *Härterei-technische Mitteilungen* **1996**, *51*, 48–55.

The effect of limited geometrical dimensions on quench stresses was studied by Yu et al. (*30*). They simulated quenching of a cylinder with diameter 30 mm and length 90 mm made of steel AISI 4142 from 860 °C into water of 20 °C. The tangential stress distributions and shapes at three different times after the start of the quenching and in the final state are shown in Figure 10. The cylinder was lowered into the water vertically, so that a short end first hit the water. After 5 s martensite formation has started at this bottom end, so that compressive stresses are created. The shape displays a slight expansion at this end. After 10 s, more martensite formation has also set in, with resulting compressive stresses. At the middle part, the cooling medium water is still in the vapor phase with low heat transfer, while it is in the nucleate boiling stage at the ends. After 15 s, the vapor stage has almost completely broken down. In the final stage after more than 150 s, compressive residual stresses prevail over the whole cylinder surface. There are steep stress gradients under the surface, and tensile residual stresses exist, except at the center line. The final shape is of the hourglass type with broad ends. Measured residual stresses are plotted as dots in the final figure. They agree reasonably well with the calculated ones. It should be pointed out that transformation plasticity was included in the calculations.

12.08.7 Surface Hardening

12.08.7.1 Definitions

In many cases, the goal is to harden the surface and not the whole workpiece in order to get a wear and fatigue-resistant surface combined with a tough core. This can be achieved by local heating of the surface before quenching, *thermal surface hardening*, or a letting carbon and/or nitrogen diffuse into the surface zone before quenching, *thermochemical surface hardening*.

Induction hardening, laser hardening, and electron beam hardening are the important types of thermal surface hardening.

12.08.7.2 Induction Hardening

Induction hardening is more complicated to understand than through hardening. Both the heating stage and the cooling stage must be considered. Static or single-shot induction hardening can be distinguished from progressive induction hardening. Using the single-shot method, a multiturn coil totally surrounds the area to be hardened; using the progressive technique, the workpiece, and a single-turn coil are moved relative to each other. The single-shot method is more readily calculated and will be described here. To calculate the heating during induction hardening, the magnetic field equation must be solved and the magnetic permeability, μ, is determined. A function fitted to experimental curves is

$$\mu = a/(b + H) + c$$

where a, b, and c are constants, and H is the magnetic field strength. The electrical resistivity must also be determined as a function of the phases present. Quenching by a water spray requires experimental data for the corresponding heat transfer function. For the description of the transformation to austenite from the starting structure, an isothermal diagram for heating (ITh diagram) is needed. To describe the transformation behavior during the subsequent cooling, an ITh diagram representative of a short austenitizing time is necessary. The austenitizing time during induction hardening is normally less than 1 min. This means that carbide dissolution has little time to take place, and therefore the type and distribution of carbides in the starting structure are important. It is well known that structures with fine carbides harden to a greater depth than structures with coarse carbides. A clear simulation of static induction hardening has been presented (*22*,*31*).

In **Figure 11**, stationary induction hardening is shown in detail, and in **Figure 12**, the agreement with experimentally measured residual stresses is shown (*22*,*24*). The calculations are carried out for the steel AISI 4142 with an induction frequency of 300 kHz. In **Figure 11(a)**, the evolution of the temperature with time at different depths is demonstrated. It is clear that the heating rate decreases at the Curie temperature, about 770 °C, and that the transformation to austenite absorbs heat (flat niveau). A short air cooling is followed by water spraying. The final hardness and martensite distributions are shown in **Figure 11(b)**. The evolution of the stress is shown in two ways, versus depth at different times, **Figure 11(c)**, and versus time for different depths, **Figure 11(d)**. In the

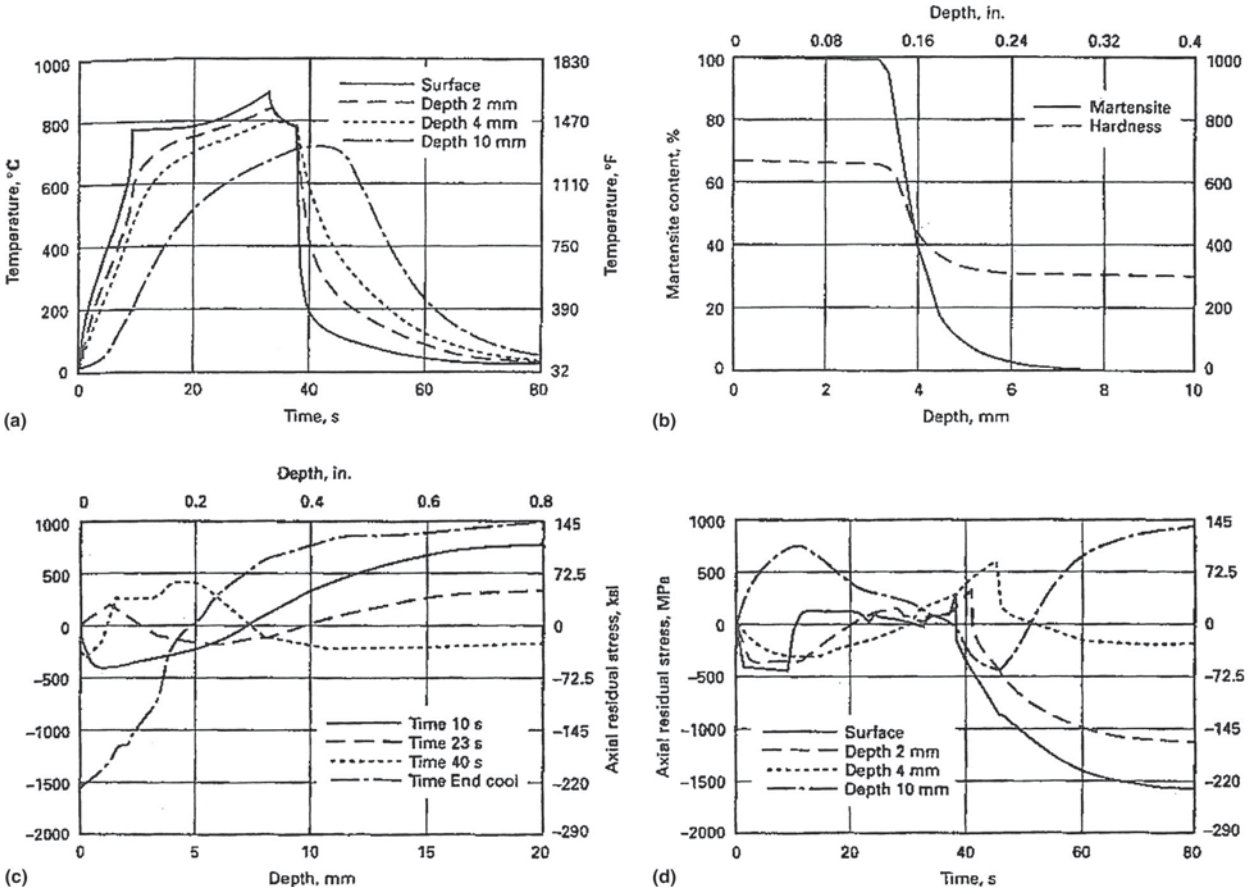

Figure 11 Calculated values for single-shot induction hardening of a 40 mm diameter cylinder steel. Induction frequency 300 kHz. (a) Temperature versus time for different depths. (b) The calculated hardness distribution. (c) Axial residual stress versus depth at different times. (d) Axial stress at different depths. Reproduced from Ericsson, T. Residual Stresses Caused by Thermal and Thermochemical Surface Treatments. In Advances in Surface Treatments; Niku-Lari, A., Ed.; Pergamon Press: Oxford, New York, Frankfurt, 1987; pp 87–113; Vol. 4; Melander, A. A Computational and Experimental Investigation of Induction and Laser Hardening. Dissertation No. 124, Linkoping University, Sweden, 1985.

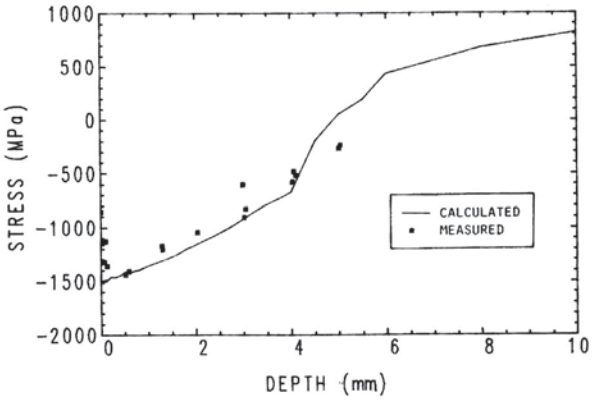

Figure 12 Comparison of calculated and measured residual stress of the same steel as in **Figure 11**. Reproduced from Ericsson, T. Residual Stresses Caused by Thermal and Thermochemical Surface Treatments. In Advances in Surface Treatments; Niku-Lari, A., Ed.; Pergamon Press: Oxford, New York, Frankfurt, 1987; pp 87–113; Vol. 4; Melander, A. A Computational and Experimental Investigation of Induction and Laser Hardening. Dissertation No. 124, Linkoping University, Sweden, 1985.

beginning, the stress becomes compressive in the heated zone but is shifted in the tensile direction when the austenite formation sets in. Only the axial stress component is shown in the figures. The computer predictions are reasonably good, as can be seen in **Figure 12**. The experimental data indicate slightly smaller compressive stresses at the surface than the calculated ones. It is not due to decarburization.

The effect of variables such as the quenching medium and the ITh diagram has also been taken into consideration. **Figure 13** shows how the hardening depth is increased when the transformation to austenite at elevated temperatures occurs more easily. The different transformation rates can be due to different steel compositions or to different prior microstructures of the same steel. The cooling is rapid enough to transform all austenite that is formed to martensite, and the residual stress distribution is only affected slightly, as shown in **Figure 13(b)**. If the water spray is replaced by oil quenching, calculation shows that the magnitude of the compressive stress peak is reduced, while the hardening depth is the same because the depth of austenitization is the same.

Tjernberg (*32*) presents measurements and calculations of residual stresses in induction-hardened shafts made of a steel SS2250 (=DIN 50CrMo4), with a diameter of 56 mm and a hardening depth of about 11 mm. Progressive induction hardening was used with a moving speed of 5 mm s^{-1} and a frequency of 2.7 kHz. For the simulation, the SYSWELD code was used. **Figure 14** shows measured and calculated axial, radial, and hoop stresses. The calculation was divided into three steps: a magnetic-thermal part, a thermal-metallurgical part, and a mechanical part. The measurements were done by the X-ray diffraction technique. There is good agreement between measurement and calculations of axial, radial, and hoop residual stresses. The hardness distribution is shown in **Figure 15**.

In this experiment with a relatively large induction hardening depth, the compensating tensile stress below the compressed layer has a maximum a few millimeter below the case depth. This type of maximum is not always observed. It can also be noted that there is a steep transition from case to core values.

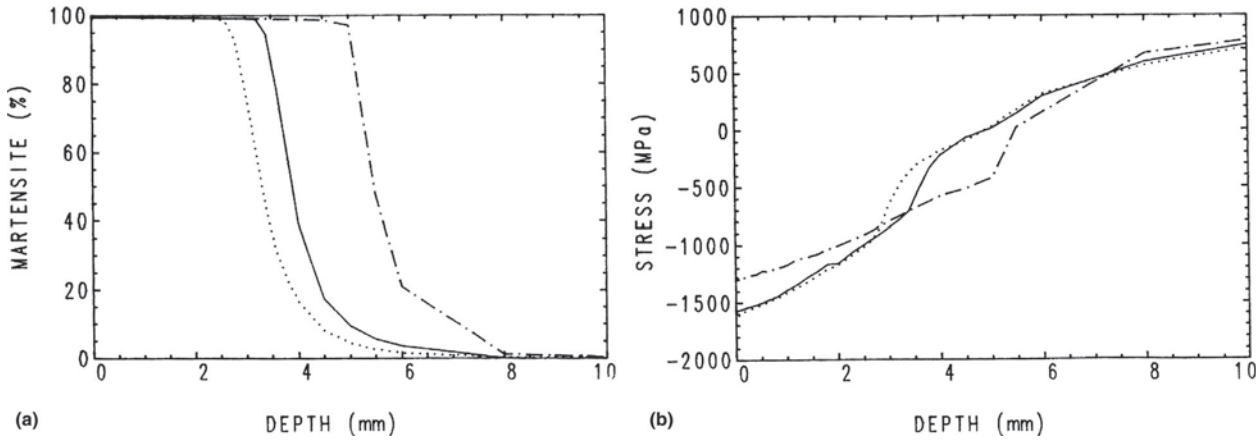

Figure 13 Calculated values of martensite distribution and residual stress after induction hardening of a 40-mm-diameter cylinder. The solid lines are calculated using an experimental ITh diagram, and the other two after a theoretical displacement to shorter and longer times of this diagram. This illustrates the effect of different prior microstructures or different steel compositions. (a) Final martensite distribution. (b) Axial residual stress profiles. Reproduced from Ericsson, T. Residual Stresses Caused by Thermal and Thermochemical Surface Treatments. In *Advances in Surface Treatments*; Niku-Lari, A., Ed.; Pergamon Press: Oxford, New York, Frankfurt, 1987; Vol. 4, pp 87–113; Melander, A. A Computational and Experimental Investigation of Induction and Laser Hardening. Dissertation No. 124, Linkoping University, Sweden, 1985.

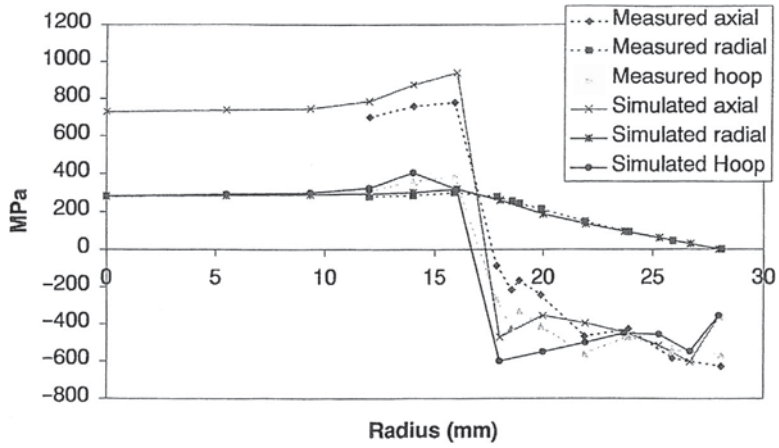

Figure 14 Measured residual stresses, corrected for removed material, compared to simulated stresses. Reproduced from Tjernberg, A. Comparison of Methods for Determining Residual Stresses in Induction Hardened Transmission Shafts. *Scand. J. Metall.* **1999**, *28* (4), 162–168.

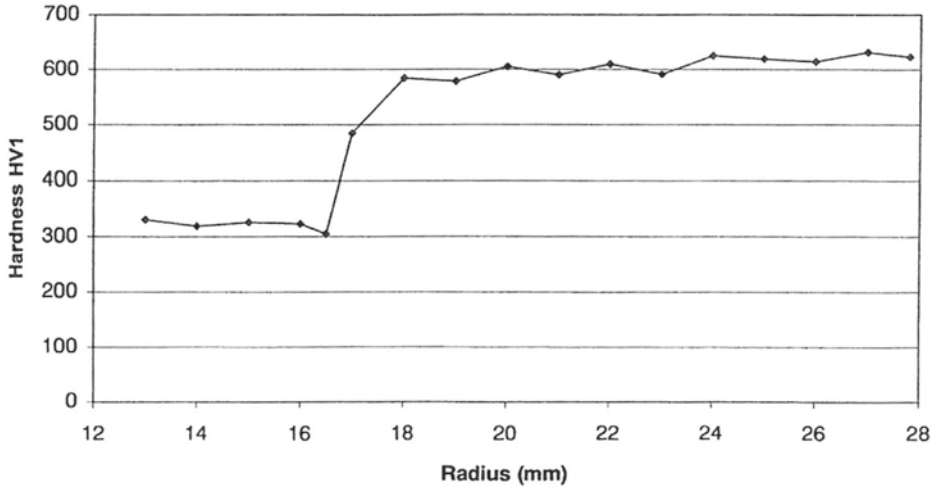

Figure 15 Measured hardness distribution for the shaft in **Figure 14**. Reproduced from Tjernberg, A. Comparison of Methods for Determining Residual Stresses in Induction Hardened Transmission Shafts. *Scand. J. Metall.* **1999**, *28* (4), 162–168.

The development of stresses during progressive induction hardening has been studied by Xu et al. (*33*,*34*) based on simulations and experiments for a Chinese standard steel 35CrMo with 0.35%C, 0.96%Cr, and 0.19%Mo and yield stress 780 MPa. **Figure 16(a)** shows the development of temperature and stresses during the heating up and cooling. S_1, S_2, S_3, and S_4 indicate sections shown in the insert in **Figure 16(b)**. The induction coil moves upward in the insert. S_1 has just started to heat and S_4 has almost cooled down. One can site the authors: During the early stage of heating up, the temperature of the whole section S_1 is lower than that of S_2, see **Figure 16(a)**. The temperature gradient along the radius generates an axial compressive stress in the surface and a tensile stress toward the center of the bar (curve S_1 of **Figure 16(b)**). Because no phase transformation occurred on this section, the stress distributions are determined by the thermal strain. When the temperature is above A_s (starting temperature for austenite), the surface compressive stresses decrease during the austenitization process (curve S_2 in **Figure 16(b)**). The formation of austenite changes the stress distribution because it involves a constriction of the volume and a marked reduction in the yield stress of the material. During the early stages of cooling (section S_3), the temperature in the core is still rising while that of the surface falls below the martensite start temperature M_s (curve S_3 in **Figure 16(b)**). At section S_4, the martensite transformation is completed in the formerly austenitic region. An axial compressive stress in the hardening layer and a tensile stress in the core are generated on this section (curve S_4 in **Figure 16(b)**). The magnitude and distribution of the stresses on section S_4 do not change significantly during subsequent cooling. This is therefore taken as the final measurements.

The authors simulated the effect of the initial yield stress of the steel on the final residual stress distribution, and it was found that both the axial stress and the hoop stress become more compressive with increased yield stress. An increase in the yield stress from 650 to 850 MPa caused an increase in axial compressive from about 750 to 850 MPa and in hoop stress from about 750 to 820 MPa. The restraining effect of the core obviously depends on the strength of the steel.

Störzel et al. (*35*) carried out simulation of progressive induction hardening with the goal of optimizing the process parameters: feeding speed of the induction coil, induced power, case depth, and residual stress. **Figure 17(a) and 17(b)** shows 3D diagrams of the result. The authors conclude that maximum compressive surface residual stress is obtained with the combination of small

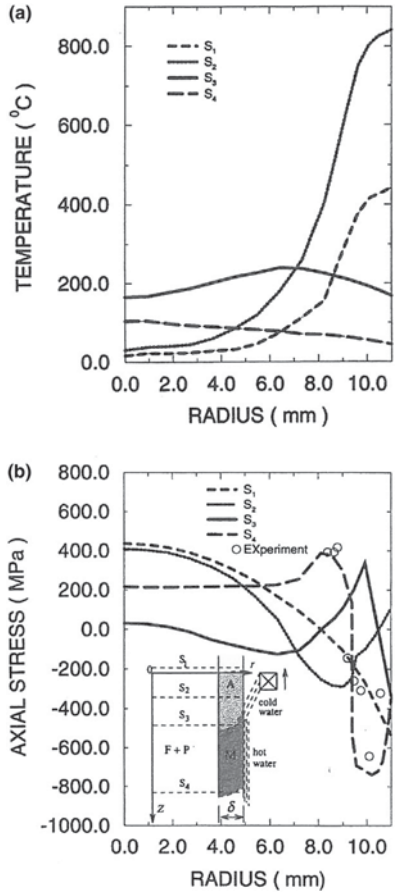

Figure 16 Variations of the calculated temperature (a) and the axial stress (b) during surface induction hardening for a cylinder of 22 mm diameter with a 1.8 mm hardened layer. S_1, $Z = -0.317$ mm; S_2, $Z = 3.317$ mm; S_3, $Z = 9.317$ mm; S_4, $Z = 300.317$ mm. A, austenite; M, martensite; F + P, ferrite + pearlite; ○, experimental value. Reproduced from Xu, D.; Li, Z.; Luo, J. Expressions for Predicting the Residual Stress in Surface Induction Hardening of Steel Bars. *Modell. Simul. Mater. Sci. Eng.* **1996**, *4* (1), 118.

induced power and small feeding speed; when the structure is martensitic in whole cross section, only small surface residual stress is obtained. By choosing a certain combination of induced power and feeding speed, a desirable surface residual stress can be obtained. The authors emphasize the need for good input data to get reliable results. This type of calculation can reduce the number of necessary experiments for process optimization and thus shorten the product development cycle.

At the edges of an induction-hardened zone, residual tensile stresses can occur (see **Figure 18**). They are probably caused by a plastic deformation in compression during heating to maximum temperature below A_1 (*36*), followed by an elastic deformation in tension during the cooling to the final temperature.

12.08.7.3 Laser Hardening

The laser surface hardening is well described in *ASM Handbook* (*37*). When a laser beam of enough high-power density impinges on a steel surface, only a fraction of the beam energy is absorbed and the rest is reflected. To increase the absorbability, the surface can be coated by substances such as carbon or manganese phosphate. The rate of surface heating can become very high, and the temperature can quickly exceed the temperature when austenite starts to form. The calculation of the austenitization can be made by help of TTT-diagrams on heating (*24*,*38*). These isothermal diagrams clearly show that the formation of austenite takes time and that the higher the temperature and the finer the starting microstructure, the shorter the time needed. Until carbide dissolution is finished, a so-called inhomogeneous austenite is obtained. The formation of martensite, bainite, pearlite, and ferrite on cooling can be calculated using programs developed by several workers. Usually, the rate of cooling is so high due to self-quenching that all austenite is transformed to martensite; that is, the depth of austenitization determines the hardened depth. High retained austenite contents have been reported in the outer layers of laser-hardened medium carbon steels (*39*).

The hardness profiles normally show a steep gradient at the case/core interphase. If the core is a martensite or a bainite tempered at a moderate temperature, a softer zone can be found next to the case due to extra tempering by the laser heating. There is a linear relationship between the magnitude of peak hardness of laser-hardened specimen and its carbon content (*40*).

$$\mathrm{HV} = 279.7 + 1024.9\mathrm{C}\ (\mathrm{w\%})$$

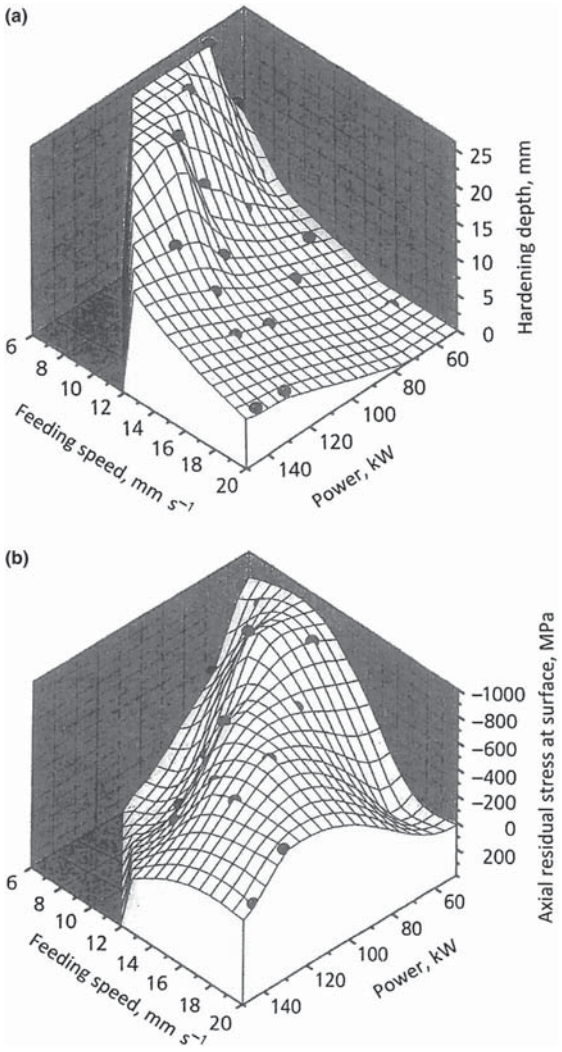

Figure 17 Calculated influence of the feeding speed and the induced power on (a) the hardening depth of a progressively hardened drive shaft and (b) residual stress at the surface. Reproduced from Störzel, K.; Schöpfel, A.; Idelberger, H. Optimierung der Prozessparameter fuer die induktive Randschichthärtung mit Hilfe numerische Simulation. *Härterei-Technische Mitteilungen* **1997**, *52*, 71.

The hardness due to laser treatment is higher than the conventional furnace hardness and is inside the so-called superhardness band (*41*).

In principle, all steels and irons that can be hardened by conventional means can also be laser hardened. Even low-carbon steels that normally cannot be induction hardened can be laser hardened due to extremely high cooling rates obtained by self-quenching. The influence of the carbide distribution is even more important than for induction hardening. A coarse carbide (pearlite islands) can give rise to martensite islands.

Laser hardening of steel in analogue with other surface-hardening processes gives rise to residual stresses in and a little below the hardened layer. The generation of residual stresses is a consequence of nonuniform permanent strains that occur during the process of heating and cooling:

- *Thermal strains due to localized heating or cooling.* It will cause residual tensile stresses both along and perpendicular to the laser-hardening track. In the surrounding material, compressive residual stresses will occur in the longitudinal direction and tensile in the transverse direction.
- *Volume changes involved in local phase transformation from austenite to martensite.* These changes will cause an increase in the specific volume, which will give compressive residual stresses in both directions. In the surrounding material, compressive residual stresses will be set up in the transverse direction and tensile in the longitudinal direction.
- *Heterogeneous plastic deformation in a nonconcurrent process depending on the time sequence of phase transformation and thermal strain.* For self-quenched specimens, a phase transformation front is expected to move from the interior outward. Stresses created by this mechanism will be compressive in the surface and tensile in the interior.

Figure 19 shows an example of experimentally measured residual stresses in a steel (*42*). The measurements have been carried out by the X-diffraction method that permits measurement in a few micrometer-thick surface layer and in an area as small as below

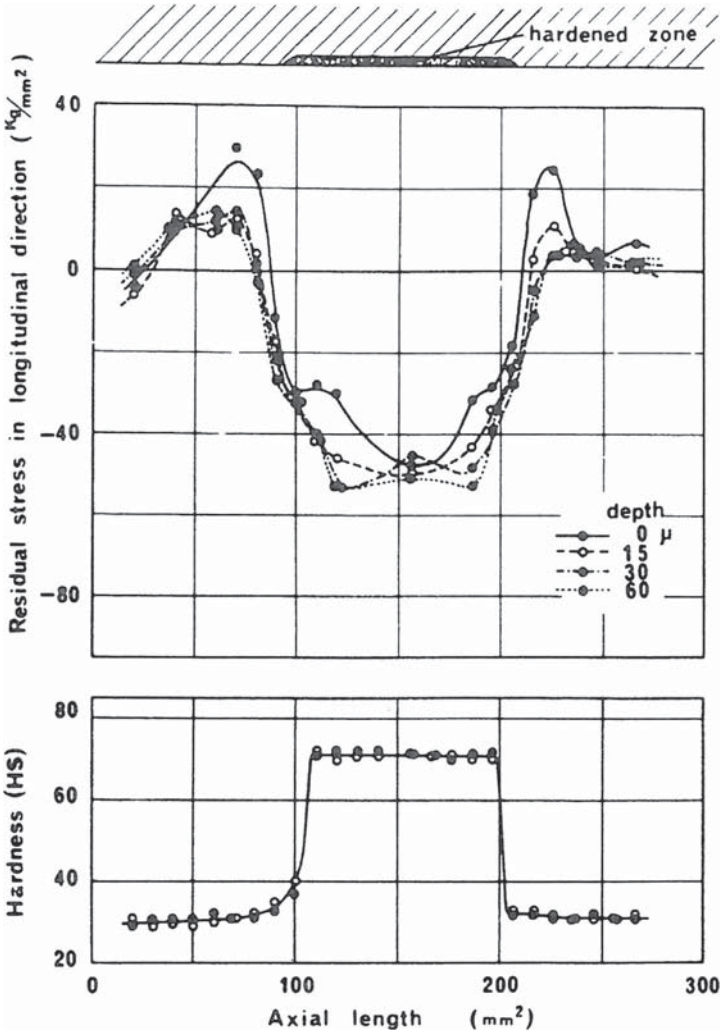

Figure 18 Residual stresses and hardness of static induction-hardened surface, diameter of specimen is 190 mm, frequency 10 kHz, and heating time 50 s. Reproduced from Ishii, K.; Iwamoto, M.; Shiraiwa, T.; Sakamoto, Y. Residual Stress in the Induction Hardened Surface of Steel. *SAE* **1971**, 710280.

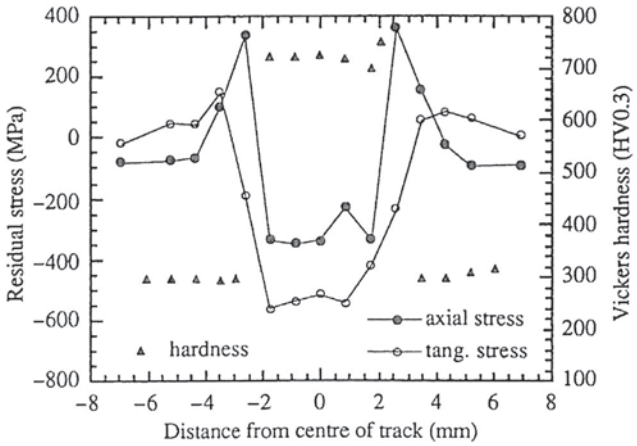

Figure 19 Residual stress distribution in AISI4140 steel, with corresponding hardness profile across a track at a depth of 125 μm below the surface. Reproduced from Lin, R. On Residual Stresses and Fatigue of Laser Hardened Steels. Dissertation No. 286, Linkoping University, Linkoping, Sweden, 1992.

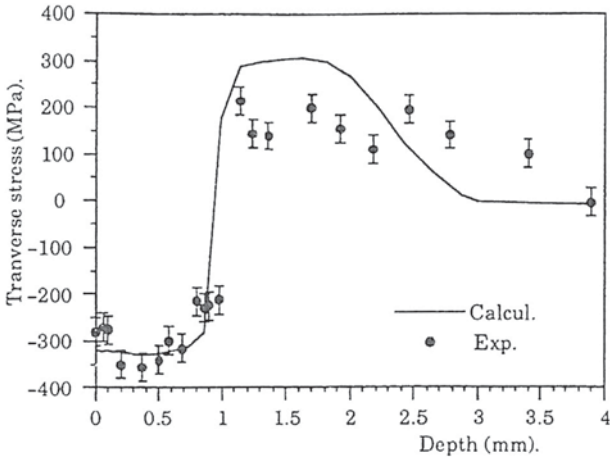

Figure 20 Residual stress distribution in the middle of a laser-hardened track in a 0.42%C steel plate. Reproduced from Denis, S.; Boufoussi, M.; Chevrier, J.; Simon, A. Analysis of the Development of Residual Stresses for Surface Hardening of Steel by Numerical Simulation: Effect of Process Parameters. In *Proceedings International Conference on Residual Stress, ICRS4*; Society of Experimental Mechanics: Baltimore, USA, 1994; pp 513–519.

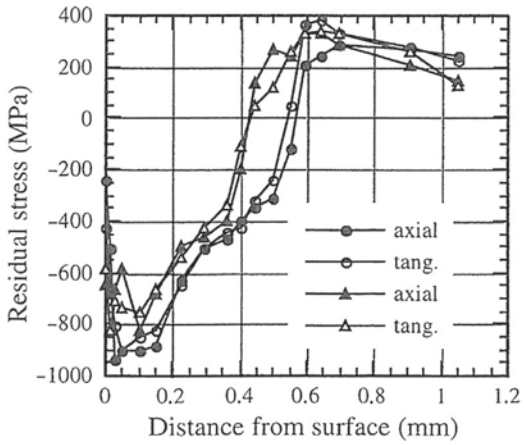

Figure 21 Residual stress profiles in laser-hardened smooth fatigue specimens of AISI4140 steel. Track center (circles) and overlapping zone (triangles). Reproduced from Lin Peng, R.; Ericsson, T. Effect of Laser Hardening on Bending Fatigue of Several Steels. *Scand. J. Metall.* **1998**, *27*, 180–190.

1 mm^2. It is interesting to note the tensile peaks on either side of the track. They are more pronounced in the longitudinal than in the transversal direction, while the compressive stress in the center is larger in the transversal direction. It is worth pointing out the close analogue between residual stress creation around welds and laser-hardening tracks. Although one can understand in principle each one of the three sources of residual stress mentioned above, their interaction is impossible to predict without doing theoretical calculations. A number of such models have been published (e.g., *43–46*). Excellent agreement between experimental and calculated values across a laser-hardened track in various steels has been achieved in another study (see **Figure 20**).

The depth where the hardness reaches the core hardness agrees with the depth of changeover from compressive surface stresses to tensile core stresses, which has also been demonstrated by computer modeling (*44*). The compressive residual stress can be increased by adding water cooling to self-cooling (*44,47*). The data in **Figure 21** is from a cylindrical specimen that was hardened along a spiral track with a certain overlap between two consecutive turns. **Figure 21** also shows the residual stress in the overlap zone, and it is compressive. It is important to study the overlap zone a little more closely because it is a potentially weak spot in fatigue. A systematic study has been made (*48*) from which **Figure 22** is reproduced. In the overlap zone 3, the steel is rehardened and next to it in the first pass a tempered zone 4 is formed. The rehardened zone is the hardest. Tensile residual stresses may exist in the tempered zones. In another study (*40*), the highest compressive stresses were measured in the rehardened zone. The contradictory stress values reported for the overlap zones are probably due to the difficulty in exactly localizing the measuring spot.

12.08.7.4 Carburizing

Carburized steels present a more complicated picture than steels with homogeneous carbon content. Already in the early 1930s, it was shown experimentally that large compressive stresses are present in carburized steel (*49*). This was explained as a result of the larger expansion of the high-carbon martensite in the surface relative to the core. Typical maximum compressive stress values vary

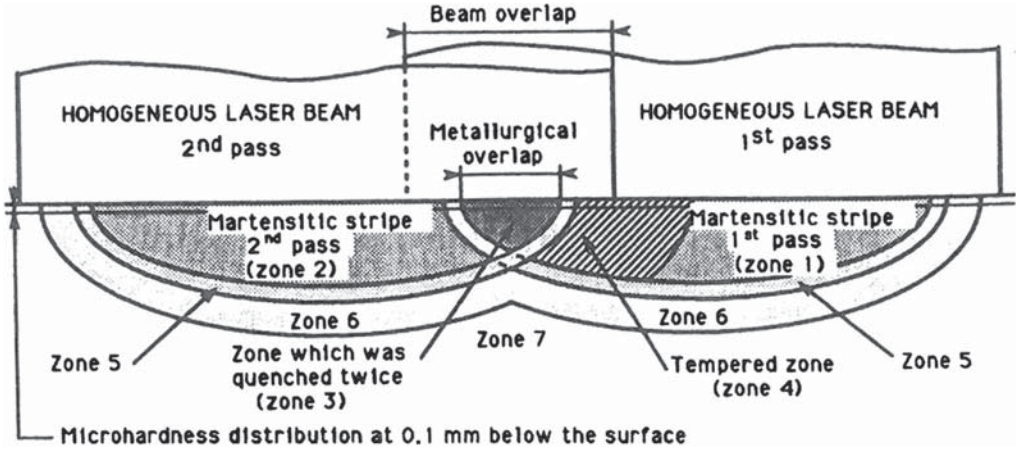

Figure 22 Sketch of area quenched and tempered during multipass treatment. Reproduced from Izery, F.; Deshors, G.; Mongis, J.; Peyre, J. DGM Informationsgesellschaft, Oberursel, Germany, 1992; p 331.

between 700 and 300 MPa. Koistinen (*50*) measured and explained qualitatively the residual stress distribution in carburized steels. The basis for his explanation is the fact that the martensite start temperature, M_s, decreases with increasing carbon content. The martensite transformation will start where the temperature first cuts the M_s curve (see **Figure 23**). The transformation then spreads outward and inward. The untransformed austenite in the surface layer is plastically strained in tension due to the core transformation. When the elongated surface is finally transformed, large compressive stresses are set up. However, the high retained austenite content close to the surface causes the maximum compressive stress to occur at 50–60% of the total case depth, corresponding to about 0.5%C in low-carbon steels. The reversal in sign of the residual stress occurs at, or very near, the case-core interphase. The statement about the position of the compressive stress maximum should not be regarded as a general rule, as will be shown in the following.

Computer modeling has been very instructive in explaining the mechanism of case hardening in greater detail. There is a wealth of literature about this subject (*13,25,51–56*).

In **Figure 24(a)–24(d)**, one can follow how the transformation of austenite starts below the surface and proceeds and how at the end the austenite in the case is partially transformed to martensite. The evolution of the stress can be seen in **Figure 25**. At first, the stress has atypical thermal distribution with tension at the surface and compression in the center. When a fair amount of the austenite has transformed in the case/core interface, the stress there is pushed into compression. When the case transforms to martensite, the stress there becomes compressive and a tensile peak appears below this layer. The tensile peak for other radii, carbon

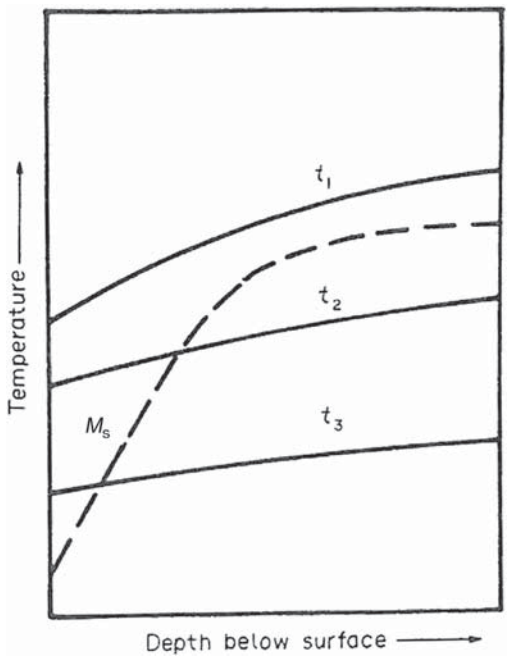

Figure 23 Temperature distribution at the time t_1, t_2, and t_3 during quenching of a carburized specimen in relation to the M_s temperature. Reproduced from Koistinen, D. The Distribution of Residual Stresses in Carburised Cases and Their Origin. *Trans. ASM* **1958**, *50*, 227–241.

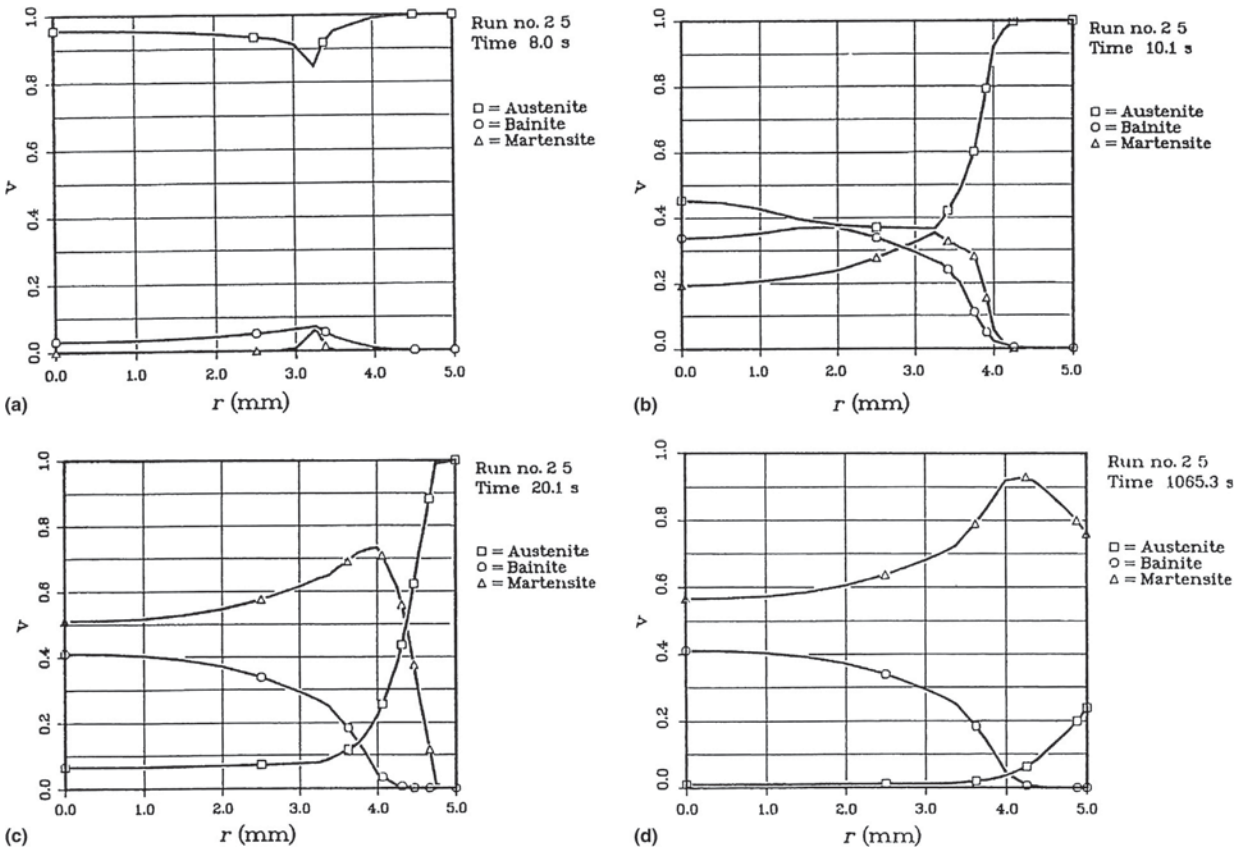

Figure 24 Computed phase contents at different times after the start of the oil quenching of a cylindrical specimen with 10 mm diameter, 1.0 mm case depth, and 0.84%C surface carbon content. The steel has 0.16%C, 0.7%Cr, 1.0%Ni. (a) At 8.0 s. (b) At 10.1 s. (c) At 20.1 s. (d) At 1065 s. Reproduced from Knuuttila, M. Computer Controlled Residual Stress Analysis and Its Application to Carburized Steel. Ph.D. Thesis No. 81, Linkoping University, Linkoping, 1982.

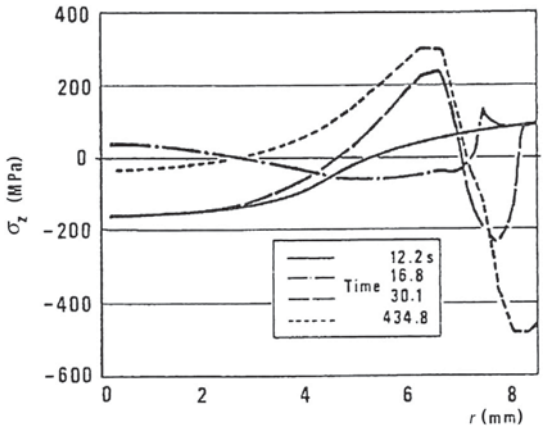

Figure 25 Calculated axial stress at 12.2, 16.8, 30.1, and 434.8 s after the start of the oil quenching of a cylindrical specimen with 17 mm diameter, 0.9 mm case depth (550 HV), and 0.8%C in the surface. Same steel as in **Figure 24**. Reproduced from Ericsson, T.; Sjostrom, S.; Knuuttila, M. Predicting Residual Stresses in Cases. In *Case Hardened Steels: Microstructural and Residual Stress Effects*; Diesburg, D., Ed.; The Metallurgical Society of AIME: Warrendale, Pennsylvania, USA, 1984; pp 113–139.

depths, or steel analysis may be missing (*56*). During the cooling, the yield stress is attained at different locations at different times, and the plastic deformation taking place greatly affects the final stress distribution. The so-called transformation plasticity will also have an important effect (*28,55*).

Usually, the residual stress in carburized steel displays a minimum (=maximum compressive stress) a little below the surface (see **Figure 25**). Distributions with an intermediate maximum has also been observed (**Figure 26**) (*51,57*). The reason for the minimum in **Figure 25** is the high retained austenite content in the surface zone. There is a shift toward the surface of the residual stress minimum for lower surface carbon contents (less retained austenite) (*57*). The depth of the residual stress minimum is also

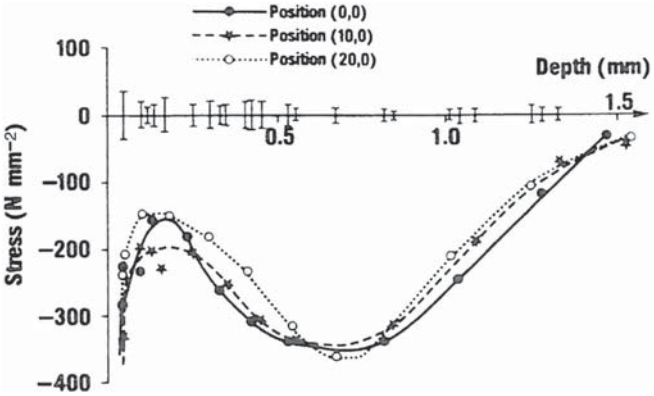

Figure 26 Residual stresses versus depth below the surface in a 10 × 50 × 80 mm rectangular specimen, 0.65 mm case depth (550 HV), and 0.82%C in the surface. The steel has 0.18%C, 0.7%Cr, 3.0%Ni, and 0.05%Mo. Reproduced from Hildenwall, B.; Ericsson, T. Prediction of Residual Stresses in Case Hardening Steels. In *Hardenability Concepts with Application to Steel*; Doane, D., Kirkaldy, J., Eds.; Met. Soc. AIME: Warrendale, USA, 1978.

strongly influenced by the specimen dimensions for a constant carbon profile as shown by (*55*,*57*). When comparing specimens of the same size, the minimum occurs approximately at the same fraction of the case depth independent of carbon profile (*55*). The depth at which the residual stress in the surface changes sign increases with the increasing diameter of a cylindrical specimen with a certain carbon profile, and at the same time the maximum compressive stress increases. The explanation is that a larger diameter means a smaller amount of martensite in the core, so the difference between the transformation strain in the case and the average transformation strain in the cylinder is increased.

With increased case depth and constant diameter, the maximum compressive stress tends to decrease (*14*,*55*), but the effect is not always significant (*58*). A more severe quenching, such as water quenching instead of oil quenching, tends to give larger compressive stresses (*57*,*58*), which is supported by calculation (*55*).

The measured residual stresses so far are in the martensite/bainite phase. But the microstructure in the high-carbon case contains fairly large percentages of retained austenite. In an extensive work by Beumelburg (*59*), the residual stress and the retained austenite content were measured in four different steels carburized to between 0.45 and 1.20%C in the surface. Most of the steels were annealed at 170 °C. As a general trend for the surface stresses, the austenite stress decreased with increased retained austenite content (9–65%) and was tensile except for more than 40% austenite. The martensite stress was in most cases compressive. In another fairly extensive study of 16 specimens (*60*) with austenite content between 15 and 32%, the stress was compressive in both phases except in one single specimen which had tensile stress in the austenite. The magnitude in the austenite was as a rule slightly smaller than in the martensite, except in the odd specimen where the magnitude in the austenite was much larger. More studies are needed to clarify the relation between the residual stress in martensite and retained austenite. The computer modeling so far has not treated the phases separately.

Subzero treatment of as-carburized steels reduces the retained austenite content due to martensite formation. It is intuitively to be expected that the martensite stress should become more compressive due to swelling of the case. Beumelburg (*59*) found a subsequent shift of the residual stress in the martensite phase in the compressive direction. A few studies, however, have shown a more complicated pattern; the compressive stress in the martensite layer just below the surface is reduced about 50 MPa, but deeper into the material it is increased about 50 MPa (see **Figure 27**).

A low-temperature temper (170 °C) is reported to shift the residual stress in the tensile direction in the martensite. A tensile shift has also been observed in the retained austenite (*57*,*59*), see details below.

Very often in gas carburizing, a thin soft layer (typically 10 μm) is formed on the surface due to oxidation of alloying elements such as Cr and Mn. The hardenability of the dealloyed layer is relatively low, and therefore fine pearlite is formed early during the cooling. This layer becomes strained in tension during martensite formation of the case, and tensile residual stresses arise (*61*). Therefore very often a few micrometer-thick layer is removed before measuring the residual stress by X-ray diffraction in the surface of gas-carburized steel.

12.08.8 Effect of Tempering on Residual Hardening Stresses

Martensitic steels are very often used in a tempered condition. One usually identifies three distinct stages of tempering (*41*).

Stage I, 100–250 °C: The formation of a transition carbide, epsilon carbide, or eta carbide and the lowering of the carbon content of the matrix martensite to about 0.25%C.
Stage II, 200–300 °C: The transformation of retained austenite to ferrite and cementite.
Stage III, above 250 °C: The replacement of the transition carbide and low-carbon martensite by cementite and ferrite.

The temperature ranges overlap depending on the tempering times used. Sometimes, a 0-stage is designated which involves carbon atoms segregation to dislocations and internal boundaries.

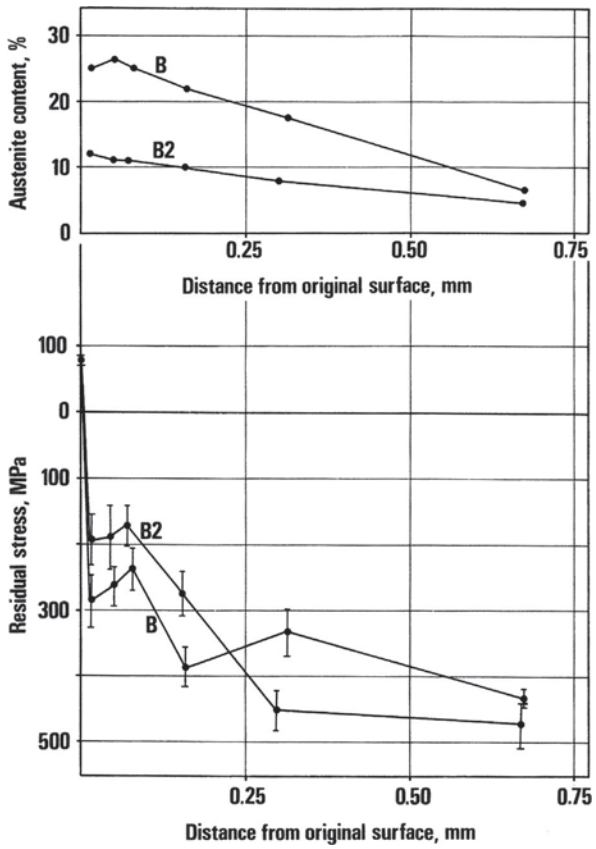

Figure 27 Measured distributions of retained austenite and residual stress versus depth below the surface in a cylindrical specimen with 15 mm diameter, 0.80 mm case depth (550 HV), and 0.85%C in the surface. Same steel as in **Figure 24**. Reproduced from Magnusson, L. Cyclic Behaviour of Carburized Steel. Dissertation No. 81, Linkoping University, Linkoping, 1980.

Relaxation of residual stress is to be expected if the stress exceeds the yield stress of the material or if density changes take place, such as the decomposition of martensite or retained austenite. The latter phenomenon is of course normally accompanied by yield stress changes. The well-known diagram of hardness versus tempering temperature for steels of various carbon content gives a guide as to when to expect residual stress relaxation (see **Figure 28**) (*41,61*). Below 100 °C, no relaxation is expected, between 100 and

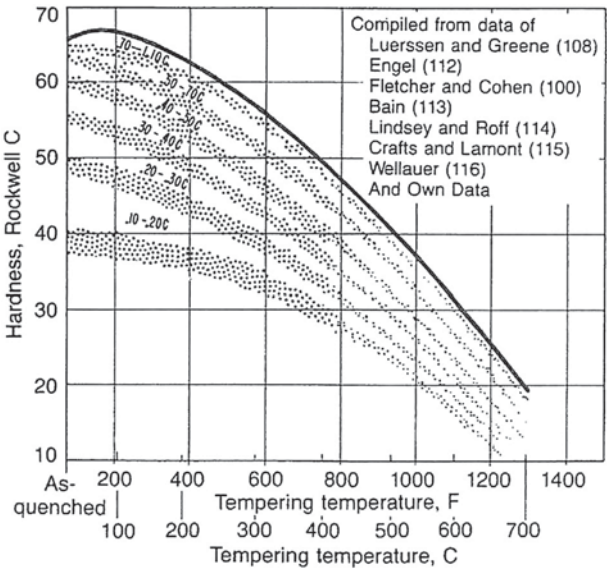

Figure 28 Decrease in hardness with increasing tempering temperature for steels of various carbon contents. Reproduced from Krauss, G. *Steels-Processing, Structure, and Performance;* ASM International: Metals Park, Ohio, 2005; p 329, Fig 17.2

200 °C some could occur, and above 200 °C residual stress relaxation should take place. Tempering below 200 °C is often applied to carburized and induction-hardened steels to reduce the risk of cracking. Tempering above about 400 °C is used to create quench and tempered steels that have mechanical properties very different from the as-quenched condition. As has been pointed out recently, much less effort has been devoted to simulating microstructure and stress evolution during the tempering process than on hardening (*62*). The reason for this fact regarding residual stresses in quench and tempered steels is probably that no or very low residual stresses remain in quench and tempered steels after high-temperature tempering. Some examples of the effect of tempering will be cited below.

Figure 29 shows the influence of homologue temperature $T(\mathrm{K})/T_m(\mathrm{K})$ on residual stress ratio $\sigma_{rs}(T)/\sigma_{rs}(293\ \mathrm{K})$ after 1 h anneal (*63*). The curves marked *f* and *g* are for hardened samples made of the carbon steels Ck22 and Ck45, respectively (AISI 1022 and 1045). No relaxation has occurred below 100 °C, and a relatively rapid relaxation is seen above this temperature.

From a very extensive study on residual stresses in carburized steel (*59*), a few results can be cited: For the steel 16MnCr5 with carburizing depth 0.9 mm and surface carbon content 0.67%C, a temper at 170 °C for 2 h shifted the surface residual stress in martensite in the tensile direction with 60–90 MPa from about 120 MPa in compression. The corresponding measurements for a surface carbon content of 1.14%C showed a tensile shift of about 150 MPa in martensite and 200 MPa in austenite. The residual stress before temper was about 100 MPa compression in martensite and 180 MPa compression in austenite, that is, relative low-surface residual stress values. In the same study, the effect of deep cooling in liquid nitrogen, −196 °C, was studied; surface carbon content was 1.14%C. The residual stress was shifted about 120 MPa in the compressive direction in martensite and about 270 MPa in the tensile direction in austenite. The retained austenite content was reduced from about 60% to about 20% by the deep cooling. Tempering after deep cooling caused a shift of about 150 MPa in the tensile direction in martensite and about 290 MPa in austenite. In all the cited cases, flat specimens with cross section 7 × 24 mm were used.

In another paper (*64*), the effect of specimen diameter, 15 and 38 mm, and tempering temperature, 180–500 °C, was studied for the steel SAE 4120RH carburized in a gas with carbon potential 1.2%. The core hardness became 37HRC and 22HRC for two diameters. The core structure consists predominantly of upper bainite in the 38-mm-diameter specimen and of martensite in the 15 mm specimen. The surface residual stress was measured after tempering at several temperatures. Below about 180 °C the residual stress was relatively constant, 300 and 150 MPa in compression for the 38 and 15 mm specimen, respectively. The difference is due to a non-martensitic core microstructure in the 38 mm specimens in contrast to martensitic in the 15 mm specimen. At 400 °C, the residual stress was about 140 MPa in compression for both types of specimen. The high temperature tempering had changed the core microstructure to become similar. The case microstructure did not depend on specimen diameter.

The effect of deep cooling touched upon above has been treated in greater detail in a study (*65*) on carburized samples of the steel En 353, with case depth 1 mm, and surface carbon content 0.75%. Six different treatments were applied: carburized (CHTUT), carburized and tempered at 150 °C for 1.5 h (CHTT), carburized and cryogenically treated at 193 K for 5 h (SCTUT), ditto plus tempering (SCTT), carburized and cryogenically treated at 77 K for 24 h (DCTUT), and ditto plus tempering (DCTT). The retained austenite content in the surface was 28% as quenched, 22% after 193 K treatment, and 14% after 77 K treatment. The tempering did not affect the values. The residual stress values down to a depth of around 300 μm are shown in **Figure 30(a)**. In **Figure 30(b)**, the residual stress values after tempering are shown. It is obvious that the 193 K treatment did not affect the residual stress and that the 193 K cryotreatment caused almost a doubling of the compressive stresses. The gradient is the same for all 77 cryotreatments before

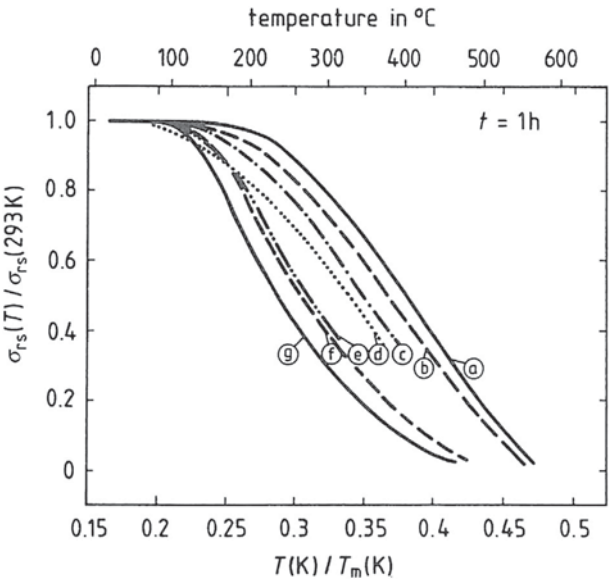

Figure 29 Influence of homologous temperature T/T_m on residual stress ratio $\sigma_{rs}(T)/\sigma_{rs}(293\ \mathrm{K})$ of steels annealed for 1 h. Reproduced from Vohringer, O.; Wohlfahrt, H. Abbau von Eigenspannungen, Härterei-Technische Mitteilungen. *Beiheft* **1983**, 144–156.

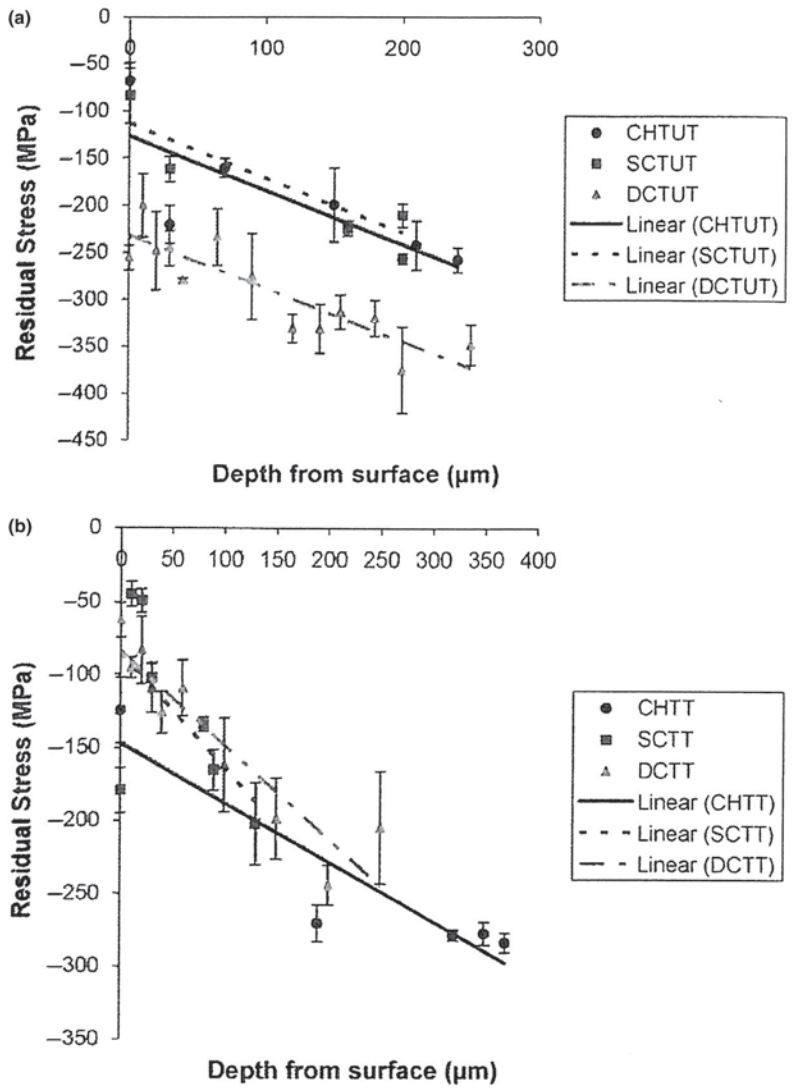

Figure 30 Distribution of residual stress in En 353 steel specimens (a) prior to tempering and (b) after tempering. Reproduced from Bensely, A.; Venkatesch, S.; Mohan Lal, D.; Nagarajan, G.; Rajadurai, A.; Junik, K. Effect of Cryogenic Treatment on Distribution of Residual Stress in Case Carburized En 353 Steel. *Mater. Sci. Eng. A* **2008**, *479*, 229–235.

tempering. Tempering did not influence the residual stress of the as-quenched and 193 K cryo-treated samples very much, which is not surprising considering the discussion in a paragraph above. Surprisingly, tempering caused a marked reduction of residual stress in the 77-K-treated samples. The authors suggest this effect to be due to cluster formation of carbon during the heating up to room temperature after the 77 K cryo-treatment and the clusters act as nuclei for finer precipitate formation during the subsequent cooling.

The last three references seem to contradict each other concerning the effect of tempering in the range 150–180 °C. A careful study of Figure 30 reveals that the residual stress values there are slightly lower after a temper at 180 °C than in the as-quenched condition. The conclusion is that the temperature range 150–180 °C is very critical.

Before leaving the subject of cryogenic treatment (deep cooling), mention should be made of a recent handbook chapter (*66*). The emphasis is on microstresses in tool steels, and not on macrostresses. The microstresses are reduced in magnitude by deep cooling in contrast to the macrostresses.

12.08.9 Effect of Fatigue on Residual Hardening Stresses

Martensitic steels are often used to make components exposed to fatigue loads. Residual hardening stresses have an important influence on the mechanical properties of martensitic steels. It is therefore important to know when fatigue loading can affect the residual stresses, especially when they can cause residual stress relaxation. There is a vast literature about the effect of residual stress

on fatigue and the relaxation of residual stress due to fatigue. Here focus is on martensitic steels of high hardness, in particular surface-hardened steels.

Residual stress relaxation can be expected when the residual stress plus the applied stress exceeds the yield stress (elastic limit) either in tension or compression. Then it should be remembered that the cyclic yield stress rather than the monotonic yield stress should be considered. **Figure 31** (*67*) shows that steels with hardness higher than about 600 HB (650 HV) cyclicly harden. A rule of thumb says that if $\sigma_{uts}/\sigma_{yield} > 1.4$ hardening is expected. **Figure 32** shows that stress relaxation at these high hardnesses requires relatively large strain amplitudes (short fatigue lives) to happen. In surface-hardened materials that have a hardness gradient (fatigue strength gradient), the situation may arise that the applied stress plus the residual stress exceeds the (cyclic) yield stress not at the surface but in a zone below the surface. A residual stress relaxation will affect the residual stress at the surface because of the residual stress equilibrium condition mentioned in an earlier paragraph. For steel of lower hardnesses and without retained austenite, the residual stress relaxes due to fatigue loading when the applied plus the residual stress exceeds 60% of the yield stress (*68*) and the first few cycles are most effective. The higher the amplitude, the faster the relaxation (*68*). The very high stability of residual stress in high-hardness martensitic steels means that shot peening, which introduces compressive residual stresses in the surface, can be very effective in increasing the fatigue resistance. It is much used but will not be discussed further here.

Compressive and tensile half-cycles affect the residual stress differently. If the residual stress is compressive, then it is the compressive half-cycles that cause relaxation. Actually, a buildup of the residual stress can be found after a tensile half-cycle. It should also be pointed out that it is mainly the residual stress in the direction of the applied stress that changes. Shot peening, for

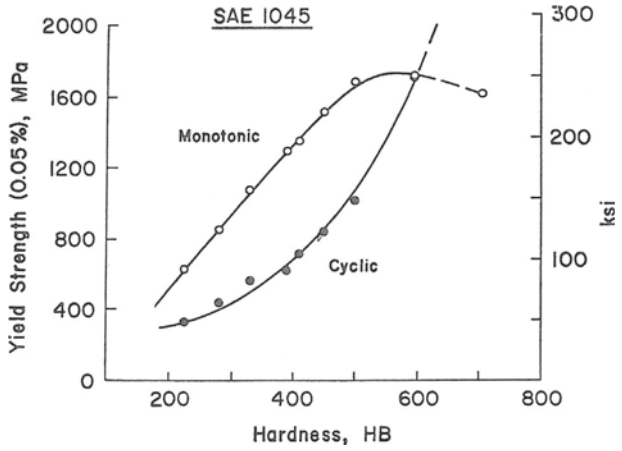

Figure 31 Influence of hardness on monotonic and cyclic yields strength for a medium-carbon steel. Reproduced from Landgraf, R.; Richman, R. *Fatigue Behavior of Carburized Steel. STP 569*; ASTM International, 1975; p 130.

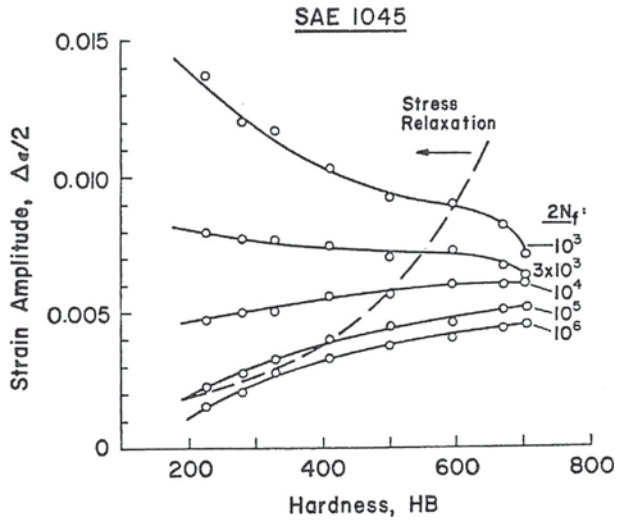

Figure 32 Fatigue and stress relaxation characteristics as a function of hardness. Reproduced from Landgraf, R.; Richman, R. *Fatigue Behavior of Carburized Steel. STP 569*; ASTM International, 1975; p 130.

instance, gives an isotropic biaxial stress state. After cycling, the residual stress component parallel to the stress amplitude is relaxed, while the other component is very little affected.

When a metastable phase is present, the fatigue cycling can induce transformation of this phase and, hence, cause a buildup of residual stress. An example is the transformation of retained austenite to martensite in carburized steel. In the study cited above (*59*), this has been studied using flat specimens in alternating bending fatigue. The residual stress was found to get more compressive in both martensite and austenite for a surface carbon content of 1.05%C and retained austenite content of 60% during the first 10 cycles and then relatively stable. The phase transformation was more complete for larger amplitudes, which meant larger compressive residual stress contributions. For specimens deep cold at −196 °C before tempering at 170 °C, virtually no changes due to fatigue loading in the residual stress in martensite was detected, but a smaller compressive shift occurred in austenite during the first 10 cycles. For specimens with surface carbon content of 0.65%C, no changes in residual stress was detected. The author contributes the changes in residual stress to transformation of retained austenite. They were about 60%C in the as-quenched 1.05%C specimens and about 10%C in the 0.65%C specimens.

In a study of fatigue of laser-hardened steel, relaxation of a residual stress depth profile was carried out (see **Figure 33**) (*42,69*). Hourglass-shaped specimens, diameter 10 mm, made of the Swedish steel SS2244 (AISI4140) was hardened with a Rofin Sinar HF1700 laser to a hardened depth of 0.46 mm and peak hardness 750 HV 0.3. The retained austenite content was 56% at the surface, 23% at a 23 μm depth, and 4% at a 30 μm depth. **Figure 33** shows the measured residual stresses after being loaded in bending at 630 MPa (surface amplitude) for 1.19×10^7 cycles. The compressive stress peak in the near surface has been reduced by about 150 MPa, and the tensile peak in the core by about 200 MPa. The most severe relaxation occurred in the region between 0.05 and 0.5 mm. The stress curves in the fatigue-loaded and fatigue-nonloaded specimens cross over each other near the zero stress level. The same degree of relaxation is found for both axial and tangential directions. In **Figure 34**, the estimated yield stress

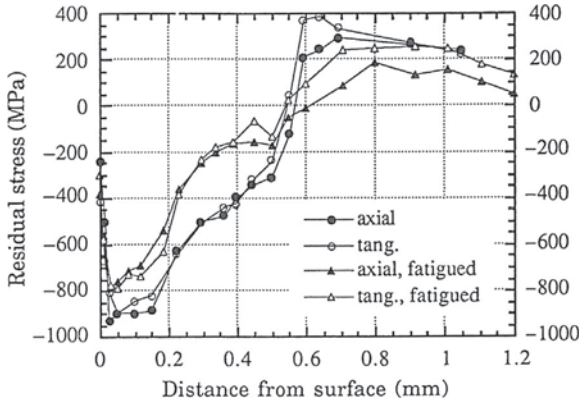

Figure 33 Residual stress distribution in smooth specimens of steel SS2244 cyclically loaded at 630 MPa for 1.19×10^7 cycles. The stress state in a specimen before fatigue is also plotted. Reproduced from Lin, R. On Residual Stresses and Fatigue of Laser Hardened Steels. Dissertation No. 286, Linkoping University, Linkoping, Sweden, 1992.

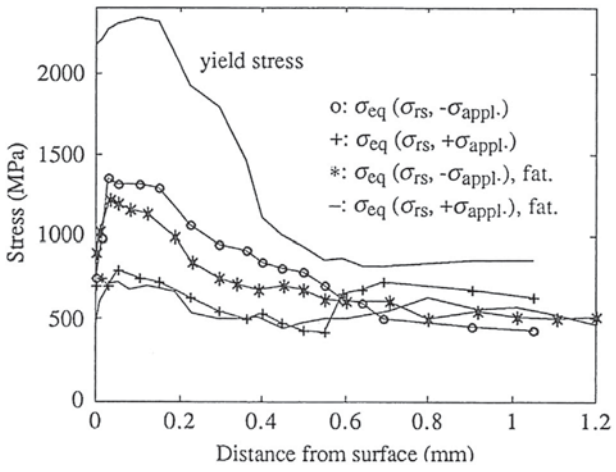

Figure 34 Depth distribution of yield stress and von Mises equivalent stress of residual and maximum applied stresses in fatigue loaded and nonloaded specimens of steel 2244. Reproduced from Lin, R. On Residual Stresses and Fatigue of Laser Hardened Steels. Dissertation No. 286, Linkoping University, Linkoping, Sweden, 1992.

σ_y and the equivalent von Mises σ_{eq} stress are shown for the same specimen as in Figure 33. The yield stress and the Mises stress have been calculated according to the expressions.

$\sigma_y = 1.289\ R_m - 392$	for $R_m \leq 982$ MPa	Ref. (*70*)
$\sigma_y = 0.893\ R_m - 3$	for $R_m > 982$ MPa	
$R_m = 3.29\ \text{HV} - 47$	for HV ≤ 445	Ref. (*71*)
$R_m = 4.02\ \text{HV} - 374$	for HV > 445	

$$\sigma_{eq} = 1/\sqrt{2}\sqrt{(\sigma_1 - \sigma_2)^2 + (\sigma_2 - \sigma_3)^2 + (\sigma_3 - \sigma_1)^2}$$

where R_m is the rupture modulus and σ_1, σ_2, and σ_3 are the axial, tangential, and radial stresses, respectively, of the sum of residual and maximum applied stresses, that is,

$$\sigma_I = \sigma_{res,I} + \sigma_{applied}$$

Compressive yield stress is assumed to be the same as tensile yield stress. The von Mises stress is always taken to be positive regardless of the sign of σ_1.

In Figure 34, it is evident that the von Mises stress is much lower than the yield stress in the hardened zone and only slightly lower in the core. Therefore, residual stress relaxation is probably caused by cyclic yielding in the core.

12.08.10 Examples of Commercial Codes for Calculation of Residual Stresses due to Martensite Hardening

A number of computer codes are based on the FE technique. The earliest works used analytical techniques and later finite difference techniques as described in a review (*51*). The field has now reached the state that a number of commercial codes are available which can even handle 3D calculations. Two compilations of codes can be mentioned (*25*,*72*). The specialized codes most widely used are SYSWELD, HEART, DEFORM HT, TS 15, and DANTE (*73*). Some general codes such as ABAQUS and ANSYS are also applied for heat treatment calculations. The software developed by the National Center for Manufacturing Sciences should also be mentioned (*53*). Finally, one can with some exaggeration state that the limiting factor is not now codes but the difficulty in finding reliable data to be used in the calculations. The most difficult to find are the mechanical high-temperature data.

See also: Controlling the Cooling Process – Measurement, Analysis, and Quality Assurance; Metallo-Thermo-Mechanical Coupling in Quenching; Austenite Formation and Microstructural Control in Low-Alloy Steels; Induction Hardening: Technology, Process Design, and Computer Modeling.

References

1. Sugianto, A.; Narazaki, M.; Kogawara, M.; Shiraayori, A.; Kim, S.-Y. Numerical Simulation and Experimental Verification of Carburizing-Quenching Process of SCr420H Steel Helical Gear. *J. Mater. Process. Technol.* **2009,** *209* (7), 3597–3609.
2. Simsir, C.; Gur, C. 3D FEM Simulation of Steel Quenching and Investigation of the Effect of Asymmetric Geometry on Residual Stress Distribution. *J. Mater. Process. Technol.* **2008,** *207* (1–3), 211–221.
3. Kang, S. H.; Im, Y. T. Thermo-Elasto-Plastic Finite Element Analysis of Quenching Process of Carbon Steel. *J. Mater. Process. Technol.* **2007,** *192–193*, 381–390.
4. Noyan, I.; Cohen, J. *Residual Stress;* Springer Verlag: New York, Berlin, Heidelberg, 1987.
5. Wolfstieg, U.; Macherauch, E. Zur Definition von Eigenspannungen. *Härterei-Technische Mitteilungen* **1976,** *31*, 2–3.
6. Hauk, V. *Structural and Residual Stress Analysis by Nondestructive Measures;* Elsevier Science BV.: Amsterdam, New York, Oxford, 1997.
7. Ericsson, T., Ed. Calculation of Internal Stresses in Heat Treatment of Metallic Materials *Mater. Sci. Technol.* **1985,** *1* (10), 754–921.
8. Lu, J., Ed. *Handbook of Measurement of Residual Stresses;* The Fairmont Press: Lilburn, Georgia, 1996.
9. *Heat Treating*; *ASM Handbook* ASM International: Metals Park, Ohio, 1991; Vol. 4.
10. Lu, J., Ed. *Handbook of Residual Stress;* Society for Experimental Mechanics: USA, 2005; Vol. 1.
11. Wallis, R. Modeling of Quenching, Residual Stress Formation, and Quench Cracking. In *Metals Process Simulation*; *ASM Handbook*; ASM International: Metals Park, Ohio, 2009; Vol. 22B, pp 547–585.
12. Totten, H., Ed. *Handbook of Residual Stress and Deformation of Steel;* ASM International: Metals Park, Ohio, 2002.
13. Ericsson, T. Residual Stresses Caused by Thermal and Thermochemical Surface Treatments. In *Advances in Surface Treatments;* Niku-Lari, A., Ed; Pergamon Press: Oxford, New York, Frankfurt, 1987; Vol. 4, pp 87–113.
14. Rose, A.; Hougardy, H. Transformation Characteristics and Hardenability of Carburizing Steels. In *Transformation and Hardenability in Steels;* Climax Molybdenum Company of Michigan, 1967; pp 155–167.
15. Rouhaud, E.; Montay, G.; Sicot, O.; Maras, A.; Francois, M. Two Dimensions Residual Stresses Analysis through Incremental Groove Machining Combined with Electronic Speckle Pattern Interferometry. *Exp. Mech.* **2009,** *49* (4), 459–469.
16. Denis, S.; Gautier, E.; Simon, A.; Beck, G. Stress-Phase Transformation Interactions – Basic Principles, Modelling, and Calculation of Internal Stresses. *Mater. Sci. Technol.* **1985,** *1* (10), 805–814.

17. Liu, C.; Yao, K.; Xu., X. J.; Liu, Z. Models for Transformation Plasticity in Loaded Steels Subjected to Bainitic and Martensitic Transformation. *Mater. Sci. Technol.* **2001,** *17* (8), 983–988.
18. Denis, S.; Gautier, E.; Sjöström, S.; Simon, A. Influence of Stresses on the Kinetics of Pearlitic Transformation during Continuous Cooling. *Acta Metall.* **1987,** *35,* 1621–1632.
19. Gautier, E.; Simon, A.; Beck, G. Plasticité de transformation durant la transformation perlitique d'un acier eutectoide. *Acta Metall.* **1987,** *35,* 1367–1375.
20. Majorek, A.; Mueller, H.; Macherauch, E. *Härterei-Technische Mitteilungen* **1996,** *51,* 11–18.
21. Thuvander, A. Prediction of Heat Treatment Distortion Using Numerical Simulation. Ph.D. Thesis, Report KTH/AMT-198, 2000.
22. Melander, M. Theoretical and Experimental Study of Stationary and Progressive Induction Hardening. *J. Heat Treat.* **1985,** *5,* 145–166.
23. Denis, S.; Farias, A.; Simon, A. Mathematical Model Coupling Phase Transformations and Temperature Evolutions in Steels. *ISIJ Int.* **1992,** *32,* 316–325.
24. Ericsson, T. Principles of Heat Treating of Steels. In *Heat Treating*; *ASM Handbook*, ASM International: Metals Park, Ohio, 1991; Vol. 4, pp 3–19.
25. Denis, S. Prévision des contraintes résiduelles induites par traitement thermique et thermochimique. *La Revue de Metallurgie* **1997,** *77,* 158–176.
26. Sjöström, S. The Calculation Residual Stress. In *Measurement of Residual and Applied Stress Using Neutron Diffraction;* Hutchings, M. T., Krawitz, A. D., Eds.; *NATO ASI Series;* Kluwer Academic Publisher: Dordrocht, Boston, London, 1992; Vol. 216, p 67.
27. Ehlers, M.; Mueller, H.; Löhe, D. Simulation der Spannungs-, Eigenspannungs-und Verzugsausbildung bei der Stahlhärtung. *Härterei-Technische Mitteilungen* **1999,** *54,* 208–215.
28. Denis, S. Considering Stress-Phase Transformation Interactions in the Calculation of Heat Treatment Residual Stresses. *J. Phys.* **1996,** *6,* 159–174.
29. Yu, H.; Wolfstieg, U.; Macherauch, E. Berechnung von Eigenspannungen mit Hilfe eines speziellen Finite-Element-Programmes. *Archiv fuer das Eisenhuettewesen* **1997,** *49,* 499.
30. Yu, H.; Schröder, R.; Graja, P.; Besserdich, G.; Majorek, A.; Hoferer, M. Zur modellierung und Simulation der Wärmebehandlung metallischer Werkstoffe. *Härterei-technische Mitteilungen* **1996,** *51,* 48–55.
31. Denis, S.; Zandona, M.; Mey, A.; Boufoussi, M.; Simon, A. Calculation of Internal Stresses during Surface Heat Treatment of Steels. In *Residual Stresses;* Hauk, V., Hougardy, H., Macherauch, E., Tietz, H.-D. E., Eds.; Residual Stresses; DGM Informationsgesellschaft: Oberursel, Germany, 1992; pp 1011–1020.
32. Tjernberg, A. Comparison of Methods for Determining Residual Stresses in Induction Hardened Transmission Shafts. *Scand. J. Metall.* **1999,** *28* (4), 162–168.
33. Xu, D.; Li, Z.; Luo, J. Expressions for Predicting the Residual Stress in Surface Induction Hardening of Steel Bars. *Modell. Simul. Mater. Sci. Eng.* **1996,** *4* (1), 111–122.
34. Xu, D.; Kuang, Z.-B. A Study on the Distribution of Residual Stress due to Surface Induction Hardening. *J. Eng. Mater. Technol.* **1996,** *118,* 571–575.
35. Störzel, K.; Schöpfel, A.; Idelberger, H. Optimierung der Prozessparameter fuer die induktive Randschichthärtung mit Hilfe numerische Simulation. *Härterei-Technische Mitteilungen* **1997,** *52,* 67–73.
36. Ishii, K.; Iwamoto, M.; Shiraiwa, T.; Sakamoto, Y. Residual Stress in the Induction Hardened Surface of Steel. *SAE* **1971**, 710280.
37. Sandven, O. In *Heat Treating, ASM Handbook*; ASM International: Metals Park, Ohio, 1991; Vol. 4, p 286.
38. Orlich, J. In *Atlas zur Wärmebehandlung der Stähle* Verlag Stahleisen: Duesseldorf, 1976; Vol. 4.
39. Chatterjee-Fischer, R.; Rothe, R.; Becker, R. *Härterei-technische Mitteilungen* **1984,** *39,* 91–98.
40. De la Cruz, P.; Odén, M.; Ericsson, T. Influence of Laser Hardening on the Fatigue Strength and Fracture of a B-Mn Steel. *Int. J. Fatig.* **1998,** *20,* 389–398.
41. Krauss, G. *Steels-Processing, Structure, and Performance;* ASM International: Metals Park, Ohio, 2005.
42. Lin, R. On Residual Stresses and Fatigue of Laser Hardened Steels. Dissertation No. 286, Linkoping University, Linkoping, Sweden, 1992.
43. Messer, K.; Bergmann, H. Stand des Laserstrahlhärtens. *Härterei-technische Mitteilungen* **1997,** *52,* 74–82.
44. Denis, S.; Boufoussi, M.; Chevrier, J.; Simon, A. Analysis of the Development of Residual Stresses for Surface Hardening of Steel by Numerical Simulation: Effect of Process Parameters. In *Proceedings International Conference on Residual Stress, ICRS4;* Society of Experimental Mechanics: Baltimore, MD, 1994; pp 513–519.
45. Domes, J.; Korner, C.; Bergmann, H. Residual Stresses in Laser Hardened Steels and Their Numerical Simulation. In *European Conference on Laser Treatment, ECLAT'94;* DGM Informationsgesellschaft: Oberursel, Germany, 1994.
46. Bailey, N.; Tan, W.; Shin, Y. Predictive Modeling and Experimental Results for Residual Stresses in Laser Hardening of AISI 4140 Steel by a High Power Diode Laser. *Surf. Coat. Technol.* **2009,** *203,* 2003–2012.
47. Cassino, F.; Moulin, G.; Ji, V. Residual Stresses in Water-Assisted Laser Transformation Hardening of 55C1 Steel. In *Fourth European Conference on Residual Stresses, ECRS4*; Denis, S.; Lebrun, J.-L.; Bourniquel, B.; Barral, M.; Flavenot, J.-F., Eds.; Cluny en Bourgogne, 1996; pp 839–849.
48. Izery, F.; Deshors, G.; Mongis, J.; Peyre, J. DGM Informationsgesellschaft, Oberursel, Germany, 1992.
49. Buehler, H.; Buchholtz, H.; Scheil, E. Eigenspannungen bei der Wärmebehandlung von Stahl. *Archiv fuer das Eisenhuettewesen* **1932,** *5,* 413–418.
50. Koistinen, D. The Distribution of Residual Stresses in Carburised Cases and Their Origin. *Trans. ASM* **1958,** *50,* 227–241.
51. Hildenwall, B.; Ericsson, T. Prediction of Residual Stresses in Case Hardening Steels. In *Hardenability Concepts with Application to Steel;* Doane, D., Kirkaldy, J., Eds.; Met. Soc. AIME: Warrendale, PA, 1978.
52. Réti, T. Residual Stresses in Carburised, Carbonitrided, and Case-hardened Components. In *Handbook of Residual Stress and Deformation of Steel;* Totten, G., Howes, M., Inoue, T., Eds.; ASM International: Materials Park, Ohio, 2002; pp 189–219.
53. Dowling, W.; Pattok, T.; Fergusson, B.; Shick, D.; Helen Gu, Y.; Howes, M. Development of a Carburizing and Quenching Simulation Tool: Program Overview. In *Second International Conference on Quenching and the Control of Distortion;* ASM International: Metals Park, Ohio, 1996; pp 349–355.
54. Aubry, C.; Denis, S.; Archambault, P.; Simon, A.; Ruckstuhl, F.; Miege, B. Prediction of Microstructures and Quenching Residual Stresses in Case Hardened Pieces Including Self-Tempering Effects. *Metall. Ital.* **1999,** *91,* 33–38.
55. Ericsson, T.; Sjostrom, S.; Knuuttila, M. Predicting Residual Stresses in Cases. In *Case Hardened Steels: Microstructural and Residual Stress Effects;* Diesburg, D., Ed.; The Metallurgical Society of AIME: Warrendale, Pennsylvania, 1984; pp 113–139.
56. Burnett, J. Evaluation of Elastic-Plastic Stresses in Quenched Carburized Cylinders by Finite Element Methods. Ph.D. Thesis, University of Akron, Akron, Ohio, 1977.
57. Coleman, W.; Simpson, M. Residual Stresses in Carburized Steel. In *Fatigue Durability of Carburized Steel;* American Society for Metals: Cleveland, 1957.
58. Motoyama, M.; Horisawa. *Residual Stress Measurements in Case Hardened Steels.* SAE 710281; Society of Automotive Engineers, 1971.
59. Beumelburg, W. Das Verhalten von einsatzgehärteten Proben mit verschiedenen Oberflächenzustanden und Randkohlenstoffgehalten im Umlauf biege,-statischen biege und Schlagbiegeversuch. Dissertation, University of Karlsruhe, Karlsruhe, 1974.
60. Knuuttila, M. Computer Controlled Residual Stress Analysis and Its Application to Carburized Steel. Ph.D. Thesis No. 81, Linkoping University, Linkoping, Sweden, 1982.
61. Hildenwall, B.; Ericsson, T. Residual Stresses in the Soft Pearlite Layer of Carburized Steel. *J. Heat Treat.* **1980,** *1,* 3–13.
62. Rajeev, P.; Jin, L.; Farris, T.; Chandrasekar, S. Modeling of Quenching and Tempering Induced Phase Transformations in Steels. *J. ASTM Int. (JAI)* **2010,** *1523,* 157–185.
63. Vohringer, O.; Wohlfahrt, H. Abbau von Eigenspannungen, Härterei-Technische Mitteilungen. *Beiheft* **1983,** 144–156.
64. Vatavuk, J.; Zicari di Monti, M.; Couto, A. The Effect of Core and Carburized Surface Microstructural Stability on Residual Stress Evolution during Tempering. *J. ASTM Int. (JAI)* **2010,** *1523,* 157–185.
65. Bensely, A.; Venkatesch, S.; Mohan Lal, D.; Nagarajan, G.; Rajadurai, A.; Junik, K. Effect of Cryogenic Treatment on Distribution of Residual Stress in Case Carburized En 353 Steel. *Mater. Sci. Eng. A* **2008,** *479,* 229–235.
66. Alexandru, I.; Bulancea, V. Effect of Cryogenic Cooling of Residual Stresses, Structure, and Substructure. In *Handbook of Residual Stress and Deformation of Steel;* Totten, G., Howes, M., InoueT, Eds.; ASM International: Materials Park, Ohio, 2002; pp 331–344.
67. Landgraf, R.; Richman, R. *Fatigue Behavior of Carburized Steel.* STP 569; ASTM International, 1975; p 130.
68. Wohlfahrt, H. Zum Eigenspannungsabbau bei den Schwingbeanspruchung von Stählen. *Härterei-technische Mitteilungen* **1973,** *28,* 288–293.

69. Lin Peng, R.; Ericsson, T. Effect of Laser Hardening on Bending Fatigue of Several Steels. *Scand. J. Metall.* **1998,** *27,* 180–190.
70. Buch, A. *Fatigue Strength Calculation*. Materials Science Surveys No. 6; Trans Tech Publications: Switzerland, 1988.
71. Kloos, K.; Velten, E. The Use of Hardness-and Residual Stress Profiles in a Scheme to Determine Fatigue Strength. In *Residual Stresses;* Macherauch, E., Hauk, V., Eds.; DGM Informationsgesellschaft Verlag, 1986; pp 203–229.
72. Besserdich, G.; Ehlers, M.; Luebben, T.; Majorek, A.; Schmitt, G.; Wiedmann, D. Weniger Verzug beim Härten durch Computer Simulation. *Härterei-Technische Mitteilungen* **1999,** *54,* 201–207.
73. Ferguson, B.; Li, Z.; Freborg, A. Modeling Heat Treatment of Steel Parts. *Computat. Mater. Sci.* **2005,** *34,* 274–281.

12.09 Distortion Engineering: Basics and Application to Practical Examples of Bearing Races

T Lübben, F Hoffmann, and H-W Zoch, IWT Stiftung Institut für Werkstofftechnik, Bremen, Germany

12.09.1	**Introduction**	299
12.09.2	**Basics of Distortion Generation**	300
12.09.2.1	Definition of Dimensional and Shape Changes	300
12.09.2.2	Fourier Analysis as a Powerful Tool for the Analysis of Distortion of Bearing Races	301
12.09.2.3	Mechanisms for Distortion of Steel Components	303
12.09.2.4	Unavoidable Size and Shape Changes	304
12.09.2.4.1	Volume Changes by Transformation	304
12.09.2.4.2	Size and Shape Changes by Thermal Stresses	306
12.09.2.4.3	Size and Shape Changes by Superposition of Thermal Stresses and Transformations	309
12.09.2.5	Avoidable Size and Shape Changes	312
12.09.3	**Collaborative Research Center 'Distortion Engineering'**	313
12.09.4	**Distortion Engineering of Bearing Races: Parameters and Variables**	316
12.09.4.1	Process Chain	316
12.09.4.2	Experimental Investigations – Processes before Heat Treatment	317
12.09.4.3	Experimental Investigations – Heat Treatment	319
12.09.4.3.1	Heating	319
12.09.4.3.2	Quenching	323
12.09.5	**Distortion Engineering of Bearing Races: Mechanisms**	324
12.09.5.1	Influence of the Carrier 'Mass Distribution (Geometry)'	325
12.09.5.1.1	Connection between Fourier Coefficients of Roundness Plots and Strains	325
12.09.5.1.2	Interpretation	328
12.09.5.1.3	Validation	328
12.09.5.2	Influence of the Carrier '(Residual) Stress Distribution'	330
12.09.5.2.1	Residual Stresses from Clamping	331
12.09.5.2.2	Stresses Resulting from Dead Load	334
12.09.5.3	Influence of the Carrier 'Temperature Distribution'	334
12.09.6	**Distortion Engineering: Compensation of Distortion**	337
12.09.6.1	Compensation Potential of Bearing Races during Machining and Heat Treatment	337
12.09.6.1.1	Machining	337
12.09.6.1.2	Heating and Austenitizing	339
12.09.6.1.3	Quenching	340
12.09.6.2	Results of Bearing Distortion Compensation at CRC 'Distortion Engineering'	340
12.09.6.2.1	Process Model	340
12.09.6.2.2	Some Experimental Details	341
12.09.6.2.3	Final Results	341
12.09.7	**Final Remarks**	342
Acknowledgment		343
References		343

12.09.1 Introduction

Dimensional and shape changes that occur during the manufacturing of metallic components cause high additional costs because they give rise to reworking or even scrap. According to a survey of the VDMA (engineering industries federation in Germany) in 1995, only in the area of power-transmission technology, the costs for the removal of distortion added up to 850 million Euros per year in Germany. Of course this savings potential was qualitatively known before. But the knowledge of the quantitative value leads to an intensification of research work in Germany.

On the one hand, an expert panel of the German heat treatment society AWT published a distortion monograph written in German in 1997 (*1*). In 2012, the fourth edition of this book appeared; all together, 32 authors from industry and universities have written parts of the monograph (*2*). It contains chapters dealing with the basics of distortion generation and the calculation of dimensional and shape changes. But the most important part is a collection of nearly 250 evaluations of papers dealing with

distortion. The above-mentioned expert panel developed a schema that is used for a uniform description of the content of the publications. One example of such a case study was published in (3). This work will be continued; besides the German *Journal of Heat Treatment and Materials*, the proceedings of conferences series like 'Quenching and Control of Distortion,' 'Distortion Engineering,' and 'Thermal Process Modeling and Computer Simulation' will especially be checked, and interesting publications will be evaluated.

On the other hand, a very important finding was that the investigation and optimization of single processes will not lead to the best possible results. In fact, an analysis of the complete manufacturing chain of the corresponding component is necessary. With this basic idea, Peter Mayr from IWT Bremen succeeded in the installation of the Collaborative Research Center (CRC) 'Distortion Engineering–Distortion Control during Manufacturing Processes' by the German Research Foundation (DFG). This project started in January 2001 and was finished at the end of 2011. During those 11 years, the 'Distortion Engineering' method – an analytic process working on three levels – was developed and adopted to total different manufacturing chains. Mainly manufacturing routes for the production of bearing races, shafts, and gears were analyzed. In the frame of cooperation projects with industrial partners, Distortion Engineering was applied to the manufacturing of aircraft skin panels, crown wheels, and rings for large size bearings.

The aim of this chapter is not to give an overview of the existing literature. Excellent summaries can be found elsewhere (e.g., (4–6)). Instead, the general basics of distortion generation will be presented by a translation of some sections of the first chapter of the German distortion monograph (Section 12.09.2). In Section 12.09.3, the CRC 'Distortion Engineering' will be introduced and the 'Distortion Engineering' method will be described. Finally, the most important results of the center concerning the production of bearing races made from SAE 52100 are summarized in the Sections 12.09.4–12.09.6 of this chapter.

12.09.2 Basics of Distortion Generation

In this section, the general basics will be described. It will contain

- definitions of size and shape changes in general and especially for bearing races,
- introduction of Fourier analysis as a powerful tool for the analysis of distortion and distortion generation,
- an overview of the responsible mechanisms for distortion of steel components,
- a systematic approach to introduce unavoidable size and shape changes, and
- an introduction of avoidable size and shape changes and the distortion potential.

12.09.2.1 Definition of Dimensional and Shape Changes

The German expert panel for distortion uses the following definitions for dimensional and shape changes:

- Size changes are alterations of the dimensions of a component without shape changes.
- Shape changes are alterations of angles and curvatures of the component.

What is the meaning of these definitions? For example, **Figure 1** shows roundness plots of a ring. The basic geometric element of it is a circle. Following the definition in a first step, the imperfect shape of the real component will be neglected. Instead, the average value of the dimensional parameter 'radius' will be calculated by, for example, minimizing the sum of squares between the

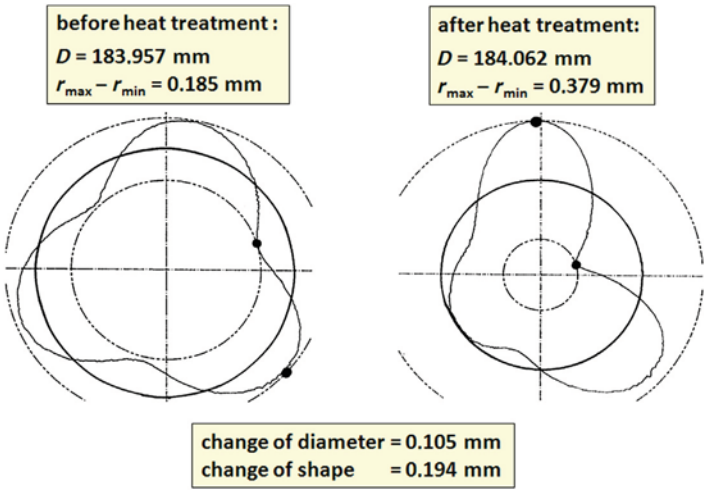

Figure 1 Roundness plots of the inner surface of a ring before and after heat treatment. Reproduced from Surm, H.; Frerichs, F.; Hoffmann, F.; Zoch, H.-W. Erweiterte Verzugsanalyse am Beispiel von Wälzlagerringen - Dem Verzug eine Richtung geben!. *HTM Z. für Werkst. Wärmebeh. Fertigung* **2008,** *63* (2), 95–103.

roundness plot and a best-fitted circle. The resulting radius is one of the dimensions of a ring without shape changes (bold line in Figure 1). The result is called a Gauss circle. Depending on the function of the component, alternatively, a circumscribed circle can be calculated in such a way that all measured points are inside the circle and the circle is as small as possible, or the circle can be determined in a way that all measured points are outside the circle and the circle is as large as possible (inscribed circle).

The results of this procedure are given before and after heat treatment as r_b and r_a. The change of radius Δr can be calculated very easily by the following equation:

$$\Delta r = r_a - r_b \quad [1]$$

In the second step, the shape change has to be calculated. The deviations from the perfect circle result from local changes of the curvature. For a ring in industrial practice, the roundness deviation OR is the most important shape parameter. It is defined as the difference between the maximum and minimum radius of the roundness plot:

$$\mathrm{OR} = r_{\max} - r_{\min} \quad [2]$$

In the finishing operation, the complete area between the concentric circles with these radii (dashed lines in Figure 1) has to be removed.

The change of the roundness deviation is given by eqn [3]:

$$\Delta\mathrm{OR} = \mathrm{OR}_a - \mathrm{OR}_b \quad [3]$$

Curvature changes are related to one basic geometric element. The second possibility for shape changes – alterations of angles – results from changes of angles between two basic geometric elements. In case of a ring, for example, the angle between the facing surface at the bottom and the inner surface can change; the result is an unwanted conicity.

For more complicated geometries, this procedure can be generalized. The first step is the definition of basic geometric elements. In the example of the ring, this element was simply a circle. Other elements could be a point, a line, a plane, a cylinder, a cone, a sphere, or a torus. The geometry of a component is defined by certain geometric characteristics such as angles or distances between its geometric elements. The determination of the describing parameters of the basic elements works by function-oriented fit algorithms as described for the ring. Then, depending on the geometry, distances between different elements or angles between them can be calculated. The distances are the dimensions of the component. The angles were mentioned above. The changes can be calculated according to eqns [1] and [3] from measurements before and after heat treatment or any other process.

12.09.2.2 Fourier Analysis as a Powerful Tool for the Analysis of Distortion of Bearing Races

In Figure 1, it can easily be seen that the value of roundness deviation is not able to characterize the distortion generation completely. Before heat treatment, the ring has a triangularity resulting from the machining process (details are given in Section 12.09.4) consisting of a well-defined direction and a corresponding amplitude. After heat treatment, the roundness is not so simple to describe. There are three directions with maxima of the radius, but the local amplitudes are different. Furthermore, the angles belonging to these maxima have changed compared to the plot before heat treatment. All of this information concerning the shape change is characterized in the classical industry-oriented description by one parameter: $\Delta\mathrm{OR} = 0.194$ mm.

The Fourier analysis is a powerful tool for the description of roundness plots and its changes by manufacturing processes. It was used for the first time in 1991 by Gunnarson for evaluation of the amplitudes of the shape change of crown wheel bores (7). The theory behind it is well known and quite simple (8). Figure 2 shows exemplarily the synthesis of a given roundness plot out of cosine functions of the orders 2, 3, and 6 (9). The complicated plot in Figure 2(a) can be described by the superposition of three simple functions with different amplitude, frequency, and phasing (Figure 2(b)–2(d)). Furthermore, the average radius of 72.5 mm has to be added.

But what has to be done if the situation is contrary, and the roundness plot is known and the amplitude and phasing of the participated orders are unknown? If the roundness plot $r(\varphi)$ were measured at N angles φ_j at equidistant positions

$$\varphi_j = \frac{2\pi \cdot j}{N} \quad \text{for } j = 0, 1, ..., N-1$$

then the trigonometric polynomial

$$T_N(\varphi) = \sum_{l=0}^{N-1} c_l \cdot \exp(i \cdot l \cdot \varphi) \quad [4]$$

with

$$c_l = \frac{1}{N} \cdot \sum_{j=0}^{N-1} r(\varphi_j) \cdot \exp\left(-i \cdot 2\pi \cdot \frac{l \cdot j}{N} \right) \quad \text{for } l = 0, 1, \ldots, N-1 \quad [5]$$

takes at φ_j the values of $r(\varphi_j)$ (8):

$$r(\varphi_j) = T_N(\varphi_j) \quad \text{for } j = 0, 1, \ldots, N-1 \quad [6]$$

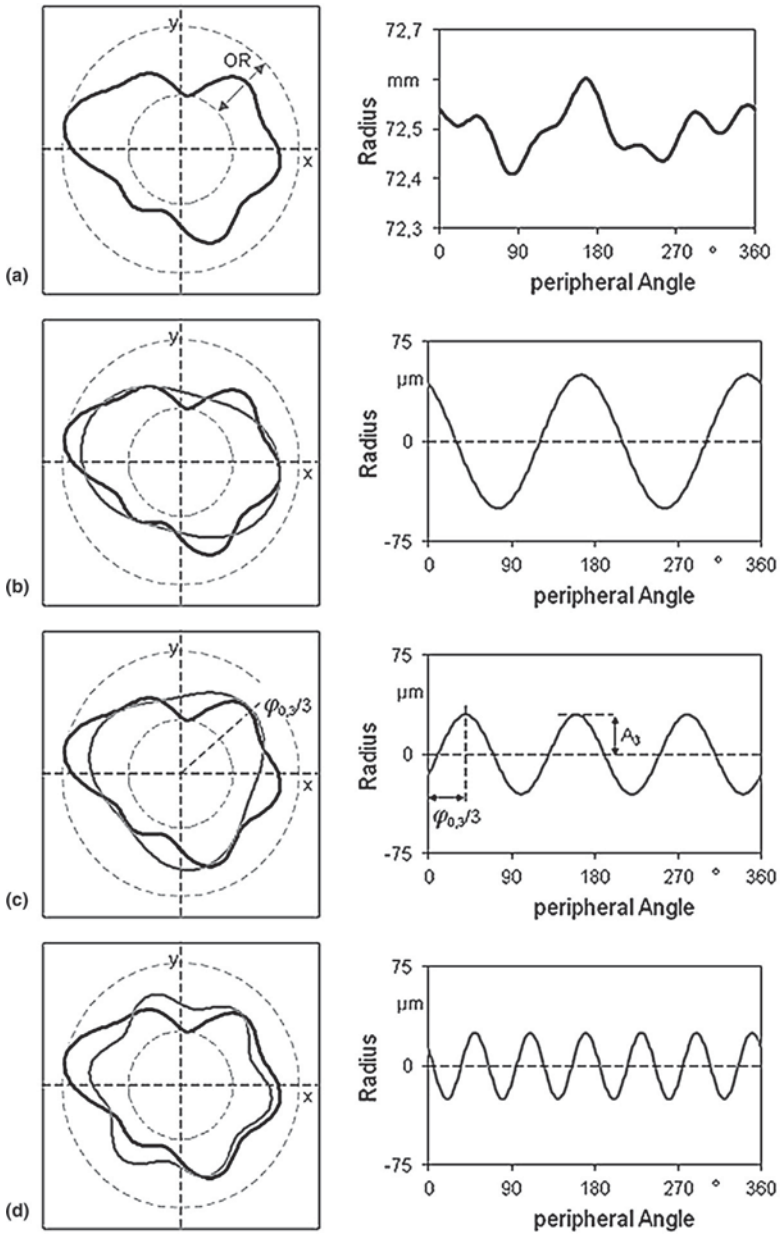

Figure 2 Roundness plots in polar (left column) and Cartesian coordinates (right column): (a) total plot, (b) portion of ovality, (c) portion of triangularity, and (d) portion of hexagonality. Reproduced from Surm, H.; Frerichs, F.; Hoffmann, F.; Zoch, H.-W. Erweiterte Verzugsanalyse am Beispiel von Wälzlagerringen - Dem Verzug eine Richtung geben!. *HTM Z. für Werkst. Wärmebeh. Fertigung* **2008,** *63* (2), 95–103.

For $l = 0$, eqn [5] yields the average radius of the ring. For all other values of l, the coefficients c_l are generally complex numbers:

$$c_l = a_l + i \cdot b_l \quad \text{for } l = 1, 2, \ldots, N-1 \qquad [7]$$

Alternatively, they can be described by the moduli A_l and the phases $\varphi_{0,l}$:

$$\begin{aligned} c_l &= A_l \cdot (\cos \varphi_{0,l} + i \cdot \sin \varphi_{0,l}) \\ A_l &= \sqrt{a_l^2 + b_l^2} \quad \text{for } l = 1, 2, \ldots, N-1 \\ \tan \varphi_{0,l} &= \frac{b_l}{a_l} \end{aligned} \qquad [8]$$

Office Excel 2007™ provides an analysis function that can be activated by installation of an 'add in.' By use of the feature 'data analysis' a fast Fourier transformation (FFT) can be used for the calculation of the coefficient c_l. In this case, the quantity N of measurement positions must be a number like 2^n. If this condition is not fulfilled, eqn [5] must be programmed by the user.

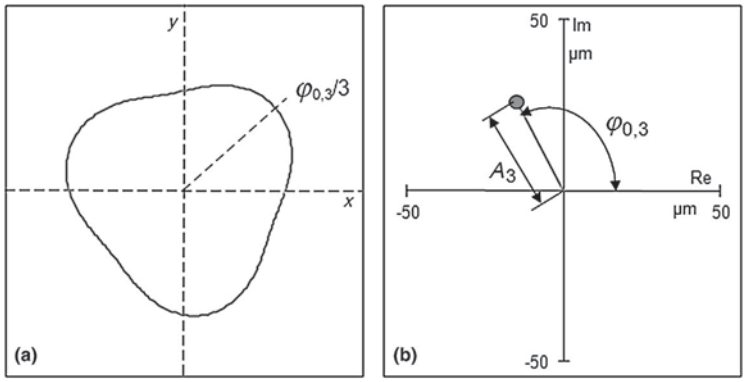

Figure 3 Distortion characterization of a pure triangularity (a) in roundness plot in the *x–y* plane and (b) in the complex plane. Reproduced from Surm, H.; Frerichs, F.; Hoffmann, F.; Zoch, H.-W. Erweiterte Verzugsanalyse am Beispiel von Wälzlagerringen - Dem Verzug eine Richtung geben!. *HTM Z. für Werkst. Wärmebeh. Fertigung* **2008,** *63* (2), 95–103.

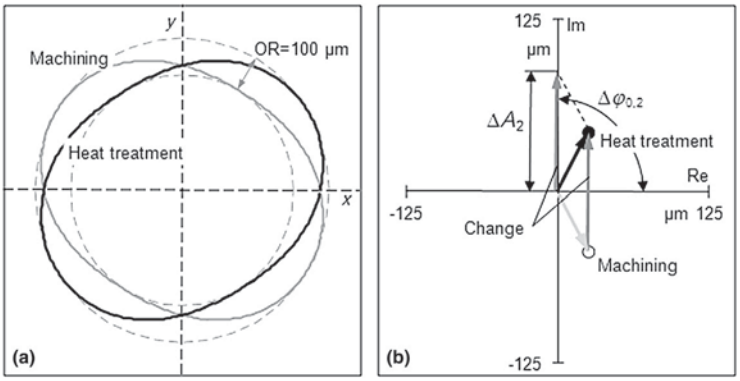

Figure 4 Calculation of the change of one distortion indicator (a) in the *x–y* plane and (b) in the complex plane. Reproduced from Surm, H.; Frerichs, F.; Hoffmann, F.; Zoch, H.-W. Erweiterte Verzugsanalyse am Beispiel von Wälzlagerringen - Dem Verzug eine Richtung geben!. *HTM Z. für Werkst. Wärmebeh. Fertigung* **2008,** *63* (2), 95–103.

Figure 3 shows an example for a roundness plot consisting of a pure third order. Only one complex number is necessary to describe this plot in the complex plane. For the interpretation, it is important to know that the phase angle $\varphi_{0,3}$ defined in the complex plane has to be divided by the number of the order I (in the example $l = 3$) to have the correct orientation of the roundness plot in the *x–y* plane.

The dimensional and shape changes of a ring can now be calculated in a straightforward way. If the coefficients c_l were calculated before and after a process from the corresponding roundness plots, the distortion can be characterized by

$$\Delta c_l = c_l^a - c_l^b \quad \text{for } l = 0, 1, 2, \ldots N-1 \qquad [9]$$

The dimensional change is given by Δc_0 and the shape changes by Δc_1, Δc_2, … . The addition and subtraction of complex numbers work in the same way as vectors were handled: one has to add or subtract the real and complex parts independently.

In Figure 4, an example is given where the roundness plot of a ring before and after heat treatment consists of a pure second order with the same amplitude but different phase angles. The corresponding description in the complex plane shows that the distortion due to heat treatment can be quantified by a change of the second-order amplitude of $\Delta A_2 = 86.6$ µm and in phase of $\Delta\varphi_{0,2} = 90°$. Keeping in mind that in the *x–y* plane the phase change has to be divided by the number of the order, we can conclude that during heat treatment an effect with an orientation of 45° has caused this distortion. This is much more information compared to the evaluation of the past, where only the amplitudes A_l were used. In the special case given in Figure 4, no distortion would have resulted from the use of the classical evaluation method.

12.09.2.3 Mechanisms for Distortion of Steel Components

Two main causes for changes in dimensions and shape are known:

- volume changes and
- deformations.

Such changes may be induced by various processes in a component (Figure 5). Volume changes can be caused on the one hand by density changes. Such modifications can result from phase transformation or precipitation processes. Both are determined by the

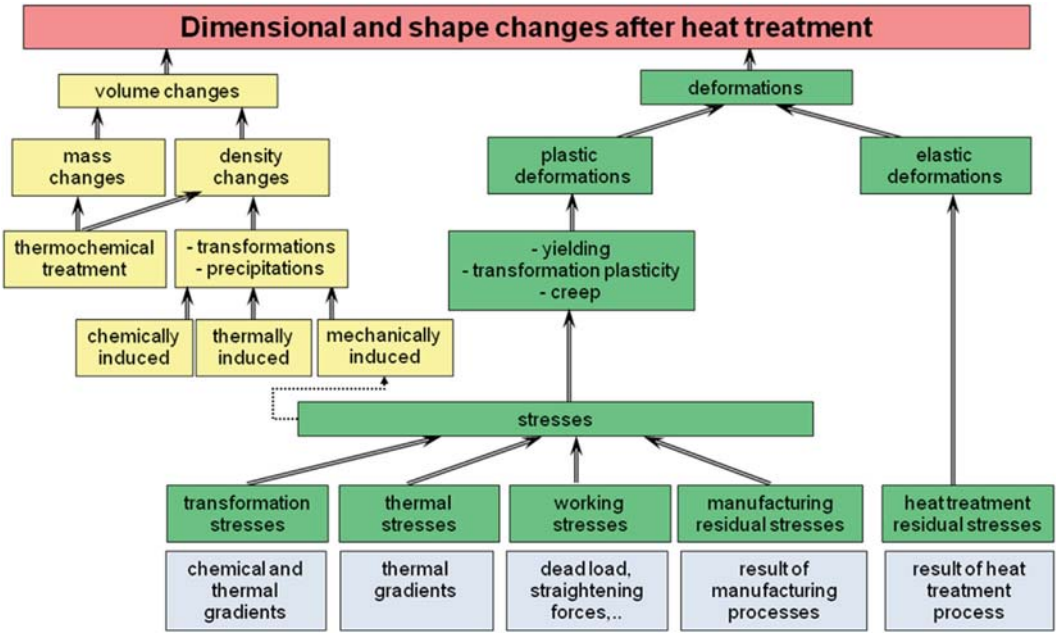

Figure 5 Causes of changes in dimensions and shape. Reproduced from Heeß, K.; Besserdich, G.; Bohn, R.; Ehlers, M.; Escher, C.; Fiderer, M.; Franz, C.; Göbel, M.; Grasemann, H. J.; Haase, P.; Hoferer, M.; Hunkel, M.; Jennes, R.; Jung, M.; Keßler, O.; Kunow, S.; Klingemann, R.; Lohrmann, M.; Lübben, T.; Majorek, A.; Miskiewicz, S.; Porzner, H.; Reinhold, P.; Schmitt, G.; Schützenhöfer, W.; Thoden, B.; Trapp, N.; Vogel, M.; Volkmuth, J.; Wägner, H.; Wiedmann, D.; Zoch, H.-W. *Maß- und Formänderungen infolge Wärmebehandlung von Stählen*, 4th ed.; Expert Verlag: Renningen, 2012. ISBN: 978-3-8169-3067-9, (in German).

(local) chemical composition and the process dependent temperature–time path. The influence of stresses on transformation behavior results in a mechanical impact to these processes too. On the other hand, volume changes can result from mass changes that occur during thermochemical treatments as, for example, carburization or nitriding.

Deformation processes may either be plastic or elastic. In the absence of external forces and moments, elastic deformations after heat treatment are always caused by residual stresses. These are the result of mainly the quenching step and are inseparable from heat-treated components.

Plastic deformation may be caused by yielding, transformation plasticity, or creep. To activate these mechanisms, stresses are necessary. Yielding occurs if the equivalent stress, which can be calculated from the – in general – multiaxial stress state, becomes larger than the yield stress. The exceeding stresses will be recovered by plastic deformation (see Chapters 12.06 and 12.08).

Contrary to this mechanism, transformation plasticity and creep do not need to exceed a minimum value. However, transformation plasticity arises only if stresses and transformation exist simultaneously (see Chapter 12.06). Creep appears at temperatures higher than 33–50% of the melting temperature given in Kelvin and depends strongly on time. Therefore, it can become important during heating processes with very low heating rates, especially at higher temperatures or during holding segments or during a carburizing process.

During heat treatment mainly a superposition of transformation and thermal stresses exists. They arise from thermal gradients and gradients in the chemical composition, some of which may be residual from the segregation that occurs during solidification. Furthermore, the dead load or straightening forces (e.g., in quenching fixtures) can generate working loads that interact with the above-mentioned stresses and therefore influence the plastic deformation. Finally, residual stresses from manufacturing processes have to be taken into account too, especially during the heating stage.

12.09.2.4 Unavoidable Size and Shape Changes

In this section, the systematic of unavoidable distortion will be introduced.

12.09.2.4.1 Volume Changes by Transformation

Let us assume that it is possible to produce a component under ideal conditions, that is,

- a component with absolutely homogeneous chemical composition and homogeneous initial microstructure,
- without any texture, and
- that a blank component without any residual stress could be produced by machining.

Let us further assume that heat treatment could be carried out under ideal conditions, including

- homogeneous heating of the component,
- very small heating rate,

- ideal charging, and
- minimum possible cooling rate with ideal heat transfer conditions.

Even under these perfect conditions, dimensional alterations will still occur if the heat treatment includes a change in the microstructure. Even without any plastic deformation, size changes unavoidably occur as a result of the relationship between specific volume and microstructure status (Figure 6 (*10*)). This diagram shows, for example, that a martensitically hardened component made from steel with 0.4% carbon experiences an unavoidable reduction in volume as a result of normalizing with very slow cooling, as a ferritic/pearlitic microstructure is produced under these conditions. This example may not be practically relevant, but it clearly indicates the principle of unavoidable size changes as a result of phase transformation. In the system developed by Wyss for unavoidable changes in dimensions and shape, this case is referred to as 'Tendency I' (Figure 7, (*11*)). The dimensional changes depend on

- chemical composition (especial carbon),
- initial microstructure,
- austenitizing conditions,

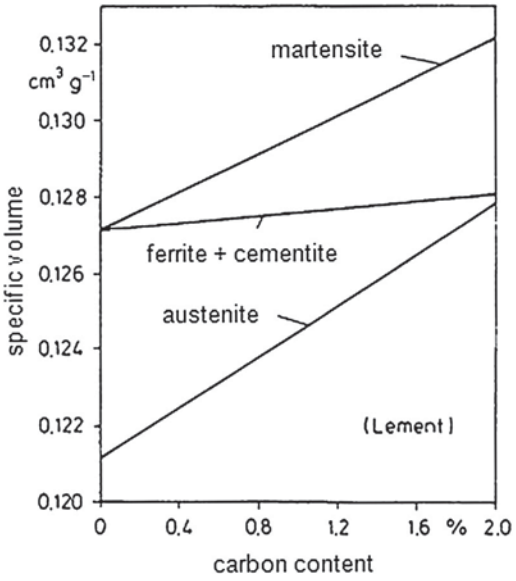

Figure 6 Effects of microstructure on the specific volume of carbon steels. Adapted from Lement, B. S. *Distortion in Tool Steels*; ASM: Metal Park, Novelty, Ohio, 1959. Reprinted with permission of ASM International. All rights reserved. www.asminternational.org.

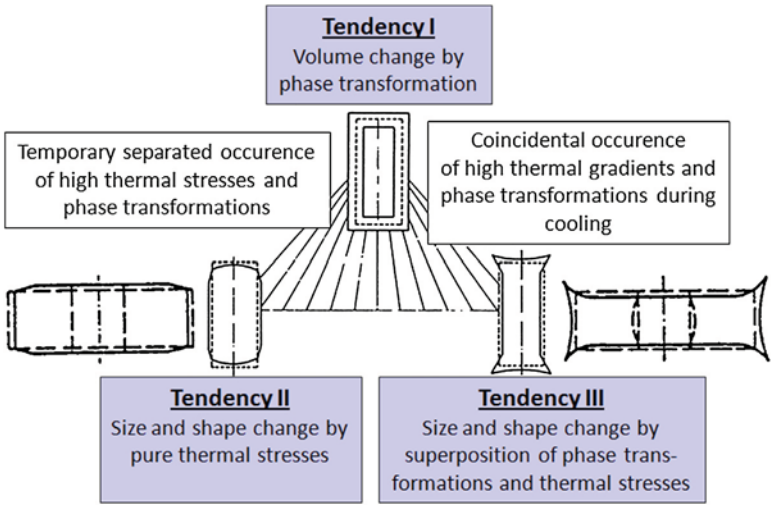

Figure 7 Three basic tendencies of unavoidable changes in dimensions and shape. Reproduced from Wyss, U. *Die wichtigsten Gesetzmäßigkeiten des Verzuges bei der Wärmebehandlung des Stahles (Hersg).* In Wärmebehandlung der Bau- und Werkzeugstähle; Benninghoff, H., Ed.; BAZ Buchverlag Basel, 1978.

- kind of transformation, and
- degree of transformation (partial, complete).

12.09.2.4.2 Size and Shape Changes by Thermal Stresses

If the cooling rate must also exceed a certain critical value in order to obtain a specified microstructure, temperature differences within the component will also occur. As a result of the temperature dependency of the specific volume, these differences create thermal stresses in the component. As indicated by the schematic cooling diagram in Figure 8 (*12*), the near-surface layer of the material initially cools faster and contracts more severely than the core. This situation leads to tensile stresses in the near-surface layer (curve *a*), in equilibrium with compressive stresses in the core. After the highest temperature difference has been reached (at *W*), the core contracts more rapidly than the near-surface layer, and at the end of the cooling process all stresses have disappeared.

This pure elastic case works only if the equivalent stress does not reach the temperature-dependent yield limit during the complete quenching process. But if the equivalent stress exceeds the yield strength of the steel, the exceeding stresses are eliminated by plastic deformation (shaded area of diagram) and the resulting stress follows curve *b*. After passing the maximum temperature difference, the stronger contraction of the core leads to an elastic reduction of the stresses at the surface (curve *c*) until the stress conditions in the material are reversed. Then the surface of the material is exposed to compressive stresses and the core to tensile stresses. After temperatures in the material have fully equalized, the stress conditions schematically indicated in the bottom right-hand part of Figure 8 remain in the material as residual stresses.

This analysis indicates that dimensional changes in this case are ultimately caused by local stresses in excess of the yield strength of the material and resulting plastic deformations. The residual stress distribution with tensile stresses in the core and compressive stresses near to the surface is typical of quenched materials without phase transformation. The corresponding changes in dimensions and shape can be described by the rule established by Ameen. According to this rule, all materials experience changes in dimensions and shape tending to approximate the shape of a sphere if thermal stresses are present during quenching (*13*). Figure 9 shows an originally square billet dead-weight body from the steel 100CrMn6 (C: 0.90–1.05, Si: 0.40–0.70, Mn: 0.95–1.25, Cr: 0.35–1.60; in weight percent) that was heated and quenched for a few hundred times, which proves Ameen's rule very impressively.

In the system established by Wyss, this case is described as tendency II (Figure 7): the larger dimension decreases and the other one increases. The effects of process and material parameters in this case can be described as follows (*14*): size changes as a result of pure thermal stresses increase with

- increasing dimensions,
- increasing quenching temperature,
- increasing quenching rate,

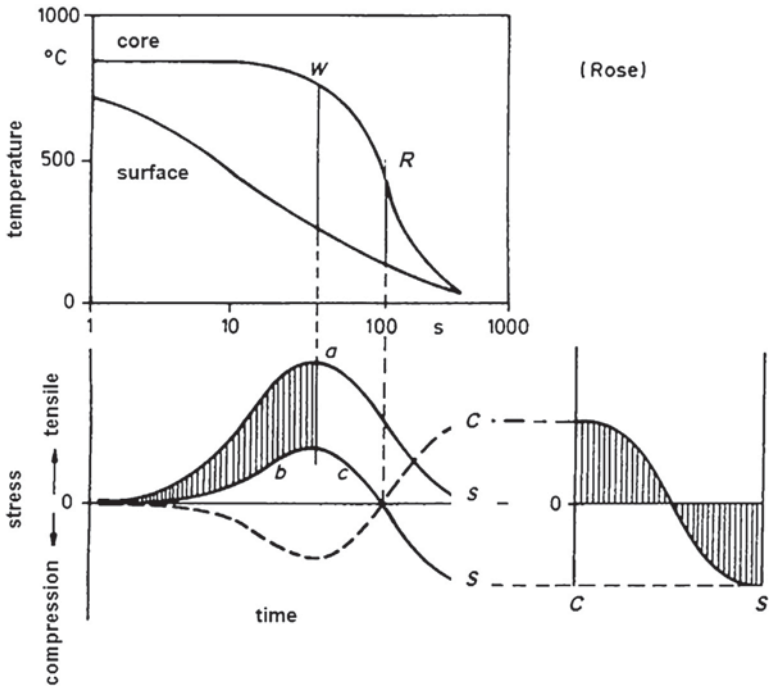

Figure 8 Creation of thermal stresses. Reproduced from Rose, A. Eigenspannungen als Ergebnis von Wärmebehandlung und Umwandlungsverhalten. *Härterei-Techn. Mitt.* **1966,** *21* (1), 1–6.

Figure 9 Dead-weight body after a few hundreds of passes through a heat treatment furnace. Original geometry: square billet (photo by Ulrich Reiβ, IWT Bremen).

- decreasing thermal conductivity,
- increasing thermal expansion, and
- decreasing yield strength.

Similar rules also apply to the heating process.

The rule of Ameen was found from the evaluation of quenching experiments with oil and water. But what happens for smaller cooling intensities? Here the investigations of Portevin and Sourdillon from 1927 give very useful results (*15*). They quenched steel bars from a temperature below A_{c1} in water and oil and received the results given in **Figure 10**. For higher quenching temperatures, the longer dimension of the bars decreases. This result is in accordance with the rule of Ameen. But for each steel grade a critical temperature exists. If the quenching temperature is smaller than the critical one, then the longer dimension increases. And this result does not conform to the rule of Ameen. **Figure 10** shows furthermore that the critical quenching temperature increases with increasing carbon content of the steel, therefore increasing the yield limit. Under the investigated conditions, oil quenching has a critical quenching temperature larger then A_{c1}.

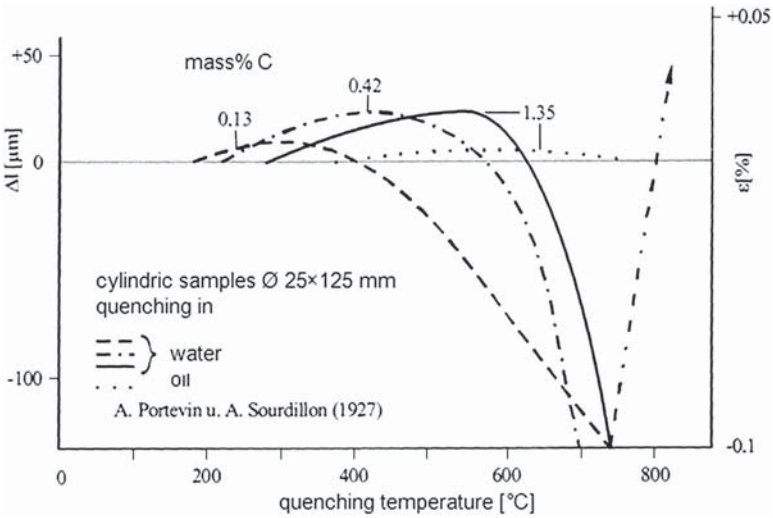

Figure 10 Length changes of steel shafts as function of quenching temperature, steel grade, and quenching medium. Reproduced from Portevin, A.; Sourdillon, A. Contribution a létude des deformations accompagnant les traitements thermiques de lacier. *Rev. Metall.* **1927,** *24* (4), 215–233.

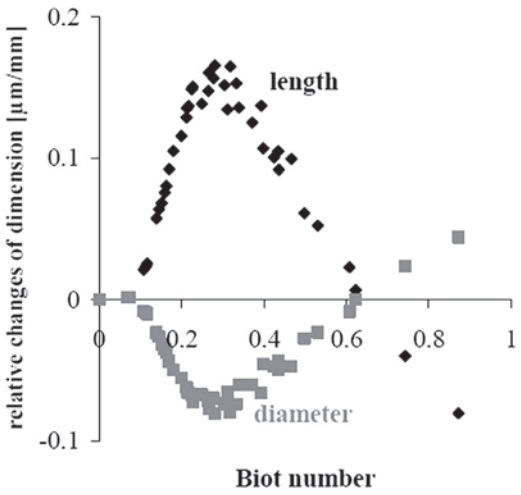

Figure 11 Dimensional changes of bars from austenitic steel SAE30300 (length/diameter ratio larger three) as function of Biot number. Reproduced from Frerichs, F.; Lübben, Th.; Hoffmann, F.; Zoch, H. -W.; Wolff, M. Unavoidable Distortion due to Thermal Stresses. In *5th Int. and European Conference on Quenching and Control of Distortion*, Berlin, 2007, pp 145–156.

These results were picked up by the CRC 'Distortion Engineering' and systematic experimental and numerical investigations of the influence of dimensions and heat transfer coefficient to the size changes were done (*16*). A few basic results are given in Figure 11. The Biot number,

$$Bi = \frac{\alpha}{\lambda} \cdot \frac{V}{S} \qquad [10]$$

where α is the heat transfer coefficient, λ the heat conductivity, V the volume, and S the surface of the sample, describes the size changes of cylinders with a length to diameter ratio of at least three for different combinations of diameter (10–50 mm), length (50–200 mm), and heat transfer coefficient quite well. Therefore, Bi is one of the dimensionless numbers that characterize the distortion behavior of components under pure thermal stress. Figure 11 shows that for small values of the Biot number, no size changes occur; the yield limit of the material will not be exceeded. For higher Biot numbers, an elongation of the cylinders results, and finally for Biot numbers larger than about 0.62, a length reduction and diameter increase occur as Ameen's rule predicts.

For discs and rings, similar dependencies of the size changes on the Biot number exists. Figure 12 compares the numerical results of bars, discs, and rings (*16*). The Biot numbers of first size changes, extreme size changes, and change of sign are nearly the same for all investigated geometries. Furthermore, it can be concluded that the largest dimensions of the simple geometries have a similar behavior – cylinder height, average ring radius, and plate radius – and the smallest dimension too (cylinder radius, ring wall thickness, and plate height). For the third dimension in between the extreme ones, no general conclusion is possible on the basis of the data in Figure 12.

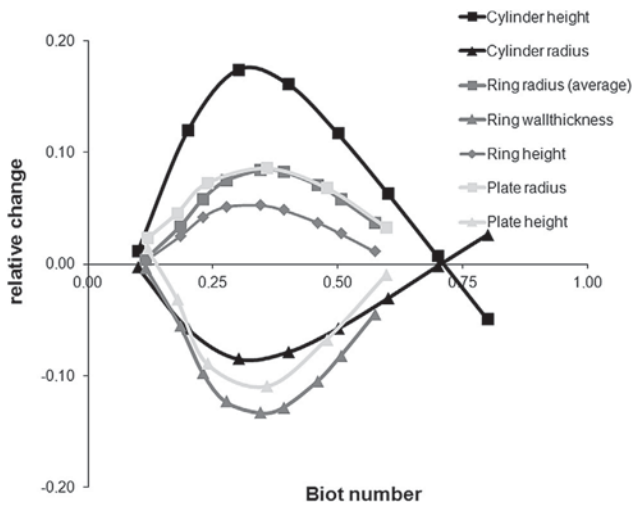

Figure 12 Size changes of simple geometries. Reproduced from Frerichs, F.; Lübben, Th.; Hoffmann, F.; Zoch, H. -W.; Wolff, M. Unavoidable Distortion due to Thermal Stresses. In *5th Int. and European Conference on Quenching and Control of Distortion*, Berlin, 2007, pp 145–156.

Besides the Biot number, only five other dimensionless numbers are necessary for the description of thermal stress–induced size changes of cylindrical bodies. They can be summarized as (16)

$$\frac{\Delta L}{L} = f\left(\frac{\alpha}{\lambda}\cdot\frac{V}{S};\alpha_{\text{th}}\cdot(T_0 - T_q);\gamma;\frac{E}{\sigma_0};\frac{E}{K};n\right)$$
$$\frac{\Delta D}{D} = g\left(\frac{\alpha}{\lambda}\cdot\frac{V}{S};\alpha_{\text{th}}\cdot(T_0 - T_q);\gamma;\frac{E}{\sigma_0};\frac{E}{K};n\right) \quad [11]$$

- α_{th}: coefficient of thermal expansion
- T_o, T_q: initial temperature and temperature of quenching medium
- γ, E: elastic properties (Poisson ratio and Young's Modulus)
- σ_0, K, n: plastic properties (yield stress and parameters of a modified Ramberg-Osgood model (16))

These dimensional numbers were identified by use of the so-called Analysis of Dimensions, and their use offers two main advantages (e.g., (17)):

- If all relevant parameters describing geometry, material, and process are known, the dimensionless numbers governing the distortion behavior of this system can be deduced. Generally, the number of dimensionless numbers is smaller than the total amount of influencing parameters.
- If the values of all dimensionless numbers of two geometrical similar bodies are equal, than the distortion behavior of this two bodies is equal too.

The second statement is true even when all parameters defining the two configurations are totally different. In fluid dynamics, this nature of dimensionless numbers is the basis for the transferability of results, for example, received with a small model in a wind tunnel to a real car or an aircraft.

But the analysis of dimensions cannot predict the functions g and f in eqn [11]. A first approach was developed by Landek et al. (18). They used averaged material properties of 28 representative austenitic steels (**Table 1**) and the corresponding standard deviations. Based on these data, a lot of finite element simulations for long bars were done. The resulting length changes were fitted by a nonlinear regression model. **Figure 13** shows the comparison between the simulated and calculated length changes. The correspondence is not perfect, but the regression model offers the possibility for an acceptable estimation of the length change when the parameters of eqn [11] are known.

Up until now, all statements were done for the distortion behavior as a result of a heat treatment process at the end of the process when the component has cooled down to room temperature. But the concept of dimensionless numbers works during a process too. In this case instead of time t, the Fourier number

$$Fo = \frac{\lambda}{\rho\cdot C_p}\cdot\frac{t}{L^2} \quad [12]$$

(ρ: density; C_p: specific heat capacity; t: time; and L: characteristic length) has to be used. Simsir has shown that besides the cooling curves, all other time-dependent results of a quenching process (e.g., martensite portion, components of stress, and strain tensor) are equal if the values of all dimensionless numbers, including the Fourier number, of two geometrically similar bodies are equal (19).

12.09.2.4.3 Size and Shape Changes by Superposition of Thermal Stresses and Transformations

In the last step of this systematization, it has to be kept in mind that a hardening process needs phase transformations during quenching, and to achieve a specific microstructure, requirements to local cooling rates have to be fulfilled. In consequence, the general case consists of a component with temperature gradients – and the corresponding thermal stresses – and phase transformations depending on the local cooling curve. In contrast to the situation in Section 12.09.2.4.1, here phase transformation gradients exist and will lead to transformation stresses. The superposition of both kinds of stresses results in a relatively complex time-dependent stress profile in the component. The plastic deformations resulting via transformation plasticity and yielding during the quenching process form the final size and shape changes. In the lower part of **Figure 14**, the stress development during a fully martensitic transformation is shown. The upper part shows schematically a CCT diagram and the cooling curves of surface and core (20). Until the

Table 1 A representative group of analyzed austenitic steels

Steel grades
27Cr–9Ni (as cast); 19Cr–10Ni–2.5Mo; 19Cr–9Ni–0.2C; 19Cr–10Ni; 19Cr–11Ni–2.5Mo; 19Cr–9Ni; 19Cr–11Ni–3.5Mo; 24Cr–13Ni; 25Cr–20Ni; X8CrNiS18.9;
AISI 201; AISI 202; AISI 205; AISI 216; AISI 301; AISI 302; AISI 304; AISI 305; AISI 308; AISI 309; AISI 310; AISI 314; AISI 315; AISI 316; AISI 317; AISI 321; AISI 329; AISI 330

Reproduced from Landek, D.; Lisjak, D.; Frerichs, F.; Lübben, Th.; Hoffmann, F.; Zoch, H.-W. Prediction of Unavoidable Distortions in Transformation-Free Cooling by a Newly Developed Dimensionless Model. In *2nd Int. Conf. on Distortion Engineering IDE 2008*, Bremen, 2008, pp 237–246.

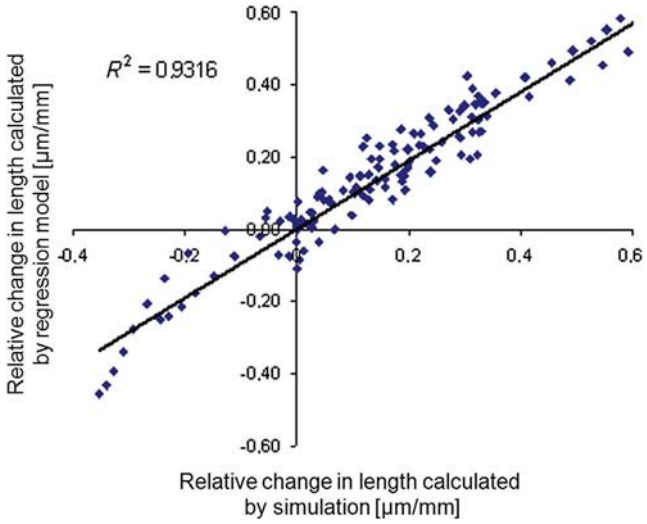

Figure 13 Correspondence between length changes after transformation-free cooling of bars made of austenitic steels calculated by numerical simulations and predicted by a regression model. Reproduced from Landek, D.; Lisjak, D.; Frerichs, F.; Lübben, Th.; Hoffmann, F.; Zoch, H.-W. Prediction of Unavoidable Distortions in Transformation-Free Cooling by a Newly Developed Dimensionless Model. In *2nd Int. Conf. On Distortion Engineering IDE 2008*, Bremen, 2008, pp 237–246.

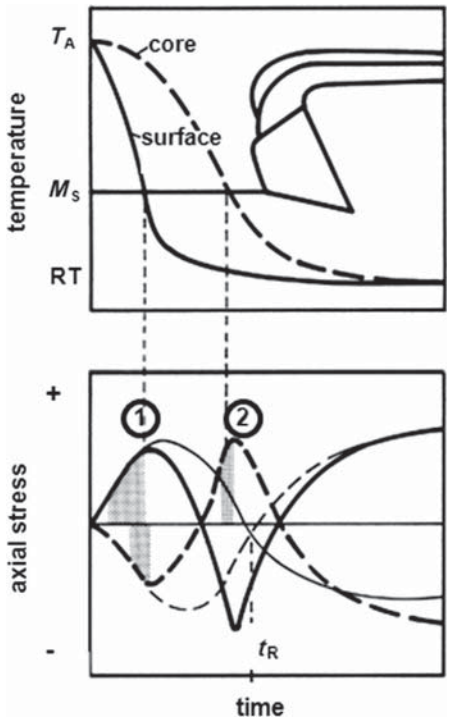

Figure 14 Example for a superposition of thermal and transformation stress (fully martensitic hardening process). Adapted from Schröder, R.; Scholtes, B.; Macherauch, E. Rechnerische und röntgenographische Analyse der Eigenspannungsbildung in abgeschreckten Stahlzylindern. *Härterei-Techn. Mitt.* **1984**, *39*, 280–291, by courtesy of Carl Hanser Verlag, Munich, Germany.

transformation of the region near the surface starts, only thermal stresses (thin lines) were generated. The martensite formation begins at the surface (point 1) and the local volume increases because of the larger specific volume of martensite (see Figure 6). As a consequence, compressive transformation stresses occur and the total stresses (thick lines) are – absolutely – reduced. In reaction, the stresses in the core (dashed lines) start to increase and plastic deformations resulting from yielding (gray marked) stop. The increase of the total core stresses continues until the transformation of the core starts (point 2). Now the same happens here as just described for the region near the surface. At the end of the quenching process, the residual stress state consists of tensile stresses at the surface and compressive stresses in the core, in contrast to the situation after quenching without transformation.

This result cannot be generalized. The stress development depends in a complex way on the interactions between transformation and cooling behavior, and the size and shape changes in a simple cylinder or ring may vary between tendency I (only size changes), tendency II (spherical shape, dimension, and shape changes), and tendency III ('wire-reel,' dimension, and shape changes) (see Figure 7). If high thermal stresses and transformations occur at different times, the results will be between sheer size changes and the spherical shape. The size changes caused by transformations and the size and shape changes caused by thermal stresses are practically added to each other. On the other hand, if thermal stresses and transformation occur at the same time, the result is the 'wire-reel' shape mentioned above (*4*,*21*).

In Figure 15 (*4*), four cases (a–d) of different interactions between thermal stresses and phase transformation are shown. In case (a), a cylinder with diameter of 100 mm and made from a steel grade SAE 1015 was quenched in oil. The maximum temperature difference between surface and core (*W*) occurs after the transformation is finished. Therefore, the resulting distortion corresponds to an approach to the spherical shape.

If the steel grade will be changed to X40Cr13 (C: 0.4–0.5%; Si: <1%; Mn: <1%; Cr: 12–14%) than point *W* is reached before the transformation starts and the distortion is similar to the first example (case (b)).

In case (c), a smaller cylinder with a diameter of 30 mm made of SAE 1030 was quenched in water. Under these circumstances, the maximum temperature difference appears during the transformation of the core but before martensite transformation of the surface starts. From the systematic of Wyss, we must conclude that the 'wire-reel' shape should result. But the experiment has shown a spherical size distortion. The reason for this can be found in the stress development. When the maximum temperature difference occurs, the core is under compression stress (see Figure 8). If now the transformation starts here, the increase of specific volume leads to an additional compressive stress. Therefore, the stress situation equates an amplified thermal stress condition with the known result in size and shape changes.

In the last example, a water-quenched cylinder made from AISI 3310 with a diameter of 100 mm was tested. In this case point, *W* occurs simultaneously with the martensitic transformation of the surface, before the core starts to form pearlite (Figure 15(d)) and therefore the 'wire-reel' distortion results.

In general, the situation is not predictable by such a simple two-shell model. Even in the simple case of pure martensitic hardening of a ring with a rectangular cross section, 30 parameters govern the distortion generation during quenching and 26 dimensionless numbers are necessary to describe the problem (*19*). If furthermore diffusion-controlled transformations have to be taken into account and/or a case-hardening process should be judged, the number of parameters increases dramatically. In such a case, only a heat treatment simulation enables one to imagine the interactions of the different mechanisms (see Chapter 12.06).

Finally, it has to be noted that the heating process can play a remarkable role in the generation of distortion (see Section 12.09.4). During this process, the thermal stresses are in many cases smaller. Therefore, in general, yielding plasticity does not play

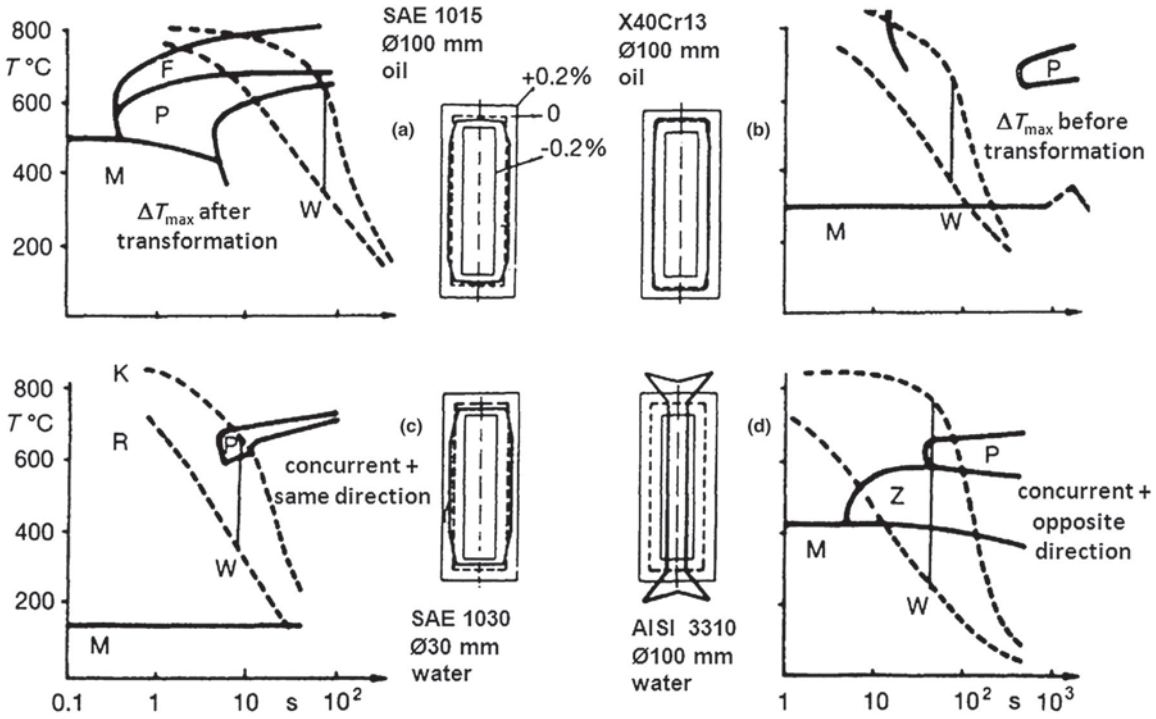

Figure 15 Size and shape changes after hardening due to different interactions between thermal and transformation stress. Reproduced from Chatterjee-Fischer, R., Beispiele für durch Wärmebehandlung bedingte Eigenspannungen und ihre Auswirkungen, Härterei-Techn. *Mitt.* **1973**, *28*, 276–288.

a major role. But transformation plasticity and creep can have a non-negligible effect. Furthermore, anisotropic effects, which result from segregations, have to be taken into account, especially during heating (e.g., (*22*,*23*)).

12.09.2.5 Avoidable Size and Shape Changes

In practice, it is of course impossible even to approach the ideal conditions mentioned in Section 12.09.2.4. But what are the important points if the real conditions have to be taken into account? **Figure 16** shows some examples of real conditions. Heat treatment of crown wheels leads in general to enormous distortion. Therefore such parts will normally be hardened in quenching presses. But what is the main reason for this result? It is easy to see that in the regions of the tooth the surface is larger and the volume is smaller compared to the lower part of the wheel. Consequently the tooth will cool down much faster, and thermal stresses between the upper and lower parts will arise and can cause a tilting of the complete gear even if all other influencing parameters are as perfect as assumed in Section 12.09.2.4. The reason for this shape change is the asymmetry of the mass distribution of the crown wheel: its geometry.

In the second example in **Figure 16**, after hardening, the ball was no longer spherical, but ellipsoid. After cutting it, an inhomogeneous, asymmetric distribution of the microstructure was found. This asymmetry results from an asymmetric distribution of the chemical composition, known as segregation. These two distributions cause complex interactions during heat treatment. The differences in the microstructure result in local differences of the volume change during austenitizing, and therefore transformation stresses occur. Furthermore, the variations in the chemical composition provoke position-dependent transformation behavior and therefore complex distributions of stress and strain development.

After heat treatment, the ring in the third example exhibits large third-order amplitude in the Fourier spectrum of its roundness plot. The distribution of residual stresses measured by the x-ray method after machining shows a similar triangularity to the roundness plot after heat treatment. It results from the interaction of clamping and turning during the machining process. During heating, these stresses will be reduced by plastic deformations which give the resulting size and shape changes.

Following these two examples, it can be concluded that not only the visible asymmetry or inhomogeneity of the mass distribution causes distortion, even the invisible asymmetries of other properties can create distortion by complicated interactions during heat treatment too. If a component inhibits such asymmetries in it, it contains a potential for distortion that is set free during the heat treatment and causes the measureable size and shape changes. This potential is called the 'distortion potential' of a component and cannot be measured. Measurable quantities are the carriers of the distortion potential. These carriers are the distributions of

- mass (geometry),
- all relevant alloying elements,
- microstructure including grain size,
- (residual) stress,
- temperature, and
- mechanical history.

From the viewpoint of process chain simulation, these carriers – with the exception of geometry – are the distributions of the state variables at the end of a process within the manufacturing chain and have to be given as initial conditions for the simulation of the next process (see Chapter 12.06). But to understand distortion generation, the interactions of the state variables during the processes have to be analyzed. Before talking about this topic and the consequences, some words have to be said about the last two carriers. The very important role of the temperature was already highlighted during the discussion of the unavoidable size and shape changes. Focusing on the avoidable distortions, inhomogeneities and asymmetries in the temperature distribution resulting not from mass distribution but from the heat transfer conditions and therefore from the process have to be taken into account. The imperfections in the temperature distribution resulting from these nonperfect conditions must be added to the effects coming from the geometry itself and cause mainly additional shape changes.

The role of the mechanical history consists of the influence of plastic deformations on effects occurring after the plasticization. One effect is the strain-hardening behavior (Bauschinger effect). Here, kinematic or isotropic behavior or mixtures of both are

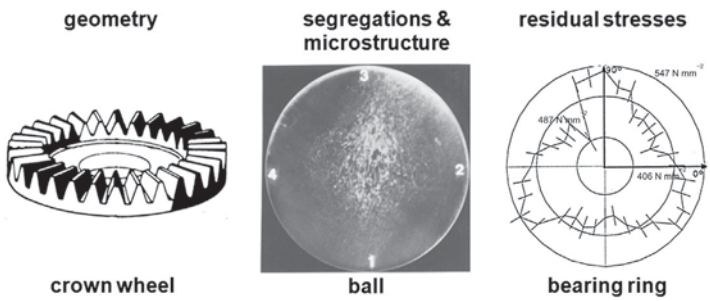

Figure 16 Real conditions – distortion potential. Reproduced from Hoffmann, F.; Kessler, O.; Lübben, Th.; Mayr, P. "Distortion Engineering" - Distortion Control during the Production Process. *Heat Treat. Met.* **2004,** *2*, 27–30.

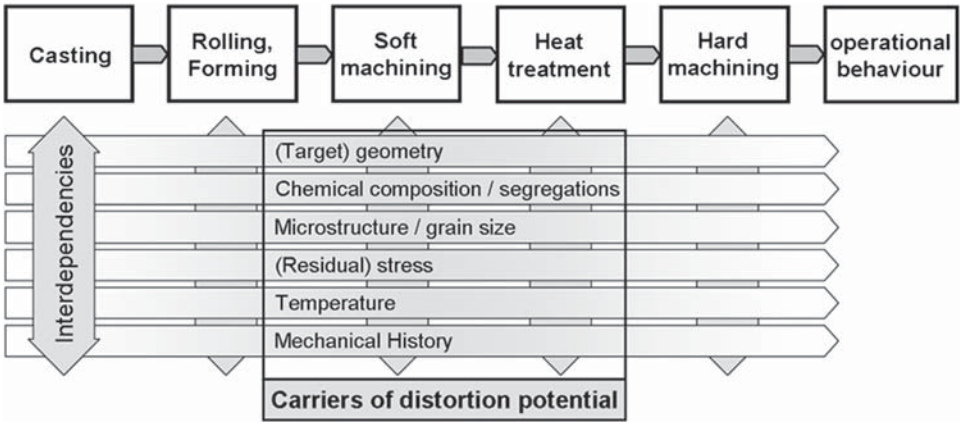

Figure 17 State variables along the process chain and its interactions (schematical description). Reproduced from Zoch, H.-W. Distortion Engineering: Vision or Ready to Application. *Mat.-wiss. u. Werkstofftech* **2009,** *40* (5-6), 342–348.

discussed. More details can be found elsewhere (e.g., (*24*)). During forming processes very high degrees of deformation occur. In this case, recrystallization effects have to be taken into account. Finally, the mechanical history can have an influence on the transformation behavior.

Figure 17 shows schematically the possible interdependencies of the state variables along the manufacturing chain. It is very important to understand that these interactions can happen during the complete path of a component from the design phase, where its geometry will be defined, over casting, rolling or forming, soft machining, heat treatment, and hard machining. Depending on the process, the modifications and interactions of the state variables can be totally different. During forming processes, there are strong modifications of the distributions of alloying elements and microstructure. During machining, these distributions will only be changed in regions near the surface of the component. Additionally, the distribution of the residual stresses will be modified. In a heat treatment process, the stress state and the microstructure in the complete component can be modified. In regions near the surface, the distributions of alloying elements can additionally be changed by wanted (carburizing, nitriding, etc.) or unwanted processes (decarburization, manganese effusion, etc.).

The geometry/mass distribution plays a particular role. On the one hand, asymmetries in the mass distribution can result in distortion even under perfect conditions, as discussed at the beginning of this subsection for the crown wheel. For this reason, a considerable amount of the distortion potential is often created during the design phase of a component. According to (*25*), this amount already reaches about 60% of the total potential of case-hardened gears.

On the other hand, the distributions of the state variables are only defined in the corresponding volume, and the process parameters like working stresses, as well as heat and mass fluxes (e.g., carbon flux) act over the surface of this volume. Furthermore, the geometry plays an active role in the distortion generation because the stress and strain distributions depend on it. In particular, the stress component normal to the surface must be zero on it. Therefore, each geometry has something like a 'transfer function.' This function defines the reaction of the geometry to deviations in the carriers from homogeneity and will be discussed in Section 12.09.4 for bearing races with rectangular cross section.

Finally, it has to be concluded that distortion is not a problem of heat treatment alone. Modifications of the carriers of distortion potential can happen in every step of the manufacturing chain. Therefore distortion is a system property and distortion control during manufacturing processes has to follow a system-oriented approach. The corresponding system is the complete manufacturing chain. According to studies carried out especially for bearing races, there are more than 200 parameters that may be relevant (*26*). This may be the reason that a system-oriented view of component distortion, emphasizing the relationships between the individual production steps, can only be found sporadically in the industry today (*27*).

12.09.3 Collaborative Research Center 'Distortion Engineering'

The CRC 'Distortion Engineering' followed the system-oriented approach since it was established by the Deutsche Forschungsgemeinschaft (DFG) at the University of Bremen in 2001. Meanwhile, it has become common knowledge that this is the only way leading to an overall minimum of distortion. Basic aims of this project were to improve the knowledge of relationships along the considered production processes, and the drawing up of a system model integrating the single production steps, which can serve to calculate the effects of the different influencing parameters on distortion. Fundamental investigations were based on simple model geometries like rings (cylindrical and conical, representative for bearing races), shafts (straight and with diameter step-down), and discs/gears (plain discs with/without bore and real gears). The corresponding materials have been through-hardening bearing steel (SAE 52100) and carburizing steel (SAE 5120). Consistently the rings have been martensitic through hardened, the shafts only blank hardened, and the discs/gears blank and case hardened. Details of the manufacturing chains are given in (*27*).

To accomplish these tasks, the CRC 'Distortion Engineering' was formed by researchers (Figure 18) from the areas of material science, mechanical and chemical engineering, metrology, application of information and communication technologies in production, industrial mathematics, and physics. They cooperated and were supported by industrial enterprises from the areas of steel production (Deutsche Edelstahlwerke, Buderus Edelstahlwerke, and Ovako Steel, Sweden), forming (Johann Hay), ball bearing manufacturing (Schaeffler KG (INA/FAG), SKF, ThyssenKrupp Rothe Erde), gearing (ZF Friedrichshafen, ZF Passau), automotive (Daimler AG), and aircraft construction (Airbus Deutschland).

One of the major achievements of the CRC was the development of the 'Distortion Engineering' methodology (Figure 19, (*28*)). Always taking into account the entire process chain, the methodology consists of three levels of investigations, starting with the identification of parameters and variables influencing distortion in every manufacturing step (Level 1). Design of experiments (DOE) allows gaining maximum output of a limited number of samples and – at the same time – shows up cross-influencing parameters and interdependencies.

After identifying the major influencing parameters, Level 2 focuses on understanding the distortion mechanisms by using the concept of distortion potential and its carriers (see Section 12.09.2.5). Modeling and simulation are helpful, and in many cases necessary tools, to fully understand the mechanisms ruling the distortion generation.

Understanding of the mechanisms does already allow minimizing of distortion, Distortion Engineering aims to compensate for distortion using the so-called Compensation Potential (Level 3). On the one hand, this approach uses the conventional method to

Figure 18 Most of the members of CRC 'Distortion Engineering' during the 3rd Int. Conf. on Distortion Engineering IDE 2011 (photo by Ulrich Reiß, IWT Bremen).

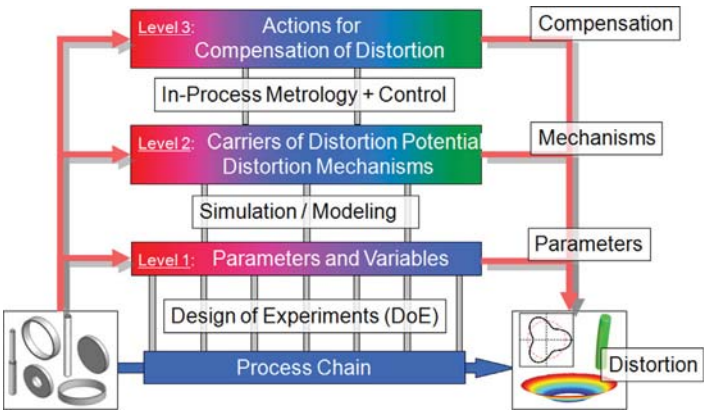

Figure 19 The methodology 'Distortion Engineering'. Reproduced from Zoch, H.-W. Distortion Engineering: Vision or Ready to Application. *Mat.-wiss. u. Werkstofftech* **2009,** *40* (5-6), 342–348.

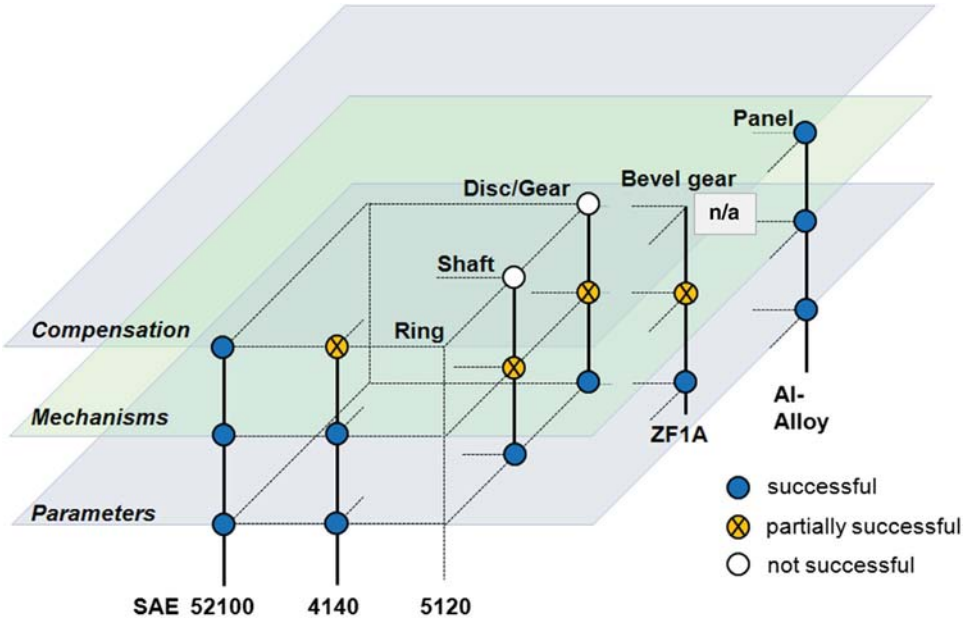

Figure 20 Fields of investigation of the CRC 'Distortion Engineering'. Reproduced from Zoch, H.-W. Distortion Engineering - Interim Results after One Decade Research within the Collaborative Research Center Distortion Engineering. *Mat.-wss. u. Werkstofftech.* **2012,** *43* (1-2), 9–15.

increase the homogeneity respectively the symmetry of the carriers of the distortion potential. But on the other hand, well-directed insertions of additional inhomogeneity/asymmetries in one or more of the distributions of the carriers can be used to compensate for the resulting size and shape changes of the existing asymmetries. For example, an inhomogeneous quenching process can be used to compensate for shape changes from the previous manufacturing process (see Section 12.09.6.1.3). An 'individual' compensation of components is principally possible, but on this level in-process measurement and control techniques are of high importance.

Figure 20 shows an overview of the fields of investigation of the CRC. It shows the geometries, materials, and the three levels of Distortion Engineering. The results gained in the different 'knots' of the CRC structure are given in a very condensed and simplified way too. As the first promising results in distortion control could be achieved well within the duration of the CRC, several so-called transfer projects with industrial partners could be started. At the end of the CRC, six transfer projects were finished, a selected number also included in Figure 20. The graph shows the relationships of the transfer projects to the basic CRC, for example, two new and different materials (SAE 4140 and carburizing steel ZF1A) with similar components (large rings and bevel gears, respectively). This close correlation allowed the required input/output data transfer between the CRC and the transfer project, thus being beneficial for both parties. Furthermore, in Figure 20 another transfer project on laser beam welding of an aluminum panel for aircraft structures is shown, successfully demonstrating that the methodology of 'Distortion Engineering' is material-independent (*29*).

Though modern techniques to extract maximum output data from a limited number of samples have been used, such as DOE, the total number of investigated model components was very high. About 1500 rings, 1000 shafts, and 1600 discs/gears passed the entire corresponding process chain, including heat treatment, and were measured after any process step. This generated a high volume of different data like geometries, microstructures, hardness distributions, and residual stresses, etc., which are stored in a knowledge management database.

One of the main targets of the CRC was the complete process chain simulation for the investigated components and manufacturing routes. Table 2 summarizes briefly the achievements, but simplifies that different software tools are necessary to model the different manufacturing processes. Data management and transfer are key issues, especially valid for the materials data for specific microstructure conditions, temperatures, etc. For SAE 52100, a database was generated, with some exceptions for SAE

Table 2 Comprehensive results in process chain simulation of CRC distortion engineering

	Casting	*Rolling*	*Forging/rolling*	*Milling*	*Heating*	*Carburizing*	*Quenching*
Ring	Not subject of CRC	No significant influence	No significant influence	Analogous model	✓	n/a	✓
Shaft		✓	Not applicable	No significant influence	✓	✓	✓
Disc/gear		✓	✓	No significant influence	✓	✓	✓

Reproduced from Zoch, H.-W. Distortion Engineering – Interim Results after One Decade Research within the Collaborative Research Center Distortion Engineering. *Mat.-wiss. u. Werkstofftech.* **2012**, *43* (1–2), 9–15.

5120 also. Yet it has to be stated that data generation is still a costly procedure, which strongly relies on collaborative work, preferably on an international basis.

12.09.4 Distortion Engineering of Bearing Races: Parameters and Variables

In this chapter, selected results of the CRC concerning the identification procedures of the most important parameters regarding distortion will be described to demonstrate the principal procedure. This will be done using the example of a bearing race manufacturing line that produces a distortion-sensitive bearing with a rectangular cross section and the dimensions $ø_o145$ mm × $ø_i133$ mm × 26 mm.

12.09.4.1 Process Chain

The very first step in defining the process chain and the corresponding parameters consisted of discussions with industrial partners from the steel industry (Deutsche Edelstahlwerke) and the ball bearing industry (FAG Komponenten AG). The aim of these discussions was, on the one hand, a minimization of the distortion potential by achieving optimum homogeneity of the distributions of the carriers of distortion potential based on the available knowledge at the start of the CRC. On the other hand, this process chain should be used as a reference manufacturing line for all investigations of the CRC.

The steps of the process chain are given in Figure 21. All rings were produced from the same heat of bearing steel SAE 52100, which was molten at the steel plant Deutsche Edelstahlwerke in an electric arc furnace. The degree of purity was adjusted by vacuum treatment. Afterwards the melt was continuously cast into ingots of a 265 × 265 mm^2 square format. The melt was electromagnetically stirred within the range of the mold to improve the homogeneity of the alloying element distribution. In further processing, the ingots were heated to deformation temperature, first bloomed, and afterwards rolled on six racks with three-roll technology to bars of 60 mm in diameter.

To forge ring blanks with the dimensions $ø_o150$ mm × $ø_i130$ mm × 30 mm, cylindrical segments with a mass of 1.190 ± 0.020 kg were sawed. For documentation of position in the raw material, each segment was numbered. Additionally, the orientation related to the original bar was marked by the insertion of a pin under a well-defined angle. The material was heated to a temperature of 1150 °C. Subsequently, hot forming was conducted in the following steps (Figure 22): upsetting the semifinished parts (deformation ratio $\varphi = -1.1$), prepunching, punching, ring rolling, and sizing. All forming processes were carried out without additional heating between the steps. The cooling from forming temperature was done in still air, and the rings did not contact each other during this process. After forging, the rings were annealed (spheroidized) and sandblasted.

All rings were machined in two steps to the desired dimension of $ø_o145$ mm × $ø_i133$ mm × 26 mm. At first, the ring was clamped at its outer surface by a six-jaw pendulum chuck (Figure 23), and the inner and one face surface was machined by longitudinal turning. This process was performed with two cuts (first cut: depth of cut $a_p = 1$ mm, second cut: $a_p = 0.5$ mm). In the second step, the inner surface of the ring was fixed by a mandrel (Figure 23) and its outer diameter and the second face surface was machined by longitudinal turning as well. This process was conducted with four cuts and a constant value of $a_p = 0.75$ mm.

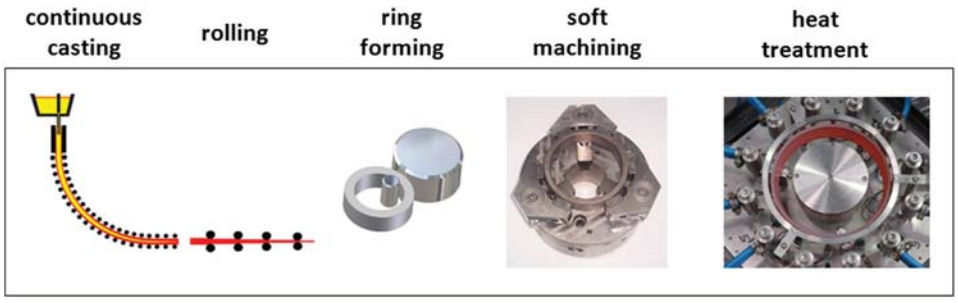

Figure 21 Processes of the investigated manufacturing line (photos by Ulrich Reiβ, IWT Bremen).

Figure 22 Process steps during hot forming (photo by Ulrich Reiβ, IWT Bremen).

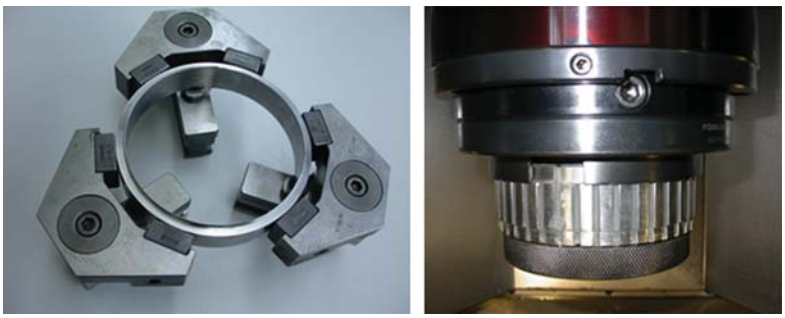

Figure 23 Clamping equipment of the reference manufacturing chain: six-jaw pendulum chuck (left) and mandrel (right) (photos by Ulrich Reiβ, IWT Bremen).

Both processes were carried out with a cutting speed $v_c = 240$ m min^{-1} and a feed $f = 0.3$ mm for the first three cuts. The last cut was done with $f = 0.1$ mm. After each set of samples, which belonged to one test variant, a new turning tool was used.

During heat treatment, the rings were batched on three points at 120° angle distance by the use of a star with three arms. All rings were positioned relative to the star by use of their marks in a well-defined way: this mark – zero position for the measurement of the angle in circumferential direction – fits to the arm of the star which showed to the right side in the furnace. For quench hardening, they were heated in 10 min to 850 °C in a preheated furnace in a protective nitrogen atmosphere in the chamber. Austenitizing time amounted to 25 min. Quenching was performed in a gas nozzle field (Figure 24), which was optimized for the requirements of ring quenching. The gas-quenching device consisted of an inner and an outer gas distributor with 36 nozzles each. The nozzles were arranged in 12 rows circumferential with three nozzles in each row. The gas-quenching device was fed with 5336 l min^{-1} nitrogen, which leads to gas velocities of about 100 m s^{-1} at the nozzle outlets. The distance between the nozzle outlets and the ring surface was 20 mm.

12.09.4.2 Experimental Investigations – Processes before Heat Treatment

The number of probably important parameters was first reduced by discussions with experts from industry from more than 200 according to Bergström et al. (*25*) to 29. In the next step, sensitivity analyses in the different processes gave a reduction to seven parameters (*30*). Furthermore in the first step only the parameters of the processes before heat treatment were analyzed. The remaining five factors and the corresponding levels are listed in Table 3 (*31*).

To investigate the influence of the alloying element distribution, a part of the material was cast without stirring (factor A). Without this technique, the distribution of the segregations becomes more inhomogeneous.

In order to investigate different deformation ratios during hot forming (factor B), the diameter of the semifinished material was reduced from 60 to 45 mm by turning. This leads to a deformation ratio during the upsetting of $\varphi = -0.52$. As a consequence of this modification, the distribution of the segregations in the rings will be changed too.

To check if the cooling from forming temperature could have an influence on distortion via a modification of the carbide size distribution, a circumferential asymmetrically cooling of the rings was realized. This was done in such a way that rings were cooled in air but one-sided beneath a heated steel plate (factor C).

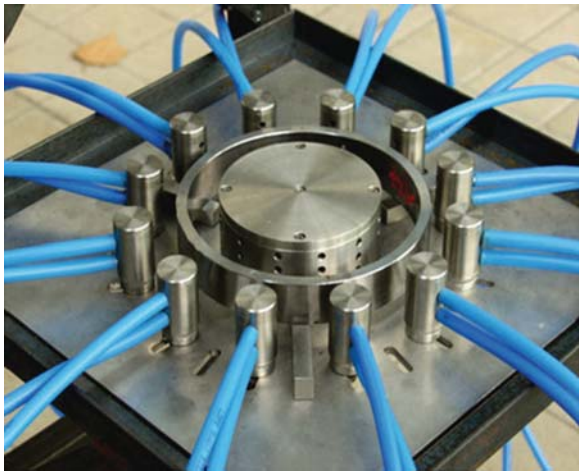

Figure 24 Gas nozzle field for ring quenching (photo by Ulrich Reiβ, IWT Bremen).

Table 3 Levels of evaluated factors in the processes before heat treatment

No.	*Factor*	*Level −*	*Level +*
A	Homogeneity of steel melt	Not stirred	Stirred
B	Deformation ratio of upsetting	−0.52	−1.1
C	Cooling after forging	Single pieces (symmetric)	Circumferential asymmetric
D	Clamping conditions	Pendulum chuck + mandrel	Three-jaw chuck + segmented jaws
E	Feed (last cut outside)	0.1 mm	0.4 mm

Reproduced from Kessler, O.; Prinz, Ch.; Sackmann, T.; Nowag, L.; Surm, H.; Frerichs, F.; Lübben, Th.; Zoch, H.-W. Experimental Study of Distortion Phenomena in Manufacturing Lines. *Mat.-wiss. u. Werkstofftech.* **2006**, *37* (1), 11–18.

To induce inhomogeneous residual stresses in a circumferential direction, a three-jaw chuck (outside) and segmented jaws (inside) were used for clamping (factor D, Figure 25).

For the last cut at the outer surface, the cutting parameter feed (factor E) was increased to $f = 0.4$ mm to influence the mean value of the residual stresses.

The experiments were planned and evaluated through the use of the 'Design of Experiments' method. The aim was to have a separation between main effects and second-order interactions. This can be ensured by using a 2_V^{5-1} DOE design in which main effects are superimposed with fourth-order interactions and second-order interactions are superimposed with third-order interactions. In general, higher order interactions are rare and can often be neglected (*32*). Thus it was assumed that the observed results are caused by the main effects or second-order interactions.

All rings were measured before and after heat treatment to evaluate the size and shape alterations due to heat treatment. The measurement program involved three circle scans at different heights at the inner and outer surfaces of the ring. In addition, flatness scans were measured at the median radius at the upper and lower face surfaces (*31*). From these measurements, the size and shape changes according to Sections 12.09.2.1 and 12.09.2.2 were evaluated. In the next step, the so-called effects were calculated. They are defined as differences between the mean results of the low and high levels of DOE (for details, see (*31,32*)). To identify significant factors and interactions on the distortion behavior of the rings, the results of the DOE experiments were evaluated by statistic analysis. The *t*-test assesses whether the means of two groups are statistically different from each other (*32*). The results of this analysis are in general classified into three different significance levels, which differ in the probability of whether an effect is really an effect or results only from statistical noise. The CRC 'Distortion Engineering' uses the levels 95% (indifferent), 99% (significant), and 99.9% (high significant) (*31*).

The main result of these investigations was that the only high significant effect on the size and shape changes results from the clamping condition. Figure 26 shows the moduli of the Fourier coefficients concerning the changes in roundness deviation of the outer surface (*31*). The second and third orders govern predominantly the change in roundness. The influence of the gas nozzle field can be seen in the relatively large amplitude of the 12th order according to the 12-nozzle rows in the circumferential direction. But a significant difference between the two levels of factor D can only be identified for the third order. The difference of the change in roundness deviation for the two clamping variants can be attributed exclusively to the difference in the third-order Fourier coefficient.

Figure 27 shows the third-order Fourier coefficients of the roundness plots of the outer surface in the complex plane. The values after machining and clamping by pendulum chuck and mandrel are quite small, as can be seen in Figure 26 as well. But the new information from this picture is that the changes have a preferred direction (negative real axis). The corresponding angle in the x–y plane is $-60 \pm 9°$. This means that this change goes into the direction between two arms of the star. In this case, the triangularity after heat treatment can be smaller than before.

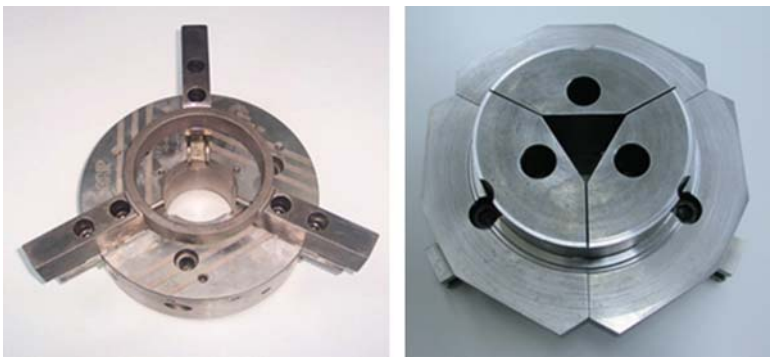

Figure 25 Clamping equipment for the generation of a more inhomogeneous residual stress distribution: three-jaw chuck (left) and segmented jaws (right) (photos by Ulrich Reiβ, IWT Bremen).

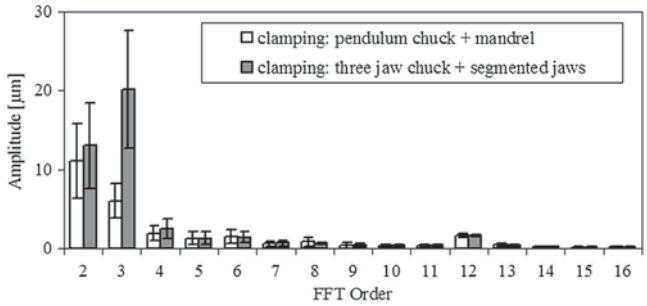

Figure 26 Comparison of the Fourier orders of the two different clamping conditions regarding the change in out-of-roundness of the outer surface (24 rings per level). Reproduced from Kessler, O.; Prinz, Ch.; Sackmann, T.; Nowag, L.; Surm, H.; Frerichs, F.; Lübben, Th.; Zoch, H.-W. Experimental Study of Distortion Phenomena in Manufacturing Lines. *Mat.-wiss. u. Werkstofftech.* **2006,** *37* (1), 11–18.

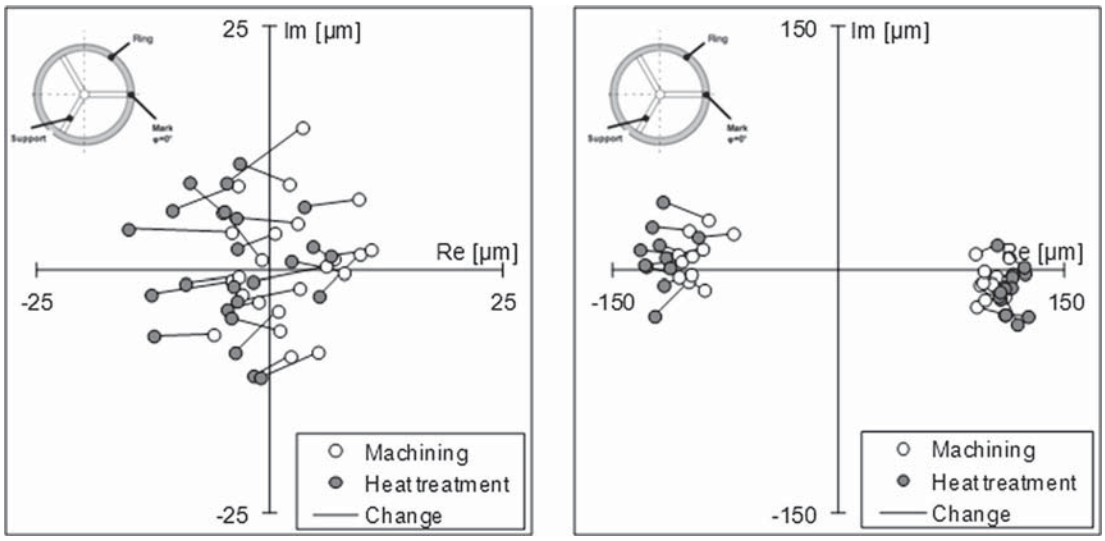

Figure 27 Complex third-order Fourier coefficients of roundness plots (outer surface) after machining and after heat treatment. Left: pendulum chuck + mandrel; right: three-jaw chuck + segmented jaw. Reproduced from Surm, H. Identifikation der verzugsbestimmenden Einflussgrößen beim Austenitisieren am Beispiel von Ringen aus dem Wälzlagerstahl 100Cr6. Dissertation, Universität Bremen, 2011, http://nbn-resolving.de/urn:nbn:de:gbv:46-00101895-17.

After clamping by three-jaw chuck and segmented jaw, the third-order Fourier coefficients are much larger and in all cases near to the real axis. After machining, this result comes from a well-oriented clamping by use of the orientation mark of each ring. But after heat treatment, the change in triangularity is oriented in the direction of the coefficient before heat treatment. The consequence of this behavior is that the triangularity has grown in each case. Furthermore, it can be seen that the average change in the negative direction of about 25 ± 9 µm is larger than in the positive direction (15 ± 4 µm).

Looking to the size changes, the effect of the clamping conditions is highly significant too. Furthermore, the interaction of clamping and feed yields a significant effect (*31*). But both have an amount on the order of 1–3 µm. For practical applications, this is not relevant.

As a consequence of these results, it can be concluded that under the given conditions the modifications of the carriers 'distribution of alloying elements' and 'distribution of microstructure' by the factors A (stirring), B (deformation ratio of upsetting), and C (cooling after forging) have no significant effect on distortion. Only the modification of the distribution of residual stresses by clamping gives a significant and relevant effect on the third-order Fourier coefficient. The resulting residual stress distributions measured by x-ray technique are shown in Figure 28. The triangularity of the residual stress distribution after clamping with three-jaw-chuck and segmented jaw correlates well with the large third-order Fourier coefficient of this variant (Figure 26).

12.09.4.3 Experimental Investigations – Heat Treatment

12.09.4.3.1 Heating

The investigations during heating were published in the doctoral thesis of Holger Surm (*33*). He identified three parameters of the heating process that could have an influence on ring distortion. These factors and the corresponding levels are listed in Table 4. Additionally, he looked for possible interactions between clamping and heating. Therefore, the influence of the clamping was

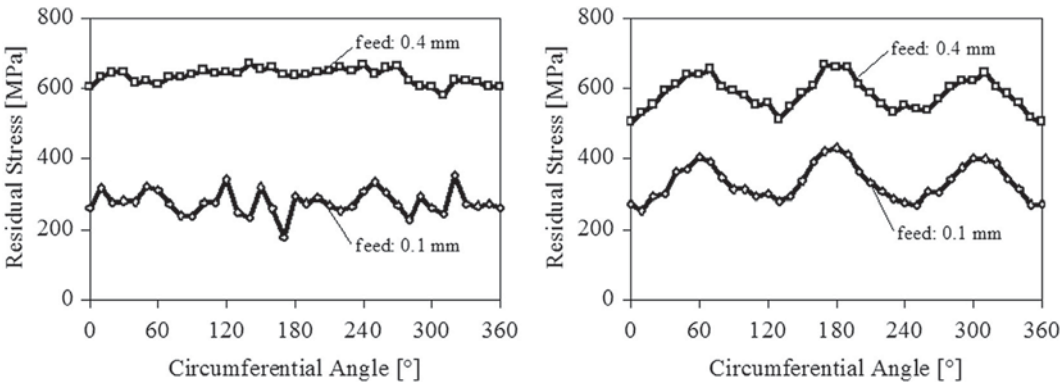

Figure 28 Residual stresses in tangential direction of the outer surface after machining. Left: pendulum chuck + mandrel; right: three-jaw chuck + segmented jaw. Reproduced from Kessler, O.; Prinz, Ch.; Sackmann, T.; Nowag, L.; Surm, H.; Frerichs, F.; Lübben, Th.; Zoch, H.-W. Experimental Study of Distortion Phenomena in Manufacturing Lines. *Mat.-wiss. u. Werkstofftech.* **2006,** *37* (1), 11–18.

Table 4 Levels of evaluated factors in the heating step

No.	*Factor*	*Level −*	*Level +*
A	Heating rate	Cold furnace	Hot furnace
B	Austenitizing conditions	850 °C 25 min	900 °C 3 min
C	Support of the rings	Two lines	Star
D	Clamping conditions	Pendulum chuck + mandrel	Pendulum chuck + segmented jaws

Reproduced from Surm, H. Identifikation der verzugsbestimmenden Einflussgrößen beim Austenitisieren am Beispiel von Ringen aus dem Wälzlagerstahl 100Cr6. Dissertation, Universität Bremen, 2011. http://nbn-resolving.de/urn:nbn:de:gbv:46-00101895-17.

investigated too. These four factors were integrated into a 2^4 DOE design that takes all possible interactions into account. All together, 16 experiments were necessary, and each of these batches contained three rings.

The heating rate was varied by the use of a cold furnace and a preheated furnace. In the first case, the core of the rings reached the austenitizing temperature after about 110 min ($\approx$7.5 K min^{-1}). When the rings were put into the preheated furnace, it took only 10 min ($\approx$83 K min^{-1}) until heating was finished (factor A). The consequence of this variation is on the one hand a simple modification of the carrier 'temperature distribution': the gradients of this distribution become larger. On the other hand, the different heating rates can initiate different amounts of the creep effect and therefore an influence on the carrier 'stress' is given too.

The second parameter 'austenitizing conditions' acts in the same direction. But here the influence of these conditions on the carbide dissolution must be taken into account. Therefore the increased temperature was combined with a reduced austenitizing time. As a consequence, the second factor level goes into the direction of a short-time heat treatment (factor B).

A variation of the ring support should check the influence of the dead load of the rings (again carrier 'stress') on the distortion generation during heating. By standard, the rings were batched on a star with three arms (diameter 10 mm) made from heat-resistant steel. Therefore the rings were lying on three points – or short lines – in 120° angle distance (**Figure 29**), from a mechanical point of view the ideal arrangement. All rings were positioned relative to the supports by use of the marks of the rings in a clear defined way: the mark was oriented relative to an arm of the star with an angle of +30°. The alternative configuration consisted of two lines with

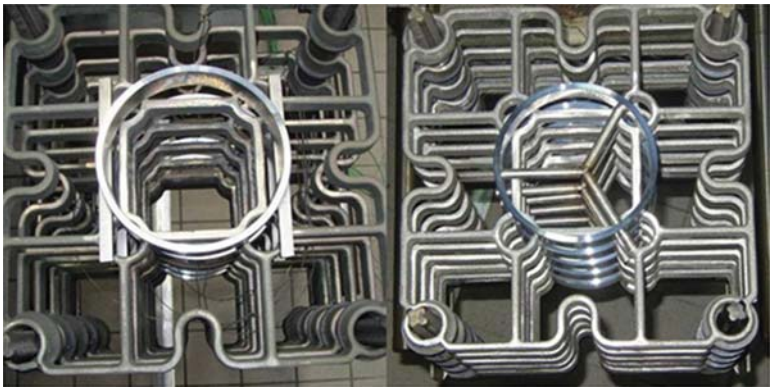

Figure 29 Levels of the factor C 'support': left: lines; right: star (photos by Ulrich Reiβ, IWT Bremen).

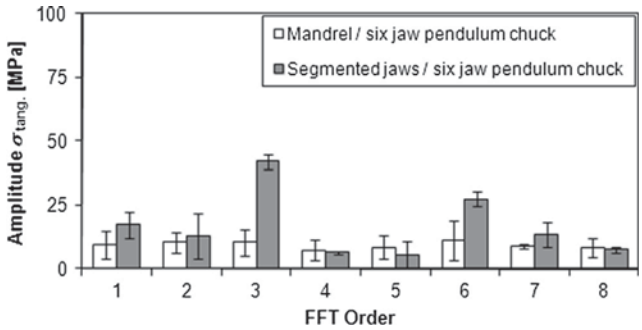

Figure 30 Influence of clamping conditions on the Fourier coefficients of the residual stress distribution (tangential direction) of the outer surface after machining (measuring position: half of the width). Reproduced from Surm, H. Identifikation der verzugsbestimmenden Einflussgrößen beim Austenitisieren am Beispiel von Ringen aus dem Wälzlagerstahl 100Cr6. Dissertation, Universität Bremen, 2011, http://nbn-resolving.de/urn:nbn:de:gbv:46-00101895-17.

quadratic cross section (10 mm): the components were lying on four lines – or small areas (factor C). The lines were positioned parallel to the back and front sides of the furnace. The ring marks were oriented to the right side of the furnace.

Besides the standard clamping, a constellation was used, which gives a modified residual stress distribution (component in tangential direction) of the outer surface. This was done by clamping the inner surface by segmented jaws instead of the mandrel (factor D). The resulting Fourier coefficients of the used clamping techniques are presented in Figure 30. Compared to the standard procedure, the Fourier coefficients of third and sixth order are significantly increased.

Differing from the reference process chain, the quenching process was replaced by a slow cooling into the furnace up to a temperature of 650 °C with a rate of 1.5 K min^{-1}. By this procedure, the transformation of the rings to a pearlitic microstructure occurs nearly at the same time over the complete volume of the rings. Therefore practically no shape changes result from inhomogeneous temperature and microstructure distribution as during the standard quenching process. The final cooling was accelerated by an agitation of the furnace atmosphere. The complete process takes nearly 800 min. To have an acceptable duration of these experiments, five rings were put into a batch, a further deviation from the reference process.

The statistical evaluation of the results showed a large number of high significant and industrial relevant effects and interactions. For lack of space, the focus will be on the Fourier coefficients of second and third orders of the roundness plots of the outer surface and the second-order coefficient of the circle plot of the *z* coordinate on the upper face surface. The results for the inner surface (respectively the lower face surface) are very similar. Size changes do not have to be considered because the resulting microstructure after the slow cooling process is a pearlitic one and therefore nearly no density changes compared to the initial microstructure (spheroidized) were found.

The change in ovality of the roundness of the outer surface is highly significantly influenced by the ring support. All other parameters have no significant and relevant influence. A change from lines to star reduces the modulus of the second-order coefficient on average by about 10 µm. Figure 31 shows the corresponding results in the complex plane. The star supported rings have

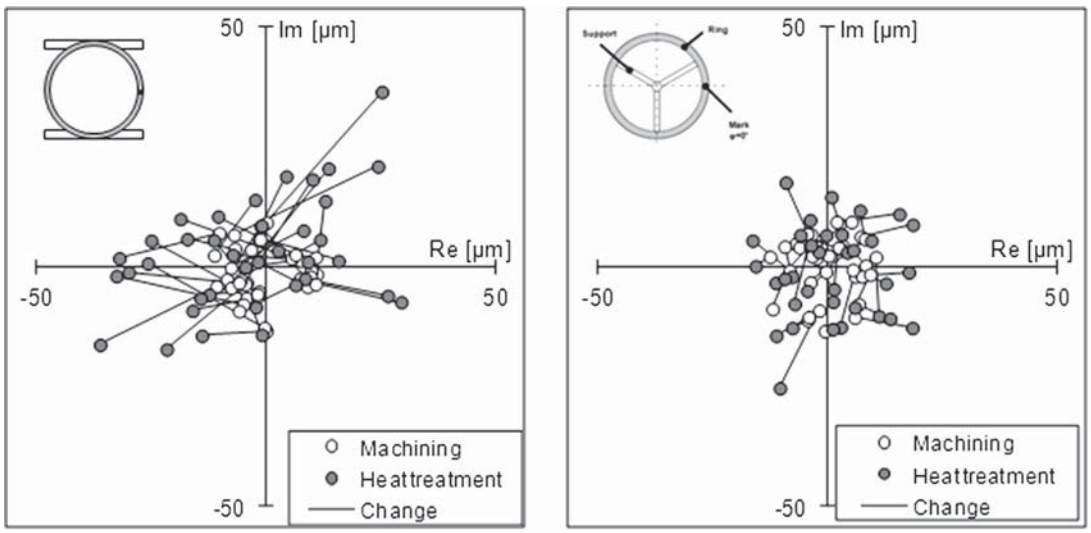

Figure 31 Complex second-order Fourier coefficients of roundness plots (outer surface) after machining and after heat treatment. Left: lines; right: star. Rreproduced from Surm, H. Identifikation der verzugsbestimmenden Einflussgrößen beim Austenitisieren am Beispiel von Ringen aus dem Wälzlagerstahl 100Cr6. Dissertation, Universität Bremen, 2011, http://nbn-resolving.de/urn:nbn:de:gbv:46-00101895-17.

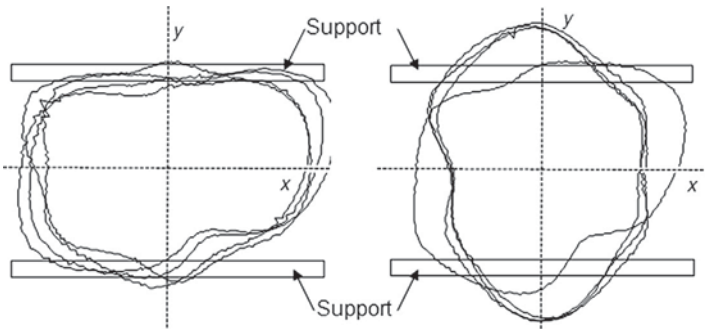

Figure 32 Characteristic roundness plots after heat treatment (outer surface) with ring support 'lines'. Left: beginning of the investigations; right: end of the investigations. Reproduced from Surm, H. Identifikation der verzugsbestimmenden Einflussgrößen beim Austenitisieren am Beispiel von Ringen aus dem Wälzlagerstahl 100Cr6. Dissertation, Universität Bremen, 2011, http://nbn-resolving.de/urn:nbn:de:gbv:46-00101895-17.

no change of ovality in a preferred direction. The complex changes are more or less randomly distributed. For the line support, the change of this coefficient goes in many cases into the direction of the negative real axis. The corresponding orientation in the x–y plane is 90°, which means that a mechanism must act which is directed perpendicular to the lines. But there are a lot of results that do not follow this trend. Some of the ovality changes are directed into the positive real axis. Figure 32 shows corresponding roundness plots. Here, it was found that at the beginning of the experiments – this means that the supports were new and therefore perfect in geometry – the largest radius of the rings was oriented parallel to the lines. At the end of the tests, the preferred orientation has changed by 90°. This effect can principally occur by shape changes of the support lines (*33*).

The change of third-order Fourier coefficient is high significantly influenced by the clamping conditions. Figure 33 again shows preferred directions. Nearly 50% of the rings with clamping by pendulum chuck and mandrel have a change of triangularity into the direction of the negative imaginary axis. The other 50% show a trend into the direction of the positive real axis. This differentiated distortion behavior can be explained by an interaction of the clamping conditions with the ring support, which was identified as a high significant effect, too.

The rings that were clamped by pendulum chuck and segmented jaws show a constant distortion behavior, as was found in Figure 27 too: the change of triangularity is oriented in the direction of the coefficient before heat treatment. The consequence of this behavior is that the triangularity has grown in all cases.

The second-order coefficient of the circle plot of the z coordinate on the upper face surface is highly significantly influenced by four factors. The largest effect comes from the ring support. By a change from line to star, an average reduction of 24 µm was found. Furthermore, a change from cold to preheated furnace gives an additional decrease of 5 µm. An interaction of these two parameters gives an effect of 6 µm. Finally, a small change (2 µm) comes from a three-factor interaction between the just mentioned parameters and the austenitizing conditions. In Figure 34, the changes of the second-order Fourier coefficient of the flatness are given. The star as ring support leads to a more or less randomly distributed change of this attribute. In the case of line support, all rings show a similar behavior. All changes happen in the positive real axis but within a scatter band. The meaning of this result is that the rings

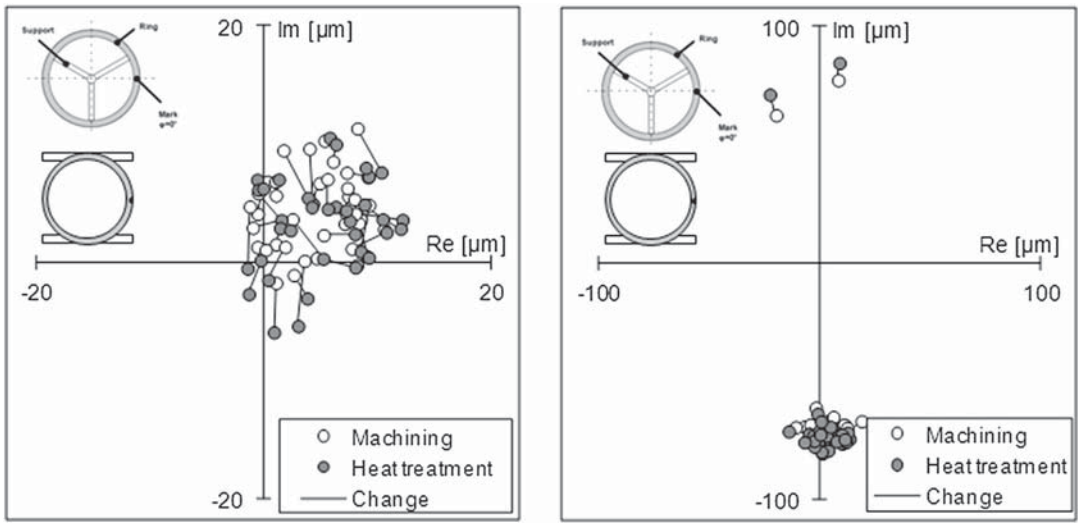

Figure 33 Complex third-order Fourier coefficients of roundness plots (outer surface) after machining and after heat treatment. Left: pendulum chuck + mandrel; right: pendulum chuck + segmented jaw. Reproduced from Surm, H. Identifikation der verzugsbestimmenden Einflussgrößen beim Austenitisieren am Beispiel von Ringen aus dem Wälzlagerstahl 100Cr6. Dissertation, Universität Bremen, 2011, http://nbn-resolving.de/urn:nbn:de:gbv:46-00101895-17.

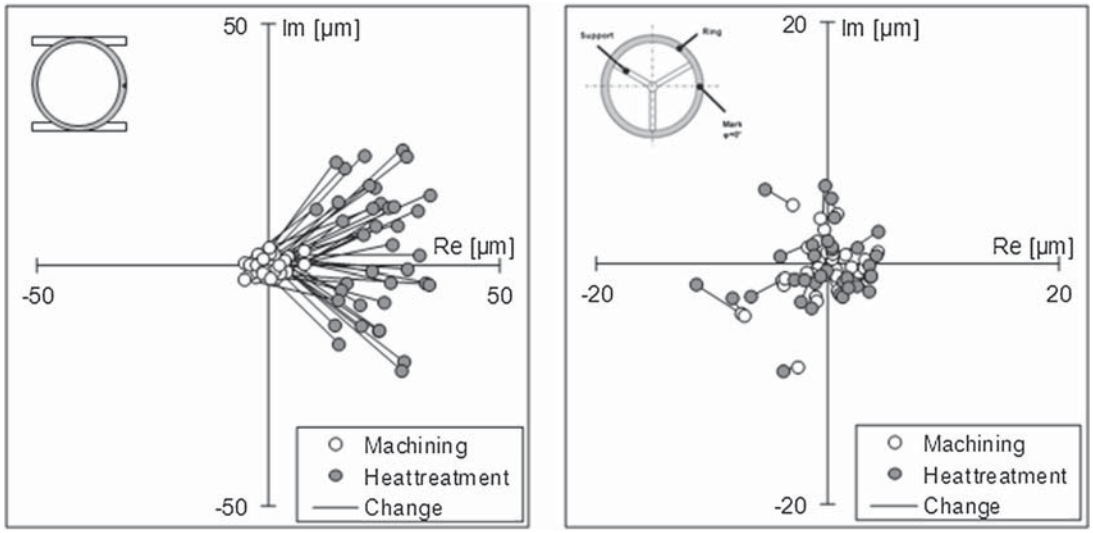

Figure 34 Complex second-order Fourier coefficients of *z* coordinate on the upper face surface after machining and after heat treatment. Left: lines; right: star. Reproduced from Surm, H. Identifikation der verzugsbestimmenden Einflussgrößen beim Austenitisieren am Beispiel von Ringen aus dem Wälzlagerstahl 100Cr6. Dissertation, Universität Bremen, 2011, http://nbn-resolving.de/urn:nbn:de:gbv:46-00101895-17.

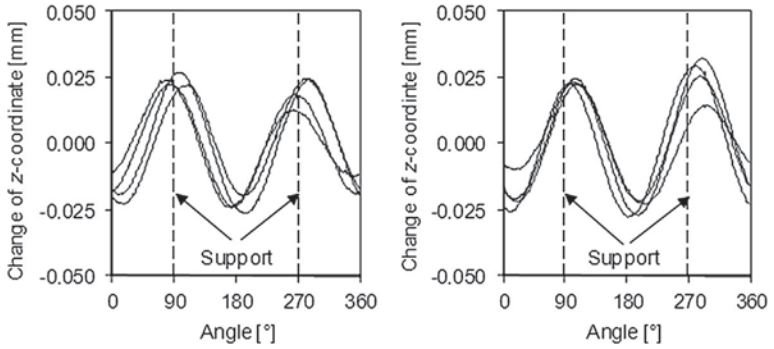

Figure 35 Characteristic flatness deviations after heat treatment (upper face surface) with ring support 'lines'. Left: beginning of the investigations; right: end of the investigations. Reproduced from Surm, H. Identifikation der verzugsbestimmenden Einflussgrößen beim Austenitisieren am Beispiel von Ringen aus dem Wälzlagerstahl 100Cr6. Dissertation, Universität Bremen, 2011, http://nbn-resolving.de/urn:nbn:de:gbv:46-00101895-17.

sag between the two lines but not in all cases perfectly into this direction. The above-mentioned effects of heating rate and interactions act only on the modulus of this Fourier coefficient. Figure 35 shows typical flatness plots. The sagging of the rings and the scattering can clearly be seen, but no effect of the above-mentioned distortion of the support lines is visible.

From these results, it can be concluded that under the given conditions, the support of the rings has a dominant influence on the distortion generation during heating. In combination with the residual stress states from machining the dead load of the rings and its interaction with the support by friction result in modifications of the carrier 'distributions of stress.' Furthermore, the detected effect of the heating rate shows that creep effects are involved in the distortion generation during heating.

12.09.4.3.2 Quenching

The investigations during the quenching process were done by Frerichs and Surm and were published in (*34*). The only parameter under investigation should have been the quenching medium, which primarily modifies the carrier 'temperature distribution.' Secondarily the carriers 'stress and microstructure distributions' were influenced too. But a variation of this process was only possible by use of different furnaces. Therefore the austenitizing process and the batch structure cannot be kept constant. The details of the heat treatments are given in Table 5. With the exception of salt bath quenching, the rings were batched on stars.

In all cases, different anisotropic size changes occur (Table 6). In particular, high pressure gas and oil quenching led to smaller changes, which may be an indication for incorrect quench hardening. Therefore, the volume change was calculated from the coordinate measurements too (Table 6). For an austenitizing temperature of 850 °C, the volume change of the ball bearing steel SAE 52100 amounts to 1.7% after a correct hardening (*35*). In this case, only the rings quenched with the used high-pressure gas quenching device fall below this threshold. The resulting microstructure of these rings should consist of an appreciable portion of bainite and/or pearlite in the martensitic matrix, which was confirmed in hardness values between 40 and 55 HRC in the quench-hardened state.

Table 5 Heat treatment conditions

Type of quenching	*Batch*	*Austenitizing*	*Quenching conditions*
Nozzle field gas quenching	Single parts	10 min 870 °C 30 min	Symmetric gas quenching
High pressure gas quenching	3 layers × 8 rings	Vacuum furnace, 5 K min^{-1} 850 °C 30 min	N_2, 10 bar, gas flow direction: top/bottom; bottom/top
Quenching in oil	3 layers × 8 rings	Vacuum furnace, 5 K min^{-1} 850 °C 30 min	High-performance quenching oil, 60 °C 5 min, agitated
Quenching in salt	1 layer, 48 rings	Done in the facility of an industrial partner	

Reproduced from Surm, H.; Frerichs, F.; Lübben, Th.; Hoffmann, F.; Zoch, H. -W. Distortion of Rings due to Inhomogeneous Temperature Distributions. *Mat.-wiss. u. Werkstofftech.* **2012**, *43* (1–2), 29–36.

Table 6 Relative size changes due to the variation of the quenching process

Quenching technology	*Mean radius (‰)*	*Height (‰)*	*Wall thickness (‰)*	*Volume (‰)*
Nozzle field gas quenching	1.96 ± 0.09	2.07 ± 0.13	2.97 ± 0.24	2.33 ± 0.16
High pressure gas quenching*	0.84 ± 0.39	0.81 ± 0.45	1.38 ± 0.40	1.01 ± 0.08
Quenching in oil	0.71 ± 0.09	2.09 ± 0.05	2.29 ± 0.10	1.70 ± 0.08
Quenching in salt	2.27 ± 0.01	2.02 ± 0.07	1.70 ± 0.05	2.00 ± 0.05

*Both types of gas flow direction: top/bottom and bottom/top. Reproduced from Surm, H.; Frerichs, F.; Lübben, Th.; Hoffmann, F.; Zoch, H. -W. Distortion of Rings due to Inhomogeneous Temperature Distributions. *Mat.-wiss. u.Werkstofftech.* **2012**, *43* (1–2), 29–36.

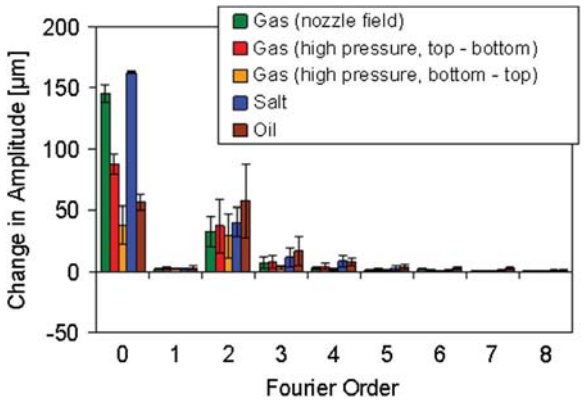

Figure 36 Comparison of the Fourier coefficients regarding the change in out-of-roundness of the outer surface for different quenching conditions. Reproduced from Surm, H.; Frerichs, F.; Lübben, Th.; Hoffmann, F.; Zoch, H.-W. Distortion of Rings due to Inhomogeneous Temperature Distributions. *Mat.-wiss. u. Werkstofftech.* **2012,** *43* (1–2), 29–36.

The rings quenched in a gas nozzle field show the maximum volume change. Keeping in mind that these rings were austenitized at 870 °C, it is clear that more carbon was dissolved and therefore a larger volume change is expected. In addition, a higher portion of retained austenite results after this heat treatment.

The change in roundness deviation is primarily controlled by a change in the second-order coefficient (Figure 36). With the exception of oil quenching, no major difference can be identified between the examined quenching technologies.

Normally, size and shape changes vary in the direction of the ring axis, which causes changes in the angle of ring raceways. For the outer raceways of the rings, the results are presented in Figure 37. The different quenching technologies lead to different alterations of the mean angle. In particular, a large standard deviation of the mean angle is noticeable. This result arises from a dependency on ring position in the batch.

In addition, the distortion behavior of the outer raceway is also characterized by a change in amplitude of the second order. For this distortion criterion, quenching in a gas nozzle field seems to be the best choice to avoid a second order in tilting. Oil quenching activates even higher order Fourier coefficients.

12.09.5 Distortion Engineering of Bearing Races: Mechanisms

In Section 12.09.4, it was shown that the carriers of distortion potential 'distribution of alloying elements' and 'distribution of microstructure' have no influence under the given conditions. Therefore, in the following sections, the influence of the remaining carriers will be analyzed and discussed.

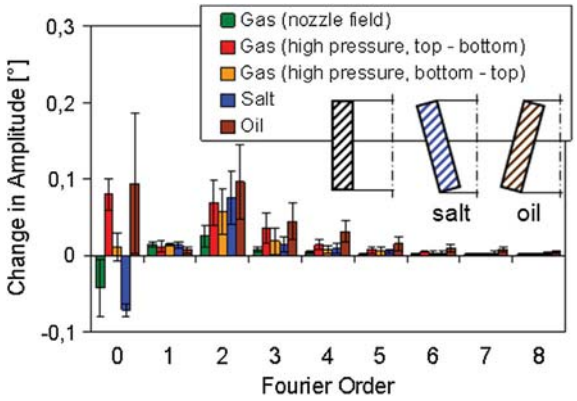

Figure 37 Comparison of the Fourier coefficients regarding the change in angle of outer face (conicity) for different quenching conditions. Reproduced from Surm, H.; Frerichs, F.; Lübben, Th.; Hoffmann, F.; Zoch, H.-W. Distortion of Rings due to Inhomogeneous Temperature Distributions. *Mat.-wiss. u. Werkstofftech.* **2012,** *43* (1-2), 29–36.

12.09.5.1 Influence of the Carrier 'Mass Distribution (Geometry)'

In this section, general interrelationships between the Fourier coefficients of a roundness plot and the strain field for bending and isotropic expansion will be derived. The results highlight the important role of the carrier 'massdistribution' during the generation of distortion. The section is based on the work of Holger Surm, Friedhelm Frerichs, and Jens Sölter, which was presented at IDE 2011 (*34,36,37*).

12.09.5.1.1 Connection between Fourier Coefficients of Roundness Plots and Strains

In a first step, it is necessary to have relations between a measured roundness plot and the curvature radius. To distinguish roundness plots and curvature radius, the first are marked with a bar (like $\overline{R}$). Furthermore, the radius of the median fiber of the ring will be used for further calculations, which is the average value of outer and inner radius:

$$\overline{R}(\alpha) = \frac{\overline{R}(\alpha)_{\text{outer}} + \overline{R}(\alpha)_{\text{inner}}}{2} \qquad [13]$$

The average radius makes it possible to describe the overall behavior of the ring by this one variable, whereas the local behavior can be described by the wall thickness $W(\alpha)$:

$$W(\alpha) = \overline{R}(\alpha)_{\text{outer}} - \overline{R}(\alpha)_{\text{inner}} \qquad [14]$$

The Fourier series of the median fiber can be written as

$$\overline{R}(\alpha) = \overline{R}_0 + \sum_{k=2}^{\infty} a_k \cdot \cos(k \cdot \alpha + \alpha_k) \qquad [15]$$

where the coefficients a_k and α_k, $k \in N$ are typical $\neq 0$. This description is equivalent to eqn [4]. The coefficient of the order $k = 1$ can be neglected because it describes only a shift of the complete ring. The corresponding curvature radius $R(\alpha)$ can be calculated in polar coordinates by (*8*)

$$\frac{\overline{R}^2 + 2 \cdot \left(\frac{\partial \overline{R}}{\partial \alpha}\right)^2 - \overline{R} \cdot \frac{\partial^2 \overline{R}}{\partial \alpha^2}}{\left(\overline{R}^2 + \left(\frac{\partial \overline{R}}{\partial \alpha}\right)^2\right)^{3/2}} = \frac{1}{R(\alpha)} \qquad [16]$$

In general, $\overline{R}(\alpha)$ is not the local curvature radius $R(\alpha)$. This is only true for an ideal ring.

The calculation of the curvature in general gives quite complex equations. For simplification, the infinite sum in eqn [15] should be reduced to the constant term $\overline{R}_0$ (mean radius) and one additional order $k \geq 2$ of the Fourier series. In this case, without any loss of generality α_k can be set to zero. The evaluation of eqn [16] yields

$$\frac{1}{R(\alpha)} = \frac{\left(\overline{R}_0 + a_k \cdot \cos(k\alpha)\right)^2 + 2 \cdot k^2 \cdot a_k^2 \cdot \sin^2(k\alpha) + k^2 \cdot a_k \cdot \cos(k\alpha) \cdot \left(\overline{R}_0 + a_k \cdot \cos(k\alpha)\right)}{\left(\left(\overline{R}_0 + a_k \cdot \cos(k\alpha)\right)^2 + \left(k^2 \cdot a_k^2 \cdot \sin^2(k\alpha)\right)\right)^{3/2}} \qquad [17]$$

Because α_k is set to zero, $\overline{R}(\alpha)$ becomes maximal at $\alpha = 0$ (see eqn [15]). At that position, eqn [17] becomes

$$\frac{\overline{R}_0 + a_k\left(1 + k^2\right)}{\left(\overline{R}_0 + a_k\right)^2} = \frac{1}{R(0)} \qquad [18]$$

Equation [18] can be solved to a_k (only the negative square root of the solution has a physical relevance):

$$a_k = \frac{1}{2}R(0)\cdot\left(1+k^2\right) - \overline{R}_0 - \sqrt{\frac{1}{4}R(0)^2\left(1+k^2\right)^2 - \overline{R}_0\cdot R(0)\cdot k^2} \quad [19]$$

By this equation, the unknown Fourier coefficient could be calculated if the average radius of the ring and the curvature radius at the position of the maximum radius ($\alpha = 0°$) were known. The first value is easily measureable, but the second value is normally unknown. For the calculation of this parameter, two basic types of deformation of a ring have to be considered:

- bending and
- isotropic expansion.

12.09.5.1.1.1 Calculation of the Fourier coefficients in the case of pure bending

In case of a bending of a circular segment (**Figure 38**), an additional deformation that leads to a modified circuit occurs. R_0 and R represent the curvature radius of the neutral fiber ds_0 before and after the additional deformation. In this case, R_0 equals the average radius $\overline{R}_0$. The length of ds_0 is given by

$$ds_0 = R_0\cdot d\alpha_0 = \overline{R}_0\cdot d\alpha_0 = R\cdot d\alpha \quad [20]$$

Before the additional deformation occurs, the length of a fiber with a distance of r' from ds_0 is given by

$$ds\left(\overline{R}_0 + r', d\alpha_0\right) = \left(\overline{R}_0 + r'\right)\cdot d\alpha_0 \quad [21]$$

After the deformation this fiber has the length

$$ds(R + r', d\alpha) = (R + r')\cdot d\alpha \quad [22]$$

The tangential strain of the neutral fiber ds_0 is 0. In a distance r' from the neutral fiber, the tangential strain can be calculated by use of eqns [21] and [22]:

$$\varepsilon_{\text{tang}}(R + r') = \frac{(R + r')\cdot d\alpha - \left(\overline{R}_0 + r'\right)\cdot d\alpha_0}{\left(\overline{R}_0 + r'\right)\cdot d\alpha_0} \quad [23]$$

Using the side condition $ds_0 = \overline{R}_0\cdot d\alpha_0 = R\cdot d\alpha$, the unknown curvature radius can be calculated from eqn [23]:

$$R = \frac{\overline{R}_0\cdot r'}{\left(\overline{R}_0 + r'\right)\cdot\left(\varepsilon_{\text{tang}}(R + r') + 1 - \dfrac{\overline{R}_0}{\overline{R}_0 + r'}\right)} \quad [24]$$

Further on in this contribution, the considered strains are in all cases tangential strains. Therefore, it will be no longer indicated with the index 'tang.' $\varepsilon(R + r')$ in eqn [24] can be approximated by a Taylor series. Because of $\varepsilon(R) = 0$ eqn [24] can be rewritten as

$$R = \frac{\overline{R}_0}{\left(\overline{R}_0 + r'\right)\cdot\left(\dfrac{\partial\varepsilon}{\partial r'}(R) + \dfrac{1}{2}\dfrac{\partial^2\varepsilon}{\partial r'^2}(R)\cdot r' + \ldots + \left(\dfrac{1}{\overline{R}_0 + r'}\right)\right)} \quad [25]$$

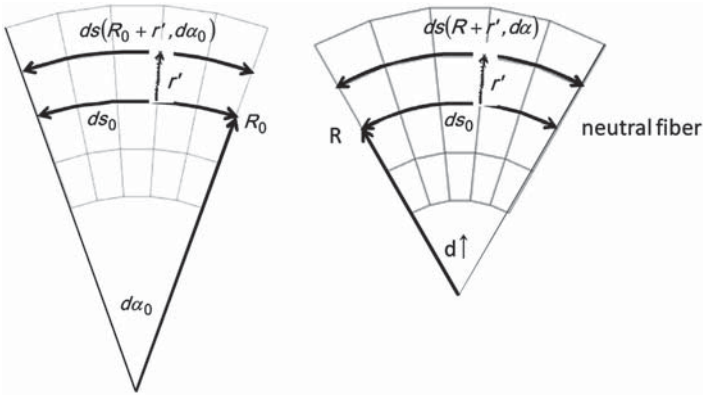

Figure 38 Change of curvature radius by an additional bending of a circular segment . Reproduced from Frerichs, F.; Lübben, Th.; Hoffmann, F.; Zoch, H.-W. Ring Geometry as an Important Part of Distortion Potential. *Mat.-wiss. u. Werkstofftech.* **2012,** *43* (1-2), 16–22.

In case of $\lim_{r' \to 0}$ eqn [5] becomes

$$R = \frac{1}{\left(\frac{\partial \varepsilon}{\partial r'}(R) + \frac{1}{\overline{R}_0}\right)} \quad [26]$$

With this equation for the curvature radius in eqn [19], the unknown Fourier coefficient can be calculated:

$$a_k = \frac{1}{2}\frac{(1+k^2)}{\left(\frac{\partial \varepsilon_{0k}}{\partial r'} + \frac{1}{\overline{R}_0}\right)} - \overline{R}_0 - \sqrt{\frac{1}{4}\frac{(1+k^2)^2}{\left(\frac{\partial \varepsilon_{0k}}{\partial r'} + \frac{1}{\overline{R}_0}\right)^2} - \frac{\overline{R}_0 \cdot k^2}{\left(\frac{\partial \varepsilon_{0k}}{\partial r'} + \frac{1}{\overline{R}_0}\right)}} \quad [27]$$

Please note that eqn [19] is only valid at $\alpha = 0°$ (see **Figure 39** (64), left picture). Therefore, $\frac{\partial \varepsilon_{0k}}{\partial r'}$ is the gradient of the tangential strain at this special position. If $\frac{\partial \varepsilon_{0k}}{\partial r'} \cdot \overline{R}_0 < 0.01$ eqn [27] can be approximated in very good agreement (difference < 1%) with

$$a_k \approx \frac{\frac{\partial \varepsilon_{0k}}{\partial r'} \cdot \overline{R}_0^2}{k^2 - 1} \quad [28]$$

By use of eqn [28], the shape of a former ideal cylindrical ring with radius $\overline{R}_0$ in the case of pure bending can be calculated by

$$\overline{R}(\alpha) = \overline{R}_0 + \sum_{k=2}^{\infty} \frac{\frac{\partial \varepsilon_{0k}}{\partial r'} \cdot \overline{R}_0^2}{k^2 - 1} \cdot \cos(k \cdot \alpha + \alpha_k) \quad [29]$$

The corresponding distribution of strain gradients is given with very good approximation by

$$\frac{\partial \varepsilon}{\partial r'}(\alpha) = \sum_{k=0}^{\infty} \frac{\partial \varepsilon_{0k}}{\partial r'} \cdot \cos(k \cdot \alpha + \alpha_k) = \sum_{k=0}^{\infty} \frac{a_k \cdot (k^2 - 1)}{\overline{R}_0^2} \cdot \cos(k \cdot \alpha + \alpha_k) \quad [30]$$

The last two equations give the possibility to calculate roundness plots if the strain gradients are known respectively vice versa to calculate the strain gradients if the Fourier coefficients of the roundness plots are known.

12.09.5.1.1.2 Calculation of the Fourier coefficients in the case of isotropic expansion

In the case of an isotropic expansion or tension, the angle $d\alpha_0$ remains unchanged (**Figure 40**). Again the curvature radius before the expansion equals the average radius. Therefore, the tangential strain of the neutral fiber can be calculated by

$$\varepsilon = \frac{ds(R) - ds(R_0)}{ds(R_0)} = \frac{R \cdot d\alpha_0 - R_0 \cdot d\alpha_0}{R_0 \cdot d\alpha_0} = \frac{R - R_0}{R_0} = \frac{R - \overline{R}_0}{\overline{R}_0} \quad [31]$$

The new curvature radius is given by

$$R = (\varepsilon + 1) \cdot \overline{R}_0 \quad [32]$$

Using this in eqn [19] and keeping in mind that this equation is only valid at $\alpha = 0°$, the Fourier coefficient a_k can be calculated by

$$a_k = \overline{R}_0 \left(\frac{1}{2}(1+k^2)(1+\varepsilon_{0k}) - 1 - \sqrt{\frac{1}{4}(1+k^2)^2(1+\varepsilon_{0k})^2 - (1+\varepsilon_{0k})k^2} \right) \quad [33]$$

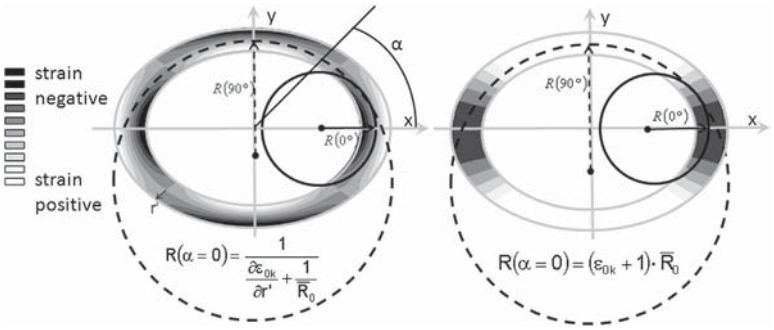

Figure 39 Strain distribution and local curvature radius $R(\alpha)$ for $k = 2$. Left: bending; right: isotropic expansion. Reproduced from Frerichs, F.; Lübben, Th.; Hoffmann, F.; Zoch, H.-W. Distortion of Conical Formed Bearing Rings made of SAE 52100. *Mat.-wiss. u. Werkstofftech.* **2009,** *40* (5-6), 402–407.

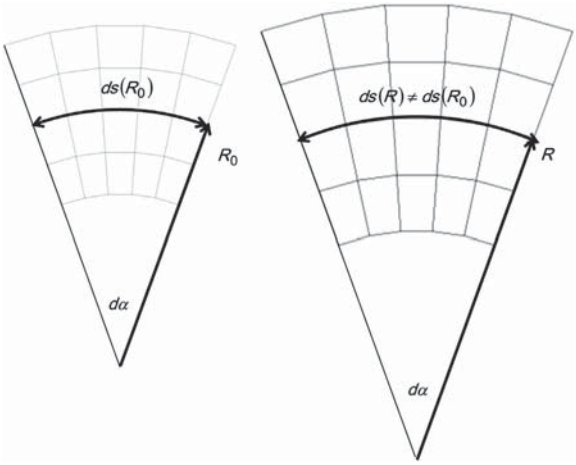

Figure 40 Change of curvature radius due to isotropic expansion. Reproduced from Frerichs, F.; Lübben, Th.; Hoffmann, F.; Zoch, H.-W. Ring Geometry as an Important Part of Distortion Potential. *Mat.-wiss. u. Werkstofftech.* **2012,** *43* (1-2), 16–22.

ε_{0k} is the strain at $\alpha = 0^\circ$ (see Figure 39, right picture). If $|\varepsilon_{0k}| < 0.005$, eqn [33] can be approximated in very good agreement (difference <1%) with

$$a_k \approx -\frac{\varepsilon_{0k} \cdot \overline{R}_0}{k^2 - 1} \qquad [34]$$

By the use of eqn [34], the shape of a former ideal cylindrical ring with radius $\overline{R}_0$ in the case of a pure isotropic strain can be calculated by

$$\overline{R}(\alpha) = \overline{R}_0 + \sum_{k=2}^{\infty} \frac{\varepsilon_{0k} \cdot \overline{R}_0}{k^2 - 1} \cdot \cos(k \cdot \alpha + \alpha_k) \qquad [35]$$

The corresponding distribution of strain is given by

$$\varepsilon(\alpha) = \sum_{k=0}^{\infty} \varepsilon_{0k} \cdot \cos(k \cdot \alpha + \alpha_k) = \sum_{k=0}^{\infty} \frac{a_k \cdot (k^2 - 1)}{\overline{R}_0} \cdot \cos(k \cdot \alpha + \alpha_k) \qquad [36]$$

12.09.5.1.2 Interpretation

In both deformation modes, the Fourier coefficients depend on a weighting factor:

$$\frac{1}{k^2 - 1} \qquad [37]$$

(see eqns [28] and [34]). Up until now, no assumptions about the sources of the strains were done. Therefore, this weighting factor is a property of the geometry 'ring' itself. But what is the consequence of this property? The answer is quite simple. If a given strain or strain gradient distribution acts into the ring, then the ring answers in such a way that the Fourier order k of this distribution is damped by the factor according to eqn [37]. An order 2 will be damped by a factor 1/3, the order 3 by 1/8, etc. The geometry itself acts as a low-pass filter.

12.09.5.1.3 Validation

Up until now, no statements were made about the kind of strain. In this subchapter, two load cases will be presented. The first is a mechanical load by clamping, the second a thermal load, as it is caused by inhomogeneous quenching in a gas nozzle field.

12.09.5.1.3.1 Mechanical loading

In industry, clamping is often done by k-jaw-chucks (typically $k = 3$ or 6) as it was done by the CRC too (Figure 25). A major drawback of these chucks is the rather punctual contact between jaw and workpiece leading to a relatively high elastic (if clamping forces are too high, even elastic–plastic) deformation.

To proof the validity of eqns [28]–[30], out-of-roundness values from an established analytical model for elastic deformations were compared with results calculated according to these equations. In addition, elastic–plastic ring deformations were simulated in 3D finite element (FE) analysis and compared to this approach too (37).

Under the given conditions for pure elastic deformation, an analytical solution is available. Marguerre gave the following equation for the radial displacement curve of a cylindrical ring, which is clamped at f equidistant points with equal forces (38):

$$\overline{R}(\alpha) - \overline{R}_0 = \frac{F_{cl} \cdot \overline{R}_0^3}{4 \cdot f \cdot E \cdot I} \left(\frac{1 + \alpha_f \cdot \cot(\alpha_f)}{\sin(\alpha_f)} \cdot \cos(\alpha) + \frac{1}{\sin(\alpha_f)} \cdot \alpha \cdot \sin(\alpha) - \frac{2}{\alpha_f} \right) \quad [38]$$

E represents the Young's modulus, I is the geometrical moment of inertia $\left(I = \frac{H \cdot W^3}{12} \right)$, and $\alpha_f = \frac{\pi}{f}$, F_{cl} is the total clamping force. In this solution, lateral contractions (Poisson ratio) are neglected too. In the interval $[0,\alpha_f]$, eqn [38] has a maximum at $\alpha = \alpha_f$ and a minimum at $\alpha = 0$. Therefore, the amplitude of the order f can be approximated by half of the out-of-roundness (37):

$$a_f \approx \frac{\overline{R}(\alpha_f) - \overline{R}(0)}{2} = \frac{F_{cl} \cdot \overline{R}_0^3}{4 \cdot f \cdot E \cdot I} \left(\frac{\alpha_f - \sin(\alpha_f)}{1 + \cos(\alpha_f)} \right) \quad [39]$$

For a constant clamping force, a strong decrease of the amplitudes a_f resulting from eqn [39] occurs (Figure 41, black bars), which is not proportional to $(k^2-1)^{-1}$. But if the clamping forces for different numbers of clamping jaws were chosen in such a way that the strain energy in the ring is constant, then eqns [39] and [28] give very similar results (37).

Furthermore, Sölter has analyzed elastic–plastic loading by use of the FE software ABAQUS. He evaluated the roundness deviations $\overline{R}(\alpha) - \overline{R}_0$ and the distribution of the strain gradients for different numbers of clamping jaws (2, 3, 4, and 6) in loaded and unloaded cases. The clamping force was chosen in such a way that the same elastic strain energy results after unloading. The evaluation consists of an FFT of the distributions of roundness deviation and strain gradient. The first gives directly the Fourier coefficients a_k according to eqn [29]. In the second case, these coefficients can be calculated by eqn [30]. In Figure 42, the ratio a_k/a_2

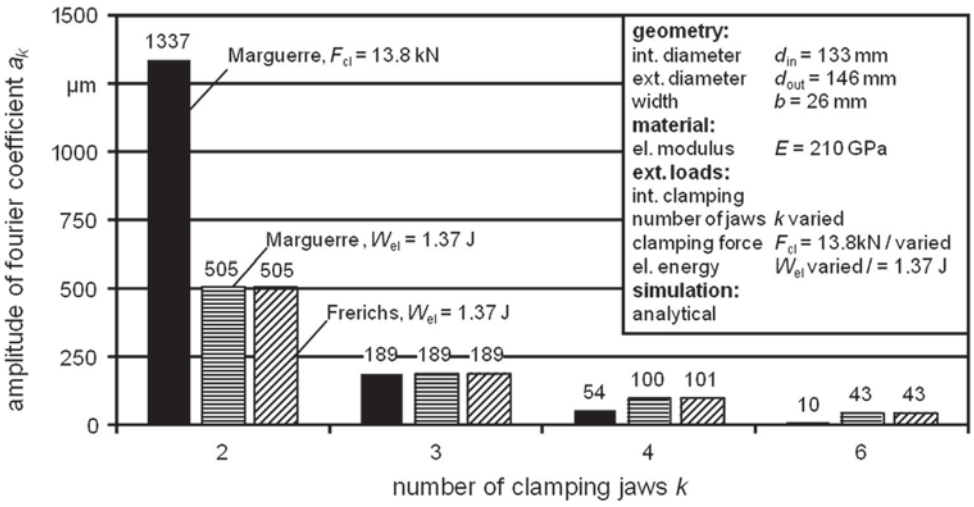

Figure 41 Dependence of Fourier coefficient on the number of clamping jaws (black: constant clamping force, eqn [39]; horizontal pattern: constant elastic energy, eqn [39]; upward diagonal pattern: constant elastic energy, eqn [28]) (reproduced from Sölter, J. Relationship between Strain Distributions and Shape Deviations of Rings Caused in Clamping. *Mat.-wiss. u. Werkstofftech.* **2012,** *43* (1–2), 23–28).

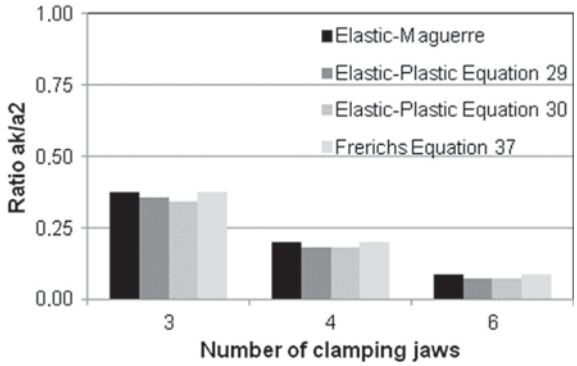

Figure 42 Comparison of the ratio a_k/a_2 resulting from different approaches (unloaded state).

is presented for these evaluations in the unloaded state. Additionally, the results of the Marguerre equation (eqn [39]) and the Frerichs approach (eqn [28]) are included. There are some smaller differences between Marguerre and Frerichs on the one hand and the FE results on the other hand. In the loaded state, these differences are much smaller. Sölter explains the deviations by the negligence of lateral contraction in the simplified models (*37*).

Based on these results, it can be concluded that the ring itself acts as a low-pass filter in the case of external loads. Moreover, the elastic–plastic FE analysis shows directly that shape deviations can be related to the internal strain state. Even if the origin of elastic shape deviations are plastically deformed material regions, the error of eqn [28] is quite small (at most 5% in the analyzed cases $k = 2, 3, 4, 6$).

12.09.5.1.3.2 Thermal loading

To proof low-pass filter function of rings for thermal loads, the gas nozzle field of the CRC 'Distortion Engineering' (**Figure 24**) was used for the generation of controlled inhomogeneous temperature fields during quench hardening (*34*). This was done by adjusting different varying flow fields with equal amplitudes in the sole Fourier orders 2, 3, and 6. Only variations of the gas flow field concerning the outer raceway were adjusted. The inner gas distribution was kept constant. This procedure ensures on one hand that the rings were hardened correctly. On the other hand, the strain respectively the strain gradient distribution in radial direction was constant for all investigated orders.

The results of these tests are given in **Figure 43** (*34*). The mean change in radius of the rings is not affected by the variation of quenching conditions (order 0). In spite of a homogeneous cooling, a change in the second order of the outer raceway is identified due to heat treatment. Nearly the same distortion behavior can be evaluated when the rings were quenched in a nonuniform way with a variation of the gas flow field in the third and sixth orders. This constant distortion behavior may be caused by releasing of distortion potential during heat treatment, which was introduced during the manufacturing of the rings.

Nonuniform quenching with high amplitude in Fourier order 2 results in a large ovality of the outer raceway in the quenched state. Similar results are identified if nonuniform quenching is realized with the same high amplitude in Fourier order 3 or 6, respectively. Compared to the other cases, a larger change in the corresponding shape changes of the outer raceway is caused. But the value of the amplitude of the corresponding Fourier order decreases with increasing order even though nonuniform quenching was always done with the same amplitude in the gas flow field.

A comparison of theoretical and experimental change in amplitude due to nonuniform quenching is given in **Figure 44**. The experimental ratio a_k/a_2 for the different Fourier orders has nearly the same values compared to the theoretical prediction according to eqns [28] and [34].

Therefore it can be stated that the ring itself acts as a low-pass filter for thermal loading too. For practical reasons, it has to be concluded that inhomogeneous carriers of the distortion potential should not have low orders in their Fourier spectrum. Second and third order periodicities must especially be avoided.

12.09.5.2 Influence of the Carrier '(Residual) Stress Distribution'

In Section 12.09.4, it was shown that two kinds of stress-based interactions between a ring and its surrounding can occur. On the one hand, the clamping process and the resulting residual stress distribution can be correlated to the related roundness plots. On the other hand, interactions with the support based on the dead load of the rings and the corresponding stresses and friction between both appear and can lead to shape changes too.

As it was shown in **Figure 28** in the case of clamping with pendulum chuck and mandrel, a homogeneous residual stress distribution in circumferential direction resulted. Therefore, it can be assumed that in this case, the reduction of these stresses during

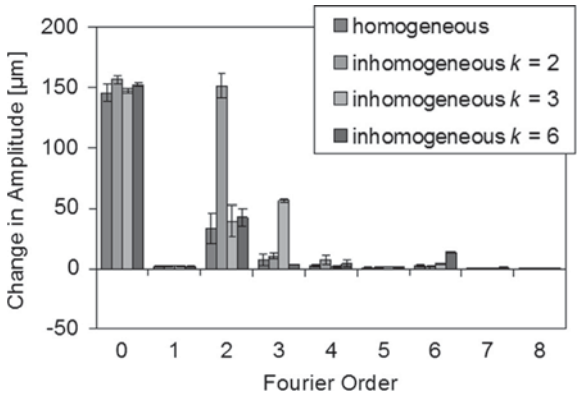

Figure 43 Change in amplitude of different Fourier orders due to nonuniform gas quenching. Adapted from Surm, H.; Frerichs, F.; Lübben, Th.; Hoffmann, F.; Zoch, H.-W. Distortion of Rings due to Inhomogeneous Temperature Distributions. *Mat.-wiss. u. Werkstofftech.* **2012**, *43* (1–2), 29–36, by courtesy of Wiley-VCH, Weinheim, Germany.

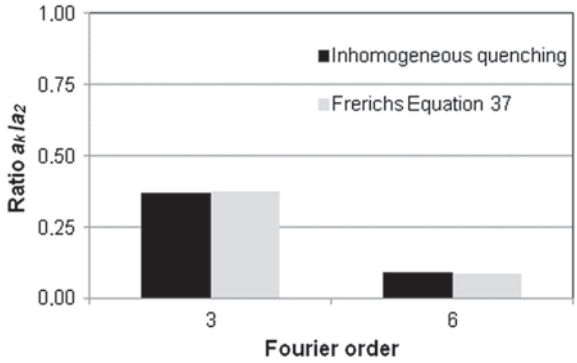

Figure 44 Comparison of theoretical and experimental ratio a_k/a_2 due to nonuniform quenching.

heating will not influence the third-order Fourier coefficients in Figure 27, left picture. So, the observed change must be a consequence of the interaction between dead load and support. This interaction leads to a change of triangularity in the direction between the support points of the star (60°, 180°, and 300° in the x–y plane). Depending on the third-order coefficient resulting from clamping and machining, an increased or decreased triangularity will occur.

In the case of a clamping process with periodical residual stress state (Figure 28, right picture), the change of third-order Fourier coefficient is oriented in the direction of this coefficient after machining (Figure 27, right picture). This means that the existing triangularity after machining will be increased exactly in the direction of the maxima in the roundness plot by the reduction of the residual stress state during heating. Furthermore, an asymmetry in this diagram can be seen: the changes in the direction of the negative real axis are larger than in the opposite direction. This behavior can be explained by the interaction of the ring with the support. In the first case, both effects are acting in the same direction: the maxima in the x–y plane are positioned at the angles 60°, 180°, and 300° and these are exactly the directions of the changes by the support. In the second case, the two effects act in opposite directions: the maxima of the roundness plot are oriented in the directions 0°, 120°, and 240° combined with unchanged directions of the star support. Therefore, both effects are acting in opposite directions, resulting in a smaller increase of the triangularity.

Figure 33 shows a very similar behavior in the investigation of the heating process when the modified orientation between star support and ring (rotation of 30°) is taken into account.

The second-order Fourier coefficient of the roundness plots will not be influenced by a star support. But a strong effect of the line support was found (Figures 31 and 32). Here the same basic effects – dead load and friction lead to stresses – should act.

In the case of the deformation of the circle plot of the z coordinate of the upper and lower surface similar results were found (Figures 34 and 35). Here, purely the dead load results in stresses.

For a better understanding, the aspects of distortion generation from residual stresses after clamping and dead load during heating will be analyzed in the next two sections, which are mainly based on the work of Holger Surm.

12.09.5.2.1 Residual Stresses from Clamping

To understand why the third-order Fourier coefficient of the rings increases, simulations of the heating process for rings with periodical triangularity after machining will be presented in this subsection. To do this, a lot of models based on the software SYSWELD were developed. In Figure 45, an overview of the necessary simulation steps is given. An unsolved problem was the simulation of the machining process of a complete bearing. To the best of the authors' knowledge, it has not been possible up until now to do this in sufficient detail because of the enormous calculations times that would be necessary. Therefore an artificial model was developed (39), which calculates the distribution of the residual stress tensor for the complete volume of a bearing. Simulation prestudies with a variation of the residual stress distribution have clearly shown that a change in roundness deviation after machining will only occur if the stress distribution is inhomogeneous in radial and tangential direction simultaneously. The most effective distribution is given if between inner and outer residual stress field, a phase shift of half a period exists (33). In this case, large bending stresses are present.

According to the experiments described in Section 12.09.4.2, the modeling of clamping was done for segment jaws (inside) and three-jaw chuck (outside). To have minimal changes in wall thickness, a phase shift of 60° between the clamping jaws for inner and outer clampings was well directed adjusted.

The model generates a radius and residual stress distribution after machining that is very similar to measured ones (40,41). Figure 46 shows simulation results in comparison with measured values. The Fourier spectra of the residual stress distributions near the outer surface are very similar. The same is true for the comparison of the depth profile.

Figure 47 shows the calculated distributions of radius and residual stresses for inner and outer surfaces after machining. A phase shift of 60° – 50% of the periodicity – between the residual stress distribution of the inner and outer surfaces resulted from this. This shift was illustrated by micromagnetic measurements (42). Therefore, it can be concluded that large bending moments were present before the heating process was started (see above).

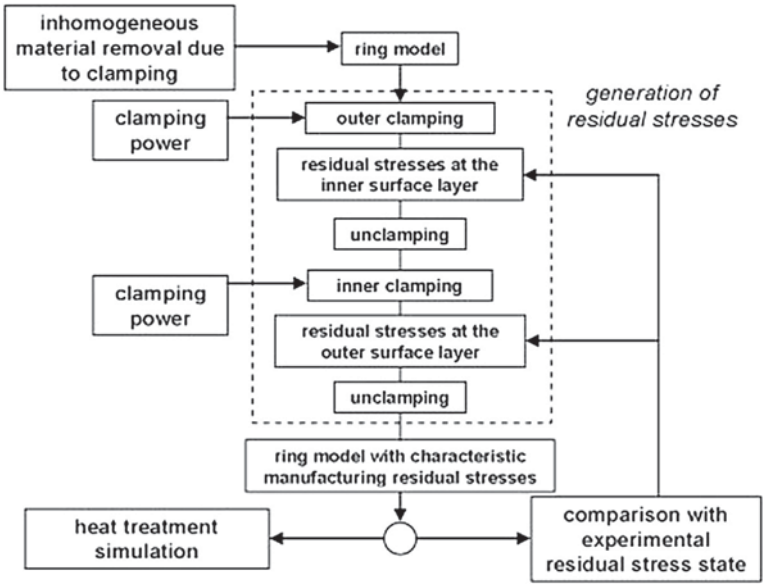

Figure 45 Simulation steps for the investigation of the residual stress influence on distortion generation during heating. Reproduced from Surm, H.; Hoffmann, F. Influence of Clamping Conditions on Distortion during Heating of Bearing Rings. *Mat.-wiss. u. Werkstofftech.* **2009,** *40* (5-6), 397–401.

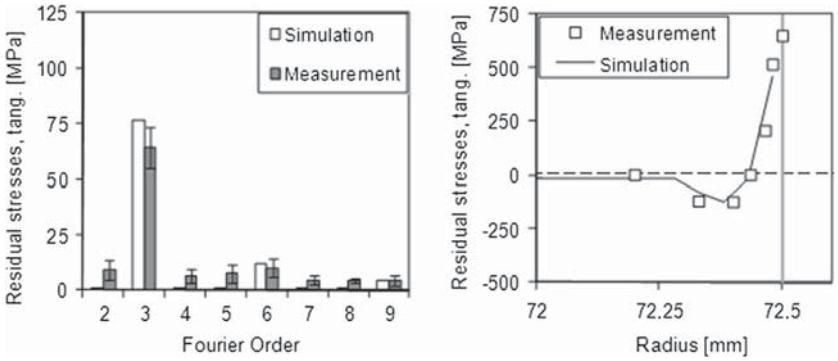

Figure 46 Comparison of measured residual stresses (tangential component) and results of the corresponding model. Left: Fourier spectrum of the stress distribution in circumferential direction; right: depth profile near the outer surface. Adapted from Surm, H. Identifikation der verzugsbestimmenden Einflussgrößen beim Austenitisieren am Beispiel von Ringen aus dem Wälzlagerstahl 100Cr6. Dissertation, Universität Bremen, 2011. http://nbn-resolving.de/urn:nbn:de:gbv:46-00101895-17.

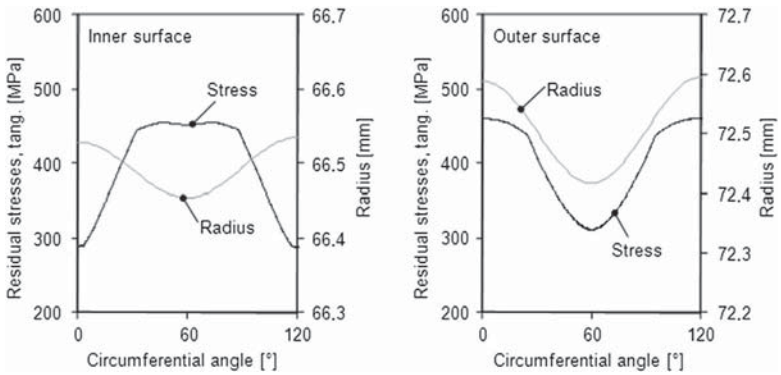

Figure 47 Comparison of simulated stress and radius distribution. Left: inner surface; right: outer surface. Reproduced from Surm, H. Identifikation der verzugsbestimmenden Einflussgrößen beim Austenitisieren am Beispiel von Ringen aus dem Wälzlagerstahl 100Cr6. Dissertation, Universität Bremen, 2011, http://nbn-resolving.de/urn:nbn:de:gbv:46-00101895-17.

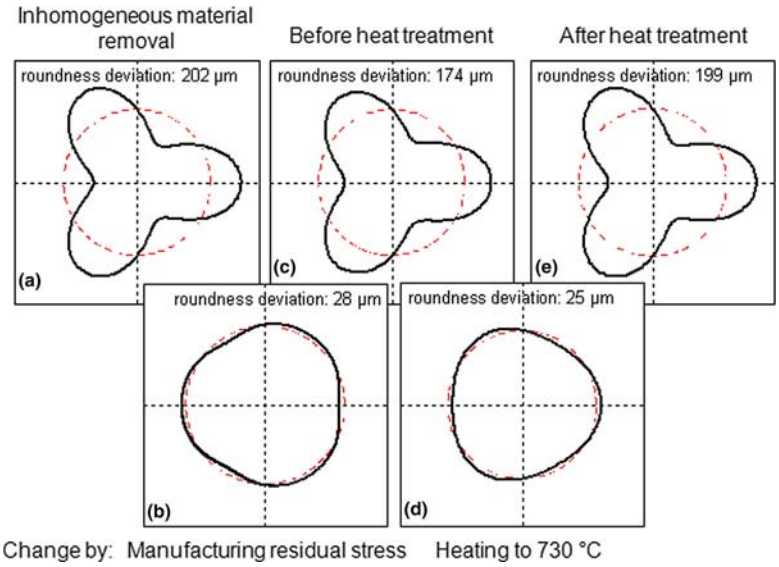

Figure 48 Roundness plots of the inner surface at different steps (upper row) and corresponding changes (lower row). Adapted from Surm, H. Identifikation der verzugsbestimmenden Einflussgrößen beim Austenitisieren am Beispiel von Ringen aus dem Wälzlagerstahl 100Cr6. Dissertation, Universität Bremen, 2011. http://nbn-resolving.de/urn:nbn:de:gbv:46-00101895-17, by courtesy of Dr Holger Surm.

The heating simulation was done up to a temperature of 730 °C by use of a measured heating curve as the boundary condition. Creep and yielding were taken into account (*43*). For space limitations, only a few results can be presented here. Detailed results of the different stress distributions after the single steps according to **Figure 45** are shown by Surm (*33*).

In the simulation of the inhomogeneous material removal during machining due to clamping, a roundness deviation of about 200 µm for the outer ring surface was used as input (**Figure 48(a)**). This equals the average value of the experimental investigations. After generation of manufacturing residual stresses, a decrease of roundness deviation of 28 µm can be observed because the maximum changes of the roundness plot are oriented in the direction of the minima (**Figure 48(b)**). This shape change results from elastic deformations. In the next step, a homogeneous heating of the ring was calculated. At a temperature of 730 °C, a change of the roundness deviation of 25 µm can be evaluated. The corresponding changes of the third-order coefficient acts in the same direction than the original Fourier coefficient (**Figure 48(d) and 48(e)**). The amplitude is nearly the complete amount of the elastic deformation from the machining process.

A comparison of the calculated changes in the third-order Fourier coefficient of the roundness plots with the measured values shows an underestimation: 12.5 instead of 19 µm (*33*). The main reason for this difference comes from the influence of the star support. In Section 12.09.4.2, it was shown that this interaction can result in an increased triangularity of about 5 µm (see **Figure 27**). In the simulation, the interaction of the ring with the support was not taken into account. Furthermore, the elastic deformation of the ring was not completely removed. About 3 µm would result after a completion of the heating process. **Figure 49** shows this and the fact that the third Fourier coefficient of roundness plots correlates quite well to the same order of the

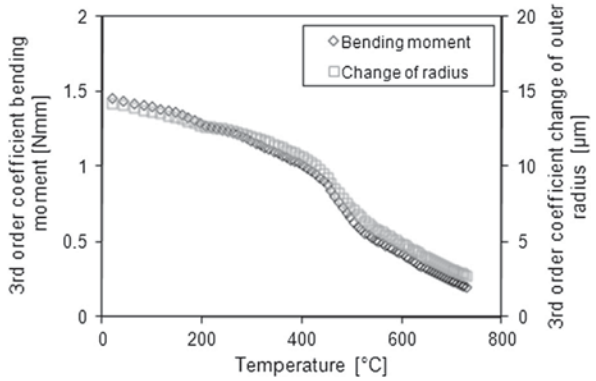

Figure 49 Comparison of third-order coefficients of bending moment and change of radius (outer surface) during continuous heating to 730 °C. Reproduced from Surm, H. Identifikation der verzugsbestimmenden Einflussgrößen beim Austenitisieren am Beispiel von Ringen aus dem Wälzlagerstahl 100Cr6. Dissertation, Universität Bremen, 2011, http://nbn-resolving.de/urn:nbn:de:gbv:46-00101895-17.

bending moment. Last but not least, it should not be forgotten that an artificial model was used for the generation of the residual stress state. The result for the tangential and axial component of the stress tensor was proofed. But the other components were not checked.

Nevertheless, it can be concluded that the interaction of the bending moment with the plasticization mechanisms of yielding and creep are at last responsible for the increase of triangularity. Therefore, the degree of inhomogeneity of the residual stress distribution after machining, and especially the gradients in the radial direction, determines the magnitude of the change of roundness deviation.

12.09.5.2.2 Stresses Resulting from Dead Load

To analyze the interaction of line supports and the ring, simulations using the software ABAQUS were done. The ring was assumed to be free of residual stresses. A contact model that needs as input the friction coefficient between support and ring was used. The heating process was again calculated using a measured cooling curve as the boundary condition. Deviating from Section 12.09.5.2.1, the austenitizing process must be simulated in this case too. The transformation model, which is based on a Johnson-Mehl-Avrami equation (see Chapter 12.06), and the corresponding parameters were published in (*44*). For modeling plastic deformation, two approaches were used:

1. Creep
2. Creep + transformation plasticity

The parameters of these models were received from (*45*). The only unknown parameter was the friction coefficient between support and ring, which can depend on temperature. Measurements of this quantity could not be done. Therefore simulations with a systematic variation of a temperature independent coefficient and plasticity model 2 were done. The left picture of **Figure 50** shows the results of this study. First of all, the simulated direction of the ovality is parallel to the lines as it was found in the experiments with a geometrically perfect line support (**Figure 32**, left picture). Up to a value of about 0.27, only a small ovality results. For larger values, a jump occurs with dramatically increased values of the second-order coefficient. But keep in mind that the given data are the results at austenitizing temperature and cannot be compared with the measurements.

To understand this result, the right-hand side picture of **Figure 50** shows the temperature dependency of the ovality. For a friction coefficient of 0.2, nearly no shape change occurs, if only creep is taken into account. If transformation plasticity is added to the model, ovality is formed during the transformation and at austenitizing temperature a modulus of about 30 μm results.

For an overcritical value of friction (0.3), the simulation forecasts that the ring adheres on the support and by the continuous expansion the second-order coefficient increases continuously. Only when the plasticity model 2 was used, the ovality was reduced by transformation plasticity to values of about 200 μm.

Up until now, no in-process measurement of the ovality was successful with an adequate accuracy. Furthermore, the simulations include some uncertainties concerning the models for contact and friction and the corresponding parameter. Therefore a final judgment of the acting distortion mechanism is not possible. Nevertheless the studies have shown that the given explanations are principally possible.

12.09.5.3 Influence of the Carrier 'Temperature Distribution'

First of all, in this section, the results of two simple temperature distributions on the corresponding roundness plots will be analyzed to receive an impression about the sensitivity of the strain distribution for such an inhomogeneity (*46*). The first case is defined by

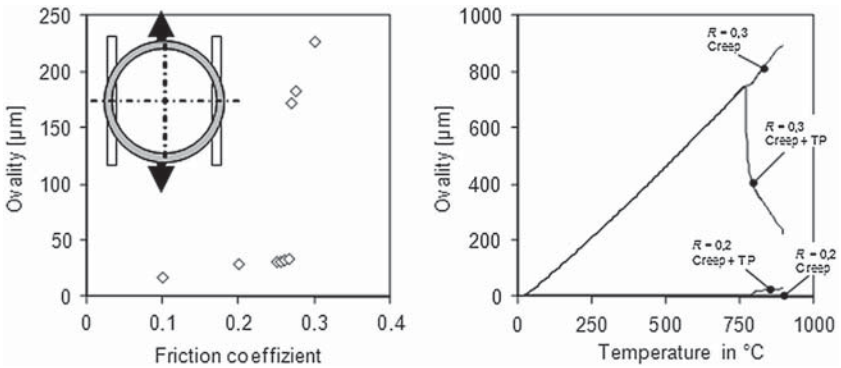

Figure 50 Module of the second-order Fourier coefficient as function of friction coefficient (left-hand side) and temperature (right-hand side). Adapted from Surm, H. Mechanismen der Verzugsentstehung bei Wälzlagerringen aus 100Cr6. *HTM J. Heat Treat. Mat.* **2012**, *67* (5), pp 291–303, by courtesy of Carl Hanser Verlag, Munich, Germany.

eqn [40]. This temperature field has a linear behavior in the radial direction and varies with frequency k in the circumferential direction:

$$T(\alpha, r') = T_0 + \frac{\Delta T}{W} \cdot \cos(k\alpha) \cdot (r' - \overline{R}_0) \quad r' \in \left[\overline{R}_0 - \frac{W}{2};\ \overline{R}_0 + \frac{W}{2}\right] \qquad [40]$$

The resulting strain gradient at $\alpha = 0$ can be calculated using the thermal expansion coefficient α_{th}:

$$\frac{\partial \varepsilon_{0k}}{\partial r} = \frac{\Delta T \cdot \alpha_{th}}{W} \qquad [41]$$

Using eqn [28], the corresponding Fourier coefficient a_k is given by

$$a_k \approx \frac{\frac{\Delta T \cdot \alpha_{th}}{W} \cdot \overline{R}_0^2}{k^2 - 1} \qquad [42]$$

For the investigated ring, a ΔT of 2 K results in a second-order Fourier coefficient a_2 with a module of about 13 µm. For such a small temperature difference, which occurs in every furnace, quite a large effect appears.

The second example is a temperature field without a gradient in the radial direction:

$$T(\alpha) = T_0 + \frac{\Delta T}{2} \cdot \cos(k\alpha) \qquad [43]$$

The resulting maximum strain is given by

$$\varepsilon_{0k} = \frac{\Delta T}{2} \cdot \alpha_{th} \qquad [44]$$

Using eqn [34], the corresponding Fourier coefficient a_k results in

$$a_k \approx \frac{\frac{\Delta T \cdot \alpha_{th}}{2} \cdot \overline{R}_0}{k^2 - 1} \qquad [45]$$

For the investigated ring type, the second temperature field gives a second-order Fourier coefficient of about 0.6 µm, a significant smaller value than in the first example.

Equations [42] and [45] were proofed by FE simulations. The results show that under the given conditions the quality of the approximation is good (*46*).

In general, the ratio of the Fourier coefficients of these two cases is given by

$$\frac{a_k^{(1)}}{a_k^{(2)}} \approx \frac{2 \cdot \overline{R}_0}{W} \qquad [46]$$

Equation [46] applies to all orders of Fourier coefficients. It can be concluded that radial temperature gradients in combination with tangential gradients are much more effective than pure temperature differences in circumferential directions. And this statement can be generalized. Equations [28] and [34] were derived without any assumption about the source of the strains. Therefore it can be concluded that similar results can be received for other carriers of the distortion potential too. Surm showed that the most effective residual stress distribution needs bending moments achieved by radial gradients of the stresses (Section 12.09.5.2.1). Frerichs estimated that to reach the same effects on roundness deviations as shown above, a carbon inhomogeneity lower than 0.01 mass-% can be sufficient if an adequate distribution of carbon with radial gradients exists (*46*).

Up until now only elastic strains were discussed. To receive a distorted component, plasticization must be taken into account. During a quenching process, creep will not occur because of its small duration. Therefore only two mechanisms are possible: yielding and transformation plasticity. To understand which of it acts for different quenching processes, the experiments described in Section 12.09.4.3.2 were repeated with a steel grade, which shows no phase transformation (SAE 304). The resulting change of radius is significantly smaller because no change of volume can occur (**Figure 51**, left picture). This change increases from gas to salt and oil quenching respectively and correlates with an increasing Biot number and therefore growing radial temperature gradients. Similar results were presented in **Figure 12**.

The higher-order Fourier coefficients follow the same principle. From gas to salt and oil quenching, the heat transfer coefficient increases which results in growing radial temperature gradients. Consequently the elastic deformation according to eqn [44] increases too if a temperature inhomogeneity in circumferential direction is present. This must have been the case for second and third order for oil quenching and can principally be explained by variations in the flow field during quenching. Then, the final step is the excess of the yield limit.

The comparison of these results with the data off bearing rings (SAE 52100, **Figure 36**) shows the additional effect of transformation plasticity. Most of the shape changes result from this plasticization mechanism. To demonstrate this, Surm and Frerichs presented simulation results of an inhomogeneous quenching process in a gas nozzle field (*34*). They chose quenching conditions in such a way that no yielding occurs. Their results clearly show that in this case roundness deviations result only from transformation plasticity.

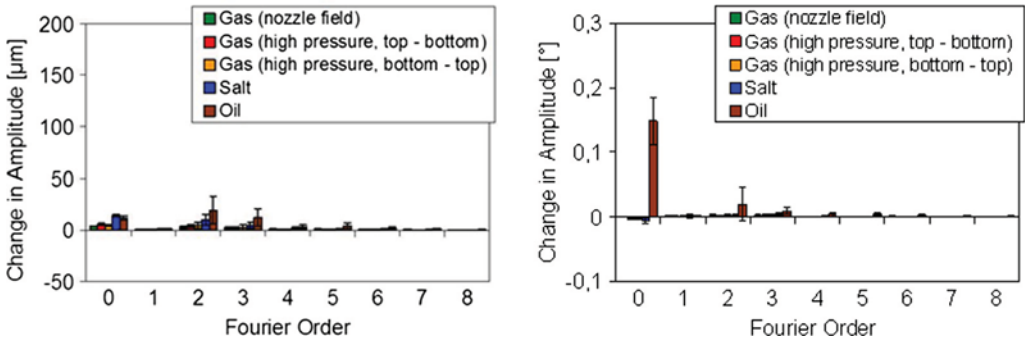

Figure 51 Change in roundness plots (left) and angle of outer surface (right) for rings of SAE 304 – moduli of Fourier coefficients. Reproduced from Surm, H.; Frerichs, F.; Lübben, Th.; Hoffmann, F.; Zoch, H.-W. Distortion of Rings due to Inhomogeneous Temperature Distributions. *Mat.-wiss. u. Werkstofftech.* **2012,** *43* (1-2), 29–36.

Until now strain analysis was not done for axial gradients in the strain distribution. Therefore no quantitative estimation of the angles of outer and inner raceways can be given. But principally the same philosophy can be applied: strain gradients in axial and circumferential directions will result in changes of the angles of outer and inner raceways and, in interaction with the above-mentioned mechanisms of plasticity, shape changes will occur. For rings made of SAE 52100, the results were presented in **Figure 37**. The right picture of **Figure 51** shows the results for the rings made from the austenitic steel SAE 304. Only for oil quenching, changes of the zero and second order were found. The average value of the austenitic steel is not significantly different from the bearing steel result. But the change of the second-order coefficient is much smaller. Here again the additional effect of transformation plasticity generates this increase.

The principal explanation for these results comes from the specific behavior of quenching in evaporating fluids. In this case, at the beginning of quenching, a vapor film is formed around the complete component. For horizontal batched rings, the breakdown of the vapor film starts at the lower edge of the rings. At this position, the heat transfer is dramatically increased because of the direct contact between ring and fluid (*47*). The borderline between the region with vapor and direct contact moves upwards and can clearly be identified in a video documentation of such a quenching process (**Figure 52**, left pictures). With some delay, a second front starts to move downwards from the upper edge. If the position of the two fronts were measured, the so-called rewetting kinematic can be illustrated as it is shown in **Figure 52** (right picture). If the large differences in heat transfer are taken into account, then from this figure a strong asymmetry in the temperature distribution in axial direction can be expected. The interaction of the corresponding strain and stress distribution with yielding and transformation plasticity will lead to the measured average change in angle of outer surface. The second-order effect will result from temperature gradients in the circumferential direction.

Finally, it can be concluded that with increasing radial gradients of the temperature distribution, more and more care must be taken to avoid gradients in the circumferential direction. For axial gradients, the strain analysis was not done. But the authors believe that similar results will be received and therefore asymmetries in the axial temperature distributions should be avoided too.

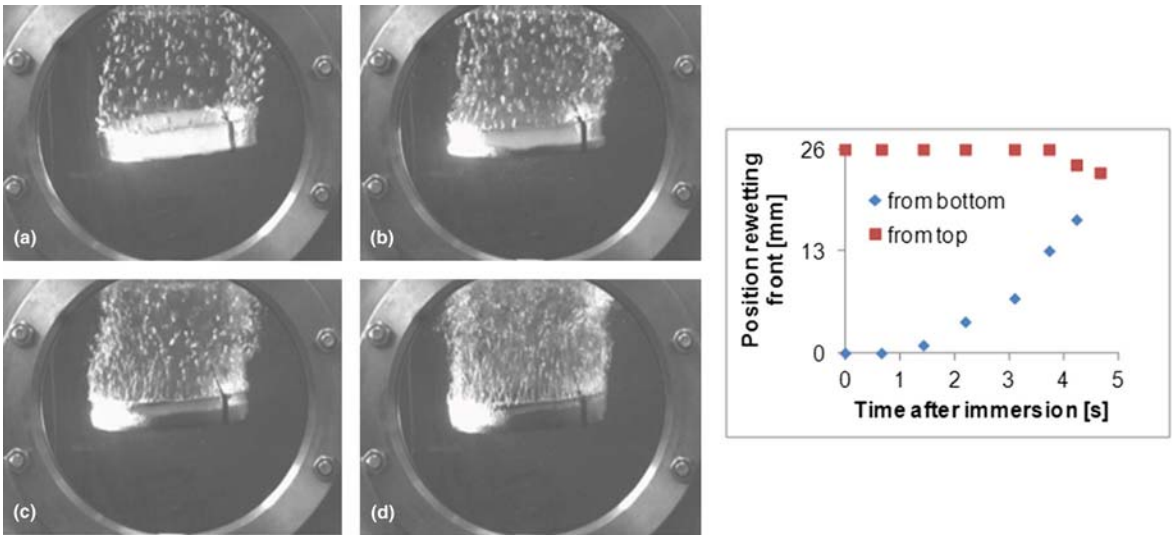

Figure 52 Quenching of a bearing in oil after different times (left-hand side) and corresponding rewetting kinematic (right-hand side). Reproduced from Lübben, Th.; Frerichs, F. Quenching of Bearing Races - Influence of Rewetting Behavior on Distortion. In *6th International Quenching and Control of Distortion Conf. Proc., Quenching Control and Distortion*; ASM International. http://www.asminternational.org/content/Events/qcd/.

12.09.6 Distortion Engineering: Compensation of Distortion

Distortion compensation can be achieved on different levels of complexity. The simplest one is the increase of homogeneity respectively symmetry of the carriers of the distortion potential in the single manufacturing steps as it was and will be done, the classical way. More complicated is the use of directed insertions of additional inhomogeneities/asymmetries in one or more of the distributions of the distortion potential carriers. On this level two, different approaches are possible. If the scatterings of size and shape changes are small, then compensation can be done during process planning. In this case, a preproduction has to be done. The resulting size and shape changes can be used to calculate corrected dimensions and angles of the component or to create an inhomogeneous modification of one of the other carriers of distortion potential. This can happen, for example, when the melting batch is changed and the modified hardenability gives a varying microstructure distribution, or if the fiber flow in basic bodies of gears results in a 'dishing' of the gear (*62*).

The second approach has to be used if an 'individual' processing of a component becomes necessary. This has to be done if the scattering of the distortion is too large and cannot be reduced by other measures. Such an 'individual' compensation of components is possible, but on this level, in-process measurement and control techniques are of high importance. The CRC has investigated different measuring techniques. Good results were received for the in-process measurement of wall thickness during turning by use of ultrasound (*48*). But during heating (by laser triangulation) and quenching (by tactile sensors and optical sensors based on extrinsic intensity modulation), the CRC did not succeed because of insufficient measuring accuracy (*49*).

12.09.6.1 Compensation Potential of Bearing Races during Machining and Heat Treatment

Especially for the bearings under investigation, compensation can only work in the processes construction design, machining, heating, and quenching (see Sections 12.09.4 and 12.09.5). The definition of modified dimensions regarding the size changes can be done during the design phase and will not be discussed. The compensation potential of heat treatment consists of modifications of roundness by inhomogeneous heating and/or quenching processes. Variations of the wall thickness distribution cannot be compensated during these processes. Therefore machining must produce bearings with a constant wall thickness over the complete circumference. Roundness compensation during heat treatment can only be done for the second and third order because of the strongly decreasing transfer function of a ring (Section 12.09.5.1). Based on this philosophy, the compensation potential of the relevant manufacturing steps will be introduced in the next subsections.

12.09.6.1.1 Machining

Within the CRC, several methods have been investigated and developed to minimize roundness and wall thickness deviations by use of flexible clamping devices (*50*). An overview of these techniques is presented in **Figure 53**. Besides the geometrical aspects, another important objective of compensation is to maintain the flexibility of the processes to ensure economical machining. Especially in the manufacturing of low lot sizes, techniques applying the clamping forces locally are often used to ensure a high range of clamping diameter. The reduction of contact area, like chucks with three hardened top jaws for instance, is combined with a low achievable part quality due to high elastic part deformations caused by process and clamping forces.

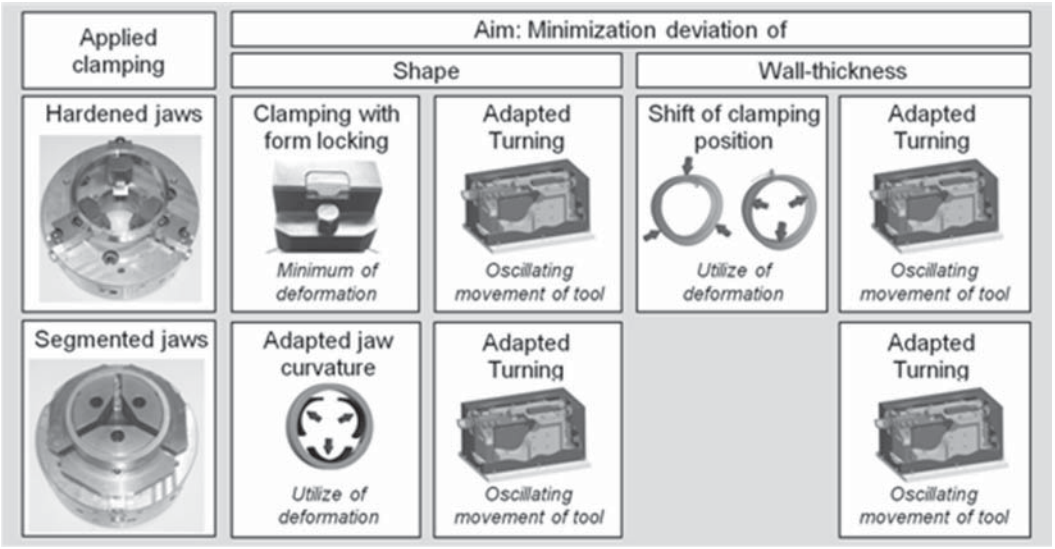

Figure 53 Different approaches of compensation methods.

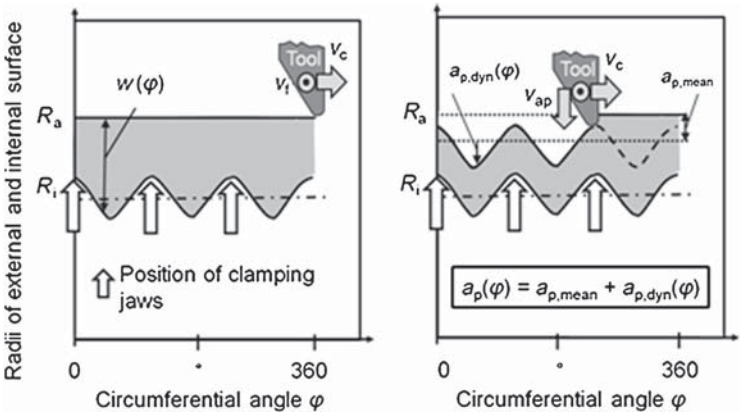

Figure 54 Wall thickness distributions after clamping by applying a three-jaw chuck. Left: conventional turning; right: adapted noncircular turning. Reproduced from Beekhuis, B.; Stoebener, D.; Brinksmeier, E. Adapted Non-Circular Soft Turning of Bearing Rings - Impact of Process Machine Interactions on Compensation Potential. *Procedia CIRP* **2012,** *1*, 540–545.

An approach to minimize deformation due to applying reduced clamping forces by using form locking jaws as well as utilizing deformation for leveling wall thickness deviation is described in (*51*). The elastic deformation caused by clamping with segmented jaws can also be utilized for compensation of shape deviation (*52*). The solution for flexible 'individual' processing is the turning with adapted depth of cut based on measured geometric deviations within the turning center. The dynamic motion of the cutting tool is provided by a long stroke tool actuator (*53,55*). This approach of geometric adapted machining was used in the final optimized manufacturing chain of the CRC 'Distortion Engineering' (see Section 12.09.6.2). In this process, the rings were first clamped externally with three hardened jaws and machined by internal longitudinal turning. After measuring the shape deviation of the inner diameter in the machine by a tactile sensor, it was finally cut with adapted depth of cut ($Di = 133$ mm). Then the rings were clamped from the inside similarly with three hard jaws and were machined to the second last external diameter. Thereafter the wall thickness deviation was measured by use of an ultrasonic measuring device, which was developed by the CRC (*48*). From these data, the harmonic tool track for the last cut was calculated. During the final external cut to diameter of 145 mm, the position of the tool was controlled by a Fast Tool Servo according to the calculated path. Wall thickness deviations were thus compensated by a well-defined harmonic depth of cut (*54*). **Figure 54** compares the resulting wall thickness distribution with the situation after conventional turning.

As discussed in Section 12.09.5.2.1, clamping a ring with three hard jaws leads to a triangular deformation. But furthermore, eccentric and oval shape deviations on its outer surface, as well as wall thickness deviations can result (**Figure 55**, left picture). These Fourier orders result from the transfer of the inner blank deficits to the machined surface (*55*). The benefit of the geometric error compensation is shown in the right picture of this figure. Independently from the feed value, the first- and third-order coefficients of wall thickness and outer radius plots can be significantly reduced by this technique, whereas the second-order coefficients cannot

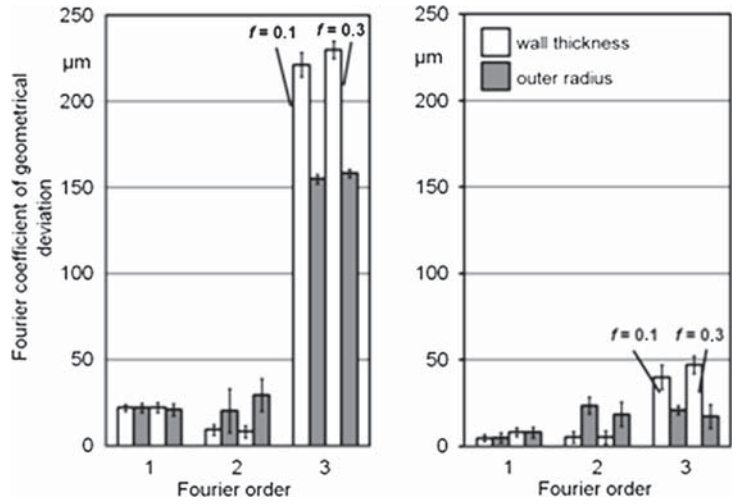

Figure 55 Comparison of shape deviations after circular (left) and noncircular turning. Reproduced from Brinksmeier, E.; Beekhuis, B.; Goch, G.; Stöbener, D. Non-Circular Soft Turning of Bearing Rings - A Method to Minimize Geometric Deviations. In *Proc. CIRP - 2nd Int. Conf. Process Machine Interaction PMI*, 2010, Vancouver, Canada, Published on CDROM, ISBN: 978-0-9866331-0-2.

be influenced. The remaining roundness deviations are not critical, because they can be reduced by inhomogeneous heating and/or quenching. But the third-order coefficient of the wall thickness distribution (about 40 μm) is a deficiency which cannot be compensated during heat treatment. Up until now, the change of the ring deformation due to

- dynamic and static cutting forces,
- the decrease of stiffness caused by material removal,
- thermal strain, as well as
- altering residual stress state of the machined surface

was neglected for the calculation of the tool path. Furthermore vibrations of spindle of the turning center due to alternating cutting forces were not taken into account too (*54*,*55*). For these topics, further work is necessary.

12.09.6.1.2 Heating and Austenitizing

For the evaluation of the compensation potential by an asymmetrical heating, respectively, austenitizing process a special furnace with six independently controllable heating zones was constructed (*56*). The heaters were mounted around the outer surface of the rings as it is shown schematically in **Figure 56**. Therefore the resulting temperature gradients in the radial direction are positive.

To evaluate the compensation potential, different heating cycles with position-dependent set-values for the six heating zones were investigated. In an experimental study, the influence of different heating zone arrangements during nonuniform austenitizing was tested (*57*). In this example, the set temperature of different heating zones was increased from 850 to 900 °C for a process time of 10 min. Over this entire time, the temperatures of the other heating zones remain at the set temperature of 850 °C. Finally, the rings were quenched in the gas nozzle field by a uniform gas distribution. By this process, the temperature inhomogeneity is transformed into an inhomogeneous distribution of the solved carbon. This leads to a variation of the martensite start temperature and consequently small variations in the retained austenite portion. Furthermore, thermal and transformation strains follow via their carbon dependency the foregoing temperature inhomogeneity.

The resulting changes in the module of the second- and third-order Fourier coefficients (outer surface) are given in **Figure 56**. The uniform austenitizing process shows the typical values of about 30 and 10 μm, respectively, resulting from the distortion potential of the manufacturing process. An increase in the oval shape is detected when using heating zone arrangements HZ1245 and HZ123. Regarding a change in the third order, no effect can be attributed due to nonuniform austenitizing (*57*).

To understand this disappointing result, some simulations were done which have taken all relevant effects into account:

- Carbide dissolution during the complete heating and austenitizing process.
- Transfer of the distribution of solved carbon to the quenching simulation.
- Influence of carbon content on the transformation kinetics (Koistinen-Marburger equation).
- Carbon-dependent strains for austenite and martensite.

The inhomogeneous part of the austenitizing process was modeled by a variation of the surrounding temperature with a second-order periodicity. This is a simplification in comparison to the experimental conditions. The amplitude of this distribution was varied. Furthermore, simulations were done with the assumption of a higher surrounding temperature at the inner surface of the ring, a condition that is not realizable with the CRC furnace. From the simulations, the radial and tangential temperature distributions immediately before the quenching process were evaluated. Furthermore the resulting second-order coefficients of the outer surface were extracted. **Figure 57** shows these ovality data as function of the tangential and radial temperature differences, respectively. The left picture of this figure corresponds approximately to the situation in the used furnace: a small positive temperature gradient in radial direction and comparable large gradients in the tangential direction. The compensation potential for ovality is in the range of 20 μm.

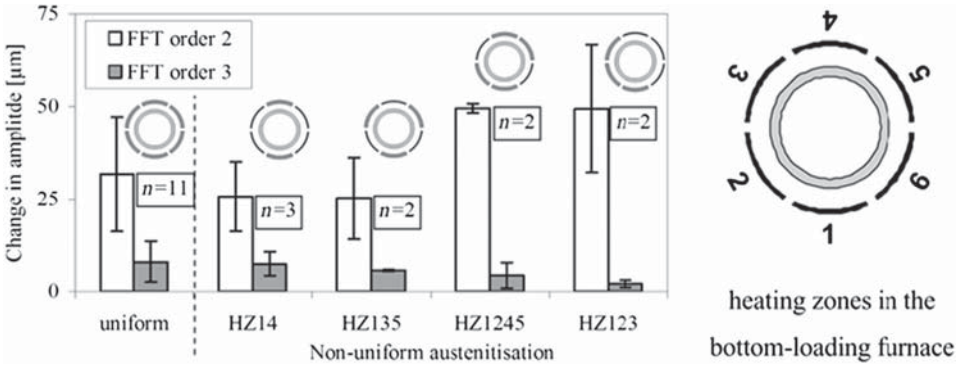

Figure 56 Shape changes of inhomogeneous austenitized bearings (HZ14: increased set value for heating zones 1 and 4). Reproduced from Lütjens, J.; Surm, H.; Hunkel, M.; Gafsi, G.; Renken, V.; Schüttenberg, S. Compensation of Roundness Deviations of Bearing Rings by Heat Treatment. *Mat.-wiss. u. Werkstofftech.* **2012,** *43* (1–2), 48–55.

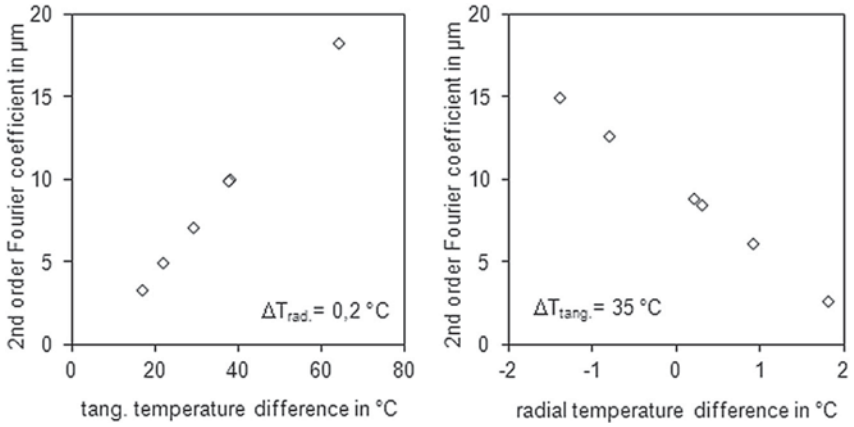

Figure 57 Simulated module of second-order Fourier coefficient after austenitizing with different temperature gradients in circumferential (left) and radial direction (right).

The right picture demonstrates again the huge influence of radial gradients. Only a few Kelvin are necessary to achieve the same effect that very much larger tangential gradients can produce. But only negative gradients act in this way. Consequently the heating must occur mainly from the inner surface. This very important result was not known in the construction phase of the furnace. Therefore its compensation potential is comparably poor. On the other hand, furnaces are normally built in this way and consequently their distortion potential is small.

12.09.6.1.3 Quenching

For the evaluation of the compensation potential by an asymmetric quenching process, the experiments presented in Section 12.09.5.1.3 for the validation of the transfer function of the mass distribution can be used (**Figure 43**). Nonuniform quenching with high amplitude in Fourier order 2 results in roundness plots with second-order coefficients of about 150 µm. Experiments without a second order produce a constant ovality of about 30 µm which results from the distortion potential that was introduced during the manufacturing of the rings. Therefore, only 120 µm are usable for distortion compensation. For the third order, the usable value is about 40 µm.

12.09.6.2 Results of Bearing Distortion Compensation at CRC 'Distortion Engineering'

The evaluation of the compensation potential showed that it can be used under the given conditions only during machining and quenching steps. The scattering of the distortion in the standard manufacturing chain was in an acceptable order. Therefore, the following compensation strategy was applied:

1. Machining of the rings with in-process measurement of the wall thickness distribution and active compensation by adapted noncircular turning.
2. Homogeneous heating and austenitizing.
3. Quenching of the rings with active compensation by inhomogeneous gas flow distribution. Determination of the control parameter by a preproduction series.

12.09.6.2.1 Process Model

During the work of the CRC different approaches for the calculation of distortion compensation by asymmetric quenching were tested. The basic task was to find a model that determines the gas flow of the 12 available nozzle columns in the circumferential direction (**Figure 24**) depending on the second- and third-order coefficients of the roundness distribution measured after machining respectively after austenitizing. Dijkman used a radial basis functions network (*58*,*59*). Lütjens et al. used polynomial relations between amplitudes and phases of roundness changes and the corresponding data of the nozzle field (*57*). They tested this type of model with roundness changes measured by a coordinate measuring machine (CMM) and tactile sensors integrated in the nozzle field (*49*). Experimental and numerical investigations showed that these models are not able to handle a constant distortion, which is introduced by the heat treatment process. The final model presented during the third IDE in 2011 does not use amplitude and phases of the Fourier coefficients but works with the corresponding real and imaginary parts. It takes two effects into account (*60*), which result from the release of the distortion potential during heat treatment:

- Fourier coefficients of the roundness before heat treatment can be enlarged by the factors f_k during heat treatment (see Section 12.09.4.3), and
- constant Fourier coefficients c_k^{const} can occur.

These parameters depend on the complete manufacturing chain. The approach for the necessary compensation of the kth order coefficient by quenching can be written as

$$c_k^{\text{comp}} = (1 + f_k) \cdot c_k^{\text{preHT}} + c_k^{\text{const}} \qquad k = 2,\ 3 \qquad [47]$$

c_k^{comp} and c_k^{preHT} are the Fourier coefficients of the roundness change resulting from the quenching or measured before heat treatment, respectively.

The final step is the calculation of the necessary gas flow distribution $\dot{m}(\varphi_j)$. The values of this function at the 12 nozzle rows can be calculated by

$$\frac{\dot{m}\left(\varphi_j\right)}{\dot{m}_{\max}} = 0.5 + K \cdot \left[\text{Re}\left(c_2^{\text{comp}}\right) \cdot \cos(2 \cdot \varphi_j) + \text{Re}\left(c_3^{\text{comp}}\right) \cdot \cos(3 \cdot \varphi_j) - \text{Im}\left(c_2^{\text{comp}}\right) \cdot \sin(2 \cdot \varphi_j) - \text{Im}\left(c_3^{\text{comp}}\right) \cdot \sin(3 \cdot \varphi_j)\right]$$
$$\varphi_j = j \cdot \frac{\pi}{6} \quad j = 1,\ 2, \ldots, 12 \qquad [48]$$

$\dot{m}_{\max}$ is the maximum gas flow at each nozzle. K has to be chosen in such a way that only positive values between 0 and 1 result from eqn [48]. It has to be mentioned that this approach neglects interactions between second- and third-order effects.

12.09.6.2.2 Some Experimental Details

The manufacturing chain for the following experiments was not only modified in the above-mentioned processes. Furthermore another melt was used and the ring blanks were made by hot tube rolling and cutting of the blanks from the tube. The heat treatment was completed by an additional cooling step to 0 °C and a tempering process (180 °C 2 h). These steps were added because a tempering after inhomogeneous quenching results in a modified roundness change (about 10%). The determination of distortion was now done by use of a CMM after tempering.

To exclude influences from a manual handling of the rings from the furnace to the gas nozzle field, a largely automated heat treatment facility for single-part hardening with high reproducibility has been built by the CRC (57). The austenitizing parameters were chosen to 870 °C 30 min. The realization of the mass flow distribution was done by twelve 3/2-way coaxial magnetic valves. This kind of valve uses an on/off operation mode controlled by a computer with short pulses (here: 1 s). During the on-status, the gas flows through to the nozzles, and during the off-status it is redirected to the surrounding via a bypass. Each of the valves receives one-twelfth of the total mass flow. The percentage of the on-status time was chosen proportional to the necessary local mass flow according to eqn [48]. The average value over all valves was chosen to 50%. This choice enables a reduction and an increase of the local flow with the same mass flow.

12.09.6.2.3 Final Results

The preproduction consisted of 11 tests. Based on the parameter estimation of this comparable small series, the production was started. By use of these additional results, the model parameters were improved iteratively (60). Table 7 lists the resulting parameters after 12 rings. The amplifying factor f_2 for the second order is about 50% larger than the third-order amplification factor f_3. The modulus of the constant change of ovality c_2^{const} is more than twice as large as the corresponding value for the third order, c_3^{const}.

Figure 58 shows the shape changes in the complex plane. It can be seen that the average module of ovality was reduced from 37 to 20 μm and in the third order even an improvement from 36 to 12 μm results. Figure 59 shows the results from the viewpoint of practice. Here the costs for rework depend on the roundness deviation. It can clearly be seen that average roundness and its scattering are considerably reduced. Nevertheless, the compensation is not perfect. The remaining shape changes, especially in the second order, are not understood in detail as of now. Possible explanations are

- small inhomogeneities in the material (see Section 12.09.5.3),
- other variable distortion potentials in the rings,
- inaccuracies in the orientation of the rings in the nozzle field, and
- interactions between the compensation measures for second and third orders.

Table 7 Parameter of the process model after preproduction of 11 rings and production of 12 rings

Order k *(–)*	f_k *(–)*	c_k^{const} *(μm)*
2	0.6	10 + 13i
3	0.41	−3 − 7i

Reproduced from Lütjens, J.; Surm, H.; Hunkel. H. Compensation of SAE 52100 Bearing Ring Distortion during Gas Nozzle Field Quenching. In *6th International Quenching and Control of Distortion Conf. Proc., Quenching Control and Distortion*, 2012, http://www.asminternational.org/content/Events/qcd/.

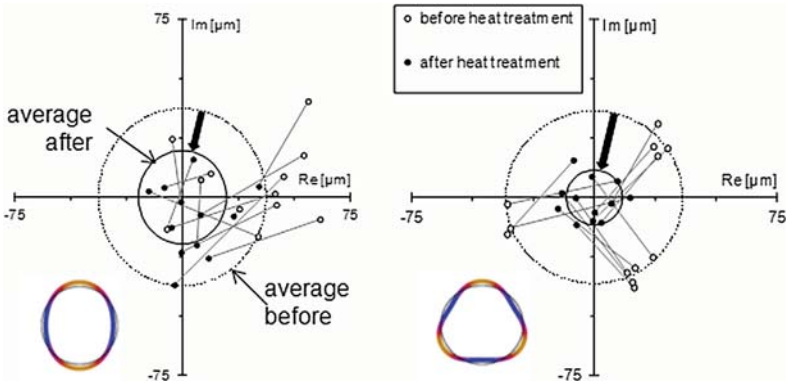

Figure 58 Results of the compensation by inhomogeneous quenching: second- (left) and third-order (right) Fourier coefficients before and after heat treatment. Reproduced from Lütjens, J.; Surm, H.; Hunkel, H. Compensation of SAE52100 Bearing Ring Distortion during Gas Nozzle Field Quenching. In *6th International Quenching and Control of Distortion Conf. Proc., Quenching Control and Distortion;* 2012. http://www.asminternational.org/content/Events/qcd/.

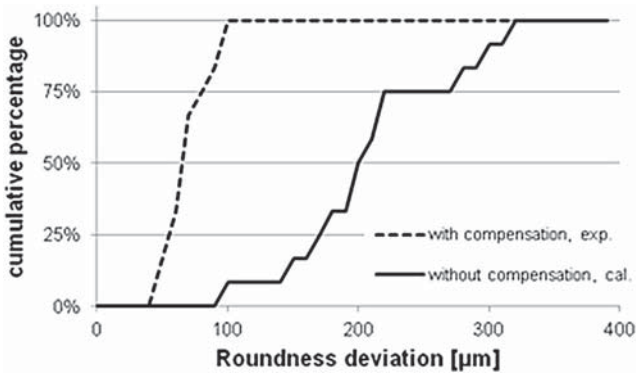

Figure 59 Influence of compensation by inhomogeneous quenching on the cumulative distribution of roundness deviation. Reproduced from Lütjens, J.; Surm, H.; Hunkel, H. Compensation of SAE52100 Bearing Ring Distortion during Gas Nozzle Field Quenching. In *6th International Quenching and Control of Distortion Conf. Proc., Quenching Control and Distortion;* 2012. http://www.asminternational.org/content/Events/qcd/.

12.09.7 Final Remarks

This overview about the work of the CRC Distortion Engineering was done especially for bearing races with a rectangular cross section. The investigations of bearing races with conical cross section, of shafts, discs and gears made from a case hardening steel could not be mentioned here because of space limitations. The small modification of the ring cross section introduces a huge additional distortion potential that leads to tilted rings. Some interesting results can be found in (*34*,*61*). An open question concerning the influence of the modified mass distribution on the tilting behavior is the strain analysis for the axial direction. The authors are sure that a similar transfer function as for the circumferential direction can be found.

The investigations of the manufacturing chains dealing with case hardening steels showed that other carriers of the distortion potential are important also. In these chains, the distributions of microstructure and alloying elements are responsible for the distortion generation too. Because of the larger dimensions, residual stresses from machining and clamping are not so important. The geometry itself will have a transfer function too. But up until now no investigations were done. The role of the temperature distribution is a smaller one, and consequently the compensation potential of the quenching process is smaller, which means that larger gradients are necessary which cannot be achieved by the very well controllable quenching process in gas nozzle fields. But active distortion compensation can be done for discs and gears by different approaches, which are described by Brinksmeier et al. (*62*). Furthermore an overview about Distortion Engineering of disc and gear manufacturing will be published in the new edition of the ASM Handbook *Heat Treating of Irons and Steels*.

The influence of the segregations on distortion of shafts was described and modeled by Martin Hunkel (e.g., (*22*)). The application of these investigations on the process chain simulation of discs is described by Simsir et al. (*23*).

No details of process simulation were presented in this chapter because this information will be given by Tatsuo Inoue in the Chapter (12.06) *Metallo-thermo-mechanical modeling of quenching process*. But it should be mentioned that a complete data set for the quenching simulation of components made from the ball bearing steel SAE 52100 was published by Acht et al. (*63*,*35*). A corresponding paper for the case hardening steel SAE 5120 is planned.

Finally, the authors wants to encourage the readers of this chapter to think about the idea of Distortion Engineering, use it, improve it, and hopefully complete it eventually in the near future.

Acknowledgment

The authors would like to thank the members of the expert panel 'Size and shape changes due to heat treatment' of AWT for their approval to translate some sections of the German distortion monograph. Many thanks to Björn Beekhuis, Friedhelm Frerichs, Martin Hunkel, Jörn Lütjens, and Holger Surm for their readiness to discuss some open questions and to proofread sections of this chapter.

See also: Metallo-Thermo-Mechanical Coupling in Quenching; Residual Stresses Produced by Quenching of Martensitic Steels.

References

1. Heeß, K., et al. *Maß- und Formänderungen infolge Wärmebehandlung - Grundlagen, Ursachen, Praxisbeispiele,* 1st ed.; Expert Verlag: Renningen, 1997 (in German).
2. Heeß, K.; Besserdich, G.; Bohn, R.; Ehlers, M.; Escher, C.; Fiderer, M.; Franz, C.; Göbel, M.; Grasemann, H. J.; Haase, P.; Hoferer, M.; Hunkel, M.; Jennes, R.; Jung, M.; Keßler, O.; Kunow, S.; Klingemann, R.; Lohrmann, M.; Lübben, T.; Majorek, A.; Miskiewicz, S.; Porzner, H.; Reinhold, P.; Schmitt, G.; Schützenhöfer, W.; Thoden, B.; Trapp, N.; Vogel, M.; Volkmuth, J.; Wägner, H.; Wiedmann, D.; Zoch, H.-W. *Maß- und Formänderungen infolge Wärmebehandlung von Stählen,* 4th ed.; Expert Verlag: Renningen, 2012. ISBN: 978-3-8169-3067-9 (in German).
3. Zoch, H.-W., Collaborative Research Centre Distortion Engineering', University of Bremen, Germany. *Int. Heat Treat. Surf. Eng.* **2011,** *5* (1), 4–6.
4. Berns, H. Verzug von Stählen infolge von Wärmebehandlung. *Z. Werkstofftech.* **1977,** *8,* 149–157.
5. Totten, G. E.; Bates, C. E.; Clinton, N. A. *Handbook of Quenchants and Quenching Technology;* ASM International: Materials Park, Ohio, 1993.
6. Pan, J. Factors Affecting Final Part Shaping. In *Handbook of Residual Stress and Deformation of Steel;* Totten, G., Howes, M., Inoue, T., Eds.; ASM International: Materials Park, Ohio, 2002; pp 159–182.
7. Gunnarson, S. Einfluss der Stranggussform auf den Verzug eines einsatzgehärteten Tellerrades aus Stahl. *Härterei-Techn. Mitt.* **1991,** *46* (4), 216–220.
8. Bronstein, I. N.; Semendjajew, K. A. *Taschenbuch der Mathematik,* 20. Auflage; Verlag Harri Deutsch: Thun und Frankfurt/Main, 1981.
9. Surm, H.; Frerichs, F.; Hoffmann, F.; Zoch, H.-W. Erweiterte Verzugsanalyse am Beispiel von Wälzlagerringen – Dem Verzug eine Richtung geben!. *HTM Z. für Werkst. Wärmebeh. Fertigung* **2008,** *63* (2), 95–103.
10. Lement, B. S. *Distortion in Tool Steels;* ASM: Metal Park, Novelty, Ohio, 1959.
11. Wyss, U. Die wichtigsten Gesetzmäßigkeiten des Verzuges bei der Wärmebehandlung des Stahles (Hersg). In *Wärmebehandlung der Bau- und Werkzeugstähle;* Benninghoff, H., Ed.; BAZ Buchverlag: Basel, 1978.
12. Rose, A. Eigenspannungen als Ergebnis von Wärmebehandlung und Umwandlungsverhalten. *Härterei-Techn. Mitt.* **1966,** *21* (1), 1–6.
13. Ameen, E. Dimension Changes of Tool Steels during Quenching and Tempering. *Trans. ASM* **1940,** *28,* 472–512.
14. Chatterjee-Fischer, R. Beispiele für durch Wärmebehandlung bedingte Eigenspannungen und ihre Auswirkungen. *Härterei-Techn. Mitt.* **1973,** *28,* 276–288.
15. Portevin, A.; Sourdillon, A. Contribution a létude des deformations accompagnant les traitements thermiques de lacier. *Rev. Metall.* **1927,** *24* (4), 215–233.
16. Frerichs, F.; Lübben, Th.; Hoffmann, F.; Zoch, H.-W.; Wolff, M. Unavoidable Distortion due to Thermal Stresses. In *5th Int. and European Conference on Quenching and Control of Distortion*, Berlin, 2007, pp 145–156.
17. Hutter, C.; Jöhnk, K. *Continuum Methods of Physical Modelling – Continuum Mechanics, Dimensional Analysis, Turbulence;* Springer: Berlin, Heidelberg, 2004.
18. Landek, D.; Lisjak, D.; Frerichs, F.; Lübben, Th.; Hoffmann, F.; Zoch, H. -W. Prediction of Unavoidable Distortions in Transformation-Free Cooling by a Newly Developed Dimensionless Model. In *2nd Int. Conf. On Distortion Engineering IDE 2008*, Bremen, 2008, pp 237–246.
19. Şimşir, C.; Lübben, Th.; Hoffmann, F.; Zoch, H.-W. Dimensional Analysis of the Thermomechanical Problem Arising during Through-Hardening of Cylindrical Steel Components. *Comput. Mater. Sci.* **2010,** *49,* 462–472.
20. Schröder, R.; Scholtes, B.; Macherauch, E. Rechnerische und röntgenographische Analyse der Eigenspannungsbildung in abgeschreckten Stahlzylindern. *Härterei-Techn. Mitt.* **1984,** *39,* 280–291.
21. Wyss, U. Die Wärmebehandlung von Bau- u. Werkzeugstählen. *Microtecnic* **1969,** *23,* 3–6.
22. Hunkel, M. Modelling of Phase Transformations and Transformation Plasticity of a Continuous Casted Steel 20MnCr5 Incorporating Segregations. *Mat.-wiss. u. Werkstofftech.* **2012,** *43* (1–2), 150–157.
23. Simsir, C.; Hunkel, M.; Lütjens, J.; Rentsch, R. Process-Chain Simulation for Prediction of the Distortion of Case-Hardened Gear Blanks. *Mat.-wiss. u. Werkstofftech.* **2012,** *43* (1–2), 163–170.
24. Simsir, C.; Dalgic, M.; Lübben, Th.; Irretier, A.; Wolff, M.; Zoch, H.-W. The Bauschinger Effect in the Supercooled Austenite of SAE 52100 Steel. *Acta Mater.* **2010,** *58,* 4478–4491.
25. Bergström, C. M.; Larsson, L.-E.; Lewin, T. Reduzierung des Verzuges beim Einsatzhärten. *Härterei-Techn. Mitt.* **1988,** *43,* 36–40.
26. Volkmuth, J. Eigenspannungen und Verzug. *Härterei-Techn. Mitt.* **1996,** *51* (3), 145–154.
27. Hoffmann, F.; Kessler, O.; Lübben, Th.; Mayr, P. "Distortion Engineering" – Distortion Control during the Production Process. *Heat Treat. Met.* **2004,** *2,* 27–30.
28. Zoch, H.-W. Distortion Engineering: Vision or Ready to Application. *Mat.-wiss. u. Werkstofftech* **2009,** *40* (5–6), 342–348.
29. Schimanski, K.; von Hehl, A.; Zoch, H.-W. Influences of Welding Parameters on Distortion. *Int. J. Microstruct. Mater. Prop.* **2010,** *5* (4/5), 436–445.
30. Clausen, B.; Lübben, Th.; Frerichs, F.; Klein, D.; Kusmierz, R.; Nowag, L.; Prinz, C.; Surm, H. Prozesskettenübergreifende Analyse der Verzugsentstehung am Beispiel von Wälzlagerringen. *HTM Z. Werkst. Wärmebeh. Fertigung* **2004,** *59* (1), 35–44.
31. Kessler, O.; Prinz, Ch.; Sackmann, T.; Nowag, L.; Surm, H.; Frerichs, F.; Lübben, Th.; Zoch, H.-W. Experimental Study of Distortion Phenomena in Manufacturing Lines. *Mat.-wiss. u. Werkstofftech.* **2006,** *37* (1), 11–18.
32. Scheffler, E. *Statistische Versuchsplanung und –auswertung;* Dt. Verl. F. Grundstoffindustrie: Stuttgart, 1997.
33. Surm, H. Identifikation der verzugsbestimmenden Einflussgrößen beim Austenitisieren am Beispiel von Ringen aus dem Wälzlagerstahl 100Cr6. Dissertation, Universität Bremen, 2011, http://nbn-resolving.de/urn:nbn:de:gbv:46-00101895-17.
34. Surm, H.; Frerichs, F.; Lübben, Th.; Hoffmann, F.; Zoch, H.-W. Distortion of Rings due to Inhomogeneous Temperature Distributions. *Mat.-wiss. u. Werkstofftech.* **2012,** *43* (1–2), 29–36.
35. Acht, C.; Dalgic, M.; Frerichs, F.; Hunkel, M.; Irretier, A.; Lübben, Th.; Surm, H. Ermittlung der Materialdaten zur Simulation des Durchhärtens von Komponenten aus 100Cr6. Teil 2: Parameter zum Umwandlungsverhalten – Beurteilung des Datensatzes anhand von Bauteilversuchen. *HTM J. Heat Treat. Mat.* **2008,** *63* (6), 362–371.

36. Frerichs, F.; Lübben, Th.; Hoffmann, F.; Zoch, H.-W. Ring Geometry as an Important Part of Distortion Potential. *Mat.-wiss. u. Werkstofftech.* **2012,** *43* (1–2), 16–22.
37. Sölter, J. Relationship between Strain Distributions and Shape Deviations of Rings Caused in Clamping. *Mat.-wiss. u. Werkstofftech.* **2012,** *43* (1–2), 23–28.
38. Marguerre, K. *Technische Mechanik, zweiter Teil: Elastostatik;* Springer-Verlag: Berlin, Heidelberg, New York, 1976.
39. Surm, H.; Keßler, O.; Hoffmann, F.; Zoch, H.-W. Manufacturing Residual Stress States in Heat Treatment Simulation of Bearing Rings. *Mat.-wiss. u. Werkstofftech.* **2006,** *37* (1), 52–57.
40. Surm, H.; Hoffmann, F. Influence of Clamping Conditions on Distortion during Heating of Bearing Rings. *Mat.-wiss. u. Werkstofftech.* **2009,** *40* (5–6), 397–401.
41. Sölter, J. Modeling and Simulation of Ring Deformation due to Clamping. *Mat.-wiss. u. Werkstofftech.* **2009,** *40* (5–6), 380–384.
42. Epp, J.; Hirsch, T. Procedure for Nondestructive RS-Measurements of Inner Surfaces of Ball Bearing Components. In *57th Denver X-ray Conf. and 8th Int. Conference on Residual Stresses (ICRS-8)*, on CDROM, Denver 2008.
43. Surm, H.; Rath, J. Mechanismen der Verzugsentstehung bei Wälzlagerringen aus 100Cr6. *HTM J. Heat Treat. Mat.* **2012,** *67* (5), 291–303.
44. Surm, H.; Kessler, O.; Hoffmann, F.; Zoch, H.-W. Modelling of Austenitizing with Non-Constant Heating Rate in Hypereutectoid Steels. In *3rd International Conference on Thermal Process Modeling and Computer Simulation*, Budapest, 2006, on CDROM.
45. SFB 570 Final Report Project C1, 2008–2009, www.sfb570.uni-bremen.de (in German).
46. Frerichs, F.; Lübben, Th.; Hoffmann, F.; Zoch, H.-W. Effects of Inhomogeneous Distribution of Distortion Potential on Out of Roundness of Rings. In *4th International Conference on Thermal Process Modeling and Computer Simulation*, Shanghai, 2010, on CDROM.
47. Lübben, Th.; Frerichs, F. Quenching of Bearing Races – Influence of Rewetting Behavior on Distortion. In *6th International Quenching and Control of Distortion Conf. Proc., Quenching Control and Distortion;* ASM International. http://www.asminternational.org/content/Events/qcd/.
48. Stöbener, D.; Goch, G. In-Process Measurements of Wall Thickness Deviations during Turning. *Mat.-wiss. u. Werkstofftech.* **2009,** *40* (5–6), 420–425.
49. Gafsi, H.; Goch, G. Semi-Optical in-Process-Metrology to Determine the Roundness Deviation of Bearing Rings during Heat Treatment. *Mat.-wiss. u. Werkstofftech.* **2012,** *43* (1–2), 125–129.
50. Beekhuis, B.; Stöbener, D.; Brinksmeier, E.; Goch, G. Compensation of Part Distortion in Soft-Turning of Bearing Rings. *Mat.-wiss. u. Werkstofftech.* **2012,** *43* (1–2), 42–47.
51. Grote, C.; Brinksmeier, E.; Garbrecht, M. Distortion Engineering in Turning Processes with Standard Clamping Systems. *Mat.-wiss. u. Werkstofftech.* **2009,** *40* (5–6), 385–389.
52. Sölter, J.; Grote, C.; Brinksmeier, E. Influence of Clamping Strategies on Roundness Deviations of Turned Rings. *Mach. Sci. Technol.* **2011,** *15,* 338–355.
53. Dijkman, M.; Stöbener, D.; Allers, S.; Kuhfuss, B.; Goch, G. In-Process Control of Cutting Depth during Turning. In *SICE Annual Conference*, Takamatsu, 2007, pp 2984–2989.
54. Beekhuis, B.; Stoebener, D.; Brinksmeier, E. Adapted Non-Circular Soft Turning of Bearing Rings – Impact of Process Machine Interactions on Compensation Potential. *Procedia CIRP* **2012,** *1,* 540–545.
55. Brinksmeier, E.; Beekhuis, B.; Goch, G.; Stöbener, D. Non-Circular Soft Turning of Bearing Rings – A Method to Minimize Geometric Deviations. In *Proc. CIRP – 2nd Int. Conf. Process Machine Interaction PMI*, 2010, Vancouver, Canada, Published on CDROM, ISBN: 978-0-9866331-0-2.
56. Surm, H.; Karsch, T.; Kessler, O.; Zoch, H.-W. Out-of-Roundness Change of Bearing Rings due to Non-Uniform Heating. In *5th International Conference on Quenching and Control of Distortion*, Berlin, 2007, pp 233–240.
57. Lütjens, J.; Surm, H.; Hunkel, M.; Gafsi, G.; Renken, V.; Schüttenberg, S. Compensation of Roundness Deviations of Bearing Rings by Heat Treatment. *Mat.-wiss. u. Werkstofftech.* **2012,** *43* (1–2), 48–55.
58. Dijkman, M.; Goch, G. Distortion Compensation Strategies in the Production Process of Bearing Rings. *Mat.-wiss. u. Werkstofftech.* **2009,** *40* (5–6), 443–447.
59. Dijkman, M. Automated Compensation of Distortion in the Production Process of Bearing Rings. Dissertation Universität Bremen, Verlagshaus Mainz GmbH, Aachen, 2009, ISBN: 3-86130-745-6.
60. Lütjens, J.; Surm, H.; Hunkel, H. Compensation of SAE52100 Bearing Ring Distortion during Gas Nozzle Field Quenching. In *6th International Quenching and Control of Distortion Conf. Proc., Quenching Control and Distortion;* 2012. http://www.asminternational.org/content/Events/qcd/.
61. Frerichs, F.; Lübben, Th.; Hoffmann, F.; Zoch, H.-W. Distortion of Conical Formed Bearing Rings made of SAE 52100. *Mat.-wiss. u. Werkstofftech.* **2009,** *40* (5–6), 402–407.
62. Brinksmeier, E.; Lübben, Th.; Fritsching, U.; Cui, C.; Rentsch, R.; Sölter, J. Distortion Minimization of Disks for Gear Manufacture. *Int. J. Mach. Tools Manuf.* **2011,** *51,* 331–338.
63. Acht, C.; Dalgic, M.; Frerichs, F.; Hunkel, M.; Irretier, A.; Lübben, Th.; Surm, H. Ermittlung der Materialdaten zur Simulation des Durchhärtens von Komponenten aus 100Cr6. Teil 1: Einleitung - Charakterisierung des Werkstoffs und der Wärmebehandlung - Grundsätzliche Überlegungen - Beschreibung von Abhängigkeiten - Thermo-physikalische Kennwerte - Thermo-mechanische Kennwerte. *HTM J. Heat Treat. Mat.* **2008,** *63* (5), 234–244.
64. Frerichs, F.; Lübben, Th. Analysis of the Distortion Potential within Bearing Rings. In *6th International Quenching and Control of Distortion Conf. Proc., Quenching Control and Distortion;* 2012. http://www.asminternational.org/content/Events/qcd/.
65. Zoch, H.-W. Distortion Engineering – Interim Results after One Decade Research within the Collaborative Research Center Distortion Engineering. *Mat.-wss. u. Werkstofftech.* **2012,** *43* (1–2), 9–15.

12.10 Austenite Formation and Microstructural Control in Low-Alloy Steels

KD Clarke, Los Alamos National Laboratory, Los Alamos, NM, USA

12.10.1	**Introduction**	345
12.10.2	**Austenite Formation**	345
12.10.3	**Typical Heat Treatments and Processing of Austenite**	348
12.10.4	**Effects of Microstructure, Composition, and Heating Rate on Austenite Formation**	352
12.10.4.1	Carbon Steel	352
12.10.4.2	Alloy Steel – Chromium	352
12.10.4.3	Additional Considerations	358
12.10.5	**Austenite Structural Development**	358
12.10.6	**Summary**	359
References		359

12.10.1 Introduction

In order to understand steel processing, it is essential to understand the formation and development of austenite (γ-iron), the high-temperature solid face-centered cubic phase. Steel is often heated from room temperature to form austenite multiple times during industrial processing, as high-temperature austenite requires less energy to deform and shape, and it can be used to effectively control the final microstructure. In addition, recent developments in advanced high-strength low-carbon sheet steels (AHSS) utilize novel thermal and deformation processing paths (*1*), resulting in room temperature-stabilized austenite that can be tailored to achieve specific mechanical properties tailored to a given application. With a little understanding of the physical metallurgy of steel, these variations in processing also allow the microstructure, and therefore properties, of a given piece of steel to be varied significantly solely with controlled variation in mechanical and thermal processing. The results of heat treatment and deformation are critically dependent on the condition of the prior austenite, even though many low-alloy steels do not contain much, if any, austenite in service. The wide variety of ways that the condition of the austenite can be controlled and manipulated during processing is a significant reason for the broad ranges of steel properties available with very small changes in composition. This flexibility makes steel the most important structural material in the modern world.

Many excellent resources are available that discuss the details of austenitizing thermal treatments (*2–18*), including introductory and specialized textbooks, reference texts, and conference proceedings. This chapter will focus on common austenitizing heat treatments and the details of austenite formation from various room temperature microstructures, including references to recent studies. It is important to understand how austenite forms in order to understand the motives behind common austenitizing heat treatments; these differences in austenite condition that are available to the metallurgist then allow for control of the final microstructure.

12.10.2 Austenite Formation

For heat treatment of steels, the first resource to become familiar with is the iron–cementite equilibrium phase diagram, which shows the equilibrium phases in iron–carbon alloys for a given temperature and composition. The iron–carbon equilibrium phase diagram (*10*) presented in **Figure 1** shows carbon levels up to 7 wt.%, but steels are iron–carbon alloys only up to approximately 2 wt.%, which is the limit of carbon solubility in austenite. The dashed lines show iron–graphite equilibrium phase stability, which requires extremely long times to attain at low temperatures and carbon levels, and is primarily of interest for cast irons, which have greater than 2 wt.% carbon. The solid lines indicate metastable iron–cementite (Fe_3C, or carbide) equilibrium, which is referred to for all practical steel-processing considerations.

Steels are generally classified by carbon content, with hypoeutectoid (below 0.77 wt.% carbon), eutectoid (at 0.77 wt.% carbon), or hypereutectoid (above 0.77 wt.% carbon) steels, each of which has a solid solution of carbon in austenite at high temperature. Below the A_1 temperature of 727 °C (referred to as the eutectoid or lower critical temperature), the equilibrium mixture is body-centered cubic ferrite (α-iron) and cementite. Note that various values are reported for the eutectoid composition and temperature, varying from 0.76 to 0.83 wt.% carbon and from 722 to 732 °C, but consensus-accepted values are 0.76–0.77 wt.% carbon and 727 °C, respectively (*10,19*). However, a binary Fe–C alloy without any impurities is rarely considered, and alloying changes vary the eutectoid composition and temperature significantly, so exact values are somewhat impractical. Phase stability changes as a function of composition are discussed in this chapter.

For hypoeutectoid steels, a phase field of ferrite and austenite is stable up to the A_3 temperature. This phase field is commonly referred to as the 'intercritical' phase field, because it occurs between the lower and upper intercritical temperatures. For hypereutectoid steels, an austenite–cementite phase field occurs between A_1 and A_{cm}, and austenite is stable above A_{cm} (both A_3 and A_{cm}

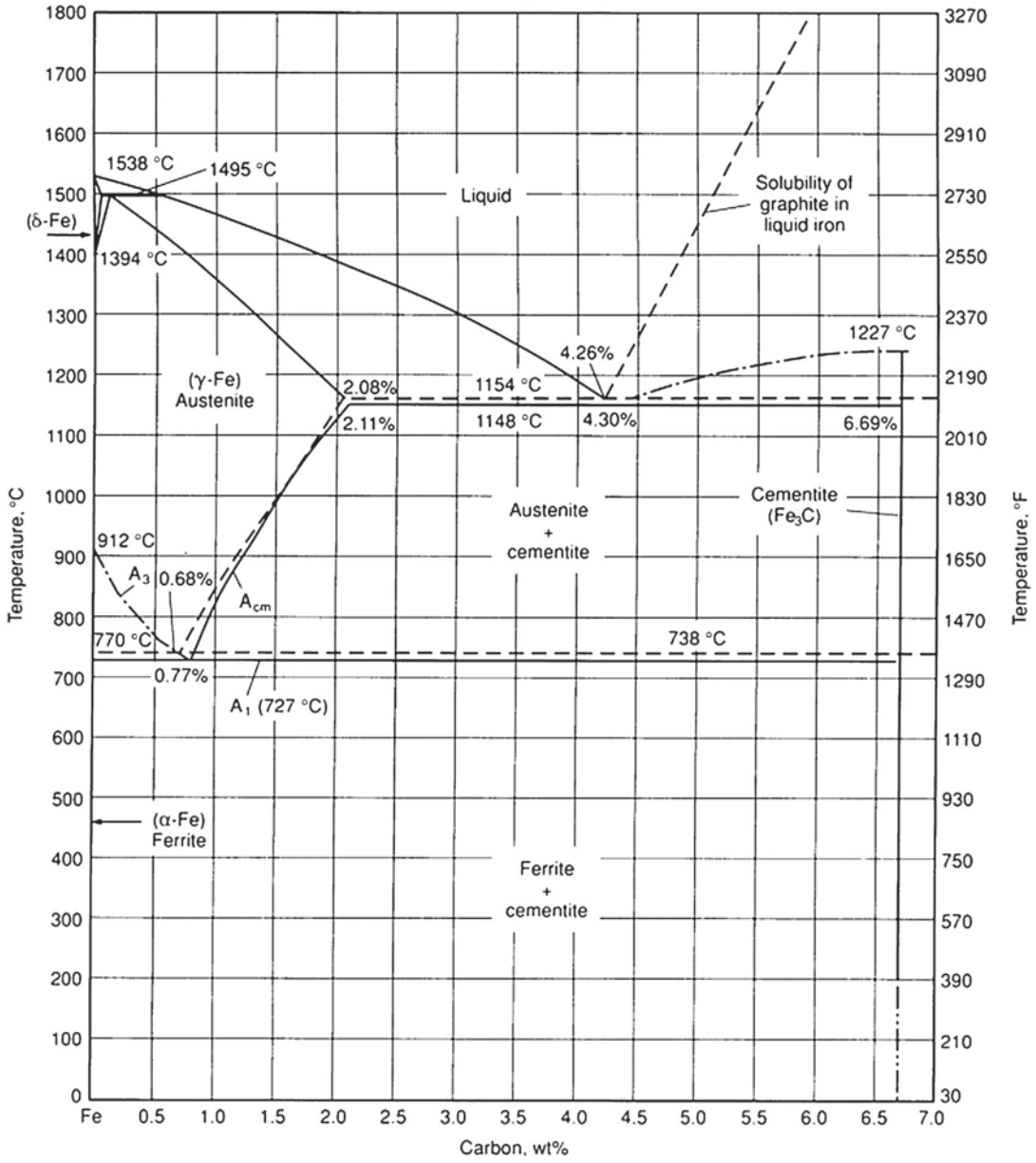

Figure 1 Carbon-rich region of the iron–carbon (solid lines) and iron–graphite (dashed lines) equilibrium phase diagram. Reproduced from Ericsson, T. Principles of Heat Treating of Steels, Heat Treating. In *ASM Handbook*, ASM International, 1991; Vol. 4, pp 3–19.

are referred to as the upper critical temperature). Finally, the phase diagram in Figure 1 is also applicable only to equilibrium conditions (essentially quasistatic heating or cooling rates), and therefore all equilibrium transformation temperatures are generally denoted with a nonsubscript 'e,' such as Ae_1, Ae_3, and Ae_{cm}. Since the transformation temperatures can vary significantly with increasing heating or cooling rates, common nomenclature for on-heating and on-cooling transformation temperatures is Ac_1 and Ar_1, which are derived from the French words for heating (*chauffage*) and cooling (*refroidissement*), respectively, and should be quoted with heating or cooling rate data for practical utility.

Upon heating an iron–carbon alloy of the eutectoid carbon composition, it will begin to transform directly from the room temperature starting microstructure (pearlite, bainite, martensite, or some combination) to austenite at the eutectoid temperature, 727 °C. Hypoeutectoid steels will begin to form austenite but retain ferrite until reaching the A_3 temperature. Steels heated within the ferrite-plus-austenite phase field are said to be intercritically annealed, and this process can be used to create room temperature microstructures with various volume fractions of ferrite and martensite (transformed from austenite). At present, intercritical annealing typically concerns sheet steels that can be processed with relatively consistent through-thickness heating and cooling rates, which result in homogeneous microstructures and are difficult to apply successfully to thick sections where significant microstructural gradients occur due to heat transfer considerations. Hypereutectoid steels form austenite while retaining cementite

up to the A_{cm} temperature and are fully austenitic above A_{cm}. Thus, the carbon composition in a given steel is the first major factor determining heat treatment temperature, since all steels experience some processing in the austenite, austenite-plus-ferrite, or austenite-plus-carbide phase field, regardless of carbon content.

Any other chemical additions, whether intentionally added or not, affect equilibrium transformation temperatures and composition as noted in this chapter. For example, increasing Cr tends to increase the Ae_1 temperature (stabilizing ferrite), whereas increasing Mn decreases the Ae_1 temperature (stabilizing austenite). Generally, Mn, Cu, and Ni are austenite stabilizers, whereas Ti, Mo, W, Al, P, Si, V, and Cr are ferrite stabilizers, and all of these elements other than Al, P, and Si stabilize cementite and form carbides (*10*,*20*). For practical purposes, all alloying elements also tend to lower the eutectoid carbon concentration (*10*). **Figure 2(a)** shows a plot of the effects of individual alloying elements, along with calculated pseudobinary sections of iron–carbon

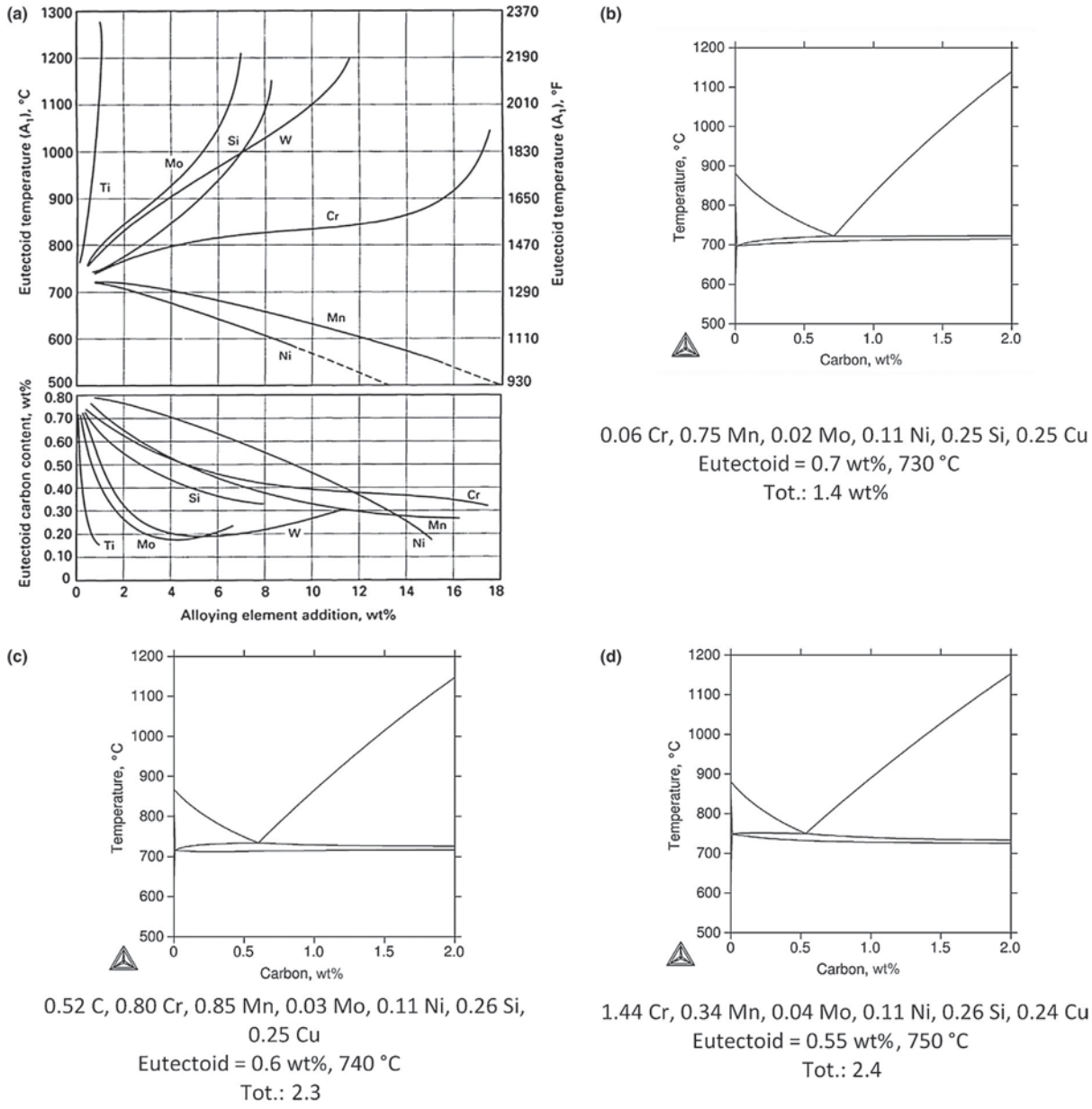

Figure 2 (a) Effect of individual alloying elements on equilibrium phase stability as a function of average composition in wt.%. Reproduced from Ericsson, T. Principles of Heat Treating of Steels, Heat Treating. In *ASM Handbook*, ASM International, 1991; Vol. 4, pp 3–19. (b–d) Calculated changes in pseudobinary iron–carbon sections of equilibrium phase diagrams with indicated changes in average composition in accordance with 10XX, 51XX, and 52XXX steels, respectively, showing significant changes in phase stability with composition changes in low-alloy steels. Calculations made with ThermoCalc. Reproduced from Clarke, A.J.; Speer, J.G.; Miller, M.K.; Hackenberg, R.E.; Edmonds, D.V.; Matlock, D.K.; Rizzo, F.C.; Clarke, K.D.; De Moor, E. Carbon Partitioning to Austenite from Martensite or Bainite during the Quench and Partition (Q&P) Process: A Critical Assessment. *Acta Mater.* **2008,** *56,* 16–22.

equilibrium phase diagrams for steels with compositions corresponding to typical AISI 10XX, 51XX, and 52XXX steels, shown in Figure 2(b)–2(d) (*21*), respectively. Even though the total alloying additions sum to below 3 wt.% for each case, the phase diagrams change significantly. First, a three-phase field becomes apparent in all cases where ferrite, austenite, and cementite are all stable. The eutectoid carbon composition decreases with total alloying content, and the addition of chromium in amounts of 0.8 and 1.4 wt.% appears to be the major factor in increasing the eutectoid transformation temperature by 20 °C. Thus, the substitutional alloy content is another major factor in determining heat treatment temperatures. Generally, appropriate heat treatment temperatures are available in the *Heat Treater's Guide* (*13*), but new alloys or nonstandard thermal cycles (e.g., induction heating) may require some adjustment to recommended practice.

12.10.3 Typical Heat Treatments and Processing of Austenite

Common heat treatments, such as full annealing, spheroidizing, normalizing, intercritical annealing, homogenizing, and hardening, are discussed. There are many resources available that cover various processes in greater detail or give specific thermal cycles for a given steel composition (*2–18*), but the basics of these thermal treatments are summarized here.

The purpose of full annealing is to erase the previous room temperature microstructure and soften previously strain-hardened material, generally for ease of subsequent deformation processing or machining. Full annealing is assumed when the term 'annealing' is used without precursors. In order to fully anneal hypoeutectoid steel, it must be heat treated to just above the Ae_3 temperature. For example, 1015 steel (0.15 wt.% carbon) would be annealed at 900 °C, whereas 1045 steel (0.45 wt.% carbon) would be annealed at 845 °C, since the Ae_3 transformation temperature decreases with increasing carbon content (*13*). The material is held at the annealing temperature, typically for 1 h, and then furnace-cooled slowly. This annealing treatment produces a coarse ferrite–pearlite microstructure and the lowest strength for a given alloy, which is most useful for subsequent cold deformation processes.

For hypereutectoid compositions, annealing is performed above the Ae_1 temperature, since the preferred microstructure for subsequent heat treatment or machining is ferrite and spheroidized carbides. For example, 52100 is annealed at 790 °C, and the material must then be cooled very slowly to allow austenite to transform to ferrite, avoid other transformations, and allow carbides to coarsen (carbon diffusion to carbides). This type of annealing is referred to as a spheroidizing anneal. If it is necessary to further spheroidize carbides for machinability or deformation processing, subsequent treatments are performed just below the lower critical temperature, which is used for medium- and high-carbon steels. Spheroidizing treatments can take many hours, but they may be the only way to effectively machine medium- and high-carbon steels, which can have high strength even with a coarse pearlite microstructure. For hypereutectoid steels, cycling above and below the lower critical temperature has also been used to refine the microstructure (*22*).

Both hypoeutectoid and hypereutectoid steels can be normalized, a process that is used to erase heavily cold-worked microstructure or the effects of hot forging. Normalizing creates a fine, equiaxed austenite grain size and a subsequent fine room temperature microstructural scale that is easier to process or heat treat, and results in improved toughness. Normalizing involves heating to temperatures above the upper critical temperature, allowing austenite formation to complete, and cooling in air. Slightly higher austenitizing temperatures and a faster cooling rate are the primary differences between normalizing and full annealing, and they result in a fine, equiaxed, room temperature grain size. It should be noted that normalizing is often applied to parts forged at very high temperatures where austenite grain size may be very coarse. Austenite grain growth kinetics increase with temperature, and rapid grain growth occurs above approximately 1050 °C, even in killed steels with fine AlN precipitates (**Figure 3(a) and 3(b)**) (*17,18*). These precipitates control austenite grain growth until the dissolution temperature is reached, which coincides with the grain growth temperature (**Figure 3(c)**) (*3*). Since forging can require very high temperatures, a subsequent normalizing treatment is used to refine the austenite grain size and room temperature ferrite–pearlite microstructure.

As mentioned in this chapter, intercritical annealing treatments can be used to create microstructures with fixed ferrite and austenite volume fractions, resulting in controlled volume fractions of ferrite and martensite and/or bainite. Intercritically annealed steels are generally quenched from the two-phase field, and the quench is commonly the final heat treatment before the steel is put into service. This practice results in products with excellent strength and ductility combinations, and is used to produce dual-phase (DP) steel, for example. For this reason, intercritical annealing is an extremely important process in the production of AHSS low-carbon sheets, and knowledge of precise phase stability and control of alloy content is necessary.

Homogenizing heat treatments are used to reduce the elemental segregation that occurs during casting of steels. Steels solidify by the growth of dendritic crystals, which reject alloy and impurity elements into the liquid according to equilibrium phase solubility requirements, resulting in the phenomenon of interdendritic segregation (*3*), which causes both macro- and microsegregation. Macrosegregation refers to gradual changes in average composition over large distances (centimeters to meters) as solidification progresses, and it can require extremely long times (days) at high temperatures to erase, which is not generally a practical remedy during industrial processing. Microsegregation refers to localized concentration gradients that are a product of solidification and that span distances of millimeters or less. Dendritic segregation is a common example, which results in banded microstructures in rolled material. An example of microstructurally banded steel is shown in **Figure 4** (*21*); this results from chromium segregation in hot-rolled 52100 steel. The banding scale is on the order of 50 microns and varies from 1.2 to 2.0 wt.% chromium. It is evident that this type of composition variation can affect local phase stability, as shown by the calculated equilibrium phase fractions in **Figure 4**. Removing this type of segregation still requires long heat treatment times at high temperatures. Based on **Figure 5** (*21,23*),

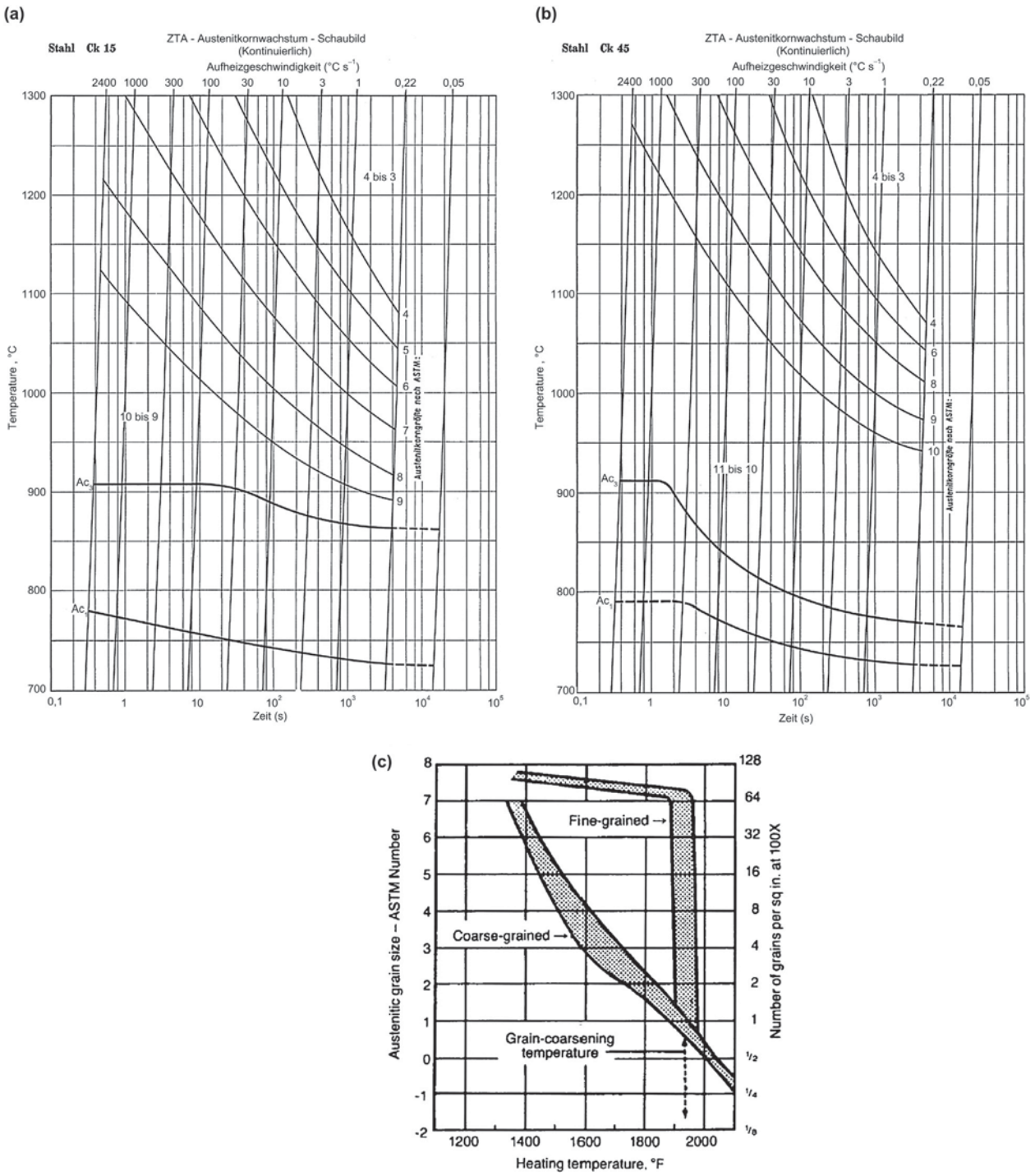

Figure 3 Austenite grain growth in (a) Ck 15 and (b) Ck 45 steel as a function of heating rate and maximum temperature. Aluminum and nitrogen contents in the Ck 15 steel are 0.006 and 0.0037, respectively (semikilled). Aluminum and nitrogen contents in the Ck 45 steel are 0.014 and 0.0115, respectively (killed). Reproduced from Orlich, J.; Rose, A.; Wiest, P. *Atlas zur Wärmebehandlung der Stähle, Band 3;* Verlag Stahleisen M.B.H.: Düsseldorf, Germany, 1973 and Orlich, J.; Pietrzeniuk, H.-J. *Atlas zur Wärmebehandlung der Stähle, Band 4;* Verlag Stahleisen M.B.H.: Düsseldorf, Germany, 1976. (c) Generalized austenite grain size as a function of temperature for slow heating rates, showing grain-coarsening temperature for fine-grained, killed steels (approx. 1050 °C), indicating the dissolution temperature of AlN precipitates, and gradual austenite grain growth in coarse-grained steels. Reproduced from Krauss, G. *Steels Processing, Structure, and Performance*; ASM International: Materials Park, OH, 2005.

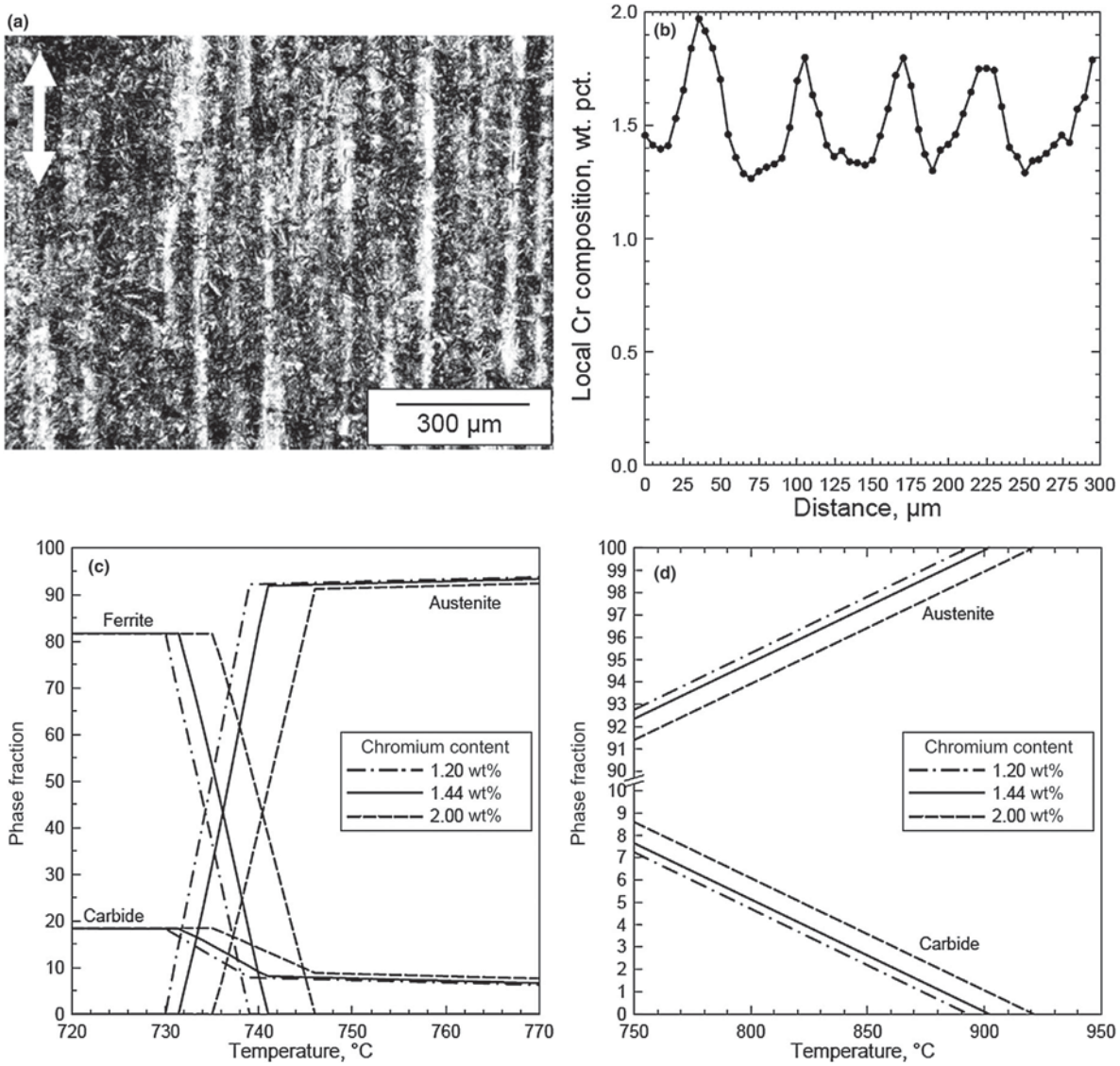

Figure 4 (a) Optical micrograph of spheroidized 52100 steel showing microstructural blanding parallel to the rolling direction (arrow), nital etch. (b) Microprobe results of chromium concentration variation in the steel depicted in (a) over 300 μm. Equilibrium phase content during (c) ferrite-to-austenite and (d) carbide dissolution based on calculated phase stability with variations in chromium content equivalent to those measured in the microprobe analysis in (b). Calculations made in ThermoCalc. Reproduced from Clarke, K.D. The Effect of Heating Rate and Microstructural Scale on Austenite Formation, Austenite Homogenization, and As-quenched Microstructure in Three Induction Hardenable Steels. Ph.D. Thesis, Colorado School of Mines: Golden, CO, 2008.

chromium can diffuse 10 microns in 1000 s at 1200 °C, so eliminating this segregation would take a minimum of 5000 s (approximately 1.5 h), which would not be desirable, as it would also greatly increase the austenite grain size. However, it has been shown that real homogenization times take longer than diffusion estimates would predict, primarily due to the decreasing driving force as segregation is reduced. In plain-carbon steels, manganese banding is often found in hot-rolled steels, and a study (*24*) examining the homogenization times required to remove 95% of the manganese segregation in hot-rolled 4145 steel found that 100 h at 1200 °C are needed. Chemically banded microstructures are of particular concern when considering surface-hardened components that are heat treated using high-heating-rate methods (induction or flame hardening), or heat treatments that use intercritical annealing and local phase stability control to create complex final microstructures, such as those for AHSS (*1*,*25*–*27*).

Hardening heat treatments in steels are used to create martensitic or perhaps bainitic microstructures, and they require fast cooling rates from austenite to avoid transformation into pearlite. **Figure 6** (*10*) shows a continuous cooling diagram for steel containing 0.45 wt.% carbon. In order to avoid forming pearlite, a very fast quench rate is necessary from the austenitizing temperature, with the temperature of the material having to cool to below 500 °C within a few seconds. For this alloy, the hardenability is low enough (i.e., required quench rates are very fast) that it is difficult to achieve the desired quench rate to get a fully martensitic microstructure. Increasing alloy content or manipulating grain size can be used to increase hardenability (*3*).

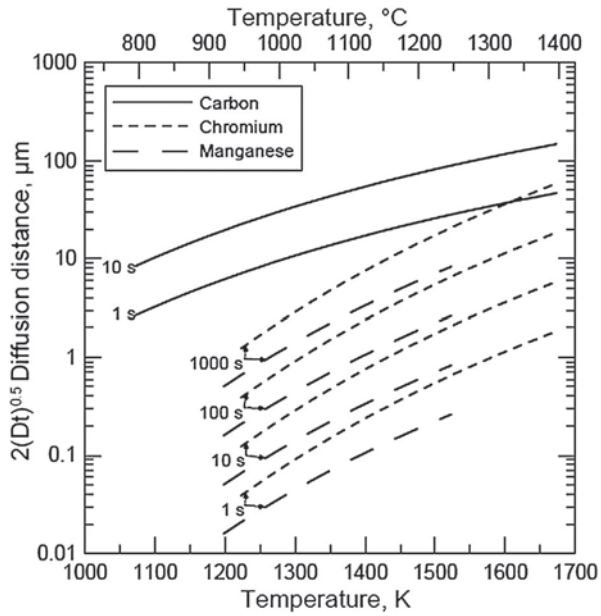

Figure 5 Diffusion distance in austenite at isothermal holds for indicated times, estimated from $L = 2\sqrt{Dt}$, where L represents the diffusion distance in centimeters, D is the diffusion coefficient of the diffusing species in austenite ($cm^2\ s^{-1}$), and t is time in seconds. Reproduced from Clarke, K.D. The Effect of Heating Rate and Microstructural Scale on Austenite Formation, Austenite Homogenization, and As-quenched Microstructure in Three Induction Hardenable Steels. Ph.D. Thesis, Colorado School of Mines: Golden, CO, 2008. Diffusion coefficients from: Shewmon, P. *Diffusion in Solids*, 2nd ed.; TMS: Warrendale, PA, 1989.

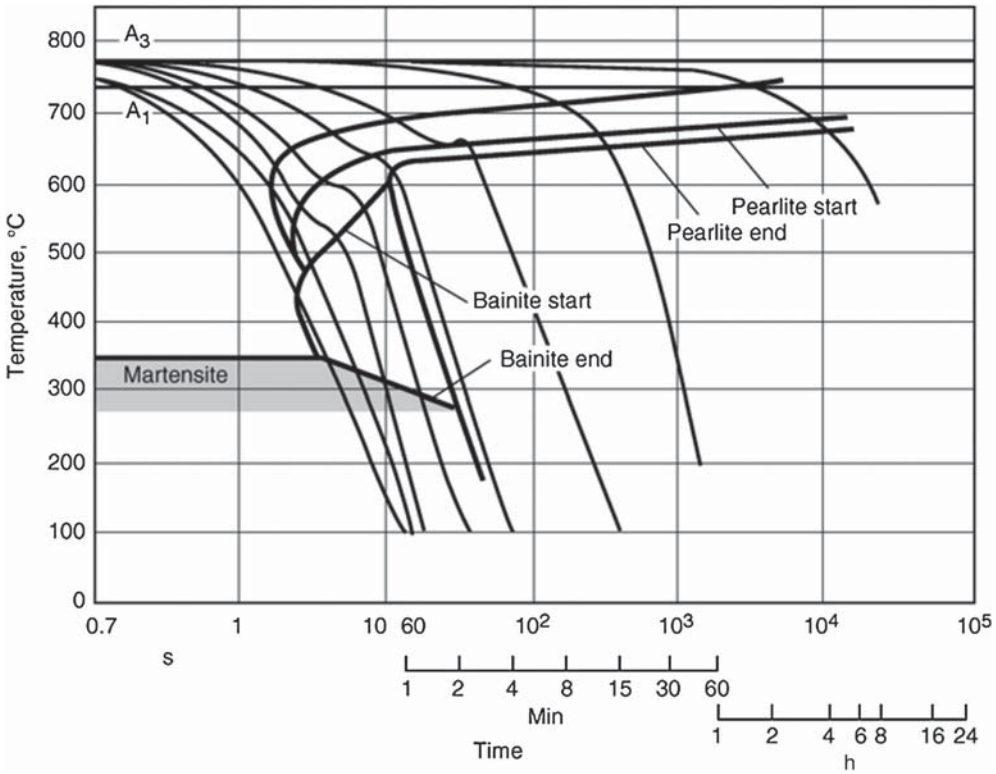

Figure 6 Continuous cooling transformation diagram for 1045 steel, indicating the cooling rates required to achieve specified final microstructures. Reproduced from Ericsson, T. Principles of Heat Treating of Steels, Heat Treating. In *ASM Handbook*; ASM International, 1991; Vol. 4, pp 3–19.

12.10.4 Effects of Microstructure, Composition, and Heating Rate on Austenite Formation

In addition to the equilibrium temperature at which austenite becomes stable for a given steel composition, the rate at which austenite forms (kinetics) also varies with initial microstructure, composition, austenitizing temperature, and heating rate. The kinetics of a given reaction means that the simple equilibrium iron–cementite phase diagram must be supplemented with diagrams incorporating composition, microstructure, and the rate at which reactions take place, such as the continuous-heating time–temperature–austenitization (TTA) diagram. An excellent resource for a wide selection of TTA diagrams is the *Atlas zur Wärmebehandlung der Stähle* (*15–18*), an encyclopedic four-volume resource produced between 1961 and 1976 that includes continuous-heating and isothermal-hold TTA diagrams for most steel compositions in common use at the time, in addition to excellent data on recommended heat treatment, effects of chemistry variations, hardenability, isothermal austenite decomposition, continuous cooling transformation, carburizing, austenite grain size, as-quenched hardness, martensite start temperatures, and micrographs of resulting microstructures.

Here, we focus on the formation of austenite by examining continuous-heating TTA diagrams for plain carbon and chromium alloy steels with various starting microstructures, as shown in **Figures 7–11**. This series demonstrates the effects of the heating rate, starting microstructure, and composition. The examples focus on chromium substitutional alloying, but the concepts also apply to other solid-solution alloying elements.

12.10.4.1 Carbon Steel

Figure 7 shows continuous-heating TTA diagrams for Ck 15 and Ck 45 steels (equivalent to AISI 1015 and 1045), each starting from ferrite–pearlite initial microstructures (*17,18*).

The TTA diagram shows that the initial transformation from ferrite–pearlite to austenite (Ac_1) occurs at much higher temperatures with increasing heating rate, increasing from approximately 730 °C to nearly 790 °C. At high enough temperatures, austenite can be stable without carbon (911 °C in **Figure 1**), but at these lower temperatures austenite requires dissolved carbon to be stable. On heating, therefore, austenite nucleates at the carbides, which supply carbon to the growing austenite grains. Carbon must also diffuse from the carbide through the austenite to the growth front in order to allow further austenite growth, resulting in diffusion-controlled growth kinetics. Thus, the carbide dissolution and carbon diffusion kinetics are critical to austenite formation kinetics. In the case of a ferrite–pearlite microstructure, nucleation occurs at pearlite grain boundaries (*3*). For the continuous-heating TTA shown in **Figure 7**, it is also important to recognize that the ferrite-plus-pearlite-plus-austenite temperature range for the 1045 steel also increases with the increasing heating rate, which, as is shown in this chapter, is an effect of a coarse initial microstructure. Finally, in order to achieve homogeneous austenite, with respect to carbon, even higher temperatures are required, which can be very important to the subsequent transformations that occur when cooling this austenite to room temperature. Homogenization of substitutional alloying element segregation, as discussed in this chapter, requires very long times.

The effects of carbon content are also evident in **Figure 7**, with the Ac_3 temperature for the lower carbon steel significantly higher than for the 1045 steel, and thus requiring significantly higher austenitization temperature (approximately 860 °C vs 770 °C) for slow heating rates. The recommended standard austenitizing temperatures for annealing or normalizing these grades are similar – respectively 885 and 915 °C for 1015, and 845 and 900 °C for 1045 (*13*) – but do show that the 1015 composition requires higher temperatures for austenitizing. However, when heating rates are increased much higher than 100 °C s^{-1}, the transformation temperatures are nearly equal, due to the kinetics of carbide dissolution and carbon diffusion required to form austenite: for the 1015 microstructure, the carbon diffusion distance is greater, since there is more ferrite, whereas for the 1045 microstructure, the larger volume fraction of carbides that must dissolve is likely the primary process controlling the rate of full austenitization. It is also important to note that the temperature at which homogeneous (i.e., no carbon gradients) austenite occurs is similar at high heating rates. The rate of carbon diffusion, as an interstitial element, is fast relative to substitutional elements, but heating rates above 1000 °C s^{-1} are fast enough so that it must be considered a rate-limiting process; see **Figure 5** (*21,23*). The starting microstructure in **Figure 7** also shows significantly spheroidized pearlite for the 1045 starting microstructure, which suggests that the dissolution kinetics may be sluggish relative to a starting microstructure of pearlite with fine lamellae. Several studies have been performed on the effect of microstructural scale on 1045 austenitization kinetics (*21,28–30*). One study (*21,28*) compared a hot-rolled microstructure with 30 vol.% ferrite and a larger pearlite colony size with a normalized microstructure with 40 vol.% ferrite and a smaller pearlite colony size. Results are shown in **Figure 8**. Although the apparent effect on the transformation temperatures is small, the change in as-quenched hardness is dramatic: the normalized starting microstructure responds to austenitization heat treatment much more quickly than the coarser hot-rolled microstructure. These results show that, for industrial nonequilibrium heating or cooling rate processing, the use of a normalizing treatment to refine grain size is beneficial to achieve a faster austenitization response, which requires shorter heat treatments and lower maximum temperatures.

12.10.4.2 Alloy Steel – Chromium

When additional alloying and variations in microstructure are considered, the TTA diagram can vary significantly. Here, we consider chromium alloying effects on transformation behavior for a $46Cr_2$ composition with a ferrite–pearlite starting microstructure and a $41Cr_4$ composition with a tempered martensite starting microstructure, as shown in **Figure 9** (*17,18*). Both compositions fall

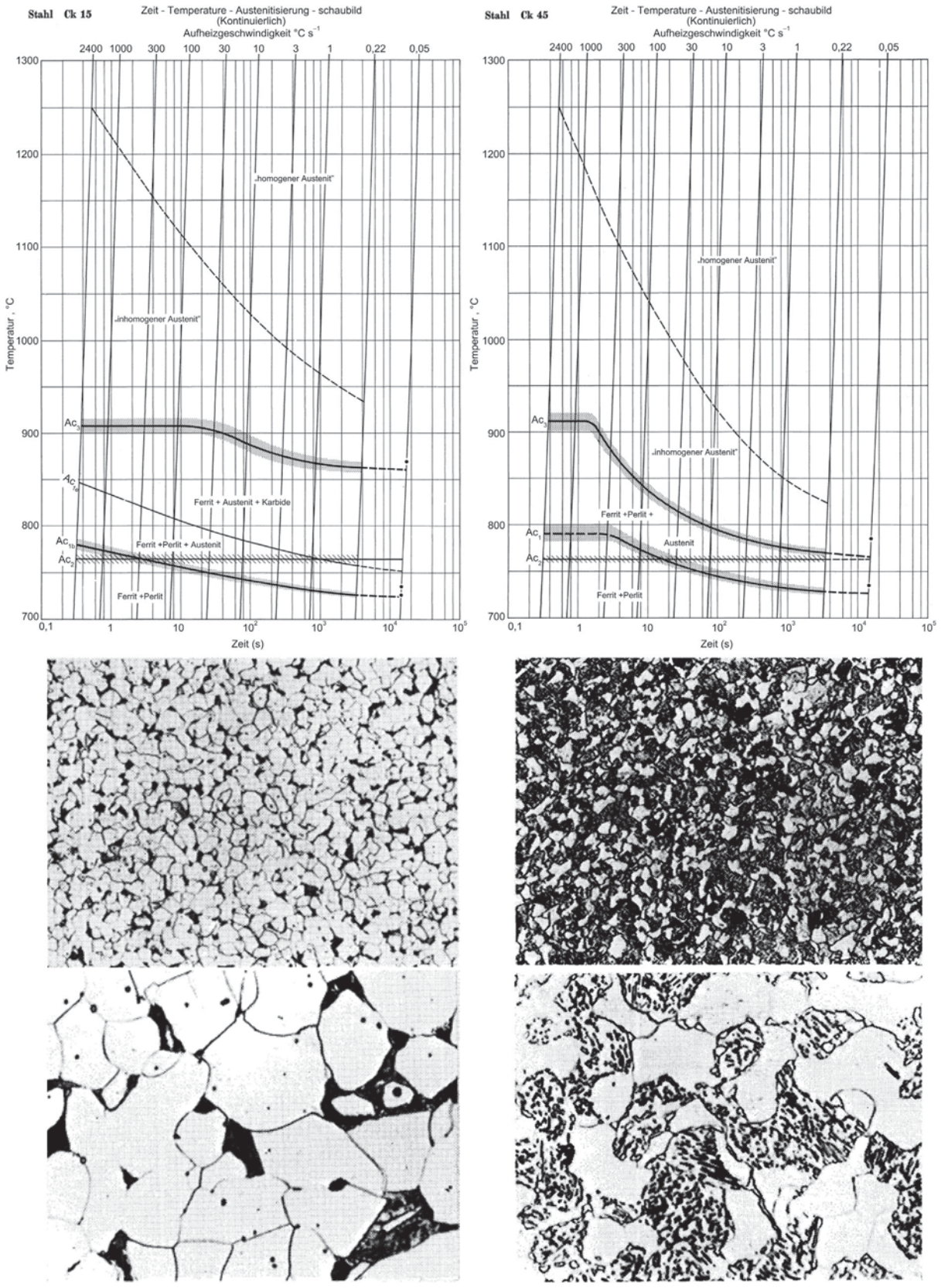

Figure 7 Continuous-heating time–temperature–austenitization (TTA) diagrams and optical micrographs of starting microstructures for Ck 15 (left) and Ck 45 (right) steels with ferrite–pearlite starting microstructures. Note that the pearlite for the Ck 45 steel is partially spheroidized, resulting in large carbides. Reproduced from Orlich, J.; Rose, A.; Wiest, P. *Atlas zur Wärmebehandlung der Stähle, Band 3*; Verlag Stahleisen M.B.H.: Düsseldorf, Germany, 1973 and Orlich, J.; Pietrzeniuk, H.-J. *Atlas zur Wärmebehandlung der Stähle, Band 4*; Verlag Stahleisen M.B.H.: Düsseldorf, Germany, 1976.

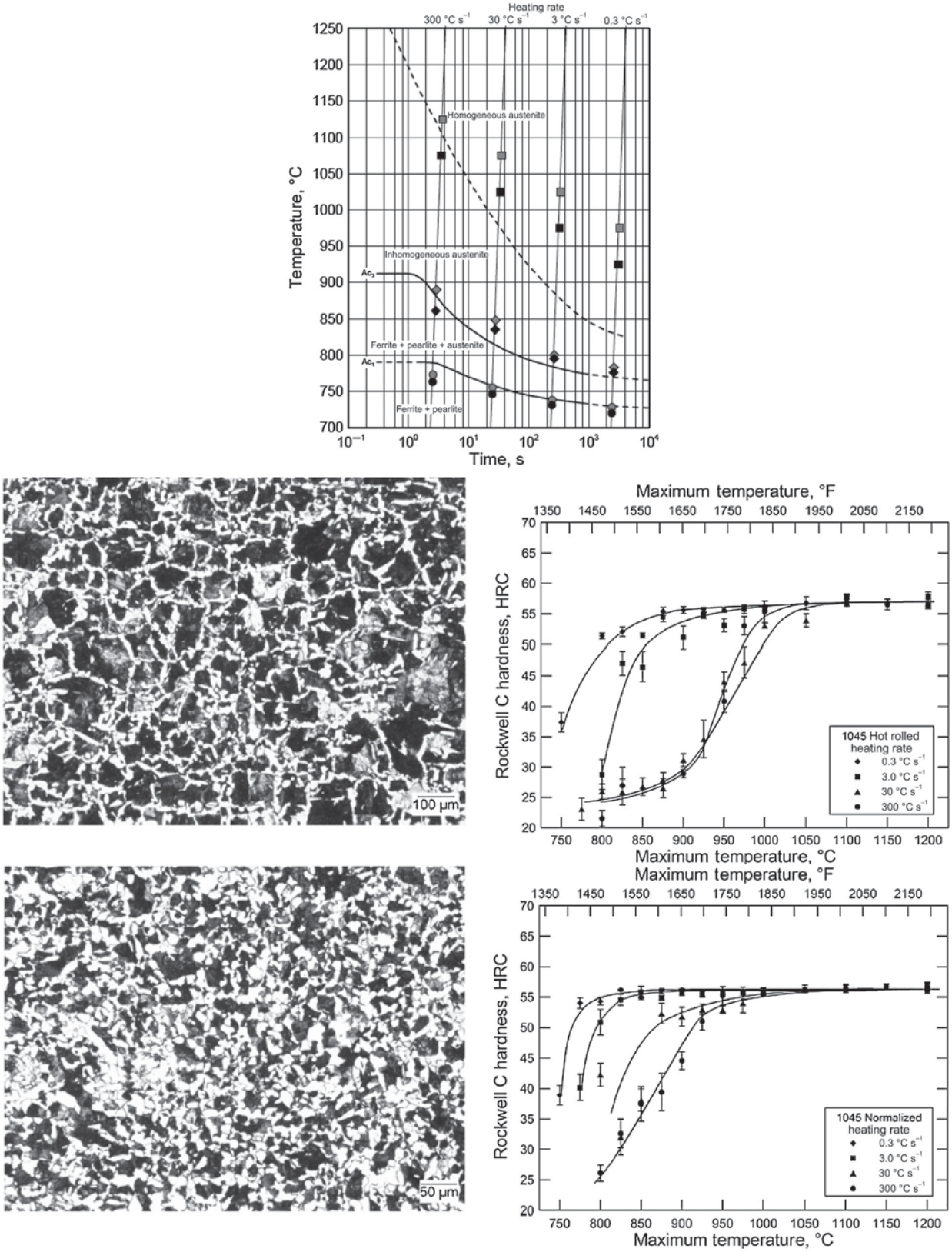

Figure 8 Measured changes in on-heating transformation temperatures for hot-rolled and normalized 1045 steel (top), along with optical micrographs of starting microstructures and final hardness for each microstructure (middle row: hot-rolled; bottom row: normalized). Reproduced from Clarke, K.D. The Effect of Heating Rate and Microstructural Scale on Austenite Formation, Austenite Homogenization, and As-quenched Microstructure in Three Induction Hardenable Steels. Ph.D. Thesis, Colorado School of Mines: Golden, CO, 2008 and Lee, S.-J.; Clarke, K.D.; Van Tyne, C.J. An On-Heating Dilation Conversional Model for Austenite Formation in Hypoeutectoid Steels. *Metall. Mater. Trans. A* **September 2010,** *41* (9), 2224–2235.

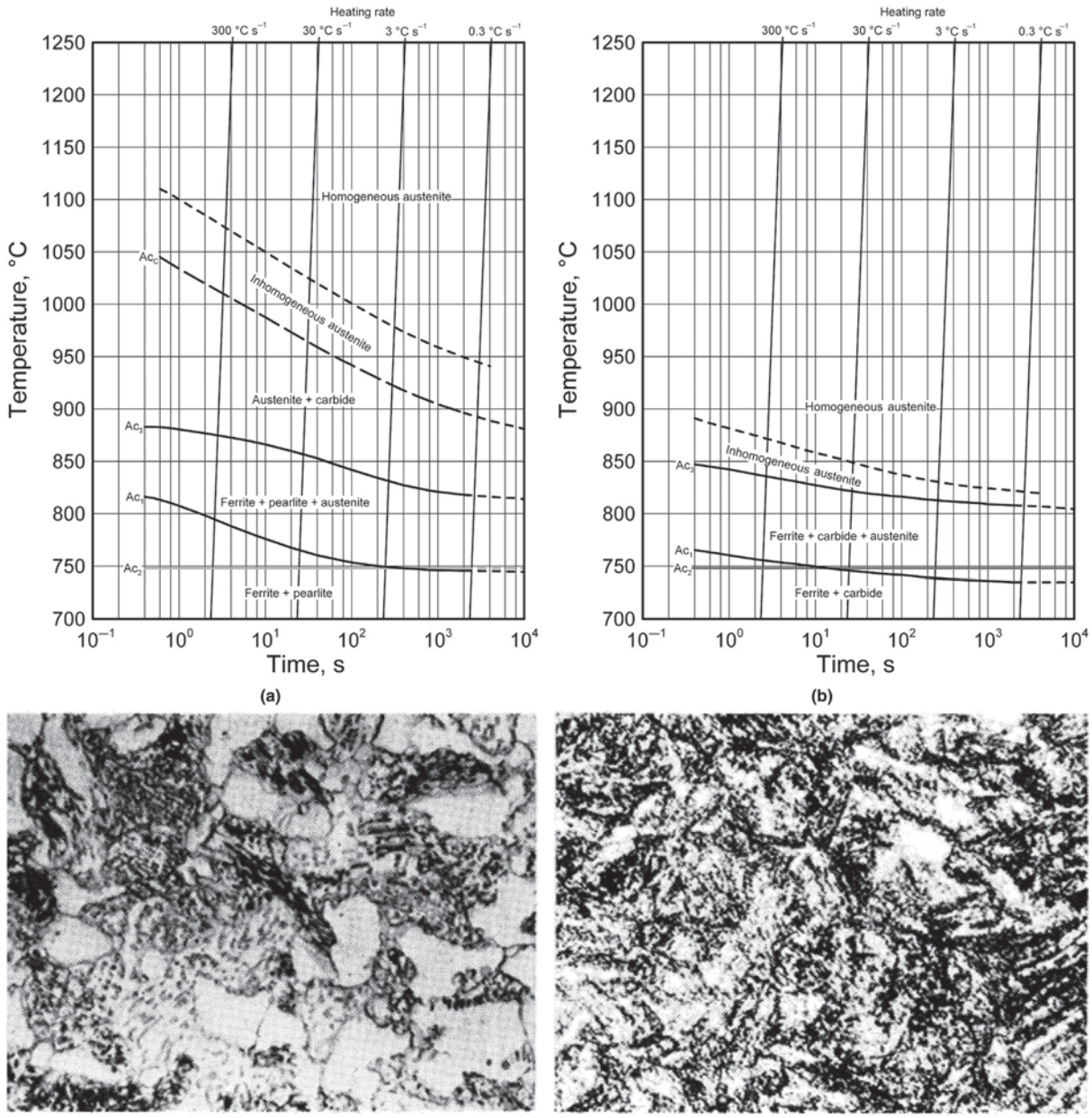

Figure 9 Continuous-heating time diagrams for (a) 46Cr2 and (b) 41Cr4 steels with optical micrographs of starting microstructures of (a) ferrite–pearlite, and (b) martensite. Compositions are similar to that of AISI 5150. Reproduced from Orlich, J.; Rose, A.; Wiest, P. *Atlas zur Wärmebehandlung der Stähle, Band 3*; Verlag Stahleisen M.B.H.: Düsseldorf, Germany, 1973 and Orlich, J.; Pietrzeniuk, H.-J. *Atlas zur Wärmebehandlung der Stähle, Band 4*; Verlag Stahleisen M.B.H.: Düsseldorf, Germany, 1976.

within values for AISI 5150H alloy, with the exception of a low-carbon content (0.4 wt.%) and minor Mo addition (0.04 wt.%) in 41Cr4. Standard annealing and normalizing temperatures for 5150 are 830 and 870 °C, which are just above the Ac_3 temperatures shown in Figure 9.

In the example given here of carbon steels (Figures 7 and 8), the effect of microstructure scale was difficult to determine, since the level of carbon was significantly different (Figure 7) or the effect was subtle (Figure 8). For the example shown in Figure 9, however, the effects of coarser microstructures are evident, with an increasing scale of microstructure increasing the effect of the heating rate, because austenite formation is a nucleation and growth process. For chromium-alloyed steels in particular, the dissolution of the resultant chromium-enriched carbides is slower than for carbides in plain-carbon steels. At slow heating rates, the effect is relatively small, but as heating rates increase, the change in transformation temperatures is much greater for the ferrite–pearlite starting structure, even though the material chemistry is very similar. In fact, carbides are still undissolved in the ferrite–pearlite initial microstructure above 1000 °C when considering the highest heating rates. In a study of induction-heated specimens of 5150 steel,

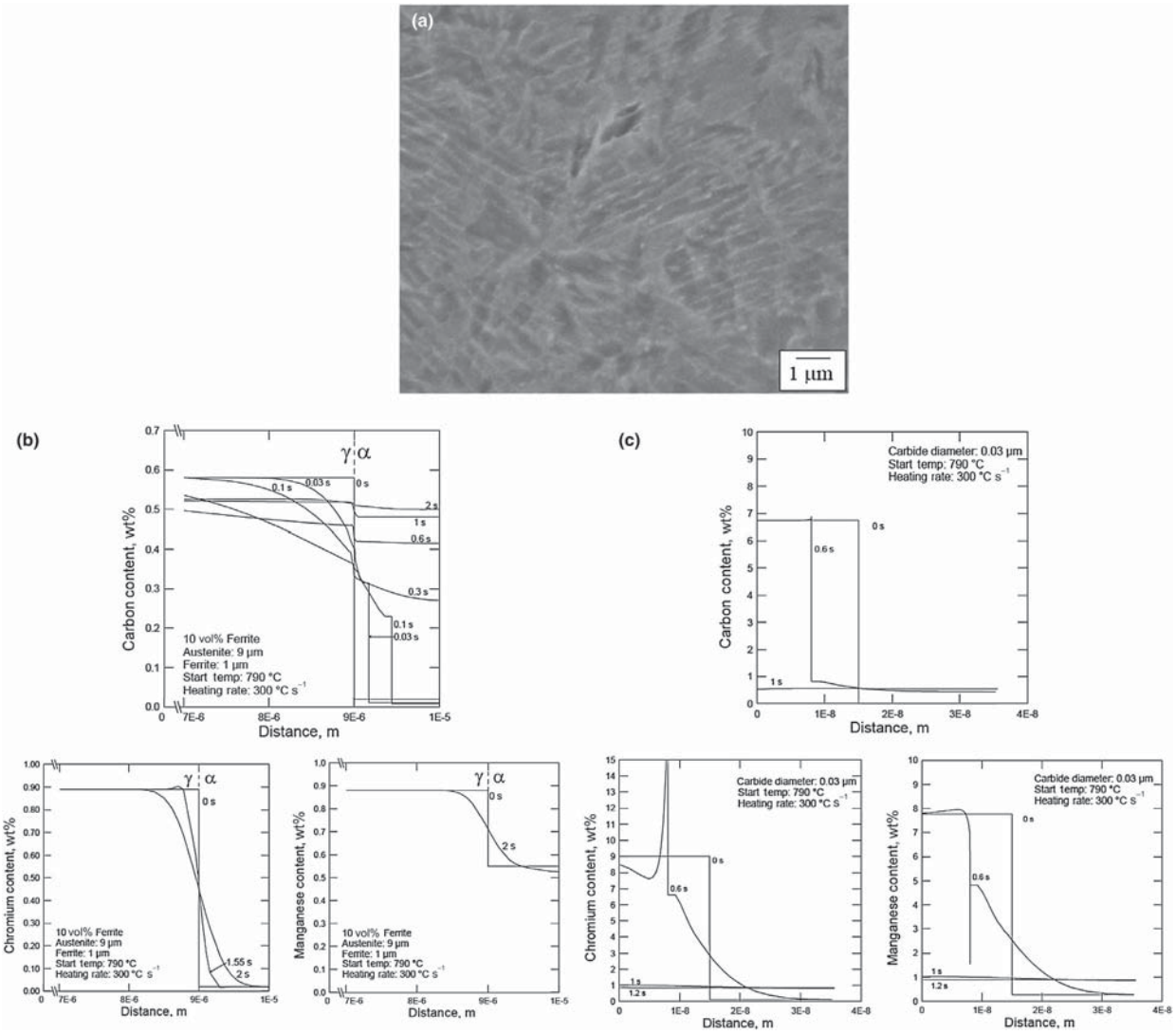

Figure 10 (a) Scanning electron micrograph showing evidence of retained carbides for a 5150 hot-rolled starting microstructure continuously heated to 900 °C at 300 °C s^{-1} and immediately quenched. The measured hardness and dilatometric analysis suggest full austenitization. Reproduced from Clarke, K.D. The Effect of Heating Rate and Microstructural Scale on Austenite Formation, Austenite Homogenization, and As-Quenched Microstructure in Three Induction Hardenable Steels. Ph.D. Thesis, Colorado School of Mines: Golden, CO, 2008; Clarke, K.D.; Van Tyne, C.J. The Effect of Heating Rate and Prior Microstructure on Austenitization Kinetics of 5150 Hot-Rolled and Quenched and Tempered Steel. In *Materials Science & Technology 2007*; TMS: Detroit, MI, 2007 and K.D. Clarke, Van Tyne, C.J.; Hackenberg, R.E.; Vigil, C.J. Induction Hardening 5150 Steel – Effects of Initial Microstructure and Heating Rate, winner of the 2010 HTS/Bodycote Best Paper in Heat Treating Award, March 2, 2010, announced in Adv. Mater. Processes, August, 2010. Published in the *J. Mater. Eng. Perform.* **2011,** *20* (2),161–168; also published electronically in ASM Heat Treating Society Industrial Heat Treating and HTPro eNews April 6, 2010. (b, c) Dictra diffusion calculations showing calculated diffusion distances of carbon, chromium, and manganese from (b) austenite into ferrite (simulating transformation of proeutectoid ferrite after pearlite regions have transformed to austenite), and (c) carbide into austenite (simulating carbide dissolution in an austenite field). (b) Suggests very little substitutional diffusion into prior ferrite regions. (c) Shows carbide dissolution is dependent on the diffusion of substitutional alloy away from the carbide. Reproduced from Clarke, K.D. The Effect of Heating Rate and Microstructural Scale on Austenite Formation, Austenite Homogenization, and As-Quenched Microstructure in Three Induction Hardenable Steels. Ph.D. Thesis, Colorado School of Mines: Golden, CO, 2008.

it was found that evidence of prior pearlite lamellae was obvious in the microstructure at temperatures well above Ac_3 (*21*,*31*,*32*) (see **Figure 10(a)**), although maximum as-quenched hardness was achieved. These carbide remnants have been referred to as 'ghost pearlite' (*33*) and were not found in 1045 steels with similar starting microstructures and high-rate heat treatments (*21*). This, along with hardness values that indicate most carbon is in solution, suggests that these remnants of pearlite may simply be locally high chromium concentrations, which result from partitioning of chromium to pearlitic carbides and slow diffusion of chromium relative to carbon, as shown in **Figure 5**. Metallographic evidence of chromium partitioning is evident, since there is a significant etching response. However, other substitutional elements, such as manganese, may also partition to carbides but would not be

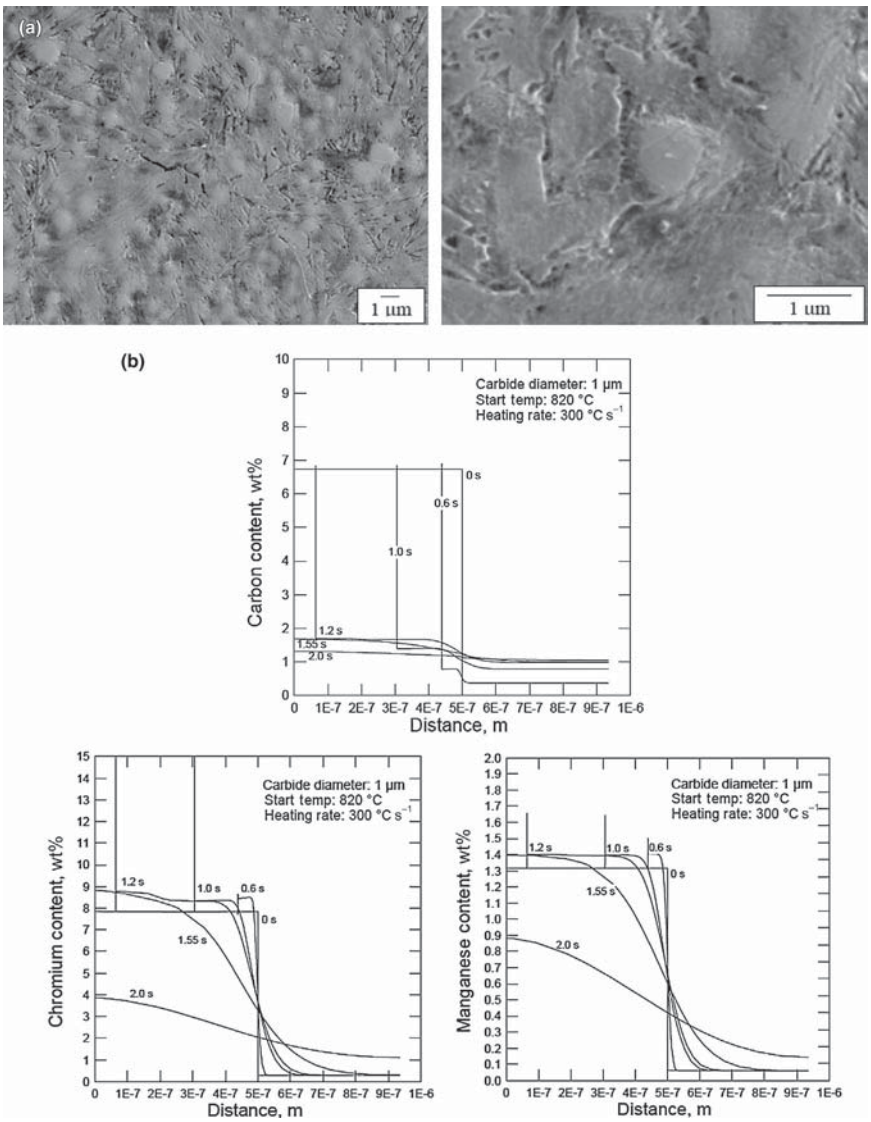

Figure 11 (a) Scanning electron micrographs of prior-spheroidized 52100 steel heated at 300 °C s^{-1} to 1200 °C, and the resulting evidence of alloy partitioning to locations of prior carbides. (b) Dictra diffusion calculations showing that significant chromium and manganese segregation remains after carbide dissolution (after 1.2 s). Reproduced from Clarke, A.J.; Speer, J.G.; Miller, M.K.; Hackenberg, R.E.; Edmonds, D.V.; Matlock, D.K.; Rizzo, F.C.; Clarke, K.D.; De Moor, E. Carbon Partitioning to Austenite from Martensite or Bainite during the Quench and Partition (Q&P) Process: A Critical Assessment. *Acta Mater.* **2008,** *56,* 16–22.

evident metallographically since manganese does not reduce etch attack significantly like chromium. Therefore, the Dictra simulations presented in Figure 10 (*21*) also suggest that chromium and manganese diffusion from substitutional alloy-partitioned carbides slows carbide dissolution during high-rate, short-time heat treatments. In addition, substitutional diffusion to prior ferrite regions results in significant concentration gradients. Although these locally high concentrations occur over very short distances, there may be subsequent effects on the local phase stability, microstructure formation, mechanical and fatigue properties, or corrosion resistance of materials with this remnant chromium or manganese segregation.

A further example of austenite formation kinetics with chromium alloying is 52100 steel, a hypereutectoid carbon composition with nominally 1.5 wt.% chromium, which is generally heat treated from a heavily spheroidized carbide condition, as shown in Figure 11, that requires significant time for dissolution (*21,34–36*). After heating at 300 °C s^{-1} to 1200 °C, remnant carbides remain, but regions where carbides fully dissolved are also evident, likely because of remnant alloy originally partitioned to the carbide. The accompanying Dictra calculations show that maximum temperatures above 1400 °C for high heating rates would still not eliminate the substitutional alloy segregation to the locations of prior carbides. Again, this suggests that high-rate heating results in chemically inhomogeneous microstructures, and there is every reason to suspect that the limited diffusivity of substitutional species results in local inhomogeneity even during slower heat treatment.

12.10.4.3 Additional Considerations

A significant number of articles have been published on the formation of austenite (*21*,*28*–*99*) over many years. However, there appears to be renewed interest in austenite formation over the past decade because of the new processing routes that are either in use or being considered for first- and second-generation AHSS (low-carbon sheet) applications (*1*), which include DP, complex-phase, transformation-induced plasticity (TRIP), lightweight steels with induced plasticity (L-IP), shear band strengthened, and twinning-induced plasticity (TWIP). In addition, research is ongoing to determine the viability of enhanced DP steels, modified TRIP, ultrafine-grained bainite, quenching and partitioning (Q&P), flash processing, lower manganese TWIP and TRIP, and high manganese TRIP as the third generation of AHSS, where it is expected that final microstructures consisting of ferrite, austenite, and martensite will be required to meet strength and ductility requirements (*1*). Although the specifics of each process will not be discussed in detail here, it is obvious that composition and microstructure are the key variables that can be selectively controlled to produce product properties to meet industry requirements. The addition of higher quantities of substitutional alloying elements such as manganese, chromium, silicon, aluminum, cobalt, nickel, and others affects the phase stability of austenite, and this must be considered during processing. Controlling grain size and incorporating steels that deform via twinning rather than slip also pose challenges for processing austenite and affect the formation and development of austenite. Finally, these new processing paths may also include deformation of the austenite to mechanically decrease grain size, as microalloying approaches may no longer be compatible with alloying strategies.

Intercritical heat treatments used to tailor specific volume fractions of ferrite and martensite and/or bainite should also be examined. During intercritical annealing, austenite forms with carbon content that is specified by a horizontal tie line between the A_3 and the ferrite phase field (essentially zero carbon). The lever rule can be used to calculate phase fraction (*2*), but the intercritical temperature used determines the austenite carbon content. Obviously, small variations in temperature and phase stability for these heat treatments will result in large changes in phase fraction and austenite carbon content, and thus precise understanding of the equilibrium phase stability for the particular composition is vital, along with accurate process control. Using intercritical annealing can result in ferrite-plus-martensite microstructures, or can be designed to create austenite with high carbon or other alloy levels, which can stabilize austenite to room temperature, assuming no competing phases (carbides) form during cooling. Alloying with aluminum or silicon can impede carbide growth. Additionally, an important consideration when alloying with significant amounts of aluminum is that full austenitization may not be possible.

In addition to composition, heating rate, and microstructural-scale effects, residual driving force within the microstructure can affect austenitization. Cold work and untempered martensite are two examples of potential energy stored within the microstructure. Many modern steel-processing paths utilize intercritical heat treatment in order to tailor microstructure with optimized volumes of ferrite and martensite (or bainite) to design steels with high strength and good ductility. Recent advances in high-strength steels may also require postquenching heat treatments in microstructures that retain austenite to room temperature via carbon stabilization and the prevention of carbide formation. The local stability is therefore critically important to the final properties.

Cold-worked materials tend to recrystallize before austenite formation in standard furnace heat treatments. However, it has been shown that heating rates above some critical value (*97*–*99*) result in a reduction in the required hold times to achieve a given amount of austenite formation, as recrystallization during austenitization increases the rate of austenite formation. It would follow that untempered martensite microstructures may alter austenite formation kinetics if a critical heating rate is used to limit tempering before entering the austenite phase field, if tempering and austenitization can occur simultaneously.

12.10.5 Austenite Structural Development

Once austenite formation is complete, the condition of austenite as a function of heat treatment is of critical importance to the final properties of the steel. In particular, austenite grain size has an important effect on subsequent processing. The temperatures and times at which steels are heat treated in the austenite phase field can have significant effects on austenite grain size. Several ways to control austenite grain size include using aluminum additions, microalloying, and thermomechanical processing (*3*,*4*,*6*,*8*,*9*).

Aluminum and nitrogen additions have been shown to minimize austenite grain growth up to 1000 °C in standard furnace heat treatments (*3*). As shown in **Figure 3**, differences in austenite grain growth occur as a function of aluminum content for continuously heated steels. The Ck 15 steel has 0.06 wt.% aluminum (semikilled), whereas the Ck 45 steel has 0.14 wt.% aluminum (killed), and their austenite grain growth rates are substantially different, especially when considering slow heating rates. Very specific quantities of aluminum and nitrogen are required to form aluminum nitride (AlN) particles that pin austenite grain boundaries up to 1000 °C. If the aluminum content is below 0.08 wt.%, there are not enough particles to pin grain boundaries, whereas if the aluminum content is above 0.15 wt.%, the particles tend to coarsen and be ineffective in pinning grain boundaries. Note that above 1000 °C for slow heating rates, the aluminum nitride precipitates dissolve, and very similar grain sizes are found for both steels. At higher heating rates, it is interesting to note that the dissolution kinetics of aluminum nitrides results in small grain sizes in the fully aluminum-killed steel up to very high temperatures (over 1100 °C at 100 °C s^{-1}). It is therefore possible to use rapid-heating techniques up to higher maximum temperatures than would ordinarily be considered, as long as hold times at a temperature are minimized or eliminated.

Other alloying elements, such as titanium, vanadium, and niobium, are often used in low-alloy steels as microalloying additions to control austenite grain size. These microalloying additions perform a similar function to aluminum in killed steels, but are used in conjunction with nitrogen or carbon to control the stability and solubility of the desired precipitate (*3*).

As mentioned in this chapter, high-temperature austenite has greatly reduced resistance to deformation, and it is therefore favorable to deform steels in the austenite phase field whenever possible. Thermomechanical processing of steels in the austenite phase field, in conjunction with controlled recrystallization, can also be used to minimize austenite grain size and therefore also the final grain size in the transformed microstructure. In microalloyed steels, austenite recrystallization may be suppressed by precipitation of fine microalloy carbonitride particles, resulting in grain structures elongated in the rolling direction. This process is known as controlled rolling. More detailed reviews of thermomechanical processing in steels are available in the literature, for example Refs. (*3*,*4*,*8*,*9*).

12.10.6 Summary

Austenite plays a key role in the processing of steels, and the condition of austenite that is formed during processing can be controlled to optimize the subsequent in-service microstructure. Many austenitization heat treatments have been optimized over decades for specific alloy compositions and processing capabilities. However, there is no 'ideal' austenitic microstructure for every application. It is generally advantageous to minimize austenite grain growth during processing, while ensuring the alloy content in the microstructure is as homogeneous as possible. Grain growth can be controlled by controlling processing temperatures, microalloying, or thermomechanical processing. Austenite composition and homogeneity should be carefully considered for high-heating-rate processes (e.g., surface induction hardening), and they may become more significant with modern developments in low-carbon AHSS sheets, which require precise processing paths and a thorough understanding of local phase stability.

The breadth of available austenite microstructures, however, affords the steel metallurgist a wide variety of processing opportunities that are not available in other alloy systems. This allows steel to persist as the most important structural material in the modern world, and it has resulted in major advancements in steel applications continuously for over a century. Recent improvements in process capabilities and theoretical understanding in steels suggest this trend will continue into the foreseeable future.

See also: Mathematical Modeling of Weld Phenomena. Part 1: Finite-Element Modeling; Bonding Technologies in Manufacturing Engineering; Review of Microstructures, Mechanical Properties, and Residual Stresses of Ferritic and Martensitic Stainless-Steel Welded Joints; Advances in Fused Deposition Modeling; Laser-Assisted Additive Manufacturing for Metallic Biomedical Scaffolds.

References

1. DeMoor, E.; Gibbs, P. J.; Speer, J. G.; Matlock, D. K. Strategies for Third-Generation Advanced High-Strength Steel Development. *AIST Trans.* **2010,** *7,* 133–144.
2. Callister, W. D.; Rethwisch, D. G. *Materials Science and Engineering, an Introduction,* 8th ed.; Wiley and Sons: New York, NY, 2010.
3. Krauss, G. *Steels Processing, Structure, and Performance;* ASM International: Materials Park, OH, 2005.
4. Brooks, C. R. *Principles of the Heat Treatment of Plain Carbon and Low Alloy Steels;* ASM International: Materials Park, OH, 1996.
5. Brooks, C. R. *Principles of the Surface Treatment of Steels;* Technomic: Lancaster, PA, 1992.
6. Brooks, C. R. *Heat Treatment of Ferrous Alloys;* McGraw-Hill: New York, NY, 1979.
7. Abbaschian, R.; Abbaschian, L.; Reed-Hill, R. E. *Physical Metallurgy Principles,* 4th ed.; Cengage Learning: Stamford, CT, 2008.
8. Leslie, W. C. *The Physical Metallurgy of Steels;* Hemisphere: Marietta, OH, 1981.
9. De Cooman, B. C.; Speer, J. G. *Fundamentals of Steel Product Metallurgy;* AIST, 2011.
10. Ericsson, T. Principles of Heat Treating of Steels, Heat Treating. In *ASM Handbook;* ASM International, 1991; Vol. 4, pp 3–19.
11. Rajan, T. V.; Sharma, C. P.; Sharma, A. *Heat Treatment: Principles and Techniques;* Prentice-Hall: New Delhi, India, 2006.
12. Grossman, M. A.; Bain, E. C. *Principles of Heat Treatment,* 5th ed.; American Society for Metals: Metals Park, OH, 1964.
13. Unterweiser, P. M. *Heat Treater's Guide Standard Practices and Procedures for Steel;* American Society for Metals: Metals Park, OH, 1982.
14. Damm, E. B.; Merwin, M. J. *Austenite Formation and Decomposition;* TMS: Warrendale, PA, 2003.
15. Wever, F.; Rose, A.; Peter, W.; Strassburg, W.; Rademacher, L. *Atlas zur Wärmebehandlung der Stähle, Band 1;* Verlag Stahleisen M.B.H: Düsseldorf, Germany, 1961.
16. Rose, A.; Hougardy, H. *Atlas zur Wärmebehandlung der Stähle, Band 2;* Verlag Stahleisen M.B.H: Düsseldorf, Germany, 1972.
17. Orlich, J.; Rose, A.; Wiest, P. *Atlas zur Wärmebehandlung der Stähle, Band 3;* Verlag Stahleisen M.B.H: Düsseldorf, Germany, 1973.
18. Orlich, J.; Pietrzeniuk, H.-J. *Atlas zur Wärmebehandlung der Stähle, Band 4;* Verlag Stahleisen M.B.H: Düsseldorf, Germany, 1976.
19. C (Carbon) Binary Alloy Phase Diagrams. In *Alloy Phase Diagrams*; *ASM Handbook*; ASM International, 1992; Vol. 3, pp 2.109–2.116.
20. DeMeyer, M.; Vanderschueren, D.; DeCoomen, B. C. The Influence of the Substitution of Si by Al on the Properties of Cold Rolled C–Mn–Si TRIP Steels. *ISIJ Int.* **1999,** *39* (8), 813–822.
21. Clarke, K. D. The Effect of Heating Rate and Microstructural Scale on Austenite Formation, Austenite Homogenization, and As-quenched Microstructure in Three Induction Hardenable Steels. Ph.D. Thesis, Colorado School of Mines: Golden, CO, 2008.
22. Kayali, E. S.; Sunada, H.; Oyama, T.; Wadsworth, J.; Sherby, O. D. The Development of Fine Structure Superplasticity in Cast Ultrahigh Carbon Steels through Thermal Cycling. *J. Mater. Sci.* **1979,** *14,* 2688–2692.
23. Shewmon, P. *Diffusion in Solids,* 2nd ed.; TMS: Warrendale, PA, 1989.
24. Anderson, P.I. Induction Hardening Response of Ferrite and Pearlite Banded Steel. M.S. Thesis, Colorado School of Mines: Golden, CO, 2005.
25. Clarke, A. J.; Speer, J. G.; Miller, M. K.; Hackenberg, R. E.; Edmonds, D. V.; Matlock, D. K.; Rizzo, F. C.; Clarke, K. D.; De Moor, E. Carbon Partitioning to Austenite from Martensite or Bainite during the Quench and Partition (Q&P) Process: A Critical Assessment. *Acta Mater.* **2008,** *56,* 16–22.
26. Clarke, A. J.; Speer, J. G.; Matlock, D. K.; Rizzo, F. C.; Edmonds, D. V.; Santofimia, M. J. Influence of Carbon Partitioning Kinetics on Final Austenite Fraction during Quenching and Partitioning. *Scr. Mater.* **2009,** *61,* 149–152.
27. Gibbs, P. J.; De Moor, E.; Merwin, M. J.; Clausen, B.; Speer, J. G.; Matlock, D. K. Austenite Stability Effects on Tensile Behavior of Manganese-Enriched Austenite Transformation-Induced Plasticity Steel. *Metall. Mater. Trans. A* **2011,** *42,* 3691–3702.
28. Lee, S.-J.; Clarke, K. D.; Van Tyne, C. J. An On-Heating Dilation Conversional Model for Austenite Formation in Hypoeutectoid Steels. *Metall. Mater. Trans. A* **September 2010,** *41* (9), 2224–2235.

29. Misaka, Y.; Kiyosawa, Y.; Kawasaki, K.; Yamazaki, T.; Silverthorne, W. O. *Gear Contour Hardening by Micropulse Induction Heating System.* document 970971; Society of Automotive Engineers, 1997; pp 121–130.
30. López, V.; Fernández, J. M.; Belló, J. M.; Ruiz, J.; Zubiri, F. Influence of Previous Structure on Laser Surface Hardening of AISI 1045 Steel. *ISIJ Int.* **1995,** *35* (11), 1394–1399.
31. Clarke, K. D.; Van Tyne, C. J. The Effect of Heating Rate and Prior Microstructure on Austenitization Kinetics of 5150 Hot-rolled and Quenched and Tempered Steel. In *Materials Science & Technology 2007;* TMS: Detroit, MI, 2007.
32. Clarke, K. D.; Van Tyne, C. J.; Hackenberg, R. E.; Vigil, C. J. Induction Hardening 5150 Steel – Effects of Initial Microstructure and Heating Rate. *J. Mater. Eng. and Perform.* **2011,** *20* (2), 161–168.
33. Medlin, D. J.; Krauss, G.; Thompson, S. W. Induction Hardening Response of 1550 and 5150 Steels with Similar Prior Microstructures. In *1st International Conference on Induction Hardening of Gears and Critical Components.* Indianapolis, IN*;* 1995.
34. Clarke, K. D.; Van Tyne, C. J. Effect of Prior Microstructure Scale and Heating Rate on Carbide Dissolution and Austenite Formation in Spheroidized 52100 Steel. In *27th Forging Industry Technical Conference and Energy Summit;* Forging Industry Association: Ft. Worth, TX, 2007.
35. Lee, S.-J.; Clarke, K. D. A Conversional Model for Austenite Formation in Hypereutectoid Steels. *Metall. Mater. Trans. A* **Dec. 2010,** *41* (12), 3027–3031.
36. Lee, S.-J.; Clarke, K. D. A Quantitative Investigation of Cementite Dissolution Kinetics for Continuous Heating of Hypereutectoid Steel. *Metall. Mater. Trans. A*, submitted for publication.
37. Bénéteau, A.; Weisbecker, P.; Geandier, G.; Aeby-Gautier, E.; Appolaire, B. Austenitization and Precipitate Dissolution in High Nitrogen Steels: And In-Situ High Temperature X-ray Synchrotron Diffraction Analysis Using the Rietveld Method. *Mater. Sci. Eng. A* **2005,** *393,* 63–70.
38. Caballero, F. G.; Capdevila, C.; García de Andrés, C. Influence of Scale Parameters of Pearlite on the Kinetics of Anisothermal Pearlite-to-Austenite Transformation in a Eutectoid Steel. *Scr. Mater.* **2000,** *42,* 1159–1165.
39. Cai, X.-L.; Garrat-Reed, A. J.; Owen, W. S. The Development of Some Dual-Phase Steel Structures from Different Starting Microstructures. *Metall. Trans. A* **1985,** *16,* 543–557.
40. Datta, D. P.; Gokhale, A. M. Austenitization Kinetics of Pearlite and Ferrite Aggregates in a Low Carbon Steel Containing 0.15 Wt. Pct. C. *Metall. Trans. A* **1981,** *12,* 443–450.
41. Durban, C.; Durand, D.; Chevre, P. Determination of Austenitic Transformation during Fast Heat Treatment in Heat Treating. In *Proceedings of the 17th ASM Heat Treating Society Conference Proceedings Including the 1st International Induction Heat Treating Symposium;* 1997.
42. Garcia, C. I.; DeArdo, A. J. Formation of Austenite in 1.5 Pct Mn Steels. *Metall. Trans. A* **1981,** *12,* 521–530.
43. Garcia, C. I.; DeArdo, A. J. Formation of Austenite in Low Alloy Steels. In *International Conference on Solid-Solid Phase Transformations;* Aaronson, H. I., et al., Eds.; TMS-AIME: Warrendale, PA, 1982; p 855.
44. Judd, R. R.; Paxton, H. W. Kinetics of Austenite Formation from a Spheroidized Ferrite–Carbide Aggregate. *Trans. Metall. Soc. AIME* **1968,** *242,* 206–215.
45. Klier, E. P.; Troiano, A. R. Ar in Chromium Steels. *Trans. Metall. Soc. AIME* **1945,** *162,* 175–185.
46. Lenel, U. R. TTT Curves for the Formation of Austenite. *Scr. Metall.* **1983,** *17,* 471–474.
47. Molinder, G. A Quantitative Study of the Formation of Austenite and the Solution of Cementite at Different Austenitizing Temperatures for a 1.27% Carbon Steel. *Acta Metall.* **1956,** *4,* 565–571.
48. Nemoto, M. The Formation of Austenite from Mixtures of Ferrite and Cementite as Observed by HVEM. *Metall. Trans. A* **1977,** *8,* 431–437.
49. Puskar, J. D.; Dykhuizen, R. C.; Robino, C. V.; Kelley, J. B.; Burnett, M. E. Austenite Formation Kinetics during Rapid Heating in a Microalloyed Steel. In *41st Mechanical Working and Steel Processing Conference;* The Iron and Steel Society (ISS), 1999; Vol. 37, pp 625–635.
50. Roberts, G. A.; Mehl, R. F. The Mechanism and the Rate of Formation of Austenite from Ferrite–Cementite Aggregates. *Trans. ASM* **1943,** *31,* 613–650.
51. Roosz, A.; Gacsi, Z.; Fuchs, E. G. Isothermal Formation of Austenite in Eutectoid Plain Carbon Steel. *Acta Metall.* **1983,** *31* (4), 509–517.
52. Schmidt, E.; Damm, E. B.; Sridhar, S. On the Rate and Mechanism of Interface Migration during Austenitization of 4118 Steel. In *Proceedings of International Conference on New Developments in Long and Forged Products: Metallurgy and Applications. 2006;* AIST: Warrendale, PA:, 2006; pp 203–215.
53. Schmidt, E.; Damm, E. B.; Sridhar, S. A Study of Diffusion- and Interface-Controlled Migration of the Austenite/Ferrite Front during Austenitiztion of a Case-Hardenable Alloy Steel. *Metall. Trans. A* **2007,** *38,* 244–260.
54. Speich, G. R.; Demarest, V. A.; Miller, R. L. Formation of Austenite during Intercritical Annealing of Dual Phase Steels. *Metall. Trans. A* **1981,** *12,* 1419–1428.
55. Speich, G. R.; Szirmae, A. Formation of Austenite from Ferrite and Ferrite–Carbide Aggregates. *Trans. Metall. Soc. AIME* **1969,** *245,* 1063–1074.
56. Wycliffe, P.; Purdy, G. R.; Embury, J. D. Austenite Growth in the Intercritical Annealing of Ternary and Quaternary Dual-Phase Steels. In *Fundamentals of Dual Phase Steels;* TME-AIME: Warrendale, PA:, 1981; pp 58–83.
57. Wycliffe, P.; Purdy, G. R.; Embury, J. D. Growth of Austenite in the Intercritical Annealing of Fe–C–Mn Dual Phase Steels. *Can. Metall. Q.* **1981,** *20* (3), 339–350.
58. Yang, D. Z.; Brown, E. L.; Matlock, D. K.; Krauss, G. The Formation of Austenite at Low Intercritical Annealing Temperatures in a Normalized 0.08C–1.45Mn–0.21Si Steel. *Metall. Trans. A* **1985,** *16,* 1523–1526.
59. Yang, J. R.; Bhadeshia, H. K. D. H. Reaustenisation in Steel Weld Deposits. In *Proceedings of an International Conference on Welding Metallurgy of Structural Steels;* The Metallurgical Society of the AIME: Warrendale, PA, 1987; pp 549–563.
60. Yang, J. R.; Bhadeshia, H. K. D. H. The Bainite to Austenite Transformation or Reaustenitisation from Bainite. In *Proceedings of an International Conference: Phase Transformations '87;* Institute of Metals: London, 1988; pp 203–206.
61. Yang, J. R.; Bhadeshia, H. K. D. H. Reaustenitisation Experiments on Some High-strength Steel Weld Deposits. *Mater. Sci. Eng. A* **1989,** *118,* 155–170.
62. Yang, J. R.; Bhadeshia, H. K. D. H. Continuous Heating Transformation of Bainite to Austenite. *Mater. Sci. Eng. A* **1991,** *131,* 99–113.
63. Epp, J.; Surm, H.; Kessler, O.; Hirsch, T. In-Situ X-ray Investigations and Computer Simulation during Continuous Heating of a Ball Bearing Steel. *Metall. Trans. A* **2007,** *38,* 2371–2378.
64. Schmidt, E.; Wang, Y.; Sridhar, S. A Study of Nonisothermal Austenite Formation and Decomposition in Fe–C–Mn Alloys. *Metall. Trans. A* **2006,** *37,* 1799–1810.
65. Zhang, X.; Liu, W.; Sun, D.; Li, Y. The Transformation of Carbides during Austenitization and Its Effect on the Wear Resistance of High Speed Steel Rolls. *Metall. Trans. A* **2007,** *38,* 499–505.
66. Caballero, F. G.; Capdevila, C.; García de Andrés, C. Influence of Pearlite Morphology and Heating Rate on the Kinetics of Continuously Heated Austenite Formation in a Eutectoid Steel. *Metall. Trans. A* **2001,** *32,* 1283–1291.
67. Caballero, F. G.; Capdevila, C.; García de Andrés, C. Kinetics and Dilatometric Behaviour of Nonisothermal Ferrite – Austenite Transformation. *Mater. Sci. Technol.* **2001,** *17,* 1114–1118.
68. Caballero, F. G.; Capdevila, C.; García de Andrés, C. Modeling of Kinetics and Dilatometric Behaviour of Austenite Formation in a Low-Carbon Steel with a Ferritic Plus Pearlite Initial Microstructure. *J. Mater. Sci.* **2002,** *37,* 3533–3540.
69. García de Andrés, C.; Caballero, F. G.; Capdevila, C. Dilatometric Characterization of Pearlite Dissolution in 0.1C–0.5Mn Low Carbon Low Manganese. *Scr. Mater.* **1998,** *38,* 1835–1842.
70. García de Andrés, C.; Caballero, F. G.; Capdevila, C.; Bhadeshia, H. K. D. H. Modeling of Kinetics and Dilatometric Behavior of Nonisothermal Pearlite-to-Austenite Transformation in an Eutectoid Steel. *Scr. Mater.* **1998,** *39* (6), 791–796.
71. Kapoor, R.; Kumar, L.; Batra, I. S. A Dilatometric Study of the Continuous Heating Transformations in 18wt.% Ni Maraging Steel Grade 350. *Mater. Sci. Eng. A* **2003,** *352,* 318–324.
72. Puskar, J. D.; Dykhuizen, R. C.; Robino, C. V.; Kelley, J. B.; Burnett, M. E. Austenite Formation Kinetics during Rapid Heating in a Microalloyed Steel. *Iron Steelmaker* **2000,** *27,* 27–34.

73. Reed, R. C.; Akbay, T.; Shen, Z.; Robinson, J. M.; Root, J. H. Determination of Reaustenitisation Kinetics in a Fe–0.4C Steel Using Dilatometry and Neutron Diffraction. *Mater. Sci. Eng. A* **1998,** *256,* 152–165.
74. Grach, G.; Lusk, M.T.; Jou, H.-J.; Ludtka, G.; Elliot, W.H.; Shick, D.; Dicastanzo, G.; Walton, H. Effect of Austenitization Hold Time and Temperature on Matrix Carbon Content and Martensite Kinetics in 52100. Unpublished draft, 2004.
75. Lyasotsky, I. V.; Shtansky, D. V. Formation of Austenite and the Kinetics of Cementite Dissolution in Steels with a Recrystallized Structure of Granular Pearlite under Laser Heating. *Phys. Met. Metallogr.* **1993,** *75* (1), 77–82.
76. Mioković, T.; Schulze, V.; Vöhringer, O.; Löhe, D. Prediction of Phase Transformations during Laser Surface Hardening of AISI 4140 Including the Effects of Inhomogeneous Austenite Formation. *Mater. Sci. Eng.* **2006,** *435–436,* 547–555.
77. Rödel, J.; Spies, H.-J. Calculation of Temperature Fields and Austenite Formation during Electron Beam Hardening. In *Surface Modification Technologies VIII: Proceedings of the Eighth International Conference on Surface Modification Technologies;* Nice, France, pp 638–650.
78. Rödel, J.; Spies, H.-J. Modeling of Austenite Formation during Rapid Heating. *Surf. Eng.* **1996,** *12,* 313–318.
79. Yakovleva, I. L.; Schastlivtsev, V. M.; Tabatchikova, T. I. Experimental Observation of Diffusionless Formation of Austenite in a Steel with Pearlitic Structure upon Laser Heating. *Phys. Met. Metallogr.* **1993,** *76* (2), 179–187.
80. Shtansky, D. V.; Inden, G. Phase Transformation in Fe–Mo–C and Fe–W–C Steels – II. Eutectoid Reaction of M23C6 Carbide Decomposition during Austenitization. *Acta Mater.* **1997,** *45,* 2879–2895.
81. Babu, S. S.; Elmer, J. W.; Vitek, J. M.; David, S. A. Time-Resolved X-ray Diffraction Investigation of Primary Weld Solidification in Fe–C–Al–Mn Steel Welds. *Acta Mater.* **2002,** *50,* 4763–4781.
82. Elmer, J. W.; Palmer, T. A.; Babu, S. S.; Zhang, W.; DebRoy, T. Direct Observations of Austenite, Bainite, and Martensite Formation during Arc-Welding of 1045 Steel Using Time-Resolved X-ray Diffraction. *Weld. J.* **2004,** 244S–253S.
83. Palmer, T. A.; Elmer, J. W.; Babu, S. S. Observations of Ferrite/Austenite Transformations in the Heat Affected Zone of 2205 Duplex Stainless Steel Spot Welds Using Time Resolved X-ray Diffraction. *Mater. Sci. Eng. A* **2004,** *A374,* 307–321.
84. Zhang, W.; Elmer, J. W.; DebRoy, T. Kinetics of Ferrite to Austenite Transformation during Welding of 1005 Steel. *Scr. Mater.* **2002,** *46,* 753–757.
85. Caballero, F. G.; Capdevila, C.; Garcia de Andres, C. Modeling of the Interlamellar Spacing of Isothermally Formed Pearlite in a Eutectoid Steel. *Scr. Mater.* **2000,** *42,* 537–542.
86. Dykhuizen, R. C.; Robino, C. V.; Knorovsky, G. A. A Method for Extracting Phase Change Kinetics from Dilatation for Multistep Transformations: Austenitization of a Low Carbon Steel. *Metall. Trans. B* **1999,** *30,* 107–117.
87. Katsamas, A. I. A Computational Study of Austentite Formation Kinetics in Rapidly Heated Steels. *Surf. Coat. Technol.* **2007,** *201,* 6414–6422.
88. Shtansky, D. V.; Nakai, K.; Ohmori, Y. Pearlite to Austenite Transformation in an Fe–2.6Cr–1C Alloy. *Acta Mater.* **1999,** *47* (9), 2619–2632.
89. Zhao, L.; Vermolen, F. J.; Wauthier, A.; Sietsma, J. Cementite Dissolution at 860 °C in an Fe–Cr–C Steel. *Metall. Trans. A* **2006,** *37,* 1841–1850.
90. Liu, Z. K.; Höglund, L.; Jönsson, B.; Ågren, J. An Experimental and Theoretical Study of Cementite Dissolution in an Fe–Cr–C Alloy. *Metall. Trans. A* **1991,** *22,* 1745–1752.
91. Liu, Z. K.; Ågren, J. Morphology of Cementite Decomposition in an Fe–Cr–C Alloy. *Metall. Trans. A* **1991,** *22,* 1753–1759.
92. Li, Z.-D.; Miyamoto, G.; Yang, Z.-G.; Furuhara, T. Kinetics of Reverse Transformation from Pearlite to Austenite in an Fe-0.6 Mass Pct C Alloy and the Effects of Alloying Elements. *Metall. Mater. Trans. A* **2011,** *42,* 1586–1596.
93. Chae, J.-Y.; Jang, J.-H.; Zhang, G.; Kim, K.-H.; Lee, S. L.; Bhadeshia, H. K. D. H.; Suh, D.-W. Dilatometric Analysis of Cementite Dissolution in Hypereutectoid Steels Containing Cr. *Scr. Mater.* **2011,** *65,* 245–248.
94. Miyamoto, G.; Usuki, H.; Li, Z.-D.; Furuhara, T. Effects of Mn, Si, and Cr Addition on Reverse Transformation at 1073 K from Spheroidized Cementite Structure in Fe-0.6 Mass% C Alloy. *Acta Mater.* **2010,** *58,* 4492–4502.
95. Palizdar, Y.; San Martin, D.; Brown, A. P.; Ward, M.; Cochrane, R. C.; Brydson, R.; Scott, A. J. Demonstration of Elemental Partitioning during Austenite Formation in Low-Carbon Aluminium Alloyed Steel. *J. Mater. Sci.* **2011,** *46,* 2384–2387.
96. Lee, S. J.; Mola, J.; De Cooman, B. C. Conversion Model for the Martensitic Transformation of Banded Austenite in a Ferrite Matrix. *Metall. Mater. Trans. A* **2012,** *43,* 4921–4925.
97. Azizi-Alizamini, H.; Militzer, M.; Poole, W. J. Austenite Formation in Plain Low-Carbon Steels. *Metall. Mater. Trans. A* **2011,** *42,* 1544–1557.
98. Kulakov, M.; Poole, W.J.; Militzer, M. The Effect of the Initial Microstructure on Recrystallization and Austenite Formation in DP600 Steel. Submitted to MMTA December 2012.
99. Rudinzki, J.; Bottger, B.; Prahl, U.; Bleck, W. Phase-field Modeling of Austenite Formation from a Ferrite Plus Pearlite Microstructure during Annealing of Cold-Rolled Dual-Phase Steel. *Metall. Mater. Trans.* **2011,** *42,* 2516–2525.

This page intentionally left blank

12.11 Quench and Tempered Martensitic Steels: Microstructures and Performance

G Krauss, Colorado School of Mines, Golden, CO, USA

12.11.1	**Introduction**	363
12.11.1.1	Processing and Heat-Treatment Considerations	364
12.11.2	**Martensite Formation and Crystallographic Considerations**	364
12.11.2.1	Martensite Transformation Kinetics and Morphologies	365
12.11.2.2	Tempered Martensitic Microstructures	367
12.11.3	**Deformation, Strengthening, and Mechanical Properties of Quench and Tempered Martensitic Microstructures**	368
12.11.4	**Fracture and Low-Toughness Phenomena in Carbon and Low-Alloy Carbon Steels**	372
12.11.5	**Summary**	377
References		377

12.11.1 Introduction

As-quenched martensitic microstructures have the highest hardness and strength that can be produced in a given steel. Such microstructures are subjected to tempering treatments that lower strength, but increase fracture resistance, toughness, and ductility. For example, Figure 1 shows the wide range of engineering stress–strain curves and mechanical performance that can be produced in 4340 steel quenched and tempered at various temperatures for 1 h (*1*). The 4340 steel contains nominally 0.40% carbon, 1.80% nickel, 0.59–0.80% chromium, and 0.25% molybdenum, and is widely used for applications that require good combinations of high strength and toughness. The carbon provides microstructural features that make possible the high strengths, as described in this chapter, and the nickel, chromium, and molybdenum provide hardenability that makes it possible to form martensite in heavy sections, as is described in Chapter 12.03 (*2*). The purpose of this chapter is to describe the effect of carbon content, alloying, martensite formation, and tempering on producing the complex microstructural systems that compose quench and tempered carbon and low-alloy carbon steels, and to relate the microstructural components of those systems to mechanical performance as demonstrated in Figure 1. Some heat-treatment conditions and steel chemistries produce microstructures sensitive to brittle fracture, and the roles that carbon content and microstructures produced by quench and tempering play in such performance of high-strength steels are also discussed in this chapter.

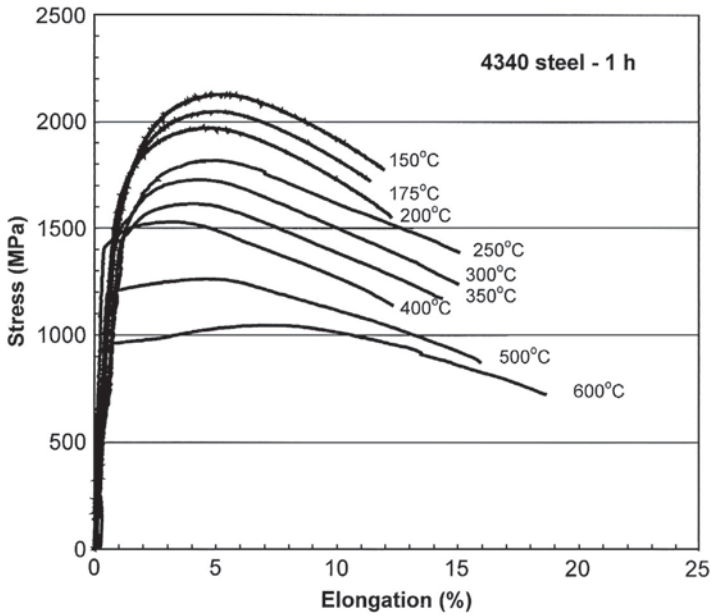

Figure 1 Engineering stress–strain curves for 4340 steel quenched to martensite and tempered at the temperatures shown. Courtesy of Young-Kook Lee.

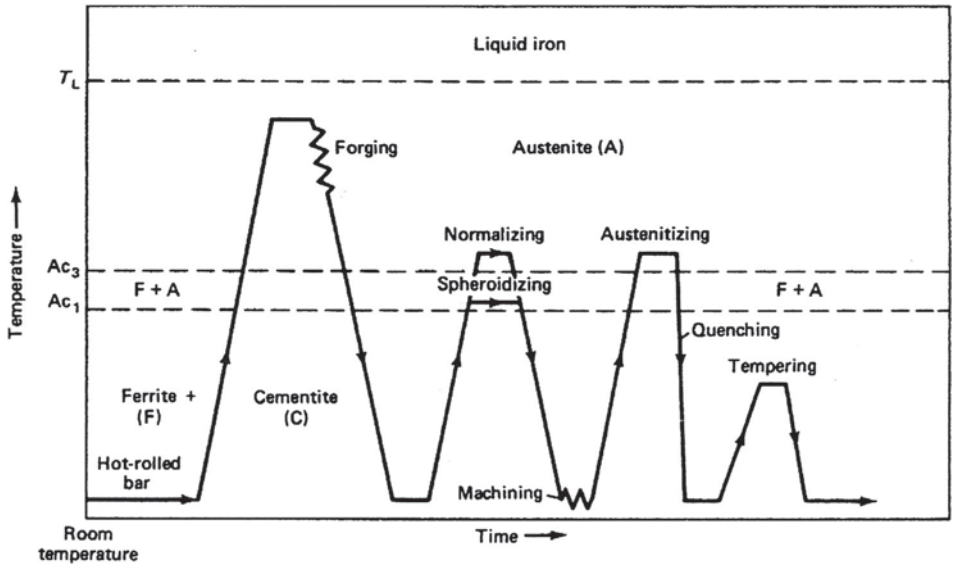

Figure 2 Schematic diagram of the thermal operations that might be applied to produce quench and tempered microstructures. Reproduced from Krauss, G. *Steels: Processing, Structure, and Performance*; ASM International: Materials Park, OH, 2005.

12.11.1.1 Processing and Heat-Treatment Considerations

Although martensitic microstructures are produced in all types of steel products, including flat rolled automotive sheet steels, low-carbon plate steels, and tubular steel products, steel bars, sometimes referred to as long products, are the hot rolled shape most subjected to quench and tempering heat treatments that provide finished mechanical properties for demanding applications. Those applications include machine parts, gears, bearings, shafts, and tools of all sorts. Figure 2 shows a schematic sequence of time–temperature operations that may be applied to produce finished hardened microstructures.

Electric arc furnace steelmaking with scrap steel and subsequent ladle refining and continuous strand casting is today a major source of bar steels (*3*), and as shown in Figure 2, hot rolled bars may be forged into more complex shapes at high temperatures.

Finished properties are produced by the three heat treatment steps of austenitizing, quenching, and tempering. Austenitizing and the modeling, heat transfer, phase transformations, residual stress development, and measurement of cooling that occur during quenching are all considered in state-of-the-art engineering detail in other chapters of this volume, and provide knowledge essential for high-quality manufacture of heat-treated components. This chapter supplements the other contents of this volume by characterizing in detail the microstructure and substructures of tempered martensite and how those structures affect finished steel performance. Martensitic microstructures that are of various carbon contents and tempered at various temperatures not only compose the microstructure of through-hardened steel parts, but also are major components, in some form or another, of other heat-treated steel systems. For example, martensite is formed on the surface of induction-hardened steels with lower strength core structures; high-carbon martensite is formed on low-carbon steel microstructures by atmosphere- or vacuum-carburizing; and nitriding is often performed on the surfaces of quench and tempered martensitic microstructures.

12.11.2 Martensite Formation and Crystallographic Considerations

Martensite crystals form in parent austenite crystals by diffusionless, shear-type mechanisms (*1*,*4*–*7*). The martensitic transformation, in the case of iron–carbon alloys and carbon steels, requires a change in crystallographic lattice from face-centered cubic austenite to body-centered tetragonal martensite. The shear mechanisms and absence of diffusion require close crystallographic coupling of the austenite and martensite; for example, close-packed planes of atoms in austenite, $\{111\}_A$, become close-packed planes in martensite, $\{110\}_M$, as reflected in eqns [1] and [2] below. Such well-known orientation relationships between the two phases in ferrous alloy systems have been determined by X-ray diffraction. The Kurdjumov–Sachs relationship states that

$$\begin{matrix}\{111\}\text{A ll}\{101\}\text{M}\\ \langle 110\rangle\text{A ll}\langle 111\rangle\text{M}\end{matrix} \quad [1]$$

and the Nishiyama relationship states that

$$\begin{matrix}\{111\}\text{A ll}\{011\}\text{M}\\ \langle 112\rangle\text{A ll}\langle 011\rangle\text{M}.\end{matrix} \quad [2]$$

Martensite crystals form parallel to composition-dependent, crystallographic planes in austenite, planes that are referred to as habit planes. Crystallographic theory assumes that the habit planes are unrotated and undistorted, and that the change in shape between the austenite and a martensite crystal are produced by homogeneous plane strain (*4*,*8*,*9*). Further, theory requires that the plane strain for the transformation depends in part on the change in crystallographic lattices from austenite to martensite – a change, however, that does not fully meet the requirement for producing plain strain and unique habit planes. Another deformation, referred to as the lattice-invariant deformation, is also required to maintain a given habit plane. The latter deformation is accomplished through plastic deformation by dislocations and/or fine twins, and, together with the volume differences between the crystal structures of austenite and martensite, contributes to the fine substructure within martensite crystals.

The fact that there is no diffusion during martensitic transformation means that the martensite theoretically inherits exactly the same chemical composition as the austenite from which it forms. Thus, the more carbon in solution in austenite in a given steel, the more carbon is trapped in a martensitic crystal structure. The carbon atoms are much smaller than iron atoms, go into interstitial sites between iron atoms, and displace the iron atoms. Consequently, the more carbon atoms in martensite, the greater is the displacement of iron atoms, producing tetragonal unit cells, with one axis greater than the other two, instead of the cubic unit-cell structure of body-centered cubic ferrite without carbon. Increasing carbon content significantly increases the **c** or tetragonal lattice parameter of martensitic unit cells, and as the **c** parameter increases there is a slight decrease in the **a** parameters of the unit cell (*10*).

12.11.2.1 Martensite Transformation Kinetics and Morphologies

When the diffusion-dependent transformations of austenite to ferrite, cementite, pearlite, and/or bainite are suppressed, martensite begins to form in austenite crystals or grains at a temperature referred to as the martensite start temperature, M_s. The more shear resistant the austenite, the lower the M_s. Carbon most strongly affects M_s temperatures but most other alloying elements in steels also tend to reduce M_s temperatures. The following widely used equation formulated by Andrews for low-alloy steels shows the dependence of M_s on carbon and alloy content (in weight percent) (*11*).

$$M_s(^\circ\mathrm{C}) = 539 - 423\ \mathrm{C} - 30.4\ \mathrm{Mn} - 12.1\ \mathrm{Cr} - 17.7\ \mathrm{Ni} - 7.5\ \mathrm{Mo} \quad [3]$$

The amount of martensite formed in a given steel is time-independent, since no diffusion is involved, and it depends only on the thermodynamic driving force as approximated by the temperature difference between M_s and the lowest quench temperature. For carbon steels Koistinen and Marburger (*12*) showed that the amount of martensite formed, f, depends on the temperature difference between M_s and quench temperature, ΔT, according to the following equation.

$$f = 1 - \exp\ -\left(1.10 \times 10^{-2}\Delta T\right) \quad [4]$$

Thus, for example, the lower the M_s temperature of a given steel, the smaller the amount of martensite formed, and the larger the amount of austenite retained on reaching room temperature. **Figure 3** shows a schematic diagram of M_s temperatures as a function of carbon content superimposed on the iron–carbon phase diagram. The strong effect of carbon on lowering the M_s temperatures of iron–carbon alloys and steels is shown.

Figure 3 also shows the approximate carbon ranges of iron–carbon alloys and steels in which two quite different morphologies of martensite develop. Examples of the two morphologies, lath and plate, are shown in **Figure 4**. The terms *lath* and *plate* are based on the shapes of the martensitic crystals: lath or board-shaped for the martensite that forms in low- and medium-carbon steels, and plate-shaped for the martensite that forms in high-carbon steels (*1*,*13*–*16*). However, in addition to the shapes of the crystals, there

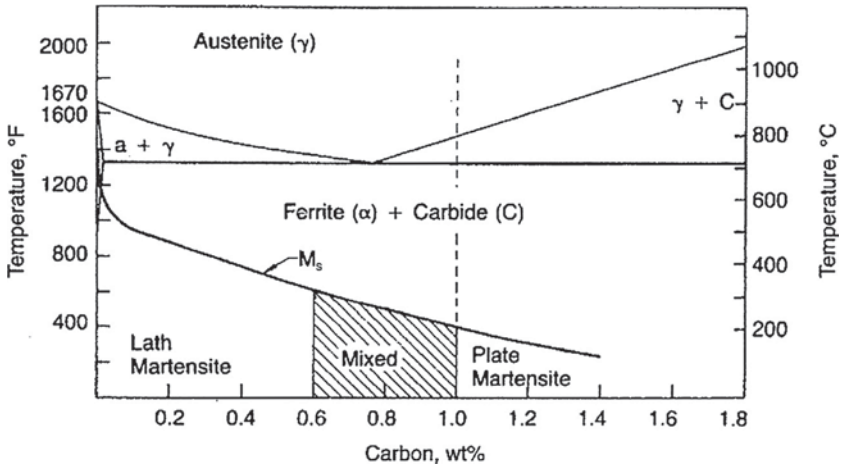

Figure 3 Schematic diagram of M_s temperatures as a function of austenite carbon content superimposed on the iron–carbon diagram. Also shown are the approximate ranges of carbon content in which lath and plate martensite morphologies develop.

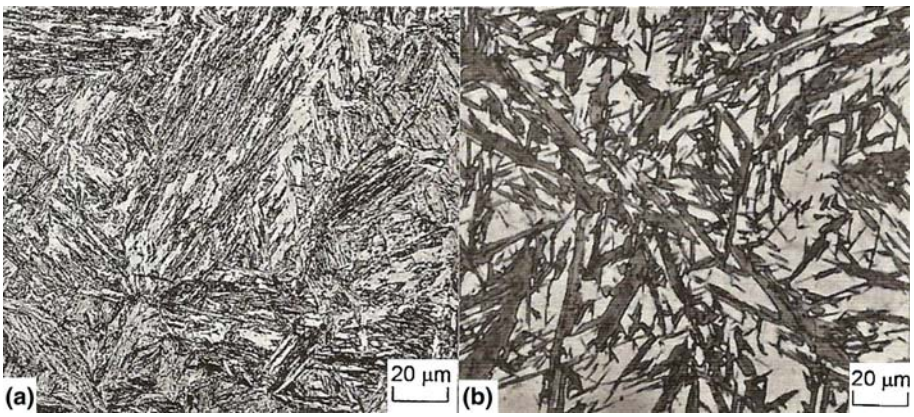

Figure 4 (a) Lath martensite in 4130 steel quenched to martensite and tempered at 150 °C and (b) plate martensite in the high-carbon case of a carburized steel. The martensite plates etch dark, and the intervening white areas are retained austenite. Light micrographs, nital etches.

are other significant differences in the two types of martensite morphologies. Lath martensite crystals are very fine. **Figure 5** shows the distribution of lath widths, as determined by electron microscope measurements of replicas and thin foil samples, in an iron-0.2% carbon alloy (*17*). The dashed line marks the 0.5 micron resolution of the light microscope; thus, the figure shows that the widths of most of the martensite crystals are finer than this resolution limit. In contrast, crystals of plate martensite tend to be much larger and are often readily observable in the light microscope, as demonstrated in **Figure 4**.

In addition to the differences in the shape and sizes of the crystals that form in lath and plate martensite, there are many other associated differences in the two types of martensitic microstructures: retained austenite contents, crystal distributions, and substructures within the crystals. As demonstrated in **Figure 4**, plate martensitic microstructures have large amounts of retained austenite, a consequence of low M_s temperatures and reduced temperature differences to drive the transformation to martensite. Retained austenite is also present in lath martensitic microstructures, but in smaller amounts than in high-carbon alloys and steels. The austenite is retained in thin layers between parallel crystals of martensite and therefore, as is the case for most of the martensite crystals themselves, is not resolvable in the light microscope. Interlath retained austenite in lath martensites is also a function of carbon content and may vary from 2% in 4130 steel, which contains nominally 0.30% carbon (*18*) to 9% in 5160 steel, which contains nominally 0.60% carbon (*19*).

The distributions of martensite crystals in the austenite grains in which they form are also quite different in lath and plate martensitic microstructures. In plate martensites, the crystals are nonparallel and form zigzag arrangements, as shown in

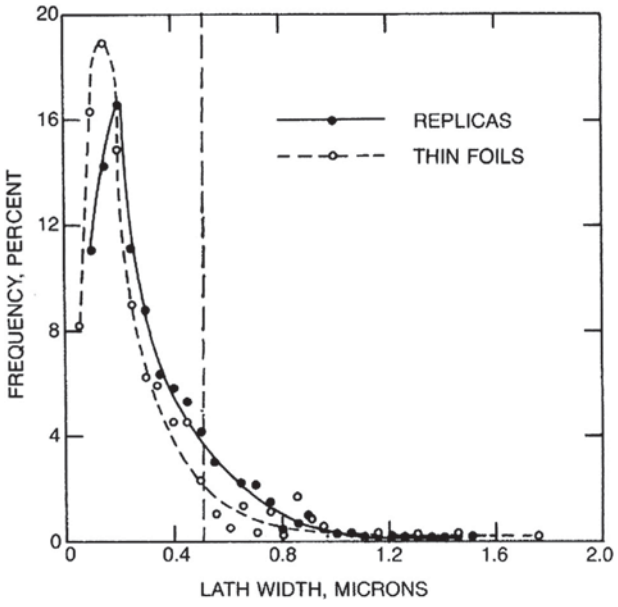

Figure 5 Distribution of martensite crystal widths in lath martensite in an iron-0.2% carbon alloy. The vertical dashed line marks the resolving power of the light microscope. Reproduced from Apple, C. A.; Caron, R. N.; Krauss, G. Packet Microstructure in Fe-0.2 pct Carbon Martensite. *Metall. Trans.* **1974**, *5*, 593–599.

Figure 4(b). The latter arrangements are due to irrational habit planes such as $\{259\}_A$, which can have up to 24 different variants or orientations in austenite (20). In contrast, the fine martensite crystals in lath martensitic microstructures form parallel to one another, as shown in Figure 4(a) and may have the same orientation in regions termed blocks (21) or may have $\{557\}_A$ habit planes closely clustered around a given $\{111\}_A$ in regions termed packets (13–15). There are only four variants or orientations of $\{111\}$ planes in a given austenite crystal; therefore, the $\{557\}$ crystals in a lath martensitic microstructure appear to be arranged with much more order than those in plate martensite. Each austenite grain may transform to several packets: thus the finer the austenitic grain size, the finer the packet size (22).

Not shown in Figure 4 is the fine structure or substructure within the martensite crystals, the elements of which are nanometer-sized and much finer than resolvable in the light microscope. In plate martensite, plastic accommodation as required by the martensitic shear transformation is largely accomplished by very fine twins, or combinations of twins and dislocations, consistent with the fact that twinning is a low-temperature deformation mode. Lath martensite crystals form at higher temperatures, where deformation is effectively accomplished by the linear crystal defects termed *dislocations*, and very high dislocation densities within lath martensite crystals, as high as 10^{12} cm^{-2} have been estimated (23). There is also evidence that the dislocation densities in lath martensite crystals increase with carbon content (24–26), a factor that contributes to increases in strength of low-temperature-tempered low- and medium-carbon steels with increasing carbon content, as discussed below.

12.11.2.2 Tempered Martensitic Microstructures

As noted earlier, almost all steels quenched to martensite are tempered, a final heat-treatment step that produces the final properties and microstructures for specific applications. Tempering may be performed at any temperature below the temperature at which austenite begins to form in a given steel. That temperature is defined as the lower critical temperature on heating, Ac_1, and is 727 °C for iron–carbon alloys. Alloying elements such as Ni and Mn lower Ac_1 and Cr and Mo raise Ac_1 temperatures. The large range of possible tempering temperatures produces a wide range of microstructures and properties, as shown in Figure 1. A number of review papers have been published to document the evolving understanding of the changes produced by tempering (27–31).

The most stable microstructure of steels at room temperature is a combination of a coarse-grained, carbon-free, body-centered cubic ferrite matrix with dispersed spherical cementite particles, a microstructure referred to as a spheroidized microstructure. Coarse grains reduce the grain boundary area, and spheroidization minimizes the interface area per unit volume of particles – both factors that reduce energy and promote stability. In contrast, as-quenched martensitic microstructures, as described above, are highly unstable by virtue of supersaturation with carbon and other alloying elements, fine martensite crystal sizes and associated high-crystal boundary areas, retained austenite, and high densities of crystal imperfections. Increasing time–temperature tempering intensity makes possible the continuous diffusion-controlled transition of the martensitic microstructures to eventually stable ferrite-carbide microstructures.

Although there is considerable carbon atom rearrangement in martensite, namely, the segregation of carbon to dislocation strain fields, during quenching and near room-temperature aging (23,32,33), the major structural and property changes of commercial interest produced by tempering are based on the formation of carbides, the transformation of retained austenite, and changes in matrix substructure. These changes have been classified in a system with four stages developed largely by Morris Cohen and his colleagues (34–37). Stage 1 is based on very fine-scale precipitation of transition carbides in response to the supersaturation of the as-quenched martensite, with carbon in the tempering temperature range of 100–200 °C. The carbide is not the more stable cementite, Fe_3C, (θ), and has been identified as epsilon carbide, $Fe_{2.4}C$, (ε), with a hexagonal crystal structure (38), or eta carbide (η), Fe_2C, with an orthorhombic crystal structure (39,40).

Figure 6 shows transition carbides in a portion of a large crystal of lath martensite in 4130 steel tempered at 150 °C. The transition carbides, 2–5 nm in size, appear as very fine, bright features, in very high density, in this highly magnified transmission electron micrograph. Also shown, as bright elongated features parallel to the horizontal axis of the micrograph, are regions of interlath retained austenite, not shown is the high density of dislocations between and on which the transition carbides have precipitated within the martensite crystals.

Stage 2 tempering is associated with the transformation of retained austenite to cementite and ferrite. Figure 7 shows the progress of this transformation as a function of tempering temperature in two medium-carbon, low-alloy steels (18). As shown, the transformation of retained austenite and cementite formation typically occurs in most steels at tempering temperatures between 200 and 300 °C. In steels with high silicon content, over 1.00%, the transformation is deferred to higher temperatures because silicon has very low solubility in cementite (41,42). Thus the formation of cementite cannot proceed because diffusion of silicon, a very sluggish process, must occur from potential sites for cementite nucleation.

In Stage 3 tempering cementite precipitation replaces transition carbide distributions, at tempering temperatures beginning at 200 °C (43), and the carbon content of the martensite drops to effectively zero, producing a matrix structure of body-centered cubic ferrite. The early stages of Stage 3 overlap Stage 2, but Stage 3 proceeds to much higher tempering temperatures as the cementite distributions coarsen and the dislocation contents are reduced by recovery mechanisms and the as-quenched martensite crystals coarsen. Depending on alloy content, cementite coarsening can be slowed because of incorporation of alloying elements into the cementite or the formation of alloy carbides by the carbide-forming elements molybdenum and chromium (44). The latter changes are sometimes referred to as fourth-stage tempering, and require high tempering temperatures and long times, typically at temperatures around 600 °C, because of the sluggish diffusion of the substitutional alloying elements Cr, Mo, and Mn. Figure 8 shows the microstructure of martensite in 4130 steel tempered at 650 °C. The parallel alignment of martensite crystals persists, but

Figure 6 Transition carbides (the fine bright features) within a crystal of lath martensite and interlath retained austenite (the elongated bright features) in 4130 steel tempered at 150 °C. Dark-field transmission electron micrograph taken with diffracted beams from transition carbides and retained austenite. Courtesy of Mauro Losz.

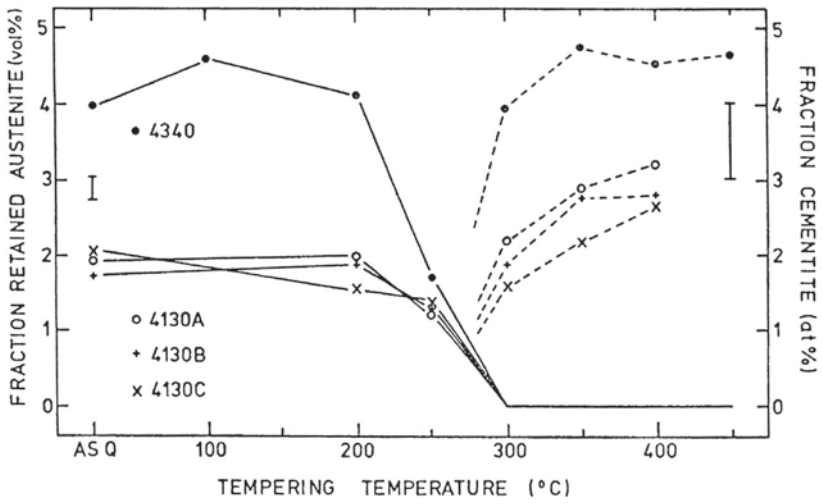

Figure 7 The effect of tempering on retained austenite and cementite contents in 4130 and 4340 steels as determined by Mossbauer spectroscopy (*18*).

distributions of coarse carbide particles within the martensite crystals and at the interfaces between the martensite crystals have replaced the fine transition carbide distributions shown in Figure 6. The original martensite crystals have coarsened, and the dislocation densities within the crystals have been substantially reduced by recovery mechanisms (*1,45*).

12.11.3 Deformation, Strengthening, and Mechanical Properties of Quench and Tempered Martensitic Microstructures

As noted earlier, martensitic steels can be tempered at any temperature below Ac_1, but commercially two major tempering temperature ranges are typically used. Low-temperature tempering (LTT) is applied between 150 and 200 °C and produces very high strengths based on the fine structure shown in Figure 6. High-temperature tempering (HTT) is applied very roughly between 500 and 650 °C, depending on desired properties and alloying, and produces microstructures similar to those shown in Figure 8.

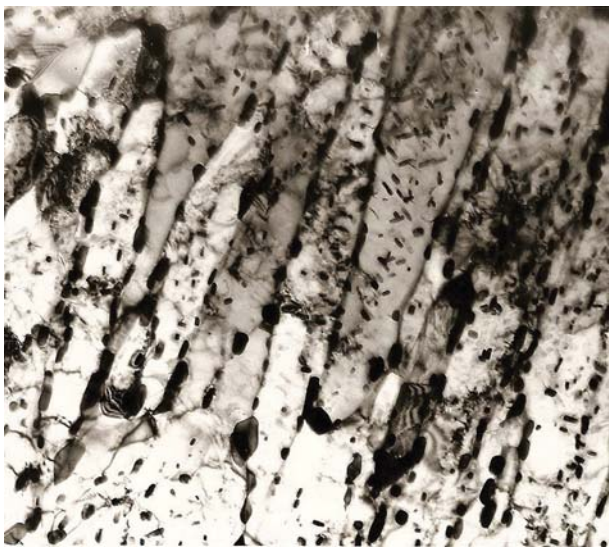

Figure 8 Microstructure of tempered martensite produced by tempering 4130 steel at 650 °C. Bright field transmission electron micrograph. Courtesy of Rick Woldow.

The dominant phase formed in quenched steel is martensite, in the form of very fine crystals, but many other components make up the microstructural systems of quench and tempered microstructure. Table 1 lists these features, their influence on strengthening, and the effect of tempering on each microstructural component (*46*). Some features in LTT microstructures are completely replaced during HTT, and some features are associated with embrittlement phenomena rather than strengthening. The various microstructures, their influence on mechanical performance, and the importance of carbon content are discussed below.

Figure 1 shows the great range of deformation behavior and mechanical properties that can be produced in a single medium-carbon steel as a function of quenching and tempering. However, the deformation response of quenched and tempered steels is very much dependent on the carbon content of a steel and its austenite prior to quenching (*47–49*). For example, Figure 9 shows

Table 1 Microstructural components in quenched and tempered low- and medium-carbon steels, their effect on mechanical behavior, and the effect of increased tempering[a]

Microstructural component	*Mechanical contribution*	*Effect of increasing tempering*
Inclusions	No strengthening; fracture initiation sites	None
Retained carbides after austenitizing	Microvoid initiation sites during ductile fracture	None during LTT; coarsening during HTT
Dislocations in martensite crystals	Major strengthening component in LTT steels	Major decreases due to recovery mechanisms
Eta/epsilon transition carbides in martensite crystals	Major strengthening component in LTT steels	Replaced by cementite after tempering above 200 °C
Martensite crystal boundaries	Minor strengthening component in LTT steels	Residual martensite crystal boundaries are a major source of HTT strengthening
Retained austenite	Stress-induced transformation to martensite in LTT steels; above 200 °C transforms to carbides and causes tempered martensite embrittlement	Transforms to cementite and ferrite above 200 °C; silicon retards cementite formation
Martensite packet and/or block boundaries	Minor strengthening component in LTT steels	Intrapacket structure coarsens with increasing tempering
Prior austenite grain boundaries	Minor strengthening component; sites for impurity and alloying atom segregation and intergranular fracture	Largely unchanged unless tempered martensite recrystallizes at very high HTT
Cementite and/or alloy carbides formed during tempering	In low-alloys steels Mn, Cr, and Mo retard coarsening and retard strength decreases during HTT tempering	During HTT, carbides contribute dispersion strengthening, may precipitate, and may cause secondary hardening
Nitrides, carbides, and/or carbo-nitrides formed by V, Nb, or Ti	May retard austenite grain growth during austenitizing; retard coarsening during HTT tempering	May precipitate during HTT, may contribute secondary hardening

[a]Reproduced from Krauss, G. Martensitic Microstructural Systems in Carbon Steels and Susceptibility to Hydrogen Embrittlement. *AIST Trans.* **2011**, *8*, 188–195.

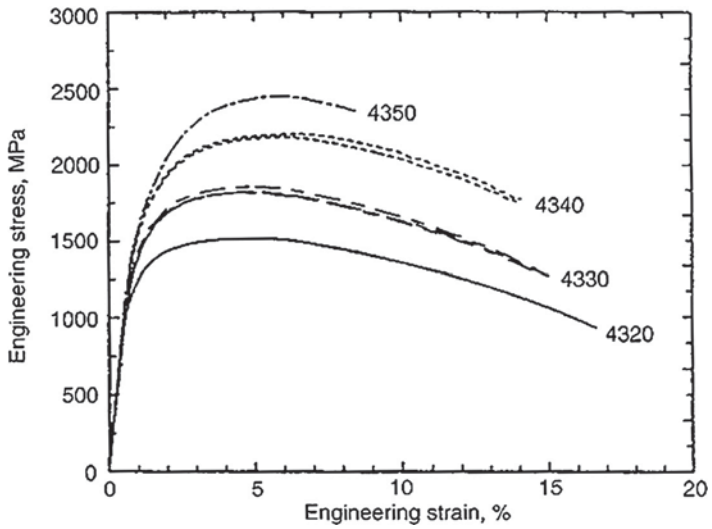

Figure 9 Engineering stress–strain curves for 43xx steels with varying carbon contents after tempering at 150 °C for 1 h. Courtesy of J. A. Sanders and, Krauss, G. *Steels: Processing, Structure, and Performance*; ASM International: Materials Park, OH, 2005.

engineering stress–strain curves for four low-alloy 43xx steels identical in alloy content but varying in carbon content from 0.20% in the 4320 steel to 0.50% in the 4350 steel. All specimens were identically tempered in the LTT range at 150 °C for 1 h. The steels all show continuous yielding, but ultimate tensile strengths and total ductilities of the various steels are very much dependent on carbon content: the higher the carbon content, the higher the ultimate tensile strengths, as developed by higher rates of strain hardening prior to necking.

The dependence of strain hardening on carbon content correlates with the fine structures of LTT martensite crystals as shown in Figure 6. The higher the carbon content, the higher the densities of fine transition carbides and dislocations in martensite crystals and the higher the shear stresses required to generate dislocation motion and the generation of dislocations that sustain plastic deformation. In LTT microstructures tempered in the first stage of tempering, retained austenite is thermally stable, but during deformation it mechanically transforms to martensite at very low strains, even below those at which yield strengths are typically measured, contributing to very high initial strain hardening rates (*50*,*51*).

The strain hardening process is described by the following equations developed by Kuhlmann-Wilsdorf (*52*).

$$\tau = \tau_0 + \textbf{const}\ \mathbf{Gb/l} = \tau_0 + \alpha \mathrm{Gb}\ \boldsymbol{\rho}^{1/2} \qquad [5]$$

where τ is the shear stress to move dislocations at a given flow stress, τ_0 is the shear stress for dislocation motion without other obstacles, **G** is the shear modulus, **b** is the Burgers vector of active dislocations, **l** is the active dislocation length at a given flow stress, $\boldsymbol{\rho}$ is the dislocation density, and constants are noted. The key relationship in these equations that explains strain hardening is the relationship between **l** and the fine structure of martensite. The smaller the **l**, the higher the shear stresses required at a given flow stress to move that dislocation length. Higher transition carbide densities reduce **l**, as do higher densities of dislocations, since more dislocation intersections act as pinning points and reduce **l**. Thus, higher flow strengths are produced in higher carbon martensites that have higher transition carbide densities and higher dislocation densities (*24*–*26*). As plastic deformation proceeds, more and more dislocations are generated, and their intersections continually reduce **l**, producing increases in flow stress during uniform plastic deformation. Eventually, strain hardening cannot keep up with applied stress, uniform plastic deformation within the gauge lengths of tensile specimens ceases, and necking instability occurs at the ultimate tensile strength (*53*,*54*). Deformation continues during postuniform strain in the neck and initiates microvoid formation around hard particles such as inclusions and carbides, leading eventually to ductile fracture surfaces characterized by coalesced microvoids. An example of ductile fracture is shown later as Figure 14 of this chapter.

Figure 9 shows clearly that the high tensile strengths in LTT microstructures with higher carbon contents are due to increased rates of strain hardening. Also shown are the very much reduced amounts of postuniform deformation in the higher carbon steels, a result explained by determining the true stress at fracture by dividing applied load at fracture by the reduced specimen area in the neck. Such calculations show that all LTT samples regardless of carbon content have about the same fracture strength of about 4000 MPa (*55*). Thus, the lower carbon steels need much more postuniform necking strain to reach that fracture stress, while the high-carbon LTT steels, by virtue of their high strain hardening rates and high ultimate tensile strengths, need much less post-uniform necking strain to reach fracture.

Microstructural changes during tempering are a function of both time and temperature. Although tempering time is often held constant during experimental studies, typically 1 h, Figures 10 and 11 show hardness and ultimate tensile strengths, respectively, for LTT 43xx steels as a function of a temperature–time parameter (*55*). Such parameters are referred to as Hollomon–Jaffe

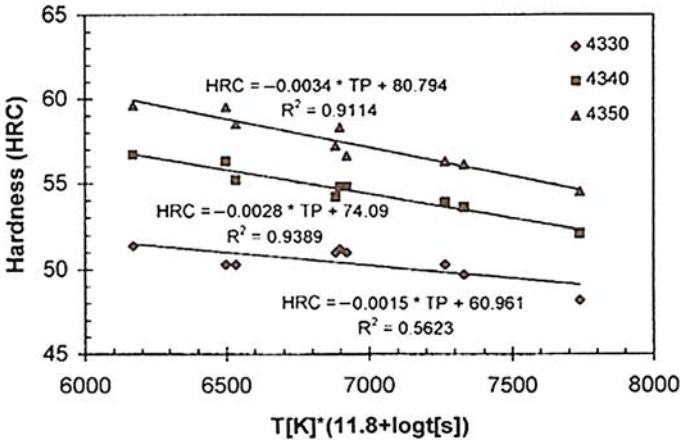

Figure 10 Hardness as a function of a time–temperature parameter for LTT 43xx steels. Reproduced from Saeglitz, M.; Krauss, G. Deformation, Fracture and Mechanical Properties of Low-Temperature-Tempered Martensite in SAE 43xx Steels. *Metall. Mater. Trans. A* **1997**, *28A*, 377–387.

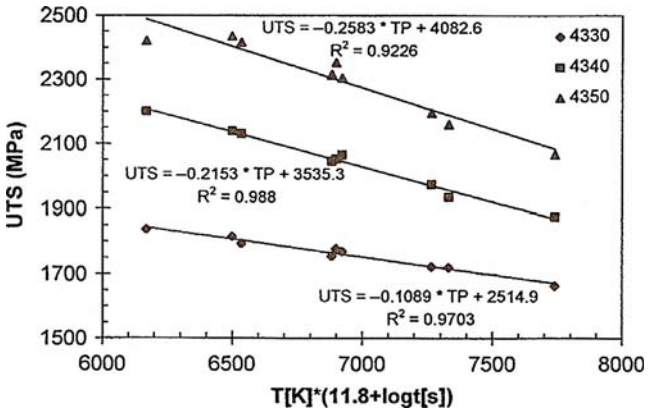

Figure 11 Ultimate tensile strengths as a function of a time–temperature parameter for 43xx LTT steels. Reproduced from Saeglitz, M.; Krauss, G. Deformation, Fracture and Mechanical Properties of Low-Temperature-Tempered Martensite in SAE 43xx Steels. *Metall. Mater. Trans. A* **1997**, *28A*, 377–387.

parameters, and the log term for time, although of importance, reflects the much smaller effect of time, compared to temperature, on the diffusional processes that occur during tempering. **Figures 10 and 11** were obtained by testing specimens tempered in the 150–200 °C LTT range for times of 10 min, 1 h, and 10 h. Temperature in the parameter is in Kelvin, time in seconds. Again, the strong effect of carbon content is shown, with the consistently higher hardness and strengths of the 4340 and 4350 steels relative to those of the 4330 steel. However, as tempering intensity in Stage 1 tempering increases, hardness and strength decrease, as the dislocation densities decrease and the transition carbides coarsen with increasing LTT tempering, increasing the **l** parameter in eqn [5].

The strength of martensitic microstructures decreases significantly after HTT tempering due to the microstructural changes noted in **Figure 8**. Dislocation contents are significantly reduced due to recovery mechanisms, and the very fine transition carbides are replaced by distributions of coarser cementite particles within and at the boundaries of tempered martensite crystals. Strengthening in these microstructures is now controlled by the small sizes of the residual martensite crystals, that is, grain boundary strengthening, and dispersion strengthening by cementite particles within the tempered martensitic matrices. As is shown in **Figure 1**, the high rates of strain hardening typical of LTT are now significantly reduced. **Figure 12** demonstrates these changes in strain hardening, as reflected by the difference between yield strength and tensile strength as a function of tempering of martensitic 4340 steel.

Alloying elements, especially the carbide-forming elements manganese, molybdenum, and chromium, at high tempering temperatures greatly reduce the rate of softening produced by microstructural coarsening (*56*). During LTT, microstructural changes are primarily controlled by carbon diffusion, but during HTT the carbide-forming elements are able to diffuse and are incorporated into cementite, reducing coarsening. Fine-alloy carbides may also precipitate. **Figure 13** shows the effect of increasing amounts of molybdenum on increasing hardness and reducing softening during HTT (*57*). The hardness peaks centered around 600 °C for samples tempered for 1 h are due to the precipitation of Mo_2C and are referred to as being produced by secondary hardening. Typically, low-alloy carbon steels contain 0.50% molybdenum or less, with larger amounts sometimes added to tool steels. Nevertheless, **Figure 13** illustrates the changes that may develop during high-temperature tempering due to alloying.

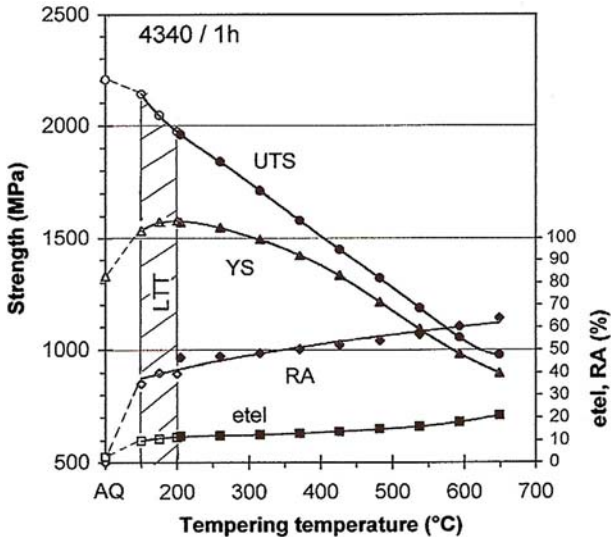

Figure 12 Mechanical properties of quenched 4340 steel as a function of tempering temperature. Reproduced from Krauss, G. *Steels: Processing, Structure, and Performance*; ASM International: Materials Park, OH, 2005.

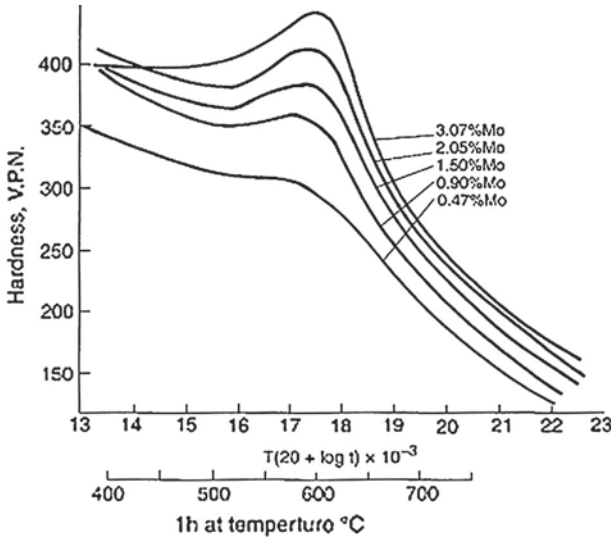

Figure 13 Effect of molybdenum alloying on hardness changes during HTT. Reproduced from Rollason, E. C. *Fundamental Aspects of Molybdenum in Transformation of Steel*. Climax Molybdenum, London, undated.

12.11.4 Fracture and Low-Toughness Phenomena in Carbon and Low-Alloy Carbon Steels

In addition to strength, toughness or fracture resistance is an important characteristic of hardened steels. Although the strength desired may vary greatly depending on requirements for yield strength, wear resistance, or fatigue resistance, good performance of quench and tempered steels is based on plastic deformation that leads to ductile fracture. Thus, although steels may be selected based on fatigue resistance (typically, one-half of the ultimate tensile strength) or load-carrying capacity based on resistance to plastic deformation or changes in dimensions as measured by yield stress, should those design stresses be exceeded, the ability to deform and resist fracture by ductile mechanisms is an important characteristic of safe steel performance. As discussed above, plastic deformation produces strain hardening that leads to ultimate tensile strength prior to the initiation of ductile fracture by microvoid nucleation, growth, and coalescence at hard particles and inclusions. Figure 14 shows the ductile fracture surface of 4350 steel quenched and tempered at 150 °C. In this example, many small microvoids have formed around small carbide particles, about 50 nm in size, that were not dissolved during austenitizing prior to quenching.

Although there are a wide range of tempering conditions that produce good combinations of strength and fracture resistance in hardened steels, there are chemical compositions and tempering conditions that produce microstructures sensitive to reduced toughness and brittle fracture behavior. In such microstructures, fracture develops with limited or no plastic deformation. Figure 15

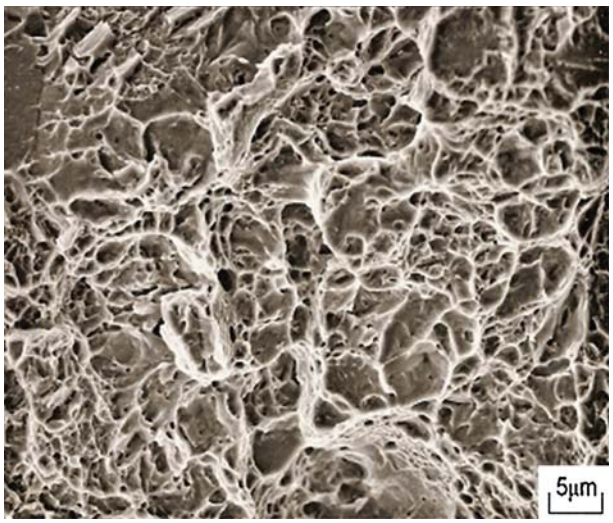

Figure 14 Ductile fracture surface after tensile testing of 4350 steel quenched and tempered at 150 °C. SEM micrograph.

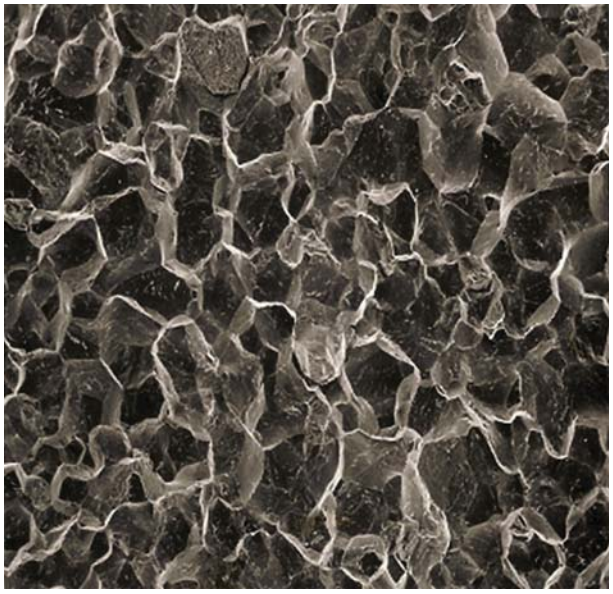

Figure 15 Intergranular brittle fracture in 52100 steel austenitized at 965 °C, oil quenched and tempered at 250 °C. SEM micrograph, 100×. Courtesy of D. Yaney.

shows an example of brittle intergranular fracture that is characteristic of many of the embrittlement mechanisms described below. The grain boundaries along which the fracture occurs are the austenite grain boundaries produced during austenitizing, and in view of the fact that the austenitic grain structure no longer exists after quenching, are referred to as prior austenite grain boundaries. Figure 15 shows intergranular fracture in a 52100 steel austenitized at 965 °C, a temperature much higher than normally used for this steel.

Figure 16 shows a fracture map based on combinations of tempering temperature and carbon content of quenched carbon and alloy steels. The various fracture modes develop as a result of tensile or bending loads at around room temperature. At subzero temperatures, screw dislocations in body-centered tetragonal and body-centered cubic crystal structures lose their ability to cross slip. Therefore, steels with such structures undergo a transition from ductile to brittle cleavage fracture with decreasing temperature (*58*). Subzero ductile to brittle cleavage transition temperatures are not shown in Figure 16, but would be a consideration of steels for application at severe low temperatures.

The medium-carbon LTT steels that develop the highest strengths, as described relative to Figure 9, show good ductile fracture resistance based on their carbon content. However, if the carbon content of an LTT steel exceeds 0.5%, as-quenched and as-quenched and low-temperature-tempered microstructures are highly sensitive to brittle intergranular fracture (*47,49,59*). This embrittlement is termed **quench embrittlement** because no tempering is required. The high-carbon steels are embrittled by carbon

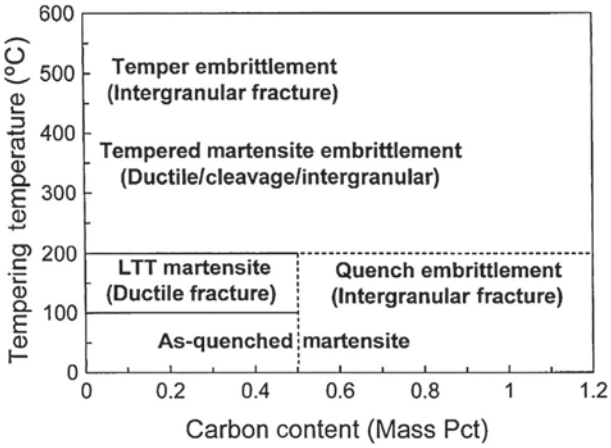

Figure 16 Fracture modes a function of tempering temperature and austenite carbon content of martensitic carbon and alloy steels subjected to tensile and bending loadings. Reproduced from Krauss, G. Deformation and Fracture in Martensitic Carbon Steels Tempered at Low Temperatures. *Metall. Mater. Trans. A* **2001**, *32A*, 861–877.

and phosphorus segregation to austenite grain boundaries during austenitizing and cooling, and may be subject to quench cracking as well as cracking under loads below typical ultimate tensile strengths. Despite the sensitivity to quench embrittlement, high-carbon LTT steels can be hardened and used if subjected to nontensile loading or if case hardened, as by carburizing, by which surface compressive loads that offset applied tensile loads are produced.

Another important way to minimize susceptibility to quench embrittlement in high-carbon steels is to intercritically austenitize in the carbide/austenite phase field. The resultant undissolved carbides maintain fine austenite grain sizes and reduce the carbon content of the austenite, reducing grain boundary fracture sensitivity. Intercritical austenitizing is widely used for high-carbon bearing steels; one reference reports that the carbon content of intercritically heated austenite in a 1.00% carbon steel may be as low as 0.55%, with the balance of the carbon tied up in carbide particles (*60*). Even in lower carbon steels, such as AISI 5160 steel containing 0.60% carbon, low austenitizing temperatures that do not dissolve all carbides may minimize susceptibility to intergranular quench embrittlement fractures (*61*).

Tempering at temperatures between about 300 and 400 °C reduces strength and hardness below those produced by tempering at lower temperatures, and would be expected to increase ductility and toughness. However, this is not the case because of the embrittlement phenomenon referred to as **tempered martensite embrittlement** (*62–64*). This change in fracture resistance is caused by the transformation of retained austenite during the second stage of tempering, as shown in **Figure 7**. Depending on steel carbon content, the fracture may be intergranular, transgranular cleavage, or ductile. **Figure 17** shows the energy absorbed by high strain rate fracture of Charpy V-Notch (CVN) specimens as a function of tempering temperature for several low-alloy steels. The 41xx steels contain nominally 1% Cr and 0.20% Mo and carbon contents of 0.30, 0.40, and 0.50% as shown in (*65*). The 52100 steel contains nominally 1.0% carbon and 1.50% Cr (*66*). Low phosphorous levels in the 41xx steels were 0.002% and high levels 0.02%. In the 52100 steel, the low P level was 0.009% and the high was 0.023%. The impact energy of as-quenched microstructures is low but improves significantly in samples tempered at 200 °C, that is, tempered in the first stage of tempering where retained austenite is still stable. However, samples tempered above 200 °C undergo the decrease in impact toughness that is associated with tempered martensite embrittlement. New coarse carbides are produced by the transformation of retained austenite. If the carbon content is high enough, as in the 4140 and 4150 steels, and with the presence of phosphorus, the embrittlement occurs by intergranular cracking along prior austenite grain boundaries. In the absence of phosphorus, the high-carbon content of the retained austenite produces coarse interlath carbides and causes transgranular cleavage fracture through the martensitic microstructure (*62*). In the 4130 steel, the carbon content is not high enough to cause intergranular fracture, but the new carbide particles produced by the transformation of retained austenite introduce additional microvoid initiating sites that lower toughness (*64*).

An important effect shown in **Figure 17** is the very strong effect of carbon on the fracture resistance of quench and tempered steels. Increasing carbon strongly drives down impact energy in all tempered microstructures, even when fracture is ductile, as is the case after tempering at 200 °C. This result is attributed to the very high strain hardening rates of the LTT substructures and consequently the limited energy-absorbing deformation required to reach fracture stresses in the high-carbon steels. This effect is so strong in the LTT 52100 steel that the absorbed CVN energy in samples tempered at 200 °C is little different from that of 52100 samples tempered in the tempered martensite embrittlement temperature range.

Temper embrittlement is arguably the oldest recognized embrittlement unique to steel composition, heat treatment, and service parameters, with references dating back to the late 1800s (*67*). It has been known that this embrittlement developed only after heating in or through the temperature range 375–575 °C, that alloy steels were most sensitive, that fracture was brittle and along prior austenite grain boundaries, and that phosphorus, antimony, tin, and arsenic were thought to be associated with the embrittlement. **Figure 18** shows the increase in ductile to brittle transition temperature with increasing time and temperature in the temper embrittlement range (*67,68*). The times for substantial temper embrittlement are long, consistent with either slow cooling

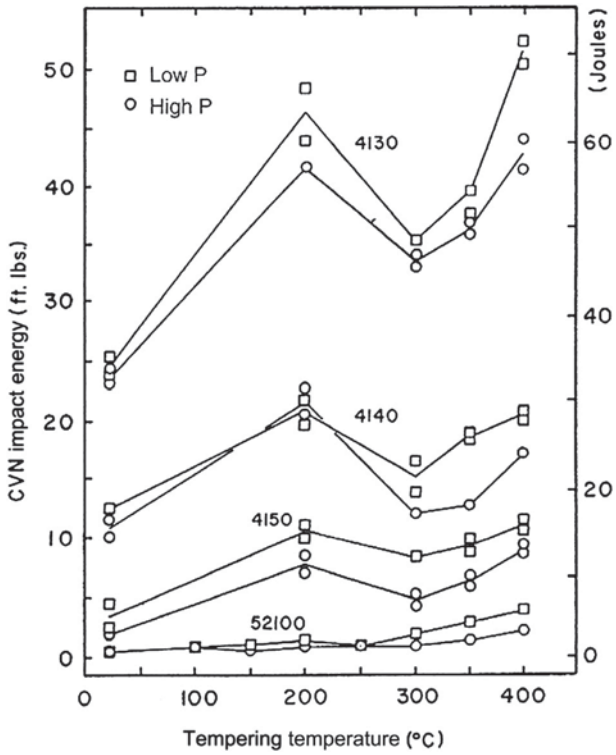

Figure 17 Room-temperature impact toughness as a function of tempering temperature in several low-alloy steels. Data from Zia-Ebrahimi, F. A Study of the Mechanisms of Tempered Martensite Embrittlement in Low-Alloy Medium-Carbon Steels. Ph.D. Thesis, Colorado School of Mines, Golden, Colorado, 1982 and Yaney, D. L. The Effects of Phosphorus and Tempering on the Fracture of AISI 52100 Steel. M.S. Thesis, Colorado School of Mines, Golden, Colorado, 1987.

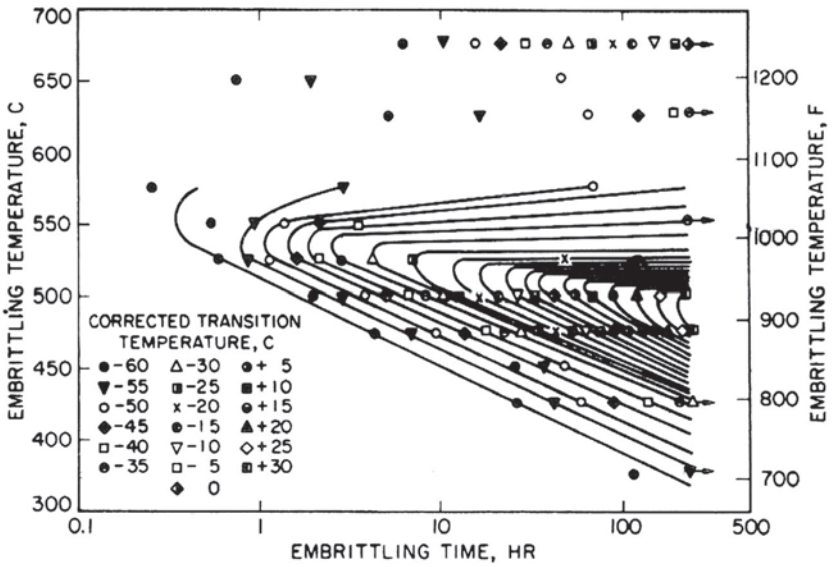

Figure 18 Temper embrittlement temperature and time ranges. The curves show isothermal curves for increasing ductile to brittle transition temperatures for a 0.39% C steel containing 0.79% Mn, 1.26% Ni, and 0.77% Cr. After Jaffe, L. D.; Buffum, D. C. Isothermal Temper Embrittlement. *Trans. ASM* **1950**, *42*, 604–618, as published in McMahon, C. J. Jr, Temper Brittleness – An Interpretive Review. In *Embrittlement in Steel*, Special Technical Publication No. 107; American Society for Testing and Materials, 1968, pp 127–167.

and heating of heavy sections or service at high temperatures, as for example large shafts and rotors for power generating equipment. As with all of the intergranular embrittlement mechanisms, no features are detectable at prior austenite grain boundaries in light and scanning electron microscopes, and Auger Electron Spectroscopy with its high-depth resolution was necessary to identify chemical elements on grain boundary fracture surfaces. It was found that not only were impurity elements such as phosphorus present in very shallow, atomic-sized layers at grain boundaries, as is the case for the quench and tempered martensite embrittlements, but also substitutional elements such as nickel were segregated to the boundaries (*69*). The fact that large substitutional elements, with their low diffusivities, must segregate accounts for the long times required for temper embrittlement to develop. More recently, the elements manganese and silicon have also been linked to temper embrittlement (*70*).

Although **hydrogen embrittlement** is not shown in **Figure 16**, it may impact every heat-treated condition and steel shown. Hydrogen may be introduced into steel by steelmaking, welding, electroplating, exposure to hydrogen sulfide containing environments, and other atmospheric conditions such as exposure to seawater. Critical amounts of hydrogen may not only make steels more susceptible to intergranular brittle fractures, as described relative to **Figure 16**, but may also limit plasticity and initiate brittle transverse cracks, depending on steel chemistry and microstructure. The pervasive nature of hydrogen fracture has led to a very large hydrogen embrittlement literature, only a small part of which is cited here, and to the development of a number of strategies that minimize susceptibility: vacuum degassing during steelmaking (*71*), slow cooling of large sections of steel (*71*), baking treatments of electroplated components (*72*), and HTT to reduce sensitivity to hydrogen sulfide steel products exposed to sour oil and gas environments (*73*). Nevertheless, hydrogen embrittlement remains a critical limitation for some applications of quench and tempered steels.

Although hydrogen has negligible solubility in body-centered cubic ferrite or body-centered tetragonal martensite at room temperature (*74*), two factors cause hydrogen to build up to, remain at critical levels, or contribute in ways that cause unexpected fracture: diffusion of hydrogen to areas of localized tensile stress, and microstructural trapping sites for hydrogen. The diffusion of hydrogen atoms to localized regions means that often hydrogen fractures are time dependent. **Figure 19** from the early work of Troiano and his colleagues shows a number of the features of hydrogen embrittlement of high strength quench and tempered steel (*75*). Baking was used to control hydrogen levels: The shorter the baking time, the more hydrogen retained in the specimen by cadmium plating. The specimens were notched, and the resulting stress concentration on loading caused hydrogen to diffuse to notches and initiate intergranular cracking. Thus, not only are there immediate decreases in fracture strength due to high retained hydrogen content, but there are also further reduced fracture strengths with increasing time at stress as more and more hydrogen diffuses to stressed areas at notches. For every level of hydrogen, **Figure 19** shows that there is a stress below which fracture will not occur. This characteristic has led to the term *static fatigue curves* for this behavior, analogous to curves with endurance limits for high-cycle mechanical fatigue. With increasing baking time, more hydrogen diffuses from the specimens, and it takes longer, hours or

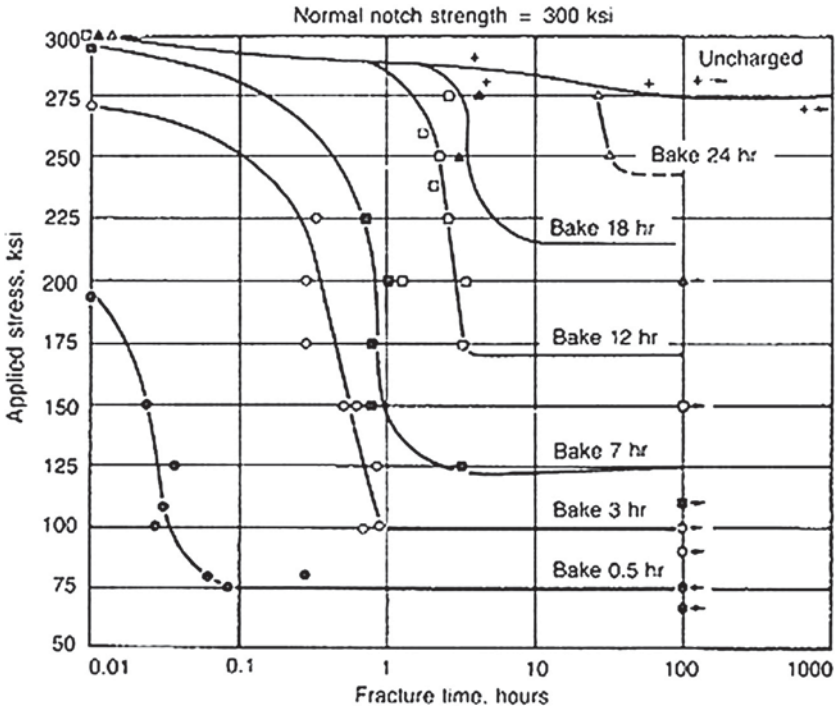

Figure 19 Static fatigue curves for quench and tempered 4340 steel notched specimens charged with hydrogen, cadmium plated, and baked for various times at 150° C to reduce hydrogen content. Reproduced from Johnson, H. H.; Morlet, J. G.; Troiano, A. R. Hydrogen, Crack Initiation, and Delayed Failure in Steel. *Trans. TMS-AIME* **1958**, *212*, 528–536.

more, for hydrogen to reach critical fracture levels. Eventually, hydrogen is reduced to harmless levels, providing the basis for long-time baking treatments to remove hydrogen from electroplated parts (*72*).

In addition to the attraction of hydrogen to regions where the crystal lattice of the matrix tempered martensite is expanded by residual stresses, hydrogen is also attracted to microstructural and substructural features of quench and tempered steels. These features are referred to as trapping sites for hydrogen and are classified into reversible and irreversible sites (*76*). Reversible trapping sites have low-interaction energy with hydrogen, and hydrogen can attach to or leave these sites at or close to room temperature. Irreversible traps have high-interaction energy with hydrogen, and hydrogen cannot leave unless the steel is heated to much higher temperatures than room temperature. Every microstructural component of quench and tempered martensitic systems shown in **Table 1** may be a trapping site for hydrogen (*46*). For example, dislocations are reversible sites and strongly attract hydrogen because of tensile stresses around the dislocation cores. Resulting concentrations of hydrogen not only cause low-stress fracture but also prevent cross slip and limit plastic deformation and ductility (*77,78*). In contrast, inclusions and carbide particles are considered to be irreversible hydrogen trapping sites (*71,76*). Research regarding hydrogen embrittlement is ongoing, and the reader is encouraged to search the literature if hydrogen is a factor in the application of a potential heat-treated steel.

12.11.5 Summary

The above discussion has described the microstructure and mechanical performance of carbon and low-alloy carbon steels produced by quenching to martensite and tempering. Very high strengths and moderate toughness can be produced by quenching and LTT at temperatures between 150 and 200 °C, and moderate strengths and very high toughness can be produced by quenching and HTT tempering at temperatures between 500 and 650 °C. These combinations of properties are produced by microstructures and substructures that control dislocation motion, dislocation multiplication, and strain hardening that produce the yield and ultimate tensile strengths required for demanding applications. Limitations to load-carrying capability relative to fracture by ductile and brittle mechanisms dependent on steel chemistry and heat-treatment conditions are also directly related to microstructure and fracture.

Although considerable information and well-established guidelines are available for the selection and manufacture of high-performance heat-treated steels, considerable further study to optimize structure and performance would be beneficial. Weight reduction, higher performance, safe application, and economy are essential current and future requirements for load-carrying heat-treated steels. Relative to satisfying these needs, the many other chapters of this volume on thermal engineering provide valuable information regarding the achievement of optimum performance by control and modeling of heat-treatment processing and the achievement of high performance not only through hardening but also through surface-hardening systems and heat treatments for economical carbon and low-alloy carbon steels. It is hoped that these interacting sets of analysis will provide the information base for the selection and manufacture of steels for ever more demanding future applications.

References

1. Krauss, G. *Steels: Processing, Structure, and Performance;* ASM International: Materials Park, OH, 2005.
2. Canale, L.C. F.; Albano, L.; Totten, G. E.; Meekisho, L. Hardenability of Steel. Vol. 12, 2014, 39–97.
3. *Bar Steels: Steel Products Manual;* Association for Iron & Steel Technology: Warrendale, PA, 2010.
4. Wayman, C. M. *Introduction to the Crystallography of Martensite Transformations;* MacMillan: New York, 1964.
5. Cohen, M. The Strengthening of Steel. *Trans. TMS-AIME* **1962,** *224,* 638–656.
6. Bilby, B. A.; Christian, J. W. The Crystallography of Martensite Transformations. *JISI* **1961,** *197,* 122–131.
7. Petty, E. R. *Martensite, Fundamentals and Technology;* Longman: London, 1979.
8. Wechsler, M. S.; Lieberman, D. S.; Read, T. A. On the Theory of the Formation of Martensite. *Trans. TMS-AIME* **1953,** *197,* 1503–1515.
9. Bowles, J. S.; MacKenzie, J. K. The Crystallography of Martensite Transformations. *Acta Metall.* **1954,** *2,* 129–137, 138–147, 224–234.
10. Cheng, L.; Bouger, A.; Keijser, De; Th, H.; Mittemeyer, E. J. Lattice Parameters of Iron-Carbon and Iron-Nitrogen Martensites and Austenites. *Scripta Metall. Mater.* **1990,** *24,* 509–514.
11. Andrews, K. W. Empirical Formulae for the Calculation of Some transformation Temperatures. *JISI* **1965,** *203,* 721–727.
12. Koistinen, D. P.; Marburger, R. E. A General Equation Prescribing the Extent of the Austenite-Martensite Transformation in Pure Iron-Carbon Alloys and Plain Carbon Steels. *Acta Metall.* **1959,** *7,* 59–60.
13. Marder, A. R.; Krauss, G. The Morphology of Martensite in Iron-Carbon Alloys. *Trans. ASM* **1967,** *60,* 651–660.
14. Marder, A. R.; Krauss, G. The Formation of Low-Carbon Martensite in Fe-C Alloys. *Trans. ASM* **1969,** *62,* 957–964.
15. Krauss, G.; Marder, A. R. The Morphology of Martensite in Iron Alloys. *Metall. Trans.* **1971,** *2,* 2343–2357.
16. Maki, T.; Tsuzaki, K.; Tamura, I. The Morphology of Microstructure Composed of Lath Martensites in Steels. *Trans. Iron Steel Inst. Jpn.* **1986,** *20,* 207–214.
17. Apple, C. A.; Caron, R. N.; Krauss, G. Packet Microstructure in Fe-0.2 pct Carbon Martensite. *Metall. Trans.* **1974,** *5,* 593–599.
18. Williamson, D. L.; Schupmann, R. G.; Materkowski, J. P.; Krauss, G. Determination of Small Amounts of Retained Austenite and Carbide in a Hardened Medium Carbon Steel by Mossbauer Spectroscopy. *Metall. Trans. A* **1979,** *10A,* 379–382.
19. Wong, J.; Matlock, D. K.; Krauss, G. Effects of Induction Tempering on Microstructure, Properties and Fracture of Hardened Carbon Steels. In *43rd MWSP Conference Proceedings,* Vol. XXXIX; ISS, 2001; pp 21–36.
20. Greninger, A. B.; Troiano, A. R. Crystallography of Austenite Decomposition. *Trans. AIME* **1940,** *140,* 307–336.
21. Marder, J. M.; Marder, A. R. The Morphology of Iron-Nickel Massive Martensite. *Trans. ASM* **1969,** *62,* 1–10.
22. Swarr, T.; Krauss, G. The Effect of Structure on the Deformation of As-Quenched and Tempered Martensite in an Fe-0.2 pct C Alloy. *Metall. Trans. A* **1976,** *7A,* 41–48.
23. Speich, G. R. Tempering of Low-Carbon Martensite. *Trans. TMS-AIME* **1969,** *245,* 2552–2564.
24. Norstrom, L.-A. On the Yield Strength of Quenched Low-Carbon Lath Martensite. *Scand. J. Metall.* **1976,** *5,* 159–165.

25. Kelly, P. M.; Kehoe, M. The Role of Dislocations and Interstitial Solute on the Strength of Ferrous Martensite, in New Aspects of Martensitic Transformations. *Suppl. Trans. JIM* **1976,** *17,* 399–404.
26. Morito, S.; Nishikawa, J.; Maki, T. Dislocation Density within Lath Martensite in Fe-C and FeNi Alloys. *ISIJ Int.* **2003,** *43,* 1475–1477.
27. Speich, G. R.; Leslie, W. C. Tempering of Steel. *Metall. Trans.* **1972,** *3,* 1043–1054.
28. Imai, Y. Phases in Quenched and Tempered Steels. *Trans. Jpn. Inst. Met.* **1975,** *16,* 721–734.
29. The Peter, G. Winchell Symposium on the Tempering of Steel. *Metall. Trans. A* **1983,** *14A,* 991–1145.
30. Krauss, G. Tempering and Structural Change in Ferrous Martensitic Structures. In *Phase Transformations in Ferrous Alloys;* Marder, A. R., Goldstein, J. I., Eds.; TMS: Warrendale, PA, 1984; pp 101–123.
31. Speich, G. R.; Taylor, K. A. Tempering of Ferrous Martensites. In *Martensite;* Olson, G. B., Owen, W. S., Eds.; ASM International: Materials Park, OH, 1992; pp 243–275.
32. Leslie, W. C.; Sober, R. J. The Strength of Ferrite and Martensite as Functions of Composition, Temperature, and Strain Rate. *Trans. ASM* **1967,** *60,* 459–484.
33. Miller, M. K.; Beaven, P. A.; Smith, G. D. W. A Study of the Early Stages of Tempering of Iron-Carbon Martensites by Atom Probe Field Ion Microscopy. *Metall. Trans. A* **1981,** *12A,* 1197–1204.
34. Lement, B. S.; Averbach, B. L.; Cohen, M. Microstructural Changes on Tempering Iron-Carbon Alloys. *Trans. ASM* **1954,** *46,* 851–881.
35. Lement, B. S.; Averbach, B. L.; Cohen, M. Further Study of Microstructural Changes on Tempering Iron-Carbon Alloys. *Trans. ASM* **1955,** *47,* 291–319.
36. Werner, F. E.; Averbach, B. L.; Cohen, M. The Tempering of Iron-Carbon Martensite Crystals. *Trans. ASM* **1957,** *49,* 823–841.
37. Roberts, C. S.; Averbach, B. L.; Cohen, M. The Mechanism and Kinetics of the First Stage of Tempering. *Trans. ASM* **1953,** *45,* 576–604.
38. Jack, K. H. Structural Transformations in the Tempering of High Carbon Martensitic Steel. *JISI* **1951,** *169,* 26–36.
39. Hirotsu, Y.; Nagakura, S. Crystal Structure and Morphology of the Carbide Precipitated from Martensitic High Carbon Steel during the First Stage of Tempering. *Acta Metall.* **1972,** *20,* 645–655.
40. Williamson, D. L.; Nakazawa, K.; Krauss, G. A Study of the Early Stages of Tempering in an Fe-1.2 pct C Alloy. *Metall. Trans. A* **1979,** *10A,* 1351–1362.
41. Barnard, S. J.; Smith, G. D. W.; Garret-Reed, A. J.; Vander Sande, J. Atom Probe Studies: 1) Role of Silicon in Tempering of Steel and 2) Low Temperature Chromium Diffusivity in Bainite. In *Solid–Solid Phase Transformations;* TMS-AIME, 1982; pp 881–885.
42. Owen, W. S. The Effect of Silicon on the Kinetics of Tempering. *Trans. ASM* **1954,** *46,* 812–829.
43. Lee, H.-C.; Krauss, G. Intralath Carbide Transitions in Martensitic Medium-Carbon Steels Tempered between 200 and 300°C. In *Fundamentals of Aging and Tempering in Bainitic and Martensitic Steel Products;* Krauss, G., Repas, P. E., Eds.; ISS: Warrendale, PA, 1992; pp 39–43.
44. Baker, R. G.; Nutting, J. The Tempering of 2 1/4 Cr 1 Mo Steel after Quenching and Normalizing. *JISI* **1959,** *192,* 257–268.
45. Caron, R. N.; Krauss, G. The Tempering of Fe-C Lath Martensite. *Metall. Trans.* **1972,** *3,* 2381–2389.
46. Krauss, G. Martensitic Microstructural Systems in Carbon Steels and Susceptibility to Hydrogen Embrittlement. *AIST Trans.* **2011,** *8,* 188–195.
47. Krauss, G. Heat Treated Martensitic Steels: Microstructural Systems for Advanced Manufacture. *ISIJ Int.* **1995,** *35,* 349–359.
48. Krauss, G. *Verformung und Bruch, Hrterei-Technische Mitteilungen*, 1991; Vol. 46, pp 7–12.
49. Krauss, G. Deformation and Fracture in Martensitic Carbon Steels Tempered at Low Temperatures. *Metall. Mater. Trans. A* **2001,** *32A,* 861–877.
50. Baozhu, G.; Losz, J. M. B.; Krauss, G. Substructure and Flow Strength of Low-Temperature Tempered Medium Carbon Martensite. In *Proceedings of the International Conference on Martensitic Transformations;* The Japan Institute of Metals, 1986; pp 367–374.
51. Zaccone, M. A.; Krauss, G. Elastic Limits and Microplastic Response in Ultrahigh Strength Carbon Steels. *Metall. Trans. A* **1989,** *20A,* 188–191.
52. Kuhlmann-Wilsdorf, D. Theory of Workhardening 1934–1984. *Metall. Trans. A* **1985,** *16A,* 2091–2108.
53. Leslie, W. C. *The Physical Metallurgy of Steels;* McGraw-Hill Book Company: New York, 1981.
54. Matlock, D. M.; Zia-Ebrahimi, F.; Krauss, G. Properties and Strain Hardening of Dual-Phase Steels. In *Deformation, Processing, and Structure;* Krauss, G., Ed.; American Society for Metals: Metals Park, OH, 1984; pp 47–87.
55. Saeglitz, M.; Krauss, G. Deformation, Fracture and Mechanical Properties of Low-Temperature-Tempered Martensite in SAE 43xx Steels. *Metall. Mater. Trans. A* **1997,** *28A,* 377–387.
56. Grange, R. A.; Hribal, C. R.; Porter, L. F. Hardness of Tempered Martensite in Carbon and Low-Alloy Steels. *Metall. Trans. A* **1977,** *8A,* 1775–1785.
57. Rollason, E. C. *Fundamental Aspects of Molybdenum in Transformation of Steel*. Climax Molybdenum, London, undated.
58. Krauss, G.; McMahon, C. J., Jr. Low Toughness and Embrittlement Phenomena in Steels. In *Martensite;* Olson, G. B., Owen, W. S., Eds.; ASM International: Materials Park, OH, 1992; pp 295–321.
59. Hyde, R. S.; Matlock, D. K.; Krauss, G. Quench Embrittlement: Intergranular Embrittlement due to Cementite and Phosphorous in Quenched Carbon and Alloy Steels. In *40th MSWP Conference Proceedings;* ISS: Warrendale, PA, 1998; pp 921–928.
60. Van de Sanden, J. Martensite Morphology of Low Alloy Commercial Steels. *Pract. Metallogr.* **1980,** *17,* 238–248.
61. Reguly, A.; Strohaeker, T. R.; Krauss, G.; Matlock, D. K. Quench Embrittlement of Hardened 5160 as a Function of Austenitizing Temperature. *Metall. Mater. Trans. A* **2004,** *34A,* 153–162.
62. Materkowski, J. P.; Krauss, G. Tempered Martensite Embrittlement in SAE 4340 Steel. *Metall. Trans. A* **1979,** *10A,* 1643–1651.
63. Bandyopadhyay, N.; McMahon, C. J., Jr. The Micro-Mechanisms of Tempered Martensite Embrittlement in 4340-Type Steels. *Metall. Trans. A* **1983,** *14A,* 1313–1332.
64. Zia-Ebrahimi, F.; Krauss, G. Mechanisms of Tempered Martensite Embrittlement in Medium Carbon Steels. *Acta Metall.* **1984,** *32,* 1767–1777.
65. Zia-Ebrahimi, F. A Study of the Mechanisms of Tempered Martensite Embrittlement in Low-Alloy Medium-Carbon Steels. Ph.D. Thesis, Colorado School of Mines, Golden, Colorado, 1982.
66. Yaney, D. L. The Effects of Phosphorus and Tempering on the Fracture of AISI 52100 Steel. M.S. Thesis, Colorado School of Mines, Golden, Colorado, 1987.
67. McMahon, C. J., Jr. *Temper Brittleness – An Interpretive Review, in Embrittlement in Steel*. Special Technical Publication No. 107; American Society for Testing and Materials, 1968, 127–167.
68. Jaffe, L. D.; Buffum, D. C. Isothermal Temper Embrittlement. *Trans. ASM* **1950,** *42,* 604–618.
69. Guttmann, M.; Dumoulin, Ph.; Wayman, M. The Thermodynamics of Interactive Co-segregation of Phosphorus and Alloying Elements in Iron and Temper Brittle Steels. *Metall. Trans. A* **1982,** *13A,* 1693–1711.
70. Bodnar, R. L.; Ohhashi, T.; Jaffe, R. I. Effects of Mn, Si, and Purity on the Design of 3.5 NiCrMoV and 2.5 Cr-1 Mo Bainite Alloy Steels. *Metall. Trans. A* **1989,** *20A,* 1445–1460.
71. Fruehan, R. J. A Review of Hydrogen Flaking and Its Prevention. *ISS Trans.* **1997,** 61–69.
72. ASTM. *Standard Guide for Post-Coating Treatments of Steel for Reducing Risk of Hydrogen Embrittlement*, Specification B 850.
73. Tuttle, R. N., Kane, R. D., Eds. *H_2S Corrosion in Oil and Gas Production – A Compilation of Classic Papers;* NACE: Houston, 1981.
74. Turkdogan, E. T. *Fundamentals of Steelmaking*. Book 656; The Institute of Materials: London, 1996; p 96.
75. Johnson, H. H.; Morlet, J. G.; Troiano, A. R. Hydrogen, Crack Initiation, and Delayed Failure in Steel. *Trans. TMS-AIME* **1958,** *212,* 528–536.
76. Pressouyre, G. M. A Classification of Hydrogen Traps in Steel. *Metall. Trans. A* **1979,** *10A,* 1571–1573.
77. McMahon, C. J., Jr. Effects of Hydrogen on Plastic Flow and Fracture in Iron and Steel. In *Hydrogen Effects in Metals;* Bernstein, I. M., Thompson, A. W., Eds.; TMS-AIME, 1981; pp 219–233.
78. Wei, F.-G.; Hara, T.; Tsuchida, T.; Tsuzaki, K. Hydrogen Trapping in Quenched and Tempered 0.42C-0.30 Ti Steel Containing Bimodally Dispersed TiC particles. *ISIJ Int.* **2003,** *43,* 539–547.

12.12 Microstructure and Properties of Gas Carburized Steels

J Grosch, Technische Universität Berlin, Berlin, Germany

12.12.1	**Introduction**	379
12.12.2	**Fundamentals – Carbon and Hardness Profiles**	379
12.12.3	**Morphology of Carburized Microstructures**	384
12.12.4	**Further Microstructural Features**	392
12.12.5	**Special Applications of Carburizing**	398
12.12.6	**Properties**	398
12.12.6.1	Fatigue Behavior	399
12.12.6.2	Fatigue Properties of Carburized Microstructures	399
12.12.6.3	Toughness and Ductility	404
12.12.7	**Summary**	408
References		409

12.12.1 Introduction

Nearly all components in technical products are loaded by constant or by repetitively applied forces or momentums such as bending or torsion, which result in a heterogeneous state-of-stress with maximum stress values at the surface of components. The function of a component usually requires complex geometries with changes in size and with notches causing stress gradients. Therefore, even a (less common) homogeneous tensile state-of-stress is locally heterogeneous.

Case hardening establishes a gradient case to core microstructure with high strength in the case and a lower strength in the core. The strength properties of these graded microstructures fit excellently with the heterogeneous state-of-stress. In the diffusion step of the carburizing process, carbon diffuses in the austenite phase field into the case of carburizing steels and creates a carbon profile with surface carbon contents of usually 0.6–0.7% up to 1% and a core carbon content of 0.15% to (0.20–0.23)% depending on the carbon content of the selected carburizing steel. Quenching transforms the austenite into martensite with the desired hardness profile of high case hardness and a less hard core (more details on the carburizing technique, see, i.e., Refs. (*1–5*)). In addition, the martensitic transformation creates a residual stress distribution with compressive residual stresses in the case and tensile residual stresses toward the core. Surface hardness, hardness profile and residual stress distribution together are responsible for the high fatigue and wear resistance of the carburized microstructure and a sufficient toughness behavior, which combines the high ductility of the soft core microstructure with the rather low ductility of the hard case microstructure. These combined properties lead to the highest values that can be reached in *one* part.

12.12.2 Fundamentals – Carbon and Hardness Profiles

The one feature that exclusively defines carburized microstructures is the carbon profiles described by the parameters case carbon content, depth of case and core carbon content. Carbon potential control makes it possible to exactly adjust different carbon profiles in carburizing steel as well as the same carbon profile (**Figure 1**) in differently alloyed carburizing steels (**Figure 2**).

The depth of case, usually defined at 0.32% carbon and in commercial practice up to about 5 mm, is controlled by the diffusion time. All steels are named according to the standards valid at the time of the respective investigation. Most of the microstructures and related properties reported here are taken from investigations (*6–11*) on the carburizing steels (according DIN 17210) 15CrNi6, 14CrNi14 and 14CrNi18. Therefore, the given correlations between the parameters of carburizing, microstructures and properties are valid in common and can be compared directly. The chemical composition in weight-percent is given in **Table 1**.

The carbon content dissolved in the austenite controls the martensitic transformation and the martensite morphology, which change according to the carbon profile from case to core (for a detailed discussion of martensite see, among others, Refs. (*12–15*)). The martensitic – diffusionless – transformation is enforced by undercooling the austenite phase by quenching, and starts when the martensite start temperature M_s is reached. M_s depends predominantly on the carbon content in the austenite and less distinctly on the substitutional alloy elements and the austenite grain size. The equation

$$M_s(^\circ\mathrm{C}) = 512 - 453\cdot\mathrm{C} - 16.9\cdot\mathrm{Ni} + 15\cdot\mathrm{Cr} + 217\cdot\mathrm{C}^2 - 71.5\mathrm{C}\cdot\mathrm{Mn} - 67.6\cdot\mathrm{C}\cdot\mathrm{Cr} \quad [1]$$

given by Andrews (*16*) on the basis of a regression calculation describes pretty well the behavior of carburized steels and is shown in **Figure 3** for an unalloyed and a high alloyed carburizing steel to demonstrate the decrease of M_s with increasing carbon content and, less markedly, with the alloying content. The martensitic transformation of carburized microstructures is finished after an

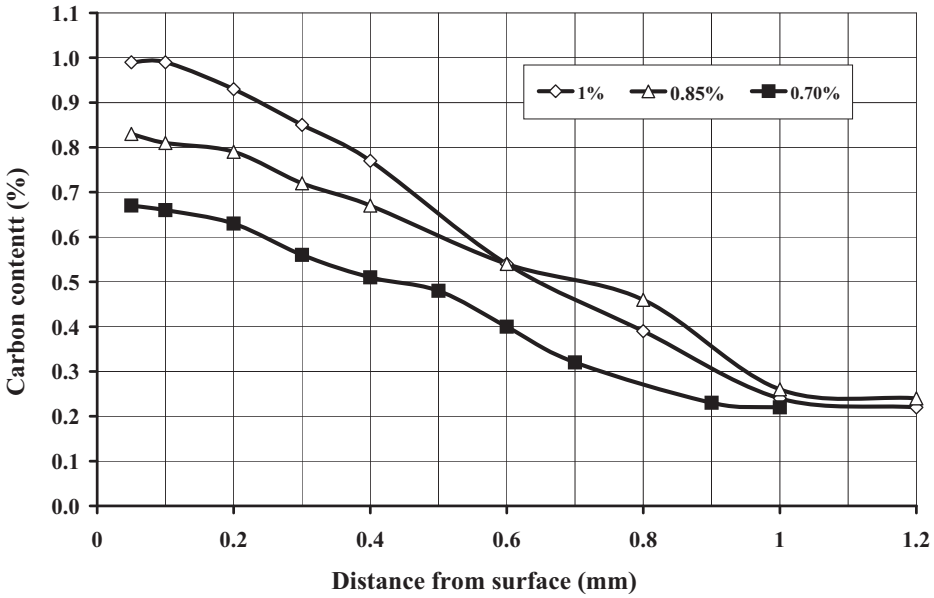

Figure 1 Carbon profiles, different case carbon contents. 15CrNi6; 925 °C → oil, 60 °C.

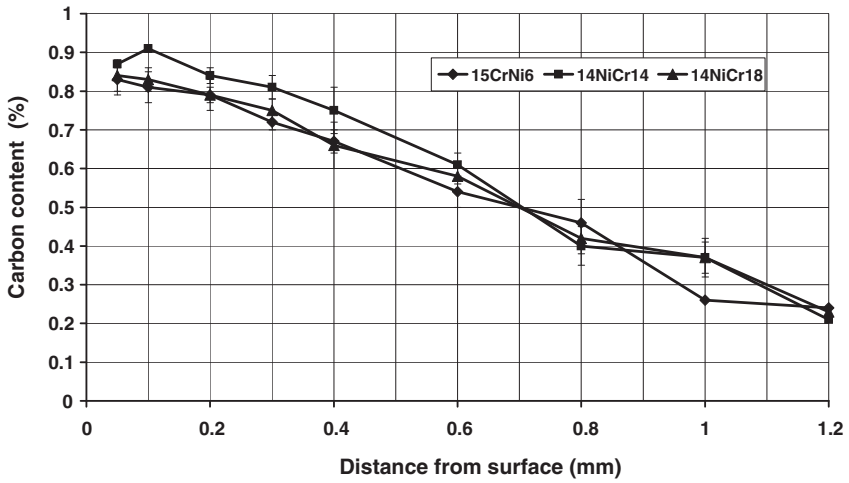

Figure 2 Carbon profiles of alloyed carburizing steels, case carbon content 0.85%; 925 °C → oil, 60 °C.

Table 1 Chemical composition of three steels

Steel	*C*	*Si*	*Mn*	*Cr*	*Ni*	*Al*	*P*	*Si*
15CrNi6	0.17	0.26	0.58	1.58	1.44	0.036	0.014	0.028
14NCr14	0.13	0.25	0.46	0.73	3.50	0.033	0.014	0.011
14NiCr18	0.13	0.22	0.48	0.93	4.36	0.033	0.014	0.010

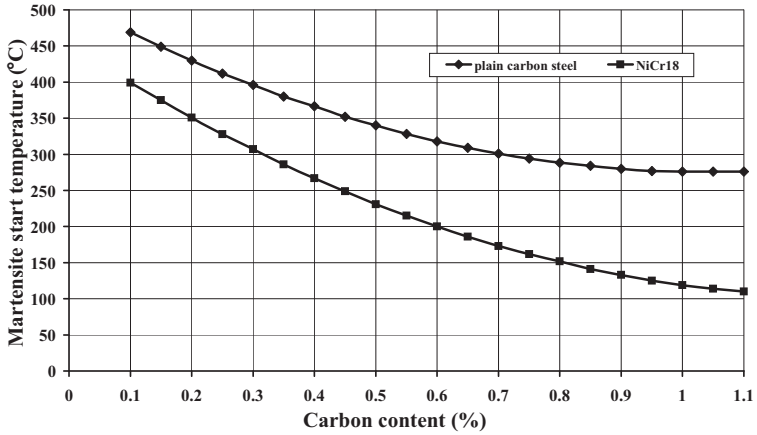

Figure 3 Martensite start temperatures, calculated after Andrews, K. W. Empirical Formula for the Calculation of Some Transformation Temperatures. *J. Iron Steel Inst.* **1965**, *203*, 721–727.

undercooling of about 200° below M_s, which means that with the high carbon contents of the case microstructure and especially with alloyed steels, the martensite finish temperature drops below the temperature T_0 of the quenching media and that the athermal martensitic transformation remains incomplete. The nontransformed austenite volume remains as retained austenite in the microstructure. The amount of retained austenite depends predominantly on the carbon content and, at constant carbon content on the alloying content, **Figure 4**.

The relation of martensite and retained austenite in the microstructure can be calculated (*17*) according to

$$V_M = 1 - \exp(-0.01 \cdot \Delta T) \qquad [2]$$

and is calculated in **Figure 5** with the values of the martensite start temperature given in **Figure 3** and a quenching temperature T_0 of 20 °C for $\Delta T = M_s - T_0$, the influence of both carbon and alloying content shows clearly.

The carbon content dissolved in the parent austenite (γ) phase determines the hardness of martensite, resulting primarily from the supersaturation of the ferrite (α) phase with the interstitial soluted carbon atoms, the elastic distortion of the body-centered-tetragonal martensite and the high dislocation and twin density from the plastic deformation accompanying the $\gamma \rightarrow \alpha$-transformation. Alloying elements have a negligible influence on martensite hardness but determine the depth of transformation at equal carbon contents.

Therefore, it is useful to describe the hardenability in carburizing with the hardenability of the case and the hardenability of the core. The hardenability of the case is determined by the carbon content only and can be controlled by the parameters of the carburizing process, especially by the carbon potential. The hardness of the martensite depends linearly (see, e.g., **Figure 6**) on the carbon content (*18–20*) and can be calculated with several formulas developed by regression calculations.

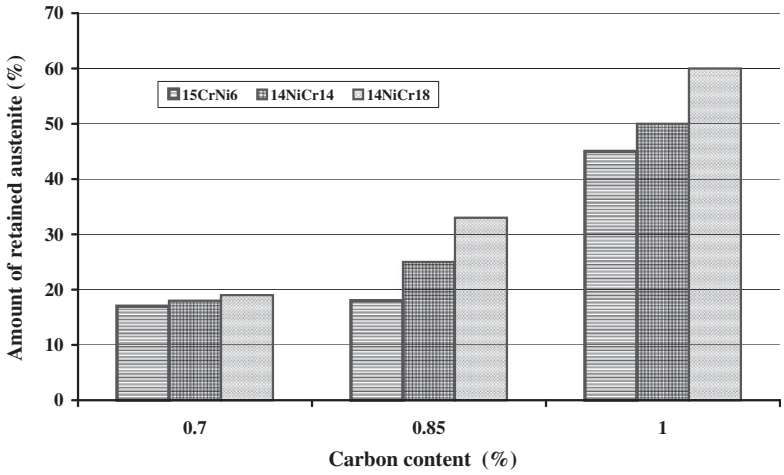

Figure 4 Effect of surface carbon content and alloy composition on retained austenite content (maximal values, CHD = 1 mm, 180 °C, 1 h).

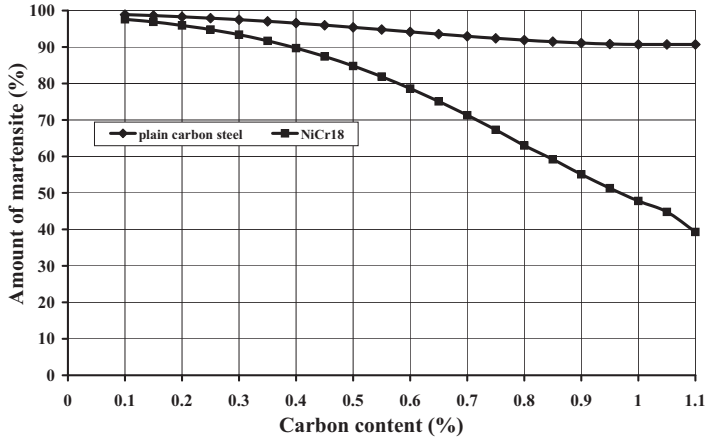

Figure 5 Austenite transformation, calculated after Koistinen, D. P.; Marburger, R. E. A General Equation Describing the Extent of Austenite-martensite Transformation in Pure Carbon–iron Alloys and Plain Carbon Steel. *Acta Metall.* **1959**, *7*, 59, M_s temperatures according to **Figure 3**.

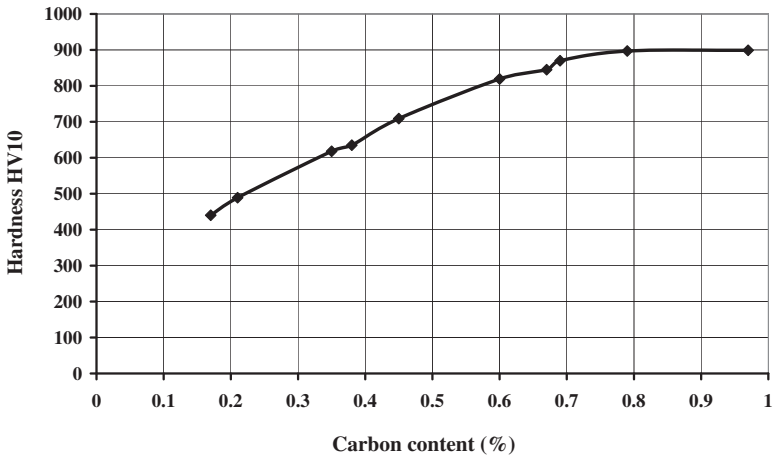

Figure 6 Effect of carbon content on martensite hardness.

The results of (*21*)

$$\text{Hardness martensite} = 20 + 60\sqrt{C}(\text{HRC}); \quad C \leq 0.6\% \qquad [3]$$

describe hardness values at the upper scatter band, those of (*22*)

$$\text{Hardness martensite} = 29 + 51(C)^{0.7}(\text{HRC}), \quad C \leq 0.6\% \qquad [4]$$

mean hardness values.

The hardenability of the core can be influenced by materials selection because the level of carbon content of carburizing steels is comparable. Especially alloy elements such as Nickel or Manganese, which do not form carbides, enhance the core hardenability (**Figure 7(a)**) with only a small difference in the influence between 3.2%Ni and 4.6%Ni, **Figure 7(b)**.

All efforts to enhance the hardness of martensite in iron–carbon alloys proved unsuccessful. The proposal to improve the hardenability of carburizing steels by adding small quantities of rare earth metals (*23–25*) could not be confirmed (*26*). Iron solutes 0.094% Cerium at 900 °C and 0.047% Cerium at room temperature, although on the basis of an alloy according to C15 two experimental alloys EX94 with 0.094% RE (0.092% Cerium and 0.002% Lanthanum) and EX57 with 0.057 RE (0.047% Cerium and 0.010 Lanthanum), were produced. These experimental alloys and a steel C15 – offering the poorest hardenability of commercial carburizing steels – have been carburized in one batch and quenched in water or oil respectively. The carbon acceptance did not improve by alloying with rare-earth metals (**Figure 8**), and there was no evidence of the proposed beneficial effect of rare earth metals on hardenability (**Figure 9**, quenched in water and **Figure 10**, quenched in oil).

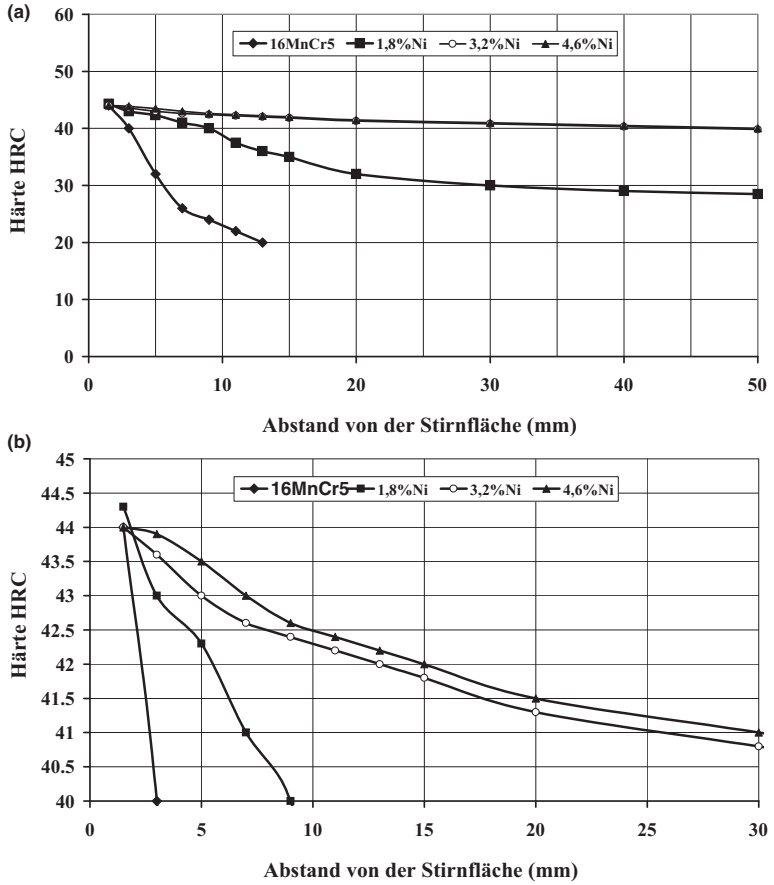

Figure 7 (a) Influence of alloy composition of carburizing steels on core hardness. (b) Influence of alloy composition of carburizing steels on core hardness, detail from Figure 7(a).

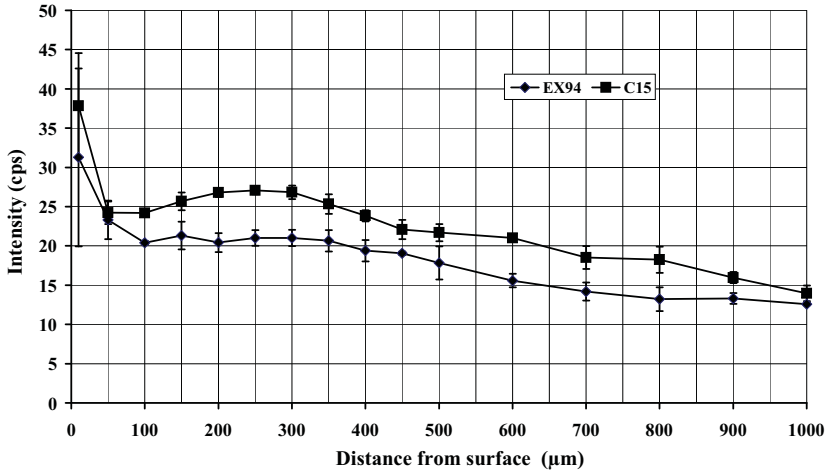

Figure 8 Effect of rare earth on carbon profiles (comparison of results of EDX-analysis, counts per seconds are not calibrated into carbon content).

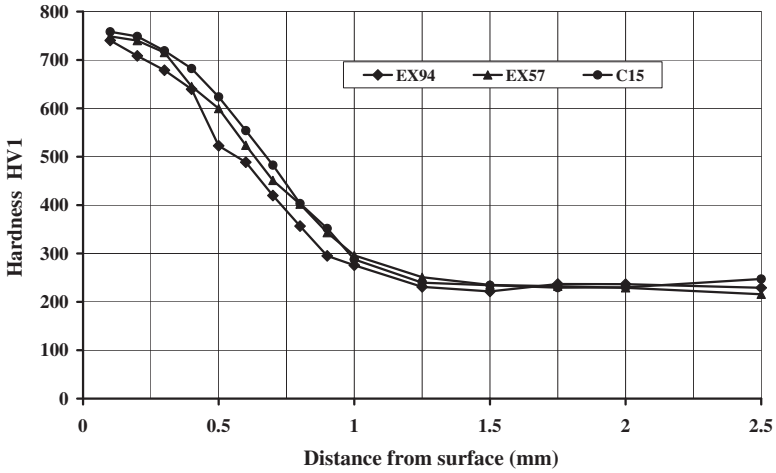

Figure 9 Effect of rare earth on hardenability: hardness profiles, quenched in water.

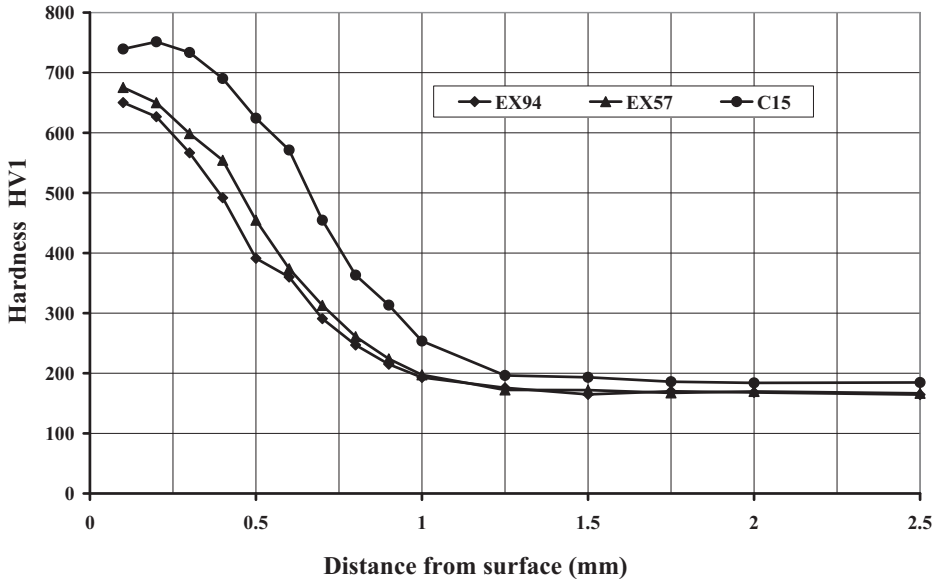

Figure 10 Effect of rare earth on hardenability: hardness profiles, quenched in oil.

12.12.3 Morphology of Carburized Microstructures

The plastic deformation accompanying the martensitic transformation is connected with twinning in microstructures with high carbon content, i.e., low martensite start temperatures, and with dislocation movement in microstructures with low carbon content, i.e., high martensite start temperatures (*27*). The morphology of martensite depends strongly on twin or dislocation type of the plastic deformation. The microstructures are shown mainly in light micrographs, some scanning electron micrographs are added when the higher magnification of the scanning electron microscopy was helpful. Transmission electron microscopy is a widely used investigation method in fundamental research but not common in the heat treating practice.

In case of microstructures with carbon contents of 0.6% and more, the face-centered austenite transforms in single martensite plates starting from nuclei at the austenite grain boundaries. The plates develop in the direction of their habit planes consecutive with different orientation in the austenite grain (progressive or fractal partitioning of the austenite grain). This martensitic microstructure is called plate martensite and, as described earlier, in carburized microstructures is always linked with retained austenite. Therefore, plate martensite can be shown in the high magnification of a scanning electron micrograph only. **Figure 11** illustrates, as far as possible with a plane cross section through a three dimensional structure, clearly visible the random distribution of the martensite planes in different sizes. The light micrographs show the dark etched midribs of the martensite plates and the white, nonetched retained austenite. **Figures 12–14** show characteristic carburized case microstructures of plate martensite and

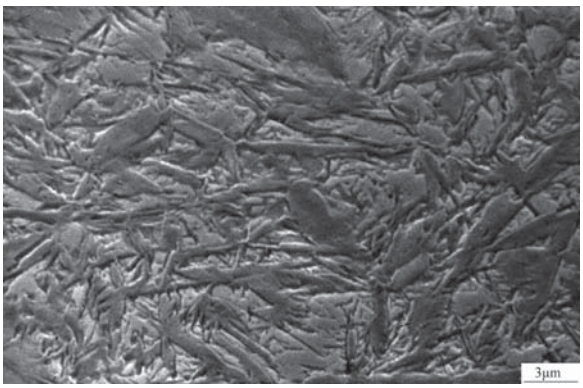

Figure 11 Plate martensite, 0.7% case carbon content, 16MnCr5. Scanning electron micrograph.

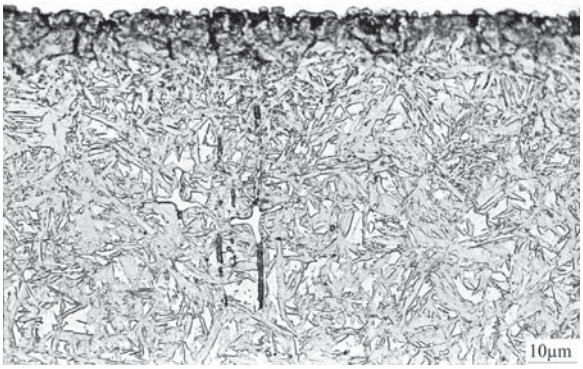

Figure 12 Plate martensite and retained austenite, 0.85% case carbon content, 15NiCr6. (Light micrograph, etched with nital).

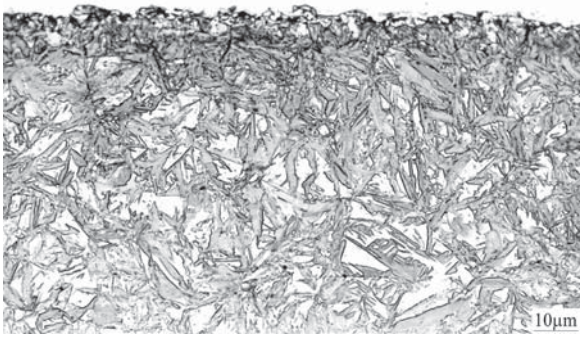

Figure 13 Plate martensite and retained austenite, 0.85% case carbon content, 14CrNi14 (light micrograph, etched with nital).

retained austenite. The case carbon content is 0.85%, the amount of retained austenite has been varied with increasing Nickel content. The white microstructural region at the surface is a consequence of surface oxidation (see the following section). The structure of the martensite plates is distinctively visible in the differential interference contrast (dic) microscopy technique (Figure 15), as with dic microscopy small changes in the surface show more clearly.

At low carbon contents, below approximately 0.3% (0.4%), the elastic strains along the martensite plates are reduced by dislocation movement. The martensite plates, also nucleating at the austenite grain boundary, align parallel to each other in packets. Several packets with different orientations to each other develop. This morphology of martensite is called lath martensite and shows clearly in the scanning electron micrograph (Figure 16). The light micrographs of lath martensite represent the core microstructure (Figures 17 and 18), the alloy composition has no visible influence. The martensitic transformation requires sufficient quenching intensity, which is, especially in large components, not always reached. The core then transforms according to the TTT-diagram into lath martensite, bainite, ferrite, and pearlite (Figure 19).

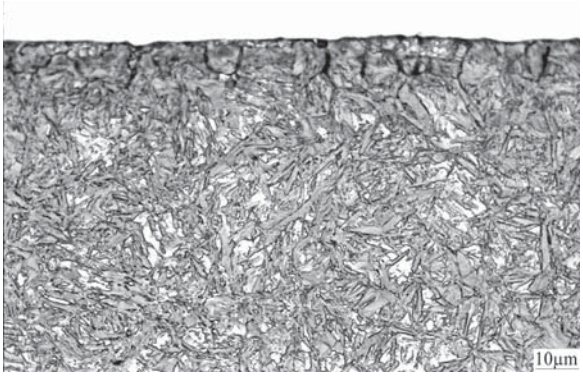

Figure 14 Plate martensite and retained austenite, 0.85% case carbon content, 14CrNi18 (light micrograph, etched with nital).

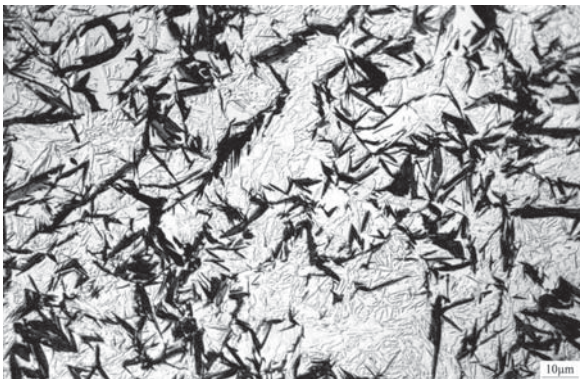

Figure 15 Plate martensite and retained austenite, 1.0% case carbon content, 14NiCr18, differential interference contrast microscopy (light micrograph, etched with nital).

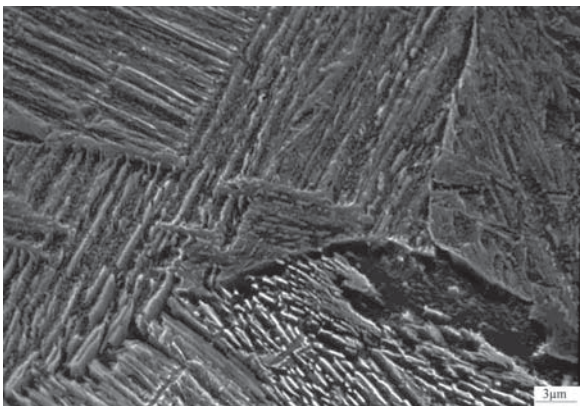

Figure 16 Lath martensite, core microstructure, 16MnCr5 (SAE 5115). Scanning electron micrograph.

Austenite transforms into both lath and plate martensite at carbon contents from 0.3% to 0.5%, depending on the alloy composition. The resulting microstructure is called mixed martensite (Figures 20 and 21) and represents the transition from plate martensite and retained austenite in the case to lath martensite in the core.

The martensitic transformation takes place within the austenite grains, and the austenite grain size therefore determines the maximum length of the first-formed martensite plates, reflecting the effect of austenite grain size on the martensitic microstructure. The (prior) austenite grain boundaries must be etched separately as they are not visible in matrix-etched microstructures. (The length of the usually dark etched midribs of the plates, Figure 15, allow a hint on the grain size.). Fine and uniformly distributed grains (Figure 22) are demanded especially for a good toughness performance. A grain size distribution with few large grains and

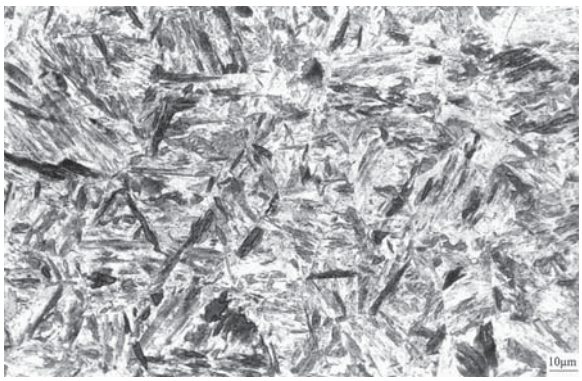

Figure 17 Lath martensite, core microstructure, 15CrNi6 (light micrograph, etched with nital).

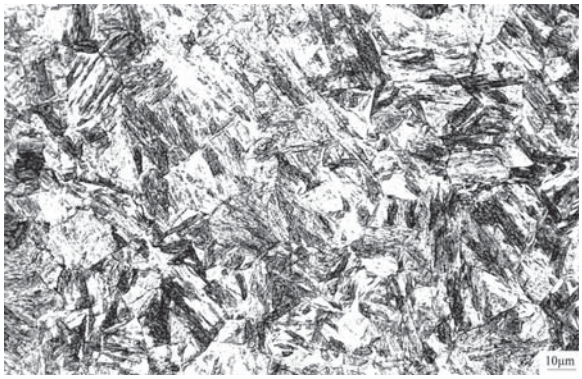

Figure 18 Lath martensite, core microstructure, 14NiCr14 (light micrograph, etched with nital).

Figure 19 Lath martensite, bainite, ferrite, and pearlite in the core microstructure, 16MnCr5 (light micrograph, etched with nital).

many fine grains (Figure 23) may seem to yield an acceptable mean grain size when using quantitative grain size measurement methods but the large grains diminish toughness and grindability.

The discussed distribution in the carburized microstructure can be summarized easily with hardness profiles as illustrated for equal steel and several carbon contents in Figure 24, corresponding to the carbon profiles in Figures 1 and 25 (which in turn corresponds to the carbon profiles in Figure 2) for constant carbon content and various alloyed carburizing steels. Both figures show the effect of retained austenite on the case hardness. The decreasing hardness toward the surface is a consequence of the increasing amount of retained austenite but can be influenced near the surface by the applied load of hardness measurement, Figure 26. Hardness HV1 given in DIN EN ISO 2639 should be substituted by HV0.1 for hardness measurements in a distance from surface smaller than 0.1 mm. The hardness profiles furthermore contain the case depth CHD, according to DIN EN ISO 2639 the distance from surface at the limiting hardness of 550 HV1/HV0.1. The limiting Vickers hardness 550 HV1 corresponds according to DIN EN

Figure 20 Mixed martensite, 14NiCr14, ~0.4%C (light micrograph, etched with nital).

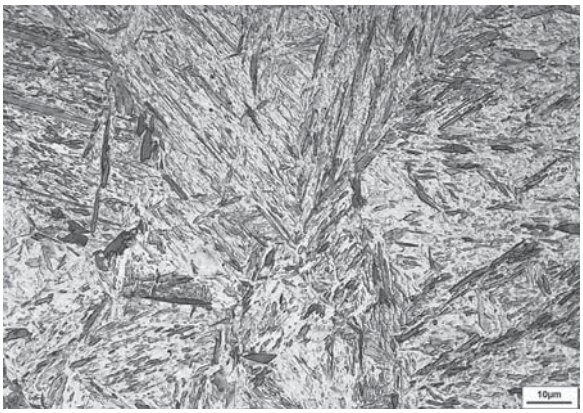

Figure 21 Mixed martensite, 14NiCr14, ~0.4%C (light micrograph, etched with nital).

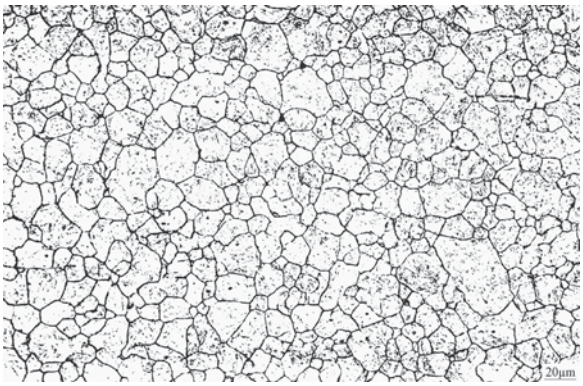

Figure 22 Prior austenite grain boundaries, 15CrNi6 (light micrograph).

ISO 18265 with a Rockwell hardness of about 50 HRC. This hardness is reached, calculated by formulas [3] and [4], in martensite with 0.32% carbon content, which is used to determine the diffusion time for a given case depth.

The residual stress distribution in a carburized component is the result of plastic deformation caused by thermal and transformation stresses, depending on the geometry of the component, heating and quenching conditions and the parameters of the martensitic transformation (*28–30*). See **Figure 27** as an example for the residual stress distribution affiliated to the hardness profiles of **Figure 4**.

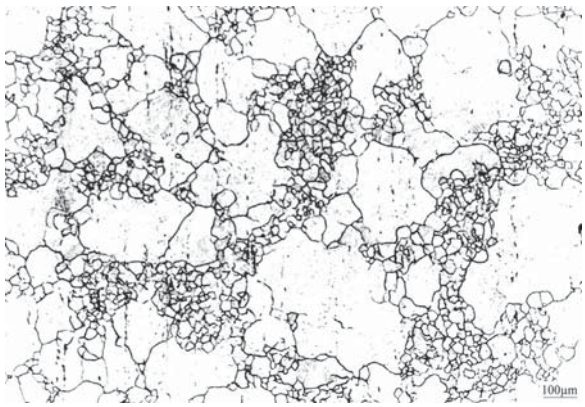

Figure 23 Prior austenite grain boundaries, 16MnCr5 (light micrograph).

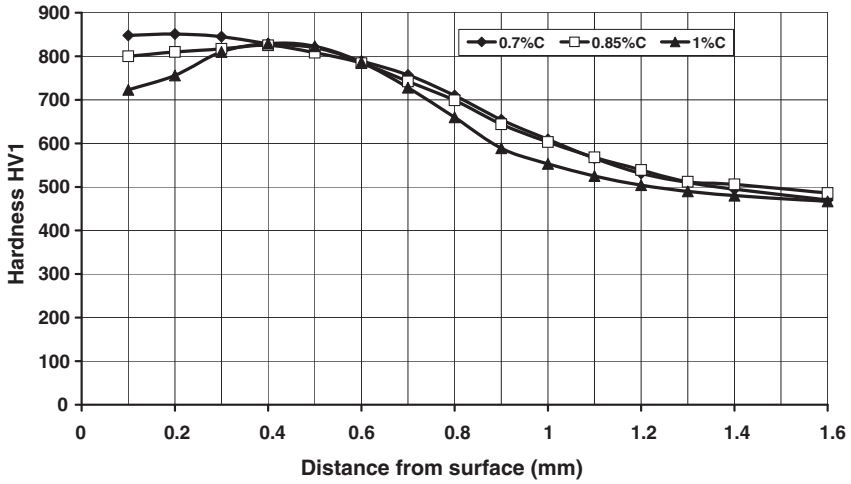

Figure 24 Effect of case carbon content on hardness profiles. 15CrNi6, 925 °C → oil, 60 °C.

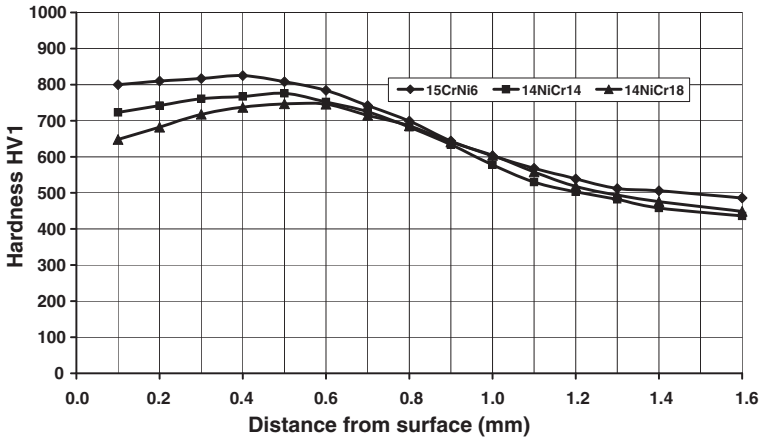

Figure 25 Effect of alloy composition on hardness profiles. Case carbon content 0.85%, 925 °C → oil, 60 °C.

Almost all carburized microstructures are tempered, usually 1 h or 2 h at 180 °C. At this temperature, carbon atoms diffuse from the supersaturated martensite of the case and form carbides FexCy, thus reducing the distortion of the microstructure. Toughness and grindability improve without a loss of hardness below the demand of the carburizing practice '60 HRC ≈ 700 HV10 ore more.' Figure 28, surface hardness, and Figure 29, hardness profile, prove that this demand cannot be reached with higher carbon and alloy content. The carbide precipitations are not visible in light micrographs. The core microstructure does not change by tempering since

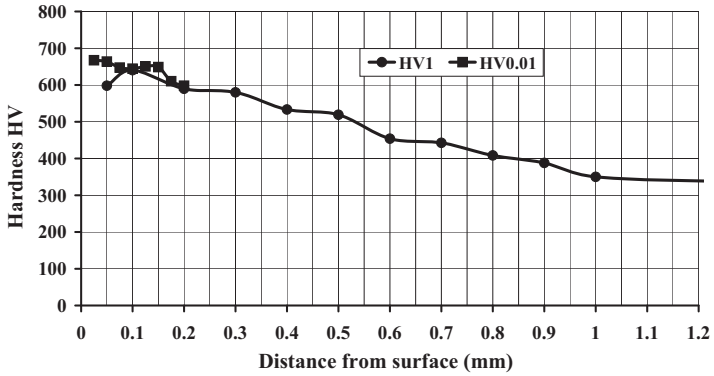

Figure 26 Effect of Vickers load on the results of hardness measurements.

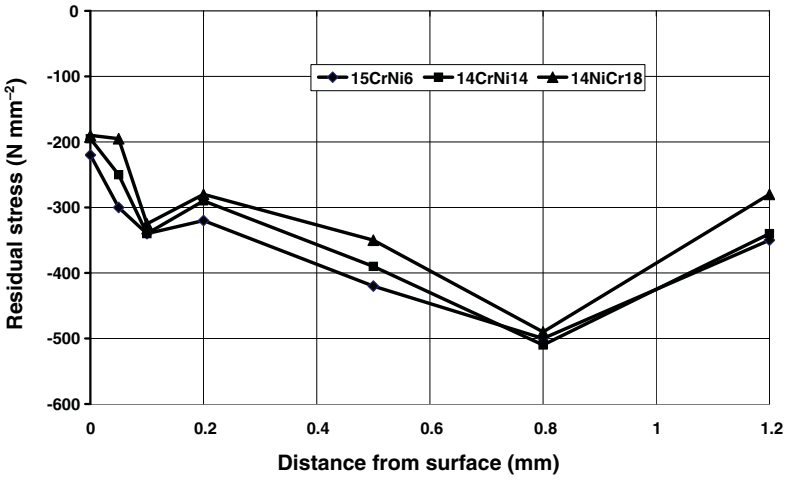

Figure 27 Residual stresses in carburized microstructures. Case carbon content 0.85% (925 °C → oil, 60 °C).

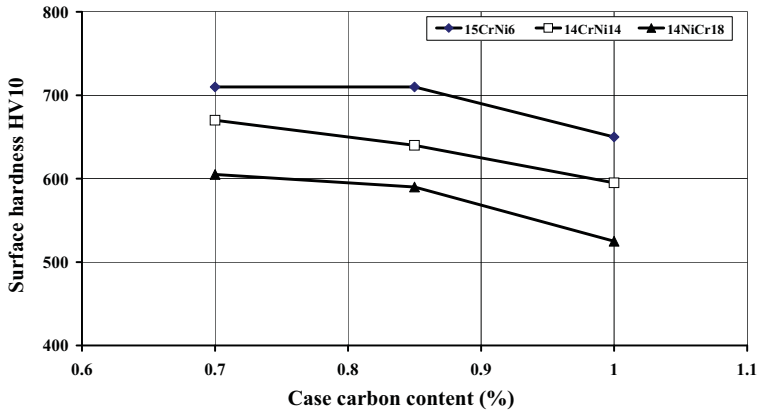

Figure 28 Effect of case carbon content and alloy composition on surface hardness. 925 °C → oil, 60 °C; 180 °C, 1 h; CHD = 1 mm.

about 0.2% carbon is segregated at dislocations (*31*). The carburized microstructure is in a nonequilibrium status after tempering, a long-time exposure of carburized components at temperatures in the range of tempering leads to a further reduction of hardness (Figure 30).

An important effect of tempering which may decide the occasionally asked question 'tempering or not tempering' is the effusion of hydrogen. All carburizing atmospheres contain hydrogen, which diffuses at carburizing temperatures easily into the steel.

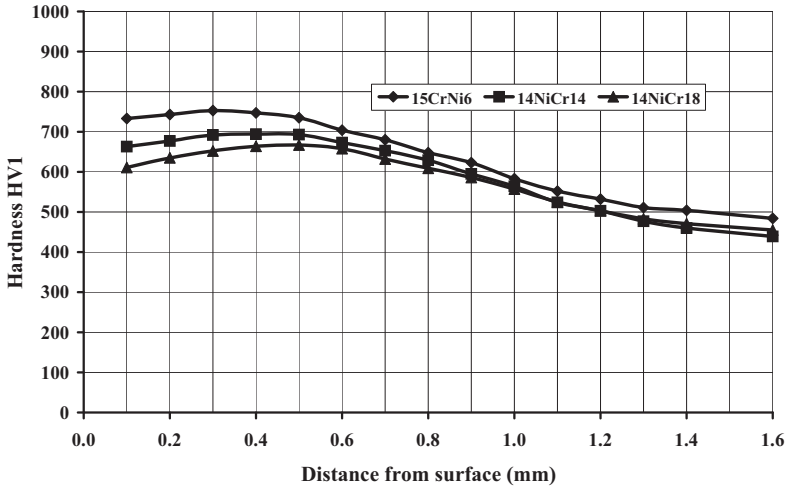

Figure 29 Effect of tempering on hardness profiles. Case carbon content 0.85%; 925 °C → oil, 60 °C; 180 °C, 1 h; CHD = 1 mm.

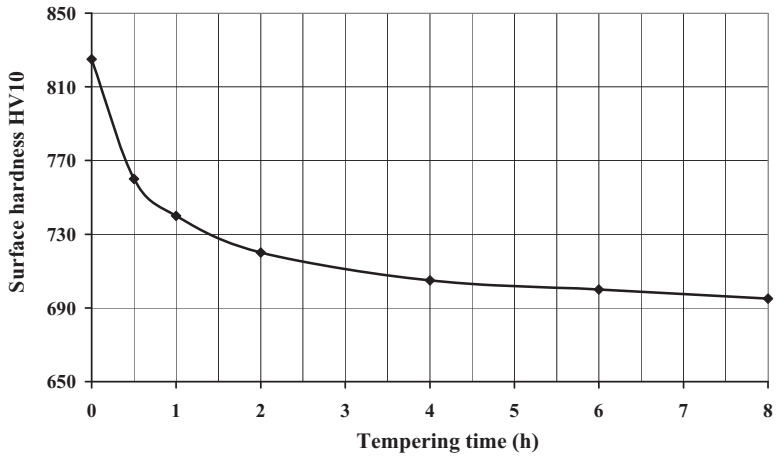

Figure 30 Effect of tempering time on surface hardness. Tempering temperature 200 °C, 16MnCr5.

Figure 31 (*32*) shows the intake of hydrogen when carburized in commercially used atmospheres. Hydrogen effuses during tempering, Figure 32 (*33*), mainly in the first hour. Oxide layers decelerate the effusion rate although tempering should be done as soon as possible after quenching.

Retained austenite transforms into the equilibrium phases ferrite and cementite when thermally activated. The transformation rate is, as valid for all thermally activated processes, proportional to the temperature and to the square root of time as demonstrated in Figure 33 (*34*).

A detailed calculation of the transformation of retained austenite is given (*35*) by

$$RA^* = RA_0 \cdot \exp\left\{ -t \cdot c \cdot \exp\left(-\frac{Q}{RT}\right)\right\} \quad [5]$$

with RA* amount of transformed retained austenite, RA_0 amount of retained austenite after quenching, t tempering time (s), c coefficient ($1–3 \cdot 10^{10}$ (s^{-1})), Q activation energy ($1322 \cdot 10^5$ J mol^{-1}), R universal gas constant (831 446 J mol^{-1} K^{-1}), T tempering temperature (K). Figure 34 shows the result of the equation for $c = 1 \cdot 10^{10}$. It follows that the transformation of retained austenite is completed at temperatures of about 300 °C, unfortunately combined with an unacceptable loss of hardness.

The martensitic transformation proceeds by deep cooling and the amount of retained austenite obtained by quenching at room temperature is further reduced, Figure 35. Deep cooling is much more effective than tempering. The hardness of deep cooled microstructures, Figure 36, is remarkably higher than the hardness of microstructures quenched to room temperatures (see Figure 25), the effect of alloying elements becomes small as the hardness of martensite depends on carbon content only. Double reheated carburized microstructures contain less retained austenite than direct quenched microstructures, with a further beneficial effect of deep cooling (Figure 37). Double reheating, however, is costly and scarcely used in practice. Deep cooling creates high

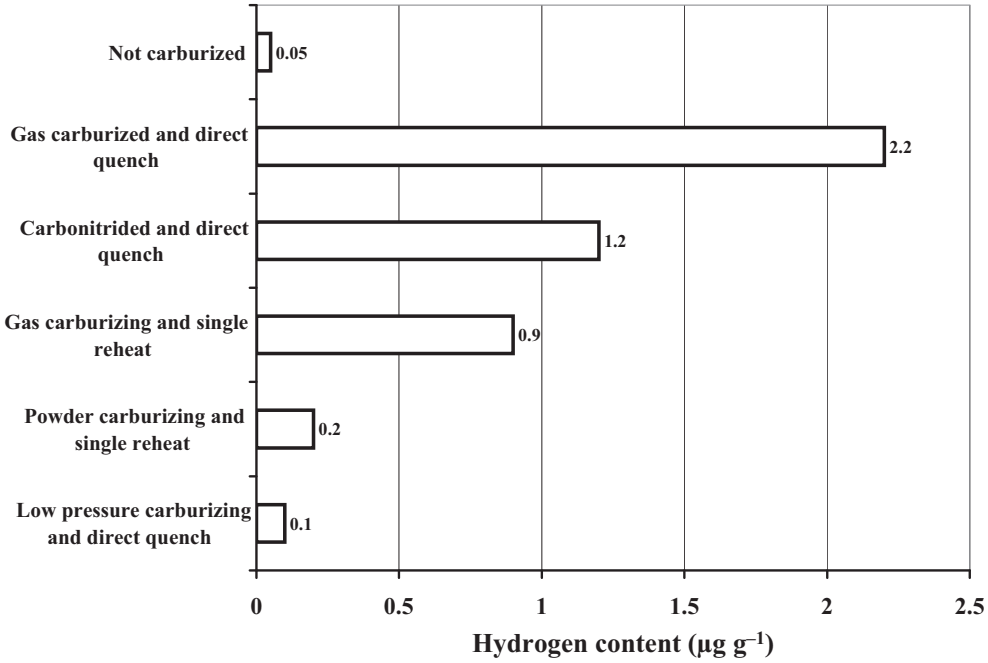

Figure 31 Hydrogen content in quenched carburized microstructures, measured with hot gas extraction at 800 °C. 20MoCr4. Adapted from Streng, H.; Grosch, J.; Razim, C. Wasserstoffaufnahme und –abgabe beim Einsatzhärten und Anlassen. *Härterei Techn. Mitt.* **1987**, *42*, 245–260.

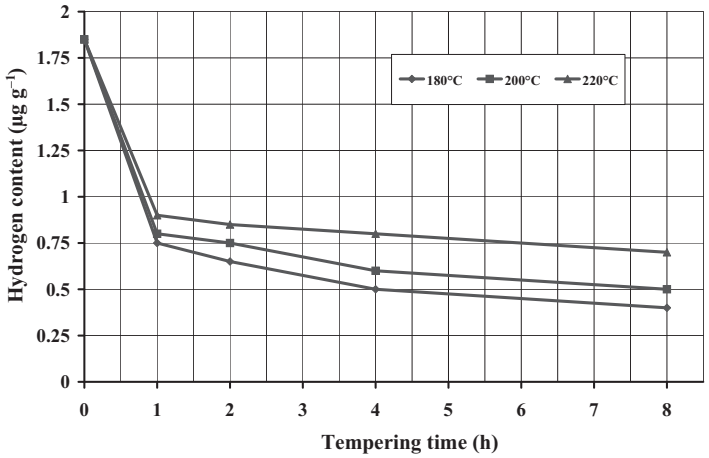

Figure 32 Effusion of hydrogen during tempering (20MoCr4). Hydrogen measured with hot gas extraction at 800 °C. Adapted from Streng, H.; Razim, C.; Grosch, J. Influence of Hydrogen and Tempering on Toughness of Case-hardened Structures. In *Carburizing – Processing and Performance*; Krauss, G., Ed.; ASM, 1989, 311–317.

tensile residual stresses in the austenite phase (*14*,*36*), **Figure 38**, which remain in the tensile range even after tempering, **Figure 39**. Therefore, deep cooling is less suitable for dynamically stressed components.

12.12.4 Further Microstructural Features

Carburizing atmospheres contain, with the exception of plasma and low pressure carburizing methods, oxygen which reacts at carburizing temperatures to form oxides in particular with silicon, manganese and chromium, and which can decarburize the microstructures. *Surface oxidation* and, as the diffusion along grain boundaries is faster than in the matrix, intergranular surface oxidation is inevitable in these atmospheres (*37*–*39*), **Figures 40 (unetched) and 41**. Surface oxidation impairs the performance of carburized microstructures because alloy elements in oxides do not further contribute to hardenability, and a softer microstructure develops which tends toward tensile residual stresses. Scanning electron micrographs show clearly that the martensite plates end

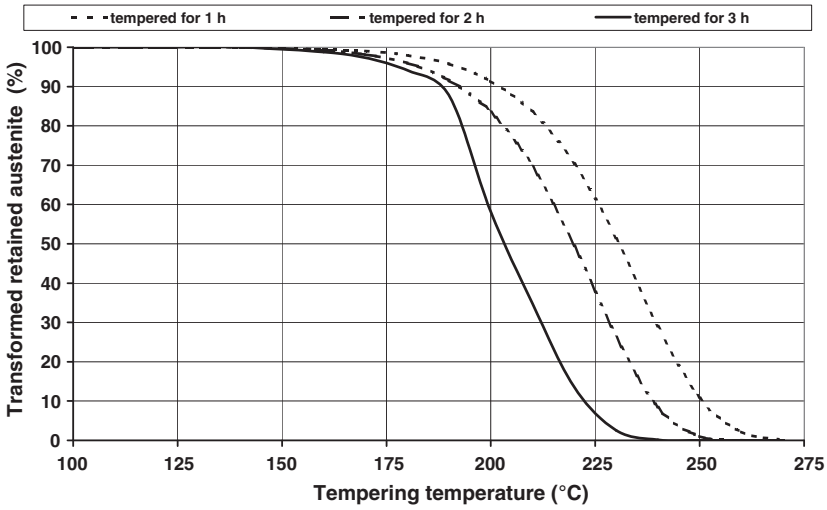

Figure 33 Transformation of retained austenite. Calculated after Lucas, G.; Nützel, H. Untersuchungen über die Umwandlung des Restaustenits in niedrig legierten Stählen mit rd 1%C. *Archiv Eisenhüttenwesen* **1966**, *37*, 981–987.

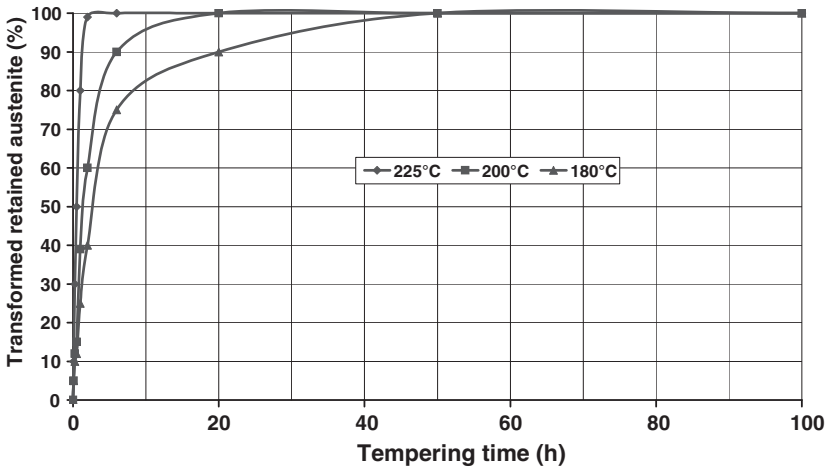

Figure 34 Transformation of retained austenite during tempering, steel 1.2%C. Adapted from Balliett, T. A.; Krauss, G. The Effect of the First and Second Stages of Tempering on Microcracking in Martensite of an Fe-1,22% C Alloy. *Met. Trans. A* **1976**, *7A*, 81–86.

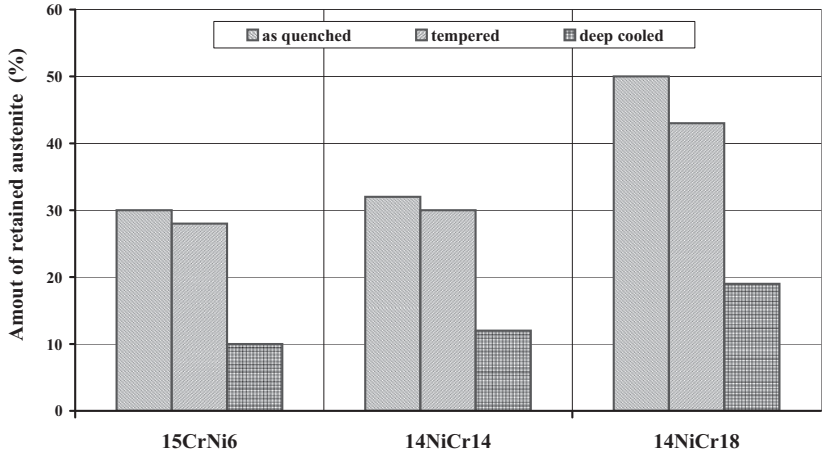

Figure 35 Influence of alloy composition and heat treatment on the amount of retained austenite in carburized steels. Case carbon content 0.85%.

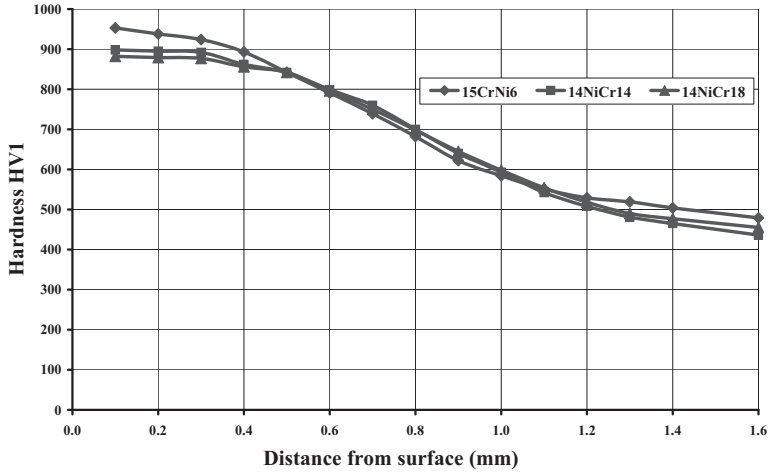

Figure 36 Hardness profiles of deep cooled carburized microstructures. (925 °C → oil, 60 °C; deep cooled at −196 °C; case carbon content 0.85%; CHD = 1.0 mm).

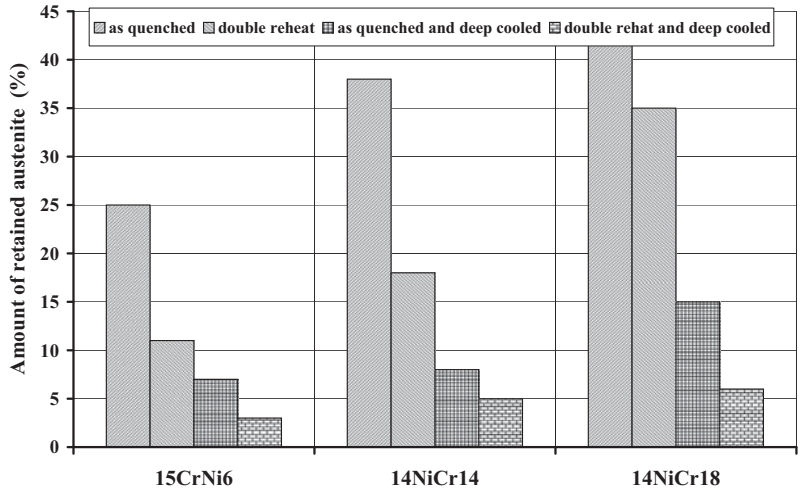

Figure 37 Retained austenite in double reheated and deep cooled carburized microstructures, case carbon content 0.85%.

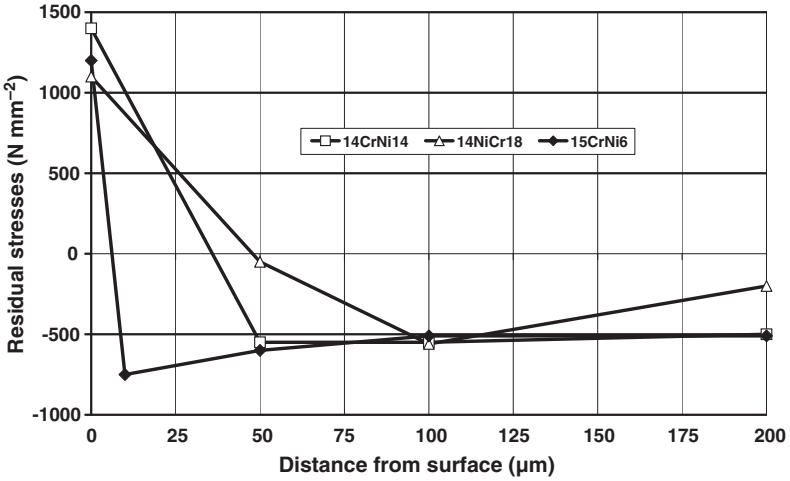

Figure 38 Residual stresses in the austenite phase of deep cooled nickel-alloyed carburized microstructures. 925 °C → oil, 60 °C; deep cooled at −196 °C; case carbon content 0.85%; CHD = 1.0 mm. Reproduced from Genzel, C.; Reimers, W.; Schwarz, O.; Grosch, J. Restaustenit und Eigenspannungs-verteilung in tiefgekühlten einsatzgehärteten Gefügen. In *Eigenspannungen und Verzug durch Wärmeeinwirkung*; Aurich, D., Kloos, K.-H., Lange, G., Macherauch, E., Eds.; DFG-Wiley-VCH: Weinheim, 1999; pp 115–119.

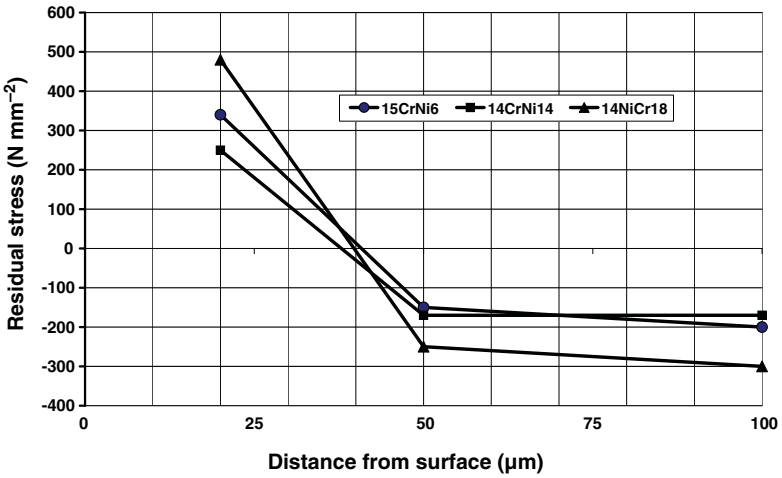

Figure 39 Residual stresses in the austenite phase of deep-cooled and tempered nickel-alloyed carburized microstructures 925 °C → oil, 60 °C; deep cooled at −196 °C; 180 °C, 1 h; case carbon content 0.85%; CHD = 1.0 mm. Reproduced from Genzel, C.; Reimers, W.; Schwarz, O.; Grosch, J. Restaustenit und Eigenspannungs-verteilung in tiefgekühlten einsatzgehärteten Gefügen. In *Eigenspannungen und Verzug durch Wärmeeinwirkung*; Aurich, D., Kloos, K.-H., Lange, G., Macherauch, E., Eds.; DFG-Wiley-VCH: Weinheim, 1999; pp 115–119.

Figure 40 Intergranular surface oxidation, 15CrNi6, unetched microstructure.

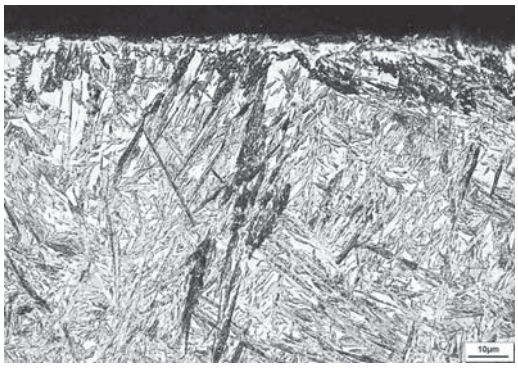

Figure 41 Effect of surface oxidation on carburized microstructure. X19NiCrMo4 (light micrograph, etched with nital).

below the surface, Figure 42. Manganese determines the size and silicon the depth of surface oxidation (*40*). Silicon segregations can establish extreme intergranular surface oxidation, Figure 43. The plasma and low pressure carburizing processes use C_2H_2 or CH_4 as carbon sources, the atmospheres are free of oxygen, surface oxidation does not occur. However, in the low pressure of these atmospheres, below 30 mbar, manganese effuses and thus the hardenability also deteriorates.

In carburized microstructures, *carbides* can be precipitated. Coarse, bone-like carbides (Figure 44) and carbides on grain boundaries (Figure 45) result from faults in carbon potential control or in quenching and lead to a decline in toughness properties. Microstructures with spherical and uniformly dispersed carbides in the martensitic matrix, Figure 46, are produced specifically to improve the wear resistance.

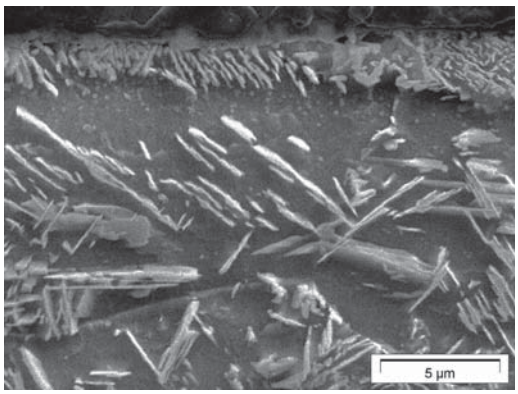

Figure 42 Effect of surface oxidation on carburized microstructure. X19NiCrMo4. Scanning electron micrograph; detail from **Figure 41**.

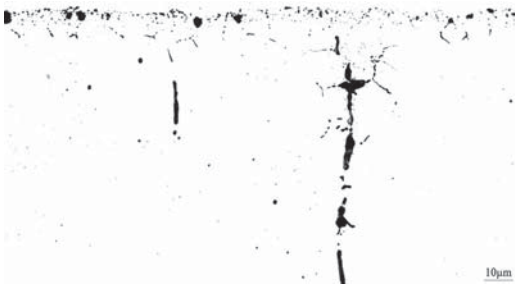

Figure 43 Extreme intergranular surface oxidation, as-polished surface, 14NiCr18.

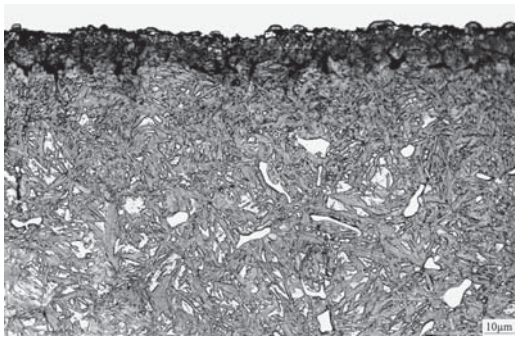

Figure 44 Carbides in a carburized microstructure, 15CrNi6 (light micrograph, etched with nital).

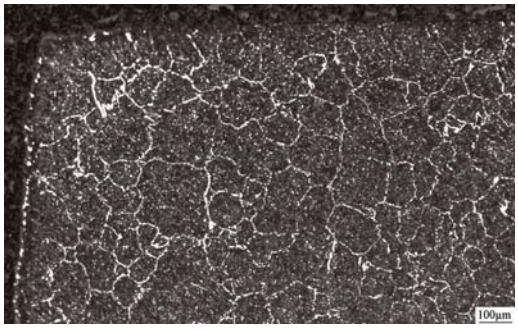

Figure 45 Carbides on (prior austenite) grain boundaries, 16MnCr5 carburized (light micrograph, etched with nital).

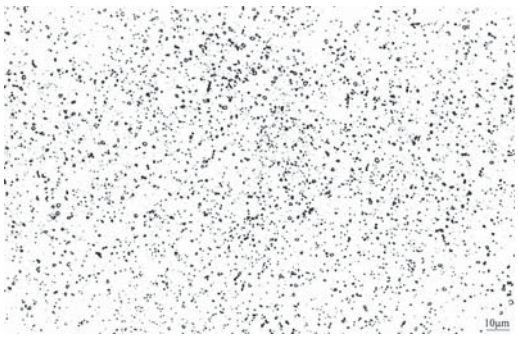

Figure 46 Homogeneous carbide precipitation in carburized 15CrNi6 (light micrograph, etched with nital).

Nonmetallic inclusions such as oxides and sulfides as well as banded structures originate from the steel making process and cannot be altered by carburizing. Manganese sulfides are usually longitudinal from hot forming and reduce the ductility if the applied forces act vertically to the inclusions. Figure 47 demonstrates manganese sulfides in the fracture surface of a carburized component which failed in service. The spherical inclusions in Figure 47 are hard aluminum oxides, which remain stable during hot forming. Those oxides can initiate subsurface fatigue fracture, Figure 48.

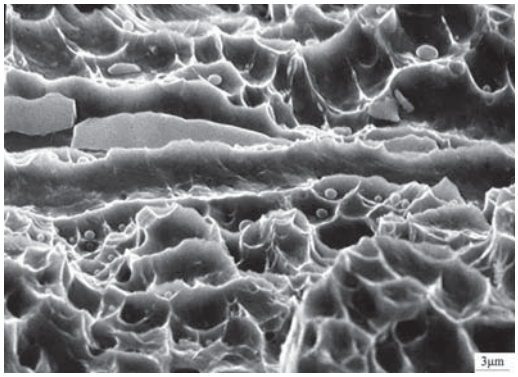

Figure 47 Manganese sulfides and (Al-) oxides in the fracture surface of carburized 16MnCr5. Scanning electron micrograph.

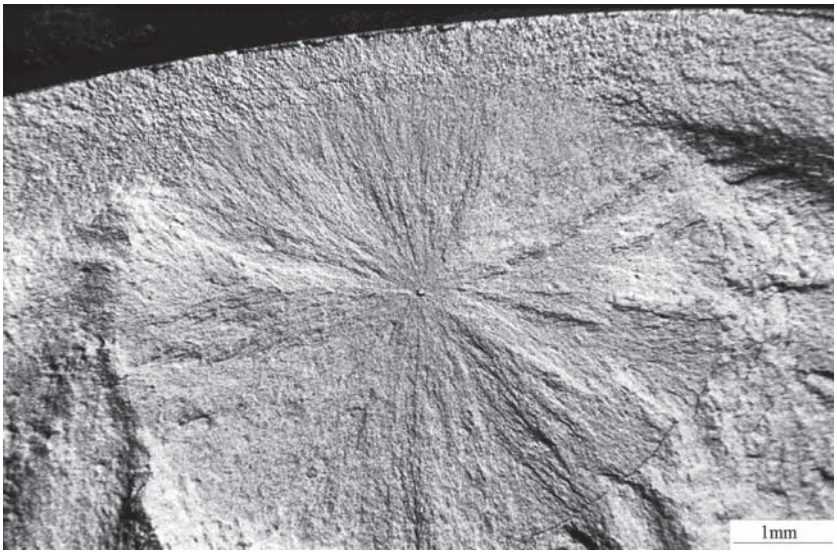

Figure 48 Subsurface fatigue fracture initiation. (14NiCr14) Scanning electron micrograph.

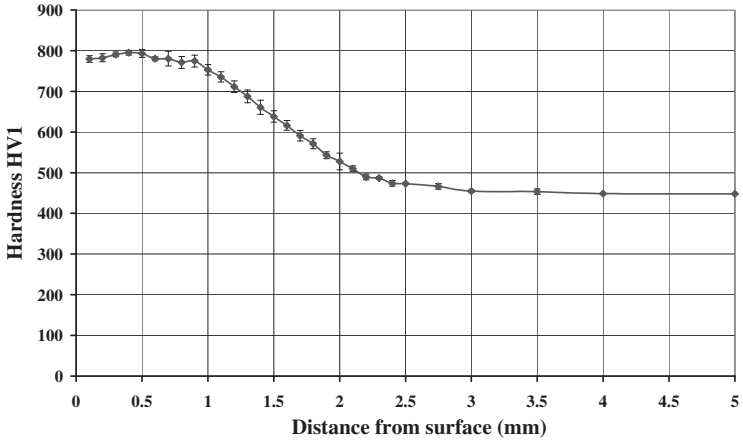

Figure 49 Hardness profile of X12MoCrNiV4-4-2. (M50NiL). Specimen ground before hardness measurement. 950 °C, 1 h → 1070 °C → N_2, 6 bar → 540 °C, 2 h → −80 °C, 30 min → 540 °C, 2 h.

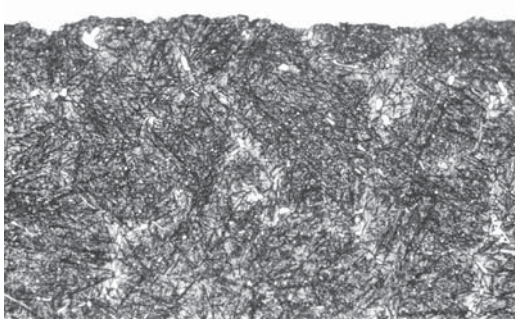

Figure 50 Microstructure of X12MoCrNiV4-4-2 (M50NiL). Surface hardness 760 ± 6 HV10. 950 °C, 1 h → 1070 °C → N_2, 6 bar → 540 °C, 2 h → −80 °C, 30 min → 540 °C, 2 h (light micrograph, etched with nital).

12.12.5 Special Applications of Carburizing

Gears exposed to high temperature operating conditions require a high hot wear resistance. On the basis of the molybdenum high speed tool steel 80MoCrV42-16 (trade name M50), the carburizing steel X12MoCrNiV4-4-3 (trade name M50NiL) was developed which in the carburized condition combines the properties of a graded microstructure with the hot wear resistance of high speed steels (*41,42*). The complex heat treatment process together with the hardness profile is depicted in **Figure 49**. Carbide precipitation is inevitable when carburizing this high alloyed steel, **Figure 50**.

Stainless steels can be carburized after activating their oxide layer. The amount of dissolved chromium decreases by the precipitation of chromium carbides and can drop below 13%Cr, the limit for corrosion resistance. Carburized austenitic stainless steels are nonmagnetic and therefore suited for applications in which wear resistance and nonmagnetic behavior are required but corrosion resistance is not necessary. Carburized steels such as X7CrCoNiMoV13-5-2-2 (trade name Pyrowear) keep their corrosion resistance when a sufficient amount of chromium is dissolved in the austenite and martensite, and carbide precipitation is avoided by suitable tempering procedures.

The strengthening of the case microstructure of austenitic stainless steels by supersaturated dissolved carbon in the austenite (*43–46*) does per definition not belong to carburizing.

12.12.6 Properties

Carburizing is the heat treatment process that is mainly selected for improving the mechanical fatigue strength as well as the rolling contact fatigue strength of components. In gears, the tooth root is stressed by mechanical fatigue and the tooth flank by rolling contact fatigue, therefore gears (and steering elements) are typical carburized components. In addition to the fatigue properties, carburized components should have enough toughness to withstand impacts without (catastrophic) fracture and, in service even more important, enough ductility to avoid cracks, which can start premature fatigue failure.

12.12.6.1 Fatigue Behavior

Repeatedly applied loads, which are lower than the limiting load in a single application, result in cyclic stresses and strains in the material and activate dislocation processes causing cyclic strain hardening and cyclic strain softening. Uneven dislocation movements in one cycle can result in irreversible plastic strain, which accumulates during cyclic loading, damages the originally flawless material, and starts crack initiation. In homogeneous microstructures with a homogeneous state of stresses, the plastic strain starts in the bulk and concentrates with ongoing cyclic loading more and more at and in regions near the surface. Cracks nucleate preferably in grains at the surface, propagate stable, eventually become unstable and cause macroscopic fracture (for detailed discussion of fatigue, see among others Refs. (47,48)).

In the design of components the fatigue behavior of materials is usually given in *S*–*N*-curves (Wöhler diagrams) in which the number of cycles to failure *N* is plotted depending on the applied loads or, in relation to a cross section, on the amplitude of the cyclic stresses *S*. However, the results of a great many available investigations can rarely be compared quantitatively because of the large number of parameters that influence the *S*–*N*-curves such as specimen geometry (length and cross section, notch geometry, surface conditions), test conditions (type of loading, frequency, cooling, number of stress levels) and after all, heat treatment. In addition, several near identical specimens tested under constant test conditions at the same stress level fail at different numbers of cycles. **Figure 51** (49) shows results of rotating bending tests with notched specimens of steel 16MnCr5 with a considerable scattering of the number of cycles to failure in the range of finite life, in which all specimens fail, and in a transition range in which, at a given stress amplitude, some specimens fail, whereas others run through to a fixed limiting number of cycles. Therefore, *S*–*N*-curves of body-centered-cubic materials should be described by a range of finite life and a transition range, for both of which the probabilities of failure or of survival are calculated statistically (50). The arcsin-$\sqrt{P}$-method has proved an appropriate way for the calculation of the probability *P* and is applied in **Figure 52** (49) as probability of failure $P = 5\%$ and $P = 95\%$ to the results of **Figure 51**. The probability of failure $P = 5\%$ as the lower limiting line of the transition range leads in **Figure 52** to the fatigue strength $\sigma_D = 480\ \text{N mm}^{-2}$, the statistically safe value for a limiting number of cycles $N_G = 5 \times 10^7$. This example shows the importance of the determination of the limiting number of cycles in an investigation program. A limiting number of cycles 10^7 instead of the chosen 5×10^7 would have resulted in about $100\ \text{N mm}^{-2}$ higher values of the fatigue strength at $P = 5\%$. The development of statistically evaluated *S*–*N*-curves consumes time and money; it is understandable that the variety of the numerous parameters has so far not been investigated in total. The following description of the correlations between the parameters of carburized microstructures and their fatigue behavior is based as far as possible on statistically evaluated results; otherwise tendencies only are available as mentioned above. Case hardening is useful for components loaded with heterogeneous states of stresses, in consequence most of the reported results are from rotating bending tests or from cantilever bending tests.

12.12.6.2 Fatigue Properties of Carburized Microstructures

Carburized microstructures can be characterized with the hardness profiles and the residual stress distribution, as described earlier. In the concept of the local fatigue resistance (51–53), the residual stresses are considered as mean stresses (54). This approach is acceptable as long as the residual stresses are not reduced by plastic flow, which occurs in microstructures of high hardness. Negative mean stresses, i.e., compressive residual stresses, enlarge the allowed stress field and increase the fatigues limits (52,55,56). The local

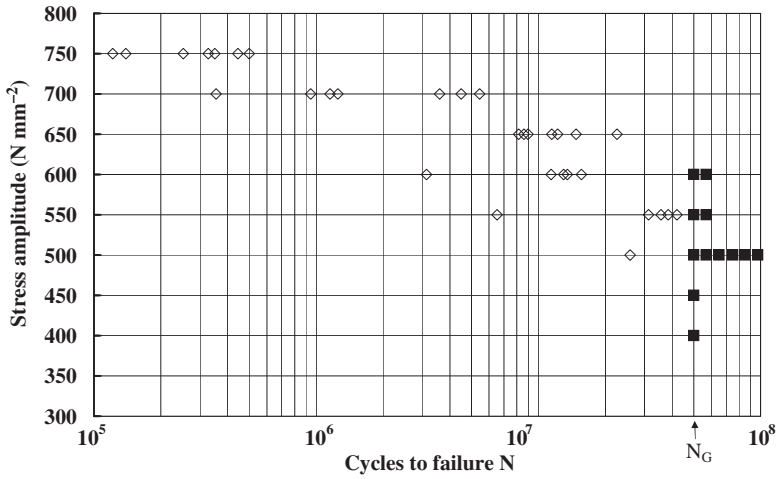

Figure 51 Results of rotating bending tests, steel 16MnCr5: quenched to 60 °C; $\alpha k = 2.01$, case carbon content 0.7%, CHD = 0.5 mm, N_G limiting number of cycles 5×10^7, open symbols: broken specimens, full symbols: run through to N_G. Reproduced from Dressel, K.; Grosch, J. Einfluß des Anlassens auf Bauteil- und Bearbeitungs eigenschaften einsatzgehärteter Bauteile, FVA-Bericht 679, 2002.

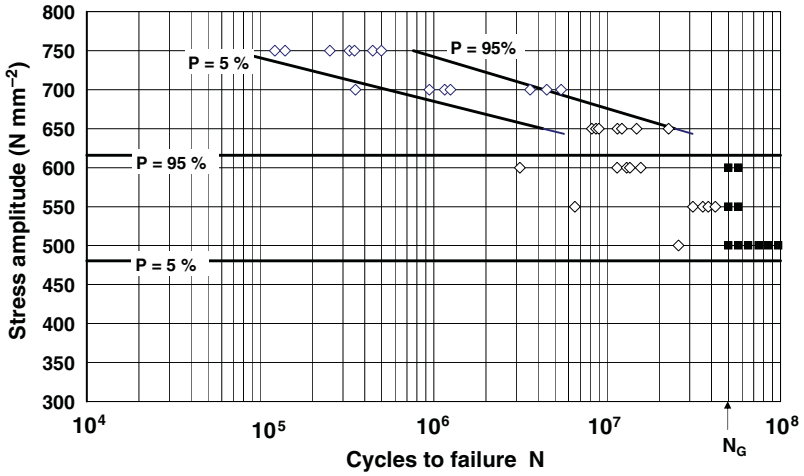

Figure 52 Results of rotating bending tests, steel 16MnCr5: quenched to 60 °C; $\alpha k = 2.01$, case carbon content 0.7%, CHD = 0.5 mm, N_G limiting number of cycles 5×10^7, open symbols: broken specimens, full symbols: run through to N_G. Reproduced from Dressel, K.; Grosch, J. Einfluß des Anlassens auf Bauteil- und Bearbeitungs eigenschaften einsatzgehärteter Bauteile, FVA-Bericht 679, 2002.

fatigue strength resulting from the interaction of the hardness profile and the residual stress distribution is a material property that resists the loading stresses (**Figure 53**, (*57*)).

The surface properties become decisive when steep loading stress distributions, i.e., steep stress gradients χ and especially when notch stresses are applied because then failure starts at the surface. Lower loading stresses can initiate cracks beneath the surface, especially if the core strength or the case depth is too low (see **Figure 53**). Inhomogeneities in the microstructure, such as nonmetallic inclusions or segregations, reduce the strength locally and can promote subsurface crack initiation. The concept of the local fatigue resistance has been confirmed in numerous investigations and serves, as well as the Weibull failure probability concept (*58,59*), as a basis for the calculation of the fatigue strength of carburized components (*60,61*).

The amount of retained austenite is well suited to describe, with one value, the influence of the heterogeneous case microstructure, determined by case carbon content, the heat treatment conditions and the material, on the fatigue behavior of carburized steels. The predominant number of results show that the fatigue strength decreases with increasing case carbon content and, as a consequence, increasing amounts of retained austenite (*62–65*), contrary results are less common (*66,67*). **Figure 54** shows results of rotating bending tests with unnotched specimens of steel 16MnCr5 with case carbon contents of 0.6%C corresponding to 5% retained austenite and of 1.4%C corresponding to 90% retained austenite. The fatigue strength decreases with increasing amounts of retained austenite (*62*). The results in **Figure 55** (*64*) are valid for cantilever bending of specimens from steel SAE8719 with equal case carbon content and different carburizing procedures which also influence the austenite grain size (**Figure 56**, (*64*)). The specific

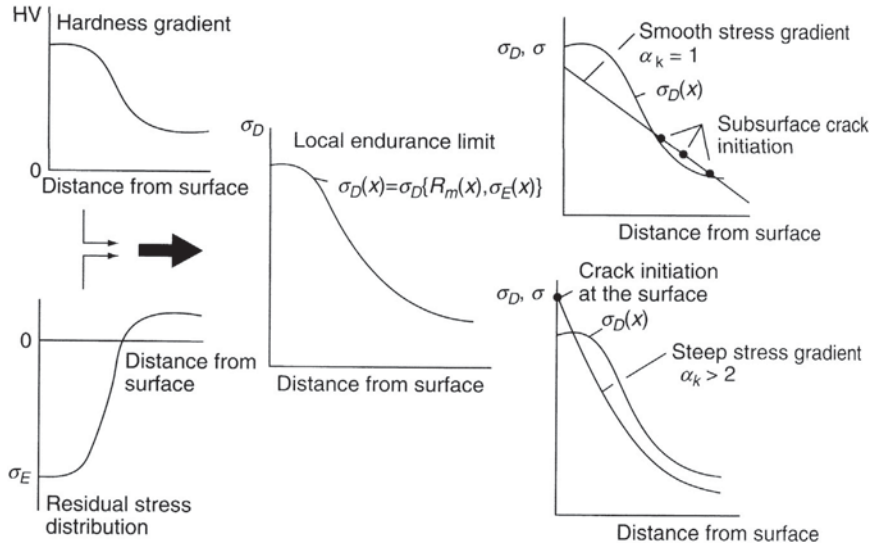

Figure 53 Concept of the local endurance limit. Reproduced from Kloos, K. H. Festigkeits- und Verschleißeigenschaften induktiv randschichtgehärteter Proben und Bauteile. *Härterei Techn. Mitt.* **1989**, *44*, 157–165.

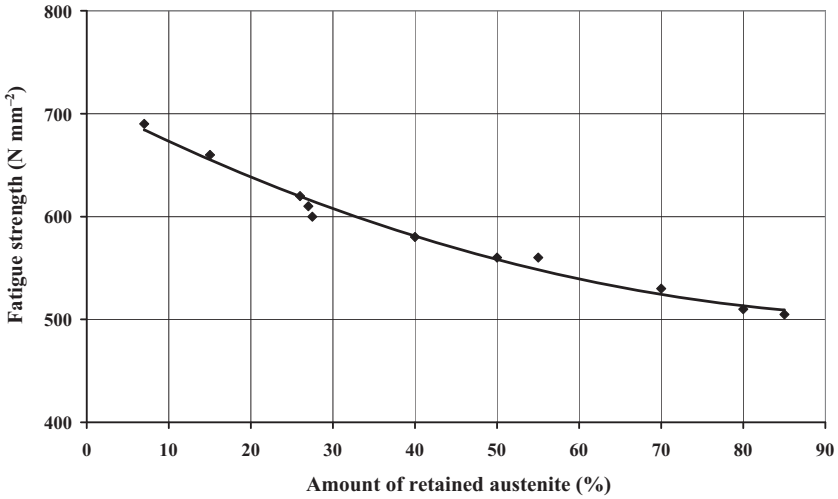

Figure 54 Influence of retained austenite on fatigue strength. Adapted from Beumelburg, W. Das Verhalten von einsatzgehärteten Proben mit verschiedenen Oberflächenzuständen und Randkohlenstoffgehalten im Umlaufbiege-, statischen Biege- und Schlagbiegeversuch. Diss. Universität (TH) Karlsruhe, 1973.

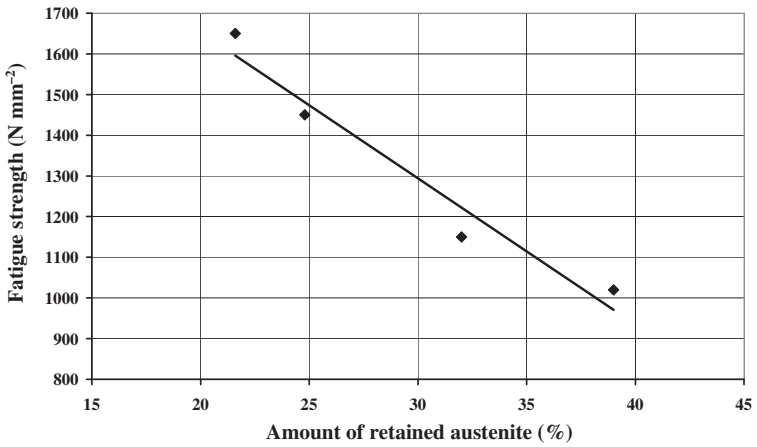

Figure 55 Influence of retained austenite on fatigue strength. Cantilever tests. Adapted from Pacheco, J. L.; Krauss, G. Microstructure and High Bending Fatigue Strength, Carburized Steels; Krauss, G., Ed.; Lakewood, 1989; pp 227–237.

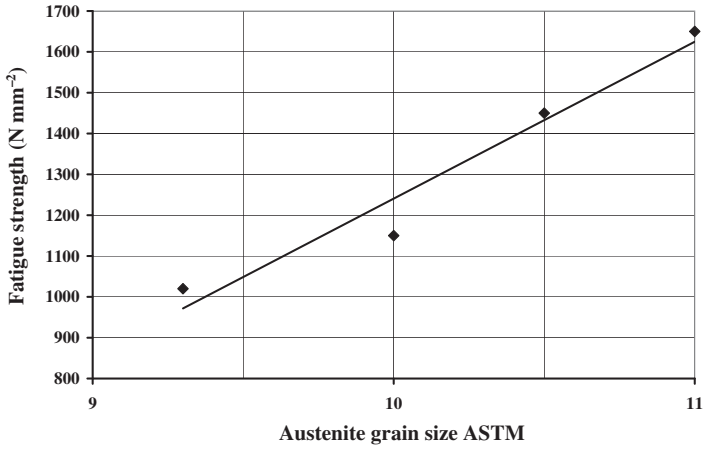

Figure 56 Influence of austenite grain size on fatigue strength. Cantilever tests. Adapted from Pacheco, J. L.; Krauss, G. Microstructure and High Bending Fatigue Strength, Carburized Steels; Krauss, G., Ed.; Lakewood, 1989; pp 227–237.

influence of both parameters on the fatigue strength cannot be discussed separately so it remains an open question whether the retained austenite or the grain size – or more likely both – are responsible.

Results from rotating bending tests with specimens of nickel alloyed carburizing steels (*68–70*) show maximum fatigue strength at medium amounts of retained austenite (**Figure 57**). Obviously, the better ductility of nickel alloyed martensite (*71–73*) predominates the detrimental influence of the heterogeneous martensite-retained austenite microstructure. Molybdenum has similar effects (*74*). The beneficial effect of nickel becomes obvious by varying the nickel content of microstructures carburized to equal case carbon content, **Figure 58** (*70*). The fatigue strength P10 of the specimens with the higher nickel content is more than 50% higher, although contrary to the concept of the local fatigue resistance, the values of hardness and of compressive residual strength of the higher nickel alloyed microstructure are lower. In practice, carburized microstructures are tempered at temperatures of about 180 °C to enhance ductility and grindability although, according to the concept of local fatigue resistance, the lower hardness and compressive residual stress values of tempered microstructures result in lower fatigue strength, as shown in **Figure 59** for rotating bending tests with steel 16MnCr5 (*49*). The best values of the fatigue strength in these experiments are obtained with the martempered microstructure but could not generally be confirmed.

In hard microstructures with a low ability to plastic deformation fatigue cracks start at the surface with intergranular growth in a few grains, **Figure 60**, and then turn to transgranular growth, **Figure 61**. Therefore, the prior austenite grain size and the properties of the grain boundaries in carburized microstructures are essential parameters for the start and growth of cracks. Coarse (austenite) grain size with relatively small grain boundary surface is susceptible to segregation during the diffusion treatment. A comparison of

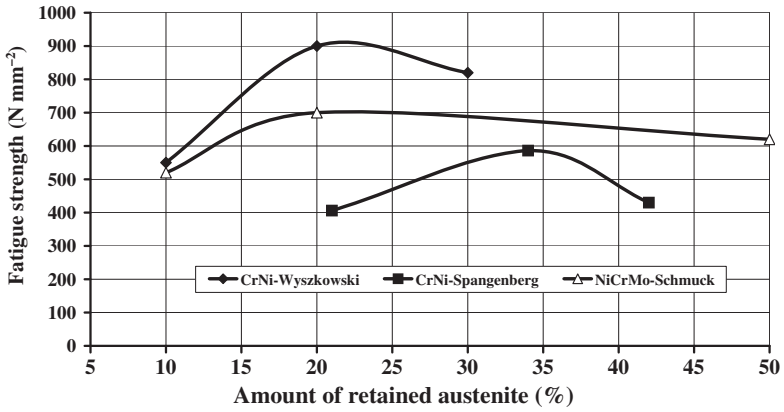

Figure 57 Influence of retained austenite on fatigue strength of nickel-alloyed steels. Rotating bending tests. Adapted from Wyszkowski, J.; Priegnitz, H.; Ratkiewicz, A.; Gozdzik, E. *Rev. Met.* **June 1971**, 411 (cit. in: Prado 69); Prado, J. M., Arques, J. L. Influence of Retained Austenite on the Fatigue Endurance of Carbonitrided Steels. *J. Mater. Sci.* **1984**, *19*, 2980–2988; Spangenberg, S.; Grosch, J.; Scholtes, B. Untersuchungen zum Einfluß des Restaustenits auf die Schwingfestigkeit einsatzgehärteter Proben. *HTM Z. Werkst. Wärmebeh. Fertigung* **2004**, *59*, 12–17.

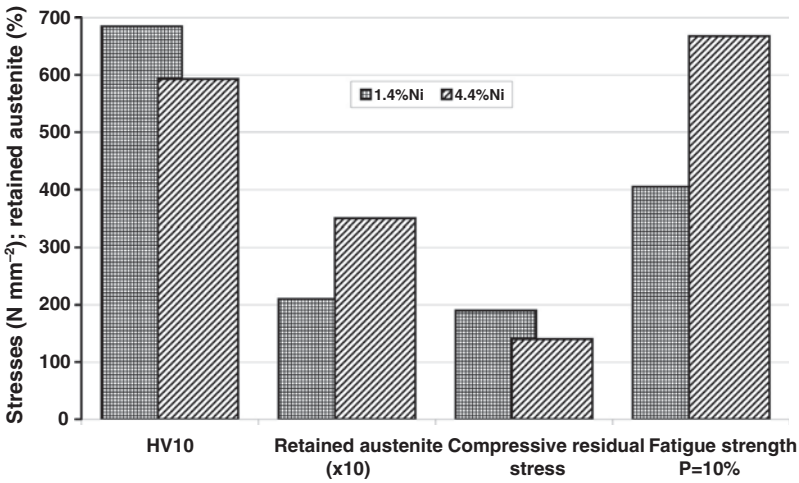

Figure 58 Fatigue strength of nickel-alloyed steels: rotating bending tests, case carbon content 0.7%; CHD = 1 mm; ak = 1.64. Adapted from Spangenberg, S.; Grosch, J.; Scholtes, B. Untersuchungen zum Einfluß des Restaustenits auf die Schwingfestigkeit einsatzgehärteter Proben. *HTM Z. Werkst. Wärmebeh. Fertigung* **2004**, *59*, 12–17.

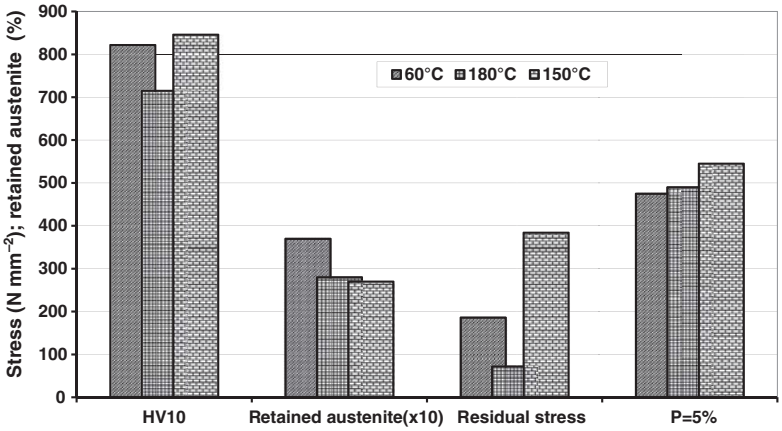

Figure 59 Results of rotating bending tests, steel 17CrNiMo6: quenched to 60 °C; tempered at 180 °C, martempered at 150 °C, $\alpha k = 2.01$, case carbon content 0.7%, CHD = 0.5 mm, N_G limiting number of cycles. Reproduced from Dressel, K.; Grosch, J. Einfluß des Anlassens auf Bauteil- und Bearbeitungs-eigenschaften einsatzgehärteter Bauteile, FVA-Bericht 679, 2002.

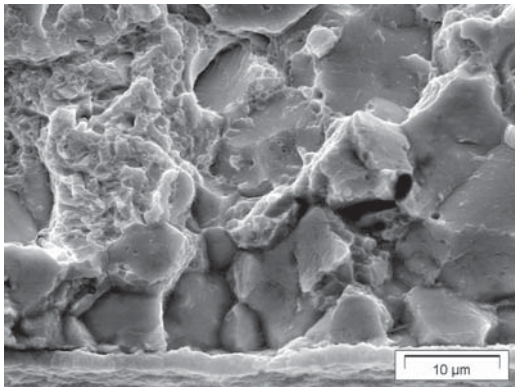

Figure 60 Intergranular start of a fatigue fracture, 17CrNiMo6; case carbon content 0.7%; CHD = 0.5 mm, as quenched, $\sigma = 500$ N mm^{-2}; cycles to failure $2.08 \cdot 10^7$. Scanning electron micrograph.

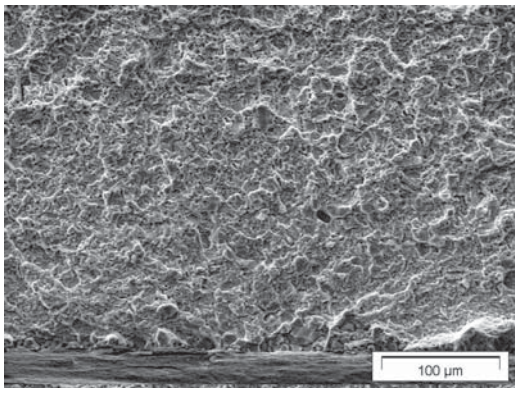

Figure 61 Transgranular growth of a fatigue fracture, 17CrNiMo6; case carbon content 0.7%; CHD = 0.5 mm, as quenched, $\sigma = 500$ N mm^{-2}; cycles to failure $2.08 \cdot 10^7$. Scanning electron micrograph.

the fatigue strength of carburized steels with different phosphorus contents (*75*) serves as an example to show the deleterious influence of phosphorus segregation, **Figure 62**. The damage of the case microstructure by surface intergranular oxidation and the loss of alloy elements establishing the hardenability during carburization in oxygen containing atmospheres (*61,62,76*), as well as the damage by manganese effusion and thermal etching effects during carburization in oxygen free atmospheres (*77–79*), are detrimental to the fatigue strength. **Figure 63** shows an example of the effect of surface intergranular oxidation (*62*).

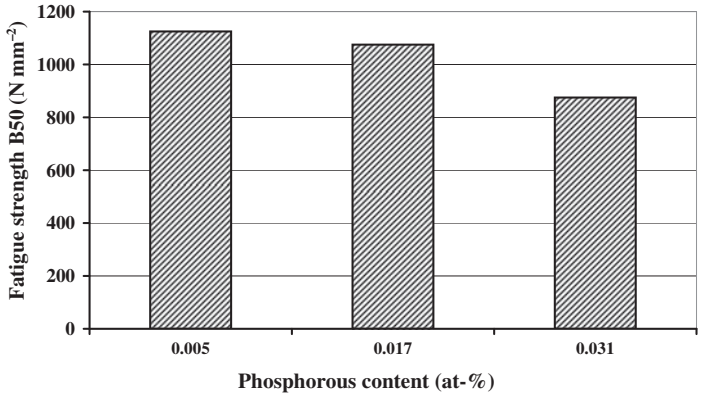

Figure 62 Influence of phosphorous content on fatigue strength, cantilever tests. Adapted from Hyde, R. S.; Matlock, D. K.; Krauss, G. Phosphorous and Carbon Segregation: Effects on Fatigue and Fracture of Gas-carburized Modified 4320 Steel. *Metall. Trans.* **1994**, *25A*, 1229–1240.

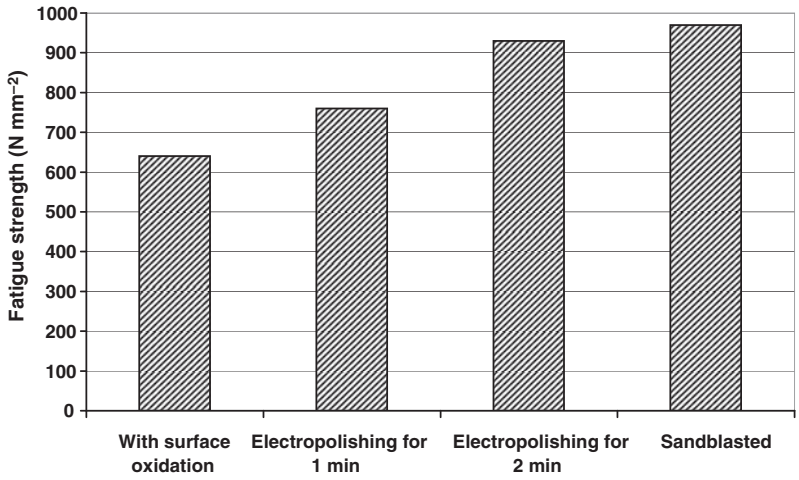

Figure 63 Influence of intergranular surface oxidation on fatigue strength of steel 20MoCr4. Rotating bending tests, $\alpha k = 1$, $N_G = 10^7$, surface carbon content 0.67%. Adapted from Beumelburg, W. Das Verhalten von einsatzgehärteten Proben mit verschiedenen Oberflächenzuständen und Randkohlenstoffgehalten im Umlaufbiege-, statischen Biege- und Schlagbiegeversuch. Diss. Universität (TH) Karlsruhe, 1973.

The influence of the case hardening depth is linked with a size effect already known from components that were not surface hardened. The advantages of case hardening decrease with increasing size. In consequence, the effect of the case hardening depth on the fatigue strength should be described in relation to the diameter of the specimen, CHD/d, for quantitative comparisons with equal case hardness. Figure 64 (*80,81*) proves that a related case hardness depth CHD/d of about 10–20% results in optimal fatigue strength, and also illustrates the important influence of the specimen geometry.

12.12.6.3 Toughness and Ductility

The toughness of carburized composite materials is dominated by two major parameters; all the other parameters are of much less influence (*82*).

The first dominating parameter is the distribution of the microstructures, which can be described by the specific case depth CHD/d, determined as the relation of case depth CHD in the maximum stressed cross-section to the total cross-section d of the component. With an increasing amount of hard microstructure in the case the resistance of the component to impact loads decreases significantly as shown by impact loads and absorbed energy (Figure 65, (*83*)). With a specific case depth of more than 30%, there is no further advantage in carburizing, the toughness has reached the level of a through-hardened microstructure. Each point in Figure 65 represents the mean value of six test results. A total of 50 alloyed carburizing steels were investigated in the carburized and the blank carburized condition, completed with the results of through hardened steels simulating a case depth of 100%. The specimens have been machined from rod material. The toughness measured with specimens taken in longitudinal direction is considerably higher than the toughness from specimens taken vertically (Figure 65). Manganese sulfides orientated in longitudinal direction during hot forming weaken the microstructures when stressed in vertical direction (see also Figure 48), main

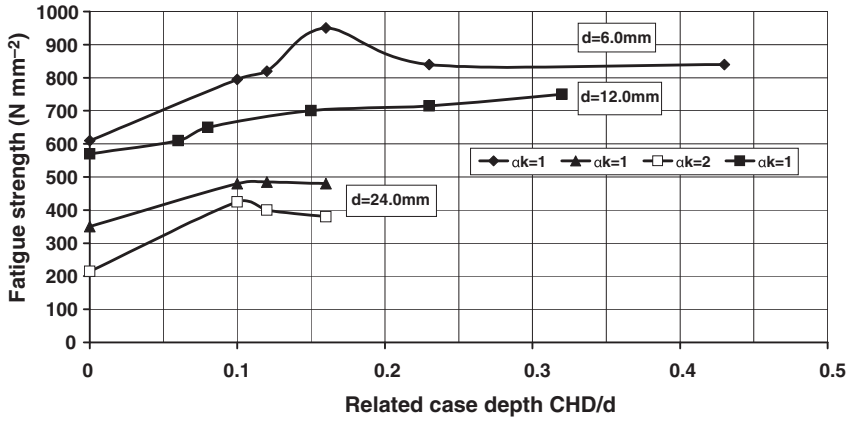

Figure 64 Influence of the related case depth CHD/*d* on fatigue strength. Adapted from Wiegand, H.; Tolasch, G. Über das Zusammenwirken einzelner Faktoren zur Steigerung der Biegewechselfestigkeit einsatzgehärteter Proben. *Härterei Techn. Mitt.* **1967**, *22*, 213–220; Kloos, K. H.; Fuchsbauer, B.; Magin, W.; Zankov, D. Übertragbarkeit von Probe-Stab-Schwingfestigkeitseigenschaften auf Bauteile. *VDI-Berichte* **1979**, *354*, 59–72, Düsseldorf, VDI-Verlag.

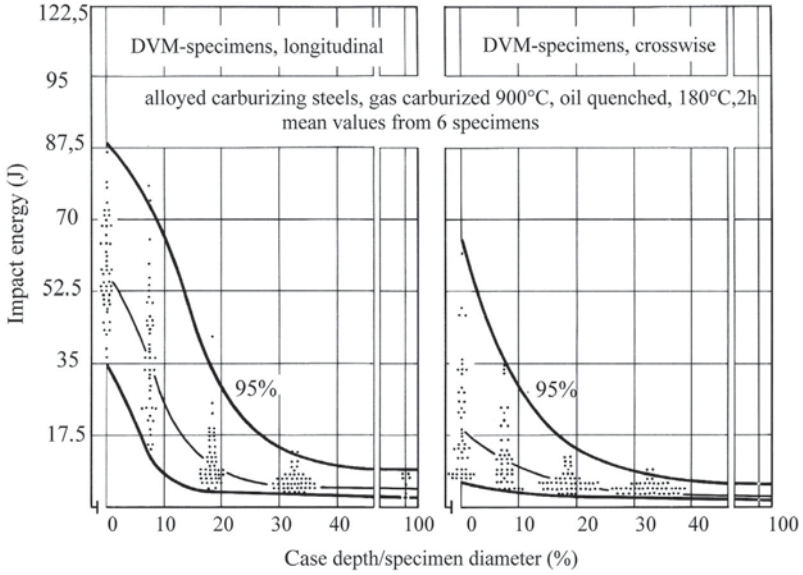

Figure 65 Influence of the related case depth CHD/*d* on the impact energy. Reproduced from Grosch, J.; Wicke, D. Bruchverhalten und Duktilität schlagbeanspruchter einsatzgehärteter Gefüge. *Härterei Techn. Mitt.* **1982**, *36*, 227–235.

parameter is the amount of sulfur. When comparing the toughness of carburized components it is always necessary to refer to the influence of material, design and heat treatment in particular *and* on the same specific case depth in order to avoid wrong conclusions. The results in Figure 66 show also that the toughness of carburized components is described satisfactorily by the instrumented impact test, which can be carried out easily.

The second dominating parameter is the carbon content in case and core, which determines microstructures and properties (Figure 66, (*84*)). Carbon contents for maximum hardenability (0.6–0.7%) are needed in the case and low carbon contents according to DIN EN ISO 10084 are of advantage in the core. Again, it should be mentioned that only the properties of those microstructures can be compared which have equal carbon profiles. The amount of retained austenite has no significant effect on fracture toughness (Figure 67, (*84*)).

The two results allow the conclusion that for the toughness of carburized components, the specific case depth should be as small as possible (this will almost always conflict with the requirements of high fatigue, high contact fatigue and high wear resistance performance), the carbon content in the case should be close to 0.6–0.7%, which can be easily maintained in computer controlled gas carburizing, and that the design should avoid single overloads. Good examples for design performance are the load characteristics of automatic gear boxes and of manual gear boxes (*85*).

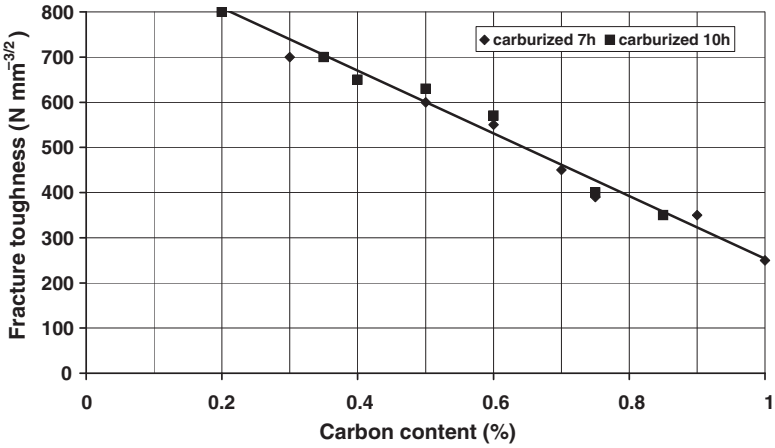

Figure 66 Fracture toughness of the carburized case. SAE4820, 925 °C → 840 °C → martempered 170 °C. Adapted from Smith, Y. E.; Diesburg, D. E. Fracture Resistance in Carburizing Steels. Part I: Fracture Toughness. *Met. Prog.* **May 1979**, 68–73.

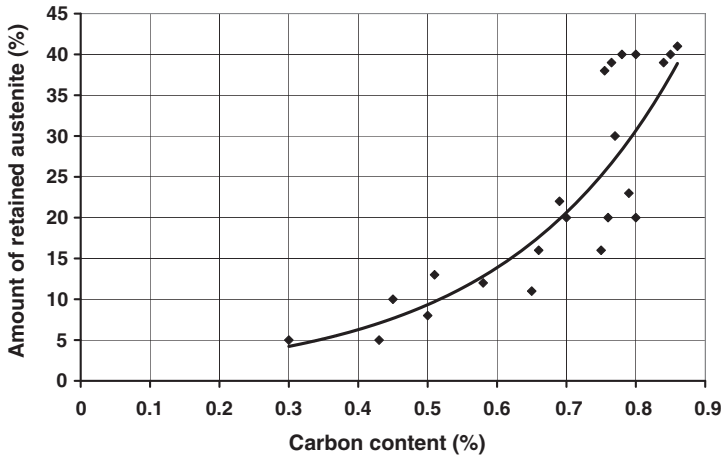

Figure 67 Amount of retained austenite in the case. SAE4820, 925 °C → 840 °C → martempered 170 °C. Adapted from Smith, Y. E.; Diesburg, D. E. Fracture Resistance in Carburizing Steels. Part I: Fracture Toughness. *Met. Prog.* **May 1979**, 68–73.

As gears become smaller and smaller in the development of new products, the imposed loads become higher and the specific case depths deeper. Overload fracture caused by unstable cracks can usually be avoided, nevertheless stable cracks due to inevitable single overloads are dangerous and must be avoided because those cracks can initiate damage by fatigue, pitting and wear and shorten the in-service time of a carburized component. The fatigue strength in particular is markedly lowered by cracks.

The toughness of a carburized component with constant case depth and already optimized carbon content can only be further improved by a higher ductility of the case microstructure. The range of results in **Figure 66** points to a possible improvement because according to **Figure 68** (*83*) the higher values belong to carburizing steels alloyed with nickel whereas the lower values belong to carburizing steels which are not alloyed with nickel. The ductility of the case can be characterized adequately with the bending-crack-stress of slow bend tests, the bending stress which initiates the first crack in the case (*62,83,86*). The bending-crack-stress can be improved significantly by alloying with nickel (*73*). The beneficial effect of nickel is more distinctive with double reheated microstructures (**Figure 69**) than with direct quenched microstructures (**Figure 70**) and of course in both heat treatments tempered microstructures are more ductile than the nontempered ones. Nickel suppresses or hinders the carbide precipitation during quenching from austenitization temperature (*87*) and improves, especially in the tempered, less distorted condition, the distribution of lattice defects in the matrix resulting in a more homogeneous slip distribution (*72*). The beneficial effect of double reheating is probably due to a minor influence of segregations to the grain boundaries as the grains are rebuilt during austenitization. The amount of retained austenite increases with increasing nickel content, which additionally improves the ductility as retained austenite locally transforms stress-induced into martensite. The increasing volume creates compressive stresses which increase the resistance against crack nucleation (*67,88*). The residual stresses have obviously no influence on the bending-crack-stress as carburized microstructures with residual stresses and through hardened microstructures without residual stresses have comparable values of the bending-crack-stress (**Figure 71**, (*10*)).

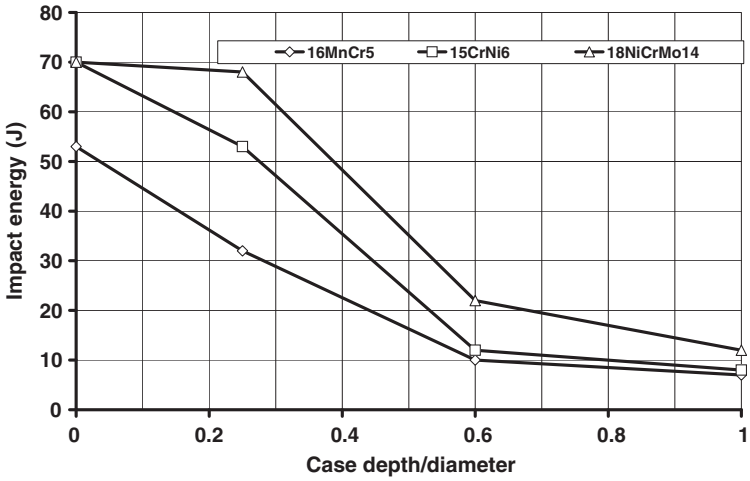

Figure 68 Influence of the related case depth CHD/*d* and the nickel content on the impact energy. DVM specimens. Reproduced from Grosch, J.; Wicke, D. Bruchverhalten und Duktilität schlagbeanspruchter einsatzgehärteter Gefüge. *Härterei Techn. Mitt.* **1982**, *36*, 227–235.

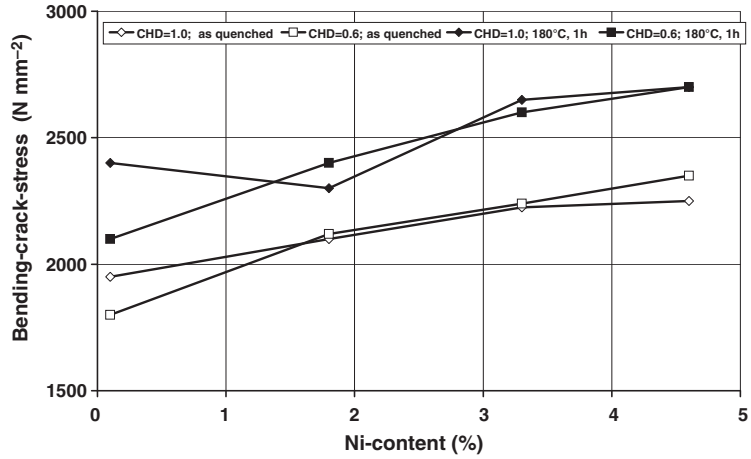

Figure 69 Effect of Nickel on the bending crack stress. Double reheated 925 °C → 60 °C and 840 °C → 60 °C. Reproduced from Thoden, B.; Grosch, J. Festigkeits- und Verformungsverhalten nickellegierter einsatzgehärteter Gefüge bei Biegebeanspruchung. *Härterei Techn. Mitt.* **1990**, *45*, 7–15.

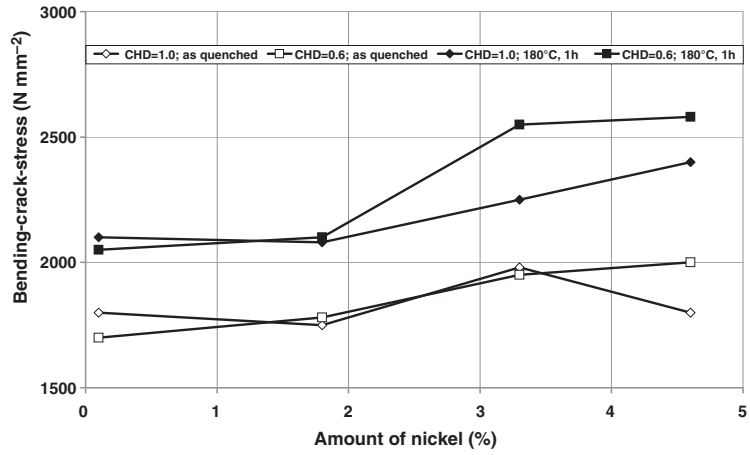

Figure 70 Effect of Nickel on the bending crack stress. Direct quench 925 °C → 60 °C. Reproduced from Thoden, B.; Grosch, J. Festigkeits- und Verformungsverhalten nickellegierter einsatzgehärteter Gefüge bei Biegebeanspruchung. *Härterei Techn. Mitt.* **1990**, *45*, 7–15.

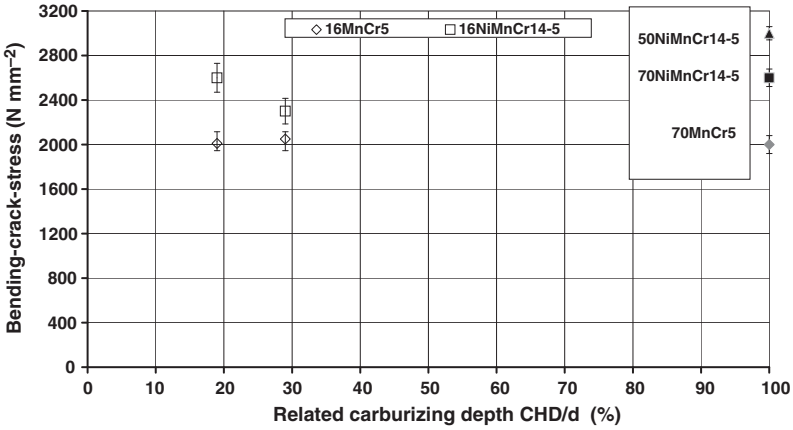

Figure 71 Bending crack stress of carburized and of quenched and tempered microstructures with the same carbon content. Adapted from Genzel, C.; Reimers, W.; Schwarz, O.; Grosch, J. Restaustenit und Eigenspannungs-verteilung in tiefgekühlten einsatzgehärteten Gefügen. In *Eigenspannungen und Verzug durch Wärmeeinwirkung*; Aurich, D.; Kloos, K. -H.; Lange, G.; Macherauch, E., Hrsg., Eds.; DFG-Wiley-VCH: Weinheim, 1999; pp 115–119.

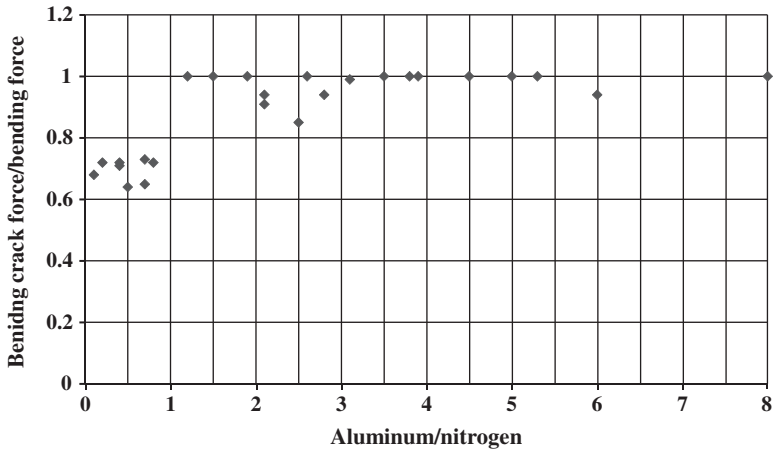

Figure 72 Effect of grain size on the ductility of direct quenched microstructures. 16MnCr5, 25 melts. 900 °C, 4 h → oil/50 °C; 180 °C, 2 h; CHD = 0.71 mm; case carbon content 0.7%C. Reproduced from Grosch, J.; Wicke, D. Bruchverhalten und Duktilität schlagbeanspruchter einsatzgehärteter Gefüge. *Härterei Techn. Mitt.* **1982**, *36*, 227–235.

As discussed earlier, the austenite grain size determines the maximal length of the martensite plates and, in consequence, the martensitic structure. Generally, microstructures with fine grains are more ductile than those with coarse grains. The effect of the grain size in a carburized microstructure is obvious in Figure 72, in which the relation σ_c/σ_b of the bending-crack-stress σ_c to the bending stress σ_b is plotted over the relation Al/N of the contents of aluminum and nitrogen. Values of $\sigma_c/\sigma_b > 1$ indicate brittle behavior with cracks nucleated at stress values below the bending stress. The ratio Al/N is used to determine the grain size stability at carburizing temperature, a ratio of three and more is required to avoid grain growth (*89*).

12.12.7 Summary

Heat treatment specifications for carburizing with which the heat treater can work must contain the required surface hardness and case depth, instructions for tempering, and the steel quality together with its chemical composition. Such a specification describes implicitly the hardness profile and in consequence the necessary carbon profile to be established in the diffusion step of carburizing as well as the hardenability and the influences of alloy elements on the carbon potential.

The carbon profile is the characteristic feature of the carburized components and determines the microstructures after quenching consisting of plate martensite and retained austenite in the case, i.e., at high carbon contents, and of lath martensite in the core with the carbon content of the selected steel or, depending on the hardenability and the size of the component, of a heterogeneous microstructure of lath martensite, bainite, pearlite and ferrite. In the transition range from case to core, both martensite morphologies develop simultaneously to a microstructure that is called mixed martensite. The hardness of martensite depends on

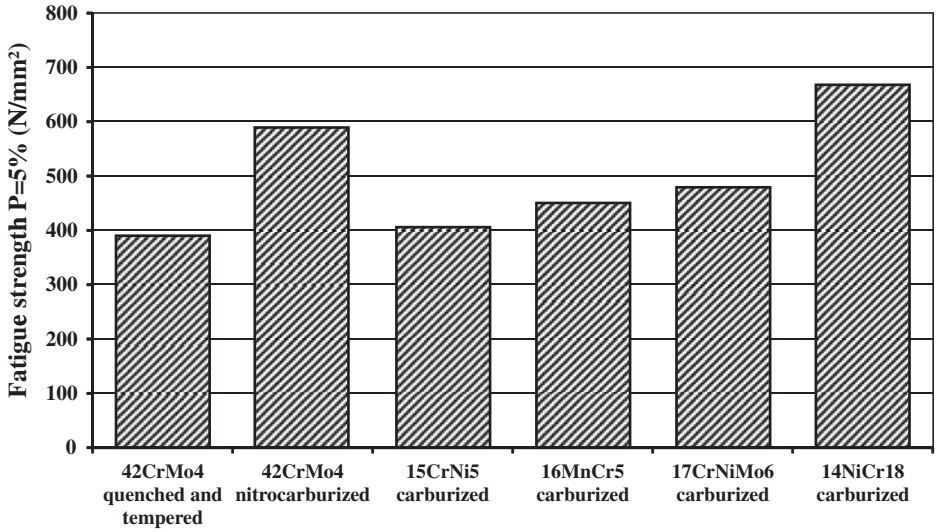

Figure 73 Comparison of the fatigue strength of some carburized and nitrided steels. Rotating bending tests, ak = 1.6. Carburized results adapted from Dressel, K.; Grosch, J. Einfluß des Anlassens auf Bauteil- und Bearbeitungs-eigenschaften einsatzgehärteter Bauteile, FVA-Bericht 679, 2002; Spangenberg, S.; Grosch, J.; Scholtes, B. Untersuchungen zum Einfluß des Restaustenits auf die Schwingfestigkeit einsatzgehärteter Proben. *HTM Z. Werkst. Wärmebeh. Fertigung* **2004**, *59*, 12–17.

the carbon content only; the macro-hardness of the case is determined by the amount of the softer retained austenite. Therefore, the amount of retained austenite is an important parameter for the properties of carburized microstructures. The martensitic transformation is accompanied by the formation of a residual stress distribution with compressive residual stresses in the case and tensile residual stresses in the region below the case and, inevitably, with distortion.

Hardness profile and residual stress distribution establish the superior fatigue resistance of carburized components, the main reason for this heat treatment. Governing parameters are the relation of case depth to the diameter of the component – most results recommend a ratio of 0.1–0.2 for best values, and the amount of retained austenite – most results indicate that the fatigue resistance decreases with an increasing amount of retained austenite. Therefore, in practice the carbon content of the case is kept at 0.6–0.7%. In deep cooling treatments, more austenite is transformed to martensite and higher hardness values are reached but the compressive residual stresses in the austenite phase change to tensile stresses, which is why deep cooling is not recommended for dynamically loaded components. Nickel and, less effective, molybdenum are reported to enhance the fatigue resistance, as illustrated by comparing the fatigue strength values P10 of differently heat treated specimens, Figure 73.

Carburized components should have sufficient toughness to withstand single overloadings without fracture or crack initiation. The relation of the hard case to the size of the component is the predominant parameter for toughness, and it is easy to understand that the toughness decreases with increasing thickness of the hard case in a component. The ductility of the case microstructure is enhanced by tempering and in addition by alloying with nickel. An important reason for every tempering treatment is the effusion of hydrogen.

Changes in the case microstructure by surface oxidation or effusion of manganese, grain coarsening, segregations and precipitation of coarse carbides can diminish the performance of carburized components.

References

1. Parrish, G. *Carburizing;* ASM: Materials Park, OH, 1999.
2. Davis, J. R. *Surface Hardening of Steels;* ASM: Materials Park, OH, 2002.
3. Krauss, G. *Steels: Processing, Structure and Performance;* ASM: Materials Park, OH, 2005.
4. Grosch, J. Heat Treatment in Gaseous Atmospheres. In *Steel Heat Treatment;* Totten, G., Ed.; CRC Press: New York, 2007; pp 415–474.
5. Grosch, J. *Einsatzhärten,* 3rd ed.; Expert-Verlag: Renningen, 2011.
6. Schwarz, O.; Thoden, B.; Grosch, J. Biegefestigkeit einsatzgehärteter und vergüteter Ni-Cr-Mn-legierter Gefüge. *Härterei Techn. Mitt.* **1991,** *46,* 317–326.
7. Genzel, C.; Reimers, W.; Schwarz, O.; Grosch, J. Development of the Residual Stress State in Carburized Steels due to the Austenite Transformation by Deep-cooling. In *DGM Info;* Hauck, V., Hougardy, H.-P., Macherauch, W., Tietz, H. D., Eds.; Gesellschaft: Oberursel, 1993; pp 129–138.
8. Schwarz, O.; Grosch, J.; Genzel, C.; Reimers, W. Gefüge und Eigenspannungen tiefgekühlter und angelassener einsatzgehärteter Stähle. *Härterei Techn. Mitt.* **1994,** *49,* 134–141.
9. Grosch, J.; Schwarz, O. Retained Austenite and Residual Stress Distribution in Deep Cooled Carburized Microstructures. In *Carburizing and Nitriding with Atmospheres;* Grosch, J., Morral, J., Schneider, M., Eds.; ASM, 1995; pp 71–76.
10. Genzel, C.; Reimers, W.; Schwarz, O.; Grosch, J. Restaustenit und Eigenspannungs-verteilung in tiefgekühlten einsatzgehärteten Gefügen. In *Eigenspannungen und Verzug durch Wärmeeinwirkung;* Aurich, D., Kloos, K.-H., Lange, G., Macherauch, E., Eds.; DFG-Wiley-VCH: Weinheim, 1999; pp 115–119.

11. Spangenberg, S. Untersuchungen zur Schwingfestigkeit einsatzgehärteter Stähle. Fortschrittsberichte VDI Nr. 602, Düsseldorf, 2000 (Diss. TU Berlin, 1999).
12. Krauss, G.; Marder, A. R. The Morphology of Martensite in Iron-carbon Alloys. *Trans. ASM* **1967,** *60,* 651–660.
13. Christian, J. W. Martensitic Transformation. In *Physical Metallurgy;* Cahn, R. W., Ed.; North Holland Publ. Comp: Amsterdam, 1970; pp 552–587. Chapter 10.
14. Nishiyama, Z. *Martensitic Transformation;* Academic Press: London, 1978.
15. Olsen, G. B.; Owen, W. S. In *Martensite;* ASM: Materials Park, OH, 1992.
16. Andrews, K. W. Empirical Formula for the Calculation of Some Transformation Temperatures. *J. Iron Steel Inst.* **1965,** *203,* 721–727.
17. Koistinen, D. P.; Marburger, R. E. A General Equation Describing the Extent of Austenite-martensite Transformation in Pure Carbon-iron Alloys and Plain Carbon Steel. *Acta Metall.* **1959,** *7,* 59.
18. Gerber, W.; Wyss, U. Härtbarkeit und Vergütbarkeit der Stähle. *Von-Roll-Mitt.* **1948,** *7* (2/3), 13–49.
19. Rose, A. Wärmebehandelbarkeit der Stähle. *Stahl Eisen* **1965,** *85,* 1229–1240.
20. Krauss, G. Martensite Transformation, Structures and Properties in Hardenable Steels. In *Hardenability Concepts and Applications to Steel;* Doane, D. V., Kirkaldy, J. S., Eds.; AIME: Warrendale, 1978; pp 229–248.
21. Just, E. Formeln der Härtbarkeit. *Härterei Techn. Mitt.* **1968,** *23,* 85–100.
22. Wyss, U. Kohlenstoff- und Härteverlauf in der Einsatzhärtungsschicht verschieden legierter Einsatzstähle. *Härterei Techn. Mitt.* **1988,** *43,* 27–35.
23. Zhiru, L.; Mufu, Y.; Fayi, Z.; Jingdong, C. A Study on Direct Quenching Process of Gear Made by Steel 20Cr2Ni4A Carburized at Low Temperature and High Concentration with Rare Earth. In *1995 Carburizing and Nitriding with Atmospheres. Conference Proceedings;* Grosch, J., Morral, J., Schneider, M., Eds.; ASM: Materials Park, OH, 1995; pp 149–155.
24. Yuan, Z.-X.; Yu, Z.-S.; Tan, P.; Song, S.-H. Effect of Rare Earth on the Carburization of Steel. *Mater. Sci. Eng.* **1999,** *A267,* 62–166.
25. Bell, T.; Sun, Y.; Lui, Z.; Yan, M. Rare-earth Surface Engineering. *Heat Treat. Met.* **2000,** *1,* 1–8.
26. Grosch, J. Einsatzhärten und Nitrieren von mit Seltenen Erden mikrolegierten Stählen. In *Proc. A3TS/AWT-Tagung Wärmebehandlung zur Härtung der Oberfläche. Straßburg;* 2006.
27. Thomas, G. Electron Microscopy Investigations of Ferrous Martensites. *Metall. Trans.* **1971,** *2,* 2373–2385.
28. Rose, A. Eigenspannungen als Ergebnis von Wärmebehandlung und Umwandlungs-verhalten. *Härterei Techn. Mitt.* **1966,** *21,* 1–6.
29. Macherauch, E.; Wohlfahrt, H.; Wolfstieg, U. Zur zweckmäßigen Definition von Eigenspannungen. *Härterei Techn. Mitt.* **1973,** *28,* 201–211.
30. Schröder, R.; Scholtes, B.; Macherauch, E. Rechnerische und röntgenographischéEigenspannungsausbildung in abgeschreckten Stahlzylindern. *Härterei Techn. Mitt.* **1984,** *39,* 280–292.
31. Speich, G. R.; Leslie, W. C. Tempering of Steel. *Metall. Trans.* **1972,** *3,* 1043–1054.
32. Streng, H.; Grosch, J.; Razim, C. Wasserstoffaufnahme und –abgabe beim Einsatzhärten und Anlassen. *Härterei Techn. Mitt.* **1987,** *42,* 245–260.
33. Streng, H.; Razim, C.; Grosch, J. Influence of Hydrogen and Tempering on Toughness of Case-hardened Structures. In *Carburizing – Processing and Performance;* Krauss, G., Ed.; ASM: Materials Park, OH, 1989; pp 311–317.
34. Balliett, T. A.; Krauss, G. The Effect of the First and Second Stages of Tempering on Microcracking in Martensite of an Fe-1,22% C Alloy. *Met. Trans. A* **1976,** *7A,* 81–86.
35. Lucas, G.; Nützel, H. Untersuchungen über die Umwandlung des Restaustenits in niedrig legierten Stählen mit rd 1%C. *Archiv Eisenhüttenwesen* **1966,** *37,* 981–987.
36. Kim, C.; Diesburg, D. E.; Buck, R. M. Influence of Sub-zero and Shot-peening Treatments on Impact and Fatigue Properties of Case Hardened Steels. *J. Heat Treat.* **1981,** *2,* 43.
37. Koslowskii, I. S.; Kalinin, A. T.; Novikova, A. Y.; Lebedova, E. A.; Reonanova, A. I. Internal Oxidation during Case-hardening of Steel in Endothermic Atmospheres. *Met. Sci. Heat Treat.* **1967,** *25,* 157–161.
38. Chatterjee-Fischer, R. Internal Oxidation during Carburizing and Heat Treating. *Metall. Trans.* **1978,** *9A,* 1553–1560.
39. Hoffmann, R.; Vogel, W. Randoxidation – Ursache, Ausmass, Auswirkung. *Härterei Techn. Mitt.* **2002,** *57,* 49–56.
40. Gondesen, B.; Hoffmann, F. T.; Mayr, P.; Laumen, C.; Holm, T. Influence of Process Gases on Carbon Pick-up and Sooting during Low Pressure and Plasma Carburising. In *Progress in Heat Treatment and Surface Engineering;* Mittemeijer, E. J., Grosch, J., Eds.; ASM: Materials Park, OH, 2000; pp 95–104.
41. Averbach, B. L.; Bingzhe, Lou; Pearson, P. K.; Fairchild, N. E.; Bamberger, E. N. Fatigue Crack Propagation in Carburized High Alloy Bearing Steels. *Metall. Trans.* **1985,** *16A,* 1253–1265.
42. Carey, S.; Herring, D. Low-pressure Carburizing Development of M50NiL. *Heat Treat. Prog.* **May/June 2007,** 43–46.
43. Kolster, B. H. Verschleiß- und korrosionsfeste Schichten auf austenitischen Stählen. *VDI-Berichte* **1984,** *506,* 107–113.
44. Collins, S.; Williams, P. Low-temperature Colossal Supersaturation. *AMP* **2006,** *164,* 32–33.
45. Christiansen, T. L.; Somers, M. A. J. Low Temperature Gaseous Surface Hardening of Stainless Steel. *HTM J. Heat Treat. Mater.* **2011,** *66,* 109–115.
46. Baudis, U.; Chavanne, H.; Maurin-Perrier, P. Surface Hardening of Austenic Stainless Steel/Durofer SH. In *Encyclopedia of Tribology*; Wang, Q. J.; Chung, Yip Wah, Eds.; Springer-Verlag, in press.
47. Suresh, S. *Fatigue of Materials,* 2nd ed.; Cambridge University Press: Cambridge, 2006.
48. Christ, H. J. *Ermüdungsverhalten Metallischer Werkstoffe,* 2nd ed.; Wiley-VCH: Weinheim, 2009.
49. Dressel, K.; Grosch, J. Einfluß des Anlassens auf Bauteil- und Bearbeitungs-eigenschaften einsatzgehärteter Bauteile, FVA-Bericht 679, 2002.
50. Dengel, D. Die arcsin √P-Transformation–ein einfaches Verfahren zur graphischen und rechnerischen Auswertung geplanter Wöhlerversuche. *Z Werkstofftechnik* **1975,** *6,* 253–361.
51. Starker, P. Der Größeneinfluß auf das Biegewechselverhalten von Ck45 in verschiedenen Bearbeitungs- und Wärmebehandlungszuständen. Diss. Universität (TH) Karlsruhe, 1981.
52. Mittemeijer, E. J. Fatigue of Case-hardened Steels: Role of Residual Macro- and Microstresses. *J. Heat Treat.* **1983,** *3,* 114–119.
53. Velten, E. Entwicklung eines Schwingfestigkeitskonzeptes zur Berechnung der Dauerfestigkeit thermochemisch randschichtverfestigter bauteilähnlicher Proben. Diss. TH Darmstadt, 1984.
54. Goodman, J. *Mechanics Applied to Engineering;* Longmans Green: London, 1899.
55. Zürn, J. Einfluß der Mittelspannung auf die Schwingfestigkeit einsatzgehärteter Stähle am Beispiel 20MoCr4 und 16MnCr5. Diss. TU Berlin, 1986.
56. Streng, H. Zähigkeitsoptimierung Einsatzgehärteter Stähle. Diss. TU Berlin, 1986.
57. Kloos, K. H. Festigkeits- und Verschleißeigenschaften induktiv randschichtgehärteter Proben und Bauteile. *Härterei Techn. Mitt.* **1989,** *44,* 157–165.
58. Weibull, W. Zur Abhängigkeit der Festigkeit von der Probengröße. *Ingenieur-Archiv* **1959,** *28,* 360–362.
59. Heckel, K.; Köhler, J. Experimentelle Untersuchung des statistischen Größeneinflusses im Dauerschwingversuch an ungekerbten Stahlproben. *Z. Werkstofftechnik* **1975,** *6,* 52–54.
60. Kuttner, T.; Zieger, H. Berechnung der Dauerschwingfestigkeit einsatzgehärteter zylindrischer Körper mit dem Konzept der lokalen Dauerfestigkeit. *Härterei Techn. Mitt.* **1992,** *47,* 367–375.
61. Schleicher, M.; Bomas, H.; Mayr, P. Berechnung der Dauerfestigkeit von gekerbten und mehrachsig beanspruchten Proben aus dem einsatzgehärteten Stahl 16MnCr5. *Härterei Techn. Mitt.* **2001,** *56,* 84–94.
62. Beumelburg, W. Das Verhalten von einsatzgehärteten Proben mit verschiedenen Oberflächenzuständen und Randkohlenstoffgehalten im Umlaufbiege-, statischen Biege- und Schlagbiegeversuch. Diss. Universität (TH) Karlsruhe, 1973.
63. Diesburg, D. E.; Eldis, G. T. Fracture Resistance of Various Carburized Steels. *Metall. Trans.* **1978,** *9A,* 1561–1570.
64. Pacheco, J. L.; Krauss, G. Microstructure and High Bending Fatigue Strength, Carburized Steels; Krauss, G., Ed.; ASM International: Lakewood, 1989; pp 227–237.
65. Krauss, G. Microstructures, Residual Stresses and Fatigue of Carburized Steels. In *Quenching and Carburising;* The Institute of Metals, 1993; pp 205–225. Book 566.
66. Richman, R. H.; Landgraf, R. W. Some Effects of Retained Austenite on the Fatigue Resistance of Carburized Steel. *Metall. Trans.* **1975,** *6A,* 955–964.

67. Brandis, H.; Reimers, H.; Schmidt, W.; von den Steinen, A. Einfluß des Restaustenitgehaltes auf die mechanischen Eigenschaften einsatzgehärteter Stähle. *Härterei Techn. Mitt.* **1983,** *38,* 63–71.
68. Wyszkowski, J.; Priegnitz, H.; Ratkiewicz, A.; Gozdzik, E. *Rev. Met.* **June 1971,** 411 (cit. in: Prado 69).
69. Prado, J. M.; Arques, J. L. Influence of Retained Austenite on the Fatigue Endurance of Carbonitrided Steels. *J. Mater. Sci.* **1984,** *19,* 2980–2988.
70. Spangenberg, S.; Grosch, J.; Scholtes, B. Untersuchungen zum Einfluß des Restaustenits auf die Schwingfestigkeit einsatzgehärteter Proben. *HTM Z. Werkst. Wärmebeh. Fertigung* **2004,** *59,* 12–17.
71. Johnson, R. J. The Role of Nickel in Carburizing Steels. *Met. Eng. Quart.* **1975,** *15,* 1–8.
72. Kwon, H.; Kim, C. H. Fracture Behaviour in Medium-carbon Martensite Si- and Ni- Steel. *Metall. Trans.* **1986,** *17A,* 1173–1178.
73. Thoden, B.; Grosch, J. Festigkeits- und Verformungsverhalten nickellegierter einsatzgehärteter Gefüge bei Biegebeanspruchung. *Härterei Techn. Mitt.* **1990,** *45,* 7–15.
74. Bacher, M. Verformungs- und Bruchverhalten verschieden wärmebehandelter Einsatzstähle. Diss. TU Karlsruhe, 1987.
75. Hyde, R. S.; Matlock, D. K.; Krauss, G. Phosphorous and Carbon Segregation: Effects on Fatigue and Fracture of Gas-carburized Modified 4320 Steel. *Metall. Trans.* **1994,** *25A,* 1229–1240.
76. Laue, S.; Bomas, H.; Hoffmann, F. T.; Mayr, P. Untersuchungen zum Einfluß des Randschichtzustandes auf die Schwingfestigkeit einsatzgehärteter Proben aus dem Stahl 16MnCr5. *HTM Z. Werkst. Wärmebeh. Fertigung* **2004,** *59,* 199–210.
77. Edenhofer, B. Case-hardening – A Process with New Evolutions and Perspectives. In *Progress in Heat Treatment and Surface Engineering;* Mittemeijer, E. J., Grosch, J., Eds.; ASM: Materials Park, OH, 2000; pp 75–93.
78. Kleff, J.; Kellermann, I.; Mallener, H.; Wirth, M.-S. Niederdruck-Aufkohlen mit Hochdruckgasabschrecken – Leistungsvergleich mit konventionellem Einsatzhärten. *HTM Z. Werkst. Wärmebeh. Fertigung* **2002,** *60,* 257–266.
79. Clausen, B.; Laue, S.; Burtchen, M.; Hoffmann, F. T.; Mayr, P. Randschichtschädigung infolge Niederdruckaufkohlung. *Härterei Techn. Mitt.* **2003,** *58,* 13–19.
80. Wiegand, H.; Tolasch, G. Über das Zusammenwirken einzelner Faktoren zur Steigerung der Biegewechselfestigkeit einsatzgehärteter Proben. *Härterei Techn. Mitt.* **1967,** *22,* 213–220.
81. Kloos, K. H.; Fuchsbauer, B.; Magin, W.; Zankov, D. Übertragbarkeit von Probe-Stab-Schwingfestigkeitseigenschaften auf Bauteile. *VDI-Berichte* **1979,** *354,* 59–72. Düsseldorf, VDI-Verlag.
82. Grosch, J. Fundamentals of Carburising and Toughness of Carburised Components. In *Quenching and Carburising;* The Institute of Metals, 1993; pp 227–250. Book 566.
83. Grosch, J.; Wicke, D. Bruchverhalten und Duktilität schlagbeanspruchter einsatzgehärteter Gefüge. *Härterei Techn. Mitt.* **1982,** *36,* 227–235.
84. Smith, Y. E.; Diesburg, D. E. Fracture Resistance in Carburizing Steels. Part I: Fracture Toughness. *Met. Prog.* **May 1979,** 68–73.
85. Lang, O. R. Dimensionierung komplizierter Bauteile aus Stahl im Bereich der Zeit- und Dauerfestigkeit. *Z. Werkstofftechnik* **1979,** *10,* 24–29.
86. Pacheco, J. L.; Krauss, G. Gefüge und Biegewechselfestigkeit einsatzgehärteter Stähle. *Härterei Techn. Mitt.* **1990,** *45,* 77–83.
87. Obermeyer, H. K.; Krauss, G.; Toughness; Intergranular. Fracture of a Simulated Carburized Case in EX-24 Type Steel. *J. Heat Treat.* **1980,** *1,* 31–39.
88. Zaccone, M. A.; Kelly, J. B.; Krauss, G. Strain Hardening and Fatigue of Simulated Case Microstructures in Carburized Steel. In *Carburized Steels;* Krauss, G., Ed.; ASM, 1989; pp 249–265.
89. Dressel, P. G.; Kohlmann, R.; Kremer, H.-J.; Stanz, A. Der Einfluß der Bedingungen beim Walzen und Wärmebehandeln von Stabstahl auf das Austenitkornwachstum von Einsatzstählen. *Härterei Techn. Mitt.* **1984,** *39,* 112–119.

This page intentionally left blank

12.13 Development of Compound Layer and Diffusion Zone during Nitriding and Nitrocarburizing of Iron and Steels

MAJ Somers, Technical University of Denmark, Kgs. Lyngby, Denmark

12.13.1	**Introduction**	413
12.13.2	**Thermodynamic Principles of Nitriding and Nitrocarburizing**	414
12.13.2.1	Gas–Solid Reactions	414
12.13.2.2	Equilibrium between Gas and Solid	415
12.13.3	**Kinetics of Compound Layer Formation**	418
12.13.4	**Nitriding of Steels**	423
12.13.4.1	Heat-Treatable Steels Containing Nitride-Forming Elements (Nitriding Steels)	423
12.13.4.2	Stainless Steels	425
12.13.5	**Modeling**	431
12.13.5.1	Modeling the Diffusion Zone in Fe–M Alloys	431
12.13.5.2	Modeling of Stress–Depth Profiles in the Diffusion Zone	434
12.13.5.3	Modeling Expanded Austenite in Stainless Steel	434
12.13.5.4	Modeling Compound-Layer Growth	434
References		436

12.13.1 Introduction

Gaseous thermochemical surface treatments such as nitriding and nitrocarburizing belong to the most versatile surface engineering processes of steels and allow improvement of the performance of components with respect to fatigue, wear, and atmospheric corrosion. The case developing during treatment can be subdivided in a compound layer at the surface and a diffusion zone underneath. The compound layer consists of iron (carbon) nitrides γ'-Fe_4N_{1-x} and ε-$Fe_2(N,C)_{1-z}$, while the diffusion zone consists of alloying element (carbo)nitrides (e.g., CrN and AlN), or a supersaturated interstitial solution of nitrogen in a metallic matrix. The compound layer provides wear resistance and, particularly after postoxidation, enhanced performance with respect to atmospheric corrosion. The diffusion zone is responsible for dramatic improvement of materials performance with respect to fatigue, by evoking a compositionally induced compressive residual stress profile. In contrast with case hardening by carburizing, the surface-hardening effect obtained by nitriding/nitrocarburizing is not achieved by a martensitic transformation in the material. As a consequence, no major volume changes and distortions, which are among the drawbacks of carburizing, will occur during nitriding/nitrocarburizing.

A wealth of industrial process conditions is available commercially. The processes can be subdivided into gaseous, salt bath, and plasma based, depending on the medium that provides the nitrogen (and carbon) species to the workpiece surface. For completeness, fluidized bed and pack nitriding processes should also be mentioned. As compared to gas, salt bath, and plasma processes, these methods are not applied on a large scale. The purpose of this chapter is not to give an overview of all the available commercial possibilities or to give a survey of different processes; for such overviews, the interested reader is referred to other Handbooks. Generally, the difference between nitriding and nitrocarburizing is as follows. Classical nitriding is performed in the temperature range 480–530 °C for 20–80 h, and the main purpose is the development of a diffusion zone to enhance the fatigue performance of a component. On the other hand, nitrocarburizing is performed at 540–590 °C, and its main objective is the development of a compound layer with good wear and tribological performance. This chapter conveys the basics of the influence of incorporating nitrogen during nitriding, and nitrogen and carbon during nitrocarburizing, on the microstructure of the developing case. This will be primarily done for gaseous treatments. A gaseous nitriding/nitrocarburizing medium was chosen because it allows accurate control and monitoring of the gas composition and, thus, targeted surface engineering of the components with maximum flexibility. Furthermore, from a scientific point of view, the use of gases allows a precise thermodynamic definition of the essential parameters governing the processing. The basic mechanisms of microstructure formation revealed by such gaseous treatment are transferable to salt, bath, and plasma treatments, even though the principle of transfer of species from the nitriding/nitrocarburizing medium to the workpiece relies on another mechanism.

First, this chapter deals with various aspects of the thermodynamics and kinetics of microstructure evolution during thermochemical treatment with gaseous nitriding and nitrocarburizing. Thereafter compound layer formation on iron, as a model case, is described during nitriding and nitrocarburizing. Development of the diffusion zone in nitriding steels is treated, followed by a description of the development of a supersaturated solid solution in stainless steels, so-called expanded austenite. Residual stresses arising during nitriding and nitrocarburizing in the diffusion zone of steels are included in this discussion because they play a paramount role in the fatigue performance of such alloys. The chapter concludes with aspects of modeling of compound layer growth, diffusion zone growth, and expanded austenite growth.

12.13.2 Thermodynamic Principles of Nitriding and Nitrocarburizing

12.13.2.1 Gas–Solid Reactions

The gas–solid interactions to be discussed here are simple and concern nitriding in NH_3/H_2 and nitrocarburizing in $NH_3/CO/CO_2/H_2/H_2O$ or $NH_3/C_xH_y/H_2$ gas mixtures. Atmospheric pressure applies in all cases discussed in this chapter. Dissociation reactions at (all available) solid surfaces within the furnace provide the atomic species that can be adsorbed at the workpiece surface, which subsequently may be incorporated into the solid state or leave the surface again. For nitriding in NH_3/H_2, adsorbed nitrogen atoms can diffuse into the solid phase ϕ (*1*,*2*):

$$NH_3 \rightleftarrows N_{ad} + \frac{3}{2}H_2 \qquad \text{[Ia]}$$

$$N_{ad} \rightleftarrows [N]_\phi \qquad \text{[Ib]}$$

or, upon development of molecular nitrogen, leave the surface again:

$$N_{ad} + N_{ad} \rightleftarrows N_2 \qquad \text{[Ic]}$$

In principle, reaction (Ic) is thermodynamically preferred to reaction (Ib), but the kinetics prevails such that nitriding according to reaction (Ib) is possible. For temperatures below 460 °C, reaction (Ic) can be neglected, as N_2 molecules cannot desorb from the surface. Generally, the importance of reaction (Ic) in the total nitriding reaction increases with temperature and nitrogen content in the phases developing at the surface. The consequences of this will be demonstrated in this chapter.

For nitrocarburizing, both carburizing and nitriding reactions can occur. Because of the presence of hydrogen, carburizing according to the following scheme is kinetically preferred (*3*):

$$CO_2 + H_2 \rightleftarrows CO + H_2O \qquad \text{[IIa]}$$

$$CO + H_2 \rightleftarrows C_{ad} + H_2O \qquad \text{[IIb]}$$

$$C_{ad} \rightleftarrows [C]_\phi \qquad \text{[IIc]}$$

Carburizing could also proceed according to:

$$2CO \rightleftarrows C_{ad} + CO_2 \qquad \text{[IId]}$$

followed by reaction (IIc), but reaction (IId) is much slower than reaction (IIb).

Additionally, the following reactions can occur (*1*):

$$CO + NH_3 \rightleftarrows HCN + H_2O \qquad \text{[IIIa]}$$

$$HCN \rightleftarrows N_{ad} + C_{ad} + \frac{1}{2}H_2 \qquad \text{[IIIb]}$$

which are promoted by the presence of catalytic surfaces in the furnace, as, for example, the furnace lining or fixtures. Alternatively, HCN could be used as the carburizing agent because it provides both nitrogen and carbon. Because of the toxicity of this gas and safety regulations involved, its application in industrial practice is not likely.

For the case that the nitrocarburizing gas mixture is based on unsaturated hydrocarbons like acetylene (C_2H_2) or propene (C_3H_6), the carburizing reaction proceeds by (*4*):

$$C_xH_y \rightleftarrows xC_{ad} + \frac{y}{2}H_2 \qquad \text{[IIe]}$$

The advantage of such gases would be easier control of the gas atmosphere as no oxygen is present. On the basis of reactions (Ia), (IIb), (IId), and (IIe), the activities of adsorbed nitrogen, a_N, and carbon, a_C, can be defined at 1 bar pressure:

$$\begin{aligned}
a_N &= K_{Ia} \cdot K_N \quad K_N = \frac{p_{NH_3}}{p_{H_2}^{3/2}} \\
a_C &= K_{IIb} \cdot K_C \quad K_C = \frac{p_{CO} p_{H_2}}{p_{H_2O}} \\
a_C &= K_{IId} \cdot K_{Cb} \quad K_{Cb} = \frac{p_{CO}}{p_{CO}^2} \\
a_C &= K_{IIe} \cdot K_{Cx} \quad K_{Cx} = \sqrt[x]{\frac{p_{C_xH_y}}{p_{H_2}^{y/2}}}
\end{aligned} \qquad \text{[IV]}$$

where K_{Ia}, K_{IIb}, K_{IId}, and K_{IIe} are the temperature-dependent equilibrium constants of reactions (Ia), (IIb), (IId), and (IIe), respectively, and K_N and K_C are nitriding potential and carburizing potential, respectively. Only for the case that the gas-phase

reaction (IIa) is in equilibrium will the carbon activities imposed by reactions (IIb) and (IId) be equal. However, this is generally not the case (5); thus, the carburizing potential for reaction (IIb) is determining. Nevertheless, the homogeneous water shift reaction (IIa) is often, erroneously, assumed to be in equilibrium, and K_C for reaction (IId) is provided as it is more straightforwardly measured (6).

12.13.2.2 Equilibrium between Gas and Solid

The stability of the various iron-based nitrides with respect to the nitriding potential and the temperature was systematically investigated more than 80 years ago by Lehrer on iron powder in flowing ammonia/hydrogen gas mixtures (7). The results obtained are depicted in the so-called Lehrer diagram (Figure 1), which allows selection of the optimal combination of nitriding potential and temperature for either promoting or avoiding the compound layer. Along the lines drawn in this diagram two solid phases coexist with the streaming NH_3/H_2 gas mixture, while elsewhere only one solid phase can exist.

The stability ranges of the iron nitrides follow from the Fe–N phase diagram (Figure 2), which shows that γ'-Fe_4N_{1-x} has a narrow homogeneity range, comparable in width to ferrite. Note that this narrow homogeneity range corresponds to a broad composition range in the gas mixture, and consequently a broad nitrogen activity range, as reflected by the Lehrer diagram (Figure 1). The ε-Fe_2N_{1-z} phase has a broad homogeneity range and, for temperatures below the eutectoid temperature 592 °C, is first stabilized at nitrogen contents beyond those necessary to stabilize γ'-Fe_4N_{1-x}. Actually, the Fe–N phase diagram in Figure 2 and the phases present in this diagram are thermodynamically metastable with respect to Fe and N_2. (It should be realized that, in contrast to ordinary phase diagrams that apply at 1 bar, the Fe–N phase diagram in Figure 2 is not a phase diagram of the pure

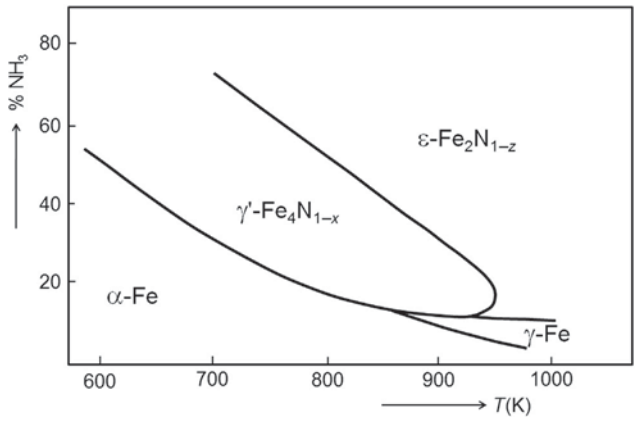

Figure 1 Lehrer diagram, depicting the stability of Fe–N phases as a function of temperature and the NH_3 content in a gas flow of NH_3 and H_2. The lines indicate the combination of temperature and NH_3 content where two phases coexist with the gas flow. Reproduced from Lehrer, E. Z. Elektrochem. **1930**, *36*, 383–392.

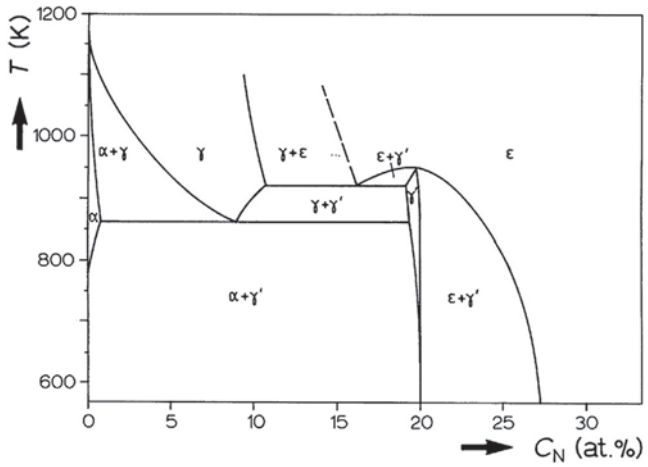

Figure 2 Fe–N phase diagram showing the homogeneity ranges of Fe–N phases as a function of phase composition and temperature. The diagram is based on imposed equilibrium studies between pure iron and NH_3/H_2 gas mixture at 1 bar total pressure.

components Fe and N_2 at 1 bar. Instead, it depicts a projection of the solubility lines in the three-dimensional temperature-composition-pressure space onto an arbitrary temperature–composition plane. The Fe–N phase diagram of the pure components at 1 bar would only show a vanishingly low solubility of nitrogen in ferrite; the iron-nitrides would require a physical pressure of N_2 of several GPa's, which can be chemically 'realized' at a physical pressure of 1 bar by NH_3/H_2 gas mixtures.) This metastability is analogous to the metastability of Fe_3C with respect to Fe and graphite in the Fe–C phase system, albeit that for Fe–N a solid–gas equilibrium applies rather than a solid–solid equilibrium, as for Fe–C.

The composition of the Fe–N phases can be accurately controlled by adjusting the nitriding potential, as depicted in so-called absorption isotherms (see references (*8*,*9*) and **Figure 3** with examples for γ'-Fe_4N_{1-x} and ε-Fe_2N_{1-z}). These compositions would in principle be expected at the surface of a growing compound layer (see below). Mathematical equations to reconstruct a thermodynamical description of the Fe–N system – i.e., Lehrer diagram, absorption isotherms, and Fe–N diagram – were collected in (*10*).

Systematic studies on the Fe–N–C system date back to the mid-1960s when Naumann and Langenscheid (*11*) published their phase stability diagram for iron powder nitrocarburized in flowing NH_3–H_2–CO gas mixtures (**Figure 4**) (*11*) (as a pendant to the Lehrer diagram) and several isothermal sections of the iron-rich corner of the ternary Fe–N–C phase diagram (**Figure 5(a)**) (*12*). Unfortunately, the water vapor content (pH_2O) in the applied gas mixtures was not provided, which implies that the carbon activity in the phase diagram is undetermined (see eqn [4]). This hinders a straightforward thermodynamic approach of the available data. Nevertheless, the important qualitative conclusion that can be drawn from **Figures 4** and **5(a)** is that the presence of a carbon containing gas in the nitrocarburizing atmosphere stabilizes the ε-phase toward lower ammonia contents and lower nitrogen

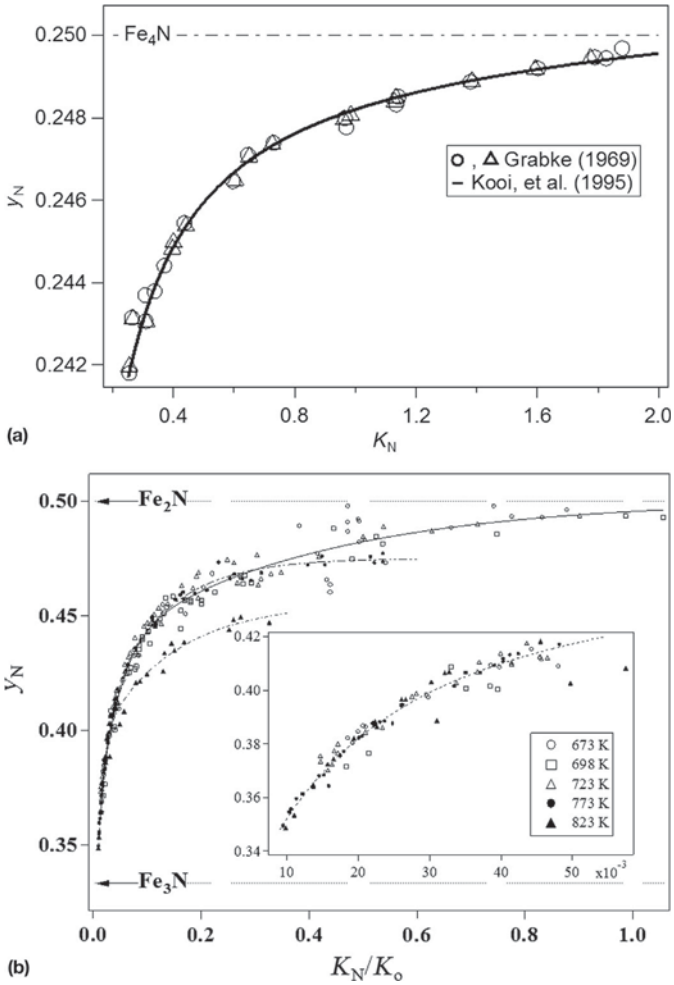

Figure 3 Absorption isotherms for nitrogen in γ'-Fe_4N_{1-x} ((reproduced from Kooi, B. J.; Somers, M. A. J.; Mittemeijer, E. *J. Metall. Mater. Trans. A* **1996**, *27*, 1063–1071), experimental data from (Grabke, H. J. Ber. Bunsengesell. *Phys. Chem.* **1969**, *73*, 596–601)) (a) and ε-Fe_2N_{1-z} (reproduced from Somers, M. A. J.; Kooi, B. J.; Ma1dzinski, L.; Mittemeijer, E. J.; van der Horst, A. A.; van der Kraan, A. M.; van der Pers, N. M. *Acta Mater.* **1997**, *45*, 2013–2025) (b), depicting the nitrogen fraction, y_N, as a function of the nitriding potential K_N. The nitrogen fraction y_N is expressed as the number of N atoms per Fe atom. K_0 in (b) is a temperature dependent normalizing factor and obeys $K_0 = -4.92 + \frac{5.39\ \ 10^3}{T}$. For temperatures above 450 °C (723 K) the maximum nitrogen content no longer approaches $y_N = 0.5$ as for temperatures up to 450 °C, because a stationary state rather than equilibrium is achieved between gas mixture and solid state, as a consequence of N_2 desorption from the surface. Reproduced from Somers, M. A. J.; Kooi, B. J.; Ma1dzinski, L.; Mittemeijer, E. J.; van der Horst, A. A.; van der Kraan, A. M.; van der Pers, N. M. *Acta Mater.* **1997**, *45*, 2013–2025.

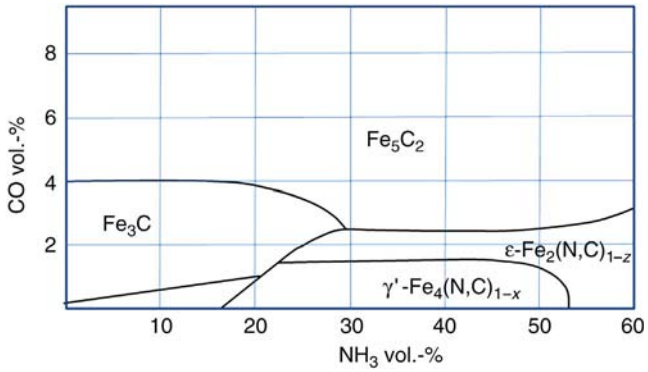

Figure 4 Phase stability diagram for Fe–C–N phases in dependence of the CO and NH_3 contents in NH_3–CO–H_2 gas mixtures at a temperature of 500 °C (773 K) for 120 min. Reproduced from Naumann, F. K.; Langenscheid, G. L. *Arch. Eisenhüttenwes.* **1965**, *36*, 677–682.

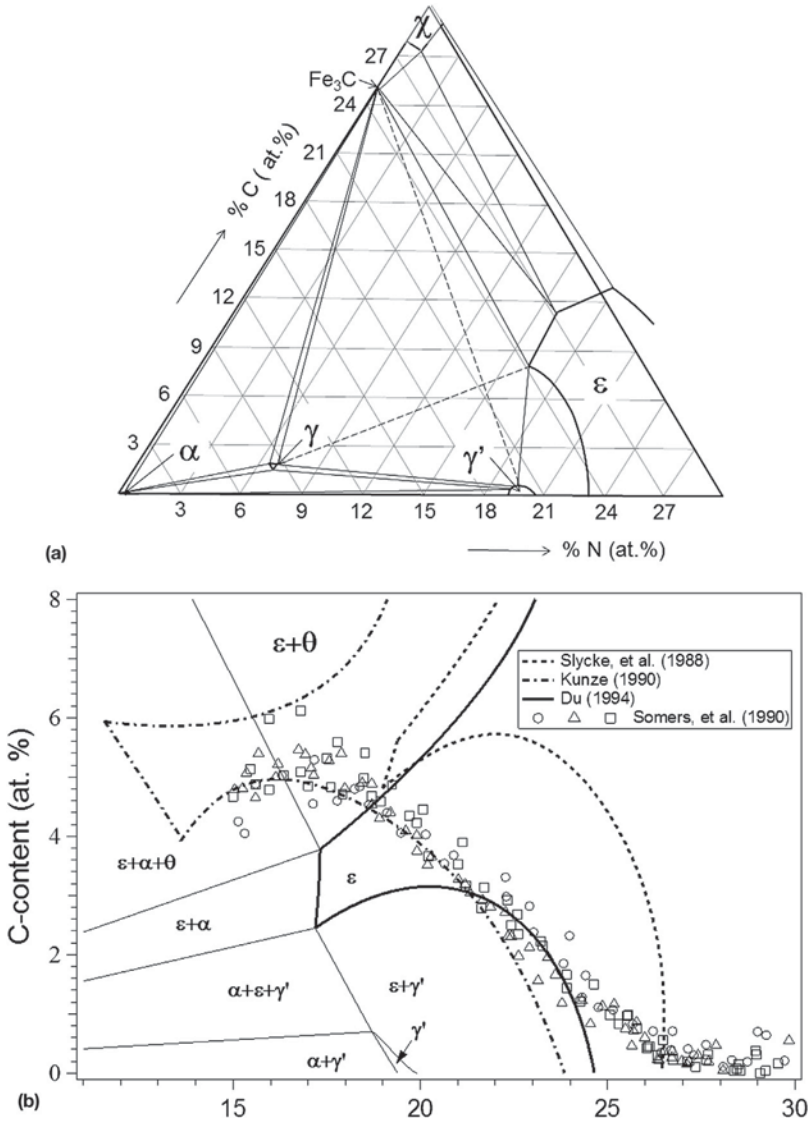

Figure 5 (a) Isothermal section at 570 °C (843 K) of the Fe–N–C phase diagram obtained by interpolation among data at 550 °C (823 K) and 600 °C (873 K) (reproduced from Naumann, F. K.; Langenscheid, G. L. *Arch. Eisenhüttenwes.* **1965**, *36*, 583–590). (b) Comparison of experimental composition data for ε-phase and several attempts to model the Fe–N–C phase diagram as presented in Slycke, J.; Sproge, L.; Ågren, J. *Scand. J. Metall.* **1988**, *17*, 122–126; Du, H. J. *Phase Equilibria* **1994**, *14*, 682–693; and Kunze, J. *Härterei-Tech. Mitt.* **1996**, *51*, 348–355.

contents and suppresses the development of the γ'-phase. The part of the ternary Fe–N–C phase diagram of most relevance for ferritic nitrocarburizing is the one proposed to apply at 575 °C (**Figure 5(a)**) and is based on an interpolation of data at 550 and 600 °C. This phase diagram should be applied with care, because the phase boundaries can only be considered approximate as a consequence of the linear interpolation. Generally, under practical, as well as laboratory, conditions, deviations from the phase boundaries in the Fe–N–C diagram were observed. Several attempts to calculate the iron-rich corner of the Fe–N–C phase diagram have been published over the years. As thermodynamic data is lacking for the pure phases involved (see above), these calculations were based on combining mathematical descriptions for binary Fe–N and Fe–C diagrams (*13–17*) and additional composition data (*18*) for the Fe–N–C phases in as-grown compound layers presuming local equilibrium at phase boundaries of the ε-phase with other phases in the compound layer/diffusion zone interface. Phase boundaries of the ε-phase in the Fe–N–C phase diagram as calculated by (*13,16,17*) are shown in **Figure 5(b)**. The large spread among the results of the various evaluations indicates the sensitivity of the numerical models for the input data and the assumptions made (*19,20*).

12.13.3 Kinetics of Compound Layer Formation

The development of the compound layer during nitriding proceeds along the stages depicted in **Figure 6** (*21*). Thermodynamically, the first phase developing at the surface of iron on gaseous nitriding is γ'-Fe_4N_{1-x}. A driving force for its nucleation develops upon exceeding the maximum solubility of nitrogen in iron in the region adjacent to the surface (**Figure 6(a)**). The incubation time for the nucleation of γ' nitride depends on the actual nitrogen content at the surface, which is the net effect of a competition between the fluxes of nitrogen atoms arriving at the surface and the fluxes of nitrogen atoms leaving the surface (**Figure 7**) (*10,19*). Provided that the flux of ammonia molecules toward the surface is sufficiently high, the flux of arriving nitrogen atoms is controlled by the dissociation rate of ammonia (reaction (Ia)); the fluxes of nitrogen atoms leaving the surface are due to the diffusion of nitrogen

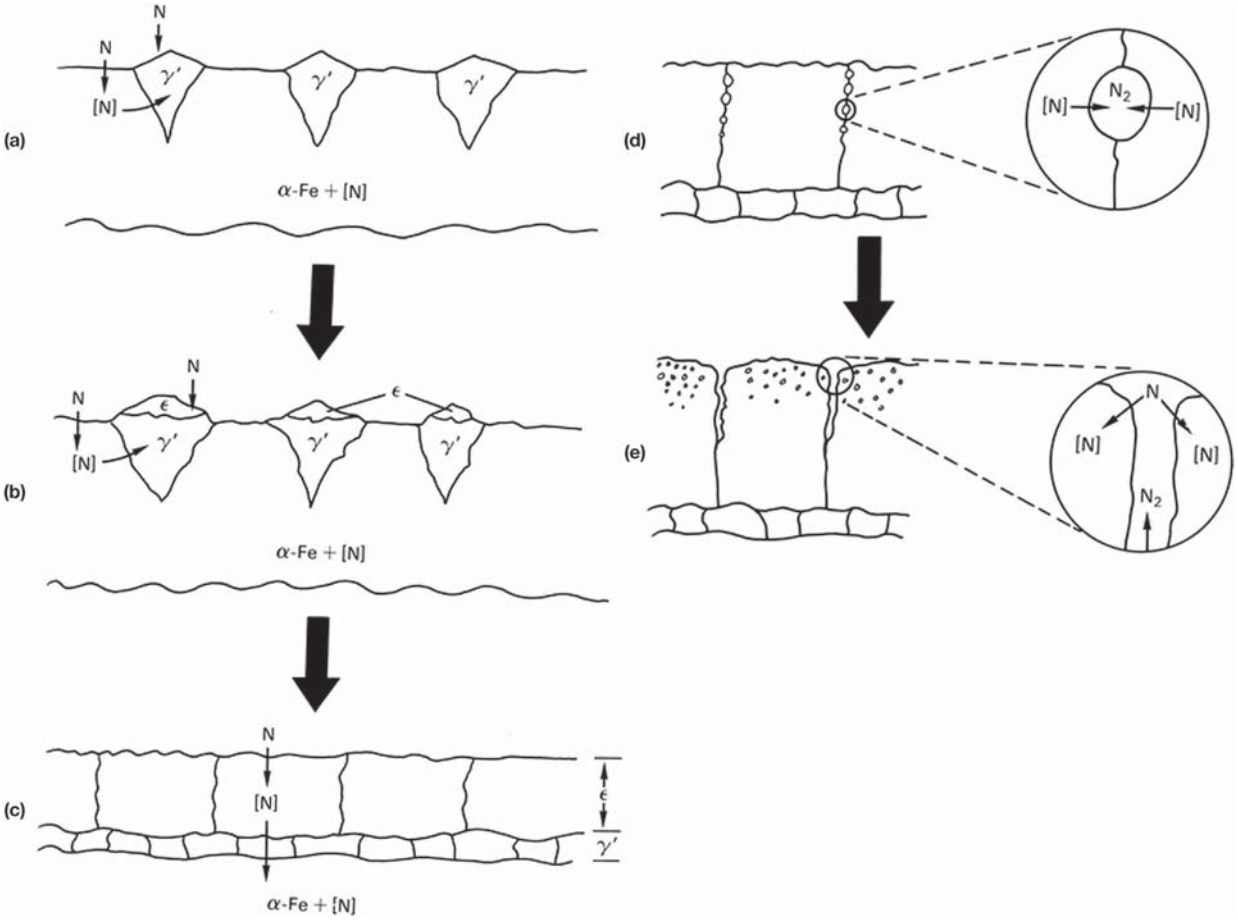

Figure 6 Stages of compound layer formation during nitriding of iron at a temperature below 592 °C (865 K): (a) nucleation of γ'-Fe_4N_{1-x}, at the iron surface (b) development of ε-Fe_2N_{1-z} on top of γ'-Fe_4N_{1-x}, (c) nitrogen-diffusion-controlled growth of the ε/γ' double layer, (d) development of N_2 filled pores at energetically favorable sites, (e) coalescence of pores into pore channels. Reproduced from Somers, M. A. J.; Mittemeijer, E. J. *Härterei-Tech. Mitt.* **1992**, *47*, 5–13.

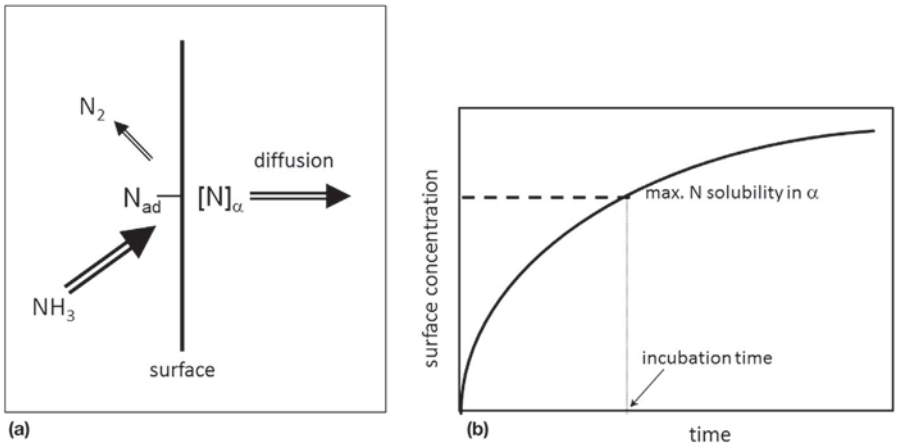

Figure 7 Balance of fluxes at the iron surface during nitriding (a) leads to gradual increase of the surface concentration of nitrogen and an incubation time for γ'-Fe_4N_{1-x} nucleation (b). Reproduced from Somers, M. A. *J. Heat Treat. Met.* **2000**, *27*, 92–102.

atoms into the solid state (reaction (Ib)) and the development and desorption of N_2 (reaction (Ic)). After the nucleation of γ' nitride ε-phase can nucleate on top (**Figure 6(b)**). Coalescence of dual-phase nuclei establishes a ε/γ'-bi-layer, which grows under the influence of nitrogen diffusion through the layer (**Figure 6(c)**). In this stage, both γ' and ε layers grow parabolically with time (**Figure 8(e)** (*22*)).

The thickness ratio of the ε and γ' layers in the compound layer depends on the nitriding parameters temperature and nitriding potential. In principle, the thickness ratio should be time independent, provided that coupled growth of the ε and γ' layers is strictly diffusion controlled. The effect of the nitriding potential is illustrated in **Figure 8(a)–(d)** (*22*) for the nitriding conditions provided in the caption.

As a consequence of the inherent metastability of iron nitrides at 1 bar with respect to Fe and N_2 (see above), porosity develops in the compound layer on prolonged nitriding. The associated development of N_2 is first observed at energetically favorable nucleation sites in the region with the highest nitrogen content, that is, near the surface at grain boundaries, where the highest driving force for N_2 development occurs (**Figure 6(d)**). On continued nitriding (or during aging), the pores coalesce and form pore channels, which allow the gas mixture to reach the interior of the porous nitride layer (**Figure 6(e)**).

On *nitrocarburizing* the nucleation of the phases constituting the compound layer depends on the competition of the surface reactions (I) and (II). The carburizing reaction (IIb) usually proceeds much faster than the nitriding reaction (Ib). Furthermore, ferrite has a lower solubility for carbon than for nitrogen. Hence, the maximum carbon content dissolvable in the substrate surface is exceeded earlier than the nitrogen solubility (**Figure 9**), and an iron-carbide or an iron-carbonitride nucleates. The nucleation of γ' iron nitride is suppressed because of the low solubility of carbon in this phase (cf. **Figures 4 and 5(a)**). The development of the composition and morphology of the compound layer is schematically shown in **Figure 10** (*21*). On nitrocarburizing pure iron, the first phase appearing at the surface is cementite (θ-Fe_3C) (*5*). The appearance of the iron-carbonitride phase ε-$Fe_2(N,C)_{1-z}$ (after cementite nucleation) in the compound layer is promoted by a high nitriding potential and is retarded by a high carburizing activity. So far, ε-phase has not been observed to nucleate as the first phase at the iron surface during nitrocarburizing.

After the initial development of cementite, the ε-phase becomes dominant in the compound layer on prolonged treatment. The content of cementite decreases and, eventually, cementite disappears, provided that the carburizing potential is lower than that necessary to stabilize cementite. Concurrently, the amount of γ' phase increases (see **Figure 10(b)**), particularly in the part of the compound layer adjacent to the substrate along with a redistribution of the carbon initially incorporated. Due to the relatively slow kinetics of ammonia dissociation at the iron surface and the concurrent nitrogen desorption, which initially allow a strong absorption of carbon, the composition of the compound layer evolves such that the nitrogen content at the surface increases gradually with time, while the corresponding carbon content decreases complementarily (*5*,*18*). Eventually, analogous to nitriding, a continuous γ'-layer underneath the ε-layer can develop, provided that the initially incorporated carbon is redistributed and does not hinder its development. Upon the development of porosity in the compound layer, an additional mechanism for the incorporation of carbon into the compound layer from the nitrocarburizing atmosphere becomes possible (**Figure 10(d)** (*23*)): the uptake of carbon in the porous part of the compound layer at some distance from the surface. This mechanism is explained by the presence of molecular nitrogen in the porous region which, according to the Le Chatelier-van 't Hoff principle, suppresses the dissociation of NH_3 (cf. reaction (I)) and consequently promotes the uptake of carbon at these locations. In addition to this purely thermodynamical explanation, a slower dissociation rate of ammonia (because of N_2) and the slow refreshment of the gas mixture in the pores should also be taken into consideration. Prolonged incorporation of carbon in the porous part leads to the formation of cementite, first along the pore channels (**Figure 10(e)**). Later, cementite develops as a continuous (porous) layer sandwiched in-between nitrogen-rich ε-phase at the surface and carbon-rich, nitrogen-poor ε-phase underneath (**Figure 10(f)**) (*23*).

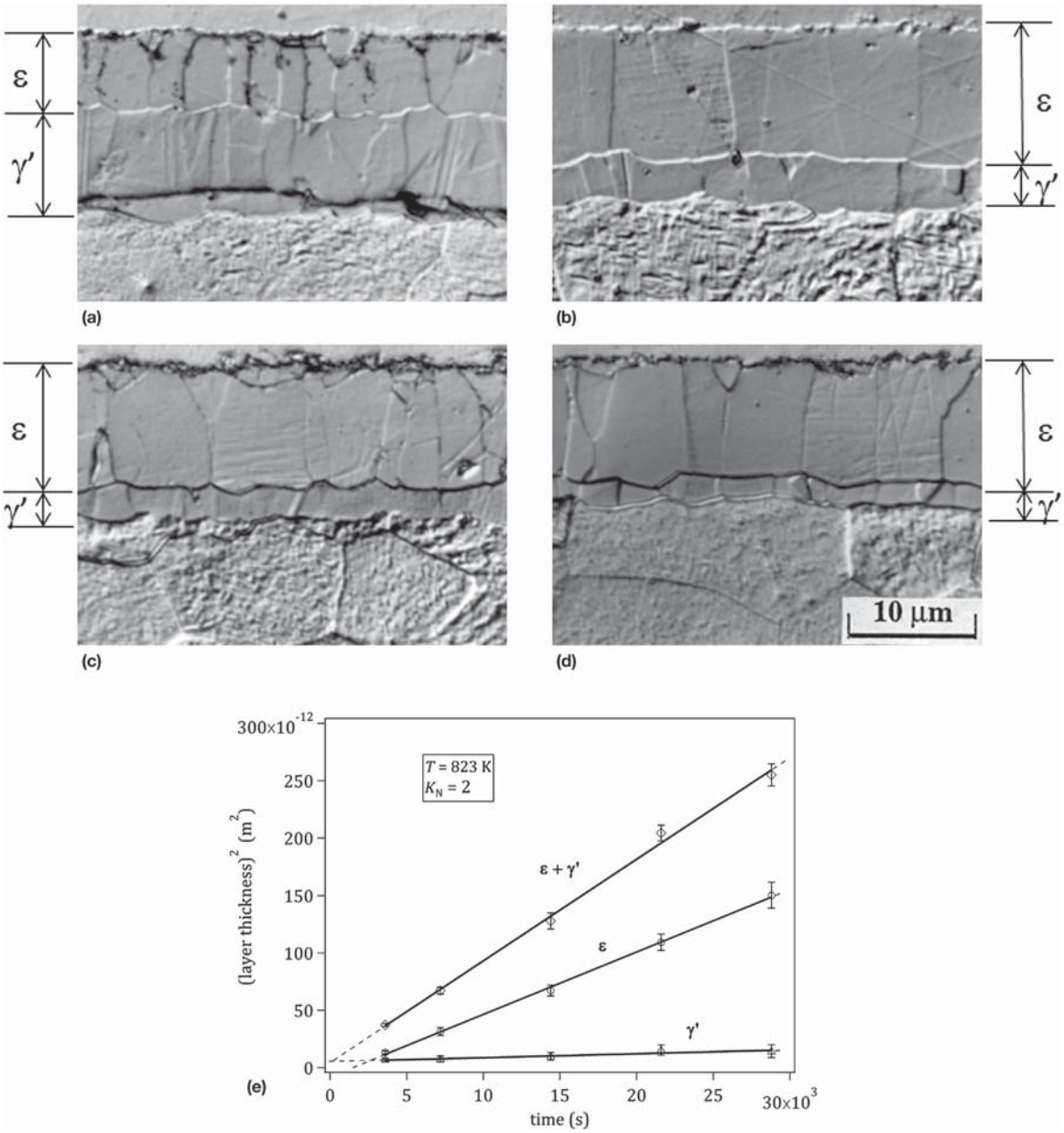

Figure 8 ε/γ' double layers on pure iron obtained at 550 °C (823 K) for various conditions of nitriding potential, K_N (pressures in atm), and nitriding time, t, (a) $K_N = 2$, $t = 10$ h; (b) $K_N = 4$, $t = 6$ h; (c) $K_N = 6$, $t = 3$ h; (d) $K_N = 8$, $t = 3$ h; (e) growth kinetics of ε/γ' double layer at 550 °C (823 K) and $K_N = 2$. Reproduced from Somers, M. A. J.; Ma1dzinski, L.; Gommers, A. W. J. Unpublished work. Delft University of Technology, 1996.

A few examples of compound layers developing during nitrocarburizing are shown in Figure 11 (*22*). The effect of a (too) high carburizing potential is clearly observed from comparing the compound layers in Figure 11(a) and (b), which were obtained after a 3 h treatment at 570 °C. The only difference between the process conditions is a partial replacement of half the volume of CO by CO_2. In a CO containing gas mixture, a higher carburizing potential can be achieved on nitrocarburizing than in a gas containing only CO_2. Consequently, Hägg carbide and cementite (cf. Figure 4) developed in the compound layer in Figure 11(a) and hinder fast growth of the compound layer, because these carbide phases can dissolve only small amounts of nitrogen and act as a diffusion barrier (see below). Replacing part of the CO with CO_2 a relatively thick, carbon lean, ε/γ' double layer develops, showing the onset of porosity close to the surface. The supply of carbon from the substrate for nitrocarburizing conditions as in Figure 11(b) follows from Figure 11(c), where a thick, almost monophase ε-carbonitride, compound layer is shown with only a small amount of γ'-nitride and abundant porosity.

As suggested by Figure 11, the composition of the compound layer developing during nitrocarburizing has a large influence on the growth kinetics. Comparison of compound layers grown for different combinations of nitrogen activity (a_N) and carbon activity

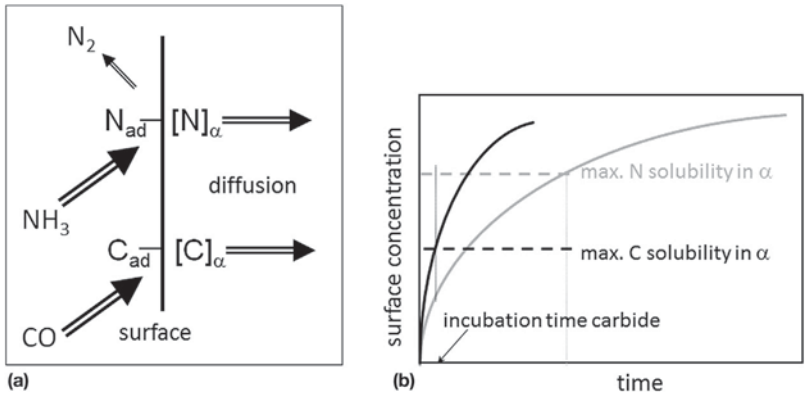

Figure 9 Balance of fluxes at the iron surface during nitrocarburizing (a) leads to gradual increase of the surface concentrations of nitrogen and carbon (b). The faster uptake of C and the lower solubility of C in α-Fe, lead to shorter incubation time for carbide than for nitride.

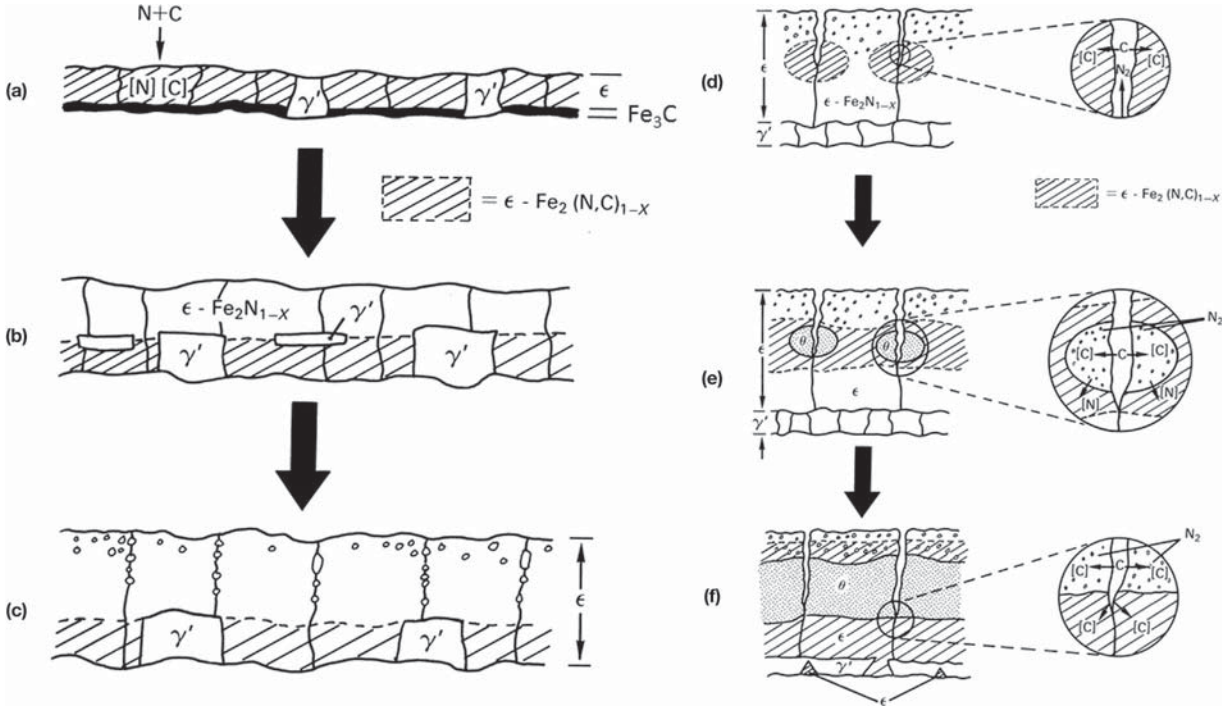

Figure 10 Stages of compound layer development during nitrocarburizing of iron at a temperature below 592 °C (865 K): (a) nucleation of cementite, ε carbonitride, and γ' nitride; (b) development of ε nitride; (c) development of porosity in ε-nitride; (d) incorporation of carbon through pore channels in ε-layer; (e) development of porous cementite layer along pore channels; (f) development of porous cementite layer sandwiched in-between ε-layers and replacement of γ'-nitride by carbon stabilized ε-carbonitride under uptake of carbon through pore channels. Reproduced from Somers, M. A. J.; Mittemeijer, E. J. *Härterei-Tech. Mitt.* **1992**, *47*, 5–13.

(a_C) has revealed that essentially three stages of growth can be distinguished (Figure 12) (*5,19*). Stages I and III are characterized by relatively slow layer growth kinetics, while stage II represents relatively fast layer growth kinetics. The transition from stage I to stage II coincides with a change of the dominant phase in the compound layer from cementite (and/or Hägg carbide) to ε-phase. Acceleration of the layer growth kinetics from stage I to stage II is a consequence of the larger diffusive flux of interstitial atoms through ε-phase as compared to the diffusive flux through cementite (and/or Hägg carbide). The diffusive flux of interstitial atoms depends on the mobility of the atoms and the maximum possible composition range; the latter is reflected by the homogeneity range in the Fe–N–C phase diagram (Figure 5(a)). As mentioned above, the disappearance of cementite as a more or less continuous sublayer in the compound layer depends on the combination of a_N and a_C. The higher the nitriding potential, the sooner can interstitial atoms diffuse through the compound layer via ε-phase bridging the cementite sublayer and the sooner does stage II of rapid growth succeed stage I. Apparently, for the compound layer shown in Figure 11(a) stage I growth applies.

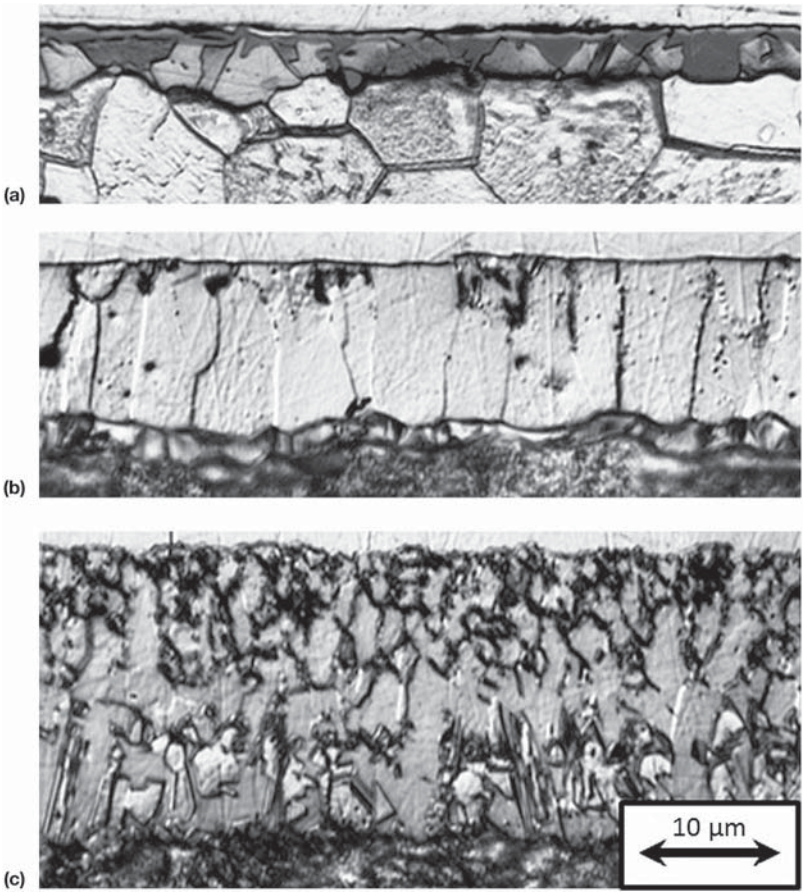

Figure 11 Cross-sectional micrographs of compound layers obtained after nitrocarburizing at $T = 570\,^{\circ}C$ (843 K) for $t = 3$ h. (a) Fe treated in 55% NH_3–35% H_2–10% CO (a high-carbon activity); (b) Fe nitrocarburized in 55% NH_3–35% H_2–5%CO_2–5%CO; (c) Fe-0.4 C nitrocarburized in 55% NH_3–35% H_2–5%CO_2–5%CO. Reproduced from Somers, M. A. J.; Ma1dzinski, L.; Gommers, A. W. J. Unpublished work. Delft University of Technology, 1996.

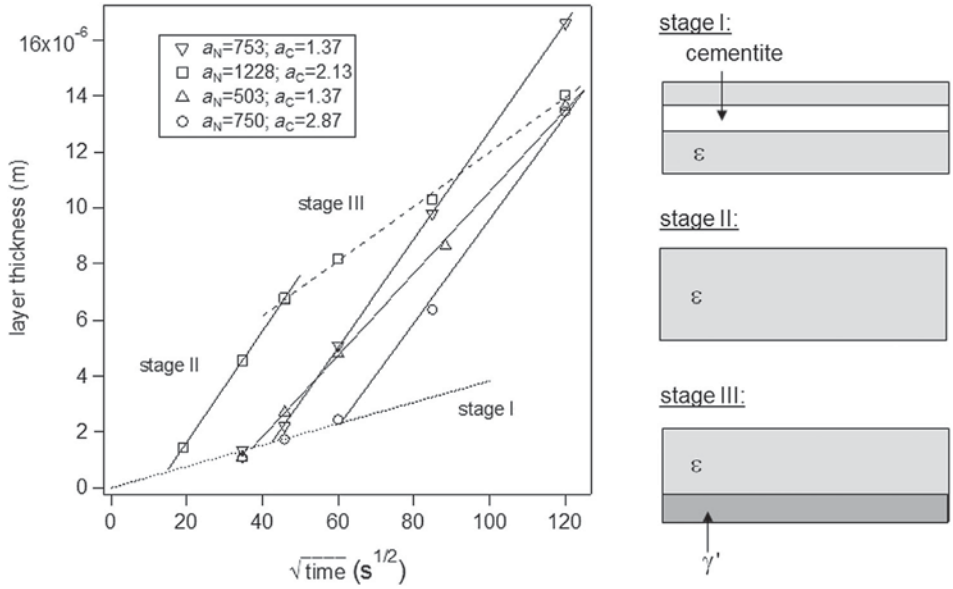

Figure 12 Kinetics of compound layer growth during nitrocarburizing of iron can be subdivided in three stages (I, II, III). Data points are for various combinations of nitrogen activity (a_N) and carbon activity (a_C) in the gas phase. Reproduced from Du, H.; Somers, M. A. J.; Ågren, *J. Metall. Mater. Trans. A* **2000**, *31A*, 195–211 and Somers, M. A. *J. Heat Treat. Met.* **2000**, *27*, 92–102.

In stage II of compound layer growth, the rate-determining step is the diffusion of interstitials (mainly nitrogen) through ε-phase, which extends from the surface to the layer/substrate interface (Figure 12). The transition from stage II to stage III is associated with the presence of a γ'-layer in-between the ε-phase and the underlying ferrite. As the carbides, γ'-nitride has a relatively narrow homogeneity range as compared to ε-phase. Isolating the ε-phase from direct contact with the substrate by the appearance of γ'-nitride retards layer growth kinetics (cf. Figure 11(b)). If carbon is provided by the substrate, the development of γ'-nitride in-between ε-carbonitride and the substrate can be prevented (Figure 11(c)). Accordingly, a stage II to stage III transition of layer-growth kinetics does not occur and rapid growth continues. The main purpose of nitrocarburizing is obtaining a thick compound layer in a relatively short time. Hence, stage II growth is promoted.

The application of hydrocarbons instead of CO/CO_2 as the carbon-supplying agents in the gas phase shows exactly the same mechanisms of carbon uptake as revealed in Figure 10 (*4*).

12.13.4 Nitriding of Steels

In the previous section (12.13.3), the development of a diffusion zone underneath the compound layer was omitted. As long as no nitride-forming alloying elements are present, the diffusion zone at the nitriding temperature is a solution of nitrogen in ferrite. During cooling the iron-based nitrides γ'-Fe_4N_{1-x} and α''-$Fe_{16}N_2$ (*24,25*) develop from a supersaturated solid solution, because the solubility of nitrogen in ferrite decreases with temperature. If cementite is present in the substrate, this phase can be transformed into ε-phase (*26*). For other steels than plain carbon steels a different picture emerges. Below the nitriding of heat-treatable steel containing nitride forming elements and the nitriding/nitrocarburizing of stainless steels, an emerging application, are discussed.

12.13.4.1 Heat-Treatable Steels Containing Nitride-Forming Elements (Nitriding Steels)

In steels containing alloying elements as, for example, Cr, Al, Mo, V, and Ti, which are stronger nitride formers than iron, nitrides of type M_mN_n (M = Cr, Al, Mo, V, Ti) develop preferentially. Extensive investigations have been done on the nitriding of binary Fe–M alloys (e.g., (*27–39*)) and some ternary iron-based alloys (e.g., (*40–43*)). From these investigations the picture emerges that if these nitride-forming alloying elements are in solid solution in the matrix, a dispersion of nanoscale platelike nitrides forms in the matrix for the nitrides with a NaCl-type lattice (CrN, TiN, VN) (Figure 13) and a hard diffusion zone develops. Early work (*28,29,31,35*) suggested that the developing platelets were mixed substitutional-interstitial atom clusters (including iron (*36*)) rather than nitrides. Recent work appears to confirm that the platelets are actually alloying element nitrides (*37–43*). As long as the nanoscale plates are coherent with the ferrite matrix, an enhanced solubility of nitrogen is experienced, so-called excess nitrogen (*32,34–47*). Part of the excess nitrogen adsorbs at the platelet matrix interface, and the remaining part is dissolved in the strained ferrite matrix (see Figure 14); only the nitrogen dissolved in ferrite can be considered mobile, the adsorbed nitrogen should be considered trapped. The growth of the diffusion zone is rate-controlled by the diffusion of nitrogen in the ferrite matrix (*31,46,47,48,49*). The capacity for binding nitrogen in the diffusion zone increases with the alloying element content. Generally, it is observed that the higher the content of strong nitride-forming elements in ferrite, and, hence, the larger the capacity for binding nitrogen in the diffusion zone, the slower does the diffusion zone grow. If a compound layer has developed at the surface, the compound layer is the thinner the higher is the concentration of nitride-forming alloying elements in the diffusion zone (see also Section 12.13.5). An example of diffusion zone growth for a typical nitriding steel under typical nitriding conditions is shown in Figure 15.

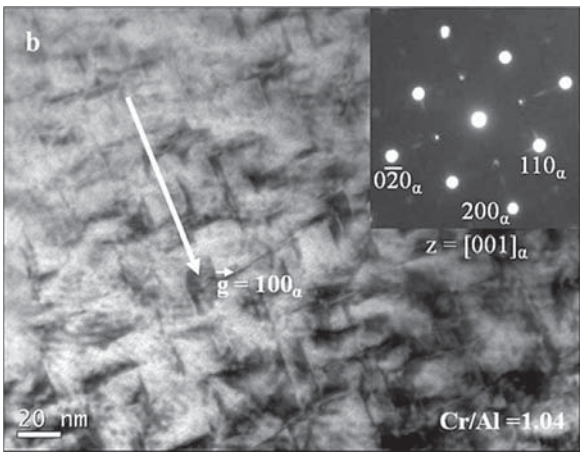

Figure 13 Coherent nitride platelets in the diffusion zone of a nitrided Fe–Cr–Al alloy (0.75 at.% Cr and 072 at.% Al). The platelets are of mixed-type $Cr_xAl_{1-x}N$. Electron diffraction pattern shows that a Baker-Nutting orientation relationship applies for the nitride platelets and the ferrite matrix. Reproduced from Jung, K. S.; Schacherl, R. E.; Mittemeijer, E. *J. Phil. Mag.* **2011**, *91*, 2382–2403.

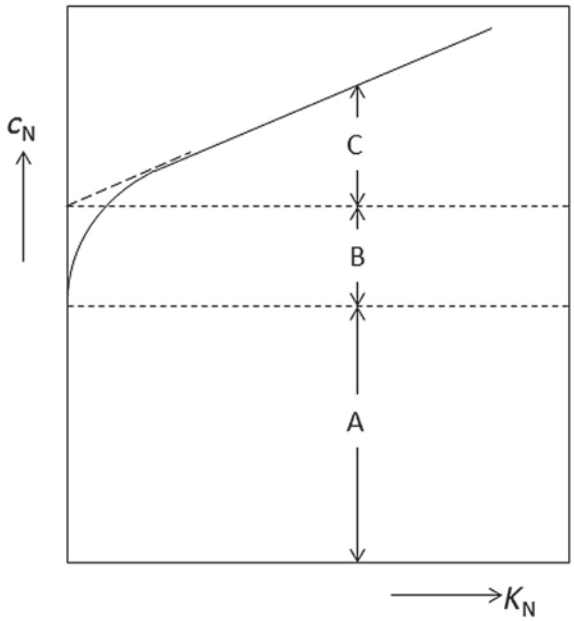

Figure 14 Schematic presentation of an absorption isotherm, that is, the amount of nitrogen absorbed as a function of the nitriding potential K_N. Three energetically different types of nitrogen are distinguished: nitrogen incorporated in stoichiometric nitride M_mN_n (A), nitrogen adsorbed at the platelet/matrix interface (B), and nitrogen interstitially dissolved in strained ferrite (C). Reproduced from Somers, M. A. J.; Lankreijer, R. M.; Mittmeijer, E. *J. Phil. Mag. A* **1989**.

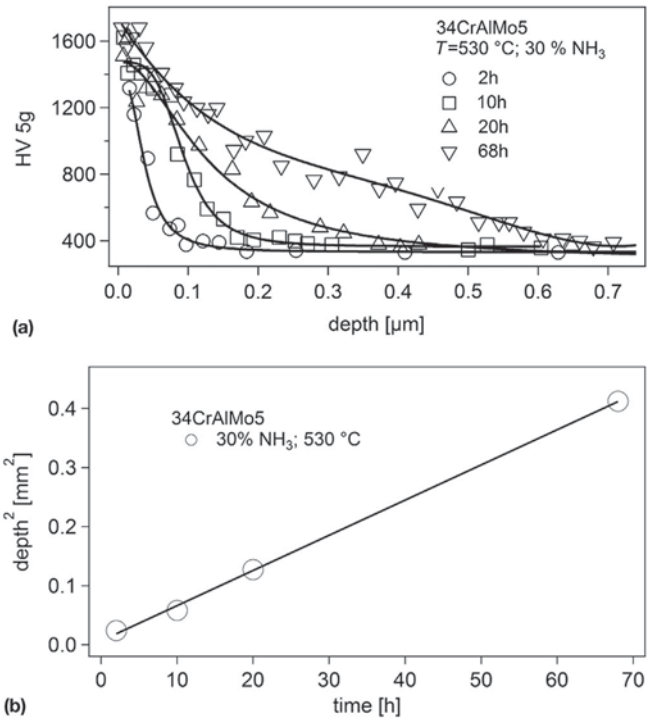

Figure 15 Hardness profiles (a) and depth of the diffusion zone (b) of nitrided 34CrAlMo5 (a nitriding steel). Nitriding conditions 530 °C (803 K) and a gas mixture of 30% NH_3 and 70% H_2. Reproduced from Hansen, I. C. M.Sc. Thesis, Technical University of Denmark, 2010.

On nitriding steels the carbides in the ferrite matrix are gradually transformed into (carbo)nitrides. The carbon atoms released by this transformation can either leave the steel, for example, by CH_4 development at the surface, or diffuse deeper into the steel. As formation and desorption of CH_4 at the usual nitrocarburizing temperatures proceeds slowly, ahead of the advancing nitriding front an enhanced carbon content accumulates, which establishes growth of the primary carbides (*50*,*51*). An example of carbon accumulation ahead of the nitriding front and carbon depletion close to the surface is shown in **Figure 16** for an Fe–Cr–C alloy (model steel) (*51*,*52*). In the microstructure of the diffusion zone, the carbon released by conversion of primary carbides develops cementite along grain boundaries lying within 45° inclined to the surface for strain energy minimization reasons. Ahead of the nitriding front, carbon contributes to growth of primary carbides (*51*,*52*). The grain boundary cementite can subsequently be transformed into carbon-rich ε-phase and eventually grain boundary γ'-nitride (*52*,*53*). (**Figure 17**). The occurrence of carbides/nitrides along grain boundaries is an unwanted microstructure and should be avoided, as it may enhance the risk for crack initiation at these locations. Comparing the morphology of such grain boundaries in fine- and coarse-grained steels shows that a fine-grained material is preferred, as the grain boundary phases remain relatively thin (**Figure 17**) (*53*). The major contribution to materials performance improvement by the diffusion zone is provided by the development of dispersed alloying element nitrides. They are responsible for the hardness increase by precipitation hardening and induce the compressive residual stress profile as a consequence of the misfit with the matrix. The contribution of primary carbides transformed into (carbo)nitrides is negligible (*51*,*52*). For this reason it is important that a sufficient level of nitride-forming alloying elements is dissolved in ferrite. The growth of primary carbides ahead of the advancing nitriding front leads to a reduction of the concentration of dissolved nitride forming elements, and thus to a lower amount of alloying element nitrides at larger depth.

The effect of alloying element concentration, nitriding time, and nitriding temperature on the stress distribution in the diffusion zone is summarized in **Figure 18** (*54*). Stress buildup is considered to be caused by nitride precipitation, while stress relaxation is a consequence of carbon depletion and overaging of the nitrides. Clearly, the higher the concentration of nitride-forming alloying elements, the higher is the compressive residual stress in the diffusion zone, the shallower is the diffusion zone and the steeper is the stress gradient at the case–core transition. For increasing nitriding time, the contribution of carbon depletion becomes more pronounced and the maximum in compressive residual stress is shifted to larger depth, while its magnitude decreases. This latter is a consequence of the lower free alloying element content associated with growth of the primary carbides (see above (*51*,*52*)). Lastly, an increase of the nitriding temperature contributes to a deeper diffusion zone as growth proceeds faster, but also a lower maximum compressive residual stress, resulting from more carbon depletion and faster overaging (*54*).

12.13.4.2 Stainless Steels

Stainless steels rely on the presence of chromium in solid solution, which allows the development and maintenance of a passive layer at the surface. Nitriding/nitrocarburizing is generally not considered good practice as treatment in the conventional temperature range 490–580 °C will lead to the precipitation of CrN. Although this provides a hardening effect, the stainless character is lost as free chromium is no longer available to maintain the passive layer. Since the mid-1980s, several processes have been developed that enable low-temperature surface hardening of stainless steel at temperatures below 440 °C (for a historical review, see Ref. (*55*)). A schematic TTT diagram is given in **Figure 19** and demonstrates the allowable treatment time at low temperature before precipitation of Cr-nitrides occurs. In this temperature range interstitially dissolved elements as nitrogen and carbon diffuse over a relatively long

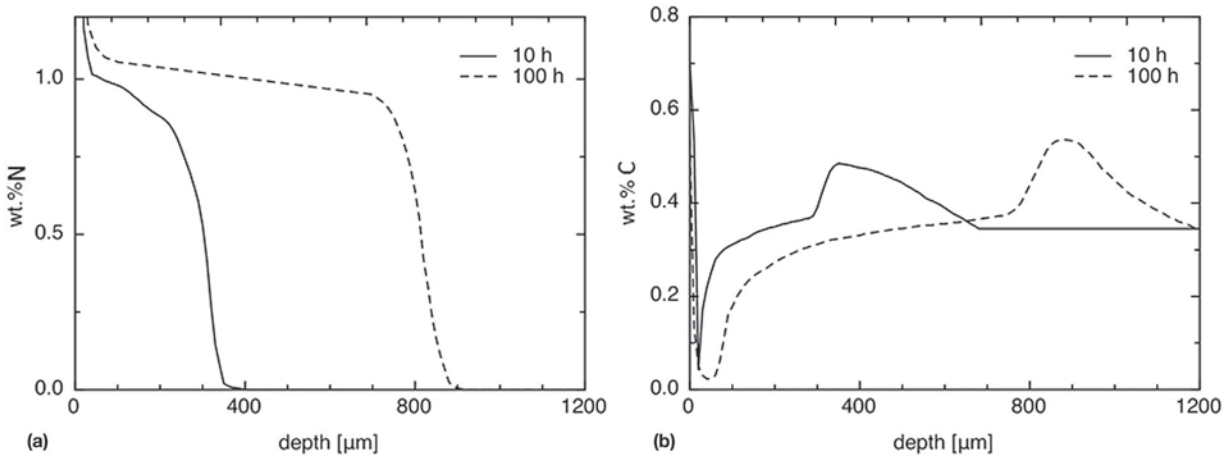

Figure 16 Composition depth profiles for nitrogen (a) and carbon (b) for a Fe–Cr–C alloy (3.0 wt.% Cr, 0.35 wt.% C) nitrided at 550 °C (823 K) for 10 and 100 h. Profiles were determined with Glow Discharge Optical Emission Spectroscopy (GDOES). Reproduced from Jegou, S.; Kubler, R.; Barrallier, L.; Somers, M. A. *J. HTM J. Heat Treat. Mat.* **2011**, *66*, 135–142.

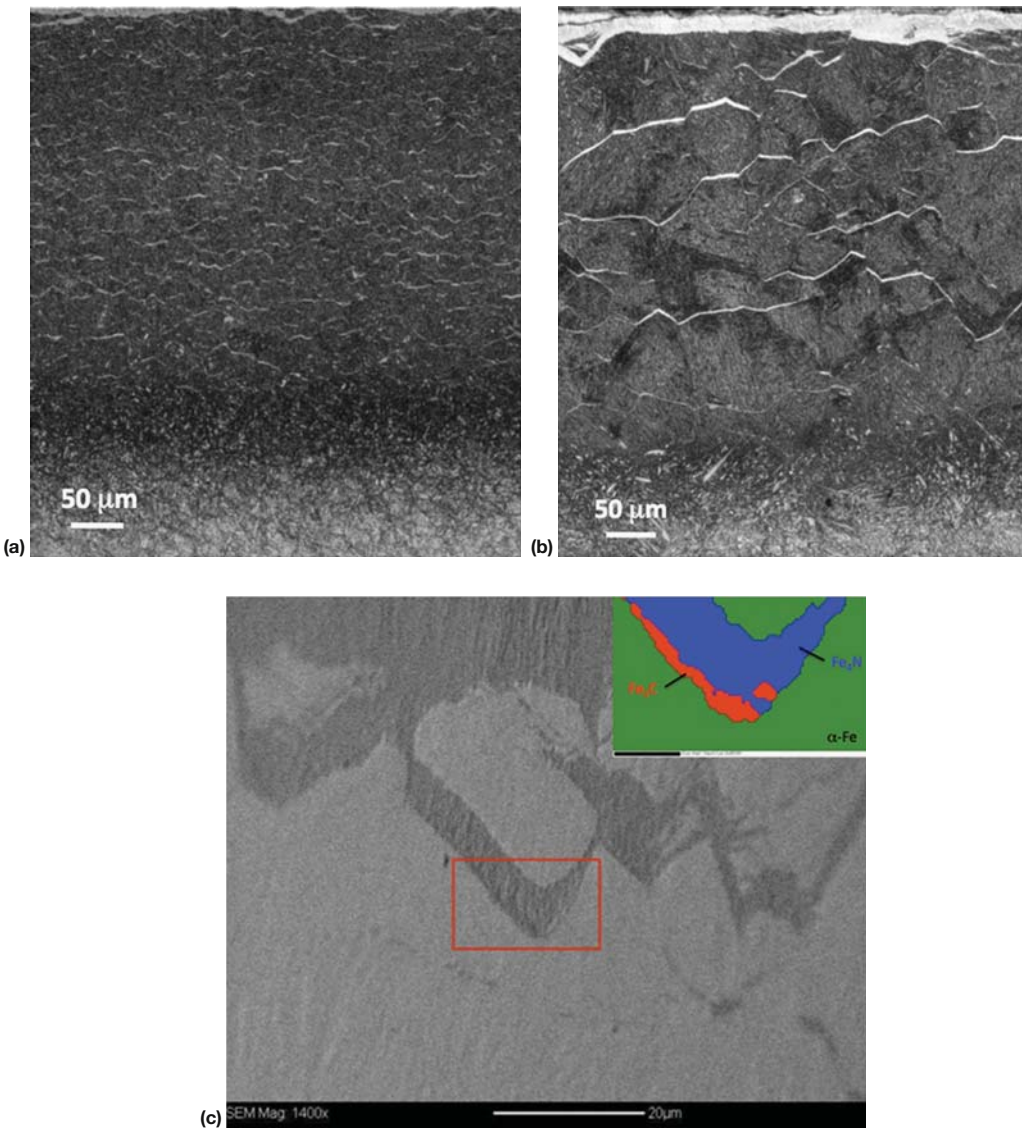

Figure 17 Cross-sections of the diffusion zone in 33CrMoV12 9 nitrided at 520 °C (793 K) for 100 h. Since the steels in (a) and (b) have an average grain size of 15 μm and 85 μm, respectively, the network of (converted) carbides along grain boundaries appears differently. EBSD investigation of grain boundary phase close to the compound layer shows that it consists of cementite (Fe_3C), upon which γ'-Fe_4N has developed. Reproduced from Jegou, S. Ph.D. Thesis, ENSAM ParisTech, 2009.

distance while substitutionally dissolved elements can be considered stationary. Consequently, the development of nitrides or carbides proceeds relatively slowly, that is, slow enough to establish a nitrogen or carbon-rich case that is free of chromium-nitrides/carbides. These processes produce a case that is essentially a solid solution of high amounts of nitrogen (and/or carbon) in austenite, so-called expanded austenite, or in case of martensite, expanded martensite (see reviews in (*56,57*)). Initially, plasma processes were employed, because surface activation by removal of the passive film through sputtering is an inherent step in such treatments. In the later years also, gaseous treatments with *in-situ* surface activation have reached maturity (*58–65,66*). This allows an exploitation of the flexibility of gaseous processes. Since austenitic stainless steel is most widely applied, the principles of low-temperature surface hardening will be demonstrated for this class of stainless steels. Gaseous processes enable the largest flexibility and straightforward thermodynamic definition as regards process parameters, and are therefore treated exclusively.

Nitriding AISI 316 for 22 h at 445 °C at various nitriding potentials allows a variation of the composition–depth profile and the depth to which expanded austenite can be found (**Figure 20**). Evidently, a colossal amount of nitrogen can be dissolved in the developing case; contents of up to 61 nitrogen atoms per 100 metal atoms have been realized in thin foils of uniform composition (*66*), which corresponds to about 38 at.% N. Nitrogen solubilities in this composition range are far beyond the maximum solubility for nitrogen in iron austenite, which is about 10 at.% at $T = 650$ °C (**Figure 2**). An explanation for the very high nitrogen solubility is the occurrence of short-range ordering of chromium and nitrogen (or carbon) atoms, which leads to nitrogen occupation of

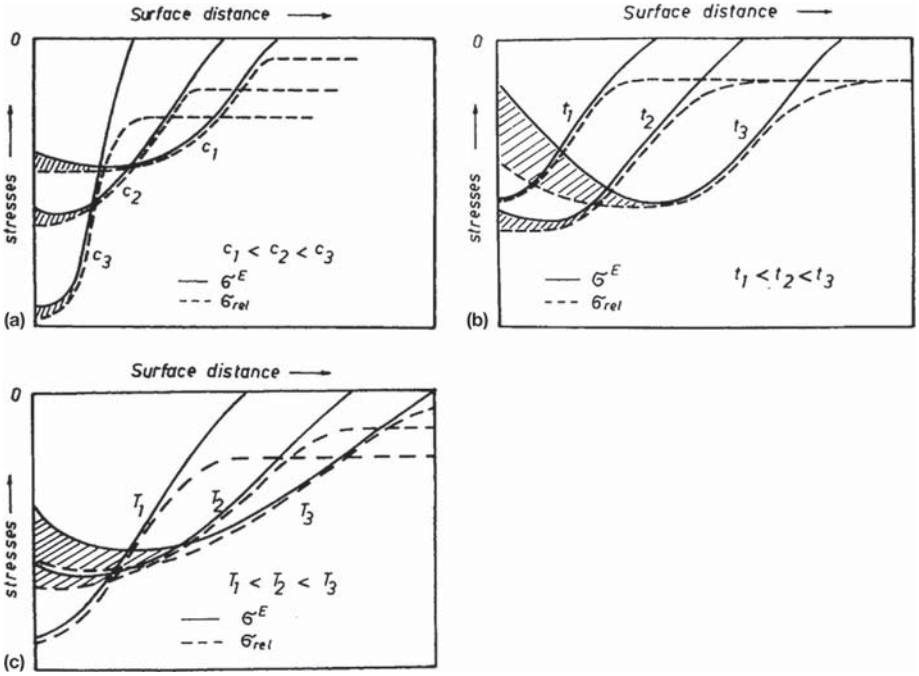

Figure 18 Evolution of residual stress profiles in the diffusion zone with concentration of nitride formers, *c* (a), with nitriding time *t* (b), with nitriding temperature, *T* (c). The shaded areas mark stress relaxation as a consequence of decarburization and overaging (σ_{rel} = relaxation stress; σ_E = elastic stress due to volume mismatch). Reproduced from Oettel, H.; Schreiber, G. In *Proc. Nitrieren und Nitrocarburieren*; Mittemeijer, E. J., Grosch, J., Eds.; AWT: Wiesbaden, 1991; pp 139–151.

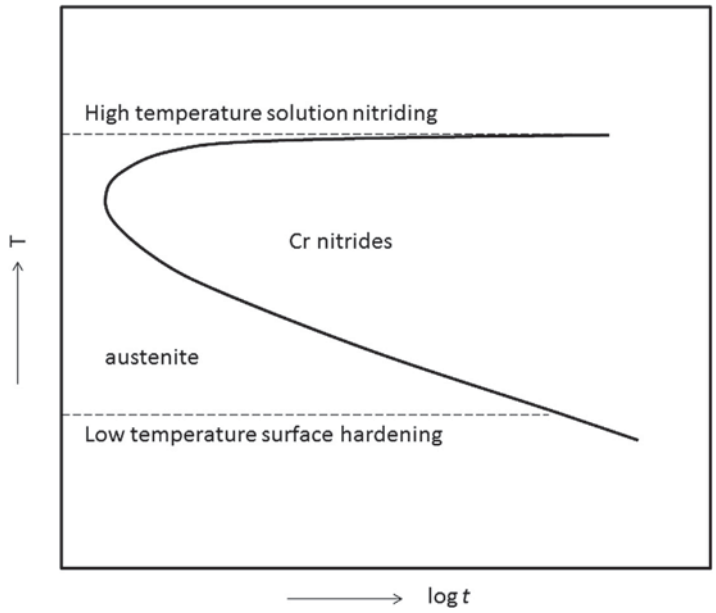

Figure 19 Schematic TTT diagram of austenite with a high nitrogen content. In order to prevent the development of chromium nitrides either a high-temperature treatment, combined with fast cooling, or a longtime low-temperature treatment should be applied. Typically, high-temperature solution nitriding is performed above 1050 °C (1325 K), and low-temperature surface hardening is performed below 450 °C (723 K).

octahedral interstices adjacent to chromium atoms. For the lowest nitrogen content in expanded austenite, that is, for Cr:N = 1:1, on average each Cr atom is coordinated by three neighboring N atoms (*67*).

During nitriding of austenitic stainless steel, an almost featureless case develops at the surface (**Figure 21**), indicating that this zone is more difficult to dissolve in the etchant (aqua regia) than the unaffected austenite. The clear transition from expanded austenite to austenite is only seemingly marked by an interface in **Figure 21**. However, this is an etching effect caused by a steep change in composition and associated abrupt change in electrochemical properties rather than an

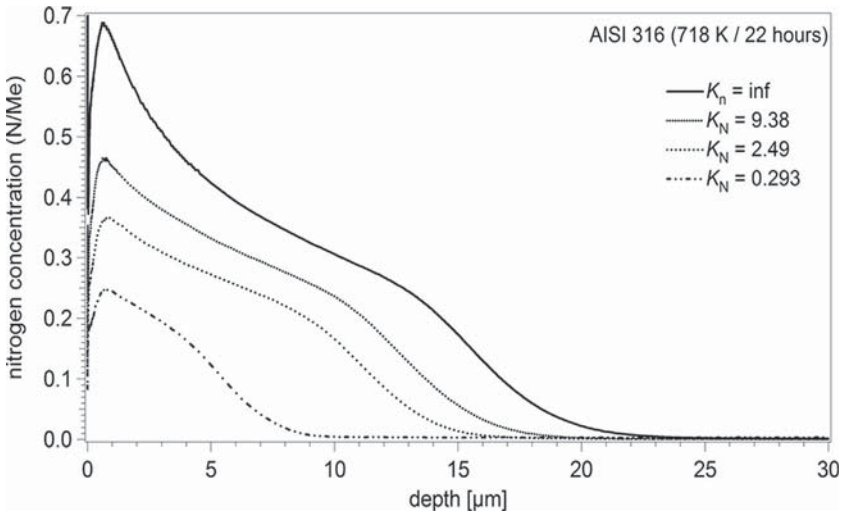

Figure 20 Nitrogen concentration–depth profiles of AISI 316 after nitriding at 445 °C (718 K) for 22 h and nitriding potentials as indicated. Concentration–depth profiles were determined with GDOES, nitrogen content is given N atom per metal atom. Reproduced from Christiansen, T. L.; Somers, M. A. *J. Int. J. Mater. Res.* **2009**, *100*, 1361–1377.

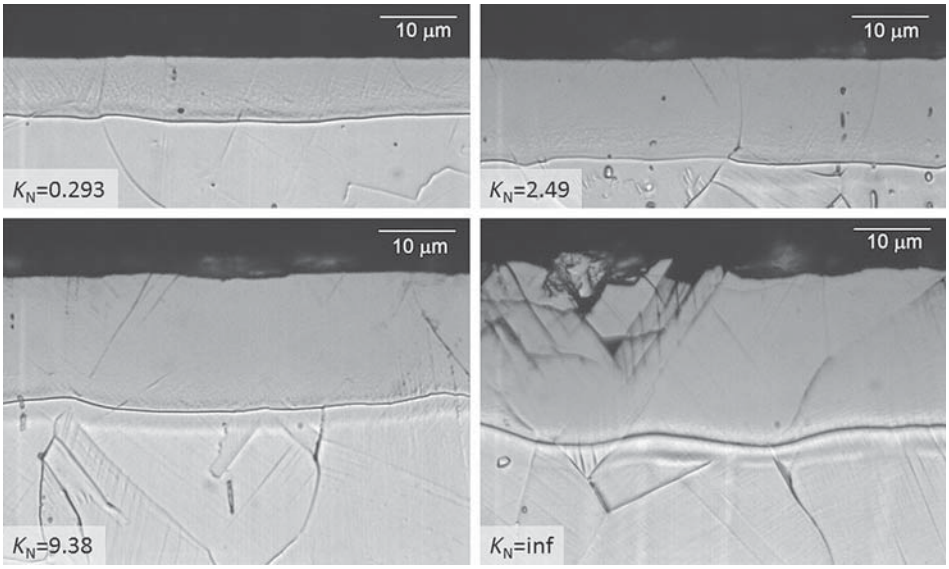

Figure 21 Cross-sections of AISI 316 nitrided at 445 °C (718 K) for 22 h in NH_3–H_2–N_2 gas mixtures, with nitriding potentials indicated in the micrographs. Reproduced from Christiansen, T.; Somers, M. A. *J. Surf. Eng.* **2005**, *21*, 445–455 and Christiansen, T.; Somers, M. A. *J. Metall. Mater. Trans. A* **2006**, *37*, 675–682.

interphase interface. A continuation of grain boundaries from austenite into the developed case proves that the case is merely a (supersaturated) solid solution in nitrogen and not a new phase; if a new phase had developed, a surface layer would appear with a grain structure that differs from that in the core. Therefore, rather than S-phase, as this zone was dubbed in the mid-1980s (*68*), the designation *expanded austenite* is more appropriate. The colossal increase in interstitial atom content in austenite leads to solid-solution strengthening and a spectacular increase in hardness. Examples of the increase in hardness in the nitrided (and carburized) case are shown in **Figure 22**. X-ray diffraction investigation of nitrided stainless steel AISI 316 shows that the austenite peaks in the diffractogram are shifted to lower Bragg angles as a consequence of the expansion of the austenite lattice (**Figure 23**). In addition to the widening of the face-centered cubic lattice, the development of huge (elastic) compressive residual stresses in the case (**Figure 24**) and the introduction of stacking faults as a consequence of plastic deformation, contribute to a shift of the peaks of expanded austenite. Generally, the higher the nitrogen content, the larger these shifts are (*69*). The compressive residual stresses are huge indeed and are directly related to the expansion of the austenite lattice that is coherent with the austenite from which it was formed. Initially, that is, for low nitrogen (or carbon)

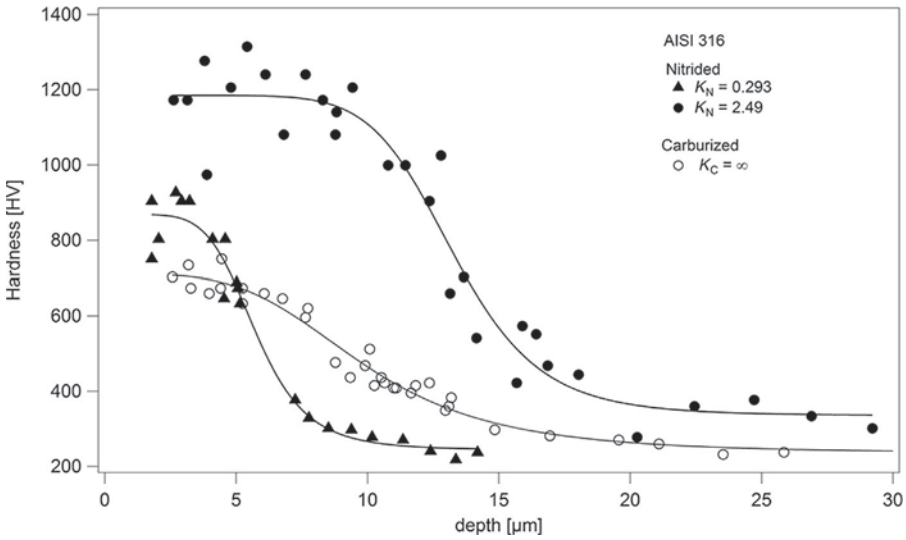

Figure 22 Hardness–depth profiles of AISI 316 nitrided at 445 °C (718 K) for 22 h in NH_3–H_2–N_2 gas mixtures, with nitriding potentials indicated, or carburized at 507 °C (780 K) for 6 h in a CO–H_2–N_2 gas mixture. The lines are fitted by a Hill equation and show a sharper case–core transition for nitrided than for carburized material. Reproduced from Christiansen, T.; Somers, M. A. *J. Surf. Eng.* **2005**, *21*, 445–455.

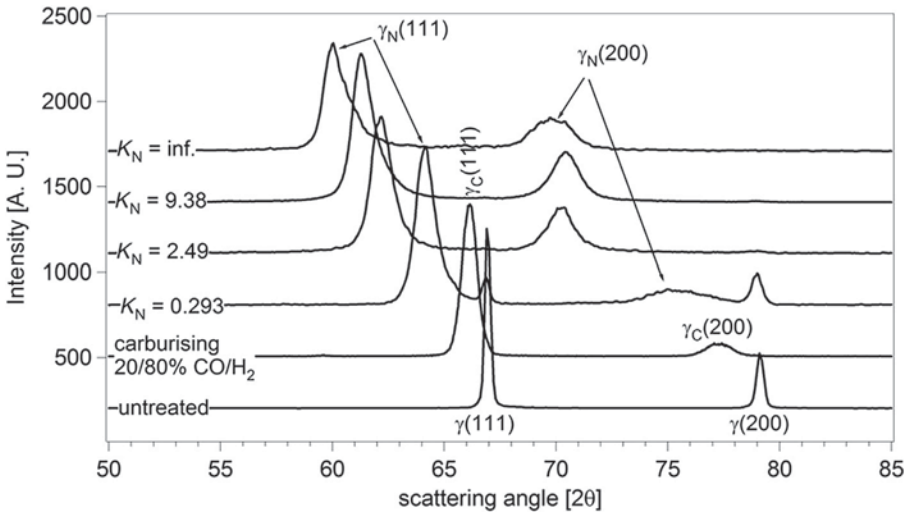

Figure 23 X-ray diffractograms of AISI 316 nitrided at 445 °C (718 K) for 22 h in NH_3–H_2–N_2 gas mixtures, with nitriding potentials indicated, or carburized at 507 °C (780 K) for 6 h in a CO–H_2–N_2 gas mixture. Expanded austenite is identified by the presence of a shift of the austenite peaks to lower Bragg angles, indicated by γ_N and γ_C. Reproduced from Christiansen, T.; Somers, M. A. *J. Surf. Eng.* **2005**, *21*, 445–455.

content, the dilation of the lattice is accommodated elastically; for higher nitrogen content, plastic deformation, as manifested by grain rotation and grain push-out, develops (*70, 71*). For the highest nitrogen contents, brittle fracture is induced in the upper part of the nitrided case (cf. **Figure 21**). Under practical conditions, the nitrogen content should be kept below, say, 25 at.% N.

The transition from the hardened case to the unaffected austenite occurs within a narrow depth range, thereby enhancing the risk for pressing the hard shell into the soft underlying steel in case of a surface load. A remedy can be found in implementing a gradual transition from case to core by gaseous nitrocarburizing or by a two-stage process, that is, nitriding preceded by carburizing (*60*). By these processes, the hardened case consists of a zone of nitrogen-expanded austenite and a zone of carbon-expanded austenite underneath (**Figure 25**). The interstitial atom content in carbon-expanded austenite lies in the range from 0 to 16 at.% C, whereas for nitrogen-expanded austenite at least a nitrogen content corresponding to the Cr content is present (*56*). Hence, carbon bridges the gap in interstitial atom content between unaffected austenite and nitrogen expanded austenite. Accordingly, smooth composition-depth, hardness-depth, and residual stress–depth profiles can be tailored with a nitrocarburizing treatment (see **Figure 25**).

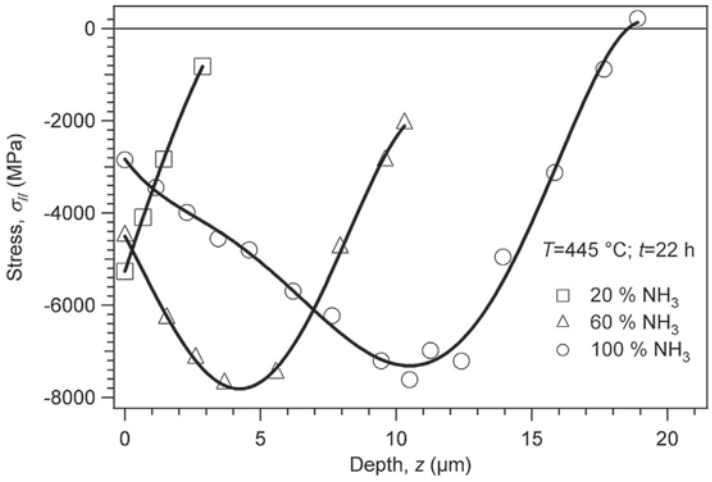

Figure 24 X-ray diffraction residual stress–depth profiles for AISI 316 nitrided at 445 °C (718 K) for 22 h in NH_3–H_2–N_2 gas mixtures, with the ammonia contents indicated, and for a carburized sample. Reproduced from Christiansen, T. L.; Somers, M. A. *J. Int. J. Mater. Res.* **2009**, *100*, 1361–1377.

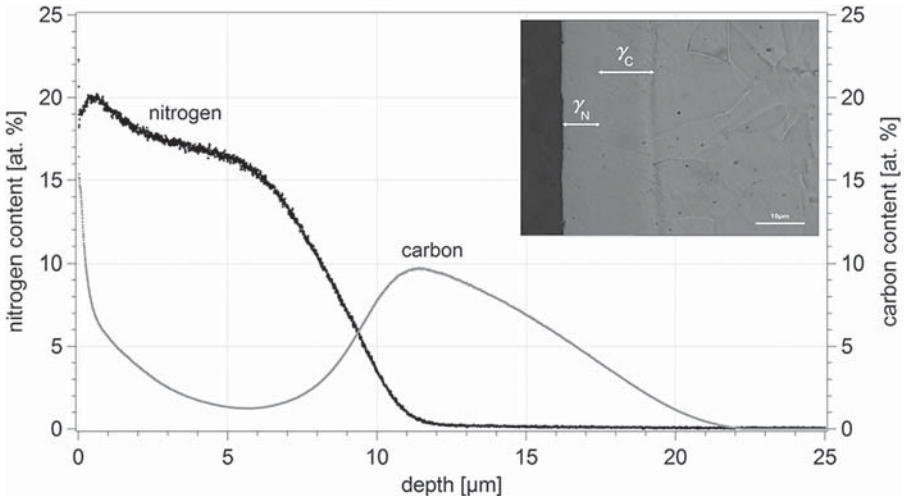

Figure 25 Nitrogen and carbon–depth profiles (GDOES) of AISI 316 nitrocarburized by linear heating from room temperature up to 475 °C (748 K) followed by immediate cooling in urea. Cross-section shows subdivision in a nitrogen and carbon containing expanded austenite. Reproduced from Christiansen, T. L.; Hummelshøj, T. S.; Somers, M. A. J. PCT WO, 2011 009463–A1.

For the case of heavy loading of the surface, the load-bearing capacity of the austenite should be enhanced further. The simplest solution would be to extend the duration of the nitriding/nitrocarburizing treatment. However, this enhances the risk for the precipitation of CrN and associated loss of the anticorrosion properties. For such demanding applications, the low-temperature surface-hardening treatment can be preceded by a high-temperature solution nitriding treatment (*72*), which dissolves a relatively low amount of nitrogen into austenite up to a depth of several millimeters. On cooling from the solution nitriding temperature, care should be taken that no CrN or Cr_2N develops (see the schematic TTT diagram in **Figure 19**).

The notion that expanded austenite is a supersaturated solid solution implies that a large driving force exists for decomposition by the precipitation of CrN (or chromium-based carbides M_5C_2, $M_{23}C_6$ and M_7C_3 for carbon-expanded austenite). The decomposition of nitrogen-expanded austenite was investigated systematically, and it was observed that both CrN and N_2 develop at temperatures above 450 °C (*73*). The development of N_2 occurs because the Cr:N ratio in expanded austenite is at least 1:1, implying that the amount of nitrogen in solid solution is higher than necessary to form stoichiometric CrN. The precipitation of CrN is promoted by the presence of favorable nucleation sites as dislocations and is therefore a major challenge in the surface hardening of heavily plastically deformed components. A recrystallization anneal prior to nitriding reduces the risk for CrN development, but simultaneously annihilates the strengthening effect of work hardening on the core of the component. In those cases where a strengthened core is necessary for optimal product performance, the low-temperature nitriding treatment can be preceded by high-temperature solution nitriding, such that the loss in strength associated with annihilation of work hardening is (partly) compensated by solid solution strengthening to a large depth (*72*).

12.13.5 Modeling

Modeling of the developing case during nitriding and nitrocarburizing has been an active field of research since the advent of the personal computer. In this section, the basics of modeling the growth kinetics of the diffusion zones in stainless steels and heat-treatable steels as well as the compound layer during nitriding are described. Since compound layer formation during nitrocarburizing is a most complicated mechanism, this is not included as no satisfactory models have been published. For reasons of clarity, the development of a diffusion zone is given first, because it is more straightforward and elaborates on descriptions given in many standard textbooks in physical metallurgy. It is assumed that growth of the nitrided case is governed by the diffusion of nitrogen atoms and that the long-range diffusion of metal atoms can be neglected. As nitrogen diffusion proceeds by an interstitial diffusion and metal atoms diffuse substitutionally, this assumption is justified.

12.13.5.1 Modeling the Diffusion Zone in Fe–M Alloys

For one-dimensional diffusion of nitrogen in the x-direction, Fick's first law describes the flux of nitrogen atoms, j_N, through a plane (this is not necessarily a lattice plane) at depth x_0:

$$J_N|_{x=x_0} = -D_N \frac{dc_N}{dx}\bigg|_{x=x_0} \quad [1]$$

where D_N and c_N are diffusion coefficient and nitrogen concentration, respectively. More importantly, Fick's second law expresses how the concentration in a volume element in-between the planes x_0 and $x_0 + dx$ changes within time increment, dt, as a consequence of different fluxes of nitrogen atoms entering and leaving the volume element:

$$\frac{\partial c_N}{\partial t} = -\frac{\partial J_N}{\partial x} = \frac{\partial}{\partial x}\left(D_N \frac{\partial c_N}{\partial x}\right) \quad [2]$$

If it can be assumed that the diffusion coefficient is constant and does not change with concentration (position), eqn [2] is reduced to:

$$\frac{\partial c_N}{\partial t} = D_N \frac{\partial^2 c_N}{\partial x^2} \quad [3]$$

Frequently, an equation of the type in eqn [3] is used in standard textbooks in Materials Science to describe the evolution of a concentration profile during diffusion of an interstitial (N or C) in austenite. A general solution of eqn [3] is:

$$c_N = A + B \ erf\left\{\frac{x}{\sqrt{2D_N t}}\right\} \quad [4]$$

where A and B depend on the boundary conditions of the diffusion problem. Taking the initial concentration of nitrogen in austenite as c_0 and the surface concentration as c_s, it is obtained:

$$\frac{c_N - c_0}{c_s - c_0} = 1 - erf\left\{\frac{x}{2\sqrt{D_N t}}\right\} \quad [4b]$$

For the growth of a diffusion zone wherein alloying element nitrides precipitate during growth, the solution proposed to describe the kinetics of internal oxidation (*74*) could serve as a zeroth order approximation (*48*). This implies that an infinitely strong interaction between nitrogen and the alloying elements occurs, such that a nitrogen atom on arrival at the advancing nitriding front is immediately captured by an unbound alloying element atom to form nitride. It is assumed that the reaction of nitrogen with alloying element can be expressed as:

$$mM + nN = M_m N_n \quad [5]$$

and the $M{:}N = m{:}n$ ratio for the nitrogen bound to nitride. Then the following continuity equation (cf. **Figure 26**), giving the increment in diffusion zone thickness $d\xi$ for a time increment dt, applies:

$$\left\{\frac{n}{m} C_M\right\} \cdot d\xi = J^{\phi} \cdot dt \quad [6]$$

where c_M is the concentration of nitride-forming alloying elements, and J^{ϕ} is the average flux of nitrogen through the matrix phase ϕ in the diffusion zone. From this continuity equation and application of Fick's first law, $J^{\alpha} = -D_N^{\alpha}\frac{\Delta c_N^{\alpha}}{\Delta x} = D_N^{\alpha}\frac{c_{N_s}^{\alpha}}{\xi}$, with $c_{N_s}^{\alpha}$ the concentration of nitrogen *dissolved in ferrite* (note that $c_{N_s}^{\alpha}$ is not identical to c_s in **Figure 26**. It holds $c_{N_s}^{\alpha} = c_s - \frac{n}{m}c_M$ at the surface and D_N^{α} the diffusivity of nitrogen in ferrite, the growth rate of the diffusion zone becomes:

$$\frac{d\xi}{dt} = \frac{K}{\xi} \quad [7a]$$

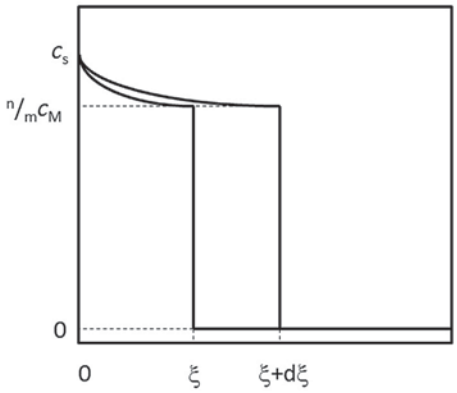

Figure 26 Schematic composition–depth profile for internal nitriding of an Fe–M alloy with an infinitely strong nitride former (e.g., Ti).

with

$$K = D_N^{\alpha} \frac{m c_{N_s}^{\alpha}}{n c_M} \qquad [7b]$$

which, upon integration, yields

$$\xi^2 = 2 D_N^{\alpha} \frac{m c_{N_s}^{\alpha}}{n c_M} t + C \qquad [7c]$$

where C is an arbitrary integration constant that could express an incubation time. Clearly, increasing the alloying element concentration c_M leads to a reduction of the growth rate of the diffusion zone, provided that all other parameters remain constant. Note that eqn [7] does not apply for c_M=0.

The above internal nitriding model applies for an infinitely strong interaction between alloying elements and nitrogen, where no nitrogen can be dissolved in the matrix when unbound nitride-forming alloying elements are present. In reality, the interaction is more moderate and a certain simultaneous solubility of nitrogen and alloying element is possible, as expressed by the solubility product of M and N, which is taken as $K_{sol} = c_M^m \cdot c_N^n$, where c_j is the concentration of element j. Note that the solubility product is the reciprocal of the equilibrium constant for eqn [5]; that is, $K_{M_m N_n} = \frac{1}{a_M^m \cdot a_N^n}$, with a_j the activity of component j in solid solution (prior to precipitation), assuming M and N obey an ideal solution so that activity a_j is replaced by the concentration c_j. Sun and Bell (*49*) developed a model that took the solubility product of the alloying-element nitride into consideration, as well as the possible development of a γ'-Fe_4N compound layer. Schacherl et al. (*46*) extended the model for development of the nitrogen concentration profile in the diffusion zone by including excess nitrogen, that is, the nitrogen dissolved in addition to the stoichiometric nitride and the equilibrium nitrogen content in the ferrite matrix, and applied it to nitriding of Fe–Cr (*46*) and later to Fe–V (*47*). A distinction should be made between strongly bound, immobile (trapped) excess nitrogen and mobile excess nitrogen. The immobile nitrogen is considered to be adsorbed at the nitride/ferrite interface and is reflected by replacing n by $n + \delta$ in eqn [5], where δ reflects the nitrogen adsorbed at the platelet/matrix interface (cf. the distance B in **Figure 14**). The mobile excess nitrogen is dissolved in the ferrite matrix and contributes to the flux of nitrogen atoms through the diffusion zone. A flow scheme of the model is given in **Figure 27**. This model describes excellently the evolution of the nitrogen concentration profile on nitriding of binary Fe–Cr alloys with various Cr contents (**Figure 28**) and shows that the mobile nitrogen has a pronounced influence on the thickness of the diffusion zone, while trapped nitrogen contributes to the total nitrogen content in the diffusion zone. Rather than nitride formation, Kamminga and Janssen (*75*) considered trapping of nitrogen atoms by alloying elements, implying that the nitrogen atoms are only temporarily trapped by the alloying elements and not infinitely strongly bound as in a nitride. Although their model could describe the results by Sun and Bell (*49*) more satisfactorily than the model in (*49*), still a discrepancy exists with the nitrogen profiles developing in more complex steels. A disadvantage of the trap model is the occurrence of unknown trap depths for the various alloying elements. Neither of the models presented so far includes the redistribution of carbon occurring during development of the diffusion zone in steels.

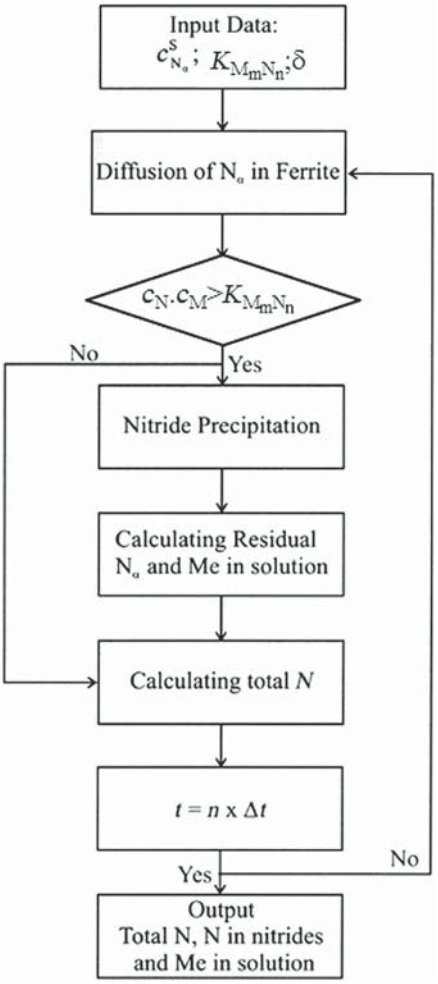

Figure 27 Flowchart for calculating the nitrogen-concentration profile in the diffusion zone for an alloy with a nitride former of intermediate strength (e.g., Cr), incorporating trapped excess nitrogen adsorbed at the platelet/nitride interface and mobile excess nitrogen dissolved in strained ferrite (cf. **Figure 14**).

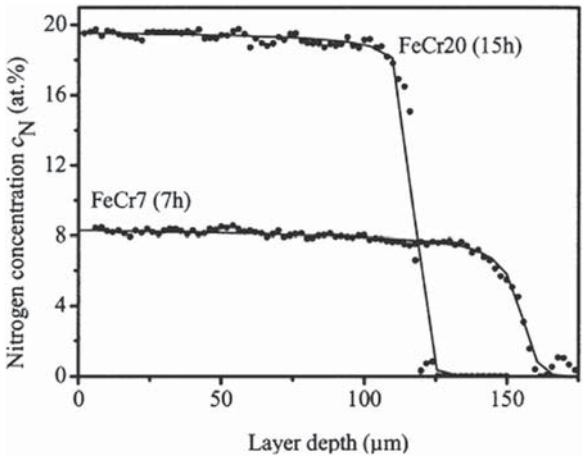

Figure 28 Nitrogen concentration–depth profile in two Fe–Cr alloys after nitriding at 580 °C (853 K) for the times indicated. The data were obtained by electron probe microanalysis (EPMA) and the lines were calculated by the model in **Figure 27**, taking contents of trapped and mobile excess nitrogen as fit parameters.

12.13.5.2 Modeling of Stress–Depth Profiles in the Diffusion Zone

Stress–depth profiles in the diffusion zone were recently demonstrated to be straightforwardly predictable from the concentration–depth profiles for nitrogen and carbon in the diffusion zone. Jegou et al. (*51,52*) used experimental nitrogen and carbon concentration profiles shown in **Figure 16**, together with the metallic composition of alloy, as input for ThermoCalco to calculate the equilibrium phase fractions of the nitrides and carbides as a function of depth. Taking the equilibrium phase fractions and the molar volumes of the various phases provided the unconstrained volume change as a function of depth. By constraining the volume changes, residual stress profiles were obtained that correspond quantitatively to the experimentally determined stress–depth profiles (**Figure 29**).

12.13.5.3 Modeling Expanded Austenite in Stainless Steel

The development of a nitrogen concentration profile in expanded austenite is not associated with nitride precipitation. Hence, it is expected that a diffusion model including trapping of nitrogen by nitride forming elements in solid solution would describe this case satisfactorily. A model to describe the evolution of nitrogen-concentration profiles in expanded austenite during plasma nitriding was presented by Martinavicius et al. (*76*). In their model, they incorporated trapping (with unknown trapping coefficients as fit parameters) of nitrogen as well as sputtering away of the surface by the plasma. Furthermore, they assumed that the diffusion coefficient of nitrogen in expanded austenite is independent of the nitrogen concentration. These models, with several fit parameters, could provide a satisfactory (mathematical) description of the nitrogen concentration profile. However, as demonstrated convincingly, the assumption of constant diffusivity in expanded austenite is untenable and in fact shows strong dependence on the nitrogen concentration (*77*). Christiansen et al. (*78*) adopted the model from (*46,49*) and generalized the model by using eqn [2] instead of eqn [3], thus allowing a composition-dependent diffusion coefficient. They also included a possibility to keep the surface concentration constant. The nitrogen concentration in excess of the solubility product was considered to be short range ordered (trapped) with Cr up to a ratio Cr:N = 1:1, that is, mathematically equivalent to the formation of CrN as in the models in (*46,49*). This model provided a qualitative correspondence with experimental and simulated nitrogen-concentration depth profiles. Comparison of the rate of nitrogen incorporated in expanded austenite as observed experimentally with those simulated by the model showed that a major discrepancy occurred. The most likely cause for this discrepancy was shown to be the occurrence of a composition-induced stress profile in the expanded austenite zone, which influences both the thermodynamics of expanded austenite, as reflected in a lower surface concentration of nitrogen, and the diffusion coefficient by the pressure effect and an enhanced chemical potential gradient induced by a stress gradient. A preliminary estimate of the contribution of stress-induced diffusion on layer growth indicated that this effect can account for enhanced layer growth by a factor 2 for the case of expanded austenite (*79*). A first attempt to include the contribution of stress-assisted diffusion in expanded austenite zones was presented by Galdikas and Moskalioviene (*80*).

12.13.5.4 Modeling Compound-Layer Growth

A compound layer consisting of an ε (top) and a γ' layer (bottom) is considered. The nitrogen concentration–depth profile over such a layer is shown schematically in **Figure 30(a)**. At the interfaces of the layers and the adjacent phase, a discontinuity in the

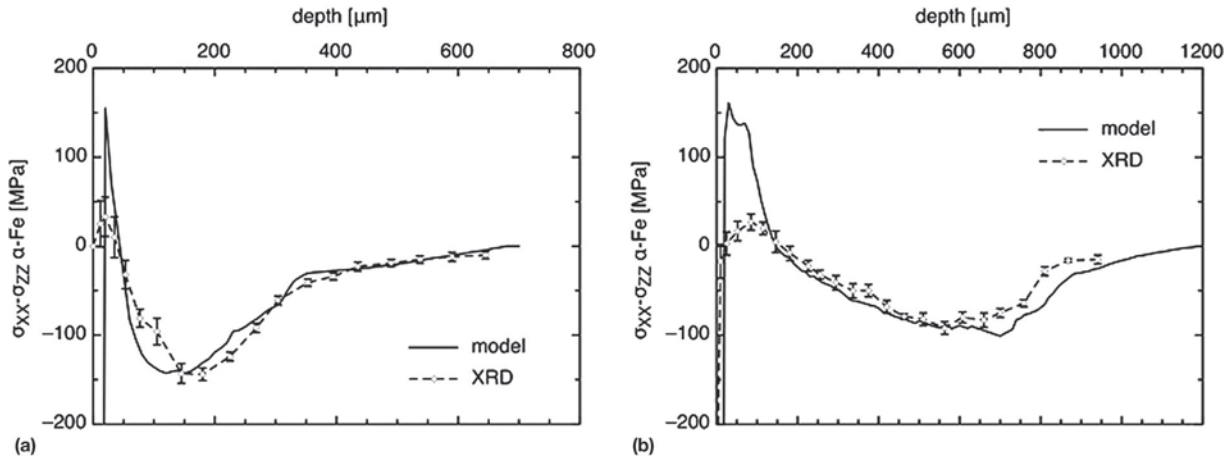

Figure 29 Calculated residual stress profiles in the ferrite matrix of Fe–3 wt.% Cr–0.35 wt.% C nitride at 823 K (550 °C) for (a) 10 h and (b) 100 h in comparison with experimental data determined by X-ray diffraction stress determination. The calculated profiles were obtained from the nitrogen and carbon concentration profile in **Figure 16**, combined with calculated equilibrium phase composition and specific volumes of the phases developed. Reproduced from Jegou, S.; Kubler, R.; Barrallier, L.; Somers, M. A. *J. HTM J. Heat Treat. Mat.* **2011**, *66*, 135–142; Jegou, S.; Barrallier, L.; Kubler, R. *Acta Mater.* **2010**, *58*, 2666–2676 and Jegou, S. Ph.D. Thesis, ENSAM ParisTech, 2009.

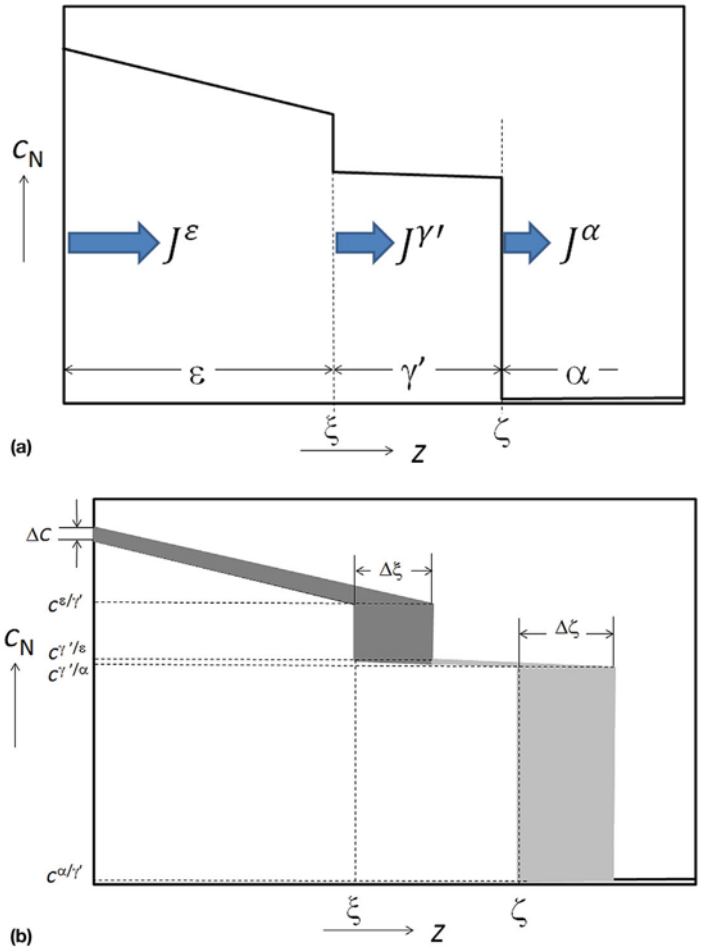

Figure 30 Nitrogen concentration–depth profile for an ε/γ' double layer. (a) Growth of the ε and γ' layers is determined by the difference of the fluxes entering and leaving these layers. (b) The amounts of nitrogen accumulating in the ε and γ' layers are represented by the dark and light gray areas, respectively. While the layer grows, the surface concentration increases.

nitrogen concentration occurs. The growth of the nitride layers is described by the continuity equations for the layers, implying that the difference in flux of nitrogen atoms entering and leaving the layers is accumulated in the layer and used for maintaining the nitrogen concentration profile and layer growth. Mathematically, the shifts of the interfaces at ξ and ζ over distances $d\xi$ and $d\zeta$, respectively, within time interval dt can be described as (*81*):

$$W^{\varepsilon} \cdot d\xi = (J^{\varepsilon} - J^{\gamma'}) \cdot dt \qquad [8a]$$

$$W^{\gamma'} \cdot (d\zeta - d\xi) = (J^{\gamma'} - J^{\alpha}) \cdot dt \qquad [8b]$$

where W^{j} is the accumulated amount of nitrogen in the layer of phase ϕ and J^{ϕ} is the flux of N atoms entering phase ϕ. The composition profiles in the ε and γ' sublayers can be approximated by straight lines if the fluxes in the respective layers are taken as the average flux over the layer. Furthermore, recognizing the gradual increase of the nitrogen content at the surface (cf. **Figure 7(b)**), a time-dependent surface concentration of nitrogen should be adopted. In **Figure 30(b)** the accumulated nitrogen atoms in the ε and γ' nitride layers are represented by the dark and light gray areas, respectively. A comparison of a model for double-layer growth presuming local equilibrium at the surface and the model in **Figure 30(b)**, shows that only a marginal change of the layer growth kinetics is obtained (**Figure 31(a)**). On the other hand, the model in **Figure 30(b)** provides a much more realistic prediction of the nitrogen concentration profile in the compound layer (**Figure 31(b)**) (*82,83*). The influence of a diffusion zone underneath the compound layer has serious implications for the growth rate of the compound layer. According to eqn [8], the growth rates of the various layers are coupled. If a diffusion zone is present underneath the compound layer, an increase of J^{α} as compared to J^{ε} implies that less nitrogen is accumulated in the compound layer. Hence, a thinner compound layer will result than for the case where the capacity for nitrogen in the diffusion zone is limited. This is indeed observed in practice, the compound layer on strongly alloyed steels is considerably thinner than on plain carbon steel.

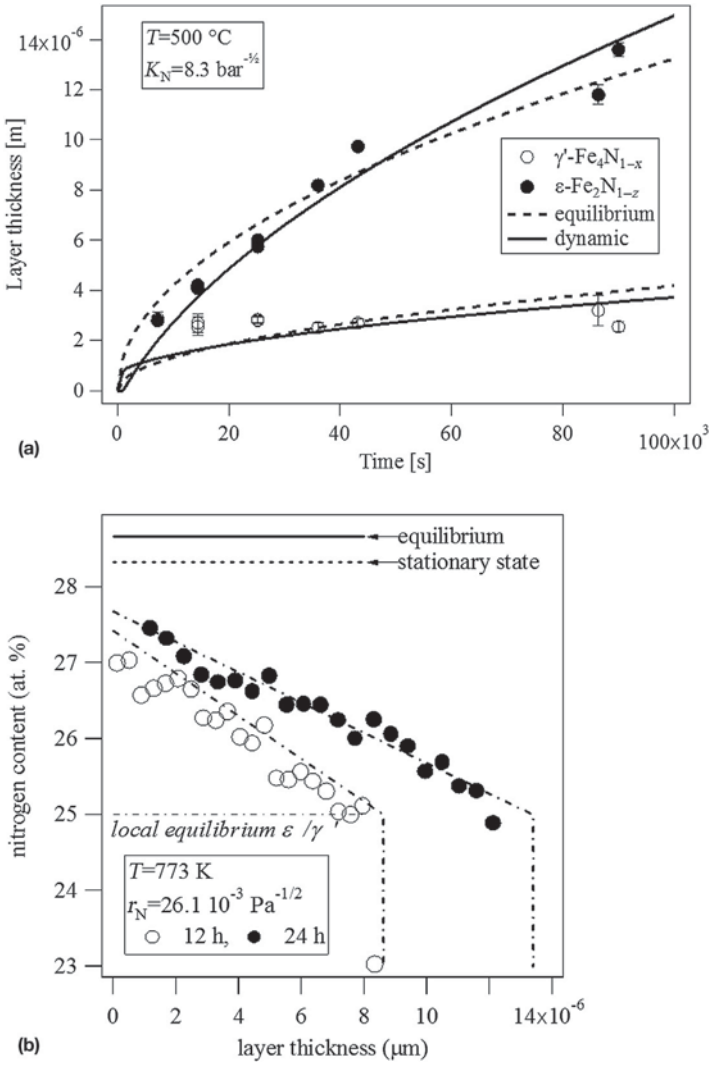

Figure 31 (a) Layer growth kinetics for an ε/γ' double layer, described by a model assuming local equilibrium at the surface of a dynamic state, where the surface concentration of nitrogen increases with time (cf. **Figure 30**); (b) evolution of nitrogen concentration–depth profile. Data were determined by EPMA; drawn lines were modeled with the model in **Figure 30**. Reproduced from Somers, M. A. J.; Friehling, P. B. *Härterei-Tech. Mitt.* **2002**, *57*, 415–420.

References

1. Slycke, J.; Sproge, L. *Surf. Eng.* **1989,** *5,* 125–140.
2. Mittemeijer, E. J.; Slycke, J. *Surf. Eng.* **1996,** *12,* 152–162.
3. Grabke, H. J. *Mater. Sci. Forum* **1994,** *154,* 69–85.
4. Pedersen, H.; Christiansen, T. L.; Somers, M. A. J. *HTM J. Heat Treat. Mater.* **2011,** *66,* 76–81.
5. Du, H.; Somers, M. A. J.; Ågren, J. *Metall. Mater. Trans. A* **2000,** *31A,* 195–211.
6. Winter, K.-M.; Hoja, S.; Klümper-Westkamp, H. *HTM J. Heat Treat. Mater.* **2011,** *66,* 68–75.
7. Lehrer, E. *Z. Elektrochem.* **1930,** *36,* 383–392.
8. Kooi, B. J.; Somers, M. A. J.; Mittemeijer, E. J. *Metall. Mater. Trans. A* **1996,** *27,* 1063–1071.
9. Somers, M. A. J.; Kooi, B. J.; Małdziński, L.; Mittemeijer, E. J.; van der Horst, A. A.; van der Kraan, A. M.; van der Pers, N. M. *Acta Mater.* **1997,** *45,* 2013–2025.
10. Mittemeijer, E. J.; Somers, M. A. J. *Surf. Eng.* **1997,** *13,* 483–497.
11. Naumann, F. K.; Langenscheid, G. L. *Arch. Eisenhüttenwes.* **1965,** *36,* 677–682.
12. Naumann, F. K.; Langenscheid, G. L. *Arch. Eisenhüttenwes.* **1965,** *36,* 583–590.
13. Slycke, J.; Sproge, L.; Ågren, J. *Scand. J. Metall.* **1988,** *17,* 122–126.
14. Kunze, J. *Nitrogen and Carbon in Steel: Thermodynamics;* Akademie Verlag: Berlin, 1990.
15. Du, H.; Hillert, M. *Z. Metallkd.* **1991,** *82,* 310–316.
16. Du, H. *J. Phase Equilibria* **1994,** *14,* 682–693.
17. Kunze, J. *Härterei-Tech. Mitt.* **1996,** *51,* 348–355.

18. Somers, M. A. J.; Colijn, P. F.; Sloof, W. G.; Mittemeijer, E. J. *Z. Metallkd.* **1990,** *81,* 33–43.
19. Somers, M. A. J. *Heat Treat. Met.* **2000,** *27,* 92–102.
20. Somers, M. A. J. *Int. Heat Treat. Surf. Eng.* **2011,** *5,* 7–16.
21. Somers, M. A. J.; Mittemeijer, E. J. *Härterei-Tech. Mitt.* **1992,** *47,* 5–13.
22. Somers, M. A. J.; Małdziński, L.; Gommers, A. W. J. Unpublished work. Delft University of Technology, 1996.
23. Somers, M. A. J.; Mittemeijer, E. J. *Surf. Eng.* **1987,** *3,* 123–137.
24. Dijkstra, J. *J. Metals* **1949,** *1,* 252.
25. Jack, K. H. *Proc. Roy. Soc. A* **1951,** *208A,* 216.
26. Mittemeijer, E. J.; Straver, W. T. M.; van der Hoeven, J. B.; van der Schaaf, P. J. *Scr. Metall.* **1980,** *14,* 1189.
27. Brenner, S. S.; Goodman, S. B. *Scr. Metall.* **1971,** *5,* 865–870.
28. Mortimer, B.; Grieveson, P.; Jack, K. H. *Scand. J. Metall.* **1972,** *1,* 203–209.
29. Pope, M.; Grieveson, P.; Jack, K. H. *Scand. J. Metall.* **1973,** *2,* 29–34.
30. Kirkwood, D. H.; Atasoy, O. E.; Keown, S. R. *Met. Sci.* **1974,** *8,* 49–55.
31. Jack, K. H. *Proc. Heat Treatment '73;* The Metals Society: London, 1975; pp 39–50.
32. Jack, D. H. *Acta Metall.* **1976,** *24,* 137–146.
33. Wagner, R.; Brenner, S. S. *Acta Metall.* **1978,** *26,* 197–206.
34. Hekker, P. M.; Rozendaal, H. C. F.; Mittemeijer, E. J. *J. Mater. Sci.* **1985,** *20,* 719–729.
35. Rickerby, D. S.; Henderson, S.; Hendry, A.; Jack, K. H. *Acta Metall.* **1986,** *34,* 1687–1699.
36. Ginter, C.; Torchane, L.; Dulcy, J.; Gantois, M.; Turpin, T.; Malchère, A.; Esnouf, C. *Metall. Ital.* **2006,** *98,* 29–35.
37. Vives Díaz, N. E.; Hosmani, S. S.; Schacherl, R. E.; Mittemeijer, E. J. *Acta Mater.* **2008,** *56,* 4137–4149.
38. Clauss, A. R.; Bischoff, E.; Hosmani, S. S.; Schacherl, R. E.; Mittemeijer, E. J. *Metall. Mater. Trans.* **2009,** *40A,* 1923–1934.
39. Hosmani, S. S.; Schacherl, R. E.; Mittemeijer, E. J. *J. Mater. Sci.* **2009,** *44,* 520–527.
40. Jung, K. S.; Schacherl, R. E.; Bischoff, E.; Mittemeijer, E. J. *Surf. Coat. Technol.* **2010,** *204,* 1942.
41. Jung, K. S.; Schacherl, R. E.; Mittemeijer, E. J. *Phil. Mag.* **2011,** *91,* 2382–2403.
42. Schacherl, R. E.; Mittemeijer, E. J. *Mater. Sci. Forum* **2012,** *706–709,* 2583–2588.
43. Jung, K. S.; Meka, S. R.; Schacherl, R. E.; Bischoff, E.; Mittemeijer, E. J. *Metall. Mater. Trans.* **2012,** *43A,* 934–944.
44. Podgurski, H. H.; Davis, F. N. *Acta Metall.* **1981,** *29,* 1–9.
45. Somers, M. A. J.; Lankreijer, R. M.; Mittmeijer, E. J. *Phil. Mag. A* **1989,** *59,* 353–378.
46. Schacherl, R. E.; Graat, P. C. J.; Mittemeijer, E. J. *Metall. Mater. Trans. A* **2004,** *35,* 3387–3398.
47. Hosmani, S. S.; Schacherl, R. E.; Mittemeijer, E. J. *Metall. Mater. Trans. A* **2007,** *38,* 7–16.
48. Lightfoot, B. J.; Jack, D. H. *Proc. Heat Treatment '73;* The Metals Society: London, 1975, 59–65.
49. Sun, Y.; Bell, T. *Mater. Sci. Eng. A* **1997,** *224,* 33–47.
50. van Wiggen, P. C.; Rozendaal, H. C. F.; Mittemeijer, E. J. *J. Mater. Sci.* **1965,** *20,* 4561–4582.
51. Jegou, S.; Kubler, R.; Barrallier, L.; Somers, M. A. J. *HTM J. Heat Treat. Mat.* **2011,** *66,* 135–142.
52. Jegou, S.; Barrallier, L.; Kubler, R. *Acta Mater.* **2010,** *58,* 2666–2676.
53. Jegou, S. Ph.D. Thesis, ENSAM ParisTech, 2009.
54. Oettel, H.; Schreiber, G. In *Proc. Nitrieren und Nitrocarburieren;* Mittemeijer, E. J., Grosch, J., Eds.; AWT: Wiesbaden, 1991; pp 139–151.
55. Christiansen, T. L.; Somers, M. A. J. In *Thermochemical Surface Engineering of Steels: Improving Materials Performance;* Mittemeijer, E. J., Somers, M. A. J., Eds.; Woodhead Publishing, 2014.
56. Christiansen, T. L.; Somers, M. A. J. *Int. J. Mater. Res.* **2009,** *100,* 1361–1377.
57. Dong, H. *Int. Mater. Rev.* **2010,** *55,* 65–98.
58. Williams, P. C.; Marx, S. C. US Patent 6,093,303, 25 July 2000.
59. Somers, M. A. J.; Christiansen, T.; Møller, P. DK174707 B1 and EP 1521861 B1.
60. Christiansen, T.; Somers, M. A. J. *Surf. Eng.* **2005,** *21,* 445–455.
61. Williams, P. C.; Marx, S. C. US Patent 6,547,888, 15 April 2003.
62. Cao, Y.; Ernst, F.; Michal, G. M. *Acta Mater.* **2003,** *51,* 4171–4181.
63. Michal, G. M.; Ernst, F.; Kahn, H.; Cao, Y.; Oba, F.; Agarwal, N.; Heuer, A. H. *Acta Mater.* **2006,** *54,* 1597–1606.
64. Somers, M. A. J.; Christiansen, T. PCT: WO 2006136166_A1, 2006.
65. Christiansen, T. L.; Hummelshøj, T. S.; Somers, M. A. J. *Surf. Eng.* **2011,** *27* (8), 602–608.
66. Christiansen, T.; Somers, M. A. J. *Metall. Mater. Trans. A* **2006,** *37,* 675–682.
67. Oddershede, J.; Christiansen, T. L.; Ståhl, K.; Somers, M. A. J. *Scr. Mater.* **2010,** *62,* 290–293.
68. Zhang, Z. L.; Bell, T. *Surf. Eng.* **1985,** *1,* 131–136.
69. Christiansen, T. L.; Hummelshøj, T. S.; Somers, M. A. J. *Surf. Eng.* **2010,** *26,* 242–247.
70. Templier, C.; Stinville, J. C.; Renault, P. O.; Abrasonis, G.; Villechaisse, P.; Rivière, J. P.; Drouet, M. *Scr. Mater.* **2010,** *63,* 496–499.
71. Stinville, J. C.; Villechaisse, P.; Templier, C.; Rivière, J. P.; Drouet, M. *Acta Mater.* **2010,** *58,* 2814–2821.
72. Hummelshøj, T. S.; Christiansen, T. L.; Somers, M. A. *J. PCT WO* **2012**, 146254-A1.
73. Christiansen, T.; Somers, M. A. J. *Z. Metallkd.* **2006,** *97,* 79–88.
74. Meijering, J. L.. Wiley Interscience, New York, NY. *Adv. Mater. Res.* **1971,** *5,* 1.
75. Kamminga, J.-D.; Janssen, G. C. A. M. *Surf. Coat. Technol.* **2006,** *200,* 909–912 and 5896–5901.
76. Martinavicius, A.; Abrasonis, G.; Möller, W.; Templier, C.; Rivière, J. P.; Declémy, A.; Chumlyakov, Y. *J. Appl. Phys.* **2009,** *105,* 093502.
77. Christiansen, T. L.; Somers, M. A. J. *Int. J. Mater. Res.* **2008,** *99,* 999–1005.
78. Christiansen, T. L.; Dahl, K. V.; Somers, M. A. J. *Mater. Sci. Technol.* **2008,** *24,* 159–167.
79. Christiansen, T. L.; Somers, M. A. J. *Defect Diff. Forum* **2010,** *297–301,* 1408–1413.
80. Galdikas, A.; Moskalioviene, T. *Comput. Mater. Sci.* **2010,** *50,* 796–799.
81. Somers, M. A. J.; Mittemeijer, E. J. *Metall. Mater. Trans. A* **1995,** *26,* 57–74.
82. Somers, M. A. J.; Friehling, P. B. *Härterei-Tech. Mitt.* **2002,** *57,* 415–420.
83. Somers, M. A. J. *J. Phys. IV France* **2004,** *120,* 21–33.
84. Grabke, H. J. *Ber. Bunsengesell. Phys. Chem.* **1969,** *73,* 596–601.
85. Hansen, I. C. M.Sc. Thesis, Technical University of Denmark, 2010.
86. Christiansen, T. L.; Hummelshøj, T. S.; Somers, M. A. J. PCT WO, 2011 009463–A1.

This page intentionally left blank

12.14 Case Structure and Properties of Nitrided Steels

H-J Spies and A Dalke, Institute of Materials Engineering, Freiberg, Germany

12.14.1	**Microstructure and Development of Nitrided Cases**	439
12.14.2	**Nitridability of Steels**	448
12.14.3	**Properties of Nitrided Steels**	454
12.14.3.1	Overview	454
12.14.3.2	Residual Stresses	455
12.14.3.3	Mechanical Properties	458
12.14.3.3.1	Strength Behavior at Monotonic Load, Hardness, and Toughness	458
12.14.3.3.2	Strength Behavior at Cyclic Load	464
12.14.3.4	Corrosion Behavior	471
12.14.3.5	Tribological Behavior	476
12.14.3.5.1	Overview	476
12.14.3.5.2	Layer Structure and Wear Behavior	477
12.14.4	**Selection of Steels and Nitriding Conditions for the Manufacture of Load-Specific Nitrided Cases**	481
12.14.4.1	Overview	481
12.14.4.2	Selection of Load-Specific Nitrided Cases	482
12.14.4.3	Nitriding Behavior of Components	484
Appendix: Chemical Composition of the Investigated Steels		485
References		486

12.14.1 Microstructure and Development of Nitrided Cases

Nitriding has been used industrially for a long time and to a large extent to improve the wear and corrosion resistance as well as the fatigue strength of ferrous engineering components. Compared to other surface engineering technologies, it is characterized by an unequaled application variety that is based on the structure of the nitrided cases and the multitude of nitridable materials. All iron materials are nitridable beginning with cast iron and unalloyed as well as low-alloyed steels to high-alloyed stainless steels and high-alloyed powder-metallurgical processed tool-steels.

Nitride layers consist in most cases of an outer layer of iron nitrides or iron carbonitrides, the compound layer, and below a layer of α-iron hardened by nitride precipitations, the diffusion layer, also called precipitation layer. This, for other thermochemical treatments unattainable combination of a ceramic hard coating with nonmetallic structure supported by a zone of precipitation hardened α-iron, ensures the wide property range of nitride cases.

Nitriding under industrial conditions is today done within a temperature range of 400–650 °C, but preferentially between 500 °C and 590 °C, which is below the A_{c1}-temperature of the iron–nitrogen system. Due to this, it is also called 'ferritic nitriding' in the Anglo-Saxon literature. However, the A_{c1}-temperature of the iron–nitrogen system is considered to be an orientation value. Dependent on the chemical composition of the base material, the transition temperature can considerably differ from this value. If the nitriding temperature exceeds the transition temperature at which austenite forms, nitrogen–austenite is formed. The resulting transition layer, which is formed during cooling, can consist of martensite, bainite, and retained austenite and braunite (eutectoid ferrite-iron nitride (Fe_4N)), respectively, depending on the cooling conditions.

Figure 1 gives an idea of the case structure generated by means of nitriding. It shows the nitrided case of unalloyed and alloyed steel, respectively. The compound layers can be distinguished from the diffusion layer below by a visibly distinctive phase boundary. The microstructure of the shown unalloyed steel consists of ferrite and pearlite. A characteristic of the diffusion layer of unalloyed steels after a slow cooling from nitriding temperature and subsequent aging, respectively, are the needle-shaped iron nitride precipitates (Figure 2). In the case of fast cooling, one gains ferrite supersaturated with nitrogen. The submicroscopic nitrides, which are formed during the nitriding of alloyed steels, lead to an increased etching of the precipitation layer compared to the non-nitrided core material.

The precipitation of nitrides and the nitrogen supersaturation of the ferrite, respectively, cause an increase in surface hardness and the generation of compressive residual stresses. The differences between the hardness profiles of nitride layers of unalloyed and alloyed steels are clearly visible (Figure 1). The higher hardness of the compound layer and the larger hardness increase within the nitrided case of the steel 16MnCr5, compared to the steel C15, are due to the precipitation of submicroscopic chromium nitrides.

The constitution of nitrided cases can be largely modified by means of varying the nitriding conditions. An example of the constitution of the compound layer, in which ε-nitride and γ'-nitride coexist, is shown in Figure 3. The phase structure, the chemical composition, and the growth rate of the compound layer are defined by the chemical potentials of nitrogen and carbon. For a high nitrogen and carbon supply, the compound layer consists of ε-(carbo)nitride $Fe_2(N,C)_{1-x}$ and secondary γ'-nitride Fe_4N within the outer zone. It passes over to a zone consisting predominantly of γ'-nitride. The outer zone of the compound layer is more or less

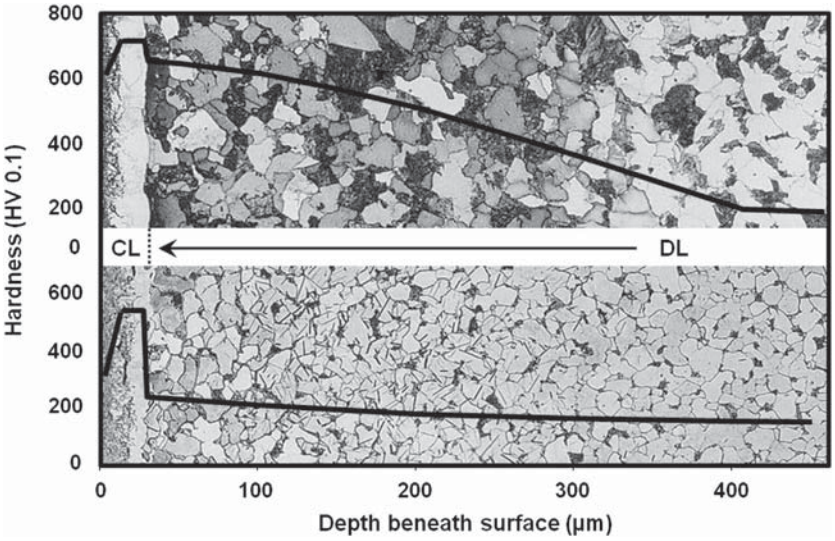

Figure 1 Microstructure and hardness profile of the case of gas-nitrided C15 and 16MnCr5, slow cooling conditions, CL: compound layer, DL: diffusion layer.

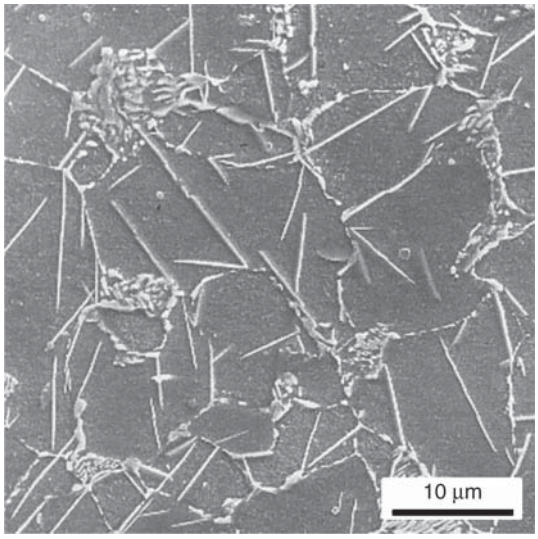

Figure 2 Iron nitride precipitations in ferrite grains within the diffusion layer of gas-nitrided C15, SEM image.

riddled with pores and can also contain oxides and sulfides, depending on the applied processes. Within the compound layer, alloy nitrides, and in particular cases also alloy carbides, are embedded depending on the nitriding conditions and the base material. By means of a systematic reduction of the nitrogen supply it is possible to generate compound layers that preferentially consist of γ'-nitride or to generate nitrided cases without any compound layer (bright nitriding), respectively.

A thermodynamic reasonable process control by the adjustment of defined chemical potentials of nitrogen and carbon is currently only possible using gaseous media, like in the case of gas nitriding and gas nitrocarburizing. In contrast, today, in the case of bath and plasma nitriding, a deliberate change of the effective chemical potentials of nitrogen and carbon is still not possible. Therefore, in these processes, the control of the structure of the nitrided case is empirical.

The reactivity of the process gases used for gas nitriding and nitrocarburizing treatments is characterized by means of the potentials of nitrogen, carbon, and oxygen, which are defined as nitriding potential, carbon potential, and oxidation potential (*1-4*).

$$K_N = p(NH_3)/p(H_2)^{3/2} \quad [1]$$

$$K_O = p(H_2O)/p(H_2) \quad [2]$$

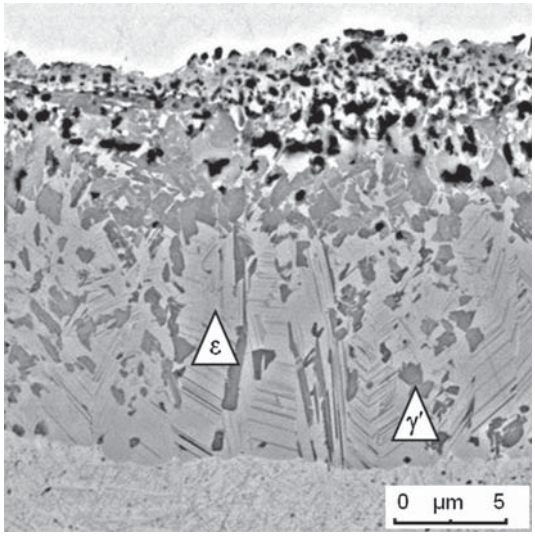

Figure 3 Example for the structure of a ε/γ′-compound layer (ε-phase: light gray; γ′-phase: dark gray).

$$K_C^W = p(CO) \cdot p(H_2)/p(H_2O) \quad [3]$$

$$K_C^B = p(CO)^2/p(CO_2) = K_C^W \cdot K_W \quad [4]$$

The nitriding potential K_N [1] results from the dissociation of ammonia. The oxidation potential K_O [2] results from the water reaction, and the carbon potential can be defined on the basis of the water gas reaction [3] and the Boudouard reaction [4], respectively. Thereby K_W is the equilibrium constant of the water gas reaction. During gas nitriding and nitrocarburizing using industrial conditions, the setting of the water and water gas equilibrium, respectively, is established. Since only one partial hydrogen pressure and one water partial pressure exist within the reaction gas, the chemical potentials of nitrogen, oxygen, and carbon are linked with each other; i.e., these chemical potentials are not independent process variables. Therefore, a change in the combination of the K_N-, K_C-, and K_O-values is only possible by means of changing the fresh gas composition (*2*).

The influence of the nitriding potential and nitriding temperature during gas nitriding on the adjustable phases at the surface and the nitrogen content of the ε-phase can be depicted in an extended Lehrer diagram (*3*,*4*). In the case of nitrocarburizing, some reference values concerning the influence of the nitriding and carburizing potential on the composition of the ε-carbonitrides can be deduced from thermodynamic calculations done by Kunze (*5*,*6*). Especially for controlling the cementite formation, further thermodynamic effort is needed (*7*). For both nitriding and nitrocarburizing, the existence of a local equilibrium between the process gas and the surface of the component is presupposed. Within the solid state below the surface, diffusion and precipitation processes considerably influence the case microstructure. Moreover, it has to be considered that the relations between the composition of the solid phase and the chemical potentials of nitrogen and carbon are applicable only for pure iron. However, for practical usage, these diagrams derived from thermodynamic calculations are feasible approximations (*2*).

A well-founded understanding of the processes occurring during the formation of nitrided cases is an important requirement for a technically based selection of materials and nitriding conditions. Therefore, in the following, the formation as well as the development of nitrided cases is described.

At sufficiently high nitrogen supply of the nitriding media, the nitrogen gets initially interstitially dissolved within the ferritic matrix and diffuses into the iron material. If the saturation limit for nitrogen is reached in the near surface matrix, nucleation of γ′-nitrides (Fe_4N) occurs. At continuously high nitrogen supply, ε-nitrides Fe_2N_{1-x} nucleate upon the γ′-nitride nucleations. Finally, with increasing nitriding time, a compact two-phase compound layer is formed by means of nucleation coalescence (*8*).

Thereby, an equilibrium stage exists between the ε- and γ′-phase of the compound layer as well as the γ′-phase and the solid solution of α-iron that has reached the nitrogen saturation limit (cf. **Figure 4(a)**). The nitrogen concentration $C^{\alpha}_{N\gamma'/\alpha}$ equates the maximum of nitrogen solubility within the ferrite, which is in the equilibrium stage with the γ′-phase. At the surface, the adjusting nitrogen concentration within the ε-nitride $C^{\varepsilon}_{N,\,max}$ depends on the nitrogen supply of the nitriding media, which can be described by the nitrogen potential K_N in the case of gas nitriding as mentioned before. The sandwich character of the compound layer can get lost during cooling by means of the formation of secondary γ′-phases out of the ε-nitrides.

A previous oxidation or oxinitriding treatment facilitates the nucleation of iron nitrides. In these cases, the surface has a more homogeneous nitride coverage and the compound layer a slightly higher thickness as well as an increased content of ε-nitride. An example is shown in **Table 1** (*9*). Analog results were obtained for plasma-nitrided unalloyed and low-alloyed steels (*10*). Also in the case of bath nitriding, oxygen within the salt melt leads to an accelerated compound layer growth.

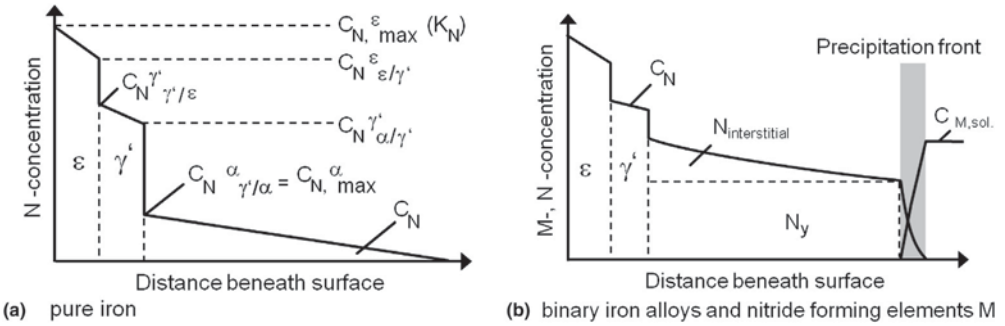

Figure 4 Structure of nitrided case (schematic), concentration distribution of nitrogen, (a) pure iron C_N, $C_N^{\gamma'}$, C_N^{α}: Concentration of nitrogen in the ε-, γ′-, α-phase, (b) binary iron alloys nitride-forming elements N_y: stoichiometric bonded nitrogen to MN_x and adsorbed at the nitride/matrix interface, $C_{M,sol.}$: Concentration of nitride-forming element M, soluted in matrix, C_N: Concentration of nitrogen. Reproduced from Spies, H.-J.; Bergner, D. Innere Nitrierung von Eisenwerkstoffen. *Härterei-Tech. Mitt.* **1992**, *47*, 346–356.

Table 1 Influence of oxidizing potential on structure of nitrided case; nitriding potential K_N: 6.0; nitriding temperature T_N: 550 °C; nitriding time t_N: 30 min

					Phase content, %			
Steel	*Oxidizing potential K_O*	*Compound layer thickness, μm*	*Nitrogen content[a], wt.%*	*Method[b]*	*α-Fe*	*ε-Fe_2N_{1-x}*	*γ′-Fe_4N*	*Fe_3O_4*
C15	<0.1	1.2–2.3	10.2	CEMS	3	97	–	–
				XRD	17	45	38	–
	<0.1[c]	1.9–2.7	10.3	CEMS	9.5	90.5	–	–
				XRD	15.0	48	37	–
	0.28–0.30	2.9–3.7	11.2	CEMS	3.0	95	–	2.0
				XRD	9.0	62	20	9.0
31CrMoV9	<0.1	0–2.5	3.2–10.7	CEMS	12.6	87.4	–	–
				XRD	67.0	18.0	15	–
	<0.1[c]	0.5–3.0	4.1–10.5	–	–	–	–	–
	0.28	3.9–5.5	11.3	CEMS	2.1	92.1	–	5.8
				XRD	–	85		13

[a]Surface analysis: electron probe microanalysis (EPMA).
[b]Information depth: CEMS (conversion electron Mössbauer spectroscopy) 100–200 nm; XRD 2.5–3.5 μm.
[c]Preoxidized: 350°C, 1 h.

Reproduced from Spies, H.-J.; Schaaf, P.; Vogt, F. Einfluß von Sauerstoffzusätzen beim Gasnitrieren auf den strukturellen Aufbau von Nitrierschichten. *Mat.-wiss. u. Werkstofftech* **1998**, *29*, 588–594.

The compound layer growth is also strongly influenced by the alloying elements within the iron. The basic relation between the alloyed elements within the ferrite and the growth of ε(γ′)-compound layers is described in Figure 5 (*11*) on the example of binary iron alloys nitrided at 550 °C for 24 h. Accordingly, at constant nitriding conditions with increasing alloying concentration, the thickness of the compound layer decreases element specifically.

The inner nitrided case below the compound layer, the diffusion layer, is a multiphase zone the structure of which is characterized by the nitrogen solid solution, but mainly through nitride precipitation of iron and its alloying elements. The growth of the layer is defined by the interaction of diffusion and precipitation processes. For a better understanding of the processes going on during nitriding of technical ferrous materials, it is advantageous to first examine these procedures for pure iron and binary iron alloys.

In pure iron, the nitrogen is dissolved within the diffusion layer at nitriding temperatures. The layer growth is, as it is typically for diffusion processes, characterized by temperature and time of the nitriding treatment. For slow cooling conditions from nitriding temperature, the dissolved nitrogen precipitates as γ′-nitride (Fe_4N) and metastable α″-nitride ($Fe_{16}N_2$), respectively (Figure 2).

In binary iron alloys containing nitride-forming elements, e.g., titanium, chromium, aluminum, molybdenum, the solute nitrogen forms small, fine dispersed nitride precipitates, which have a thickness of only some atom layers, at nitriding temperature.

Because of the small solubility products of these nitrides, the alloying elements are nearly completely precipitated as nitrides. The mismatch between the volumes of nitride and matrix results in local lattice distortions. These distortions cause a relative high strengthening and increased nitrogen solubility of the iron matrix. The additionally existing nitrogen, besides the stoichiometric bonded and the interstitial nitrogen, is called excess nitrogen. It can be present both directly at the interface nitride/matrix and also interstitially dissolved within the expanded matrix (*12–14*). With increasing nitriding time and temperature, a coarsening of the precipitated nitrides can occur, indicated by a hardness decrease.

The extent of hardness increase is specifically for each alloying element. One example for the effect of individually alloying elements on the maximum hardness obtained after nitriding at 524 °C for 48 h is shown in Figure 6 (*15*). The influence of the

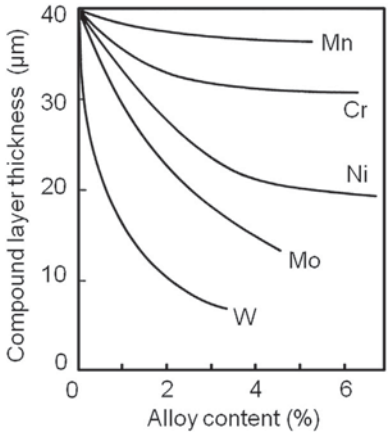

Figure 5 Influence of alloying elements on compound layer thickness; gas nitrided at 550 °C for 24 h. Reproduced from Lachtin, J. M. *Physikalische Grundlagen des Nitrierens*; Maschgis: Moskau, 1948. vgl. auch Lachtin, J. M.; Kogan, J. D. Nitrieren von Stählen. Maschinostrojenije Moskau, 1976.

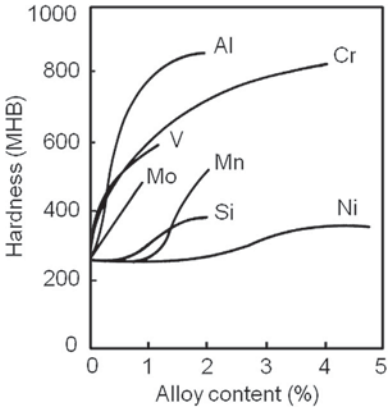

Figure 6 Influence of different alloying elements on maximum hardness of nitrided steels; gas nitrided at 524 °C for 48 h, MHB: Montron Brinell hardness, test load for total indentation depth of 9/5000″ (0.0457 mm). Reproduced from Homerberg, V. O. Nitriding. *The Iron Age* **15 October 1936**, *137*, 49–98.

nitride formers chromium and vanadium on the precipitation hardening effect is in a comparable range. In contrast, at equal concentrations, aluminum causes a considerably stronger hardness increase. The effect of these three nitride formers on the precipitation hardening significantly decreases above a concentration range of 1 wt.%.

In the case of binary alloys, the surface hardness reaches a saturation value of 1300–1400 HV0.3, independent on the alloying element (*16–18*). After reaching this level, the surface hardness does not change, despite the increasing concentration of nitride-forming elements. Accordingly, with regard to the surface hardness increase, optimal alloying contents can be defined. For Fe–Ti and Fe–V alloys, the saturation value is reached at a concentration of about 3.2 at.% (*17,18*).

The nitriding of binary alloys applying sufficiently high nitrogen supply and nitriding time also leads to a sandwich case structure consisting of an ε- and/or γ′-nitride compound layer and a diffusion layer (**Figure 4(b)**). The nitrogen concentration profile within the diffusion layer is defined by the nucleation rate of the nitrides. The nucleation rate depends on the magnitude of interaction between nitrogen and alloying element, the element concentration, and the nitriding temperature (diffusion rate, temperature dependency of solubility products of the nitrides) (*8,19*). The concentration profile shown in **Figure 4(b)** is obtained for a strong interaction. At the diffusion front of the nitrogen, the alloying elements precipitate as nitrides completely, and the diffusion front is also the precipitation front. In case of a weak interaction between nitrogen and alloying elements, the formation and growth of nitride precipitates are defined by the diffusion of the alloying elements. The precipitation front dissipates into a precipitation area, which can extend to the whole thickness of the case. The maximal nitrogen concentration is reached only at the interface to the compound layer. A similar effect is due to a hindered nucleation e.g., for Fe–Al alloys (*12,19*).

Chromium being very important for nitriding steels is an alloying element that has an intermediate concentration-dependent interaction. This is shown in **Figure 7**. For the given nitriding conditions, a strong interaction exists at higher chromium contents. Due to the steep increase of the nitrogen concentration and hardness as well as the hardness plateau in the case of 4.6% Fe–Cr alloy, it can be assumed, that the precipitation of chromium nitrides takes place nearly completely at the diffusion front. Due to these preconditions, the influence of the chromium diffusion on the precipitation process is insignificant. For a low chromium

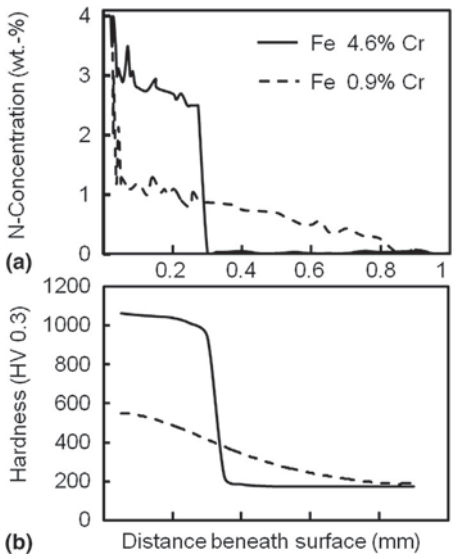

Figure 7 Concentration profile of nitrogen and hardness profile in nitrided case of Cr–Fe alloys; $T_N = 570\,^{\circ}C$, $t_N = 32$ h: (a) concentration profile and (b) hardness profile.

concentration (0.9%), a weak interaction exists. The maximal nitrogen concentration and maximal hardness are only reached at the changeover of the diffusion layer to the compound layer. The precipitation rate is controlled by the chromium diffusion. The precipitation front, which falls close to the diffusion front in case of higher chromium contents, dissipates and extends to nearly the complete depth of the diffusion layer, like a kind of a diffuse precipitation area.

The diffusion layer growth for a given temperature is determined by the nitriding time and the concentration of the nitride-forming elements. Figure 8 shows the influence of the alloying element concentration within α–iron on the thickness of the diffusion layer according to Lachtin et al. (*11*). These results have been confirmed by investigations done on binary Fe–Cr, Fe–V, and Fe–Ti alloys. They show that the square of nitride case depth is linear increasing with time and linear decreasing with rising alloying content (*17*,*18*,*20*).

In contrast to the already described binary alloys, commercially used ferrous materials contain defined contents of carbon. Their nitriding behavior differs mainly due to the interaction between nitrogen and carbon and the decarburizing effect of the nitriding medium. Furthermore, commercial alloyed steels usually contain several nitride-forming elements, which has to be considered.

The presence of carbon leads to a change in the structure of the compound layer. At comparatively low nitrogen supply, in the cementite existing within the ferritic matrix, fine dispersed alloyed carbides formed during heat treatment as well as pearlite grains within ferritic/pearlitic microstructures are transformed into nitrides and carbonitrides. A part of the carbon that gets released during the transformation diffuses toward the surface, contrary to the nitrogen diffusion. This is supported by the decarburizing effect of the nitriding medium in case of plasma and gas nitriding. The diffusion rate of carbon within the compound layer is of a minor dimension and hinders the carbon transport up to the surface.

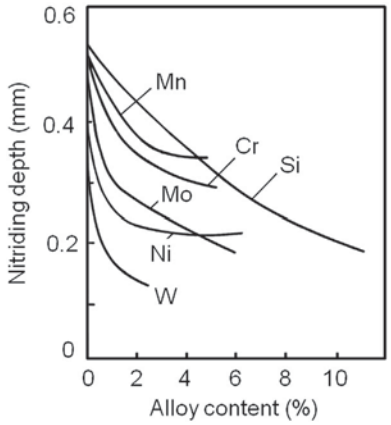

Figure 8 Influence of alloying elements on nitriding depth, gas nitrided at 550 °C for 24 h. Reproduced from Lachtin, J. M. *Physikalische Grundlagen des Nitrierens*; Maschgis: Moskau, 1948. vgl. auch Lachtin, J. M.; Kogan, J. D. Nitrieren von Stählen. Maschinostrojenije Moskau, 1976.

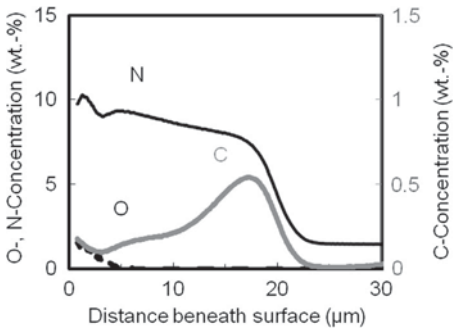

Figure 9 Concentration profile of nitrogen and carbon in a compound layer of gas-nitrided steel 42CrMo4, carbon enrichment in the lower area of compound layer; $T_N = 550\,^{\circ}C$, $t_N = 16$ h.

The enrichment of carbon within the compound layer promotes the formation of the ε-phase. Opposite to the ferritic matrix, the ε-phase has a higher solubility for carbon (at 550 °C, α-iron: 0.003%, ε-nitride: 3.8%), which therefore has a considerably lower chemical potential. Depending on the structure and thickness of the compound layer as well as the carbon release within the diffusion layer, an abrupt enhancement of the carbon concentration appears within the compound layer at the changeover to the diffusion layer (inner carburization). One corresponding example is shown in **Figure 9**. Besides the presence of γ′-nitride and ε-nitride at the interface compound layer/diffusion layer, also ε-carbonitride exists due to the inner carburization. Hence, the sandwich structure of the compound layer being characteristic for pure iron and carbon-free iron alloys gets lost. During nitriding and nitrocarburizing, a direct change between the ε-carbonitride phases into the ferrite is possible. This notice made consistently was also proved by means of thermodynamic calculations (*5*).

The relatively low amounts of soluble carbon within the ferrite at nitriding temperature slightly influence the solubility of nitrogen within the iron. Therefore, the settings within the diffusion layer of unalloyed steels generally correspond to pure iron. In contrast, considerable differences result at the presence of nitride-forming elements. For nitriding steels preferentially alloyed with chromium and aluminum are used. Depending on their application, these steels can also contain further nitride formers, e.g., molybdenum, vanadium, and tungsten. Except aluminum, all nitride-forming elements are also carbide formers. Therefore, during nitriding they can exist dissolved within the ferrite both as alloyed carbides and alloyed cementite, respectively. Corresponding to the described binary iron alloys, the alloying elements, dissolved within the ferrite, and the nitrogen, diffused into the material, form nitrides, which lead to a hardness increase depending on the alloying content. The cubic face-centered nitrides of chromium, of vanadium, and of molybdenum are completely mixable with each other. Within chromium-alloyed, heat-treatable steels, chromium nitrides exist, which contain also vanadium and molybdenum.

The setting level of the nitride formers to carbide is defined by the carbon content and the heat treatment condition of the steel. During tempering of alloyed steels, first a low-alloyed cementite $(Fe,M)_3C$ is formed. Within this cementite, the relation between iron atoms and the atoms of the carbide-forming elements is approximately the one within the matrix. When the annealing temperature rises above 450–500 °C a redistribution of the alloying elements takes place. The carbide formers enrich within the carbide phase and within the ferritic matrix their content decreases. Cementite can absorb a high amount of alloying elements, especially chromium, but also molybdenum and vanadium. Due to this it can be assumed that within common heat-treatable steels containing chromium contents up to 3% and slight amounts of molybdenum and vanadium, both for the normalized and the quenched and tempered condition the nitride-forming elements are mainly present as alloyed cementite $(Fe,M)_3C$. Comparable results are also available for low-alloyed cold and hot working steels. In contrast, high-alloyed ledeburitic steels contain, besides the secondary carbides, also numerous primary carbides.

The alloyed cementite and the secondary alloyed carbides of heat treatable steels and low-alloyed tool steels get destabilized by the diffusion of nitrogen into the material and transform into nitrides. In dependency of the carbide composition more or less complex mixed nitrides are formed. The *in situ* transformation of the carbides formed during tempering occurs under retention of the exterior form and therefore does not lead to a hardness enhancement (*21*). With increasing setting of the nitride formers to carbide, i.e., with increased carbon content of the steel and rising tempering temperature the hardness enhancement decreases.

The primary carbides of ledeburitic steels behave very different opposite to the nitrogen diffusing inside the material. At adequate long nitriding time, the primary $(Cr,M)_7C_3$-carbides of the ledeburitic chromium steels transform into nitrides due to the higher affinity of chromium to nitrogen. This is shown on a concentration profile in **Figure 10**. Within the base material the profile of the carbon distribution is an image of the chromium distribution. Within the diffusion layer nitrogen takes over the role of carbon. Independent of the chromium content, the profile of the carbon concentration within this zone is characterized by the precipitation of carbon, which is squeezed out of the carbides, at the grain boundaries. Also the transformation of primary carbides occurs without noticeable changing of morphology. A polycrystalline aggregate of (Cr,M)N and ferrite takes over the place of the primary $(Cr,M)_7C_3$-cristallite (*21*).

In contrast to the ledeburitic chromium steels there are no hints of local nitrogen enrichment within the precipitation layer of high-speed steels. The primary ledeburitic MC-carbides being rich on vanadium are transformed into nitrides very slowly (*8*). This

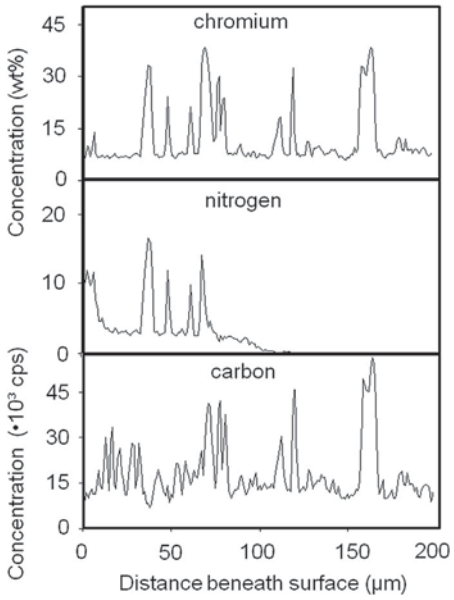

Figure 10 Concentration profile of nitrogen, carbon, and chromium in the case of gas-nitrided steel X155CrVMo12-1, carbon concentration in counts per second (cps); $T_N = 570\,^{\circ}C$, $t_N = 8$ h.

can be due to kinetic reasons. Inside carbides and nitrides of this type, the diffusion coefficient of nitrogen is very low. According to Lachtin and Kogan the diffusion coefficient of vanadium nitride at 550 °C is about a magnitude of 10^{16} lesser compared to the ferrite (*22*).

The release of carbon at the precipitation front, being mainly a result of the transformation of temper carbides, influences its previously mentioned redistribution during nitriding. The distortion of the matrix lattice caused by nitride precipitation leads to an increased solubility of carbon (excess carbon) and promotes its diffusion into the tensile stress area, being ahead of the diffusion front of the nitrogen. Depending on the steel composition, the carbon precipitates as cementite and alloyed carbides, respectively.

Mainly in the case of chromium-alloyed heat-treatable steels and tool steels, the enrichment of carbon in front of the diffusion layer can be distinguished by means of metallographic analysis due to an increased etching behavior (**Figure 11**). For higher contents of carbon and chromium, the carbon enrichment is clearly pronounced. For the steel X40CrMoV5.1 the carbon concentration reaches nearly the 3-fold of the nominal value at a distance to the surface of 325 µm, see **Figure 12**. The peaks in carbon concentration within the diffusion layer are a result of cementite precipitation at the grain boundaries.

For steels free of chromium and alloyed with aluminum, such an enrichment of carbon in front of the diffusion zone has not been observed yet (*23*). Since these steels do not contain alloyed carbides, no release of carbon takes place within the precipitation front.

Independent of the carbon enrichment in front of the diffusion layer, which is characteristic for steels alloyed with chromium, the main amount of carbon released as a result of the nitride formation diffuses toward the surface due to the strong decarburizing effect of the nitriding media and the high diffusion rate owing to the lattice distortion.

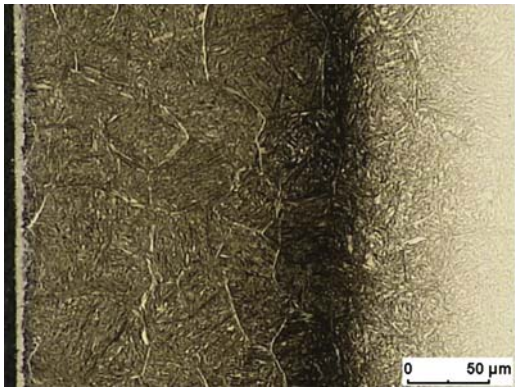

Figure 11 Microstructure of the nitrided case of the steel X38CrMoV5-1, etchant: nital; $T_N = 570\,^{\circ}C$, $t_N = 6$ h.

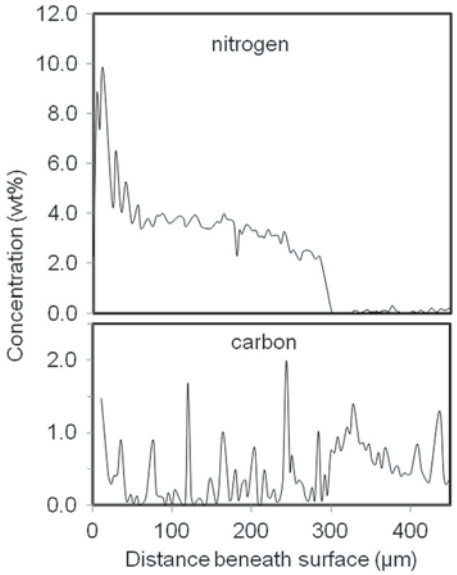

Figure 12 Concentration profile of nitrogen and carbon in case of a gas oxinitrided steel X40CrMoV5-1; $T_N = 500\,^{\circ}C$, $t_N = 96$ h.

The level of carbon redistribution depends on the alloying content of the base material and the nitriding conditions. It rises with increasing contents of nitride-forming elements. Therefore, it is more pronounced for the steel X38CrMoV5.1 compared to the steel 31CrMoV9 at equal nitriding conditions. Analog results have been obtained during investigations of conventional Cr–Al alloyed steels (*23*).

The nitriding potential has an important influence on the carbon redistribution. Thick ε-compound layers impede an effective decarburization due to the low diffusion rate of carbon within the ε-solid solution. Carbon precipitates stress-induced as cementite at grain boundaries parallel to the surface within the diffusion layer (*8,24*). Therefore, cementite precipitations at former austenite grain boundaries, being more or less parallel to the surface, are characteristic of the microstructure of the nitrided case of steels alloyed with chromium (>2% Cr). These precipitates had been termed wrongly in the past as 'nitride fibers' and 'nitride precipitates,' respectively, and had been explained by an excess nitriding.

The diffusion coefficient of carbon within the γ′-nitride is 6–15 fold higher compared to the one within the ε-nitride. For this reason, thin γ′-nitride compound layers facilitate an effective decarburization and thus the suppression of cementite precipitations at grain boundaries near surface areas. This has been consistently proved for plasma and controlled gas oxinitriding (*3*). As it is shown in **Figures 13 and 14** on the example of gas oxinitriding, the amount of grain boundary precipitations can be influenced by controlling the structure of the compound layer and a bright nitriding, respectively, with the help of the nitriding potential K_N.

The case structure of nitrided alloyed steels, resulting from the previously described relations, is schematically represented in **Figure 15**. The dimensions of the different areas, i.e., the thickness of compound layer as well as diffusion layer and decarburized zone, are characterized by the alloying content and the nitriding conditions. The hardness increase and the amount of excess nitrogen depend on the kind, stability, and amount of the formed nitride precipitations. In case of a particle growth as a result of re-dissolution the hardness, the residual stresses and therefore the content of nitrogen decrease.

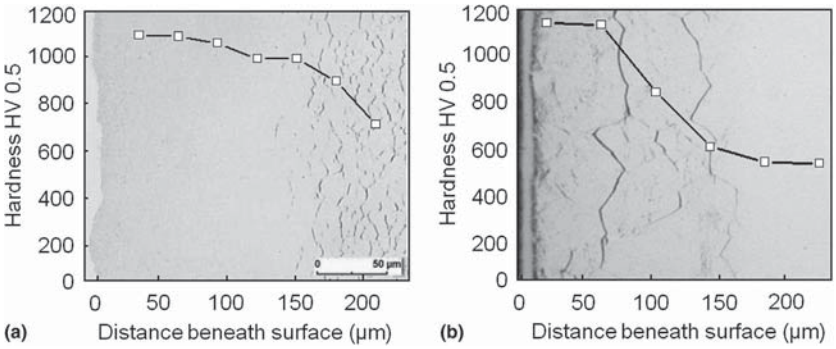

Figure 13 Cementite precipitation and hardness profile in the case of differently gas oxinitrided components: X38CrMoV5-1, etchant: alkaline sodium picrate solution. (a) $T_N = 560\,^{\circ}C$, $t_N = 32$ h, $K_N = 0.4$ and (b) $T_N = 570\,^{\circ}C$, $t_N = 8$ h, $K_N = 2.5$.

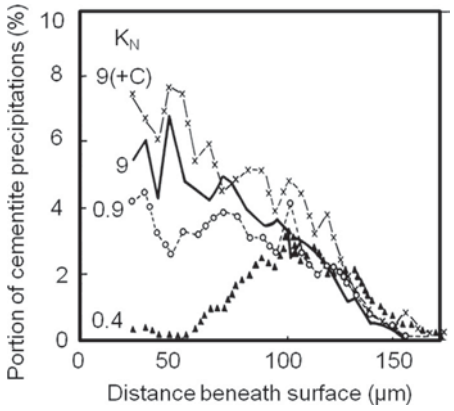

Figure 14 Influence of nitriding potential K_N on the amount of cementite precipitations at grain boundaries in the case of gas oxinitrided steel X38CrMoV5-1, $T_N = 550\,^{\circ}C$, $t_N = 24$ h. Reproduced from Spies, H.-J. Stand und Entwicklung des kontrollierten Gasnitrierens. *Neue Hütte* **1991**, *36*, 255–262.

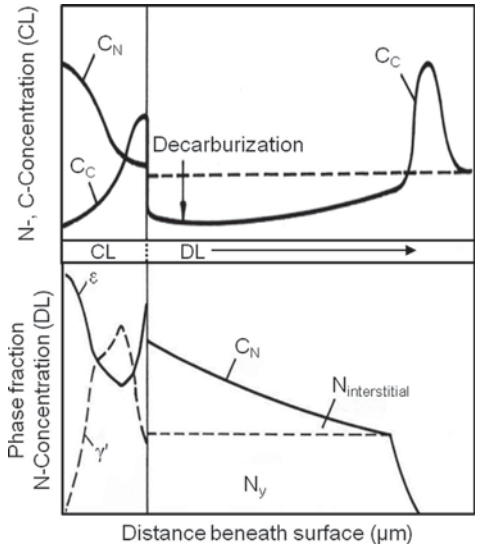

Figure 15 Structure of nitrided case of alloyed steels (schematic); N_y: stoichiometric bonded nitrogen and excess nitrogen; C_C: Carbon concentration; C_N: Nitrogen concentration. Reproduced from Spies, H.-J.; Bergner, D. Innere Nitrierung von Eisenwerkstoffen. *Härterei-Tech. Mitt.* **1992**, *47*, 346–356.

Owing to the low solubility product of most nitrides and the slight diffusion rate of the nitride-forming elements, the stability of the nitride precipitations is relatively high. Therefore, compared to other surface layers like case-hardened martensitic layers, nitrided cases are characterized by a high stability against thermal loads (see also Section 12.14.3.3).

12.14.2 Nitridability of Steels

The main function of nitriding consists of the formation of nitride-containing cases of a defined structure. Based on this, the nitridability can be defined as "…the response of an iron material at nitriding, characterized by the change of alloying content and structural constitution of the case depending on the nitriding conditions (*25*)."

As manufacturing property, it describes the response of an iron material toward defined nitriding conditions. For the comparison of materials, it is necessary to reduce the variety of possible nitriding conditions by setting limits with selected standard conditions.

Based on the definition of the nitridability, the evaluation and the specification of the structure of nitrided cases have to be examined as a unit. The characterization of the case structure has been established by means of metallographic analysis, microanalytical methods, and hardness measurements. Thereby, in this case the hardness is not a property but an indicator of the material and structural changes within the case. For describing the precipitation-hardening process during nitriding, the hardness increase (extent of strengthening), the nitriding hardness depth (total depth of hardening), and the hardness profile within the

diffusion zone (hardness plateau, extension of the transition zone between case (case hardness: maximal hardness of the diffusion layer near the compound layer) and core hardness) are important.

By characterizing the nitridability through thickness and microstructure of the nitrided case as well as the level, depth, and profile of the strengthening, also the essential parameters of the load behavior of the case are comprised. Therefore, the evaluation of the nitridability implicates the load-related specification of the case structure.

With the discussion of nitridability, being a function of chemical composition and microstructure of the base material, based on the structural case constitution, it has to be differentiated between the influences of the microstructure of the compound layer and the precipitation process as well as the microstructure of the diffusion layer.

The thickness of compound layer decreases with increasing alloying content, as shown in **Figure 5**, at constant nitriding conditions. This conclusion is proved consistently by results published in the literature that concern the growth of the compound layer on technical ferrous materials during nitriding and nitrocarburizing. One example is depicted in **Figure 16** (*26*).

The phase structure and the growth rate of the compound layer are also to a great extent influenced by the inner carburization (cf. Section 12.14.1). It is more strongly pronounced in the case of alloyed steels due to the release of carbon out of alloyed carbides and the higher diffusion velocity of carbon. An example is shown in **Figure 17** in which the phase profiles of γ'-compound layers of the steels C 20 and 20MnCr5, generated at a low nitriding potential, are compared (*27*).

For both steels, the compound layer directly at the surface nearly exclusively consists of γ'-nitride generated due to the low nitriding potential. For the steel 20MnCr5, the inner carburization leads to an increased content of ε-carbonitrides, especially at the changeover between the compound layer and diffusion layer. In contrast, in the case of the steel C 20, within the lower zone of the compound layer contents of ε-carbonitrides up to only 2% appear. This demonstrates that mono-phase γ'-compound layers on alloyed steels can only be generated by using a strongly decarburizing nitriding atmosphere due to the inner carburization.

In the case of alloyed steels, the inner carburization promotes the growth of the compound layer and gives an explanation of differences from the previously mentioned general relations. For steels with equal alloying content containing carbon up to 0.5%,

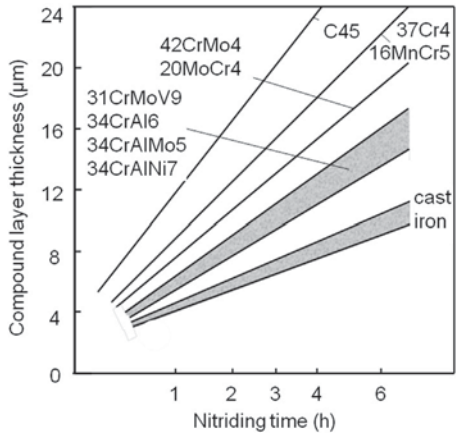

Figure 16 Compound layer growth of different steels at T_N: 580 °C. Reproduced from Eysell, F. W. Verfahrensvarianten und Anlagen zu Nitrocarburieren in Gas. *Zeitschr. für wirt. Fertig. (ZwF)* **1982**, *77*, 292–299.

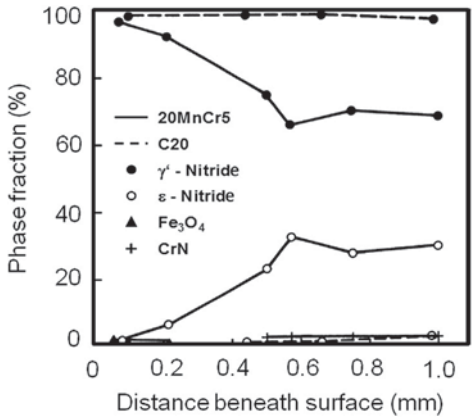

Figure 17 Phase profile of compound layers of steels C20 and 20MnCr5 gas oxinitrided at 570 °C for 32 h, $K_N = 0.8$. Reproduced from Schubert, T. Variationsmöglichkeiten des Gefüges der Verbindungsschichten beim kontrollierten Gasnitrieren. Dissertation, Bergakademie, Freiberg, 1986.

the thickness of the compound layer increases with increasing carbon content. Also for steels alloyed with aluminum, the lattice distortion caused by the precipitation of aluminum nitride leads to an intensified carbon transport up to the surface and thus to anomalies of the compound layer growth (*23*).

Besides the chemical composition, also the heat treatment condition of the base material influences the microstructure and the thickness of the compound layer. The fine dispersed temper carbides of the quenched and tempered condition avoid the formation of diffusion columnar grains during nitriding, which is characteristic for the normalized microstructure. A microstructure with a fine distribution of nitrides is generated. The thickness of the compound layer on normalized microstructures can reach up to 30% above those compound layers generated on a quenched and tempered microstructure. During nitriding of normalized low carbon steels at temperatures of about 500 °C, the changeover of compound layer to diffusion layer is often not formed as a compact diffusion front. Plate-shaped nitride areas, starting from the grain boundaries and reaching into the ferrite, are characteristic for this microstructure (*23*,*28*). An example is shown in **Figure 18**. Ferritic-pearlitic microstructures γ′-nitrides and ε-carbonitrides can appear side by side at the lower compound layer area due to the transformation of pearlite grains in ε-carbonitrides (**Figure 19**).

Concerning the influence of the base material on the microstructure and hardness distribution within the diffusion layer, considerable individual results for a variety of nitriding conditions and a broad material range have been published in the literature. During nitriding with the formation of a compound layer, it can be assumed that the growth of the diffusion layer is not determined by the processes occurring at the interface of the nitriding medium and base material but by the diffusion reaction of nitrogen into the ferritic matrix. The mass transfer at the interface of the reactive medium and metal has no influence on the velocity of the internal nitriding. Under these conditions, the hardening within the diffusion layer, being independent of the applied nitriding process and

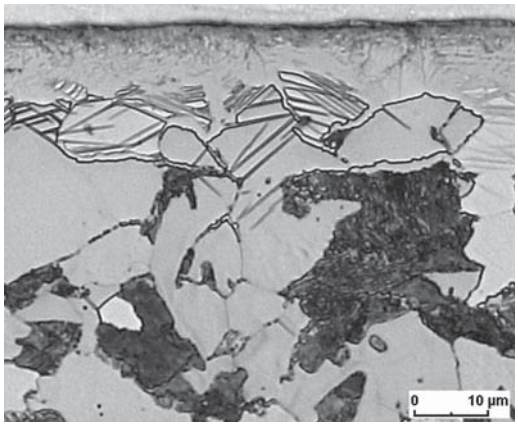

Figure 18 Plate-shaped growth of nitride phases within the interface compound layer/diffusion layer, steel 16MnCr5, normalized, gas oxinitrided at 510 °C for 16 h.

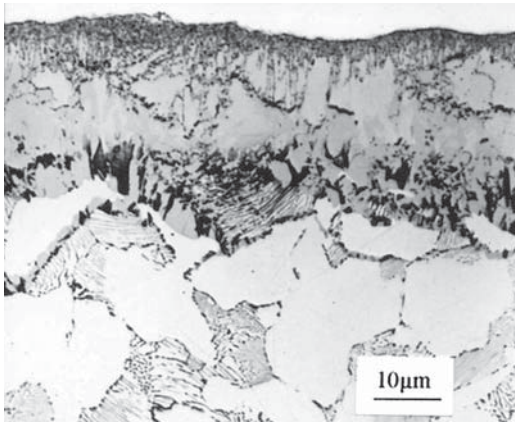

Figure 19 γ′-nitrides and ε-carbonitrides in the lower area of compound layer of gas oxinitrided steel C25, normalized, etchant: alkaline sodium picrate solution, $T_N = 570$ °C, $t_N = 8$ h.

nitriding potential, results from the temperature and time interaction of nitrogen with the matrix material. Figure 20 impressively underlines that the hardness profile within the diffusion layer is not affected by the composition of the reaction gas. These facts allow a summarized explanation of the influences on the formation of the diffusion layer. Figure 20 illustrates at the same time, again impressively, the influence of the chromium concentration on the interaction with nitrogen.

For unalloyed steels, the decrease of the nitrogen diffusion rate, being a result of the carbon dissolved within the ferrite and the impediment of the diffusion with growing amount of pearlite, lead to a decrease of the nitriding depth with increasing carbon content (Figure 21) (29). In case of alloyed steels, it has long been known that an increasing content of nitride-forming elements lead to increased surface hardness values and to decreased thicknesses of the diffusion layer (Figures 6 and 8). These conclusions resulting for binary iron alloys are consistently proved by investigations concerning the growth of nitride cases on different alloyed commercially ferrous materials. As one corresponding example, Figure 22 shows the growing profiles of the nitrided case for different steels.

The most used nitride formers applied in steels are chromium and aluminum. Nitriding steels mostly contain small amounts of vanadium and molybdenum for improving the temper resistance and for decreasing the sensitivity against tempering embrittlement. The influence of these elements on the nitridability can be comprehended by means of the summation of the amount of substance of the nitride formers. Due to their low concentration, it is possible to disregard their element-specific effect.

The results of the influences of chromium on the internal nitriding of technically used steels can be summarized as follows:

- With growing content of chromium, the maximal reachable nitrogen content within the diffusion layer increases. Depending on the nitriding temperature, it rises considerably above the stoichiometric bonded nitrogen content to (Cr, M) N given by the nitride-forming elements (excess nitrogen). Parallel to the chromium content, the nitrogen absorption per unit surface area increases (8).

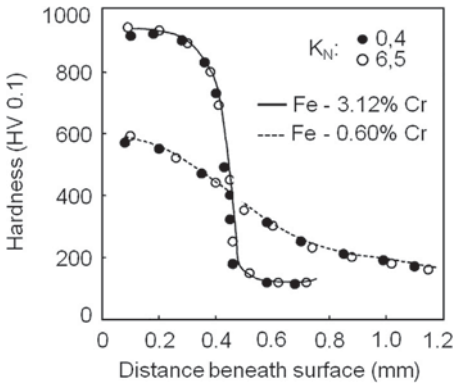

Figure 20 Influence of nitriding potential K_N and chromium content on the hardness profile in nitrided cases of Fe–Cr alloys. Reproduced from Spies, H.-J.; Böhmer, S. Beitrag zum kontrollierten Gasnitrieren von Eisenwerkstoffen. *Härterei-Tech. Mitt.* **1984**, *39*, 1–6.

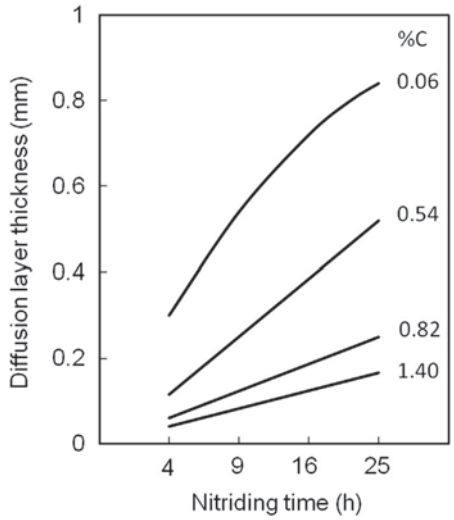

Figure 21 Influence of carbon content on the diffusion layer (needle zone) growth, Fe–C alloys, gas nitrided at 550 °C. Reproduced from Eilender, W.; Meyer, O. Über die Nitrierung von Eisen und Eisenlegierungen I. *Arch. Eisenhüttenwes* **1930/31**, *4*, 343–352.

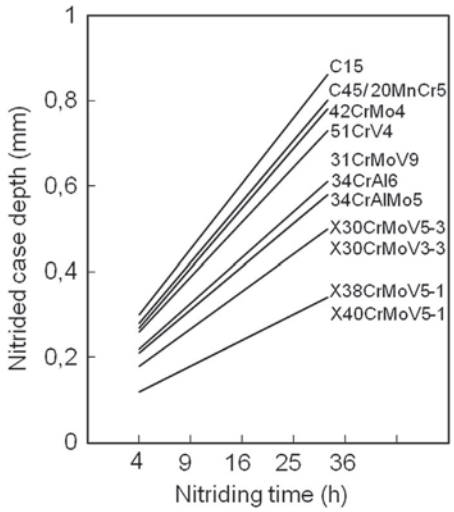

Figure 22 Nitrided case growth of different steels, T_N: 570 °C.

- The hardness increases and the maximal compressive residual stresses increase with increasing chromium content. At comparable chromium contents, the hardness increase decreases with increasing carbon content (Figure 23). From Figure 23 it can be depicted that the hardness increase is directly proportional to the square root of the alloying content (at.%).
- For chromium steels the concentration in at.% can be replaced as a first approximation by the mass percent (wt.%) due to the slight differences between the relative atomic mass of iron and chromium.
- For steels containing chromium contents up to 5%, the hardness increase strongly depends on the heat treatment condition of the base material. The maximum is reached for the normalized and hardened condition. A tempering temperature above 500 °C leads, with rising tempering parameter, to a strong decrease in hardness.
- For steels with a ferritic-pearlitic microstructure, the hardness increase within the pearlite grains is clearly reduced compared to the one within the ferrite grains (Figure 24).
- Increasing chromium contents clearly reduce the hardening depth d, according to the relation $d^2 \sim (\text{at.\% Cr})^{-1}$.

The influence of the carbon content and the heat treatment condition on the height of hardening can be explained by the change of concentration of nitride formers dissolved within the ferrite by means of a differing content of their bonding as carbide.

The previously mentioned relations are depicted in Figure 25. With equal chromium content, the steels X38CrMoV5-1 and X6CrMo5 mainly differ in carbon concentration and thus in the level of carbide-forming ability. For steel X6CrMo5, a strong interaction exists due to the high chromium concentration in the matrix. The hardness steeply increases at the diffusion front at approximately 80% of the case hardness. The significantly lower chromium concentration within the matrix of X38CrMoV5-1 leads

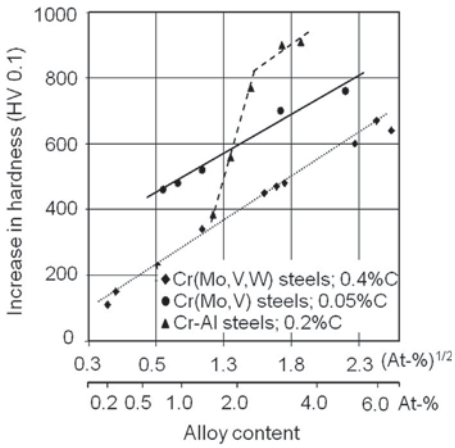

Figure 23 Increase of hardness as a function of the concentration of nitride-forming elements, gas oxinitrided; Cr(Mo,V,W)-steels (0.4% C) and Cr(Mo,V)-steels (0.05% C): 550 °C/32 h; Cr,Al-steels (0.2% C): 570 °C/48 h. Reproduced from Spies, H.-J.; Bergner, D. Innere Nitrierung von Eisenwerkstoffen. *Härterei-Tech. Mitt.* **1992**, *47*, 346–356.

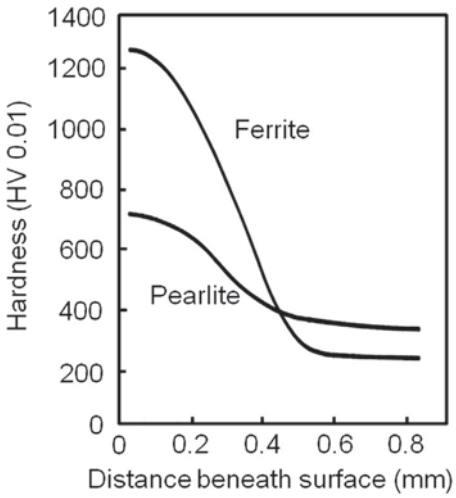

Figure 24 Hardness profile in ferrite and pearlite of a nitrided case of steel 42CrMo4, gas oxinitrided at 570 °C for 16 h. Reproduced from Spies, H.-J.; Bergner, D. Innere Nitrierung von Eisenwerkstoffen. *Härterei-Tech. Mitt.* **1992**, *47*, 346–356.

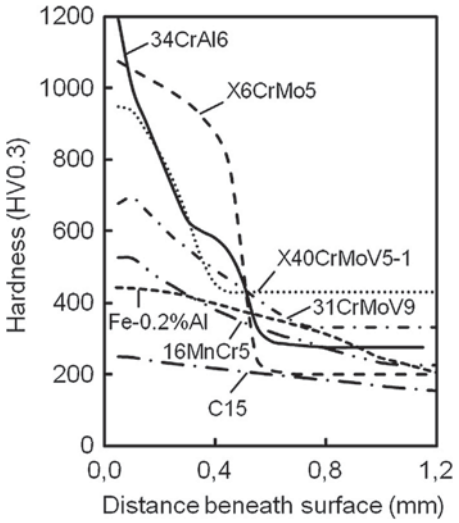

Figure 25 Hardness profiles in the case of nitrided different steels, $T_N = 570\,°C$, $t_N = 32\,h$.

to a more weak interaction. Within its diffusion layer, the hardness continuously increases and reaches a maximum value first before the changeover to the compound layer.

For steels alloyed with aluminum a high hardness increase is very characteristic. As shown in **Figures 23 and 25**, low contents of aluminum within unalloyed and low-alloyed chromium steels already cause a considerable hardness increase (*16*,*23*). Depending on the nitriding conditions, the strong effect of aluminum on the precipitation hardening significantly decreases above a defined content (see Section 12.14.1, **Figure 6**). For the example shown in **Figure 23**, also above an amount of substance of 0.9 at.% Al (the basis alloy of Cr–Al steels contains 1.45 at.% Cr; above an Al addition of 0.9 at.% Al (sum of nitride formers: 2.35 at.%) equates the rising in hardness increase of mainly Cr-alloyed steels) only a slight hardness increase can be reached.

The higher the hardness increase compared to chromium for a given amount of substance, the higher content of excess nitrogen and the higher decarburizing rate of steels alloyed with aluminum can be explained by a major distortion of the matrix lattice due to precipitated aluminum nitrides. As mentioned in Section 12.14.1, there are remarkable differences between the kinetics of nitride precipitations within iron–chromium and iron–aluminum alloys. The hexagonal structure of aluminum nitride expected for the equilibrium state strongly differs from the ferritic matrix. Therefore, its nucleation is highly impeded (*19*,*30*). The modified precipitation kinetics significantly influences the strengthening increase within the diffusion layer of Cr–Al alloyed steels. After a significant hardness enhancement within the diffusion front, the hardness reaches it maximum value directly below the surface, cf. **Figure 25**.

The high inner carburization of chromium–aluminum alloyed steels promotes the growth of the compound layer. Thus, also in case of low nitrogen supply, the compound layer contains a large amount of ε-carbonitride (*23*).

12.14.3 Properties of Nitrided Steels

12.14.3.1 Overview

The change of the composition and structural constitution of the case due to nitriding causes modifications of its chemical, mechanical, and physical properties as well as the micro geometric shape of the surface. As described in previously, nitrided cases usually consist of a thin hard layer of iron nitrides, the compound layer, which is supported by a layer of precipitation hardened α-iron, the diffusion layer. The constitution of nitrided cases can be broadly modified by means of the variation of the nitriding conditions and the materials selection.

The hardness of compound layers is significantly defined by the amount and distribution of pores as well as its phase structure. Within the porous free region, it can reach hardness values up to 1200 HV0.02. Depending on the nitriding conditions, the chemical composition, and the heat treatment condition of the base material, the hardness increase within the diffusion layer can reach values up to 1200 HV0.3.

The relationship between the structure, the fundamental properties, and the engineering performance of nitrided cases is shown in Figure 26 (*31*). It can be seen that the sensitivity of nitrided components toward tribological, chemical, and electrochemical attack is mainly controlled by the structure of the compound layer. In contrast to this, their behavior under cyclic mechanical and thermal loads predominantly depends on the structure of the diffusion layer. Obviously, significant performance characteristics like, e.g., the wear behavior and the initial crack behavior under mechanical stresses, are defined by the combined effect of the compound layer and diffusion layer structure.

The high hardness of the compound layer and its nonmetallic structure provide an increased resistance against abrasive and adhesive wear. In this regard, it has been proven that ε-nitrides have a higher wear resistance compared to γ′-nitrides because of their hexagonal structure and their higher hardness. The porous seam that is a special characteristic of ε-nitride has a favorable influence on the running-in behavior and leads to a good contact pattern.

Iron nitrides can be passivated and show increased resistance against neutral salt solutions, atmospheric corrosion, and tribooxidation. Their corrosion resistance increases in the order of γ′-nitride – ε-nitride – ε-carbonitride.

The precipitation of nitrides in the diffusion layer causes increased strength and formation of compressive residual stresses. By means of nitriding, the possibility of case strengthening up to depths >0.5 mm in combination with the appearance of compressive residual stresses leads to a significant increase in contact fatigue resistance as well as fatigue resistance and thermal fatigue resistance. Moreover, the possibility of an effective reduction of the notch sensitivity by means of nitriding has to be referred.

As a characteristic of the precipitation hardening, these effects are also retained at higher temperatures. Therefore, nitrided cases have considerably increased hot strength and thermal stability. A quantitative imagination of the tempering stability of nitrided hot

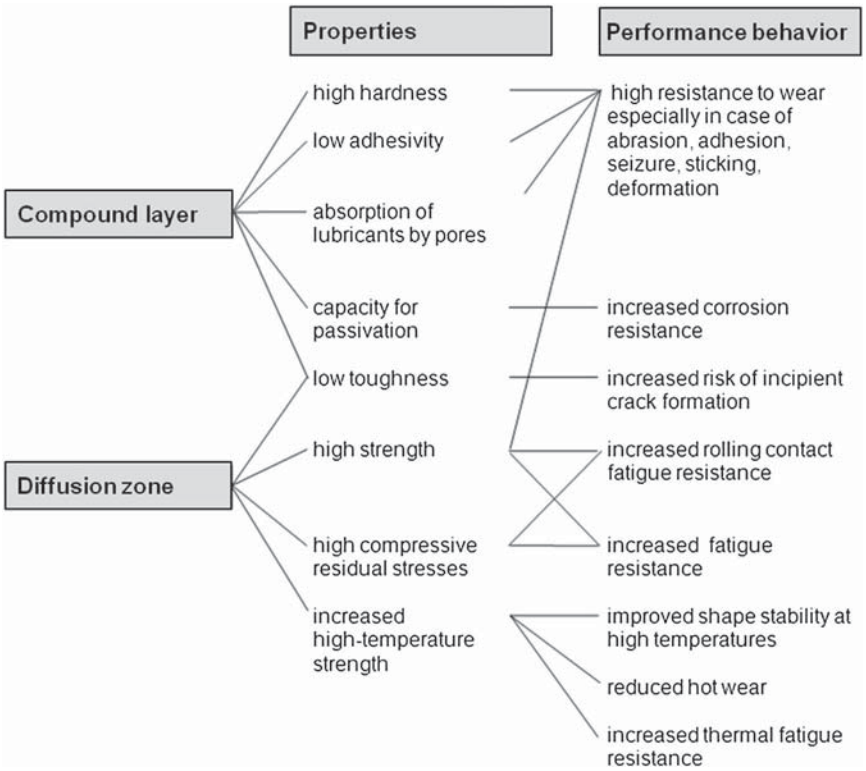

Figure 26 Structure, properties, and performance behavior of nitrided cases.

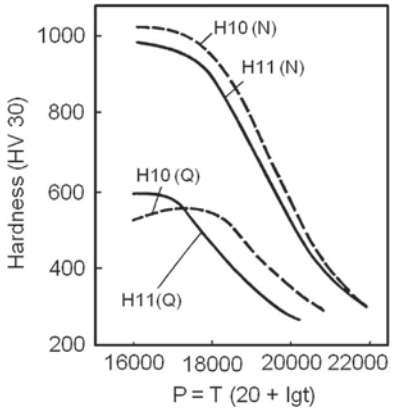

Figure 27 Main tempering curves of the steels H10 and H11 in the initial conditions Q (quenched and tempered) and N (quenched and nitrided).

working steels is given in Figure 27. As can be seen, within the range of the tempering parameter 16 000 to 19 000, the hardness of the nitrided case exceeds the hardness of quenched and tempered steels about 350–430 HV30. The precipitation conditions generated at low nitriding temperatures are characterized by a relatively high stability, which is also effective at test temperatures above the nitriding temperature.

The level of residual stresses generated due to the volume change during nitriding is limited by creep processes. In this way, the high temperature strength of nitrided cases influences the fatigue behavior of nitrided components by the height of the maximal residual stresses.

The increase of the strength of the case is connected with a decrease in ductility. The fracture toughness of diffusion layers can be classified in the known correlation between hardness and ductility. For a high surface hardness, the fracture toughness is in the lower scatter limit of the one obtained for ledeburitic tool steels. An important disadvantage predominantly under dynamic loads is the low toughness of compound layers. As a result of their structure, their fracture toughness is at the upper limit of the toughness of hard coatings.

The unique combination of a thin hard coating with a thicker, strengthened supporting layer is characteristic only for nitrided cases. Hence, an application variety of nitriding arises which is unequalled by other surface engineering technologies. Compared to case hardening or thermal surface hardening, the relatively low treatment temperatures ensure low dimensional and shape changes but also limit the obtainable diffusion depths.

12.14.3.2 Residual Stresses

A characteristic of nitrided cases is macroscopic compressive residual stresses that significantly influence the behavior of nitrided components under cyclic mechanical loads. They arise due to gradients of macro and micro expansions mainly caused by the nitride formation. Within the compound layer, the volume and thermal expansion, being a result of the iron nitride formation, are generating macroscopic residual stresses due to different coefficients of the thermal expansion between ferrite as well as ε- and γ′-nitrides. A further contribution is given by the formation of pores and the precipitation of secondary γ′-nitride during cooling (*32*). For compact ε-nitride layers, tensile stresses appear at near-surface areas, which change into compressive residual stresses with increasing distance to the surface.

In ε(γ′)-compound layers of the steel 31CrMoV9, compressive residual stresses in the range of −640 to −790 MPa are measured in the lower compound layer area within the γ′-nitride and the ε-nitride, respectively (*32*).

At nitriding temperatures, the interstitial solution of nitrogen causes lattice expansions within the diffusion layer of unalloyed steels. For slow cooling conditions, further volume expansions are generated due to the precipitation of α″- and γ′-nitrides and the different thermal expansion coefficients between the nitrides and the ferritic matrix.

The residual stresses generated in this way are generally lower than −200 MPa (*33,34*). For a fast cooling from nitriding temperature, additional thermal stresses arise. The resulting residual stresses can reach maximum values of −400 to −500 MPa (*34*), which can be reduced at room temperature by means of a natural aging.

Within the diffusion layer of iron materials alloyed with nitride-forming elements, macroscopic residual stresses are mainly formed by gradients of the volume expansions caused by nitride precipitations. Analogous to the increase of hardness, the height of the residual stresses is primary defined by the concentration of nitride-forming elements dissolved within the ferritic matrix (*33–35*). Besides the nitride formation and the excess nitrogen within the matrix, the volume expansion is influenced by the material specific redistribution of carbon as described in Section 12.14.2.

The height of the compressive residual stresses generated by the volume expansion is limited by the stress relaxation as a result of creep processes as well as the precipitation plasticity (*34–37*). In this way, the creep behavior of the nitrided case at nitriding temperature defines the height of the maximal residual stresses. Just like the surface hardness, the hardness increase, and the hot

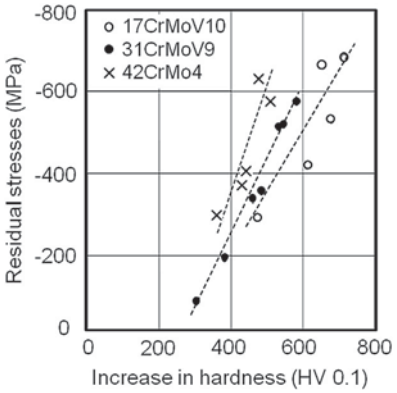

Figure 28 Correlation between maximum residual compressive stress and increase in hardness, determined for different nitrided conditions of steels 17CrMoV10, 31CrMoV9, and 42CrMo4. Reproduced from Spies, H.-J. Stand und Entwicklung des kontrollierten Gasnitrierens. *Neue Hütte* **1991**, *36*, 255–262.

hardness, the creep behavior results from the strength properties of the base materials but particularly from the precipitation contribution during nitriding and the corresponded modifications of the matrix structure.

Therefore, relationships exist between the factors that characterize the precipitation behavior during nitriding such as surface hardness, hardness increase, hot hardness, and the height of compressive residual stresses. These relationships are remarkably complex due to the multitude of influencing parameters. As depicted in **Figures 28** and **29** there are material-specific as well as temperature- and time-specific dependencies.

The thermal activity of the creep processes increasing with rising nitriding temperature causes the clear decrease of the residual stresses within the examined temperature range (500–570 °C) compared to the decrease of the hot hardness. It explains the influence of the nitriding temperature on the correlation between the height of the residual stresses and the hot hardness as shown in **Figure 29**.

An example for the influence of steel composition on the profile of the residual stresses within the nitrided case is shown in **Figure 30**. The hardness increase and the compressive residual stresses are enhanced with rising content on nitride-forming elements dissolved within the ferrite. The strengthening depth decreases and a steep drop down in the profile of hardness and compressive residual stresses occurs. The differences between the steels 31CrMoV9 and 17CrMoV10 result from the different grade of chromium being bonded as carbide.

In contrast to the hardness, the maximal compressive residual stresses do not appear in the near-surface area. The decrease of the compressive residual stresses in the near-surface region and the surface distance of the maximum of the residual stresses are mainly defined by the material-specific decarburization, which is also dependent on the nitriding conditions, as well as the stress-induced redistribution of the cementite (*34*).

With rising nitriding temperature, the creep strength of the nitrided cases decreases and the decarburization increases. As can be seen in **Figure 31**, this leads to a decrease of the maximal compressive residual stresses and an enlargement of the surface distance of the residual stress maximum. An extension of the nitriding time at constant nitriding temperature causes the same effect, see **Figure 32**. The tension relaxation increasing with nitriding time results in a considerable decrease of the maximal compressive residual stresses.

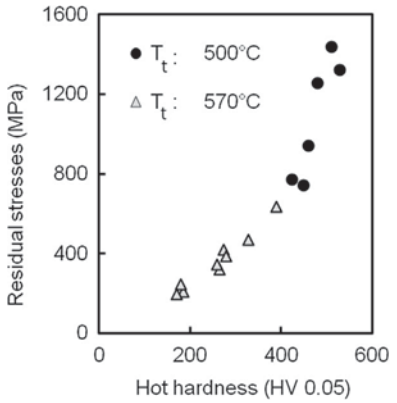

Figure 29 Relation between maximum residual stress and corresponding hot hardness at nitriding temperature.

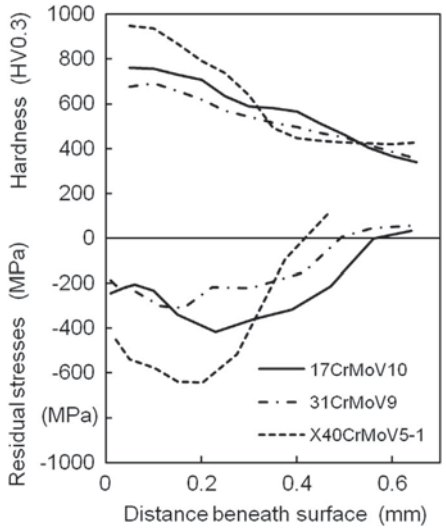

Figure 30 Profiles of hardness and residual stresses in nitrided case of steel 17CrMoV10, 31CrMoV9, and X40CrMoV5, $T_N = 570\,^{\circ}C$; $t_N = 32$ h.

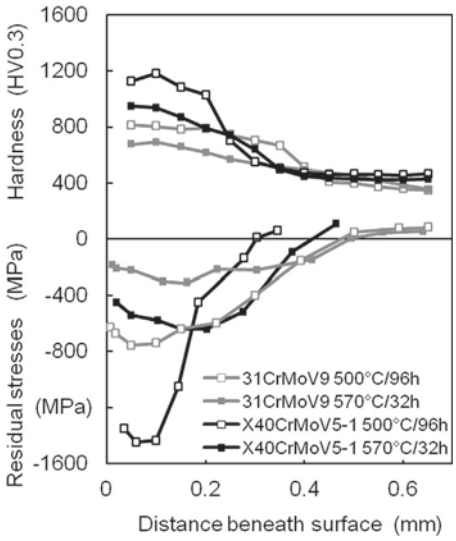

Figure 31 Influence of nitriding temperature on hardness and residual stress profiles of steel X38CrMoV5-1 and 31CrMoV9.

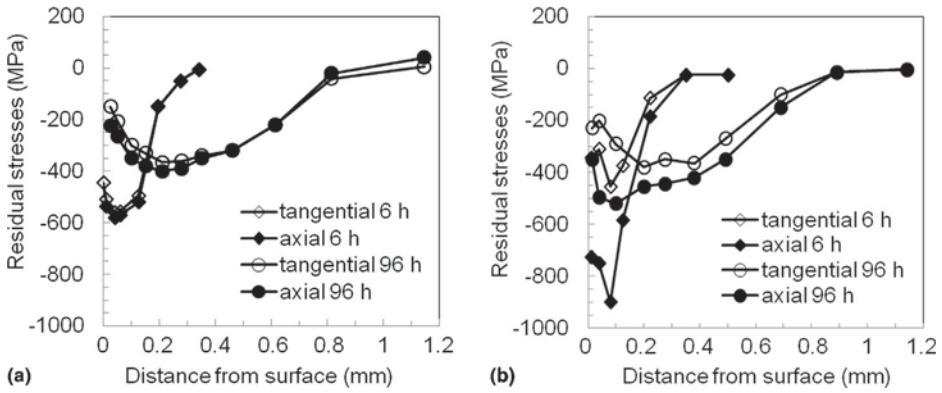

Figure 32 Influence of nitriding time on residual stress profile of nitrided case of steel 31CrMoV9, $T_N = 550\,^{\circ}C$, sample diameter: 17 mm; (a) plain samples $K_t = 1$; (b) notched samples $K_t = 2$.

Figure 32 simultaneously depicts also the influence of geometrical effects. The compressive residual stresses in axial and tangential directions do not differ for plane cylindrical samples. In contrast, for notched samples the strain impediment in the notch ground causes axial and tangential stresses of different levels. For low nitriding depths (nitriding times of 6 h), the axial stresses are more than doubled compared to the tangential stresses. These differences decrease with increasing nitriding time and increasing component size.

The described relations give some hints for the materials selection and the choice of the nitriding conditions in the case of high demands on the residual stress condition. Thus, it is, e.g., possible to specifically enhance the hardness increase and the compressive residual stresses by means of an increase of the nitride-forming elements within the ferrite and the decrease of the nitriding temperature and meet high demands on the fatigue strength behavior.

12.14.3.3 Mechanical Properties

For the service behavior of nitrided components, different areas are of importance, depending on the depth effect of the load. The effect of tribological stresses, for example, is preferentially confined on the direct surface layer. In contrast to this, the fatigue and crack behavior depend both on the strength of the surface layer and the core and on the residual stresses within the case and the core. Thereby, the transitions between the single load cases are fluent. The characterization of the mechanical behavior of surface compounds needs to be done depending on the load case, including the determination of local and global properties of the materials compound.

The large microstructure and property gradients in nitrided cases demand testing methods with a high spatial resolution for determining the local properties. Therefore, the indentation methods with their load-depending resolution belong to the fundamental test methods for characterizing the mechanical properties of nitrided layers. The conventional hardness measurement, which can often be correlated to other mechanical properties, is still successfully applied for evaluating the surface hardness and the hardness distribution at cross-sectional and angle polished samples. Besides this, the indentation fracture mechanics for characterizing the toughness of brittle surface layers have been established (*38,39*). With this test method, the local fracture toughness is calculated from the length of the crack, which develops in the tensile strength field of a Vickers hardness indentation, and the normal load (*40*). The crack initiation on a Vickers mark indentation being characteristic for nitride layers is exemplarily shown in Figure 33.

Another possibility of localizing the load is the formation of an inhomogeneous stress distribution having stress gradients that exceed the strength gradients within the surface layer e.g., by means of notches and bending. The change in toughness $K_c(\rho)$ of notched samples in dependence on the notch radius ρ can be used for estimating the toughness of surface layers. Beneath a material-specific critical notch radius ρ_0 the notch toughness remains constant and is considered to be an appraised value for the fracture toughness (*39,41,42*). One fracture example is shown in Figure 34. It describes the notch toughness of different nitrided samples of the steel 20MnCr5N (N = normalized) in dependence of the notch radius. The critical notch radius $\rho_0 = 25\ \mu m$ is within the magnitude of known values obtained for the case hardened steels (*41*).

12.14.3.3.1 Strength Behavior at Monotonic Load, Hardness, and Toughness

The strength behavior at monotonic mechanical loads is described by the resistance of a material against permanent plastic deformation and fracture. In dependence of the ductility and the load conditions, the plastic deformation prior to and during fracture can be very different. Therefore, the materials strength behavior is additionally also defined by its ductility and toughness.

The strength properties of nitrided steels are significantly conditioned by the microstructure and the properties of the diffusion layer, as suggested in Figure 26. An idea of the extremely broad property spectrum is shown on the example of the hardness profile within the diffusion layer of selected steels in Figure 25.

By means of alloying the steels with up to 5% Cr as well as 1% Al, it is possible to specifically modify the case hardness of the diffusion layer between 250 and 1200 HV0.3. Even higher values of case hardness are obtained in the case of high-alloyed tool steels and stainless steels.

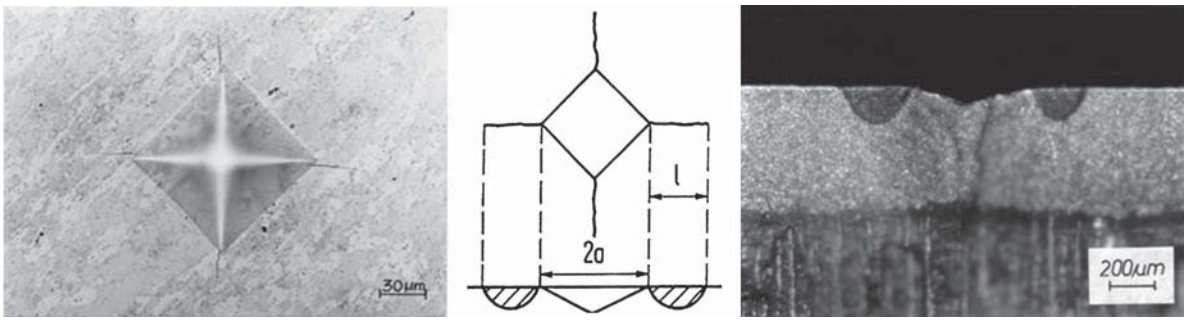

Figure 33 Characteristic crack formation on a Vickers indentation mark within a nitrided layer.

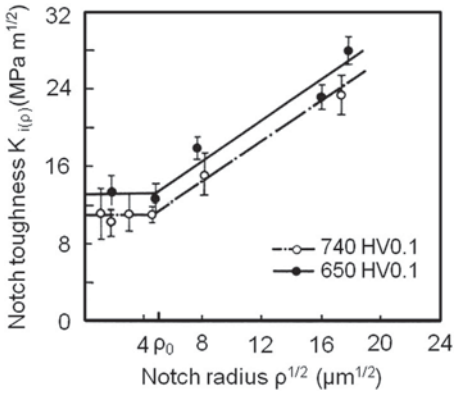

Figure 34 Notch toughness as a function of notch radius, steel 20MnCr5, normalized and differently nitrided.

As shown in Figure 31, besides the influence of the chemical composition, the hardness profile can be specifically controlled in a wide range by means of the variation of the nitriding parameter. The height of compressive stresses is essentially defined by means of the nitriding temperature as explained in Section 12.14.3.2. By decreasing the nitriding temperature from 570 to 500 °C, the compressive stresses within the nitrided case of the steels 31CrMoV9 and X40CrMoV5-1 are more than doubled (Figure 31).

The change in hardness of the nitrided cases causes also a different fracture behavior. For low-alloyed steels, the hardness of the near-surface area of the diffusion layer is in the range of 250–400 HV0.3, which corresponds to the characteristic values obtained for low-alloyed quenched and tempered steels. Bright nitrided components made of unalloyed steel exhibit a similar fracture behavior like such steels. Nitriding is therefore also used to improve the strength behavior of sheet metal parts made of unalloyed steels (*43*). The hardness of the nitride layer of 31CrMoV9 of about 750–850 HV reaches the one of hardened cold working steels. The surface hardness of X38CrMoV5-1 of about 900–1150 HV0.3 exceeds the hardness of hardened high-speed steels (64–66 HRC/ 850–920 HV). The fracture behavior of nitrided layers on these steels is therefore comparable to the fracture behavior of hardened tool and high-speed steels, which are both well known for their low toughness.

The fracture toughness of nitride layers can be classified in the established correlation of hardness and fracture toughness (Figure 35). At comparable hardness, the fracture toughness of the surface layer on quenched and tempered nitrided steels reaches the toughness of hardened high-speed steels. An inferior toughness is shown by steels having a normalized microstructure. In the area of hardness decrease within the diffusion layer, the toughness increases to the toughness level of the base material, in the case of quenched and tempered steel 31CrMoV9 to 125–140 MPa $m^{1/2}$ (Figure 36). Due to the higher hardness (950–1250 HV), the diffusion zones of hardened cold working steels have a lower toughness. With a value of 11–13 MPa $m^{1/2}$, it is above the toughness of compound layers, but increases only slightly at the changeover to the hardened base material. The fracture toughness of a ledeburitic chromium steel (X210Cr12, X155CrVMo12-1) with a hardness of 55–58 HRC is about 23–25 MPa $m^{1/2}$ (*44*).

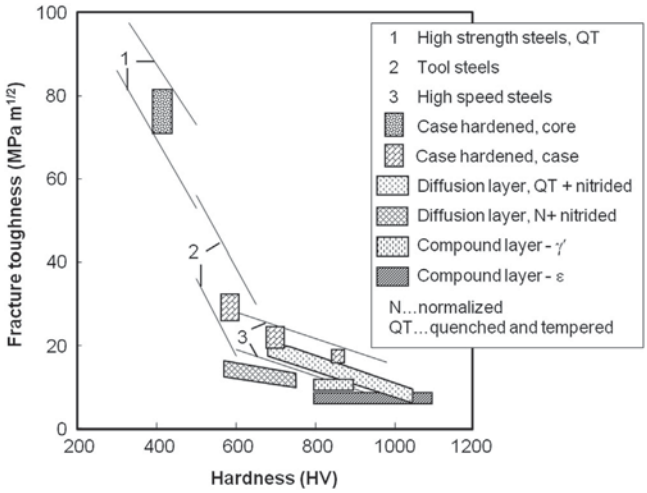

Figure 35 Hardness and fracture toughness of steels (1, 2, 3), case hardened and nitrided surface layers.

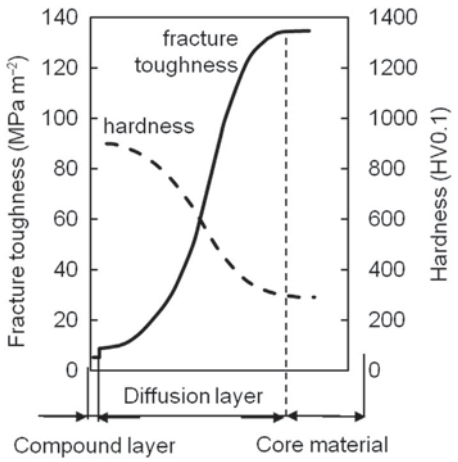

Figure 36 Variation of toughness and hardness in a nitrided case, schematic description on the example of steel 31CrMoV9.

A characteristic of compound layers is their high hardness and their nonmetallic structure as well as the resulting low toughness. Depending on the nitriding parameter and the chemical composition of the steel, they may contain varying amounts of γ′-nitrides, ε-phase with different nitrogen and carbon content, cementite, and various alloyed nitrides and carbides. Besides, compound layers contain also pores in varying amount and distribution. The hardness of compound layers is significantly defined by the mentioned components existing in varying amounts and distribution. In the pore-rich zone, the hardness is normally lower than 600 HV0.025. For unalloyed steels, the highest hardness values are obtained in the pore-free area of ε-carbonitride layers. In the case of alloyed steels, the hardness of the pore-free zone is defined by the amount of alloyed nitrides.

The dependency of the microhardness of compound layers of gas oxinitrided and bath nitrocarburized samples on the sum of nitride-forming elements (ΣMe = Cr + Mo + V + W) is shown in **Figure 37**. The microhardness of the gas oxinitrided sample has been determined by means of the Martens hardness measurement; in the case of the bath nitrocarburized samples, the Vickers hardness measurement was used (*45*). Therefore the hardness values are not comparable. Nevertheless, the same dependency exists for the influence of the alloying elements independent on the nitriding process (gas/bath nitriding) and the process parameter. This proves that the hardness of the compound layer is primarily defined by the chemical composition of the base material. Obviously the influence of the nitriding process is marginal. The toughness of compound layers, which can be determined by means of the indentation fracture mechanics, is between 6 and 10 MPa m$^{1/2}$, which is at the upper limit of the toughness of hard coatings; γ′-layers have a higher toughness compared to ε-layers (*38*,*42*).

If a nitrided sample is loaded by tension or bending, the yielding of the core material is initiated above a surface compound specific stress, but the core will be constrained from yielding by the unyielded case.

The composite will continue to deform elastically until the strain is sufficient to crack the brittle tensile loaded case. The distances between the initiated cracks depend on the strength properties of the material compound and the ratio of the layer thickness to thickness of the core material (*46*). Already at relative low tensile stresses a multitude of close adjoined micro cracks are developed

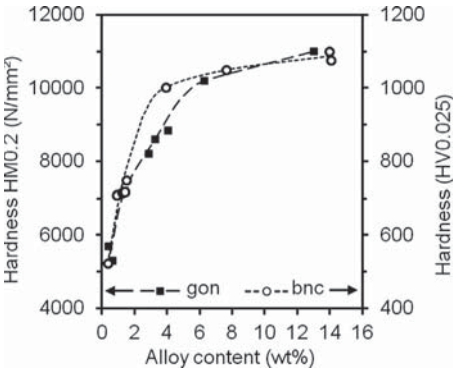

Figure 37 Compound layer microhardness as function of sum of nitride-forming elements (ΣMe = Cr + Mo + V + W) for various steels after salt bath nitrocarburizing (T_N = 580 °C, t_N = 1.5 h) and after gas oxinitriding (T_N = 570 °C, t_N = 32 h). Reproduced from Slyke, J.; Sproge, L. Kinetics of the Gaseous Nitrocarburising Process. *Surf. Eng.* **1989**, *5*, 125–140.

within the compound layer which are intercepted at the phase boundary compound/diffusion layer. During a further increase of tension load also the diffusion layer cracks in higher constant distances. As a result, a multiple notched sample of the core material is generated. The reduction in area, which characterizes the ductility of the surface layer compound, strongly decreases. With dependency on the layer structure also the tensile strength is reduced.

For equal nitrided case depths, the incipient crack stress is defined by the case hardness (Table 2). With decreasing surface hardness, i.e., with increasing toughness, the ratio of the incipient crack stress to tensile strength of the core material is increased. For constant sample geometry and surface hardness, the incipient crack stress decreases with increasing effective nitrided case depth. This is shown, for example, by the results of four point bending tests in Table 3. During these tests, the diffusion layer cracked even before reaching the 0.1 mm bending limit. At an effective nitrided case depth of 0.41 mm, the incipient crack stress decreased in this example to 70% of the 0.1 mm bending limit of the unnitrided core material.

The fracture behavior of the cracked nitrided samples and components is characterized by the toughness properties of the layer compound. The case hardness of the nitrided layer of unalloyed steels is, as mentioned, about 250–350 HV and thus in the range of the core hardness of quenched and tempered steels. The numerous cracks generated within the compound layer of these steels due to high tensile or bending loads get intercepted at the changeover to the diffusion layer. Also in case of high loads, the diffusion layer keeps their good ductility.

The cracks within the diffusion layer of quenched and tempered steels are intercepted and blunted at the end of the diffusion layer by the ductile core material through a plastic deformation of the crack tip area. A corresponding example is shown in Figure 38. The crack initiation depth in this case is equivalent to the effective nitrided case depth. The stress intensity is characterized by the component geometry, the crack initiation depth, and the effective load. If the stress intensity reaches the fracture toughness of the core material due to a further increase of the nominal stress, a ductile residual fracture occurs. At a given fracture toughness, the fracture stress decreases with increasing crack initiation depth – effective nitrided case depth.

The fracture behavior of nitrided components made of quenched and tempered steels differs significantly from the fracture behavior of case-hardened components. For equal hardness, the fracture toughness of case-hardened layers exceeds the fracture toughness of nitrided layers; therefore their resistance against the formation of cracks is slightly enhanced (Figure 35). Due to the higher hardness, the hardened core material has a considerable lower fracture toughness compared to the high-tempered nitrided steel (Figure 39) and thus a lower fracture resistance (*41*).

Also for nitrided tools made of ledeburitic cold working steels, the cracks generated during the crack initiation phase are intercepted by the base material. As can be seen in Figure 39 on the example of the toughness profile of the surface layer of nitrided ledeburitic cold working steel X210Cr12, the difference between the fracture toughness of the nitrided layer and the core material is

Table 2 Tensile properties of nitrided steels

		Nitrided case					
Steel/treatment		*CL (μm)*	*Nhd (mm)*	*Ch HV0.1*	*UTS (MPa)*	*ICS[a] (MPa)*	*RA[b] %*
X38CrMoV5-1	QT	–	–	–	1602	–	53
	Nit	12	0.21	1230	1598	1308	8
32CrMoV12-28	QT	–	–	–	1325	–	53
	Nit	8	0.21	1150	1318	1182	4
56NiCrMoV7	QT	–	–	–	1179	–	54
	Nit	12	0.21	700	1184	1082	5

[a]Incipient crack strength.
[b]Reduction of area.

Table 3 Bending properties of nitrided steel X38CrMoV5-1

	Nitrided case					
Treatment	*CL (μm)*	*Nhd (mm)*	*Ch HV0.1*	*Bending strength $\sigma_{0.1}$ (MPa)*	*ICS[a] σ_f (MPa)*	*$\sigma_{0.1}/\sigma_f$[b]*
QT	–	–	–	1745	–	–
Nit	7	0.11	1110	1820	1700	0.97
Nit	0–2	0.20	1020	1850	1710	0.98
Nit	17	0.29	1060	1785	1380	0.79
Nit	25	0.41	1070	1685	1225	0.70

[a]Incipient crack strength.
[b]$\sigma_{0.1}$ Nit/σ_f QT.

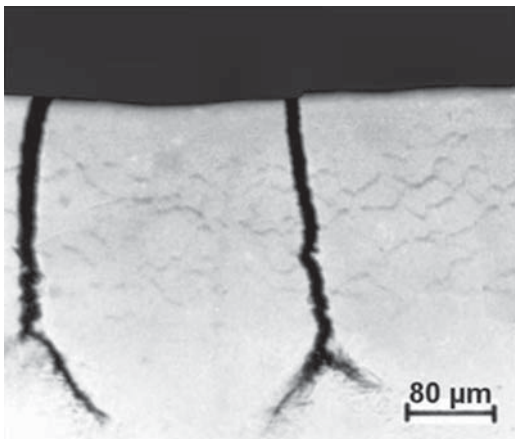

Figure 38 Cross-section of a particular strained bending nitrided specimen, showing cracks blunting at the beginning of the core, steel: 31CrMoV9.

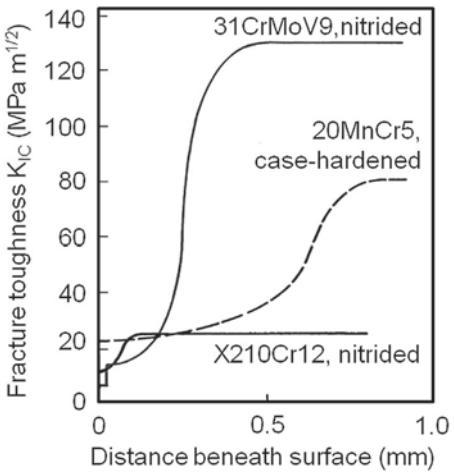

Figure 39 Variation of toughness in the case of the nitrided steels 31CrMoV9 and X210Cr12 as well as the case-hardened steel 20MnCr5.

very low (*44*). Hence, for only a slight increase of the nominal load, an instable crack propagation occurs, which leads to a brittle residual fracture.

The tolerable crack length/nitrided case depth can be evaluated from the permissible stress intensity (fracture toughness) of the base material, the nominal load, and the component geometry. Due to the low fracture toughness for tools made of high-speed steels and ledeburitic cold working steels, effective nitrided case depths in the range of 30–60 µm are permissible. By means of a reduction of the notch sharpness, the influence of the geometry can be decreased and the permissible effective nitrided case depth can be increased. This is depicted in **Figure 40** on the results of investigations concerning the notch toughness of different nitrided samples of the steel 165CrMoV46 at dynamic load, load velocity $\dot{K} \approx 10^6 \mathrm{MPam}^{1/2}\mathrm{s}^{-1}$.

In contrast to static tests on low-alloyed nitrided steels, the fracture toughness characterizes the toughness of the layer compound nitrided layer-base material. As shown in **Figure 40** the notch sensitivity of the layer compound increases with increasing surface hardness and growing effective nitrided case depth. In first-order approximation, its fracture toughness equates the toughness of the base material.

As described in Section 12.14.3.1, nitride layers are featured by a high thermal strength due to the high thermal stability of the alloyed nitrides precipitated at nitriding temperature. An impression of this is given by the hot hardness profile within the nitride layer of a cold working steel X6CrMo4 and the hot working tool steel X40CrMoV5-1 shown in **Figure 41**. The nitride layer hardness of X40CrMoV5-1 exceeds the core hardness more than the double value, both at 500 °C and at 570 °C. Steel X6CrMo4 reaches the hot hardness of X40CrMoV5-1 despite the lower alloying content. This can be attributed to the influence of carbon on the available concentration of nitride-forming elements within the matrix as mentioned in Sections 12.14.1 and 12.14.2. In the case of steel X38CrMoV5-1 the chromium being bonded as carbide is not available for an effective precipitation hardening. A characteristic of the precipitation structure generated at nitriding temperature is their relatively high thermal stability. This is clearly depicted in **Figure 42** on the example of the influence of the test temperature on the hot hardness. The thermal stability legitimates the

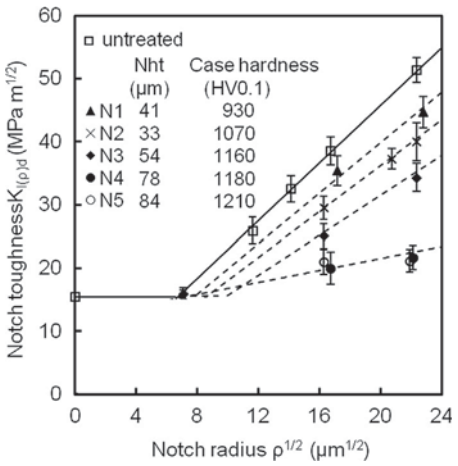

Figure 40 Influence of the case structure on the notch toughness of differently nitrided steel 165CrMoWV46 at dynamic load, $\dot{K} \approx 10^6$MPa m$^{1/2}$s^{-1}.

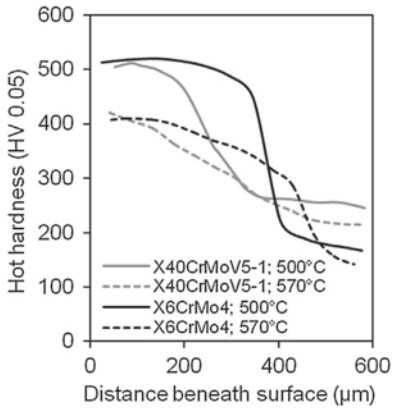

Figure 41 Hot hardness profiles in differently nitrided case of steels X6CrMo4 and X40CrMoV5-1; $T_N = 500\,°C$, $t_N = 96$ h; $T_N = 570\,°C$, $t_N = 32$ h.

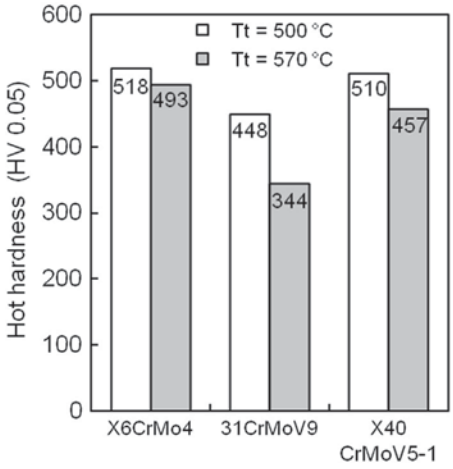

Figure 42 Case hot hardness of different steels, nitrided at $T_N = 500\,°C$, $t_N = 96$ h, tested at $T_t = 500\,°C$ and $570\,°C$.

application of nitrided components, e.g., nitrided hot working tools and valves, even at temperatures above the nitriding temperature.

12.14.3.3.2 Strength Behavior at Cyclic Load

For decades, nitriding has been successfully used for enhancing the fatigue behavior of components, including, for example, gears, springs, crankshafts, and axle shafts, but especially parts that are subjected to complex cyclic mechanical, tribological, and chemical loads. Investigations by Mailänder (*47,48*) already proved that the fatigue strength of nitrided samples is defined by the core strength and the nitriding time (nitrided case depth), cf. **Figure 43**.

Nitrided components are distinguished by a low notch sensitivity and insensitivity against the surface roughness. The enhancement of the fatigue strength is notably high for sharp notched components, i.e., for high stress gradients (*35,48*), see **Tables 4 and 5**. With increasing component diameter, the stress gradients decrease. Thus, the effect of nitriding on the enhancement of the fatigue strength decreases. For notched samples having a diameter of 100 mm, the increase in fatigue strength up to 136% through nitriding is still significant (**Table 5**). According to data of Sauer (*49,50*), the fatigue strength of rods with 200 mm in diameter is still enhanced by nitriding up to 114%.

The increase of the fatigue strength by means of nitriding can be explained by the strengthening of the surface layer and the formation of compressive residual stresses. The effect of residual stresses can be equalized to a mean stress and can be described quantitatively, for example, by the approach of Goodman (*52,53*) and the modified damage parameter of Smith, Watson, and Topper (*54,55*) (SWT), respectively. In contrast to the Goodman approach, the SWT parameter considers in a first approximation also the effect of the residual stresses on the crack propagation (*54*). Experimental investigations proved that the results are in good agreement with the dependence of fatigue limit on the value of residual stresses, which was estimated on the basis of the SWT approach (*55*).

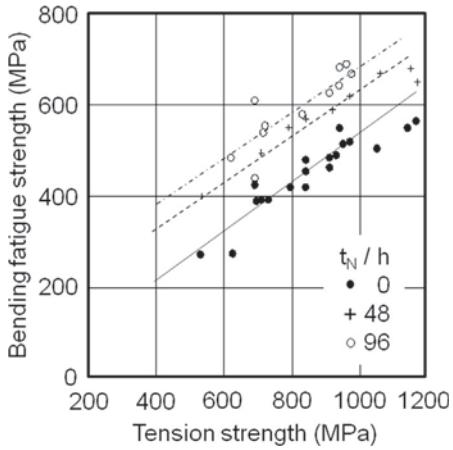

Figure 43 Bending fatigue strength of quenched and tempered and nitrided samples according to Mailänder, T_N: 500 °C, specimen diameter: 7.5 mm. Reproduced from Mailänder, R. Über die Dauerfestigkeit von nitrierten Proben. *VDI-Z* **1933**, *77* (10), 272–274.

Table 4 Rotating bending fatigue strength of nitrided steels according to H. Wiegand

				Rotating bending fatigue strength						Fatigue notch factor K_f	
				σ_{bf}[a] (MPa)			$\sigma_{bf,\ n}$[b] (MPa)				
Steel type	$R_{m,\ core}$ *(MPa)Nitrided*	*Nitriding Temperature (° C) Time (h)*		*Non-nitrided*	*Nitrided*	*Enhancement of* σ_{bf} *(%)*	*Non-nitrided*	*Nitrided*	*Enhancement of* $\sigma_{bf,\ n}$ *(%)*	*Non-nitrided*	*Nitrided*
Cr–Mo–Al – Nit-steel[c]	883	520	45	471	667	+41	235	–	–	2.0	–
Cr–Mo–V – Nit-steel[c]	1177	520	45	559	716	+28	255	588	+130	2.19	1.23
C – QT-steel[c]	834	480	45	431	667	+55	245	441	+80	1.76	1.51
Cr–Mo – QT-steel[c]	1079	500	45	549	824	+50	265	520	+96	2.07	1.59

[a] σ_{bf}: determined on a plane rotating bending sample (6,5 mm ø).

[b] $\sigma_{bf,\ n}$: determined on a notched rotating bending sample (notch depth: 0.5 mm; notch radius: 0.5 mm).

[c] Nit: nitriding, QT: quenched and tempered.

Reproduced from Wiegand, H. Nitrieren im Motorenbau. *Härterei-Tech. Mitt.* **1942**, *1*, 166–185.

Table 5 Influence of sample diameter on bending fatigue strength of quenched and tempered nitrided steels

		$K_t^d = 1$		$K_t^d = 2$		
Steel[a]	*Sample diameter (mm)*	σ_{bf}[b] *(MPa)*	*IF*[c]	$\sigma_{bf,}$[b] *(MPa)*	S[c]	K_f^d
31CrMoV9QT	7.5	473	–	335	–	1.41
	17	438	–	252	–	1.74
	38	402	–	239	–	1.68
30CrNiMo8QT	10	436	–	287	–	1.52
	80	394	–	230	–	1.71
	100	–	–	222	–	–
31CrMoV9QT,Nit[e]	7.5	651	1.37	620	1.85	1.05
	17	508	1.16	465	1.85	1.09
	38	450	1.12	366	1.53	1.23
30CrNiMo8QT,Nit[f]	10	651	1.49	609	2.12	1.07
	80	457	1.16	310	1.35	1.47
	100	–		303	1.36	–

[a]QT: quenched and tempered, Nit: nitrided.

[b]Fracture possibility, $P = 50\%$.

[c]Incremental factor, IF: σ_{bf} – nitrided/σ_{bf} – non-nitrided.

[d]K_t: stress concentration factor, K_f: fatigue notch factor.

[e]Nitriding hardness depth: 0.5 mm; case hardness: 735 HV0.3; core hardness: 280 HV0.3.

[f]Nitriding hardness depth: 0.4 mm; case hardness: 690–716 HV0.3; core hardness: 305 HV0.3.

Reproduced from Kloos, K. H. a.o. Quatitative Bewertung des oberflächentechnischen Größeneinflusses plasmanitrierter Probestäbe bei Umlaufbiegung und Zug-Druck-Beanspruchung. *Härterei-Tech. Mitt.* **1984**, *39*, 165–172 and Spies, H.-J., et al. Abschätzung der Schwingfestigkeit nitrierter bauteilähnlicher Proben mit Hilfe normierter Wöhlerstreubänder. *Mat.-wiss. u. Werkstofftech* **1996**, *27*, 60–71.

The depth-depending hardness and residual stress distribution cause a depth depending 'local net fatigue strength' $\sigma_{NFS}(x)$. This concept of local fatigue strength attributed to Woodvine (*56,57*) has been established for evaluating the influencing variables on the fatigue behavior of surface hardened components (*55–58*). **Figure 44** gives an example of Woodvine analysis of carburized steel. The comparison of the local fatigue strength with the local stress distribution $\sigma_a(x)$ can be used to assess the potential crack initiation position.

In case of a flat load induced stress distribution, the fatigue failure in the high cycle region arises by local crack initiation due to inhomogeneities in the microstructure, in particular nonmetallic inclusions within the core near the strengthened case (incipient crack position 1). This damage development is characteristic for unnotched or low-notched parts and especially for components having high diameter. In this case, the fatigue strength is defined by the properties of the core material, particularly its strength and its purity grade as well as the nitriding depth-dependent incipient crack depth. This explains the mentioned insensitivity against the surface conditions and low notches.

The increase of the stress gradient due to high stress amplitudes in the finite life region as well as sharp notches leads to a shifting of the failure location, which characterizes the fracture development, to the component surface fracture, see **Figure 45**. **Figure 46** illustrates the two types of fatigue fracture surfaces.

As arising from **Figure 45**, the transition from core controlled to case controlled fracture depends on both the profile of the applied stress and the profile of the net fatigue strength, which is defined by the hardness profile and residual stress profile. High

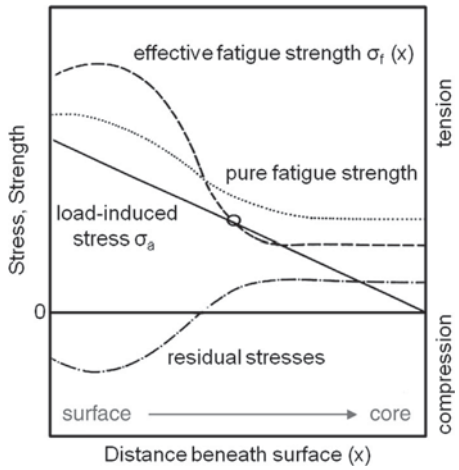

Figure 44 Woodvine analysis of carburized steel fatigue specimens, predicting subcase/surface origin of failure. Reproduced from Woodvine, J. G. R. The Behavior of Case-Hardened Parts under Fatigue Stresses. *Iron Steel Inst., Carnegie Scholarship Mem.* **1924**, *13*, 197–237.

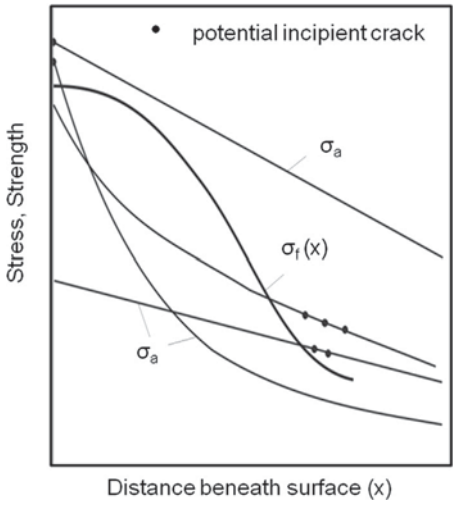

Figure 45 Possible flaw sites in dependence of the local fatigue limit $\sigma_{AD}(x)$ and the loading stress $\sigma_a(x)$, schematic.

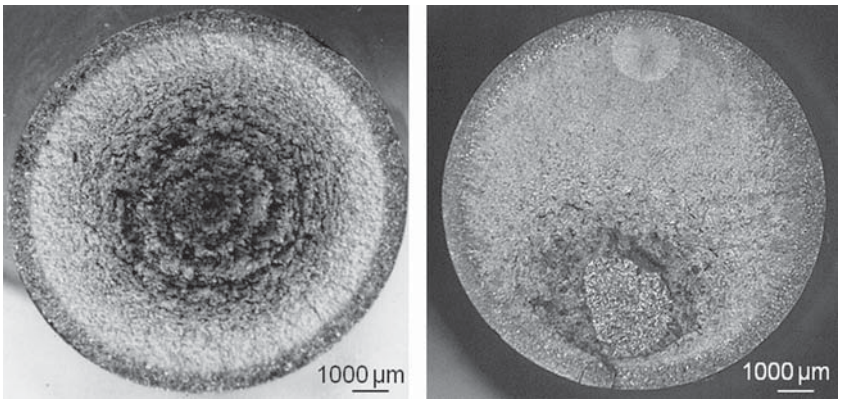

Figure 46 Case-controlled and core-controlled fracture, left: surface cracking, centric residual fracture, right: subsurface cracking, excentric residual fracture.

compressive residual stresses significantly increase the net fatigue strength and therefore extend the crack initiation position zone beneath the surface to higher stress amplitude values and higher stress gradients, respectively.

For all crack initiation positions, especially at loads within the region of the fatigue limit, a multiple crack initiation formation can occur (*59,60*). The cracks being exposed by the fracture do not always exist within one level. Therefore, molded fracture zones with steps and moonscapes can be formed (**Figure 47**). This is clearly evident for the influence of the stresses volume on the crack initiation and thus the fatigue strength.

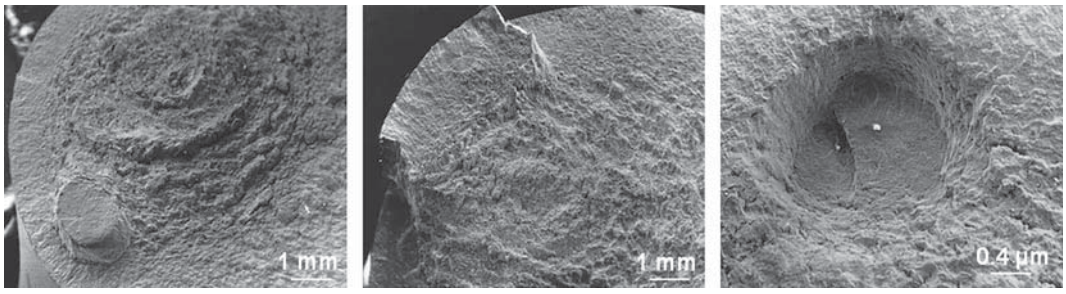

Figure 47 Facets of multiple subcase nuclei.

The further fracture development is influenced by the toughness of the hardened surface layer and the core material. This is clearly depicted by a schematic image of the fracture phases of nitrided and case-hardened steels for the crack initiation beneath the surface (Figure 48).

For nitrided steels, the cracks are not growing up to the surface. The local stable crack growth of the incipient crack is interrupted by unstable crack propagation within the diffusion layer if the stress intensity reaches a critical value, the local fracture toughness. A circumference edge crack is formed, which gets intercepted by the ductile core material. This is followed by a global stable crack growth within the core material (ductile fatigue), which is generally finished due to a final ductile rupture at adequate crack depth. The area affected by fatigue before the final failure is large.

For case-hardened steels, the fracture toughness of the case-hardened surface layer, which exceeds the fracture toughness of nitrided cases, is not reached by the maximum stress intensity of the subsurface cracks. The initiated cracks grow up to the surface and generally no circumferential edge crack is formed. The fatigue fracture is unilaterally extended from the incipient crack position. The lower core toughness compared to high tempered nitrided steels (cf. Figure 39) leads to a final failure by brittle fracture. The connected lower static residual strength leads to a major residual fracture surface.

Information of the toughness of the diffusion layer is yielded from the geometry of the subsurface incipient cracks. The stress intensity at the transition from local stable crack propagation to unstable crack propagation within the diffusion layer can be calculated from the position, size, and shape of the incipient crack rosette as well as the nominal load (*60*). In first approximation it is an estimated value for the fracture toughness of the diffusion layer in this area.

The fracture toughness and the notch toughness are both influenced by the microstructure (normalized or quenched and tempered before nitriding) of the diffusion layer and its hardness, as shown in examples in Table 6. The values are at the upper scatter limit of the parameter for the diffusion layer determined by means of the notch fracture mechanics. In view of the high hardness and toughness gradients within this area, it is comprehensible.

The fatigue strength of smooth and low notched components especially having higher diameter is determined by the aforesaid described fracture development through the change of the crack initiation position, which is influenced by the load and the layer structure (Figure 45). Thus, the fatigue strength results from the superposition of the S–N scatter bands of the core material and the

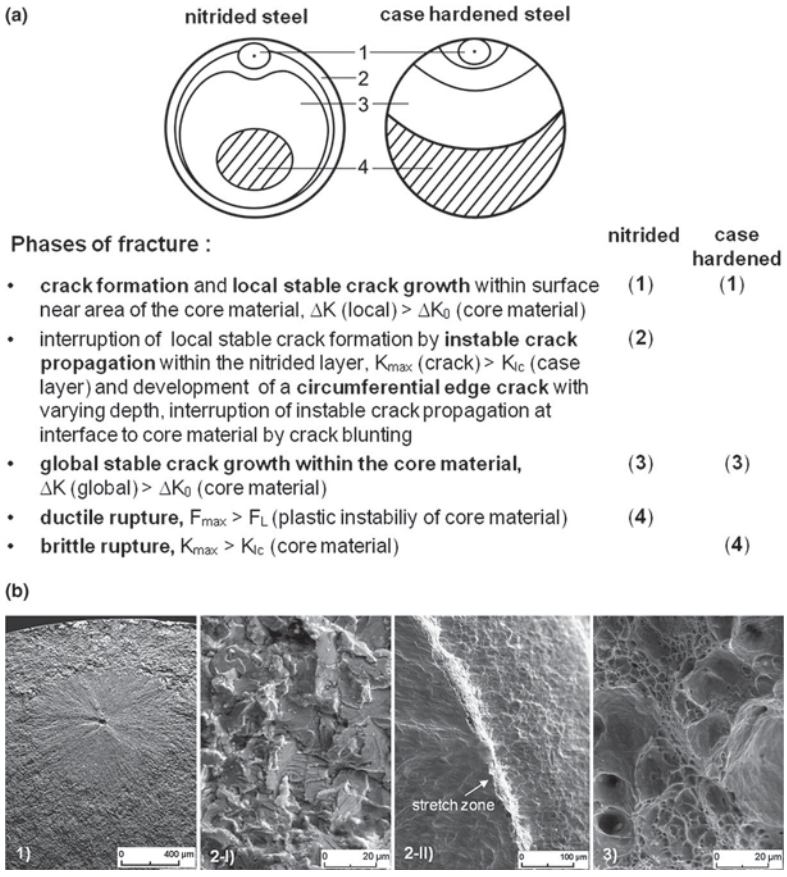

Figure 48 Fatigue fracture development of nitrided and case-hardened steels at core-controlled crack initiation, (a) schematic, (b) examples of fracture appearance at different fracture phases (SEM): (1) initial crack with transition to brittle fracture within case, (2-I) brittle fracture of nitrided case, (2-II) brittle fracture of nitrided case with a stretch zone at the transition to the core, (3) final ductile rupture.

Table 6 Layer structure, fatigue strength, and toughness of the case of nitrided steels

Steel[a]	Hardness HV0.3		Nitriding hardness depth (mm)	σ_{bf}[b] (MPa)	S–N curve – exponent k	Fracture toughness (MPa $m^{1/2}$)	Core toughness (MPa $m^{1/2}$)
	Case	Core					
20MnCr5N	630	190	0.42	490	14.1	14.0–16.3	13.6–14.6
20MnCr5QT	600	250	0.44	670	9.3	17.9–18.9	16.2–18.2
31CrMoV9QT	780	275	0.47	750	9.7	15.8–18.0	13.8–16.0

[a]N: normalized, QT: quenched and tempered.
[b]Bending fatigue strength, fracture possibility, $P = 50\%$, plane sample, diameter: 7 mm.

near-surface area of the nitrided case, as shown in Figure 49. The scatter appearing during the incipient crack formation is depicted in Figure 49(b). For the given example, the change of the incipient crack position occurs at stress amplitudes between 1060 MPa and 1150 MPa and cycles between $1.5 \cdot 10^4$ and $5.5 \cdot 10^4$.

The case-controlled fatigue behavior in the low cycle area is characterized by the properties of the near-surface region of the nitride layer and especially through the height, stability, and depth distribution of the residual stresses as well as the hardness profile within the near-surface region. A linear relation between hardness and fatigue resistance exists only for hardness values up to 500 HV. At higher hardness values, the fatigue resistance increases only marginally with dependence on the purity grade, i.e., the inner notch effect (*58*,*61*).

But the surface hardness significantly determines the stability of the residual stresses. The nitrided layer has an increased fatigue behavior and decreased incipient crack strength compared to the base material (see also Section 12.14.3.3.1). This explains the increased overload sensitivity, i.e., the sensitivity against maximum and medium stresses, respectively, of nitrided components. This leads to a smooth profile of the S–N curve of the surface zone. The change of the incipient crack position is visible in a change of the S–N curve slope as depicted in Figure 49 (*62*).

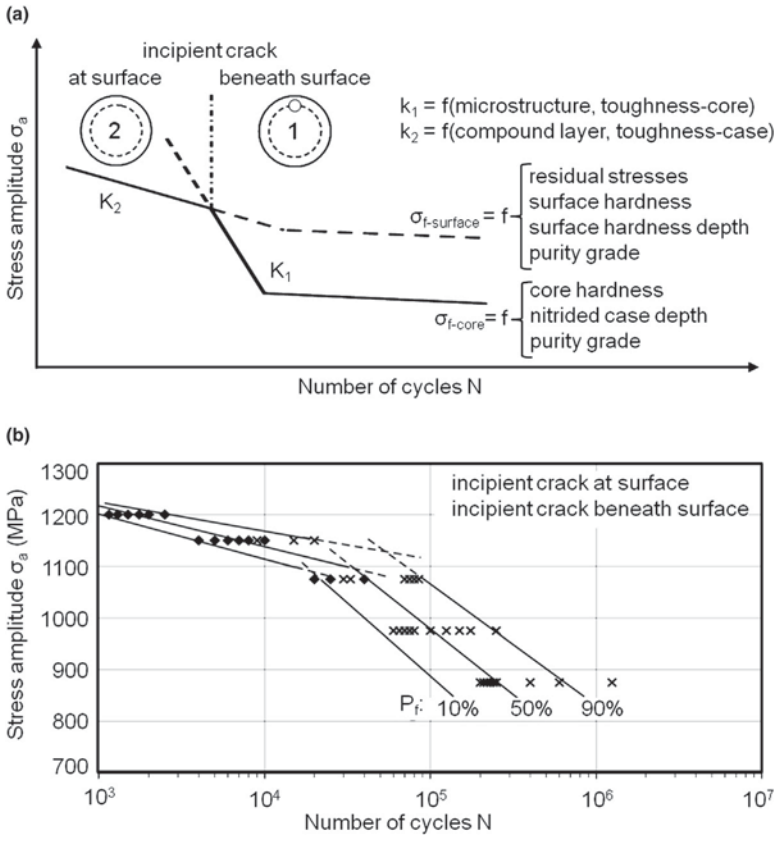

Figure 49 S–N curves in finite life region at core-controlled crack initiation, superimposition of SN curves of case and core material, (a) schematic image, influencing parameter on the cyclic strength; (b) scatter band of finite life strength of nitrided unnotched samples of 20MnCr5QT steels, fracture probability $P_f = 10\%$, 50%, and 90%. Reproduced from Spies, H.-J.; Tan, N. D.; Vogt, F. Einfluss des Aufbaues von Nitrierschichten auf die Schwingfestigkeit gekerbter Proben. *Härterei-Tech. Mitt.* **1993**, *48*, 153–161.

The slope of the S–N curves is described by the gradient exponent k. High values of k mark a low slope and thus a high overload sensitivity. The slope of the S–N curve in the high cycle regime k_1 is determined by the incipient crack formation behavior of the core material and the duration of the stable growth of the subsurface cracks, i.e., the effective nitrided case depth and the toughness of the diffusion layer.

The slope in the area of the intermediate fatigue k_2 is significantly defined by the incipient crack formation behavior of the nitride layer, which is mainly controlled by the phase structure of the compound layer and the toughness of the diffusion layer. This is proved by results of investigations shown in **Table 7**, which have been obtained on notched and differently nitrided samples of the steel 20MnCr5 having an incipient crack formation at the surface. Accordingly, removal of the ε-nitride layers as well as a γ′-nitriding result in a decrease of the overload sensitivity. The same effect is obtained for quenched and tempered nitrided samples compared to normalized nitrided samples due to the higher toughness of the diffusion layer.

The fatigue behavior in the high cycle region, which is controlled by the crack initiation beneath the surface, is characteristic for a wide field of component sizes, as the following examples show. For notched components, the transition of core-controlled fatigue to case-controlled fatigue occurs, in dependence on the nitride layer structure with increasing component diameter, only at relatively high stress gradients (sharp notches). For the steel 31CrMoV9 (Ncd = 0.5 mm), for example, surface incipient cracks appeared in the high cycle region for a notch root diameter of 50 mm first at notch factors $K_t > 3$ (*stress concentration factor*: $K_t = \sigma_{notch}/\sigma_{nom}$; σ_{notch}: greatest stress at the notch root; σ_{nom}: nominal stress). **Figure 50** shows a sub-surface crack nucleus within the fatigue fracture surface of a nitrided shouldered shaft made of 34CrNiMo6 steel (Ncd = 0.44 mm) of 190/160 mm in diameter after a load in the region of the fatigue limit. The starting point of the crack is situated within the core material in a depth of 2.16 mm beneath the surface.

The case-controlled fatigue behavior in the high cycle range is limited for sharp-notched components having a low diameter. The influence of notches on the fatigue behavior of nitrided samples of small diameter is shown in **Figure 51** on the example of 20MnCr5 steel. For the better characterization of the effect of nitriding, the respective values of each variant have been normalized related to the fatigue limit of the polished unnotched and unnitrided specimen. With increasing notch effect, i.e., with increasing stress gradient, the supporting effect is significantly rising. The fatigue strength reduction factor K_f (*fatigue notch factor:* $K_f = \sigma_c/\sigma_{cnom}$; σ_c: fatigue limit of the unnotched body; σ_{cnom}: nominal stress at the fatigue limit of the notched body) is clearly smaller compared to the notch factor K_t. The enhancement of the linear slope of the fatigue endurance limit, defined by the gradient exponent k, increases with increasing notch effect.

For the given specimen cross-section, the enhancement of the notch factor K_t from 1 to 2 leads to a displacement of the incipient crack position up to the surface. The significantly higher fatigue limit of the nitride layer extensively compensates the effect of the

Table 7 Fatigue strength and layer structure of notched nitrided samples of steel 20MnCr5, $K_t = 2$

	Compound layer		*Hardness HV0.3*		*Nitriding hardness – depth*	*Residual stresses*[a]	σ_{bWK}[b]	*S–N curve – exponent*[b]
Initial condition	*Type*	*Thickness (μm)*	*Case*	*Core*	*(mm)*	*(MPa)*	*(MPa)*	k
Normalized	γ′	8				−300	574	19.3
	ε(γ′)	22	670	190	0.49	−350	593	29.0
	ε(γ′)	0[c]				−350	596	21.0
Quenched and tempered	γ′	9				−255	608	11.2
	ε(γ′)	22	645	262	0.52	−315	670	15.8

[a]Distance to surface: 50 μm.

[b]Bending fatigue strength, notched samples ($K_t = 2$), fracture possibility, $P = 50\%$; sample diameter within notch root: 7.5 mm.

[c]Compound layer removed/grinded.

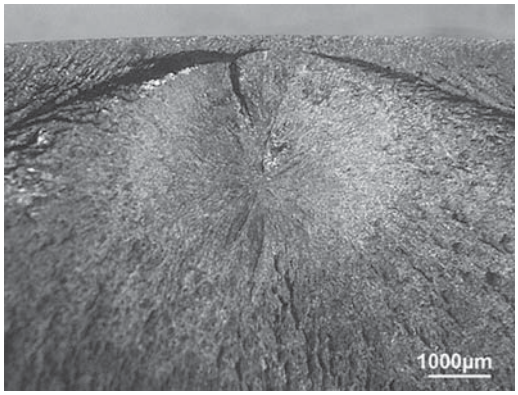

Figure 50 SEM fractograph of a subcase crack nuclei within fatigue crack area of a shouldered axle with diameter of 190/160 mm.

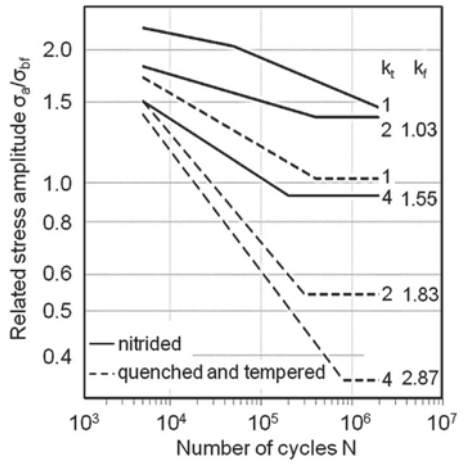

Figure 51 S–N curves of quenched and tempered as well as quenched, tempered and nitrided steel 20MnCr5 for different stress concentration factors, reffering to rotating bending endurance fatigue strength of quenched and tempered smooth samples, $P_B = 50\%$. Reproduced from Spies, H.-J.; Tan, N. D.; Vogt, F. Einfluss des Aufbaues von Nitrierschichten auf die Schwingfestigkeit gekerbter Proben. *Härterei-Tech. Mitt.* **1993**, *48*, 153–161.

notches so that the fatigue limit of unnotched and notched specimens ($K_t = 2$) is within the same magnitude. The scatter bands of the transition area determined for both notch factors do not differ practically (Figure 52). In contrast, for equal incipient crack position, the enhancement of the notch effect from $K_t = 2$ to $K_t = 4$ causes a clear decrease of the fatigue limit (Figure 51). Anyhow, the strength is far in excess of the value resulting from the higher notch factor, and the fatigue strength reduction factor $K_f = 1.55$ is significantly lower compared to the notch factor $K_t = 4$.

In contrast to the fatigue endurance limit, the fatigue strength for finite life of nitrided notched specimens is considerably influenced by the change of the incipient crack position. The bisection of the fatigue life range occurring for the unnotched specimens is not appearing. As explained before, the incipient crack formation at the surface results in a significant decrease of the S–N curve slope.

The demands for the high fatigue strength of nitrided components, resulting from the outlined relations between the fatigue behavior and the structure of the nitrided layer, are very complex. They are explained and underpinned on the schematic diagram in Figure 49(a). The fatigue endurance limit of plane and low notched specimens is core controlled. A high fatigue limit requires primarily a high nitrided case depth and high core strength as well as a high purity grade (Figure 43).

The behavior in the field of finite life fatigue strength and operational stability is controlled by the change of the failure location. By a change at higher stress amplitudes, i.e., high fatigue strength of the nitrided layer, the lower overload sensitivity being characteristic for the core controlled fracture, can be better used. An example is shown in Figure 53. The nitrided samples of the steels 20MnCr5 and 31CrMoV9 significantly differ in surface hardness from each other but show only marginal difference in core hardness, effective nitriding depth, and consequently fatigue strength. Clearly, differences exist in the fatigue finite life behavior due

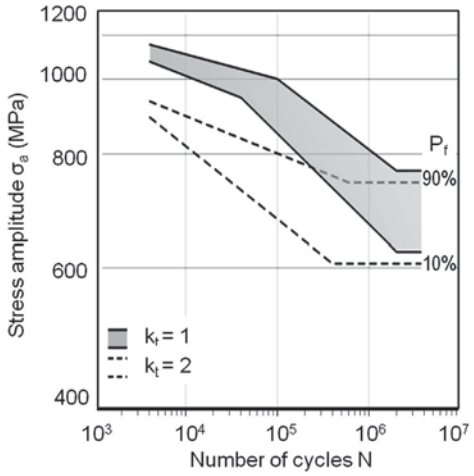

Figure 52 S–N curves of nitrided steel 20MnCr5 for stress concentration factors $K_t = 1$ and $K_t = 2$; $P_f = 50\%$. Reproduced from Spies, H.-J.; Tan, N. D.; Vogt, F. Einfluss des Aufbaues von Nitrierschichten auf die Schwingfestigkeit gekerbter Proben. *Härterei-Tech. Mitt.* **1993**, *48*, 153–161.

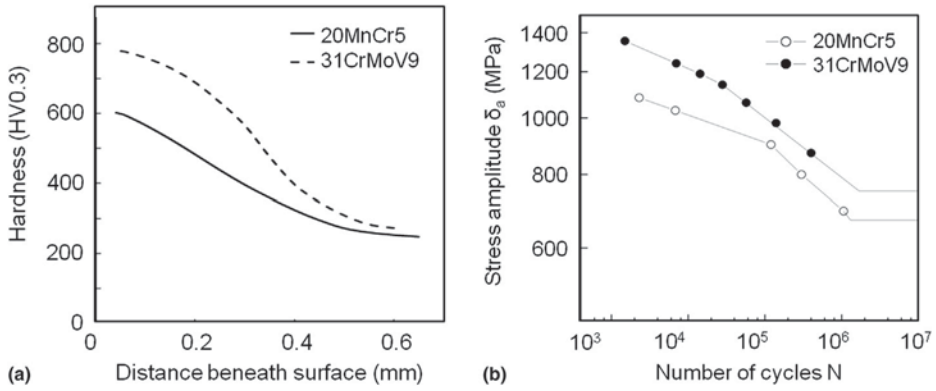

Figure 53 Hardness profile and S–N curves of nitrided samples, steels 20MnCr5 and 31CrMoV9.

to the higher surface hardness of 31CrMoV9 as well as its higher and more stable compressive residual stresses. The transition between case- and core-controlled failure for steel 31CrMoV9 takes place first at higher stress amplitudes and lower cycle numbers.

High fatigue strength of the near-surface area of the nitride layer is achieved by means of high and stable compressive residual stresses with its maximum beneath the surface. With increasing hardness the stability of the residual stresses against a stress relaxation during the load and their effect on the fatigue strength increases. Therefore, a high stability and a high effect of the residual stresses require a high strengthening of the surface layer. Limits for the strengthening arise from the decreasing toughness and the connected enhancement of the maximum stress sensitivity due to the increase in hardness.

The height of residual stresses is defined by the nitride precipitation and stress relaxation processes, which depend on nitriding temperature and time, as explained in Section 12.14.3.2. High compressive residual stresses can therefore only be generated at relatively low nitriding temperatures and adequate high temperature stability of the nitrided layer. For a given nitriding parameter, the high temperature stability and the hardness increase depend on the amount of nitride-forming elements and their level of setting as carbide.

The opposed effect of toughness and hardness as well as high temperature stability requires a component-specific optimization and the consequences for the material selection and the definition of the nitriding temperature.

The toughness of the diffusion layer depends, besides its hardness, on the initial microstructure. Quenched and tempered microstructures exhibit a significantly higher toughness after nitriding compared to normalized microstructures.

A high load in the field of finite life fatigue and operational stability requires, for a case-controlled failure, high incipient crack fatigue strength and an inhibition of the crack propagation by means of high and stable compressive residual stresses, which increase in core direction. A high toughness of the surface layer, γ'-compound layers, and grinded compound layers decreases the incipient crack affinity of the surface. For bright nitriding as well as for removing the white layer by chemical reduction, a negative influence of the height and distribution of the residual stresses has to be considered (*46*).

It has to be pointed out that high strength material conditions, thus also nitrided layers, react extraordinarily sensitively to nonmetallic inclusions and microstructural inhomogeneities (*63*,*64*). For nitrided components, the appearance of late fractures also above the cycle limit of 10^7 load cycles, which is used for conventionally defining the fatigue life limit, has to be faced. In dependency of the purity grade, microstructure inhomogeneities, micronotches, and other imperfections, the incipient crack position can be located at the surface as well as beneath the surface.

12.14.3.4 Corrosion Behavior

In the early nineteenth century, it was already known that iron nitrides are characterized by an increased resistance against neutral and alkaline media. The increase of the corrosion resistance of components made of iron and steel by means of gas nitriding was the subject of many patents at the beginning of the twentieth century. However, the application of nitriding for improving the corrosion resistance of components had still been a niche technology in the leading industrial nations for a long time. Only the Soviet Union industrially used the technologies of gas and salt bath nitriding for corrosion protection in a broad extent since the 1930s. It was known, for example, that ε-nitride layers showed a considerably better resistance against sea water compared to compound layers consisting of γ'-nitrides. Weathering tests in different climates proved the unchanged appearance of ε-nitride layers after a removal time of about 1 year.

Intensive research work within the last 40 years consistently proved the increased resistance of compound layers against neutral salt solutions and atmospheric corrosion. This is particularly valid in the case of their resistance against pitting corrosion caused by chloride ions. The corrosion resistance of compound layers is defined by its phase constitution and its chemical composition. An illustration of the broad property range of variably generated compound layers is given in **Figure 54** and **Table 8**. As it can be seen, the corrosion resistance increases in the order of γ'-nitride, ε-nitride, and ε-carbonitride. The resistance of ε-nitride layers is

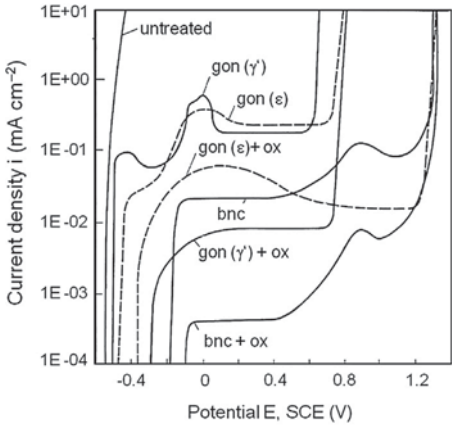

Figure 54 Potentiodynamic anodic current density/potential curves of differently treated samples of steel 20MnCr5, 0.9 M NaCl-electrolyte; gon: gas oxinitrided, bnc: bath nitrocarburized, ox: post-oxidized. Reproduced from Ebersbach, U.; Friedrich, S.; Nghia, T.; Spies, H.-J. Elektrochemische Korrosionsuntersuchungen an gasoxinitriertem und salzbadnitrocarburiertem Stahl in Abhängigkeit vom Aufbau der Nitrierschicht. *Härterei-Tech. Mitt.* **1991**, *46*, 339–349.

Table 8 Layer structure and corrosion behavior, extended

Layer parameter						
Thickness (μm)	*Structure*	*Salt-spray test*[a]	*Immersion test*[b] *(mg Fe/100 ml)*	*Corrosion potential*[c] E_{cor}, *SCE (mv)*	*Passive current density*[c] *(μA cm^{-2})*	*Pitting potential*[c] E_{pit}, *SCE (mv)*
10–14	γ′	8	143.0	−490 to −510	180	580–605
	γ′ – oxidized	23	4.6	−280 to −300	200	700–765
	ε(γ′)	8	3.3	−320 to −370	100	550–670
	ε(γ′) – oxidized	35	1.4	−190 to −210	10–20	1000–1200[e]
20–25	ε(γ′) – oxidized	43	0.7	–	10–20	1000–1200[e]
13–15	ε(C)[d]	–	–	−250 to −320	10–20	1240–1300[e]
13–15	ε(C) – oxidized	–	–	−170 to −210	0.1–3.4	1220–1280[e]
40	Hard chromium	8	2.5	–	0.02	620–740

[a]Test cycles up to first corrosion; cycles: 8 h: 35 °C, 0.5% NaCl pH = 6.5–7.2; 16 h: 20 °C, relative humidity, 75%.
[b]Test solution after Machu-Schiffmann: 50 g l^{-1} NaCl; 10 ml l^{-1} glacial acetic acid; 5 g l^{-1} 30% H_2O_2 solution; pH = 3, test duration: 4 h.
[c]Electrolyte: 0.9 M NaCl.
[d]ε(C): ε-carbonitride.
[e]Transpassivation potential E_t.

Reproduced from Ebersbach, U.; Friedrich, S.; Nghia, T.; Spies, H.-J. Elektrochemische Korrosionsuntersuchungen an gasoxinitriertem und salzbadnitrocarburiertem Stahl in Abhängigkeit vom Aufbau der Nitrierschicht. *Härterei-Tech. Mitt.* **1991**, *46*, 339–349.

significantly defined by the height of the nitrogen content (see Table 9). ε-Carbonitride layers obtaining a nitrogen and carbon concentration of about 8.6% show an optimal pitting corrosion resistance (65).

The corrosion resistance of nitrided cases can be additionally improved by means of oxidation after nitriding (Table 8). Oxidized nitrided cases considerably exceed the corrosion resistance of hard chromium cases and today, they are widely used as a substitute of such layers (67–70).

Depending on the applied treatment technology, the corrosion behavior of oxidized compound layers can differ significantly. It is considerably defined by the composition of the compound layers beneath the oxide layer and the structure of the oxide layer.

Table 9 Electrochemical behavior of ε-nitride layers in dependence from nitrogen concentration, pure iron, layer thickness: 9–11 μm

Layer	*Nitrogen concentration, wt.%*	*Pitting potential*[a] E_{pit}, *mV*	*Passive current density*[a], *mA cm^{-2}*
ε(γ′) – 7%N	7.2	640–700	0.1
ε(γ′) – 7%N-oxidised	8.9	1150–1200[b]	0.01–0.02
ε(γ′) – 9%N	9.2	1200–1350[b]	0.01–0.02

[a]Electrolyte: 0.9 M NaCl.
[b]Transpassivation potential E_t.

Reproduced from Winkler, H. P.; Spies, H.-J.; Schubert, T. Korrosionsverhalten nitrierter Eisenwerkstoffe. In Freiberger Forschungshefte; pp 49–54. Leipzig.

An oxidation at temperatures below 500 °C and times between 0.5 h and 1.5 h has been established. Under these conditions, the nitrogen, which is displaced from the near-surface areas, enriches, e.g., beneath the oxide layer. Thereby, the enriched layer reaches depths of about 8–9 μm depending on the oxidation conditions. This ensures satisfying corrosion resistances also in the case of layer wear due to an interaction of tribological and chemical loads (*67*). The results of investigations on the resistance of an oxidized compound layer against pitting corrosion, shown in **Figure 55**, confirm this conclusion. The pitting corrosion potential considerably decreases first after a layer removal of more than 8 μm.

An example of the chemical composition and the microstructure of an oxidized compound layer exhibiting a high corrosion resistance is depicted in the SEM micrograph in **Figure 56**. The compound layer mainly consists of ε-phase, in the lower areas of a nearly pore free ε-carbonitride etched dark grey and, in the near-surface areas, it consists of the light grey ε-nitride (**Figure 56(a)**). Tracks of γ′-nitride appear in the lower regions of the layer, identifiable on the white, nonetched areas. The critical value of the sum of nitrogen and carbon content being in the range of 8.6% is first underrun in a surface distance of 12.5 μm (**Figure 56(b)**).

Besides the resistance against pitting corrosion, the uniform corrosion behavior matters to describe the comprehensive corrosion behavior of nitrided cases. It can be specified by the free corrosion potential E_{cor} and free corrosion current i_{cor}. For the characterization of the uniform corrosion behavior, the reciprocal polarization resistance R_p^{-1} is often used (*68*). The reciprocal polarization resistance, measured in the vicinity of the free corrosion potential, is inversely proportional to the free corrosion current. As shown in **Table 8**, there are clear differences between the free corrosion potentials of γ′- and ε-compound layers. Starting from γ′-nitride layers to oxidized layers and ε-nitride layers to ε-carbonitride layers, the free corrosion potential is shifted in the noble direction.

The reciprocal polarization resistance provides the possibility of precisely characterizing the corrosion behavior of the ε-phase with dependence on their chemical composition described by the concentration ratio [C]/[N + C]. The results of investigations on low-alloyed steels, which have been differently nitrocarburized, are shown in **Figure 57**. As a results out of it ε-carbonitrides of the concentration range of [C]/[N + C] = 0.02–0.2 exhibit a considerably better corrosion behavior. The reciprocal polarization resistance decreases about more than 1 order of magnitude. Pure ε-nitrides und ε-carbonitrides containing high carbon contents show considerably worse uniform corrosion behavior.

Compound layers also exhibit an increased resistance against the attack of molten metals. Again, this property can be improved by means of a subsequent oxidation. This has been proved by investigations on samples of the steel X38CrMoV5-1 nitrided

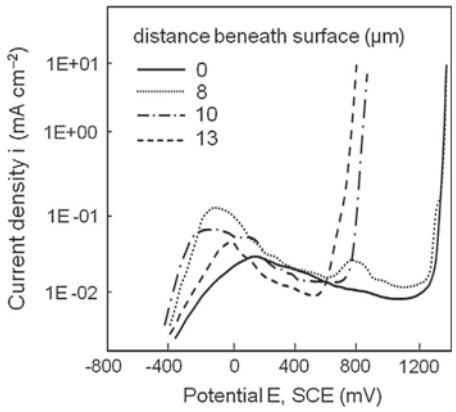

Figure 55 Change of potentiodynamic anodic current density/potential curves of nitrided and post-oxidized steel S355 with increasing distance from the surface; compound layer thickness 20 μm; 0.9 M NaCl electrolyte. Reproduced from Winkler, H. P.; Spies, H.-J.; Schubert, T. Korrosionsverhalten nitrierter Eisenwerkstoffe. In Freiberger Forschungshefte; pp 49–54. Leipzig.

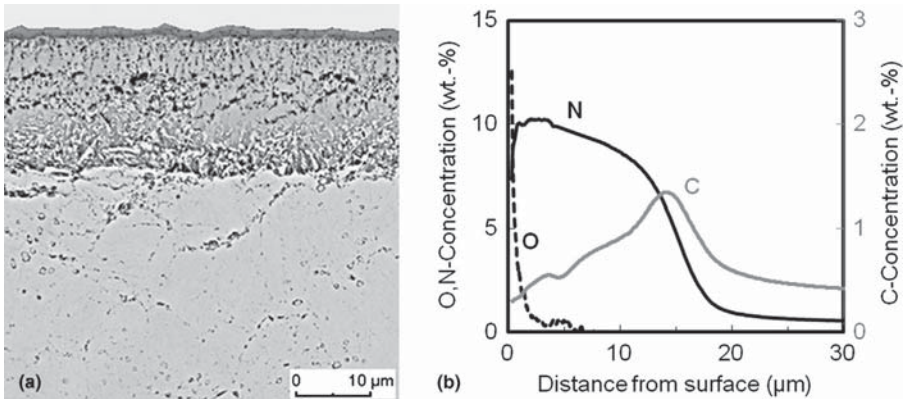

Figure 56 Gas nitrocarburized and oxidized compound layer of steel 42CrMo4: (a) microstructure, etchant: alkaline sodium picrate solution and (b) concentration profile.

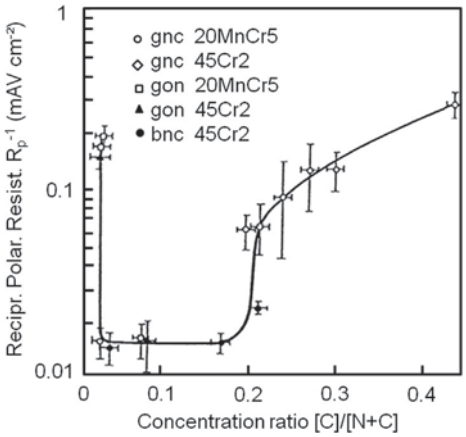

Figure 57 Reciprocal polarization resistance of nitrided and nitrocarburized samples in dependence on the concentration ratio [C/C + N] in the ε-phase, steels: 20MnCr5 and 45Cr2; 0.9 M NaCl electrolyte, gnc: gas nitrocarburized, gon: gas oxinitrided, bnc: bath nitrocarburized. Reproduced from Ebersbach, U.; Friedrich, S.; Nghia, T. Structure and Corrosions Behavior of Nitride Layers. In *Proc. Surf. Eng*; DGM Informges: Bremen, 1993; pp 299–304.

differently. Thereby, the mass of the samples lost after a 4 h attack of molten aluminum at 735 °C was determined. Due to a nitriding with generating a compound layer the mass lost determined on non-nitrided samples decreased on the average of 580 mg cm^{-2} to 85 mg cm^{-2}. An oxidation of the compound layer results in a further decrease of the mass lost to 32 mg cm^{-2}.

The development of processes for generating oxidized carbonitrided layers started from the development of the Q and QPQ process in the 1980s (*70*). Nearly at the same time the NITROTEC process was developed in Great Britain (*43*). The QPQ process, developed out of the tuff nitride Q process, consists of a salt bath nitrocarburizing treatment with an oxidizing quenching followed by a polishing step and a requenching in an oxidizing atmosphere. In the NITROTEC process, gas nitrocarburizing is followed by oil quenching, post-oxidizing, and impregnation with a corrosion-inhibiting sealant protection. Also, recent investigations proved that a polymer post-impregnation treatment definitively increases the corrosion resistance of oxinitrided steels (*71*,*72*).

For the generation of oxidized carbonitrided layers having optimal corrosion behavior, a multitude of process variants are available today. Besides the bath nitrocarburization, gas nitrocarburization and plasma nitrocarburization are also used. Due to the development of the controlled nitriding, it is possible today, for all three processes, to generate ε-carbonitride layers having a high corrosion resistance by means of adjusting the defined nitrogen and carbon contents.

On austenitic and ferritic stainless steels, no compound layer is generally formed under normal nitriding conditions. The bonding of chromium within the precipitation layer results in a breakdown of its corrosion resistance. A possibility of improving the tribological load capacity of these steels by simultaneously keeping the excellent corrosion resistance offers a nitriding or carburizing treatment at temperatures below 450 °C. The formation of precipitates causing a depletion of chromium in the matrix is strongly impeded in this temperature range. Depending on temperature and time of this low-temperature treatment, the nitrogen or carbon within the case remain, dissolved. A strongly dilated austenite, an expanded austenite (γ_N or γ_C), is generated, which is distinguished by a high hardness and high compressive residual stresses (*73*).

An illustration of the influence of the treatment conditions on the corrosion behavior of stainless austenitic steels conveys the results of electrochemical investigations shown in **Figures 58 and 59**. The pitting corrosion behavior in aqueous 0.5 M NaCl solutions and the passivation behavior in dilute H_2SO_4 solutions (0.05 M) have been characterized by means of potentiodynamic measurements using a potential feed rate of 0.2 V h^{-1} (NaCl) and 1.8 V h^{-1} (H_2SO_4), respectively.

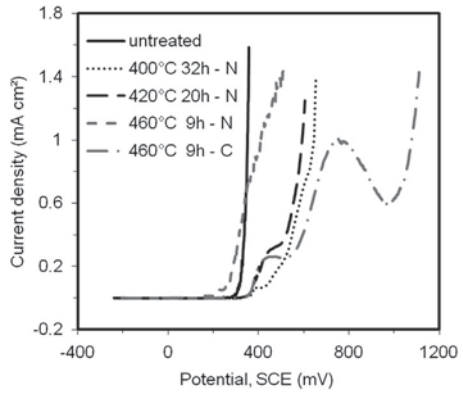

Figure 58 Anodic polarization curves of differently treated samples of steel X2CrNiMo17-12-2; 0.9 M NaCl-electrolyte, N: nitrided, C: carburized. Reproduced from Spies, H.-J.; Bell, T.; Kolozsvary, Z. Thermochemical Surface Treatment of Stainless Steels at Low Temperatures. *Härterei-Tech. Mitt.* **2010**, *65*, 11–21.

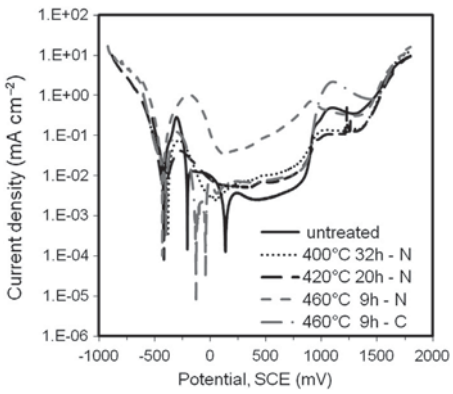

Figure 59 Anodic polarization curves of differently treated samples of steel X2CrNiMo17-12-2; 0.05 M H_2SO_4 electrolyte. N: nitrided, C: carburized. Reproduced from Spies, H.-J.; Bell, T.; Kolozsvary, Z. Thermochemical Surface Treatment of Stainless Steels at Low Temperatures. *Härterei-Tech. Mitt.* **2010**, *65*, 11–21.

As can be seen in Figure 58, the resistance against pitting corrosion is considerably increased by means of nitriding as well as carburization. Only the nitriding treatment applying 9 h at 460 °C resulted in a decrease of the pitting corrosion potential within the less noble areas. For this treatment condition, metallographic investigations showed the formation of chromium nitride precipitates at grain boundaries within the near-surface regions. In contrast, layers generated by means of carburization under comparable treatment conditions have been free of precipitation. This is evidence of the higher thermal stability of the expanded carbon austenite as described in the literature several times (*75*).

In contrast to pitting corrosion, the passivation behavior is not changed by a low-temperature nitriding treatment at 400–420 °C compared to the initial condition (Figure 59). This is clear evidence for the formation of a single-phase, precipitation-free surface layer. The chromium depletion within the region near the grain boundaries caused by the precipitation of chromium nitrides during the nitriding treatment of 460 °C for 9 h considerably influences the developing of the current density potential curve. Being characteristic for a starting intercrystalline corrosion, the current density for passivation and the current density within the passive region clearly increase. In contrast, between the profiles of the current density potential curve obtained on a carburized sample, treated at 460 °C for 9 h, and the initial condition nearly no difference exists. So, also the passivation behavior confirms the higher thermal stability of the expanded austenite.

Due to the attractive possibilities for improving the tribological load capacity of stainless steels without losing their corrosion resistance, the low-temperature nitriding treatment of these steels have been the subject of intensive research work for the last 20 years. Based on deepened knowledge concerning the thermal stability of expanded austenite, the work resulted in the development of industrially used treatment processes.

An overview of the characteristics of nitriding, carburizing, and nitrocarburizing processes at low temperatures is given in Table 10. The duplex layers generated by means of nitrocarburizing and the combination of carburization and nitriding, respectively, exhibit the high surface hardness of nitrided cases as well as the high thickness and the smooth hardness profile of carburized layers. Thus, they combine the advantages of nitriding and carburizing. Varying the carbon supply and the temperature and time, respectively, of the single processes for a sequential treatment and the variation of nitrogen and carbon potential during a duplex treatment, respectively, modifies their structural constitution within broad limits (*74*). Hence, for numerous applications, such layers provide optimal solutions. Between layers with equal compositions, which are generated by means of different processes, no fundamental differences exist.

Table 10 Characteristics of low-temperature nitriding, carburizing, and nitrocarburizing according to Bell and Sun, extended

	Process		
Features	*Nitriding*	*Carburizing*	*Nitrocarburizing*
Temperature, °C	300–450	300–520	300–450
Layer thickness, μm	2–15	5–45	5–30
Layer uniformity	Good	Very good	Very good
Layer structure	Precipitation-free expanded austenite		
Corrosion resistance	Good	Good	Good
Surface hardness, HV0.05	1400–1600	900–1100	1400–1600
Hardness profile	Abrupt	Gradual	Gradual
Wear resistance	Very good	Good	Very good
Layer toughness	Poor	Very good	Good
Load-bearing capacity	Low	High	High

Reproduced from Bell, T.; Sun, Y. Low Temperature Plasma Nitriding and Carburizing of Austenitic Stainless Steels. In *Stainless Steel 2000, Proc. Int. Sem. Osaka/Japan, 2000*; Maney Publ: London, 2001; pp 275–288.

12.14.3.5 Tribological Behavior

12.14.3.5.1 Overview

The surface load of a component due to contact and relative movement of a counterbody is called tribological load. It is primarily operative within the material areas that form the surface. The indicated changes of shape, size, and amount of a part as well as material loss within the surface layer are described by the wear behavior as a property of a tribosystem. The wear behavior depends on the load as well as the combined properties of the friction counterparts. Therefore, it is significantly more complex and difficult to overview in contrast to the behavior at mechanical load of a component volume.

By means of model wear tests the friction and wear behavior of materials, which is dependent on many influencing factors, can be described, but only in rough approximation.

The results concerning the wear behavior of nitrided components published in the literature are very different from each other and partly contradictory. This is comprehensible due to the numerous nitriding and nitrocarburizing processes being industrially used in practice and therefore resulting variation range in nitride layer structure as well as the complex effect of tribological loads.

The characterization of the wear behavior of materials through the classification of their resistance to the separate or superimposed effect of the wear mechanisms of abrasion, adhesion, tribo-oxidation, and contact fatigue has been proved.

Abrasion conventionally defines a material removal by means of micro cutting as a result of a two-body abrasion. It arises at solid friction and mixed friction first of all due to mechanical interaction of the roughness heights of the contact partner in the micro scale. These can lead to a material removal due to micro shear fracture, micro brittle fracture, and micro fatigue fracture. The resistance of a material to the effect of these elementary processes is defined by its strength. Thus, the material's resistance against abrasive wear is directly proportional to its hardness. This is also valid for the wear resistance of compound layers (*76*) as depicted in **Figure 60**.

Adhesive wear arises due to the formation of atomic bonds between the friction partners and a following shearing outside the initial contact area. It presupposes an approach on atomic scale distance due to a plastic deformation and adequate bonding forces. A high resistance against adhesive wear requires a low plastic deformability of the micro contact areas and a reduction of the formation of adhesive bindings. Therefore, the hardness and crystal structure have a strong influence on adhesion. Compared to metals having a fcc and bcc crystal structure, hexagonal metals exhibit a minor adhesive behavior (*77,78*). The ε-nitrides and carbonitrides of iron have a high hardness as well as a hexagonal crystal structure and therefore a strongly limited plastic deformability. Due to the at least partially covalent bindings, the density of metallic electrons available for adhesive bindings is very low (*77*). Compound layers consisting of ε-nitride and carbonitride are distinguished by high resistance against adhesive wear.

Tribochemical reactions being frictionally induced modify the strength properties of the surface areas due to the formation of oxide layers. With solid friction and mixed friction, they generally lead to a decrease of the wear resistance due to the promotion of loose debris particles. In contrast to this, for lubricated combinations, adherent thin reaction layers are formed acting wear reductive.

Contact fatigue occurs at loads in rolling contacts, which are frequently accompanied by slip and sliding contacts. The slip for bearings is about 3%, and for gears 24%. Contact fatigue, for example, is a major cause of failure in rolling-elements bearings, gear teeth, wheel-rail contacts, and rolling mill rolls. Contact fatigue behavior is defined by the strength and residual stress distribution within the area of the load maximum. Its depth position beneath the surface is defined by the height of the normal load and the contact geometry. A change in the load condition due to frictional tangential loads leads to yielding of the material at considerably lower surface pressures. Therefore, the increase of the slip causes a decrease of the rolling contact strength. The increase of the slip

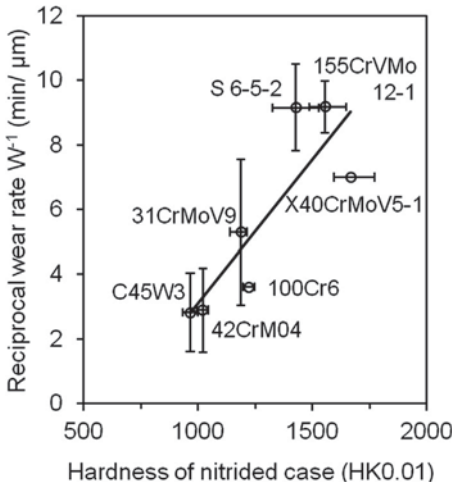

Figure 60 Resistance of compound layers, 5 µm distance beneath the surface, against two-body abrasion, grinding test, SiC grit 600. Reproduced from Habig, K.-H.; Li, Y. Rauheits- und Verschleißprüfungen an Verschleiß-Schutzschichten. *Härterei-Tech. Mitt.* **1982**, *37*, 180–192.

from 3% up to 24% caused, for example, a decrease of the rolling contact strength (10^8 cycles) of nitrided samples of the steel 31CrMoV9 from 3400 MPa to 3000 MPa.

High local compressive residual stresses and high local strength ensure a high resistance against fatigue damage of the surface area compared to volume fatigue. Irreversible changes of the material condition during the whole life cycle are characteristic for the effect of the load during a rolling contact (*79–81*). Therefore the rolling contact strength is only strength for finite life.

12.14.3.5.2 Layer Structure and Wear Behavior

Based on the depth effect of the load, the behavior of nitrided steels during abrasion, adhesion, and tribo-oxidation is mainly characterized by the structure of the compound layer. The properties of the diffusion layer are essentially for the behavior during contact fatigue due to the connected load and contact geometry-dependent increased depth effect.

One example for a typical hardness profile within the nitrided case of a low-carbon non-alloy steel is shown in **Figure 61**. In the area of the pore seam, the hardness increases from 400 HK0.025 to a maximum value of 1100 HK0.025 within the nonporous ε-zone. Within the diffusion layer, it decreases almost immediately to the core hardness of 180 HK0.025 (*82*). Resulting from the described relations, an analogue profile is obtained for the wear resistance to abrasive/adhesive loads (**Figure 62**). The porous seam, having a low wear resistance, is attached to the porous free zone of the compound layer, which is distinguished by a high resistance against abrasion and adhesion due to its high hardness and phase composition. Within the diffusion layer of unalloyed steels, the wear resistance, according to the hardness decrease, rapidly decreases to the base material level (*83*).

The pore-conditioned increased running-in wear can be desired in the case of a sliding load because of the improved geometry matching and connected improved contact pattern, respectively, and therefore leading to decreased specific contact surface pressure (*84*). In contrast to this, for numerous component assemblies, especially for closed tribosystems, a minor abrasion during the running-in-period and therefore a minor porous seam are requested.

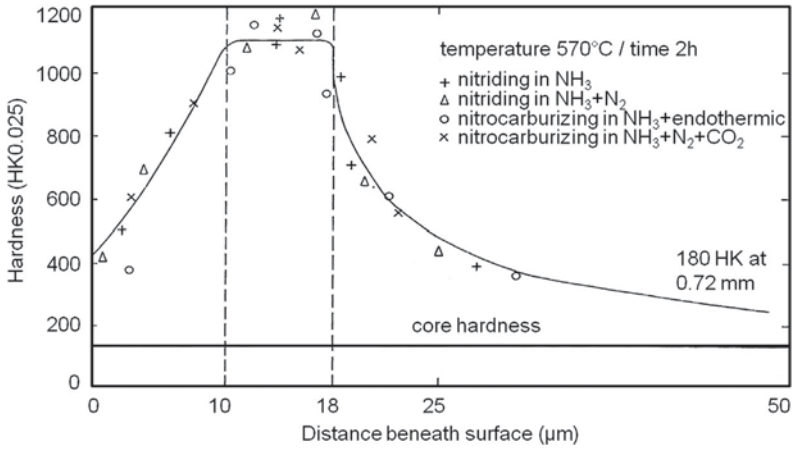

Figure 61 Effect of nitriding and nitrocarburizing followed by oil quenching on case hardness profile of non-alloy low carbon steel. Reproduced from Dawes, C.; Tranter, D. F.; Smith, C. G. *Reappraisal of Nitrocarburizing and Nitriding When Applied to Design and Manufacture of Non-alloy Steel Automobile Components*, *Heat Treatment '79*; The Metals Soc: London, 1980; pp 60–68.

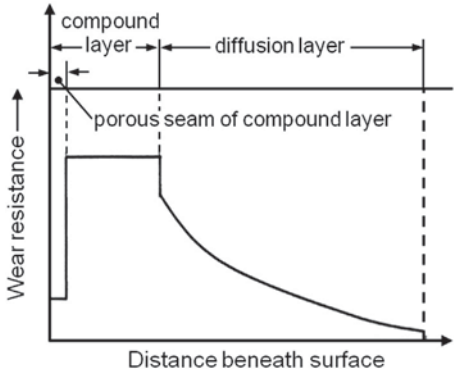

Figure 62 Wear resistance of nitrided layers as function of distance from surface. Reproduced from Hoffmann, F., et al. Verschleiβwiderstand nitrierter und nitrocarburierter Stähle. *Härterei-Tech. Mitt.* **1997**, *52*, 376–386.

As expected, the wear behavior of compound layers is remarkably influenced by the phase composition. Based on the described reasons for the verification of an optimal resistance against adhesion and abrasion, a high amount of ε-phase within the compound layer is desired. A high carbon content, which increases with increasing depth within the compound layer, is recommended due to the major wear resistance of the ε-carbonitride compared to the ε-nitride (*84,85*). For selected loads, also thin porous free γ′-layers have been proved. Concerning the influence of the compound layer thickness on the wear behavior, different and conflicting results have been reported. This can be traced to the extremely different effects of tribological loads, which are strongly dependent on the structure of tribological systems. The optimal structure of the compound layer is always load specific and therefore very different.

Due to an oxidation of compound layers, their hardness increases, especially in the range of the porous seam (*86*). A very significant hardness increase was proved in case of bath-nitrocarburized samples (**Figure 63**). It can be attributed to the strong porosity that is characteristic for this nitriding process. The hardness increase and the modified behavior against a tribo-oxidation cause a significant improved wear behavior both at adhesive and abrasive loads (*86–89*).

Results of investigations on nitrided as well as nitrided and oxidized samples of steel C45 are given in **Table 11**. The resistance to abrasion was evaluated with the abrasion energy density, which was determined by means of scratch tests at the surface after the removal of the porous seam within a depth of 5 μm (*89*). For characterizing the sliding wear behavior, the linear wear intensity was determined with a tribometer according to Siebel/Kehl. As can be seen in **Table 11**, oxidation of the compound layer causes an increase in surface hardness and in abrasive energy as well as a decrease of the linear wear intensity. It is remarkable that the effect of the oxidation could be proved by means of the scratch test even in a depth of 5 μm. This can be traced to the increase of nitrogen concentration due to the oxidation, which has been discussed in relation to the corrosion behavior of oxidized compound layers in Section 12.14.3.4. The depth effect of the oxidation is also clearly visible at the hardness profile shown in **Figure 63**.

An idea of the wear behavior of sliding combinations of differently treated steels at dry friction on air is given in **Table 12**. At this load, the material combination of quenched and tempered steels C60 and C45 shows the lowest wear resistance. They fail due to strong adhesive–abrasive wear. For the contact combination of hardened and tempered steels showing hardness values above 400 HV, wear reductive reaction layers are generated, which lead to a decrease in wear coefficient of one order of magnitude. Contact combinations of steels nitrided with a compound layer and nitrocarburized, respectively, follow. Their wear coefficients differ only

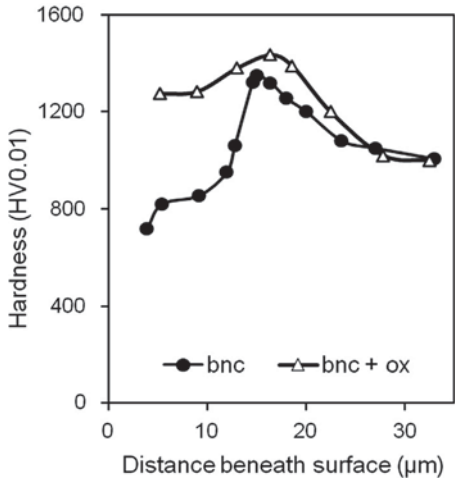

Figure 63 Effect of post-oxidation on case hardness profile of bath nitrocarburized steel 20MnCr5. Reproduced from Nghia, T. T. Korrosions- und Verschleißverhalten von nitrierten und nitrocarburierten Stählen. Dissertation, TU-Bergakademie, Freiberg, 1994.

Table 11 Wear behavior of gas oxinitrided and oxidized compound layers, steel C45

Compound layer thickness (μm)	*Type*	*Surface hardness (HV1)*	*Abrasion energy density ($J\,mm^{-3}$)*[a]		*Wear intensity*[b] *($m\,m^{-1}$)*
			Surface	*5 μm depth*	
12–14	ε(γ′)	585	6.7	9.3	$2.0 \cdot 10^{-9}$
	ε(γ′) – oxidized[c]	696	9.3	12.4	$0.9 \cdot 10^{-9}$
19–21	ε(γ′)	616	6.3	8.8	$2.9 \cdot 10^{-9}$
	ε(γ′) – oxidized[c]	648	8.3	11.6	$1.2 \cdot 10^{-9}$

[a] $\omega_R = W_A \cdot V_R^{-1}$; W_A = abrasion energy, V_R = scratch volume.
[b] Linear wear intensity $W_l = d_W\,s^{-1}$; d_W = wear depth, s = wear way (length).
[c] Oxidized: about 1 μm Fe_3O_4.

Reproduced from Spies, H.-J.; Mothes, A.; Pursche, G. Zum Verschleißverhalten oxydierter Nitrier-schichten. *Schmierungstechnik 1989*, *20* (6), 177–178.

Table 12 Wear coefficient of sliding couples of differently heat-treated steels during dry friction in air

			Surface layer		
Wear rate[a,b] *($mm^3\ N^{-1}\ m^{-1}$)*	*Steel*	*Heat treatment*[c]	*Hardness*	*Phases*	*Thickness (μm)*
$4.3 \cdot 10^{-4}$	C60	QT/560/1 h	300 HV10	temp. Ms	
$4.1 \cdot 10^{-4}$	C45	QT/550 °C/1 h	289 ± 11 HV10	temp. Ms	
$4.3 \cdot 10^{-5}$	C60	QT/430 °C/1 h	~450 HV10	temp. Ms	
$2.8 \cdot 10^{-5}$	C45	QT/220 °C/0.5 h	592 ± 30 HV10	temp. Ms	
$2.0 \cdot 10^{-5}$	C110W1	QT/220 °C/1 h	724 ± 27 HV10	temp. Ms	
$1.6 \cdot 10^{-5}$	C110W1	Q	904 ± 57 HV10	Ms	
$1.6 \cdot 10^{-5}$	42CrMo4	BNC/570 °C/2 h	370–530 HV0.05	ε-$Fe_{2-3}N$ (FeS)	14
$1.5 \cdot 10^{-5}$	42CrMo4	BNC/580 °C/2 h	715 HV0.05	ε-$Fe_{2-3}N$	14
$1.4 \cdot 10^{-5}$	34CrAlNi7	GN/520 °C/72 h	~900 HV0.2	$\varepsilon + \gamma'$	50
$1.2 \cdot 10^{-5}$	C45	GNC/570 °C/2 h	554 HV0.2	ε-$Fe_{2-3}N$	8
$1.0 \cdot 10^{-5}$	42CrMo4	GNC/570 °C/2.5 h	810 HV0.05	ε-$Fe_{2-3}N$	9
$7.9 \cdot 10^{-6}$	42CrMo4	BNC/570 °C/2 h	722 ± 29 HV0.2	ε-$Fe_{2-3}N$	13
$7.2 \cdot 10^{-6}$	42CrMo4	PN/500 °C/36 h	900 HV0.05	γ′-Fe_4N	4
$4.3 \cdot 10^{-7}$	34CrAlNi7	GN/520 °C/72 h	~900 HV0.05	CL abraded (grind down)	

[a]Pin on disc, $F_N = 5$ N and 10 N; $v = 0.1$ m s^{-1}; $s = 1000$ m, equal material of pin and disc.

[b]Wear rate $k = W_V \cdot F_N^{-1}\ s^{-1}$; W_V = wear volume, F_N = normal load, s = sliding distance.

[c]QT: quenched and tempered, Q: quenched, BNC: bath nitrocarburized, GN: gas nitrided, GNC: gas oxinitrided, PN: plasma nitrided.

Reproduced from Habig, K.-H.; Chatterjee-Fischer, R.; Hoffmann, F. Untersuchungen des Gleit und Furchungsverschleißes an thermochemisch behandelten Stählen. *Mat.-wiss. u. Werkstofftech* **1982**, *13*, 207–215.

by a factor of 2.2. A systematic influence of the nitriding treatment and the phase composition, respectively, was not noticed. Such relations can only be detected by a detailed characterization of the compound layer structure. The low k-value of the sliding contact combination of the gas-nitrided steel 34CrAlNi7 with the compound layer removed indicates that hard diffusion layers exhibit a high wear resistance for the given load.

The sliding wear resistance of unalloyed and low-alloyed steels nitrided with a compound layer exceeds the resistance of contact combinations of steels having a microstructure of carbon-rich martensite (Table 12, steel C110W1) and is situated at their upper limit, respectively (*90*). Tribologically loaded components with contact combinations of nitrided unalloyed and low alloyed steels have therefore been proved, especially with regard to their high resistance against adhesion, within numerous industrial applications, e.g., automotive and engine industry, hydraulic industry, power train, and conveyor technique.

This is depicted in Figure 64, which shows the surface microstructure of a nitrided gear tooth flank of a truck gear box after a running duration of 600 000 km and for comparison also the microstructure of the unloaded tooth root. It is clearly visible that only a small part of the porous seam has been removed due to the load. The wear-conditioned removal is about 1–3 μm compared to the layer thickness within the tooth root.

The wear behavior of diffusion layers is primarily characterized by their hardness. Their resistance against adhesive wear is structurally dependent and very low. At room temperature, it does not significantly differ from the behavior of hardened as well as quenched and tempered steels having equal hardness. Of importance is the high thermal stability of nitrided microstructures

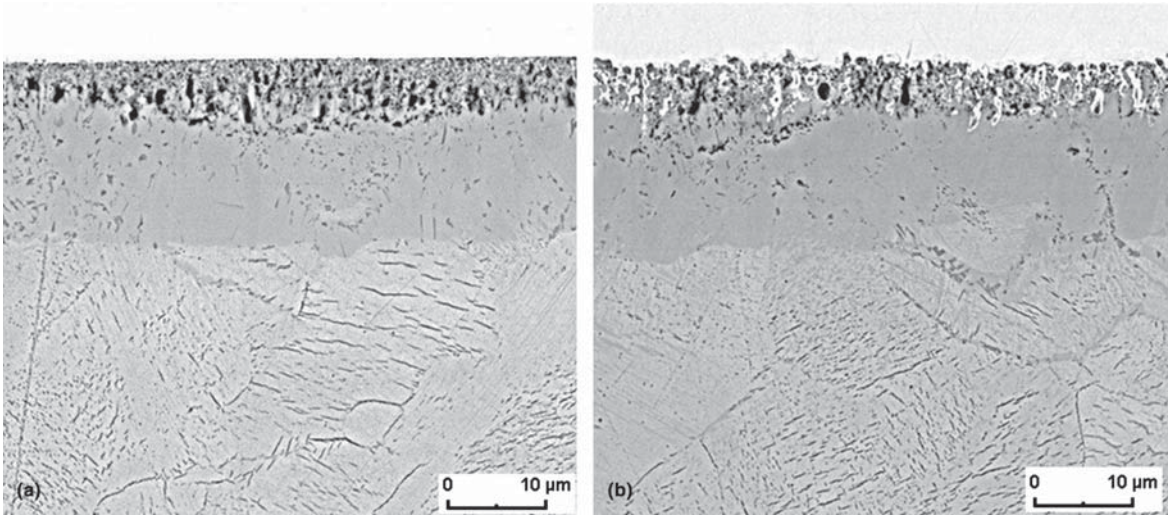

Figure 64 Microstructure of nitrided case of a gear after 600 000 km running time, steel C45 (a) tooth flank and (b) tooth root.

strengthened due to precipitation hardening, as described in Section 12.14.3.3. Their high hot strength gives nitrided components that are thermal and tribologically loaded, e.g., tools for hot forging, a high resistance against hot wear.

For industrial applications, the increased resistance of diffusion layers against rolling contact wear is of great importance. It is mainly defined by the hardness and residual stress profile. A high resistance to the effect of the shear stresses induced by the surface pressure requires a strength profile that considers the load specification by means of an adequate high and deep strengthening.

Table 13 depicts the results of rolling contact wear tests at nitrided and case-hardened samples of steels 20MnCr5, 31CrMoV9, and X38CrMoV5-1. They were determined on cylindrical sample of 20 mm in diameter. The tests were performed on a two-plate rolling contact testing apparatus with wick-feed lubrication and velocity-vibration sensor. The values given in **Table 13** for the absolute height of the fatigue strength after 3×10^7 over-runs result from the test conditions, especially from the contact geometry and the slide of 8%. The presented strength values are not transferable to components, but they allow the determination of relations between structure and rolling contact strength.

From the results it can be reasoned that considerable differences in hardness depth, core hardness, and compound layer structure do not significantly influence the rolling contact strength. The values obtained for nitrided samples are within the range of 4334–4442 MPa. Only the samples of the conditions 7 and 8 having surface hardness of 788 HV0.1 and 935 HV0.1 exhibit significantly higher rolling contact strength. This could be due to the strength and residual stress distribution within the area of the load maximum, which is situated at a depth of about 180–220 μm beneath the surface for the given test conditions. In a comparable depth, the hardness of the conditions 3–6 is in the range of 570–620 HV0.1, in contrast for condition 7 at 685–700 HV0.1 and for condition 8 at 760–770 HV0.1. The high diffusion layer hardness of the steel X38CrMoV5-1 in the range of the load maximum and in combination with the high compressive residual stresses (635 MPa adverse to 375 MPa) leads at equal normal load to a lower local plastic deformation and therefore to a lower material stress. This explains the high rolling contact strength.

The rolling contact strength of case-hardened samples classifies within the dependency being described for nitrided samples. This is also confirmed by industrial experience whereby no differences exist between case-hardened and nitrided components at low load depths. Limits for the nitriding result from the reachable diffusion depth. Due to the low treatment temperatures, compared to the case hardening, the depth is clearly beneath the ones that can be reached after case hardening.

Also the wear behavior of stainless ferritic, austenitic, and ferritic-austenitic steels can be significantly improved by nitriding and nitrocarburizing, respectively. The chromium nitrides and carbides formed within the case at common treatment temperatures between 500 and 600 °C lead to chromium depletion of the matrix and a strong decrease of the corrosion resistance. Therefore, stainless steels are nitrided within this temperature range only in exceptional cases. Through an adequate low treatment temperature, the formation of precipitates can be suppressed, and thus the corrosion resistance is kept. A surface microstructure consisting of expanded austenite is developed which is characterized by high hardness and high compressive stresses (compare also Section 12.14.3.4 corrosion behavior) (*73*).

The sliding wear behavior determined by means of a pin-on-disc tribometer at atmospheric dry friction conditions, **Figure 65**, can be considerably improved by a low temperature treatment (*74*). The highest wear resistance offer plasma nitrided samples (PN), due to a lower case hardness the wear resistance of carburized samples (PC) is slightly decreased. The outer case of nitrocarburized samples (PNC) consists of expanded nitrogen austenite; its wear behavior is therefore comparable to the one of nitrided samples. The surface of gas oxinitrided samples consists of a thin magnetite layer and beneath it a layer of expanded nitrogen austenite. This explains the higher wear rate compared to plasma nitrided samples. Samples of the duplex steel show a structural related higher wear resistance.

The influence of plasma nitriding and gas oxinitriding on the rolling wear behavior of AISI 304 steel at solid friction is shown in **Figure 66**. Also in the case of such a load condition, nitriding leads to a significant enhancement of the wear resistance. However, the increase in wear resistance during these test conditions is clearly lower compared to the pin-on-disc test. Also, the order of

Table 13 Layer structure and rolling contact strength of differently treated samples of steels 20MnCr5, 31CrMoV9, and X38CrMoV5-1

		Hardness (HV0.1)			*Compound layer*		
Steel	*Treatment*[a]	*Case*	*Core*	*Thickness*[b] *(mm)*	*Thickness (μm)*	*Structure*	*Rolling contact strength*[c] *(MPa)*
20MnCr5	CH	760	500	0.52	–	–	4303
20MnCr5	CH	760	500	0.72	–	–	4501
20MnCr5	GON	640	200	0.55	30	ε(γ′)	4442
20MnCr5	GON	600	200	0.63	11	γ′(ε)	4222
20MnCr5	GON	630	265	0.67	21	ε(γ′)	4438
31CrMoV9	GON	735	330	0.40	Bright		4372
31CrMoV9	GON	788	345	0.53	9	γ′(ε)	4596
X38CrMoV5-1	GON	935	430	0.38	9	γ′(ε)	4709

[a]CH: case hardened; GON: gas oxinitrided.

[b]Limit of hardness: core hardness + 50 HV0.1.

[c]Slip: 8%; limit of rolling cycles: $3 \cdot 10^7$.

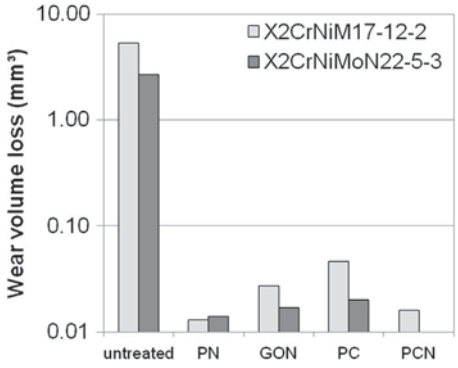

Figure 65 Wear volume of differently treated samples, $T_N = 420\,^{\circ}C$, $t_N = 20$ h; pin-on-disc test, $F_N = 10$ N, counterbody: hard metal ball with 10 mm diameter, wear distance: 600 m (untreated), 1200 m (treated).

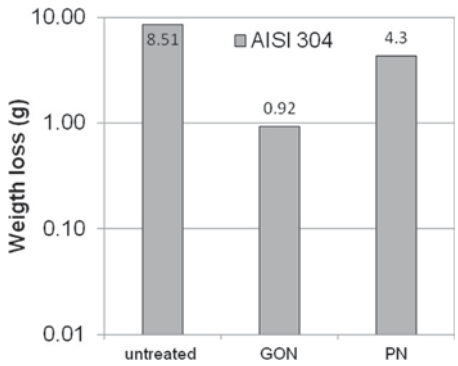

Figure 66 Accumulated weight loss from a pair of wheels under dry condition, Amsler rolling-sliding wear test (slip: 10%), test time: 1.5 h; load F_N: 500 N; AISI 304 steel; $T_N = 420\,^{\circ}C$, $t_N = 20$ h. Reproduced from Spies, H.-J.; Bell, T.; Kolozsvary, Z. Thermochemical Surface Treatment of Stainless Steels at Low Temperatures. *Härterei-Tech. Mitt.* **2010**, *65*, 11–21.

precedence is changed. For the given test conditions, the lowest wear rates have been exhibited by the gas oxinitrided samples. This could be a result of a modified wear mechanism due to the mentioned magnetite layer.

The relations described reveal that the wear behavior of nitrided components and tools strongly depend on the test conditions and the load conditions for a specific application. The use of these generalized relations requires their specification by a preferably comprehensive analysis of the respective tribosystem. Thereby, the friction condition (solid body friction, mixed friction) and the wear mechanism have to be estimated, from which the function of the system is jeopardized the most (function limitative effect). In view of the great variety of actual loads, only from this it is possible to conduct a preselection of suitable materials and treatment conditions.

12.14.4 Selection of Steels and Nitriding Conditions for the Manufacture of Load-Specific Nitrided Cases

12.14.4.1 Overview

As arising from Sections 12.14.1 and 12.14.2 the structure of nitrided cases can be modified in wide limits. For nitriding, in contrast to other techniques, this opens up a large scale of possible applications for the formation of load-specific nitrided surface layers.

The exploitation of the high property potential of nitrided layers requires the generation of designed surfaces by means of a controlled nitriding.

> Controlled nitriding involves the application of nitriding technologies to achieve optimal properties of structural components for specific applications by means of the formation of nitrided layers with a defined load specific layer structure. This involves also the design of load and nitriding specific components (25,31)

At present, only gas nitriding and nitrocarburizing technologies offer the right set of conditions for thermodynamically based process control. During plasma nitriding, the nitriding potential of the plasma is adjusted by means of the process gas composition (ratio of nitrogen to hydrogen) and the plasma parameter.

Prerequisites for controlled nitriding and nitrocarburizing are as follows:

- Knowledge about the optimal structure of the composite nitrided case/substrate for a given specific load as a basis for an application-oriented selection
- Knowledge about the nitriding behavior of components in dependence from the material and the nitriding conditions, as a basis for the selection of the substrate material and the process parameter
- Monitoring and control of the nitriding parameter in the case of gas processes, especially the chemical potentials of nitrogen, carbon, and oxygen in the process gas

The basic concept of controlled nitriding, the natural sequence of events involved in the manufacture of components using nitriding procedures, can be summarized as in **Figure 67**. The decision to modify specifically the properties of the surface signifies that some existing properties of the substrate are necessary for the component to fulfill its function satisfactorily and economically acceptable. The first step is to determine the required engineering properties of the surface/substrate compound. The selection of the substrate material implies, the requirements on the volume properties, the heat treatment condition, and the required nitridability, i.e., the concentration of nitride-forming elements.

The heat-treating condition before nitriding has to be selected based on the requirements of the substrate properties and the layer toughness. The necessary concentration of nitride-forming elements can be estimated from the in Section 12.14.2 and 12.14.3.2 explained relations between the chemical composition and the hardness increase as well as the residual stresses by consideration of the nitriding conditions and the heat-treating condition of the substrate.

The nitriding parameters as well as the nitriding potential, nitriding temperature, and nitriding time are selected on the basis of the nitriding behavior of the components.

For *in situ* monitoring and control of the nitriding parameter in gas phase processes (*gas nitriding and nitrocarburizing*) for more than 20 years, oxygen sensors, based on ion conducting solid electrolytes, have been proved successfully. In the last few years, the development of hydrogen sensors has complemented the solid electrolyte sensors in a practical way.

12.14.4.2 Selection of Load-Specific Nitrided Cases

From the relationships between the structure and properties of nitrided cases indicated in Section 12.14.3 recommendations result for the selection of load-specific nitrided cases (**Table 14**). These recommendations are greatly simplified. The types of load mentioned in the first column include a large number of specific applications. Hence the resulting demands on the case properties cannot be met by a defined single layer. Therefore the recommendations should be adapted to the specific applications on the basis of a system analysis. This applies to the selection of the thickness, the phase, and chemical composition of the compound layer, as well as the hardness and residual stress distribution in the diffusion layer, which are strongly influenced by the substrate material and the nitriding temperature.

The variety of actual loads also explains the differing literature data due to the nonunanimous opinions of specialists on the optimum structure for specific applications.

The required support of the compound layer depends on the surface pressure. For low surface pressure, it is possible to use non-alloyed steel or cast iron as substrate. The requirements in surface hardness or hardness increase and case depth compared with the non nitrided substrate material grow with increasing surface pressure.

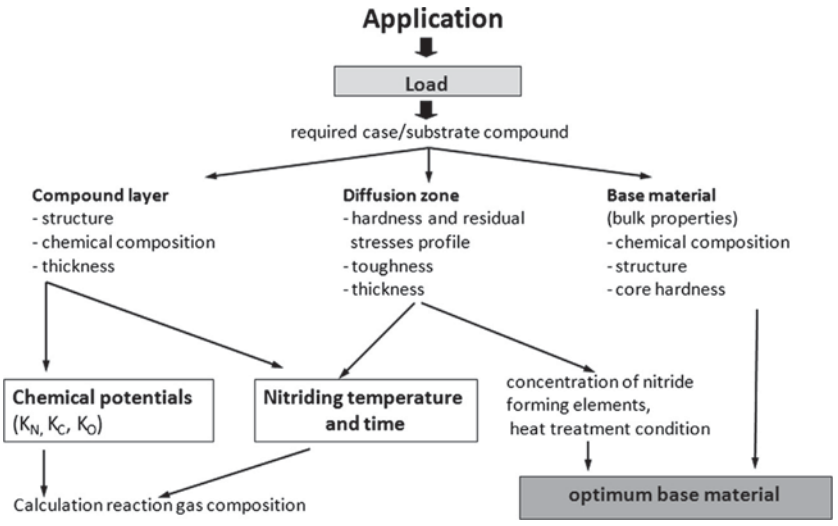

Figure 67 Basic concept of controlled nitriding, sequence for selection of base material and nitriding conditions.

Table 14 Recommendations for the selection of load-specific nitrided cases

Load	Compound layer		Diffusion zone
	Type	*Thickness (μm)*	
Abrasive wear	ε(N,C) – ox.[a], ε(γ′), γ′	>10	High surface hardness depth
Adhesive wear	ε(N,C) – ox.[a], ε	>10	High surface hardness
Corrosion	ε(N,C) – ox.[a], ε(N,C), ε	15–20	Less importance
Molten metal	ε(N,C) – ox.[a], ε	>10	Less importance
Contact fatigue	ε(N,C), ε, γ′, without comp. layer	0…<10	High: ● Surface hardness (>600 HV0.1) ● Nitriding hardness depth > 0.35 mm ● Case depth > 0.15 mm ● Toughness[b] ● Internal stresses
Fatigue	Less importance		High: ● Surface hardness, ● Core hardness, ● Hardness increase ● Case depth, ● Toughness[b] ● Internal stresses
Thermal fatigue	Less importance		High: ● Surface hardness (>1000 HV0.1) ● Case depth

[a] ε-carbonitride, oxidized.

[b] High toughness implies compound layer: without, γ′, ε(<10 μm) diffusion zone: decarburized, without Fe_3C precipitates at grain boundaries pretreatment: quenched and tempered.

This requires the application of steels preferential alloyed with chromium and aluminum. For high resistance against contact fatigue, volume fatigue, and thermal fatigue the, necessary structure of the diffusion zone (high residual stresses, high surface hardness, hardness increase, hardness profile) can also be achieved only by using alloyed steels and the selection of adequate treatment conditions.

Selected examples for the improvement of the service behavior of components through nitriding are given in **Table 15**. They underline the conclusion in **Figure 26** on the application variety of nitriding and substantiate the recommendations for the layer selection in **Table 14**. Due to the fact that the improvement of the service behavior also for comparable components strongly depends on the specific load profile, the effect of nitriding on the service behavior is given only qualitatively in **Table 15**. For example, by means of nitriding, the production volume of reamers can be increased up to the 1.3–6.6 fold depending on the machining material. With dependence on the stress, the production volume of hot working dies can be increased up to the 1.2–6 fold by means of controlled nitriding.

Table 15 Examples for improved service behavior of components through nitriding

Component	*Material*	*Structure of compound layer type/thickness (μm)*	*Nitriding-hardness depth (mm)*	*Fatigue strength*[a]	*Wear*	*Thermal fatigue Resistance*[a]	*Corrosion*
Crankshaft	C45,42CrMo4, 31CrMoV9	ε(γ′) ≈20	0.2–0.6	++	++		
Camshaft	GGL, remelted surface layer	ε(γ′) – ox. ≈20	Secondary[b]		++		
Gearbox parts	16MnCr5, 42CrMo4	γ′; ε ≦10	0.3–0.8	++	++		
Piston rod	S355	ε(γ′) – ox. ≈20	Secondary		+		++
Valve spring	50CrV4, OTEVA 90SC[c]	Bright, <1 μm	≦0.1	++			
Splined hub	C35	ε(γ′) – ox. ≈20	Secondary		++		++
Reamer	S 6-5-2	Without compound layer	≦0.03		++		
Die insert	X38CrMoV5-1	ε(γ′) ≦20	≦0.35		+	++	
Thread rolling tool	X155CrVMo12-1	Without compound layer	≦0.1		++		
Die casting mold	X38CrMoV5-1	ε(γ′) – ox. ≧10	≦0.1		++	++	

[a] +: Improvement compared to base material.

[b] Supporting effect of the remelted surface layer.

[c] 0.6% C, 2% Si, 0.85% Mn, 0.95% Cr, 0.1% V, 0.3% Ni.

12.14.4.3 Nitriding Behavior of Components

The selection of nitriding conditions assumes extensive knowledge of the nitriding behavior of components. An idea of the numerous influencing factors on the nitriding behavior that have to be considered is shown in Figure 68.

The change of component properties caused by the nitriding is determined by the interaction between the component and the reaction gas during heating, holding, and cooling in dependence on the initial condition of the component and the temperature-time characteristic. As mentioned in Figure 68, the result of nitriding, e.g., gas nitriding, is also influenced by the process and furnace parameters, e.g., the gas throughput and gas circulation.

Besides the nitridability of the base material, also the structure of the surface layer resulting from the component processing, the surface roughness, possible deformation-, reactive-, and absorption layers, residual stresses, and other difficult controllable variables significantly influence the nitriding result.

An increasing surface roughness favors the nucleation of iron nitrides and thus the growth of the compound layer. Tailings of grinding emulsions and washing agents can lead to passivation, which avoids the formation of an equal nitride layer or, in extreme case, the nitriding itself. Hence, for the selection of the nitriding conditions and the material, it is necessary to consider both the material-specific nitridability and the processing specific influences.

The influence of the manufacturing on nitriding behavior increases from the unalloyed steels via chromium alloyed quenched and tempered and hot working steels to stainless steels due to the raising chromium content. A successful nitriding of chromium alloyed steels, especially at a low nitriding potential and at temperatures below 500 °C, thus requires an activation of the surface. Today, this is possible for all industrial nitriding and nitrocarburizing processes.

One way for a thermodynamically controlled surface activation offers the controlled gas oxinitriding by setting a defined material-specific oxidation potential above the oxidation limit of iron but below the oxidation limit of iron nitrides. In the initial stages of the gas oxinitriding, the passive layer will be destroyed by the external oxidation of iron. This leads to a faster growth rate and uniform formation of the compound layer with a higher content of ε-nitride. In this way, the gas oxinitriding provides a uniform nitriding for temperatures up to 350 °C. This is, for example, of great importance for the low-temperature nitriding of stainless steels and springs as well as tools made of cold work steels. The technology for surface activation by controlled-gas oxinitriding has proven extremely successful in the industry (3).

Details for the selection of the nitriding conditions can be taken from an illustration of fundamental influencing factors on the nitriding results (Figure 69). The nitriding result is described by the parameters that mainly define the service behavior, the compound layer thickness clt, the case hardness Ch (Ch – case hardness: maximal hardness of the diffusion layer near the compound layer.), the hardness increase ΔH, the nitrided hardness depth Nhd, the case hardness depth Chd, the parameter Δx/Nhd, and the height of the residual stresses σ_E. The ratio Δx/Nhd characterizes the hardness profile within the diffusion layer resulting from the interaction strength between nitrogen and the alloying elements. As described in Section 12.14.1, for a weak interaction, the surface hardness is reached below the surface, the surface hardening depth is low, and the value of Δx/Nhd converges to the value 1. In contrast, for a strong interaction (Δx/Nhd converges to the value 0), the ratio Chd/Nhd converges to the value 1, thus such a hardness profile ensures a high resistance against a failure caused by fatigue and wear (Table 14).

This overview points out that the nitriding potential mainly determines the growth rate and the constitution of the compound layer. In contrast, the structure and the extent of strengthening of the diffusion layer for the nitriding with a compound layer formation are largely independent from the nitriding potential. The hardness and the residual stresses profile is influenced primarily by the material as well as the nitriding temperature and time. The chemical potential of the nitriding media, which is described by the nitriding potential K_N in case of gas nitriding (Figure 69), matters only in special cases, e.g., for the suppression of cementite precipitation due to a bright nitriding.

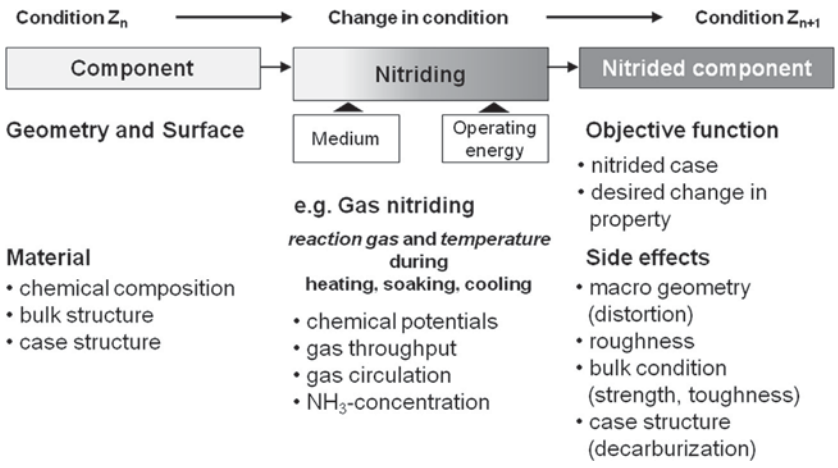

Figure 68 Nitriding behavior of components.

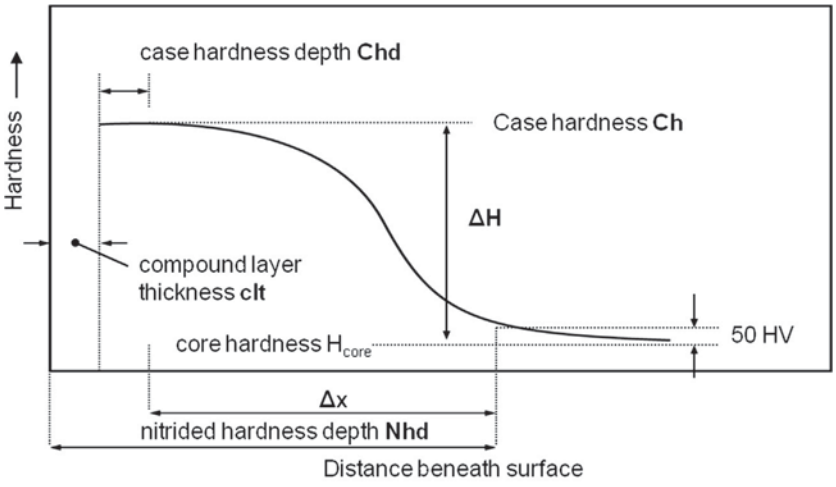

		clt	Ch	ΔH	Nhd	Chd	Δx/Nhd	σ_E
nitriding conditions								
T_N ↑		↑	=↓	=↓	↑	↑	=↓	↓
t_N ↑		↑	=↓	=↓	↑	↑	=↓	↓
K_N ↑		↑	=	=	=	=	=	=
substrate material								
Composition:	Cr ↑	=↓	↑	↑	↓↓	↑	↓	↑
	Al ↑	↑	↑↑	↑↑	=↓	↓	↑	↑↑
	C ↑	=↑	↓	↓	=↓	↓	↑	↓
Structure:	N	=	=↑	↑	=	↑	↓	=↑
	QT (T ↑)	=	↓	↓	=	↓	↑	↓

N: normalized QT: quenched and tempered T: tempering temperature

Figure 69 Effect of nitriding conditions and base material on the nitriding result; schematic description; N: normalized, QT: quenched and tempered, T_t: tempering temperature; according to Lightfood and Jack extended. Reproduced from Lightfood, B. J.; Jack, D. H. Kinetics of Nitriding with and without White-Layer Formation. London. In *Proc. Heat Treatment '73. Met. Soc*; **1975**; pp 59–66.

Appendix: Chemical Composition of the Investigated Steels

Designation		*Composition (wt.%)*						
DIN	*AISI/UNSI SAE*	*C*	*Mn*	*Cr*	*Mo*	*Ni*	*V*	*Others*
S355	–	≤0.22	1.25	–	–	–	≤0.10	–
C15	C1015	0.15	0.45	–	–	–	–	–
C20	–	0.20	0.55	–	–	–	–	–
C25	C1025	0.25	0.55	–	–	–	–	–
C45	C1045	0.45	0.65	–	–	–	–	–
C60	C1060	0.60	0.75	–	–	–	–	–
C110W1	110W1	1.10	0.20	–	–	–	–	–
16MnCr5	–	0.16	1.15	0.95	–	–	–	–
17CrMoV10	–	0.17	0.40	2.85	0.25	–	0.15	–
20MnCr5	–	0.20	1.25	1.15	–	–	–	–
20MoCr4	–	0.20	0.85	0.45	0.45	–	–	–
30CrNiMo8		0.30	0.65	2.00	0.40	2.00	–	–
31CrMoV9	–	0.30	0.55	2.50	0.20	–	0.15	–
34CrAl6	–	0.34	0.75	1.35	–	–	–	Al: 1.0
34CrAlMo5	Nitralloy 135	0.34	0.55	1.15	0.20	–	–	Al: 1.0

(*Continued*)

Designation		Composition (wt.%)						
DIN	AISI/UNSI SAE	C	Mn	Cr	Mo	Ni	V	Others
34CrNiMo6	–	0.34	0.65	1.50	0.25	1.50	–	–
34CrAlNi7	–	0.34	0.55	1.65	0.20	1.0	–	Al: 1.0
37Cr4	–	0.37	0.75	1.0	–	–	–	–
42CrMo4	4142	0.42	0.75	1.05	0.25	–	–	–
45Cr2	–	0.45	0.65	0.50	–	–	–	–
51CrV4	6150	0.51	0.90	1.05	–	–	0.20	–
100Cr6	L3	1.00	0.35	1.50	–	–	–	–
X6CrMo4	–	≤0.07	≤0.20	3.75	0.45	–	–	–
X6CrMo5	P4	≤0.07	0.30	4.80	0.50	–	0.10	–
X30CrMoV3-3	H10	0.30	0.30	3.00	2.75	–	0.55	–
30WCrV17-9	–	0.30	0.30	2.50	–	–	0.55	W: 4.3
X38CrMoV5-1	H11	0.38	0.40	5.15	1.30	–	0.45	–
X40CrMoV5-1	H13	0.40	0.40	5.15	1.35		1.00	
56NiCrMoV7	242	0.56	0.85	1.00	0.45	1.70	0.10	–
X155CrVMo12-1	D2	1.55	0.40	12.0	0.85	–	0.85	–
165CrMoWV46	–	1.65	0.30	11.50	0.65	–	0.25	W: 0.50
X210Cr12	–	2.10	0.40	12.0	–	–	–	–
S6-5-2	M2	0.90	≤0.40	4.20	5.0	–	1.85	W: 6.35
X2CrNiMo17-12-2	316	≤0.03	2.00	17.5	2.25	11.5	–	–
X2CrNiMoN22-5-3	31803	≤0.03	2.00	22.0	3.0	5.5	–	N: 0.1–0.22

References

1. Böhmer, S.; Spies, H.-J.; Berg, H.-J.; Zimdars, H. Oxygen Probes for Controlling Nitriding and Nitrocarburising Atmospheres. *Surf. Eng.* **1994,** *10,* 129–135.
2. Spies, H.-J.; Berg, H.-J.; Zimdars, H. Fortschritte beim sensorkontrollierten Gasnitrieren und –nitrocarburieren. *Härterei-Tech. Mitt.* **2003,** *58,* 189–197. see also: *Int. Heat Treat. Surf. Eng.* **2007**, *1*, 64–72.
3. Lehrer, E. Über das Eisen-Wasserstoff-Ammoniak-Gleichgewicht. *Z. Elektrochem.* **1930,** *36,* 383–392.
4. Automated Gaseous Nitriding Controlled by Nitriding Potential, SAE, AMS 2759/10; May 1999.
5. Kunze, J. *Nitrogen and Carbon in Iron and Steel Thermodynamics;* Akademie Verlag: Berlin, 1990.
6. Kunze, J. Thermodynamische Gleichgewichte im System Eisen-Stickstoff-Kohlenstoff. *Härterei-Tech. Mitt.* **1996,** *51,* 348–354.
7. Leineweber, A.; Gressmann, T.; Mittemeijer, E. J. Simultaneous Control of the Nitrogen and Carbon Activities during Nitrocarburising of Iron. *Surf. Coat. Technol.* **2012,** *206,* 2780–2791.
8. Spies, H.-J.; Bergner, D. Innere Nitrierung von Eisenwerkstoffen. *Härterei-Tech. Mitt.* **1992,** *47,* 346–356.
9. Spies, H.-J.; Schaaf, P.; Vogt, F. Einfluß von Sauerstoffzusätzen beim Gasnitrieren auf den strukturellen Aufbau von Nitrierschichten. *Mat.-wiss. u. Werkstofftech* **1998,** *29,* 588–594.
10. Spies, H.-J.; Reinhold, B.; Berg, H.-J. Einfluß von Sauerstoff beim Plasmanitrieren. *Härterei-Tech. Mitt.* **2007,** *62,* 13–18.
11. Lachtin, J. M. *Physikalische Grundlagen des Nitrierens;* Maschgis: Moskau, 1948. vgl. auch Lachtin, J. M.; Kogan, J. D. Nitrieren von Stählen. Maschinostrojenije Moskau, 1976.
12. Podgurski, H. H.; Knechtel, H. E. Nitrogenation of Fe-Al Alloys. *Trans. Met. Soc. AIME* **1969,** *245,* 1595–1608.
13. Jack, D. H. The Structure of Nitrided Iron-Titanium Alloys. *Acta Metall.* **1976,** *23,* 137–146.
14. Podgurski, H. H.; Davis, F. N. Thermochemistry and Nature of Nitrogen Absorption in Nitrogenated Fe-Ti Alloys. *Acta Metall.* **1981,** *29,* 1–9.
15. Homerberg, V. O. Nitriding. *The Iron Age* **15 October 1936,** *137,* 49–98.
16. Fry, A. The Theory and Practice of Nitrogen Case Hardening. *J. Iron Steel Inst.* **1932,** *135,* 191–222.
17. Kirkwood, D. H.; Atasoy, ÖE.; Keown, S. R. The Structure of Annealed Iron-Titanium Alloys. *Metal Sci. J.* **1974,** *8,* 49–55.
18. Bor, S.; Atasoy, ÖE. The Nitriding of Fe-V Alloys. *Metall. Trans.* **1977,** *8A,* 2514–2518.
19. Lightfood, B. J.; Jack, D. H. Kinetics of Nitriding with and without White-Layer Formation. In *Proc. Heat Treatment '73. Met. Soc;* 1975, pp 59–66, London.
20. Schacherl, R. E.; Graat, P. C. J.; Mittemeijer, E. J. The Nitriding Kinetics of Iron Chromium Alloys. *Metall. Mater. Trans. A* **2004,** *35A,* 3387–3398.
21. Leroy, C.; Michel, H.; Gantois, M. Etude des transformation de phases associes a la niturationde aciers allies an chrome. In *Proc. 2. Int. Congr. Heat Treatment of Metals*; pp 207–218. Florence.
22. Lachtin, J. M.; Kogan, J. D. *Structure and Strength of Nitrided Alloys;* Metallurgia: Moskau, 1982.
23. Wiedemann, R.; Oettel, H.; Bergner, D. Ungewöhnliche Verbindungsschichtbildung beim Nitrieren Al-legierter Stähle und ihre Ursachen. *Härterei-Tech. Mitt.* **1991,** *46,* 301–307.

24. Mirdha, S.; Jack, D. H. Characterization of Nitride 3% Chromium Steel. *Metal Sci.* **1982,** *16,* 398–404.
25. Spies, H.-J.; Böhmer, S. Beitrag zum kontrollierten Gasnitrieren von Eisenwerkstoffen. *Härterei-Tech. Mitt.* **1984,** *39,* 1–6.
26. Eysell, F. W. Verfahrensvarianten und Anlagen zu Nitrocarburieren in Gas. *Zeitschr. für wirt. Fertig. (ZwF)* **1982,** *77,* 292–299.
27. Schubert, T. Variationsmöglichkeiten des Gefüges der Verbindungsschichten beim kontrollierten Gasnitrieren. Dissertation, Bergakademie, Freiberg, 1986.
28. Homerberg, V. O.; Walsted, J. P. *A Study of the Nitriding Process, Part1.* ASST Nitriding Symposium, 1929, 56–99.
29. Eilender, W.; Meyer, O. Über die Nitrierung von Eisen und Eisenlegierungen I. *Arch. Eisenhüttenwes* **1930/31,** *4,* 343–352.
30. Biglari, M. H.; Brakman, C. M.; Mittemeijer, E. J.; Van der Zwaag, S. The Kinetics of the Internal Nitriding of Fe-2Al pct Al Alloy. *Metall. Mater. Trans. A* **1995,** *26A,* 765–776.
31. Spies, H.-J. Stand und Entwicklung des kontrollierten Gasnitrierens. *Neue Hütte* **1991,** *36,* 255–262.
32. Oettel, H.; Ehrentraut, B. Makroskopische Eigenspannungen in der Verbindungsschicht gasnitrierter Stähle. *Härterei-Tech. Mitt.* **1985,** *40,* 183–187.
33. Koch, M. Eigenspannungen nach Nitrieren und Einsatzhärten. In: Eigenspannungen und Lastspannungen. *Beiheft Härterei-Tech. Mitt.* **1982,** 112–121.
34. Oettel, H.; Schreiber, G. Eigenspannungsbildung in der Diffusionszone. In *Tagungsband "Nitrieren und Nitrocarburieren";* 1991, AWT: Wiesbaden; pp 139–151.
35. Wiegand, H. Nitrieren im Motorenbau. *Härterei-Tech. Mitt.* **1942,** *1,* 166–185.
36. Daves, W.; Fischer, F. D. Finite-Element-Simulation komplexer Wärme-behandlungsphänomene am Beispiel des Nitrierens. *BHM* **1996,** *141,* 204–208.
37. Spies, H.-J.; Berns, H.; Ludwig, A.; Bambauer, K.; Brusky, U. Warmhärte und Eigenspannungen nitrierter Stähle. *Härterei-Tech. Mitt.* **1998,** *53,* 359–366.
38. Spies, H.-J. Zähigkeit von Nitrierschichten auf Eisenwerkstoffen und ihre Kennzeichnung. *Härterei-Tech. Mitt.* **1986,** *41,* 365–369.
39. Möhler, W. *Untersuchungen zur Bruchzähigkeit und zum Wälzverschleißverhalten nitrierter Stähle;* Dissertation, Bergakademie, Freiberg, 1987.
40. Ponton, C. B.; Rawlings, R. D. Vickers Indentation Fracture Toughness Test. *Mater. Sci. Technol.* **1989,** *5,* 865–872, 961–976.
41. Schmidtmann, E.; Kopfer, G. Beurteilung des Bruchverhaltens einsatzgehärteter Stähle durch Kennziffern der Bruchmechanik. *Arch. Eisenhüttenwes* **1981,** *52,* 483–489.
42. Spies, H.-J. Untersuchung des mechanischen Verhaltens von Randschichten. *Mat.-wiss. u. Werkstofftech* **1995,** *26,* 68–77.
43. Dawes, C.; Tranter, D. F. NITROTEC Surface Treatment – The Development and Application of New Gaseous Nitrocarburising Concepts in the Design and Manufacture of Automobile Components. Paper: Int. Foundry Heat Treat. Conf., Johannesburg, South Africa, Nov. 1982, pub. In Heat Treat. Metals, 1982, 85–90 and tz. für Metallbearbeitung, 1984, 78, 32–38.
44. Spies, H.-J.; Claus, R. Zur Bewertung des Bruchverhaltens nitrierter Stähle für Kaltarbeitswerkzeuge bei dynamischer Belastung. *IfL-Mitt.* **1987,** *26* (4), 105–112.
45. Slyke, J.; Sproge, L. Kinetics of the Gaseous Nitrocarburising Process. *Surf. Eng.* **1989,** *5,* 125–140.
46. Jack, D. H.; Winnik, S. Effect of Process Variables on the Fatigue Resistance of Nitride Steel, *Heat Treatment '79;* The Metals Soc.: London, 1980; pp 169–177.
47. Mailänder, R. Über die Dauerfestigkeit von nitrierten Proben. *VDI-Z* **1933,** *77* (10), 272–274.
48. Mailänder, R. Eigenspannungen und Biegewechselfestigkeit verstickter Stahlproben. *Arch. Eisenhüttenwes* **1936,** *10,* 257–261.
49. Sauer, G. Verhalten eines salzbadnitrierten Kohlenstoffstahles bei Umlaufbiegebelastung unter berücksichtigung der Probengröße. *Industrieanzeiger* **1965,** *87,* 95–104 and 799–804.
50. Kloos, K. H. a.o. Quatitative Bewertung des oberflächentechnischen Größeneinflusses plasmanitrierter Probestäbe bei Umlaufbiegung und Zug-Druck-Beanspruchung. *Härterei-Tech. Mitt.* **1984,** *39,* 165–172.
51. Spies, H.-J., et al. Abschätzung der Schwingfestigkeit nitrierter bauteilähnlicher Proben mit Hilfe normierter Wöhlerstreubänder. *Mat.-wiss. u. Werkstofftech* **1996,** *27,* 60–71.
52. Thomson, R. F. *Summary. Proc. Fatigue Durability of Carburized Steel;* ASM: Cleveland, Ohio, Oct. 1956, 1957; pp 106–115.
53. Macherauch, E.; Kloos, K. H. Bewertung von Eigenspannungen. *Härterei-Tech. Mitt.* **1982,** *37.* Beiheft, 175–194.
54. Fuchs, H. O. The Effect of Self Stresses on High Cycle Fatigue. *J. TEVA* **1982,** *10,* 168–173.
55. Spies, H.-J. Fatigue Behavior of Nitrided Steels. *Steel Res.* **1993,** *64,* 441–448.
56. Woodvine, J. G. R. The Behavior of Case-Hardened Parts under Fatigue Stresses. *Iron Steel Inst., Carnegie Scholarship Mem.* **1924,** *13,* 197–237.
57. Robinson, G. H. The Effect of Surface Condition on the Fatigue Resistance of Hardened Steel, 1957, pp 11–46. In *Proc. Fatigue Durability of Carburized Steel;* ASM: Cleveland, Ohio, Oct. 1956.
58. Kloos, K. H.; Velten, E. Berechnung der Dauerschwingfestigkeit von plasmanitrierten bauteilähnlichen Proben unter Berücksichtigung des Härte- und Eigenspannungsverlaufs. *Konstruktion* **1984,** *36,* 181–188.
59. Jones, B. K.; Martin, J. W. Fatigue Failure Mechanisms in a Nitride En 41B Steel. *Met. Technol.* **1978,** 217–221.
60. Spies, H.-J.; Scharf, M.; Kaldor, M. Zur Fraktographie des Ermüdungsbruches nitrierter Stähle. *Neue Hütte* **1985,** *30,* 107–110.
61. Spies, H.-J.; Griesbach, R. Einfluss des Nitrierens auf die Schwingfestigkeit von Vergütungsstählen. *Maschinenbautechnik, Berlin* **1985,** *34,* 224–229.
62. Spies, H.-J.; Tan, N. D.; Vogt, F. Einfluss des Aufbaues von Nitrierschichten auf die Schwingfestigkeit gekerbter Proben. *Härterei-Tech. Mitt.* **1993,** *48,* 153–161.
63. Dengel, D. Zur Dauerfestigkeit nitrierter Stähle. *Härterei-Tech. Mitt.* **2002,** *57,* 316–326.
64. Murakami, Y. Material Defects as the Basis of Fatigue Design. *Int. J. Fatigue* **2012,** *41,* 2–10.
65. Ebersbach, U.; Friedrich, S.; Nghia, T.; Spies, H.-J. Elektrochemische Korrosionsuntersuchungen an gasoxinitriertem und salzbadnitrocarburiertem Stahl in Abhängigkeit vom Aufbau der Nitrierschicht. *Härterei-Tech. Mitt.* **1991,** *46,* 339–349.
66. Ebersbach, U.; Friedrich, S.; Nghia, T. Structure and Corrosions Behavior of Nitride Layers. In *Proc. Surf. Eng;* DGM Informges: Bremen, 1993; pp 299–304.
67. Winkler, H. P.; Spies, H.-J.; Schubert, T. Korrosionsverhalten nitrierter Eisenwerkstoffe. In *Freiberger Forschungshefte;* Leipzig; 1987; pp 49–54.
68. Bonhoeffer, K. F. Über das elektrochemische Verhalten von Eisen. *Z.f. Elektrochem.* **1951,** *55,* 151–154.
69. Wahl, G. Salzbadnitrocarburieren nach dem QPQ-Verfahren. *VDI-Zeitschrift* **1984,** *126,* 811–818.
70. Wahl, G. Anwendung der Salzbadnitrocarburierung bei kombinierter Verschleiß- und Korrosionsbeanspruchung. *Zeitschr. für wirt. Fertig. (ZwF)* **1982,** *77,* 501–506.
71. Doche, M. L.; Meynie, V.; Mazille, H.; Deramaix, C.; Jacquot, P. Improvement of the Corrosion Resistance of Low-Pressure Nitrided and Post-Oxidised Steels by a Polymer Impregnation Final Treatment. *Surf. Coat. Technol.* **2002,** *154,* 113–123.
72. Steyer, P.; Millet, I.-P.; Mazille, H.; Peyre, J.-P.; Jaquot, P.; Hertz, D. Influence of Post Treatments on Corrosion Behavior of Gas Nitrocarburised Steels. *Surf. Eng.* **2003,** *19,* 173–178.
73. Bell, T. Current Status of Supersaturated Surface Engineered S-Phase Materials. *Key Eng. Mater.* **2008,** *373–374,* 289–295.
74. Spies, H.-J.; Bell, T.; Kolozsvary, Z. Thermochemical Surface Treatment of Stainless Steels at Low Temperatures. *Härterei-Tech. Mitt.* **2010,** *65,* 11–21.
75. Bell, T.; Sun, Y. Low Temperature Plasma Nitriding and Carburizing of Austenitic Stainless Steels. In *Stainless Steel 2000, Proc. Int. Sem. Osaka/Japan, 2000;* Maney Publ: London, 2001; pp 275–288.
76. Habig, K.-H.; Li, Y. Rauheits- und Verschleißprüfungen an Verschleiß-Schutzschichten. *Härterei-Tech. Mitt.* **1982,** *37,* 180–192.
77. Habig, K.-H. Reibung und Verschleiß von gehärteten, nitrierten und borierten Stahl-Gleitpaarungen in Luft und im Vakuum. *Z. Metallkde* **1984,** *75,* 630–634.
78. Sikorski, M. E. The Adhesion of Metals and Factors that Influence it. *Wear* **1964,** *7,* 144–162.
79. Voskamp, A. P. Microstructural Changes during Rolling Contact Fatigue. Thesis, TU Delft, 1997.
80. Ringsberg, J. W. Life Prediction of Rolling Contact Fatigue Crack Initiation. *Int. J. Fatigue* **2001,** *23,* 575–586.
81. Sandström, J. Subsurface Rolling Contact Fatigue Damage of Railway Wheels – A Probabilistic Analysis. *Int. J. Fatigue* **2012,** *37,* 146–152.
82. Dawes, C.; Tranter, D. F.; Smith, C. G. Reappraisal of Nitrocarburizing and Nitriding When Applied to Design and Manufacture of Non-alloy Steel Automobile Components, *Heat Treatment '79;* The Metals Soc: London, 1980; pp 60–68.
83. Hoffmann, F., et al. Verschleißwiderstand nitrierter und nitrocarburierter Stähle. *Härterei-Tech. Mitt.* **1997,** *52,* 376–386.
84. Razim, C.; Rodrian, U. Untersuchungen zum Schichtaufbau und Verschleißverhalten hochbelasteter, nitrierter Schraubenräder. *Härterei-Tech. Mitt.* **1985,** *40,* 141–149.
85. Schröter, W.; Uhlig, W. Zum Verschleißverhalten nitridhaltiger Schichten. *Schmierungstechnik* **1980,** *11,* 9–15.

86. Nghia, T. T. Korrosions- und Verschleißverhalten von nitrierten und nitrocarburierten Stählen. Dissertation, TU-Bergakademie, Freiberg, 1994.
87. Woska, R. Einfluss der Zusammensetzung der Nitrierschicht auf das Mischreibungsverhalten. *Härterei-Tech. Mitt.* **1983,** *38,* 10–17.
88. Werner, G.; Ziese, J. Anwendung physikalischer Oberflächenmessmethoden an gegossenen Nockenwellen mit dem Ziel, durch definiertes Nitrieren und Oxidieren die Lebensdauer zu erhöhen. *Härterei-Tech. Mitt.* **1984,** *39,* 156–163.
89. Spies, H.-J.; Mothes, A.; Pursche, G. Zum Verschleißverhalten oxydierter Nitrier-schichten. *Schmierungstechnik* **1989,** *20* (6), 177–178.
90. Habig, K.-H.; Chatterjee-Fischer, R.; Hoffmann, F. Untersuchungen des Gleit und Furchungsverschleißes an thermochemisch behandelten Stählen. *Mat.-wiss. u. Werkstofftech* **1982,** *13,* 207–215.

12.15 Induction Hardening: Technology, Process Design, and Computer Modeling

VI Rudnev and D Loveless, Inductoheat Inc., Madison Heights, MI, USA

12.15.1	**Introduction**	490
12.15.1.1	Basic Principles of Induction Hardening	490
12.15.1.2	Skin Effect and Its Classical Definition	496
12.15.1.3	Magnetic Wave Phenomenon	497
12.15.1.4	Eddy Current Cancellation	499
12.15.2	**Design Considerations for Induction-Hardening Processes**	499
12.15.2.1	Effect of Prior Microstructure and Heating Rates	499
12.15.2.2	Obtaining Fully Martensitic Structures	502
12.15.2.3	Superhardening Phenomenon	504
12.15.2.4	Induction-Hardening Coil Designs	505
12.15.2.4.1	Copper Selection and Coil Fabrication	505
12.15.2.4.2	Single-Shot Inductors	507
12.15.2.4.3	Scanning Inductors	508
12.15.2.4.4	Progressive Inductors	510
12.15.2.4.5	Specialty Inductors	511
12.15.2.5	Magnetic Flux Concentrators	513
12.15.2.5.1	Physics of Magnetic Flux Concentration	514
12.15.2.5.2	Selecting Flux Concentrator Materials	515
12.15.2.5.3	Flux Concentrator's Materials Trade-Off	517
12.15.2.5.4	Common Misconception	518
12.15.2.5.5	Design and Application Features	519
12.15.2.5.6	Electromagnetic Shielding, and Prevention of an Undesirable Temper-Back	519
12.15.2.5.7	Summary of Using Magnetic Flux Concentrators	522
12.15.3	**Computer Modeling**	523
12.15.3.1	Governing Equations	525
12.15.3.2	Numerical Computation Techniques	527
12.15.3.3	Limitations of Generalized All-Purpose Commercial Software	529
12.15.3.3.1	Challenges in Simulation Inline Multicoil Continuous Induction Heating	530
12.15.3.3.2	Challenges in Modeling an Induction Scan Hardening	530
12.15.3.4	Conclusion	532
12.15.4	**Induction-Hardening Systems and Applications**	533
12.15.4.1	Induction Hardening of Automobile Crankshafts	533
12.15.4.1.1	Clamshell or Split Inductors	533
12.15.4.1.2	Nonencircling U-Shaped Inductors Requiring Crankshaft Rotation	534
12.15.4.1.3	Nonrotational Hardening of Crankshafts: The SHarP-C Process	536
12.15.4.2	Induction Hardening of Gears	540
12.15.4.2.1	Coil Design and Heating Modes	541
12.15.4.3	TSH Technology for Hardening Complex Geometry Parts	546
12.15.4.4	Induction Hardening of Hand Tools and Bits for the Mining Industry	548
12.15.5	**A Review of Modern Power Supplies for Induction Hardening**	552
12.15.5.1	Introduction	552
12.15.5.2	History of Power Supplies for Induction Heat Treating	553
12.15.5.3	Unique Terminology	554
12.15.5.4	Power Electronic Components	554
12.15.5.5	Induction-Hardening Parameters	556
12.15.5.6	Common Power Supply Types	557
12.15.5.6.1	AC to DC Converter	558
12.15.5.6.2	DC to AC Inverter	559
12.15.5.6.3	Load Matching Circuits	561
12.15.5.7	Commonly Used Circuit Topologies	562
12.15.5.7.1	Voltage Source Inverters	562
12.15.5.7.2	Current Source Inverters	566

12.15.5.8 Conclusion 568
12.15.6 Load Matching Induction-Hardening Power Supplies 569
12.15.6.1 Simple Examples 570
12.15.6.2 Load Connection Types 570
12.15.6.2.1 Matching the Parallel Resonant Load 570
12.15.6.2.2 Matching the Series Resonant Load 575
12.15.7 Conclusion 578
References 578

12.15.1 Introduction

The induction heat treatment of metals represents a wide range of applications (*1*). This includes annealing (subcritical and intercritical), normalizing, hardening, tempering, and stress relieving of a variety of workpiece geometries. The most popular application of induction heat treatment is the hardening of steels and cast irons. The three most common forms of induction hardening are surface hardening (case hardening), through hardening, and selective hardening.

12.15.1.1 Basic Principles of Induction Hardening

The aim of induction hardening of steels and cast irons is to provide a martensitic layer on specific areas of the workpiece to increase the hardness, strength, fatigue, and wear resistance, while allowing the remainder of the part (if required) to be unaffected by the process.

The typical procedure for induction hardening involves heating the component to the austenizing temperature range, holding it at a temperature long enough for essentially complete austenitic microstructures to form, then rapidly cooling the alloy until it is below the M_s temperature. Intense spray quenching allows replacement of the diffusion-dependent transformation processes by a shear-type transformation, producing a much harder constituent called martensite. Hardening may be done either on the surface of the workpiece or throughout its entire cross-section.

Figure 1 shows three examples representing three forms of induction-hardening applications: induction surface hardening of camshaft lobes (top); induction through hardening of carbon steel pins (middle); and selective induction hardening of the head of the hammer (bottom).

Induction hardening is a complex combination of electromagnetic, heat transfer, and metallurgical phenomena involving many factors. Both, heat transfer and electromagnetic phenomena are nonlinear and tightly interrelated; because the physical properties of heated materials depend strongly on both temperature and magnetic field intensity. The metallurgical phenomenon is also a nonlinear function of temperature, heating intensity, cooling severity, alloy chemical composition, prior microstructure, and other factors. The basic electromagnetic phenomenon of induction heating is quite simple and discussed in several books (*1–9*) including college physics.

Because of the physics of the electromagnetic induction phenomena, the heating can be localized to areas where the metallurgical and mechanical changes are desired.

The goal of induction surface hardening is to provide a martensitic layer on surface areas (external and/or internal) of the workpiece without affecting the rest of the part. **Figure 2** shows a small portion of the virtually endless variety of steel and cast iron components that can be induction surface hardened. This includes but is not limited to different transmission and engine components (e.g., axles, CV joint, camshafts, crankshafts, gears, cylinders, connecting rods, rocker arms, etc.), fasteners (e.g., bolts, screws, studs), off-road, farm, and mining equipment (i.e., shafts, clutch plates, pins, track links), cutting tools, bearings, inner/outer races sprockets, spindles, skid plates, fixtures, and the list goes on and on (*1–9*). The variety of geometries of components that undergo induction hardening and the diversity of required hardness patterns call for a variety of hardening inductors. Some of those inductors are shown in **Figure 3**.

In contrast to surface hardening, the goal of through hardening is to form a martensitic structure throughout the workpiece. For this to occur, the entire cross-section of the component to be through hardened is raised above the austenization temperature A_{c3} and then rapidly cooled to produce a consistent martensitic structure through the entire cross-section. The ability of the component to be through hardened depends on the hardenability of the steel, quenching conditions, grain size, and parts' geometry. Through hardening may be needed for parts requiring high strength, such as snowplow blades, chain links, truckbed frames, valve-spring wire, drill bits, and certain fasteners.

Both induction through and surface (case) hardening can be localized to a component's particular areas (e.g., its ends or its middle sections), a process often referred to as selective hardening.

The tempering process takes place after steel is hardened, but it is no less important. The transformation to martensite through quenching creates a very hard and low toughness structure. Untempered martensite retains a high level of residual stresses and typically is too brittle for many commercial applications, except for a small group of components that primarily require wear resistance. Reheating of as-quenched steels and cast irons for tempering produces a microstructure of tempered martensite. A variety of microstructures and mechanical properties of steels and cast irons can be produced by tempering, including increasing toughness,

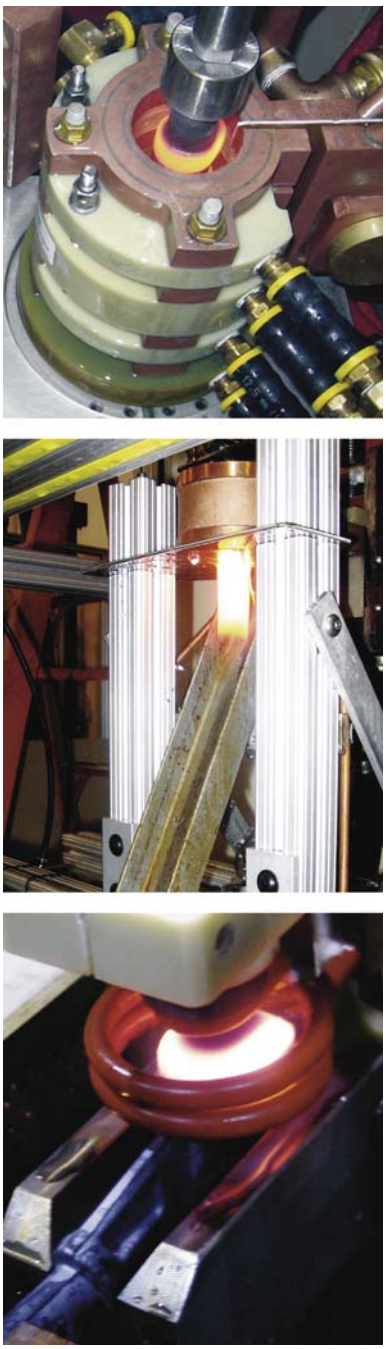

Figure 1 Examples of induction hardening: induction surface hardening of camshaft lobes (top), induction through hardening of carbon steel pins (middle), and selective induction hardening of the head of the hammer (bottom). Courtesy of Inductoheat Inc.

yield strength, and ductility; relieving internal stresses; eliminating brittleness; and, in some cases, improving the shape stability of as-quenched components (*10,11*).

A conventional way of tempering is to run the parts through a tempering oven or furnace (gas-fired or infrared), which is often located in a separate production area and therefore requires extra space, labor, and time for part transportation. Tempering in the furnace is a time-consuming process that typically takes 1–4 h. Short-time induction tempering was developed to overcome these drawbacks.

Time and temperature are two of the most critical parameters of tempering. In shorter-time induction tempering, in order to provide the similar effect as in longer-time oven tempering, it is necessary to utilize higher temperatures (*1,10*). There are several ways to determine the time–temperature correlation between conventional long-time low-temperature furnace tempering and short-time higher temperature induction tempering, including the Hollomon–Jaffe equation and the Grange–Baughman

Figure 2 Examples of the virtually endless variety of steel and cast iron components that can be induction hardened. Courtesy of Inductoheat Inc.

tempering correlation. Discussion of induction tempering is outside the scope of this chapter, and we suggest readers review Refs. (*1*,*5*,*10*,*11*).

The physics of heating by electromagnetic induction can be described as follows (*1*). An alternating voltage applied to an inductor or induction coil terminals produces an alternating electrical current flow in the coil circuit, which in turn generates in its surroundings a time-variable magnetic field. This magnetic field induces eddy currents in the workpiece located inside the coil or in its close proximity. It is imperative to remember that eddy currents could also be induced in other electrically conductive objects that are located near the coil. Induced currents (also called eddy currents) have the same frequency; however, direction of their flow is opposite to the coil current flow. Eddy currents produce heat by the Joule effect (I^2R). No contact is required between the workpiece and induction coil. **Figure 4** shows a longitudinal cross-section of an inductor with the surrounding magnetic field occurring inline through hardening of carbon steel rods. The inductor comprises two six-turn solenoid induction coils connected electrically in a series.

Unlike carburizing and nitriding furnaces, the performance of induction heaters first and foremost is affected by the electromagnetic properties of the heated metal. The electromagnetic properties of materials encompasses a variety of characteristics, including magnetic permeability, electrical resistivity (its reciprocal electrical conductivity), saturation flux density, coercive force, and many others (*1*). While recognizing the importance of all electromagnetic properties, two of them are electrical resistivity (its reciprocal electrical conductivity) and magnetic permeability, which have the most pronounced effect on the performance of an induction heating system, coil efficiency, and selection of main design and process parameters.

The ability of material to easily conduct electric current is specified by electrical conductivity σ. The reciprocal of the conductivity σ is electrical resistivity ρ. The units for ρ and σ are Ω-meters and mho m^{-1}, respectively. Both σ and ρ can be used in engineering practice; however, most engineering data books contain primarily electrical resistivity data. Therefore, the value of ρ will be used here.

For some electrically conductive materials, electrical resistivity decreases with temperature. However, for a great majority of steels and cast irons, electrical resistivity increases, with temperature being a nonlinear function. **Table 1** shows the variation of electrical resistivity (μΩ*m) versus temperature for three steel grades (AISI 1023, 1080, and 4130) (*12*).

Grain size has a noticeable effect on electrical resistivity, as well as plastic deformation, prior heat treatment, and some other factors. At the same time, the effect of temperature and chemical composition are two of the most pronounced factors.

Relative magnetic permeability μ_r indicates the ability of a material (i.e., carbon steel) to conduct the magnetic flux better than vacuum or air. μ_r is a nondimensional parameter. Relative magnetic permeability may have a pronounced effect on coil calculation, electromagnetic field distribution, and selection of process parameters. The constant $\mu_0 = 4\pi \times 10^{-7}$H m^{-1} is called the

Figure 3 Specifics of the inductor design is typically application-oriented. Courtesy of Inductoheat Inc.

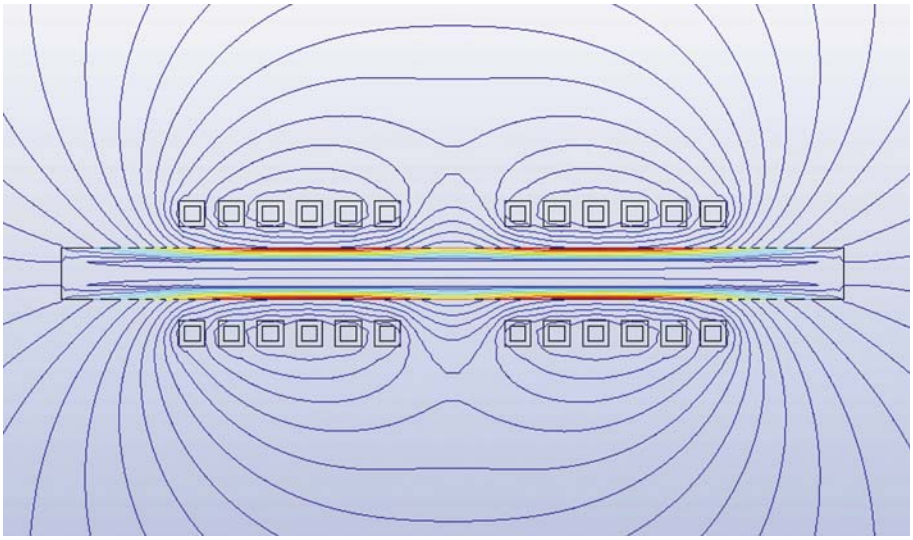

Figure 4 Longitudinal (axial) cross-section of an inductor with the magnetic field used for inline through hardening of carbon steel rods. Inductor comprises two six-turn solenoid induction coils connected in series.

Table 1 Electrical resistivity (μΩ*m) variation versus temperature for three steel grades

	Temperature, °C						
Steel grade	*21*	*200*	*400*	*600*	*700*	*900*	*1000*
AISI 1023	0.169	0.292	0.487	0.758	0.925	1.136	1.167
AISI 1080	0.18	0.308	0.505	0.772	0.935	1.164	1.191
AISI 4130	0.223	0.342	0.529	0.786	0.945	1.137	1.171

Source: Rothman, M. F. *High-Temperature Property Data: Ferrous Alloys*; ASM Int., 1988.

permeability of free space (the vacuum). The product of relative magnetic permeability and permeability of the free space is called magnetic permeability μ and corresponds to the ratio of the magnetic flux density (B) to magnetic field intensity (H).

A material's ferromagnetic property is a complex function of grain structure, chemical composition, frequency, temperature, and magnetic field intensity. Figure 5 shows an illustration of the complex relationship among μ_r, temperature, and magnetic field intensity for medium carbon steel (*13*). Magnetic permeability decreases with increasing temperature in the majority of induction heating applications. The temperature at which a ferromagnetic body becomes nonmagnetic is called the Curie temperature (Curie point). When the temperature of ferromagnetic material approaches the Curie point, magnetic material gradually loses its magnetic properties, becoming nonmagnetic with $\mu_r = 1$ upon exceeding the Curie temperature.

It is important to recognize that the same kind of carbon steel at the same temperature and frequency can have noticeably different values of μ_r due to differences in power applied to induction coil affecting the intensity of the magnetic field (H). For example, μ_r of magnetic steels commonly used in induction hardening at the initial stage of heating can vary from values of about $\mu_r = 6$ to values exceeding 60, depending on the magnetic field intensity (H) and temperature (T).

Chemical composition is another factor that makes a marked effect on the Curie temperature. The Curie point of plain carbon steel corresponds to the A_2 critical temperature on the iron–iron-carbide phase transformation diagram. Therefore, even among the plane carbon steels, the Curie temperature might be noticeably different due to the carbon content variation. For example, the Curie point of plain carbon steel AISI 1020 being about 768 °C is clearly different from 732 °C, which is typical for steel AISI 1060. Depending on the heat intensity (°C s^{-1}), there can be some shifting of the Curie temperature due to thermal hysteresis.

As magnetic materials (i.e., carbon steels) are being induction heated from room temperature, the alternating magnetic flux field causes the magnetic domains of the material to oscillate as the magnetic domains change their polar orientation every cycle. This oscillation is called magnetic *hysteresis*, and a certain amount of heat is produced by the friction when the domains oscillate.

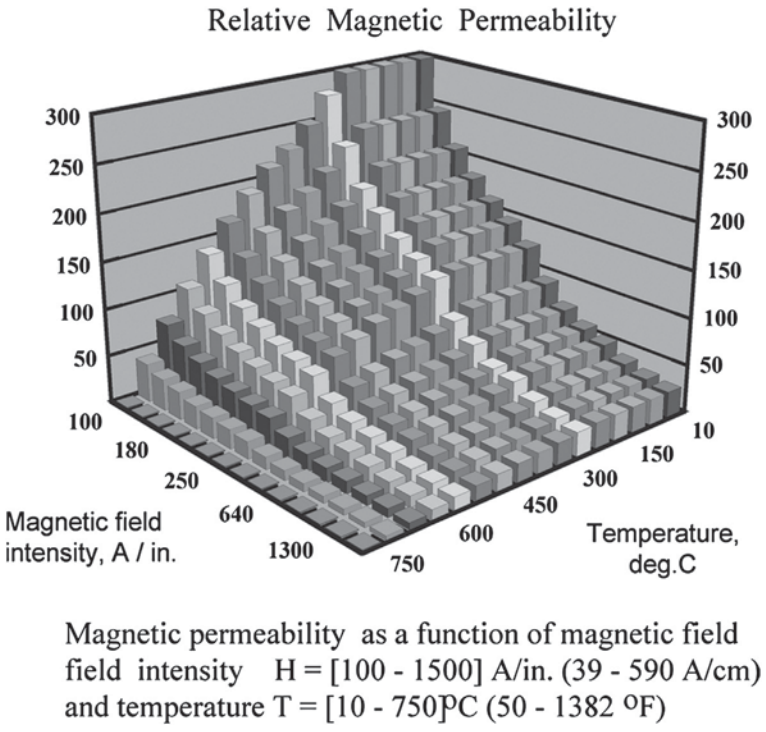

Figure 5 An illustration of the complex relationship among μ_r, temperature, and magnetic field intensity for medium carbon steel. Reproduced from Rudnev, V., Demidovich, V. Advanced Computation Software for Everyday Use in Modern Induction Heat Treating. *Proceedings of 17th ASM Heat Treating Conference,* Indianapolis, 15–18 Sept., 1997; pp 551–555.

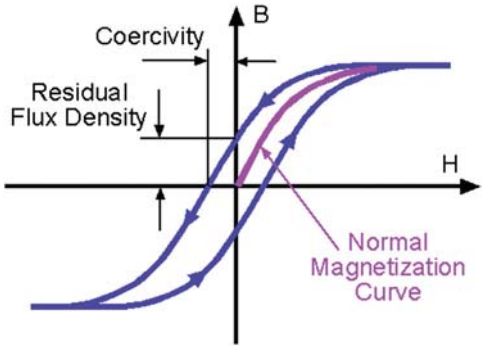

Figure 6 An illustration of the magnetic hysteresis.

Upon being heated above the Curie temperature, steels become nonmagnetic, no reversal of domains can occur, and magnetic hysteresis ceases. Figure 6 shows an illustration of magnetic hysteresis and the effect of the strength of magnetic field.

For the great majority of induction surface hardening applications, a heating effect due to magnetic hysteresis losses does not typically exceed 9–12% and for through hardening – 6–8% compared to the amount of heat generated by the eddy current (Joule heat). However, in some low-temperature applications, where magnetic material retains its magnetic properties during the entire heating cycle (e.g., induction tempering, low-temperature stress relieving), hysteresis heat generation can reach greater and more appreciable values compared to Joule heat generated by eddy current.

Similar to electromagnetic properties, the thermal properties of heated materials (including specific heat and thermal conductivity) are also nonlinear functions of the temperature. Three of the most critical thermal properties of heated materials are thermal conductivity, specific heat, and surface heat losses due to thermal radiation and convection. All of these thermal properties are also nonlinear functions of chemical composition, microstructure, and temperature. Tables 2 and 3, respectively, show variation of specific heat J/(kg *^{o}K) and thermal conductivity W/(m*^{o}K) versus temperature for three steel grades (AISI 1023, 1080, and 4130).

The value of specific heat designates an ability of material to absorb the heat. Steel has the ability to absorb more heat as temperature increases. This means that more energy is required to heat steel when it is hot than when it is cold.

Thermal conductivity k designates the rate at which heat travels across a thermally conductive workpiece. A material with a higher k value conducts heat faster than a material with a low k. Therefore, in through hardening applications, it is advantageous to have high thermal conductivity. However, in selective hardening, a high value of k is often a disadvantage because of its tendency to promote the heat-soaking action and attempt to equalize the temperature distribution within the heated workpiece.

Surface heat losses represent another nonlinear thermal property that takes place during induction heating. Surface thermal losses combine convection losses described by the well-known Newton's law of heat convection and thermal radiation according to the Stefan–Boltzmann law of thermal radiation.

Table 2 Specific heat (J kg^{-1}*^{o}K) variation versus temperature for three steel grades

	Temperature, °C						
Steel grade	*50–100*	*150–200*	*250–300*	*350–400*	*550–600*	*650–700*	*750–800*
AISI 1023	486	519	557	599	749	846	950
AISI 1080	490	531	565	607	712	770	–
AISI 4130	477	523	544	607	741	829	837

Source: Rothman, M. F. *High-Temperature Property Data: Ferrous Alloys*; ASM Int., 1988.

Table 3 Thermal conductivity (W m^{-1}*^{o}K) variation versus temperature for three steel grades

	Temperature, °C						
Steel grade	*100*	*200*	*400*	*600*	*700*	*800*	*1000*
AISI 1023	51.2	49	42.7	35.6	31.8	26.1	27.2
AISI 1080	48.1	45.2	38.1	32.7	30.1	24.4	26.8
AISI 4130	42.7	41.7	39	34.1	31	30	28

Source: Rothman, M. F. *High-Temperature Property Data: Ferrous Alloys*; ASM Int., 1988.

12.15.1.2 Skin Effect and Its Classical Definition

Due to several electromagnetic phenomena, the eddy current density and the induced power density (heat source) distribution within the workpiece are not uniform, potentially causing a nonuniform temperature profile. In some processes, it is desirable to have some nonuniform heat distribution, but, in others, it creates some challenges. A nonuniform current distribution can be caused by several electromagnetic phenomena, including (1) skin effect, (2) proximity effect, (3) ring effect, (4) slot effect, and (5) electromagnetic end and edge effects. Reference (*1*) discusses these effects in detail.

Whenever someone is discussing any induction heating application, reference is often made to the skin effect phenomenon that is a fundamental property of induction heating. This phenomenon can be clearly observed during the induction heating of any electrically conductive body located inside an induction coil (**Figure 7**). Skin effect represents a nonuniform distribution of an alternating current within the workpiece cross-section. According to this phenomenon, eddy currents induced within the workpiece will primarily flow in the surface layer (the 'skin' layer); where the majority of all induced power (about 86%) will be concentrated. The thickness of this layer is called the reference depth or current penetration depth, δ. The value of penetration depth varies with the square root of electrical resistivity and inversely with the square root of frequency and relative magnetic permeability according to expression [1]:

$$\delta = 503\sqrt{\frac{\rho}{\mu_r F}} \qquad [1]$$

where ρ is the electrical resistivity of the metal, Ω*m; μ_r is the relative magnetic permeability; and F is frequency, Hz, δ in meters.

Mathematically speaking, the penetration depth δ is the distance from the surface of the conductor toward its core at which the current decreases exponentially to 1/exp, its value at the surface. The power density at this distance will decrease to $1/\exp^2$, its value at the surface.

Figure 8 illustrates the skin effect, showing the commonly accepted understanding regarding current density distribution being reduced from the workpiece surface toward the core. At distance equal to one penetration depth (δ) from the surface, the magnitude of the current will retain approximately 37% of its surface value. However, the power density retains only about 14% of its surface

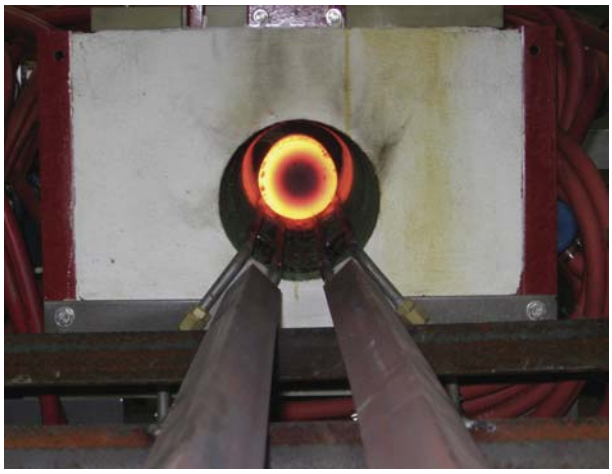

Figure 7 Skin effect can be clearly observed during induction heating of any electrically conductive body located inside an induction coil. Reproduced from Rudnev, V. Computer Modeling Helps Identify Induction Heating Misassumptions and Unknowns. *Ind. Heat.* **October, 2011,** 59–64.

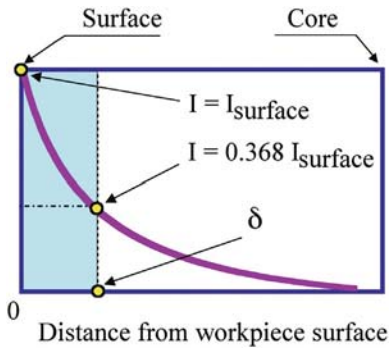

Figure 8 Current density distribution versus distance from surface of the workpiece due to the skin effect.

value at a one-penetration depth distance, because power relates to a current as I^2R. From this, one can conclude that about 63% of the current and 86% of the induced power in the workpiece will be concentrated within a surface layer of thickness δ. The fact that practically all induced power (heat sources) is concentrated within the current penetration depth emphasizes the importance of having a clear understanding of skin effect appearance during induction heating.

Engineers often calculate the distribution of the current density along the workpiece thickness (radius) using Bessel functions or numerous charts that are readily available to determine values of δ versus temperature when heating different materials using various frequencies.

Unfortunately, many people are not aware that the widely used assumption regarding current and power distribution due to a skin effect is not valid for a great majority of induction surface hardening applications. Computer modeling helps to uncover this common erroneous assumption (*14*).

It is imperative to remember that the widely accepted assumption of the exponential distribution of induced current and power is only appropriate for a solid body (workpiece) having both constant electrical resistivity and magnetic permeability. Therefore, realistically speaking, this assumption can be made for only some unique cases of induction heating and heat treating, such as induction heating of nonmagnetic materials to relatively low temperatures (i.e., preheating prior to curing or bonding) or heating nonmagnetic materials that exhibit insignificant changes in their electrical resistivity during the heat cycle.

For the great majority of induction surface hardening applications, the power density (heat source) distribution is not uniform and there always are thermal gradients within the heated workpiece. These thermal gradients result in nonuniform distributions of electrical resistivity and, in particular, magnetic permeability within the heated workpiece. The presence of these nonlinearities leads to the fact that the common definition of current penetration depth does not 'fit' its principal assumption.

12.15.1.3 Magnetic Wave Phenomenon

If the frequency has been chosen correctly for induction surface hardening, the thickness of the nonmagnetic surface layer – the layer that is heated to above the Curie temperature for purposes of its austenization – is somewhat less than the current penetration depth in hot steel. The desirable frequency is often chosen in such a way that it produces a current penetration depth that will be 1.2–2 times the required case depth at the end of heating.

In induction surface hardening, the power density distribution along the radius/thickness has a unique wave shape (*1,6*) that differs significantly from the commonly assumed exponential distribution. Here, the power density has its maximum value at the surface and decreases toward the core. But then, at a certain distance from the surface, the power density suddenly starts increasing again, reaching a maximum value before it starts a final decline (**Figure 9**, right).

In 1960, a hypothesis regarding a 'magnetic-wave' phenomenon was independently introduced by Simpson (*9*) and Lozinskii (*4*). Both scientists intuitively felt that there should be conditions in which the power density distribution would differ from that of the traditionally accepted exponential form. They provided a qualitative description of this phenomenon based on their intuition. At the time, a quantitative assessment of this phenomenon could not be developed due to a limitation in computer modeling capabilities to simulate tightly coupled electrothermal phenomena. Of course, it also was not possible to accurately measure the power/current density distribution inside the solid workpiece during induction heating, without disturbing an eddy current flow. The first publication that provides a quantitative evaluation of a magnetic-wave phenomenon was published in (*8*), with further research provided in (*1,6,13,14*).

Tightly coupled electromagnetic-thermal software enables a quantitative estimation of the magnetic-wave phenomenon. **Figure 9** shows the temperature profile (**Figure 9**, left) and power density distribution, (**Figure 9**, right), along the radius of a 36 mm

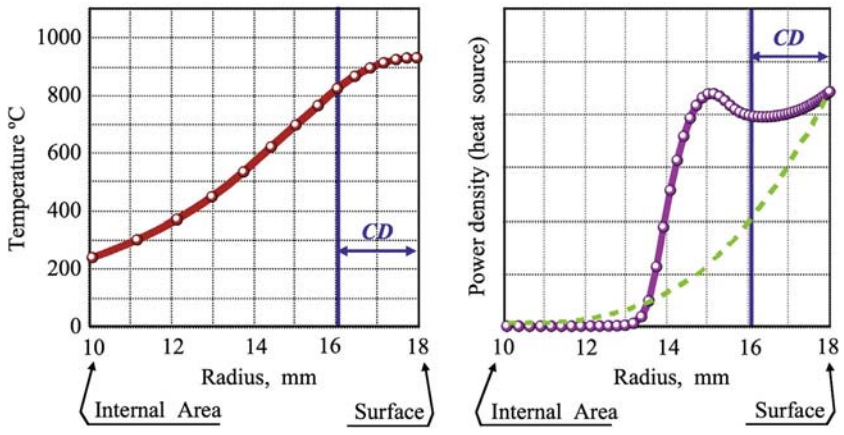

Figure 9 Solid lines represent radial distribution of temperature (left) and power density (right) when induction surface hardening carbon steel shafts using 10 kHz. Required case depth is 2 mm. The dashed curve in the graph at right is the commonly assumed exponential power density distribution. Reproduced from Rudnev, V., Demidovich, V. Advanced Computation Software for Everyday Use in Modern Induction Heat Treating. *Proceedings of 17th ASM Heat Treating Conference,* Indianapolis, 15–18 Sept., 1997; pp 551–555.

in diameter medium carbon steel shaft at the final stage of heating using a frequency of 10 kHz. For comparison, the dotted curve illustrates the common assumption of an exponential curve for power density distribution and the solid curve shows an actual magnetic wave distribution obtained as a result of computer simulation (14).

The main cause of a magnetic wave relates to the differences in magnetic properties of the surface and subsurface regions. In the majority of induction hardening, the carbon steel retains its magnetic properties in the subsurface region; the surface region is nonmagnetic, being heated above A_{c3} critical temperature for austenization. In some cases, this phenomenon can manifest itself in formation of the maximum value of heat sources being located in an internal subsurface layer of the workpiece and not at its surface.

The phenomenon of the wavelike distribution of power density has a marked effect on the choice of frequency that would allow providing the required hardness depth. Therefore, in induction surface hardening the selection of optimal frequency is not as obvious a task as it might appear using rules of thumb, or as it was presented in the great majority of publications devoted to induction heating, based on the commonly accepted assumption of the exponential heat source distribution.

It is important to be aware that the magnetic-wave phenomenon of power density distribution does not appear solely along the radius/thickness of the workpiece. It also occurs when studying three-dimensional (3D) power density distribution. The causes for its appearance remain the same. Numerical computer modeling using appropriate software helps to reveal a complexity of magnetic-wave phenomenon.

Figure 10 shows an example of the selective induction-hardening application – the top and bottom end regions of the cup-shaped component required being selectively hardened. The area between those two regions should retain ductility, and its hardening was prohibited (*14*).

Because of the symmetry of components, only one-half of it (the right half) was modeled using finite-element analysis (FEA). **Figure 11** shows FEA mesh (left) and computer-simulated magnetic field distribution (right) at the final stage of heating using two two-turn inductors and U-shaped magnetic flux concentrators. Frequency is 25 kHz.

The plot of the magnetic field distribution (**Figure 11**, right) clearly indicates the demarcation of the cup's regions heated both above and below the Curie temperature. The concentration of magnetic field lines can be clearly seen. The magnetic-wave phenomenon appears at a magnetic–nonmagnetic border. The sequential dynamics of temperature profiles during induction heating is shown in **Figure 12**.

The magnetic wave was not the only physical phenomenon that was required to be taken into consideration in order to accurately simulate the induction selective hardening process and determine an optimal coil design that resulted in a desirable temperature distribution. Some of the challenges in this case study were related to the following phenomena (*14*):

From an electromagnetic perspective: It was necessary to ensure the balance among three electromagnetic effects: proximity effect, 'ring' effect, and end effect. Each of those effects influences the distribution heat generation and temperature profile. By determining an optimal coil design and process recipe, it was possible to balance those electromagnetic effects and obtain desirable final temperature distribution.

From a heat transfer perspective: During the heating cycle, the presence of colder neighboring areas creates greater cooling effect (the cold sink effect) experienced by end regions. This means that during the heating cycle, due to thermal conductivity, uneven amounts of heat will be removed from different areas of the required heat zones. This demands designing inductors that can intentionally distribute power density nonuniformly, compensating an intensive heat sink effect and producing a required temperature pattern at the end of heating.

From a design perspective: It was important to come up with a relatively simple, cost-effective, and robust coil design that would provide hardening selective end areas of the component with high and repeatable quality and with minimum shape distortion.

Computer modeling precisely addressed the presence of the above-discussed process features and determined an optimal inductor design, taking into consideration a complex 3D appearance of the magnetic wave phenomenon (radial and longitudinal).

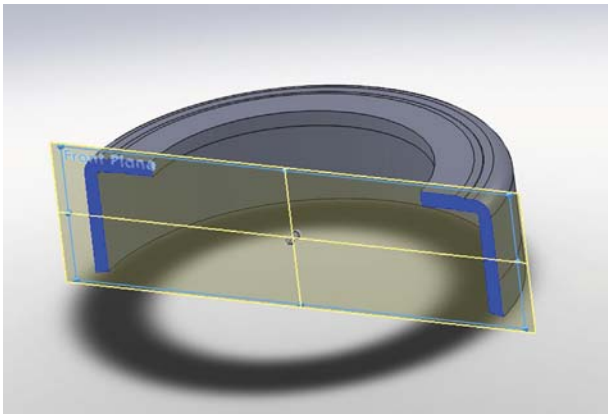

Figure 10 Selective areas of cup-shaped components required induction through hardening.

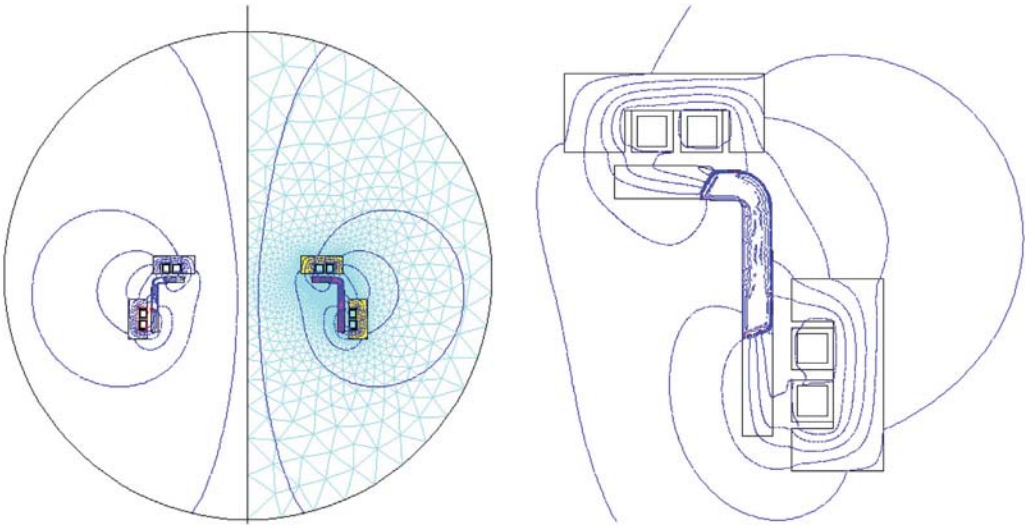

Figure 11 FEA mesh (left) and computer-simulated magnetic field distribution at the final stage of heating (right) using two-turn inductors and U-shaped magnetic-flux concentrators when selective hardening of end regions of cup-shaped component. Due to the symmetry of the component, only the right half was modeled.

12.15.1.4 Eddy Current Cancellation

In through hardening applications, the relationship between workpiece diameter-to-penetration depth (in case of solid cylinders) and thickness-to-current penetration depth (for flat or rectangular workpieces) is critical for obtaining high heating efficiency and an ability to reach austenizing temperatures.

The cross-sectional size of the solid cylinder required to be through hardened must be at least 3 times (but preferably 4 times) that of the eddy current penetration depth; otherwise current cancellation might occur. This is because induced eddy currents circulating in the opposite sides of the solid cylinder are oriented in opposite directions. Upon reaching by the current penetration depth certain values compared to the physical size of the workpiece (i.e., diameter or thickness), they might start canceling each other, dramatically reducing heat intensity and heating efficiency.

In order to avoid this cancellation, frequencies for through hardening of the solid cylinders should be selected in such a way that the current penetration depth does not exceed approximately one-fourth the diameter for solid cylinder parts and one-half the thickness for flat workpieces (i.e., plates) when using solenoid coils. When the cylinder diameter is less than four penetration depths or a plate thickness less than two penetration depths, the electrical efficiency of induction coil will be rapidly decreasing.

When through hardening tubular components, the phenomenon of current cancellation is more complex and is a nonlinear function of at least three parameters: ratio 'wall thickness-to-δ,' ratio 'tube diameter-to-δ,' and specifics of inductor design (*1*). Numerical computer modeling helps to determine conditions when current cancellation can be avoided.

12.15.2 Design Considerations for Induction-Hardening Processes

12.15.2.1 Effect of Prior Microstructure and Heating Rates

The first step in designing an induction-hardening machine is to specify the required hardness pattern, including the surface hardness, case depth, and hardness transition zone. The hardness pattern is directly related to temperature distribution and is controlled by selection of frequency, time, power, and workpiece/coil geometry.

When hardening steel parts, the critical temperatures are often determined based on the iron–iron carbide ($Fe–Fe_3C$ diagram) phase transformation diagram. This widely used diagram is a plot of temperature versus carbon content (*10*,*15*) and shows the effects of heating or cooling of the steel on transformations in its crystal structure. It is also used to determine the temperature ranges over which certain heat treatments may be carried out.

However, it is important to be aware that this diagram might be misleading in the majority of induction-hardening applications because it is valid only for the equilibrium condition of plain carbon steel.

A major requirement of an equilibrium condition is sufficiently slow heating and absence of thermal hysteresis. The induction process simply does not qualify because the heating rate, or heat intensity, often exceeds 100 °C s^{-1} and in some cases reaches 1000 °C s^{-1} and even higher. Such intensive heating drastically affects the kinetics of austenite nucleation and growth during heating, shifting it to higher temperatures (**Figure 13**) in order to create sufficient conditions for the required diffusion-based processes (related to carbide dissolution, austenite formation, and obtaining a homogeneous austenitic structure with a uniform distribution of carbon).

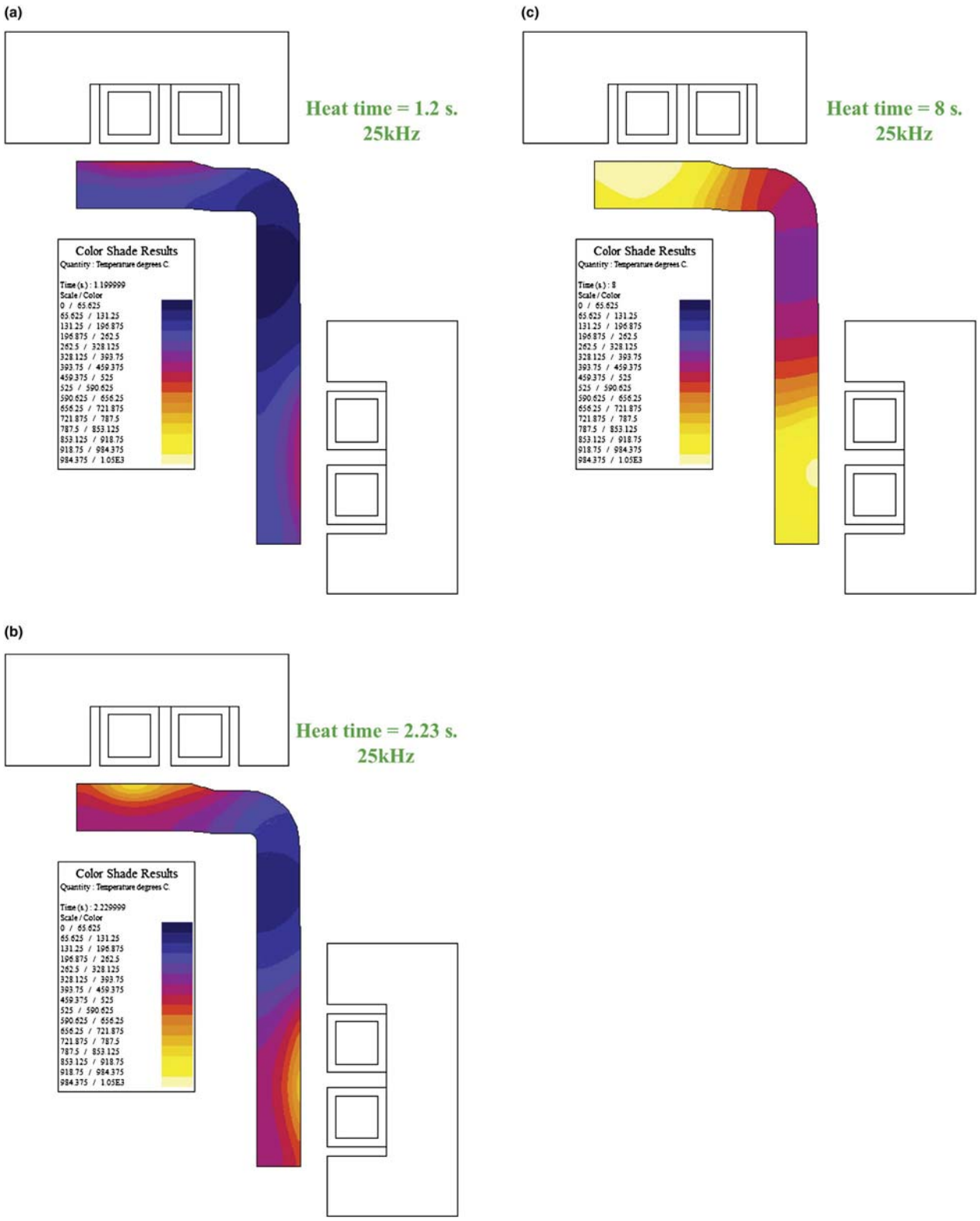

Figure 12 Computer simulation of the sequential dynamics of selected areas of cup-shaped components using two two-turn inductors and U-shaped magnetic-flux concentrators when selective hardening of end regions of cup-shaped component. Due to the symmetry of the component, only the right half was modeled. Courtesy of Inductoheat Inc.

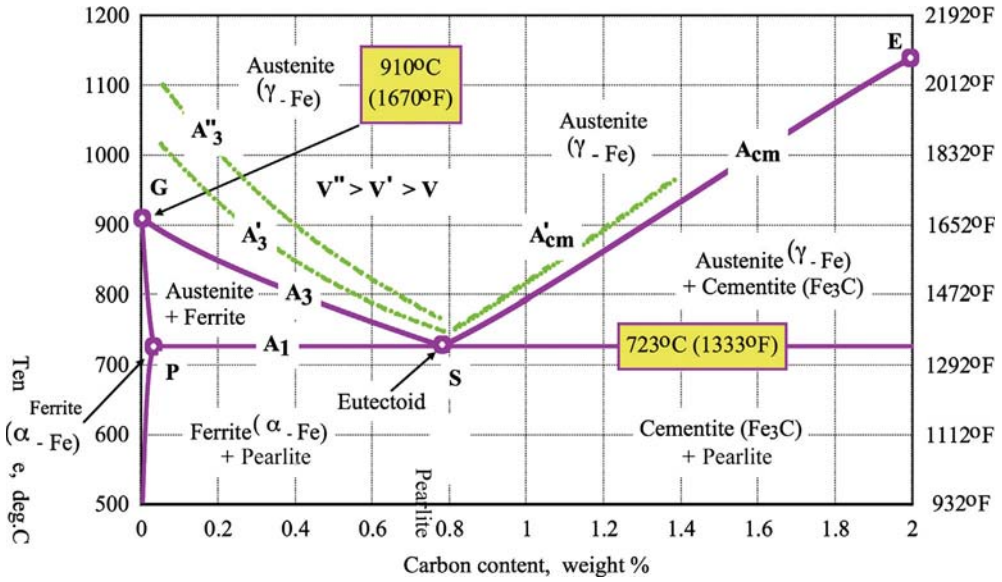

Figure 13 Lower portion of the Fe–Fe_3C equilibrium phase transformation diagram and its variation when an intensive heating rate is used. Note: A_3'', A_3', A_3, and A_{cm} at heating rates (°C s^{-1}) V', V, and V, respectively ($V' > V > V$). Reproduced from Rudnev, V. Metallurgical Insights for Induction Heat Treaters, Part I: Induction Hardening Temperatures. In *Heat Treating Progress*, ASM Int., May/June, 2007; pp 15–17.

The presence of heterogeneous austenite can result in an unacceptable structure of as-quenched parts. Upon quenching, the decomposition of heterogeneous austenite first begins in regions with lower carbon concentration. This results in a respective increase of the M_s temperatures and corresponding shift of the continuous cooling transformation curve (CCT curve) to the 'left.' The CCT curve of regions with excessive amounts of carbon will be shifted in the opposite direction with a respective decrease of the M_s temperatures, resulting in a potential corresponding heterogeneity of the as-quenched structure.

Probably the most comprehensive study on the correlation of heat intensity to the ability to obtain homogeneous austenite was conducted by J. Orlich, A. Rose, and their colleagues at the Max Planck Institute fur Eisenforschung GmbH in Dusseldorf, Germany (*16,17*). They developed atlases that consist of more than 500 pages of nonequilibrium time-temperature-austenizing diagrams for a variety of steels after they have been rapidly heated using heat intensities from 0.05 to 2400 °C s^{-1}. Those diagrams should be used by induction-hardening practitioners instead of the conventional Fe–Fe_3C diagram in determining the most suitable hardening temperatures of steels.

Besides nonequilibrium heating and cooling conditions, an appreciable amount of residual elements, alloying elements, and pressure can noticeably affect hardening temperatures as well.

The microstructure of steel prior to heat treatment (sometimes also referred to as the initial structure, structure of the parent material, or structure of the 'green' part) also has a pronounced effect on the hardening results and a selection of required process parameters (*18*). These parameters include the austenizing temperature and the amount of time the part is required to be held at that temperature. As can be seen from **Figure 14**, the required induction-hardening temperature range for AISI 1042 plain carbon steel depends not only on the heat intensity but also on the material's prior microstructure (*19*):

880 °C to 1093 °C, for annealed prior microstructures;
840 °C to 1000 °C, for normalized prior microstructures; and
820 °C to 930 °C, for quenched and tempered microstructures.

Over the years, the effect of prior structure on heating rate has been studied in numerous publications, including (*1,5,6,10,11,15–34*) and can be basically explained as follows.

A quench and tempered prior structure is the most favorable. It ensures rapid transformation, which allows a reduction in the temperature required for austenite formation. This prior structure is associated with a fast and consistent response of the steel to induction hardening, with minimum amounts of grain growth, shape/size distortion, and surface oxidation; a minimum required heating energy; and a well-defined 'crisp' hardness pattern having a sharp and narrow transition zone. This type of initial structure can also result in higher hardness and a deeper hardened case depth than characterizes other prior structures.

If the initial microstructure of a steel component has a significant amount of coarse pearlite and, most importantly, coarse ferrites or clusters or bands of ferrites, then the structure cannot be considered favorable. Ferrite is practically a pure iron and does not contain a sufficient amount of the carbon required for martensitic transformation. Pure ferrite consists of less than 0.025% carbon. Large areas (clusters or bands) of ferrite require a long time for carbon to diffuse into carbon-poor areas. Those ferrite clusters or bands could act as one very large grain of ferrite and will often be retained in the austenite upon rapid heating (*1,20,21*). After quenching, a complex ferritic–martensitic microstructure can form. Scattered soft and hard spots and poor mechanical properties

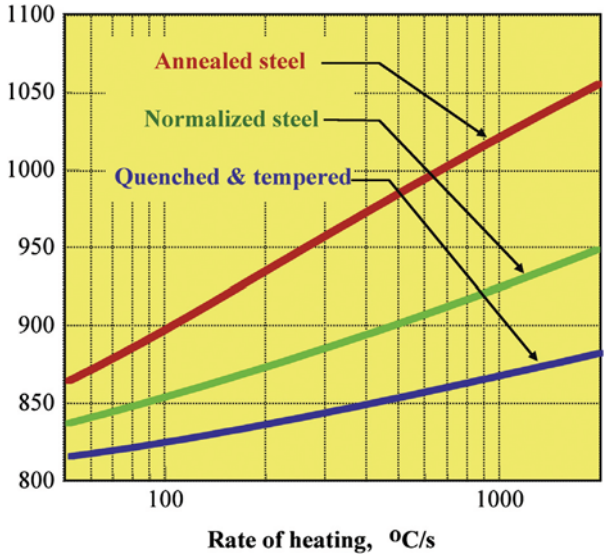

Figure 14 Effect of initial microstructure and heating rate on A_3 critical temperature for AISI 1042 steel. Reproduced from Feuerstein, W.; Smith, W. *Trans. ASM* **1954,** *46*, 1270.

characterize this structure. Appreciably elevated temperatures and longer heating times are required to austenitize steels that have these structures. It is strongly recommended that severely segregated and banded initial microstructures in 'green' parts be avoided.

Steels with large stable carbides (i.e., spheroidized microstructures) also have poor response to induction hardening and result in the need for prolonged heating/soaking and significantly higher temperatures to complete austenitization. Longer heating times lead to grain growth, the formation of coarse martensite, extended transition zone, excessive oxidation/decarburization, and increased shape distortion. Coarse martensite has a negative effect on such important properties as toughness, impact strength, and bending fatigue strength, and is susceptible to cracking.

Therefore, when one is determining appropriate induction-hardening temperatures for a carbon steel component, it is imperative to bear in mind the limitations of the equilibrium Fe–Fe_3C phase transformation diagram and to take into account heating intensity and the microstructure of the 'green' part.

As opposed to other heat-treating techniques, induction hardening is significantly affected by variation of steel's chemical composition. Therefore, a favorable initial metal condition also includes tight control of the specified chemical composition of steels (i.e., H-steels) and cast irons. Wide compositional limits cause surface hardness and case depth variation. Consequently, tight control of the composition reduces possible variation of the heat-treat pattern resulting from multiple steel/iron sources. Microstructurally and chemically segregated structures and banded initial microstructures of 'green' components should be avoided.

All commercial grades of steels contain limited amounts of additional chemical elements that happened to be in steel as traces or residual impurities in the raw materials or were added to the melting pot in order to create certain conditions during the steelmaking process. Excessive amounts of these elements, their heterogeneous distribution, and the presence of appreciable-size stringers can result in stagger hardness and strength degradation. For example, the presence of large stringers of manganese sulfide inclusions can act as the stress raisers promoting intergranular cracking. Sulfur level, copper, phosphorus, and nitrogen content should be closely controlled.

Besides chemical composition control and prior microstructure, the surface condition of the heat-treated component is another factor that can have a pronounced effect on heat-treating practice. Voids, microcracks, notches, and other surface and subsurface discontinuities, as well as other stress concentrators, can initiate cracking during hardening when the steel goes through the expansion–contraction cycle; thermal gradients and stresses can reach critical values and 'open' notches and microcracks (*1,20,21*). Conversely, a homogeneous metal structure with a smooth surface free of voids, cracks, notches, and the like improves heat-treating conditions and positively affects important workpiece characteristics, such as bending fatigue strength, endurance limit, impact strength, and parts' durability and life.

12.15.2.2 Obtaining Fully Martensitic Structures

In induction hardening of steels, the ability to obtain a certain degree of martensitic structure is often the measure of the success of the process. Martensite is a supersaturated solid solution of carbon in ferrite with a body-centered tetragonal (BCT) structure. Upon rapid cooling, carbon is trapped in the crystal structure. High hardness develops in the steel as a result of the distortion that occurs during the transformation from face-centered cubic (FCC) austenite to BCT martensite and the fine dislocation substructure that develops in the martensite crystals during the diffusionless, shear transformation (*10,11,15,33*).

Martensite formation is governed by the shear-type (diffusionless) transformation of austenite; that is, the transformation occurs almost instantaneously upon reaching a certain temperature. Since the transformation is diffusionless, the initially created martensite plates do not grow in size with time. Instead, new plates continue to form upon further cooling.

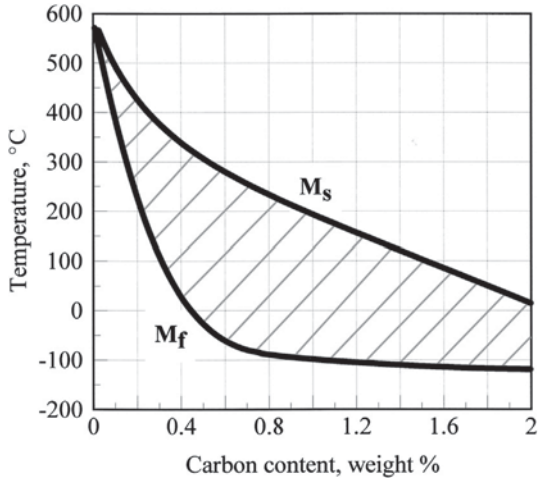

Figure 15 M_s and M_f temperatures as function of carbon content according to Gulyaev, A. *Metallurgy*; Metallurgia: Moscow, Russia, 1977.

If the continuous cooling transformation (CCT) diagram of steel is shifted far to the left, the cooling curve might enter the upper transformation-start region practically despite the quench severity, preventing the formation of an entirely martensitic microstructure. In such cases, the final microstructure of the hardened layer will consist of a combination of martensite and some upper transformation products (such as pearlite and bainite). Although a fully martensitic structure might not be obtained, the amount of upper transformation products can be appreciably small (practically speaking) and, depending on the application, might not noticeably affect component mechanical properties.

Martensitic transformation occurs over a temperature range between the M_s (martensite start) and M_f (martensite finish) temperatures. The range depends on the steel's chemical composition and, from a practical perspective, cannot be changed by varying quench severity. If quenching is interrupted at a certain temperature within the martensite transformation range, no further transformation to martensite will occur. However, the transformation will resume upon further cooling.

In plain carbon steels, the M_s to M_f temperature range is directly related to the carbon content. Some authors have provided charts for rough estimation of those temperatures (**Figure 15**) (*37*). M_s temperatures for the majority of steels are well established. In contrast, M_f temperatures are not well determined and are affected by many factors. For example, recent studies conducted by George Krauss revealed that even relatively low-carbon steels always contain some retained austenite meaning that M_f temperatures actually never reached, certainly on quenching to room temperature (*125*).

The carbon content and amount of martensite that form directly determine the maximum hardness of a given steel. In the 0.2–0.65% carbon content range, the hardness of the steel is proportional to the carbon content.

M_f temperatures for plain carbon steels with high carbon content, cast irons, and some alloy steels are well below room temperature. Thus, even if quench severity is sufficient to miss the upper transformation region of the CCT diagram, a fully martensitic structure will not be obtained within the hardened layer. The existence of a noticeable amount of untransformed austenite – retained austenite – will be unavoidable (**Figure 16**).

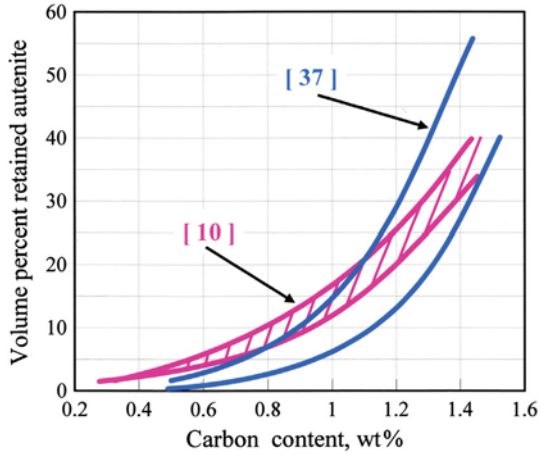

Figure 16 Retained austenite as a function of carbon content according to Krauss, G. *Steels: Heat Treatment and Processing Principles*; ASM Int., 2005; Gulyaev, A. *Metallurgy*; Metallurgia: Moscow, Russia, 1977.

In plain carbon steels that have carbon content below 0.5%, the retained austenite is typically less than 2%. It is well accepted that it is difficult to accurately measure this amount of retained austenize using light optical microscopy. As carbon content increases, so does retained austenite, rising to around 6% in steels with 0.8% C and perhaps exceeding 30% for steels with 1.25% C.

The amount of retained austenite also increases with increasing hardening temperatures. Alloying elements that lower the M_s temperature often increase the amount of retained austenite. Besides carbon content and alloying elements, the temperature of the quenchant can also affect the amount of retained austenite. Several relations (i.e., Harris–Cohen correlation, etc.) exist to calculate the amount of retained austenite in a given steel based on the temperature difference between M_s and quench.

Cryogenic treatment can be used to transform retained austenite into martensite. An untempered fully martensitic structure has low toughness.

Case study: In the past, some induction heat treaters have been confused by observing the presence of nonmartensitic structures in induction-hardened parts where, based on conventional metallurgical practice and widely used heat-treating diagrams, a fully martensitic structure should have been obtained. An example follows.

- *Observation # 1*: After induction heating and quenching of a steel component, there was no evidence of ferrite/pearlite networking. This led the heat treater to conclude that austenitization had been completed.
- *Observation # 2*: Metallographic examination revealed no evidence of excessive grain growth, scale formation, or decarburization; this finding supported the idea that the final temperature had not been too high. This result was verified by measuring the surface temperature of the heated component.
- *Observation # 3*: Based on data provided by the steel's manufacturer, the M_f temperature was above the temperature of the quenchant. Quench time, concentration, and severity of cooling were sufficient to cool the heated component below the M_f temperature and miss the 'nose' of the CCT curve.

Analysis: These observations led the heat treater to expect a fully martensitic structure to be obtained after quenching. However, metallographic examination revealed a small amount of nonmartensitic transformation products.

An improper assumption had been made: The absence of ferrite/pearlite networking in martensite does not mean that homogeneous austenite had been obtained. One characteristic of inhomogeneous austenite is a nonuniform distribution of carbon.

After fast heating, a ferrite/pearlite networking may not exist, but there might still be an inhomogeneous distribution of carbon in the austenite. Instead of a ferrite/pearlite networking, there could be some localized carbon-enriched areas and regions where the carbon concentration is noticeably reduced. Since both the M_s and M_f temperatures depend on carbon content; the high- and low-carbon areas of the part with inhomogeneous austenite will have different CCT curves upon quenching. As a result, these areas have different critical cooling rates, and other, nonmartensitic transformation products may appear in the predominantly martensitic structure. A longer time for austenizing temperature is required to reduce the heterogeneity of austenite and to fix this problem.

Carbon content influences not only the maximum achievable surface hardness and case depth, but also the transition zone. For example, eutectoid steels always have a shorter transition zone compared with that of hypoeutectoid steels (assuming thermal conditions upon heating and quenching are similar).

12.15.2.3 Superhardening Phenomenon

Surface hardness of case-hardened parts can be slightly higher than surface hardening of identical parts that are through hardened. This phenomenon sometimes is referred to as superhardening. Because of this phenomenon, for given carbon steel, the surface hardness of a part surface hardened using induction could be 2–4 HRC (Rockwell Hardness, scale-c) higher than is normally obtained for a given carbon content for through-hardened steel (*126*).

The superhardening phenomenon is not completely understood, and its origin has not been established. However, it can be attributed to several factors, including higher residual stresses and final microstructure (carbide shape and density, retained austenite, dislocation density of the martensitic matrix, grain size, and others). The short heating cycle results in fine austenitic grain sizes that occur because, in induction hardening, the steel typically is at the austenitizing temperature for a short time, reducing the possibility of grain growth.

Another factor that might contribute to superhardening is the higher lattice strain from appreciable residual compressive stresses at the surface of the part when its internal regions and, in particular, the core remain at a lower temperature or at ambient temperature.

In addition, the existence of a cold core that serves as a cold heat sink has a marked effect on the severity of the cooling rate during quenching. In a majority of induction surface hardening applications, the core temperature does not rise significantly due primarily to a pronounced concentration of electromagnetic energy within the surface layer (skin effect), high heat intensity, and short heating time. As a result, heat transfer from the surface of the workpiece to its core during the heating stage is not sufficient to significantly raise the core temperature (*1*). The total quench severity during the quenching stage of heat treating is a product of the severity of surface cooling by the quenchant and internal cooling due to thermal conduction of heat from the hot surface toward the cold core – the so-called cold heat sink phenomenon (*38,39*). A cold core complements surface quenching by further increasing the cooling intensity at the surface and subsurface regions of the part. In contrast, in most cases hot internal areas of the through-heated parts provide undesirable thermal support to a part's surface region that is being quenched by a quenchant by decreasing the total value of quench severity.

The phenomenon of the superhardening of induction surface- (case-) hardened parts is particularly noticeable in steels with a carbon content of 0.35–0.65%, case depths less than 0.125 in. (3.2 mm), and heat times less than 4 s. A prior microstructure also has a pronounced effect on the appearance of the superhardening phenomenon. Fine-grain homogeneous normalized prior structures, as well as quenched and tempered structures, have a greater chance to exhibit superhardening. Annealed and spheroidized prior structures seldom reveal this phenomenon. In some cases, the superhardening phenomenon could allow a user to apply a lower steel grade (lower carbon content) without sacrificing the desired surface hardness and hardness profile.

Case study. According to end-quench hardenability test data adapted from *Heat Treating Guide: Practice and Procedures for Irons and Steels*, the maximum hardness range for AISI 1038 steel at a distance of 1 mm from a quenched surface should not exceed 58 HRC and can be as low as 51 HRC (*40*). However, induction surface hardening practice shows that when hardening the pins and main journals of a crankshaft using nonrotational SHarP-C technology (heat time is about 3–4 s and case depth is approximately 1.8–2.5 mm) using a low-concentration polymer quench, hardness readings at 1 mm below the part's surface can often be 60–61 HRC. Even at a distance of about 2 mm below the surface, the hardness remains at the same 60–61HRC level instead of the expected maximum hardness of 55 HRC as predicted by the end-quench hardenability test (*40*). Experience reveals that it was possible to provide a sufficient cooling severity and obtain surface hardness of about 53–56 HRC by just relying exclusively on the cold sink effect (no use of liquid quenchant).

12.15.2.4 Induction-Hardening Coil Designs

An inductor configuration depends on specifics of the particular application that include but are not limited to geometry of the workpiece, heating mode, production rate, required heating profile, available power/frequency source, and the material handling (i.e., how the part is moved into the inductor or the inductor indexes into the heating position, whether rotation of the part is required, or how the part is transferred after heat treatment). **Figure 3** shows a small sample of a virtually endless number of coil designs for induction hardening.

Generally speaking, inductors for induction-hardening applications can be divided into four major categories: scanning, progressive, single-shot, and special inductors (*1*).

12.15.2.4.1 Copper Selection and Coil Fabrication

As discussed in (*1,41–43*), copper is almost exclusively used for coil fabrication instead of other metals because of its unique properties that include, but are not limited to, good electrical and thermal conductivities, inherent corrosion resistance, and superior cold and hot workability and other mechanical properties. Copper's availability and cost are other important factors that make it an excellent choice for coil fabrication. Oxygen-free (OFC) copper grade as well as some other copper grades are used.

The electrical conductivity of copper, σ_{Cu}, is an important physical property that dramatically affects the life of the induction coil because the electrical conductivity of a material is a measure of how easily it conducts electric current. The reciprocal of σ_{Cu} is electrical resistivity, ρ_{Cu}. Electrical conductivity of a particular copper grade can also be expressed in comparison to a volume conductivity of 100% of the International Annealed Copper Standard, written 100% IACS (*44*).

Electrical resistivity of copper varies with temperature, chemical composition, metal structure, and grain size, and depends strongly on purity. Phosphorus, tin, selenium, tellurium, and arsenic are some of the typical impurities found in commercially pure copper. Impurities distort the copper lattice, affecting ρ_{Cu} to a considerable extent. Even relatively small amounts of impurities or trace elements, including oxygen (which oxidizes copper), can appreciably increase copper's electrical resistivity, leading to a corresponding increase in coil electrical resistance and kW losses dissipated within the inductor (*42*).

As for most metals, ρ_{Cu} rises with temperature. Uncounted heat dissipation within the copper causes an increase in coil electrical resistance and correspondent increase in kW losses. Therefore, it is important to make sure that copper is sufficiently water-cooled.

Although alloying copper can noticeably improve certain mechanical properties and corrosion resistance, it also reduces the material's thermal conductivity. This decreases the capability of water-cooled passages to remove the heat and properly cool an inductor and reduce the ability to avoid the localized overheating due to the less intensive heat removal because of diminished thermal conduction.

Hardening inductors are typically CNC (computerized numerical control) machined from a solid copper block, thus making them rigid, durable, and repeatable. CNC machined inductors and utilization of 'quick-change' devices guarantee precision of coil fabrication and alignment with respect to hardened component eliminating or dramatically reducing the amount of time required to 'tweak' new coil after replacement and reduce downtime. As an example, **Figure 17** shows a semifinished single-shot inductor being CNC machined from a single copper block.

Copper tubing (rectangular or round cross-section) is also used for coil fabrication. Copper tubing is often annealed to improve its ductility, bending properties, and workability. When sharp bends, complex coil shapes, or small diameters are required, bending or brazing assembles components of coils made from tubing. Joints are often overlapped, creating so-called tongue and groove joints (*1*).

Different alloys (fillers) can be used for copper brazing. Good wetting and free-flow characteristics are critical. A silver-base brazing alloy that contains 35–45% Ag is commonly used for brazing coil parts (*1*). To provide sound joints, the joint gaps

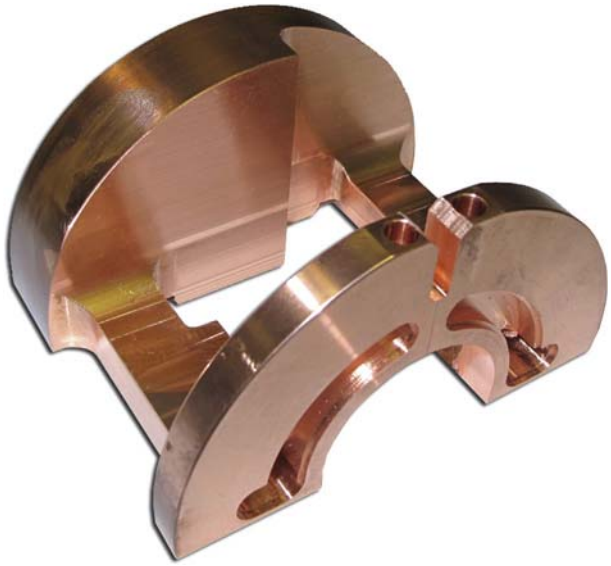

Figure 17 Semifinished single-shot inductor being CNC machined from a single copper block.

(clearances) should be held to a minimum but be sufficient enough for the silver-base alloy to flow freely into the joint due to capillary action.

Even though silver has superior electrical and thermal properties compared with copper, the fact that joint gaps are filled by a silver-base material remains an area of concern because trapped gases, porosity, and the presence of oxides and other elements increase the electrical resistance of the joint area compared with that of solid copper. Excessive kW losses occur in the joints (unless the joint is located in a portion of the coil that is not expected to carry electrical current) and make them noticeably weaker (*42*). If the induction coil contains numerous brazed joints and, in particular, if there are 90° joints, then water flow in cooling coil turns could be impeded, requiring booster pumps.

Reduction of braze joints, particularly in current-carrying areas, is imperative for fabrication of long-lasting inductors. Improvements in copper-bending technology have a significant positive effect on the coil life and up-time of induction heating systems. For example, rectangular copper tubing 6 mm × 6 mm and 1 mm wall can be easily bent into a complex shape having 90° bends and can even be double twisted at angles of nearly 180° without collapsing its walls.

The majority of inline inductors and inductors for heating internal surfaces are multiturn solenoid coils that are typically fabricated using round, square, and rectangular copper tubing. It is important to remember that the work hardening of copper occurs with deformation. This is the reason why coil builders anneal the tubing every few bends, keeping copper ductile and preventing wall collapse and copper fracture. When forming close bends or fabricating coils using small-diameter copper tubing (i.e., 4-mm-diameter round tubing), it is desirable to fill it with fine-particle sand or low melting temperature material. This helps to prevent the collapse of tubing during its bending.

It is imperative to remember that the main goal of coil copper is to conduct electrical current. Therefore, inevitably some kW losses will be generated within the coil copper due to Joule losses. Additional heat is absorbed by copper due to thermal radiation and convection from workpiece surface. Therefore, it is essential that water-cooling passages and amount of flow are sufficient to provide required cooling. All means should be taken to minimize the heat generation in coil copper.

The heating face copper wall thickness should increase as frequency decreases. This fact is directly related to the current penetration in the copper and the copper edge effect, and it holds true for both coils machined from solid copper and coils made of tubing.

A quick estimate of current penetration depth, δ_1, in the copper, within the 15–75 °C range can be calculated using the following formula:

$$\delta_1,\ \text{mm} = 70/(\text{frequency},\ \text{Hz})^{1/2} \quad [2]$$

In order to avoid unnecessary efficiency reduction, a current-carrying copper tubing wall (d_1) should be greater than $d_1 > 1.6\ \delta_1$ (*1*). A coil tubing wall thinner than 1.6 δ_1 reduces coil efficiency due to an increase in kW losses. In some cases, the copper tubing wall d_1 can be noticeably thicker than 1.6 δ_1 (*43*) because it may be mechanically impractical to use a tubing wall thickness of, for example, 0.2 mm.

There are several common ways to protect induction coils from the sometimes harsh environment in which they operate. In most hardening applications, the workpiece surface is heated to a temperature above 900 °C. The impact of thermal radiation and convection from the heated part complements kW losses generated within the coil copper and can be detrimental to the coil copper degradation. This emphasizes an importance of proper water cooling and the design of the cooling passage. Coil cooling should be as close to the heating face as possible, particularly when U-shaped flux concentrators are used.

Cast refractory liners or ceramic guides can be added to induction systems (when space is available) to protect the coil copper from accidental touching of the workpiece and to improve its thermal efficiency. This design concept is often used in inline multicoil systems. If a liner is damaged, it can usually be easily replaced without having to remove the inductor from the heating system. This reduces equipment downtime in applications such as inline heat treatment of multiple rods or tubes. Unfortunately, the use of refractory necessitates having greater copper-to-workpiece gaps negatively affecting coil electrical efficiency.

Total efficiency of the induction coil (η) is a combination of both coil thermal efficiency (η_{th}) and coil electrical efficiency (η_{el}) (*1*):

$$\eta = \eta_{el}\eta_{th} \quad [3]$$

The value of η_{el} represents the ratio of the power induced in the workpiece to the total power that comprises workpiece power and electrical losses in the coil copper, electrically conductive bodies located in the close proximity to induction coil and transmission losses. The value of (η_{th}) indicates the amount of thermal losses compared to the heating power and includes heat radiation and convection, as well as thermal losses due to thermal conduction to fixtures, liners, support structures, and the like.

As mentioned above, thermal insulation or refractory materials can significantly decrease surface thermal losses. At the same time, the use of refractory results in a larger coil-to-workpiece air gap. This inevitably results in deterioration of electromagnetic coupling between the induction coil and heated workpiece, and accordingly leads to decreased coil electrical efficiency (*1*).

Therefore, on the one hand, refractory allows improving a coil thermal efficiency. On the other hand, it reduces coil electrical efficiency. A decision to use or not to use the refractory is always a reasonable compromise. In some cases, it is advantageous to have as small a coil-to-workpiece air gap as possible, maximizing coil electrical efficiency; in others, it is preferable to use a refractory and decrease surface heat losses and more than compensate for the loss of energy with a greater coil-to-workpiece air gap. In the great majority of induction-hardening applications, reducing an air gap is the most popular approach. Numerical computation helps to make an appropriate decision regardless of whether use of a refractory would be beneficial.

At higher frequencies, coil currents are typically lower. Frequency reduction is usually associated with coil current increase and a correspondent increase of electromagnetic forces experienced by an inductor and its vibration. Therefore, more attention must be paid to coil support and brazed joints. Nonmagnetic metal studs or electrically nonconductive structures held together with an insulator provide added support.

When designing and fabricating hardening inductors, it is important to consider the electromagnetic field in the immediate vicinity of the inductor. The use of low-resistivity nonferrous materials (preferably electrically nonconductive) in the area close to the inductor is recommended. Fasteners and washers used to connect bus-work to the inductor should also be nonferrous and preferably nonconductive. The rule of thumb: ferrous materials should be located at least one coil diameter away from the coil. More precise recommendations can be obtained by using computer modeling (*6*).

12.15.2.4.2 Single-Shot Inductors

Setups in which the external or internal surface is induction hardened at one time with an inductor that remains stationary with respect to the part are called *single-shot* operations (**Figures 18** and **19**). Typically, single-shot inductors are used for parts with complex geometries and parts that require complex heating patterns. As an example, **Figure 18** shows a single-shot inductor for hardening internal areas of constant velocity automotive front wheel drive components, and **Figure 19** shows a single-shot inductor for hardening the complex geometry component. In both cases, heat-treated components are static during heating and quenching.

Although encircling solenoid coils are the most electrically efficient inductors, in some single-shot applications, nonencircling inductors are used for a single-shot hardening of symmetrical parts. As an example, **Figure 20**, left, shows a single-shot hardening of a carbon steel shaft having numerous diameter changes, shoulders, and spline. Single-shot profiled inductors are often used for hardening such shafts (**Figure 20**, right). With this type of inductor, the induced currents flow longitudinally rather than circumferentially (except the crossover region under horseshoe-shaped copper loops). Single-shot inductors are typically custom made to

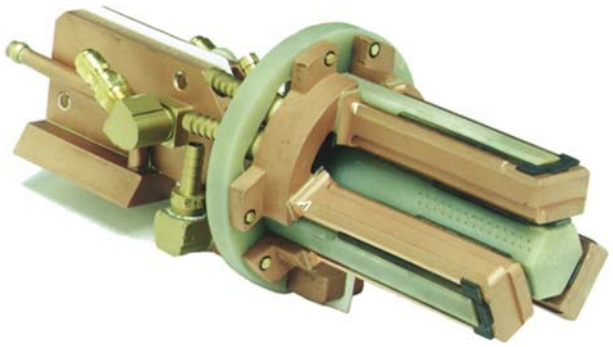

Figure 18 Single-shot inductor for hardening internal areas of constant velocity automotive front wheel drives components. Courtesy of Inductoheat Inc.

Figure 19 A single-shot inductor for hardening complex geometry component. Courtesy of Inductoheat Inc.

induction harden a particular component. This inductor design has become popular for surface hardening of various types of shafts in high-volume production lines. The shaft must be rotated during operation to ensure uniform heating of the surface. Depending on application specifics, rotation speeds range from 60 to 500 rpm. Shorter heating times require faster rotation speeds. Typically, at least six rotations per heat cycle are required. Quenching can be incorporated into inductor design, or it can take place at different places using a quench device that can be positioned below an inductor.

12.15.2.4.3 Scanning Inductors

Parts with a high degree of rotational or axial symmetry are often induction hardened using scanning techniques in which the parts are moved progressively through the coil; alternatively, the coil moves along the workpiece length/height. Thus, with scan hardening only a small portion of the workpiece is induction hardened at any given time. Scan inductors have become popular for surface hardening and through hardening of various types of shafts in high-volume production lines. As an example, **Figure 21** shows a vertical dual-spindle system for induction scan hardening of the steel shafts. Scan rate and coil power are varied during scanning to allow proper accommodation of changes in shaft geometry. The trade-off is coil cost and power supply size that are typically much greater for single-shot inductors than for scan inductors.

Scan inductors are particularly attractive for hardening elongated workpieces for which a single-shot method would substantially increase the cost of power supply, coil, tooling, and auxiliary equipment. Scan inductors also provide superior flexibility compared to single-shot inductors allowing operating components of various lengths.

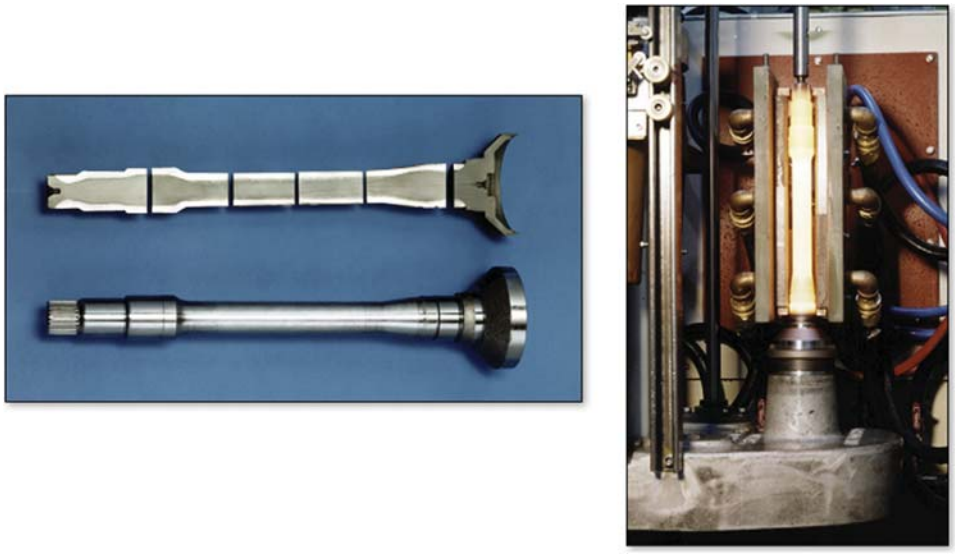

Figure 20 Nonencircling single-shot inductor for hardening shafts. Courtesy of Inductoheat Inc.

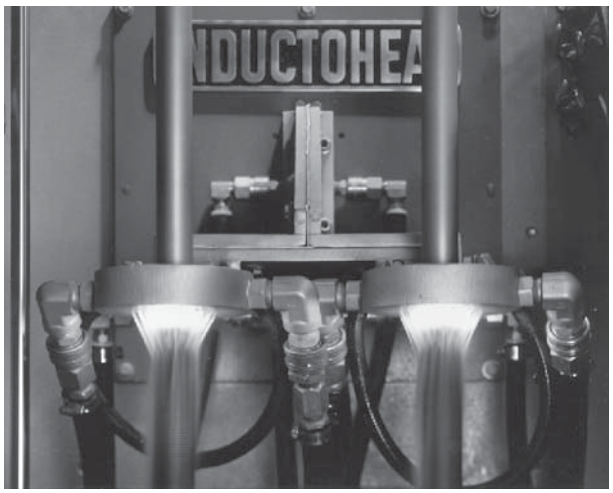

Figure 21 Dual-spindle systems for induction scan hardening of carbon steel shafts. Courtesy of Inductoheat Inc.

Scan inductors (vertical or horizontal) may be one or more turns. Figure 22(a) shows examples of two-turn coils for scan hardening of straight shafts (Figure 22(b)). Those coils require using spray quench followers. In contrast, Figure 23 shows a cross-section of the machined integrated quench scan inductor (MIQ inductor) used in the dual-spindle shaft hardening system shown on Figure 21. Both a coil-cooling chamber and a quench chamber are clearly visible.

The required number of turns is determined by the ability to load match (also called impedance match or load tune) the coils to the power supply and/or by specific process requirements. The impedance (load) matching process is particularly important if

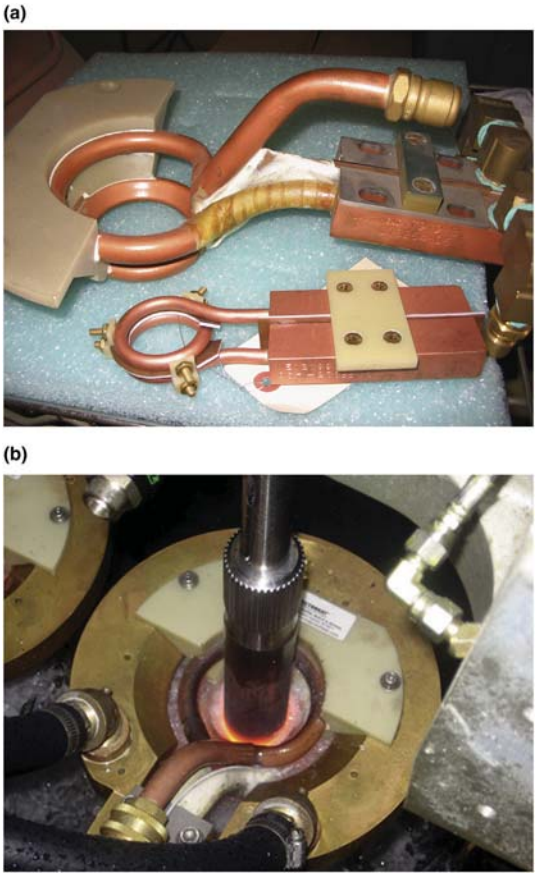

Figure 22 Examples of two-turn coils for scan hardening of straight shafts. Courtesy of Inductoheat Inc.

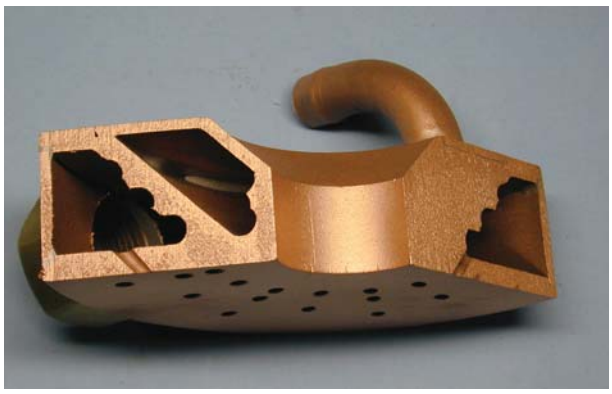

Figure 23 Machined integral quench inductor. Courtesy of Inductoheat Inc.

maximum power is required from the power supply. There should be a balance in power, voltage, frequency, and current to achieve the desired heat intensity and heating pattern. The term *load matching* or *load tuning* is used to describe this process and will be discussed further.

Scan coils with wider heat faces allow faster scan rates, because with the longer inductor, the part will be in the inductor for a longer period of time; this means that the scan rate can be higher.

One main restriction for using the wide heating face scan coils is related to the longer and gradual pattern run-outs and potential difficulty in meeting some hardness pattern specifications when sharp transition is required. Hardness pattern controllability sometimes suffers when wide-face inductors are used.

Single-turn inductors with narrow heating faces are used for hardening fillets with small radiuses and/or where sharp pattern run-outs (cutoffs) are required. An example is the case in which a pattern must end near a snap ring groove. Inductors with narrow heating faces are also useful for obtaining a short transition zones (both axial and radial).

Hairpin inductors are often used for scan-hardening flat surfaces. Transverse flux inductors have limited use in induction through hardening due to its high sensitivity.

12.15.2.4.4 Progressive Inductors

Progressive heating is used for hardening long parts (i.e., wires, rods). Long parts are typically induction hardened horizontally because they are more readily processed in a horizontal manner. However progressive heating is not limited by horizontally processed parts.

The inductors for progressive heating follow the same design principles as conventional scanning or static inductors. A great majority of progressive inductors are multiturn solenoid coils (see **Figure 24**). Progressive heating is used to heat progressively moving workpieces. Progressive inductors comprise a single coil or a number of coils. Sequential heating-soaking stages take place when several inline coils are used. The different heating stages may have diverse power levels and frequencies to optimize heating conditions. Coil design should accommodate the specifics of using different frequencies and power levels.

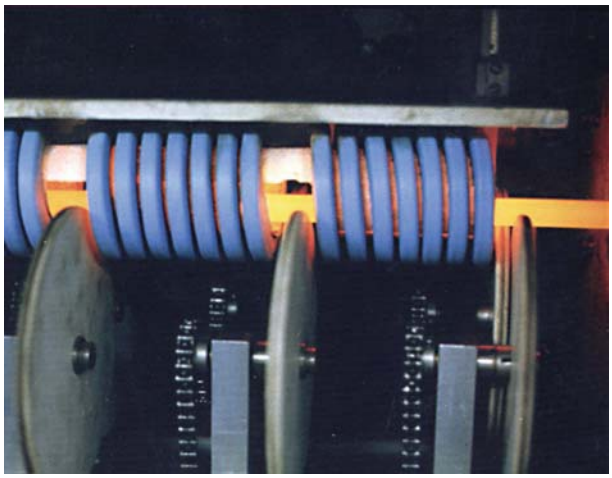

Figure 24 High-frequency progressive heating. Courtesy of Inductoheat Inc.

Just as the current penetration depth in the part is related to the frequency, so is the depth of current flow in the inductor. The wall thickness of the inductor copper tubing might need to be adjusted to accommodate the frequency. As the frequency is decreased, the required copper tubing wall thickness might need to be increased as well, and special measures might require enhancing the coil's rigidity. This is because lower frequencies are usually accompanied by a greater magnitude of current that inevitably leads to greater magnetic forces.

12.15.2.4.5 Specialty Inductors

Over the years industry has developed a family of special or specialty inductors that address specific feature(s) of a particular induction-hardening application. Several considerations affect the selection of a particular specialty inductor style, including:

- Shape of the workpiece
- Area to be heated or hardening pattern requirements
- Material-handling specifics
- Process parameters selection (frequency, power density, time of heating, etc.)
- Specifics of quenching
- Required production rate, etc.

Specialty inductors include the following inductor styles:

- Pancake inductors
- Butterfly inductors
- Split-return inductors
- Hairpin inductors
- U-shaped inductors for hardening crankshafts
- Active-passive inductors for hardening crankshafts and camshafts
- Clam shell or split inductors
- Profiled inductors
- Inductors for heating internal surfaces (ID inductors)
- Master inductor-changeable inserts
- Inductor with doors and doorless inductors for heating flat workpieces
- Channel coils
- 'C'-core inductors
- Multiplace inductors
- Transverse flux inductors
- Traveling wave inductors, etc.

Space limitation does not permit discussing all styles of specialty inductors here. For those who are interested in studying in detail different styles of specialty inductors, we suggest reviewing the following references (*1–9,15,47–58*). The discussion here regarding specialty inductors will be limited to only some of them.

12.15.2.4.5.1 Coils for hardening internal surfaces (ID coils) and hairpin inductors

Induction heating of the internal surface(s) of a workpiece can be used for applications such as hardening, tempering, annealing, shrink fitting, stress relieving, and brazing. **Figure 25** shows a variety of different inductor styles for heating internal surfaces, including solenoid-type cylindrical single-turn and multiturn coils and hairpin inductors. The specifics of designing internal inductors as well as the peculiarity of the selection of process parameters are discussed in (*1,55*).

Single-turn and multiturn solenoids are often used for heating internal surfaces. Internal coils are typically made of copper tubing that is spiral wrapped the same way a solenoid is wrapped. In some cases, the head of the internal inductor is machined from a solid copper bar (**Figure 25**, bottom photos) providing a rigid and robust structure and minimizing the end effect of coil helix. Since the return leg of the inductor usually goes through the center of the coil, the smallest outside diameter (OD) of solenoid-type inside diameter (ID) coils is usually limited to about 12 mm, but 19 mm is more typical.

If the workpiece has an ID less than 20 mm, then hairpin inductors are sometimes used, requiring part rotation (**Figure 25**, middle-right). Hairpin-type inductors are usually bent or brazed copper tubing and resemblance of the inductor's loop shape to a lady's hairpin. The magnetic flux concentrator must be positioned between the legs of the hairpin inductor to improve heating efficiency and reduce coil current.

12.15.2.4.5.2 Pancake inductors

Pancake inductors are used for selective heating of flats, discs, and plates, as well as for heating large mill rolls in the paper-making industry. The shape of these types of inductors can be round, square, rectangular, or odd shaped. The term *pancake* is used to describe the typical flat round shape of the inductor. This type of inductor has the appearance of an electrical stovetop burner. **Figure 26** shows a typical pancake coil for heating a flat circular pattern of a workpiece.

In some cases, the turns of a pancake coils are profiled having various turn-to-workpiece gaps and a density of winding of coil turns. This helps to control end effects and the dead-spot in the middle.

Figure 25 Inductors for hardening internal surfaces. Courtesy of Inductoheat Inc.

In the great majority of applications, pancake inductors are used for single-shot or static heating. In others, these inductors are used for scan heating.

12.15.2.4.5.3 Split-return inductors and butterfly coils

Split-return inductors are used in various induction heat-treating applications, including hardening (*1*). As an example, **Figure 27** shows split-return inductors for use in pipe seam annealing (top) and selective hardening (bottom) applications (*56*).

The main (center) leg of a split-return inductor splits into two return legs. **Figure 28** illustrates an electrical circuit of a split-return inductor. Current density in the main leg is double that in the return legs. Therefore, the power density (heat source) under the main leg is about four times higher than the power density under its return legs. This ratio can be further increased if the width of copper

Figure 26 Pancake inductor. Courtesy of Inductoheat Inc.

tubing of return legs is greater than the width of copper for the main leg, or if a flux concentrator is applied for the main leg, resulting in further increased power density in a narrow band of the workpiece located under the main leg.

Figure 29 shows what is commonly referred to as a butterfly inductor, which essentially is a multiturn split-return inductor resembling the shape of a butterfly (*1,56*). A butterfly inductor uses two pancake inductors (the 'wings'), and the turns are wound so that the center turns of the coil are all in the same direction (the 'body'), creating the highest power density region that provides the main heating, similar to split-return inductors discussed above. The inductor often applies a magnetic flux concentrator around the center turns of the coil. This helps to increase heat intensity under the center of the coil.

There are several modifications of butterfly-type inductors, including a single-butterfly and a double-butterfly inductor used for tooth-by-tooth induction hardening of large gears.

12.15.2.5 Magnetic Flux Concentrators

Magnetic flux concentrators (also called flux controllers, intensifiers, diverters, or magnetic shunts) are made from high-permeability, low-power-loss materials. They are routinely used in induction-hardening applications (Figure 30), helping to

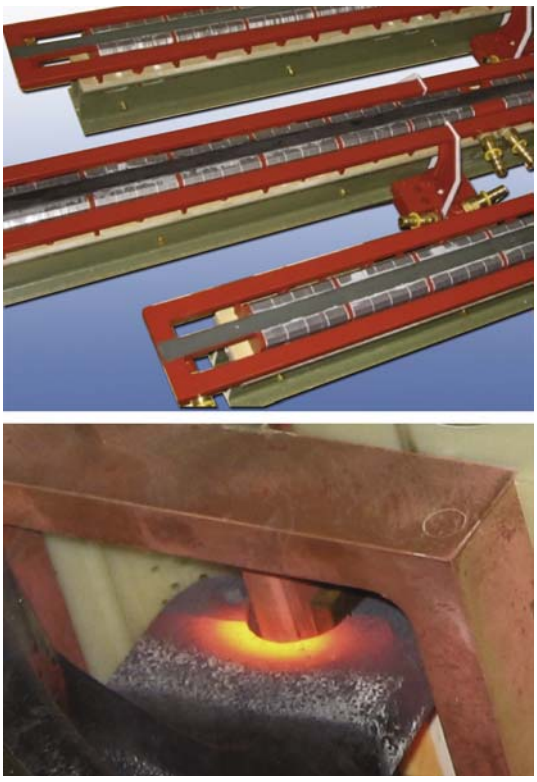

Figure 27 Split-return inductors for use in pipe seam annealing (top) and selective hardening (bottom) applications. Courtesy of Inductoheat Inc.

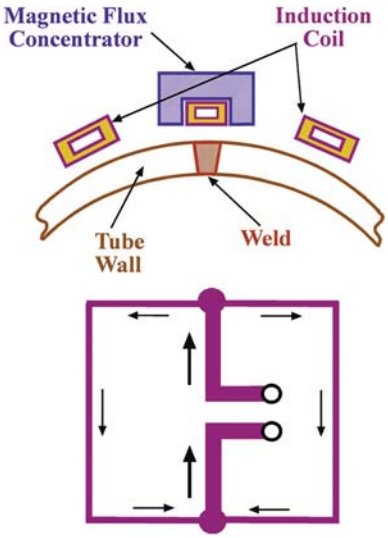

Figure 28 A sketch of an electrical circuit of a split-return inductor. Reproduced from Rudnev, V. Systematic Analysis of Induction Coil Failures and Prevention. Part 14: Split-Return Inductors and Butterfly Inductors. *ASM Int., Materials Park, Ohio. Heat Treat. Prog.* **March/April, 2009,** 17–19.

concentrate magnetic flux lines in a manner similar to that of magnetic cores in power transformers and AC motors (*1,7,8,57–59*). In some cases, magnetic flux concentrators are credited with turning a seemingly impossible development task into a fairly reasonable one. Magnetic flux concentrators have three traditional functions in induction hardening:

- They provide a selective heating of certain areas of the workpiece.
- The improve the electrical parameters of the heating inductor (including electrical efficiency and coil power factor).
- They act as an electromagnetic shield preventing or dramatically reducing the undesirable heating of adjacent electrically conductive regions.

12.15.2.5.1 Physics of Magnetic Flux Concentration

Without a concentrator, the magnetic flux would spread around the inductor or current-carrying conductor and create an electromagnetic link with the electrically conductive bodies located in close proximity. The magnetic flux concentrator forms a magnetic path to channel the coil's main magnetic flux in a well-defined area outside the coil, preventing or dramatically reducing the heat intensity of electrically conductive surroundings (*57–59*).

The electrical current distribution (AC current) in an isolated conductor of a square cross-section is shown in **Figure 31(a)**. As can be seen, the AC current distribution within the conductor's cross-section is not uniform. Taking into consideration that the great

Figure 29 A butterfly inductor. Courtesy of Inductoheat Inc.

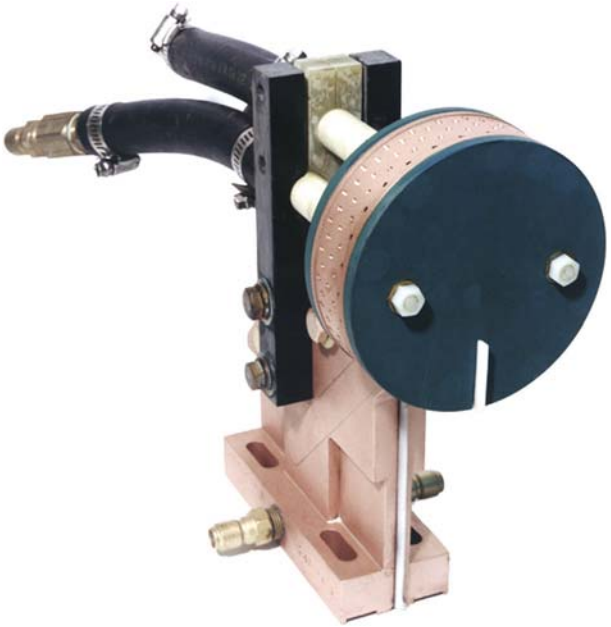

Figure 30 Inductor for scan hardening internal surfaces consists of magnetic flux concentrators located on coil's ID and its ends. Courtesy of Inductoheat Inc.

majority of inductors are fabricated from copper that is a good electrical conductor having low values of electrical resistivity and the fact that medium- and radio frequencies are the most typical frequencies applied in induction hardening, the skin effect in inductors is always pronounced, resulting in a concentration of electrical current in the thin-surface layer. The thickness of that surface layer is quite small and relates to a value of current penetration depth into copper δ_{Cu} at a particular frequency (**Table 4**). The maximum value of the current density is located within corner regions of the conductor of the rectangular cross-section.

Current distribution changes upon bringing another electrical conductor within a close proximity to a current-carrying conductor are shown in **Figure 31(b)**. Due to the electromagnetic proximity effect, a significant portion of the conductor's current will flow near the surface that faces another electrical conductor, for example, a workpiece. The balance of the current will be concentrated in the side regions of the conductor.

When a U-shaped magnetic flux concentrator is placed around the electrical conductor (e.g., around a single-turn induction coil), practically all coil current will be shifted toward a coil 'open'-surface region. In other words, the concentrator 'squeezes' the current to an open surface, as shown in **Figure 31(c)** (*59*). Concentrating the current within the surface of the coil that faces the workpiece improves coil-to-workpiece electromagnetic coupling, which in-turn, improves the coil's electrical efficiency and reduces the amount of power required for heating.

Another factor that results in a reduction of power demand to do a heating job involves the flux concentrator's ability to localize the magnetic field (**Figure 31(d)**). The flux concentrator prevents a major portion of the external magnetic field from propagating outside the concentrator. In other words, it localizes the heated area. As a result, it reduces the mass of heated metal and leads to an increase of an induced power density (heat sources) in the workpiece's areas required to be heated. This is the second factor associated with a reduction of power needed to accomplish the required heat treatment.

12.15.2.5.2 Selecting Flux Concentrator Materials

Flux concentrator materials include laminations, pure ferrites, and numerous proprietary iron-based and ferrite-based composites (e.g., Fluxtrol, MagShape, Ferrotron, and Alphaform), including single- and multiple-phase alloys (*1*,*60*,*74*–*76*).

Different applications may call for different materials and their grades. The selection decision should be based on a variety of factors. Typically, higher values of relative magnetic permeability, electrical resistivity, thermal conductivity, Curie point, saturation flux density, and ductility are sought, while lower values of hysteresis loss, Joule loss, and coercive force are desirable. Additional factors in a given material's favor include the ability to be cooled and to withstand high temperatures, thermal expansion, resistance to chemical attack by quenchants, high compressive and tensile strength, good machinability, impact strength and/or formability, density, ease of installation and removal, ability to monitor its working condition, structural homogeneity, low anisotropy, and low cost (*59*).

In induction hardening, the materials typically used as flux concentrators are soft magnetic in nature; that is, they are magnetic only when an external electromagnetic field is applied (*60*). In a magnetic field, these materials can change their magnetization rapidly without much friction. They are characterized by a tall and narrow magnetic hysteresis loop of a relatively small area (**Figure 6**). Larger area of hysteresis loop associates with greater losses.

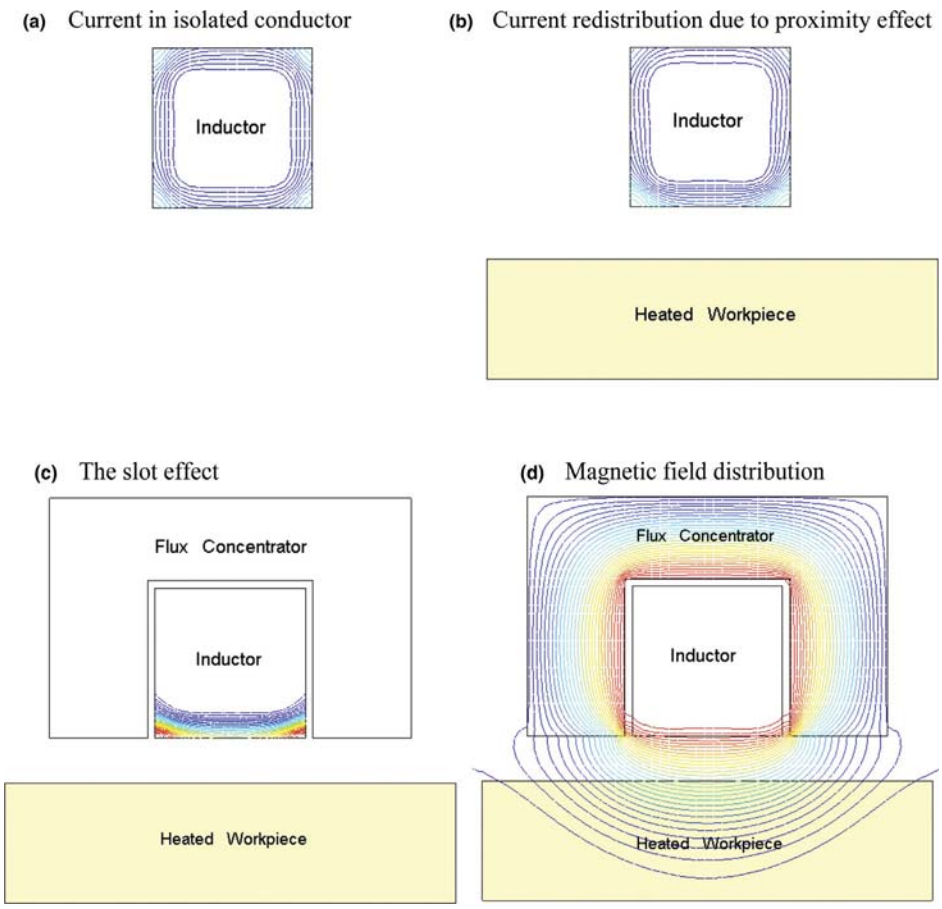

Figure 31 Computer modeling of coil current and magnetic field distribution. (a) Current distribution in an isolated conductor (coil). (b) Current redistribution in a conductor in close proximity to an electrically conductive workpiece. Due to the proximity effect, a significant part of the conductor's current flows near the surface that faces the load (the open surface). (c) When a magnetic flux concentrator is placed around the workpiece, practically all of the current in the coil is concentrated on the open surface (the slot effect). This improves coil-to-workpiece magnetic coupling, which results in improved coil electrical efficiency. (d) A reduction in required coil power also can be attributed to the flux concentrator's ability to localize the magnetic field. Reproduced from Rudnev, V. An Objective Assessment of Magnetic Flux Concentrators. *ASM Int., Materials Park, Ohio. Heat Treat. Prog.* **Nov./Dec., 2004,** 19–23.

Soft-magnetic materials usually have a relatively uniform structure, low anisotropy, and randomly arranged magnetic domains. Random domains correspond to a minimum energy configuration – zero magnetization – when their magnetic effects cancel each other. However, the domains can be easily rearranged by applying an external magnetic field. The direction of domain rearrangement will correspond to the direction of the applied field. In this case, the material behaves as a temporary magnet.

In addition to a desirable high relative magnetic permeability and saturation flux density, magnetic flux concentrator materials also should have electrical resistivity and thermal conductivity values that are as high as possible. A high electrical resistivity reduces eddy current losses that in turn reduce its temperature increase during the heating cycle, improving the overall electrical efficiency.

High thermal conductivity helps extend the service life of concentrators by equalizing temperature distribution and reducing the tendency to have localized overheating ('hot spots') caused by a high-density magnetic flux and heat radiation from the workpiece's surface.

One of the most important magnetic properties of a flux concentrator is related to a low value of hysteresis loss. This quality is derived from the magnetization curve (Figure 6) and consists of (*1*)

1. a cycle of magnetization in one direction;
2. a reversal of the applied magnetic field, which results in demagnetization of previously magnetized material and its magnetization in the opposite direction; and
3. another reversal process resulting in magnetization in the original direction.

Table 4 Current penetration depth into pure copper δ_{Cu} versus frequency at ambient temperature

Frequency, kHz	*1*	*3*	*10*	*30*	*70*	*200*	*500*
δ_{Cu}, mm	2.16	1.2	0.68	0.39	0.26	0.15	0.1

Hysteresis loss is characterized by the conversion of electromagnetic energy into thermal energy when magnetic domains are rearranged during the hysteresis cycle, and is proportional to the area of the hysteresis loop and the frequency. A wide opening in the magnetization curve and a high-applied frequency correspond to a high hysteresis loss.

The hysteresis loss should be as small as possible because its value associates with a temperature rise in the flux concentrator. Too high a temperature increase can cause a loss of the concentrator's magnetism and, therefore, its fast degradation, a reduction in coil efficiency as well as variation in the induction-hardening pattern, and a worsening process repeatability.

A flux concentrator material also should have a coercive force that is as small as possible. A theoretically perfect concentrator with maximum efficiency would have no magnetization remaining after the external magnetic field falls to zero.

Flux concentrator properties can be obtained from manufacturer data sheets or can be measured using the appropriate test instruments.

One should also be alert to overheating of the flux concentrator: the corners and end-faces of laminations tend to overheat due to electromagnetic end effects and magnetic saturation requiring special design arrangements and, often, the use of several types of magnetic flux concentrators.

12.15.2.5.3 Flux Concentrator's Materials Trade-Off

The flux concentrator materials most commonly used in induction hardening are of the following types (*1,7,8,59,74–76*):

1. Laminations
2. Magneto-dielectric materials
   - Electrolytic iron-based materials
   - Carbonyl iron-based materials
   - Pure ferrites and ferrite-based materials
3. Soft, formable materials
4. Multiple-phase alloys

The use of laminations as flux concentrators in induction heating (**Figure 32**) was a spin-off from the motor and transformer industry. Laminations are punched out of grain-oriented magnetic alloys (Ni–Fe and Si–Fe alloys). Some laminations are made from nanocrystalline alloys. Stacks of laminations are used effectively from line frequency to 30 kHz. There also have been cases where laminations were used successfully at higher frequencies (50 kHz and higher, e.g., Nano™ laminations). Individual laminations must be electrically isolated from each other. Special coatings of individual laminations (i.e., mineral and/or organic coating) provide electric insulation.

The thickness of individual laminations should be held to a minimum to keep eddy-current losses sufficiently low. The typical thickness range of individual laminations is 0.02–0.8 mm. Thinner laminations are used for higher frequencies, while laminations thicker than 0.3 mm typically are chosen for frequencies below 1 kHz.

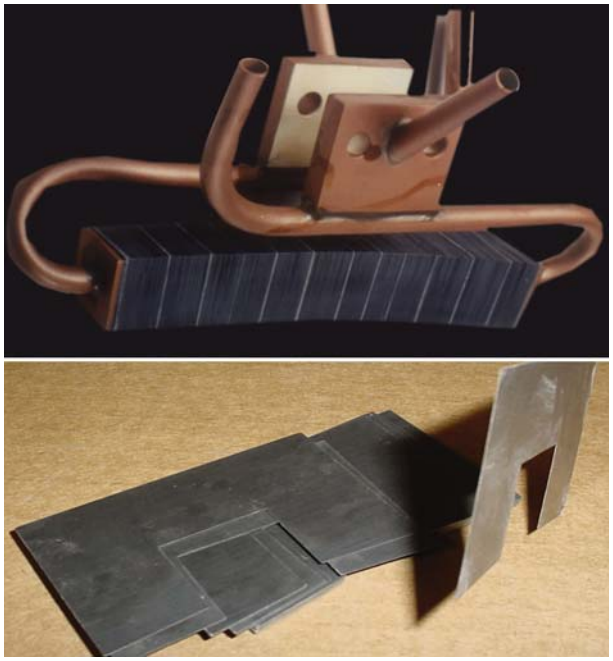

Figure 32 Laminations are among the materials used for flux concentrators. They are punched out of grain-oriented magnetic alloys, and stacks of them are used effectively from line frequency to 30 kHz. The typical thickness is 0.02–0.8 mm. Reproduced from Rudnev, V. An Objective Assessment of Magnetic Flux Concentrators. *ASM Int., Materials Park, Ohio. Heat Treat. Prog.* **Nov./Dec., 2004,** 19–23.

Flux concentrators made of laminations are not problem-free (*61*). For example, laminations are particularly sensitive to aggressive environments, including quenchants. Rust and degradation can result. The magnetic properties of laminations can be degraded by an increase in coercive force and subsequent hysteresis loss increase. If the individual laminations are not firmly clamped together, they could start to vibrate, resulting in mechanical damage of coating, coil copper, noise generation, and eventually premature failure of the coil or process.

Laminations expose appreciable heterogeneous properties; magnetic, electric, and thermal properties. End-faces of laminations are prone to overheat due to electromagnetic end effects, requiring special design arrangements.

On the plus side, laminations are relatively inexpensive and can withstand high temperatures better than other materials. Lamination stacks also can be used to support the induction coil while being insulated from it. Another advantage is that laminations have a high relative permeability and the highest saturation flux density (from 1.4 to 1.8 T) when strong magnetic fields are applied (typical case of induction hardening). This means that laminations are better able to retain their magnetic properties in the strong magnetic fields.

Pure ferrites and iron-based powder materials also are often used in induction hardening. Ferrites are dense ceramics made by mixing iron oxide (FeO) with oxides or carbonates of one or more other metals such as nickel, zinc, or magnesium. In relatively weak magnetic fields, ferrites have very high magnetic permeabilities ($\mu_r = 2000+$). Some of the main drawbacks to ferrites are related to their brittleness, low-saturation flux density, and low Curie point ($\sim$220 °C). Note that, above the Curie point, magnetic materials lose their magnetic properties. Poor machinability and low thermal shock resistance and impact strength are other drawbacks of ferrites.

Some ferrite-based and iron-based powder materials have noticeably improved machinability, thermal conductivity, and magnetic flux density compared to ferrites. This includes different grades of Fluxtrol and MagShape, for example. **Figure 30** shows an example of applying magnetic flux concentrators fabricated from Fluxtrol material. This MIQ-type inductor was used for induction hardening of internal surfaces of the workpiece. Substantially reduced heterogeneity of physical properties is another advantage of concentrators made from powder composites.

In order to assure a quick delivery, manufacturers of ferrite-based and iron-based powder flux concentrators are usually kept in stock premachined blocks of a particular shape at their facilities. When needed, those blocks can be shipped for customized final machining. For example, **Table 5** shows the standard stock sizes from the MagShape shipping list (*75*).

Some flux concentrator materials are supplied in a soft, formable condition and can easily be molded into a shape sufficiently accurate for development purposes and subsequently machined, if desired, to exact tolerances (*1*). Alphaform is an example (**Figure 33**).

Depending on the application, a magnetic flux concentrating 'device' can be made from a single material or more than one material. For example, in a split-return coil, laminations can be located at the middle of the coil and iron- or ferrite-based powder materials placed at the coil ends. Such a design is cost-effective and electrically efficient and increases the life of the concentrator because it takes into account the field distortion due to the electromagnetic end effect that would result in additional losses if laminations with their heterogeneous magneto-thermal properties were used at the coil ends (*59,61*).

12.15.2.5.4 Common Misconception

There is a common misconception that the use of magnetic flux concentrators automatically leads to increased coil efficiency. As it has been explained in Ref. (*1*), flux concentrators improve the efficiency of the process partly by improving the electromagnetic coupling between the workpiece surface and the current-carrying region of the inductor, as well as by reducing stray losses (due to reduced reluctance of the air path).

However, the electrical resistance of any magnetic flux concentrator is far from being infinite. Therefore, since the flux concentrator is an electrically conductive body and is positioned in close proximity to current-carrying regions of the inductor being exposed to a high-density magnetic flux. This results in some inevitable power loss and generating the heat within it (via the Joule effect and hysteresis losses). Increased power loss within a concentrator could negatively affect the electrical efficiency of an inductor.

The first two factors (reduced electromagnetic coupling distance and reduced stray losses) tend to counteract the third (power loss), and any change in coil electrical efficiency will be the sum of all three factors (*1*).

Conclusion. In some applications, flux concentrators can help to improve heating efficiency; in others, no improvement will be noted or efficiency may even drop. For example, there usually is no appreciable improvement in coil efficiency when concentrators are used in induction applications such as tempering, stress relieving, shrink-fitting, and subcritical annealing. The same can be said for the long solenoid-type induction coils (multiturn coils) used to heat billets, bars, and rods prior to forging, rolling, upsetting, and extrusion.

Table 5 Examples of MagShape flux concentrator standard stock sizes

Sizes of round type concentrators, mm										
30 × 50	40 × 50	50 × 50	60 × 50	70 × 50	75 × 50	80 × 50	90 × 50	100 × 50	125 × 25	150 × 25
Sizes of rectangular type concentrators, mm										
100 × 100 × 50	100 × 100 × 25	100 × 75 × 25	100 × 50 × 25	100 × 25 × 25	75 × 75 × 25	75 × 50 × 25	75 × 25 × 25	50 × 50 × 50	50 × 50 × 25	50 × 25 × 25

Reproduced from www.magshape.com.

Figure 33 Some flux concentrator materials are supplied in a softened condition and can easily be formed into a shape sufficiently machined, if desired, to exact tolerances. Reproduced from Rudnev, V. An Objective Assessment of Magnetic Flux Concentrators. *ASM Int., Materials Park, Ohio. Heat Treat. Prog.* **Nov./Dec., 2004,** 19–23.

On the other hand, appreciable improvements in electrical efficiency can be achieved when flux concentrators are applied to certain types of induction-hardening coils. Examples include channel, hairpin, odd-shaped, spiral-helical, and pancake inductors; electromagnetically short solenoid-type coils (single-turn or two-turn coils); and inductors used to heat internal surfaces (ID coils).

12.15.2.5.5 Design and Application Features

In most cases, the application of magnetic flux concentrators does not require re-engineering of the induction system. However, when a concentrator is used, higher current densities can be generated on certain areas of the coil, for example within copper tubing corners (Figure 31(c)). This could hasten the onset of stress cracking (by work hardening of the copper, for example) if the original coil design was susceptible to this condition. Therefore, consideration must be given to coil wall thickness, coil cooling, and the positioning of quench holes, which are frequently located near the coil surface edges in scan inductors. Care also should be taken at the corners of flux concentrators because of their tendency to saturate and/or overheat due to electromagnetic end effects and thermal edge effects. The initiation of stress fractures can almost always be minimized or eliminated by a well-thought-out coil design (*61*).

It also is important to remember that the impedance of a straight coil can be much different than that of one having a magnetic flux concentrator. Therefore, it is necessary to check that the coil properly load matches the power supply after the concentrator has been installed.

Special care should be taken when applying magnetic flux concentrators to multiturn coils, because the voltage across the coil turns can reach appreciable values, and a short current path may develop through the concentrator, resulting in arcing and eventual failure. In this case, the reliability of the concentrator's electrical insulation plays an essential role in coil design.

12.15.2.5.6 Electromagnetic Shielding, and Prevention of an Undesirable Temper-Back

A major concern in the induction hardening of complex-shape parts is the potential for undesirable heating of adjacent areas that already have been hardened (*58*). This temper-back or annealing is particularly important when hardening camshafts with closely positioned lobes (e.g., tri-lobe cams), gears (tooth-by-tooth), and other critical components.

Due to electromagnetic field propagation, eddy currents are induced not only in the workpiece, which is located under the inductor heating face, but in adjacent areas as well. Without a concentrator, the magnetic flux would spread around the coil and link with any electrically conductive surroundings, which could include neighboring areas of the part (cam lobes, for example) and possibly areas of the induction-heating machine or fixture. Induced eddy currents produce heat, which can cause undesirable metallurgical changes that could potentially negatively affect components working conditions.

Flux concentrators allow electromagnetically decoupling of the induction coil from adjacent electrically conductive components, drastically reducing undesirable heating of these areas and the extent of temper-back, as well as improving the reliability of functioning robotic devices.

As an example, Figure 34 shows a sketch of an induction camshaft hardening system and the magnetic field distribution around a single-turn cylindrical inductor. Without a concentrator, the magnetic flux spreads around the bare coil and could create an appreciable electromagnetic link with electrically conductive regions located in the coil's close proximity. As a result, eddy currents will be induced there, generating Joule heat. This heat can cause undesirable metallurgical changes in those areas. For example, edge areas of camshaft lobes that were induction hardened in previous process stages can be softened (Figure 34, top) during heating of the subsequent heating stage when the next lobe will be induction hardened (*58*).

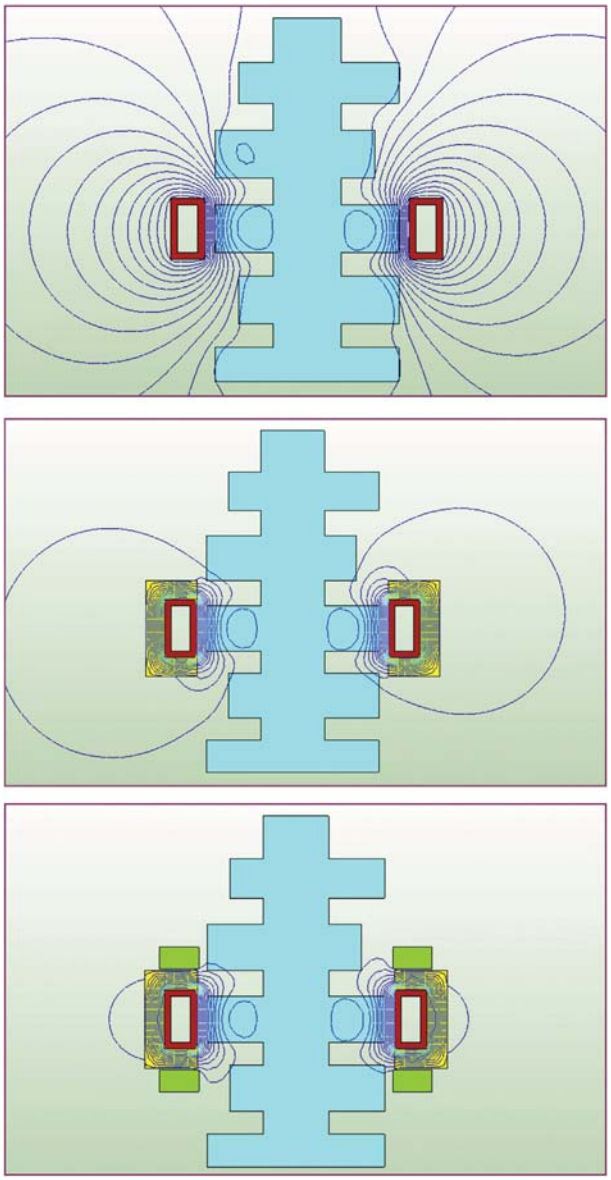

Figure 34 Electromagnetic control of undesirable temper back of previously hardened camshaft lobes. Reproduced from Rudnev, V. Simulation of Induction Heat Treating. In *Metals Process Simulation;* Furrer, D. U., Semiatin, S. L., Eds.; ASM Int., 2010; pp 501–546.

When a U-shaped magnetic flux concentrator is wrapped around that single-turn inductor (Figure 34, middle), a much smaller portion of the electromagnetic field of the coil will link with adjacent lobes and outside the coil. Depending on a camshaft's geometry and coil design specifics, the reduction of power density induced at the corners and edges of neighboring lobes can exceed 4- to 12-fold compared to a bare coil. This substantially reduces the probability of undesirable temper-back.

Further reduction of the external magnetic field can be achieved by using a combination of U-shaped concentrators and Faraday rings (Figure 34, bottom).

Multiple coils are involved in some induction heat-treating applications. Strong electromagnetic interaction can be formed between coils because of the relatively short distances between them. This creates the potential for certain undesirable electromagnetic effects, such as an arbitrary power transfer between coils. In these applications, flux concentrators can also be used as electromagnetic shields, drastically reducing magnetic interaction between coils.

Appreciable external magnetic fields can 'confuse' the robot's working conditions when loading, holding, and/or unloading parts. Acting as electromagnetic shields, flux concentrators electromagnetically decouple the induction coil from adjacent electrically conductive devices, drastically reducing undesirable external magnetic fields and improving the reliability of robotic systems and other electronic devices.

The effectiveness of concentrators acting as magnetic shields depends on such factors as frequency, magnetic field intensity, material properties, and the geometry of the induction system. Mathematical modeling can reveal a magnetic field distribution outside of the induction coil and determine their shielding effect (*6*).

Flux concentrators are often effectively used in applications requiring induction heating of selected areas of the workpiece. Induction brazing, soldering, selective hardening, tempering, stress relieving, annealing, shrink fitting, localized warm and hot forming and bending are some of such applications. Compared to applications that require heating the entire workpiece, selective heating involves several important process characteristics related to magnetic field concentration in a particular area of the workpiece, grossly affecting coil design, optimal frequency, and coil electrical parameters selection. Flux concentrators help to effectively control electromagnetic end effects in those applications. As an example, **Figures 35** and **36** show the results of FEA computer simulation of induction heating a selected area of a steel rail.

Butterfly-type inductors positioned on both sides of a rail provide selective heating. Current flowing in the center turns is in the same direction, generating the main heating effect. Top and bottom turns represent the so-called return lags of the inductor, with current flowing in a direction opposite to current of center turns. The FEA mesh and magnetic field distribution of both coils is

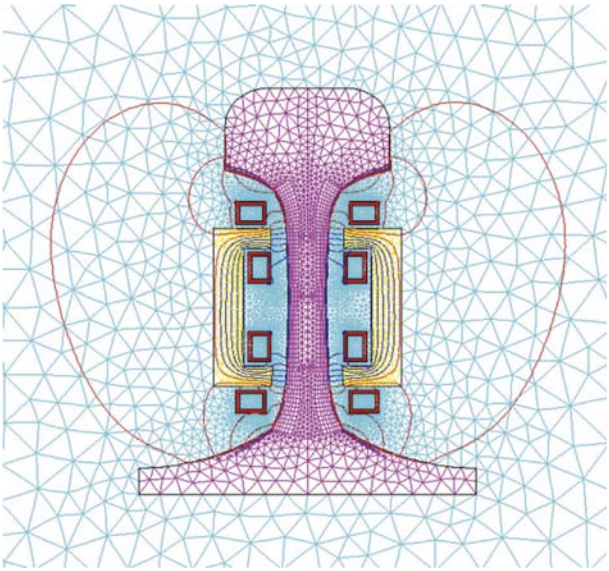

Figure 35 Results of computer simulation of induction heating a selected area of a steel rail. FEA mesh and magnetic field distribution.

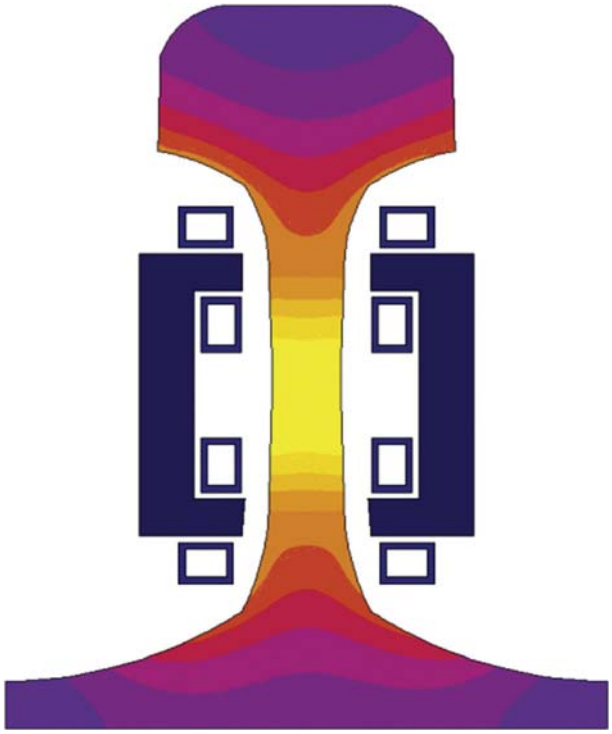

Figure 36 Results of computer simulation of induction heating a selected area of a steel rail. Temperature distribution.

shown in Figure 35. The main heating is provided by the center turns, while heating generated by return lags helps compensate the cold sink effect of adjacent regions, particularly during rail transportation to the subsequent operation in the manufacturing process. Temperature distribution at the final stage of induction heating is shown in Figure 36.

U-shaped lamination stacks positioned around the center turns have a twofold impact on the performance of butterfly-type inductors:

- They serve as magnetic flux-concentrators to boost the heating intensity of center turns.
- They provide electromagnetic decoupling of coil turns, with currents flowing in opposite directions; this also increases overall coil electrical efficiency.

12.15.2.5.7 Summary of Using Magnetic Flux Concentrators

Advantages. Magnetic flux concentrators can improve the induction heat-treating process by the following:

- Reducing the induction coil's required power and current levels
- Improving the electrical efficiency of the process and decreasing energy consumption
- Making it possible to selectively heat specific areas of the workpiece
- Obtaining a superior hardening patterns
- Minimizing geometric distortion of the induction-hardened workpiece
- Preventing undesirable heating of adjacent areas (shielding effect)
- Reducing rejects, rework, and scrap
- Lengthening equipment life
- Shortening the cycle time
- Improving the reliability of electronic devices working in proximity to induction coils
- Eliminating or dramatically reducing exposure of personnel to external electromagnetic fields

Figures 30, 37(a), and 37(b) present three examples of magnetic flux concentrators playing a critical role in the performance of ID scan hardening, a single-shot inductor for hardening spring clutch, and inner ring hub hardening, respectively.

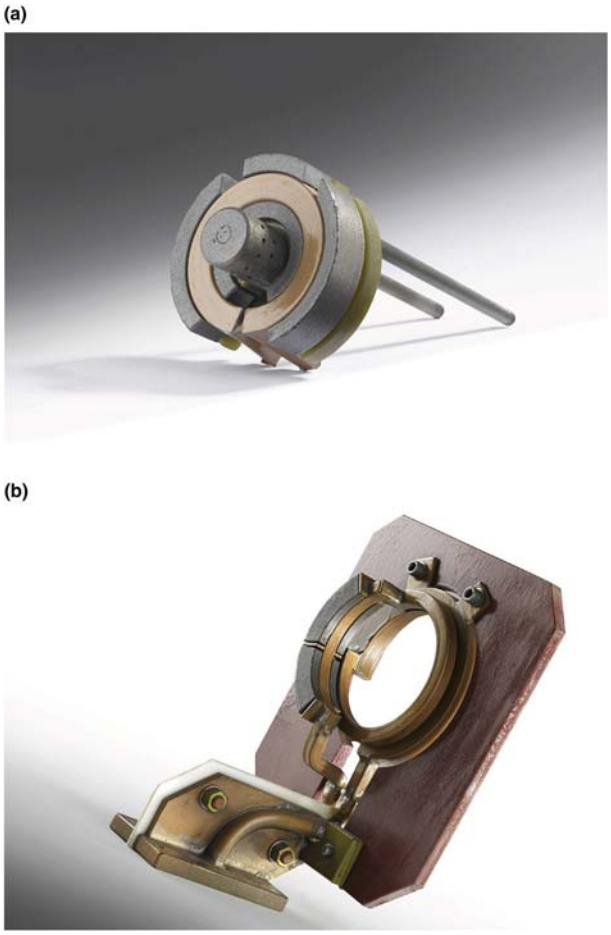

Figure 37 (a) Example of using magnetic flux concentrator on a single-shot hardening inductor for spring clutch. (b) Example of using magnetic flux concentrator for inner ring hub hardening. Courtesy of MagShape S.r.l., Montecchio Magg., Italy.

Caveats: There is an expense associated with adding a flux concentrator to an existing inductor. A common saying among those familiar with induction heating is, "If a good part can be effectively produced without a flux concentrator, there is no reason to add to coil cost."

Concentrators also degrade in service. As soon as they are installed, their ability to concentrate magnetic fields begins to slowly decline due to, for example, degradation and rusting of magnetic particles, degradation of binders (in composite materials), or isolation coating (in laminations).

Reliability of the installation of flux concentrators is another major concern. Flux concentrators typically are soldered, screwed, or sometimes (e.g., iron-based and ferrite-based composite concentrators) even simply glued to the induction coil. They usually are positioned in areas of high magnetic flux density, where electromagnetic forces can be substantial. Over time, these forces can potentially cause the concentrator to loosen and unexpectedly shift or move to an improper position, resulting in improper hardening, thereby negatively affecting overall product quality and process repeatability.

Another possible cause of concentrator loosening is unstable temperature conditions. During the processing cycle, the concentrator can be heated to 260 °C and even higher, followed by cooling during quenching to ambient temperature. In typical hardening applications, this repetitive heating and cooling are accompanied by a volumetric expansion and contraction of the concentrator, which can cause it to unglue, loosen, and move. That movement can also cause variations in heating and hardening patterns. Besides that, it is important to be aware that ferrites as well as ferrite-based and iron-based flux concentrators have quite low maximum temperatures. For example, according to data obtained from one of the manufacturers of flux concentrators, the maximum temperature of some iron-based and ferrite-based composite concentrators is only 250 °C for a long-term use and 300 °C for short-term use. If the temperature of iron-based and ferrite-based powder concentrators exceeds its maximum permissible level, its binder (different types of epoxies) starts to deteriorate and disintegrate uncontrollably. This might negatively affect the overall robustness and repeatability of the induction system.

An unexpected change in the hardening pattern can be very serious. In the automotive industry, for example, it can result in the recall of many thousands of vehicles to replace the defective part. To prevent such a situation, flux concentrators should be examined on a scheduled basis and repaired, if necessary. In some cases, special electronic monitoring devices can be installed to indicate changes in concentrator performance. Unfortunately, those devices add substantially to total system cost.

12.15.3 Computer Modeling

In the last decade, when discussing subjects related to a computer modeling of induction heating, the word *usefulness* has been replaced by the word *necessity*. Modern computer simulation is capable of effectively simulating electromagnetic and thermal phenomena for many processes, including those that involve electromagnetic induction. Combination of a sophisticated engineering background with advanced process simulation software gives induction heating professionals the unique ability to analyze, in just a few hours, complex technological processes. It offers the ability to predict how different, interrelated, and nonlinear factors may impact the transitional and final thermal conditions and shows what must be accomplished to improve process effectiveness and determine the most appropriate process recipes, and serves as a comfort factor when designing new systems allowing avoiding unpleasant surprises, shortening the learning curve, and reducing development time (*70–73*).

Over the years, industry has accumulated numerous rules of thumb in regard to calculating the basic induction-hardening process parameters. Some of these recommendations are discussed in (*1–6,15*).

As an example, **Figure 38** consists of a chart developed by industry for choosing frequency, power density, and heat time for surface (case) hardening of solid cylinders (i.e., straight shafts) without irregularities. **Table 6** presents estimated power requirements for induction hardening of spur gears.

Guidelines for selection of frequency and power for through hardening, normalizing, and annealing are similar to other induction applications that require through heating of workpieces (*1–4*). If frequency is too low, then an eddy current cancellation within the heated component takes place, resulting in poor coil electrical efficiency (except for applications utilizing transverse flux and traveling wave inductors). When the frequency is too high, however, the skin effect will be highly pronounced, resulting in a current concentration in a very fine surface layer compared to the diameter/thickness of the workpiece. In order to provide sufficient heating of the core by thermal conduction, a long heating time is needed, leading to potential surface overheating, excessive decarburization, scale, grain growth, and other undesirable phenomena associated with achieving high temperatures. The rule of thumb suggests that in order to avoid noticeable current cancellation the ratio 'Radius/δ' > 1.6. This condition results in a reasonable compromise between in-depth heating effect and relatively insignificant coil electrical efficiency reduction due to minor eddy current cancellation.

An estimation of the process parameters based on a single formula rule of thumb was popular from the 1960s through the 1990s. Although those techniques were easy to employ, they were very subjective, with inherent major restrictions limiting their use for quick estimation of only ballpark parameters of induction heating systems (*1–3*). Such overly simplified estimation techniques always posed the danger of yielding erroneous and inadequate results.

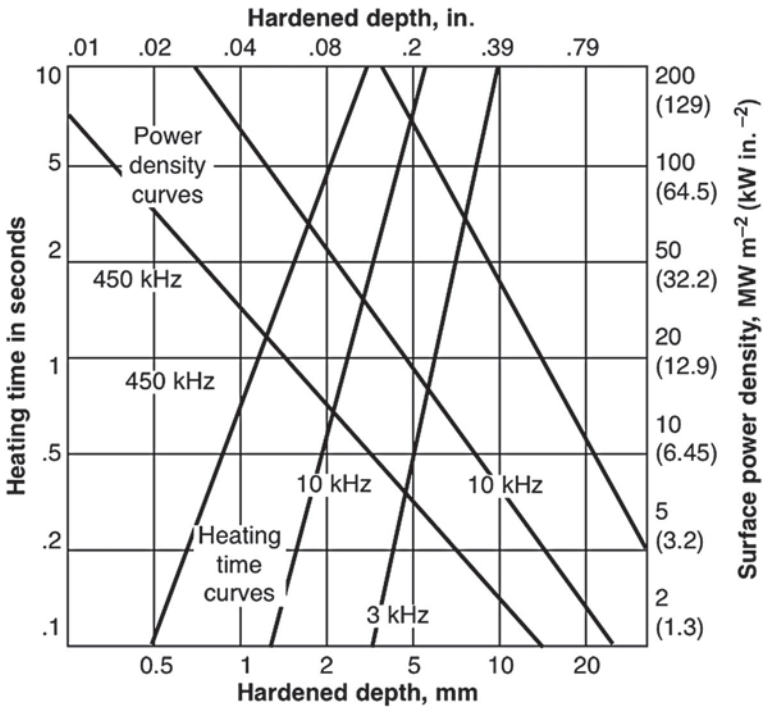

Figure 38 Interrelationship among heating time, surface power density, and hardened depth for various frequencies. Reproduced from ASM Handbook, *Heat Treating*; ASM Int., 1991; Vol. 4.

Table 6 Ballpark estimation of power requirements for induction hardening of gear teeth

		Approx. length of tooth profile		*Surface area per tooth*[a]			
Tooth	*Diametral pitch*	*mm*	*in.*^{2}	*cm*^{2}	*in.*^{2}	*Power per tooth*[b] *kW*	*Total power required*[c] *kW*
A	3	50	2.0	12.9	2.0	20	800
B	4	38	1.5	9.7	1.5	15	600
C	5	33	1.3	8.4	1.3	13	520
D	6	25	1.0	6.5	1.0	10	400
E	7	23	0.9	5.8	0.9	9	360
F	8	19	0.75	4.8	0.75	7.5	300

[a]*For a face width of 25 mm (1 in.).*

[b]*At a power density of 1.55 kW cm*$^{-2}$ *(10 kW in.*$^{-2}$*).*

[c]*For a gear having 40 teeth.*

Reproduced from ASM Handbook, Heat Treating; ASM Int., 1991; Vol. 4.

It is imperative to keep in mind that most rules of thumb are extremely subjective and are only related to a selection of frequency and power when single-shot hardening or scan hardening of regular shaped cylinders (i.e., solid shafts) are made from plain carbon steels.

Besides, rules of thumb usually assume hardening fine-grain normalized homogeneous ferritic–pearlitic prior structures with carbon content of about 0.4–0.5%. As discussed earlier, the microstructure of steel prior to heat treatment has a pronounced effect on the results of induction hardening and the required process parameters such as austenitizing temperature and the amount of time the part is required to be held at that temperature for a carbon homogenization.

At the same time, the shapes of the majority of induction-hardened components are far from being simple, solid cylinders. Even those parts that belong to the group of generally cylindrical-shape components have certain design features that could make them prone to overheating or underheating upon induction heating, dramatically affecting hardness patterns. Typical examples are parts containing longitudinal and/or transverse holes, keyways, grooves, shoulders, flanges, diameter changes, undercuts, hollow areas, splines, and sharp corners (**Figure 39**). However, such features are not unique as they are commonly found on many transmission and engine components (*45*). Erroneous and inadequate results can be obtained when single-formula rules-of-thumb estimation techniques are used to determine process parameters when heat-treating irregularly shaped workpieces with certain design features.

Recent achievements in the development of modern computers, the increasing complexity of induction-hardening applications, increasing demands to manufacture higher quality parts, in combination with the necessity of improving process cost-effectiveness

Figure 39 Representative part having various geometrical discontinuities. Reproduced from Rudnev, V. Computer Modeling Helps Prevent Failures of Heat Treated Components. *Adv. Mater. Process.* **October, 2011,** 28–33.

by shortening the learning curve and reducing development time that are naturally related to reducing delivery time of equipment, have significantly restricted the usefulness of simplified formulas, as well as analytical and seminumerical methods.

Rather than using simplified estimation techniques with numerous restrictions and questionable accuracy, modern induction heating specialists turned to highly effective numerical simulation methods such as finite differences, finite elements, edge elements, finite volumes, boundary elements, and others. Numerical techniques are widely and successfully used in the simulation of coupled electromagnetic, heat transfer, and metallurgical phenomena. Each of those numerical modeling techniques has certain *pros* and *cons*, and each has been used alone or in combination with others (*1*,*6*,*8*,*46*,*47*).

Generally speaking, in order to simulate an induction heat-treating system, it is necessary to model several process stages, including heating, soaking, dwelling, cooling during quenching, and reheating for tempering or stress-relieving (*1*).

It is important to remember that any computational analysis can at best produce only results that are derived from the properly determined physical properties of heated materials and correctly defined governing equations.

The first important step in any computer simulation is obtaining physical properties of heated materials versus temperature from properly conducted experiments or trustful sources. As discussed above, electromagnetic and thermal properties nonlinearly vary with temperature, chemical composition, microstructure, grain size, and the like.

The interrelated nonlinear nature of the material properties dictates the necessity of developing special computational algorithms coupled together with electromagnetic and thermal phenomena (*1*,*47*).

The second, though equally important, step in any mathematical simulation is to choose an appropriate theoretical model that correctly represents the technological process or phenomena.

12.15.3.1 Governing Equations

The technique of calculating electromagnetic fields depends on the ability to solve Maxwell's equations. Maxwell's equations represent a set of equations that describe an interrelated nature of electric and magnetic fields. For general time-varying electromagnetic fields, when there are no substantially fast-moving components, Maxwell's equations in differential form can be written as (*1*,*6*,*62*–*66*)

$$\nabla \times \mathbf{H} = \mathbf{J} + \frac{\partial \mathbf{D}}{\partial t} \qquad \text{(from Ampere's law)} \qquad [4]$$

$$\nabla \times \mathbf{E} = -\frac{\partial \mathbf{B}}{\partial t} \qquad \text{(from Faraday's law)} \qquad [5]$$

$$\nabla \cdot \mathbf{B} = 0 \qquad \text{(from Gauss's law)} \qquad [6]$$

$$\nabla \cdot \mathbf{D} = \rho^{\text{charge}} \qquad \text{(from Gauss's law)} \qquad [7]$$

where **E** is electric field intensity, **D** is electric flux density, **H** is magnetic field intensity, **B** is magnetic flux density, **J** is conduction current density, and ρ^{charge} is electric charge density.

Equations [4]–[7] consist of special symbols: ∇, $\nabla\cdot$, and $\nabla\times$ that are used in vector algebra to shorten an expression of particular differential operation without having to carry out the details designating following mathematical operations, respectively: gradient (*grad*), divergence (*div*), and curl (*curl*). The fundamental laws governing the general time-varying electromagnetic field can be written not only in differential form (eqn [4] through [7] but in integral form as well: see expressions [8] to [11] (*62–66*)

$$\oint_C \mathbf{H}\cdot \mathrm{d}l = \int_S \mathbf{J}\cdot \mathrm{d}A + \int_S \frac{\partial \mathbf{D}}{\partial t}\cdot \mathrm{d}A \quad \text{(from Ampere's law)} \tag{8}$$

$$\oint_C \mathbf{E}\,\mathrm{d}l - \int_C \mathbf{B}\times v\cdot \mathrm{d}l = -\frac{\mathrm{d}}{\mathrm{d}t}\int_S \mathbf{B}\cdot \mathrm{d}A \quad \text{(from Faraday's law)} \tag{9}$$

$$\oint_S \mathbf{B}\cdot \mathrm{d}A = 0 \qquad \text{(from Gauss's law)} \tag{10}$$

$$\oint_S \mathbf{D}\,\mathrm{d}A = \int_V \rho^{\text{charge}}\mathrm{d}V \qquad \text{(from Gauss's law)} \tag{11}$$

where dV represents differential of volume 'V' surrounded by surface 'S,' dA denotes differential vector element of surface region 'A' with small magnitude and direction normal to surface 'S,' dl represents vector element of path length that is tangential to contour 'C' surrounded surface 'c,' and v is instantaneous velocity of element dl.

Some numerical modeling methods (e.g., boundary element method) apply the integral form of Maxwell equations; while others (e.g., finite element method (FEM) and finite-difference method (FDM)) typically utilize its differential form.

The Maxwell's eqns (4–7) are in indefinite form because the number of equations is less than the number of unknowns. These equations become definite when the relations between the field quantities are specified. The following constitutive relations are additional and hold true for a linear, isotropic medium:

$$D = \varepsilon\varepsilon_0 E \tag{12}$$

$$B = \mu_r\mu_0 H \tag{13}$$

$$J = \sigma E \quad \text{(Ohm's law)} \tag{14}$$

where the parameters ε, μ_r, and σ denote, respectively, the relative permittivity, relative magnetic permeability, and electrical conductivity of the material; and $\sigma = 1/\rho$, where ρ is electrical resistivity.

Similarly to the magnetic permeability of free space μ_0, the constant $\varepsilon_0 = 8.854\times 10^{-12}\ \mathrm{F\ m^{-1}}$ is called the permittivity of free space. Both relative magnetic permeability μ_r and relative permittivity ε are nondimensional parameters and have very similar meanings. Similar to μ_r, relative permittivity (or dielectric constant) indicates the ability of a material to conduct the electric field better than vacuum or air.

The great majority of applications involve induction heating of metals; the impact of induced conduction current density **J** into total heat generation is much greater than the impact of displacement current density $\frac{\partial D}{\partial t}$. It is for this reason that, in the modeling of induction hardening, the impact of displacement current is often neglected.

It is important to realize that depending on the magnetic and electric properties, certain quantities of the electromagnetic field can be continuous or discontinuous on different sides of an interface divided into two different mediums. Designating two different media with a common interface by subscripts 1 and 2, the basic field vectors must satisfy the following boundary conditions (*62–66*):

$$(B_2 - B_1)\cdot n = 0 \tag{15}$$

$$(H_2 - H_1)\times n = J^{\text{surface}} \tag{16}$$

$$(E_2 - E_1)\times n = 0 \tag{17}$$

Boundary conditions [15]–[17] can be interpreted as follows. According to eqn [15], the normal component of the magnetic flux density B is continuous across the interface of medium 1 and 2. In the presence of the surface current J^{surface}, as it follows from eqn [16], the tangential components of the magnetic field strength H are discontinuous across the two media with a magnitude of J^{surface}. If the surface current is absent (it is the case of electrically conductive materials), then the tangential component is continuous and the right side of eqn [16] will be 0. According to eqn [17], the tangential components of the electric field intensity E are continuous across the interface. Expressions [15]–[17] can be very helpful in providing one of the simple tests whether the results of numerical computer modeling are physically correct. Physical interpretation of Maxwell's equations is provided in (*1,62–66*).

The transient thermal process in a metal workpiece can be described by the Fourier equation (*1, 67–69*):

$$c\gamma\frac{\partial T}{\partial t} + \nabla\cdot(-k\nabla T) = Q \tag{18}$$

where T is temperature; γ is the density of the metal, c is the specific heat, k is the thermal conductivity of the metal, and Q is the heat-source density produced by eddy currents per unit time in a unit volume (so-called heat generation). This heat-source density is obtained as a result of solving the electromagnetic problem.

It is important to be aware that an assumption of the steady-state heat transfer cannot be used for modeling thermal processes of induction hardening because, according to the steady-state approach, the temperature would remain constant at a given point of heated component, for all time. However, during induction hardening, temperature distribution of the component varies with time. Therefore, only the transient (time-dependent) approach should be used to model thermal processes that take place in induction hardening. With a transient heat transfer, the temperature is a function not only of the space coordinates but of time as well.

Equation [18], with suitable boundary and initial conditions, represents the 3D temperature distribution at any time and at any point in the workpiece. The initial temperature condition refers to the temperature profile within the workpiece at time $t = 0$. The initial temperature distribution is usually uniform and corresponds to the ambient temperature. However, in some cases, the initial temperature distribution is nonuniform due to the residual heat that is retained after previous technological process (i.e., self-tempering and induction hardening with interrupted quenching).

For most induction heating problems, thermal boundary conditions represent a combined effect of surface heat losses due to thermal radiation and convection, and they can be expressed as

$$-k\frac{\partial T}{\partial n} = \alpha(T_s - T_a) + c_s\left(T_s^4 - T_a^4\right) + Q_s \qquad [19]$$

where $\partial T/\partial n$ is the temperature gradient in a direction normal to the surface at the point under consideration, α is the convection surface heat-transfer coefficient, c_s is the radiation heat-loss coefficient, Q_s is the surface loss (i.e., during quenching or as a result of workpiece contact with cold rolls, water-cooled guides or liners, etc.), and n denotes the normal to the boundary surface. In many cases Q_s is not a constant and depends on surface conditions and surroundings.

As one may see from eqn [19], the heat losses at the workpiece surface are highly nonlinear. If the heated body is geometrically symmetrical along the axis of symmetry, the Neumann boundary condition can be formulated as

$$\frac{\partial T}{\partial n} = 0 \qquad [20]$$

The Neumann boundary condition implies that the temperature gradient in a direction normal to the axis of symmetry is zero. In other words, there is no heat exchange at the axis of symmetry.

In the case of heating a cylindrical workpiece, eqn [18] can be rewritten as [21]

$$c\gamma\frac{\partial T}{\partial t} = \frac{\partial T}{\partial Z}\left(k\frac{\partial T}{\partial Z}\right) + \frac{1}{R}\frac{\partial}{\partial R}\left(kR\frac{\partial T}{\partial R}\right) + Q \qquad [21]$$

However, when heating rectangular workpieces (i.e., heat transfer in plate, RCS bars, or slab), eqn [18] can be written in Cartesian coordinates as

$$c\gamma\frac{\partial T}{\partial t} = \frac{\partial T}{\partial X}\left(k\frac{\partial T}{\partial X}\right) + \frac{\partial}{\partial Y}\left(k\frac{\partial T}{\partial Y}\right) + \frac{\partial}{\partial Z}\left(k\frac{\partial T}{\partial Z}\right) + Q \qquad [22]$$

Equations [21] and [22] with boundary conditions [19] and (20) are the most popular equations for mathematical modeling of the heat-transfer processes in induction heating and heat treating.

Depending on application specifics, computer simulation analysts are often used in simplified forms of the governing equations. Some of those simplifications include an assumption of a time-harmonic electromagnetic field (a quasistationary assumption). Under this assumption, it is possible to conclude that the electromagnetic field quantities in Maxwell's equations are harmonically oscillating functions with a single frequency. Another simplification deals with the fact that for the great majority of induction-hardening applications the velocity of component movement is appreciably small compared to applied frequency. The piecewise continuous nature of material properties is postulated in the great majority of mathematical modeling of induction hardening.

An appreciable amount of electromagnetic and thermal simulations can also be effectively modeled using two-dimensional assumptions instead of 3D models, resulting in a correspondent reduction of time required for computer modeling, data preparation and visualization.

There are several ways to couple the electromagnetics and heat transfer when modeling induction heating, including a two-step approach, indirect coupling, and direct coupling. A critical review of the applicability of these coupling techniques is provided in (*1,47*).

12.15.3.2 Numerical Computation Techniques

Many mathematical modeling methods and programs already exist or are under development. Work in this field is done in universities, including Leibniz University of Hannover (Hannover, Germany), Padua University (Padua, Italy), Michigan State University, and the University of Latvia (Riga, Latvia), research laboratories; large companies such as Inductoheat, Inc.; and specialized software companies such as Cedrat, ANSYS Corp., Comsol Group, Infolytica Inc., Integrated Engineering Software Inc., ESI Group, Ansoft Corp., and Vector Fields Inc. Not a single universal computational method is optimum for solving all

induction heating problems. For each application or family of similar applications, certain numerical methods or software are preferred.

In recent years, the FEM has became a dominant numerical simulation tool for a variety of engineering applications, including thermal induction (*1,47,77–83*). Although FEA is a very effective modeling technique, it cannot be considered an ultimate computational tool for all induction heating applications. In some cases a combination of different numerical methods is more effective, whereas in others FEA is preferred.

let us briefly review a simple example; any numerical computer modeling technique (including FDM and FEM) requires a network mesh of the modeling area. That network includes induction coil(s), the heated workpiece, magnetic flux concentrators (if applied), fixtures, and other electrically conductive bodies located in close proximity to induction coils. The specifics of mesh generation affect the accuracy of simulation, required time for pre- and post-processing, as well as actual time to run numerical simulations. As an example, **Figure 40** shows network meshes for three of the most popular numerical computer modeling techniques (*6,70,71*).

Even a cursory look at a comparison of network meshes reveals that depending on the specifics of a particular induction application, a certain type of mesh generation technique could be a decisive factor in the selection of numerical simulation techniques that would suit best for modeling a particular application.

It is easy to apply the FDM method when the modeling area has regular geometries: cylindrical or rectangular. The orthogonal mesh discretizes the area of simulation (i.e., induction coil, workpiece, flux concentrator, etc.) into a finite number of nodes (**Figure 40**, left). Because of the orthogonal mesh (grid), the discretization algorithm is quite simple. An approximate solution of the governing equation is found at the mesh points defined by the intersections of the lines. This method provides a pointwise approximation of the differential equation and is quite universal because of its generality and its relative simplicity to apply.

The FEM is another group of numerical simulating techniques devoted to obtaining an approximate solution for different technical problems, including those encountered in induction heating. This numerical technique was originally applied in mechanical engineering. Later, applications of FEM have expanded to other areas of engineering.

The FDM provides a pointwise approximation; however, the FEM provides an elementwise approximation of the governing equations. According to FEM, the area of study is divided into numerous finite elements (mesh) as shown on **Figure 40**, middle.

FDM is usually not as well suited as FEM for simulation of induction systems with complicated shaped boundaries or in the case of a mixture of materials and forms. In this case, FEM has a distinct advantage over FDM.

Electromagnetic field distribution in the air, in most cases of inductor design, can be considered useless information. Such information might be of interest only during the final design stage when evaluating electromagnetic field exposure from the induction heater. The need to always carry out a computation of the electromagnetic field in the air can be considered a noticeable disadvantage of both the finite-difference and finite-element methods, in particular for elongated multicoil systems.

The boundary element method (BEM) requires discretization only of the boundaries of the electrically conductive components of the induction system (**Figure 40**, right). This substantially simplifies one of the most time-consuming parts of numerical model preparation (that is meshing) compared to FDM and FEA and dramatically reduces a time of computation.

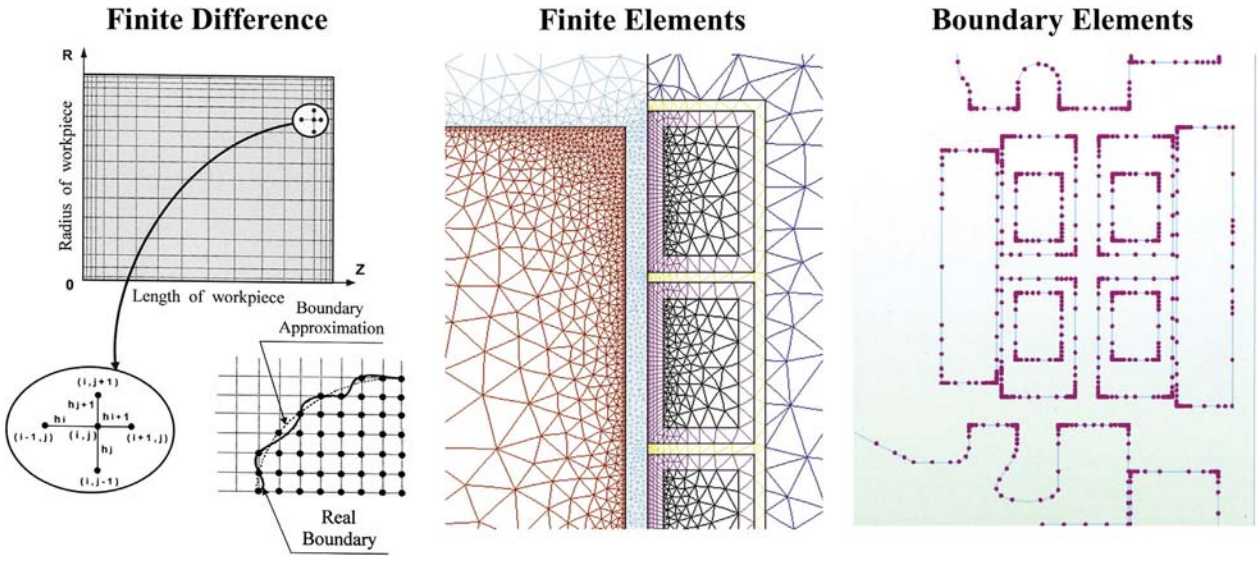

Figure 40 A comparison of network meshes for the three most popular computer modeling techniques used in induction heating: finite difference (FDM), finite element (FEM), and boundary element (BEM). Reproduced from Rudnev, V. *Tips for Computer Modeling Induction Heating Processes, Part 1;* Forge, July, 2011.

Figure 41 High-frequency multicoil inline induction heater. Courtesy of Inductoheat Inc.

The multicoil induction heater is often used for a high-speed heat treatment, including hardening, subcritical annealing (process annealing) of wires, stripes, and tubes. Several multiturn induction coils are positioned inline, and a workpiece continuously moves through them (Figure 41).

Quite often the length of such induction systems exceeds 10 m, and, in some cases (depending on a production rate), can be as long as 30 m and even longer. As discussed above, both FDM and FEA require mesh generation not only within the heated workpiece and induction coil(s), but also in the air around it due to electromagnetic field propagation outside of induction coils. This leads to a necessity to generate enormously large mesh and to expend an extraordinary long time for execution of simulation when generalized programs are used.

In contrast to FDM and FEM, BEM applies an integral form of Maxwell's equation as a governing equation for the electromagnetic problem. This allows taking into consideration only conductive bodies in the computation. Since with BEM, unknowns are only located on the boundaries or interfaces, it only requires discretization of the boundaries of the electrically conductive components of the induction system. This substantially simplifies one of the most time-consuming parts of the numerical model preparation when FDM and FEM are used.

Such advantages as the reduction of computation time, simplicity, user-friendliness of the mesh generation, and good accuracy (particularly when working with nonmagnetic materials or materials with linear properties) make this technique quite attractive in certain applications compared to other methods. In some cases of substantially nonlinear material properties, an error can be accumulated in solving internal problem using BEM. In cases like this, BEM is used to solve external electromagnetic problems, and FEM or FDM is used to solve internal electromagnetic problems. Such an approach utilizes the best of different numerical methods.

References (*1*,*6*) discuss the *pros* and *cons* of different computer modeling methods and their applicability to simulate induction heating processes.

12.15.3.3 Limitations of Generalized All-Purpose Commercial Software

Many of the commercial codes used for computer modeling of induction heating processes are all-purpose programs that were primarily developed for modeling electrothermal processes taking place in electrical machines, motors, medical devices, circuit breakers, nondestructive testing (NDT), transformers, and magnetic recording systems, and were later adapted to some induction heating needs.

The necessity to sell products to as many customers as possible forces software developers to produce a universal simulation tool that can be used by much larger industries compared to induction heat treating.

As a result, certain process subtleties related to induction heating might be 'overlooked' by developers or unreasonably simplified. Regardless of the well-recognized impressive capabilities of modern commercial software, many of the generalized programs experience difficulties in taking into consideration certain features of a particular induction heating application. This might include the following:

- Heated workpiece can simultaneously move, rotate, or oscillate in respect to induction coil(s).
- Most induction-hardening operations combine heating and spray-quenching stages. Some computer modeling challenges of spray quenching are related to complex interaction between the surface of the hot steel and spray quench, which comprises hydrodynamic structure of the spray quench, temperature, pressure, flow and type of the quenchant, as well as design specifics of the quenching device.

- The presence of thermal refractory and necessity to take into consideration thermal radiation view factors (the Lambert's law of thermal radiation).
- In some applications (i.e., contour hardening of gears), induction hardening is accomplished by using dual frequency power generators that allowing to apply two different frequencies simultaneously to a heating coil.
- Existence of nonuniform *initial* temperature distributions and presence of interrupted heating and/or quenching.
- Presence of the comet tail effects in induction scan hardening.
- Presence of end plates, guides, fixtures, tooling, liners that might deform electromagnetic and thermal field distributions.
- Presence of transient technological stages (e.g., thermal holding, the 'cold' start, 'hot' start, etc.) in inline induction system that comprise a number of coils.

Lack of ability to properly take all or some of the above-discussed factors into consideration could lead to erroneous modeling results. An attempt to simulate inline multicoil continuous heating application or induction scan hardening might unpleasantly surprise a computer modeling analyst who might try using generalized all-purpose software (*70–72*).

12.15.3.3.1 Challenges in Simulation Inline Multicoil Continuous Induction Heating

Progressive or continuous induction is a popular method of heating wires, rods, bars, strips, small- and medium-size billets when they are moved through an inline multicoil horizontal induction heater. This heating method assumes that the workpiece is sequentially (progressively) heated while passing through different coils of the induction heating line (*1,46,71,72*). The purpose of heating may be through-hardening, subcritical annealing, tempering, or heating prior to hot working or coating.

One of the challenges presented by inline induction heating arises from the fact that the surface-to-core temperature profile continues to change as the workpieces pass through the line of induction coils (**Figures 24** and **41**). The line can be quite long, often exceeding 10 m, but in some cases it can be as long as 30 m. Coils can be connected to different power supplies, or several coils might have a complex series or parallel electrical connections and individual design features. Electromagnetic field distortion due to coil end effects and the presence of heating/soaking stages between coils must be taken into consideration.

In order to optimize system performance and determine the most suitable design and process parameters, it is often necessary to analyze two transient process stages: 'cold' start and 'hot' start. The term *cold start* represents a process condition when the induction heater was switched off for a sufficiently long time (e.g., after a holiday) and its thermal refractory has been cooled down to an ambient temperature.

In contrast, the term *hot start* designates a condition marked by a relatively short interruption in the process cycle (e.g., due to temporary issues related to short interruptions in the operation of machines subsequent to induction). A short interruption leads to partial refractory cooling and its temperature being appreciably high.

Suppose the analyst knows the physical properties of the refractory's material, its thickness and the geometry of the induction system, and, therefore, fully expects to be able to evaluate the effect of 'cold start' and 'hot start' versus a steady state and determine what would be the most appropriate process recipe to compensate the differences in refractory temperature.

Suddenly, the analyst might realize that purchasing all-purpose software does not allow imputing the specifics of a refractory design and/or take into consideration either a continuous movement of the workpiece along the multicoil heating line or consideration coil end effects. At the best, manuals might suggest that the user is somehow supposed to quantify an effect of a refractory on the workpiece's thermal boundary condition taking place due to convection and radiation surface heat losses. Unexpectedly, such common design features of any inline multicoil induction heater might become an obstacle in using generalized commercial modeling software (*70–72*).

12.15.3.3.2 Challenges in Modeling an Induction Scan Hardening

As stated earlier, the typical procedure for induction hardening involves heating the component to the austenizing temperature, holding it at a temperature for a period sufficiently long for completion of the formation of homogeneous austenite, then rapidly cooling (typically using a spray quench), allowing the formation of martensite. Scan hardening is one of the most popular induction techniques for hardening elongated parts with a rotational or axial symmetry or when hardening surfaces of flat components are required.

When designing scan-hardening inductors and developing optimal process recipes, it is imperative to properly model not only heating but the spray-quenching stage as well. Otherwise, crucial aspects of the scan-hardening process might be missed, having a negative impact on modeling accuracy and its usefulness.

Unfortunately, a negative aspect of the great majority of commercially available all-purpose software is that they have a limited capability to accurately take into consideration not only spray quenching that is subsequent to heating, but also a comet-tail effect, as well as pre- and post heating effects that appeared due to the external magnetic field propagation and axial heat flow due to thermal conduction when trying to model induction scan hardening.

The case study below presents an example of proper simulation of scan hardening using Inductoheat's proprietary software.

Figure 42 shows the results of computer modeling the sequential dynamics of induction scan hardening a hollow shaft, using a two-turn machined integral quench (MIQ) inductor with an L-shaped flux concentrator ring (frequency = 9 kHz) (*6,70*).

First (see **Figures 42(a)** and **42(b)**), a 2.6 s power dwell is applied to properly preheat the shaft's fillet area. During this stage, an inductor is energized but does not move, and quenching is not applied. Upon completing the dwell stage, the shaft fillet is

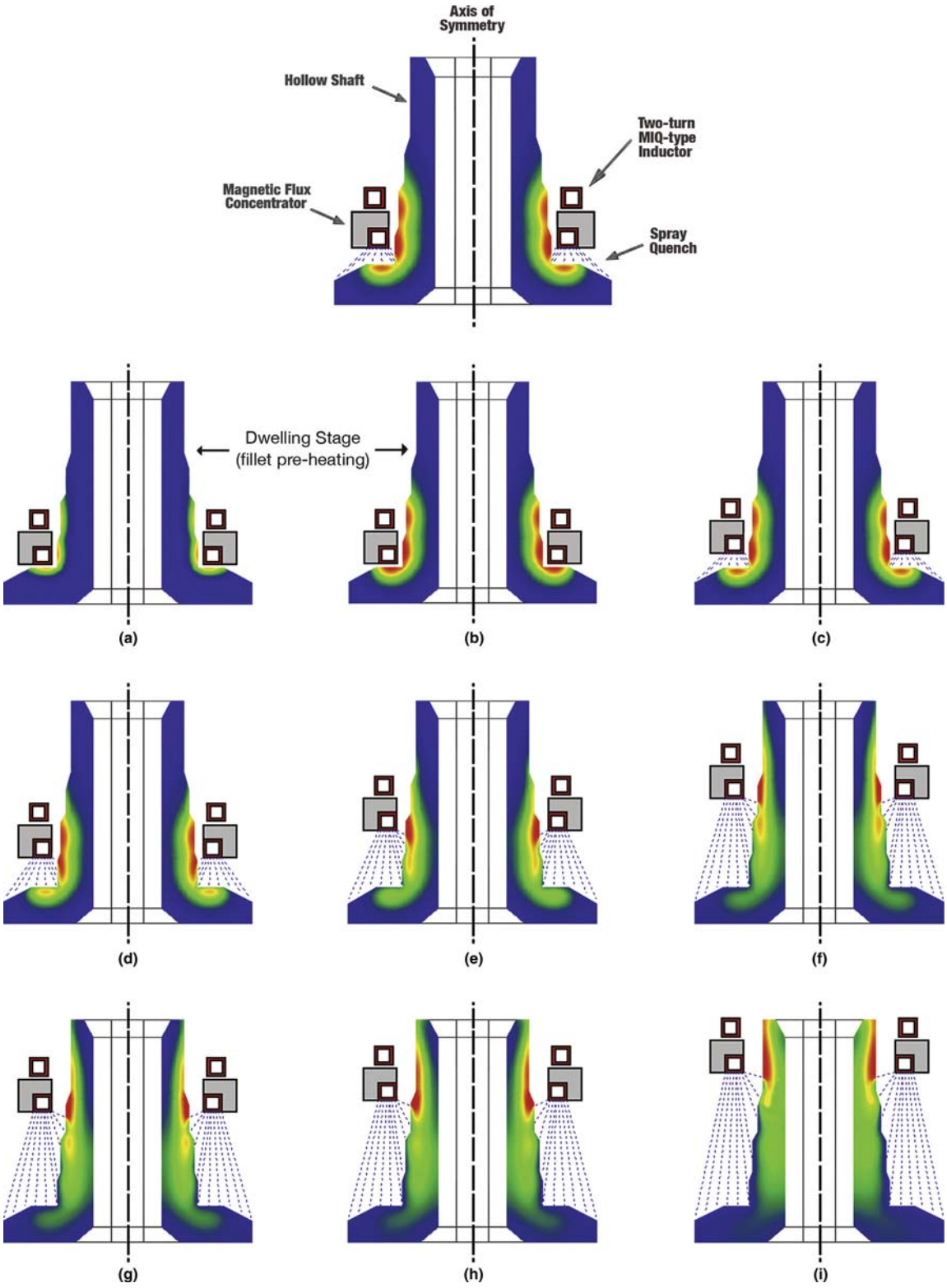

Figure 42 Computer simulation of the sequential dynamics of induction scan hardening a hollow shaft using a two-turn machined integral quench (MIQ) inductor with an L-shaped magnetic flux concentrator ring (frequency = 9 kHz). Reproduced from Rudnev, V. Computer Modeling of Induction Heating: Things to be Aware off, Things to Avoid. *Ind. Heat.* **May, 2011,** 41–45.

sufficiently preheated and scanning begins. Scan rate and coil power are varied during scanning to allow proper accommodation of changes in shaft geometry. Computer modeling reveals several important process subtleties (*6,70*):

- During induction scanning, appreciable heating of the shaft begins at a distance a good deal above the top copper turn, creating a preheating effect. Factors responsible for preheating are heat flow in the axial direction due to thermal conduction and propagation of the external magnetic field generating appreciable heat sources outside of induction coil.
- The presence of an external magnetic field outside the induction coil is also responsible for the postheating of shaft areas located immediately below the bottom turn, and, in some cases, even in regions where the subsequent quenchant impinges the shaft surface. The combination of insufficient quenching and relatively short distance between the exit end of induction coil and the area where quenchant impinges the workpiece surface can dramatically reduce quench severity due to an induction heating effect of the external field of the coil. This can create conditions for crossing the nose of the CCT (continuous cooling transformation) curve, resulting in the formation of mixed structures with the presence of upper transformation products (e.g., bainitic/pearlitic structures or 'ghost' networking). Such microstructures are notorious for scattering and lower hardness readings.
- The electromagnetic proximity effect and the coil end effect cause the hot spots that appear on the shoulder near a shaft diameter change (regardless of the coil power reduction there). During scanning, the magnetic field preferably couples to the shoulders, leading to a power density surplus at those locations. The presence of hot spots produced by a power surplus necessitates a prolonged cooling to remove excessive heat, ensuring martensitic formation and obtaining sufficient hardness. At the same time, a heat deficit could occur in the undercut region and transition area near the shaft's smaller diameter.

It is imperative to take into consideration a comet-tail effect when developing a scan-hardening process recipe. **Figure 43** shows the magnified temperature patterns of the intermediate process scanning stage (**Figure 42(f)**). The comet-tail effect manifests itself as a heat accumulation in shaft subsurface regions below the scan inductor, being pronounced in the areas of a diameter change. Upon quenching, the temperature of the shaft surface can be cooled sufficiently below the M_s temperature. At the same time, the heat accumulated in the shaft subsurface might be sufficient for tempering back as-quenched surface regions and could potentially result in the appearance of soft spots within the case depth. Sufficient quench-out is essential to prevent this undesirable phenomenon.

To optimize temperature distribution prior to quenching, complex process control algorithms are required, with a varying power and scan rate when the coil approaches geometrical irregularities. The necessity of determining multiparameter control algorithms leads to long development times in the lab using the trial-and-error method, with a number of components being wasted. The learning curve can be considerably shortened, and the number of parts required for trials can be dramatically reduced thanks to computer modeling.

12.15.3.4 Conclusion

It is important to be aware that some critical feature(s) of a particular induction heating and heat-treating application could be a limiting factor for all-purpose software. This could create considerable challenges in applying generalized commercial codes, forcing an analyst to make ill-defined assumptions that might dramatically affect the accuracy and usefulness of simulations.

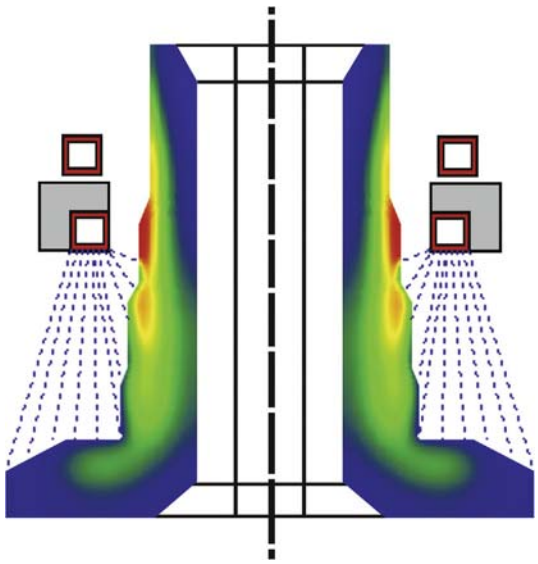

Figure 43 The comet-tail effect manifests itself as a heat accumulation in shaft subsurface regions below the scan inductor. Reproduced from Rudnev, V. Computer Modeling of Induction Heating: Things to be Aware off, Things to Avoid. *Ind. Heat.* **May, 2011,** 41–45.

Scientists and engineers of Inductoheat Inc. routinely utilize a variety of commercial software. In addition, the Inductoheat professionals developed proprietary application-oriented programs that take into consideration process specifics and important subtleties.

Our experience shows that there is no single universal computational method that optimally fits all induction applications. Taking into consideration the specifics and subtleties of a wide variety of induction heating processes, we find that a number of subject-oriented and highly effective software are preferable to searching for a single universal code. For similar problems, certain numerical methods or software are preferred.

12.15.4 Induction-Hardening Systems and Applications

The typical induction-hardening system comprises several components, including:

- Power supply (i.e., typically medium or high frequency inverter)
- Heat station
- Heating inductor
- Quench system
- Water-cooling system
- Control, monitoring, and quality assurance devices
- Workstation (workpiece handling and fixtures)

Varieties of hardening inductors were discussed in Section 12.15.2.4 of this chapter. A separate chapter of this volume is devoted to quenchants and quenching techniques. Aspects of power supplies, load matching, control, monitoring, and quality assurance will be discussed at the end of this chapter (Sections 12.15.5 and 12.15.6). This section reviews some of the most popular induction hardening applications.

12.15.4.1 Induction Hardening of Automobile Crankshafts

Crankshafts are widely used in internal combustion engines, pumps, compressors, and so on, and belong to the group of the most critical auto components typically weighing between 12 and 40 kg, depending on the engine (*84,85*).

A crankshaft, typically cast or forged, comprises a series of crankpins (pins) and main journals (mains) interconnected by counterweights (**Figure 2**, top left). Steel forgings, nodular iron castings, microalloy forgings, and austempered ductile iron castings are among the materials most frequently used for crankshafts (*1*).

Crankshaft journals were induction hardened using one of two alternative processes: band hardening or band and fillet hardening. According to band hardening, bearing surfaces are induction hardened. Roll or ball hardening of the fillet areas are applied after induction hardening, inducing compressive residual stresses there. With induction band and fillet hardening, fillets and bearing surfaces are induction hardened. The specifics of a particular crankshaft and its operating conditions call for one of those alternative hardening techniques.

Taking into consideration that the diameters of the crank's journals (mains and pins) are much smaller compared to the external dimensions of the counterweights, the conventional encircling-type coils could not freely pass from one journal to another. This feature necessitates developing specific inductor designs for induction hardening the crankshaft's journals.

12.15.4.1.1 Clamshell or Split Inductors

Clamshell or split inductors (**Figure 44**) were developed in the 1950s and have been used for induction hardening of crankshafts since that time. No rotation of the crankshaft is required. Short coil life, poor reliability, and low production rate were some of the main drawbacks of these inductors (*86*). The short coil life resulted from the need to break the electrical current flow by having high-current contacts.

When the inductor is closed, it must be clamped with sufficient pressure, ensuring good electrical contact between the movable parts of the coil. Practically speaking, no contact surfaces of a coil are perfectly smooth, and, regardless of the amount of contact surface polishing and cleaning, air pockets and contaminated islands of the contact area will always be present, forcing the coil current to flow through the localized contact points (*86*). This results in localized overheating, contact burning, and arcing, ultimately leading to premature coil failure. Regardless of the applied pressure, the quality of the electrical contacts degrades after multiple openings and closings of the coil. Contaminants quickly build up on contact surfaces in the production environment. This further increases electrical resistance and Joule losses of the contact area, increasing the electrical resistance of transitional areas between contact surfaces that continuously change during coil operation, resulting in poor reliability and variation in the power induced within the heated component while power at the coil terminals remains unchanged. Heat treaters often were required to continuously increase the contact pressure to compensate for a clamshell coil surface deterioration with time. Sometimes it even led to copper deformation in clamping areas, unpredictable inductor performance, and its premature failure(*1,85,86*).

Those factors limited the use of this technology for hardening of bearing surfaces when appreciably low production rates are required.

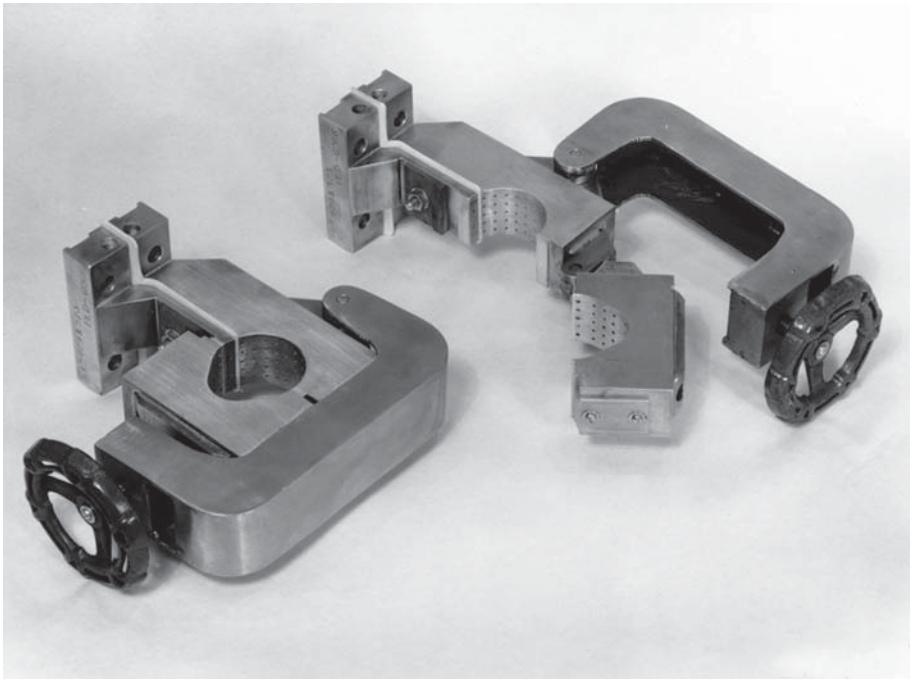

Figure 44 Clam shell or split inductor with integral quench for hardening camshaft lobes. Reproduced from Rudnev, V.; Loveless, D.; Cook, R.; Black, M. *Handbook of Induction Heating*; Marcel Dekker: NY, 2003.

12.15.4.1.2 Nonencircling U-Shaped Inductors Requiring Crankshaft Rotation

Nonencircling U-shaped inductors were almost exclusively used from the 1960s to the year 2000 to induction harden the bearing surfaces of automotive crankshafts (*1,84*). According to this process, each crankpin and main journal was heated by bringing a U-shaped inductor close to the pin or main bearing surface while the crankshaft was rotated about its main axis. Since the pins axes were offset radially from the main axis, the pins orbited the main axis. The circular orbital motion of such a heavy system should be maintained quite precisely, with a special control tracking system providing a power modulation for each heated crank's feature during its rotation (**Figure 45**). U-shaped inductors rode on the journal surface while a crankshaft rotated during heating using carbide guides (also called spacers or locators).

Several obvious drawbacks are associated with this technology, namely (*84,85*):

- High maintenance cost.
- Utilization of nonencircling U-shaped inductors demands having critically small 'journal-to-inductor's copper' air gaps (0.25–0.4 mm). Each U-shaped inductor consists of 6–10 carbide guides leading to time-consuming setup training and experience in the proper installment and adjustment of the locators and still allows for human error. Besides, each locator is simply one more part that can go wrong leading to a hardness pattern shifting.
- Carbides 'ride' on the bearing surfaces heated to temperatures exceeding 900 °C. This makes it difficult to precisely monitor the carbides' wear and to maintain the required 0.25–0.4 mm gaps. Due to the small air gaps and uncontrollable wear of carbide guides, the U-shaped inductor often accidentally touches a rotating crank surface during operation. This results in water leaks, premature copper failure, and appreciable equipment downtime and negatively affects the quality of heat-treated journals (e.g., pattern shifting, an appearance of 'soft' spots on as-hardened surfaces).
- Nonencircling U-shaped inductors inherently produce a nonsymmetric heating pattern at any given time because heat is applied to only less than a half portion of the crankshaft journal (**Figure 45**). The rest of the pin/main undergoes a 'soaking-cooling' cycle. The nonsymmetrical heating nature of U-shaped inductors can potentially result in nonuniform hardness profiles and requires relatively prolonged heat times (7–20 s), which, in turn, leads to heating appreciable metal masses resulting in excessive distortion of the crankshaft.
- A combination of prolonged heating times, moist working environment, and critically small inductor copper-to-bearing surface gaps results in copper deterioration due to stress-corrosion and stress-fatigue cracking and potentials for arcing. All these factors negatively affect coil life expectancy.
- Bulky system design and noisy operation associated with the necessity of moving massive induction heating and quenching systems often weigh over 900 kg and wear out flexible cables.
- U-shaped inductors are typically fabricated using one of two techniques: copper bending or brazing. In both cases, precision and repeatability of fabrication of complex-geometry inductors (**Figure 45**) is always a concern, negatively affecting the repeatability of hardness patterns after installing new inductors requiring appreciably long validation process.

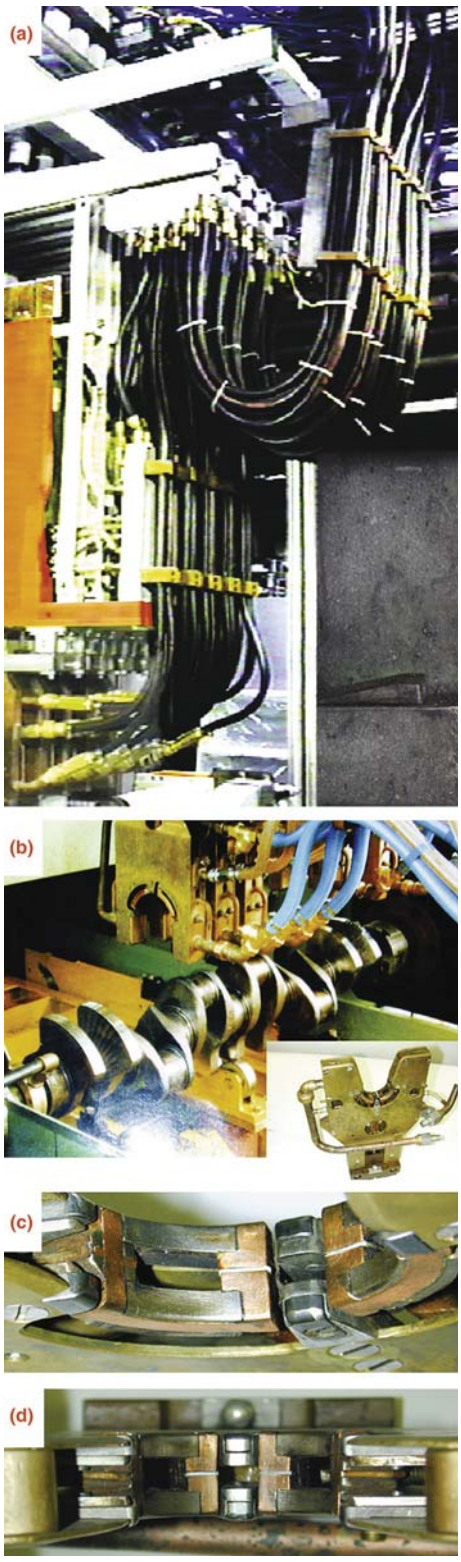

Figure 45 Rotational hardening process utilizes a number of U-shaped inductors. Note: Carbide guides (locators) are required. Reproduced from Doyon, G.; Brown, D.; Rudnev, V.; Desmier, G.; Elinski, J. Taking the Crank out of Crankshaft Hardening. *Ind. Heat.* **December, 2008,** 41–44.

- High system sensitivity may also negatively affect pattern repeatability and could also lead to a short tooling life.
- Safety concerns due to the presence of multiple moving heavy machine parts and cables.

12.15.4.1.3 Nonrotational Hardening of Crankshafts: The SHarP-C Process

In order to induction harden crankshaft's journals while not having to rotate the crankshaft, a patented nonrotational technology SHarP-C (Stationary Hardening Process for Crankshafts) was introduced in early 2000 (*87,88*). Following its first appearance, this technology was further 'fine-tuned' becoming a proven advance process that eliminates the need to rotate the crankshaft while at the same time removing the drawbacks of the interrupted high-current contacts associated with clamp-type inductors. **Figure 46** shows the CrankPro® machine, which implements a SHarP-C technology. This patented technology was specifically developed for high production rates when heat treating automotive crankshafts.

According to a patented nonrotational crankshaft hardening process, an inductor consists of two sections (**Figure 47**): a bottom (active) inductor and a top (passive) inductor. The bottom inductor, being active, is connected to a medium-frequency inverter, while the top inductor (passive) represents a short circuit (a loop). The bottom inductor is stationary, while the top inductor can be opened and closed. Each inductor has two semicircular areas where the crankshaft's features will be placed (*87,88*).

Figure 46 CrankPro machine implements Inductoheat's patented nonrotational crankshaft hardening and tempering technology (SHarP-C). Courtesy of Inductoheat, Inc.

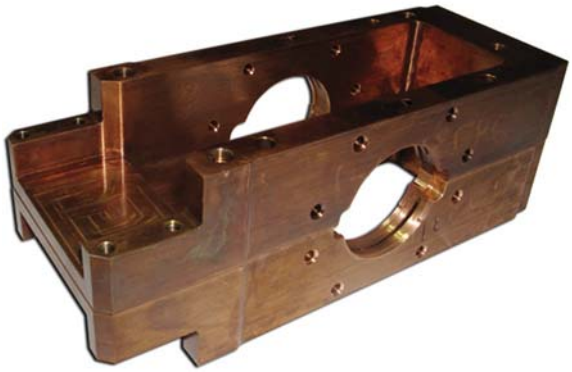

Figure 47 SHarP-C inductor for nonrotational Crankshaft hardening. Courtesy of Inductoheat Inc.

Robot or gentry loading a crankshaft into the heating position, the top inductor pivots into a 'closed' position and the power is applied from the power supply to the bottom (active) inductor. The current starts to flow in the bottom inductor. Being electromagnetically coupled to a top inductor, a current flowing in the bottom inductor induces the eddy currents to start to flow in the top inductor creating currents oriented in the opposite direction compared to a source current (similar to transformer effect).

According to this technology, top and bottom inductors provide the simultaneous hardening of two journals, helping to increase a production rate. A modified SHarP-C inductor can be used for induction hardening of only a single bearing or multiple bearings, if required.

As can be seen from our discussion, electromagnetically speaking, any heated feature of the crankshaft (e.g., pins, mains, and oil seal) 'sees' the SHarP-C inductor as a classical fully encircling solenoid coil (*84,85,87,88*), naturally increasing the heating uniformity along a perimeter of the crankshaft's journals and maximizing electrical efficiency.

This patented nonrotation induction-hardening and tempering technology provides several principal benefits such as simple operation, superior reliability, quality, maintainability, and cost reduction. Other benefits include (*84,85*):

- Heat patterns are 'locked in place' and very repeatable since neither the crankshaft nor the coils are moving during the induction-hardening process. **Figure 48** shows the hardness pattern for the pin journal of the V-8 crankshaft.
- No wearing of the locators/guides/spacers involved. The SHarP-C process utilizes inductors, which do not require contact guides, or complex and expensive noncontact coil positioning and tracking systems of any kind. This increases control reliability and simplifies process monitoring.
- Being CNC machined from solid copper block, inductors are more robust, rigid, and repeatable. The inductor does not have any brazed or bended parts. This eliminates inductor distortion and its shape variation during the fabrication and hardness pattern drift associated with shape variation of inductor. **Figure 49** shows a side-by-side comparison of the rigidity and complexity of the U-shaped inductor (top) versus the SHarP-C inductor (bottom). There are far fewer components involved in the patented SHarP-C inductor design, meaning higher reliability because of the smaller numbers of parts that can go wrong.
- On average, the required heat time for hardening has been reduced fourfold, being in the range of 2–4 s, and provides several principal benefits, including energy reduction and improved shape/size distortion. During heat treating, the crankshaft rests on

Figure 48 Nonrotational hardening process provides crankshaft pins and mains with superior microstructural properties. Reproduced from Doyon, G.; Brown, D.; Rudnev, V.; Desmier, G.; Elinski, J. Taking the Crank out of Crankshaft Hardening. *Ind. Heat.* **December, 2008,** 41–44.

Figure 49 A side-by-side comparison of rigidity and complexity of U-shaped inductor (top) versus SHarP-C inductor (bottom). Reproduced from Rudnev, V.; Doyon, G.; Brown, D. Innovative Induction Heating Technologies. Pittsburgh. In *Proc. of Materials Science & Technology Conf.* (MS&T-08); 5–9 Oct., 2008.

V-blocks, and its journals are heat treated sequentially. As an example, Figure 50 shows a sequence of hardening of V-8 crankshaft. Reduction of total indicated runout (TIR) distortion is traditionally one of the most important factors in the heat treating of crankshafts. Because of the short heat time, the core of the journal remains relatively cold during the whole heat treating cycle, acting as a shape stabilizer and reducing shape distortion. TIR directly affects the amount of metal required to grind. One of the most important factors that have a pronounced effect on distortion is the amount of heat generated within the crankshaft body and an ability to keep its core temperature below the elasticity limit while surface heating a journal. The greater the amount of heated metal, the greater the metal's expansion, which in turn causes greater distortion. Appreciable reduction of the heat time associated with this process leads to only a small mass of metal being heated. The core temperature at the end of heating does not typically exceed 300 °C, and core temperature of about 220 °C being more typical. A sufficiently cold core acts as a shape stabilizer. The heat-affected zone is minimized, resulting in a corresponding reduction of metal expansion and, obviously, in minimization of size and shape distortion. Thanks to the above-discussed factors, distortion of the crankshaft bearings is usually less than 25 microns after using nonrotational SHarP-C technology.

- Crankshaft pins and mains have superior microstructural properties. These include the noticeable reduction of grain growth, decarburization, and intergranular oxidation of the pin/main surface. The hardened pattern is clearly defined and 'crisp' (Figure 48) without the 'fuzzy transition zone' that is present when longer heat times are employed using nonencircling U-shaped inductors. The case depth consists of fine-grain martensitic microstructure. Surface compressive stresses obtained when applying SHarP-C technology are imperative for prevention of surface crack development. Intensive theoretical and computer modeling studies in developing optimal process recipes have been conducted in cooperation with leading world experts such as Dr Lynn Ferguson, Deformation Control Technology, Inc., to provide a favorite distribution of transitional and residual stresses of heat-treated cranks (Figure 51).
- The need to have the surface of crankshaft journals at a high temperature for prolonged periods, which is required by rotational technology, is potentially often associated with such an undesirable metallurgical phenomenon as grain boundary liquation. This phenomenon substantially increases brittleness and sensitivity to intergranular cracking, in particular of the oil-hole area. Thanks to the process features of nonrotational technology, copper profiling of inductors, and other know-how, this undesirable phenomenon has been eliminated.

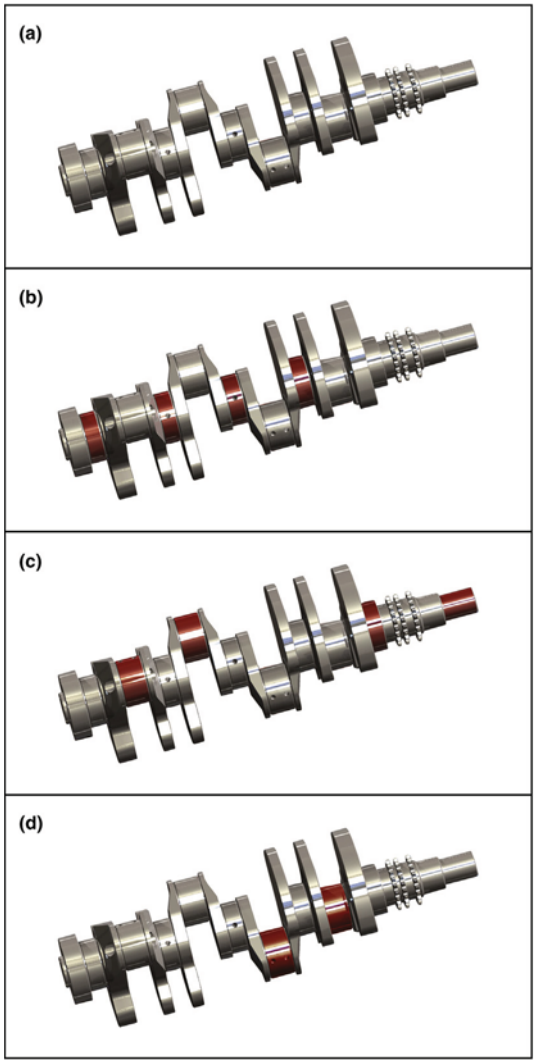

Figure 50 Sequence of induction hardening bearing journals of V-8 crankshaft.

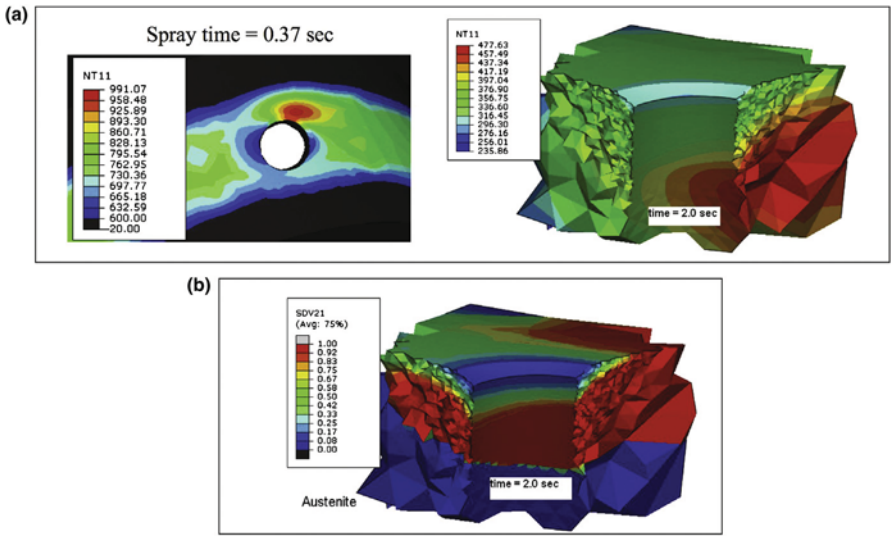

Figure 51 Computer modeling of temperature profiles during spray quenching of crankshaft journal (a) and prediction of austenite transformation (b). Courtesy of Deformation Control Technology, Inc.

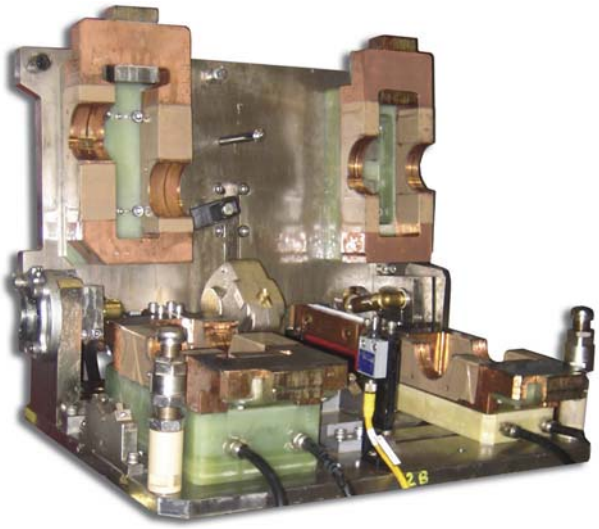

Figure 52 Pallet with inductors for a nonrotational SHarP-C technology. Reproduced from Doyon, G.; Brown, D.; Rudnev, V.; Desmier, G.; Elinski, J. Taking the Crank out of Crankshaft Hardening. *Ind. Heat.* **December, 2008,** 41–44.

- Coil-to-journal air gaps are substantially larger when the SHarP-C coils are used compared to air gaps required by the rotational crankshaft hardening process. This creates a favorable condition to reduce stress corrosion and stress fatigue of coil copper dramatically increasing a tooling life.
- Accurate CNC fabrication of SHarP-C inductors and utilization of a 'quick change' pallet approach (**Figure 52**) guarantee that inductor pallets are automatically aligned with respect to the crankshaft after coil replacement. No time-consuming process adjustments are required to 'tweak' each inductor after replacement. Unitized construction allows quick, error-free, 'production-ready' factory installation and start-up, substantially reducing downtime.
- Since rotation of the crankshaft is not required, it is not necessary to move heavy structures often weighing over 900 kg through the orbital path during heating. Nor are there high-current electrical contacts or flexible cables to wear out. There is only the 'open-close' action of the passive section of the SHarP-C inductor. All these improve safety aspects in operating equipment and its ergonomics.

Conclusion. Nonrotational SHarP-C technology is an increasingly popular process used for the crankshaft's band hardening of journal-bearing surfaces when medium- and high-production rates are required. The rotational process utilizing nonencircling U-shaped inductors continues to be the most widely used process for crankshaft fillet hardening applications requiring hardening of the split pins and undercuts.

12.15.4.2 Induction Hardening of Gears

Gear performance characteristics (including load condition and operating environment) dictate the required surface hardness, core hardness, hardness profile, residual stress distribution, grade of the steel, and its prior microstructure (*1,89–94*).

In contrast to carburizing and nitriding, induction hardening does not require heating the whole gear. With induction, heating can be localized to only those areas in which metallurgical changes are required. For example, the flanks, roots, and tips of gear teeth can be selectively hardened.

External spur and helical gears, worm gears and internal gears, bevel gears, racks, and sprockets are among the parts that are routinely induction hardened (*1,89–96*). A sampling of parts can be seen in **Figure 53**.

Gear operating conditions, the required hardness, and cost are important factors to consider when selecting materials for induction-hardened gears. Plain carbon steels and low-alloy steels containing 0.4–0.55% carbon content are commonly specified. Examples include AISI 1045, 1552, 4140, and 4340. In some cases, high-carbon steels are used (i.e., AISI 1065, 1070, 1080, 52100).

Tooth surface hardness after hardening and tempering is typically in the 50 to 60 HRC range, depending on the application specifics. Core hardness depends primarily on steel chemical composition and its prior treatment (referred to as microstructure of a 'green' gear). For example, for quenched and tempered prior structures core hardness is usually in the 29–36 HRC range. (The importance of having 'favorable' prior microstructure for short-time induction hardening has been discussed earlier in Section 12.15.2.1 of this chapter.)

Besides chemical composition and prior microstructure, the surface condition of the gear is another factor that can have a pronounced effect on gear hardening. Microcracks, notches, and other surface and subsurface discontinuities as well as surface stress raisers can initiate cracking during hardening when the metal goes through the expansion–contraction cycle. Thermal gradients and stresses can reach critical values and 'open' notches and microcracks. Conversely, a homogeneous steel structure with

Figure 53 External spur and helical gears, worm gears and internal gears, bevel gears, racks, and sprockets are among the parts that are typically induction hardened. Courtesy of Inductoheat Inc.

a smooth surface free of voids, cracks, notches, and the like improves the heat-treating conditions and positively affects important gear characteristics, such as bending fatigue strength, endurance limit, impact strength, durability, and gear life.

Medium frequency and, in particular, high frequency have a tendency to overheat sharp corners and edges; therefore, it is highly desirable that gear teeth are reasonably chamfered for optimum results in the heating process.

The first step in designing an induction gear-hardening machine is to specify the required surface hardness and hardness profile. Generally speaking, eight widely accepted gear-hardening patterns (*1*,*91*,*92*) can be achieved with induction hardening:

1. Flank hardening
2. Flank and tip hardening
3. Hardening of tooth tip
4. Root hardening
5. Through hardening of entire tooth and root
6. Semicontour hardening (nonuniform pattern)
7. Contour hardening (uniform pattern)
8. Flank and root hardening

Reference (*1*) provides a comprehensive review of those patterns, their applicability, pros and cons, their achievability using different induction-hardening techniques, and the effect of those patterns on gear load-carrying capacity and gear life.

A through-hardened medium- and large-size gear teeth with hardness exceeding 62 HRC are typically too brittle and might experience a premature fracture. It is also important to have a sufficient hardened case depth to be able to adequately provide the required gear tooth strength and other properties. Insufficient hardness as well as an interrupted ('broken') hardness profile at tooth contact areas or in the root region will shorten gear life due to poor load-carrying capacity, premature wear, tooth bending fatigue, rolling contact fatigue, pitting, and spalling, and can even result in some plastic deformation of the teeth (*95*,*96*).

12.15.4.2.1 Coil Design and Heating Modes

Generally speaking, gears are induction hardened by either encircling the gear with a coil (so-called spin hardening using a single shot or scanning heating modes) or, in larger gears and pinions, by heating them 'tooth-by-tooth' with either 'gap-by-gap' or 'tip-by-tip' hardening.

12.15.4.2.1.1 Tooth-by-tooth hardening of gears

The tooth-by-tooth hardening can be applied to external and internal gears and pinions (*1,89,91*). Applied frequencies with tooth-by-tooth hardening are usually in the range of 1–30 kHz. At the same time, there are some cases when radio frequencies are used, but it is typically when submerged hardening techniques is applied.

Coil geometry depends on the shape of the teeth and the required hardness pattern. According to the tip-by-tip technique, an inductor encircles a body of single tooth. At the present time, this technique is used very seldom because hardness patterns obtained with this technique have limited use.

The gap-by-gap technique is much more popular than the tip-by-tip concept and requires the inductor to be symmetrically located between two flanks of adjacent teeth (**Figure 54**). Inductors can be designed to scan heat only the root and/or flank of the tooth, leaving the tip and tooth core tough and ductile (**Figure 55**). Scanning rates can be quite high, reaching 8 mm per second and even higher.

Both tip-by-tip and gap-by-gap techniques are typically not very suitable for small and fine pitch gears (modules smaller than 6). There are many variations of coil designs applying these principles. Two of the most popular inductor designs are shown in **Figure 56**.

Gears hardened by using the gap-by-gap technique can be fairly large, having ODs of 5 m or more; they can weigh several tons. As an example, **Figure 57** shows a tooth-by-tooth induction gear-hardening machine for a large bearing ring for a wind energy turbine with teeth located on the ID of the ring (*89*). A bearing ring OD exceeds 3.5 m, and the maximum weight surpasses 5 tons. The required case depth is 2.5–3.5 mm. The *z*-axis scan height (tooth width) is 0.35 m. Precise inductor fabrication techniques, inductor rigidity, and superior alignment techniques are required. Special locators or electronic tracing systems are often used to ensure proper inductor positioning in the tooth space. Thermal expansion of metal during heating should also be taken into consideration when determining the proper inductor-to-gear tooth air gap. After ring loading and initial coil positioning, the process runs automatically based on an application recipe.

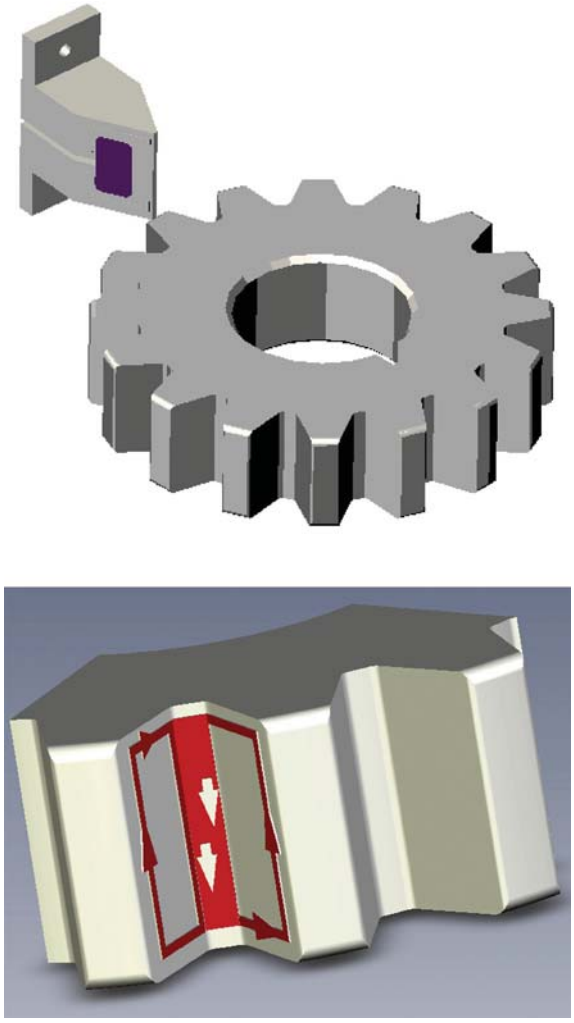

Figure 54 Gap-by-gap induction hardening of gears. Reproduced from Rudnev, V.; Loveless, D.; Cook, R.; Black, M. *Handbook of Induction Heating*; Marcel Dekker: NY, 2003.

Figure 55 Gear-hardened pattern using gap-by-gap hardening. Courtesy of Inductoheat Inc.

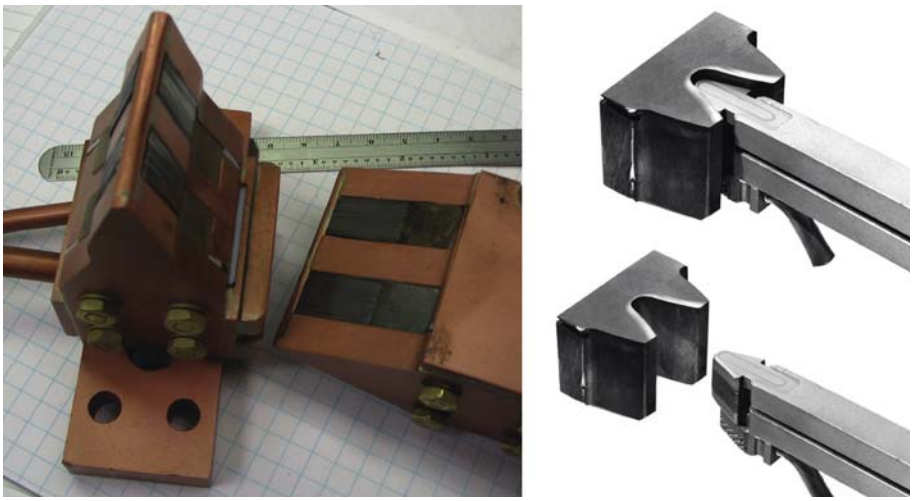

Figure 56 Two of the most popular inductor designs for gap-by-gap hardening. Courtesy of Inductoheat Inc.

Figure 57 Induction gear-hardening machine for a large-diameter ring for a wind-turbine generator with teeth located on the inside diameter of the ring. The bearing ring OD can be as large as 3.5 m, the required case depth is 2.5–3.5 mm, the *z*-axis scan height (tooth width) is 350 mm, and the maximum weight exceeds 5 tons. Courtesy of Inductoheat-HWG, Germany.

There is a limitation to applying this method for hardening internal gears. Typically, it is required that the internal diameter of the gear exceed 0.2 m and, in some cases 0.25 m or more (depending on tooth geometry).

Both tip-by-tip and gap-by-gap hardening is a time-consuming process with a low production rate. Power requirements for these techniques are relatively low and depend on the production rate, type of steel, case depth, and tooth geometry. Modest power requirements can be considered an advantage, because if spin hardening is used for hardening large gears, it could require an appreciable amount of power that could diminish the cost effectiveness of the hardening (*89*).

One of the challenges presented by tooth-by-tooth hardening is related to the appearance of undesirable tempering back of the previously hardened area. An undesirable tempering back can take place for two main reasons: The first deals with inducing eddy currents by an external magnetic field of the heating inductor in the tooth regions that were already hardened.

The second reason is associated with the thermal conductivity phenomenon. All hardenable steels have relatively high thermal conductivities. Heat is transferred by thermal conduction from a high-temperature region of the gear surface to its lower-temperature region. According to Fourier's law, the rate of heat transfer is proportional to the temperature difference and the value of thermal conductivity. During hardening, the surface temperature reaches a relatively high value exceeding the critical temperature A_{c3}. Therefore, when heating one side of the tooth, there is a danger that the opposite side of the gear tooth will be heated by thermal conduction to temperatures of the tempering range, resulting in undesirable tempering back of previously hardened regions.

Whether or not a hardened face of a tooth will be oversoftened depends on the applied frequency, gear module, tooth shape, heat time, and hardened case depth. In the case of shallow and moderate case depth and large teeth, the root of the tooth, its fillet, and the bottom of the tooth flank typically are not excessively overheated because the massive area below the tooth root provides a sufficient cold sink. This helps to protect the previously hardened side of the tooth from undesirable tempering back.

An addendum region of the tooth and its tip can be considered areas of concern, having the potential for tempering back because there is a relatively small mass of metal there. Besides, the heat has only a short distance to travel from one to the other side of the tooth.

Specially designed spray cooling blocks are applied to eliminate or dramatically reduce undesirable tempering back. Depending on the tooth shape, some tempering back might be unavoidable. In the properly designed system, this tempering back is typically insignificant, well controlled, and acceptable. In some cases, a submerged induction gear-hardening technique is used (*1*).

12.15.4.2.1.2 Spin hardening of gears

Spin hardening is particularly appropriate for small and medium-size gears (*1,90,92–94*). Gears are rotated during heating to ensure an even distribution of energy. Single-turn or multiturn solenoid inductor encircles the entire gear. Hardness pattern uniformity and repeatability depend strongly on the relative positions of gear and induction coil, and the ability to maintain the gear concentricity in respect to the coil.

With spin hardening, five parameters affect obtaining hardness patterns: frequency, power, cycle time, coil geometry, and specifics of quenching. **Figure 58** illustrates a diversity of induction-hardening patterns that were obtained with variations in heat time, frequency, and power (*92*).

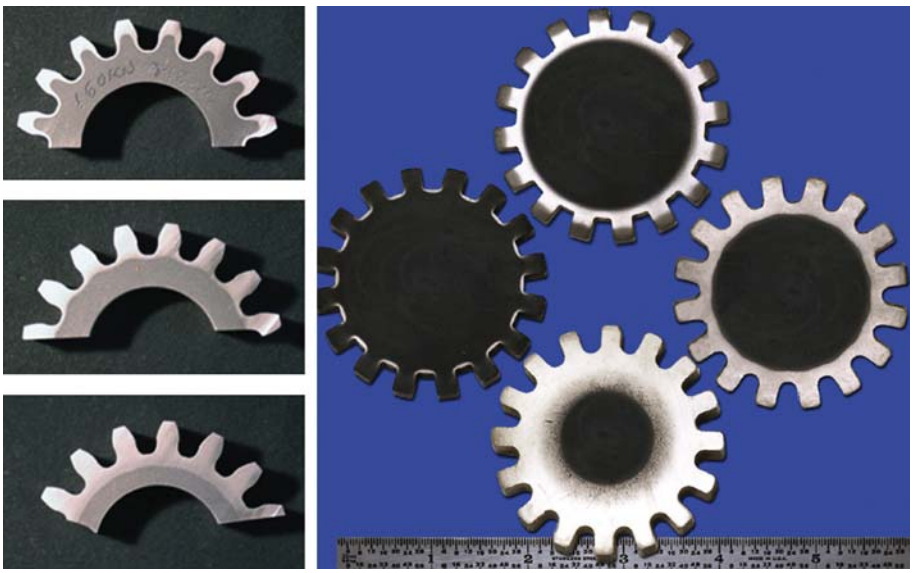

Figure 58 Diversity of hardness patterns obtained with induction spin hardening. Courtesy of Inductoheat Inc.

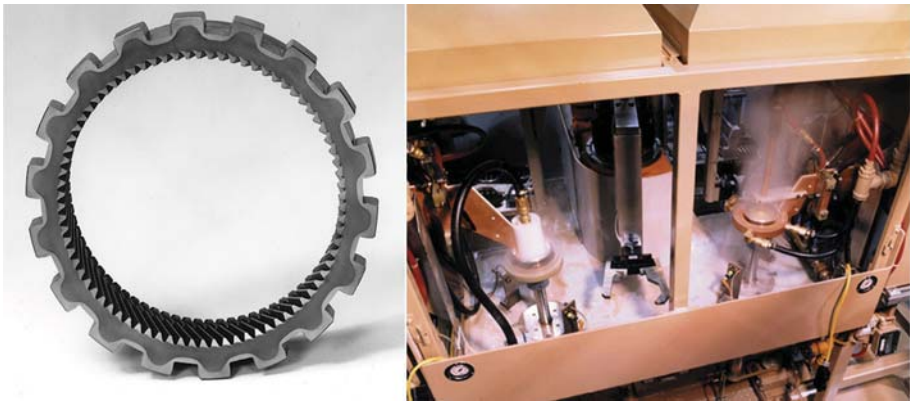

Figure 59 Induction hardening of automotive transmission component with smaller, helical teeth on the ID and large teeth on the OD. Courtesy of Inductoheat Inc.

As a rule, when it is necessary to harden only the tooth tips, a higher frequency and high-power density should be applied. To harden the tooth roots, use a lower frequency. A high-power density generally results in a shallow pattern, while a low-power density produces a deeper pattern with wide transition zones.

Figure 59 shows a two-post induction gear-hardening machine (*1*). The gear being heat treated in this application is an automotive transmission component for a parking brake with fine helical teeth on the ID and large teeth on the OD. The hardening of the ID gear teeth requires a higher frequency than the OD. Therefore, a frequency of 10 kHz was chosen for OD hardening, and 200 kHz was chosen for ID hardening. After heat is off, quenchant is applied to the hot gear in place. This practically instantaneous quench provides a consistent metallurgical response. Quenching reduces the gear temperature to the quenchant temperature or the temperature suitable for forming sufficient amount of martensite and for ensuring safe gear handling. Gears are conveyed to the machine, where a cam-operated robot then transfers them to the hardening station.

In some cases, a dual frequency is used to induction harden gears. The dual-frequency concept has been developed in an attempt to obtain a contour hardness pattern and to minimize gear distortion after hardening. According to the earlier dual-frequency concept (*1,90*), two different power supplies were required. The idea of using two different frequencies to produce the desired contour-like hardness pattern has been around since the late 1950s. Since then, several companies have pursued this idea, and different names and abbreviations have been used to describe it. Regardless of the differences in process recipes, the basic idea remains the same (*92*).

The gear is induction preheated to a temperature determined by the process features, typically being 350 to 100 °C below the critical temperature A_{c1}. Usually, preheating is accomplished by using medium frequency (3–10 kHz) depending upon gear size and tooth profile. Lower frequency results in greater eddy current penetration depths, which lead to a more in-depth preheating effect of root area and partially to heat the flank regions. Preheat times are typically from several seconds to a minute, depending on the size and shape of the gear teeth and its prior microstructure. Obviously, preheating reduces the amount of energy required for the final heat.

After preheating, there might be a soak time typically ranging from 2 to 5 s to achieve a more uniform temperature distribution across the teeth of the gear. Depending on the application, preheat can consist of several stages (the so-called preheat power pulses).

Final heat times can range from less than 1 s to several seconds. A high-frequency (30–450 kHz) and high-power density are applied during the final heating stage. At this stage, more intensive heating of flanks and tips regions takes place. Selected frequency allows the eddy current to penetrate to the desired depth, providing after both stages (preheat and final heat) a reasonable compromise in obtaining contour-like hardness patterns of the gear teeth.

With the conventional dual coil arrangement, one coil provides preheating, and another coil final heating. Both coils work simultaneously if the scanning mode is applied. In the case of a single-shot mode, a two-step index-type approach is used.

In some cases, dual-frequency machines produce parts having lower distortion and having more favorable distribution of residual stresses compared with using single-frequency techniques. However, depending on tooth geometry, the time delay between low-frequency preheating and high-frequency final heating could have a detrimental negative effect for obtaining truly contour hardened patterns or minimization of tooth distortion.

Further improvement in obtaining true contour hardening (Figure 60) is related to the development of a single coil simultaneous dual-frequency gear hardening, which utilizes an inverter that generates simultaneously dual frequency output signal. Low frequency helps to austenitize the roots of the teeth, and high frequency helps to austenitize the teeth flanks and tips simultaneously (*90*).

Sometimes, it is not advantageous to have two different frequencies working simultaneously all the time. Depending on the gear geometry, it is often preferable to apply lower frequency at the beginning of the heating cycle; after achieving a desirable root heating, the higher frequency can complement initially applied lower frequency, completing a job by working simultaneously (*90*).

Figure 60 Contour-hardened gears. Courtesy of Inductoheat Inc.

As an example, Figure 61 shows Inductoheat's machine for an induction hardening of internal wide-face, gear-like component, having a minor gear diameter of 176 mm and a major gear diameter of 186 mm using a single-shot simultaneous dual-frequency heating. The total power exceeds 1200 kW comprising medium-frequency (10 kHz) and high-frequency (120–400 kHz) modules working not just simultaneously, but in any sequence desirable to optimize the properties of heat-treated gears.

12.15.4.3 TSH Technology for Hardening Complex Geometry Parts

Over the years, gear manufacturers and induction heat treaters have gained knowledge resulting in quieter, lighter, and lower cost gears and other critical components that have an increased load-carrying capacity to handle higher speeds and torques.

Michigan-based ERS Engineering Corporation has worked with its European partners to develop a unique steel metallurgy and hardening process that allows replacing carburizing with induction hardening for a wide range of complex-shaped components, including parts previously thought to be impossible to induction harden successfully (*1*,*93*,*97*). Figure 62 shows complex gear-like geometry components that used to be difficult to harden by conventional induction hardening. In the past all of these components used to be carburized, but not any more. TSH Technology allows one to induction contour harden those components.

TSH Technology is a combination of controlled low hardenability (LH) low-alloy steels and special induction-hardening techniques. TSH steels were originally developed by professor K. Z. Schepeljakovskii and successfully used for more than a decade. However, recent breakthroughs in the further excelling of TSH steels substantially widen the range of their applications (*93*,*97*).

TSH steels have reduced the tendency to grain growth during heating into the hardening temperature range, providing fine-grain martensite with extremely high compressive stresses at the tooth surface. They can be substituted for more expensive standard steels typically used for conventional induction hardening or carburizing grades. TSH steels have significantly less alloying elements such as manganese, molybdenum, chromium, and nickel than the majority of conventional low-alloy steels.

Different applications may call for slightly different steel chemical compositions and process recipes. As an example, Table 7 shows two of the most typical compositions of TSH steels (60LH and 80LH) versus some carburized steel grades (8620H and 4320H).

With TSH Technology, components are typically through heated and then are rapidly quenched. The hardened depth is mainly controlled by the steel's chemical composition. Therefore, even though components made from TSH steels are often heated through, their limited hardenability allows obtaining well-defined and crisp hardness case depth at the surface (Figures 63 and 64).

In the past, it was practically impossible to induction harden the parts shown on Figures 62–64, due to a combination of shape complexity and sizes. Now it is possible to get those uninterrupted contour-like hardness patterns by using a simple operation: through heating using low intense–low frequency inverters and water quenching. Notice that the spiral bevel pinion (Figure 63) was induction hardened on OD, ID, and teeth region using a single operation producing an uninterrupted case hardness pattern. There are several important factors associated with TSH Technology (*93*):

- TSH steels incorporate significantly smaller amounts (3–8 times less) of alloying elements such as manganese, molybdenum, chromium, and nickel, compared to traditionally used low-alloy steels.

Figure 61 Inductoheat's single-coil dual-frequency system comprises medium-frequency (10 kHz) and high-frequency (120–400 kHz) modules working simultaneously or in any sequence desirable. Total power exceeds 1200 kW. Courtesy of Inductoheat Inc.

- TSH steels require using low- and medium-induction hardening frequency (1–25 kHz). This reduces equipment capital cost (including the reduction of power supply cost). It also dramatically reduces the probability of overheating a part's edges, tips, and sharp corners that could occur due to electromagnetic end and edge effects when the RF heating frequencies used are typical for conventional induction-hardening processes.
- Formation of high compressive residual stresses (up to 600 MPa/85ksi) at the surface.
- The hardened depth is primarily controlled by the steel's chemical composition and initial microstructure. The heat-treating process is repeatable and robust.
- Formation of fine-grain and in some cases ultra-fine-grain martensitic structures within the case depth (**Figure 65**) allows improving both toughness and strength of induction-hardened components. Core structure is a mixture of bainite and pearlite, resulting in a good combination of core ductility and strength.

TSH Technology is far less sensitive than conventional induction hardening to the imperfections of parts' positioning during heating (e.g., a part's wobbling due to a bearing wear, when component rotates during the heat cycle).

Figure 66(a) shows 330-mm-diameter helical bull gear (module 6.8 mm, number of teeth = 47; weight = 13.8 kg) that has been induction hardened according to TSH Technology. **Table 8** shows the chemical composition of this gear. In order to obtain such a contour-like hardness pattern (**Figure 66(b)**) using encircling inductor and the conventional induction-hardening technique and taking into consideration the size of that helical gear, it would require applying medium frequency and large amounts of heating power for a very short time to form contoured austenitic layer at the gear surface (97).

In contrast to the conventional induction-hardening process, the required kW of power supply can be dramatically reduced with TSH Technology, because it does not demand the formation of a contour-like austenized layer prior to quenching and does not require a short heat time. This permits using lower power inverters, meaning lower capital cost.

The TSH Technology is an extremely promising technology that was developed to replace thermochemical heat-treating processes, such as carburizing, carbonitriding, nitriding, or furnace direct hardening, which is currently widely used. Its benefits are particularly noticeable when induction case hardening medium and large-size complex-shaped components.

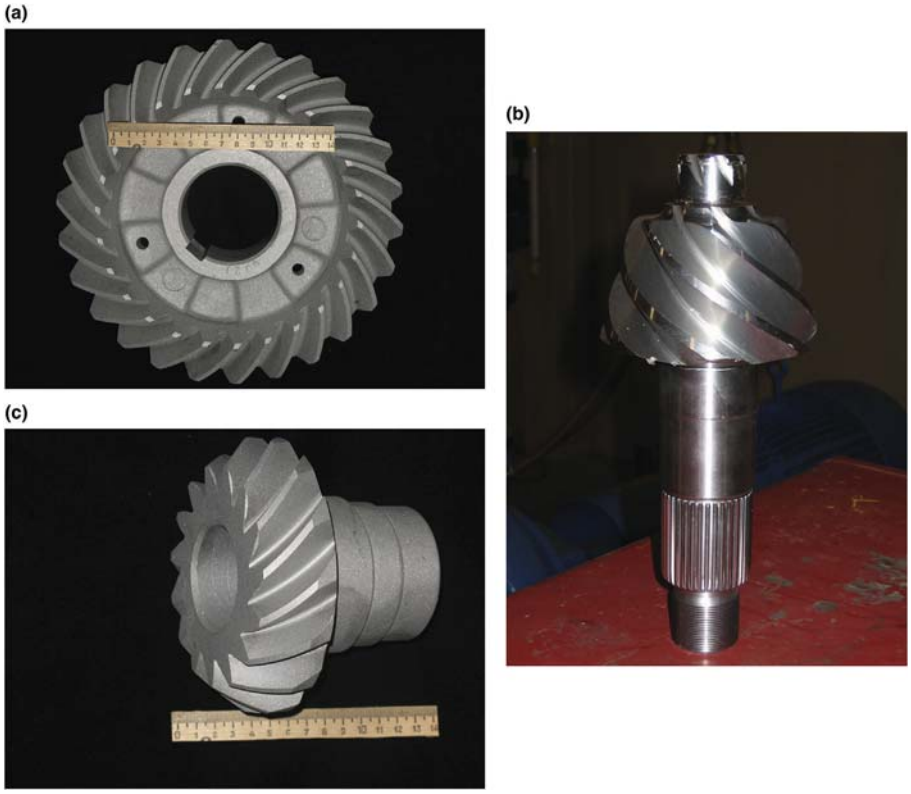

Figure 62 Complex gear-like components that used to be difficult to harden by conventional induction hardening. Now those components can be induction surface hardened by TSH Technology. Reproduced from Brayman, S.; Kuznetsov, A.; Nikitin, S.; Binoniemi, B.; Rudnev, V. Contour Hardening Bevel, Hypoid, and Pinion Gears; *Gear Solutions* Sept., 2011, 30–35; *Breakthrough Contour Hardening;* Bulletin of ERS Engineering Corporation, September, 2011.

Applicability of the TSH Technology is not limited to gears. Bushings, transmission shafts, king pins, ball joints, driveshaft and differential crosses, bearings, coils, and leaf springs are also good candidates for TSH Technology. Figure 67 shows carrier pin with simultaneous OD and ID hardening using a single frequency of 3 kHz. Pin OD is 32 mm. Note that there are two holes: transverse (6 mm diameter) and longitudinal (12 mm diameter). All required areas of the pin, including outside surface and both inside surfaces, have an impressive uninterrupted hardness pattern.

12.15.4.4 Induction Hardening of Hand Tools and Bits for the Mining Industry

Specific geometry parts are used for hand tools and in the mining industry requiring heat-treating selected areas. Due to its ability to selectively heat certain areas, induction heating is often a preferable choice for hardening and tempering hammers, wrenches, chisels, drill bits, and the like. Components consisting of a combination of thick and thin sections present a certain challenge for heat treaters due to nonuniform heating characteristics. For example, during heating, the thick sections may not come up to the required temperature as quickly as thin sections.

Table 7 A comparison of typical chemical composition (%) of two low-hardenability TSH steels versus carburized grades

	60LH	*80LH*	*8620H*	*4320H*
C	0.55–0.63	0.77–0.83	0.17–0.23	0.17–0.23
Si	0.10–0.30	0.10–0.25	0.15–0.35	0.15–0.35
Mn	0.10–0.20	0.10–0.20	0.60–0.95	0.40–0.70
Cr	<0.15	<0.25	0.35–0.65	0.35–0.65
Ni	<0.25	<0.25	0.35–0.75	1.55–2.0
Cu	<0.30	<0.30	–	–
S	<0.04	<0.04	<0.04	<0.04
P	<0.04	<0.04	<0.035	<0.035

Reproduced from Brayman, S.; Kuznetsov, A.; Nikitin, S.; Binoniemi, B.; Rudnev, V. Contour Hardening Bevel, Hypoid, and Pinion Gears; Gear Solutions, Sept., 2011, 30–35.

Figure 63 Spiral bevel pinion was induction hardened using TSH Technology. Courtesy of ERS Engineering Corp.

Figure 64 Automotive journal cross was induction hardened using TSH Technology. Courtesy of ERS Engineering Corp.

In addition, thick sections might have a substantially more intense thermal sink effect, which manifests itself in less intense heating and noticeably faster heat reduction during a part's transportation from the heating stage to a quenching position. This condition is addressed by using induction coil profiling and special process settings to help overcome the problem.

Thickness variations in parts having a complex geometry can create some difficulties in obtaining the required heat-treating patterns during quenching as well. For example, the cooling rate of quenched sprayed thinner sections is markedly different from that for massive sections, which can require the use of special adjustments in inductor design and/or quench block.

It is important to remember that too thin cross-sections might also present difficulties in obtaining sufficient heating due to a potential eddy current cancellation and inability to reach required temperatures for obtaining homogeneous austenite.

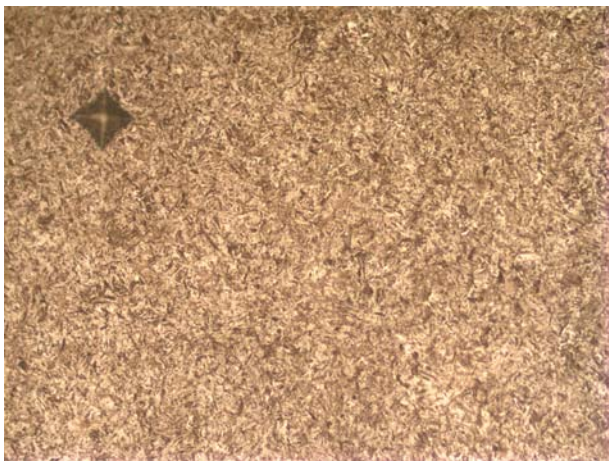

Figure 65 Fine-grain martensitic structure of induction surface hardened automotive journal cross. 400X. Nital etch.

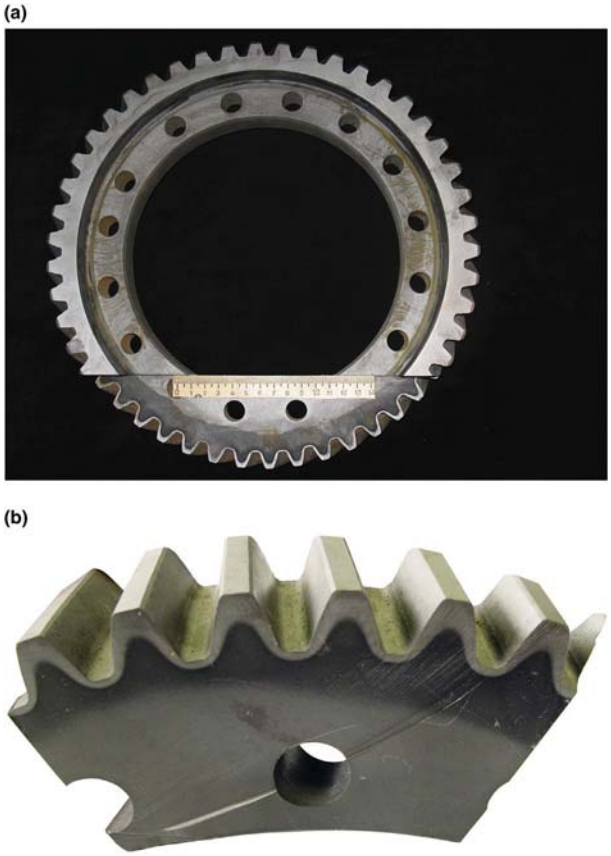

Figure 66 Helical gear induction hardened according TSH Technology. Courtesy of ERS Engineering Corp.

Sharp corners and poor chamfering or rounding of holes and edges can lead to the occurrence of local overheating, resulting in excessive thermal stresses and excessive grain growth and grain boundary liquation, which could cause the formation of cracks.

In some cases, product engineers prefer to have a lower hardness in certain areas (e.g., the undercut area). That is, they sometimes prefer having a martensitic–bainitic structure instead of a fully martensitic microstructure. This provides some ductility and toughness and allows reducing the probability of cracking under impact load and premature failure.

The proper choice of design parameters (applied frequency, power density, coil geometry, use of flux concentrators, steel grade selection, etc.) allows the heat treater to obtain the required heat-treating pattern even in cases when an undesirable combination of electromagnetic end effect and thermal edge effects seems unsuitable for hardening by induction.

Table 8 Shows the chemical composition of inductively hardened helical gear shown in **Figure 66** (Study was conducted by STORK® Climax Research Services, Inc.)

Element	*%*	*Method*
C	0.77	ASTM E1019-08
S	0.014	ASTM E1019-08
P	<0.005	ISO-14707:2000E (Glow discharge)
Si	0.08	ISO-14707:2000E (Glow discharge)
Mn	0.06	ISO-14707:2000E (Glow discharge)
Cr	0.17	ISO-14707:2000E (Glow discharge)
Ni	0.06	ISO-14707:2000E (Glow discharge)
Mo	<0.02	ISO-14707:2000E (Glow discharge)
V	<0.008	ISO-14707:2000E (Glow discharge)
Al	0.0088	ISO-14707:2000E (Glow discharge)
Cu	0.04	ISO-14707:2000E (Glow discharge)
Ti	0.09	ISO-14707:2000E (Glow discharge)
Nb	<0.008	ISO-14707:2000E (Glow discharge)

Figure 67 Induction machine for hardening the working surfaces of wrench jaws. Different hardness patterns are noticeable for parts having appreciable differences in section thickness near the hardened surface area. Courtesy of ERS Engineering Corp.

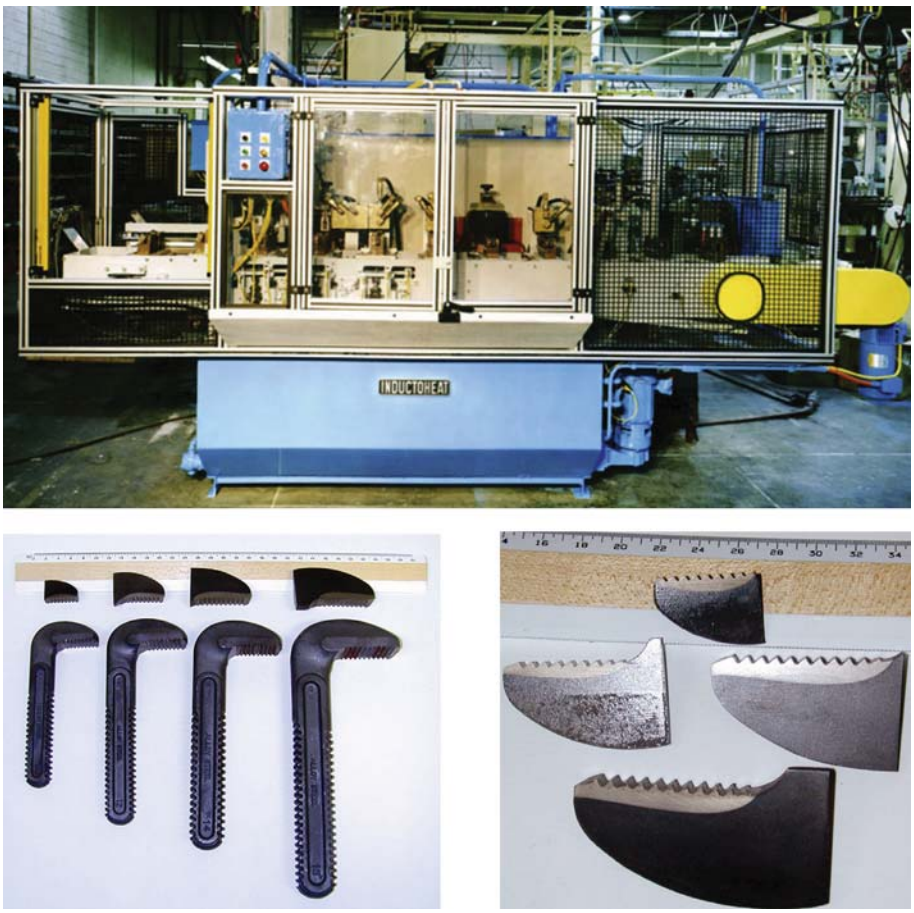

Figure 68 Simultaneous brazing the working tips and induction hardening of mining tool bits. Courtesy of Inductoheat Inc.

As an example, Figure 68 shows an induction machine for hardening and tempering the working surface of wrench jaws as well as etched cross-sections that reveal uniform hardness patterns of parts, despite having appreciable differences in masses of metal near the hardened surface area.

Many times, induction hardening is combined with another operation, thereby increasing the effectiveness of an entire process. For example, Figure 69 shows simultaneous induction hardening of mining tool bits and brazing the working tips. Very careful temperature control is required to reach an optimal temperature profile that provides required thermal conditions for tool bit hardening and obtaining desirable brazing conditions to get sound joint between a carbide tip and the nest of the tool bit. Numerical computer simulation provides important assistance in determining an optimal temperature distribution.

Space limitation does not permit further discussion of induction-hardening applications. For those who would like to study physics and process the specifics of other induction heating and heat-treating applications, we recommend review of the following publications (*1–9,15,47–51,91–100*).

12.15.5 A Review of Modern Power Supplies for Induction Hardening

12.15.5.1 Introduction

Power supplies for induction hardening change the available utility line frequency and voltage to single-phase power at a frequency appropriate for producing the required heat-treat pattern. Most power supplies for induction heat treating convert incoming 50- or 60-cycle power to DC and switch the DC using power semiconductor switches in an inverter configuration to produce single-phase AC power. This AC power is then applied to the induction coil through a load matching network consisting of passive power electronic components.

No single power supply design can efficiently satisfy the requirements of the many widely varying induction heat-treat applications (*101*). Each application has an optimum heating frequency, power level and inductor parameters including voltage, current

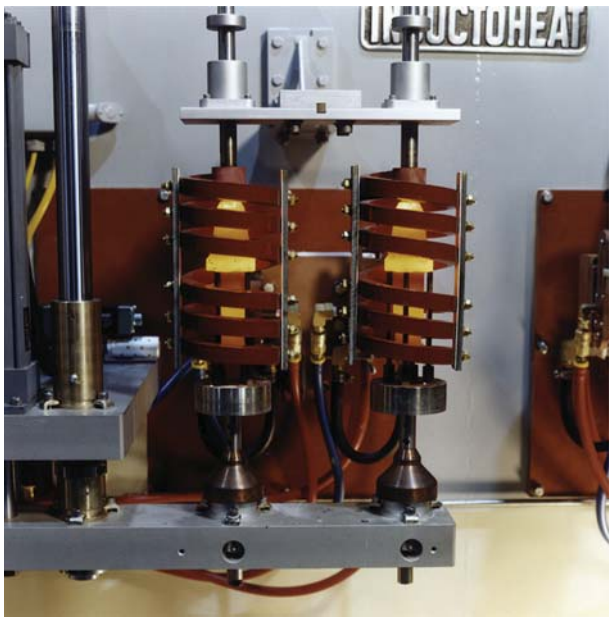

Figure 69 Simultaneous induction hardening of mining tool bits and brazing the working tips. Courtesy of Inductoheat Inc.

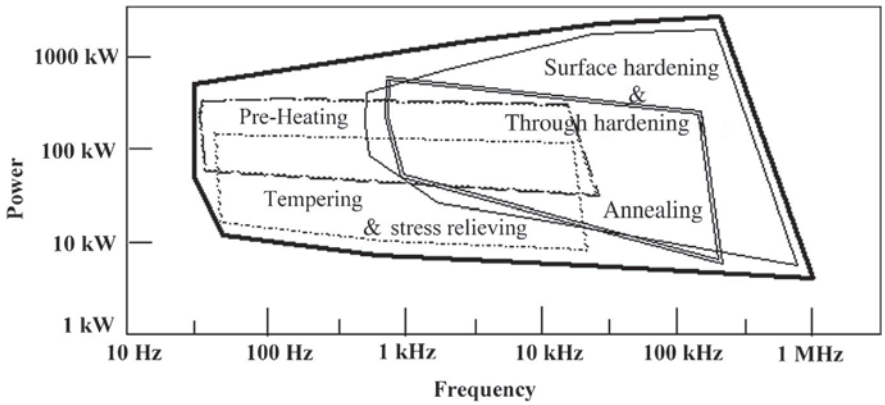

Figure 70 Power–frequency diagram for typical induction heat-treating applications.

and power factor. For this reason, many different circuits and components have been used in the various induction heating power supplies in use today (*103*). Figure 70 shows graphically the power and frequency range commonly used in a variety of induction heat-treating applications (*1*).

12.15.5.2 History of Power Supplies for Induction Heat Treating

In the early days of induction hardening, line frequency was used for very low frequency applications while spark gap generators and vacuum tube oscillators were used for shallow case-hardening applications requiring high frequency. Applications requiring frequencies from 500 Hz to 10 kHz commonly employed motor-generator sets capable of up to 300 kW of output power per set.

The invention of the power semiconductor switch in the late 1960s revolutionized the way power for induction hardening could be produced. The thyristor or silicon controlled rectifier (SCR) was the first power semiconductor to be widely used in the inverter circuit of solid-state power supplies for audio frequency (500 Hz–10 kHz) heating. Many of these units are in use today. Also in the late 1960s and early 1970s many integrated circuits were introduced that made possible precise control and monitoring of the induction heating process.

Most modern induction-hardening power supplies being produced today use high-power low-loss transistors in the inverter with sophisticated microprocessor-based control electronics to provide precise control, monitoring, and fault diagnostics.

12.15.5.3 Unique Terminology

There are many unique terms and abbreviations that are commonly used by induction heat-treat specialists. Terminology that may be found in this section on power supplies and load matching is defined below (*104*).

Buttons –Taps –Studs: The individual terminal connections on the load-matching capacitors above the porcelain insulators. Connection of a button involves installing a conducting copper strap or washer between an existing copper bus and the capacitor termination, thus making an electrical connection between a section of the capacitor and the bus.

Cans: Load matching resonant circuit capacitors.

Choke: An inductor that is placed in a circuit to restrict conduction of high-frequency current.

Converter: A switching circuit for changing alternating current into direct current.

Efficiency: The ratio of actual power output of the power supply or induction heating coil to the power input.

Harmonic Distortion: Higher frequency components caused by the switching action of a semiconductor converter or an inverter.

Inverter: A switching circuit for changing direct current into alternating current.

KVAR: A rating term for capacitors that specifies the amount of reactive volt-amperes that the capacitor can supply to the circuit when operated at a specific voltage and frequency.

Over the Hump: A condition whereby a swept frequency power supply is operating beyond the resonant frequency of the output, or load circuit.

Power Factor (cos φ): The cosine of the phase angle between the voltage and the current in a circuit. A low or poor input power factor of a power supply means that a higher input current is required to produce a given output power. A low or poor output power factor from a power supply means that a higher kVA or product of output voltage times output current is required to produce a given output power.

Resonance: For a series circuit, resonance occurs at the frequency at which the vector sum of the capacitive and inductive reactance is equal to zero, the power factor (cos φ) is equal to 1, and the impedance is at its minimum value. For a parallel circuit, resonance also occurs at the frequency at which the capacitive and inductive reactances are equal and the impedance of the parallel circuit is at its maximum.

RFI: Radio frequency interference radiated from an induction heating power supply or its load. This radiation is usually caused by transients resulting from switching of the power semiconductors.

Tank Circuit: The components in the resonant portion of the induction heating circuit, usually consisting of capacitors, transformers, and the induction coil. These components may be connected in series or parallel, depending on the type of power supply used.

Trombone Bus: A bus that is designed to slide in and out of the receiving bus to change the circuit inductance and allow adjustment of the load frequency, voltage, and power.

Tuning or Matching the Load: The process of adjusting the circuit capacitance, inductance, and impedance in order to heat the workpiece most effectively with the components available.

12.15.5.4 Power Electronic Components

Power electronic components, including capacitors, inductors, resistors, transformers, and various power semiconductors, are common to all modern induction-hardening power supplies and their load matching networks. For those with little or no knowledge of electronics, a basic description of the components is presented using mechanical analogies.

Inductors or coils, as they are commonly referred to, have inductance and oppose any change in electric current. Inductance is like inertia in a mechanical system, and the inductor is like a flywheel that opposes a change in rotational speed.

Capacitors have the capacity to store electric charge just as a spring is able to store energy in the form of tension.

Resistors have resistance that resists the flow of current and generates heat just as brakes have friction, resist motion, and generate heat.

Transformers are used to match the impedance of two portions of a circuit. This means that a transformer can reduce voltage and increase current or alternately increase voltage and decrease current while maintaining the same volt amp product on output as on the input. This is similar to a gear box in a mechanical system that is used to match the speed and torque of two portions of the system.

When an inductor, capacitor, and resistor are connected together, a resonant circuit is formed. It is resonant at the frequency where the inductive reactance (X_L) and capacitive reactance (X_C) are equal and the Q or quality factor of the circuit is equal to X_L/R. Therefore, the smaller the resistance the higher the Q.

Diode or Rectifier: The diode passes electric current in one direction and blocks flow in the opposite direction. The schematic symbol and waveshapes associated with a rectifier are shown in **Figure 71**.

Silicon-Controlled Rectifier (SCR) or Thyristor: The SCR or thyristor is like a diode in that it will conduct current in the forward direction and block conduction in the reverse direction. However, the SCR will conduct in the forward direction only after receiving a trigger pulse at its gate. Current flow in the forward direction will stop only after the voltage across the SCR has reversed, and forward-blocking capability is restored after reverse voltage is maintained for a certain amount of time referred to as turn-off-time or TOT. The schematic symbol and waveshapes associated with a thyristor are shown in **Figure 72**.

Transistors: The transistor is also designed to conduct current in only one direction. A relatively small level of voltage applied to its control terminal (base or gate) is able to control large amounts of current flow through the transistor. The control signal

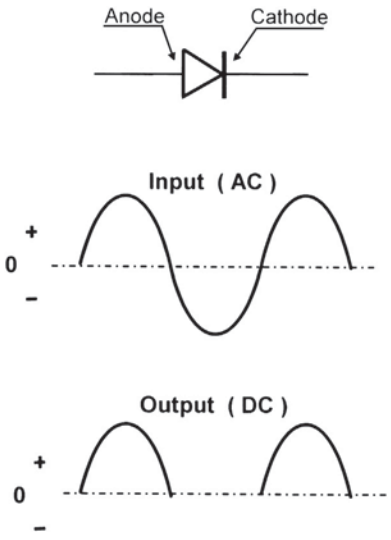

Figure 71 Symbol and waveshapes of diode.

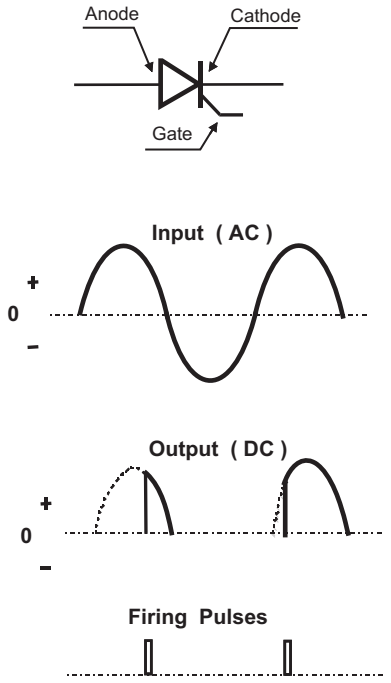

Figure 72 Symbol and waveshapes of thyristor.

can turn on current flow and also turn it off. Two basic types of transistors are commonly used for high-power switching in modern induction heating power supplies. The schematic symbol and waveshapes associated with a transistor are shown in Figure 73.

The MOSFET (metal oxide silicon field effect transistor) is a fast-switching transistor with relatively blocking high voltage that requires very little power to control. Power MOSFETs are made by connecting thousands of transistor cells in parallel on a single silicon substrate. Still higher power switching capability is accomplished by mounting several of these multitransistor substrates on a single heat sink in a power module.

The IGBT (insulated gate bipolar transistor) generally has higher current and higher voltage than the MOSFET but somewhat slower switching. In the IGBT, two transistor technologies are combined. The very fast switching speed and low-control power of the MOSFET form the control end, and the high voltage and high current of the bipolar transistor make up the power-handling portion, resulting in a transistor that combines the best of both in the IGBT.

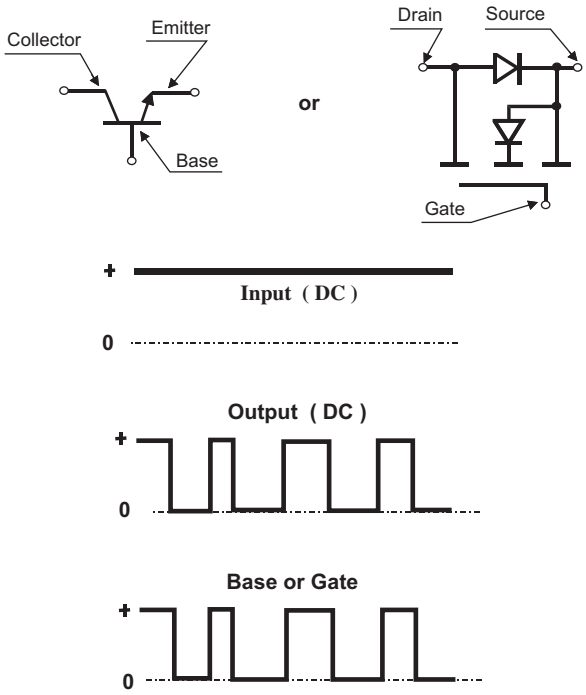

Figure 73 Symbol and waveshapes of transistor.

12.15.5.5 Induction-Hardening Parameters

As discussed in detail in the preceding sections of this text, each induction-hardening application requires the specific process parameters of power, frequency, and heat time to obtain the desired metallurgical pattern. The power versus frequency relationship for common induction heat-treating applications is shown in Figure 70. Many power supply types and models have been developed to match these widely varying application requirements.

Frequency is a most important heating parameter because it directly controls the depth of induced heat source penetration. Frequency is also an important factor in the design of induction heating power supplies. The power components used in these power supplies must be capable of performing reliably and efficiently at the applied frequency. Figure 74 shows the types of power semiconductors that are commonly used for various power/frequency combinations. Large areas of overlap exist where more than one type semiconductor switch may be used.

The physical size and shape of the workpiece, the desired heat-treat pattern, the electromagnetic properties of the workpiece material, along with the geometry of the heating coil, determine the specific coil voltage, current, and power factor or *Q*. These parameters must be known to ensure that the power supply is capable of delivering the required power to the coil. Most induction power supplies are able to match a reasonable range of heating coil parameters.

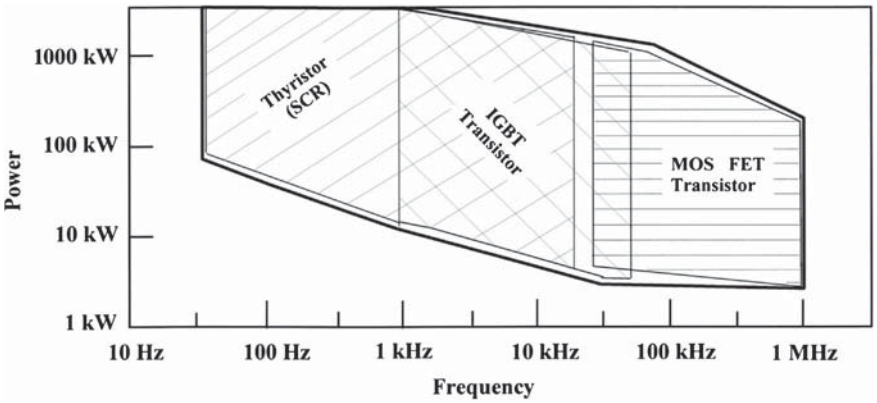

Figure 74 Power–frequency diagram for semiconductor inverters.

12.15.5.6 Common Power Supply Types

The simplified block diagram in Figure 75 applies to nearly all induction heat-treat power supplies. The input is usually a three-phase line frequency (50 or 60 Hz) at a voltage between 220 and 575 V. The first block represents the conversion from AC to DC. This converter may provide a fixed DC voltage or a variable DC voltage or current to the inverter section. The inverter switches the DC input to produce a single-phase output at the desired heating frequency. The load matching section adapts the output of the inverter to the voltage and current levels required by the induction-hardening coil. The control section communicates with the load matching and inverter sections and in some cases the converter section to adjust the output to the coil to match the parameters set by the command inputs.

Many books and technical papers discuss the design and theory of operation of the various types of induction heat-treat power supplies (*1,101–116*), presenting in-depth technical details. Space limitation does not permit detailed discussion of all aspects of modern power supply design in this chapter. Only the most commonly used power circuits and control combinations are discussed here, providing some insights into the advantages and disadvantages of modern induction-hardening power supplies.

The principal design features of various power supply configurations most commonly used for induction hardening are shown in Figure 76. The two major types, described in more detail later, are the voltage fed and the current fed systems. The chart further divides each of these types by the DC source (fixed or variable), the particular mode of inverter control, and the load circuit configuration (series or parallel).

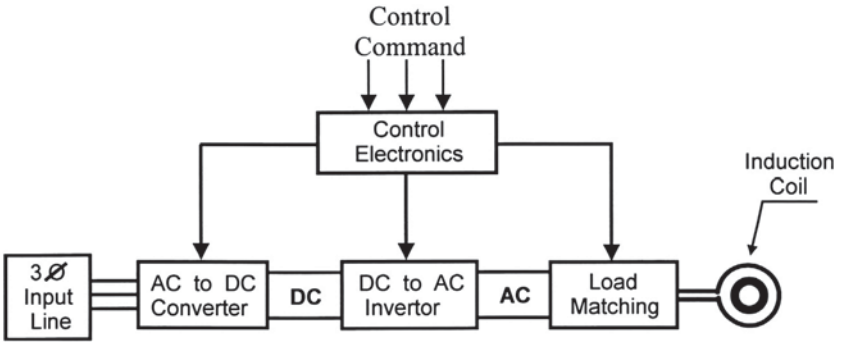

Figure 75 Basic block diagram of induction-hardening power supply. Reproduced from Loveless, D. An Overview of Solid State Power Supplies for Induction Heating, 33. *Metal Producing* **August, 1995**.

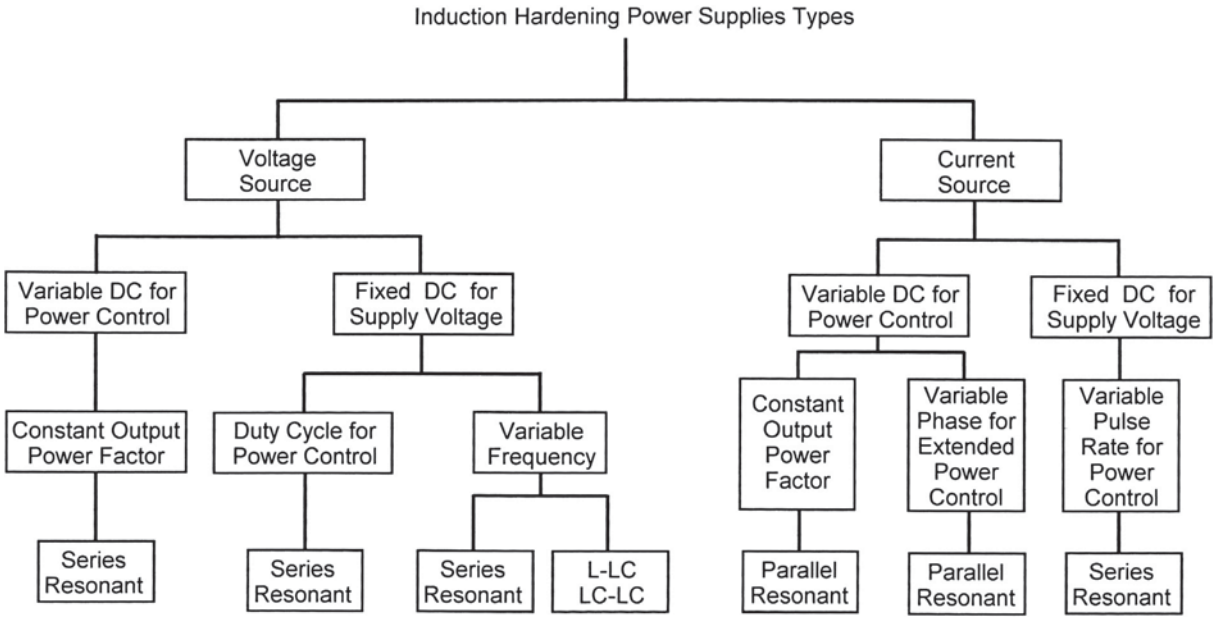

Figure 76 The principal design features of various power supply configurations.

12.15.5.6.1 AC to DC Converter

Four basic AC to DC converters are used. The simplest is the uncontrolled three-phase (six-pulse) rectifier. The average DC output voltage of this rectifier is a fixed 1.35 times the rms voltage of the input line-to-line voltage. The most common input line voltages are 400 V and 480 V, resulting in DC output voltages of 540 VDC and 650 VDC, respectively. The input line power factor of this converter is quite high and typically varies from 0.930 to 0.955. A schematic diagram and waveshapes are shown in **Figure 77**.

The second type of converter is the phase-controlled three-phase (six-pulse) rectifier shown in **Figure 78**. Control of the DC voltage output of the rectifier is accomplished by delayed turn on time of the thyristors relative to the input AC line. This relatively simple converter can be used to regulate the output power of the power supply by controlling the DC supply voltage or current to the inverter. One disadvantage of the phase-controlled rectifier is that operation at reduced output voltage causes the input line power factor to decline to a value less than is usually acceptable to modern power quality specifications (*117*). Another disadvantage of the phase-controlled rectifier for power control is the response time limitation that is due to the relatively low frequency of the input line.

The third converter is a combination of the uncontrolled three-phase (six-pulse) rectifier and a transistor (typically IGBT) switch mode (buck) regulator as shown in **Figure 79**. This converter has the high-input power factor of the uncontrolled rectifier and fast control response that results from the relatively high pulse width modulation (PWM) rate of the switch mode (buck) regulator.

A disadvantage of all three of these converters is the high level of harmonic content of the input line current. This harmonic current can be dramatically reduced through use of a multiphase transformer and parallel rectifiers to obtain a 12-, 18-, or 24-pulse rectifier. A 12-pulse rectifier and its current and voltage waveshapes are shown in **Figure 80**. **Table 9** compares the typical current harmonic content and input line power factor of the 6-, 12-, and 24-pulse rectifiers (*118*).

The fourth converter is actually a group of converter circuits that employ transistors (usually IGBTs) to reduce line current harmonic content, improve the input power factor, and control the output DC voltage. This is accomplished by Pulse Width

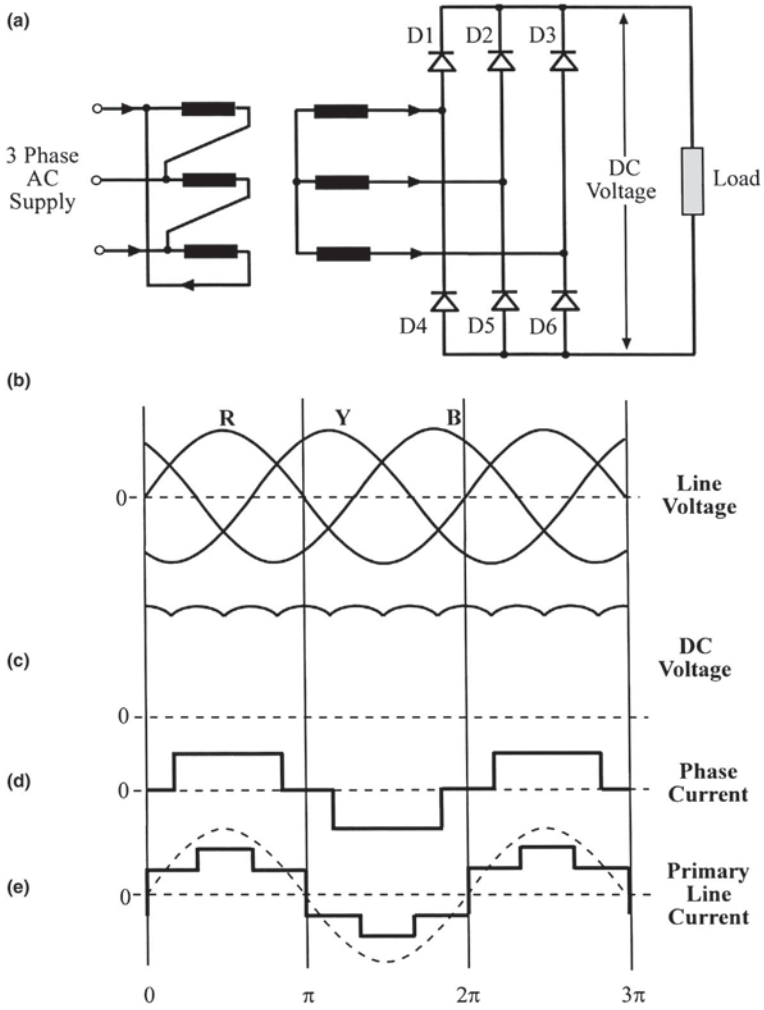

Figure 77 The uncontrolled three-phase (six-pulse) rectifier.

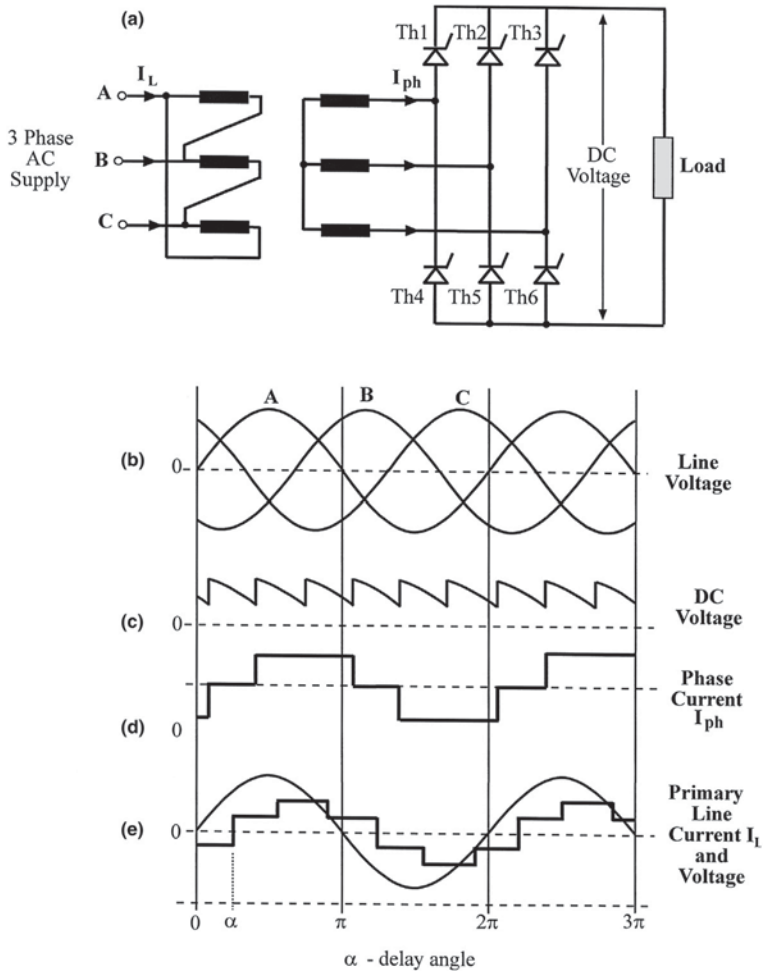

Figure 78 The phase controlled three-phase (six-pulse) rectifier and waveshapes.

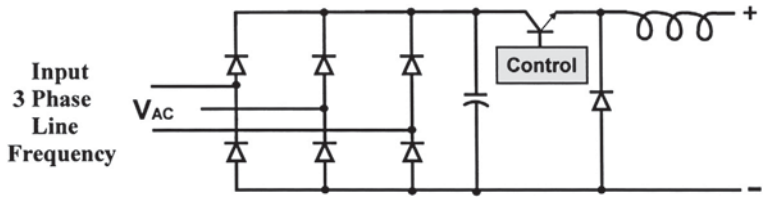

Figure 79 Transistor switch mode regulator for three-phase (six-pulse) uncontrolled rectifier.

Modulating (PWM) the switching transistors to control when and how much current is passed from the input line to the converter output. Inductors and capacitors provide the energy to smooth both the input line current and output voltage of the converter. A schematic of one such active converter circuit and its waveshapes are shown in Figures 81 and 82.

12.15.5.6.2 DC to AC Inverter

The function of the inverter section of an induction-hardening power supply is to change the DC voltage from the converter section to single-phase AC power at the frequency used for heating. The two basic inverter circuits commonly used are the full bridge (also called as H-bridge) and the half bridge. A less common inverter circuit used in induction heating is the quarter-bridge or single-switch inverter.

The full-bridge inverter schematically is usually drawn in the form of an H with a switch in each leg and the load in the center as shown in Figure 83. An AC output across the output circuit is obtained by first left to right (solid arrows). After turning S1 and S2 off, switches S3 and S4 are then closed, causing current to flow right to left (dash arrows). This process is repeated at a rate that provides the desired heating frequency.

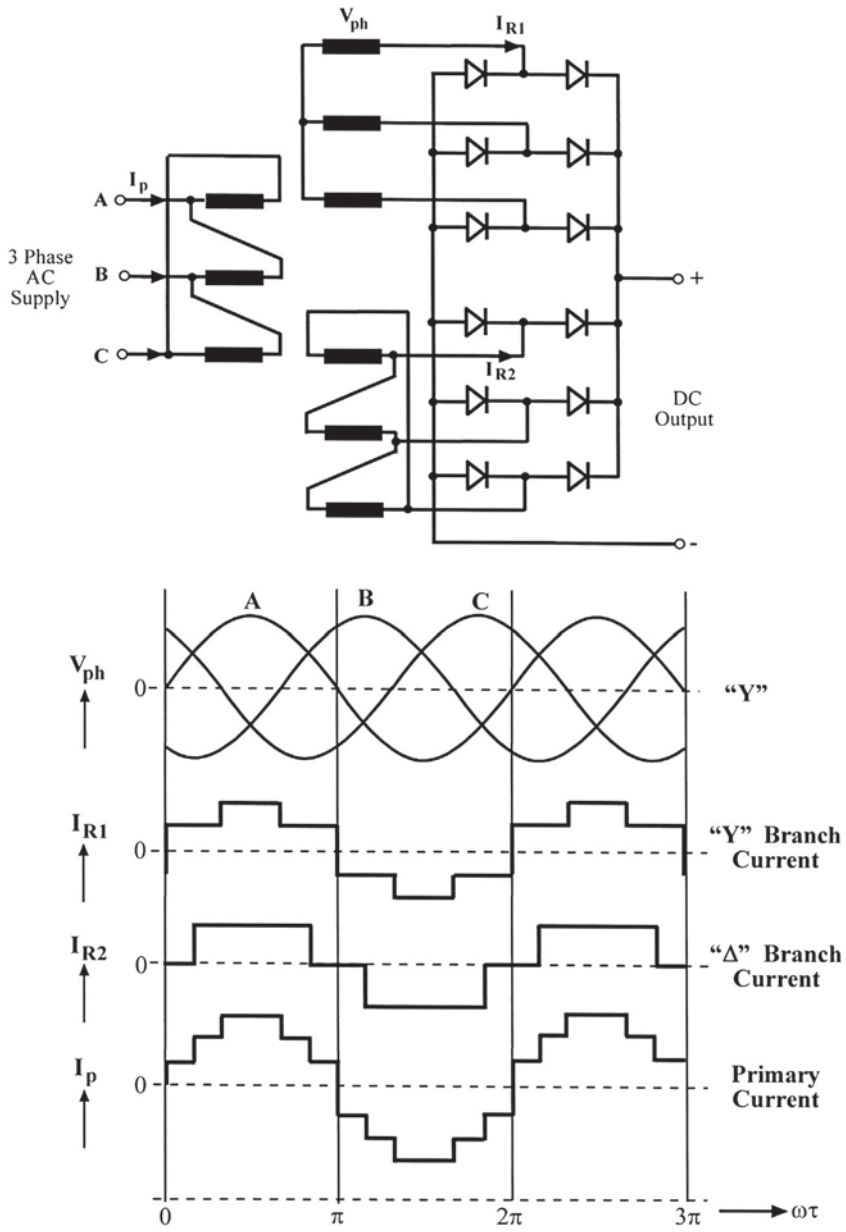

Figure 80 Diagram of a 12-pulse rectifier and its current and voltage waveshapes.

Table 9 Comparison of percentage of current harmonics T.H.D. and power factor (P.F.) for 6-, 12-, and 24-pulse rectifiers as percentage of the fundamental

	Order of harmonics								*T.H.D.*	*P.F.*
Inverter pulses	*5th*	*7th*	*11th*	*13th*	*17th*	*19th*	*23rd*	*25th*		
6	17.5%	11%	4.5%	2.9%	1.5%	1%	0.9%	0.8%	21.5%	0.955
12	2.6%	1.6%	4.5%	2.9%	0.2%	0.1%	0.9%	0.8%	6.0%	0.989
24	2.6%	1.6%	0.7%	0.4%	0.2%	0.1%	0.9%	0.8%	2.0%	0.999

Reproduced from Fishman, O. DC Line Distortion for Static Power Converters Used in Induction Melting. *Inductotherm Bull.* **2001**.

The half-bridge inverter as shown in Figure 84 requires only two switches and two capacitors. The two capacitors connected in series provide a neutral connection to one side of the output circuit. An AC output across the output circuit is obtained by first turning on switches S1, causing current to flow from right to left (solid arrows). After turning S1 off, switch S2 is then closed, causing current to flow left to right (dash arrows). This process is repeated at a rate that provides the desired heating frequency.

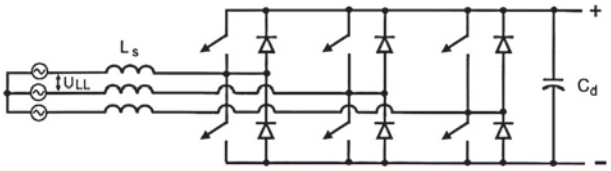

Figure 81 A schematic of an active converter circuit.

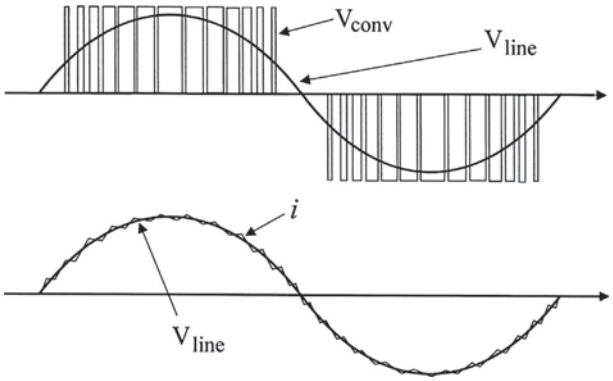

Figure 82 Waveshapes of an active converter circuit of **Figure 81**.

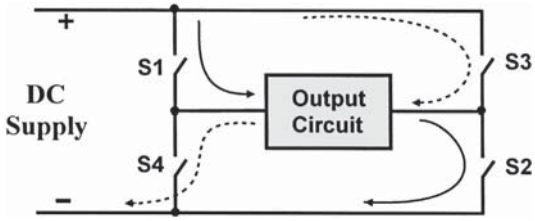

Figure 83 The full-bridge inverter.

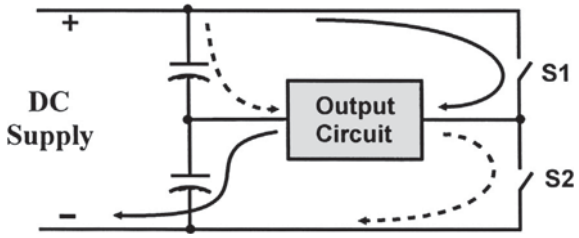

Figure 84 The half-bridge inverter.

The quarter-bridge or single-switch inverter is shown in **Figure 85**. Closure of the switch S1 causes sinusoidal pulses of current to flow in the series resonant load circuit connected across the switch. This inverter configuration is discussed later.

12.15.5.6.3 Load Matching Circuits

The load matching circuit has two functions. First, it provides resonance with the induction heating coil at or near the desired heating frequency. As will be discussed in subsequent paragraphs, this resonant circuit can be either in series or parallel. Operation of the inverter at the resonant frequency of the output circuit is advantageous because at this frequency the voltage and current applied to the circuit are in phase.

Second, the process of load matching (load tuning) matches the output impedance of the inverter to the impedance of the load. The meaning of impedance matching and the process of load matching will be discussed in detail in Section 12.15.6.

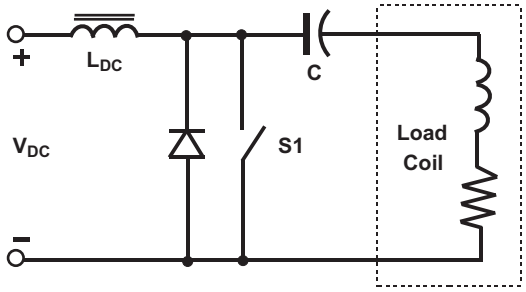

Figure 85 The quarter-bridge or single-switch inverter.

12.15.5.7 Commonly Used Circuit Topologies

As shown in Figure 76, power supply circuits for induction heating are one of two types, voltage source and current source.

Voltage source inverters have a filter capacitor across the DC bus to provide a stable voltage that is switched by the inverter bridge and a series reactive component (capacitor or inductor) coupling the inverter to the load as shown in the simplified schematic diagram (Figure 86). The most popular voltage source inverters fall into one of three categories: the simple series output, the LC–LC (series inductor-capacitor coupled to a parallel resonant capacitor-inductor load), and the L–LC (inductor coupling to a parallel resonant capacitor-inductor load).

Current source inverters have a large inductor (this large inductance inductor should not be confused with the heating inductor) in the DC current path feeding the inverter to provide a stable source of DC current.

12.15.5.7.1 Voltage Source Inverters

12.15.5.7.1.1 Voltage source inverter with simple series output

The voltage source inverter is one of the most popular induction heating power supply types and is used in power supplies having output frequencies that range from 90 Hz to 1 MHz. The inverter is either full bridge (Figure 86) or half bridge, and the semiconductor switches can be thyristors (SCRs), IGBTs, or MOSFETs. Inverters for generating relatively low heating frequencies (from 90 Hz to 6 kHz) may still use thyristors (SCRs) to switch current. The large majority of modern power supplies for induction hardening use the IGBT modules for operation in the frequency range below 100 kHz. Higher frequency supplies employ the much faster MOSFET transistors to switch at frequencies from 50 kHz to 1 MHz.

Four control methods are used to adjust the output power of the voltage source series inverter: (1) sweep frequency below resonance, (2) sweep frequency above resonance, (3) DC voltage control at resonance, and (4) duty cycle control at resonance. Figure 87 illustrates the power versus frequency relationship and the power control range for operation below, above, and at load resonant frequency.

Switching the voltage-fed inverter below resonance is illustrated by showing the bridge output voltage (Figure 88, trace 1) and the output current waveshape (trace 2). This mode of control must be employed when thyristor switches are used because

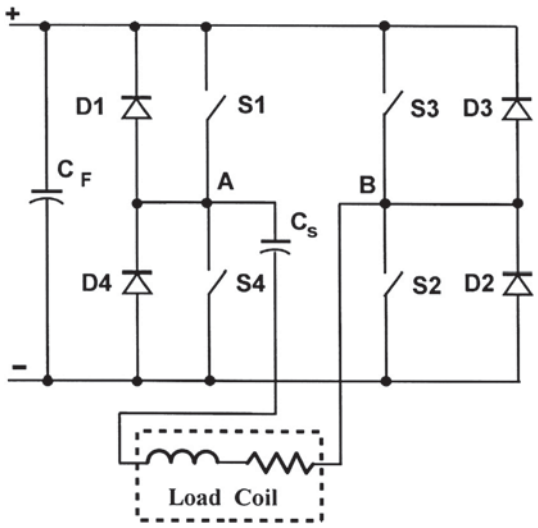

Figure 86 Voltage source inverter with series-connected output.

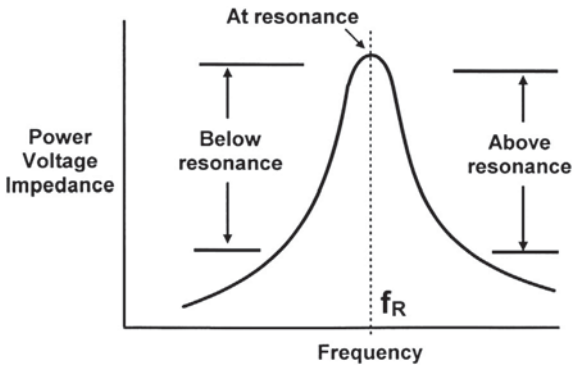

Figure 87 Power versus frequency relationship and the power control range for operation below, above, and at load resonant frequency.

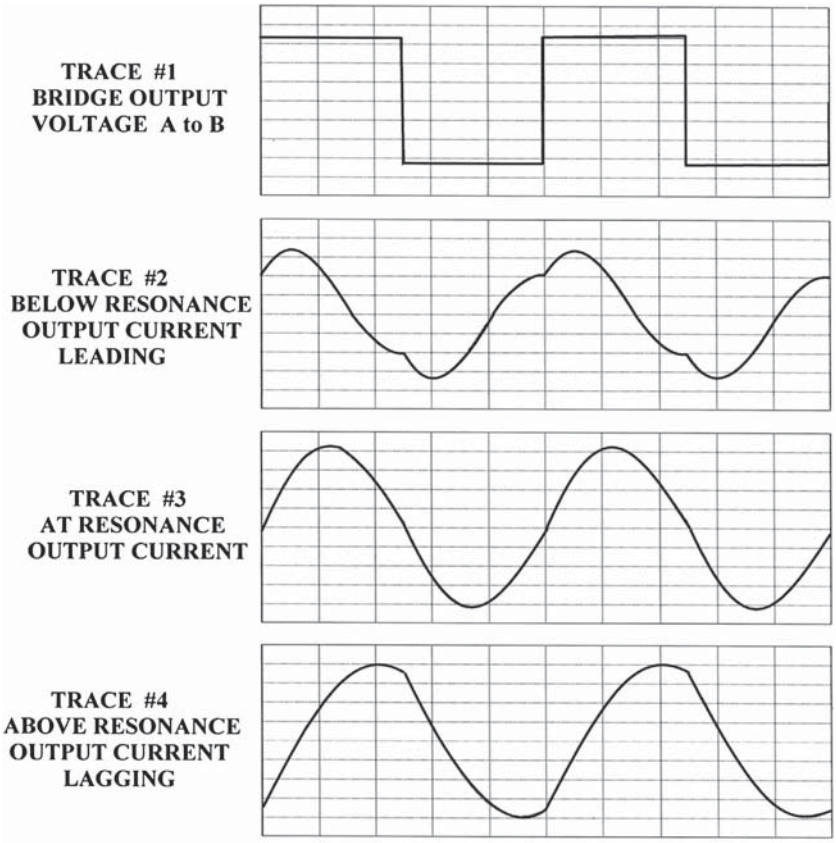

Figure 88 Waveshapes of switching of the voltage-fed inverter. Reproduced from Rudnev, V.; Loveless, D.; Cook, R.; Black, M. *Handbook of Induction Heating;* Marcel Dekker: NY, 2003.

antiparallel diode conduction must follow thyristor conduction for a sufficient time to allow the thyristor to turn off. This minimum TOT requirement limits the practical use of thyristors to frequencies below 10 kHz. The nductoheat Statipower 6 is an example of this type of inverter (*104*). The Inductoheat SP12 using IGBTs is also switched below resonance to control power from a constant-voltage DC source.

The above resonance switching mode of control has become most popular, especially when IGBTs are used. In this case, the conducting switches (S3 and S4) are turned off prior to the current reaching zero. This forces the current to flow in the diodes (D1 and D2) that are across the nonconducting switches (S1 and S2). These switches (S1 and S2) can then be turned on and will conduct as soon as the load current changes direction. The newer IGBTs have an advantage in this case because they have very low turn-off switching losses and the antiparallel diode switching losses are eliminated as well, which allows for more output power per IGBT than when switching below resonance. The Inductoheat SP16 (full bridge) and UP16 (half bridge) employ IGBT modules switched above resonance to control output power.

The third method of control is possible because transistors do not require TOT and therefore can be operated at resonance as illustrated by the output current waveshape (Figure 88, trace 3). In this case, there is little or no diode conduction, and the transistor is switched while the current is at zero, thus minimizing all switching losses and maximizing inverter power rating and efficiency. Operation at resonance means that the output power factor is unity and maximum power is being transferred from the DC source to the load. To regulate power in this case, the DC supply voltage must be controlled. The Inductoheat SP11 is operated at resonance and the power is controlled by a pulse width modulated (PWM) switch mode (buck) regulator.

In the fourth method of control, the inverter is switched at resonance and supplied by a constant voltage DC source. Power is controlled by varying the duty cycle of the inverter output. This is accomplished by providing a separate square wave gate control signal to each half of the inverter H Bridge at the load resonant frequency while shifting the phase of one relative to the other. The greater the phase difference between the square waves, the lower the output power. The bridge output voltage and the resulting output current for operation at reduced output power are shown in Figure 89.

The voltage-fed inverter supplies a square wave voltage at the output of the bridge, and the load determines the current drawn through the bridge. In nearly all heat-treatment applications, an output transformer is required to step up the current available from the inverter to the higher level required by the induction heating coil. The secondary of this transformer is connected directly to the heating coil when the heating frequency is 30 kHz or less and the coil voltage is less than 250 V. In higher frequency applications where the coil voltage is greater, the series resonant capacitor is usually placed in the secondary circuit of the transformer and in series with the heating coil.

12.15.5.7.1.2 Voltage source inverter with series LC connection to a parallel load (LC–LC)

The voltage source inverter can be connected to a parallel resonant load or 'Tank' circuit. One method employs a series connection of inductor and capacitor or LC circuit to couple the inverter current to the parallel resonant load, as shown schematically in Figure 90. In this case, the magnitude of the inverter current and its waveshape is set by the value of the inductor and capacitor and the inverter operating frequency. The LC–LC power supply commonly uses thyristors (SCRs) in the inverter bridge and operates in the frequency range below load resonance.

A very important feature of this style of inverter is that the internal series circuit isolates the bridge from the load. This protects the inverter from load faults caused by shorting or arcing and from 'badly' tuned loads, making it one of the most robust thyristor-based induction power supplies available for heat treatment.

A second feature of this series-parallel LC–LC configuration is realized when the internal series circuit is tuned to the third harmonic of the firing frequency. The power supply is then capable of developing full power into the parallel tank circuit tuned to either the fundamental firing frequency or the third harmonic. The waveshapes present in this style of inverter are shown in Figure 91. Trace 1 shows the voltage waveshape at the output of the bridge. Trace 2 shows the bridge output current to the load; trace 3 is the load current when the load is tuned to the fundamental or firing frequency. The corresponding waveshapes for operation with the load tuned to the third harmonic of the firing frequency are shown in trace 4.

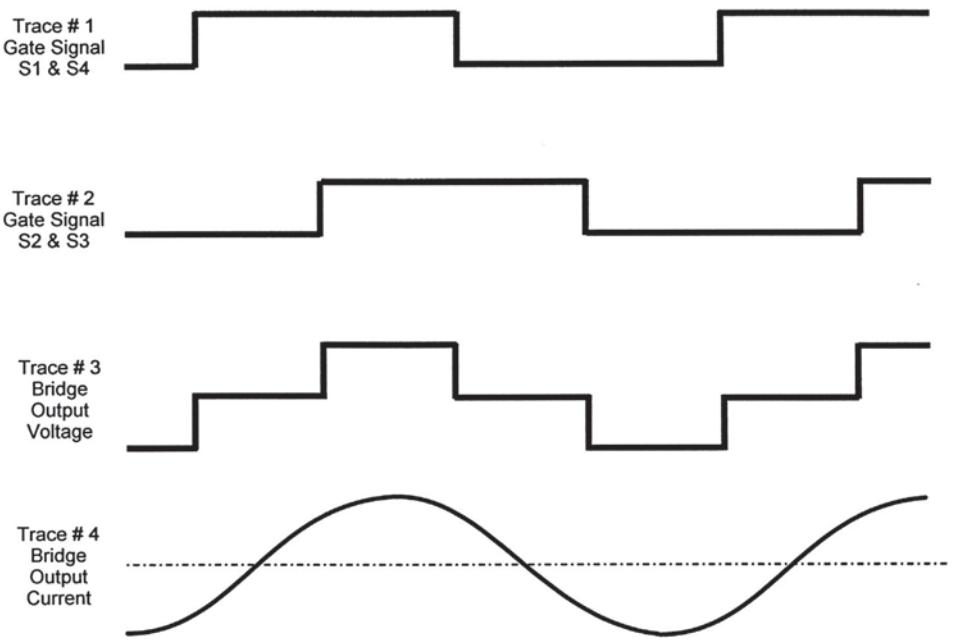

Figure 89 The bridge output voltage and the resulting output current for operation at reduced output power.

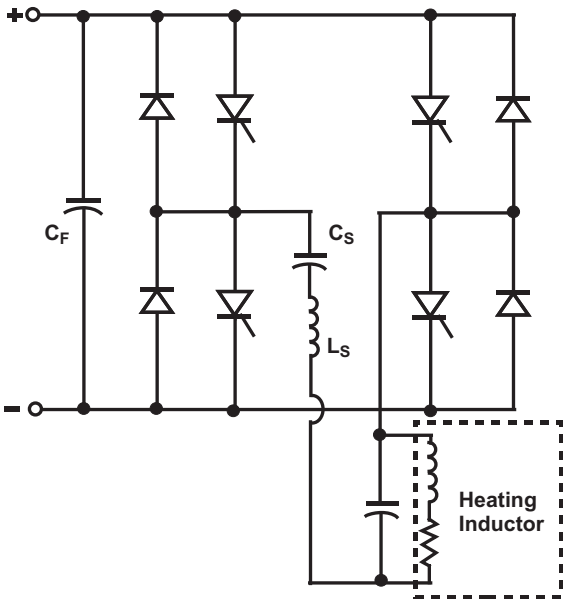

Figure 90 Voltage source inverter with a series connection to a parallel load. Reproduced from Loveless, D. An Overview of Solid State Power Supplies for Induction Heating, 33. *Metal Producing* **August, 1995**.

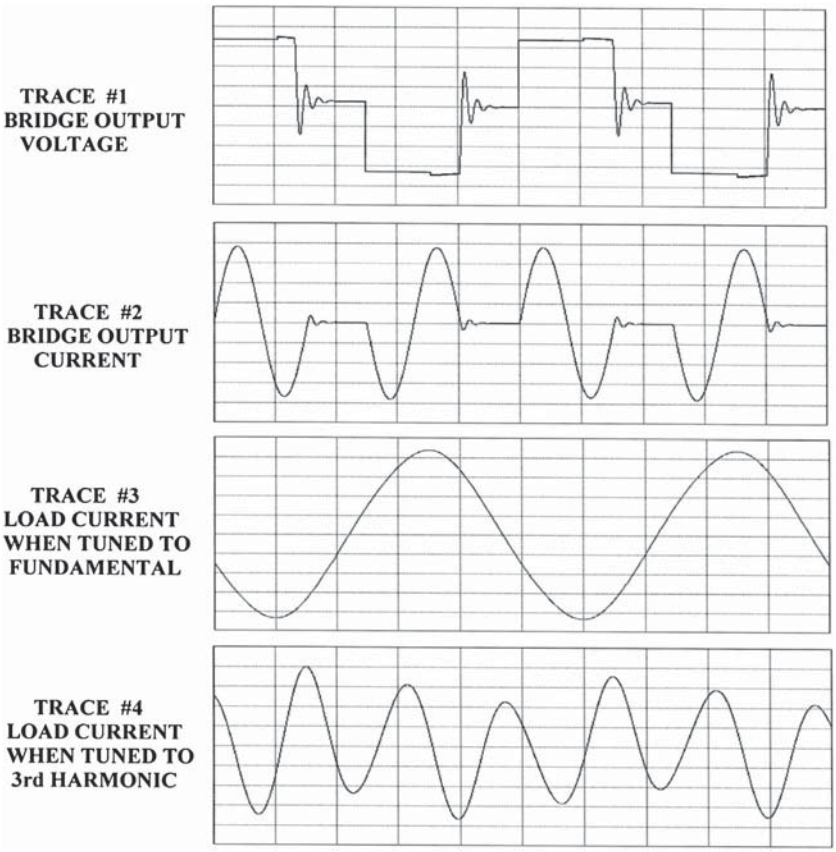

Figure 91 Waveshapes of the voltage source inverter with series connection to a parallel load. Reproduced from Rudnev, V.; Loveless, D.; Cook, R.; Black, M. *Handbook of Induction Heating;* Marcel Dekker: NY, 2003.

For example, the Inductoheat Statipower 5 family of induction heat-treating power supplies are produced in three dual-frequency models: 1 and 3 kHz, 3.2 and 9.6 kHz, and 8.3 and 25 kHz, with a power range of 150–1500 kW. Because load current is not required for commutation, this system can be operated with the output shorted for easy troubleshooting.

12.15.5.7.1.3 Voltage source inverter with series inductor connected to a parallel load (L–LC)

A second method for connecting a voltage source inverter to a parallel resonant load is commonly referred to as L–LC. Transistors either IGBT or MOSFET are the power switching components most commonly used in this type of inverter. Control of output power is accomplished by a sweep frequency operation either below or above the load resonant frequency. In addition to sweep frequency control, a form of pulse with modulation of the conduction time of the bridge switches may be used to limit the peak current output from the inverter. This PWM control allows for operation into a shorted load and also permits testing of the power supply with its output short circuited. An example of an L–LC inverter is the Inductoheat SP18 power supply that applies this circuitry (Figure 92).

12.15.5.7.2 Current Source Inverters

12.15.5.7.2.1 Current source with parallel load

The most common current source inverter for induction hardening is the full bridge connected to a parallel resonant load circuit. Thyristors (SCRs) have been used in this inverter configuration for many years and continue to be used today for applications requiring 10 kHz or less.

When the power switching is done with thyristors, the current-fed inverter must be operated above the resonant frequency of the parallel resonant load to provide TOT to the thyristors. As illustrated by the waveshapes of Figure 93, the voltage across the output of the bridge is a sine wave (trace 1) and the current (trace 2) is a square wave. This is just the reverse of the voltage-fed inverter, where the voltage is a square wave and the current is a sine wave. The DC bus voltage across the bridge after the large inductor L_{dc} (trace 3) resembles a full-wave rectified sine wave. The bus voltage is forced negative from the time the bridge is switched until the load voltage reaches zero. This time must be sufficiently long to provide TOT to thyristors that are no longer conducting. The voltage across the thyristor switches are shown in traces 4 and 5 of Figure 93, with the negative portion of the waveshape noted as TOT.

Power control is accomplished by varying the DC bus voltage at the output of the converter. When a controlled rectifier is used, a poor input power results when the rectifiers are not full on and the DC bus voltage is less than maximum. To improve or maximize the input power factor over a range of load voltages, a second mode of power control can be employed. This control increases the output voltage on the load by changing the phase of thyristor turn on relative to the phase of the load voltage. As the phase difference is increased, TOT is increased and the output voltage rises to increase power to the load. This means that with a properly matched load, the input power factor can be maintained near unity from less than 50% power to 100% power.

Figure 92 Inductoheat's transistorized power supply Statipower SP-18, 600 kW/30 kHz. Courtesy of Inductoheat Inc.

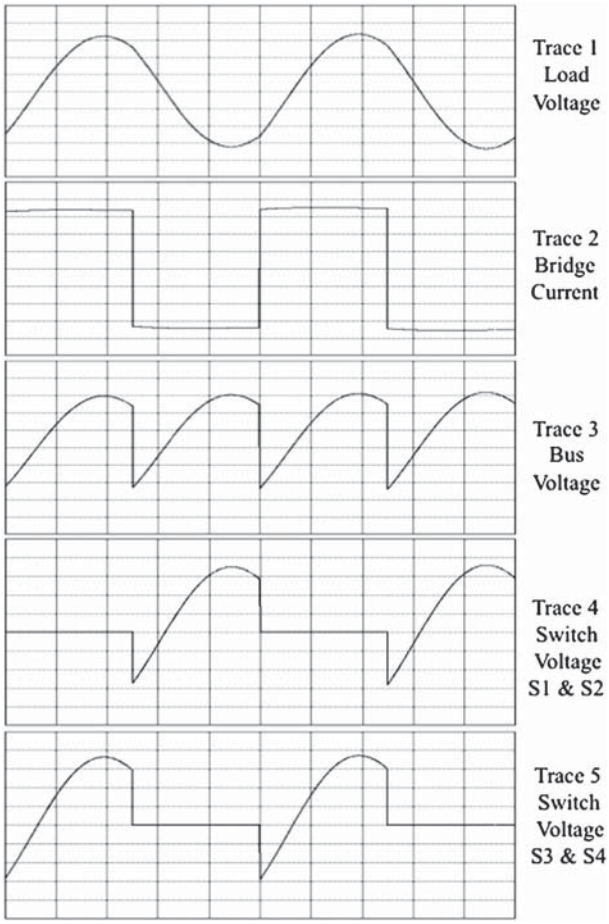

Figure 93 The waveshapes of a current source with parallel load. Reproduced from Rudnev, V.; Loveless, D.; Cook, R.; Black, M. *Handbook of Induction Heating;* Marcel Dekker: NY, 2003.

Transistors are used today in the inverter bridge of the current-fed inverter at frequencies from 90 Hz to 1 MHz because they can be switched very fast and do not require TOT. In this case, the inverter can be operated at the resonant frequency of the parallel resonant tank circuit as shown in Figure 94. One diagonal of the bridge containing transistors T1 and T2 is turned on as transistors T3 and T4 of the other diagonal are turned off. This switching or commutation is done at a time when the voltage across the load, inverter bus, and transistors is at or very near zero. The inverter waveshapes obtained in this mode of operation are shown in Figure 95. Switching at zero voltage minimizes the switching losses in the transistors and therefore allows for much higher frequency operation. When the inverter frequency is locked to the natural resonant frequency of the load, the output power must be regulated by controlling the input current to the inverter. This is accomplished by using one of the variable-voltage AC to DC converters described earlier.

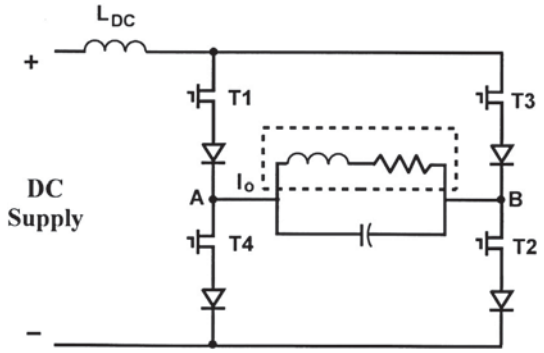

Figure 94 Current source full-bridge transistor inverter. Reproduced from Loveless, D. An Overview of Solid State Power Supplies for Induction Heating, 33. *Metal Producing* **August, 1995**.

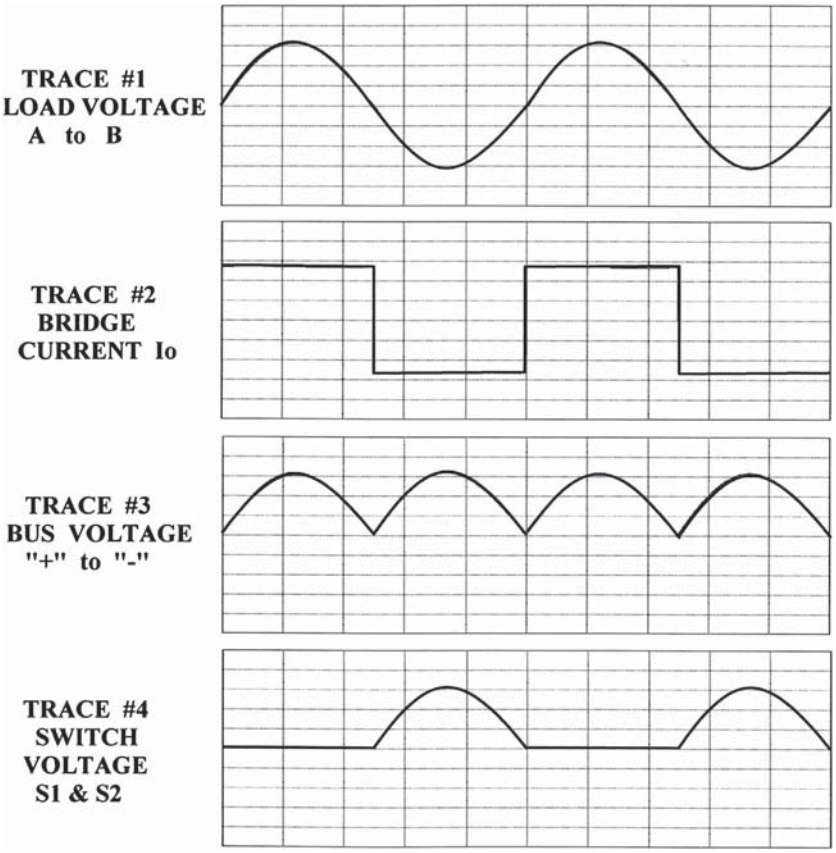

Figure 95 Current source inverter waveshapes at resonance. Reproduced from Rudnev, V.; Loveless, D.; Cook, R.; Black, M. *Handbook of Induction Heating*; Marcel Dekker: NY, 2003.

12.15.5.7.2.2 Current source with series load

The quarter bridge or single-switch inverter is considered to be a current source inverter because it has a large inductor in the DC current path that provides a stable source of DC current to the inverter. The power switch can be a thyristor or a transistor for frequencies below 30 kHz and only a transistor for higher frequencies. **Figure 85** shows a simplified circuit diagram. When switch S1 is turned on, DC current continues to flow from the DC source through the large inductor and also from the series load-tuning capacitor C_S, discharging it through the load coil. The resulting load current pulse, shown in **Figure 96**, trace 2, is nearly sinusoidal, with the first half-cycle of current passing through the switch and the second half-cycle through the diode. During this portion of the period, current is rising in the input inductor. When current stops flowing in the diode, the energy stored in the input inductor causes direct current to flow in the output circuit, recharging the series load-tuning capacitor C_S. The frequency of the output sine wave is determined by the series capacitor and the load coil inductance. For operation at high frequencies, the power semiconductor switch T can be left on, allowing the load circuit to ring (oscillate) for more than one cycle. It is this resonant frequency that primarily determines the penetration depth of the induction heating current. The firing rate of the inverter regulates the output power level, and therefore, the quarter bridge power supply uses a simple fixed voltage AC to DC converter.

12.15.5.8 Conclusion

Several references were made earlier to different types of power supplies and their features. It should be clear at this point why induction heating manufacturers developed a family of different types of power supplies (**Figure 97**). Each power supply best fits the needs of a certain family of induction heating applications, optimizing operational conditions. In some applications (e.g., simultaneous dual-frequency gear hardening), heat-treating power supply could combine two or even more inverters to better suit the specifics of a particular application. One of these power supplies is shown in **Figure 61** and was discussed in Ref. (*90*).

Some power supplies have more flexibility, providing an ability to independently change the frequency and output power during the scan-hardening process 'on the fly.' One of these power supplies is STATITRON-IFP inverter, which allows for independent change of frequency in the 5–40 kHz range and power in a range of 75–360 kW in a single module system.

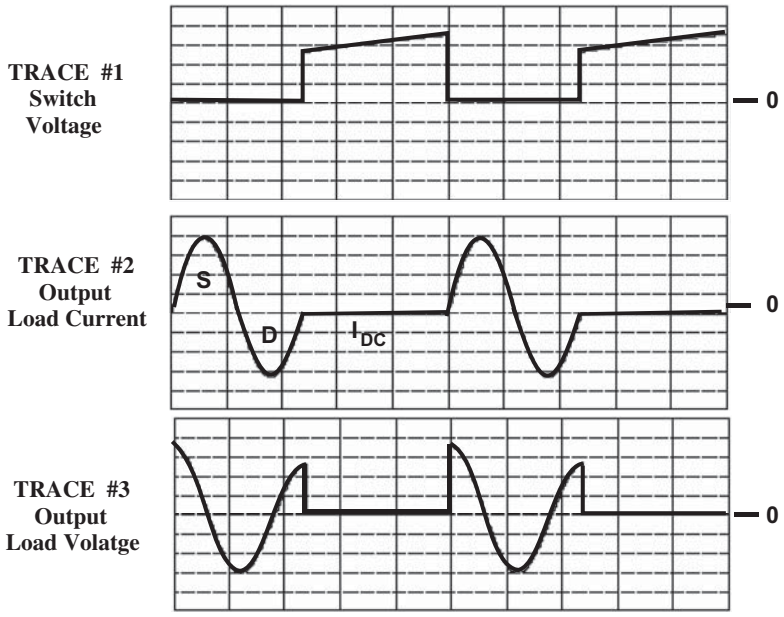

Figure 96 Wave shapes for quarter CE bridge or single-switch inverter. Reproduced from Rudnev, V.; Loveless, D.; Cook, R.; Black, M. *Handbook of Induction Heating*; Marcel Dekker: NY, 2003.

Figure 97 Family of highly efficient Inductoheat's power supplies for various induction heating applications. Courtesy of Inductoheat Inc.

12.15.6 Load Matching Induction-Hardening Power Supplies

Modern induction-hardening systems are made up of a specific power supply type, an induction heating coil with a workpiece, and a load matching network. The load matching network may be physically located within the power supply cabinet or in a separate enclosure commonly referred to as the heat station. Components typically in the heat station include variable ratio transformers, capacitors, and in some cases matching (tuning) inductors. Induction power supplies are available in many types and models, each with a given maximum power, voltage, and current rating that will operate over a specified frequency range. The load matching network is essential because seldom does the output current or output voltage perfectly match the corresponding requirements of the induction heat-treat coil, and in that case rated output power cannot be obtained.

12.15.6.1 Simple Examples

One example of the need to match a power source to a load is the simple lighting circuit having a 120 V supply and a 12 V, 12 W light bulb. The 12 W light bulb with 12 V applied would draw one amp of current (12 W/12 V = 1 A) and its resistance by Ohm's law would be 12 ohms (12 V/1 A = 12 Ω). If connected directly to the 120 V supply, it would draw 10 amps of current (120 V/12 Ω = 10 A) and dissipate 1200 W (120 V × 10 A = 1200 W), causing it to fail in a 'flash.' Matching the 120 V supply to a 12 V bulb is easily accomplished by inserting a transformer with a 10 to 1 ratio between the source and the load. This transformer then steps the secondary voltage down by a factor of 10 providing 12 V, and the bulb then draws the required 1 A. At the same time, the primary current is only 0.1 amp, which is one-tenth of the secondary current. Interestingly, the volt amp product of the source or primary (120 V × 0.1 A = 12 VA) is equal to the volt amp product of the load or secondary (12 V × 1 A = 12 VA). This example shows how a transformer provides an impedance match between the source and the load but does not change the VA product (assuming appreciably small losses in the transformer).

The load matching of an induction heat-treating system is more complex due to the presence of reactive components. Coils used in induction hardening have two electric components. One is a resistive component that causes heat to be generated, as in the case of the light bulb of the example above. A second component is the inductance, which results from the magnetic field that is generated by the flow of AC current through the coil. Each of these components can be measured and are referred to as resistance (R) in Ohms and inductance (L) in Henrys. The opposition to current flow that is caused by inductance (L) is called inductive reactance (X_L) and is dependent on frequency ($X_L = 2\pi fL$) and electromagnetic properties of the workpiece. The ratio of these two components (X_L/R) is referred to as the Q of the coil. It is important to realize that Q is not constant during the heating cycle. This is because, among other factors, R and L are functions of temperature that varies during the heating cycle. An average value of Q over the cycle time is often used for load matching calculations. The range of average values of Q of induction-hardening coils is typically in the range from 3 to 8, and it is lower at a beginning of the heating cycle when steel retains its magnetic properties and increases at the end of the heating.

It would be beneficial to review the following simple example to better appreciate the effect of Q on load matching. Is a power supply rated at 100 kW, 800 V, and 250 amps compatible with an induction heating coil that needs 100 kW, 40 V, and 10 000 amps at 10 kHz to produce the desired hardening pattern? As in the light bulb example above, a transformer with a ratio of 20:1 (800/40 = 20) will match the power supply voltage to the coil voltage. In this case, the current from the power supply to the transformer primary would be 10 000/20 or 500 amps, which is much more than the 250 amps available from the power supply.

By adding capacitance to tune the load circuit to resonate at or near the operating frequency of 10 kHz, the current is reduced to 100 kW/800 V or 125 amps, which is well within the output current rating of the power supply. Tuning the load circuit to the desired heating frequency can also be regarded as correcting the load power factor of the work coil to near unity. In this case the load resonating capacitor would be called a power factor correction capacitor.

12.15.6.2 Load Connection Types

The two basic types of induction heating load connections are parallel and series circuits. The parallel circuit, shown in Figure 98, is used with power supply types that have a specific output voltage rating for full-power operation. From the previous Section 12.15.5.7 on *Modern Power Supplies for Induction Hardening*, the types that use the parallel load connection are the voltage source LC–LC, the voltage source L–LC, and the current source with parallel load.

The series load shown in Figure 99 is used with the voltage source with series load and with the current source quarter bridge with series load.

12.15.6.2.1 Matching the Parallel Resonant Load

Figure 87 shows a typical curve of frequency versus power, voltage, and impedance. This shows that as the frequency applied to the parallel resonant load is brought nearer to its resonant frequency, the impedance, voltage, and power will

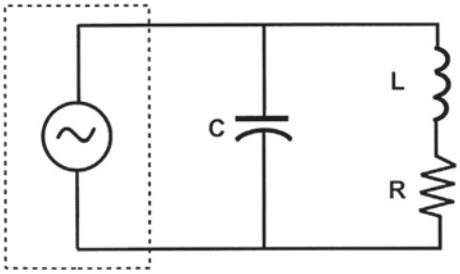

Figure 98 Parallel circuit for induction heating.

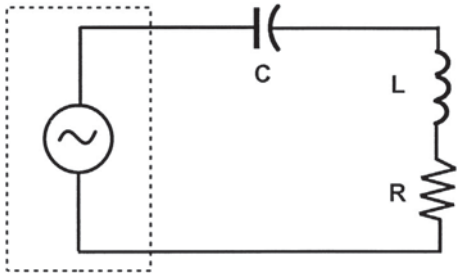

Figure 99 Series circuit for induction heating.

increase until all three parameters reach their maximum at resonance. The voltage source inverters using sweep frequency control operate just above or just below resonance to adjust power. When variable DC or PWM is used to control power, the inverter operates at the load resonant frequency. It is therefore important to adjust the load matching components to obtain a resonant frequency as close as possible to the operating frequency required to obtain the desired hardening pattern.

The first step in load matching is to determine the output capabilities of the power supply.

The second step is to determine the power in kilowatts, coil voltage, and the frequency that must be supplied to coil terminals for obtaining the desired induction-hardening result. This can be done based on rules of thumb, extrapolation of data from previous application of similar hardening inductors, or from the results of computer modeling. Transmission losses (including bus-bar losses and a voltage drop) should be included into consideration separately.

The next step toward obtaining an acceptable load match is to estimate the Q of the work coil. As mentioned earlier, the Q of most induction-hardening coils is between 3 and 8. For example, a low Q (2–4) is typical when heating steel below Curie temperature with a closely coupled coil. Heating steel above the Curie point or with a loosely coupled, relatively large air gap between coil and workpiece will result in a high Q (5–15).

Using the estimated values of power and Q, we can calculate the KVA of the load by

$$\text{KVA} = \text{kW} \times Q \qquad [23]$$

The induction heat-treating system uses capacitors that are designed for use at a specific frequency, rated voltage, and KVAR where

$$\text{KVAR} = \frac{2\pi f C V^2}{10^9} \quad \text{where } C \text{ is in } \mu\text{F} \qquad [24]$$

It should be noted here that the nameplate KVAR rating of a capacitor is at the nameplate frequency and voltage. Operation at another voltage or frequency will result in an operating KVAR value that is different from the rated KVAR.

When the load is tuned to resonance, the KVAR of the capacitor is approximately equal to the KVA of the load. Therefore, by combining the equations above, an estimate of the capacitance can be made by using the following expression:

$$C \approx 10^9 \times \text{kW} \times Q / 2\pi f V^2 \qquad [25]$$

The two most common parallel resonant load matching circuits are shown in Figures 98 and 100. Most induction-hardening applications use single-turn, two-turn, or three-turn induction coils (heating inductors) that require less than 250 V applied to the coil terminals to obtain the required heating power. In this case, the secondary windings of a variable ratio transformer are connected directly to the induction coil, and the resonant or 'tuning' capacitor is connected across the primary windings of this transformer as shown in Figure 100. Changing the transformer ratio affects the resonant frequency of the load as well as the amount

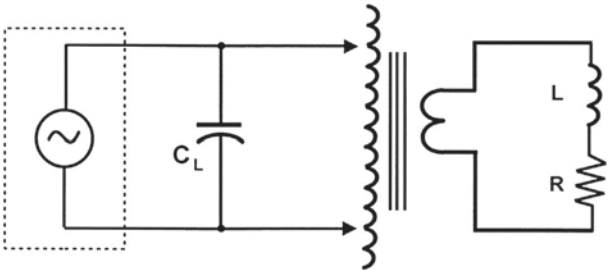

Figure 100 Parallel resonant circuit for low-voltage heating coil.

of voltage step down. To more clearly illustrate the load matching process, let us assume that the following induction-hardening parameters are given or estimated (assuming frequency of 10 kHz):

Power supply	*Induction coil estimates*
Rated kW = 150 kW	Required kW = 120 kW
Rated voltage = 800 V	Coil voltage = 60 V at 120 kW
Max current = 380 amps	Coil $Q = 5$

Since the maximum voltage rating of the load matching capacitor and transformer is 800 V, the operating voltage at 120 kW can be set by

$$C_S \text{ voltage} = 800\text{V} * \sqrt{\left(\frac{120}{150}\right)} = 715\text{ V}$$

The value of capacitance in microfarads is estimated using the formula:

$$C_S \approx 10^9 \times \text{kW} \times \frac{Q}{2\pi f V^2} = 10^9 \times 120 \times 5/2\pi \times 10\ \ 000 \times (715)^2 \approx 18.7\ \mu\text{F}$$

The variable transformer ratio can be calculated by

$$T_R = 715\text{ V}/60\text{ V} = 11.92\text{; therefore a ratio of 12:1 will be used.}$$

Having determined the matching component values based on rough estimates of the induction coil parameters, it is useful to run a heating cycle and record the actual power, voltage, and operating frequency. With this data, the estimates can be refined and the load match further improved. Continue the above example using the following, taken during the trial heating cycle:

Power = 110 kW
Voltage = 800 V (Volt Limit)
Frequency = 11.5 kHz

The actual coil voltage at 110 kW is then 800/12 or 66.7 V.

To increase the power to the required 120 kW at 700 V, the coil voltage must be

$$\text{Coil Voltage} = 66.7\text{ V} \times \sqrt{\frac{120}{110}} = 69.7\text{ V}$$

The new transformer ratio should be changed to

$$T_R = 700\text{ V}/69.7\text{ V} = 10.04\text{; therefore a ratio of 10:1 will be used.}$$

This change of transformer ratio will increase the resonant frequency by the inverse of the ratio change:

$$F = 11.5\text{ kHz} \times \frac{12}{10} = 13.8\text{ kHz}$$

The resonant frequency varies inversely as the square of the capacitance. Therefore, to obtain the desired operating frequency of 10 kHz, the value of the capacitor should be increased to

$$C = 18.7\ \mu\text{F} \times \left(\frac{13.8}{10}\right)^2 = 35.6\ \mu\text{F}$$

Having determined a new transformer ratio and load matching capacitance, we should run another heating cycle to verify that the desired results have been achieved. The procedure above may be repeated if the results of this test show that further fine tuning of the load matching is required.

The procedure for matching the simple parallel resonant load is summarized by the following steps:

1. Determine the output capabilities of the power supply.
2. Estimate the power, frequency, and coil voltage that will be required to achieve the desired hardening pattern.
3. Estimate the Q of the heating coil.
4. Calculate the KVAR and capacitance value.
5. Calculate the transformer ratio.
6. Run the heating cycle with a new setup and record the actual power, voltage, and frequency.
7. Recalculate the transformer ratio and capacitor value.

8. Run the heating cycle and record actual power, voltage, and frequency.
9. Repeat until acceptable parameters are obtained.

A trial-and-error approach to load matching may also be used, but this method usually takes more time and effort to achieve and satisfactorily match. This method requires that a heat run be made after each adjustment of capacitance or transformer ratio. **Table 10** indicates the desired change (increase or decrease) in a particular operating parameter and the direction of required adjustment (increase or decrease) of capacitance or transformer ratio to achieve the desired change.

Specialized test equipment is available to ease the load matching process. The load frequency analyzer (LFA) available from Inductoheat, Inc. is shown in **Figure 101**. When LFA is connected to an induction heating load, it will indicate the resonant frequency and allow a rough estimate of load *Q*. It is a solid-state, portable instrument that quickly determines the resonant frequency of the induction heating load without heating (*119*). This equipment eliminates time-consuming setup and prevents the waste of production parts typically used during trial-and-error techniques and the heating and cutting process. To operate the analyzer, simply plug it into an outlet and select the frequency range. Load the workpiece into the inductor and place the clip leads across the heat station capacitor bus. By adjusting the frequency of the LFA, the resonance is determined by the level indicated on the bar graph. With adjustments to the machine's transformer and capacitor connections, the desired heating frequency can easily be achieved.

12.15.6.2.1.1 Matching the parallel resonant LC–LC load

The process of load matching the LC–LC power supply to its load is the same as the process used for the simple parallel resonant load in Section 12.15.6.2.1 except that the LC coupling components in the output of the power supply have an effect on the resonant frequency of the system. In order to determine the correct value of the tuning capacitor, the effective capacitance of the inverter output must be subtracted from the parallel resonant load tuning capacitance found by the procedure described in Section 12.15.6.2.1.

A diagram of a typical LC–LC power supply and load is shown in **Figure 102**. The LC networks in the inverter output (L_S and C_S) are net capacitive at the operating frequency of the inverter. The value of L_S and C_S are fixed for a given power rating. For example, in the Inductoheat SP5 the value of C_S is typically 43 μF per 100 kW of output power rating. A 150 kW unit would therefore have a C_S value of 64 μF. The effect of this capacitance on load tuning is reduced by the square of the inverter output transformer ratio (1:4), which in this case would be $C_{S\ eff} = 64\ \mu F/16 = 4\ \mu F$. Therefore, the load tuning procedure for a 150 kW LC–LC power supply is the same as that for the parallel resonant load in Section 12.15.6.2.1 except that the actual installed capacitance is the calculated tuning capacitor (C_L) value reduced by $C_{S\ eff}$ of 4 μF.

The procedure for matching the Parallel Resonant LC–LC Load is summarized by the following steps:

1. Determine the output capabilities of the power supply.
2. Estimate the power, frequency, and coil voltage that will be required to achieve the desired hardening pattern.
3. Estimate the *Q* of the heating coil.

Table 10 Trial-and-error load matching

Parameter	*Increase* ↑ *Decrease* ↓	*Adjust*	
		Capacitor	T_x *ratio*
Voltage	↓	↑	↓
	↑	↓	↑
Frequency	↓	↑	↑
	↑	↓	↓
Current	↓	↓	↑
	↑	↑	↓

Figure 101 Portable load frequency analyzer. Courtesy of Inductoheat Inc.

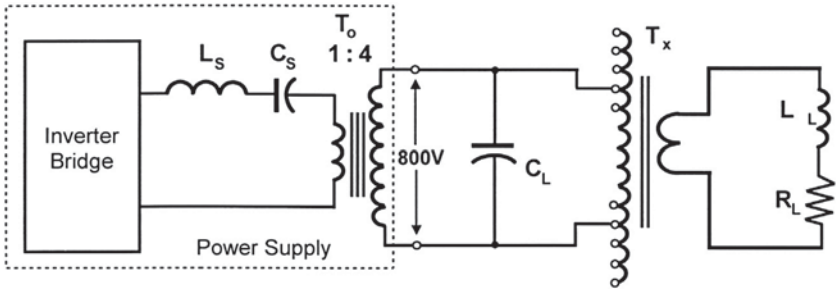

Figure 102 LC–LC output and load circuit.

4. Calculate the KVAR and capacitance value C_L and subtract the effective series capacitance $C_{S\ eff}$ to determine the capacitor value to install.
5. Calculate the transformer ratio.
6. Run the heating cycle with the new setup and record the actual power, voltage, and frequency.
7. Recalculate capacitor value C_L and transformer ratio as in steps 4 and 5 above.
8. Run the heating cycle and record the actual power, voltage, and frequency.
9. Repeat until acceptable parameters are obtained.

12.15.6.2.1.2 Matching the parallel resonant L–LC load

The L–LC power supply has an inductor L_S in series with the power supply output as shown in **Figure 103**. The value of L_S depends on the power rating and nominal frequency of the power supply. For example, in the Inductoheat SP18, the value of L_S in a 150 kW, 10 kHz power supply would be 60 μH. This inductance counteracts some of the load tuning capacitance, in effect raising the resonant frequency of the output circuit.

To quantify this effect, the equivalent inductance related to the parallel resonant load circuit is found by multiplying the inductance L_S by the inverse square of the turns ratio: $L_{S\ equiv} = 60\ \mu H\ (2/3)^2 = 26.7\ \mu H$. This inductance value is in effect across the load resonant capacitor C_L, and therefore the value of the load resonant capacitor calculated by the process outlined in Section 12.15.6.2.1 must be increased by a compensating capacitance value that will offset this equivalent inductance. The value of compensating capacitance C_{comp} is calculated using the following formula:

$$C_{comp} = \frac{1}{(2\pi F)^2 L} \quad \text{if } L_{S\ equiv} = 26.7\ \mu H \text{ then : } C_{comp} = \frac{1}{(2\pi 10\ 000)^2 26.7\ \mu H} = 9.5\ \mu F$$

The value of the capacitance actually installed to properly match the Parallel Resonant L–LC Load is the sum of the C_L value as calculated in Section 12.15.6.2.1 for a simple parallel resonant load and the compensating capacitance C_{comp} calculated above.

The procedure for matching the Parallel Resonant L–LC Load is summarized by the following steps:

1. Determine the output capabilities of the power supply.
2. Estimate the power, frequency, and coil voltage that will be required achieve the desired hardening pattern.
3. Estimate the Q of the heating coil.
4. Calculate the KVAR and capacitance C_L value and add the compensating capacitance C_{comp}.
5. Calculate the transformer ratio.
6. Run the heating cycle with the new setup and record the actual power, voltage, and frequency.
7. Recalculate the capacitor value and transformer ratio as in steps 4 and 5 above.
8. Run the heating cycle and record the actual power, voltage, and frequency.
9. Repeat until acceptable parameters are obtained.

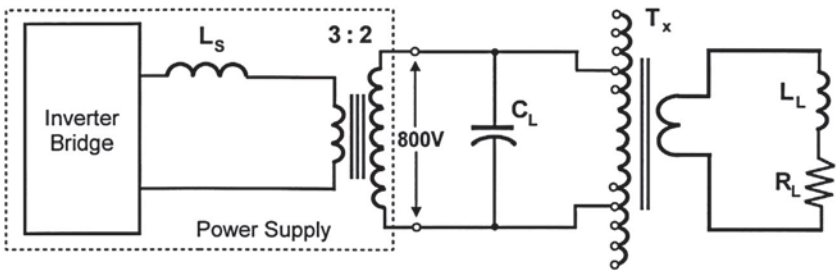

Figure 103 L–LC output and load circuit.

12.15.6.2.2 Matching the Series Resonant Load

The series resonant load has a frequency versus power, voltage, and current response curve that is the same as that of the parallel resonance load, with power, voltage, and current, all reaching a maximum at resonance as shown in Figure 104. The impedance of the series resonant load is high off resonance and minimum at resonance, as shown in Figure 105. This is opposite to the impedance curve of the parallel resonant load. The series resonant load is usually connected to a voltage source power supply having an output transformer T_X with various ratios to provide higher output current than is available from the inverter bridge. As explained in Section 12.15.5.7.1.1, voltage source inverters using sweep frequency control operate just above or just below resonance to adjust power. When variable DC or PWM is used to control power, the inverter operates at the load resonant frequency. It is therefore important to adjust the load matching components to obtain a resonant frequency as close as possible to the output frequency required to obtain the desired hardening pattern.

The two most common series resonant load matching circuits are shown in Figure 106 for high-voltage and high-frequency loads and in Figure 107 for low-voltage loads. Induction-hardening applications are usually accomplished using a tightly coupled

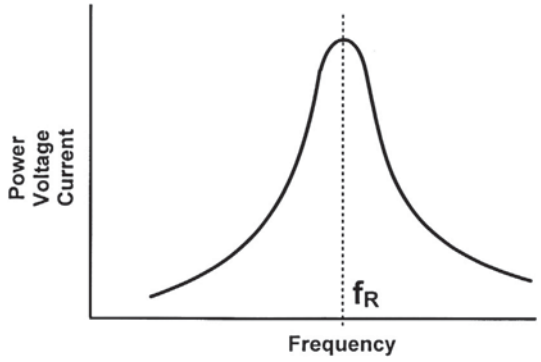

Figure 104 Frequency versus power, voltage, and current response curve for the series resonant load.

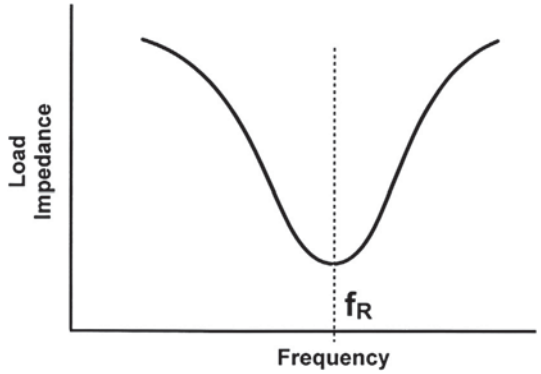

Figure 105 The impedance of the series resonant load.

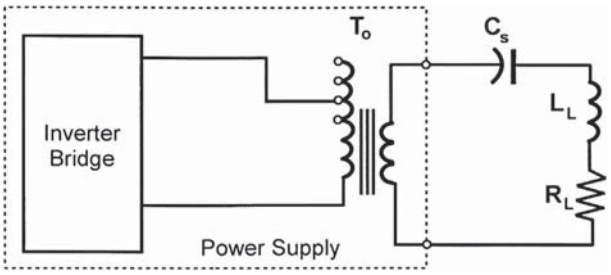

Figure 106 Series resonant high-voltage load circuit.

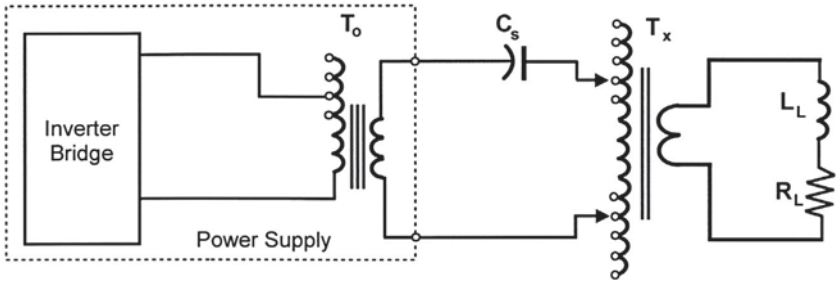

Figure 107 Series resonant low-voltage load circuit.

single-turn heating coil that requires relatively high current and low voltage. In this case, the secondary of a variable ratio transformer is connected directly to the work coil, and the resonant or 'tuning' capacitor C_S is connected in series with the primary of this transformer, as shown in Figure 107. Changing the transformer ratio affects the resonant frequency of the load as well as the amount of current stepup/voltage step down. The load matching procedure is described here for the low-voltage circuit of Figure 107, with a variable ratio transformer connected to the load coil. However, this procedure may also be used in load matching the high-voltage circuit of Figure 106 by setting the ratio of T_X to 1:1.

Voltage source power supplies with simple series load circuits as described in Section 12.15.5.7.1.1 have a nominal output current rating as opposed to a nominal output voltage rating, as is the case for supplies operating in parallel resonant loads.

The first step in load matching is to determine a few important power supply parameters. These include power rating, nominal frequency, output current rating, DC bus voltage, and available output transformer T_O ratios. Also determine the voltage rating of the load matching series capacitor C_S and matching transformer T_X.

The second step is to determine the power in kilowatts, coil voltage, and the frequency that must be supplied to obtain the desired induction-hardening result. This can be done based on rules of thumb, from extrapolation of data from previous application of similar applications, or from the results of computer modeling.

The next step toward obtaining an acceptable load match is to estimate the Q of the work coil. As mentioned earlier, the Q of most induction-hardening coils is between 3 and 8. For example, a low Q (2–4) is typical when heating steel below the curie temperature with a closely coupled coil. Heating steel above the curie point or with a loosely coupled inductor (large air gap between coil and workpiece) will result in a high Q (5–15).

To illustrate further the load matching process, the following induction-hardening parameters are given or estimated. Parameters similar to those used in the example of parallel resonant load matching in Section 12.15.6.2.1 will be used to simplify comparison of the load tuning process.

Power supply	*Load matching*	*Work coil estimates*
Rated kW = 150 kW	C_S voltage rating = 800 V	Required kW = 120 kW
Frequency = 10 kHz	T_X voltage rating = 800 V	Coil voltage ≈ 60 V at 120 kW
Max current = 375 A		Coil $Q \approx 5$
DC bus voltage = 650 V		
T_0 ratios 3:1 to 12:1		

Since the maximum voltage rating of the load matching capacitor and transformer is 800 V, the operating voltage at 120 kW can be set by

$$\text{Operating voltage} = 800\ \text{V} * \sqrt{\left(\frac{120}{150}\right)} = 715\ \text{V}$$

The load matching transformer ratio is then calculated by

$$T_{X\ \text{ratio}} = \frac{715\ \text{V}}{60\ \text{V}} = 11.9;\ \text{therefore, a ratio of 12: 1 will be used.}$$

The value of series resonant capacitance C_S in microfarads is estimated using the formula:

$$C_S = \frac{\text{kW} * Q * 10^9}{2\pi f V^2} = \frac{120 * 5 * 10^9}{2 * \pi * 10\ \ 000 * 715^2} = 18.7\ \mu\text{F}$$

The ratio of output transformer in the power supply T_X for the initial setup is found by dividing the estimated load coil Q by a factor of $K_f = 1.2$ (specific for L-LC power supply design) when using a full bridge inverter power supply. In this example,

$$T_{X\ \text{ratio}} = \frac{Q}{1.2} = \frac{5}{1.2} = 4.17;\ \text{therefore, a ratio of 4:1 will be used.}$$

The current in the capacitor C_S is found by the following formula:

$$I_{C_s} = V * 2\pi fC = 700 * 2 * \pi * 10\ 000 * 18.7 * 10^{-6} = 822\ \text{A}$$

Calculate the inverter output current to verify that the inverter current does not exceed the maximum of 375 A using the following:

$$I_{\text{INV}} = \frac{I_{C_s}}{T_{X\ \text{ratio}}} = \frac{822\ \text{A}}{4} = 205\ \text{A}$$

This is well within the current limit. Having determined the matching component values based on rough estimates of the work coil parameters it is useful to run a heating cycle and record the actual power, voltage, and operating frequency. With this data, the estimates can be refined and the load match further improved. Continue the above example using the following taken during the trial heating cycle:

Power = 110 kW
Voltage = 800 V (Volt limit)
Inverter current = 270 A
Frequency = 11.5 kHz

The KVAR of the C_S is then

$$\text{KVAR} = \frac{2\pi fCV^2}{10^9} = 864,\ \text{where } C \text{ is in } \mu\text{F}$$

From this data a new estimate of coil Q can be made:

$$Q \approx \frac{\text{KVAR}}{\text{kW}} \approx 864/110 \approx 7.85$$

The actual coil voltage at 110 kW is then 800/12 or 66.7 V.
To increase the power to the required 120 kW at 700 V, the coil voltage must be

$$\text{Coil Voltage} = 66.7\ \text{V} \times \sqrt{\frac{120}{110}} = 69.7\ \text{V}$$

The new transformer ratio should be changed to

$$T_R = 700\ \text{V}/69.7\ \text{V} = 10.04;\ \text{therefore, a ratio of 10:1 will be used.}$$

This change of transformer ratio will increase the resonant frequency by the inverse of the ratio change:

$$F = 11.5\ \text{kHz} \times \frac{12}{10} = 13.8\ \text{kHz}$$

The resonant frequency varies inversely as the square of the capacitance. Therefore, to obtain the desired operating frequency of 10 kHz, the value of the capacitor should be increased to

$$C = 18.7\ \mu\text{F} \times \left(\frac{13.8}{10}\right)^2 = 35.6\ \mu\text{F}$$

The actual Q of the load coil is found to be 7.85; therefore a new inverter output transformer ratio is determined by

$$T_{X\ \text{ratio}} = \frac{Q}{1.2} = \frac{7.85}{1.2} = 6.54.\quad \text{Therefore, a ratio of 7:1 will be used.}$$

The current in the capacitor C_S is found by the following formula:

$$I_{C_s} = V * 2\pi fC = 700 * 2 * \pi * 10\ 000 * 35.6 * 10^{-6} = 1566\ \text{A}$$

Calculate the inverter output current to verify that the inverter current does not exceed the maximum of 375 A using the following:

$$I_{\text{INV}} = \frac{I_{C_s}}{T_{X\ \text{ratio}}} = \frac{1566\ \text{A}}{7} = 224\ \text{A}$$

This is well within the current limit. Having determined a new load matching transformer ratio, series capacitance, and inverter output transformer ratio, another heating cycle should be run to verify that the desired results have been achieved. The procedure above may be repeated if the results of this test show that further load matching is required.

The procedure for matching the simple series resonant load is summarized by the following steps:

1. Determine the output capabilities of the power supply.
2. Estimate the power, frequency, and coil voltage that will be required to achieve the desired hardening pattern.
3. Estimate the Q of the heating coil.
4. Determine the operating voltage of the load matching transformer and series capacitor.
5. Calculate the matching transformer to be used.
6. Calculate the KVAR and series capacitance value.
7. Calculate the inverter output transformer ratio.
8. Run the heating cycle with the new setup and record the actual power, voltage, current, and frequency.
9. Recalculate load Q, matching transformer ratio, series capacitor value, and the inverter output transformer ratio.
10. Run the heating cycle and record the actual power, voltage, current, and frequency.
11. Repeat steps 8, 9, and 10 until the power supply is in regulation and without limits throughout the heating cycle.

12.15.7 Conclusion

Because of space limitation, only a small portion of the virtually endless variety of subjects related to induction-hardening technologies were discussed here. Components made of steels and cast irons that undergo induction hardening include different transmission and engine components (e.g., axles, CV joint, camshafts, crankshafts, gears, cylinders, connecting rods, rocker arms, etc.), fasteners (e.g., bolts, screws, studs), off-road, farm, and mining equipment (i.e., shafts, clutch plates, pins, track links), cutting tools, bearings, inner/outer races sprockets, spindles, skid plates, fixtures, and the list goes on and on. The variety of geometries of components that undergo induction hardening and diversity of required hardness patterns call for a variety of hardening inductors. Some of those inductors are shown in Figure 3.

For readers who would like to further study subjects related to induction hardening (including but not limited to a formation of initial, transitional, and residual stresses, a part's distortion and its control, failure analysis of heat-treat components, induction tempering versus oven tempering, etc.), we provide an extensive list of publications below. Numerous technical articles can be found at http://www.inductoheat.com/articles.php.

If someone needs clarification regarding certain subjects discussed in this chapter or has a question regarding induction heating or induction heat-treating application, we encourage you to contact us via e-mail: rudnev@inductoheat.com or loveless@inductoheat.com.

References

1. Rudnev, V.; Loveless, D.; Cook, R.; Black, M. *Handbook of Induction Heating;* Marcel Dekker: NY, 2003.
2. *Induction Heating, Course 60;* ASM International: Metals Park, OH, 1986.
3. Orfueil, M. *Electric Process Heating;* Battelle Press: Columbus, OH, 1987.
4. Lozinskii, M. G. *Industrial Applications of Induction Heating;* Pergamon: London, 1969.
5. Semiatin, S. L.; Stutz, D. E. *Induction Heat Treatment of Steel;* ASM International: Metals Park, OH, 1986.
6. Rudnev, V. Simulation of Induction Heat Treating. In *Metals Process Simulation;* Furrer, D. U., Semiatin, S. L., Eds.; ASM Int.: Materials Park, OH, 2010; pp 501–546.
7. Rudnev, V.; Cook, R.; Loveless, D.; Black, M. Induction Heat Treatment: Basic Principles, Computation, Coil Construction and Design Considerations in Steel Heat Treatment. In *Equipment and Process Design;* Totten, G., Ed.; CRC Press, 2007; pp 277–394 (chapter 4).
8. Rudnev, V.; Cook, R.; Loveless, D.; Black, M. Induction Heat Treatment. In *Steel Heat Treatment Handbook;* Totten, G., Howes, M., Eds.; Marcel Dekker: New York, 1997; pp 765–872.
9. Simpson, P. G. *Induction Heating: Coil and System Design;* McGraw-Hill: NY, 1960.
10. Krauss, G. *Steels: Heat Treatment and Processing Principles;* ASM Int., 2005.
11. Honeycomb, R. W. K.; Bhadeshia, H. K. D. H. *Steels: Microstructure and Properties;* Arnold: Great Britain, 1995.
12. Rothman, M. F. *High-Temperature Property Data: Ferrous Alloys;* ASM Int.: Metals Park, OH, 1988.
13. Rudnev, V., Demidovich, V. Advanced Computation Software for Everyday Use in Modern Induction Heat Treating. Proceedings of 17th ASM Heat Treating Conference, Indianapolis, 15–18 Sept., 1997; pp 551–555.
14. Rudnev, V. Computer Modeling Helps Identify Induction Heating Misassumptions and Unknowns. *Ind. Heat.* **October, 2011,** 59–64.
15. ASM Handbook, *Heat Treating;* ASM Int.: Materials Park, OH, 1991; Vol. 4.
16. Atlas zur Warmebehandling der stahle. In Orlich, J., Rose, A., Wiest, P., Eds.; Verlag Stahleisen: Dusseldorf, Germany, 1973; Vol. 3.
17. Orlich, J.; Pietrzeniuk, H.-J. Atlas zur Warmebehandling der stahle. In *Zeit-temperatur-austenitisierung-schaubilder,* Vol. 4; Verlag Stahleisen: Dusseldorf, Germany, 1976.
18. Rudnev, V. Metallurgical Insights for Induction Heat Treaters, Part 1: Induction Hardening Temperatures. *Heat Treat. Prog.* **May/June, 2007,** 15–17.
19. Feuerstein, W.; Smith, W. *Trans. ASM* **1954,** *46,* 1270.
20. Rudnev, V. Metallurgical 'Fine Points' of Induction Hardening: Part 1. *Ind. Heat.* **March, 2005,** 37–42.
21. Rudnev, V. Metallurgical 'Fine Points' of Induction Hardening: Part 2. *Ind. Heat.* **May, 2005,** 41–47.
22. Coryell, J. J.; Matlock, D. K.; Speer, J. G. The Effect of Induction Hardening on the Mechanical Properties of Steel with Controlled Prior Microstructures. *Proc. Int. Conf. Materials Science & Technology* **2005,** 3–14.
23. Cunningham, J. L.; Medlin, D. J.; Krauss, G. Effects of Induction Hardening and Prior Cold Work on a Microalloyed Medium Carbon Steel. *Proc. of the 17th ASM Heat Treating Conference, Indianapolis,* **1997,** 575–584.
24. Shutts, A. *Effects of Heating Rate and Prior Microstructure on SAE 1541 Forging Steel.* Report MT-SCR-004-012; Forging Industry Educational and Research Foundation, April, 2004.
25. Medlin, D.; Krauss, G.; Thompson, S. Induction Hardening Response of 1550 and 5150 Steels with Similar Prior Microstructures. Indianapolis. In *Proc. of 1st Int. Conference on Induction Hardening of Gears and Critical Components;* May, 1995; pp 57–65.

26. Smith, K.; Wise, J.; Krauss, G. A Microstructural Analysis of Rapid Austenite Formation in Induction Hardened Steels. Gothenburg, Sweden. In *Proc. of the 5th ASM Heat Treatment and Surface Engineering Conference;* June, 2000.
27. Favenyesi, T.; Medling, D.; Matlock, D.; Krauss, G. The Effect of Prior Microstructure on the Fatigue of Induction Hardened AISI 1050 Steel. In *Proc. of 40th MWSP Conference;* ISS, 1998; pp 733–740.
28. Cunningham, J. Effects of Induction Hardening and Prior Cold Work on a Microalloyed Medium Carbon Steel. M.S. Thesis MT-SRC-096-024, Colorado School of Mines, Golden, CO, August, 1996.
29. Clarke, K. D.; Van Tyne, C. J. *Effect of Prior Microstructure and Heating Rate on Austenite Formation Kinetics in Three Steels for Induction Hardened Components*. Progress Report; Colorado School of Mines: Golden, Colorado, December, 2005.
30. Clarke, K. D.; Van Tyne, C.; Vigil, C. *Induction Hardening 5150 Steel – Effect of Initial Microstructure and Heating Rate*. Joined Progress Report; Colorado School of Mines and Los Alamos National Laboratory, 2006.
31. Clarke, K. D.; Van Tyne, C. J. *Effect of Prior Microstructure Scale and Heating Rate on Carbide Dissolution and Austenite Formation in Spheroidized 52100 Steel*, Report of Advanced Steel Processing and Products Research Center at the Colorado School of Mines, 2006.
32. Rollmann, J.; Kaiser, B.; Kloos, K.; Berger, C. Intrinsic Material Properties after Short Time Austenization. In *Proc. of the 17th ASM Heat Treating Conference;* Indianapolis, 1997; pp 777–781.
33. Brooks, C. *Principles of the Heat Treatment of Plain Carbon and Low Alloy Steels;* ASM Int.: Materials Park, OH, 1996.
34. Canale, L. C. F.; Brooks, C. R.; Rudnev, V. The Effect of Prior Microstructure on the Hardness and Residual Stress Distribution in Induction Hardened Steels, *Proc. SAE Int. Off-Highway Congress;* Las Vegas, Nevada, March, 2002.
35. Semiatin, S. L.; Stutz, D. E. *Induction Heat Treatment of Steel;* ASM Int.: Metals Park, OH, 1986.
36. Troiano, A. R.; Greninger, A. B. The Martensite Transformation. *Metal Prog.* **April, 1946,** *50* (2), 303–307.
37. Gulyaev, A. *Metallurgy;* Metallurgia: Moscow, Russia, 1977.
38. Rudnev, V. Metallurgical Insights for Induction Heat Treaters, Part 2: Spray Quenching. *Heat Treat. Prog.* **August, 2007,** 19–20.
39. Rudnev, V. Metallurgical Insights for Induction Heat Treaters, Part 3: Limitations of TTT and CCT Diagrams. *Heat Treat. Prog.* **Nov./Dec., 2007,** 23–25.
40. *Heat Treating Guide: Practice and Procedures for Irons and Steels;* ASM Int.: Materials Park, Ohio, 1995.
41. Rudnev, V. *Systematic Analysis of Induction Coil Failures and Prevention. Part 1: Introduction*. Heat Treat. Prog.; ASM Int.: Materials Park, Ohio, August, 2005, 25–26.
42. Rudnev, V. *Systematic Analysis of Induction Coil Failures and Prevention. Part 3: Coil Copper Selection*. Heat Treat. Prog.; ASM Int.: Materials Park, Ohio, Nov./Dec., 2005, 19–20.
43. Rudnev, V. *Systematic Analysis of Induction Coil Failures and Prevention. Part 7: Fabrication of Hardening Inductors*. Heat Treat. Prog.; ASM Int.: Materials Park, Ohio, Sep./Oct., 2006, 17–18.
44. Joseph, G., Kundig, K. J. A., Eds. *Copper: Its Trade, Manufacture, Use, and Environmental Status;* ASM Int.: Materials Park, Ohio, 1999.
45. Rudnev, V. Computer Modeling Helps Prevent Failures of Heat Treated Components. *Adv. Mater. Process.* **October, 2011,** 28–33.
46. Rudnev, V. Simulation of Induction Heating Prior to Hot Working and Coating. In *Metals Process Simulation;* Furrer, D. U., Semiatin, S. L., Eds.; ASM Int., 2010; pp 475–500.
47. Special Issue of IJMPT, Geneva, Switzerland. In *Induction Heating & Hardening & Welding;* Grum, J., Rudnev, V., Eds.; 2006.
48. Curtis, F. W. *High Frequency Induction Heating;* McGraw-Hill: NY, 1950.
49. Zinn, S.; Semiatin, S. L. Coil Design and Fabrication. Part 1: Basic Design and Modifications. *Heat Treat.* **June, 1988,** 32–36.
50. Zinn, S.; Semiatin, S. L. Coil Design and Fabrication. Part 2: Specialty Coils. *Heat Treat.* **August, 1988,** 29–32.
51. Zinn, S.; Semiatin, S. L. Coil Design and Fabrication. Part 3: Fabrication Principles. *Heat Treat.* **October, 1988,** 39–41.
52. Rudnev, V. Systematic Analysis of Induction Coil Failures and Prevention. Part 8: 'Gap-by-gap' Gear Hardening Coils. ASM Int., Materials Park, Ohio. *Heat Treat. Prog.* **Nov./Dec., 2006,** 19–20.
53. Rudnev, V. Systematic Analysis of Induction Coil Failures and Prevention. Part 9: Clamshell Inductors. ASM Int., Materials Park, Ohio. *Heat Treat. Prog.* **Jan./Feb., 2007,** 17–18.
54. Rudnev, V. Systematic Analysis of Induction Coil Failures and Prevention. Part 10: Contactless Inductors. ASM Int., Materials Park, Ohio. *Heat Treat. Prog.* **March/April, 2007,** 15–16.
55. Rudnev, V. Systematic Analysis of Induction Coil Failures and Prevention. Part 12: Inductors for Heating Internal Surfaces. ASM Int.., Materials Park, Ohio. *Heat Treat. Prog.* **July/August, 2008,** 21–22.
56. Rudnev, V. Systematic Analysis of Induction Coil Failures and Prevention. Part 14: Split-Return Inductors and Butterfly Inductors. ASM Int., Materials Park, Ohio. *Heat Treat. Prog.* **March/April, 2009,** 17–19.
57. Rudnev, V.; Cook, R. Magnetic Flux Concentrators: Myths, Realities and Profits. *Metal Heat Treat.* **March/April, 1995**.
58. Rudnev, V.; Cook, R.; Loveless, D. Keeping your Temper with Magnetic Flux Concentrators, Modern Application News, Nov., 1995.
59. Rudnev, V. An Objective Assessment of Magnetic Flux Concentrators. ASM Int., Materials Park, Ohio. *Heat Treat. Prog.* **Nov./Dec., 2004,** 19–23.
60. Bozorth, R. *Ferromagnetism;* IEEE Press: Piscataway, NJ, 1993.
61. Rudnev, V. Systematic Analysis of Induction Coil Failures and Prevention. Part 5: Effect of Flux Concentrator on Coil Life. ASM Int., Materials Park, Ohio. *Heat Treat. Prog.* **March/April, 2006,** 21–26.
62. Landau, L.; Lifshitz, E. *Theoretical Physics*In: *The Electrodynamics of Continuous Media;* Nauka: Moscow, 1992; Vol. 8.
63. Feynman, R.; Leighton, R.; Sands, M.*The Feynman Lectures on Physics;* Addison-Wesley Publ.: Reading, MA, 1964; Vol. 2.
64. Binns, K. J.; Lawrenson, P. J.; Trowbridge, C. W. *The Analytical and Numerical Solution of Electric and Magnetic Fields;* John Wiley & Sons, Ltd: New York, 1992.
65. Hammond, P. *Electromagnetism for Engineers;* Pergamon: New York, 1978.
66. Plonus, M. A. *Applied Electromagnetics;* McGraw-Hill: New York, 1978.
67. Patankar, S. *Numerical Heat Transfer and Fluid Flow;* Hemisphere: New York, 1980.
68. Incropera, F. P.; Dewitt, D. P. *Fundamentals of Heat Transfer;* Wiley: New York, 1981.
69. Rohsenow, W. M.; Hartnett, J. P. *Handbook of Heat Transfer;* McGraw-Hill: New York, 1973.
70. Rudnev, V. Computer Modeling of Induction Heating: Things to be Aware off, Things to Avoid. *Ind. Heat.* **May, 2011,** 41–45.
71. Rudnev, V. *Tips for Computer Modeling Induction Heating Processes, Part 1;* Forge, July, 2011.
72. Rudnev, V. *Tips for Computer Modeling Induction Heating Processes, Part 2;* Forge, October, 2011; pp 25–28.
73. Rudnev, V.; Loveless, D.; Ribeiro, C.; Boomis, J. Unleashing a Superior Induction Heating Design with Computer Modeling. *Ind. Heat.* **August, 2009,** 43–47.
74. www.fluxtrol.com.
75. www.magshape.com.
76. Leschynsky, V.; Weinert, H.; Szlaferen, A. Layered Alloys for Effective Magnetic Flux Concentration in Induction Heating. *Mater. Sci. Poland* **2007,** *25* (2), 275–281.
77. Nacke, B. Recent Development in Induction Heating and Future Prospects in Industrial Applications. Padua, Italy. In *Proc. Int. Symposium on Heating by Electromagnetic Sources (HES-07);* June, 2007.
78. Baake, E.; Schulbe, H.; Nikanorov, A. Alternative Processing for Laminar Compound Materials Based on Induction Heating. Padua, Italy. In *Proceedings of Int. Symposium on Heating by Electromagnetic Sources (HES-07);* June, 2007.
79. Dughiero, F.; Forzan, M. Electromagnetic Thermal Metallurgical Models for Induction Hardening. Hannover. In *Proc. Int. Scientific Colloquium: Modeling for Electromagnetic Processing;* 2008; pp 117–118.

80. Muhlbauer, A.; Udpa, S.; Rudnev, V.; Sutjiagin, A. Software for Finite Element Modeling Induction Heating Processes. Part 1, St. Petersburg, Russia. In *Proc. 10th Russian Conf. High-Frequency Applications*; pp 36–37.
81. Barglik, J.; Czerwiński, M.; Hering, M.; Wesołowsk, M. Radiation in Modeling of Induction Heating Systems. In Wiak, S., Krawczyk, A., Dolezel, I., Eds. **2008**; Vol. 30.
82. Barglik, J.; Alendarska, J.; Dolega, D.; Smagor, A. Numerical Modeling of Induction Heating of Steel Bodies. Hannover. In *Proc. Int. Scientific Colloquium: Modeling for Electromagnetic Processing*; pp 111–116.
83. Rudnev, V. Spray Quenching in Induction Hardening Applications. *J. ASTM Int.* **2008,** *6* (2).
84. Doyon, G.; Brown, D.; Rudnev, V.; Desmier, G.; Elinski, J. Taking the Crank out of Crankshaft Hardening. *Ind. Heat.* **December, 2008,** 41–44.
85. Rudnev, V.; Doyon, G.; Brown, D. Innovative Induction Heating Technologies. Pittsburgh. In *Proc. of Materials Science & Technology Conf. (MS&T-08);* 5–9 Oct., 2008.
86. Rudnev, V. Systematic Analysis of Induction Coil Failures. Part 9: Clamshell Inductors. *Heat Treat. Prog.* **Jan./Feb., 2007,** 17–18.
87. US Patent # 6,274,857, 2001.
88. US Patent # 6,859,125, 2005.
89. Doyon, G.; Brown, D.; Rudnev, V.; Andrea, F.; Sitwala, Ch.; Almeida, E. Induction Heating Helps Put Wind Turbines in High Gear. *Heat Treat. Prog.* **September, 2009,** 55–58.
90. Rudnev, V. Single-Coil Dual-Frequency Induction Hardening of Gears. *Heat Treat. Prog.* **October, 2009,** 9–11.
91. Rudnev, V. *Induction Hardening of Gears and Critical Components. Part 1;* Gear Technology, Sep./Oct., 2008, 58–63.
92. Rudnev, V. *Induction Hardening of Gears and Critical Components. Part 2;* Gear Technology, Nov./Dec., 2008, 47–53.
93. Brayman, S.; Kuznetsov, A.; Nikitin, S.; Binoniemi, B.; Rudnev, V. *Contour Hardening Bevel, Hypoid, and Pinion Gears;* Gear Solutions, Sept., 2011, 30–35.
94. Rudnev, V. Spin Hardening of Gears Revisited. *Heat Treat. Prog.* **March, 2004,** 17–20.
95. Davis, J. R. *Gear Materials, Properties, and Manufacture;* ASM Int.: Materials Park, OH, 2005.
96. Parris, G.; Ingham, D. *The Submerged Induction Hardening of Gears;* Gear Technology, March/April, 2001, 28–40.
97. *Breakthrough Contour Hardening;* Bulletin of ERS Engineering Corporation, September, 2011.
98. Rudnev, V.; Baloy, G.; Haddad, E. Tips for Successful Induction Hardening of Steels. *Ind. Heat.* **January, 2005,** 20–24.
99. Rudnev, V. Induction Hardening Cast Iron. *Heat Treat. Prog.* **March, 2003,** 27–32.
100. www.inductoheat.com.
101. Loveless, D.; Cook, R.; Rudnev, V. Considering Nature and Parameters of Power Supplies for Efficient Induction Heat Treating. *Ind. Heat.* **June, 1995,** 33–37.
102. Cook, R.; Loveless, D.; Rudnev, V. Load Matching in Modern Induction Heat Treating. *Ind. Heat.* **September, 1995,** 39–42.
103. Loveless, D. An Overview of Solid State Power Supplies for Induction Heating, 33. *Metal Producing* **August, 1995**.
104. Loveless, D.; Cook, R.; Rudnev, V. Induction Heat Treatment: Modern Power Supplies, Load Matching, Process Control and Monitoring. In *Steel Heat Treatment Handbook;* Totten., G., Howes, M., Eds.; Marcell Dekker: New York, 1997; pp 873–911 (chapter 11B).
105. Frank, W.; Der, C. Solid State RF Generators for Induction Heating Applications. In *IEEE IAS Conference Record;* October, 1982; pp 939–944.
106. Mauch, K. Transistor Inverters for Medium Power Induction Heating Applications. In *IEEE IAS Conference Record;* October, 1986; pp 555–562.
107. Jain, P.; Dewan, S. A Performance Comparison of Full- and Half-Bridge Series Resonant Inverters in High Frequency High Power Applications. *IEEE Trans. Ind. Appl.* **March/April, 1990,** *26* (2), 317–323.
108. Kit, K. *Switch Mode Power Conversion;* Marcel Dekker: NY, 1984.
109. Vasiliev, A.; Gurevich, S.; Ioffe, J. *Power Supplies for Electrothermal Equipment;* Energoatomizdat: Moscow, 1985.
110. Loveless, D. Solid State Power Supplies for Modern Induction Heat Treating. Indianapolis. In *Proc. of 17th Heat Treating Conference;* September, 1997; pp 615–620.
111. Espi, J.; Dede, E.; Sanchis, E.; Ferreres, A. Features and Design of the Voltage-Fed L-LC Resonant Inverter for Induction Heating. Charleston. In *Proceedings of IEEE PESC;* Jun., 1999; pp 292–301.
112. Nagai, S.; Savary, P.; Nakaoka, M.; Ogiwara, H. Phase-Shifting PWM Control-Mode High-Frequency Inverter for Induction Heating Applications. In *Proceedings of Int. Conference on Power Conversion;* 1988; pp 292–301.
113. Rashid, M. H. *Power Electronics Handbook;* Academic Press: San Diego, 2001.
114. Mohan, N.; Undeland, T.; Robbins, W. *Power Electronics: Converters, Applications, and Design;* John Wiley & Sons: Hoboken, NJ, 2003.
115. Rashid, M. H.; Rashid, H. M. *SPICE for Power Electronics and Electric Power;* CRC Press, 2005.
116. Loveless, D.; Cook, R.; Rudnev, V. Induction Heat Treatment: Modern Power Supplies, Load Matching, Process Control and Monitoring. In *Steel Heat Treatment: Equipment and Process Design;* Totten, G., Ed.; CRC Press, 2007; pp 395–434.
117. IEEE Standard 519-1992. *Recommended Practices and Requirements for Harmonic Control in Electrical Power Systems;* The Institute of Electrical and Electronics Engineers: New York, 1993.
118. Fishman, O. *DC Line Distortion for Static Power Converters Used in Induction Melting*, Inductotherm Bulletin, 2001.
119. *Load Frequency Analyzer*, Inductoheat Bulletin, 2010.
120. Totten, G.; Bates, C. E.; Clinton, N. A. *Handbook of Quenchants and Quenching Technology;* ASM Int.: Materials Park, OH, 1993.
121. Grum, J. *Induction Hardening;* University of Ljubljana: Slovenia, 2003.
122. Zinn, S. *Quenching for Induction Heating;* Induction Consultants, February, 2010.
123. Canale, L. C. F., Mesquita, R. A., Totten, G. E., Eds. *Failure Analysis of Heat Treated Steel Components;* ASM Int.: Materials Park, OH, 2008.
124. Totten, G.; Howes, M.; Inoue, T. *Handbook of Residual Stress and Deformation of Steel;* ASM International: Materials Park, OH, 2002.
125. Rudnev, V. Personal Communication with Professor George Krauss, July, 2012.
126. Rudnev, V. Metallurgical Insights for Induction Heat Treaters, Part 5: Super-Hardening Phenomenon. *Heat Treat Prog.* **September, 2008**, pp. 35–37.

12.16 Microstructures and Mechanical Performance of Induction-Hardened Medium-Carbon Steels

AB Nissan and KO Findley, Colorado School of Mines, Golden, CO, USA

12.16.1	**Fundamentals of Induction Hardening**	581
12.16.1.1	Overview of the Induction-Hardening Process	581
12.16.1.2	Hysteresis Losses, Eddy Currents, and Heat Transfer	583
12.16.1.3	Alloy Content and Carbon Content Selection of Induction-Hardened Steel	585
12.16.1.4	Review of Critical Induction-Hardening Parameters	586
12.16.2	**Rapid Austenitization and Hardenability of Steel Microstructures**	587
12.16.3	**Residual Stress and Its Effects on Mechanical Properties**	590
12.16.4	**Characterization of Induction-Hardened Components**	592
12.16.5	**Strength and Fatigue of Induction-Hardened Parts**	595
12.16.5.1	Estimation of Fatigue Crack Nucleation Location	598
12.16.5.2	Fatigue Fracture Surface Location and Morphology	600
12.16.6	**Industrial Standards Relevant to Induction Hardening**	602
12.16.7	**Summary and Conclusions**	603
Acknowledgments		603
References		603

12.16.1 Fundamentals of Induction Hardening

Induction hardening is quick and cost effective, and allows for repeatable high throughput of samples with a very reliable low maintenance setup, and it offers significant advantages over other surface-hardening methods. The short time between heating and quenching does not allow sufficient time for decarburization or significant grain growth of the steel, and there is little to no distortion of the part from the heat-treatment operation. Axisymmetric or near axisymmetric parts are ideal for induction hardening, but more complex geometries such as gears can also be induction hardened.

Induction hardening is different from other case-hardening methods in that there is no chemical change at the surface of the part after induction hardening, unlike surface-hardening treatments such as carburizing or nitriding. Instead, induction hardening relies exclusively on phase transformations to create a wear-resistant case and compressive residual stresses at the surface. The resulting martensitic case as well as the compressive residual stresses improves the wear and fatigue life of induction-hardened components significantly over nonhardened components.

Any metal can be induction hardened, but ferromagnetic materials (e.g., iron or steel) are especially responsive to induction hardening due to their ferromagnetic properties. Ferromagnetic materials respond well to induction heating because both hysteresis and eddy current losses can contribute to heating in a part, depending on the frequency of the induction-hardening operation (**Figure 1**). Low-alloy steel can be effectively induction hardened to produce substantial improvements in wear and fatigue performance without the addition of expensive alloying elements, and induction-hardening equipment is also very versatile in that it can be used for either case or through hardening heat treatments as well as selectively hardening critical regions.

12.16.1.1 Overview of the Induction-Hardening Process

The basic induction-hardening setup employs a water-cooled copper conductor that surrounds the workpiece. Copper coils are used to minimize resistive heating from the high alternating current, and the coil is water cooled to prevent melting due to the high-power input. Several examples of induction coil/workpiece configurations are shown in **Figure 2**. Induction-hardening configuration design is also versatile; for example, a single surface or just the inner diameter of a tube can be heated. Induction hardening can be conducted with scanning coils or multiturn coils.

Either single-shot (stationary) or scanning (progressive) induction-hardening processes are possible with the water-cooled copper coil configuration. Single-shot induction hardening is usually conducted with a multiple-turn coil where the coil and sample do not move relative to each other (**Figure 2(a)**). Scanning induction heating involves holding the sample stationary and moving the coil up or down the workpiece at a constant scan speed (**Figure 2(b)**). The main advantage of a scanning coil is that the power input to the workpiece is concentrated into a single coil, which can allow for faster heating rates and shallower case depths depending on the size of the power source available for hardening. Additionally, the scanning induction coils can have either an integrated quench ring (**Figure 3(a)**), which is incorporated into the coil and allows for immediate quenching of the material after heating, or an external quench ring separate from the scanning coil (**Figure 3(b)**), which allows for a greater flow rate of quenchant on the sample. Single-shot coils do not have integrated quench rings and instead rely on an external quench apparatus. The workpiece is constantly rotated during both single-shot and scanning induction of axisymmetric geometries to ensure even heating.

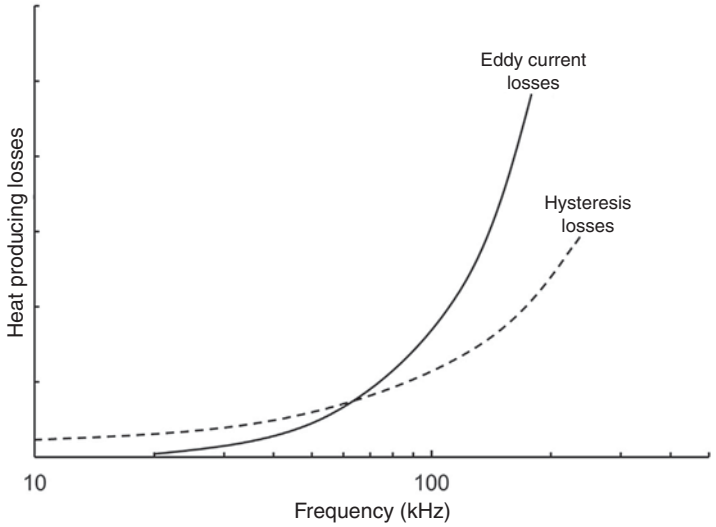

Figure 1 Heat contribution from eddy currents and hysteresis losses below the Curie temperature as a function of frequency. Adapted from Curtis, F. W. *High Frequency Induction Heating;* Lindsay Publications Inc.: Bradley, IL, USA, 1987.

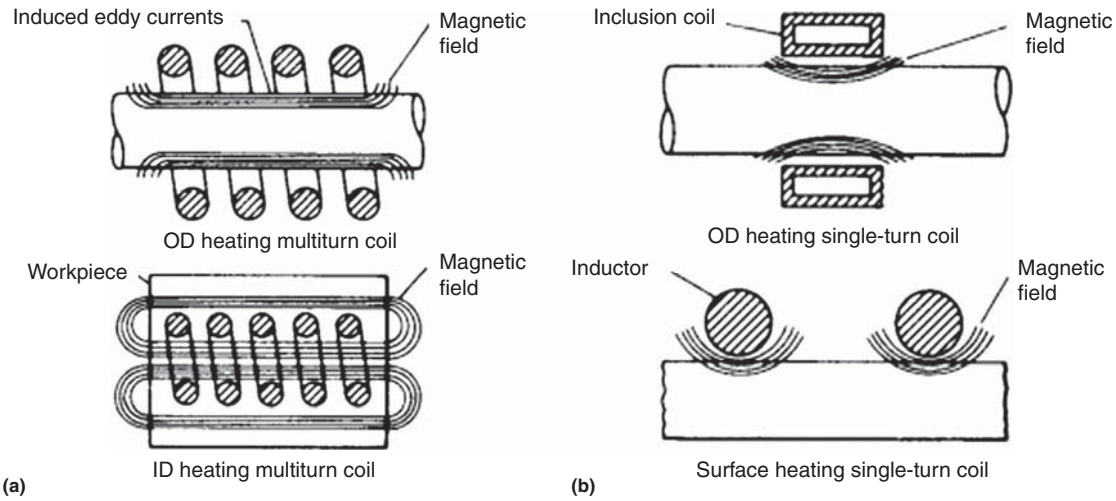

Figure 2 Typical induction coil to workpiece configuration for induction heating of (a) outer and inner diameter heating with multiturn coils and (b) outer diameter and surface heating with single turn coils. Reproduced from the Haimbaugh, R. E. *Practical Induction Heat Treating*; ASM International: Materials Park, OH, USA, 2001.

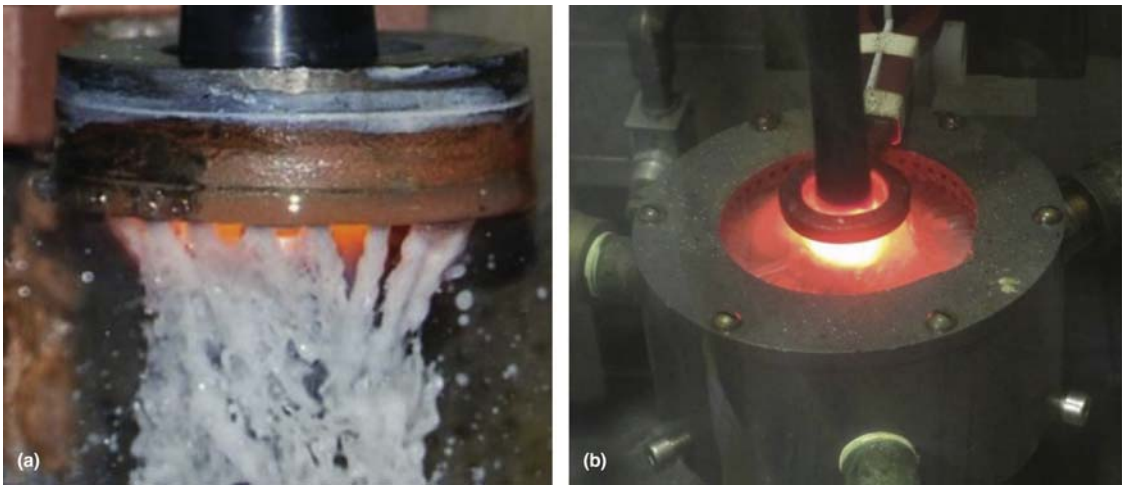

Figure 3 Scanning coil with (a) an integrated quench ring and (b) a separate quench ring.

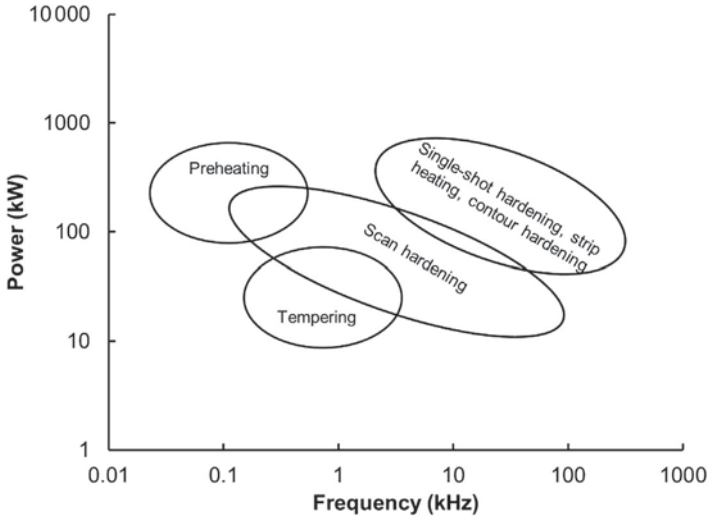

Figure 4 Typical frequency and power settings for different types of induction heating applications. Adapted from Semiatin, S. L.; Stutz, D. E. *Induction Heat Treatment of Steel;* American Society for Metals: Metals Park, OH, 1986.

The induction-hardening generator power and frequency specification varies by manufacturer and model but can range from 10 kW to 1 MW using alternating current at frequencies of 0.1 kHz to greater than 200 kHz. The power and frequency used depend on the desired case depth and on whether scanning or single-shot induction hardening is utilized (*2–5*) (**Figure 4**). As shown in **Figure 4**, single-shot hardening is usually conducted using higher power than scan hardening because the entire section to be hardened must be heated at once rather than progressively, which requires greater power. The frequency range at which scan hardening is conducted is also more variable than single-shot hardening, and the power input requirement decreases as the scan hardening frequency increases. During scan hardening, the penetration depth of magnetic induction decreases as the frequency is increased, which results in increased power densities (assuming power remains constant). Because of the increase in power density, less time is required for heating.

12.16.1.2 Hysteresis Losses, Eddy Currents, and Heat Transfer

Induction hardening is a complex interaction of both electromagnetic radiation and heat transfer. During the heating cycle, a ferromagnetic material (e.g., steel) is heated through both hysteresis and eddy current losses. Hysteresis losses dominate at frequencies less than approximately 60–70 kHz (*1*) and are caused by the rapid change of magnetic fields due to the alternating current in the induction coil. The changing magnetic field causes the domains in the ferromagnetic steel to rapidly change, which results in a hysteresis in the magnetization versus magnetic field strength behavior as shown in **Figure 5**. The magnitude of the power dissipated into the workpiece is the area encompassed within the hysteresis curve (*1–7*). As the frequency of the alternating

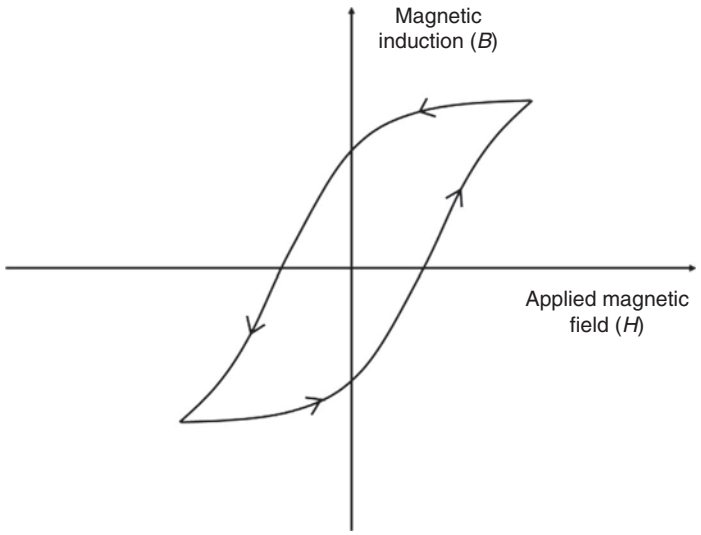

Figure 5 Typical hysteresis curve for a ferromagnetic material where *B* is the magnetic induction and *H* is the externally applied magnetic field.

current of the induction coil is increased, the hysteresis curve contracts until the forward and reverse responses are the same, and thus the power input from hysteresis losses decreases and is surpassed by eddy current losses.

Eddy current heating, also known as joule heating, is the primary form of heat input into a workpiece at frequencies greater than 70 kHz (*1*). Eddy currents are caused by local magnetization of the workpiece, which causes magnetic eddies to develop within the material. The eddies dissipate their energy into the surrounding material, resulting in heating of the workpiece. For thin sheets, assuming the magnetic field is uniform and the material is homogeneous, the power input into a workpiece due to eddy current losses is (*5*):

$$P = \frac{\pi^2 B_v^2 d^2 f^2}{6\rho D} \quad [1]$$

where B_v is the peak magnetic flux density, d is the thickness of the sheet, f is the frequency, ρ is the resistivity of the material, and D is the density of material. Thus, the power input into a workpiece increases with increasing frequency and magnetic field strength and decreases as the resistivity of the material increases.

Since the magnetic field during induction hardening of a ferromagnetic material is not uniform throughout the thickness of the part, the depth at which the majority of current and power are concentrated is referred to as the penetration depth or skin effect. The penetration depth, δ (m), is the distance from the surface into the workpiece at which the current is 37% and the power density is 14% of the current and power at the surface of the part (63% of the current and 86% of the power are contained in the penetration depth) (*7*). It can be predicted by (*8*):

$$\delta = \frac{1}{\sqrt{\pi f \mu_r \sigma}} \quad [2]$$

where f is the frequency (Hz), μ_r is the relative magnetic permeability (unitless), and σ is the electrical conductivity (S m^{-1}). The relative magnetic permeability is a ratio of the magnetic permeability (μ) of the material over the permittivity of free space (μ_o) and is given by (*9*):

$$\mu_r = \frac{\mu}{\mu_o} \quad [3]$$

Equation [3] can be approximated by:

$$\delta = \frac{500}{\sqrt{f}} \quad [4]$$

where δ is the penetration depth (mm) and f is the frequency (Hz); the equation may be applied for temperatures greater than 800°C (*10*). As a general rule of thumb for induction hardening of steel components, the penetration depth should be twice the desired case depth (*3*).

The induction-heating response of a ferromagnetic workpiece changes once the material passes through the Curie temperature, the temperature at which the material switches from ferromagnetic to paramagnetic behavior. In steel, the Curie temperature is 770 °C regardless of carbon content. Above the Curie temperature, the relative magnetic permeability becomes unity, and the

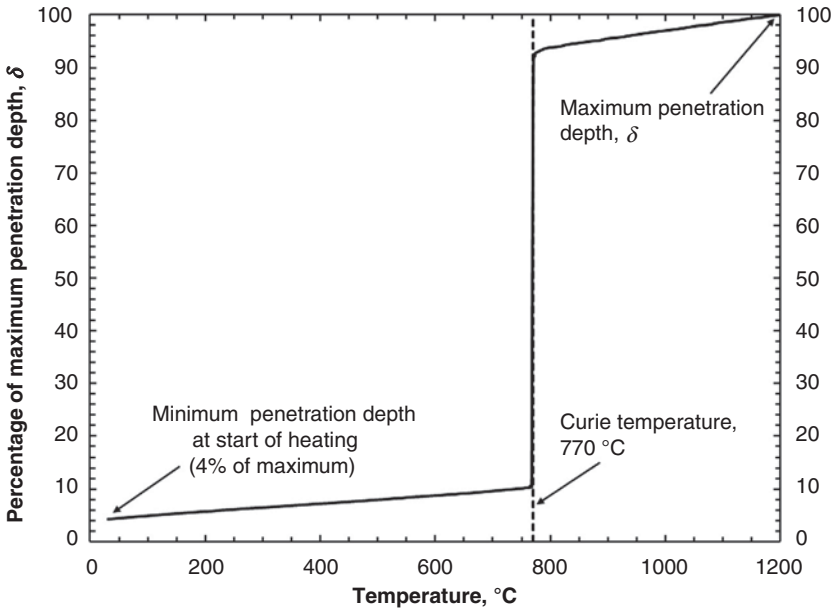

Figure 6 Penetration depth, δ, as a function of temperature for a plain carbon steel demonstrating the dramatic increase in penetration depth above the Curie temperature.

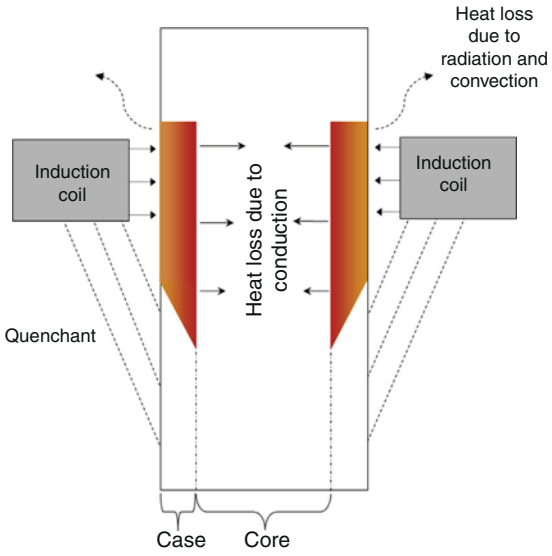

Figure 7 Scanning coil induction-hardening schematic demonstrating heat input from the induction coil as well as the heat losses from radiation, convection, and conduction.

penetration depth increases dramatically as shown in Figure 6, which plots the relative penetration depth compared to the maximum possible as a function of temperature. This increase in the penetration depth of the workpiece can result in overtempering of the core microstructure during hardening and longer heating times required for deep case depths because of more diffuse heating through the austenitized layer.

Adding to the complexity of induction hardening is that all three types of heat transfer occur during processing: conduction, convection, and radiation (Figure 7). Heat is constantly conducted from the hot surface to the cooler core, so additional heat input is required to achieve the desired temperature (such as the austenitization temperature). Furthermore, heat conduction into the interior can overtemper the microstructure at the case/core interface. Heat is also lost to the environment through radiation and, to a lesser extent, through convection. Heat loss is a major factor in determining the total heat input into the workpiece. During quenching, convection draws heat from the surface, and conduction draws heat to the surface. However, heat also conducts to the core of the workpiece until the surface of the workpiece is cooler than the core, at which point heat is then conducted from the warmer core to the cooler surface. The heat conduction processes can result in a small amount of auto-tempering of the workpiece in cases where the workpiece and case depth are sufficiently large.

12.16.1.3 Alloy Content and Carbon Content Selection of Induction-Hardened Steel

As previously stated, induction hardening, unlike other case-hardening methods, relies exclusively on the formation of martensite, with no composition change to produce a hard fatigue-resistant case and compressive residual stresses at the surface of the part. Increasing the strength of the case also increases the load-carrying capacity of the part in torsion. Because induction hardening relies on transformation of the case to martensite, carbon and alloy steels in the carbon content range of 0.4–0.5 wt. pct. C are especially suited for induction hardening to match the surface hardness expected from other surface-hardening processes (Figure 8). This carbon range allows for the high hardness (55–60 HRC) required for wear and fatigue resistance, but generally avoids the problems associated with higher carbon content steel such as quench cracking and quench embrittlement. Figure 9 shows that steels with carbon content greater than 0.5 wt. pct are susceptible to quench embrittlement, where the part becomes susceptible to brittle intergranular fracture due to cementite formation and phosphorus at prior austenite grain boundaries. However, carbon and alloy steels with carbon content outside of the 0.4–0.5 wt. pct. range are commonly used in industrial induction-hardening processes. If lower carbon steel is used, then a lower surface hardness and resulting wear resistance must be accepted. If a higher carbon content is used ($C > 0.55$ wt. pct.), precautions should be taken to ensure that quench cracking and quench embrittlement at the surface do not occur.

Plain carbon steels (i.e., 10xx series) have a limited amount of hardenability. Hardenability is the depth or maximum diameter where a 50% martensitic microstructure can be achieved; it is expressed as an ideal diameter and can be calculated for any alloy content using ASTM A255-10 'Standard Test Methods for Determining the Hardenability of Steel' (*8*). The use of alloying elements such as Ni, Mo, Mn, and Cr increases the hardenability of steel. By increasing the hardenability of an alloy, greater case depths can be achieved. In addition to alloying to improve hardenability, microalloy additions of Nb, V, Al, and Ti can be used to form carbides and nitrides that retard grain growth during the austenitizing process and improve the tempering response of the material, which may improve mechanical performance (*11*,*12*).

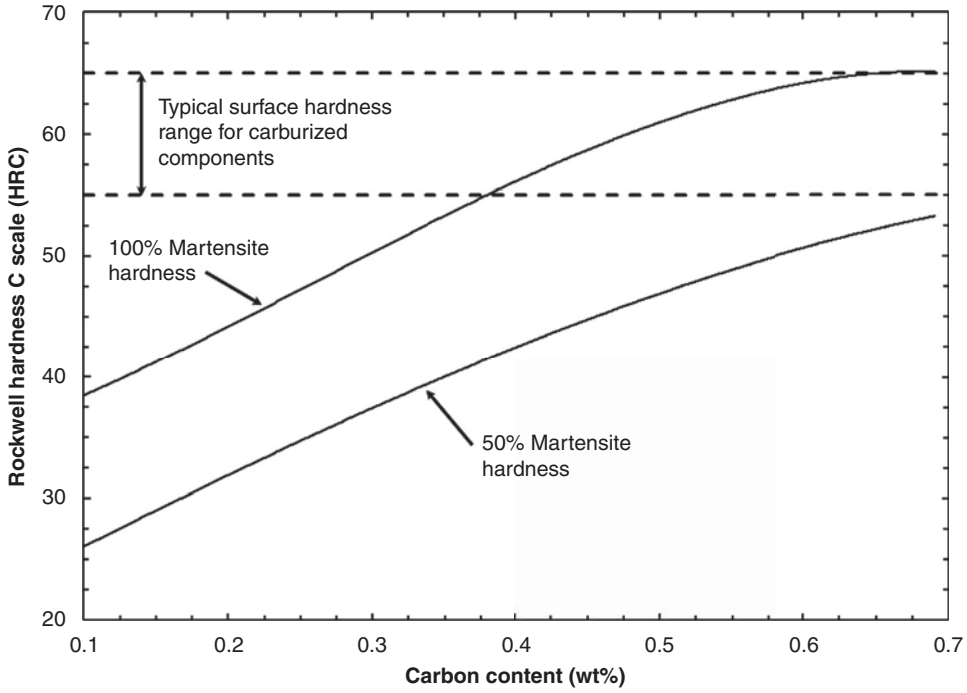

Figure 8 Hardness range for steel with different carbon contents as well as the typical hardness range for carburized components (reproduced from the *ASTM Standard A255-10, Standard Test Methods for Determining Hardenability of Steel*; ASTM International: West Conshohocken, PA, USA, reprodued from the Abbaschian, R.; Abbaschian, L.; Reed-Hill, R. R. Physical *Metallurgy Principles*, 4th ed.; Cengage Learning: Stamford, CT, 2009, Reprodued From the Kalpakjian, S.; Schmid, S. R. Manufacturing Engineering and Technology; Prentice Hall: Upper Saddle River, NJ, 2001).

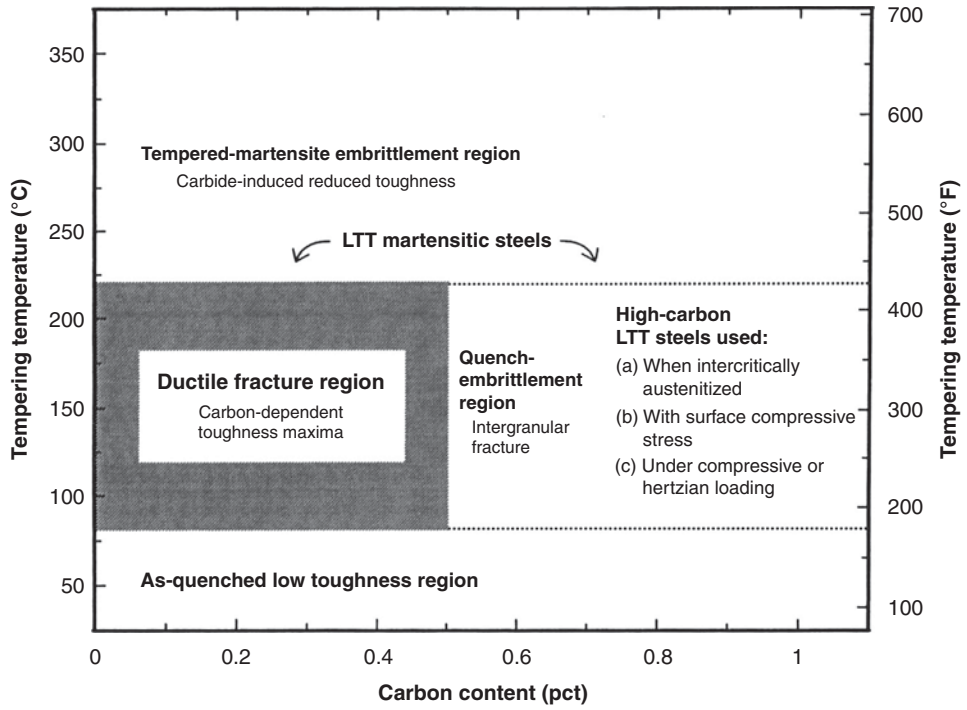

Figure 9 Schematic showing the ductile fracture region and quench-embrittlement regions as a function of tempering temperature and carbon content (reproduced from the Krauss, G. *Steels: Processing, Structure and Performance*; ASM International: Materials Park, OH, USA, 2005.).

12.16.1.4 Review of Critical Induction-Hardening Parameters

The main parameters, excluding workpiece geometry, that determine the depth and speed of heating of a given workpiece are the alternating current frequency, alternating current power, scan speed (scanning coil), dwell time (single shot coil), type of quenchant,

and coil configuration. During processing, frequency, power, and scan speed/dwell time are the quickest and least costly to change to achieve the desired case depth. However, depending on the induction-heating system frequency, power or scan speed may be fixed.

Frequency: As shown in eqns [2] and [4], frequency adjustment allows for changes in the penetration depth, δ, of the workpiece. For relatively thin workpieces, a higher frequency must be used to prevent through hardening of the material. The frequencies of induction-hardening machines are generally broken into three categories: low frequency (<10 kHz), medium frequency (10–70 kHz), and high frequency (>70 kHz) (*7*). The high-frequency range is also termed 'radio frequency.' Medium- and high-frequency are used the most often for surface hardening of steel components.

Power: A range of power settings can be used for induction hardening, from as low as 10 kW to over 1 MW of power. If, for example, more power is imparted to the workpiece, the heating rates within the skin depth region at a given frequency will be increased.

Scan speed/dwell time: If the frequency and power are held constant, changing the scan speed/dwell time can change the temperature distribution and resulting case depth within the workpiece. Increasing the scan speed may be required to prevent melting of the sample and to decrease the case depth. Lowering the scan speed may be desired if the microstructure in the workpiece does not transform readily to austenite upon heating and requires greater heat input (e.g., spheroidized microstructure).

Quenchant: A wide variety of quenchants are available in liquid (water, oil, or polymer) and gas (N, He, Ar, etc) form. Each of these media provides different levels of heat extraction at the surface of the part. Care must be taken to select a quenchant that is severe enough to form martensite at the desired case depth but not too severe as to cause quench cracking at the surface of the workpiece. For alloys with a carbon content and/or hardenability, a less severe quenchant should be utilized. Polymer-based quenchants are popular in induction-hardening applications because the percentage of polymer can be tuned to adjust the severity of the quench to the necessary level.

Coil configuration: The design of induction coils is outside the scope of this chapter, but excellent descriptions on coil design, configuration, and troubleshooting of induction coils can be found in Ref. (*2*,*3*,*7*).

Tempering conditions: The final hardness of the induction-hardened part after processing is a function not only of carbon content but also of the use of tempering after processing. A typical tempering operation after induction hardening is 176°C for one to one and a half hours. If a higher tempering temperature is used, then the surface hardness of the part will decrease, but the toughness of the case region will also increase. Because the highest possible wear and fatigue resistance in the case is generally desired, the 176°C temper is often utilized. It should be noted that independent of the tempering temperature, all induction-hardened parts should be tempered within 4 h of induction hardening in accordance with the Society of Automotive Engineers standard SAE AMS2745 (*16*).

12.16.2 Rapid Austenitization and Hardenability of Steel Microstructures

In order to form a martensitic case microstructure during induction hardening, the case microstructure must first be transformed to austenite before quenching. Induction hardening is a unique heat treatment in that the heating cycle is very short, so the extent of austenitization upon heating and at the brief hold at peak temperature is strongly dependent on the starting microstructure. Austenite can nucleate at ferrite grain boundaries, adjacent to spheroidized carbides, or within pearlite colonies; Figure 10 schematically shows nucleation of the austenite grains during heating at these various sites. Since austenite has a much higher solubility for carbon, nucleation near carbon-rich regions such as cementite is favorable. Growth of the austenite grain into the pearlite is very rapid due to the abundance of carbon from the cementite and the correspondingly short diffusion distances between carbon-rich regions in the interlamellar ferrite. Figure 11 demonstrates how austenite can nucleate at pearlite colony boundaries or at cementite lamellae at an initial time t_1; the austenite grains are denoted A_1, A_2, and A_3. Due to the slow dissolution of carbides, multiple austenite grains can nucleate within the same pearlite colony. The schematic at t_2 shows that austenite growth is more rapid at the pearlite colony boundary (*17*). If, however, the austenite is to grow into pro-euctectoid ferrite, carbon must diffuse from the cementite, which results in much slower austenite growth.

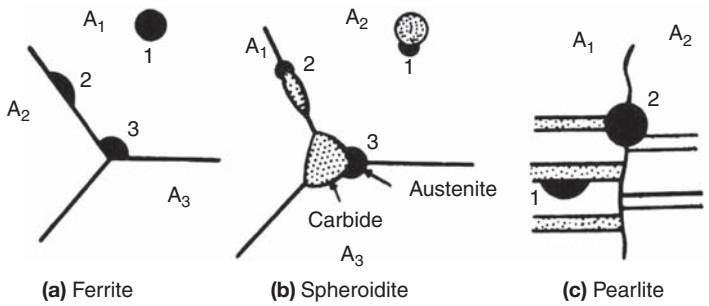

Figure 10 Austenite nucleation sites in (a) ferrite, (b) spheroidite, and (c) pearlite (reproduced from the Krauss, G. *Steels: Processing, Structure and Performance*; ASM International: Materials Park, OH, USA, 2005).

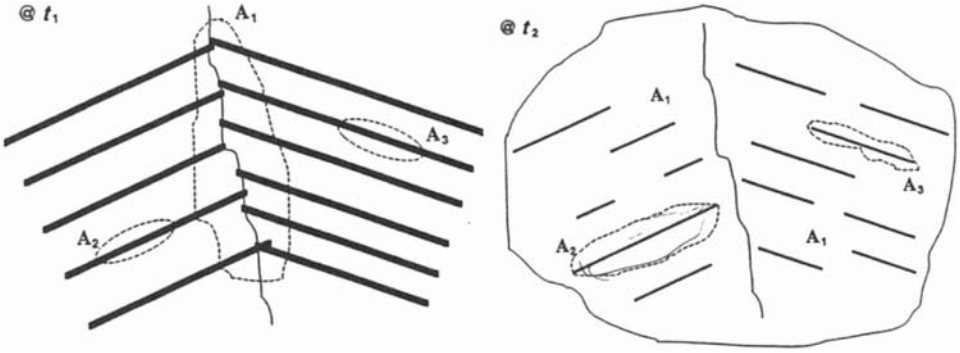

Figure 11 Austenite nucleation at the start of the nucleation and growth process in a pearlite colony (left schematic), and later within the austenite grain at remaining carbides (reproduced from the Speich, G. R.; Szirmae, A.; Richards, M. J. Formation of Austenite from Ferrite and Ferrite-Carbide Aggregates. *Trans. Metall. Soc. AIME* **1969**, *245*, 1063–1074).

Table 1 Prior microstructure, maximum surface hardness, and case depth for induction-hardened 1541 and 4140 alloys in which scan speed, power, and frequency were held constant and only prior microstructure and alloy were changed (*18*)

Prior microstructure	*Alloy*	*Max. hardness after processing, HRC*	*Case depth (50 HRC), mm*	*Surface axial residual stress, MPa*
Spheroidized	1541	55–56	1.42	−550
	4140	52–53	0.41	−550
Ferrite + spheroidized pearlite	1541	56–57	2.03	−350
	4140	57–58	1.42	−420
Ferrite + coarse pearlite (small PAGS)	1541	56–57	2.13	−400
	4140	56–57	1.02	−490
Ferrite + coarse pearlite (large PAGS)	1541	56–57	1.73	−240
	4140	57–58	1.32	−290
Quenched and tempered martensite	1541	58–59	2.74	−350
	4140	58–59	2.84	−290
As-quenched martensite	1541	58–59	3.35	−260
	4140	58–59	2.80	−310

Because diffusion is sluggish compared to the short heating time during induction hardening, an ideal microstructure would have evenly distributed carbon or a fine dispersion of carbides throughout the microstructure to allow for rapid austenitization. Table 1, taken from the work of Coryell (*18*), provides example results for the effects of alloy type and starting microstructure on the induction-hardening response. Coarse spheroidized microstructures are the slowest and least responsive to induction hardening, and as-quenched martensite responds the best to induction hardening followed by quenched and tempered martensite (*18*). Carbon is supersaturated and relatively well dispersed in as-quenched martensite and forms fine carbides upon tempering that are readily dissolved during heat treatment. Table 1 also shows that the alloy with the higher hardenability, 1541, has a higher case depth for every condition.

If the carbides within an austenite grain do not entirely dissolve during induction processing, the austenite is considered inhomogeneous. The lower carbon content of the austenite reduces the propensity for quench cracking and quench embrittlement for steels with carbon contents greater than 0.5 wt. pct. (*15*). However, if too many carbides remain in solution, the surface hardness of the induction-hardened part may be lowered. Because fully homogeneous austenite would require an almost infinite amount of time to form, austenite is considered homogeneous even if very small carbides are present.

Besides microstructure, the extent of austenitization depends on heating rate and induction process temperature. During furnace heat treating, an equilibrium Fe–C phase diagram can generally be used to determine the critical temperatures for the ferrite + austenite, A_{c1}, and austenite, A_{c3}, phase fields because the time required to reach these temperatures in a furnace are relatively sluggish. However, heating rates can be in excess of $1000\,^{\circ}C\,s^{-1}$ during induction hardening, so the influence of transformation kinetics on the critical transformation temperatures must be considered. At these high heating rates and short hold times at peak temperature, diffusion is very limited due to the short time at temperature. The A_{c3} temperature can increase by 100–300 °C from the equilibrium A_{c3} temperature. The effect of heating rate is illustrated in Figure 12, which plots the A_{c3} temperature as a function of heating rate in 1042 steel for three different starting heat-treatment conditions: annealed, normalized, and quenched and tempered (*6*). The A_{c3} temperature increases with heating rate for all three conditions, and as described previously, the microstructure with the most homogeneous distribution of carbon, the quenched and tempered condition, transforms more readily

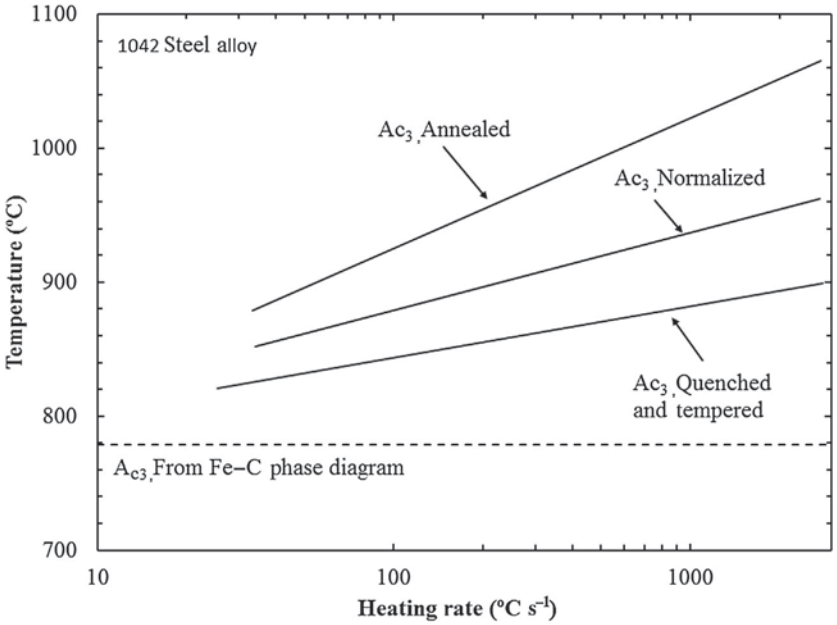

Figure 12 Differences in A_{c3} temperature for a 1042 steel alloy with three different starting microstructures at different heating rates compared to the A_{c3} temperature from the Fe–C phase diagram. Replotted from Semiatin, S. L.; Stutz, D. E. *Induction Heat Treatment of Steel;* American Society for Metals: Metals Park, OH, 1986.

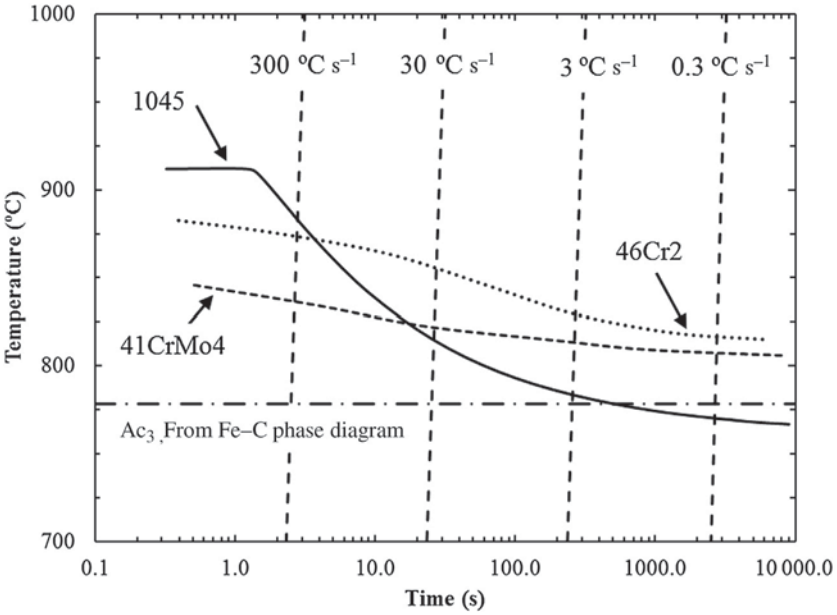

Figure 13 Effect of heating rate and alloy composition on the A_3 temperature. Replotted from Orlich, J.; Rose, A.; Wiest, P. *Atlas zue Wärmebehandlung der Stähle – Band 3, Zeit-Temperatur-Austenitisierung-Schaubilder;* Verlag Stahliesen: Düsseldorf, Germany, M.B.G.,1973.

(at lower temperatures) to austenite. Similarly, a time–temperature-austenitizing diagram is plotted in **Figure 13** for three medium-carbon steels that were induction heated at several heating rates. The critical temperature increases with increasing heat rate for all three alloys.

During induction hardening, the heating rates are high and the quench rates can be extremely high, so induction-hardened components undergo a phenomenon termed *superhardness* (*15*). This phenomenon is associated with refinement of the austenite grains during heating due to the very short time at austenitizing temperatures. The newly formed fine-grained austenite is then quenched very rapidly to form very hard martensite. Induction processing can result in a 1–5 HRC increase in hardness compared to the martensite hardness expected for a given carbon content (**Figure 14**).

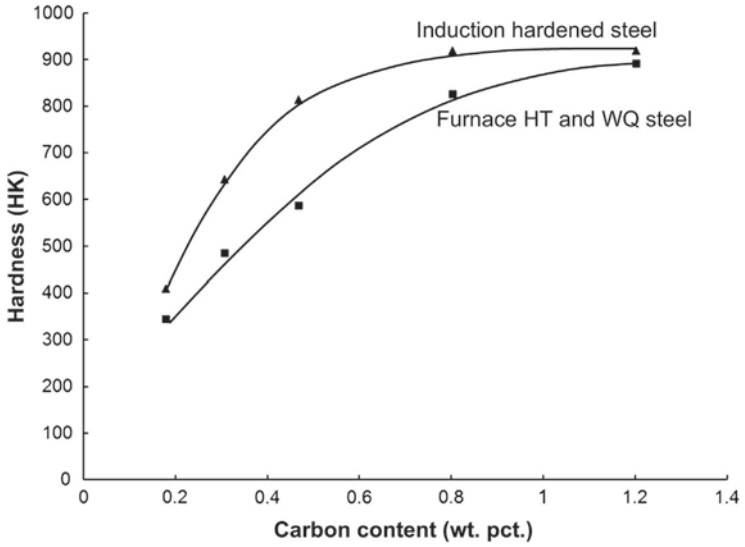

Figure 14 Hardness as a function of carbon content at the surface of induction-hardened plain carbon steels compared to the same steels subjected to furnace heat treatments (HT) and water quenching (WQ). Superhardness is observed at the surface of induction-hardened components compared to the HT and WQ steels. Adapted from Hassell, P. A.; Ross, N. V. Induction Heat Treating of Steel. In *ASM Handbook;* Vol. 4, Heat Treating, 1991.

12.16.3 Residual Stress and Its Effects on Mechanical Properties

Residual stresses can be beneficial or detrimental, depending on the residual stress profiles in the material after final processing. If the residual stresses at the surface are tensile, they are considered detrimental to the fatigue and most other mechanical properties of a component. If, however, the residual stresses at the surface of the part are compressive, the residual stresses are considered beneficial. Induction hardening generally produces a favorable residual stress profile that is compressive at the surface and tensile in the core (*21*).

Compressive stresses arise at the surface of induction-hardened parts for the following reasons:

1. Residual stresses occur after induction processing primarily due to the volume difference between austenite, ferrite, and martensite (**Figure 15**). The larger the volume change upon the decomposition of austenite (e.g., formation of martensite, pearlite, etc.), the greater the tensile or compressive residual stresses. **Figure 16** shows a schematic cooling profile of an

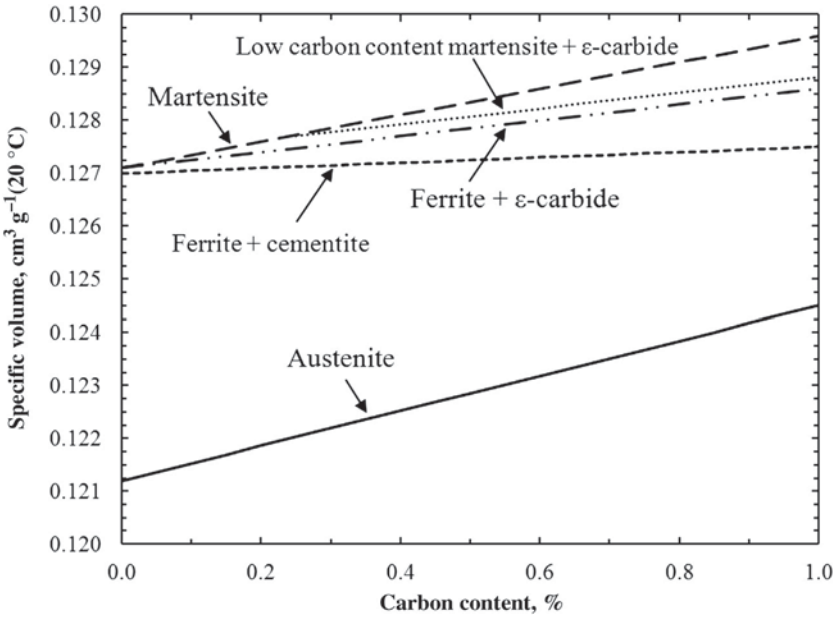

Figure 15 Specific volume of steel phases as a function of carbon content for a tool steel (reproduced from the Totten, G., Ed. *Steel Heat Treatment Handbook*; Marcel Dekker, Inc.: New York, USA, 1997).

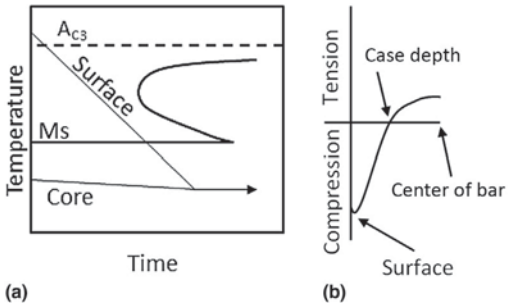

Figure 16 Example (a) CCT diagram demonstrating the cooling profile from the surface and the core of the samples and (b) the resulting residual stress profile after quenching.

induction-hardened part superimposed on a continuous cooling transformation (CCT) diagram. The outside (case) of a part transforms to austenite during induction processing, but the majority of the core microstructure is not heated to a temperature that allows for partial or full austenitization. Upon cooling, the surface of the part undergoes a phase transformation to martensite, which also involves volume expansion, while the core does not undergo a phase transformation. Thus, the volume expansion due to the phase transformation at the surface of the part results in residual compressive stresses, and the core is subjected to residual tensile stresses. Phase transformations have the largest effect on the residual stress distribution during induction processing.

2. During quenching, the surface of the part cools more rapidly and thus contracts more than the core, which initially results in residual tensile stresses at the surface and compressive stresses in the core. However, upon further cooling, the core begins to cool more rapidly and contracts more than the surface, and the residual stress profile flips so that the surface goes into compression and the core is under tension.

Many techniques such as X-ray diffraction (XRD) (*22,23*), neutron diffraction (*24*), the contour method (*25*), and the slitting (crack compliance) method (*26*) have been developed to determine residual stresses in a component. Of these four techniques for residual stress determination, XRD is the most common. The depth profile is accomplished by chemical polishing or machining with chemical polishing into the surface of the sample and retaking measurements at each target depth.

Residual stress is calculated from XRD results based on the deviation of the crystal lattice from the unstressed state. The interatomic spacing (d) of the lattice increases due to tensile residual stresses and decreases due to compressive stresses. The d-spacing is calculated from Bragg's law (*9*):

$$\lambda = 2d \sin \Theta \qquad [5]$$

where λ is the wavelength of the characteristic X-ray radiation, d is the interplanar spacing, and Θ is the angle between the incident beam (X-ray source) and the horizontal axis or the angle between the diffracted beam and the horizontal axis.

Although Bragg's law can be used to obtain residual stress values, the preferred method is the $\sin^2 \psi$ method (*23*). This method utilizes a single theta angle and relies on rotation of the sample relative to the X-ray source and detector. Using a Cr–Kα target, the ideal 2-theta angle for ferrous alloys is 156° (d-spacing of 0.117 nm (*23*)). Several ψ angles, the rotation angle of the specimen relative to the X-ray beam (**Figure 17**), are then selected such as 0, 20, 29, and 36.3, which corresponds with $\sin^2 \psi$ values of 0, 0.1170, 0.2340, and 0.3505, respectively (*23*). These angles are considered ideal because they are uniformly spaced as $\sin^2 \psi$ values.

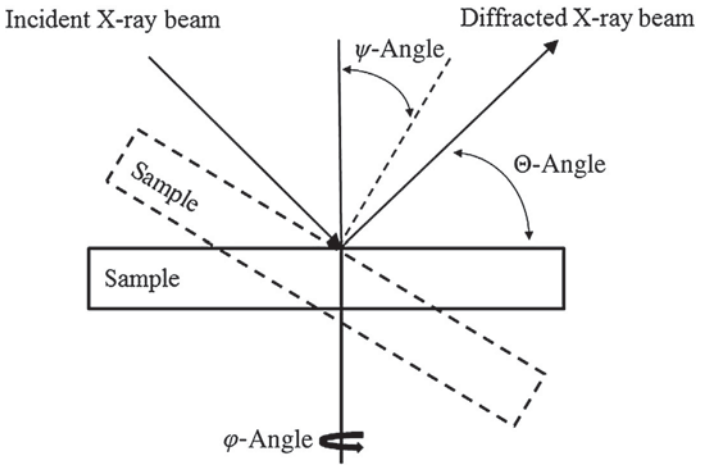

Figure 17 Schematic showing the basic geometry for stress measurements by XRD. Adapted from *Residual Stress Measurement by X-ray Diffraction;* 2003 ed., SAE International: Warrendale, PA, USA, 2003.

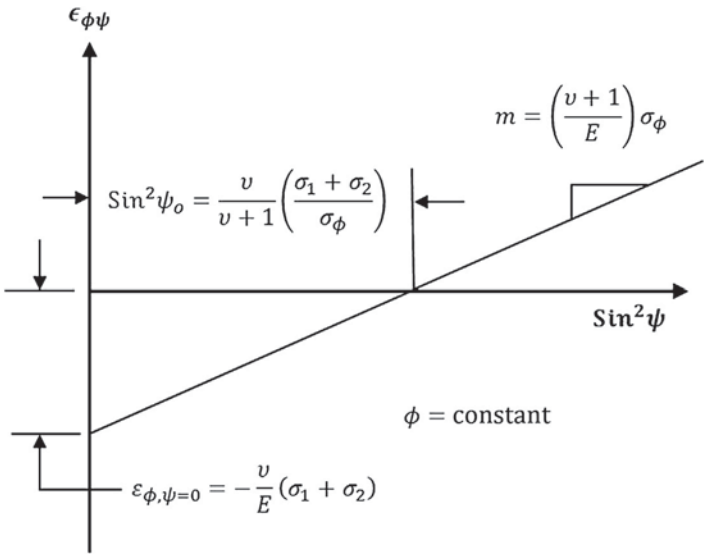

Figure 18 $\mathrm{Sin}^2\,\psi$ method of determining residual stress. Adapted from *Residual Stress Measurement by X-ray Diffraction;* 2003 ed., SAE International: Warrendale, PA, USA, 2003.

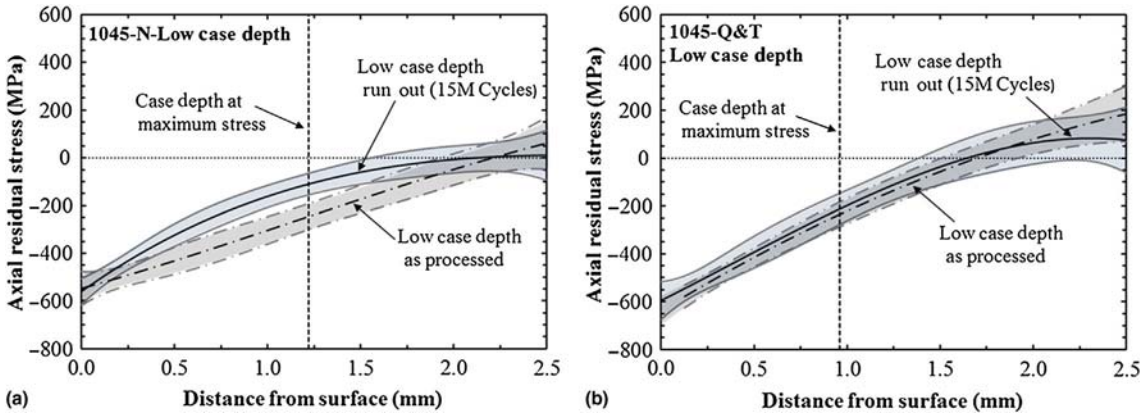

Figure 19 Residual stress profiles in induction-hardened 1045 steel fatigue specimens before fatigue testing and after fatigue testing for 15 million cycles at the endurance limit. Residual stress data are for bars that were initially (a) normalized and (b) quenched and tempered before induction hardening. For each residual stress profile, the best fit line and the 99% confidence interval are shown (reproduced from the Nissan A. B. The Effect of Microstructure and Induction Processing on Fatigue Performance and Crack Initiation of Induction Hardened Bar Steel. Ph.D. Dissertation, Colorado School of Mines, Golden, CO, USA, 2012).

The strain ($\varepsilon_{\varphi\psi}$) at each of the $\sin^2\psi$ values is then measured while holding φ and θ constant (Figure 17). These values are then plotted as shown in Figure 18. The two principal stresses, σ_1 and σ_2, can be determined by graphing $\sin^2\psi$ versus $\varepsilon_{\varphi\psi}$ and with the knowledge of Poisson's ratio (υ) and the elastic modulus (E) for the material of interest, as shown in Figure 18 (*23*). Using elasticity equations, the third principal stress, σ_3, can also be determined.

During cyclic loading, plastic deformation of the part results in relaxation of the residual stresses (*27–29*). For example, Figure 19 shows the residual stress profile generated in a medium-carbon steel, induction hardened from two different starting microstructures, immediately after induction processing and after fatigue cycling at the endurance limit. The two starting microstructures of the steel were normalized ferrite-pearlite and quenched and tempered martensite. Some relaxation of the residual stress was observed in the 1045 normalized condition, likely because the core microstructure undergoes some plastic deformation even at stresses as low as the endurance limit. However, the 1045 quenched and tempered condition, which is not as susceptible to plastic deformation due to its high strength, exhibited little to no relaxation of the residual stresses. It is expected that after fatigue cycling at stresses much greater than the endurance limit (low cycle regime), a significant amount of residual stress relaxation will occur.

12.16.4 Characterization of Induction-Hardened Components

Characterization of the workpiece after induction hardening is critical to determine whether the power, frequency, and scan rate settings are correct for the target induction-hardened depth. The quickest method to determine the case depth is to section the part,

Table 2 Macro and micro etchants to determine visually the effective case depth after induction hardening

Type of etchant	*Recipe*	*Description*	*Figure*
Macro	10 ml nitric acid (HNO_3) 90 ml ethanol	Good etching response to distinguish case and core regions	**(Figure 20a)**
Macro	10 ml hydrochloric acid (HCl) 90 ml ethanol	Adequate etching response between case and core	**(Figure 20b)**
Micro	2 ml nitric acid (HNO_3) 98 ml ethanol	Adequate etching response between case and core	**(Figure 20c)**
Micro	4 g picric acid (HNO_3) 100 ml ethanol	Good delineation of the case/core transition region	**(Figure 20d)**

rough grind (i.e., 320 grit SiC paper), and etch with any of the solutions listed in Table 2. The etchants attack the case martensite microstructure differently than the core, so the case depth can be measured with a Brinell scope or stereo microscope. Examples of etching with each of the solutions are shown in Figure 20 on an induction-hardened medium-carbon steel bar. For this alloy, the 10% nitric, 90% ethanol solution is the most effective at discerning the case and core. It should be noted that even though the macro etch reveals the case and core due to differences in microstructure, the most accurate method of determining the case depth is by microhardness measurements on a polished cross section.

Either Vickers or Knoop microhardness measurements may be employed to measure the case depth. Determination of the case depth by hardness requires more surface preparation than the visual method; a final 1 μm diamond polish is necessary to minimize variations in measurements. The highest load possible should be used for the hardness measurements in accordance with ASTM E384-11 'Standard Test Method for Knoop and Vickers Hardness of Materials' (*31*).

The microhardness profile indicates useful information about induction-hardening processing such as the extent of transformation and excess heating of the microstructure in the case/core transition region. An ideal induction-hardened microhardness traverse is shown in the schematic in Figure 21(a). When the case is fully transformed to martensite (i.e., it was fully transformed to austenite before quenching), the hardness is constant in the case region, as shown in Figure 21(a). There is also a relatively abrupt

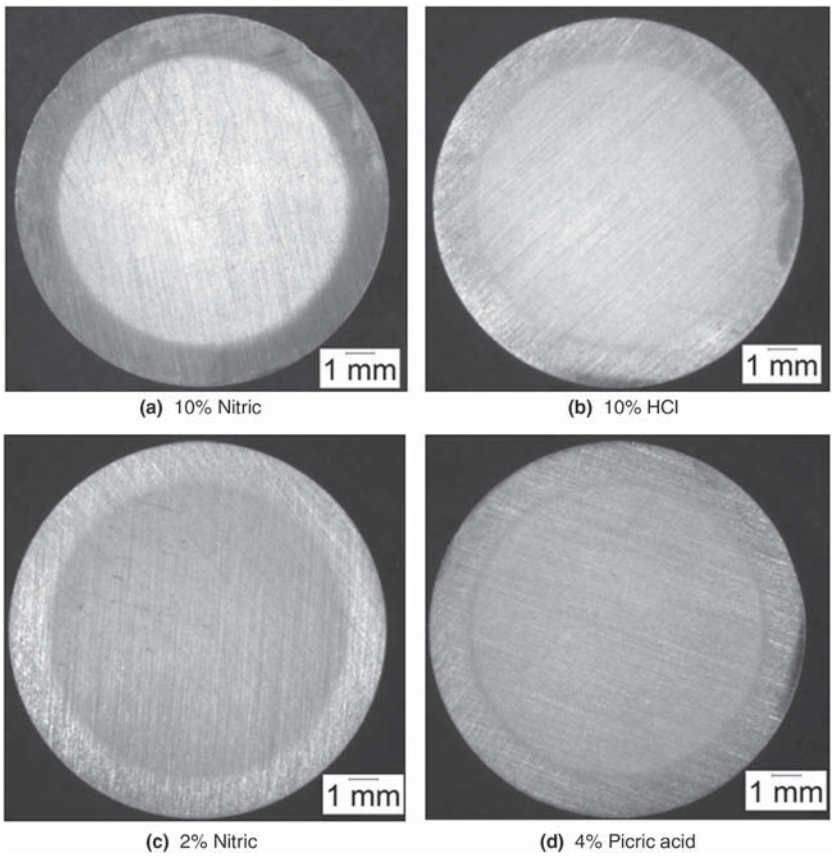

Figure 20 Macroetching response of an induction hardened shafts to (a) 10% nitric acid in ethanol, (b) 10% hydrochloric acid in ethanol, (c) 2% nitric acid in ethanol, and (d) 4% picric acid in ethanol.

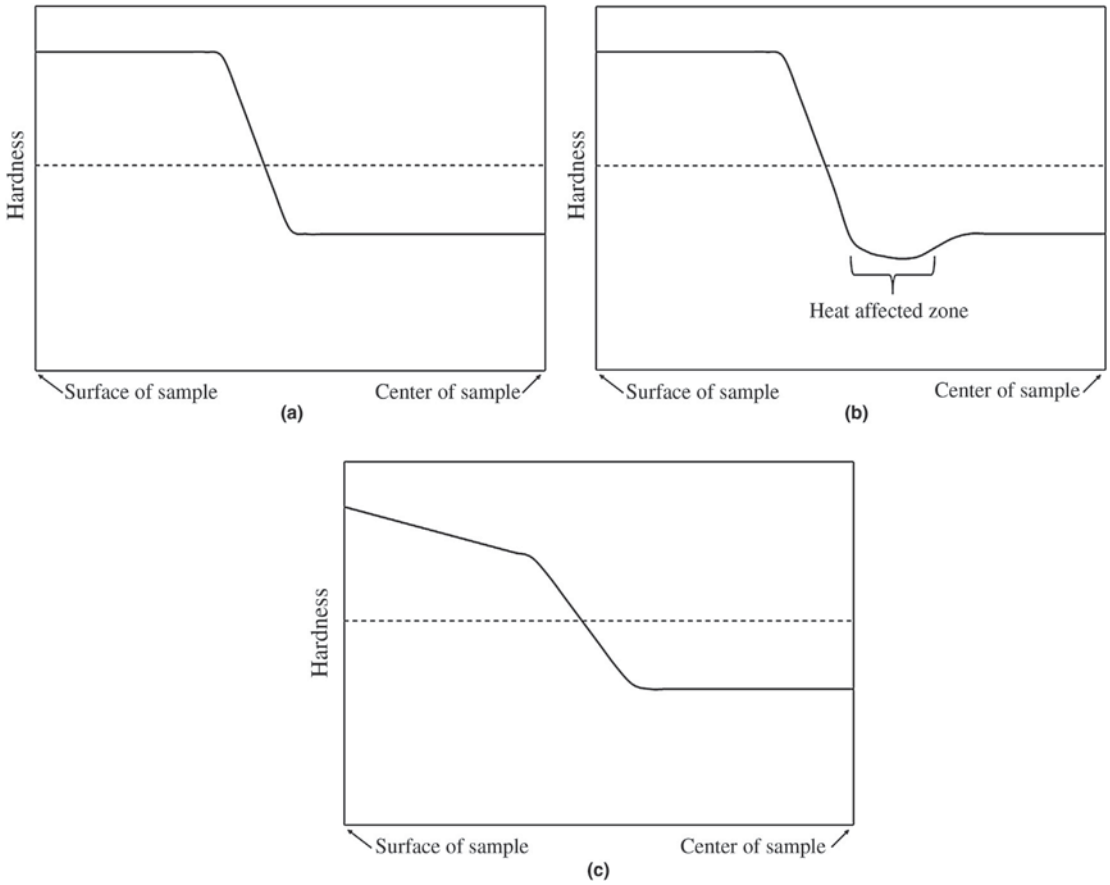

Figure 21 Microhardness profiles for determination of effective case depth. An ideal hardened profile is shown in (a), an ideal hardened profile with a heat-affected zone is shown in (b), and (c) demonstrates incomplete austenitization of the parent microstructure in the case during hardening.

case/core transition region, and the hardness at the end of the transition region of the case–core interface is near the hardness of the core microstructure. Tempered martensite core microstructures are susceptible to overtempering during induction processing, which results in decreased hardness at the end of the case–core interface transition region as shown in **Figure 21(b)**. If austenitization of the parent microstructure is not completed during induction processing, then a downward slope in hardness would be observed in the case as well as a lengthy case/core transition region (**Figure 21c**). The surface hardness is similar in both **Figures 21(a) and 21(c)**, but the case hardness profile in **Figure 21(a)** is more desirable; thus, surface hardness measurements may not be sufficient to evaluate the effectiveness of induction heat treatments.

The effective case depth by microhardness can be easily acquired after the hardness traverse is plotted similar to **Figure 21**. It is common in industry to define the effective case depth as the distance from the surface to the location that hardness falls below 50 HRC. However, this definition does not take into account carbon content. A more comprehensive definition of effective case depth is found in JIS G0559 "Steel – Determination of case depth after flame hardening or induction hardening" (*32*), which defines the effective case depth as:

● 0.23–0.33 wt. pct. C	350 HV (36 HRC)
● 0.34–0.43 wt. pct. C	400 HV (41 HRC)
● 0.44–0.53 wt. pct. C	450 HV (45 HRC)
● 0.54 wt. pct. C and greater	500 HV (49 HRC)

After microhardness measurements, the polished samples should be etched to observe the extent of microstructural transformation during hardening. For example, **Figure 22** shows the microstructure from an induction-hardened part that did not fully austenitize in the case during processing. Small ferrite grains are visible in the case region, and the volume fraction of ferrite is higher as the depth increases. The parent microstructure was composed of ferrite and pearlite. The partial transformation could be due to

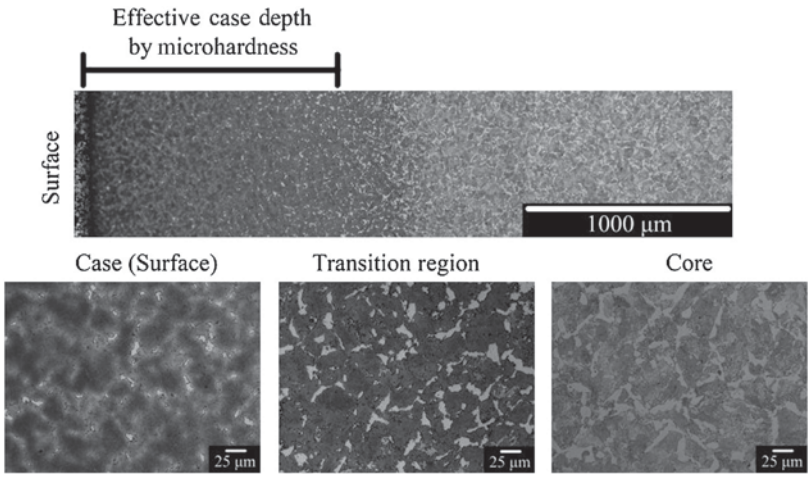

Figure 22 Optical micrographs of the microstructural gradient from the surface (left) to the core (right) of an induction-hardened 1045 normalized condition with higher magnification images of the case, transition, and core regions, 4 pct. picric acid in methanol. Note the retained ferrite at the surface of the part (reproduced from the Nissan A. B. The Effect of Microstructure and Induction Processing on Fatigue Performance and Crack Initiation of Induction Hardened Bar Steel. Ph.D. Dissertation, Colorado School of Mines, Golden, CO, USA, 2012).

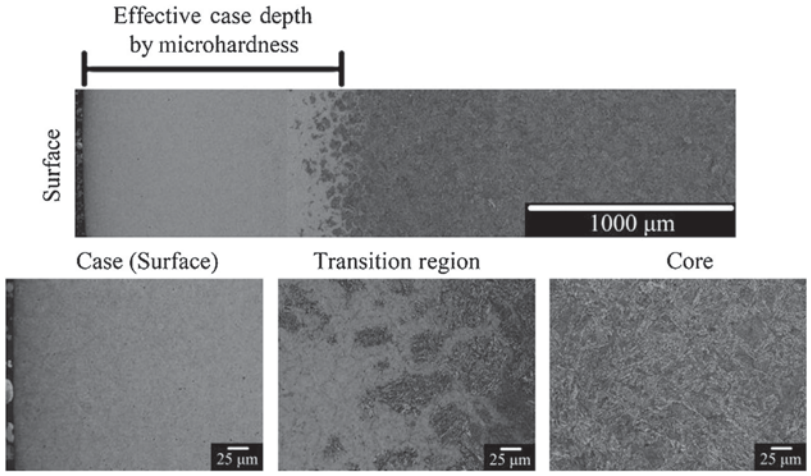

Figure 23 Optical micrographs of the microstructural gradient from the surface (left) to the core (right) of a 4145 as-hot rolled condition with higher magnification images of the case, transition, and core regions, 4 pct. picric acid in methanol (reproduced from the Nissan A. B. The Effect of Microstructure and Induction Processing on Fatigue Performance and Crack Initiation of Induction Hardened Bar Steel. Ph.D. Dissertation, Colorado School of Mines, Golden, CO, USA, 2012).

either insufficient temperature or time at temperature. The transformation kinetics could be aided through a normalizing heat treatment followed by a forced air cool to reduce the ferrite grain size in the parent microstructure. Figure 23, on the other hand, demonstrates a fully martensitic microstructure in the case, which means the case was fully austenitized during induction processing. There is also an abrupt transition from the case to the core microstructure, which is indicative of a good induction-hardening operation.

The iterative steps to determine if a part has been induction hardened properly are:

- Macro etch to observe the extent of transformation.
- Microhardness to determine the true effective case depth.
- Microstructural analysis to ensure that full transformation of the parent microstructure occurred.

12.16.5 Strength and Fatigue of Induction-Hardened Parts

The torsional, axial, and bending load-carrying capacity of components can be increased by induction hardening. This concept is illustrated in Figures 24(a) and 24(b), which are schematic plots of applied torsional stress and effective torsional strength as a function of depth from the surface of a case-hardened bar. Microhardness values can be converted to torsional yield, tensile, or

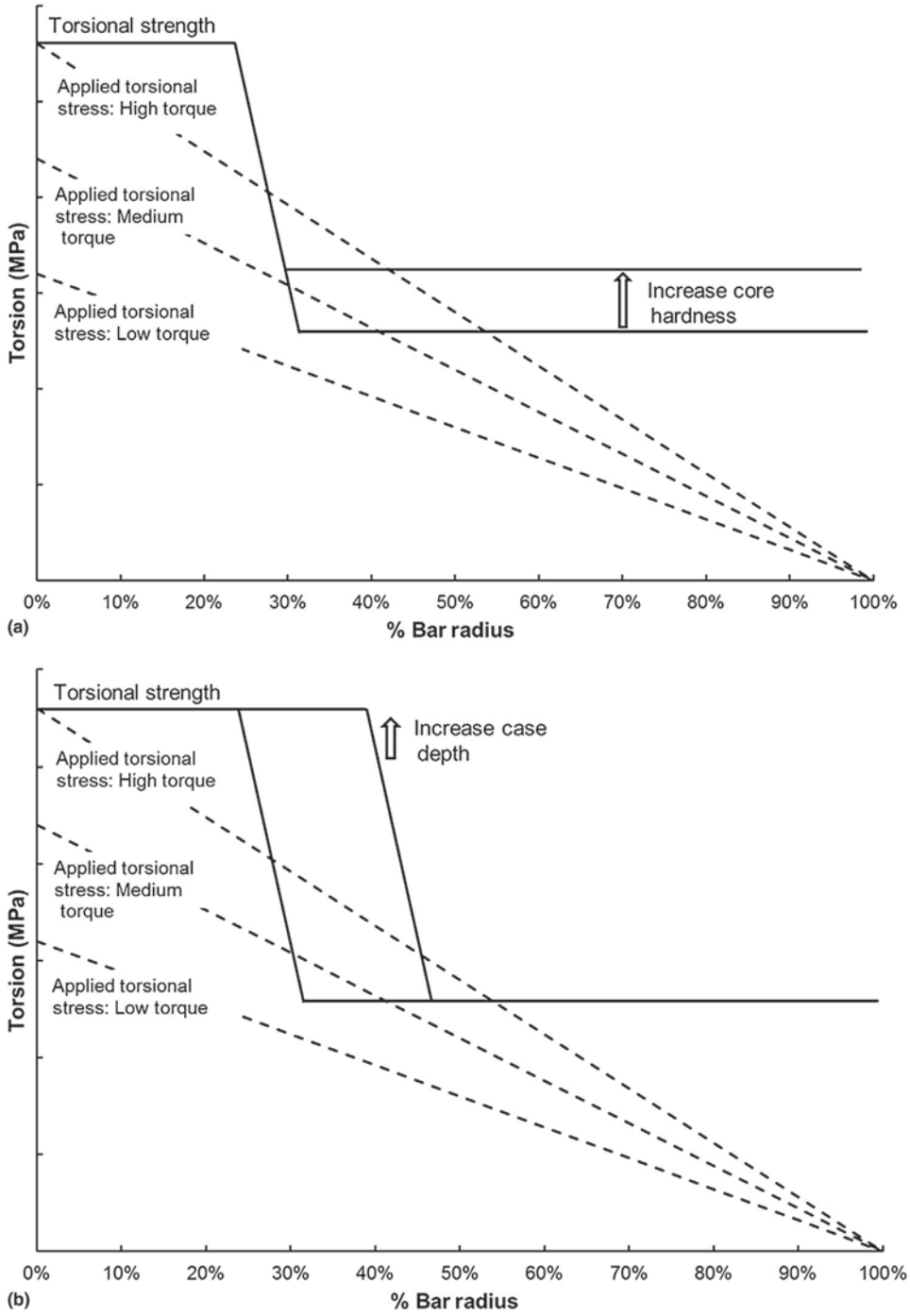

Figure 24 (a) Schematic showing applied torsional stress and torsional strength for a surface-hardened bar with two different core hardness levels. (b) Schematic showing applied torsional stress and torsional strength for a surface-hardened bar with two different case depths.

fatigue strengths; a general conversion from Vickers hardness to reversed torsional fatigue strength is 1.13*HV (*33*). The torsional stresses associated with three levels of applied torque are plotted on the figures. In **Figure 24(a)**, the torsional strength is plotted for two levels of core hardness. In the low-torque condition, the applied torsional stress does not exceed the torsional strength at any bar depth. In the medium-torque condition, the applied torsional stress is less than the torsional strength in the case but exceeds the torsional strength at the case–core interface for the lower core hardness condition. However, if the core hardness is increased, the applied stress does not exceed the material strength at any depth in the medium-torque condition. In the high-torque condition, the applied stress exceeds the torsional strength at the surface of the bar and near the case–core interface. Thus, the load-carrying capacity of a component is limited by the torsional strength at the surface. Similarly, **Figure 24(b)** shows the effects of increasing case depth for the lower core hardness condition. If the case depth is increased, the applied stress does not exceed the torsional strength at any depth in the medium-torque condition. In the high-torque condition, the torsional strength is exceeded at the bar

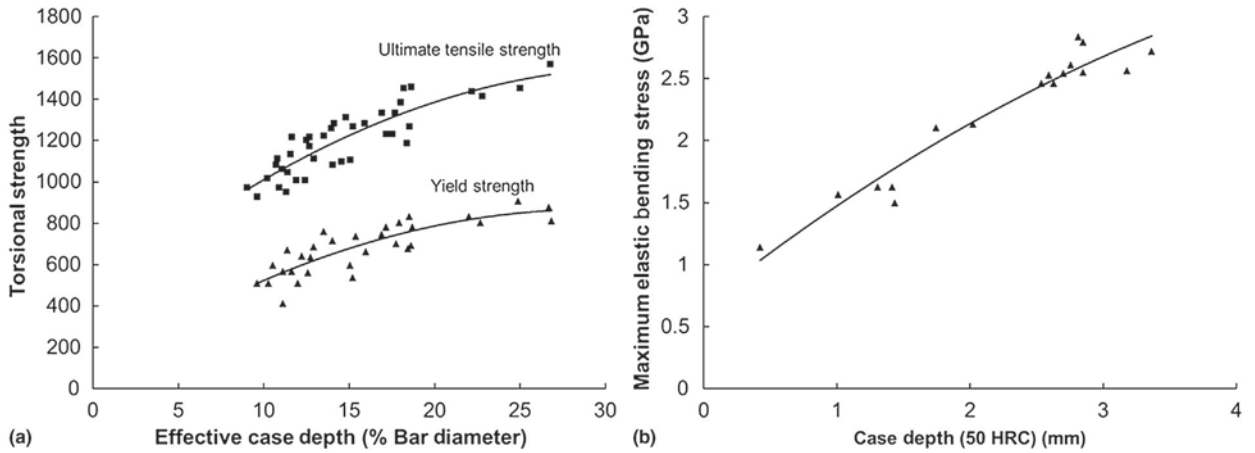

Figure 25 (a) Torsional yield and tensile strength as a function of effective case depth (depth to 40 HRC) in a variety of medium-carbon steels (reproduced from the Fett, G. A. Importance of Induction Hardened Case Depth in Torsional Applications. In *Heat Treat. Prog.* **2009**, *9*, 15–19). (b) Maximum elastic bending stress as a function of case depth (depth to 50 HRC) in 1541 and 4140 steel with a bar diameter of 12.7 mm.

surface for both case depths, which again shows there is an upper limit for increasing load capacity that is defined by the torsional strength at the surface.

The above arguments are supported by experimental data presented in **Figures 25(a) and 25(b)**. **Figure 25(a)** shows torsional strength versus effective case depth (depth to 40 HRC) in a variety of steels with carbon contents approximately between 0.4 and 0.5 wt. pct (*34*). Both yield and ultimate strength increase as case depth increases, but an upper limit is reached at an approximate case depth of 25% of the bar diameter. Scatter in the data is due to different core hardness levels and total case depths (depth to 20 HRC). Similarly, **Figure 25(b)** shows that the maximum elastic bending stress increases with increasing case depth (depth to 50 HRC) in induction-hardened 1541 and 4140 steel (*18*).

Another objective of induction hardening is to increase the fatigue resistance of components. As described previously, compressive residual stresses arise in the case, which are beneficial for fatigue resistance. The hard martensitic case increases fatigue resistance at the surface due to the increase in local strength level. Often, the core microstructure is more susceptible to fatigue damage than the case. However, in components subjected to bending or torsion loads, higher loads are necessary to cause fatigue damage in the core region than if the same microstructure was present at the surface in a noninduction-hardened component. This latter point is illustrated in **Figure 26**. **Figure 26(a)** is a plot of fatigue data from 1040, 1541, and 4140 induction-hardened steel shafts subjected to a stress amplitude of 407 MPa in torsional fatigue (*34*). The figure shows that the fatigue life increases as effective case depth, defined as the depth to 40 HRC, as a percentage of the shaft diameter increases. Similarly, **Figure 26(b)** is a plot of bending stress amplitude versus number of cycles to failure in induction-hardened calcium-treated 4140 steel (*35*). Three different case depths were assessed: 22, 29, and 39% of the bar diameter. The endurance limit increases as case depth increases.

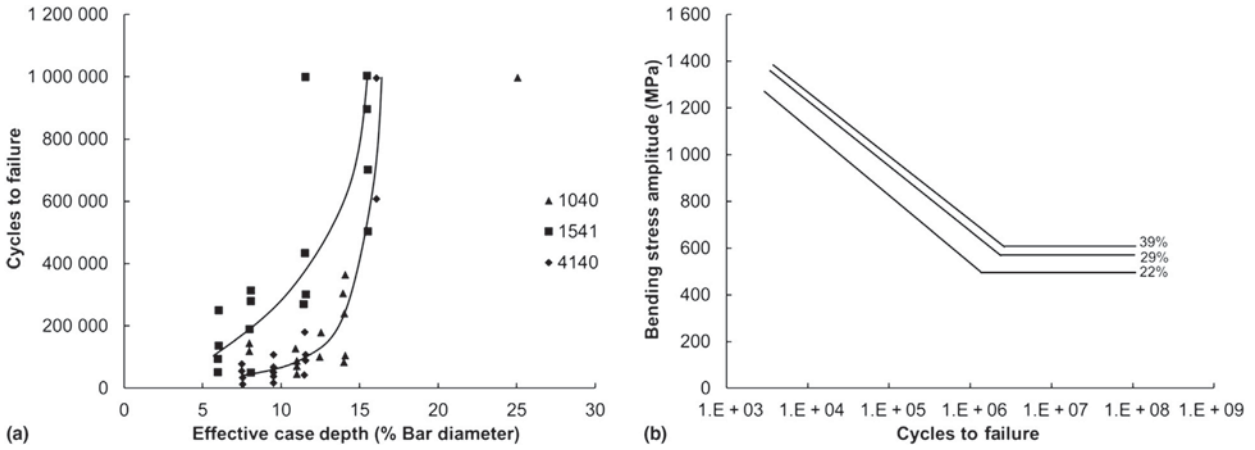

Figure 26 (a) Cycles to failure versus effective case depth as a percentage of shaft diameter for 1040, 1541, and 4140 steel shafts subjected to a stress amplitude of 407 MPa in torsion (reproduced from Fett, G. A. Importance of Induction Hardened Case Depth in Torsional Applications. In *Heat Treat. Prog.* **2009**, *9*, 15–19.). (b) Bending stress amplitude versus cycles to failure for calcium-treated 4140 steel induction hardened to 22, 29, and 39% of the bar (reproduced from the Hayne M. L. The Effect of Ferrite and Pearlite Banding on the Rotating Bending Fatigue Behavior of Induction Hardened 4040Ca4 Bar Steel. M.S. Thesis, Colorado School of Mines, Golden, CO, USA, 2010).

12.16.5.1 Estimation of Fatigue Crack Nucleation Location

Components are typically designed to operate in the low-cycle fatigue regime where the majority of the fatigue life is spent initiating a fatigue crack. Thus, it is important to determine the regions of a component that are susceptible to fatigue crack nucleation, which is dependent on the case depth. A useful tool to determine the optimal case depth is the Woodvine diagram (*36*). These diagrams were first used to determine ideal carburizing depths but can also be applied to induction-hardened components (*37*). They can determine the most likely locations for fatigue crack nucleation in a part, and both bending and axial loads can be analyzed. The location of maximum stress, whether on a smooth specimen or at a stress concentration, should be analyzed.

Similar to **Figures 24(a) and 24(b)**, the Woodvine diagram contains the applied stress from the surface of the part to the center; the applied stress is constant for a uniaxial loading condition but varies linearly from the surface to the center for torsional or bending loads. If available, the residual stress as a function of depth should be added to the applied stress to obtain an effective applied stress (residual plus applied stress). The local fatigue strength as a function of depth is superimposed on the same plot. The local fatigue strength can be estimated using data from a microhardness traverse and a relationship such as the following:

$$\text{Fatigue strength (MPa)} = 1.3695\ (\text{HV}) + 48.265 \qquad [6]$$

where HV is Vickers hardness (*33*). Equation [6] is plotted along with the 95% confidence interval in **Figure 27** for a variety of low- and high-alloy steels ranging from 0.25 to 0.55 wt pct. C.

The locations of the part susceptible to fatigue damage are predicted by the regions on the Woodvine diagram where the effective applied stress is greater than the estimated fatigue strength (**Figure 28**). A 'safe' operating load for a given case depth or ideal case depth for a given load can be determined for a case-hardened component. The analysis should consider that the fatigue strengths are only estimated values.

There are four possible outcomes from the Woodvine diagram. The first outcome (**Figure 28(a)**) is that there are no regions susceptible to fatigue crack nucleation. The second outcome (**Figure 28(b)**) is the surface of the part is susceptible to fatigue crack nucleation. In this scenario, either a lower load or a higher carbon content (which will result in greater case hardness) should be employed to increase fatigue resistance of the case. The third outcome is that both the surface and the core are susceptible to fatigue crack nucleation (**Figure 28(c)**). In this scenario, both higher carbon content and a deeper case depth should be considered if the applied load cannot be reduced. The final outcome is that the core is susceptible to fatigue crack nucleation (**Figure 28(d)**). To improve fatigue resistance for this last scenario, either a deeper case depth or higher core hardness should be considered. The latter three outcomes are for applied stresses greater than the endurance limit.

Woodvine diagrams for fatigue specimens from 1045 steel, quenched and tempered before induction hardening, and 4145 steel, as-hot rolled before induction hardening, are shown in **Figures 29 and 30**; the fatigue samples were tested in fully reversed cantilever bending fatigue. The depths where fatigue crack nucleation was experimentally observed are also plotted on the figures. The applied stress profiles on the diagrams correspond to the stress amplitude at the experimentally determined endurance limit. The Woodvine diagrams correspond to the scenario presented in **Figure 28(d)**. In both the diagrams, the applied stress plus residual stress at the surface of the part is zero or slightly compressive. All of the fatigue cracks nucleated in the subsurface of the fatigue

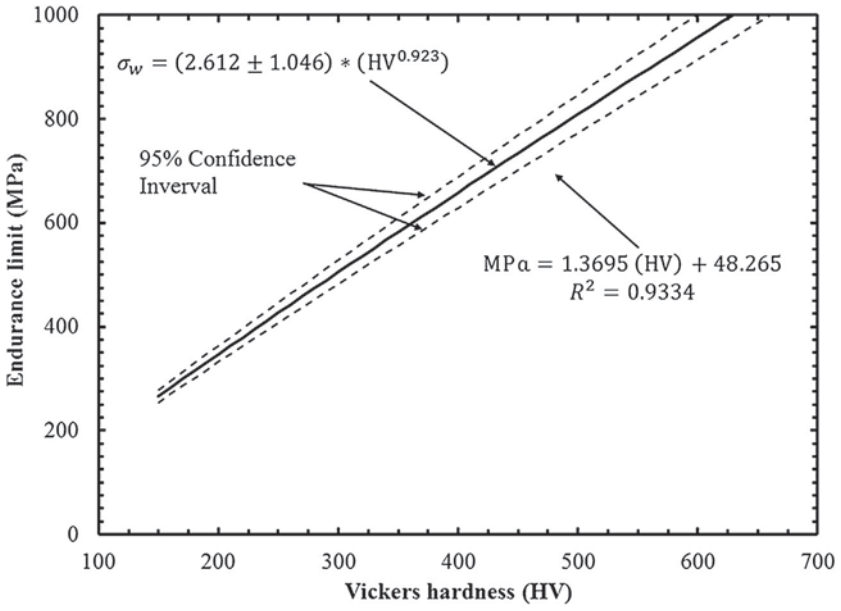

Figure 27 Relation between endurance limit and Vickers hardness for a variety of steel alloys (different alloying content and carbon content) (reproduced from the Nishijima, S. Basic Fatigue Properties of JIS Steels for Machine Structural Use; NRIM Special Report (Technical Report) No. 93–02, 2-3-12 Nakemeguro, Meguroku, Tokyo, Japan, 1993).

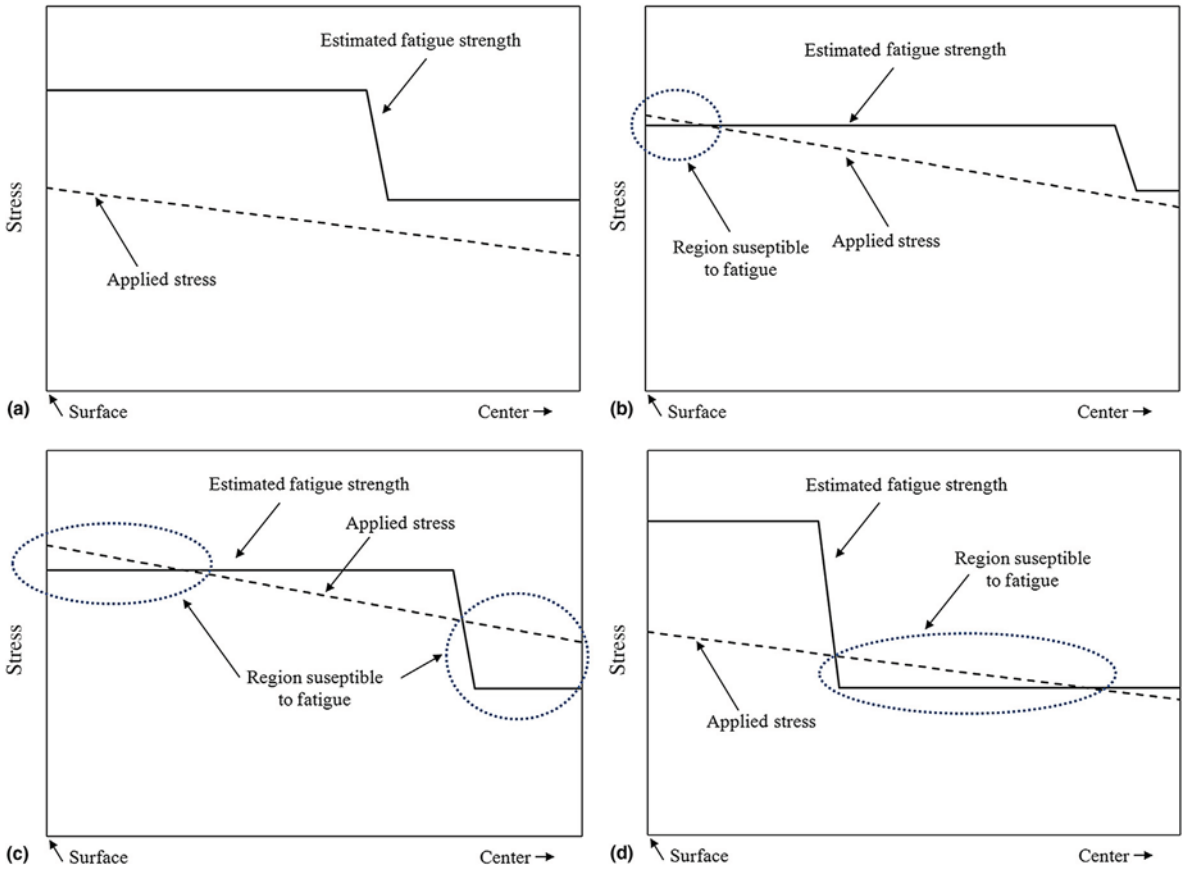

Figure 28 Locations are susceptible to fatigue failure when the estimated fatigue strength is less than the effective stress. Based on the diagram and any stress concentrators in the part either (a) no area is susceptible, (b) the surface of the part is susceptible, (c) the surface and the core are susceptible, or (d) the core is susceptible to fatigue crack nucleation.

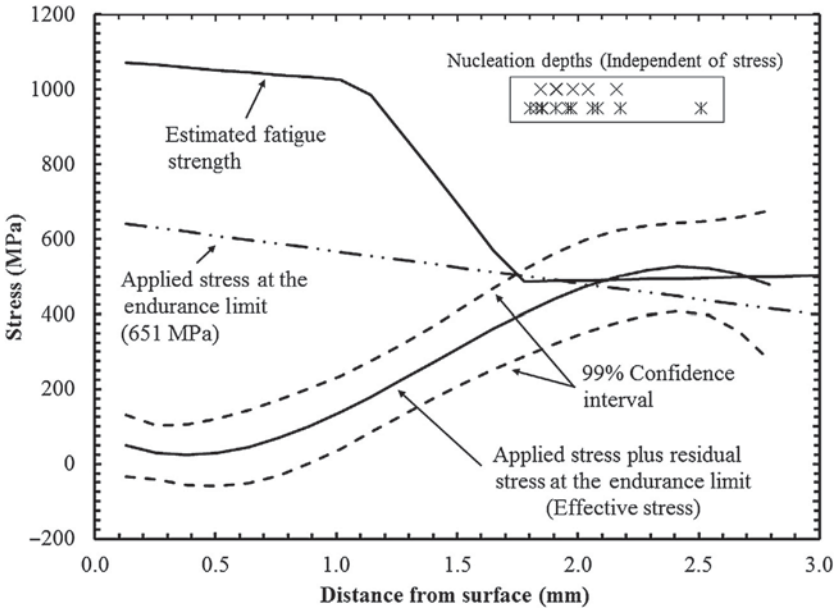

Figure 29 Woodvine diagram for the 1045 quenched and tempered induction-hardened condition, with the applied stress plotted at the endurance limit. Fatigue crack nucleation depths, independent of stress, are shown for all fractured samples and are separated into microstructural feature (X) and inclusion (⁎) nucleated fatigue cracks (reproduced from the Nissan A. B. The Effect of Microstructure and Induction Processing on Fatigue Performance and Crack Initiation of Induction Hardened Bar Steel. Ph.D. Dissertation, Colorado School of Mines, Golden, CO, USA, 2012).

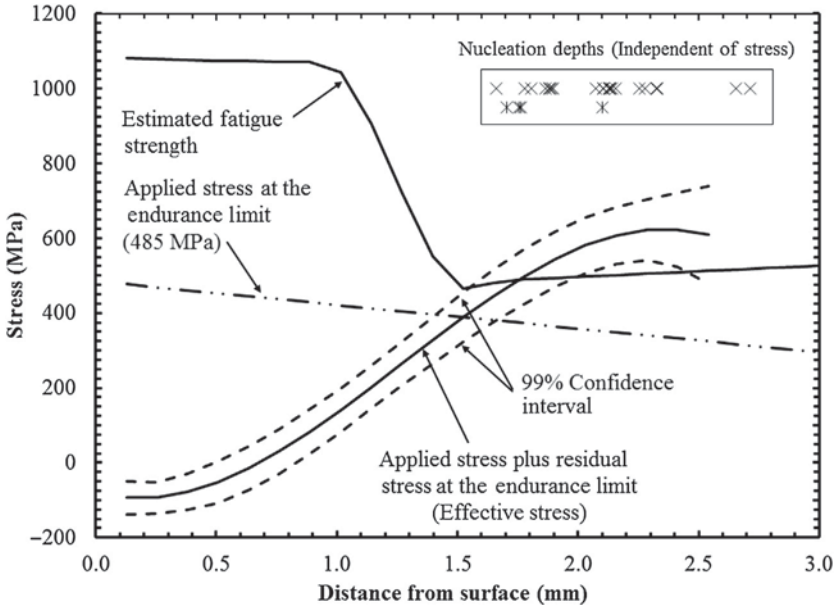

Figure 30 Woodvine diagram for the 4145 as-hot rolled induction-hardened condition with the applied stress plotted at the endurance limit. Fatigue crack nucleation depths, independent of stress, are shown for all fractured samples and are separated into microstructural feature (X) and inclusion (⁎) nucleated fatigue cracks (reproduce from the Nissan A. B. The Effect of Microstructure and Induction Processing on Fatigue Performance and Crack Initiation of Induction Hardened Bar Steel. Ph.D. Dissertation, Colorado School of Mines, Golden, CO, USA, 2012).

specimens, which is due to the low effective applied stress at the surface. Even if the residual stress profile is not considered, the applied stress at the endurance limit does not exceed the estimated fatigue strength at any point from the case to the core. There is excellent correlation between the measured depths of fatigue crack nucleation and the regions predicted to be susceptible to fatigue crack nucleation from the Woodvine diagrams. It should also be noted that even at the endurance limit, the effective applied stress in the core exceeds the estimated fatigue strength of the material in both the 1045 quenched and tempered and 4145 as-hot rolled conditions. However, fatigue cracks may not propagate if the stress in the core is not great enough to exceed the threshold stress intensity (ΔK_t) required to propagate a nucleated fatigue crack. However, at just 5 MPa above the endurance limit, finite fatigue lives were observed in these alloys, which indicates that the ΔKth required to propagate a fatigue crack was exceeded.

12.16.5.2 Fatigue Fracture Surface Location and Morphology

Fatigue crack nucleation location can vary depending on the applied stress, type of loading, local hardness of the part, case depth, and resulting residual stress profile after induction hardening. The Woodvine diagram described in the previous section is useful for determining the regions of a fatigue part susceptible to fatigue crack nucleation, but many other metallurgical factors can affect fatigue life. For example, the inclusion population in the steel, the service conditions, the hydrogen content of the steel, incorrect processing parameters (during induction hardening, tempering, or both), and surface damage on the part can adversely affect fatigue life.

Figure 31 shows fracture surfaces from induction-hardened bending fatigue specimens; **Figure 31(a)** shows a 1060 steel fracture surface, while **Figure 31(b)** shows a 1045 steel fracture surface. Both fracture surfaces exhibit subsurface crack nucleation with some characteristic fracture features. The region of crack initiation and fatigue crack growth is the flat, oval-shaped region at the case–core interface (arrows in **Figures 31(a) and 31(b)**. A higher magnification image of the subsurface crack initiation region is shown in **Figure 31(c)**. Radial marks point back to the crack initiation location. Some have attributed the flat fracture in the vicinity of crack nucleation to hydrogen embrittlement. Once the fatigue crack reaches a critical length, likely correlating to where the fracture toughness of the material is exceeded, overload fracture occurs. The overload fracture morphology is distinct between the case and core microstructures. In the brittle case microstructure, both intergranular and quasi-cleavage may be present (*30,38*), resulting in a flat macroscopic appearance. However, a very small shear lip region may be observed at the edge of the case region in **Figure 31(c)**. In the core, cleavage or microvoid coalescence may be observed depending on the core microstructure (*30,38*). The failure is more ductile in the core and has a much rougher macroscopic appearance. Surface nucleated failures are also possible in bending fatigue (*39*), but compressive residual stresses at the surface and the comparatively weak core microstructure make subsurface crack nucleation more likely.

Torsional fatigue fractures of induction-hardened components also exhibit distinct overload regions in the case and core microstructures. However, fatigue crack initiation appears different because of the different loading condition, and surface nucleated failures occur more readily. **Figure 32** shows a schematic of a shaft subjected to torsion loading and two stress elements within the

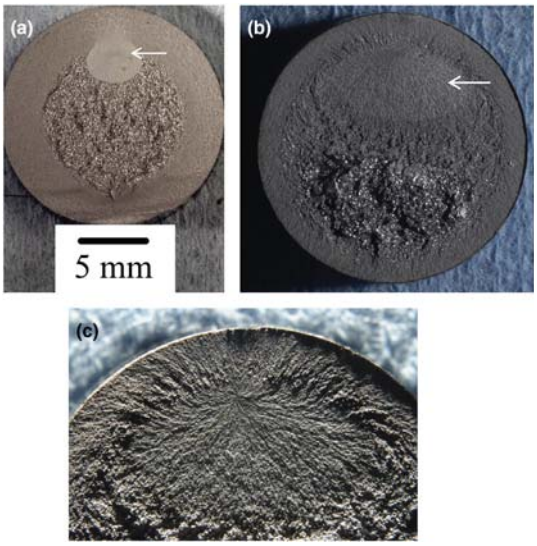

Figure 31 Fracture surfaces of (a) a 1060 induction-hardened bar with a normalized core, (b) a 1045 induction-hardened bar with a quenched and tempered core, and (c) higher magnification image of the same 1045 bar showing the crack initiation location. (Image courtesy of D.K. Matlock).

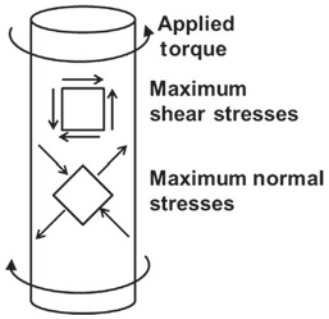

Figure 32 Schematic of a shaft subjected to a torsional load with stress elements showing the orientation of the maximum shear and normal stresses.

shaft showing the orientations with the maximum shear and normal stresses. The maximum shear stress is transverse and longitudinal with respect to the axis of the shaft, while the maximum normal stress is oriented 45° to the axis of the shaft. Cracks nucleate either on the plane of maximum shear or maximum normal stresses. At high stress or strain amplitudes where there is significant plasticity, cracks nucleate on the plane of maximum shear stress and strain. At lower stress or strain amplitudes, cracks nucleate on the plane of maximum normal stress. **Figure 33** schematically shows observed crack nucleation mechanisms in the low-, intermediate-, and high-cycle regions of a strain life plot and actual fatigue cracks in induction-hardened shafts tested at high and low shear strain amplitudes (*40*). The schematic shows that as the applied shear strain amplitude decreases, the crack orientation changes from predominately longitudinal (plane of maximum shear stress) to 45° (plane of maximum normal stress) from the specimen axis.

As presented previously, components are designed to operate in the high-cycle fatigue regime, where crack initiation is the majority of the fatigue life. Crack initiation in induction-hardened components can occur due to plastic damage in the microstructure or around inclusions, which act as small-stress concentration regions within an alloy. **Figure 34(a)** shows a scanning electron microscope (SEM) image of crack nucleation due to plastic damage in the ferrite-pearlite core microstructure of a 1045 induction-hardened steel bar subjected to bending fatigue. **Figure 34(b)** shows an SEM image of crack nucleation due to a nonmetallic inclusion in the tempered martensite core microstructure of another 1045 induction-hardened bar subjected to bending fatigue. In softer core microstructures, such as ferrite–pearlite microstructures, fatigue crack nucleation due to plastic damage in ferrite grains is more frequent. In harder core microstructures, such as quenched and tempered martensite, the regions around inclusions are the weak links of the microstructure. Nonmetallic inclusions are present in all steels. Some examples of common nonmetallic inclusions are MnS, CaS, Al_2O_3, and MgO. There are many other nonmetallic inclusions present in steel, and inclusions can be composite in nature comprising one or more compound. Current steel-melting practices can produce a high-quality low-inclusion content steel, but inclusions cannot be completely removed from steel.

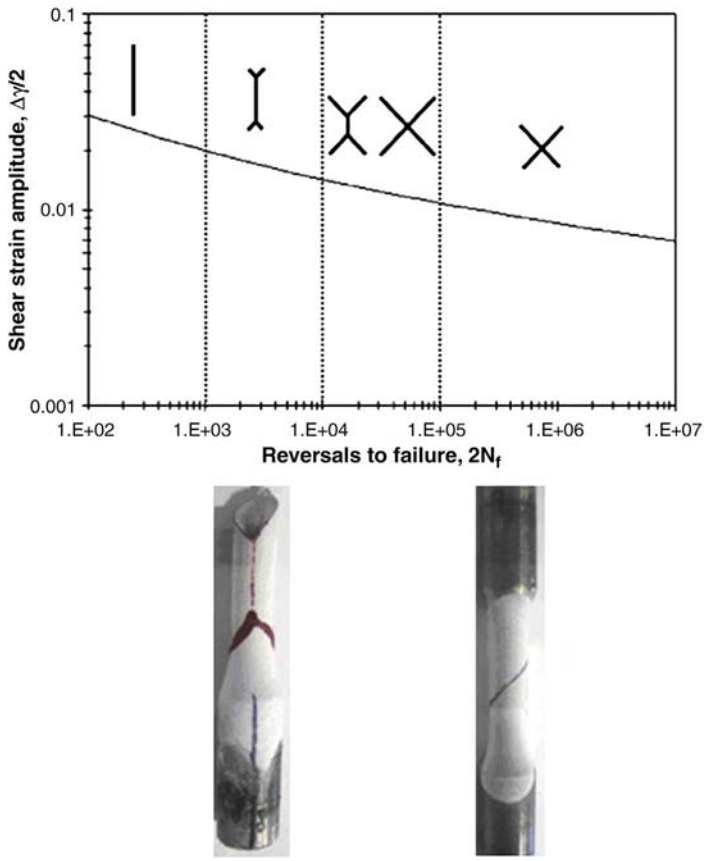

Figure 33 Schematic showing observed fatigue crack orientations in 1050 induction-hardened steel shafts at low-, intermediate-, and high-shear strain amplitudes. Two examples of fatigue cracking are shown below the schematic. Data replotted from the Cryderman, R.; Shamsaei, N.; Fatemi, A. Effects of Continuous Cast Section Size on Torsion Deformation and Fatigue of Induction Hardened 1050 Steel Shafts. *J. Mater. Process. Technol.* **2011**, *211*, 66–77.

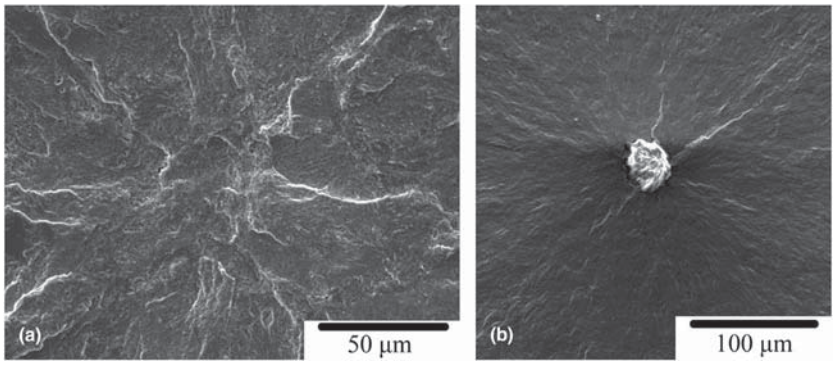

Figure 34 Examples of fatigue crack nucleation at the case–core interface in induction-hardened bars subjected to bending fatigue (a) microstructural features in a ferrite/pearlite 1045 induction-hardened steel where plastic damage likely contributed to crack nucleation and (b) an inclusion at the crack nucleation location in a 1045 quenched and tempered steel (reproduced from the Nissan A. B. The Effect of Microstructure and Induction Processing on Fatigue Performance and Crack Initiation of Induction Hardened Bar Steel. Ph.D. Dissertation, Colorado School of Mines, Golden, CO, USA, 2012).

12.16.6 Industrial Standards Relevant to Induction Hardening

- International Standard (ISO) 3754 "Steel – Determination of Effective Depth of Hardening after flame or induction hardening"
- Japanese Industrial Standard (JIS) B 6912:2002 "Process of Induction Hardening and Tempering of Iron and Steel"
- Japanese Industrial Standard (JIS) G 0559:2008 "Steel – Determination of Case Depth after Flame Hardening or Induction Hardening"
- Society of Automotive Engineers (SAE) ARP4715 "Induction Hardening of Steel Components"
- ASTM Standard A255-10, "Standard Test Methods for Determining Hardenability of Steel"
- ASTM Standard E384-11, "Standard Test Methods for Knoop and Vickers Hardness of Materials"

12.16.7 Summary and Conclusions

Induction processing is an effective method to produce case-hardened components in low- and medium- carbon steels with various microstructures. The induction processing parameters can be carefully tuned to achieve desired case depths. The induction-hardening process and alloy selection have interrelated effects on the resulting mechanical behavior, and the important parameters to consider are case depth, residual stress distribution, case and core microstructure hardness, and other microstructural features such as inclusions.

There are many opportunities for further research and development in induction-hardened steels. The development of the induction-hardened case microstructure as a function of induction process parameters and alloy should be characterized, especially with more widely available high-resolution characterization equipment such as advanced transmission electron microscopes and atom probe tomography. The role of microalloying in microstructural development and its effects on mechanical performance should also be assessed. For example, micoralloying may increase the fatigue resistance of the core microstructure and thus improve mechanical performance. Several of the fatigue research studies conducted have utilized bending fatigue tests, and crack nucleation often occurs at the case–core interface; thus, fatigue performance is controlled by the core microstructure. In contrast, torsional loads are applied to many induction-hardened part applications, and fatigue crack nucleation occurs at the surface of the part; then, the case microstructure plays a larger role. As discussed in this chapter, torsional fatigue studies have been performed, but further work is necessary to assess the effects of microstructure in the case and core on torsional fatigue performance.

Acknowledgments

The authors are grateful for the support, in writing this chapter, of the Advanced Steel Products and Processing Research Center, an industry–university collaborative research center at the Colorado School of Mines.

References

1. Curtis, F. W. *High Frequency Induction Heating;* Lindsay Publications Inc: Bradley, IL, USA, 1987.
2. Haimbaugh, R. E. *Practical Induction Heat Treating;* ASM International: Materials Park, OH, USA, 2001.
3. Zinn, S.; Semiatin, S. L. *Elements of Induction Heating: Design, Control, and Applications;* ASM International: Metals Park, OH, USA, 1988.
4. Gürm, C. H.; Pan, J. *Thermal Process Modeling of Steels;* CRC Press: New York, NY, USA, 2009.
5. Fiorillo, F. *Measurement and Characterization of Magnetic Materials;* Elsevier: Amsterdam, The Netherlands, 2004.
6. Semiatin, S. L.; Stutz, D. E. *Induction Heat Treatment of Steel;* American Society for Metals: Metals Park, OH, 1986.
7. Rudnev, V.; Loveless, D.; Cook, R.; Black, M. *Handbook of Induction Heating;* Marcel Dekker, Inc: New York, NY, USA, 2003.
8. ASTM Standard A255-10. *Standard Test Methods for Determining Hardenability of Steel;* ASTM International: West Conshohocken, PA, USA.
9. Callister, W. D. J. *Material Science and Engineering: An Introduction,* 5th ed.; John Wiley & Sons, Inc.: New York, NY, USA, 2000.
10. Thelning, K. E. *Steel and Its Heat Treating, Bofors Handbook;* Butterworth: London, UK, 1975.
11. Cunningham, J. L.; Medlin, D. J.; Krauss, G. Effects of Induction Hardening and Prior Cold Work on a Microalloyed Medium Carbon Steel. *J. Mater. Eng. Perform.* **1999,** *8,* 401–408.
12. Yaguchi, H.; Tsuchida, T.; Matsushima, Y.; Abe, S.; Iwasaki, K.; Inada, A. *Effect of Microstructures on the Fatigue Behavior of V-Added Ferrite-Pearlite Type Microalloyed Steels;* Kobelco Technology Review No. 25, 2002, pp 49–53.
13. Kalpakjian, S.; Schmid, S. R. *Manufacturing Engineering and Technology;* Prentice Hall: Upper Saddle River, NJ, 2001.
14. Abbaschian, R.; Abbaschian, L.; Reed-Hill, R. R. *Physical Metallurgy Principles,* 4th ed.; Cengage Learning: Stamford, CT, 2009.
15. Krauss, G. *Steels: Processing, Structure and Performance;* ASM International: Materials Park, OH, USA, 2005.
16. SAE Standard AMS2745. *Induction Hardening of Steel Parts;* Society of Automotive Engineers: Warrendale, PA, USA, 2001.
17. Speich, G. R.; Szirmae, A.; Richards, M. J. Formation of Austenite from Ferrite and Ferrite-Carbide Aggregates. *Trans. Metall. Soc. AIME* **1969,** *245,* 1063–1074.
18. Coryell J. J. The Effect of Induction Hardening on the Mechanical Properties of Steel with Controlled Prior Microstructure. M.S. Thesis, Colorado School of Mines, Golden, CO, USA, 2004.
19. Orlich, J.; Rose, A.; Wiest, P. *Atlas zue Wärmebehandlung der Stähle – Band 3, Zeit-Temperatur-Austenitisierung-Schaubilder;* Verlag Stahliesen, M.B.G: Düsseldorf, Germany, 1973.
20. Hassell, P. A.; Ross, N. V. *Induction Heat Treating of Steel.* In *Heat Treating;* ASM Handbook, 1991; Vol. 4.
21. Totten, G., Howes, M., Inoue, T., Eds. *Handbook of Residual Stress and Deformation of Steel;* ASM International: Materials Park, OH, USA, 2002.
22. Totten, G., Ed. *Steel Heat Treatment Handbook;* Marcel Dekker, Inc.: New York, New York, USA, 1997.
23. Society of Automotive Engineers (Etats-Unis). *Residual Stress Measurement by X-ray Diffraction: 2003 ed.* SAE International: Warrendale, PA, USA, 2003.
24. Tjernberg, A. Comparison of Methods for Determining Residual Stresses in Induction-Hardened Transmission Shafts. *Scand. J. Metall.* **1999,** *28,* 162–168.
25. *The Contour Method for Measuring Residual Stress*, [Online]; Los Alamos National Lab, January 2009. Available: http://www.lanl.gov/contour/.
26. *The Slitting (Crack Compliance) Method for Measuring Residual Stress*, [Online]; Los Alamos National Lab: January 2009. Available: http://www.lanl.gov/residual/.
27. Torres, MA. S.; Voorwald, H. J. C. An Evaluation of Shot Peening, Residual Stress and Stress Relaxation on the Fatigue Life of AISI 4340 Steel. *Int. J. Fatigue* **2002,** *24,* 877–886.
28. Zhuang, W. Z.; Halford, G. R. Investigation of Residual Stress Relaxation under Cyclic Load. *Int. J. Fatigue* **2001,** *23,* 31–37.
29. Yonetani, S.; Isoda, S. Effect of Residual Stress on Fatigue Strength of Induction Hardened Specimens of a Medium Carbon Steel. *Tetsu-to-Hagane. J. Iron Steel Inst. Jpn.* **1989,** *75,* 1362–1369.
30. Nissan A. B. The Effect of Microstructure and Induction Processing on Fatigue Performance and Crack Initiation of Induction Hardened Bar Steel. Ph.D. Dissertation, Colorado School of Mines, Golden, CO, USA, 2012.
31. ASTM Standard E384-11. *Standard Test Methods for Knoop and Vickers Hardness of Materials;* ASTM International: West Conshohocken, PA, USA, 2010.
32. JIS Standard G0559. *Steel – Determination of Case Depth After Flame Hardening or Induction Hardening;* Japanese Industrial Standards Committee: Akasaka, Minato-ku, Tokyo, Japan, 2008.

33. Nishijima, S. *Basic Fatigue Properties of JIS Steels for Machine Structural Use;* NRIM Special Report (Technical Report) No. 93–02, 2-3-12 Nakemeguro, Meguroku, Tokyo, Japan, 1993.
34. Fett, G. A. Importance of Induction Hardened Case Depth in Torsional Applications. *Heat Treat. Prog.* **2009,** *9* (6), 15–19.
35. Hayne M. L. The Effect of Ferrite and Pearlite Banding on the Rotating Bending Fatigue Behavior of Induction Hardened 4040Ca4 Bar Steel. M.S. Thesis, Colorado School of Mines, Golden, CO, USA, 2010.
36. Woodvine, J. G. R. *The Behaviour of Case-Hardened Parts under Fatigue Stresses;* Iron and Steel Institute, 1924. Carnegie Scholarship Memoirs.
37. Braisch, P. K. The Influence of Tempering and Surface Conditions on the Fatigue Behaviour of Surface Induction Hardened Parts. *Mater. Sci. Forum* **1992,** *102–104,* 319–334.
38. Santos, C. G.; Laird, C. Fractography of Induction-Hardened Steel Fractured in Fatigue and Overload. *Materials Characterization* **1997,** *39,* 25–41.
39. Clarke, C. K.; Halimunanda, D. Failure Analysis of Induction Hardened Automotive Axles. *J. Fail. Anal. Prev.* **2008,** *8,* 386–396.
40. Cryderman, R.; Shamsaei, N.; Fatemi, A. Effects of Continuous Cast Section Size on Torsion Deformation and Fatigue of Induction Hardened 1050 Steel Shafts. *J. Mater. Process. Technol.* **2011,** *211,* 66–77.